CHEMICAL ENGINEERING RESEARCH

Reports of the 4th year research projects in the Department of Chemical Engineering at Imperial College London

VOLUME 3

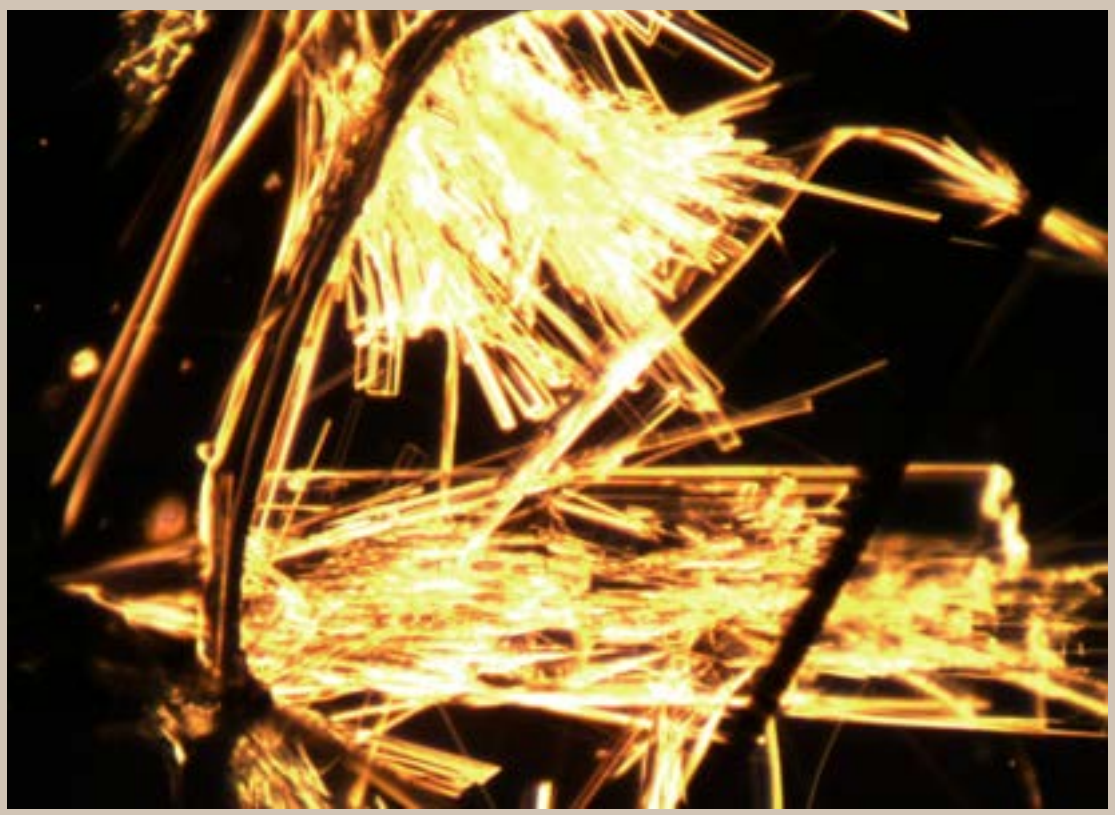

Edited by Erich A. Müller

February, 2021

CHEMICAL ENGINEERING RESEARCH

Reports of the 4th year research projects
in the Department of Chemical Engineering
at Imperial College London

Edited by Erich A. Müller

Volume 3

2021

© The Author(s) 2021.
Published by Imperial College London, London SW7 2AZ, UK
Contact details – e.muller@imperial.ac.uk

This book is a compilation of manuscripts created as part of a teaching assignment on the 4th year's Chemical Engineering CENG97005 course (Advanced Chemical Engineering Practice Research Project) . Copyright in each paper rests with its authors. The author of each paper appearing in this book is solely responsible for the content thereof; the inclusion of a paper in the book shall not constitute or be deemed to constitute any representation by Imperial College London that the data presented therein are correct or sufficient to support the conclusions reached or that the experiment design or methodology is adequate.

The book is licensed under a Creative Commons Attribution-NonCommercial-NoDerivs 3.0 Unported (CC BY-NC-ND 3.0). Under this licence, you may copy and redistribute the material in any medium or format on the condition that: you credit the author, do not use it for commercial purposes and do not distribute modified versions of the work. When reusing or sharing this work, ensure you make the licence terms clear to others by naming the licence and linking to the licence text. Please seek permission from the copyright holder for uses of this work that are not included in this licence or permitted under UK Copyright Law. https://creativecommons.org/licenses/by-nc-nd/3.0/.

The information contained in this publication is being distributed without warranty of any kind, either expressed or implied. The responsibility for the interpretation and use of the material lies with the reader. In no event shall Imperial College London be liable for damages arising from its use.

E-ISBN 978-1-9160050-2-0

First published in 2021

Preface

This volume of *Chemical Engineering Research* collects the unedited research project reports written by 4th year undergraduates (Class of 2021) of the M.Eng. course on Chemical Engineering in the Department of Chemical Engineering at Imperial College London. The research project spans for one term (Autumn) during the last year of the career and has an emphasis on independence, ability to plan and pursue original project work for an extended period, to produce a high quality report, and to present the work to an audience using appropriate visual aids. Students are also expected to produce a literature survey and to place their work in the context of prior art. The papers presented showcase the diversity and depth of some of the research streams in the department, but obviously only touch on a small number of research groups and interests. For a full description of the research at the department, the reader is referred to the departmental website[1].

The papers presented are in no particular order and they are identified by a manuscript number. Some papers refer to appendixes and/or supplementary information which are too lengthy to include. These files are available directly from the supervisors (see supervisor index at the end of the book). Some of the reports are missing, being embargoed as they contain confidential information. A few reports correspond to industrial internships, called LINK projects, performed in collaboration with Shell.

2020 was a particularly challenging year, as many experimental facilities were either temporarily closed down and/or had restricted access. This is reflected in a larger fraction of the research projects being theoretical or computational in nature.

Cover figure corresponds to an optical microscopy of crystallization of Sodium Dodecyl Sulfate needles (taken from the work of Alessia Borys, manuscript 40).

London, February 2021

[1] https://www.imperial.ac.uk/chemical-engineering

Title Index

paper	Title	page
1	Design and Optimisation of a Continuous Bioreactor for the Production and Filtration of RNA	1
2	Smart Enumeration Strategies for Candidate Enumeration Approach to Optimal Experiment Design	11
3	The Impact of Supply Chain Modelling Decisions and Policies on the Effectiveness of England's COVID-19 Supply Chain	21
4	Potential Applications of Variously Structured Semi-transparent PV Cells in an Evacuated Solar-thermal System	31
5	Investigating factors affecting student engagement with gamified learning apps	41
6	Developing a Dynamic Carbon Benchmarking Method for Building Portfolio Comparison	51
7	Process Design and Life Cycle Analysis for Methanol and Ethanol Electrooxidaton	61
8	Acoustic Levitation to Study Polymer Particle Drying for Applications in Spray Drying	71
9	Proof of Concept of Uncertainty Analysis and Sensitivity Analysis on Distributed Energy System Investment Models	80
10	Computational Modelling and Experimental Characterisation of the Fabrication of Tuneable Photonic Crystal pH Sensors	90
11	Pore Network Modelling of Diffusion in Rocks	100
12	Optimizing COVID-19 vaccine supply chain network in England: A ChAdOx1 and BNT162b2 case study	110
13	Automatic Tuning of Adaptive PID Controllers using an Artificial Neural Network	120

paper	Title	page
14	Wrong Way Behaviour of Packed Bed Reactors: Influence of Variable Velocity for a Gas-to-Liquid Reactor	130
15	Optimisation of Monoclonal Antibody Purification Process via Data-Driven and Hybrid Modelling	140
16	A Scenario-based Analysis of Vaccine Stockpiling Uncertainty during COVID-19 pandemic	150
17	Heat Integration for Cement Production with Reduced Carbon Impact using Direct Separation Reactors	160
18	Application of the SAFT-γ Mie Equation of State in Modelling of Asphaltene Precipitation	(*)
19	Evaluating an Isoprene Producing Co-culture Model of *M. trichosporium* OB_3b and *P. pastoris* using Dynamic Flux Balance Analysis	170
20	Nonsolvent-induced phase separation and breath figure arrays on a model polymer	180
21	Enhancing the Stability of Bismuth Vanadate Photoanodes with Bismuthene and Nickel Iron Oxy-Hydroxide Layers	(*)
22	Design of Novel RNA Thermometers for the Cold Shock Response in Bacterial Cells	190
23	Synthesis and Optimisation of Novel Corn Starch Superhydrophobic $CaCO_3$ Films	200
24	Process Plant Layout Optimisation and its Application to Flixborough (1974)	210
25	An assessment of the United Kingdom's carbon capture readiness for natural gas reciprocating engines	220
26	Decarbonisation of the UK Residential Sector using Spatial Agent Characterisation	230
27	Modelling Density and Viscosity of Partially Carbonated Aqueous 2-Amino-2-Methyl-1-Propanol and Piperazine for CO_2 Capture	240
28	Agent-Based Modelling of The Steelmaking Industry in India: Assessment of Preferential Pathways towards Sustainable Development	249

paper	Title	page
29	A Critical Techno-Economic and Environmental Assessment of Next Generation Energy Storage Technologies: From Lithium to Sodium & Potassium-Ion Batteries	(*)
30	A catalyst design study for the catalytic conversion of ethanol to butadiene	259
31	Catalytic Activity Profiling in a Multi-Tubular Hydrogenation Reactor for High Concentration Acetylene Streams	(*)
32	Kinematic Parameters Examination for Process Modelling of Protein Crystallisation	268
33	Application of a CHO cell Genome-Scale Metabolic Model for Bioprocess Optimisation	278
34	Identifying novel mixtures as working fluids in Organic Rankine Cycles through an improved computer-aided molecular and process design algorithm	288
35	Literature Review and Experimental Design in Producing Rigid Polyurethane Foam for Sportswear Clothing	298
36	Mathematical Modelling of Targeted Thrombolysis by a Multifunctional Nanomedicine: Effects of Clot Length and Coarseness on Recanalization Time	308
37	Depot Optimisation for Vehicle Fleet Electrification	318
38	Process Design and Techno-Economic Assessment for Biofuel Production of Excreted Octanol from Genetically Engineered Cyanobacteria	328
39	Retrofitting of the UK Gas Grid for Hydrogen Delivery	338
40	Crystallisation Behaviour and the Effects of Cooling Rate & Sample Volume of Sodium Dodecyl Sulfate in Aqueous Solution	348
41	Atomistic simulation of pH-responsive PLP-NDA	357
42	Investigation into the Decomposition Techniques Employed in Optimising a Chimeric Antigen Receptor T-Cell Therapy Supply Chain	365
43	CFD modeling of immiscible liquid-liquid dispersion in a stirred vessel	375

paper	Title	page
44	Comparative Assessment of Polynomial Optimisation Solvers	385
45	Framework for a Machine Learning Approach to Cancer Classification with IgG Glycome Profiles	395
46	Heuristic Methods to Improve and Expand the SAFT-γ Mie Database via Analysis of 13C NMR Spectroscopy	405
47	Computational Investigation on Lipid-Polymer Interactions and Intracellular Delivery for Novel Pseudopeptic Polymers	415
48	Techno-economic analysis of a novel hydrogen powered air-source absorption heat pump for domestic heating	425
49	Numerical Modelling with Particles of Taylor-Couette Graphene Exfoliation	435
50	Accurate estimates of SAFT-VR Mie parameters for single-segment species from *ab initio* calculations	(*)
51	Exploratory Framework towards Developing a Predictive Model for Teamwork in Engineering Teams	444
52	Optimising the synthesis of MIL-53(Al) on ceramic hollow fibre substrate for the adsorptive removal of diclofenac from water	454
53	Modelling of Paracetamol Crystallisation in Ethanol Solution	464
54	Investigation of the Thermodynamic Stability of the Precious Metal-Free Catalysts for the Oxygen Reduction Reaction	474
55	Investigating Entrepreneurial Intention among Chemical Engineering students and Developing tailored Entrepreneurship Education	484
56	Data-Driven State of Charge Estimation in Li-ion Batteries under Dynamic Operating Conditions	494
57	Molecular modelling absorption of solutes in amorphous domain of semicrystalline polymers	504
58	Infrared spectroscopic simulations of an absorbing layer on a non-absorbing substrate	514

paper	Title	page
59	Catalyst Design Study for the Catalytic Conversion of Ethanol to 1-Butanol and Butadiene via the Guerbet and Lebedev reactions	514
60	Polydopamine Modified Polyvinylidene Fluoride Membrane Prepared via Combined Crystallisation and Diffusion (CCD) Method	(*)
61	Surrogate Modelling of Spray Dispersion using Computational Fluid Dynamics & Machine Learning	524
62	Technoeconomic Assessment of Hybrid Renewable Energy Systems for a Hotel in Egypt	534
63	Techno-economic evaluation of green Ethylene production from CO and H_2 via Methanol-to-Olefins process	(*)
64	Techno-Economic Analysis of Photocatalytic Reduction of CO_2	546
65	Technoeconomic and Life Cycle Analysis of Single Cell Proteins	557

(*) These papers have been removed by request of the authors and/or supervisors

Author and Supervisor index at the end of the book.

Design and Optimisation of a Continuous Bioreactor for the Production and Filtration of RNA

Joseph Davidson and Laetitia Dischamps

Department of Chemical Engineering, Imperial College London, UK

December 17, 2020

Abstract

Development of new vaccine candidates through traditional technologies can lead to several years between the emergence of a new pathogen and the onset of clinical trials of the vaccine. RNA vaccines when combined with a Quality by Design (QbD) approach have shown the ability to greatly reduce these development times, allowing for rapid responses to novel pathogens. This study has considered one of the main challenges facing the production of such RNA vaccines at scale: the ability to operate the process continuously. Through computational modelling, using findings from the batch transcription process and experimental data for continuous operation, a novel bioreactor has been designed and optimised. This novel bioreactor consists of a continuous transcription reactor and an RNA product filtration by Tangential Flow Filtration (TFF). In applying the principles of QbD to these models, relationships between the Critical Quality Attributes and Critical Process Parameters can be demonstrated. The subsequent integration of the models then allows for the implementation of a recycle, noticeably decreasing costs of raw materials. Critically, continuous operation of the RNA production process has displayed a three-fold increase in productivity when compared with batch operation.

Keywords: RNA Vaccines, Quality by Design, Tangential Flow Filtration, In Vitro Transcription

1 Introduction

Vaccinations have been one of the major breakthroughs in modern medicine, eradicating certain infectious diseases such as smallpox and significantly reducing the effects of many others including polio (Di Pasquale et al., 2015). Conventional vaccines, dating back to the 18th century, have however not been as effective against rapidly evolving and emerging pathogens, such as influenza (Di Pasquale et al., 2015). RNA based vaccines have the potential to overcome these challenges due to their shorter production times as well as their safe administration and cheap manufacture (Pardi et al., 2018). RNA vaccines introduce an mRNA sequence coding for a disease-specific antigen into the body, which will then induce the cells' production of that protein and equip the immune system with the tools to fight the real pathogen if encountered (Pardi et al., 2018). Most recently, RNA technology has shown to be successful in the race for a COVID-19 vaccine this year, with both Moderna and Pfizer/BioNTech confirming a 95% efficacy after phase 3 trials with RNA vaccines (Adam and Zimm, 2020). Approval of the Pfizer/BioNTech vaccine in the UK has in turn, seen the first use of RNA vaccines outside of clinical trials (Campbell, 2020). In addition to infectious diseases, RNA vaccines show potential in dealing with other major health challenges such as allergies (Weiss et al., 2017) and cancers (Sahin et al., 2017).

RNA vaccines are a platform technology, as their production can be standardised, allowing for quick responses to epidemics (Kramps and Elbers, 2016). Indeed, different vaccines could be produced using the same production process, with the same quality control systems, rapidly and at high capacity. Therefore, the production of new vaccines can be achieved in around one tenth of the time compared to conventional vaccine production technologies (Kis et al., 2020).

Yet, the large scale production of safe and affordable vaccines using this method is limited by the current use of batch processes. Indeed, continuous operation can lead to a ten-fold increase in yield compared to batch processes (Yang et al., 2020) and can reduce operational costs by up to 55% compared to batch processes (Walther et al., 2015).

However, vaccine production is one of the most heavily regulated industries in the pharmaceutical sector,

and this safeguard means innovation can be time-consuming. Traditionally, Quality by Testing (QbT) is used to evaluate the quality of pharmaceutical products by testing the raw components, the process and the products. If a single quality standard is not met, the testing needs repeating, with no insight regarding the issue with the process (Hubert et al., 2013). This leaves the risk of mistakes being repeated, rendering QbT an enduring and demanding process. Quality by Design (QbD) was approved in 2004 as a method where the testing time and the uncertainty to evaluate pharmaceutical processes are reduced (Sangshetti et al., 2017). QbD applies science- and risk-based approaches to define a final manufacturing design space within which the quality of the product is guaranteed (Haas et al, 2014). This allows for continuous improvement because, if the design space has gained regulatory approval, then so long as operation remains within this space, changes can be introduced. The QbD process requires definition of the Quality Target Product Profile (QTPP) based on the patients' needs as well as the Critical Quality Attributes (CQA) and Critical Process Parameters (CPP). QbD also requires identification of the design space that maps the range of operating conditions that ensure the QTPP is met, then the development of a control system for the process, and finally to continuously monitor the process and to feed the process parameters to the control system (Corredor et al., 2018).

This research paper aims to explore the possibility for novel continuous production of RNA for use in vaccines through a Quality by Design framework. This endeavour is split into two sections: the RNA transcription reaction and the Tangential Flow Filtration (TFF) separation process. Continuous transcription is to be done building upon knowledge of the process from batch findings and the TFF model is to be developed and validated using experimental data. These models are then to be integrated with the potential for recycle of the removed species in the TFF stage to be explored and to allow for comparisons with batch operation.

2 Background

With the onset of the COVID-19 pandemic, the interest in the ability of RNA vaccines to fight infectious diseases has been accelerated. Despite having never had an RNA vaccine approved for use in humans before November 2020, the flexibility and speed of the processes around RNA vaccine development and production have lead to much excitement about the potential for the technology.

Van de Berg and Behmer (2019) have undertaken extensive work in the analysis of the batch production of RNA through *in vitro* transcription, using the design of experiments data available from Professor Shattock [1]. Here, a mechanistic model was created and developed based on work from Akama et al. (2012) to model the transcription process with the additional consideration of RNA degradation. Their work also took the initial steps towards applying the model and findings to inform a continuous reactor model for the *in vitro* transcription process.

With regards to TFF, the general principles behind the process are relatively well understood, however there is a significant lack of both experimental and especially modelling work in literature in the application to RNA filtration. Funkner et al. (2018) have carried out experimental work in the purification and/or conditioning of RNA with varying chain lengths after transcription from a template DNA using at least one TFF stage. The TFF used here has focused on the removal of the solutes smaller than the RNA species with the DNA template removed through digestion by addition of DNAse and $CaCl_2$. These give primarily qualitative findings from their work that can provide insight into the additional phenomena that manifest when applying TFF to RNA filtration. Limited quantitative data is available for the TFF configurations used in the process with a range of membrane specifications applied to the filtration stage.

This lack of detailed computational modelling of both the continuous RNA transcription process and the use of TFF in separation of the RNA sets the scene for the design and integration of both unit operations. In modelling the two processes together, the groundwork can be set to allow more informed decisions in design of experiments. The possibility for recycle after the TFF back to the reactor inlet can also be explored with a focus on the potential economic savings this can bring about.

King's College London are in the process of conducting experiments for the continuous production of RNA with TFF then used for the separation system. This bioreactor aims to allow for modular design with simple and efficient operation of the process to allow for high productivity. A schematic of the bioreactor is shown in figure 2.1 and forms the basis of the modelling undertaken in this study. 800 of these units then form the overall RNA production configuration.

[1] Unpublished data from Professor Shattock's team was used.

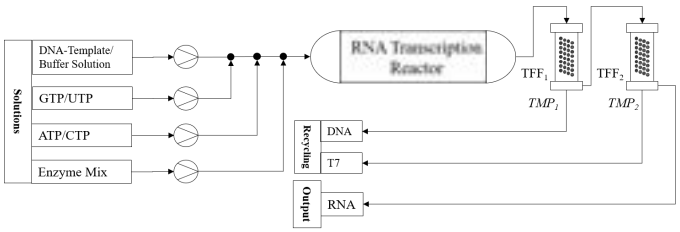

Figure 2.1: *Schematic of one unit of the King's College London's bioreactor*

3 Methodology

The RNA vaccine production requires two steps. Firstly, an *in vitro* transcription reaction step occurs where the T7 RNA polymerase enzyme uses the DNA template to transcribe the nucleotide triphosphates (NTP^{4-}) into RNA, also forming pyrophosphate (PPi) as a byproduct. PPi released by the reaction binds with Mg^{2+} and precipitates to form magnesium pyrophosphate (Mg^2PPi), this reaction is assumed negligible during our modelling (Akama et al., 2012).

Following the transcription reaction, the RNA product is purified through a separation system. For continuous operation, this separation often takes the form of Tangential Flow Filtration (TFF). The purification of the RNA enables for greater integrity over a longer period of time, which is especially important for storage and distribution (Funkner et al., 2018). It also means that the RNA can meet the purity requirements for regulatory approval (Schlake et al., 2012).

3.1 Quality by Design

3.1.1 Continuous Reactor

The CQAs and CPPs of the RNA transcription process have been determined by van de Berg and Behmer (2019). The effective RNA concentration was found to be the key process CQA, whilst a series of parameters including temperature, pH and reactant concentrations were identified as CPPs. The CPPs for a continuous system can differ to the ones for a batch system because of the difference in production process. Using the batch data from Professor Shattock's group that presented the effect of varying the initial concentrations of certain components on the RNA yield, the ranking of certain CPPs was determined. A number of parameters have an influence on the yield of the process, here, the statistical significance of the concentrations of Mg, NTP and T7RNAP were evaluated using MODDE. The batch transcription reaction process was ran experimentally with several combinations of different initial concentrations for Mg, NTP and T7RNAP. The corresponding RNA yield achieved by each combination was obtained. Using DoE, the impact of variation of these parameters in the reaction were identified (Corredor et al, 2018). Therefore, in the MODDE simulation, a Factor List of 3 process parameters was analysed: Mg, NTP and T7RNAP. At first, 63 experiments were entered, giving different RNA yields after 2, 4 and 6 hours of a batch transcription process.

3.1.2 Tangential Flow Filtration

Again applying a QbD framework, the CPPs and CQAs for the TFF process were taken from Watler and Rozembersky (2009). The CPPs are as follows: transmembrane pressure (TMP), feed concentrations, temperature and cross-flow flux. The CQAs are as follows: RNA product recovery, membrane recovery and filtrate flux rate.

Assuming that the temperature can be taken as constant through sufficient process control and that solute deposition is negligible, temperature and membrane recovery are not considered in the construction of the TFF model. This leaves three CPPs and two CQAs that become the focus of the model.

3.2 Continuous Reactor

3.2.1 Assumptions

- Constant properties of the species
- Temperature is controllable and constant
- Negligible axial mixing and frictional pressure drop in the system
- Negligible kinetic and potential energy

3.2.2 Mathematical Model

The model consists of a system of 4 ordinary differential equations (ODEs), describing the change in total RNA, PPi^{4-}, H^+,and NTP^{4-} concentration through RNA transcription and RNA degradation. The rates used to describe the reactions occuring in the reactor are shown in equations 1 and 2. The rate of transcription (1) was based on van de Berg and Behmer's work (2019) whilst the rate of degradation (2) was tailored to the expected outlet RNA concentration of 4 to 6 g/L, as defined by the team at King's College. Conjectural values were chosen for k_{deg} ($L^{10}.mol^{-10}.hr^{-1}$), n_1 and n_2.

$$V_{tr} = \frac{k_{app}[T7] \times \alpha[Mg] \times [MgNTP]}{K_2[MgNTP] + \alpha K_1[Mg] + 1} \qquad (1)$$

$$V_{deg} = k_{deg} \times [RNA]^{n_1} \times [H]^{n_2} \quad (2)$$

The concentration variation of the reactants and products was determined using the design equation for an idealised continuous PFR at steady state.

$$\frac{dX}{dV} = \frac{-r_A}{F_{A,0}} = f(X) \quad (3)$$

To integrate and solve the system of differential equations in Python, Euler's explicit method was used (Mushtaq, 2014). This method has shown to be more accurate for small step sizes (ΔL) (Brio etal., 2010), thus a high number of steps (100,000) was chosen, achieving a step size of 4.4 10^{-6}m.

$$X_{i+1} = X_i + f(X_i) \times \Delta L \quad (4)$$

3.2.3 Reactor Volume Optimisation

The degradation rate constant (k_{deg}) and orders (n_1, n_2) constitute uncertain variables, but knowing that the expected RNA yield at the outlet of the reactor is between 4 and 6 g/L, the possible values of those variables can be narrowed down. The reactor volume optimisation is then a two step process.

Firstly, the possible combinations of k_{deg}, n_1 and n_2 for which the RNA yield is in the expected interval have to be identified. For this, 1 million combinations were done: k_{deg} was varied between 1 and 5 with intervals of 0.05, while n_1 was varied between 0.5 and 1.5 and n_2 was varied between 0 and 1, both with intervals of 0.01. The model was therefore run with each of the combinations to identify the ones obtaining an RNA yield between 4 and 6 g/L.

Secondly, those successful combinations were then further run through the Python model to obtain the reactor length, for each rate of degradation, at which the RNA yield in maximized. This was done up to a reactor length of 550mm. The cross-sectional area and inlet volumetric flowrate were maintained the same as that chosen by the team at King's, whilst the residence time varied.

3.3 Tangential Flow Filtration

After the transcription reactor, the effluent is fed into a TFF unit for purification. Here, the feed stream to the TFF is separated into two streams; a retentate stream and a permeate stream due to a pressure difference being applied across the membrane. A simplified diagram of the process is given in figure 3.1.

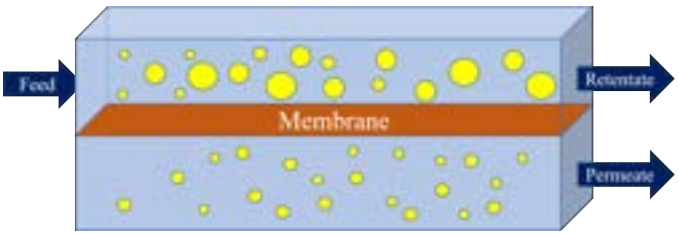

Figure 3.1: *Tangential Flow Filtration Diagram*

3.3.1 Assumptions

- Below a TMP of 30 psi and feed flux of 1000 $L.m^{-2}.hr^{-1}$, there is negligible shear degradation (Funkner et al., 2018).
- Below a TMP of 30 psi, the flux is membrane controlled (Funkner et al., 2018).
- Negligible deposition of solutes in the membrane pores (no pore blocking).
- Temperature and pH can be sufficiently controlled to be taken as constant.
- No precipitation of RNA.

3.3.2 Degradation

The TFF modelling considers degradation of the RNA through two terms: shear degradation and natural degradation. This assumes that the RNA species is made up of the four bases in equal amounts.

Shear degradation is modelled through an exponential term and is a function of the degree to which the TMP exceed the TMP where shear degradation becomes significant. This is inspired by the shear degradation of DNA modelling from Adam and Zimm (1977). From Funkner et al. (2018), shear degradation was not observed in the pressure range explored of below 2 bar (29 psi). Hence the onset of shear degradation is expected to commence at some TMP above 29 psi, although data is not available for the specific TMP and flow rate where this becomes significant.

$$V_{deg,sh} = k_{sh}(1 - e^{\alpha_{sh} Q_{ret}(TMP - TMP_{sh,onset})}) \quad (5)$$

Where the $V_{deg,sh}$ ($g.hr^{-1}$) is the shear degradation rate, k_{sh} ($g.hr^{-1}$) is the shear degradation rate constant, α_{sh} ($hr.L^{-1}.psi$) is the shear degradation exponential constant, Q_{ret} ($L.hr^{-1}$) is the retentate flow rate and $TMP_{sh,onset}$ is the TMP above which shear degradation becomes significant.

Degradation is also considered using the same term as in the reactor model, with a dependence on the RNA concentration and the H^+ concentration.

3.3.3 Permeate Flux

At sufficiently low TMP, the TFF process is membrane controlled and is dependent on the TMP (Funkner et al., 2018). The permeate flux can then be modelled through the use of a membrane controlled flux model (Watler and Rozembersky, 2009):

$$J_{per} = k \times TMP \tag{6}$$

Where J_{per} ($L.m^{-2}.hr^{-1}$) is the flux through the membrane, k ($L.m^{-2}.hr^{-1}.psi^{-1}$) is the mass transfer coefficient, TMP (psi) is the transmembrane pressure.

To account for the multiple solutes that pass through the TFF, a probability factor is incorporated to model the likelihood that each solute molecule will pass through the membrane in the permeate based on the solute's molecular weight. This is a function of the molecular weight cut-off (MWCO), which is a property of the membrane used in the process. Since water is the smallest solute in the TFF feed stream, the difference in molecular weight of each solute and water is used here, allowing for the mass transfer coefficient in the flux term to become that of water, a much more accessible quantity for a given membrane specification. The probability factor is given below:

$$PF_i = e^{-a\frac{MW_i - MW_{H_2O}}{MWCO}} \tag{7}$$

Where PF_i is the probability factor of solute i, a is the membrane correction factor, MW_i (kDa) is the molecular weight of solute i, MW_{H_2O} (kDa) is the molecular weight of water and MWCO (kDa) is the molecular weight cut-off of the membrane.

The membrane correction factor, a, can then be altered to fit the the specification of a given membrane by use of membrane's solute retention curve from experimental screening.

Below 30 psi TMP, the permeate flux through the membrane then becomes:

$$J_{per} = k_{H_2O} \times TMP \tag{8}$$

Table 1: Permeate flux mass transfer coefficients for three membrane specifications

MWCO (kDa)	k_{H_2O} ($L.m^{-2}.hr^{-1}.psi^{-1}$)
100	3.5
300	5.0
1000	6.7

The mass transfer coefficient is then found for a given membrane by plotting permeate flux at a range of TMPs and taking the gradient when pure water is used as the feed stream. The values used in the modelling are taken from Funkner et al. (2018) from experimental screening for 100 kDa and 300 kDa and 1000 kDa membranes.

The mass flow rate through the membrane is then calculated for use in the mass balance:

$$m_{per,i} = J_{per} \times SA \times PF_i \times C_{ret,i} \tag{9}$$

3.3.4 Model Development and Validation

With the flux and degradation terms defined, a mass balance is carried out for each component in the feed stream and solved at length segments along the entire length of the TFF unit. These mass balances are then solved in Python using scipy.optimize.fsolve() to give the concentrations of each component in the retentate stream. From each length segment, the retentate flux and concentrations then are used as the feed stream flux and concentrations in the next length segment for 100 length segments. The mass balance is as follows:

$$0 = v_{feed}C_{feed,i} - v_{ret}C_{ret,i} - m_{per,i} - V_{deg} \tag{10}$$

Where v ($L.hr^{-1}$) is the volumetric flow rate and C ($g.L^{-1}$) is the concentration with subscripts feed, ret and per referring to the feed, retentate and permeate streams respectively and subscript i denoting component i.

The model is then validated with the experimental data available from Funkner et al. (2018) for a single stage TFF for the recovery of the T7 RNA Polymerase. The RNA retention is then calculated for a range of RNA chain lengths and membrane specifications. Data is limited for the first stage DNA separation TFF unit so the validation of the model focuses on the second stage T7 RNA Polymerase recovery. Through this comparison with experimental data, the membrane MWCO and the membrane correction factor in the permeate flux can be found to optimise RNA separation.

The dimensions for the TFF unit of the King's College rig are then applied to the model, with a membrane surface area of 214 mm^2, residence time of 53 minutes and a 2:3 split between the retentate and permeate channels with an total channel depth of 0.5 mm.

3.3.5 TFF Design Space

Upon validation of the TFF model, a design space can then be generated through variation of the feed flux, inlet concentration and TMP. A 3D plot can therefore be generated whereby each point represents a set

of conditions for which the TFF unit is simulated and the outlet concentration of RNA is calculated and assigned a colour to allow for plotting. To narrow down the number of points, only combinations of the three considered CPPs that give a concentration factor of above 1.5 are plotted. That is, an outlet retentate concentration which is 50% greater than the inlet RNA concentration.

3.4 Reactor and TFF Model Integration

The continuous reactor and the TFF separation system are then linked, with the outlet concentrations and flow rate from the reactor fed into the separation system. The integration of the TFF model allows for the calculation of the number of doses of RNA vaccines that are produced per year from the retentate stream of the system, assuming an 80% running time and that 1.2mg of RNA is required per vaccine dose, as suggested by the team at King's College.

3.5 Recycle Stream from TFF to Reactor

Following this, the implementation of a recycle was considered at the exit of the TFF unit, feeding the permeate stream back to the inlet of the reactor. This step is economically important because raw materials account for 84.1% of costs (Kis, 2020).To implement the recycle into the model, a mass balance was performed over the junction between the recycle ($v_{recycle}$) and the desired reactor inlet stream (v_0).

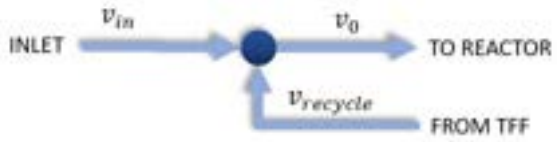

Figure 3.2: *Diagram of the recycle system*

In this study, the recycle of the NTP, Mg and T7RNAP enzyme were considered. It is important to note that the most costly raw material of the process is a compound not considered in this study, the 5' cap. A first balance was carried out on the volumetric flowrates, presented by equation 11, and then the molar concentrations of the species were balanced using equation 12. This provided the volumetric flowrate required to the inlet of the system (v_{in}), as well as the concentrations of this stream ($C_{i,0}$) required to meet the initial conditions of the feed to the reactor.

$$v_0 = v_{in} + v_{recycle} \tag{11}$$

$$v_0 C_{i,0} = v_{in} C_{i,in} + v_{recycle} C_{i,recycle} \tag{12}$$

4 Results and Discussion

4.1 Critical Process Parameters

Fitting the batch data in MODDE, a series of approximations were obtained for the CPPs. Outlying points were removed from the observed vs predicted values plot to obtain high correlation coefficients (R2 = 0.86), prediction values (Q2 = 0.75), and reproducibility (0.91) for the model. The validity of the model was negative due to MODDE fitting a linear regression to the data and a non-linear response was obtained between these factors.

The factor coefficients were then determined, presented in table 2. These can be used as a crude estimate for CPP identification.

Table 2: Coefficients of factors obtained in MODDE

Factor	**Coeff.**	***p***
Mg	-0.36	1.3e-11
NTP	-0.22	1.6e-06
T7RNAP	0.22	6.0e-07

According to Corredor et al. (2018), the CPPs have statistically significant effects when the p value is inferior or equal to 0.05, this acknowledges that these factors are CPPs. From the MODDE modelling, the CPPs can be ranked from most to least critical: Mg concentration, T7RNAP concentration and, lastly, NTP concentration.

4.2 Continuous Reactor

4.2.1 King's College reactor

The reaction constants and orders used for the transcription rate were taken from van de Berg and Behmer's work (2019). For the degradation rate, the values were initially taken to be $k_{deg} = 2.25$ $L^{10}.mol^{-10}.hr^{-1}$, $n_1 = 1$ and $n_2 = 0.1$ giving an RNA yield of 5.5 g/L. This achieves a volumetric productivity of 1.90 $g.L^{-1}.hr^{-1}$ which is three times higher than the one obtained by a batch process with the same inlet concentrations (van de Berg and Behmer, 2019). This supports that operating a process continuously is advantageous because higher productivity can be achieved.

The overall conversion of NTP to RNA was calculated as 0.29, it is low due to the degradation of RNA. Hence, more than 70% of the initial NTP concentration was present at the outlet of the reactor, emphasising the interest in implementing a recycle to the system.

4.2.2 Reactor Volume Optimisation

The optimization of the reactor is limited by the uncertainty around the RNA degradation rate: the degradation rate constant (k_{deg}) and orders (n_1, n_2) constitutes undetermined variables. Yet, it was known that the outlet yield of RNA was expected to be between 4 to 6 g/L. Therefore, 1 million simulations were performed with different combinations of values for k_{deg}, n_1 and n_2. The combinations giving an RNA yield between 4 and 6 g/L were plotted in 4.1, as possible combinations describing the rate of degradation of RNA. The RNA concentration was also found to be critical, as the degradation rate order of RNA, n_1, had to be around 1 to achieve a yield within the expected range. Indeed, performing simulations over a range of n_1 between 0 and 2, the values of n_1 plotted ranged between 0.65 and 1.15.

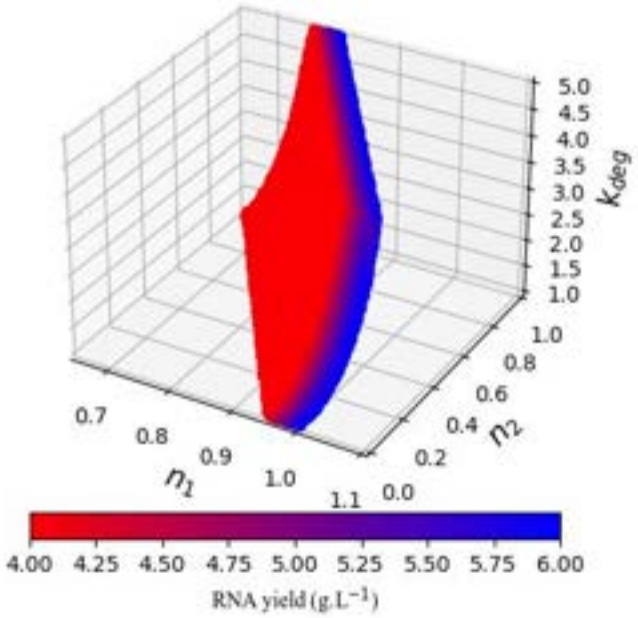

Figure 4.1: *The degradation rates obtaining a RNA yield between 4 and 6 g/L. k_{deg} is the rate constant ($L^{10}.mol^{-10}.hr^{-1}$) and n_1 and n_2 are the degradation rate orders of RNA and H, respectively.*

Following this, each successful combination of values, plotted in figure 4.1, was then run through the model to obtain the length at which the maximum RNA yield was achieved for that degradation rate. The cross-sectional area and inlet volumetric flowrate were kept constant whilst the residence time was varied according to the change in reactor volume.

From figure 4.2 it is noticeable that the vast majority of the points lay below the current reactor volume designed by the team at King's College. This shows that

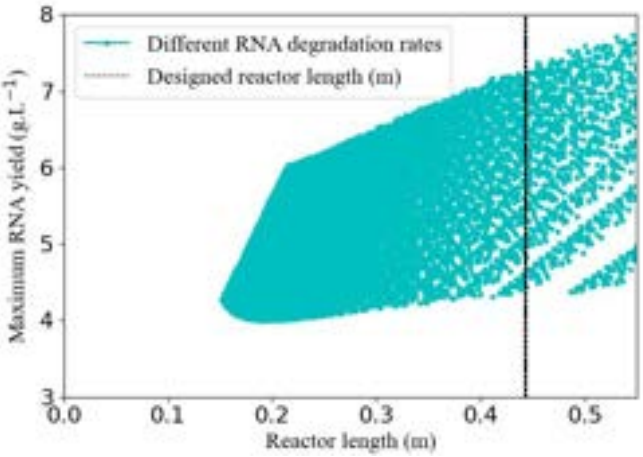

Figure 4.2: *Reactor length at which each degradation rate exhibits a maximum in RNA yield, compared to the King's College reactor length of 442.4mm.*

under the current conditions, the King's College reactor is most likely not optimised and so this leaves space for further optimisation. For instance, an increase in inlet volumetric flowrate pushes the density of points from figure 4.2 to the right, towards the designed reactor length dashed line. Therefore, an increase in inlet volumetric flowrate would increase the yield observed in the King's College reactor.

4.3 Tangential Flow Filtration

4.3.1 Probability Factor

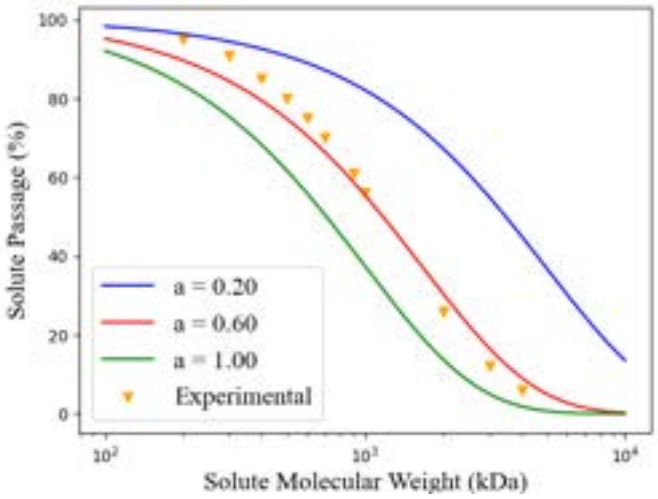

Figure 4.3: *Comparison of probability factor at varied membrane correction factor with experimental data (Watler and Rozembersky, 2009) for a range of solute molecular weights and a membrane of 1000 kDa MWCO.*

From figure 4.3, through variation of the membrane correction factor in the probability factor, an agreement with experimental data for the variation of retention with solute molecular weight is found. A value of 0.60 is then used as in the probability factor in further modelling. However, the retention profile is heavily dependent on the membrane that is utilised in the TFF process and hence needs alteration with each membrane used, both with membrane MWCO and membrane manufacturer. As a result, it is important that the general trend of the solute profile is obtained through the probability factor. In deciding upon a membrane, screening experiments would enable for the passage profiles to be plotted and then a membrane chosen to minimise the loss of RNA and maximise the passage of the other solutes. In the meantime, the probability factor used here is a relatively good approximation for the membrane retention profile.

4.3.2 Retention of RNA

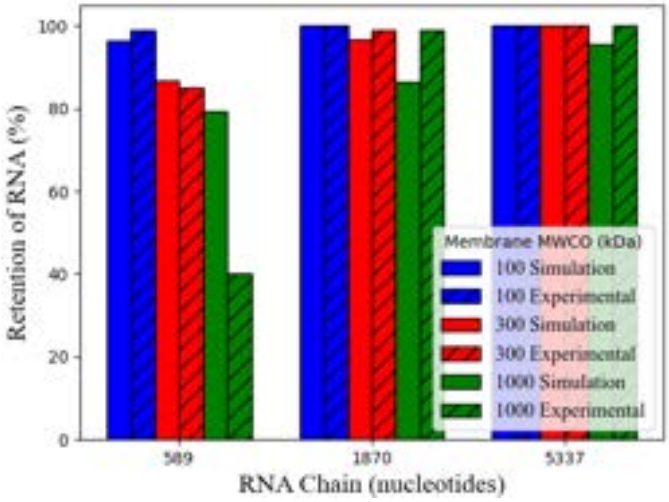

Figure 4.4: *The retention of RNA in the simulated TFF process against experimental data (Funkner et al., 2018) for a range of membrane MWCO.*

As can be seen in figure 4.4, the TFF model shows good overall agreement in the RNA retention achieved when compared with experimental data. For smaller RNA chain lengths, the model performs less well, especially for larger MWCO membrane specifications. The RNA chain length of interest in this study (10,000 nucleotides) is significantly larger than the chain lengths in the experimental data and hence close to total retention of RNA in the TFF is expected for the three membrane specifications considered. To ensure this high retention of the RNA product, a membrane MWCO of 300 kDa is taken forward in subsequent modelling.

4.3.3 TFF Design Space

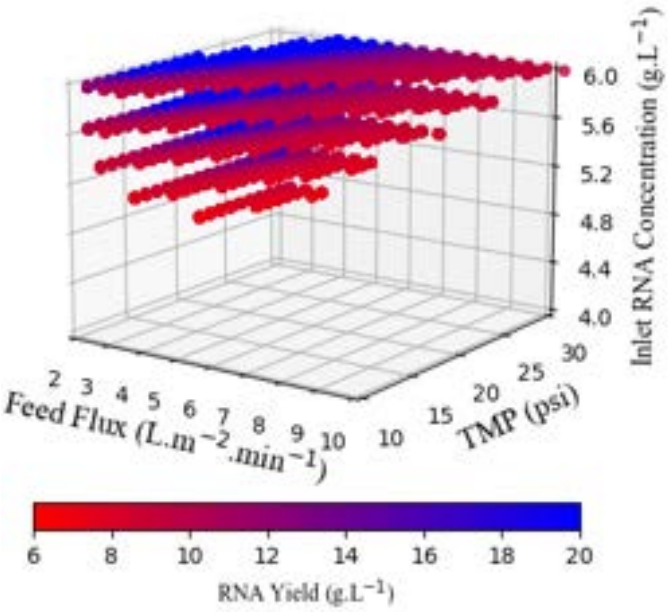

Figure 4.5: *Variation of RNA concentration in the retentate with feed flux, TMP and inlet concentration for a MWCO of 300 kDa and a concentration factor of 1.5 across the TFF.*

Figure 4.5 displays the impact of the three CPPs the TFF model considers and their effect on the yield of RNA after filtration. As the TMP is increased, there is a significant increase in the concentration of RNA in the retentate stream exiting the TFF. However, extrapolating this relationship beyond a TMP of 30 psi needs care, with an expectation that the TFF process will become gel layer driven and as such, no longer become dependent on the TMP of the unit. This being a result of larger solutes collecting near the membrane surface of the membrane but being too large to pass through. Similarly, the onset of significant shear degradation is anticipated at some point above a TMP of 30 and larger flow rates and whilst this point is not known exactly, would result in significant loss of RNA chain integrity, reducing the effective RNA concentration in the retentate. With decreasing feed flow rate, an increase in residence time is achieved and as such, a greater RNA concentration in the retentate is observed. For lower feed flux, there is also a reduction in the velocity of the stream parallel to the membrane which is likely to lead to greater net deposition of the solutes on the membrane and therefore greater pore blocking, hindering the TFF process and requiring more frequent regeneration of the membrane. This will then lead to a reduction in the productivity of the process. In feed flux,

there will be an optimal value that balances this pore blocking at low flux and the shear degradation at high flux. More detailed experimental data would be necessary to pinpoint this optimal flux as solute deposition is neglected in this modelling.

4.4 Reactor and TFF Model Integration

Following the integration of the TFF model with the reactor model, the rate of RNA vaccine doses produced per year by the whole system (800 units) was estimated. Assuming steady-state, 100 % retention of RNA and an operating time of 300 days per year, approximately 2.88×10^6 doses are produced per year for 800 units.

4.5 Recycle Stream from TFF to Reactor

By implementing the recycle, using the mass balance from equations 11 and 12, the inlet volumetric flowrate v_{in} is calculated to be of 6.12×10^{-7} L/min with a NTP concentration of 0.08 mol/L, a T7RNAP concentration of 1.65 U/L and a Mg concentration of 0.02 mol/L. The amount of savings acquired by implementing the recycle add up to a total of about 2 million dollars per year, as shown in table 3. The most significant expense is NTP, and the cost of raw NTP per year for 800 units with recycle is equal to 2 times the amount of total savings from recycling. Therefore, integration of a recycling stream is beneficial because it considerably reduces the costs of the process.

Table 3: Amount of savings per year for 800 units from recycling Mg, NTP and T7RNAP. Costs of the GMP grade materials were given by Roche.

Compound	**Savings ($/year)**
Mg	36,500
NTP	2,030,000
T7RNAP	0.0371
Total	2,070,000

5 Conclusions and Outlook

The modelling developed here has successfully given insight into the potential for such a novel method for RNA production and *in situ* separation through utilisation of a TFF system. Careful use of the findings from work previously undertaken in batch processes enabled for a more informed transition to continuous operation, especially with regards to the transcription and degradation rates. Using a QbD framework throughout allowed for the models to explore the links between the CPPs and CQAs, for both the continuous reactor and TFF, against a backdrop of limited data for such a setup. Integration of the two units was also carried out with the recycle of the permeate stream from the TFF back to the reactor inlet. Transitioning from the batch model previously developed to the continuous model has displayed a three-fold increase in productivity.

With regards to optimal operation of the bioreactor, modelling indicates that the current length of the reactor channel is likely too long and can be shortened to obtain the greatest RNA yield at the outlet. Alternatively, in that objective, the inlet volumetric flowrate can be increased. Optimal operation of the TFF unit appears to be with a TMP around 25 psi to ensure that the process remains membrane controlled, avoiding the formulation of a significant gel layer on the membrane.

Whilst the TFF model appears to provide close agreement with the experimental data used for sufficiently long RNA chains, it is important to reevaluate the model for the smaller units that King's College are looking into. When data is available for these smaller, more modular TFF units, the model can be reevaluated and improved. In turn, more detailed and complete experimental data would allow for the development a model with which greater confidence could be placed in. Here, a design of experiments method could then be applied to carefully select experiments by using the model. As the experiments are time consuming and expensive, these should be minimised.

In terms of the additional considerations for TFF application to RNA, a number of possible considerations could be made to refine the model. For example, the membrane recovery is omitted from the current model, whereby the rate of solute deposition is unknown and in turn so is time between which membrane recovery is necessary. Incorporating this into the model would allow for more detailed economic analysis as well as a more accurate estimate for the productivity of such continuous operation by factoring in the need to pause operation and recover the membrane.

Another exciting area for exploration would be the use of more innovative configurations for the continuous reactor. For example, additional inlets of NTP could be placed at a range of distances along the unit. This would allow for greater yields of the RNA at the outlet as high concentrations of NTP could be maintained along the reactor length.

6 References

Adam, R. Zimm, B. (1977). Shear degradation of DNA. *Nucleic Acids Res*, **4**(5), 1513-1537.

Akama, S. Yamamura, M. Kigawa, T. (2012). A Multiphysics Model of In Vitro Transcription Coupling Enzymatic Reaction and Precipitation Formation. *Biophysical Journal*, **102**(2), 221-230.

Brio M. Webb G. Zakharian A. (2010). Problems with Multiple Temporal and Spatial Scales. *Mathematics in Science and Engineering*, **213**, 175-249.

Campbell, M. (2020). Key Questions and Answers About the UK's First Approved COVID-19 Vaccine. *Technology Networks*.

Corredor, C. Vikstrom, C. Persson, A. Bu, X. Both, D. (2018). Development and Robustness Verification of an At-Line Transmission Raman Method for Pharmaceutical Tablets Using Quality by Design (QbD) Principles. *Journal of Pharmaceutical Innovation*, **13**(4), 287-300.

Di Pasquale, A. Preiss, S. Tavares Da Silva, F. Garçon, N. (2015). Vaccine Adjuvants: from 1920 to 2015 and Beyond. *Vaccines*, **3**(2), 320–343.

Funkner, A. Dorner, S. Sewing, S. Kamm, J. Broghammer, N. Ketterer, T. Mutzke, T. (2018). United States Patent No. US20180298372.

Haas, J. Franklin, A. Houser, M. Maraldo, D. Mikola, M. Ortiz, R. et al. (2014). Implementation of QbD for the development of a vaccine candidate. *Vaccine*, **32**(24), 2927-2930.

Hubert, C. Lebrun, P. Houari, S. Ziemons, E. Rozet, E. Hubert, P. (2014). Improvement of a stability-indicating method by Quality-by-Design versus Quality-by-Testing: A case of a learning process. *Journal of Pharmaceutical and Biomedical Analysis*, **88**, 401-409.

Kis, Z. (2020, June, 30). *Biologics: Regulatory CMC, Quality and Manufacturing* [Video file].

Kis, Z. Kontoravdi, K. Dey, A. Shattock, R. Shah, N. Engineering Physical Science Research Council. (2020). Rapid Development and Deployment of High-volume Vaccines for Pandemic Response, 2637-403X.

Kramps, T. Elbers, K. Introduction to RNA Vaccines. *RNA Vaccines*(Methods in Molecular Biology, pp. 1-11). New York, NY: Springer New York.

Mushtaq, F. (2014). Analysis and Validation of Chemical Reactors performance models developed in a commercial software platform.

Pardi, N. Hogan, M. Porter, F. Weissman, D. (2018). MRNA vaccines — a new era in vaccinology. *Nature Reviews. Drug Discovery*, **17**(4), 261-279.

Sahin, U. Derhovanessian, E. Miller, M. et al. (2017). Personalized RNA mutanome vaccines mobilize polyspecific therapeutic immunity against cancer. *Nature*, **547**(7662), 222-226.

Sangshetti, J. Deshpande, M. Zaheer, Z. Shinde, D. Arote, R. (2017). Quality by design approach: Regulatory need. *Arabian Journal of Chemistry*, **10**(S2), S3412-S3425.

Schlake, T. Thess, A. Fotin-Mleczek, M. Kallen, K. (2012). Developing mRNA-vaccine technologies. *RNA biology*, **9**(11), 1319–1330.

Tapia, F. Vázquez-Ramírez, D. Genzel, Y. Reichl, U. (2016). Bioreactors for high cell density and continuous multi-stage cultivations: options for process intensification in cell culture-based viral vaccine production. *Applied Microbiology and Biotechnology*, **100**(5), 2121-2132.

van de Berg, D. Behmer, C. (2019). Mechanistic Modelling of RNA Vaccine Production for Quality by Design. *Chemical Engineering Research: Reports of the 4th year research projects in the Department of Chemical Engineering at Imperial College London*, 454-463.

Watler, P., Rozembersky, J. (2009). Application of QbD Principles to Tangential Flow Filtration. In A. Rathore, R. Mhatre, Quality by Design for Biopharmaceuticals: Principles and Case Studies (pp. 111-126).

Walther, J. Godawat, R. Hwang, C. Abe, Y. Sinclair, A. Konstantinov, K. (2015). The business impact of an integrated continuous biomanufacturing platform for recombinant protein production. *J Biotechnol*, **10**(213), 3-12.

Weiss, R. Scheiblhofer, S. Thalhamer, J. (2017) Generation and Evaluation of Prophylactic mRNA Vaccines Against Allergy. *Methods Mol Biol.*, **1499**, 123-139.

Yang, O. Qadan, M. Ierapetritou, M. (2020). Economic Analysis of Batch and Continuous Biopharmaceutical Antibody Production: a Review. *J Pharm Innov*, **15**, 182–200.

Smart Enumeration Strategies for Candidate Enumeration Approach to Optimal Experiment Design

Weicheng Hua and Megan Sim

Department of Chemical Engineering, Imperial College London, U.K.

Abstract: Optimal experimental design (OED) is utilised to maximise information from the least number of experiments, having positive implications on both resources and time. The candidate enumeration method for solving optimal experimental design, available on Python through Pydex, is a novel approach aimed at reducing computational costs by discretising the design space. However, smarter discretisation strategies are required to achieve its full potential. In this paper, two algorithms - equipartition (EQ) and quasi-random sampling (QRS) - are developed to tackle this issue. These 2-phased methods adopt the divide-and-conquer approach to reduce computational costs without impairing solution precision. The first phase has the goal of identifying promising regions while the second phase aims to pinpoint optimal candidate locations. Two model domains were considered for this study, RSM and ODE models. For low-dimensional RSM models, EQ was found to efficiently give good precision but may exclude some optimal candidates in its final solution. QRS was outperformed by both EQ and brute force but at higher dimensions, QRS may be the only feasible method in obtaining an optimal design. For ODE models, QRS exceeds brute force in terms of efficiency for a comparable solution accuracy. In conclusion, QRS is recommended as the more promising algorithm to further develop.

Keywords: Optimal Experiment Design, Smart Enumeration Strategies, Equipartition, Quasi-Random Sampling, RSM Models, ODE Models

1 Introduction

Overview

The purpose of optimal experiment design (OED) is to design experiments that reduce the negative effects of measurement noise. This allows for less experiments to be performed and has positive implications on cost of resources and time. Generally, OED aims to maximise information from the least amount of experiments. The application of OED is widespread in many industries, including but not limited to, the process industry and nonclinical medicine (Atkinson 1996).

The optimal set of experiments is identified by solving the following optimisation program:

$$\xi^* = arg \max_{\xi} \phi \left[\mathbf{M}\right] \tag{1}$$

where ξ is the experiment design, the asterisk (*) indicates optimality, $\mathbf{M}$ is the information matrix, and the objective is to maximise ϕ which is a scalar summarisation of the information contained in [$\mathbf{M}$].

Shifting the focus to the use of OED for model calibration using the Frequentist paradigm, the information matrix [$\mathbf{M}$], can be defined as:

$$\mathbf{M} = \sum_{s=1}^{N_s} w_s A_s \tag{2}$$

$$\sum_{s=1}^{N_s} w_s = 1 \tag{3}$$

where $\mathbf{M}$ is the Fisher Information Matrix (FIM), N_s is the number of experimental supports (i.e. a unique experiment within ξ), w_s is the non-negative weight of the s^{th} experimental support and A_s is its rank-1 atomic information matrix. The weight of an experimental support is the number of times it is repeated divided by the total number of experiments conducted.

Presently, the conventional method for solving the optimisation problem in equation 1 is known as the parallel sequential approach (Franceschini and Macchietto 2008). The caveat is that in order to arrive at a global solution, good initial guesses must be fed to the formulations.

An alternative emerging method called candidate enumeration (CE) is proposed to tackle the limitations associated with the current methodology. Here, the continuous set of experimental control variables, $\boldsymbol{X}$, is discretised into a finite set of unique experiments knows as candidates. This allows for an experimental design, ξ, to be equivalently represented by a vector of experimental weights, w, which transforms the optimisation problem into:

$$w^* = arg \max_{w} \phi \left[\sum_{c=1}^{N_c} w_c A_c\right] \tag{4}$$

$$\sum_{c=1}^{N_c} w_c = 1 \tag{5}$$

where N_c is the number of candidate points in $\boldsymbol{X}$. This allows for reformulation of the problem as a linear convex optimisation program, regardless of model domain. Expensive computation of the atomic information matrices has to only be done once for each discrete experiment, as compared to continuous calculations in parallel sequential approach. The CE method is implementable on Python using the Pydex package (Kusumo 2020).

Motivation

The current approach to solving experimental design through CE enumerates candidates in a uniform grid. This is referred to as the 'brute-force' (BF) method and is illustrated by the figures below.

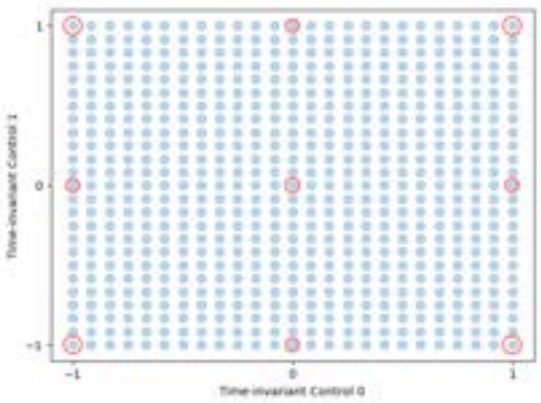

Figure 1: Brute force candidate enumeration method for a nonlinear model with 2 Time-Invariant Controls.

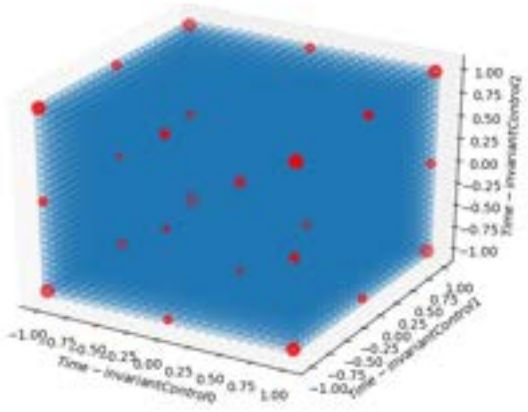

Figure 2: Brute force candidate enumeration method for a non-linear model with 3 Time-Invariant Controls.

In figure 1, each blue dot represents a discretised candidate. The number of candidates enumerated along each axis is inversely proportional to the desired precision of design. For example, a precision of 0.01 will require 101 candidates to be enumerated. The optimal experimental design is obtained as a result of solving equation 4, and candidates with non-zero weights are graphically shown using red circles, with their sizes being directly proportional to the weight of the associated candidate.

This approach works efficiently, for most degrees of precision, in lower dimensional models with fewer experimental parameters. However, as higher dimensions are explored, an exponential increase in computing power is required to maintain the level of precision. From Figures 1 and 2, it can be observed that the number of points enumerated in the 3D case is significantly larger than that in the 2D case. Consequently, the main constraint to the general implementation of CE is that it is not scalable to higher dimensions.

The motivation for this paper is thus, to introduce smart enumeration strategies to replace brute-force enumeration in an attempt to tackle the issues mentioned above. As the models used in practice are various and behave differently, there was a challenge in devising a universal solution. Hence, two algorithms were proposed, each tailored to different model domains - the equipartition (EQ) method and quasi-random sampling (QRS).

The rest of this paper comprises an overview of what is currently available in literature and definitions of key terminologies in Section 2. The methodologies for the algorithms introduced here are illustrated and their performances discussed in Sections 3 and 4 respectively. Finally, Section 5 summarises the key findings and an outlook for future improvements is suggested in Section 6.

2 Background

2.1 Terminology

Before moving forward, it is beneficial to summarise some key terminologies. These are applicable to all 3 enumeration strategies considered - brute force, EQ and QRS - unless stated otherwise.

Table 1: Definitions of terminology used throughout the paper.

Terms	Definition
Time-Invariant Controls (TIC)	Parameters that are set by the practitioner during the experiment, within user-specified bounds. These do not change with time.
Design Space	The complete region defined by the lower and upper limits of the time-invariant controls. This space includes all possible experimental designs.
Candidates	Unique experimental support with different sets of time-invariant control values within the design space.
Levels	Level values are specified based on desired precision for each dimension of the design space. The number of candidates enumerated is the product of all levels. (*Brute force and EQ only)
Experimental Effort	A percentage of the total number of experiments to be performed.
Optimal Candidates	The experimental candidates with experimental efforts greater than a user-specified tolerance, obtained in the final iteration of the algorithm. In a real world setting, these are the experimental designs for the practitioner to perform.
Promising Candidates	Experimental candidates that are selected as optimal during any iteration of the algorithm prior to the final one.
Promising Regions	Regions within the design space surrounding the promising candidates and are believed to contain the optimal candidates.

2.2 Literature

In addition to uniform grid enumeration, there are other strategies for candidate enumeration within the design space. Monte Carlo sampling involves the use of randomly generated candidates within the design region and was first applied to computer simulations in 1949 (Metropolis and Ulman 1949). As a consequence of this randomness, Monte-Carlo often leaves regions of the design space unexplored. To provide a more uniform sampling, the stratified Monte Carlo (SMC) was derived. This involves dividing the design space into regions of equal probability. Once these regions are defined, a candidate is then randomly selected from each region (Koehler and Owen" 1996). The issue with SMC sampling is that, in the best case scenario, the number of candidates scale as 2^n, where n is the number of dimensions. Hence, the strategy is not scalable to higher dimensions, where n is large, or to design spaces split into many regions (Guinta, Wojtkiewicz, and Eldred 2003.

Latin Hypercube Sampling (LHS) is similar to SMC in that the design space is also divided into smaller regions and candidates are enumerated within. The difference is that for each one-dimensional projections of the regions, there can only be one candidate (Iman and Shortencarier 1984). As opposed to a fixed lower bound on the number of candidates generated in Stratified Monte Carlo, Latin Hypercube Sampling allows for the generation of arbitrary numbers of candidates within the design space. The challenge with LHS is that there can be multiple mutations of the same design problem. Some of these designs may have poor coverage of the design space as well as high spatial correlations (Guinta, Wojtkiewicz, and Eldred 2003).

Low-discrepancy sampling (LDS) uses a deterministic algorithm to generate candidates within an n-dimensional design space, with the goal of distributing the candidates as uniformly as possible without employing a regular grid (Guinta, Wojtkiewicz, and Eldred 2003). Some of the most well known low-discrepancy sequences include Hal-

ton sequence, Sobol sequence and Poisson-Disc sampling.

In this paper, an iterative, divide-and-conquer strategy for smart-sampling of the design space is attempted where both uniform rasterisation and LDS were applied strategically. The algorithms proposed aim to break a large problem down into smaller components, making it more efficient as well as robust. This is done to outperform the brute force approach, particularly in high dimensional cases, where the method often becomes infeasible.

3 Methodology

In this section, the procedures of the proposed algorithms as well as their customisable features are outlined - starting with equipartition and followed by quasi-random sampling. Key algorithm attributes are also explained at the end of the section. Complementing Pydex, the algorithms are implemented in Python, and detailed instructions are provided.

The basis for these strategies is the iterative, divide-and-conquer approach with the goal of eliminating the need to densely enumerate within the entire design space. Both algorithms can be split into two phases - initialisation and refinement. The initialisation phase aims to identify promising regions within the design space while the refinement phase attempts to pinpoint the exact location of optimal candidates within these promising regions.

The two algorithms are distinct in the way they generate candidates and create regions within the design space. To effectively demonstrate the functionalities of these algorithms, step-by-step illustrations will be shown using the model below as an example:

$$y = \theta_0 + \theta_1(x_0) + \theta_2(x_1) + \theta_3(x_0)(x_1) + \theta_4(x_0)^2 + \theta_5(x_1)^2 \tag{6}$$

where y is the output or response variable, θ_j are the model parameters and x_i are the time-invariant controls (TIC). The number of model parameters, n_θ, is 6 and the number of TICs, n_x, is 2. The design space of this model can therefore be represented as a hypercube of n_x dimensions. The range of each dimension has been normalised to be between -1 and 1. The brute force solution to this problem is shown in figure 1.

3.1 Method 1: Equipartition

Equipartition is derived from the brute force method where dense, uniform rasterisation is only applied selectively. The intended effect is to reduce computational cost whilst maintaining precision. This algorithm is put forward as a potential solution to RSM models with design spaces of up to roughly 5 dimensions. This number might vary depending on the available computing power as well as the number of model parameters. In higher dimensions, this algorithm is not recommended as the number of candidates required to fully cover the entire design space increases exponentially. Quasi-random sampling in subsection 3.2 has therefore been developed as an alternative for these models.

Initialisation

In the initialisation step of EQ, the OED problem is solved to a much lower precision than brute force. The number of candidates enumerated is based on Caratheodory's theorem applied to OED problems.

> *There exists a solution whose number of optimal candidates is upper bounded by d, where*

$$d = \frac{n_\theta(n_\theta + 1)}{2} \tag{7}$$

The levels for each dimension are determined by taking the n_x-th root of d and rounding up the value to the nearest integer. Candidates are then uniformly enumerated over the design space and the optimisation problem in equation 4 is solved to give the first set of promising candidates. This is demonstrated below for the model based on equation 6.

$$d = \frac{6(6+1)}{2} = 21$$

$$level = \sqrt[2]{21} = 4.58 = 5 \ (for\ each\ dimension)$$

Algorithm 1: Pydex enumeration and optimisation of candidates.

```
1. initial_level = [5, 5]
   (for 2 dimensions)
2. ti_control_candidates =
   enumerate_candidates(bounds, initial_level)
   (enumerate 5x5 candidates in design space)
3. design_experiment
   (optimising the problem and
   selecting promising candidates)
```

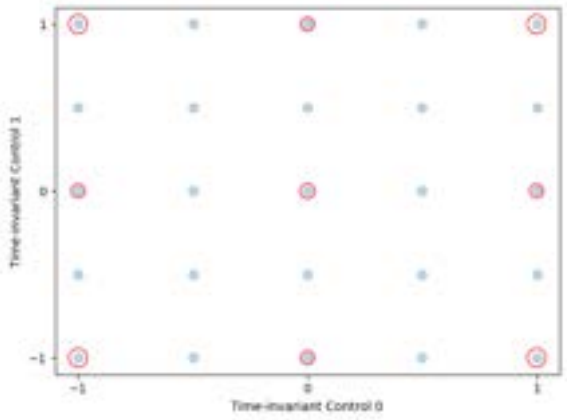

Figure 3: Initialisation phase of equipartition for example model. Of the 25 candidates enumerated, 9 are chosen as promising.

After identifying the promising candidates, the design space is split into smaller regions as shown in figure 4. Regions containing promising candidates in this step are assumed to contain the final optimal candidates and are thus kept as promising regions.

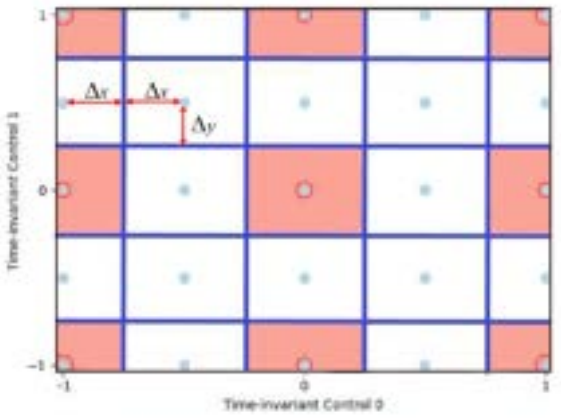

Figure 4: Partitioning of the design space into regions of length given by Δx and Δy. Promising regions are shaded in red.

Refinement

To pinpoint the optimal candidates, the problem is resolved with candidates enumerated only within the promis-

ing regions. The number of enumerated points within a promising region is consistent throughout the entire design space. This number is given by a user-specified reiteration sub-levels. Figure 5 is the second iteration, showing re-enumeration in the promising regions with user-specified sub-levels = [3,3].

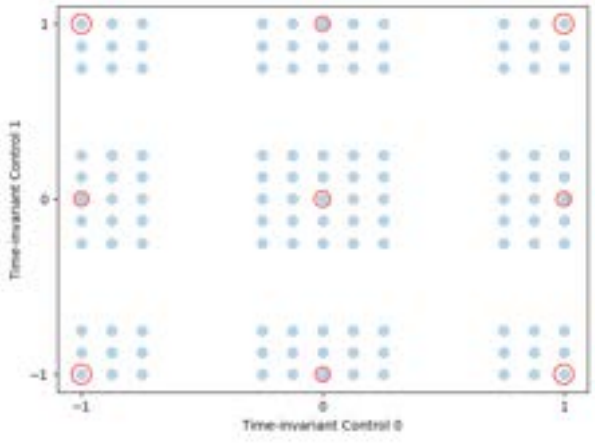

Figure 5: Second iteration following initialisation. New candidates are only enumerated in promising regions from figure 4

It can be seen that the original problem has now been divided into smaller subproblems. The number of candidates enumerated in figures 3 and 5 are both significantly less than in figure 1. This process is repeated, where each promising area is further partitioned, new Δs are calculated and a new set of promising regions defined. Candidates are again enumerated within smaller promising regions and they become more densely packed. The process is repeated until the candidate density is equivalent to the desired precision. This is detected when Δ becomes less than the user-specified termination range in all dimensions.

User-Defined Features

There is some flexibility allowed for users to tailor the algorithm to their needs.

1. TIC variable bounds – Bounds of the time-independent control variables. These are automatically normalized to be between [-1,1]
2. Termination range – Using their experience and perception, users can input comfortable values where the algorithm terminates. For example, this can be the range of experimental uncertainty. If not declared, the algorithm will take the default values to be 5% of the respective dimension ranges.
3. Sub-levels – Sub-levels are the levels for promising regions. Users can choose how densely they want to enumerate within the promising areas depending on the time available and computer capabilities. The default sub-level for all dimensions is 3.
4. User iteration – An alternative termination condition. Users can choose to run the algorithm for a certain number of iterations of their choice.
5. User candidates – Users are allowed to input candidates to be enumerated in all iterations
6. Showing plots – This is a choice between plotting figures for each iteration or only the final results.

Summary

The summary for the iterative equipartition algorithm is presented in the flowchart below.

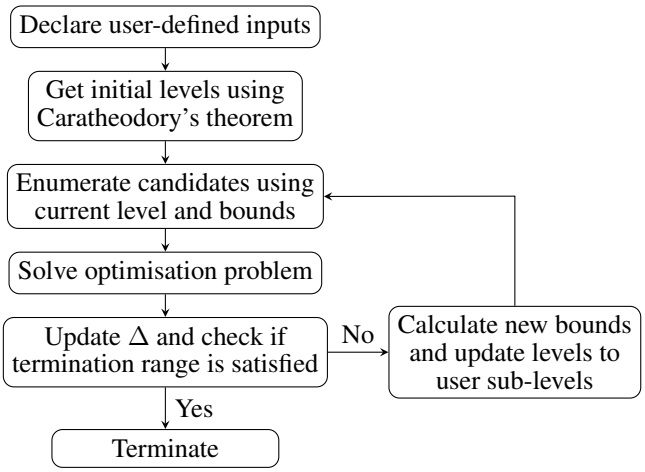

3.2 Method 2: Quasi-Random Sampling

Quasi-random sampling (QRS) differs from both brute force and equipartition in that the candidates are generated from low-discrepancy Halton sequences and are therefore unstructured. Consequently, the subregions within the design space are non-symmetric and challenging to identify. This algorithm is designed for increased robustness and proposed for RSM models above 5 dimensions as well as ODE models.

Initialisation

In QRS, the promising regions are identified through clustering of the promising candidates. The number of candidates enumerated in the first iteration is given by the upper bound d of Caratheodory's theorem as shown in equation 7. These are generated from the Halton sequence using the probability library of tensorflow (Martín Abadi et al. 2015). The results from the first iteration is shown below for model 6.

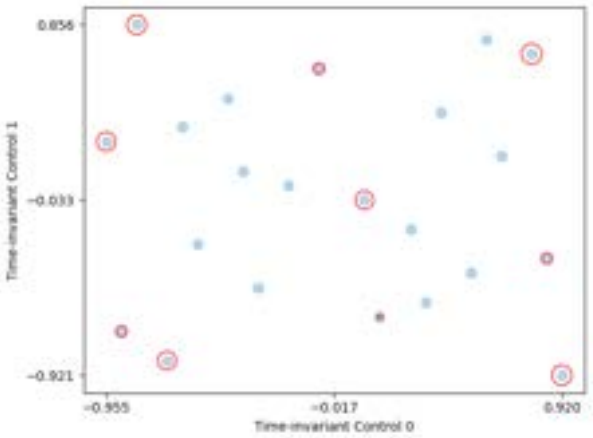

Figure 6: First iteration of the QRS initialisation phase showing non-uniform candidates. Of the 22 candidates enumerated, 10 are chosen as promising.

In each subsequent iteration, the number of new candidates generated is equal to the number of candidates enumerated in the previous iteration. These additional points are generated based on the ensuing Halton sequence elements from the previous iteration. Therefore, the total number of candidates in each new iteration is double the previous, with half of them kept from the previous iteration. The promising candidates in each iteration is stored. Using the above example, a plot of the second iteration and a table showing the course of candidate enumeration are shown below.

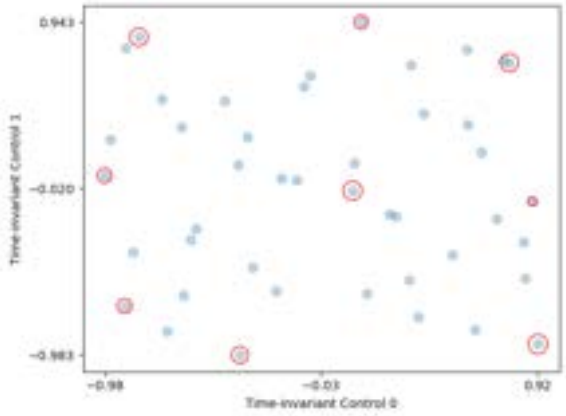

Figure 7: Second iteration of the QRS initialisation phase.

Table 2: Candidate properties in the first and second iterations.

Candidate Properties	Iteration 1	Iteration 2
Number of candidates enumerated	22	44
Number of new candidates	0	22
Halton sequence element	1 to 22	23 to 44

The termination condition depends on the rate of improvement of objective function values (OFV) between each iteration. It has been found that huge improvements in promising region location is reflected by large increases in OFV. The initialisation phase ends once there is no significant change in the OFV with each iteration. This point of diminishing returns is called a knee point and the method for detecting this is python package of the 'Kneedle' algorithm (Satopaa et al. 2011). Initialisation terminates once a consistent knee point is detected.

By the end of initialisation, promising candidates from all iterations have been compiled and promising clusters can be observed as shown in figure 8.

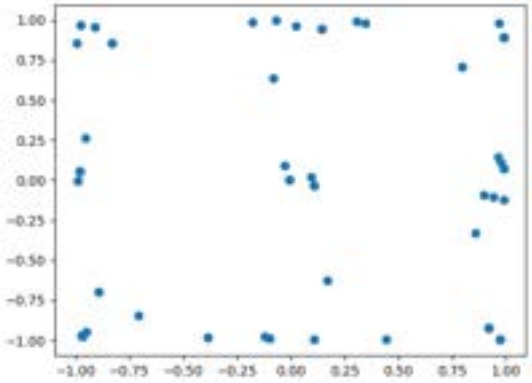

Figure 8: Promising clusters at the end of QRS initialisation. Unpromising candidates have been removed for clarity.

Refinement

In the refinement phase, identificantion of the promising regions from promising clusters is done through Voronoi tessellation. This is done using the Voronoi function in the scipy spatial library (Virtanen et al. 2020). These diagrams are drawn, with the candidates from the final initialisation iteration as centroids.

For the Voronoi regions enclosing a promising candidate, an outer bounding box is drawn surrounding these promising regions and their neighbours. The lengths, Δs, of this box are determined by the furthest vertices of the associated Voronoi regions in each dimension. An example of how a bounding box is drawn around promising Voronoi regions and their neighbours is shown in figure 9.

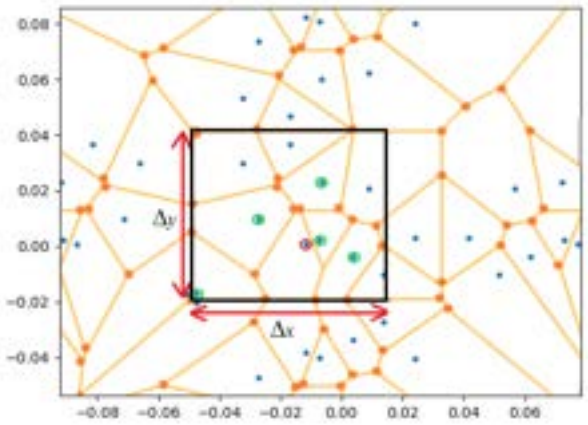

Figure 9: A snippet of a Voronoi diagram and the new bounding box in black.

In figure 9, the red circle around a blue dot indicates a promising candidate, the green circles highlight the neighbours of the promising candidates and the black box is the bounding box for this promising region. The vertices of the Voronoi regions are represented by orange dots.

New candidates are enumerated within this bounding box and the optimisation problem is solved again to obtain new promising candidates. New Voronoi regions and their corresponding bounding boxes are redrawn and this process is repeated until the Δs have been reduced to less than the termination ranges in all dimensions. The termination range is again based on the user-desired precision.

QRS Implementation for ODE Models

Two different methods of OED for ODE models are considered. In the first case, it is assumed that the practitioner is able to monitor the variables of interest at all times throughout the experiment. These OED problems can be solved without any modifications to the QRS algorithm. In the second case, it is assumed that samples can only be taken at one moment in time over the course of an experiment. This is often the case for chemical reaction experiments conducted as batch processes. Optimising for the right sampling time is therefore necessary for optimal design. For QRS, the sampling times are treated simply as an additional TIC and this increases the design space by one dimension.

User-Defined Features

Below are available customisation of the algorithm.

1. TIC variable bounds – See section 3.1.
2. Termination range – See section 3.1.
3. Showing plots – See section 3.1.
4. Refinement – Users can choose to terminate the algorithm after initialisation before the refinement phase.
5. Refinement neighbours – Users can alter the extent of neighbouring points included in the bounding box. For instance, a neighbour value of 1 means that only direct neighbours of the promising candidate are considered. A value of 2 would include the neighbours of these direct neighbours as well.
6. Optimise sampling times – For ODE models, users can choose to optimise sampling times.

Summary

The iterative quasi-random sampling algorithm is summarised in the following flowchart.

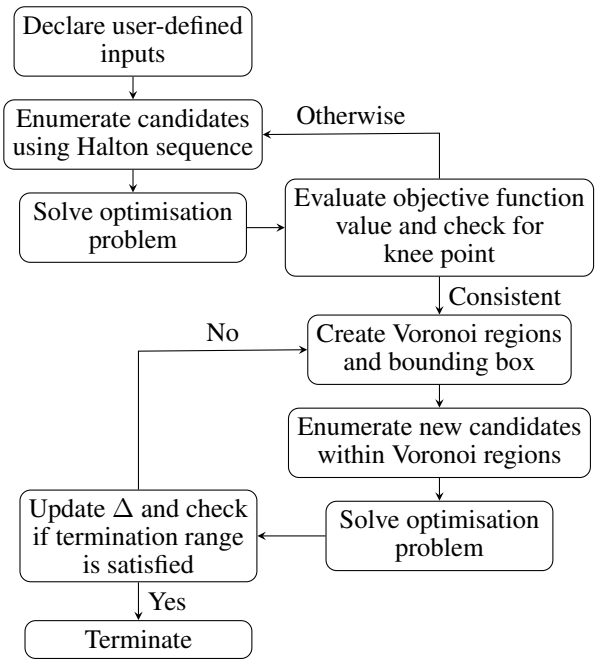

3.3 Algorithm Features

Halton Sequence

The main benefit of low-discrepancy sequences (LDS) over grid-based enumeration techniques is that an arbitrary number of candidates can be generated for design spaces of any dimensions. Halton sequences is chosen over Latin-Hypercube due to its better space filling properties (Guinta, Wojtkiewicz, and Eldred 2003). There is also an ease of computation as there is no need to recompute the entire sequence between each iteration. This is because the next elements in a Halton sequence can be computed without knowledge of the previous elements (Niederreiter 1992). Although studies have shown that Halton sequences perform worse at higher dimensions due to linear correlation issues, the number of dimensions this occurs at ($\approx$ 30) is typically not a concern for experimental design problems ("Randomized Halton sequences" 2000).

Kneedle - Knee Point Termination

The Kneedle algorithm is selected as it has a significantly lower latency for knee detection, as compared to other online knee detection methods such as the exponentially weighted moving average algorithm (Satopaa et al. 2011). Applied to QRS, the initialisation phase ideally terminates after the detection of a consistent knee point.

Alternative termination conditions that have been explored are as follows. The first was to compare the Hausdorff distances between promising candidates in each iteration and terminating once a number of unexpected increases or 'peaks' are detected. Another criterion explored was tracking the number of promising candidates and terminating once this number remains consistent for a certain amount of iterations. However, the performances of these were found to be very dependant on the model and hence, cannot be applied universally.

Voronoi Regions

A challenge when using the scipy spatial Voronoi library was trying to get the Voronoi regions defined within the TIC bounds in the first iteration, and subsequently, within promising regions. To overcome this, a pseudo bounding-box was generated by reflecting the relevant candidates across the intended bounding box. This generated Voronoi regions whose edges make up the bounding box boundaries. This is illustrated in figure 10, where an orange, rectangular bounding box formed by Voronoi edges can be observed.

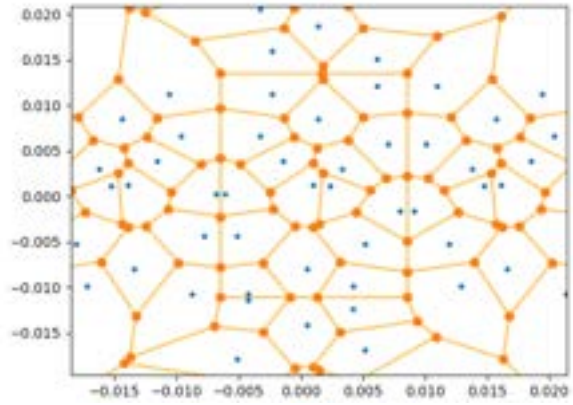

Figure 10: A snippet of a Voronoi diagram containing a pseudo-bounding box.

4 Results and Discussion

4.1 OED for RSM Models

Response surface methodology (RSM) is an assembly of statistical and mathematical tools developed by Box and Behnken in the 1950s. RSM models are used in many industries for product and process optimisation. For example, RSM can be used to optimise various food-related operations such as drying and blanching (Yolmeh M. 2017). In the pharmaceutical industry, RSM has the potential to improve drug ingestion by monitoring drug characteristics such as hardness, friability and effervescent time (A.P.K. et al. 2020).

A multitude of models were used to assess algorithm performance and similar patterns were observed. Two models are presented in this report to highlight these patterns. The first is a fourth order, non-linear, 2D model:

$$y = \theta_0 + \theta_1(x_0) + \theta_2(x_1) + \theta_3(x_0)(x_1) + \theta_4(x_0)^2 + \theta_5(x_1)^2 + \theta_6(x_0)^2(x_1) + \theta_7(x_1)^2(x_0) + \theta_8(x_0)^3 + \theta_9(x_1)^3 + \theta_{10}(x_0)^3(x_1) + \theta_{11}(x_1)^3(x_0) + \theta_{12}(x_0)^2(x_1)^2 + \theta_{13}(x_0)^4(x_1)^4$$

The second is a second order, non-linear, 3D model:

$$y = \theta_0 + \theta_1(x_0) + \theta_2(x_1) + \theta_3(x_2) + \theta_4(x_0)(x_1) + \theta_5(x_0)(x_2) + \theta_6(x_1)(x_2) + \theta_7(x_0)^2 + \theta_8(x_1)^2 + \theta_9(x_2)^2$$

Higher-dimensional models are not used to present the results as graphical illustrations are not available for those. The solving time is measured using the Time package on Python and taken as an average of 5 runs.

All the optimisation in this section is carried out using the D-optimality criterion. From equation 4:

$$\phi = log(det(\mathbf{M})) \tag{8}$$

Results from 2D Model

Below is a table of results detailing the total number of candidates enumerated over all iterations as well as the total time taken to solve, for the three algorithms considered - brute force (as control), equipartition and quasi-random sampling. All 3 were solved to a precision of 1% of the design space range in all dimensions. Figures from the final iterations are also included with the final objective function values (OFV) given in the captions.

Table 3: Total number of candidates enumerated over all iterations and time taken for 2D RSM model.

Results	BF	EQ	QRS
Total candidates	10,201	1,233	9,680
Time taken (s)	750	55	1,000

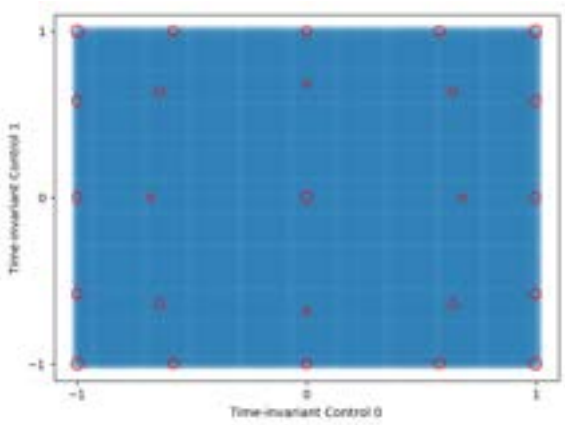

)

Figure 11: Optimal candidates using BF. OFV = -37.009.

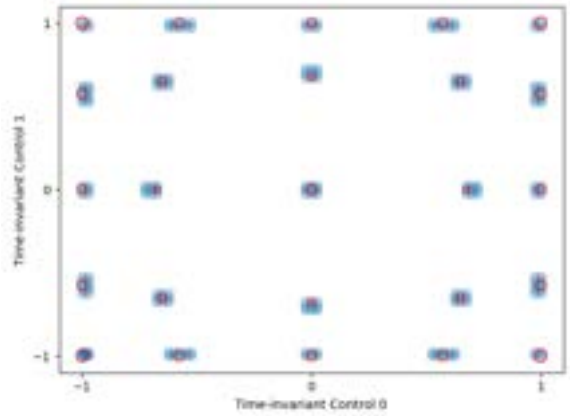

Figure 12: Optimal candidates using EQ. OFV = -37.010.

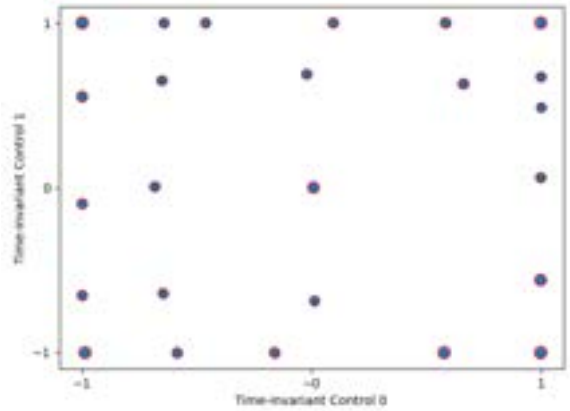

Figure 13: Optimal candidates using QRS. OFV = -37.290.

It is observed that the BF and EQ algorithms provide the same design with insignificant difference in OFV. QRS was found to be inferior in this case. Comparing figures 13 and 11 shows that QRS misses 2 optimal candidates, and the positions of the detected candidates are slightly off. Splitting of efforts between optimal candidates is seen in the top left and right corners. In addition, a symmetrical distortion from the center is seen for the top- and bottom- centre points. This may happen due to the randomness in candidate enumeration, resulting in them being very close to, but not exactly at the optimal solution. All these factors led to a lower OFV.

Results from 3D Model

Below is a table of results for the 3D model as well as figures from the final iterations. Brute force enumeration was solved to a precision of 5%. At 1%, 1,030,301 candidates need to be enumerated, making the problem infeasible due to memory limitations of a personal computer. The other two algorithms were solved to a precision of 1% and final OFVs are provided in the figure captions.

Table 4: Total number of candidates enumerated over all iterations and time taken for 3D RSM model.

Results	BF	EQ	QRS
Total candidates	9,261	2,019	32,281
Time taken (s)	450	60	8,000

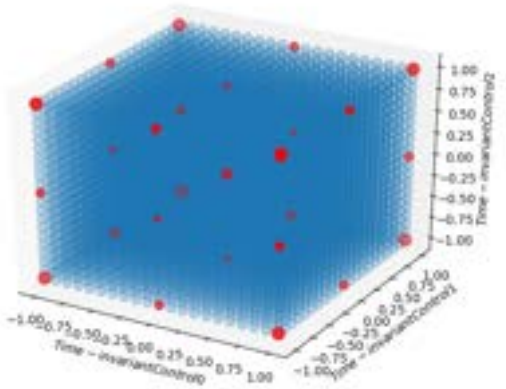

Figure 14: Optimal candidates using BF. OFV = -7.455.

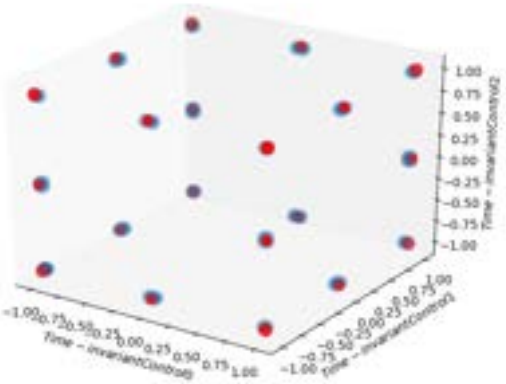

Figure 15: Optimal candidates using EQ. OFV = -7.831.

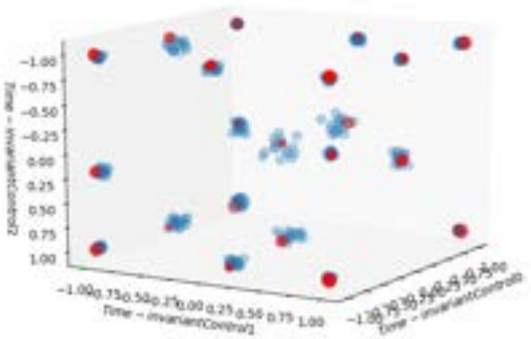

Figure 16: Optimal candidates using QRS. OFV = -7.709.

Locations of the solutions to brute force and EQ are exactly the same for enumerated candidates. However, 7 'missing' points is seen for EQ, and these are located at the centre of the cube faces. As before, QRS failed to

provide all optimal candidates, only 21 out of 27 were found. However, in this case, it managed to outperform EQ in terms of OFV.

Discussion

Comparing EQ to BF, the same design can be obtained with significantly less time. However, issues with 'missing' points may arise. This happens when candidates are not generated near enough to the actual optimal solutions and hence, Pydex is not able to pick up on these. A crude way of fixing this is by introducing user-chosen points to the set of experimental candidates. This may be useful when users have a vague idea of the optimal design. Additionally, the EQ algorithm can also be altered to ensure odd-numbered levels during initialisation so that the centre candidates are always enumerated.

Comparing QRS to BF and EQ, the former performs considerably worse than the latter two in terms of time taken. With regards to result accuracy, the QRS algorithm is at a disadvantage compared to grid based enumeration. OED for RSM are often found at the extremities of TICs as the sensitivities are greatest at these points. Solutions to low-dimensional RSM models are therefore typically symmetrical with optimal candidates at the corners, centres and edges. As candidates in QRS are synthesised using quasi-random sampling methods, it is impossible to generate candidates exactly at these points. One potential strategy of improving the accuracy of QRS is to increase the bounding box sizes in each iteration by including the neighbours of the direct neighbours. This can be done by increasing the user-defined neighbour option in the model definition Python script. This has the effect of increasing the OFV from -37.290 to -37.087 for the 2D model. Conversely, the value was reduced from -7.709 to -7.799 in the 3D model. Hence, it can be concluded that this is not a sure-fire way of fixing the problem and the strategy needs to be adopted with caution.

With regards to efficiency, logically, the higher the number of candidates enumerated, the longer the time taken. However, it can be observed that QRS may take longer to solve even when the number of candidates generated is less, as seen in table 3. This is because between each enumeration, QRS takes time to generate the Halton sequences and Voronoi diagrams. The cost of these outweighs the gains of solving a smaller CE problem.

BF enumeration has been found to produce optimal candidates with low efforts. With QRS or EQ, promising regions with optimal candidates of efforts below a user-defined tolerance are discarded during the iterations. This could be another reasoning behind the 'missing' optimal candidates. However, this might not be an issue if an equivalently high OFV is obtained. This could potentially be desirable as an equivalently good OED with less candidates means a smaller number of unique experiments, leading to a reduction in both time and resource needed.

As the dimensions of the design space increases, the initialisation phase of EQ becomes more and more computationally expensive as more candidates need to be generated. Eventually, QRS may become the only viable solution to the problem. Hence, for RSM models, it is proposed to implement equipartition at lower dimensions (e.g. below 5D), and QRS above this threshold. However, it is important to note the dependence of the algorithms on the performances of the 'library' and the 'optimiser' outsourced to solve the problem.

4.2 QRS for ODE Systems

Developing good ordinary differential equation (ODE) models are essential for many industries. They are used, in particular, in the pharmaceutical industry to describe chemical kinetics in batch reaction processes. OED aims to design experiments to maximise information on the reaction parameters. Two different ODE models based on chemical kinetics were tested for the proposed algorithms. The first (case 1) is a model of a first order irreversible reaction with one reactant A:

$$\frac{dC_A}{dt} = \theta_0 C_A \tag{9}$$

The TIC set by the user is the initial concentration of A, C_{A0}. The second (case 2) is a model based on a reversible reaction with 2 reactants, A and B, where the rate of reaction is given by:

$$\frac{dC_A}{dt} = \theta_0 e^{-\frac{\theta_1}{RT}} C_A^{\theta_2} C_B \tag{10}$$

$$\frac{dC_B}{dt} = -\theta_3 \frac{dC_A}{dt} \tag{11}$$

The TIC for experimental design in this model is the initial concentration of A, C_{A0}, and the temperature, T. Here, both optimising and non-optimising of sampling times are considered (OST).

ODE Results and Discussion

For all cases, the desired precision has been set to 0.01 of the design space range. Table 5 shows the results obtained from both case studies. Attempting to solve case 2 to the desired precision through brute force was not feasible on a personal computer. A precision of 0.05 of the design space was used instead.

In the case 1 model, it has been found that the QRS algorithm has a significantly longer run-time than brute force enumeration. The bottleneck-step in QRS is solving a problem with 2,560 candidates with 1 sampling time candidate each, while the brute force method is solving a problem with 101 candidates, each having 101 sam-

Table 5: Results obtained from designing optimal experiments for both Case 1 and Case 2 models using Bruteforce and QRS.

	Case 1		**Case 2 (Without OST)**		**Case 2 (With OST)**	
	BF	QRS	BF	QRS	BF	QRS
Candidates	[5,4.04]	[4.998,3.97]	[3.32, 273.15] [3.32, 373.15] [5, 273.15] [5, 323.15]	[3.43, 273.15] [3.44, 273.15] [3.45, 273.15] [4.99, 273.15] [4.99, 322.29]	[3.32, 273.15, 1] [3.53, 323.15, 1] [5, 273.15, 1] [5, 323.15, 0.45] [5, 323.15, 1]	[3.317, 274.4, 0.98] [4.98, 321.97, 0.99] [4.968, 274.86, 0.99] [4.989, 274.85, 0.77]
Objective Values	54.186	54.10	-30.46	-30.23	-27.68	-27.98
Time (s)	58	446	302	109	209	179

pling time candidates. When solving an OED problem the computational cost of sensitivity analysis is associated with the number of candidates while optimisation cost is dependent on the number of sampling time candidates. QRS thus increases cost for sensitivity analysis in hopes of winning it back through a decrease in cost for optimisation. However, this problem is exacerbated due to limitations with the implementation method of Pydex and the developed algorithm. Redundant calculations are done during sensitivity analysis where the sensitivities of all candidates are recalculated each iteration, even though half of these are already available from the previous iteration. The accuracy of the final results produced by both algorithms are comparable as both candidate locations and objective function values (OFV) are very similar.

In case 2, the upsides of the developed algorithm is more prevalent as the problem is solved in a shorter timeframe. The accuracy of results are also adequate when comparing both candidate locations and OFV to each other. However, a missing point at around [3.3, 323.15] as well as split efforts around the point [3.3, 273.15] can be seen. When optimizing for sampling times the points [3.53, 323.15, 1] and [5, 323.15, 1] are missing while the position of the point [4.989, 274.85, 0.77] appears to have shifted insignificantly in terms of sampling time. The lower objective function value can be explained by the fact the best experimental candidates are on the bounds of the design space (max T, min T and max C_{A0}) and thus, disadvantages the QRS algorithm as mentioned in section 4.1.

5 Conclusion

This paper has presented two potential solutions to the computationally taxing brute force approach to candidate enumeration. Generally, the algorithms introduced are shown to be promising. However, further development is needed before they are applicable to real-world problems.

From the two RSM case studies, equipartition is found to be comparable to brute force in terms of solution precision. It also outperforms brute force in terms on efficiency and speed. However, an issue with 'missing' points may come up in higher dimensions due to low initialisation density. Hence, caution must be exercised when running the algorithm at higher dimensions.

QRS was found to perform worse for RSM models due to low efficiency. Issues regarding missing points, splitting efforts as well as shifts in candidate locations have been noticed. For models with symmetrical optimal points located at the bounds of the design space, QRS is at a disadvantage as it is difficult to enumerate candidates precisely at these extremes. For ODE models, it was found that QRS is able to obtain comparable solutions in a shorter amount of time.

Generally, at higher dimensions, QRS may be the only viable solution and is thus concluded as the more promising algorithm.

6 Limitations and Outlook

Over the course of the project, several issues linked to algorithm efficiency and universal functionality of QRS were identified. Given the time constraints imposed, these were not acted upon but only discussed as below.

6.1 Algorithm Efficiency

The key objective for developing these algorithms in the first place was to improve upon the efficiency of current methods without foregoing precision. Although the two algorithms introduced have been observed to be promising within this respect, more can be done to further boost efficiency. Two efficiency-limiting factors were identified - high numbers of enumeration in QRS initialisation and expensive computation of Voronoi diagram generation.

Potential for Iteration Reduction in QRS Initialisation

One direction to explore is alternative sampling methods that could decrease convergence time in identifying the promising regions. Poisson disc sampling (PDS) is a promising alternative due to its increased uniformity. However, PDS executes poorly at lower number of points and incurs high computing cost (Bridson 2007).

Sufficient accuracy of the clusters obtained during initialisation is essential for algorithm success. However, due to the current doubling of candidates, each new iteration in initialisation becomes more computationally taxing. Decreasing this doubling ratio may reduce the maximum number of candidates enumerated in one iteration, but will lead to an increase in the number of total initialisation iterations. Instead, a'dynamic growth' model can be adopted where candidates are doubled (or more) initially and the rate of candidate growth is decreased subsequently depending on certain conditions.

Another strategy is to enumerate new candidates based on results from previous iterations. A crude way of doing this is by modifying QRS into a 'hybrid' algorithm where the distinction between initialisation and refinement is made loose. Here, refinement is carried out between each iteration in initialisation. The downside to this is that the aspect of even distribution in the overall design space is lost. A more complex but elegant approach could be the Markov Chain Monte Carlo Methods (Schwedes and Calderhead 2018) where the probability of generating new candidates in promising regions is higher than in unpromising regions. However, it is yet to be seen if such methods will improve convergence during initialisation and if the increased computational costs for candidate generation are justified.

Efficient Identification of Promising Regions

It has been found that the computation of Voronoi diagrams, especially in higher dimensions, is both time-consuming and memory-intensive. This could be because the number of vertices in Voronoi regions increases exponentially with the number of dimensions. The current approach of adding additional, artificially generated points to compute the bounding boxes only worsens the issue. Switching over from a vertex representation to an h-representation of polytopes removes the need for these artificial points. This might allow for easier computation of the boundaries which might improve overall computational efficiency (Tereshchenko, Chevokin, and Fisunenko 2013).

An alternative to detecting promising regions could be k-means clustering (VanderPlas n.d.). The bounding boxes of the promising regions for each cluster can be drawn using the minimum and maximum of candidate coordinates in all dimensions. The number of clusters can be detected by using a similar approach to 'Kneedle' with an initial lower bound given by the minimum number of initialising promising candidates (Mahendru n.d.). This is expected to reduce computational cost as computations are only performed on the augmented list of promising candidates from the initialisation run.

Reducing Memory Consumption

It was found that solving the same optimisation problem sequentially is memory-intensive with 'MOSEK'. The solver did not free up memory between each new iteration as expected. This highlights the strong dependence on outsourced libraries.

6.2 Expanding Functionality

As it stands, the algorithms introduced can only be applied to a limited scope of problems. Potential strategies for expanding this scope are discussed below.

Multiple Sampling Times

Optimisation of multiple sampling times is originally proposed to be treated as additional dimensions in the design space. However, two points that are very different geometrically may produce the same sampling time combination. For example, the points [0,1] and [1,0] which are different geometrically, results in the same combination of sampling time candidates.

Expansion to Non-Convex, Arbitrary Design Spaces

It would be likely to extend the functionality of these algorithms for the optimal design of experiments in arbitrary design spaces. To do this, it might be necessary to first develop a smart sampling methods for non-structured, high-dimensional design spaces. Algorithms have been developed for Poisson-disc sampling methods which can be used for enumerating candidates within the arbitrary design space (Quan et al. 2016).

Utilising the Atomic Information Matrix

The atomic information matrix (AIM) can be potentially be used as an indication of the locations of optimal candidates.

7 Acknowledgements

We thank Kennedy Kusumo for his guidance throughout the past 3 months. Our insightful discussions have taught us much and helped developed the algorithms we have today.

References

A.P.K., Mahapatra et al. (2020). "Application of response surface methodology (RSM) in statistical optimization and pharmaceutical characterization of a patient compliance effervescent tablet formulation of an antiepileptic drug levetiracetam". In: *Futur J Pharm Sci*. DOI: https://doi.org/10.1186/s43094-020-00096-0.

Atkinson, A. C. (1996). "The Usefulness of Optimum Experimental Designs". In: *Journal of the Royal Statistical Society. Series B (Methodological)* 58.1, pp. 59–76. ISSN: 00359246. URL: http://www.jstor.org/stable/2346165.

Bridson, Robert (2007). "Fast Poisson Disk Sampling in Arbitrary Dimensions". In: *ACM SIGGRAPH 2007 Sketches*. SIGGRAPH '07. San Diego, California: Association for Computing Machinery, 22–es. ISBN: 9781450347266. DOI: 10.1145/1278780.1278807. URL: https://doi.org/10.1145/1278780.1278807.

Franceschini, Gaia and Sandro Macchietto (Oct. 2008). "Macchietto, S.: Model-based design of experiments for parameter precision: State of the art. Chemical Engineering Science 63(19), 4846-4872". In: *Chemical Engineering Science* 63, pp. 4846–4872. DOI: 10.1016/j.ces.2007.11.034.

Guinta, Anthony A., Steven F. Wojtkiewicz, and Michael S. Eldred (2003). "Overview of Modern Design of Experiments Methods for Computational Simulations". In: DOI: 10.2514/6.2003-649.

Iman, Ronald and M.J. Shortencarier (Mar. 1984). "Fortran 77 program and user's guide for the generation of Latin hypercube and random samples for use with computer models". In:

Koehler, "J.R. and A.B. Owen" (1996). "9 Computer experiments". In: *Design and Analysis of Experiments*. Vol. 13. Handbook of Statistics. Elsevier, pp. 261–308. DOI: https://doi.org/10.1016/S0169-7161(96)13011-X. URL: http://www.sciencedirect.com/science/article/pii/S016971619613011X.

Kusumo, Kennedy (2020). *pydex*. URL: https://pypi.org/project/pydex/.

Mahendru, Khyati (n.d.). *How to Determine the Optimal K for K-Means*. URL: https://medium.com/analytics-vidhya/how-to-determine-the-optimal-k-for-k-means-708505d204eb. (accessed: 09/12/2020).

Martín Abadi et al. (2015). *TensorFlow: Large-Scale Machine Learning on Heterogeneous Systems*. Software available from tensorflow.org. URL: https://www.tensorflow.org/probability/api_docs/python/tfp/mcmc/sample_halton_sequence.

Metropolis, Nicholas and Stanislaw Ulman (1949). "The Monte Carlo Method". In: *Journal of The American Statistical Association* 44.

Niederreiter, Harald (1992). "Random Number Generator and Quasi-Monte Carlo Methods". In:

Quan, Weize et al. (2016). "Maximal Poisson-Disk Sampling via Sampling Radius Optimization". In: *SIGGRAPH ASIA 2016 Posters*. SA '16. Macau: Association for Computing Machinery. ISBN: 9781450345408. DOI: 10.1145/3005274.3005281. URL: https://doi.org/10.1145/3005274.3005281.

"Randomized Halton sequences" (2000). In: *Mathematical and Computer Modelling* 32.7, pp. 887–899. ISSN: 0895-7177. DOI: https://doi.org/10.1016/S0895-7177(00)00178-3.

Satopaa, V. et al. (2011). "Finding a "Kneedle" in a Haystack: Detecting Knee Points in System Behavior". In: *2011 31st International Conference on Distributed Computing Systems Workshops*, pp. 166–171. DOI: 10.1109/ICDCSW.2011.20.

Schwedes, Tobias and Ben Calderhead (2018). *Quasi Markov Chain Monte Carlo Methods*. arXiv: 1807.00070 [math.ST].

Tereshchenko, Vasyl, Sergii Chevokin, and Andriy Fisunenko (2013). "Algorithm for Finding the Domain Intersection of a Set of Polytopes". In: *Procedia Computer Science* 18, pp. 459–464. ISSN: 1877-0509. DOI: https://doi.org/10.1016/j.procs.2013.05.209. URL: http://www.sciencedirect.com/science/article/pii/S1877050913003529.

VanderPlas, Jake (n.d.). *In Depth: K-Means Clustering*. URL: https://jakevdp.github.io/PythonDataScienceHandbook/05.11-k-means.html. (accessed: 09/12/2020).

Virtanen, Pauli et al. (2020). "SciPy 1.0: Fundamental Algorithms for Scientific Computing in Python". In: *Nature Methods* 17, pp. 261–272. DOI: 10.1038/s41592-019-0686-2.

Yolmeh M., Jafari S.M. (2017). "Applications of Response Surface Methodology in the Food Industry Processes". In: *Food Bioprocess Technol*. DOI: https://doi.org/10.1007/s11947-016-1855-2.

The Impact of Supply Chain Modelling Decisions and Policies on the Effectiveness of England's COVID-19 Supply Chain

Thanat Wongwaisayawan and Chen Horng Tan
Department of Chemical Engineering, Imperial College London, U.K.

Abstract—

The COVID-19 pandemic continues to devastate the entire world with its catastrophic effect, claiming the lives of millions of people [1]. To solve the global pandemic, pharmaceutical companies had invested millions of dollars into the development of a COVID-19 vaccine. However, the scale of the supply chain and effort required to vaccinate the entire global population would become a major problem. This paper aims to understand how different supply chain modelling approaches can maximise the vaccine availability and minimise the vial spoiled using 3 separate experiments. These experiments being: the implementation of a prioritisation and scheduling policy, removal of a supply chain layer and the implementation of a secondary vaccine into the supply chain (Pfizer's BNT162b2 vaccine). These experiments will be implemented onto a base model, an ideal four-level supply chain, supplying the ChAdOx1 [2] candidate vaccine. The Highly Extensible Resource for Modelling Event-driven Supply chains (HERMES) software will be utilised to simulate the base model and explore the three scenarios. It was observed that the effectiveness of a vaccine prioritisation and scheduling to each group was dependant on the ratio of the actual population between each group. Moreover, the removal of a supply chain layer proved to be effective in decreasing the vaccine spoilage by decreasing storage and transit duration. Furthermore, the addition of a new vaccine into the supply chain proved to be successful, given that the storage within the already existing infrastructure was able to accommodate the increased supply. The results of these experiments can serve as a guideline for predicting the effects of macro changes to the COVID-19 supply chain.

1. INTRODUCTION

A new coronavirus disease (COVID-19) was first discovered in Wuhan, China, when an unusual cluster of pneumonia cases was discovered and reported in the Hubei Province in December 2019 [3]. COVID-19 is highly contagious and the infected individuals may not show any symptoms up to 14 days after being exposed it [3]. The delayed symptoms or sometimes asymptomatic causes the control and prevention of the spread of the virus to be incredibly difficult. This resulted in multiple lockdowns throughout the world, including two nationwide lockdowns within the United Kingdom. As COVID-19 continues to appear in many places in the world, the World Health Organization (WHO) declared the outbreak of COVID-19 a pandemic on the 11^{th} of March 2020 [3]. Lockdowns were detrimental to the economy, with risks of a global recession in the first quarter and a projected average global GDP growth of -4.9%, -10% for the UK [4]. To date, there are more than 70 million coronavirus cases worldwide with around 2.2% death rate [1]. The loss of fellow citizens and the economic downturn brought upon a worldwide effort to discover an effective vaccine to stop the COVID-19 pandemic.

Since the discovery of the new coronavirus, scientists and researchers have been working profusely to develop potential COVID-19 vaccines. As of September 2020, there are 321 vaccine candidates under development and of these, some candidates have made it to the phase three of clinical trials, showing varying degrees of success [5]. Out of the candidate vaccines, three shows the most potential; the ChAdOx1 nCoV-19 (University of Oxford and AstraZeneca), mRNA-1273 (Moderna and the National Institutes of Health), and BNT162b2 (Pfizer and BioNTech) [2].

Due to the promising outlook of some candidate vaccines, the UK had entered negotiations and ordered differing amounts of vaccines from different companies. According to the Department of Health and Social Care [6], the UK had secured early access to 355 million doses of vaccine. These vaccines include:

- Oxford / AstraZeneca : 100 million doses
- Novavax : 60 million doses
- BioNTech / Pfizer : 40 million doses
- Moderna : 5 million doses
- Janssen : 30 million doses
- GSK / Sanofi Pasteur : 60 million doses
- Valneva : 60 million doses

This paper aims to simulate a possible COVID-19 vaccine supply chain networks within England. Multiple experiments will be done to investigate the effects of making structural changes, implementation of prioritisation schedules and introduction of new vaccine into existing models, with the focus on optimising the vaccine availability and spoilage.

2. METHODOLOGY

2.1 Overview

The Highly Extensible Resource for Modelling Event-driven Supply chains (HERMES) was utilised to model and simulate the COVID-19 vaccine supply chain of England. Key components were sourced and inputted into the HERMES model chain. For example, transportation routes (with specified vehicle type, push supply policy, and exact distances between locations), storage facilities (including fridges and freezers) and 1200 Healthcare Center geographical locations [7]. HERMES was able to model the effects of varying multiple parameters on the cost and efficiency of the supply chain, enabling the macro visualisation of the supply chain. Multiple scenarios such as the removal of supply chains levels, addition of a second vaccine and scheduling policies were experimented on to the model. Due to the unforeseeable nature of the COVID-19 pandemic, data and literature related to vaccine supply chain in England is limited and scarce. To overcome this, an ideal case was simulated, acting as a "base" case.

Two ideal base cases was explored. These two cases utilised the same assumptions, only differing in the transport policy and the resulting optimised cold storage allocation. The first case had a transport frequency of once a month, whilst the second case had a transport frequency of twice a month. These models was referred to as the Base One and Base Two models. These models were tasked to administer the AstraZeneca's ChAdOx1 candidate vaccine to the entire population of England, aged 18 and above, within a period of one year. Three experiments were implemented on to the "base" cases. Firstly, effects of prioritisation and scheduling of was explored. Secondly, experiments to observe the effect of removing supply chain levels were done, decreasing the four-level to three-level. Finally, due to the success of Pfizer's BNT162b2 vaccine, with a 95% effectiveness [8] rate, the UK has started to roll out 800,000 doses [9] of the vaccine to front line workers and those at risk. Therefore, the third experiment explored the effect of adding the Pfizer vaccine to the existing supply chain.

2.2 Summary of Key Assumptions

1) Those aged 18 and above will be vaccinated within the period of one year.
2) The structures of the base models were assumed to have four separate levels.
3) Administration occurs only at the bottom most layer and upper layer will act as distribution centers.
4) The manufacturer would supply exactly as demanded (Ideal case assumption).
5) Individuals will require two doses to become immunized [2].
6) The cold storage utilised at each location was within $+100L$ of the minimum required (Readily available fridges in the UK were found to come in increments of 100L [10]).
7) Healthcare Centers would operate 5 days per week (To reflect the in-hours working days of the NHS [11]).

Further elaborations of each assumption was done below.

2.3 England's Supply Chain Base Model

2.3.1 Structure

Figure 1 depicts the structure of the supply chain. The base structure was assumed to have four separate levels. The first level was assumed to be a National store, a storage facility that acts as the starting node which handles all deliveries from the manufacturer and delivers to lower level. This level was referred to as the "National" Level. The second level was assumed to be another distribution center. This was based on the existing 8 geographical regions with the addition of London. London is a highly populated area, where the magnitude of the population [12] is similar to that of the 8 regions, hence the inclusion of London in the second level of the supply chain. This level was referred to as the "Regional" level. The subsequent third level, was also assumed to be a distribution center. This level was based on metropolitan and non-metropolitan counties, unitary authorities, and London Boroughs, totalling 87 locations. This level was referred to as the "Local Government" level. The final level consisted of all the hospitals associated with the National Health Service (NHS), totalling 1200 locations [7]. This level acted as the only administration level of the supply chain and subsequently, this level was referred to as the "Healthcare Center" level. Furthermore, Healthcare Centers was assumed to operate 5 days per week [11] to reflect the normal operating hours of the National Health Service.

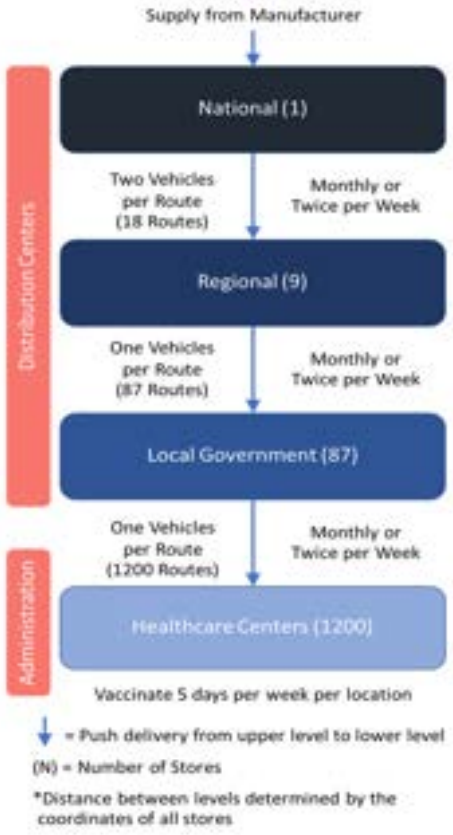

Figure 1: Structure and Brief Overview of the Supply Chain

2.3.2 Vaccine Specification

The ChAdOx1 vaccine was specified to be administered through intramuscular injection and each patient required two separate doses [13] to become fully immunised. The lifetime of the vaccine was specified to be 6 months in 2-8°C storage and when opened, would become spoiled in 6 hours [14]. The storage duration in freezers was not specified in HERMES as the long lifetime in normal fridge conditions of the ChAdOx1 deemed the usage of freezers to be redundant. So far, the specification on doses stored per vial, dosage volume, secondary packed volume and the dimensions of secondary packing has yet to be release by AstraZeneca. Hence it was assumed that each vials of vaccine was specified to carry 10 doses per vial and the secondary packing dimensions would follow the measurements for a typical 10-dose vial outlined by WHO [15], resulting in a packed volume of $5.2725cm^3$ per dose of vaccine and diluent. Furthermore, the price of the vaccine was assumed to be $3.69 per vial.

In the case of Pfizer's BNT162b2 vaccine, the storage conditions was much more extreme. The Pfizer vaccine has three separate storage lifetime and specification: the vaccine has a lifetime of up to 6 months with the usage of ultra-low temperature freezer (-70°C), 15 days in the Pfizer's thermal shippers and 5 days in 2-8°C fridges [16]. Moreover, each vial transported contained 5 doses of the vaccine [8]. Packaging specifications and dosage volume have not been released, hence it was assumed to be the same as that used in the ChAdOx1 vaccine.

2.3.3 Transport

Firstly, it was assumed that the manufacturer would supply exactly as demanded as this modelled the ideal case. Two transportation policies would be explored in the base case, transport frequency of once a month and twice a month. This would allow for the effects of transport frequency to be observed in all experiments. All levels would receive shipments from the above level (through the specification of a Route Type "push" in HERMES) on fixed schedule as seen from Figure 1. The usage of a fixed schedule was utilised to depict the situation with limited supply, where demand fetch supply was not feasible. Furthermore, transports only had 2-8 °C storage capabilities on board.

2.3.4 Demand

Only those aged 18 and above were considered due to the results of the phase 3 clinical trial [13], where it was deemed unsuitable to vaccinate those below 18. England's population data by counties and districts from the Office of National Statistics was used [12]. For simplicity, the population data was categorised into four groups, the Healthcare workers (HCW), the Senior Citizen (age 65 and above), the Adults (age 25-64) and the Young Adults (age 18-24). The overall population in each groups can be observed in Table 1. The two-dosage requirement of the vaccine resulted in a demand of over 88 million doses for the population. For simplicity, the demand at each Healthcare Center locations was the total demand within that county or district divided by the total number of Healthcare Center location within that county or district.

Table 1
Summary of Population Numbers and Percentage by Group [12, 17]

Group	Population	Percentage of Total Population (%)
HCW	1,321,704	3.0
Senior Citizens	9,759,778	22.1
Adults	28,285,508,	64.1
Young Adults	4,745,265	10.8
Total	**44,112,255**	100

2.3.5 Cold Storage

The 6 months lifetime of the ChAdOx1 vaccine in the temperature range of 2-8°C allowed the utilisation of normal refrigerators as the main means of storage. Hence, in all four levels of the base model, only 2-8°C cold storage equipment was utilised. However, due to the unprecedented nature of the pandemic, a clear list of cold storage facilities and allocation in each Healthcare Centers was not available. Therefore, for the purpose of this study, the minimum storage capacity required for each location was used. This minimum storage was found from initially simulating the model with excess storage, then the storage at each location was individually resized. The readily available cold storage available in the market are sized in increments of 100L [10], hence the storage capacity implemented within each location was $+100L$ of the minimum required.

2.4 Supply Chain Performance Metrics

Two key metrics were used to compare the performance of the models in different experiments. Firstly, vaccine availability was used:

$$Availability = \frac{Treated\ Individuals}{No.\ of\ Individuals\ Showing\ up\ to\ Vaccinate} \quad (1)$$

Vaccine availability measures the proportion of demand fulfilled by the supply. Availability lower than 100% is caused by missed vaccination opportunities due to partial or full stock out at an administration center.

Furthermore, the percentage of vaccine vials spoiled was used. This was defined as:

$$Percentage\ Vials\ Spoiled = \frac{Vials\ Spoiled}{Vials\ Procured} \quad (2)$$

This performance metric indicates the percentage vaccines that would become inactivated due to prolonged transportation or storage duration. In a case of a pandemic with limited a supply of vaccines, a high value of spoilage is undesirable.

These two metric were selected to measure the performance of the models as they were often utilised in WHO reports [18, 19]

3. EXPERIMENTS

3.1 Prioritisation and Scheduling

Due to the urgency of the COVID-19 pandemic and a limited supply of COVID-19 vaccines, the Strategic Advisory Group of Experts (SAGE) on Immunization of the World Health Organization (WHO) has developed guidelines for prioritisation

of vaccine usage. SAGE utilised three proposed broad epidemiological settings to provide rationales for priority uses of COVID-19 vaccines. Healthcare workers was prioritised over other groups as they face the highest risk of infection, which could lead them to become a transmitter of the virus. Furthermore, to efficiently reduce the mortality and morbidity rates, population groups exposed to significantly higher risk of death and illnesses was prioritised over those facing lower risks. Some other groups also being mentioned by the SAGE included social/employment groups that were unable to effectively physically distance and pregnant women. Using the four population groups mentioned in Section 2.3.4, HCW and Senior Citizens were determined to be the groups facing highest risks, whilst Adults and Young Adults faced less risks. Hence, HCW and Senior Citizens will be prioritised over Adults and Young Adults. Various prioritisation schedules were explored and listed below:

- Experiment A: 1,3,6,2 *
- Experiment B: 2,2,6,2
- Experiment C: (2,2)**,(10,10)
- Experiment D: (3,3),(9,9)
- Experiment E: (4,4),(8,8)

*The four number indicates the number of months allocated to each population in the order of HCW, Senior Citizens, Adults and Young Adults. For example, in Experiment A, HCW will be vaccinated in the first month, senior citizens will be vaccinated in the next three months, followed by the Adults in the next six months and the Young Adults in the last two months.
**Those in a bracket are grouped and vaccinated in the same period of time. For example, in experiment C, HCW and Senior Citizens will be vaccinated in the first two months together with no prioritisation among these two groups, followed by the Adults and the Young Adults together in the next ten months without any prioritisation.

3.2 Layer Removal

A multi-tier supply chain was utilised for the base model as it improved the supply chain's efficiency and resilience. However, for a robust understanding of the underlying relationship of the layers, experiments of layer removal were carried out to study and understand the effect of changing the total storage capacity of the supply chain on the performance metrics. In both the base models, the Regional and the Local Government stores were removed separately, thus creating four different models.

The models are as below:

- Experiment F: Removal of the Regional Layer
- Experiment G: Removal of the Local Government Layer

3.3 Introduction of Pfizer Vaccine to Existing Models

The Pfizer vaccine was chosen to be included in this study as the Britain's Medicines and Healthcare products Regulatory Agency claimed that the Pfizer vaccine showed 95% efficacy in the protection against the COVID-19 virus. Thus, the first 800,000 doses (out of the 40 million doses purchased) [20] was delivered to be administered to HCW and the senior citizens as they were placed at the top to the prioritisation list [21]. In order to incorporate the Pfizer vaccine into the base models, additional assumptions were made.

The base model was not able to accommodate the direct introduction of the Pfizer vaccine due to the extreme storage requirement of -70°C. Therefore, ultra-low temperature freezers were added to distribution centers, namely, the National, Regional and Local Government stores. However, HERMES was not designed for the distribution of vaccines requiring ultra-low temperature. HERMES only allows the lifetime below 0°C and between 2-8°C of the vaccine to be specified. However, as mentioned in 2.3.2, the Pfizer vaccine have three separate lifetime specifications. Therefore, a simplification of the storage specification was required to simulate the experiment.

First, the lifetime of the vaccine below 0°C inputted into HERMES was specified as 6 months, synonymous to the lifetime of the vaccine below -70°C. The updated model only utilised ultra-low temperature freezer, hence the below 0°C specification would effectively be that of the ultra-low temperature of -70°C. Moreover, to accommodate the lifetime specification in the Pfizer thermal shippers and the normal 2-8°C fridges, the 2-8°C input required in HERMES was specified as 20 days. This was the combined lifetime of 15 days in the shippers and 5 days in the fridge. Since vehicles and Healthcare Centers only had 2-8°C storage capabilities, by specifying the 2-8°C input as 20 days, HERMES would recognise that these vaccines would be transported using the special Pfizer boxes whenever the vaccines leave a distribution facility. Furthermore, when delivered to Healthcare Centers, the 20 days would take into account the lifetime of the vaccine in 2-8°C storage in the Healthcare Centers. Hence, producing a more robust simulation.

Since the prioritisation experiments done in Section 3.1 closely followed the priority list guidelines [21] released by the UK government, the following experiments were done on this Pfizer model to explore the effects of the prioritisation and scheduling policy:

- Experiment H (Base Pfizer model):Since only 40 million doses of the Pfizer vaccine was ordered by the UK government [22], the Pfizer vaccine was administered to only the Healthcare workers and Senior Citizens, whilst the AstraZeneca vaccine was used to vaccinate the Adults and Young Adults. No scheduling took place in this case.
- Experiment I (Prioritisation and Scheduling): (2,2),(10,10)
- Experiment J (Prioritisation and Scheduling): (3,3),(9,9)
- Experiment K (Prioritisation and Scheduling): (4,4),(8,8)
  Prioritisation and scheduling policies will follow the same policies described in Section 3.1.

The prioritisation experiments of the Pfizer model would reflect the current ongoing (and possibly near future) scenario where the Pfizer vaccine would be used to vaccinate as many Healthcare workers and those at risks as fast as possible. Then, when other vaccines get approved for usage, such as the ChAdOx1, these vaccines would be implemented to fill in the gap left by the Pfizer vaccine to achieve a fully vaccinated population. Furthermore, the implementation of the Pfizer vaccine would only be applied to the Base Two model. Due to the monthly shipping frequency, a minimum of 10 stock out days in each administration level would be observed, due to the

lifetime of 20 days for the transport and storage in Healthcare Centers. Therefore, the Base One model was omitted from this experiment.

3.4 Costing

For all experiments, costings were done to estimate the total cost of each model. This costing would include vaccine costs, cold storage costs, vehicle costs and energy costs (Fuel for vehicles and electricity used to run cold storage). The costing of the infrastructures such as storage buildings and facilities was not calculated as recent reports from the European Center for Disease Prevention and Control (ECDC) suggested that European governments including the UK plans to utilise already existing infrastructures [23] for the vaccination program. Hence, buildings and infrastructure costs were assumed to be 0. Furthermore, the level of involvement of each personnel would vary depending on their job description, hence the full salary of each staff member would not be contributed to the supply chain operational cost. This variability in contribution had been explored extensively in the supply chain of other countries [24], but not yet done for the UK. Since this was not within the scope of this project, staff costs were omitted.

Furthermore, the cost of vaccines per dose of the ChAdOx1 vaccine was estimated using SuperPro Designer [25] within the frame of the UK Research and Innovation (UKRI) funded project on COVID-19/SARS-CoV-2 vaccine manufacturing and supply chain optimisation (EPSRC grant number EP/V01479X/1). This estimated that the costs per dose of ChAdOx1 vaccine was $3.69 and the costs of the Pfizer vaccine was found to be $20 per dose [4]. The price of fridges were sourced from CoolMed Ltd [26] and Ethicheck Ltd [10], whilst vehicle costs were sourced from CoolKit Ltd [27].

4. RESULTS AND DISCUSSION

4.1 Base Model

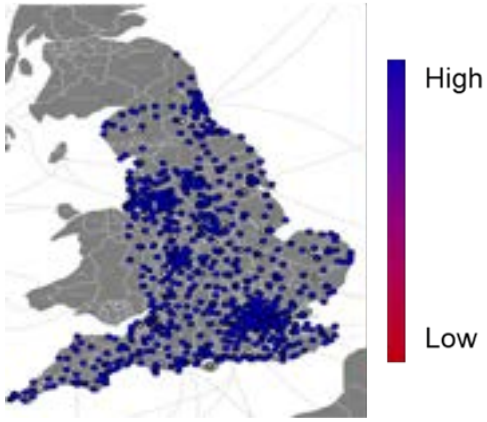

Figure 2: Base One model's Vaccine availability at Healthcare Centers

Since the base model was designed act as an ideal case, the vaccine availability and stock out days for these base cases were fixed at 100% availability and 0 stock out days (as observed from 100% availability across all Healthcare Center in Figure 2). The vaccine spoilage was shown to be 4.6% for the Base One model and 6% for the Base Two model. Furthermore, the optimised cold storage volume had a storage utilisation over 85% at each location, as shown in Figure 3. The optimised cold storage volume and storage costs by level was listed in Table 2. It was observed that the cold storage required by the Base One model was larger than that of Base Two. This was due to the trade-off between the transport frequency and cold storage required, as a higher frequency would result in lower inventory space required at each location.

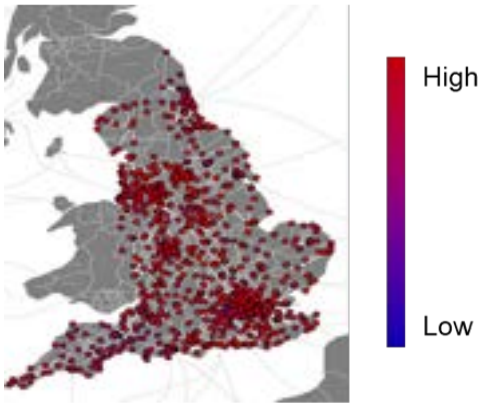

Figure 3: Base One's Cold storage utilisation at all Healthcare centers

Table 2
Summary of Optimised Cold Storage

	Cold Storage (L)		Storage Costs by Level ($)	
Level	Base One	Base Two	Base One	Base Two
National	28,000	24,000	337,610	289,380
Regional	72,600	62,000	891,116	751,960
Local Government	44,712	25,700	622,327	316,213
Healthcare Centers	238,671	220,840	2,445,308	2,095,103
Total	**383,983**	**332,540**	**4,296,361**	**3,452,656**

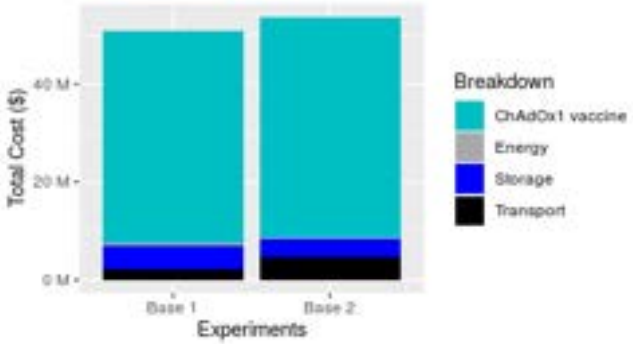

Figure 4: Annual Total Costs in Base Models

Furthermore, the total costs of the supply chain was shown in Table 2. The total cost of the Base One model was slightly lower than that of Base Two at $50.8 million compared to $53.7 million. Vaccine cost dominated in both cases, totalling $43.3 million in Base One and $ 45.1 million in Base Two. The

$1.8 million difference between the models was attributed to a slightly higher vaccine spoilage in Base Two. Transportation costs, alongside vaccine costs, was the main cause of the slightly higher cost in the Base Two model. Since the vehicles in the Base Two models were utilised more often, the cost for Base Two transportation was $2.3 million greater than Base One. Furthermore, due to the larger cold storage capacity required in Base One, the cold storage costs were $0.9 million greater in Base One compared to Base Two. However, the total cost of Base Two model remained to be greater than the Base One model.

4.2 Effects Of Prioritisation and Scheduling

As seen from Figure 5, the prioritised model results was separated into two group, Experiment A and B with relatively low vaccine availability and Experiment C,D and E with high vaccine availability.

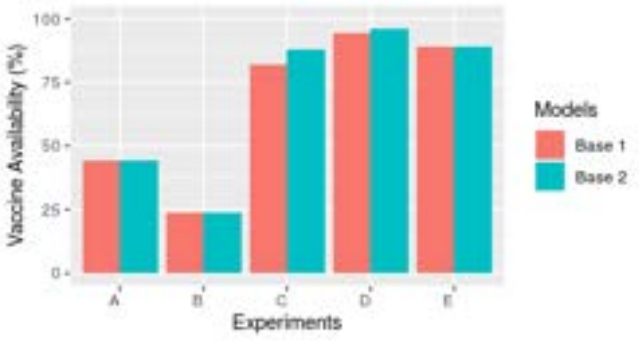

Figure 5: Vaccine Availability in Prioritisation and Scheduling Experiments

The low availability of Experiment A (Base One at 44.1%, Base Two at 44.4%) and Experiment B (Base One at 23.8%, Base Two at 23.6%) were caused by over-prioritising and over-scheduling HCW and Senior Citizens. This depicted a scenario where the time allocated for a prioritised group was far too long compared to its population, causing less time to be allocated to other groups. The shortened time allocated to the Adults and Young Adults groups resulted in an increase in monthly demand. This resulted in National and Healthcare Center storage bottlenecks, resulting in lowered availability. In both Experiment A and B, only 6 months were scheduled for Adults, even though the group accounted for more than 64% of the total demand. This resulted in multiple missed opportunities as multiple Healthcare Centers faced stock out days, decreasing the overall availability. Furthermore, this over-prioritisation effect was seen clearly from the decrease in availability from Experiment A to B. The availability decreased by more than 20%, this was attributed to due to over-scheduling HCW. Since Senior Citizens had more than 7 times the demand compared to HCW, by allocating an additional month to HCWs and decreasing a month from Senior Citizens in Experiment B, the supply chain was overwhelmed by the surge in demand from the Senior citizens, resulting in a large decrease in availability.

Additionally, it was observed that the vaccine availability improved significantly in Experiments C, D and E. This was attributed to the decision to group those exposed to high risk together, and those exposed to low risk together. This increased the total amount of time allocated to each group, hence preventing demand surges. Furthermore, the ratio of time allocated between these groups also corresponded to the ratio of demand between these groups, resulting in an optimised scheduling sequence. As seen in Table 1, the ratio of HCW + Senior Citizens : Adults + Young Adults was approximately 1:3, this reflected the ratio of time allocated between the two groups in Experiment D, hence causing the demand of each months to be relatively the same. This resulted in high availability for all three experiments, with Experiment D being the highest at 94.2% for Base One and 95.8% for Base Two. Experiment E follows behind closely at 89.0% for Base One and 89.1 % for Base Two. Experiment C, the lowest of the three, had 81.9% availability for Base One and 88.0 % for Base Two. Moreover, the availability would decrease relative to magnitude of the difference between the ratio of allocated time and the actual population ratio between each group, as seen from lowered availability in Experiment C and E. Hence to maximise availability, the prioritisation schedule should correspond roughly to the ratio of population between each group.

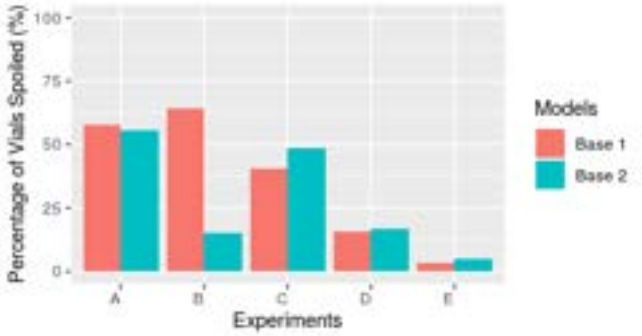

Figure 6: Total Percentage of Vials Spoiled in Prioritisation and Scheduling Experiments

Furthermore, this relationship between the ratio of time allocated and population ratio was the cause of the decrease in percentage of vials spoiled from Experiment C to D as observed in Figure 6. However, the decrease from Experiment D to E was unexpected. Since Experiment D has the optimal prioritisation schedule, one would expect the vials spoiled to be lowest in Experiment D, yet the percentage vials spoiled was lowest in Experiment E at 3.4% in Base One and 5.0% in Base Two. This decrease was attributed to the short amount of time allocated for the vaccination of Adults in Experiment E which caused a National Level bottleneck as demand surged in the last 8 months of the vaccination program. This meant that the storage capacity of the National Level was unable to accommodate the total supply needed to fulfil the demand within these months. Furthermore, since the rate at which vaccine were being administered at Healthcare Centers was much greater than previous experiments during the last 8 months, the amount of

time that vaccines had to be stored at distribution centers would decrease, decreasing the likelihood of vaccine spoilage caused by prolonged storage and transport duration.

Moreover, it was observed that Experiments A and B had vaccine spoilage greater than 50% (except for Experiment B Base Two). The high level of vaccine spoilage was caused by the Healthcare Center storage bottlenecks as demand surged during the months scheduled for Senior Citizens and Adults. This meant that the storage capacity of Healthcare Centers were not able to accommodate the large number of supplies from upper levels. This increased the inventory levels in the distribution centers, further increasing the amount of time a vaccine had to be stored in distribution levels, thereby increasing the vaccine spoilage. Furthermore, the 14.9% of vials spoiled in Base Two Experiment B may seem like an anomaly at first glance, however this was not the case. This experiment experienced a National level storage bottleneck, causing a decrease in the total amount of vaccines procured. The number of vaccines procured was 2,723,487 vials for the whole year, only 22.2% of the projected demand in the Base Two case. This storage bottleneck was not present in this experiment for Base One due to a larger overall storage capacity compared to Base Two, hence preventing this bottleneck.

Therefore, any prioritisation and scheduling policies implemented should take into consideration the ratio of population in each age group to prevent the presence of National and Healthcare Center storage bottleneck. However, National level storage bottlenecks, although would decrease the availability, may be beneficial for cases that experiences a Healthcare Center level bottleneck at the same time. The National level bottleneck would be able to limit the stock inventory in the Regional and Local Government levels, which would decrease the high level of spoilage that was often observed in cases with Healthcare Center storage bottlenecks.

4.3 Effect of Layer Removal

Figure 7 showed the vaccine availability of the ChAdOx1 vaccine in Experiments F and G where the Regional and the Local Government layer were removed. The vaccine availability ranged from 49.5% to 87.8%.

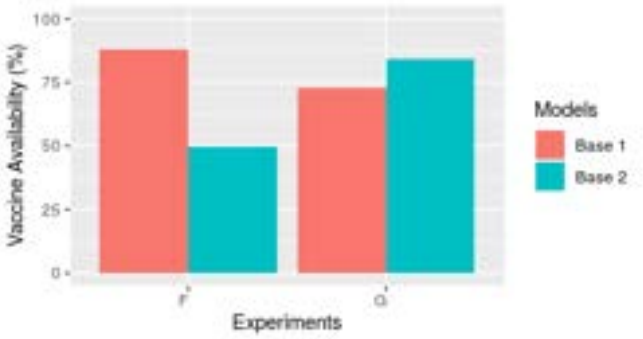

Figure 7: Vaccine Availability in Removed Layer Experiments

This result was closely related to the cold storage volume stated in Table 2. In experiment F, the vaccine availability in Base One was significantly higher than that of Base Two. The removal of the Regional layers caused the Local Government Layer to become the only "connector" between the National level and Healthcare Centers. As observed in Table 2, the total cold storage volume of the Regional level in both models were approximately 18% of their respective total cold storage volume. However, the total cold storage volume of the Base One Local Government level was 44,712 L (11.6% of the total cold storage volume), whereas the Base Two model was 25,700 L (7.7% of the total cold storage volume). Therefore, since both Local Government level storage capacities were less than that of the removed Regional stores, the Local Government level would not be able to accommodate the same magnitude of supply from the National stores, resulting in a Local Government level storage bottleneck. This bottleneck would limit the amount of vaccine being delivered to Healthcare Centers and thus reducing vaccine availability. Moreover, storage bottlenecks also caused high percentage of vial spoiled due to longer storage duration, as observed in Figure 8. Thus, Local Government level storage bottleneck was the main factor of the decreased vaccine availability.

In experiment G where the Local Government level was removed, the vaccine availability in both the models were 73.0% and 84.2% . The higher availability in the Base Two Experiment G model was due to the removed Local Government layer holding a lower proportion of the total cold storage capacity compared to its Base One counterpart (7.7% compared to 11.6%). Therefore, the bottleneck was not as serious as that in Experiment F. Even though, Experiment G models still maintained a relatively high availability, the removed storage still caused the availability to be lower than the base models.

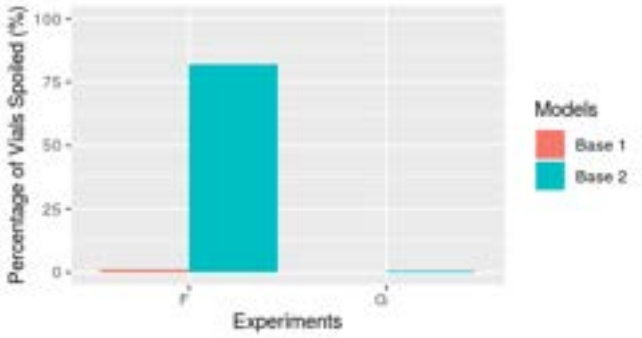

Figure 8: Percentage of Vials Spoiled in Removed Layer Experiments

Figure 8 showed the percentage of vials spoiled in Experiments F and G. It was observed that the Base One Experiment F and G models and Base Two Experiment G model had extremely low percentage of vial spoiled (1.3%, 0.1% and 0.4%). These number were lower than that of four-level base models. This was attributed to the shorter storage duration in distribution levels, due to the removal of the supply chain layer, resulting in a significant reduction of vaccine spoilage. However, Experiment F of the Base Two model was an exception as it had an extremely high percentage of vial spoilage at Base Two 82.0%. This was due to the Local Government storage bottleneck as

discussed above. Severe Local Government storage bottleneck led to longer vaccine storage duration, resulting an increase in vaccine spoilage.

During a pandemic, a three-level supply chain could be more suitable than four-level supply chain. The three-level supply chain was observed to successfully decrease the vaccine spoilage, given no extreme storage bottlenecks. Due to the very limited supply of vaccines in a pandemic, the low spoilage was a crucial factor to keep the wastage at its minimal. Furthermore, for an effective removal of supply chain layer, the removed layer should have the least percentage of the overall cold chain storage capacity. Moreover, the balance between the cold storage capacity and the shipping frequency had to be reconsidered as this would affect the amount stuck inventory and the percentage of vials spoiled.

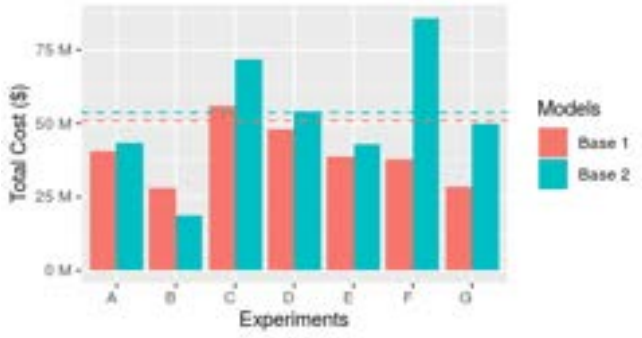

Figure 9: Annual Total Costs in Prioritisation and Scheduling Experiments and Removed Layer Experiments

It was observed in Figure 9 that vaccine costs dominated the total cost of the supply chain. This was due to the high dosage demand at 88 million doses. The dotted lines in Figure 9 depicted hosts of the base models. Most experiments had lower costs than the base models. This was the result of storage bottlenecks, causing the amount of vaccine procured to be lower than that of the base models. Experiments with a high level of vials spoiled, resulted in costs higher than that of the base models. For example, Experiment F of Base Two model had a spoilage percentage of 82 %, hence these vaccines would all be additional costs.

4.4 Effect of Introduction of Pfizer Vaccine to Existing Models

In this experiment, the Pfizer vaccine was used to vaccinate HCW and Senior citizens, a reflection of what was implemented by the UK Government. The effect of implementing the Pfizer vaccine onto an already existing infrastructure was observed in Figure 10.

Experiment H had an overall availability of 99.1%, with the ChAdOx1 availability being 100% and Pfizer's BNT162b2 being 93.28%. The 100% availability in the ChAdOx1 vaccine meant that there was close to no disruption in the distribution of the ChAdOx1 vaccine. The addition of the ultra-low temperature freezers to the distribution centers separated storage facilities for the two vaccines. Furthermore, the slightly lowered availability of the BNT162b2 vaccine was attributed to the relatively high vaccine spoilage of 23.8%, observed in Figure 11. This was due to the short lifetime of 20 days in the thermal box and normal fridge storage.

However, in experiments where prioritisation and scheduling were implemented, negative effects due to the usage of two different vaccines was observed. This negative effect was attributed to storage competition in the Healthcare Center storage and was observed in the decreasing availability of the BNT162b2 vaccine from 92.3% in Experiment I to 70.0% in Experiment K. This decrease was unusual since the time allocated for the BNT162b2 vaccine increased from 2 to 4 months. However, in the month prior to the start of the usage of the ChAdOx1 vaccine, the ChAdOx1 vaccine would have started to be delivered to the National Level and subsequently to the lower levels. This would not yet affect the BNT162b2 vaccination program due to the utilisation of different storage facility in the distribution levels. However, one to two weeks before the start of the scheduled start of the ChAdOx1 vaccination period, the ChAdOx1 vaccine would had been delivered to Healthcare Center locations. However, since the BNT162b2 administration was still being carried out and no additional cold storage added to the Healthcare Centers, this would decrease the amount of BNT162b2 vaccines at each location, causing a Healthcare level storage bottleneck and subsequently decreasing the availability. Furthermore, the time allocated for the ChAdOx1 vaccination program decreased from 10 to 8 months from Experiment I to K. This meant that the ChAdOx1 vaccine supplied to Healthcare Centers were much greater in Experiment K compared to Experiment I, causing the decrease in BNT162b2 availability.

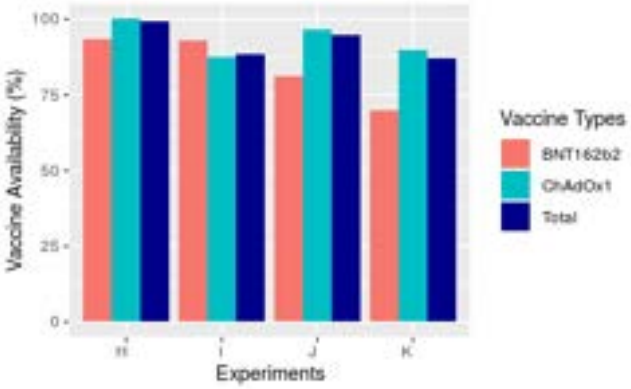

Figure 10: Vaccine Availability by Vaccine Types in Pfizer Experiments

Furthermore, the ChAdOx1 availability was observed to be 87.5%, 96.7% and 89.8% in Experiments I, J and K. This initial decrease in availability from Experiment I to J was attributed to the storage competition. Even though Experiment I had more time to vaccinate Adults (10 months compared to 9), due to the low amount of time allocated for the BNT162b2 vaccine in Experiment I (2 months compared to 3 months), the number of vaccines stored within Healthcare level storage in the last month of the allocated time for the BNT162b2 vaccine would be much greater than that of Experiment J. This

caused the level of ChAdOx1 inventory in the first month of administration to be much lower in Experiment I, resulting in missed opportunities, hence a lowered availability. However, this was not the case from Experiment J to K. There was a decrease in availability from 96.7% to 89.8%. Although the effect of storage competition still exists, this was overshadowed by a National level storage bottleneck. The decreased amount of time allocated for Adults and Young Adults caused the demand to be much greater, resulting in overwhelming the National level cold storage facilities, hence decreasing the number of vaccines received, thereby decreasing availability.

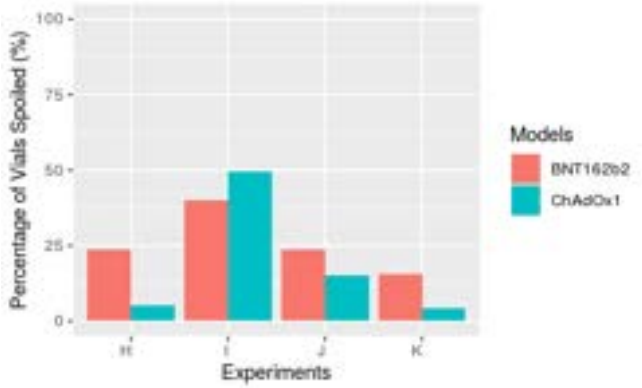

Figure 11: Percentage of Vials Spoiled in Pfizer Experiments

Moreover, a decreasing trend in vaccine spoilage was observed in both the ChAdOx1 and BNT162b2 vaccines in experiments I, J and K. The decreasing trend for the Pfizer vaccine spoilage was due to an alleviation in the Healthcare level storage bottleneck as the time allocated for the prioritisation of the Pfizer vaccine increased. From experiments I to J to K, the amount of time allocated to vaccinate the HCW and Senior Citizens increased from 2 to 3 to 4 months. This decreased the monthly demand for the BNT162b2 vaccine; hence a smaller supply of vaccines was required. This resulted in a decreased in the volume of cold storage needed for the Healthcare Centers. Since there were no additions of cold storage in the Healthcare Center levels, the unaccommodated stock was stored in the Regional and Local Government levels, resulting in high levels of vaccine spoilage when these vaccines become undelivered when the prioritisation schedule ended. Therefore, as the scheduled duration of the BNT162b2 vaccine increased, this alleviated the Healthcare Center bottleneck, decreasing the percentage of vials spoiled. However, the decreasing trend in the ChAdOx1 vaccine was not caused by a storage bottleneck in Healthcare Center. This decrease was attributed to the faster rate at which ChAdOx1 vaccines was administered, due to the increased demand. This decreased the amount of time spent in storage for the ChAdOx1 vaccine, thereby decreasing the likelihood of spoilage during storage or transportation.

Furthermore, due to the short lifetime of the Pfizer vaccine, it was expected that the percentage of vials spoiled would be higher for the Pfizer vaccine compared to the Oxford vaccine. However, the opposite was observed in Experiment I, as observed in Figure 11. The ChAdOx1 vaccine was shown to have a spoilage of 49.5% and 39.9% for the BNT162b2 vaccine. Additionally, the-lower-than expected spoilage of the Pfizer vaccine was due to a National level storage bottleneck, similar to that explain above. This resulted in lower amounts of vaccine spoilage in the Regional and Local Government levels, causing the spoilage of the Pfizer vaccine in Experiment I to be lower than that of the Oxford vaccine.

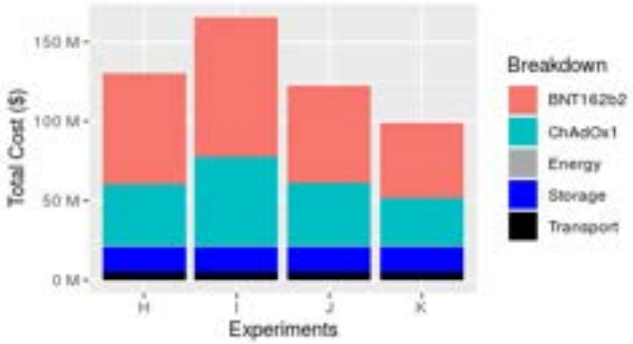

Figure 12: Annual Total Costs in Pfizer Experiments

Figure 12 showed the annual total costs from the cost of vaccines, energy costs (electricity and fuel), cold storage costs and transport costs. Moreover, the total cost of all the Pfizer implemented models were far higher than those only administering the Oxford vaccine. Model H had a total annual cost of $129.8 million, $76.1 million higher than that of the normal Base Two model. This was attributed to the higher price of the Pfizer vaccine at $20 per dose compared to $3.69 for the Oxford vaccine and the additional costs for the ultra-low freezers of $11.9 million. This caused all the cost of models I ($165.5 million), J ($122.6 million) and K ($98.7 million) to be much greater than its Oxford only counter parts in Section 4.2. Furthermore, the much higher costs seen in Model I relative to other models was due to the high levels of vaccine spoilage. This meant that a great amount of the cost procured from the Pfizer vaccine would be essentially wasted as the vaccine are not being administrated but instead, spoiled.

To conclude, National and Healthcare Center storage bottlenecks were the main cause of decreased availability when the Pfizer vaccine was implemented. Moreover, the storage competition induced Healthcare Center storage bottleneck was detrimental to the availability and vaccine spoilage as observed in Figure 10 and 11. This resulted in high vaccine costs. Hence to ensure the least disruption upon implementing a second vaccine, an excess of storage should be used, especially in the Healthcare Center levels, alongside an optimised prioritisation and scheduling policy.

5. LIMITATIONS OF THE PROPOSED MODEL

The models and experiments simulated were able to depict possible real life supply chain scenarios to a certain extent and give a crucial insight to the relationships and trade-offs within the supply chain. However, in order to improve and further investigate the model, some additional experiments have to be

done. Due to the immediate need of vaccines in the pandemic, some inputs in the models had to be assumed from ongoing research due to unreleased information from vaccine manufacturers and government organisations. Hence when information, such as secondary packed volume, and number of doses per vial, becomes available, the model should be updated to decrease the uncertainties caused by these assumptions. Even though the costs calculated gave a good visualisation of the expected costs incurred from the supply chain, the costs of the workforce were calculated (Supplementary Material Section) but not included in the report due to the uncertainty in the contribution of the salary towards the cost of the supply chain. Hence a further sensitivity analysis could be done to address this uncertainty, to provide a more robust solution.

6. CONCLUSION

The two base models and 11 experimental models were created to simulate various possible scenarios for COVID-19 vaccine distribution in England. A total of 1200 NHS Healthcare Centers were included in this study. The vaccine availability and the percentage of vials spoiled were the key performance metrics used.

After implementing experiments onto the base models, different types of storage bottlenecks were identified as the cause of lowered availability and increased percentage vials spoiled. To avoid such scenarios, upon implementing a prioritisation schedule, the proportion of time allocated to each group should reflect the population ratio to alleviates effects of National and Healthcare Center bottlenecks. Furthermore, upon removing one supply chain layer, bottlenecks will occur directly above or below that of the removed layer, given that the above or below layer has a smaller storage capacity. Hence to minimise bottleneck effects, the removed layer should hold the lowest percentage of overall total storage. However, on the bright side, the percentage of vials spoiled in a three-level supply chain was significantly lower than that in four-level supply chain due to shorter storage and transport duration. Furthermore, in the case of the addition of the Pfizer vaccine, although bottlenecks were a key cause of lowered availability, storage competition between different vaccines detrimental to the vaccine availability. These effects can be alleviated through ensuring an excess amount of storage in the Healthcare Center levels and separate storage within distribution centers.

This paper had studied the effect of different variables using 13 models to understand how to improve the efficiency of the vaccine supply chain. Nevertheless, different structures has different underlying mechanisms that affects the overall performance of the supply chain. Ultimately, the relationships highlighted the simulated COVID-19 vaccine supply chain will be able to serve as a guideline to understand these underlying relationships.

REFERENCES

[1] Worldometer coronavirus.

[2] WHO. Draft landscape of covid-19 candidate vaccines. Technical report, World Health Organisation, Dec 2, 2020.

[3] NHS Scotland. Coronavirus disease (covid-19).

[4] IMF. World economic outlook update, june 2020. Technical report, International Monetary Fund, June, 2020.

[5] Robert Chen Stephen Mayhew TungThanh Le, Jakob P. Cramer. Evolution of the covid-19 vaccine development landscape. 04 SEPTEMBER 2020.

[6] Ian Sample Jessica Elgot. uk scrambles to buy 5m doses of covid breakthrough vaccine, 16 November 2020.

[7] NHS Choices. Hospitals, 2015.

[8] Mark Fischetti. The covid cold chain: How a vaccine will get to you, Nov 19, 2020.

[9] BBC. Covid-19 vaccine: First person receives pfizer jab in uk, Dec 9, 2020.

[10] Ethicheck. Pharmacy refrigerators, 2020.

[11] NHS. Nhs out-of-hours services, Nov 16, 2018.

[12] ONS. Estimates of the population for the uk, england and wales, scotland and northern ireland. Technical report, Office for National Statistics, June 24, 2020.

[13] AstraZeneca. Azd1222 vaccine for the prevention of covid-19. Technical report, Nov, 2020.

[14] AstraZeneca. Azd1222 vaccine met primary efficacy endpoint in preventing covid-19, Nov 23, 2020.

[15] WHO. *HOW TO CALCULATE VACCINE VOLUMES AND COLD CHAIN CAPACITY REQUIREMENTS*. WHO Vaccine Management Handbook. 2017.

[16] Pfizer. Covid-19 vaccine u.s. distribution fact sheet, Nov 20, 2020.

[17] Public Health England. Seasonal flu vaccine uptake in gp patients: monthly data, 2019 to 2020. Technical report, Nov 28, 2019.

[18] Outsourcing vaccine supply chain and logistics to the private sector. 2013.

[19] Integration of vaccine supply chains with other health commodity supply chains. 2013.

[20] Michelle Roberts. Covid-19: Pfizer/biontech vaccine judged safe for use in uk, 2 December 2020.

[21] UK Department of Health and Social Care. Priority groups for coronavirus (covid-19) vaccination: advice from the jcvi, 2 december 2020. Technical report, UK Department of Health and Social Care, Dec 3, 2020.

[22] Emma Reynolds. Uk becomes first country to authorize pfizer/biontech's covid-19 vaccine, first shots roll out next week, Dec 3, 2020.

[23] ECDC. Overview of covid-19 vaccination strategies and vaccine deployment plans in the eu/eea and the uk. Dec 2, 2020.

[24] Mercy Mvundura and Kristina Lorenson. Estimating the costs of the vaccine supply chain and service delivery for selected districts in kenya and tanzania. *Vaccine*, 33(23):2697 – 2703, 2015.

[25] Demitri Petrides. Superpro designer user guide - a comprehensive simulation tool for the design, retrofit evaluation of specialty chemical, biochemical, pharmaceutical, consumer product, food, agricultural, mineral processing, packaging and water purification, 2013.

[26] Coolmed. Solid door small refrigerator cms29, 2020.

[27] Coolkit. new fridge freezer vans for sale, 2020.

Potential Applications of Variously Structured Semi-transparent PV Cells in an Evacuated Solar-thermal System

Maria Zagorulko & Gianluigi Tosti di Valminuta
17/12/2020
Department of Chemical Engineering, Imperial College London, UK

1 Abstract

A lot of research has been placed into solar panel industry over the years, investigating ways of improving the PV technology in an attempt to harness energy more effectively. Most of this research has been into Photo-voltaic (PV) and solar-thermal (PV-T) panels, but more recently semi-transparent Photo-voltaic (STPV) cells have been explored as a viable alternative to conventional PV designs. Cadmium Telluride (CdTe), perovskites, and polymers are all materials that can be used for the active layers of Semi-transparent Photo-voltaic Thermal (STPV-T) cells. In this paper, multiple examples of each material were found and their physical properties recorded. Respective electrical and thermal efficiencies in a simple panel, made up of the cell and an ideal solar-thermal absorber separated by a vacuum, were then modelled using MATLAB, and the energy efficiencies were obtained. Finally, the materials were qualitatively evaluated in terms of their availability, distribution costs and scalability.

The best cell was found to be ITO/C_{60}/Perovskite/Spiro-OMeTAD/MoO/Au, which displayed 13.5% PCE and 64.4% thermal absorber heat efficiency at astonishing 88% transparency.

Key-words: Cadmium Telluride, Perovskites, Polymer, Semi-transparent Photo-voltaic thermal, irradiance, Power Conversion Efficiency(PCE)

2 Introduction & Background

2.1 Introduction

Photo-voltaic thermal (PV-T) collectors have been in the spotlight of most governmental energy policies in 2020, as evidenced by the Green Homes Grant, which gives vouchers of up to £10,000 to homeowners making their houses more nergy efficient (Kunz (2020)). Harnessing thermal energy as a by-product of electrical energy generation could unveil a clear framework for delivering domestic and industrial heating as well as power in a sustainable way.

One of the most common solar-thermal designs is the evacuated tube system which shows higher insulating properties and improved overall efficiency of 70% (Spirit Solar Ltd (2020)) in comparison to other models. Recent progress in PVT optimal configuration has been largely concentrated around circulating fluid and PV cell's adhesive thermal properties. Nonetheless, there are multiple promising developments in solar cell industry that in tandem with thermal component could elevate the effectiveness of PV-T collectors.

Recently, there has been a rising interest in Semi-transparent Photo-voltaic cells (STPVs), which can replace windows and roofing in modern buildings to improve their efficiency and deliver power. By one estimate by Baltazar & Do (2017), BIPV windows could generate 12-21% savings in annual energy usage. Cells are able to convert visible and ultraviolet incident light into electricity, yet their application in PV-T designs is minimally reviewed. This paper focuses on comparing electrical performances of the three most common STPV materials: perovskite, polymers and cadmium telluride (CdTe) and their effect on energy distribution of the PV-T module.

2.2 Background

Of particular interest, recent studies show advances in solar cell efficiencies manufactured from perovskite-based materials. Perovskite is a calcium titanium oxide mineral ($CaTiO_3$) (Ossila ltd (2020)) that is widely used in PV modules due to its low cost and ease of manufacture.

Bailie et al. (2014) found an application of perovskite in a mechanically stacked tandem cell where a high transparency is achieved by using a silver nanowire (AgNW) top electrode that transmits 90% of light in the 530-1000nm range. The following arrangement displayed astonishing power conversion efficiency (PCE) of 18.6%.

Additionally, Guo et al. (2014) have displayed a further application of AgNWs electrode top layer in combination with zinc oxide (ZnO) as a supporting substrate for a perovskite tandem cell. The fact that they obtained a much lower PCE of 8.5% could be a result of reletively high 2.1 eV energy band gap between perovskite and the top layer, which is significantly larger than the usual for PV panels.

On the other hand, an elevated PCE of 25.5% has been achieved by Dewi et al. (2019) as a result of perovskite utilization in a 4T tandem cell with top transparent layers of Indium Tin Oxide (ITO) and Silver (Ag). Remarkably, the result was achieved with an intermediate energy band gap of 1.58 eV, which shows the importance of further research into the effect of band gaps on solar cell performance.

You et al. (2015) took a different approach to the problem, and proposed to utilise multilayer graphene as the top electrode deposited onto perovskite active layer. Among 4, 3, 2 and 1 graphene layers, the double graphene layer was proven to give the highest PCE of 12.02%. Graphene is said to be a suitable low cost alternative to a transparent silver nanowire top layer.

Another material around which there has been quite a lot of discourse is Cadmium Telluride (CdTe). CdTe was one of the first materials to be explored for photo-voltaic applications, together with amorphous Silicon (a-Si), in the mid 90s (Romeo et al. (2018)).

According to Zweibel (2008), CdTe is the only thin film technology that is cheaper than conventional crystalline Silicon panels, as well as having the smallest Carbon footprint and lowest payback time over it's life-cycle, although the toxicity of Cadmium remains a problem at the end of the panels' lives. Cdte forms the p-junction of the cell and Cadmium Sulfide (CdS) the n-junction. The latter is also known as a window layer, as it transmits most visible light. CdTe also tends to have a very efficient band gap of 1.5 eV, as the optimal band gap for photo-voltaic conversion is around 1.45 eV.

Banerjee (2015) was able to obtain an efficiency of over 20% using an $8\,\mu m$ CdTe layer with a $0.35\,\mu m$ layer of CdS. The solar cell also had transparent conductive oxide (TCO) as a transparent and conducting oxide with front contact and a back contact made of copper and gold. The general findings were that efficiency increased with CdTe thickness, and that the CdS layer thickness also showed a positive correlation with efficiency, although it had much less of an effect, as it mostly transmits the light, as well as being a much thinner layer in the first place.

Semi-Transparent Photo-voltaics (STPVs) are especially useful when used on buildings as building integrated photo-voltaics (BIPVs). They have the ability of reducing the Solar Heat Gain of the building (the thermal energy increase from absorbing solar radiation) and regulate how much light enters the building on top of generating on-site, renewable energy.

MA. Green et al. (2020) were able to achieve a very high transmittance of over

70% in the near-infrared region (NIR) of 1000 nm, combined with a respectable efficiency of 8.6% using a cell with a CdTe thickness of 900 nm in the configuration above, Figure 1. This high value of transmissivity in the NIR is key for windows as it allows light that is not as hard on the eyes to pass through.

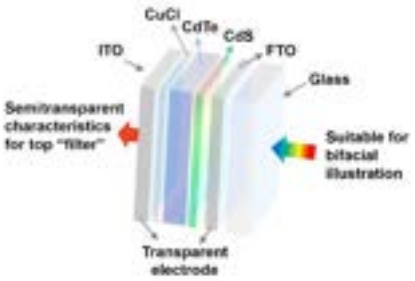

Figure 1: MA. Green et al. (2020) cell configuration

Alrashidi et al. (2019) found that their cell had a solar transmission of 12%, and visible transmission of 25%, and that their maximum solar heat gain of 20% was over 70% lower than for a single glazed window, which can be ideal for warmer climates. The team also computed a U-value of $2.7W/m^2$ vs a higher value of $5.7kw/m^2$ for the glazed window. Since the U value is the heat energy that moves through an area in a given time, this shows that the STPVs that the above experiment utilised were more efficient thermal insulators as well.

Polymers are a more recent development in the solar energy market as the active layer materials, with vast potential in the long term. Research from Li et al. (2019) shows this potential, as the study showed the ability to synthesise an original molecule (ID-4Cl), that when used in a cell with the structure ITO/PEDOT:PSS/active layer/PDINO/Au (15nm) gave an optimal PCE of 10.2% when the active layer had a thickness of 65nm, although this quickly dropped to 6.99% when its area was increased to 4 mm^2, highlighting the potential problems of scalability of this technology. The prototype also achieved an average visible transmittance of 47.6%, which shows its applicability in BIPV applications.

Hu et al. (2019) were able to achieve a PCE of 12.37% and an average visible transmittance of 18.6% for a polymer solar cell (PSC), which had an active layer made of the unique material (PM6:Y6) with thickness of 100nm , and electrodes made of Ag and Au with thicknesses of 10nm and 1nm respectively. Yu et al. (2015) also developed some PSCs, in which one-dimensional photonic crystals (1DPCs) were applied in attempt to improve the PCE. The goal was successfully achieved, increasing it from 4.87% to 5.31%. The cell also possessed a colour rendering index of 0.97, which means that the light filtered through it accurately represents the real colour of objects it shines upon. The crystals were made up of alternate layers of MoO_3 and LiF, and act in a similar way to a Bragg reflector, by reflecting part of the spectrum out and concentrating incident light.

3 Methodology

Although there is a fairly extensive research into STPV cells, the scarcity of theoretical investigation around their application in solar-thermal systems make further research necessary in order to understand the overall thermal and electrical potential. Our research focuses on the potential of a cell with an arrangement as shown in Figure 2.

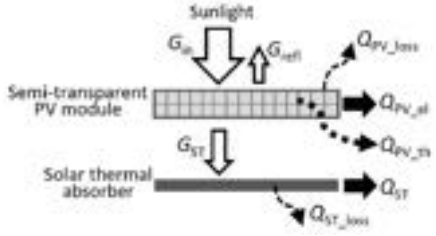

Figure 2: Physical Model of STPVT with semi-transparent cells (Huang et al. (2020)

In order to choose the dominant design for semi-transparent solar-

thermal module in Figure 2, wide literature research was undertaken to find the key model parameters and compare perovskite, CdTe and polymers as active layer materials for the solar cell. The collector above has been chosen in order to explore the maximum potential of radiative energy available to a solar-thermal absorber. Thus, conductive and convective phenomena have been ignored, as well as any heat losses within the system.

Explicitly, the model parameters allocated for the research were transmittance, absorptivity and reflectance percentages. Each respective parameter was obtained from graphical data found in literature and modelled against the solar irradiation spectrum. As incident sunlight G_{in} falls on the semi-transparent PV, absorptivity data can be applied to calculate energy retained in the solar module. Transmissivity of STPV is then employed in modelling the amount of energy available for the thermal module, while reflectivity models the energy lost on contact with the cell. The aforementioned variables were used in the equation set below.

$$Q_{PV} = \int_0^\infty G_{in}(\lambda)\alpha_{PV}(\lambda)\,d\lambda \qquad (1)$$

$$G_{ST}(\lambda) = G_{in}(\lambda) \times \tau_{PV}(\lambda) \qquad (2)$$

$$Q_{ST_{th}} = \int_0^\infty G_{ST}(\lambda)\,d\lambda \qquad (3)$$

Where G_{in} and G_{ST} are the incident radiations on the PV cell and the thermal absorber respectively, α_{PV} and τ_{PV} are the absorptivity and transmissivity of the PV cell, and Q_{PV} and $Q_{ST_{th}}$ are the total energy produced in the PV cell and the thermal energy produced by the absorber. Additionally, the power conversion efficiency was extracted for each material iteration and applied in Equation 4.

$$Q_{PV_{el}} = I_{in} \times \eta_{el} \qquad (4)$$

Where $Q_{PV_{el}}$ is the electrical power produced in the PV cell, I_{in} is the solar energy absorbed by the cell, and η_{el} is it's PCE.

Subsequently, these equations formed the basis of the MATLAB model employed to differentiate STPV-T designs. The model has facilitated the visualisation of both electrical and thermal energy distributions of the PV using Equation 5.

$$Q_{PV_{th}} = Q_{PV} - Q_{PV_{el}} \qquad (5)$$

with $Q_{PV_{th}}$ being the thermal energy produced in the cell. In order to obtain the full set of results, a number of assumptions were made. Firstly, the absorptivity data was obtained via the Equation 6 for all materials, assuming the physical accuracy of this method.

$$t + r + a = 1 \qquad (6)$$

Secondly, due to the lack of reflectance data in the literature sources, perovskite reflectivity range was obtained from graphical data provided by Hajjiah et al. (2018)) whereas polymer reflectivity was extracted from Zhang et al. (2019). Similarly, assumed reflectance for CdTe was obtained from Alrashidi (2019). Finally, the main assumption used was behind the data modeling. To develop the energy distributions across the full solar spectrum (0-2500nm), main variables were assumed to show constant values below 250nm and past 1000nm where data was not available from the sources, the absorptivity of the solar absorber was assumed to be 1, and the power loss in the cell was assumed to be negligible.

4 Results and Discussion

4.1 Spectral distribution

To create an understanding of the amount of energy available to a thermal absorber, G_{st} was calculated for each

respective material. The results, plotted against the full solar spectrum, are shown in Figure 3, 4 and 5. It was essential to see the spectral distributions for all materials in order to devise a set of designs that could be then used in future energy modeling. An ideal semi-transparent cell transmits most of the spectrum to the thermal absorber in the visible region yet also shows significant transmission in the infrared part of the spectrum. From Figure 3, it is clear that the most promising cadmium telluride designs are tandem cells with CuCl/ITO with 2% and 10% O_2 gas introduction during the design manufacture. Furthermore, Glass/TCO/CdTe/CdS/TCO semi-transparent structure displays bigger G_{st} range. This was an expected result as the aforementioned models show higher maximum transmission values compared to other CdTe based cells.

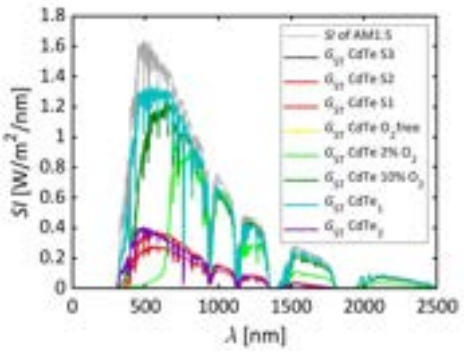

Figure 3: Spectrum Arrived at Thermal Absorber through CdTe Cells

In the perovskite selection, (refer to Figure 4), better overall spectral distribution is seen. Nonetheless, only three designs peaked in the visible region. The following layouts were dominant: FTO/Perovskite/CIGS and ITO/Perovskite/TiO_2 with 80% max. transmittance semi-transparent tandem cells and $AuMoO_3$/Perovskite/ITO where maximum transmittance was 88%.

The difference in the width of perovskite spectrum and CdTe in the visible range can be explained by the typical transmission spectra of the above materials. Perovskite cells are able transmit in 530nm $< \lambda <$ 860nm range (Trofimov et al. (2020)) while cadmium telluride STPVs transmit in a wider 380nm $< \lambda <$ 780nm range.

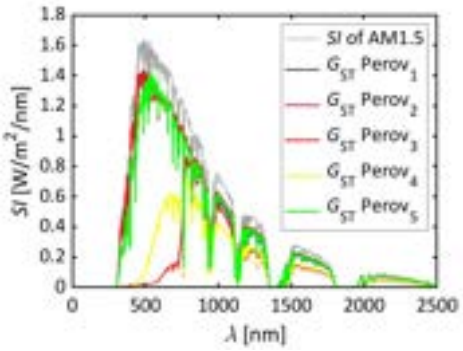

Figure 4: Spectrum Arrived at Thermal Absorber through Perovskite Cells

Polymer based designs displayed the least transmission of energy to the thermal absorber. This can be explained by much lower transparency of the top layer of the cells in contrast to CdTe and Perovskite. Semi-transparent polymer cells with incorporated one-dimensional photonic crystals (1DPC) show high transmission of 1.15 and 0.8 $W/m^2/nm$ for triple crystal pair and quadruple crystal pair respectively. Additionally, from Figure 5., cell with the structure ITO/ZnO/PTB7-Th1:COi8DFIC1.5x:IEICO-4Fx and 63% max. transmission gives the desired performance in both visible and infrared regions of spectrum.

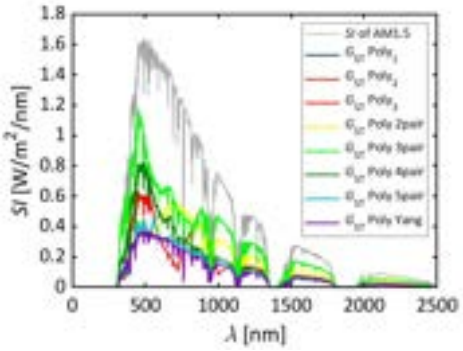

Figure 5: Spectrum Arrived at Thermal Absorber through Polymer Cells

4.2 Energy distribution

As a result of MATLAB modeling, each semi-transparent layout has shown it's electrical and thermal energy capabilities that are displayed in this section. It was obvious that materials tat had low transparency values built up a lot of heat in the PV cell itself as opposed to transmitting the energy to the thermal absorber, where it is converted more efficiently.

In fact, Figure 6 shows the CdTe cells studied by Alrashidi (2019), that have varying transparencies. We can see that with these configurations there is very little heat energy being produced at the solar thermal absorber, especially when compared to the massive amount in the PV cell itself. Although the latter could be recovered by using some fluid flowing behind the cell in a heat exchanger, the rise in temperature that would be associated with it in our cell is prohibitive, as PV cells work better at lower temperatures. This highlights the importance of a high transmittance in our STPV-T cells in order to obtain the highest efficiency possible.

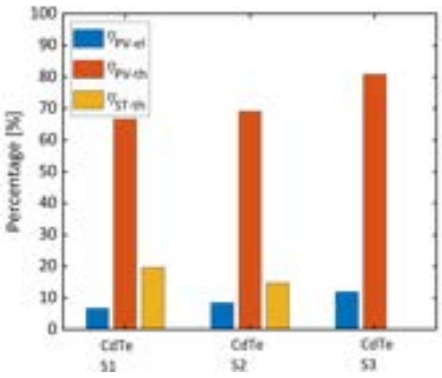

Figure 6: Energy Efficiencies of Cdte Cells with transparencies of 25%, 19%, and 0.5% respectively

Thereafter, the designs that appeared to give the most promising spectral distribution were then analysed in terms of their energy performance: both electrical and thermal. The results were then put into graphical form and differentiated.

As we can see from Figure 7, all chosen cells have shown good thermal energy meaning that incident solar energy could successfully radiate part of the solar spectrum to the thermal absorber. The highest thermal values were attained by the model with double layer of transparent conductive oxides in its structure (Glass/TCO/CdTe/CdS/TCO) which displayed 86.2% of thermal heat generation efficiency. This result is owed to the high transparency of the STPV (close to 92%). Regardless of the model performing poorly electrically, achieving only 2.0% photo-voltaic conversion, the system shows the greatest potential in solar-thermal applications.

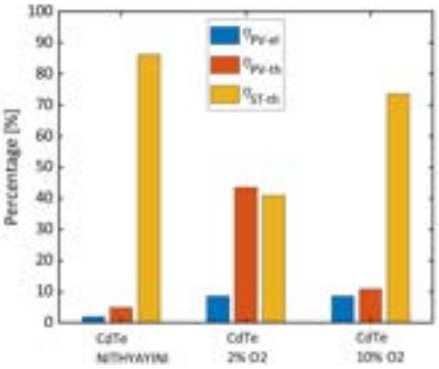

Figure 7: Energy Efficiencies of Different Cdte Cells

Better results in terms of electrical energies were achieved by tandem CdTe PV cells with oxygen ingestion at the manufacturing stage. Both designs performed at 8.6% PCE. For the CdTe cell deposited under 2% oxygen atmosphere, the PV heat is more dominant (43.5%) compared to the thermal absorber heat (40.7%) which is an unfavourable condition for effective PV-T design. On the contrary, the same cell structure with 10% oxygen incorporation has shown an astonishing 73% absorber heat energy, seven times the corresponding PV heat.

While CdTe samples displayed greater potential in terms of thermal absorber heat distributions, perovskite

based cells show higher electrical conversion across the whole set. As seen from Figure 8., the highest electrical efficiency of 25.2% was achieved by a tandem cell with ITO/Perovskite/TiO_2 structure (Perov 3 on chart). Unfortunately, the model failed to create significant thermal outputs (26% PV_{th} and 32% ST_{th}). Potentially, such performance is explained by relatively low maximum transmittance (79%) and insufficient percentage of incident light that could be spectrally split and made available to the absorber. Similar thermal performance was demonstrated by the cell with the following structure: FTO/Perovskite/CIGS (Perov 1).

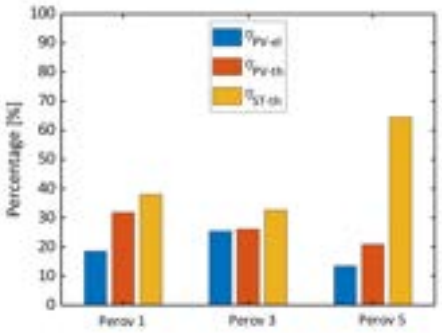

Figure 8: Energy Efficiencies of Different Perovskite Cells

From the graphical data above it is evident that the third set up (i.e.Au/MoO_3/Perovskite/ITO) is able to demonstrate the highest PV and thermal absorber heat values (20.93% and 64.4% respectively). Additionally, electrical performance of the model peaked at 13.5% showing good PV performance. This result has also consolidated the importance of the oxide use in the structure of STPV-Ts.

Polymer based cells' energy performance can be seen in Figure 9. Both cells with structural addition of 1-dimensional photonic crystals display average thermal performance in terms of PV heat and thermal absorber heat. The cell with triple pair of photonic crystals showed 55% while quadruple pair crystal cell achieved only 33% absorber heat efficiency. Nonetheless, in four pair crystal system large proportion of heat was the generation by the PV itself, signifying the importance of additional strategies being developed to utilise the heat produced in the PV module.

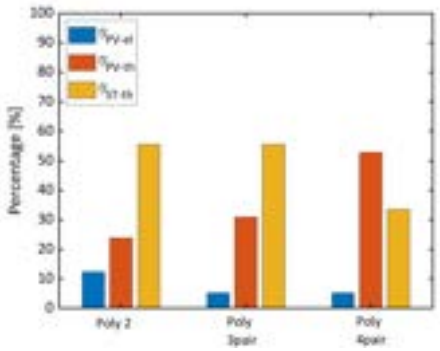

Figure 9: Energy Efficiencies of Different Polymer Cells

Unlike the 1-DPCs based designs, the polymer with the structure ITO/PEDOT:PSS/active layer/PDIN/Al (labelled as Poly 2) has shown more potential to be employed in a PV-T arrangement. High transparency (85%) of the layout has helped to arrive at 12.3% electrical and 55.5% thermal absorber efficiencies at the modelling stage.

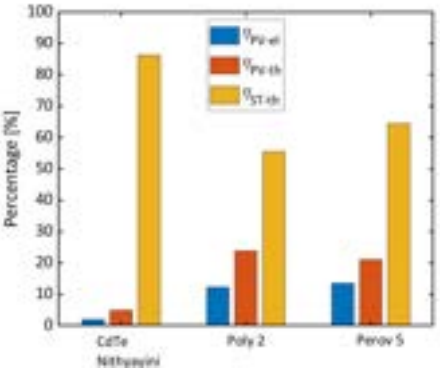

Figure 10: Energy Efficiencies of the Best Sample from each Active Layer Material

As a result of previous analysis, the well performing designs were compared to arrive at a single most-promising material for STPV-T of the study. Upon evaluation of the Figure 10., it became apparent that Perov 5 with structure ITO and fullerine as the top layers shows the

best electrical and thermal efficiencies in the current design. Thus, this material was identified having the biggest potential in STPV-T systems.

Perovskite is seen as the most promising active layer material not only due to it's energy distribution performance. All materials were investigated on the basis of their scalability, production costs and availability.

In terms of scalability, perovskite offers limited expandability as the electrical efficiency of the perovskite module falls dramatically with the increase in area.(National Renewable Energy Laboratory (2018)) Cadmium telluride, on the other hand, represents a highly scalable option, as 5% of the world's solar market is dominated by CdTe based cells. Nonetheless. cadmium is a heavy metal that on outgassing releases toxic fumes that pose danger to human's organ functions. (Matters (2016)) Polymers' scalability, in turn, depends on the initial composition of the complex chemical.

For the production costs, perovskites (Cai et al. (2016)) show much stronger market competition with 45\$/m^2 (Li et al. (2018)) versus 60\$/m^2 for organic polymer cells(GreenMatch (2020)) and 72\$/m^2 for CdTe based cells.(dmsolar LLC (2016))

Availability of the material is key for the successful implementation of any design. Cadmium telluride shows high availability values at present, however, tellurium could potentially be exhausted (current abundance: 1 part per billion in Earth's crust, similar to that of platinum). Perovskite can be found in Earth's mantle as well as in carbonate formations which are in extreme abundance. (Publishing (2005))

5 Conclusions

This study has successfully identified the capabilities of three materials in semi-transparent PV-T applications. The most promising material for the aforementioned collector design is perovskite as the solar cell's active layer. The following design has displayed considerable electrical efficiency of 13.5% and thermal absorber heat efficiency of 64.4% that could not be attained by any other design mentioned in this research.

It also showed the feasibility of semi-transparent PV use in addition to the thermal component.The research has shown massive importance of further investigation into semi-transparent solar-thermal collectors.

The above analysis can be improved as part of the wider research. For example, similar exercise could be performed with other collector designs (both conductive and convective). Furthermore, it is key to investigate the ideal manufacturing conditions for perovskite to benefit from it's performance further. Finally, modelling electrical efficiency from external quantum efficiency (EQE) rather than power conversion efficiency is advised.

6 Acknowledgements

The authors would like to thank Gan Huang (Imperial College London) for their support and guidance during this research project.

References

Alrashidi, H. (2019), 'Performance evaluation of semi-transparent cdte thin film photovoltaic for building façade applications'.
URL: *https://ore.exeter.ac.uk/repository/handle/10871/38891*

Alrashidi, H., Ghosh, A., Issa, W., Sellami, N., Mallick, T. & Sundaram, S. (2019), 'Thermal performance of semitransparent cdte bipv window at temperate climate'.
URL: *https://www.sciencedirect.com/science/article/pii/S0038092X19311892*

Bailie, C. D., Christoforo, M. G., Mailoa, J. P., Bowring, A. R., Unger, E. L., Nguyen, W. H., Burschka, J., Pellet, N., Lee, J. Z., Grätzel, M. & et al. (2014), 'Semi-transparent perovskite solar cells for tandems with silicon and cigs'.
URL: *https://doi.org/10.1039/C4EE03322A*

Baltazar, J.-C. & Do, S. L. (2017), 'Ises conference proceedings database'.
URL: *http://proceedings.ises.org/?doi=swc.2015.08.02*

Banerjee, S. (2015), 'High efficiency cdte/cds thin film solar cell'.
URL: *https://www.ijert.org/high-efficiency-cdtecds-thin-film-solar-cell*

Cai, M., Wu, Y., Chen, H., Yang, X., Qiang, Y. & Han, L. (2016), 'Cost-performance analysis of perovskite solar modules'.
URL: *https://onlinelibrary.wiley.com/doi/full/10.1002/advs.201600269*

Dewi, H. A., Wang, H., Li, J. & Thway, M. (2019), 'Return to issueprevresearch articlenext highly efficient semitransparent perovskite solar cells for four terminal perovskite-silicon tandems'.
URL: *https://doi.org/10.1021/acsami.9b13145*

dmsolar LLC (2016), 'Next generation pv for 12v system'.
URL: *https://www.dmsolar.com/cdte.html*

GreenMatch (2020).
URL: *https://www.greenmatch.co.uk/solar-energy/solar-panels/organic-solar-cells*

Guo, F., Azimi, H., Hou, Y., Przybilla, T., Hu, M., Bronnbauer, C., Langner, S., Spiecker, E., Forberich, K., Brabec, C. J. & et al. (2014), 'High-performance semitransparent perovskite solar cells with solution-processed silver nanowires as top electrodes'.
URL: *https://pubs.rsc.org/en/content/articlelanding/2015/nr/c4nr06033d*

Hajjiah, A. T., Kandas, I. & Shehata, N. (2018), '(pdf) efficiency enhancement of perovskite solar cells ...'.
URL: *https://www.researchgate.net/publication/327468874EfficiencyEnhancementofPerovskiteSolarC*

Hu, Z., Wang, Z., An, Q. & Zhang, F. (2019), 'Semitransparent polymer solar cells with 12.37% efficiency and 18.6% average visible transmittance'.
URL: *https://www.sciencedirect.com/science/article/pii/S2095927319305572?via%5C=ihub*

Kunz, N. (2020), 'Green homes grant extended until 2022: Up to £10,000 vouchers'.
URL: *https://www.greenmatch.co.uk/blog/green-homes-grant*

Li, X., Meng, H., Shen, F., Su, D., Huo, S., Shan, J., Huang, J. & Zhan, C. (2019), 'Semitransparent fullerene-free polymer solar cell with 44% avt and 7% efficiency based on a new chlorinated small molecule acceptor'.
URL: *https://www.sciencedirect.com/science/article/pii/S0143720819303365?via=ihub*

Li, Z., Zhao, Y. & Wang, X. (2018), 'Cost analysis of perovskite tandem photovoltaics'.
URL: *https://doi.org/10.1016/j.joule.2018.05.001*

MA. Green, E. D., AC. Tamboli, D. B., C. Heisler, C. S., G. Akhlesh, P. V., X. Wu, J. Z., TM. Barnes, X. W., Gorji, N., S. Lalitha, R. S., GK. Williamson, R. S., C. Li, G. C. & et al. (2020), 'Semitransparent cdte solar cell with over 70% near-infrared transmittance'.
URL: *https://link.springer.com/article/10.1007/s10854-020-04368-6*

Matters, E. (2016), 'Safety of cadmium based solar panels questioned again'.
URL: *https://www.energymatters.com.au/renewable-news/em1469/*

National Renewable Energy Laboratory, N. (2018), 'News release: Perovskite technology is scalable, but questions remain about the best methods'.
URL: *https://www.nrel.gov/news/press/2018/perovskite-technology-is-scalable-but-questions-remain-about-the-best-methods.html*

Ossila ltd, O. (2020), 'Perovskites solar cell structure, efficiency amp; more'.
URL: *https://www.ossila.com/pages/perovskites-and-perovskite-solar-cells-an-introduction*

Publishing, M. D. (2005), 'Perovskite'.
URL: *https://rruff.info/doclib/hom/perovskite.pdf*

Romeo, A., Artegiani, E. & Menossi, D. (2018), 'Low substrate temperature cdte solar cells: A review'.
URL: *https://reader.elsevier.com/reader/sd/pii/S0038092X18301713?token=FE817E7D309472718C*

Spirit Solar Ltd, S. (2020), 'Solar thermal vs solar pv - what's the difference?'.
URL: *https://www.spiritenergy.co.uk/kb-solar-thermal-vs-solar-pv*

Trofimov, P., Pushkarev, A., Sinev, I. & Fedorov, V. (2020), 'Perovskite–gallium phosphide platform for reconfigurable visible-light nanophotonic chip'.
URL: *https://pubs.acs.org/doi/10.1021/acsnano.0c01104*

You, P., Liu, Z., Tai, Q., Liu, S. & Yan, F. (2015), 'Efficient semitransparent perovskite solar cells with graphene electrodes'.
URL: *https://onlinelibrary.wiley.com/doi/abs/10.1002/adma.201501145*

Yu, W., Jia, X., Long, Y., Shen, L., Liu, Y., Guo, W. & Ruan, S. (2015), 'Highly efficient semitransparent polymer solar cells with color rendering index approaching 100 using one-dimensional photonic crystal'.
URL: *https://pubs.acs.org/doi/10.1021/acsami.5b02039*

Zhang, J., Xu, G., Tao, F., Zeng, G., Zhang, M., Yang, Y. M., Li, Y. & Li, Y. (2019), 'Highly efficient semitransparent organic solar cells with color rendering index approaching 100'.
URL: *https://onlinelibrary.wiley.com/doi/abs/10.1002/adma.201807159*

Zweibel, K. (2008), 'A solar grand plan'.
URL: *https://www.scientificamerican.com/article/a-solar-grand-plan/*

Investigating factors affecting student engagement with gamified learning apps

Mason Banks and Manjeeta Matabudul
Department of Chemical Engineering , Imperial College London, U.K.

Abstract
Gamified learning applications have been a source of increasing interest in the modernisation of teaching in higher education settings. To successfully incorporate gamified apps into the learning process, attitudes and behaviours of the students and lecturers involved and their relationship to the app must be studied. The following study utilised the Atrivity app within a Chemical Engineering course at Imperial College London to investigate the factors affecting student engagement with gamified learning apps. Interventions to promote the app were undertaken, such as vouchers and social media advertisements, while questionnaires and focus groups were conducted and analysed through correlations. It was found that the interventions had no bearing on app usage due to feature limitations of the app and its integration into the course structure. It was also discovered that the new remote learning environment has influenced the various factors affecting student motivation to use gamified learning apps, indicating a pivot towards individualised learning apps as opposed to ones of a competitive nature. This finding provides scope for future research into the use of gamified apps in remote learning environments.

Introduction
Traditional higher education learning methods, mainly through lectures, involving the passive absorption of content, are less effective in encouraging students to take ownership of their learning and apply concepts learnt[1]. Active learning has proven to promote a higher order thinking and connection between knowledge to application among students[2].
In the Chemical Engineering Department at Imperial College London, considerable efforts have been made to integrate technology with teaching through the implementation of active learning platforms such as Panopto, WeBWork, Chemistry video tutorials and most recently, the 'Imperial Chem Eng Wiki' and the Atrivity app. Atrivity is a gamified quiz app including challenges, leaderboard and competition.
Gamified mobile learning apps can enable students to consolidate their knowledge and to better engage with lecture content. A study showed that the students appreciated quizzes due to their visual aspects, mobility, simplicity, and ability to give quick feedback[3]. Apps incorporating gamified elements into their design can engage and motivate students[4]. As students benefit from cumulative learning at a slow and constant pace, this can discourage "binge-learning" or "cramming" for the final exams[5].
A mobile app solely cannot help in boosting students' performance in exams. However, it can test the students' conceptual understanding so that they are in a good position to work out problem sheets and exam papers. Therefore, students need to make maximum usage of the app throughout the year rather than close to the exams.
Given that personal mobile devices are now ubiquitous[4], apps are an efficient way of reaching out to students and stimulating their interest in educational content.
Online learning has been quickly forced upon students since late March this year due to the COVID-19 pandemic. One good study habit to allow students to get the most out of online learning is through regular self-assessments[6]. Gamified learning apps can assist students with testing their progress regularly in this current learning environment. Furthermore, students can have access to the games from anywhere to play during their own time. Through peer challenges, a virtual collaborative environment is enhanced whilst minimising isolated student experiences.
Atrivity was implemented in 2018 in the first-year Chemistry and Maths modules. It has been used as a learning tool during lectures, post-lectures and during revision time, for the Chemistry course for two academic years while it was only used for one year for the Maths course. WeBWork seems to be the preferred active learning platform for the Maths module currently.
With Atrivity, students can challenge their peers in quizzes once the multiple-choice questions have been released by the facilitator of the course, which were either after covering the content or during the lectures. Further questions for the Safety and Loss Prevention (S&LP) module were released for the third-year students this year.
Currently, the app incorporates a few features promoting learners' engagement. Push notifications trigger immediate learning by capturing students' attention and help them stay up to date with the content[4]. The 'leaderboard' feature aims to make the learning more competitive and addictive due to the score-tracking component.
However, it was found that there was poor usage of the app by the students, with most of them only using the app when the lecturer asked them to do so or a few days before the exams. Low engagement is a common problem faced by educational apps[7].
Literature has shown that making the usage of the app compulsory would help in increasing the usage among the students[5]. If the quizzes were graded, students would tend to value them for more intrinsic reasons[5]. However, a few lecturers using the app in

the department have argued that they would ideally prefer if students took ownership of their learning rather than forcing it upon them.

For the gamified app to be perceived as a fun and useful learning tool, it is important that it is widely used among the students without making it mandatory. Different internal and external factors can affect student's motivation to engage with gamified learning apps.

Therefore, this research paper is concerned with **investigating the factors affecting student engagement with gamified learning apps**.

The study will look at the factors hindering the Atrivity app's usage and how some of them can be overcome. Insightful recommendations can be provided as to the direction of gamification of university-level learning using apps and the most influential factors affecting motivation to use them.

When an app is developed, effective marketing strategies ranging from social media to rewards need to be implemented for it to be successful. Factors affecting mobile behaviour before downloading apps, thus the usage, need to be determined[8].

Qualitative and numerical data will be collected from Atrivity, questionnaire surveys, interviews, and focus groups. The usage of the app will be closely monitored among third-year students for the S&LP module. A total of 6 games are available for 2 chapters for the autumn term on Atrivity. The results will include correlations between surveys' findings and a holistic approach towards the promotion of gamified learning apps.

Background

Traditional teaching methods have been found to not be sufficiently effective, thereby indicating that learning in the 21st century needs to develop into an active process. Active learning can shift the way universities act as primary drivers of societal and educational changes and allows students and lecturers to redefine learning while moving into collaborative learning and co-creation of knowledge[9].

One way of implementing active learning is through gamification of educational content. Gamification involves the use of game design elements in non-game situations and game-based learning involves using playing games to gain knowledge and skills[10.]

Gamified learning applications have been a source of increasing interest in the modernisation of teaching in higher education settings.

Studies have shown overall positive outcome with gamified learning apps and online quizzes. A previous study by Pechenkina[4] proved that active learning through gamified learning apps led to an increase in student retention rates and academic performance.

Another study by Cook and Babon[5] showed that online quizzes were an effective way to incentivize students to complete preparatory work, promote active learning and were relatively time efficient. Students showed a high level of engagement with these quizzes and valued them more as they were graded.

In a first-year engineering course, online quizzes were introduced to increase student engagement with on-campus teaching and learning activities. It was found that students appreciated the flexibility of this learning style and could be further motivated if the online quizzes were made a summative assessment task[11].

Cohen and Sasson[12] found that the average grade from written tests and online Moodle quizzes were good predictors of the grade for the final examinations and students expressed generally positive attitudes towards online quizzes. The last Moodle quiz sent to the students in the study is similar to the Atrivity quiz in the sense that they are both time-restricted and provide feedback, i.e., the final score and which questions were correctly attempted, at the end of a challenge.

A previous study on the Atrivity app found that student engagement with live in-class challenges dropped off by 77% over three sessions spanning the course of 4 months[17], indicating an engagement issue over time. The study then focused on using the app for exam preparation in the two-week lead-up. It found that although there was a 74% increase in students registering in the app, very few of those students used the app to answer questions, rather to access revision materials, indicating that when presented with traditional learning methods in an application, students are likely to select it over gamified learning which is more novel and unfamiliar.

The same study also saw sporadic low-level usage of the app throughout the month leading up to the Chemistry exam, with a large spike in challenges and training games played in the two days prior to the exam, engagement peaking on the day of the exam[17]. This exemplifies the current student attitude to the app as a tool for last-minute exam revision.

It was also found that student engagement was higher on the app when studying more difficult content[17], highlighting the importance of challenge in learning.

In addition to this, the study found that Chemistry had greater student engagement as opposed to Mathematics[17]. Engagement therefore depends on the nature of the subject as well as difficulty, as they have inherently different question styles.

Differing lecturer engagement with the app between the two subjects was also a likely cause for the discrepancy, for example automated challenges came directly from the course leader in Chemistry while in Mathematics, the challenges came from generic accounts. Furthermore, a student survey in the previous study identified most students who used the app did so because the lecturer asked them to, and when asked what would encourage them further,

a common response identified more endorsement from the lecturer as a main factor[17].
Students having previously used the Atrivity app for learning Chemistry have mentioned that they feel it is not a useful tool for learning new material, and that it does not prepare them for exam questions[17]. It is therefore important to explain the limitations of the app and its intended purpose as a way of reinforcing knowledge on a rolling-basis to consolidate fundamental concepts in parallel with traditional learning methods.
It was also identified that students who were not aware of the anonymity feature and training modes felt discouraged to use the app[17]. It is therefore important to strongly reinforce these features to include the many students who dislike the competitive nature of the challenges.
The software limitations of the app must also be carefully considered when writing questions, as it has been found that many students were discouraged from using it due to interface and display issues[17]. For example, equations not displaying correctly or images appearing blurry.

Methodology

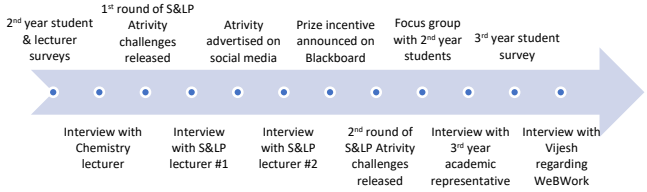

Figure 1: Project Timeline

Figure 1 shows the project timeline throughout the study, which indicates the approaches taken which aim to identify and assess the effect of several variables of which the research question is a function.
Initially, a survey questionnaire was distributed to all teaching staff in the Chemical Engineering Department. The primary goal was to identify prevailing conceptions of the usefulness of the Atrivity app to their courses, and the reasons behind. Additionally, it aimed to highlight whether lecturers thought the app needed promotion amongst staff and students, and which methods they believed would be most effective in doing so. This gave preliminary direction to the project in terms of the factors affecting motivation to prioritise and focus on later in the project.
Simultaneously, a separate survey questionnaire was sent out to 2nd year students who previously used the app in Chemistry and Mathematics courses. It served the same purpose as the lecturer survey, and the questions were designed such that the two surveys could be easily compared to help illuminate the effect of student-lecturer relationship on app usage.
All surveys were conducted securely through the Qualtrics website, with clear anonymity disclaimers given within the email invitations in line with data collection ethics guidelines.
SPSS 27 by IBM was the statistical software used to analyse the quantitative data collected from surveys, and two-tailed Pearson correlations were conducted at the 5% significance level. This was deemed the most appropriate test in determining dependences between variables pertinent to the research question. Practically, this was done by transforming the questionnaire responses into numerical matrices. For example, if a question's responses were 'disagree', 'neutral', 'agree' they would be assigned values of -1, 0, and 1, respectively. Thus, each question became a sample variable suitable for bivariate testing.
Both the reliability and validity of the surveys were also determined using SPSS. To assess the internal reliability, the Cronbach alpha value (α) was determined. The value is an indicator of how reliably the survey items measure similar constructs. The validity analysis was performed through an exploratory factor analysis. A factor reduction matrix enabled to determine the extent to which survey questions successfully measured its intended theme. Construct validity gives an indication of how closely the survey tests the hypothesis being investigated.
This ease of analysis using SPSS was a key motivation for the heavy use of the online questionnaire to gather data.
However, there are various limitations to surveys in data collection, such as inability to ask follow-up questions, and discrete response options stifling expression and potentially introducing bias. Therefore, to improve the reliability of the data gleaned from surveys, supporting interviews and focus groups were undertaken with members from each sample group.
After sending out the surveys to lecturers and students, an interview was carried out with the Chemistry lecturer who used the Atrivity app during the lectures for 2 academic years. The purpose of this interview was to investigate the previous approaches used by the lecturer to increase students' engagement with Atrivity. Open-ended style questions were mostly asked to get an in-depth understanding of what worked well and what did not. They provide a holistic look of the issues as the data is given more diversity due to the open-ended nature of the questions[13]. Based on the responses obtained, possible intervention approaches were flagged, and some were further implemented and considered throughout the course of the research study.
From the students' and lecturers' responses, a few feasible promotion strategies were implemented.

Initially, an announcement was made during the Safety and Loss Prevention lectures by the lecturer about the existence of the app and that he would be releasing challenges after covering each of the course's chapters. One PowerPoint slide included instructions on how to log in and who the students can contact if they are facing technical issues with the app. At that point, the first two sets of challenges on Chapter 2 were released to the students.

Secondly, the app was promoted on the Imperial Chemical Engineering social media platforms, namely Facebook, Twitter and Instagram, with a download link attached.

The last marketing intervention step included the introduction of a prize incentive along with a Blackboard announcement. Three new sets of games were released for Chapter 3 and the lecturer made both an in-class and Blackboard announcement regarding the rewards for the students who would perform exceptionally well in the challenges. Prizes would be given to the two students at the top of the leaderboard and these would consist of £20 and £10 Amazon vouchers for the winner and runner-up, respectively. Each challenge comprises 7 questions which were all written by last year's final year students and proofread by the lecturers. For each question, there were 3 choices and 1000 seconds available to attempt it. One would score 50 points for each correct answer. From the time of announcement, the students had 6 days to complete the challenges. The Atrivity control panel provided the relevant data regarding the level of engagement, such as the number of players registered, the number of active players in each game, the education time, and the percentage of correct answers, which were used for analysis.

After sending the questionnaire to the students, a focus group was organised with the current second-year students whereby specific open-ended questions related to the usefulness of the app and the interventions, were asked to them. One of the two participants recruited wrote some questions for Atrivity last year. From the information provided, the prize incentive was then implemented next.

After introducing the prize incentive among the third-year students, due to time limitations and the heavy schedule of the third-year students, a meeting with the year representative was held instead of a focus group, to understand the behavioural reactions from the students based on the interventions.

A final questionnaire was then sent to the third-year students, with the design being informed by the findings emergent at that point in the timeline.

Each question in the survey was designed to primarily measure one of five pre-determined themes of which the research title is a function. As indicated by Figure 2, survey items will often straddle multiple factors as the themes are interrelated.

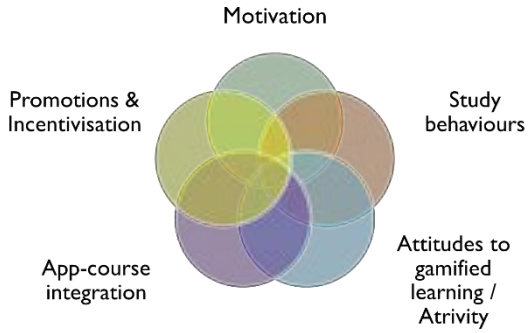

Figure 2: Venn diagram representing the 5 interrelated survey themes

As motivation is the overarching theme, each survey item measuring the four main factors influencing motivation had a supplementary question asking explicitly if a given factor positively or negatively affected it, and to what degree. This ensured that any significant correlations found between these paired survey items had a definite causal relationship and were therefore more reliable.

Students were then able to list any learning apps that they currently use and their reasons for using them and were given the chance to enter a raffle to win a £10 Amazon voucher. A third of respondents took part in the raffle, which may have impacted the reliability of the survey findings.

Correlations were finally conducted on the collected data to further investigate hidden relationships between the various themes, and reliability and validity were evaluated in a similar fashion as the initial surveys.

A few participants volunteered to join the focus groups after an email was sent out to both year groups along with the same message in the 'WhatsApp' group chats. Ethical codes were ensured for the focus groups as consent was sought and the interviewee had the choice to answer a question or end an interview. Furthermore, no monetary payment was provided to the second-year students for participation to minimise the possibility of motivating people to be untruthful in their answers which could affect the reliability of the study[14]. All the students from second year and third year were also made aware about the aim of the research project and could contact the researchers with questions and concerns.

Results and Discussion

Second-year student survey findings

From the survey sent out to the second-year students, a total of 30 responses were recorded, with some questions skipped by a few students. While 76% of the students admitted to having used Atrivity last academic year, no student perceived the app as being extremely useful and 3 students even admitted that it was extremely useless. However, overall, most students were more inclined to viewing the app

as slightly useful, thereby showing potential for the app to be promoted within the department.

Most students who did not use the app said that they did not think it was useful for exams. In first year, students tend to be overwhelmed by the transition from high school to university and thereby, tend to find difficulties in adjusting to a new learning environment. Using an app to reinforce knowledge may seem less appealing to them throughout the year, especially in situations whereby students are usually facing other issues such as home sickness, socialisation, motivation, and poor academic skills[15], which would require immediate attention. During the focus group, the students have even mentioned that first-year students tend to be more worried about exams and passing the year.

Other popular reasons for the lack of usage of the app were the poor user interface and display, and limited time scheduled to use it. With increasing competition from other learning platforms such as Khan Academy, Quizlet and Libretext, students would be more tempted to switch to these alternatives which are more user-friendly and well-established online platforms. The lifecycle of the Atrivity app with a poor user interface could be as follows:

Figure 3: Lifecycle of an app with poor user interface

Generally, apps tend to be forgotten and abandoned before the users discover their value[7]. On average, an app can retain only 40% of the initial users after nearly a month[16]. An app with a poor user interface can only accelerate the uninstallation rate (from (3) to (5) in Figure 3) among users. To increase the enthusiasm for the app usage, the technical functionalities of Atrivity need to be improved. During the focus group, the students complained that the app would crash multiple times and that they would prefer getting printed copies of the MCQs, thereby defeating the purpose of the app.

They found that the quality of the screenshot images was significantly poor, with Atrivity being unable to display equations or symbols. The students were also unable to re-attempt questions which were incorrectly answered. There are no solutions provided, which makes it harder for students to know where they went wrong in their reasoning process. However, students cannot solely rely on Atrivity for the consolidation of knowledge after lectures. Problem sheets and past exam papers usually help in preparing students to tackle complex engineering problems. It is therefore recommended that until these technical features are added for improving the user's experience, this app should be promoted as a reinforcement tool to assist the students in understanding the fundamentals[17]. This can be complemented by adding a section called "Atrivity" in the discussion board in Blackboard for the specific modules, whereby students can ask further questions to their peers and the course leader regarding the solutions to the MCQs in the app.

The student who was involved in writing the questions for the app said that he did not feel confident that the app would benefit his learning as some of the questions were his own. Due to the complaints from the students, it is best that the questions are written and proofread by experts or students from higher year groups, instead of students from the same year group. Having the questions endorsed by an expert would reassure the students in the quality of the questions and answers provided. This would minimise the chances of incorrect answers and increase the number of students who used to write questions for the app, to use it in their own spare time.

When it was asked whether the app was well incorporated, only 15% of the students agreed that this was the case. The most popular reasons for a low agreement rate were due to the limited use of Atrivity by the lecturers and tutors, as well as the intrinsic technical issues with the app. Students from the focus group supported these findings by saying that the lecturers would be only using the app when they remembered that it existed and there was no consistency. This stresses the importance of the continuous use of Atrivity by lecturers and tutors. It could be more convenient for lecturers to stop using or promoting the app during the lecture hours as time might be very limited. However, the course must be structured in such a way that the students are reminded to use the app either at the beginning or end of the lectures.

From the students' survey results, it was found that lecturers encouraged students to use the app while there was limited encouragement from tutors or GTAs during the tutorials. However, students strongly agreed that these two factors did not affect their usage. Overall, students expressed mixed opinions as to whether the app was well advertised by the department. During the focus group, the students mentioned that more innovative incentives need to be explored for promoting the usage of the app. Currently, the app incorporates gamification through the leaderboard, points-scoring and badges. Literature shows that gamification does indeed increase the engagement of students in the online learning experience[18]. Further external motivators

such as interesting prizes such as vouchers or tickets, could potentially boost engagement. Similarly, the app "HOLD" which aims to limit student distraction, allows students to accumulate points for not using their phone. These points can be used to get free cinema tickets and discount vouchers from various stores[19]. For apps having educational purposes such as HOLD and Atrivity, rewards can tend to attract students.

The students were asked to rank the different marketing strategies for encouraging usage of Atrivity (Figure 4).

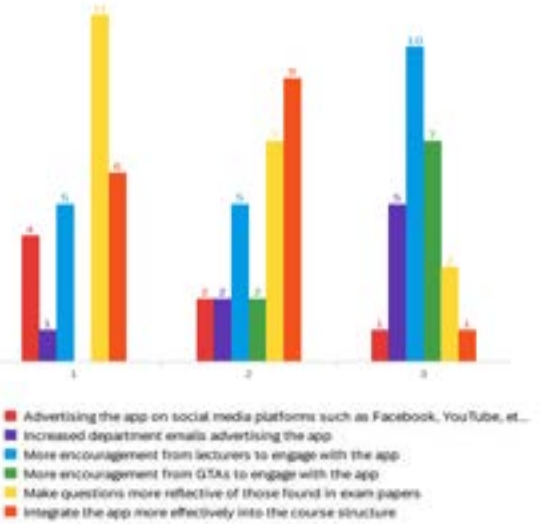

Figure 4: Number of students who ranked the top 3 marketing strategies

From Figure 4, students would prefer that the questions in Atrivity reflect those found in exam papers. The other 2 popular choices include the effective integration of the app into the course structure followed by higher encouragement from lecturers to use the app. However, even though questions could slightly reflect exam-style questions, it would be nearly impossible to fully achieve this as Atrivity can only generate one specific type of question - MCQs. For Chemical Engineering exams, questions are asked in different formats ranging from 'True or False' to long descriptive ones, whereby questions could be attempted in one line or a couple of pages. Atrivity can only support MCQs and therefore should be promoted as this reinforcement app which can test students' understanding of key concepts that would equip students with confidence to work out problem sheets and past exam papers. The app needs to be promoted in a different light as more emphasis should be put on the reinforcement purpose of this tool and the improvements, if any, along with connecting the department's intentions with students' expectations[17].

A different online platform called WeBWork was launched this year for first year and second year Maths modules. A few of students' complaints about Atrivity were tackled with WeBWork as it would recognise mathematical variables and symbols. There was simple ease of navigation and worked-out solutions were available to the students. Following a meeting with the Maths lecturer, it was found that there is a high engagement rate among the students. Having some of the questions graded was a huge push, but there were still a lot of students using WeBWork for the non-graded questions. The preliminary maths questions sent out to incoming first-year students through WeBWork seemed to very useful, especially to those students who did not have prior Further Maths background. During the focus group, the students admitted that they currently preferred WeBWork over Atrivity, even though WeBWork was not promoted through any marketing strategy.

Correlation findings from students' survey

The data obtained from the students' questionnaires yielded two significant correlations from the Pearson's test on SPSS. A positive correlation of 0.57 was found between the usage of Atrivity last year and the usefulness of the app. This shows the importance of students testing the app for themselves to find the extent to which it is useful. Some students have already formed an opinion about the app without even using it. Without any incentive, fewer students might use the app and those who do not might hold a negative feeling towards Atrivity. In this instance, it should be considered to initially grade Atrivity questions so that students can be exposed to it at least once for proper judgement of the app. During the focus group, the students have expressed enthusiasm for complementing graded coursework with Atrivity as this would force them to stay engaged with the course and not fall behind. While this initiative might not sound appealing to many students at the beginning of the year, closer to exams, they would feel more confident.

Another positive correlation of 0.48 was obtained between the usage of Atrivity last year and lecturer's encouragement to engage with the app. This result is in line with earlier survey's findings this summer, where 44% of the students used the app whenever the Chemistry course lecturer would request them to do so- either through live games or emails and push notifications[17]. However, it was also found that the students' engagement in the live games dropped with time. The focus group's interviewees argued that this was mostly due to the poor user interface of the app, rather than students disengaging with the course content due to other commitments.

Lecturers' survey findings

Only 1 lecturer of the 16 surveyed was not aware of Atrivity to some degree, however only 2 lecturers had previously used Atrivity in their courses.

28% of those who did not use the app said that it was due to not knowing how Atrivity works, while another 28% said they did not think Atrivity would add any value to their teaching sessions.

Lecturers identified the following as the most effective ways of improving student engagement with Atrivity:

- More encouragement from lecturers and GTAs to engage with app
- Integrating the app more effectively into the course structure

It was also found that on average, lecturers believe that they themselves are more likely to engage with the app if:

- Provided with tutorials on how to use the app
- Provided with example ways to incorporate the app into the structure of their course

This indicates the importance of making gamified learning apps simple and easy to use such that they can be readily implemented to facilitate the learning process, which will encourage both the staff and students to engage with it together. The only significant correlation found there was a strong association between believing the app needs promotion among students and that the app needs promotion among lecturers to improve engagement (0.72), further highlighting the importance of the student-lecturer relationship when considering motivation.

Interventions

Over the course of 6 weeks, different interventions were implemented to monitor student's engagement with the app for the S&LP module. A total of 6 games were released- 2 from Chapter 2 and 4 from Chapter 3.

The first intervention was when the lecturer made an announcement at the end of the lectures to download Atrivity to practice MCQs on Chapter 2 of the course. Following the announcement, a few students registered in the app. 3 students were active in the first game released which covered the first part of Chapter 2. However, the participation rate dropped significantly with only 1 student playing a challenge for the second game of Chapter 2. This should take into consideration that students generally tend to attend lectures at the beginning of the term, however, the attendance rate tends to drop with increasing coursework. A previous study on Atrivity showed that the most popular games were for chapters which had been covered a while ago rather than the recent ones[20].

Two weeks later, Atrivity was advertised on social media, which did not affect the engagement rate. The posts only received a few likes of approximately 5 in total, which shows a lack of interest among students. Despite social media is intensively used for marketing[21] and widely used by Chemical Engineering students within the department, it was proven that it might not be an effective platform for promoting education apps.

On week 5, the prize incentive was introduced, and this was advertised by the lecturer at the end of the week's lectures and on Blackboard. On week 6, after the deadline to qualify for winning a prize had passed, it was found that no student played all the games for Chapter 3. The prize incentive was not enough to motivate the students to score maximum number of points to win the vouchers. The timing might have affected the participation rate, as most students from the same year group were busy in their Mechanical Design project for the same module during that time. This showed that students would prioritise graded coursework over rewards for non-graded challenges.

Table 1: S&LP games data

Games	Users	Registered in App	Registered in game	Active in the game
Combustion	132	34	19	3
Fires & Explosions	132	34	4	1
Corrosion Introduction	132	34	0	0
Corrosion Kinetics- part 1	132	34	1	0
Corrosion Kinetics- part 2	132	34	0	0
Corrosion-Thermodynamics	132	34	1	1

Chapter 2 included 'combustion' and 'fires & explosions' games while the remaining games from Table 1 belonged to Chapter 3. Initially, the number of active players was lower than those registered in the game. This means that a few students opened the game but did not choose to play a challenge. Overall, the different interventions had minimal effect on students' behaviours.

Third-year student survey and interview findings

Data from the third-year student survey supplemented by an interview with the current academic course representative allowed for a deeper understanding of the causes for low engagement despite implementing a few promotion strategies. A Cronbach alpha value of 0.81 was found and every survey item successfully measured its intended theme with some overlap. Therefore, the reliability and validity of the survey items were sound.

The student awareness of the two interventions of vouchers and advertising on social media had no significant impact on student motivation to use the app.

This may be explained by some correlations of pair-wise survey items aimed to draw causal relationships between various factors and motivation:

- Student motivation to use the app strongly decreased due to issues inherent to the app. For example, there was a strong positive correlation between motivation and ease of use (0.736) and finding the app intuitive (0.618) respectively and a strong negative correlation between motivation and experiencing technical issues with the app (0.848).

- Student motivation to use the app also decreased due to the perception that the nature of the questions written for S&LP were not well suited to the quick-fire, multichoice nature of Atrivity (0.843).

- Whether or not students thought that individually challenging other students was a positive feature greatly impacted their motivation to use the app (0.775). Awareness of the training mode and perception towards it had a mild effect on the motivation of students to use the app (0.452 and 0.485 respectively).

- Students' perception of the way the app was advertised when rolled out for S&LP this year moderately influenced their motivation to use the app (0.535).

- Students' perception that the way the app was not incorporated well into the S&LP and Chemistry courses greatly diminished their motivation to use the app (0.805 and 0.711).

- Students who cut non-mandatory work from their schedules first during term-time tended to have less motivation to use Atrivity (-0.554). This makes sense as Atrivity was made non-mandatory work.

The other three main influences on motivation to use Atrivity have apparently overridden the effect of promotions and incentivisation completely in this study, therefore diminishing our ability to analyse their effects on usage of gamified apps generally.

Interestingly, students who tend to use learning apps to practise factual recall style questions tended to believe that the S&LP questions were not well suited to the quick-fire, MCQ nature of the Atrivity app (-0.585). This indicates a willingness for more factual recall style questions to be released for the app, as opposed to other types. This was corroborated during our interview with the third-year representative, who noted that the lack of feedback after conducting a long-winded calculation was unrewarding, which impacted her motivation to use the app very negatively.

On another note, it was found that 90% of 29 students who responded either 'somewhat' or 'strongly agree' that the new remote learning environment has forced them to change the way they study. In addition, several correlations seem to suggest that the remote learning environment affected students' relationship to gamified learning apps, and the way different factors influence motivation may have changed as a result.

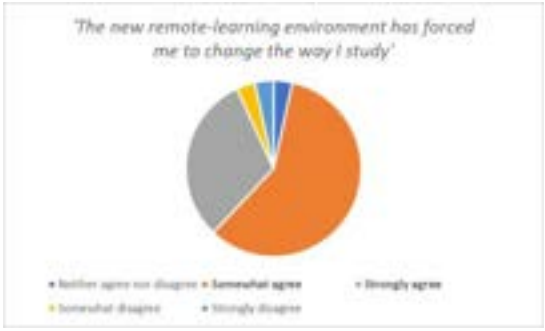

Figure 5: 'The new remote learning environment has forced me to change the way I study' response pie chart

There is a very strong positive association (0.853) between using gamified apps regularly to support your studies and having an increased willingness to use them because of the new remote learning environment. This suggests that students who integrate apps into their regular learning schedule believe that they are tools especially well-suited to this learning environment. As the environment is largely online and in isolated workspaces, students may be looking to use apps to make individualised learning more engaging or to simulate collaborative learning normally conducted in-person. Indeed, it has been found that students tend to be more 'excited about learning and [colleagues] hold them accountable and motivate them to stay engaged' when attending university in-person[22].

Furthermore, students who found that the new remote learning environment has changed the way they study expressed to a moderate degree that they found individually challenging other students not to be a positive feature of the app (-0.579). They also expressed to a lesser degree that they did not find the leaderboard to be a positive feature of the app (-0.393). This suggests that students behave less competitively in this new environment, and therefore view these focal features of Atrivity in a poorer light. Chemistry course leader Dr. Deesha Chadha expressed that students were quite enthusiastic when using Atrivity for in-class challenges and tended to aggregate into teams when competing. The diminished sense of teamwork and collegiality in the new remote learning environment may have caused this shift in study behaviour and therefore negatively impacted motivation to use Atrivity.

This is further corroborated by another data point, being that students who had increased willingness to use gamified learning apps because of the changing

learning environment expressed moderately that the individual challenge feature of Atrivity was not a positive one (-0.499), indicating that other gamified learning apps on the market are perceived as more suitable in the current scenario. Indeed, several students indicated the use of apps with non-competitive nature in the closing comments such as Quizlet, Memrise, LinkedInLearning, Magoosh and Anki which are more user-centric and aimed at self-facilitated and individualised learning.

Students who found that the new remote learning environment has changed the way they study also moderately believe that the app was not well incorporated into the S&LP course structure (-0.498). This suggests that the approach to incorporating gamified apps into such modules should change to complement the aspects of the new learning environment. Indeed, it has been found that there needs to be a concerted effort to provide a learning structure while going beyond replicating old environments, instead, using a range of collaboration tools and engagement methods that promote "inclusion, personalization and intelligence"[23].

Student attitudes towards the usefulness of gamified learning apps in university level learning or in Chemical Engineering specifically had no bearing on their motivation to use Atrivity, emphasising the importance of issues specific to this app in explaining the low usage.

In addition, 41% and 52% of students 'slightly' and 'strongly agreed' respectively that gamified learning apps can be useful for learning Chemical Engineering , while 55% and 38% of students 'slightly' and 'strongly' agreed that they can be useful for learning university level content generally. This indicates that students tend to perceive Chemical Engineering as particularly well-suited to gamified learning, and more broadly that these types of apps do have a place in the academic sphere.

Conclusion

Overall, students are very enthusiastic to engage with learning tools which incorporate technology. However, the learning tool needs to fit appropriately in the context for the students to perceive it as useful. Different routes of promotion and incentives such as vouchers and advertisements have no bearing on student motivation to use gamified learning apps if they do not find the app useful in the first place.

For complex subjects, like Chemical Engineering, gamified learning apps have the potential to be implemented. However, they need to complement the relevant course content and student behaviours appropriately if students are to be motivated to use it, which the gamification app investigated in the study, Atrivity, currently does not do.

The most effective way to encourage students to use the app is through grading the questions. In this way, students would value them more, as shown with WeBWork.

Even though, previously, students appreciated and engaged with the competitive nature of gamified learning apps, the learning style of students has changed due to a forced change in their current learning environment. Along with internal factors such as user interface and type of feedback available in the app, it has been found that external factors, such as lecturers' encouragement and a new learning environment, have had an impact on student engagement with gamified learning apps. Remote learning might not favour competition unless students are in the appropriate environment where they are all brought together virtually and encouraged to challenge their peers.

Gamified learning apps can be more effective if the usage is in a timely manner whereby students test their progress regularly throughout the academic year.

Recommendations

The results have shown that there are many internal and external factors behind gamification apps' low engagement rate. Therefore, the following recommendations can be proposed:

- Lecturers should introduce grading some of the quizzes in the app initially so that students can discover the potential of the app through their usage. This should be paired with improvement of the technical features to improve user's experience.
- When advertising gamified learning apps such as Atrivity, it should be emphasised that they are reinforcement tools and not learning tools. Students should be referred to other learning platforms such as WeBWork which is a better platform suited for complex engineering problems complemented with hints and solutions. It might be more appropriate for Maths-based questions.
- Based on the new remote learning environment, higher student engagement rate can be observed if competition-based apps are shifted to individualised or collaborative-based apps.
- Further investigate the effect of the new remote learning environment on usage of gamified learning apps by investigating other gamified learning apps and their intended purposes.

Limitations

- Small survey sample sizes (<50) may have negatively impacted the reliability of the results. 72% of respondents to the third-year survey agreed that they attend live lectures regularly. These students may therefore not represent the cohort accurately. Larger focus groups would also have been more representative of the entire cohort.
- Atrivity was used as a model to explore broader factors influencing motivation to use gamified learning apps, however its features may not be representative of the larger market of apps available.

- Although the final survey was designed with pair-wise items to ensure a causal relationship was found when conducting correlations, causation cannot be ensured between more nuanced correlations between non-pairwise items.

Acknowledgements

We would like to extend our gratitude to Dr. James Campbell who has guided us throughout the project. We would also like to thank Dr. Deesha Chadha for her assistance with SPSS and Dr. Chris Tighe and Dr. Marsha Maraj for their support in the interventions. Finally, we would like to thank all the lecturers and students who participated in the surveys and focus groups.

References

1. Bligh Donald. What's the use of lectures? *Biochemical Education*. 1972;27(3):183-184. doi:10.1016/s0307-4412(99)00047-3
2. Cook BR, Babon A. Active learning through online quizzes: better learning and less (busy) work. *Journal of Geography in Higher Education*. 2017;41(1):24-38. doi:10.1080/03098265.2016.1185772
3. Wilkinson K. The integration of mobile learning app-based quiz-games in higher education teaching of anatomical sciences. Published online June 14, 2017.
4. Pechenkina E, Laurence D, Oates G, Eldridge D, Hunter D. Using a gamified mobile app to increase student engagement, retention and academic achievement. *International Journal of Educational Technology in Higher Education*. 2017;14(1):1-12. doi:10.1186/s41239-017-0069-7
5. Cook BR, Babon A. Active learning through online quizzes: better learning and less (busy) work. *Journal of Geography in Higher Education*. 2017;41(1):24-38. doi:10.1080/03098265.2016.1185772
6. Spicer André HL. How students can make the most of online learning | Financial Times. Published 2020. Accessed November 23, 2020. https://www.ft.com/content/87077445-6a1c-4283-bc81-8077af211a12
7. Pham XL, Chen GD. PACARD: A New Interface to Increase Mobile Learning App Engagement, Distributed Through App Stores. *Journal of Educational Computing Research*. 2019;57(3):618-645. doi:10.1177/0735633118756298
8. Zolkepli IA, Mukhiar SNS, Tan C. Mobile consumer behaviour on apps usage: The effects of perceived values, rating, and cost. *Journal of Marketing Communications*. Published online 2020. doi:10.1080/13527266.2020.1749108
9. Christersson C, Staaf P. Promoting active learning in universities: Thematic Peer Group Report. *Learning and Teaching Paper*. 2019;5(January). www.eua.eu
10. Welbers K, Konijn EA, Burgers C, de Vaate AB, Eden A, Brugman BC. Gamification as a tool for engaging student learning: A field experiment with a gamified app. *E-Learning and Digital Media*. 2019;16(2):92-109. doi:10.1177/2042753018818342
11. Aziz SM, Lakes M. Online Quizzes for Enhancing Student Learning in a First Year Engineering Course Author : Published online 2003:1-8.
12. Cohen D, Sasson Irit. ONLINE QUIZZES IN A VIRTUAL LEARNING ENVIRONMENT AS A TOOL FOR FORMATIVE ASSESSMENT. *Journal of Technology and science Education*. 2015;5(3):184-193.
13. Allen M. Survey: Open-Ended Questions. In: *The SAGE Encyclopedia of Communication Research Methods*. SAGE Publications, Inc; 2017. doi:10.4135/9781483381411.n608
14. Head E. The ethics and implications of paying participants in qualitative research. *International Journal of Social Research Methodology*. 2009;12(4):335-344. doi:10.1080/13645570802246724
15. Tappu R. (17) (PDF) What are the Key Issues faced by first year undergraduates?". Published 2015. Accessed December 12, 2020. https://www.researchgate.net/publication/305826252_What_are_the_Key_Issues_faced_by_first_year_undergraduates
16. Kothari N. The 9 Key Metrics For Measuring User Engagement For Ecommerce Apps - Mofluid.com. Published 2016. Accessed December 13, 2020. https://mofluid.com/blog/the-9-key-metrics-for-measuring-user-engagement-for-ecommerce-apps/
17. Mawdsley K. Interview and Survey Report- summer 2020. Published online 2020.
18. Imran H. Evaluation of awarding badges on Student's engagement in Gamified e-learning systems. *Smart Learning Environments*. 2019;6(1):17. doi:10.1186/s40561-019-0093-2
19. Heathman A. The Hold app rewards students with cinema tickets for not checking their smartphone | London Evening Standard | Evening Standard. Published 2018. Accessed December 14, 2020. https://www.standard.co.uk/tech/hold-app-smartphone-addiction-a3778746.html
20. Mawdsley K, Mehta K. Investigating Active Learning through Atrivity to Chemical Engineering . Published online 2020:10.
21. Appel G, Grewal L, Hadi R, Stephen AT. The future of social media in marketing. *Journal of the Academy of Marketing Science*. 2020;48(1):79-95. doi:10.1007/s11747-019-00695-1
22. Li C, Lalani F. The rise of online learning during the COVID-19 pandemic | World Economic Forum. Published 2020. Accessed December 17, 2020. https://www.weforum.org/agenda/2020/04/coronavirus-education-global-covid19-online-digital-learning/
23. Burke Lilah. Long-term online learning in pandemic may impact students' well-being. Published 2020. Accessed December 17, 2020. https://www.insidehighered.com/digital-learning/article/2020/10/27/long-term-online-learning-pandemic-may-impact-students-well

Developing a Dynamic Carbon Benchmarking Method for Building Portfolio Comparison

Miles Gulliford, Richard Orlebar

1 Abstract

This work developed an industry focused, dynamic benchmarking method for assessing the carbon performance of a building portfolio, in partnership with Sainsbury's. This novel approach implemented a layered structure to predict unique carbon emission benchmarks for each of Sainsbury's stores. Multivariate linear regressions (MLR), artificial neural networks and decision trees (DT) were used to produce these benchmarks and their performance was compared. Performance indicators including model error, sensitivity analysis and classification of case study stores assessed the relevance of each technique to the application. It was concluded that DTs were most suitable for this form of benchmarking.

This model distinguished itself from previous benchmarking methods in its production of quantitative carbon residuals, indicating a store's level of over or under-performance in gCO_2ft^{-2}. These outputs were more suitable for short-term goal setting and decision making. The model was more robust to climate factors than previous methods due to the careful implementation of weather features. It was observed that the regression models proved more effective for electricity demand benchmarking than gas. This work highlights the need for further research on gas demand benchmarking.

2 Introduction

Forecasts made by the Intergovernmental Panel on Climate Change (IPCC) outline the risk of reduced economic growth and shortages in food and water in the event of global warming of 1.5°C above pre-industrial levels [1]. Thus, to keep global temperatures below this limit, net anthropogenic CO_2 emissions must reach zero by 2050. As of 2019, building operation made up 30% of global CO_2 emissions with an annual $10GtCO_2$ emitted [2]. Therefore, to avoid the severe impacts of global temperature rise, commercial building operators must face the challenge of steadily eliminating these emissions. Sainsbury's, the UK's second-largest grocer, captured 16% of the market share in 2019 [3]. For the financial year ending in 2020, Sainsbury's estimated its annual UK emissions as 0.85 $MtCO_2e$ [4]. Approximately 68.6% of these emissions were attributed to the operation of stores and supermarkets [4]; it is evident that much of Sainsbury's work in reaching their net-zero target will lie in improving the emissions profile of their portfolio.

There exists a significant amount of literature on the analysis of building energy usage and efficiency. Technical, statistical and data-driven techniques have been developed for demand prediction [5, 6], urban planning [7, 8], building diagnostics and retrofit [9, 10] as well as building performance benchmarking [11, 12].

Within the building sector, benchmarking refers to the comparison of the energy performance of similar buildings [13], typically resulting in a performance score or rating. A significant number of white-box methods [14] have been developed based on detailed industry knowledge. The most renowned of these models being the Energy-Star method [15], a benchmark designed by the US Environmental Protection Agency (EPA), whereby each building is assigned a 1-100 rating for energy performance.

While these initiatives act as a useful form of performance disclosure, their reliance on detailed technical information means they are less suited to evaluating building performance at scale. Therefore, by leveraging increased volumes of building information, black-box data-driven methods [16] show significant potential for large building portfolios.

Data-driven methods employed for building energy performance benchmarking applications include multivariate linear regression (MLR) [11], K-means clustering [12] and decision trees [17]. More nuanced and novel approaches include work by Lara et al. [18] with K-means clustering and MLR in sequence, which resulted in a higher coefficient of determination (R^2). Yalcintas' 2006 work used ANNs to predict and benchmark energy demand for different systems while modelling how retrofitting efforts would affect these benchmarks [19].

Literature gaps surrounding building energy performance, included the implementation of comprehensive weather and carbon factor data for comparison of portfolios covering different seasons and climates [16]. Furthermore, comparison of benchmarking method performance remains limited [17, 20], an opportunity exists to compare methods for benchmarking along the lines of Tso and Yau's work comparing MLR, DT and ANN performance for demand prediction [21].

As part of its partnership with Imperial, Sainsbury's provided access to data on the characteristics, electricity usage and gas consumption for all 1929 assets in its portfolio. Data on this scale offered a unique opportunity to perform research in the field of benchmarking building efficiency and inform investment strategies for a low carbon future.

This work built on the wealth of existing benchmarking techniques to develop a novel, robust methodology for comparing the carbon emissions across a portfolio, with particular attention to the mining and implementation of weather features. This allowed for

benchmarking of building performance dynamically, accounting for unmanageable factors including store age, type and climate.

Three different regression techniques for this benchmarking approach were assessed. This comparison offered compelling insights into relative feature importance and ensured a high performing final model.

This report introduces the methodologies used in construction of the three models and discusses the results of analysis. The outputs of the models provided sufficient detail to inform future investment decisions towards Sainsbury's carbon emissions goal and provide short-term targets.

3 Methodology

3.1 Data Collection and Treatment

Prior to the development of the benchmarking models, data was collected, cleaned and processed.

3.1.1 Building Data

A database of building characteristics, electricity usage and gas consumption data by four-week periods for financial years ending 2018 through 2020, was provided by Sainsbury's. This contained 1929 assets. In order to ensure the model compared like-for-like buildings and targeted operationally intense assets, only supermarkets were considered; this left 594 remaining stores. Categorical features, such as store type, were converted to binary variables, as these values could then be interpreted by the models.

3.1.2 Weather Feature Creation

Hourly temperature and humidity data were sourced from the Centre for Environmental Data Analysis (CEDA) [22]. These were loaded into an SQLite database from which they could be called easily. Data was collected for each store by matching it to its closest weather station; this was collated into the corresponding four-week periods.

Weather features created included: average humidity, heating degree days (HDD) and cooling degree days (CDD), these are shown in equations 1 and **??** below. These may be interpreted as demand on heating and cooling systems respectively over the time period considered. These values were commonly used in literature [19] as they more accurately reflected temperature effects on energy demand.

$$HDD = \sum_{i=day} v_i(T_i - T_b) \quad v_i \begin{cases} 1 & T_i < T_b \\ 0 & \text{Else} \end{cases} \tag{1}$$

$$CDD = \sum_{i=day} v_i(T_i - T_b) \quad v_i \begin{cases} 1 & T_i > T_b \\ 0 & \text{Else} \end{cases} \tag{2}$$

Here, temperature (T_i) was a daily average. To maximise the value of the HDD and CDD features, analysis of their correlation with energy consumption was completed for different baseline temperatures T_b, this was selected as 15.5°C for CDD and 12°C for HDD.

3.1.3 Carbon and Cost Factors

A carbon emissions factor (CF) represents the CO_2 produced per unit energy consumed (gCO_2e/kWh); cost factors are similar, with units of £/kWh. The Sainsbury's dataset included store specific CF values for electricity used over 2019 and annual average cost factor values for all stores; these were used to convert energy residuals to carbon and cost bases respectively. These outputs were considered more appropriate for investment decision making. A constant gas CF of 184 gCO_2e/kWh was taken from government data [23]. To account for the decarbonisation of the UK electricity mix the electricity CF values were reduced at a constant rate of 10% per year [23].

3.1.4 Feature Selection

Once all features were collected, those which would not add resolution to the model were removed by the following steps.

First, technological features were not considered as inputs to the model; this rewarded stores with lower carbon emitting technologies.

Next, variables with low variance (below 5%) were removed from consideration, as they reflected features with little change across the entire database, providing limited additional information. Likewise features with high degrees of co-variance were removed. This was to prevent the amplification of a single characteristic that would otherwise be captured in another variable: café and petrol stations were removed here as they were found to be strongly ($r > 0.6$) associated with store sales area.

Finally, analytical feature selection was undertaken using a cross-validated recursive feature elimination (RFECV) algorithm for the MLR model regression. Here, features were scored on their importance to the model (see section 3.4.4), the lowest value feature is removed and the process is repeated. The number and combination of features, which minimised model error (Mean absolute error, MAE, see equation 11) was selected for the MLR regression. The features removed in each step and final features used in each model may be found in Appendix 6.2.

3.2 Model Structure

A dynamic benchmark value for electricity and gas demand was calculated using three different regression techniques. These values were converted to an emissions basis using the carbon factors. The residual (error) of the prediction was then taken as a quantitative measure of a stores deviation from its benchmark.

To maintain valid comparisons between the three

models, a consistent layered model structure and output was defined. This was made up of five steps:

1. Data Loading
2. Data Pre-processing
   K-Means Clustering: 3 Clusters
   MLR Fitting & Prediction Modelling
   Carbon Residual calculated and stored.
3. Removal of Outliers on Carbon Residual basis.
4. Model Iteration - Final Pass
   K-Means Clustering (except Model 3)
   Fitting & Prediction Modelling:
   Model 1: Multivariate Regression
   Model 2: Artificial Neural Network
   Model 3: Decision Tree
   All Residuals calculated and stored
5. Final K-Means Clustering

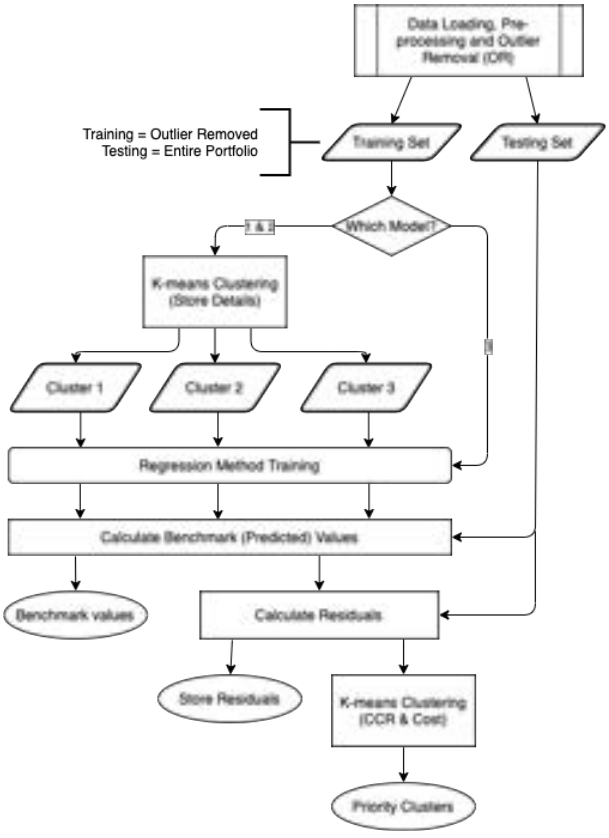

Figure 1: Model Flowsheet

Steps two to four were computed across each four-week period to produce performance benchmarks and carbon residuals. These were determined on a unit area basis to ensure they could be compared across a portfolio. Stores with negative residuals were considered over-performing while positive residuals indicated under-performance.

The quantitative nature of residuals provided concrete figures for more detailed comparison of stores and overall portfolio performance.

$$X_{Residual} = X_{Actual} - X_{Predicted} \tag{3}$$

Combined Carbon Residual (CCR) was chosen as the best output to compare stores in terms of their environmental impact as it was inclusive of gas and electricity emission components. This was calculated as a sum of carbon residuals (the products of each consumption residual and their respective carbon factors), accounting for both electricity and gas over the entire period considered:

$$CCR_{Combined} = \sum_{i=Elec,Gas} (\text{Residual}_i \times CF_i) \tag{4}$$

3.2.1 K-Means Clustering

K-means clustering is a popular method for grouping n features into k clusters in which each feature belongs to the cluster with the closest centroid.

Given a set of observations (x_1, ..., x_n), where each is a d-dimensional real vector, K-Means clustering was employed to define sets S = S_1,..., S_k with centroids μ so as to minimize the sum of square error within the group (i.e. variance):

$$arg_S min \sum_{i=1}^{k} \sum_{\mathbf{x}_i} \| \mathbf{x} - \mu \|^2 \tag{5}$$

K-means clustering, as used in steps two and four, was a useful too for breaking down the supermarkets into manageable groups with similar features to further model resolution, based on work by Lara et al. [18]. As the decision tree model created its own subsets, K-means clustering prior to implementation was deemed unnecessary in this case.

K-means clustering was also employed in step five to group stores by investment priority; this was defined as performance with respect to combined carbon and cost residuals, clustering buildings by investment criteria. A transformation function was applied to each feature, re-scaling their range to [-1, 1]; ensuring equal weighting where clustering was implemented.

3.2.2 Regression for Outlier Identification

As all model construction algorithms (see 3.3.2, 3.3.3, 3.3.4) aim to minimise prediction error, stores with abnormal electricity or gas demands will have greater influence over the regression models. This was considered undesirable as significant deviations would lead to unrealistic benchmark values for all stores.

Therefore, to prevent these outliers from excessively influencing model construction, an initial clustering and linear regression was run on the dataset using the methods detailed in 3.2.1 and 3.3.2 respectively. The resulting gas and electricity residuals were converted to an all-time carbon residual for each store, see equation 4, and was used to screen the initial dataset. Any stores beyond two standard deviations from the mean were removed, leaving approximately 95% of stores which were used for model training.

3.3 Electricity and Gas Demand Regression

3.3.1 Regression Protocol

As time-dependent data such as electricity usage, gas consumption and weather was available in four week periods, regressions were trained and predicted against each period individually. This prevented overfitting of store characteristics as each store only appeared once in each regression. Additionally, stores with no gas capacity were removed from the gas regression training sets and were assigned gas residuals of 0.

3.3.2 Model 1: Multi-variate Linear Regression (MLR)

In the first model, the MLR method was used to determine benchmark values. MLR maps a set j features **X** to a predicted output y for each of i observations, shown in equation 6 below.

$$y_i = \alpha + \sum_{j=1} \beta_j x^*_{ij} \tag{6}$$

The coefficient of each feature β_j and intercept α are determined to minimise a cost function given in equation 7.

$$E = \sum_{i=1} (y_{i,predicted} - y_{i,real})^2 \tag{7}$$

Each continuous feature was standardised using eq.8 as is common practice [24].

$$x^*_{ij} = \frac{x_{ij} - \mu_j}{\sigma_j} \tag{8}$$

3.3.3 Model 2: Artificial Neural Network (ANN)

In model 2, the ANN method was used to determine benchmark values. The ANN method maps a set j features **X** to a predicted output y for each of i observations via a network of nodes, a structure based on the way the brain learns.

There are three types of nodes in an ANN: input nodes, hidden nodes and output nodes. Each input node takes the value of a feature for a given observation. In this case the separate electricity regressor had 16 input nodes and the gas regressor had 15. Both had a single output node, corresponding to the benchmark value.

These two groups of nodes are connected by a network of m layers of n hidden nodes. These take inputs from all nodes of the previous layer and transform them according to a series of weights, as shown in equation 9. The model was arranged in a feed-forward fashion with no memory or competition between nodes.

$$y_i = \alpha + \sum_{n=1} \beta_n x^*_{in} \tag{9}$$

Where x_{in} is the output of node n from the previous layer, and y_i is the output of the node. α and β are weights assigned to minimise the model's cost function, here MAE eq. 11, as squared error metrics were thought to amplify the influence of outliers.

A network with one hidden layer and nodes equivalent to half the number of input nodes was selected as appropriate based upon previous ANN models developed for benchmarking purposes [20, 19]. The outputs of the single hidden layer were transformed by a sigmoid function as in [5] see eq. 10.

$$f(x) = \frac{1}{1 + e^{-x}} \tag{10}$$

Additionally a variable learning rate was implemented, meaning the amount all coefficients were adjusted by, decreased as the model tuning progressed. This lead to improved error in final prediction values. As in the case of MLR, continuous variables were standardised by their mean and standard deviation as in eq. 8.

3.3.4 Model 3: Decision Tree (DT)

Decision trees, when applied to continuous outcomes, are referred to as regression trees. These work by partitioning data into subsets via a series of binary splits using Boolean logic. Each point at which a decision is made is referred to as a node.

The CART (Classification and Regression Trees) algorithm was selected for decision tree construction, as it accepts continuous inputs and outputs, and has been employed for benchmarking outcomes previously [17].

For regression models, each split was made to minimise error between the mean of the generated subset and each of its datapoints. Here the error metric mean absolute error (MAE see eq. 11), was used to measure goodness of split. MAE was chosen to minimise the influence of outliers compared to squared error metrics. Decision trees use selfish decision making processes, meaning each split was optimised without consideration of decisions further down the tree. A maximum of 5 splits and minimum leaf size of 5% of stores were specified to avoid overfitting. These values were specified based on the structures of existing decision trees constructed for benchmarking outcomes [17, 25].

3.4 Model Testing

3.4.1 Model Error

Model error analysis offered invaluable insight into the performance, distribution and outcomes of each model. As numerous regressions were performed for all three models, the error metrics were taken for each period and averaged for comparison.

As MAE was utilised in construction of the regressions, it was deemed the most relevant metric for model analysis. This represented the magnitude of the average residual and is defined as:

$$MAE = \frac{\sum_i |y_{i,predicted} - y_{i,true}|}{n} \tag{11}$$

To supplement MAE, maximum error (ME) was collected for each model to provide insight into the maximum deviation from a benchmark value. This indicated the harshness of the benchmarks.

Table 1: Sample stores provided by Sainsburys

Store	Reason	Area ft^2
A	Leaking Roof	81,885
B	High Consumption	65,931
C	Leaking Roof	88,872
D	Gas Capacity	73,643
E	Largest Area	104,805
F	CHP Capacity	45,859

3.4.2 Model Validation

Sainsbury's ccollated a list of stores based on known operational history, listed in table 1. The residuals of each of these stores were qualitatively analysed to ascertain the realism and validity of each model. A full description of each store can be found in the appendix 6.4.1.

3.4.3 Confidence Intervals

To provide insight into the robustness of these methods, confidence intervals were generated for the residuals of each model. 1000 new datasests were constructed by sampling with replacement from the original database, each model was trained on each new dataset before fitting on the original set. For each store the range of residuals produced acted as confidence intervals.

3.4.4 Feature Importance

Finally, the relative importance of the features for each model were determined. As each model employs different methods to map features to their predicted values, this illustrated the impact each feature had on electricity and gas demand benchmarking. The permutation importance method was employed, as it can be applied to all regression methods ensuring comparable outcomes. This method determines the importance of feature n by measuring the impact on model error (here MAE), when observations of feature n are randomly shuffled between stores. This was repeated 10 times and the mean increase in error was taken as the feature's importance. All feature importance values were then normalised by the most important feature.

4 Results and Discussion

4.1 Model Outputs

When plotting the outputs of each model, minor differences were difficult to observe visually with a large number of datapoints. However, it was clear that for each model there existed stores which lay outside of the high density regions; these were successfully identified by the priority clustering step which highlighted similar numbers of extreme poor-performers across the models. Similar clustering patterns emerged for each model, making them easy to rearrange from worst to best, values from one to five were reassigned respectively.

Table 2 shows the cluster distributions of each model. It was evident that although the DT model distributed stores less evenly, it provided a more pessimistic prediction of the portfolio, with the most under-performing stores. On the other hand, the MLR model was the most optimistic and evenly distributed. This was due to the inherent differences between regression methods. While MLR model minimised square error which accounted more strongly for outliers, the ANN and DT methods minimised MAE, taking less account of, and therefore punishing, underperforming outliers.

Table 2: Distribution of stores by priority cluster and over vs under performance by model

Priority Cluster	MLR	ANN	DT
1	6	5	3
2	97	40	13
3	190	181	175
4	186	259	277
5	103	97	114
Performance	**MLR**	**ANN**	**DT**
Over	285	279	275
Under	297	303	307

The contribution of gas and electricity residuals to overall carbon residuals were evaluated for each model. These findings were summarised in table 3.

Table 3: Average carbon residual components and the contributions of gas and electricity residuals to these as % by model

Model	Average	Electricity	Gas
	gCO_2ft^{-2}	%	%
MLR	596	40.1	59.9
ANN	1170	41.2	58.8
DT	1150	28.8	71.2

It was found that the greater contribution of gas over the three-year period was due to its fixed carbon factor value. While the dynamic electricity CF decreased, the gas CF remained constant and large. This increased the gas weighting for each period, thereby widening the disparity between stores under and over performing in gas use. Electricity-only stores were unlikely to be identified as outstanding towards the later periods due to the overshadowing influence of gas performance. The most prominent case being the DT model, which suggested an average weighting of 71.2% by gas, this large deviation was later explained in section 4.2.1.

Using the final priority clustering to categorise and clarify which stores performed similarly with respect to emissions and costs, an interesting dependency on electric carbon factor was seen. For example, a store with high electricity consumption, hence high utility costs, was not registered as overly poor performing due to the low carbon factor of it's electricity provider; this saw the balancing out of the two factors and was able to select the worst performing stores with both high costs and emissions. This would allow Sainsbury's to target stores which under-perform in both categories, providing both a financial and sustainability incentive.

4.2 Model Comparisons

4.2.1 Model Error

The average MAE and maximum error of each model for both gas and electricity was computed, as shown below.

Table 4: MAE and Mean Max. Error for overall models, electricity regressions and gas regressions, all data to 0 d.p

Model	MAE gCO_2ft^{-2}	MME gCO_2ft^{-2}
MLR	156	1380
Electricity	139	1070
Gas	173	1700
ANN	142	1390
Electricity	128	1050
Gas	155	1730
DT	138	1960
Electricity	118	1260
Gas	158	2660

The decision tree regressions yielded the lowest mean absolute error, followed by the ANN model for electricity, while the two showed extremely similar MAE values for gas regressions. The MLR model consistently scored the highest for MAE. This suggested that the relationship between the features and electricity/gas usage intensity showed non-linear behaviour, which the ANN and DT models were able to capture. Similar results and conclusions were drawn by Yalcintas and Ozturk [20].

MME gave a strong indication of the maximum size of residuals produced by a model. The fact that MME was higher for gas regressions offered further explanation for their greater influence on store residuals shown in table 3.

Despite producing the lowest MAE the DT model showed the highest mean maximum error. This was unsurprising, as the DT model assigned a mean benchmark value to all stores within a given leaf. As these values were less tuned to each store, greater errors were produced for outliers. This harsher approach was considered favourable as it meant stores with the greatest need for investment stood out, because of the higher residuals they were assigned.

MAE was consistently higher for gas regressions than for electricity. One explanation may be that

gas demand was less comprehensively explained by features considered here, for example Mavromatidis, Acha and Shah's [9] work predicting energy use by component uses store average temperature as an input for predicting boiler energy usage which was not considered by this model.

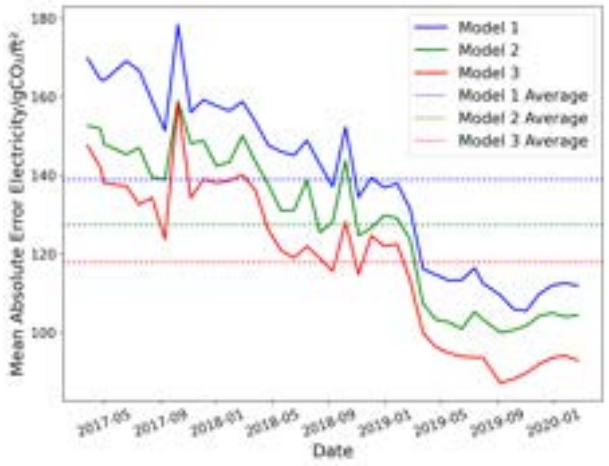

Figure 2: Mean absolute error for electricity regressor by period

Model error metrics, MAE and maximum error, were computed for each regression completed. These were averaged across cluster and plotted in Figures 2 and 3 against period.

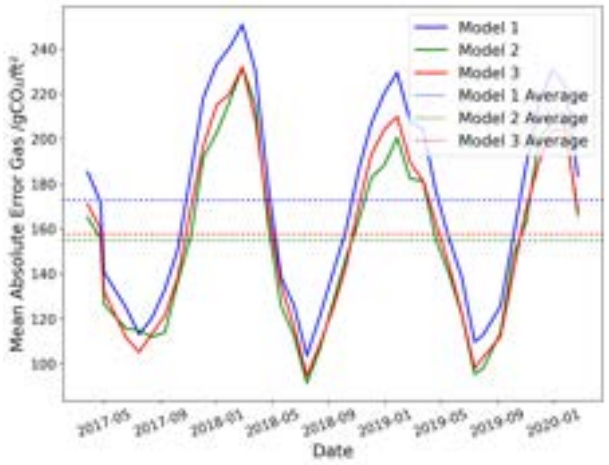

Figure 3: Mean absolute error for gas regressor by period

It was observed that MAE for model predictions trended downward for electricity, while gas prediction errors exhibited strong periodicity. This supported conclusions that dynamic benchmarks performed poorly for gas regression, as they were not able to account for seasonal demand changes.

4.2.2 Confidence Intervals

Confidence intervals for the percentile rank of each store were evaluated and found to be of consistently high magnitude. This was expected as the majority of stores have similar sized carbon residuals. Hence, a small change in the scores assigned by models would result in a disproportionate shift in ranking.

Table 5: Confidence intervals for each model's percentile position

Model	Overall %	Electricity %	Gas %
MLR	±25.8	±25.6	±32.6
ANN	±34.8	±34.9	±34.3
DT	±31.7	±30.9	±32.1

Model 1 produced the smallest confidence intervals, indicating this model was more suitable for performance prediction for new stores. The ANN model had the highest uncertainty in store ranking, this suggested it was overfitting on sample data. Hence, it was less able to predict the performance of unknown datapoints.

4.2.3 Model Validation

The ability of each model to categorise the sample stores highlighted by Sainsbury's successfully, was an important metric of applicability.

Sainsbury's considered stores A-D as their worst performing. While both leaking stores (A & C) were registered as poor-performing by all models, only model 3 (DT) identified all four stores as under-performing with respect to the carbon residuals. However, when clustered in combination with cost, they were assigned mid-to-low priority rankings. Conversely, the most noticeable model error was that models 1 and 2 suggested that stores B & D were actually over-performing (negative residuals). This was in-fact due to smaller positive electricity but greater negative gas residuals, thereby, bringing the combined carbon residual down.

It was not expected that these stores would be identified as the very worst due to deliberate correction for inherent factors such as building age in these models, and disagreement on classification of the same buildings in literature [12]. However, the DT model ranked these stores within the worst 30%. Hence, model 3 was considered the most valid, as it most appropriately categorised known worst performers.

Store F was identified as an extreme poor performer with respect to carbon residual. This was due to its use of combined heat and power technology, where power is generated through the building's heating mechanism. Though CHP lowered electricity demand, as sus-

Table 6: Carbon residual, percentile rank with lowest percentile as worst and priority cluster rank of sample stores

	Carbon gCO_2ft^{-2}			Percentile %			Cluster Rank		
Store	**MLR**	**ANN**	**DT**	**MLR**	**ANN**	**DT**	**MLR**	**ANN**	**DT**
A	2810	2780	13800	34.4	36.4	4.8	5	3	4
B	-2220	-718	9930	60.8	57.4	9.3	4	3	3
C	5410	2030	5710	23.5	40.0	21.5	3	4	3
D	-4140	-4440	4260	68.2	76.1	26.6	4	4	3
E	-19300	-17300	-9270	98.5	98.6	92.3	5	5	5
F	8260	10700	4550	17.0	10.3	25.8	4	3	4

pected, more gas was used which was also considered more carbon intensive by each model. Therefore, all models classified this store in their worst 26% of performers. Focusing only on carbon emissions, CHP technology was not as sustainable as previously thought. However, store F was still clustered into mid-low priority rankings, as gas was significantly cheaper than electricity, illustrating the balance of financial and sustainability considerations weighed by the priority clusters.

The magnitude of each carbon residual was evaluated with respect to the total carbon emissions of the store, this offered insight into the accuracy and realism of each model.

Table 7: Average carbon residual as a proportion of a stores total carbon emissions

Test	**MLR** %	**ANN** %	**DT** %
Total	-15.1	-11.8	-8.21
Under	15.0	14.1	13.2
Over	-42.3	-37.6	-30.5

All three models gave negative average total residuals, as shown in table 7. This suggests that on average a store could emit less than its carbon benchmark. It was noted that the DT model provided the most realistic figure for average store performance and was not as influenced by extreme under-performers which skewed the regressions in models 1 and 2. The underperforming stores were emitting on average 14% more than their predicted values. These were considered reasonable for each model and could be used by Sainsbury's as short term objectives as the IEA targets building energy intensity reduction of over 50% globally by 2030 [2].

An interesting observation was that during this analysis, all three models selected the same five stores as the best performing with respect to their residual contributions. With further investigation, it was revealed that these stores used far less gas than each model predicted, providing further evidence for the importance of gas residuals to these models.

4.2.4 Sensitivity Analysis

Values and parameters set within the models, such as carbon factors and costs, were subject to sensitivity analysis to assess their effect on the model outputs and performance. Each value was subject to deviations of ±10% and it's impact on carbon residual and the outlier removal step was recorded.

Although changes in cost factors had no effect on the residuals or regression outputs, the weighting of stores in the final priority clustering was significantly altered, particularly for stores with large electricity or gas residuals. This highlighted the importance of providing accurate cost factors, to ensure outputs of the model are able to accurately inform investment decisions.

Table 8: Effect of carbon factor sensitivity analysis on carbon residual magnitude and number of outliers excluded

	Electricity CF		**Gas CF**	
Model	**+10%**	**-10%**	**+10%**	**-10%**
1	15.6%	0.2%	10.5%	4.5%
2	26.8%	13.5%	-16.1%	10.6%
3	6.0%	-2.2%	7.9%	-4.3%
Excluded	+2	+1	+1	+2

Table 8 illustrates the impact of carbon factors on the average store residual for each model. While car-

bon factors were not included as a variable in the regressions, they changed the training sets at the outlier removal step, with positive and negative deviations causing an increase in outliers from under-performing and over-performing stores respectively. This result also suggested a potential local minimum within the bounds of ±10% deviations.

Though each model observed a different response to these variations, the DT model was considered best performing in this test as it showed smaller deviations, suggesting more confidence and robust predictions of the residual values.

4.2.5 Feature Importance

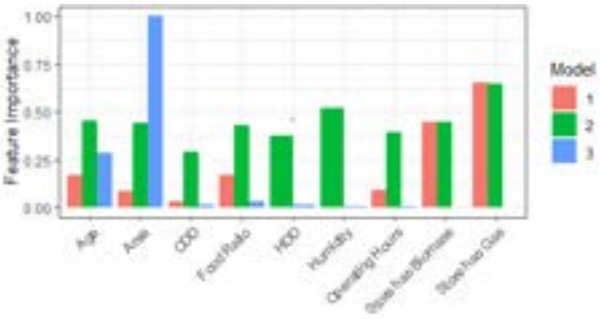

Figure 4: Feature importance by model for electricity use regression

The feature importance profile of model 2 stood out, as all features were of similar importance, for both gas and electricity benchmarking. The ANN technique creates complex mappings of inputs to outputs [20]. Hence, model 2 was more likely to force value from less influential features. This even distribution of importance implies that model 2 was overfit to these variables. This explains the extreme periodic variation of its residuals shown in appendix fig. 11, as features were assigned varying importances at every period.

The DT model ranked store area consistently as it's most important feature for electricity, with age as the only other feature of significant importance. This was understood as a reflection on the model's limited number of splits, which meant only a small number of variables could be used by the model. The model's high performance despite use of few variables gives a strong indication of its predictive power.

For electricity, model 1 assigned high importance to the features identifying whether the store has other energy sources. This offered some explanation to it's high MAE, as the models use of binary features created less incremental predictions, hence greater error.

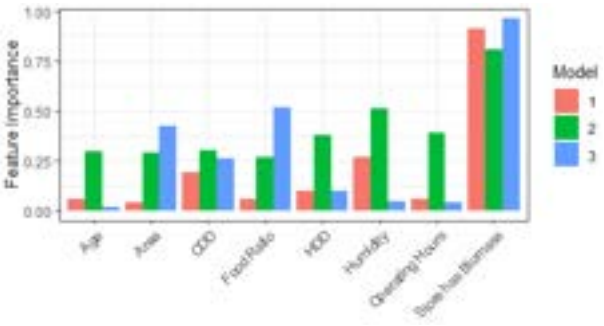

Figure 5: Feature importance by model for gas use regression

The binary feature indicating if a store had a biomass furnace was extremely important to all models for gas regression. This was unsurprising as biomass boilers are a direct substitute for gas boilers. It also offered some explanation as to the poor performance of gas regression, as the models appear to over-rely on a low resolution feature which cannot produce accurate predictions.

Weather features were more important to models 1 and 3 for gas demand prediction. As heating is the primary use of gas, it was expected to be strongly correlated with weather features.

It was of particular note that humidity was a feature of high importance in models 1 and 2, as this feature had not been utilised for benchmarking applications previously. While, humidity had been identified as a high value energy use predictor [26], Figure 5 provided further support for this observation. It was noted that a wider range of features were important to model 3 for gas use prediction. This highlights the challenges all models faced in predicting this outcome, leading them to force value from small deviations in these features.

5 Conclusions

In this work, an innovative benchmarking method has been developed using energy demand prediction models. The dynamic behaviour of the models produces unique benchmark values for stores. This allows for the provision of quantitative, realistic and comparable carbon and cost figures. The benchmarks produced allow commercial users, such as Sainsbury's, to set short-term targets as they work to decarbonise their portfolios.

The layered regression, outlier removal and clustering structure resulted in high performance, by preventing the influence of anomalous data, according to analysis. It was concluded that the decision tree based model (model 3) benchmarked performance most effectively. The simplicity and ease of interpretation of this technique as noted in other literature [17, 25] go further to highlight the suitability of DT for bench-

marking outcomes.

This work sets a precedent for the implementation of weather data for benchmarking outcomes. The analysis and selection of baseline temperature for degree day metrics offered an opportunity for creating energy demand prediction models more robust to disparate climates. Humidity was identified as a particularly important feature which had yet to be implemented in benchmarking applications.

One area identified for further work was the regressions notable limitations in gas demand prediction. This issue is expected to grow as gas carbon intensity remains high relative to electricity, which continues to decarbonise. [23].

References

[1] Masson-Delmotte, V. et al. Global warming of 1.5°c. an ipcc special report..., 2018. URL https://www.ipcc.ch/site/assets/uploads/sites/2/2019/06/SR15_Full_Report_High_Res.pdf. [Accessed 17.11.2020]. pages 1

[2] Abergel, T. , Delmastro, C. Tracking report: Tracking buildigs 2020, 2020. URL https://www.iea.org/reports/tracking-buildings-2020. [Accessed 17.11.2020]. pages 1, 8

[3] Kantar data 2019 uk grocery market share. URL https://www.kantarworldpanel.com/en/grocery-market-share/great-britain/snapshot/29.12.19/. [Accessed 02.11.2020]. pages 1

[4] J sainsbury plc climate disclosure project: Climate change 2020 report, 2020. URL https://www.cdp.net. [Accessed 17.11.2020]. pages 1

[5] Bojic M. Kalogirou, S.A. Artificial neural networks for the prediction of the energy consumption of a passive solar building. **Energy**, 25(5):479–491, 2000. pages 1, 4

[6] Rivard H. Zmeureanu R. Yang, J. On-line building energy prediction using adaptive artificial neural networks. **Energy and Buildings**, 37(12):1250–1259, 2005. pages 1

[7] Lafrance G. Lariviere, I. Modelling the electricity consumption of cities: effect of urban density. **Energy Economics**, 21(1): 53–66, 1999. pages 1

[8] R. et al. Nouvel. Combining gis-based statistical and engineering urban heat consumption models: Towards a new framework for multi-scale policy support. **Energy and Buildings**, 107(15):204–212, 2015. pages 1

[9] Acha S. Shah N. Mavromatidis, G. Diagnostic tools of energy performance for supermarkets using artificial neural network algorithms. **Energy and Buildings**, 62. pages 1, 7

[10] M. Yalcintas. Energy-savings predictions for building-equipment retrofits. **Energy and Buildings**, 40(12):2111–2120, 2008. pages 1

[11] Hui Y.V. Miu Lam Y. Chung, W. Benchmarking the energy efficiency of commercial buildings. **Applied Energy**, 83(1):1–14, 2006. pages 1

[12] Malkawi A. Gao, X. A new methodology for building energy performance benchmarking: An approach based on intelligent clustering algorithm. **Energy and Buildings**, 84. pages 1, 7

[13] X.G. Casals. Analysis of building energy regulation and certification in europe: Their role, limitations and differences. **Energy and Buildings**, 38(5):381–392, 2006. pages 1

[14] Han Y. Xu P. Li, Z. Methods for benchmarking building energy consumption against its past or intended performance: An overview. **Applied Energy**, 124(1):325–334, 2014. pages 1

[15] Webber C. Koomey J. Brown, R. Status and future directions of the energy star program. **Energy the International Journal**, 27(5):505–520, 2002. pages 1

[16] Y. et al. Wei. A review of data-driven approaches for prediction and classification of building energy consumption. **Renewable and Sustainable Energy Reviews**, 82(1):1027–1047, 2018. pages 1

[17] J. et al. Jeong. Development of an integrated energy benchmark for a multi-family housing complex using district heating. **Applied Energy**, 179(1):1048–1061, 2016. pages 1, 4, 5, 9

[18] R.A. et al. Lara. Selection of representative buildings through preliminary cluster analysis. **International High Performance BUildings Conference**, pages 1–10, 2014. pages 1, 3

[19] Yalcintas M. An energy benchmarking model based on artificial neural network method with a case example for tropical climates. **International Journal of Energy Research**, 30: 1158–1174, 2006. pages 1, 2, 4

[20] Ozturk U.A. Yalcintas, M. An energy benchmarking model based on artificial neural network method utilizing us commercial buildings energy consumption survey (cbecs) database. **International Journal of Energy Reserach**, 31(4): 412–421, 2007. pages 1, 4, 6, 9

[21] Yau K.K.W. Tso, G.K.F. Predicting electricity energy consumption: A comparison of regression analysis, decision tree and neural networks. **Energy**, 32(9):1761–1768, 2007. pages 1

[22] The natural environment research council's data repository for atmospheric science and earth observation. URL http://archive.ceda.ac.uk/. [Accessed 09.10.2020]. pages 2

[23] Energy Industrial Strategy UK Department for Business. Greenhouse gas reporting: conversion factors 2020. URL https://www.gov.uk/government/publications/greenhouse-gas-reporting-conversion-factors-2020. [Accessed 04.12.2020]. pages 2, 10

[24] Y. et al. Ding. Benchmark analysis of electricity consumption for complex campus buildings in china. **Applied Thermal Engineering**, 131:428–436, 2018. pages 4

[25] H. et al. Park. Development of a new energy benchmark for improving the operational rating system of office buildings using various data-mining techniques. **Applied Energy**, 173(1): 225–237, 2016. pages 5, 9

[26] Wakui T. Satake R. Yokoyama, R. Prediction of energy demands using neural network with model identificationby global optimization. **Energy Conversion and Management**, 50(9):319–327, 2009. pages 9

Process Design and Life Cycle Analysis for Methanol and Ethanol Electrooxidaton

Hamza Riaz Hussain and Ines Perez Tabarnero
Department of Chemical Engineering, Imperial College London, U.K.

December 17, 2020

Abstract

Whilst alcohol electrolysis for hydrogen production has been studied extensively at a laboratory scale, no industrial scale processes have ever been published for methanol or ethanol electrolysis. In this study we develop and assess four process models, two for each alcohol electrooxidation. Life cycle analyses (LCAs) are performed for these processes under various mixtures of grid power, natural gas and offshore wind power, and they are benchmarked against steam-methane reforming (SMR) and water electrolysis (WE). To assess industrial applicability, process costing was done in conjunction with the LCAs, giving a view of overall economic and environmental feasibility. The processes explored can be split into two categories: two-product, which produce hydrogen gas and potassium formate or acetate depending on whether methanol or ethanol is used; and three-product, which produce formic or acetic acid, potassium sulphate and hydrogen. The two-product electrooxidation processes are less harmful to the environment than grid-powered water electrolysis and can be highly profitable. The two-product processes are also superior to their three-product counterparts in terms of both emissions and profit.It was also shown that the processes using methanol as a feedstock are less polluting than their ethanol counterparts, and on average are also more profitable. By exploring the emissions of all processes developed in this study under different energy systems, it was found that switching to renewable energy only cuts emissions by a maximum of 2-5% and that the bulk of emissions are associated with feedstock production rather than energy consumption. The importance of feedstock selection is highlighted and opportunities to reduce their global warming potential are suggested.

Abbreviation	Meaning
AEC	Alkaline Electrolysis Cell
E	Ethanol
ED	Extractive Distillaton
M	Methanol
PEM	Proton-Exchange Membrane
PSD	Pressure Swing Distillation
SMR	Steam-Methane Reforming
WE	Water Electrolysis
3PS	Three Product Scenario
2PS	Two Product Scenario
G+NG	Grid + Natural Gas
W+NG	Offshore Wind + Natural Gas
W	Offshore Wind

Table 1: Table of abbreviations used throughout the report

1 Introduction

Across the globe, presidents and prime ministers are looking towards implementing hydrogen technology to decarbonise the energy sector. In the wake of the Covid-19 pandemic, the development of a hydrogen economy will play a significant role in stimulus packages, particularly in Europe where France and Germany[1, 2] have already earmarked €9bn each to the cause. Furthermore, the IEA estimates global demand for low-carbon hydrogen to increase from 0.36 Mtonne.yr^{-1} in 2019 to 7.92 Mtonne.yr^{-1} by 2030[3], indicating the importance of clean hydrogen generation and the opportunities for large-scale deployment.

The United Kingdom has announced up to £0.5bn of investment with the aim of achieving 5GW of low-carbon hydrogen production capacity by 2030[4]. While hydrogen already plays an important role in the economy, a low-carbon hydrogen market does not yet exist in the UK[5]. National consumption amounts to 0.7 million tonnes annually[6] and, according to the Committee on Climate Change, this needs to increase by at least one order of magnitude[7] if the UK is to met its net-zero targets in 2050. The UK Government's Clean Growth Strategy proposes three decarbonisation scenarios, where the *Hydrogen Pathway* aims to convert the current natural gas network to deliver hydrogen for home and industrial heating[6], indicating high potential for green hydrogen consumption. Additionally, the EIA has identified H_2 injection into natural gas streams as one approach to create demand[5], with projects already lined up in northern England.

Whilst most current literature on low-carbon hydrogen production delves into water electrolysis, there is limited available information on bio-based feedstock electrolysis, and to the best of the authors' knowledge there are no studies on industrial-scale methanol and ethanol electrolysis to produce hydrogen and valuable side-products simultaneously. As one of the most promising bio-feedstocks for hydrogen production[8], ethanol electrolysis is a natural choice to explore the process. Furthermore, methanol, being a cheaper and simpler compound than ethanol, is an interesting alternative to study.

This article presents a technical and economic assessment of four industrial-scale electrooxidation processes using methanol and ethanol as feedstocks with the purpose of producing heating-grade hydrogen. These processes are based on alkaline electrolysis cells (AEC), the most mature electrolysis method[9], and split into two subgroups with Section 3.1 introducing the production of hydrogen, potassium sulphate and formic/acetic acid (for methanol/ethanol respectively), and Section 3.2 introducing the production of hydrogen and potassium formate/acetate.

A life cycle analysis (LCA) is presented for each process under three different energy consumption scenarios: grid energy with natural gas, offshore wind power with natural gas, and offshore wind only. Wind power is favoured as it is the least carbon-intensive energy source for electrolysis[10], and the UK's planned access to 40GW of offshore wind by 2030[4], along with its vast potential for hydrogen storage[11, 12], makes it the perfect candidate to base the presented processes in. The major sources of social and environmental damage are identified, optimal feedstock sources are proposed and the minimum hydrogen cost is calculated to assess which processes are the most promising.

2 Background

Methanol and ethanol electrolysis have been explored for a number of years. Take, Tsurutani and Umedab showed in 2006 that a methanol-water mixture could be electrolysed to produce hydrogen at less than 60% the energy consumption of water electrolysis[13] in a direct methanol fuel cell (DMFC), framing methanol electrooxidation as a viable competitor for hydrogen generation. A number of alternative electrolysis methods have been explored, such as Tuomi *et al.*'s study of alkaline membrane electrolysis, which showed that alkaline environments enhance methanol oxidation kinetics[14], and Pham, Baba and Shudo's article on proton exchange membrane (PEM) electrolysis which, to the best of the authors' knowledge, is the only publication of experimental methanol electrolysis energy requirements per unit hydrogen[15]. These studies have helped develop an understanding of the reaction kinetics and electrolytic performance; however, they fail to consider the practicalities of large scale deployment and the associated costs.

Similarly, there is strong interest in ethanol electrolysis, with direct ethanol fuel cells (DEFCs) being particularly well-explored. Monyoncho *et al.* published a literature review of DEFCs in 2019, noting the superiority of alkaline conditions to acidic electrolysis and indicating the need to assess the potential returns of alcohol electrolysis processes[16]. Whilst Monyoncho *et al.*'s review focused on the production of energy *via* direct alcohol fuel cells (DAFCs), a route to simultaneous production of valuable chemicals and hydrogen *via* electrocatalysis was first discovered by Bambagioni *et al.*. In 2010, they showed that this process requires only one third of the electricity needed for water electrolysis[17]. Bellini *et al.* later went on to study electrocatalysts for the electrooxidation of ethanol to acetate in an aqueous potassium hydroxide solution, estimating that in producing 25kg potassium acetate, one could make a profit of €9-10.(kg H_2)$^{-1}$ [18]. However, this estimate did not account for separation systems and their associated capital and operational costs.

Moreover, without any proposed process plant designs, no robust life cycle analyses have ever been produced on methanol or ethanol electrooxidation.

3 Methods

For application to home and industrial heating, the H_2 outlet streams in all flowsheets needed to be 99.9 mol%, in accordance with the ISO 14687:2019 standard for Type I Grade B fuel[19].

The conceptual design for the processes followed the 5-level hierarchical approach proposed by Douglas[20], and was based on glucose[21] and glycerol[22] electrooxidation processes found in literature. The flowsheets were implemented on Aspen Plus V11, and the Electrolyte NRTL model with the Redlich-Kwong equation of state (ELECNRTL) method was used.

Accurate modelling of the alkaline electrolyser was outside the scope of this work. Consequently, literature values were used to model the inputs, outputs and electricity usage of the reactors for both methanol[15] and ethanol[17, 18]. In Aspen, the electrolyser was modelled as a stoichiometric reactor (RStoich) combined with a flash vessel to separate the liquid and vapour streams.

While in practice, a mixture of reactants and products would exit the reactor, 100% conversion of the alcohols was assumed. This allowed for the use of literature values to model the inputs and outputs of the electrolyser. Furthermore, results from electrooxidation processes on other bio-feedstocks such as glycerol and glucose, show respective conversions of up to 91.8% and 98.3%[21, 22], indicating that similarly high conversion in alcohol electrooxidation could be feasible, depending on residence time.

To optimise the energy usage of the systems,

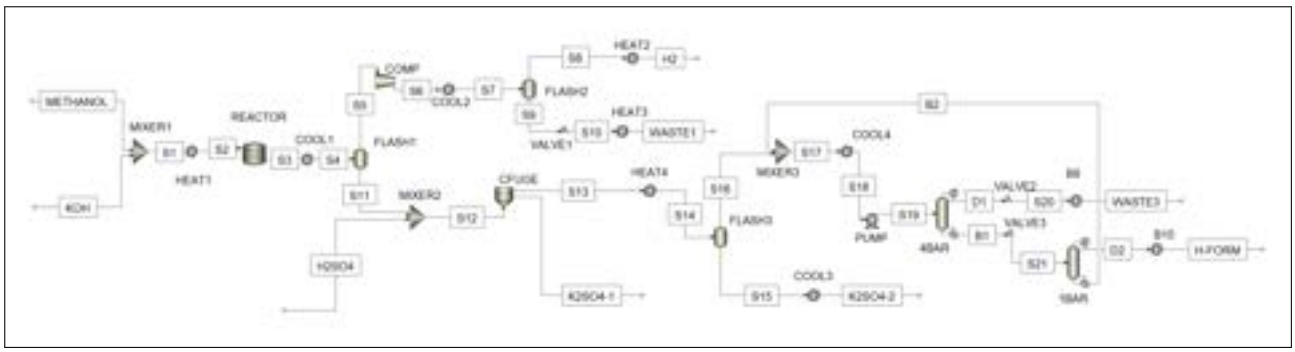

(a) Methanol 3PS process

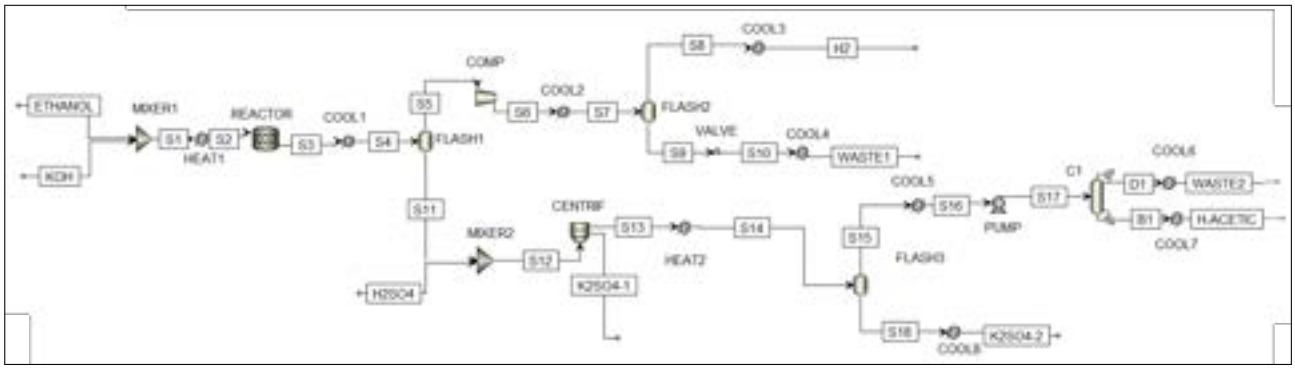

(b) Ethanol 3PS process

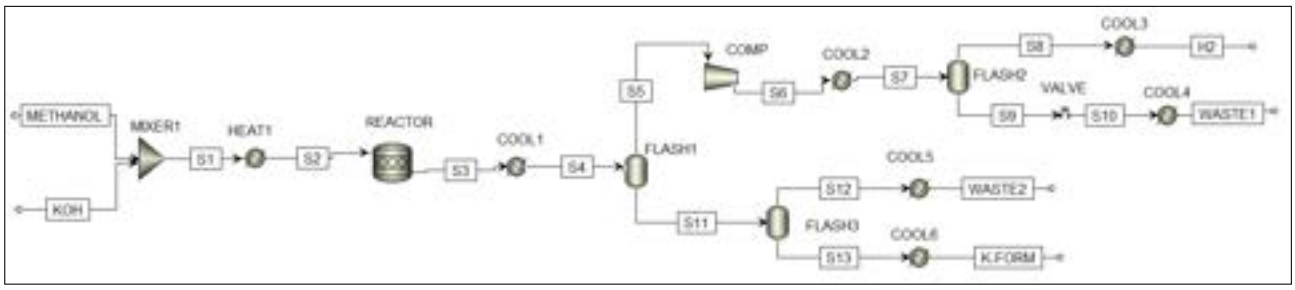

(c) Methanol 2PS process

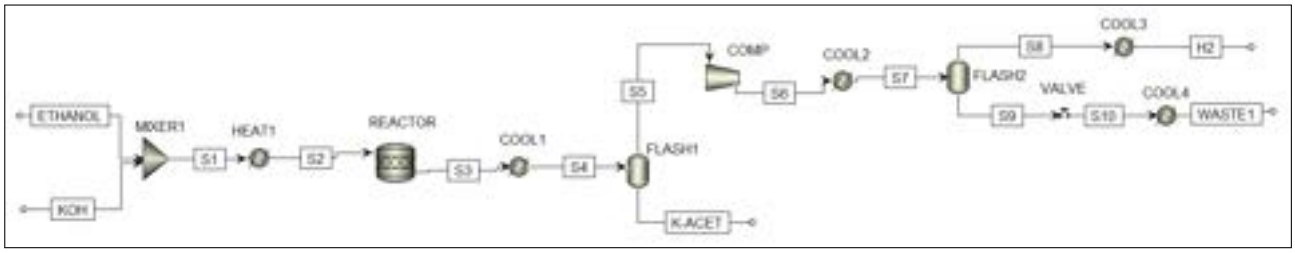

(d) Ethanol 2PS process

Figure 1: 3PS and 2PS process flow diagrams for methanol and ethanol feedstocks

heat integration was carried out *via* the construction of a minimum energy consumption network. A $\Delta T_{min} = 10°C$ was chosen to ensure good driving force for the heat exchange and avoid getting large exchange areas. Increasing the ΔT_{min} could have further reduced the exchanger area, but this would make the energy from the process harder to recover.

Two processes were designed for each alcohol feedstock. The Three Product Scenario (3PS) produces potassium sulphate and formic/acetic acid as co-products to the hydrogen, whereas in the Two Product Scenario (2PS) potassium formate/acetate is produced in conjunction with the hydrogen gas. In both the 3PS and 2PS processes pure methanol or ethanol and 30 wt% KOH solution were fed to the plant. In the 3PS processes 10 wt% H_2SO_4 was also fed to neutralise the reactor outlet.

3.1 Three Product Scenario (3PS)

As seen in Figures 1, the process for both alcohol feedstocks is identical at the beginning. Initially, the methanol/ethanol is mixed with the KOH solution and fed to the reactor. The liquid stream leaving the electrolyser is mixed with H_2SO_4 and sent to a centrifuge, where a first potassium sulphate product

stream is obtained. The remaining liquid is heated up in a flash where the rest of the K_2SO_4 is precipitated, and a mixture of organic acid and water is sent to the distillation train.

3.1.1 Methanol Separations

When using methanol as a feedstock, formic acid is produced upon mixing H_2SO_4 with the reactor outlet. The liquid fed to the distillation train is a binary mixture of formic acid and water, which forms a maximum boiling azeotrope at atmospheric pressure. This is difficult to separate using conventional distillation[23].

Two options were considered to carry out the separation: extractive distillation (ED) and pressure swing distillation (PSD). Since the azeotrope has been found to be pressure sensitive[23], PSD was selected to avoid introducing an additional chemical component to the system.

3.1.2 Ethanol Separations

For the ethanol feedstock a system was required to separate acetic acid from water. Although these components do not form an azeotrope, their separation is difficult and energy intensive due to a tangent pinch on the pure water end[24].

Multi-effect distillation (MED), ED and CD were all considered for this separation. ED was initially discarded because it would require a three-column system as well as the addition of more chemicals to the process. Multi-effect distillation seemed to be the optimal method, but when comparing it to a single column separation it was found that MED required more stages and that the energy required to run the two columns was considerably higher than implementing only one.

3.2 Two Product Scenario (2PS)

This process corresponds to the formation of potassium formate/acetate salts in addition to hydrogen gas. The reactor and hydrogen separation train are identical to those found in the 3PS processes; the difference lies in the treatment of the liquid exiting electrolyser. In this scenario the output of the reactor is not neutralised with sulphuric acid, which saves in capital and operating costs as the process does not require a complex liquid separation system. Rather, a single co-product is formed in addition to the hydrogen gas: a carboxylate salt. The minimum purities for sale of potassium formate and potassium acetate are 74 wt% and 70 wt% respectively. The potassium acetate leaving the reactor was already above this threshold, however an additional flash vessel at 125°C was implemented in the methanol process to achieve the minimum required purity.

3.3 Life Cycle Analysis

A Life Cycle Analysis was performed for the processes described above with SimaPro 8.5.2.1, using 1kg of hydrogen as the functional unit. Inventory analysis was done using the Ecoinvent 3 database, and the impact assessment was calculated using the RecipeMidpoint (H) 2016 method. Feedstock inputs were selected from the Global market, and a UK electricity grid was built using 2018 data[25, 26]. Mass allocation was implemented rather than cost allocation, since product prices vary considerably.

A cradle-to-gate system boundary was implemented, as the aim of this work was not to precisely describe the impact of the processes, but rather to compare the potential of each design from an environmental point of view. The end use of the hydrogen was not deemed relevant for this analysis, although the stages after the production processes tend to have a small influence on the impact of the hydrogen life cycle[22, 27].

3.4 Technoeconomic Analysis

A technoeconomic analysis was also performed for each of the desgins. The capital costs of the flowsheet were calculated using Guthrie's correlations reported by Douglas[20]. The electrolyser CapEx was approximated to be equal to a water electrolyser of the same size[9]. A Capital Recovery Factor of 0.106 was obtained by assuming 10% interest rate and a plant lifetime of 30 years. This allowed for the annualised capital costs of the plant to be calculated.

Ranges for feedstock costs were obtained from Alibaba, and three possible scenarios were analysed: a "best case" scenario, where feedstocks would purchased at their lowest price and the products sold at their highest; a "worst case" scenario were the inverse occurs, and an "average case" scenario.

Average UK costs were used for OpEx calculations, and the values used are displayed in Table 2. It should be noted that the wind price is the UK goal for offshore windfarms in 2030.

Utility	Value	Unit
Natural Gas [28]	0.02	$\$.kWh^{-1}$
Grid Electricity [28]	0.12	$\$.kWh^{-1}$
Wind Electricity [4]	0.13	$\$.kWh^{-1}$
Cooling Water [29]	1.72	$\$.m^{-3}$

Table 2: Utility costs

4 Results and Discussion

4.1 Process Outputs

The electrolyser approximation used in the flowsheets is in line with literature and small scale experimental values: the outlet H_2 purity reported

Process	Products	Flowrate (ktonne.yr^{-1})	Purity (wt%)	Electricity (kWh.(kg H_2)$^{-1}$)
Methanol 3PS	Hydrogen	5.34	99.9	13.49
	Potassium Sulfate	116.51	100	
	Formic Acid	59.59	96.5	
Methanol 3PS(W)	Hydrogen	5.34	99.9	179.73
	Potassium Sulfate	116.51	100	
	Formic Acid	59.59	96.5	
Methanol 2PS	Hydrogen	5.34	99.9	13.48
	Potassium formate	129.77	80.1	
Ethanol 3PS	Hydrogen	5.34	99.9	24.64
	Potassium Sulfate	116.51	100	
	Acetic Acid	73.23	91.1	
Ethanol 3PS	Hydrogen	5.34	99.9	222.75
	Potassium Sulfate	116.51	100	
	Acetic Acid	73.23	91.1	
Ethanol 2PS	Hydrogen	5.34	99.9	24.57
	Potassium Acetate	170.55	70.3	

Table 3: Output flows, purity and electricity usage for each of the processes. Note that 3PS methanol and ethanol without abbreviations represents both Grid+Natural Gas and Wind+Natural Gas, since the source of electricity does not affect the values

for a methanol electrooxidiser ranges from 95.5-97.2 mol%[13], and the modelled reactor in Aspen has an output of 96.74 mol%.

Hydrogen gas with 99.90 mol% purity was obtained as a product in a flash at 9.5 bar and 5°C, meeting the regulatory specifications to become a "zero-carbon option to replace natural gas for heat generation"[6]. However, a sensitivity analysis was carried out to assess the feasibility of plant changes should H_2 production for PEM cells become a priority. This application would require a hydrogen purity of 99.97 mol%[19]. To attain this slight increase in purity, the flash would need to be operated at 32 bar, leading to an increase in compressor duty of 82% and significantly higher capital costs, which may not be desirable.

Table 3 illustrates the product output flows as well as the plant's electricity usage. The co-product flowrates are significantly higher than those of hydrogen, highlighting the key difference between alcohol electrolysis and water electrolysis. As hydrogen price is predicted to decrease by up to 86% in the future[6], these valuable co-products can be a strong asset to mitigate risk if appropriate financial support mechanisms are not adopted for hydrogen.

Consequently, the distillation processes were optimised to achieve the highest recovery of chemicals possible, as well as optimum purity for sale. In the case of methanol 3PS, this consisted of two columns at 4 and 1 bar that achieve a formic acid purity of 96.5 wt% with 95% recovery. Similarly, the conventional distillation unit for the ethanol 3PS operating at 6 bar, achieves an acetic acid purity of 99.1 wt% with 99.8% recovery.

The electricity consumption by the plant experiences little variation from 3PS to 2PS for both alcohols. In most cases the main contributor is the electrolyser, which needs 12 kWh.(kg H_2)$^{-1}$ for methanol, and 22.7 kWh.(kg H_2)$^{-1}$ for ethanol. However, the heating and cooling duties are significant, and electricity demand increases by a factor of 13.3 (methanol) and 9.1 (ethanol) when natural gas is replaced by electrified heating in the 3PS scenarios. This shows that the 3PS distillation systems are very energy intensive and may be difficult to electrify.

4.2 Life Cycle Analysis

4.2.1 Process Comparison

Life cycle analyses (LCAs) were performed on each of the processes. The most commonly reported metrics were used for further study: global warming potential (kg CO_2eq.(kg H_2)$^{-1}$), stratospheric ozone depletion (kg CFC11eq.(kg H_2)$^{-1}$), fine particulate matter formation (kg PM2.5eq.(kg H_2)$^{-1}$) and human carcinogenic toxicity (kg 1,4-DCB.(kg H_2)$^{-1}$).

Figure 2 shows that the 2PS processes have much lower environmental impacts than their 3PS counterparts across all metrics. Furthermore, the 3PS(W) process strongly outperforms the 3PS(G+NG) and 3PS(W+NG) in the case of both ethanol and methanol usage, indicating the significant pollution associated with natural gas heating in these processes.

Notably, the most significant changes in environmental impact come from changes in process feedstock, not when the electricity source is changed. Taking methanol as an example, the transition between the 3PS(G+NG) to 3PS(W+NG) processes results in only a 2.7% change in global warming potential, but the move from 3PS(G+NG) to 2PS(G) (which does not use H_2SO_4 or natural gas) results in a 41% reduction. Furthermore, the 2PS(G) process is approximately 15% less carbon intensive than even the 3PS(W) process, indicating that the reduction in emissions comes primarily from eliminating H_2SO_4. Therefore, carbon abatement of feedstocks is critical to reduce the environmental impact of these processes. Section 4.3 discusses this in more detail.

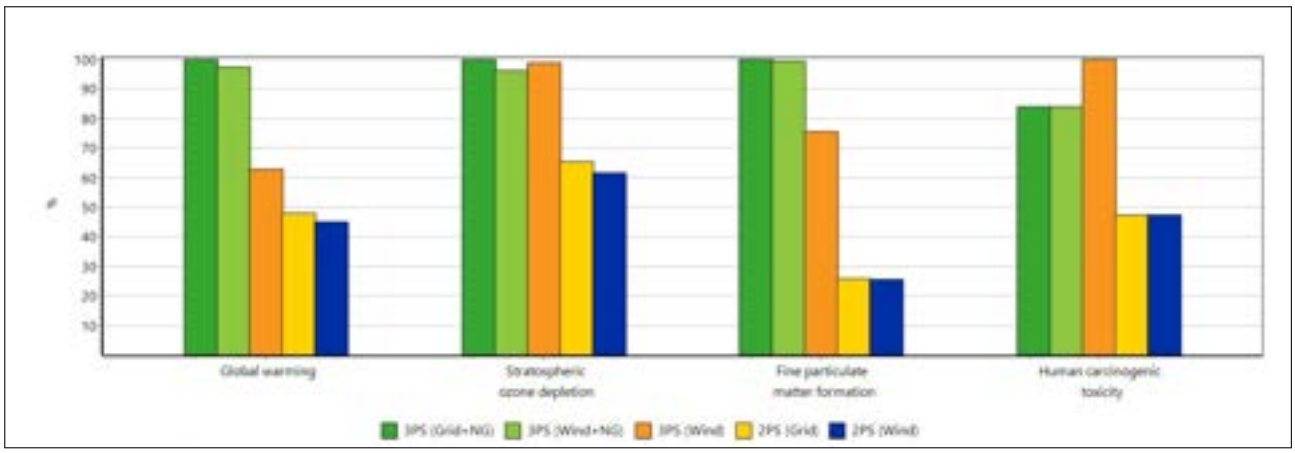

(a) Methanol process impact assessment metrics

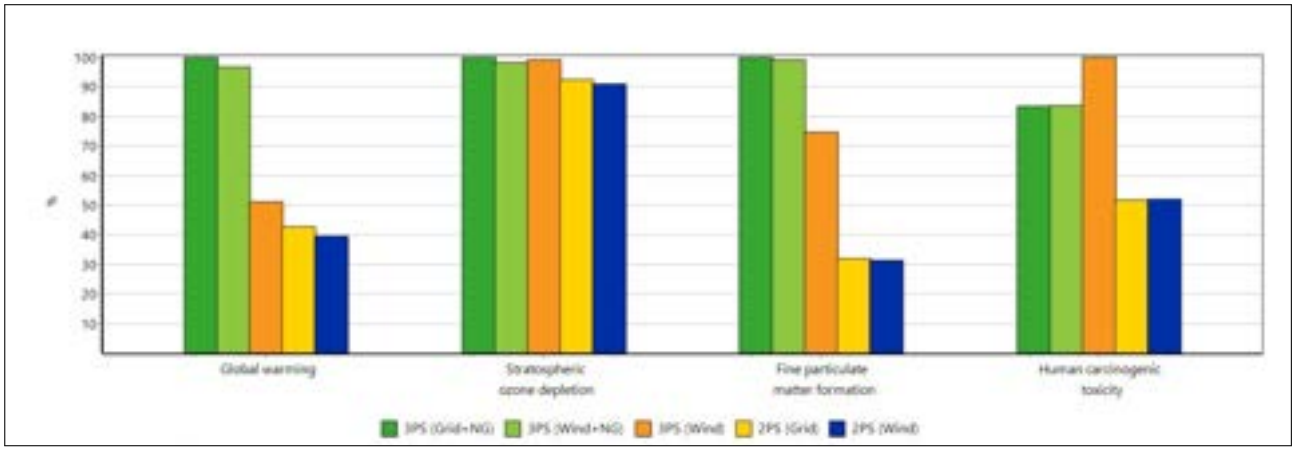

(b) Ethanol process impact assessment metrics

Figure 2: Impact assessment metrics for the methanol and ethanol processes: global warming potential, stratospheric ozone depletion, fine particulate matter formation and human carcinogenic toxicity.

4.2.2 Methanol versus Ethanol

In comparing the two lowest-impact methanol and ethanol processes, 2PS(W), it was found that methanol as a feedstock outperforms ethanol across all analysed metrics. Methanol's most pronounced advantage is in stratospheric ozone depletion, where process impacts are 80% lower than the ethanol counterpart. This is driven by the higher electricity requirements of the ethanol reactor, as significant ozone depletion is associated with the production of steel and glass fibre for wind turbine construction.

Across the remaining metrics, GWP, particulate matter formation and human toxicity, an advantage existed in favour of methanol, although it was less pronounced. It was found that between 66%-74% of emissions across the remaining metrics were derived from KOH. As potassium hydroxide is used in equal volumes in both processes, the majority of emissions are maintained in each, with methanol's advantage primarily being accounted for by the lower energy requirements of methanol electrooxidation.

4.2.3 Benchmarking

In order to assess the feasibility of the processes proposed in this paper, their emissions were benchmarked against steam-methane reforming and water electrolysis (grid- and wind-powered) as shown in Figure 3.

The 2PS processes outperformed grid-based water electrolysis on every metric, and the 3PS processes performed similarly well, with the exception of their particulate matter emissions when gas heating was implemented.

The alcohol electrolysis processes rarely outperformed wind-based water electrolysis due to feedstock-related emissions. Wind-based water electrolysis derives its emissions almost exclusively from the production of wind turbines. These emissions come primarily from steel production, with glass fibre also making up a significant portion, up to 44.5% in the case of ozone depletion. The proposed processes (excluding the electrified heating case) typically use between 25.5% (methanol)-46.6% (ethanol) of the electricity in water electrolysis; thus, the significant difference in emissions comes from the elevated emissions of feedstocks such as sulphuric acid and potassium hydroxide, as opposed to water.

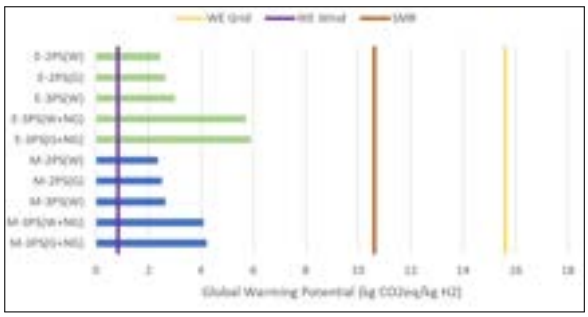

(a) Global warming potential benchmarking

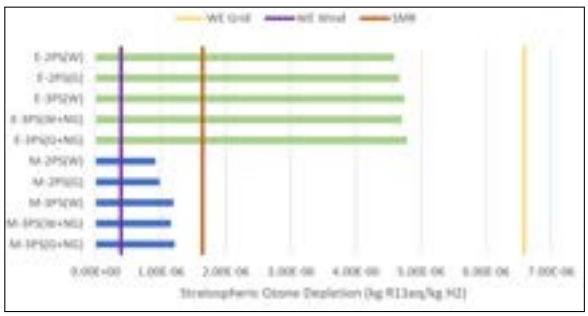

(b) Stratospheric ozone depletion benchmarking

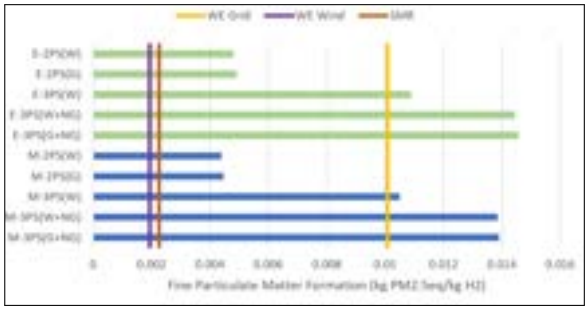

(c) Fine particulate matter formation benchmarking

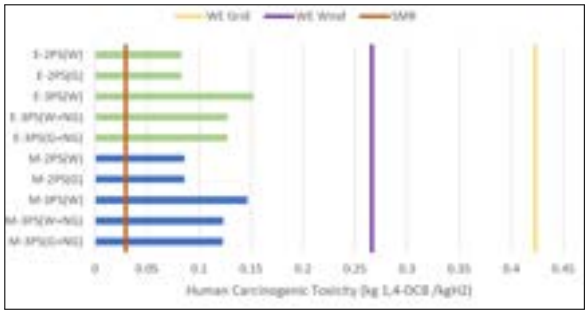

(d) Human carcinogenic toxicity benchmarking

Figure 3: All processes benchmarked against steam methane reforming (SMR) and water electrolysis using grid energy (WE Grid) and offshore wind energy (WE Wind)

The only benchmarked metric where alcohol electrolysis had a lower environmental impact than wind-based water electrolysis was in human carcinogenic toxicity, which is an emission primarily driven by steel production for wind turbines.

Methanol electrolysis was found to be level with SMR overall, outperforming SMR on on GWP and ozone depletion, but under-performing on particulate emissions and human toxicity, likely due to steel-associated emissions. Ethanol electrooxidation performed similarly, although it has elevated levels of ozone depletion due to additional energy consumption.

4.3 Emission reduction

To try to reduce the environmental impact of the processes, feedstock supply chains were analysed to locate the main emission sources. Global warming potential was selected for detailed analysis, as it is the most analysed impact category in electrolysis LCAs[30] and is the most relevant for meeting government-set emissions targets.

The carbon intensity of the potassium hydroxide feedstock was more than twice as large as any other input, so reduction in its emissions could significantly decrease the GWP of the overall process. High emissions were traced back to Indian and Chinese production of KOH, due to their coal-intensive energy grids. These emissions could be mitigated using carbon capture and storage (CCS). On the other hand, the European grid has a higher proportion of renewables and significantly less coal, therefore European-produced KOH has significantly fewer associated emissions.

The most carbon intensive stage of sulphuric acid production was found to be the production of sulphur from natural gas and petroleum. Implementation of CCS at production sites could decrease the carbon intensity of H_2SO_4. Similarly to the case of KOH, European chemical factories have a GWP almost 7% less than Rest of the World factories, so imports from countries with greener grids is recommended.

For methanol, European gas-produced heat was the biggest single contributor. Seeking methanol produced by electrified heating would be a viable option of reducing the kg CO_{2eq} associated to this feedstock, particularly if renewable energy is used.

Finally, the main impact associated with ethanol feedstocks originated from using nitrogen as a fertiliser. No significant differences between production sites at different locations were found. Consequently, cellulosic feedstocks could be purchased in lieu of cornstarch- and sugarcane-derived ethanol. Although more expensive, this feedstock has much lower environmental impact, offering both more favourable land usage and emitting less CO2. [31].

4.4 Process Costs

Due to the wide ranges in feedstock and product prices, significant profit variability was found for each of the scenarios modelled, as displayed in Figure 4. The 2PS processes are more profitable than the 3PS processes for both alcohols, being the only designs with a positive average profit. It can also

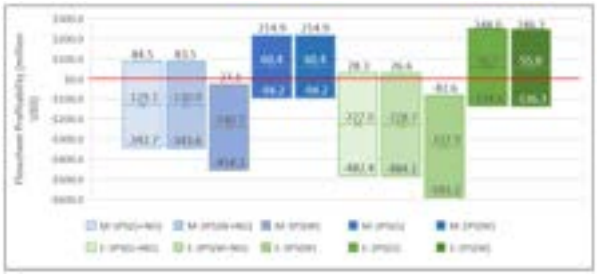

Figure 4: Profit ranges for all methanol and ethanol processes

be seen, that the 2PS processes have a 25% and 43% smaller profitability range than the 3PS scenarios for methanol and ethanol respectively, as they utilise one less feedstock. Nevertheless, the variations in feedstock and product prices for the 2PS processes pose a liability and were worth investigating. The main sources of cost variation were found to be potassium acetate (46.2% and 44.3% contribution) and potassium hydroxide (33.0% and 26.7%) for methanol and ethanol respectively.

The difference in profit between the 3PS and 2PS processes for both alcohols is driven by several factors. The principal factor is feedstock saving, since elimination of sulphuric acid from the process led to a reduction of approximately \$150M.year^{-1}. In the case of ethanol processes, the cost reduction also has a significant contribution from operational costs, primarily driven by cooling water demand. The methanol process does not have as significant a decrease in OpEx, since it requires an additional flash vessel in the 2PS process to be able to achieve a saleable potassium formate purity.

Regarding the 3PS processes for both alcohols, the methanol process yielded better results. This can be explained by the methanol process being less energy intensive. Furthermore, the methyl alcohol feedstock price is half that of ethanol, and, in terms of products, the acetic acid is only 8% more valuable than formic acid. This leads to the overall profitability of the ethanol processes being smaller than for methanol.

In order to ensure that these processes would always be profitable, a minimum hydrogen selling price (MHSP) was computed for the"worst case scenario" feedstock and product prices. These are shown in Table 4. They are significantly higher than the maximum hydrogen price found in literature[32], more than 11 times in the case of the ethanol 3PS(W) process. Looking at the difference between the ethanol process values and methanol ones, the former are much higher across all designs and energy scenarios, about 140%. Selling hydrogen at this market price is therefore completely infeasible, even if we choose the lower MHSP values associated with the methanol processes. However, a revenue support system could to be established to render these processes economically attractive. If so, these designs have great potential for reducing emissions and providing green hydrogen while wind-powered water electrolysis evolves and renewables improve penetration in energy grids.

Process	Minimum H_2 selling price \$.kg^{-1}
Methanol 3PS(G+NG)	69.13
Methanol 3PS(W+NG)	69.32
Methanol 3PS(W)	91.60
Methanol 2PS(G)	19.33
Methanol 2PS(W)	19.47
Ethanol 3PS(G+NG)	96.81
Ethanol 3PS(W+NG)	97.16
Ethanol 3PS(W)	119.12
Ethanol 2PS(G)	27.46
Ethanol 2PS(W)	27.78

Table 4: Minimum hydrogen prices for the different scenarios

The contributions of OpEx, CapEx and feedstocks to overall process cost is shown in Figure 5, where the methanol designs are taken as an example. It can be seen that the plant costs are mainly driven by feedstocks, accounting for more than 80% of total expenditure in all of the processes, except 3PS(W). When changing energy feedstocks from grid to offshore wind, there was no significant cost change, as illustrated by the transition from 3PS(G+NG) to 3PS(W+NG) and the analogous transitions in the 2PS scenarios. However, implementation of electrified heating increases the OpEx of 3PS(W) by more than 3x compared to all other designs.

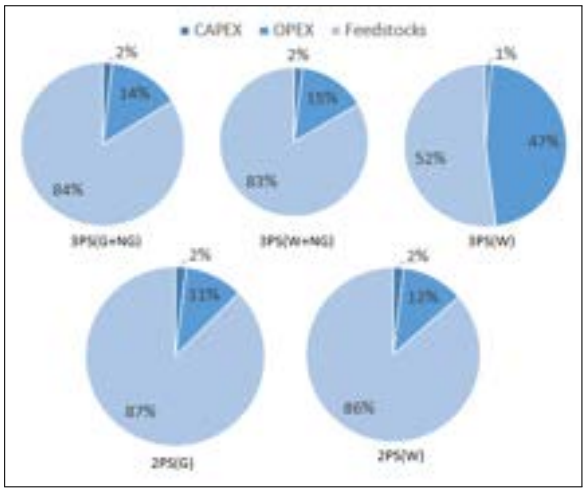

Figure 5: Cost distribution for the different methanol processes for each energy scenario

A particularly large decrease of \$110M/year in mean profit is observed when moving from the 3PS(W+NG) process to the 3PS(W) process. This is due to offshore wind energy being 670% more expensive than natural gas per kilowatt hour under the UK government's 2030 goal for wind energy costs[4, 28]. Given that wind-powered electrolysis has been shown to be the least damaging to the environment[10] it is important for industry to adopt it wherever possible; however, under current cost estimations, electrified heating with wind power in the 3PS processes is very unlikely to be feasible for at least the next 10 years.

Nevertheless, the profitability of the processes will likely evolve over time, with the projected price of renewable electricity to keep decreasing as technologies evolve[33]. Furthermore, electrified heating 3PS has significantly lower GWP and particulate matter emission metrics than the 3PS cases that used natural gas. Revenue support at the beginning of the project might increase its future profitability, making it more competitive with the other designs. Furthermore, future implementation of carbon taxes may also render the 3PS(W) process more competitive with other 3PS processes due to its lower GWP.

5 Conclusion

Demand for hydrogen is rapidly expanding in the face of climate change, and the implementation of low-carbon hydrogen is a valuable step in cutting emissions and meeting the carbon targets in the United Kingdom. Alkaline electrolysis using methanol or ethanol as feedstocks can be profitable at an industrial scale, and can help produce hydrogen gas with lower emissions than current industry standards, whilst simultaneously producing valuable chemicals as side-products.

It was shown that the most promising process is one that produces two products; hydrogen gas and a carboxylate salt (potassium formate or potassium acetate). This process is capable of generating profits of \$248M.year^{-1} and in combination with offshore wind power, this process can cut the global warming potential associated with SMR, the industry standard, by up to 80%. Furthermore, being less energy intensive than WE, this process strongly outperforms grid-powered WE across all analysed metrics: global warming potential, ozone depletion, particulate matter formation and human toxicity.During this transitory period in the energy industry, whilst energy grids are still very carbon-intensive, the proposed 2PS process could be very valuable, providing the opportunity to generate profit and reduce emissions whilst WE and renewable energy systems evolve.

The three-product processes, which produce hydrogen gas, an organic acid and potassium sulphate, have significantly higher emissions than the 2PS processes and are less profitable. The 3PS(W) system remains of interest as it approaches the low GWP characteristic of the 2PS, but does not generate profit under any current product prices. The authors note that the contents of this paper provide a snapshot of the energy industry as it currently stands; as we move towards net-zero emissions, comprehensive taxes on fossil fuels and financial support mechanisms may render the 3PS(W) system profitable and applicable in industry.

The use of methanol as a feedstock has a significantly lower environmental impact than ethanol. Furthermore, its processes are less costly, as indicated by minimum hydrogen selling prices which are on average 140% higher for ethanol. However, being primarily derived *via* methane reforming in industry, it may not be as sustainable as ethanol (mainly biomass-derived) in the long term. Future studies should include a life cycle analysis of biomethanol as a feedstock to the 2PS process to assess whether methanol electrooxidation could be feasible in the future if natural gas is phased out.

Future studies should also focus on improving the precision of experimental data for methanol and ethanol alkaline electrolysis. Testing at higher-temperature conditions (50°C-100°C) characteristic of industrial water electrolysis should be done to optimise industrial scale alcohol electrolysis. Furthermore, testing at a larger scale would allow to improve electricity consumption estimates for large electrolysers, and continuous flow systems should be analysed to optimise reactor residence time and conversion.

6 Acknowledgements

The authors would like to thank Hui Luo (Imperial College London), Nixon Sunny (Imperial College London) and Andrea Bernardi (Imperial College London) for their guidance and invaluable input.

References

[1] Victor Mallet. France launches €100bn coronavirus recovery plan. *Financial Times*, Sep 2020.

[2] Nik Martin. Germany and hydrogen — €9 billion to spend as strategy is revealed. *DW News*, Jun 2020.

[3] IEA. Hydrogen, 2020.

[4] HM Government. The ten point plan for a green industrial revolution. Nov 2020.

[5] IEA. The future of hydrogen. 2019.

[6] P. E. Dodds et al. Opportunities for hydrogen and fuel cell technologies to contribute to clean growth in the uk. *H2FC SUPERGEN*, 2020.

[7] HM Government. The clean growth strategy. 2017.

[8] Lorena Mosca, Jose Antonio Medrano Jimenez, Solomon Assefa Wassie, Fausto Gallucci, Emma Palo, Michele Colozzi, Stefania Taraschi, and Giulio Galdieri. Process design for green hydrogen production. *International Journal of Hydrogen Energy*, 45(12):7266 – 7277, 2020. Hydrogen separation/purification via membrane technology.

[9] O. Schmidt, A. Gambhir, I. Staffell, A. Hawkes, J. Nelson, and S. Few. Future cost and performance of water electrolysis: An expert elicitation study. *International Journal of Hydrogen Energy*, 42(52):30470 – 30492, 2017.

[10] Antonio Valente, Diego Iribarren, and Javier Dufour. Harmonised life-cycle global warming impact of renewable hydrogen. *Journal of Cleaner Production*, 149:762 – 772, 2017.

[11] D. Parkes, D.J. Evans, P. Williamson, and J.D.O. Williams. Estimating available salt volume for potential caes development: A case study using the northwich halite of the cheshire basin. *Journal of Energy Storage*, 18:50 – 61, 2018.

[12] Nixon Sunny, Niall Mac Dowell, and Nilay Shah. What is needed to deliver carbon-neutral heat using

hydrogen and ccs? *Energy Environ. Sci.*, 13:4204–4224, 2020.

[13] Tetsuo Take, Kazuhiko Tsurutani, and Minoru Umeda. Hydrogen production by methanol–water solution electrolysis. *Journal of Power Sources*, 164(1):9 – 16, 2007.

[14] Sami Tuomi, Annukka Santasalo-Aarnio, Petri Kanninen, and Tanja Kallio. Hydrogen production by methanol–water solution electrolysis with an alkaline membrane cell. *Journal of Power Sources*, 229:32 – 35, 2013.

[15] Anh Tuan Pham, Tomohiro Baba, and Toshio Shudo. Efficient hydrogen production from aqueous methanol in a pem electrolyzer with porous metal flow field: Influence of change in grain diameter and material of porous metal flow field. *International Journal of Hydrogen Energy*, 38(24):9945 – 9953, 2013.

[16] Evans A. Monyoncho, Tom K. Woo, and Elena A. Baranova. Ethanol electrooxidation reaction in alkaline media for direct ethanol fuel cells. In *Electrochemistry: Volume 15*, volume 15, pages 1–57. The Royal Society of Chemistry, 2019.

[17] Valentina Bambagioni, Manuela Bevilacqua, Claudio Bianchini, Jonathan Filippi, Alessandro Lavacchi, Andrea Marchionni, Francesco Vizza, and PeiKang Shen. Self-sustainable production of hydrogen, chemicals, and energy from renewable alcohols by electrocatalysis. *ChemSusChem*, 3(7):851–855, Jun 2010.

[18] M. Bellini, M. Bevilacqua, M. Innocenti, A. Lavacchi, H. A. Miller, J. Filippi, A. Marchionni, W. Oberhauser, L. Wang, and F. Vizza. Energy & chemicals from renewable resources by electrocatalysis. *Journal of The Electrochemical Society*, 161(7):D3032–D3043, 2014.

[19] Hydrogen fuel quality — product specification. part:all applications except proton exchange membrane (pem) fuel cell for road vehicles. Standard, International Organization for Standardization, Geneva, CH, 2019.

[20] James M Douglas. *Conceptual design of chemical processes*. McGraw-Hill, 1988.

[21] Wu-Jun Liu et al. Efficient electrochemical production of glucaric acid and h2 via glucose electrolysis. *Nature Communications*, 2020.

[22] Mario Simoes, Steve Baranton, and Christophe Coutanceau. Electrochemical valorisation of glycerol. *ChemSusChem*, (5):2106 – 2124, 2012.

[23] Badra Mahida, Hassiba Benyounes, and Weifeng Shen. Process analysis of pressure-swing distillation for the separation of formic acid–water mixture. *Chemical Papers*, 2020.

[24] Cătălin Pătrut, Elena Cătălina Udrea, and Costin Sorin Bildea. Separation of water-acetic acid mixtures by cyclic distillation. *U.P.B. Sci. Bull*, 2018.

[25] UK Government. Energy trends: December 2018.

[26] IEA. Data and statistics.

[27] Jamie Ally and Trevor Pryor. Life-cycle assessment of diesel, natural gas and hydrogen fuel cell bus transportation systems. *Journal of Power Sources*, 170(2):401 – 411, 2007.

[28] UK Government. Prices of fuels purchased by manufacturing industry in great britain (p/kwh) (qep 3.1.2).

[29] Sofia Figuereido. The cost of water in the process industry, 2015.

[30] Ramchandra Bhandari, Clemens A. Trudewind, and Petra Zapp. Life cycle assessment of hydrogen production via electrolysis – a review. *Journal of Cleaner Production*, 85:151 – 163, 2014. Special Volume: Making Progress Towards More Sustainable Societies through Lean and Green Initiatives.

[31] Timothy Kremer et al. N2 gas is an effective fertilizer for bioethanol production by zymomonas mobilis. *PNAS*, 112:2222–2226, 2015.

[32] Muhammet Kayfeci, Ali Keçebaş, and Mutlucan Bayat. Chapter 3 - hydrogen production. In Francesco Calise, Massimo Dentice D'Accadia, Massimo Santarelli, Andrea Lanzini, and Domenico Ferrero, editors, *Solar Hydrogen Production*, pages 45 – 83. Academic Press, 2019.

[33] Committee on Climate Change. Hydrogen in a low-carbon economy. *International Journal of Hydrogen Energy*, 2018.

IMPERIAL COLLEGE LONDON

DEPARTMENT OF CHEMICAL ENGINEERING

ADVANCED CHEMICAL ENGINEERING PRACTICE

Acoustic Levitation to Study Polymer Particle Drying for Applications in Spray Drying

Authors: Athanasios Charos, Michael Piliounis

Abstract

A laboratory scale acoustic levitator is employed to simulate the process conditions of spray drying to circumvent the difficulty in experimentally observing single droplet drying in commercial spray drying equipment. The formation and drying of model polymer particles is studied in terms of particle size, drying profile, and morphology. Mixtures of varying concentrations (1-10 % w/w) of poly(styrene) (PS) and poly(methyl methacrylate) (PMMA) in the common solvent tetrahydrofuran (THF) are examined. Three distinct drying regimes are identified and a descriptive model is proposed to describe the phenomena using extraction time, τ and diffusion exponent, α. These regimes are (i) solvent removal from droplet prior to formation of a polymer-rich skin, (ii) solvent diffusion through the forming polymer skin, and (iii) arrest of the droplet with regards to particle size and morphology. Results indicate that higher polymer concentrations lead to a transition to regime 2 at shorter times, giving rise to earlier polymer skin formation and larger final particles. Scanning Electron Microscopy is employed to validate the formation of hollow particles predicted by the large Peclet number (Pe= 6300), and examine surface porosity imparted from the condensation and organization of water droplets on the surface of the polymer skin.

Keywords: Acoustic Levitation, Spray Drying, Polymer Particles, Drying

1 Introduction

Spray Drying is a well-established industrial process with an estimated equipment market size of $ 4.5 billion in 2020,[1] and is widely used to transform valuable compounds dissolved in liquid streams into solid, stable particulate materials. It involves a liquid feed of solvent, soluble compounds, and a heating medium, usually air. The feed is introduced to the process vessel through an atomizer, which converts the liquid into a stream of droplets of $\sim 1-100\mu m$ size. Process conditions are set to ensure complete evaporation of the solvent by the time the droplets/particles reach the bottom of the vessel. The nature of the dry products depend on their physical and chemical properties and can vary between dry powders, agglomerates, or granules. Depending on the drying profile and solvent selection a range of particle morphologies can be formed including completely compact and hollow particles.[2,3]

Being cost-effective, continuous, and easily scalable for a wide range of capacities, this process is used in several industrial domains. Its ability to handle heat-sensitive compounds renders it lucrative especially for the pharmaceuticals and food processing industries.[4] Owing to the strict particle distribution achieved, it is also used in the production of catalyst supports and paint pigments.[5]

Despite the maturity of this process, little research has been done to understand the process at a fundamental level. Empirical models and heuristics are largely used for modeling and control of the process,[6,7] leading to sub-optimal operation. Computational simula-

tion of such systems is particularly challenging due to the complex heat and mass transfer phenomena and the intrinsic non-uniformity of the system (pressure, temperature, concentration, velocity gradients). Relying on predictive methods to obtain important process parameters limits the accuracy and consistency of these models.[8] Conducting physical experiments on the apparatus presents great challenges as well. Tracking fast-moving droplets/particles inside a complicated gas flow regime and harsh process conditions give rise to repeatability and reliability concerns. Besides, the co-existence of solid, liquid, and gas-phase contributes greatly to the inherent complexity of the system.

Polymer particles are often created by spray drying,[9] and are widely used due to their easy manufacturing, wide applicability, and compatibility with numerous biological and chemical systems. Characteristic properties of such particles include mechanical stability, significant load capacity, and consistent shape and morphology, dependent on the manufacturing process.[10]

This study examines the drying of single droplets containing a single solvent, a polymer and mixtures of polymers until the formation of polymer microparticles. Acoustic levitation is employed to keep the droplet stationary without any external interference. Eliminating mechanical contact ensures no heterogeneous nucleation effects. This novel approach greatly simplifies the system at hand while also allowing easy monitoring of the droplet throughout the experiment. Zaitone and Tropea conducted experiments comparing forced convection drying in induced airflow to acoustically levitated droplet drying. They concluded that for high airflow rates (as is in the spray drying process), the two methods are in agreement in the physical parameters describing the drying process.[11] Therefore, acoustic levitation is a valid approach to simulate the spray drying process and study single droplets. By removing the droplet's spatial variation, we are able to achieve significantly higher repeatability of the process and consistency of the results. It is acknowledged that this approach does not capture all the complex phenomena occurring inside a spray dryer vessel, it provides however sufficient conditions to study the overall drying process, polymer skin formation, morphology, and structure of the particles.

The work presented determines the role of polymer concentration on the drying kinetics, morphology and size of polymer particles. Differences between PMMA, PS and their mixture will provide useful insights on the spray drying process on two levels. Firstly, given the scarcity of accurate experimental results, the presented data and analysis contributes significantly to the efforts already made by the scientific community. Secondly, identifying the physical phenomena that take place during the process will provide a more reliable for computational simulations to be performed, ultimately enhancing process control of the industrial process.

2 Materials and Methods

2.1 Experimental Setup

Experiments were performed using analytical grade polymers and solvent. Polymethylmethacrylate (PMMA) of 74 kg/mol was synthesised in house through radical polymerisation and Polysterene (PS) of 50.4 kg/mol was sourced from Polymer Laboratories Ltd. As a base solvent, anhydrous THF, dried with 4 Å molecular sieves was sourced from Merck & Co. Polymer solutions of PMMA/THF, PS/THF and a three component system of PMMA/PS/THF (50-50 polymer concentration) were prepared at various concentrations ranging from 10% w/w total polymer concentration down to 1% w/w. Experiments were performed under ambient conditions (T=20.5 °C and relative humidity (RH)= 52%).

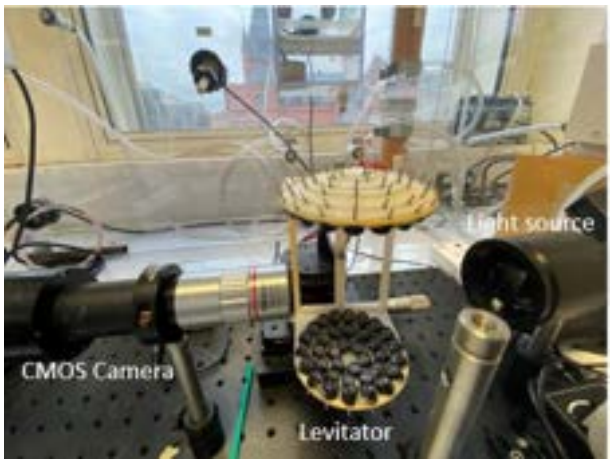

Fig. 1 Experimental setup. From left to right: CMOS camera, acoustic levitator and light source. The opposite facing transducers are depicted in the middle, levitating a droplet for reference.

To achieve acoustic levitation, a TinyLev levitator was used which employed two sets of ultrasonic transducers mounted on two curved interfaces, opposite to each other (see Figure 1). The transducers' frequency was set to 40kHz in air.[12]

Liquid droplets in the μm scale were placed at the nodal point by a 13 mm diameter hypodermic needle, attached to a 0.3 mm diameter NORM-JECT syringe. The experiments were conducted within a Coy humidity control chamber containing a Watlow EZ-ZONE heater and

a ETS Micro-controller Model S-100 as well as temperature and humidity sensors to maintain stable conditions. To capture high resolution images of the drying droplet-particle, a tube microscope with 5X Mitutoyo Plan Apo objective (focal length = 200 mm) was connected to a Basler ac2040-90uc CMOS camera. Images were taken for seven (7) minutes after the deposition of the droplet at 0.5 frames per second (fps). The sequence of images obtained for each droplet-particle were analysed using ImageJ, an image processing software, monitoring the particle radius change with time. Calibration of the setup was performed yielding a 1.106:1 μm:pixel ratio. Scanning Electron Microscopy (SEM) was employed to analyse the surface morphology and structure of the particles. Apparatus used was a Zeiss Auriga, with accelerating voltage of 5kV.

2.2 Methods

Previous research,[13] has proposed that the dimensionless Peclet number can be used to characterize the droplet drying process. It is expressed as:

$$Pe = \frac{k}{D_s},^{14} \tag{1}$$

where k is the solvent evaporation rate and D_s the diffusivity of the solute.

For low Peclet number (Pe ≤ 1) the diffusion of the solute is faster than the recession rate of the surface resulting in dry, non-hollow particles which are expected to have little or no void space,[15]. Such particles are beyond the scope of this project. This study focuses on particles with large Peclet number (Pe ≥ 2). Large Peclet number results in increased local concentration of the solute (polymer) at the droplet surface which leads to shell or skin formation and therefore hollow particles.[16]

Compression forces due to the acoustic field resulted in the deformation of the droplet into an oblate spheroid (see Figure 2a). Particles were described using an ellipse approximation, with the image processing software reporting the change of minor and major radii over time. The use of the equivalent particle radius was proposed and validated (see subsection 3.1) to simplify data analysis:

$$R_{eq} = \sqrt[3]{R_{minor}R_{major}^2} \tag{2}$$

$$Q_{wa} = \sqrt[3]{Q_{minor}Q_{major}^2} \tag{3}$$

where R_{eq} is the equivalent radius and Q_{wa} the weighted average for major and minor radii properties. Unless otherwise stated, $R(t) = R = R_{eq}$ throughout this report.

For the pure THF droplets, evaporation was modelled using the following empirical equations, previously used in microfluidics literature to describe droplet solvent extraction,[17,18] and evaporation according to boundary layer theory respectively,[19] :

$$R(t) = (R_0 - R_\infty)(1 - \frac{t}{\tau})^\alpha + R_\infty \tag{4}$$

$$\frac{R^2(t)}{R_0^2} = 1 - \beta\frac{t}{R_0^2} \tag{5}$$

where R(t) is the droplet radius at time t, R_0, R_∞ the initial and final droplet radii, τ the extraction time, α the exponent accounting for type of diffusion ($\alpha = 0.5$ for pure Fickian diffusion), β the evaporation coefficient.

For pure solvent evaporation $R_\infty = 0$ as explained in section 3.1. Physically, τ represents the time where the solvent droplet is expected to completely evaporate assuming no water condensation due to air humidity occurs. Note that, Equations 4, 5 are equivalent in the ideal case of $R_\infty = 0$ and $\alpha = 0.5$. Additionally, the alpha value of 0.5 yields a $t^{0.5}$ dependence expected from pure Fickian diffusion.

For the polymer-THF solutions, a more descriptive model was required to accurately describe the drying process including polymer skin formation and kinetic arrest of the particle:

$$R(t) = (R_0 - R^*)(1 - \frac{t}{\tau_1})^{\alpha_1} + (R^* - R_\infty)(1 - \frac{t-\tau_1}{\tau_2})^{\alpha_2} + R_\infty \tag{6}$$

where R(t) is the particle radius at time t, τ_1, τ_2 are extraction times, R_0, R^*, R_∞ the initial, cross-over and final droplet radii. This expression was formulated to account for the initial unhindered solvent evaporation (term 1) and the solvent diffusion through the polymer skin (term 2). To validate the equivalent radius approximation, the model describing the pure solvent droplet evaporation was tested for the minor and major radii values reported by imageJ, using data from three (3) runs. The results of the physical parameters obtained in these two cases were averaged using Equation 3 and compared to the values obtained through the R_{eq} method.

Throughout this report, uncertainty in measurements is quantified with the standard deviation method:

$$\sigma = \sqrt{\frac{\Sigma(x_i - \mu)^2}{N}} \tag{7}$$

where x_i is the value of a parameter for run i, μ is the average value of the the parameter x_i over all runs considered and N is the number of runs considered.

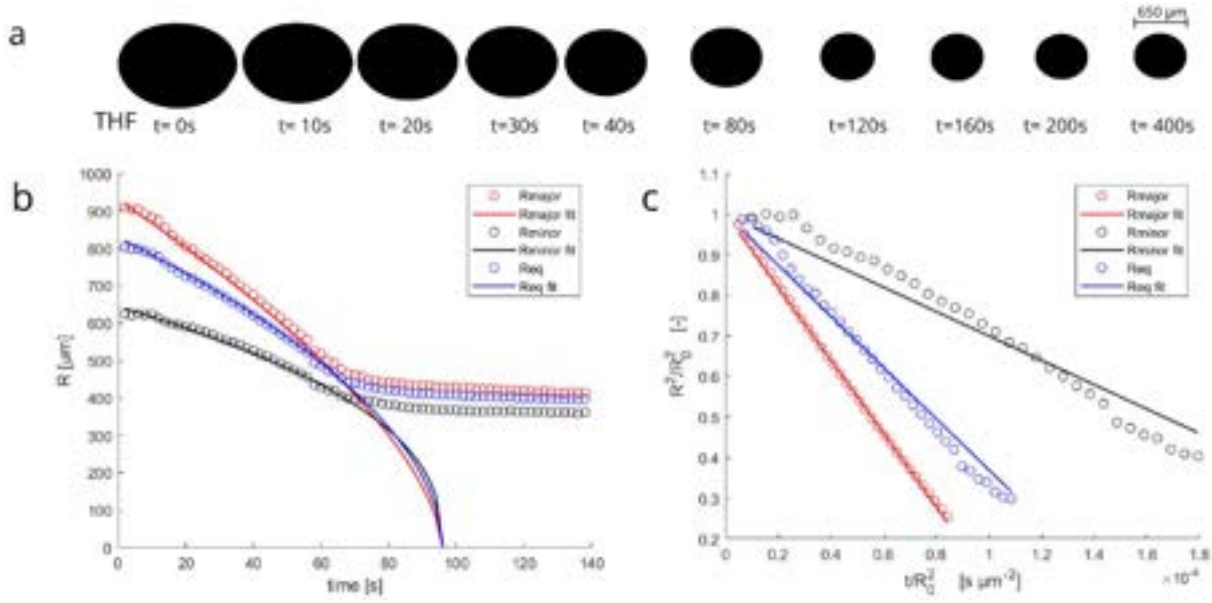

Fig. 2 (a) Sequence of images featuring a pure THF droplet drying. Initial size reduction is rapid. No further decrease is visible after 120 seconds. After t=120 s, no further decrease in size is visible. **(b)** Experimental results obtained for the major, minor and equivalent radius, normalised by the respective initial value. The proposed model shows good agreement for all dimensions examined, with consistent extraction time $\tau = 96$ s. **(c)** Experimental data and model fits for the major, minor and equivalent radii. The constant gradient lines represent the term β $[\mu m^2 s^{-1}]$.

3 Results and Discussion

3.1 Pure Solvent Evaporation

The evaporation of pure solvent droplets can be described by evaporation models based on film theory,[20] assuming that due to rapid internal mixing, a uniform temperature distribution exists.[21]

Images taken during the drying process of a pure THF droplet are exhibited in Figure 2a. Initial size reduction is rapid, with the droplet major radius reaching half it's initial size in approximately 40-50 seconds. Further size reduction is much slower and the droplet attains its final size at approximately 120 seconds. As explained below, the latter statement is justified by water condensation on the droplet surface.

To validate the use of the equivalent radius method, the descriptive model for the solvent evaporation was used with the experimental values obtained for the major and minor radii. To minimise the degrees of freedom, extraction time (τ) is kept constant and the α, β parameters are allowed to vary. In Figure 2b, the continuous lines intersect the time axis at precisely $t = \tau = 96$ s, physically representing the time that a pure THF droplet is expected to completely evaporate, when water condensation is not present. In Figure 2c, the gradients of the straight lines represent β. Using Equation 3, the weighted averages of the α, β values are obtained as reported in Table 1 and are in agreement with the values obtained via the R_{eq} method.

The consistency of the results obtained give sufficient evidence of accuracy of the R_{eq} method, thus allowing its use in this report.

Table 1 Parameter values obtained by the major, minor, weighted average and equivalent radius analysis. Weighted average values obtained by equation 3

	$\tau[s]$	$\alpha \pm \sigma$ [-]	$\beta \pm \sigma$ $[\mu m^2 s^{-1}]$
Major	96	0.63 $\pm$0.02	9000 $\pm$400
Minor	96	0.40 $\pm$0.01	3000 $\pm$150
W. Average	96	**0.54** $\pm$0.01	**6240** $\pm$50
Equivalent	96	**0.53** $\pm$0.01	**6300** $\pm$25

In theory, Equation 4 assumes that the final droplet radius $R_\infty = 0$, however results detailed in Figure 2a, 2b indicate that $R_\infty \neq 0$. In practise, during the drying process, the volatile solvent causes an evaporative cooling effect which leads to a decrease of the particle surface temperature. Under the conditions explored (RH=52%, T=20.5°C), water condensation on the surface is significant,[22] and is the primary reason behind the falling rate of solvent evaporation as well as the final droplet size. Upon condensation, water diffuses inside the droplet, as THF and water are fully miscible, and THF continues to evaporate until the droplet comprises entirely of water. In the beginning, the latter process is significantly faster leading to droplet size reduction. Later on it be-

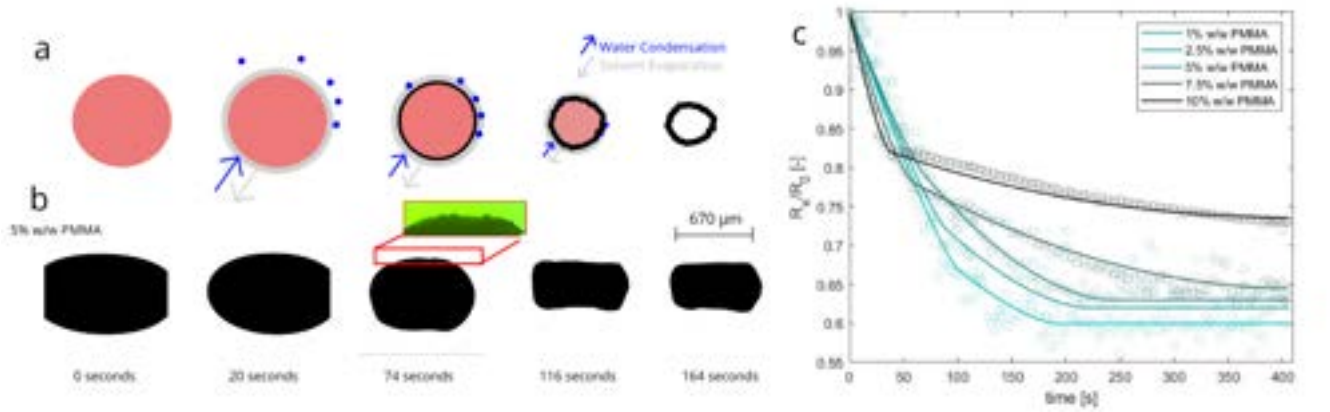

Fig. 3 (a) Schematic of the drying of a polymer-solvent droplet towards particle formation. Blue dots represent water condensation and coalescence on polymer skin (denoted by black outline). A solvent-free and hollow particle is obtained with mechanical stability and rough surface morphology. **(b)** Images sequence of a 5% w/w PMMA droplet drying.The first two images are slightly cropped as the droplet exceeded the camera frame. The inset from instance of 74 s shows water condensation on the skin surface. **(c)** Normalized R_{eq} progression with time for all PMMA concentrations examined (1-10 % w/w). The three distinct drying regimes are visible especially for lower concentrations. Inconsistent data due to particle vibrations were discarded.

comes progressively slower as the water content inside the droplet increases. The final size is attained when the droplet, consisting primarily of water, returns to ambient temperature. The radius change is then dictated by the evaporation of water which is slow.

3.2 Solvent - Polymers Systems

Analysing the change of the equivalent droplet-particle radius with respect to time (Figure 3b), three (3) distinct regions are identified. The first two regions correspond to separate drying regimes whose end is signified by a sharp inflection point in the curves, or kink. The third region is the plateau to which each particle reaches, signifying the kinetic arrest. At this point, diffusion of solvent through the thick polymer skin continues until the cavity of the particle is dry. These regimes are identified irrespective of polymer or concentration. Given the constant temperature and humidity, any difference must result from the difference in initial droplet size, polymer type or concentration.

3.2.1 First Regime

This drying regime is associated with the first term of Equation 6 and the corresponding key parameters α_1 and τ_1. It is characterised by rapid solvent evaporation leading to significant droplet size reduction. Diffusion exponent (α_1) values show slight increase with increasing polymer content, retaining values in the range [0.8,1.6]. Interestingly, the polymer molecules affect solvent diffusion at this early stage. The non-constant values of α_1 and the deviation from 0.5, show the system's digress from ideal Fickian diffusion. This observation is in agreement with published literature where α_1 has been used to account for dynamic interfacial effects, hydrodynamics and demixing.[23]

Polymer molecules solvated in a liquid experience little polymer-polymer interactions at relatively low concentrations. Increasing the polymer concentration up to a threshold value (specific to every polymer-solvent system), leads to negligible change in physical properties. Once this value is exceeded, polymer-polymer interactions affect the physical properties of the solution, giving rise to a gel.[24] In droplet drying, the threshold concentration is exceeded at the droplet surface and not the entire droplet volume, giving rise to a polymer skin which later becomes the outer edge of the particle. This behaviour can be validated by approximating the system's Peclet number:

$$Pe \sim \frac{6300 \times 10^{-12}}{10^{-12}} = 6300 \gg 2 \tag{8}$$

where the numerator corresponds to the calculated solvent evaporation rate (β) and the denominator to the solute diffusivity in THF.[25] The value of the dimensionless number exceeds the threshold value and therefore accumulation of polymer at the receding droplet interface is expected which ultimately leads to skin formation and hollow particles.

Solvent evaporation at the droplet surface effectively increases the local polymer concentration. Little mass transfer resistance allows for the quick diffusion of the solvent to the surface, thus keeping the local concen-

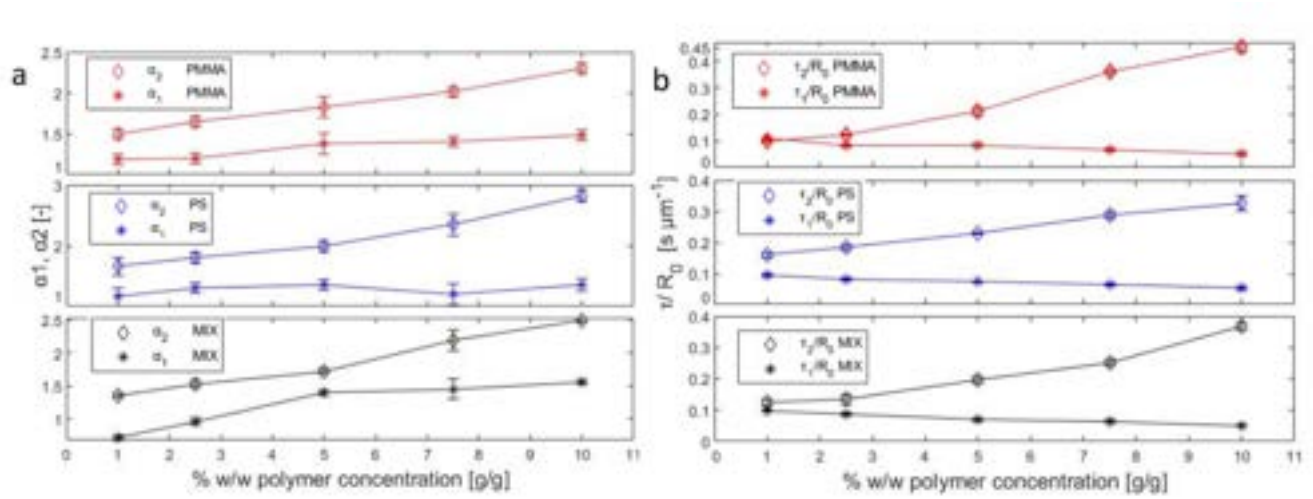

Fig. 4 Key parameters of the descriptive model, plotted with respect to concentration for all the solvent-polymers systems examined. In both cases, error bars represent standard deviation. **(a)** Diffusion exponents α_1 and α_2 both showed increase with increasing polymer concentration. **(b)** The extraction times τ_1 and τ_2 diverge with increasing concentration, resulting in longer second regime.

tration below the threshold value. The driving force to this process is the concentration gradient between the droplet surface and the droplet core ($C_{core} - C_{surface}$).[26] However, as evaporation progresses, the solvent content of the droplet decreases causing the decrease of C_{core} and the driving force. Inevitably, the threshold concentration is exceeded and the polymer molecules entangle sufficiently to physically crosslink and solidify, forming a surface skin. This event is described in this analysis by $\tau_1[s]$ and $R^*[\mu m]$ representing the elapsed time and droplet radius at the onset of cross-linking. Special attention was given to τ_1 due to its importance in the spray drying process.

Extraction time (τ_1) shows consistent decrease with increasing concentration, however, given the parameter's dependence on the droplet size, the values reported have been normalized by the initial droplet radius in Figure 4b. This is expected as the magnitude of polymer-polymer interactions increase with concentration, resulting in faster skin formation.

Different polymers exhibited different extraction times. The diffusivity of the polymer in the solvent is identified as an important parameter that can justify the observed trend. The high molecular weight of PMMA and its slightly slower diffusion, forces it to accumulate more at the surface leading to faster skin formation. The mixture of the two polymers exhibits intermediate results, hinting at a linear relationship between the discussed polymer properties and the skin formation time. Other factors that might contribute to the differences between the systems are glass transition temperature, polydispersity and crystallinity.

The regime of constant drying rate,[11] ends when the solvent diffusion to the particle surface becomes smaller than the evaporation rate, marking the onset of the skin formation. Further solvent evaporation is controlled by the diffusion of solvent through the skin, a process which becomes incrementally slower.

3.2.2 Second Regime

This intermediate regime features smooth parabolic curves in the R_{eq} vs time plots, reconciling the initial rapid size reduction of the first regime to the plateau representing the third regime (see Figure 3c). The curvature of the graph suggests progressively hindered diffusion as the gradient of the curve smoothly approaches zero and the particle approaches kinetic arrest. Diffusion exponent α_2 increases with polymer concentration, retaining values in the range [1.3, 2.8]. The significant deviation from ideal Fickian diffusion is expected, as the solvent must diffuse through a porous skin. The time length of this regime, expressed by the difference $\tau_2 - \tau_1$, varies with polymer content. Physically, it represents the time between the onset of skin formation and kinetic arrest of the particle. Low concentration experiments feature significantly smaller time periods for this regime because τ_1 increases and τ_2 decreases simultaneously (Figure 4b).

The thickening process of the polymer skin (*i.e.* polymer shell formation) is incremental and not spontaneous. Polymer entanglement and cross-linking initially occurs at the outer edge of the particle, but then propa-

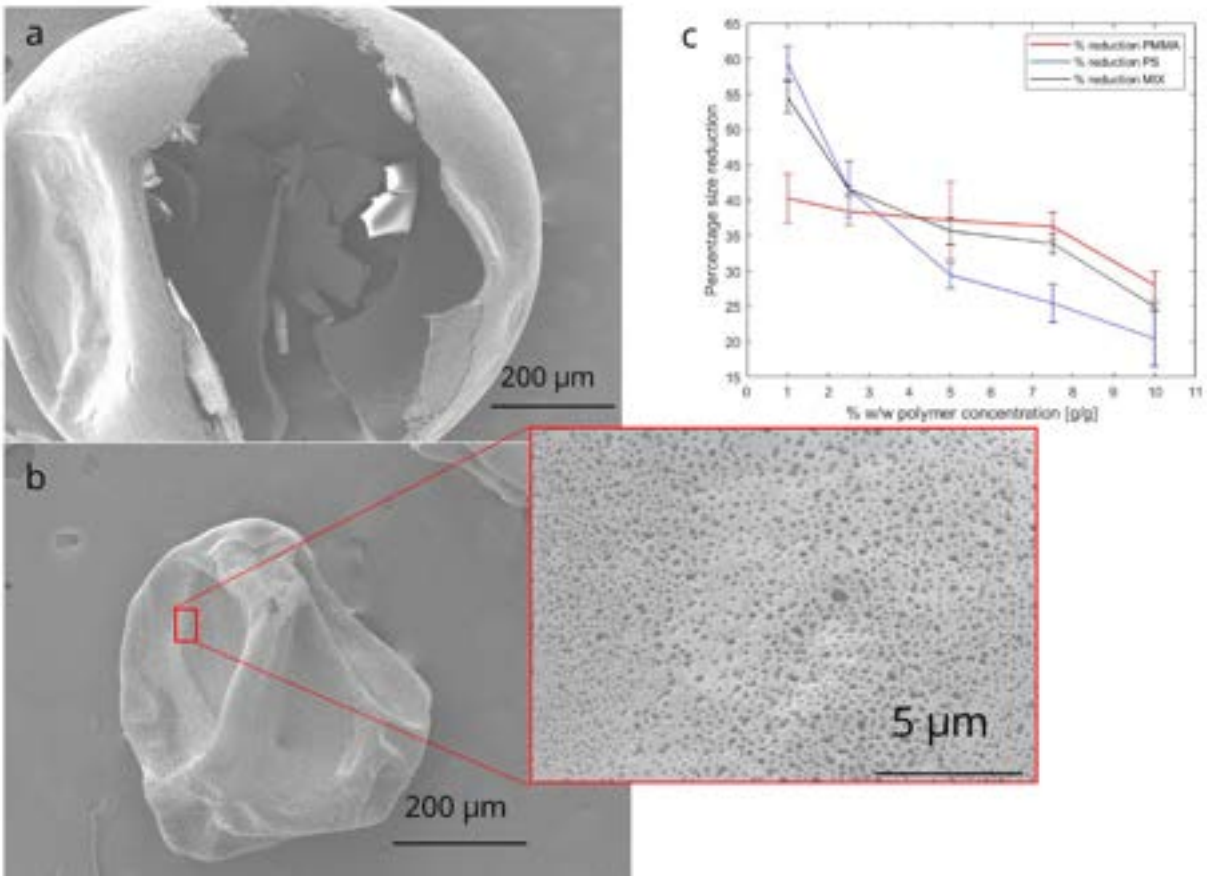

Fig. 5 (a) Scanning Electron Microscopy image of polymer 10% PMMA-PS mixture particle. Hollow spherical particle with large cavity and intact skin and evident buckling on the left hand side due to acoustic compression. **(b)** 10% PMMA particle with significant buckling. Blowup image of the pore structure. **(c)** Percentage size reduction of the drying droplets, as they form particles $(\frac{R_0-R_\infty}{R_0}) \times 100\%$. Error bars represent standard deviation of measurements.

gates to the inside of the particle. This creates additional resistance to the solvent diffusion which effectively increases the local polymer concentration at the interface between the inner side of the skin and the liquid droplet core. The skin propagation is halted prior to reaching the droplet core, therefore creating hollow particles. This is attributed to the high volatility of the solvent as well as cavitation that occurs at the droplet core.[27]

Water condensation due to evaporative cooling occurs in this setting as well. At low polymer concentrations, water droplets stabilise on the polymer skin and coalesce to form visible droplets as in blowup of Figure 3b. It has been previously reported that presence of water in polymer-solvent mixtures affects the morphology of the particle, resulting in porous or honeycomb-like structures often called breath figure arrays.[28] This is attributed to the different evaporation rates of the liquids (water usually being the less volatile component).

The strength of interactions between the polymer and the solvent determine the size and uniformity of the pores and holes respectively. Weaker interactions allow for water to coalesce, resulting in bigger cavities in the polymer skin. On the contrary, favorable polymer-solvent interactions force water in small, uniform cavities on the skin, ultimately leading to a structured porous skin.

A limitation of the acoustic levitation method is identified here, regarding the particle shape achieved. The compression forces of the acoustic field in the z-axis, initially lead to isotropic expansion of the liquid droplet, giving rise to an ellipsoid. Once applied to the thin polymer skin, the compression forces result in skin surfaces that are perpendicular to the applied force as observed in Figure 3b. As explained above, the thickening of the polymer shell is an incremental process. As such, the skin is initially a very thin polymer layer supported on a liquid droplet. While being able to maintain its mechanical integrity, the surfaces under pressure are distorted into flat surfaces, maximising their surface area, thus minimising the applied pressure.

This behaviour is characteristic to the acoustic levitation, and is not expected in spray drying. In the latter process, small initial droplets result in spherical particles due to the high surface tension. On the contrary, a larger initial droplet size may result in distorted particles, which is the case for lactose particles used as API carriers for inhalants.[29]

3.2.3 Third Regime

All polymer-solvent systems feature a consistent dependence of final particle size to polymer content. To take into account the effect of the initial droplet size, the percentage size reduction for all the concentrations of the different systems are plotted in Figure 5c where error bars represent standard deviation of three (3) to five (5) runs. The size reduction of each droplet is highly dependent on the initial droplet size. Therefore, to remove the uncertainty of variable initial size, the percentage droplet size reduction is plotted for all polymer concentrations (Figure 5c. The observed size reduction in percentage terms, decreases with increasing concentration. This trend can be attributed to the earlier skin formation (τ_1 decreases with increasing concentration). As the skin formation occurs earlier in the process the droplet is larger.

Once the incremental skin formation has been completed, the particle has a rigid solid shell, which can undergo mechanical instabilities *e.g.* buckling.[16] At this point the equivalent radius curves of the particles plateau as in Figure 3c of the PMMA curves (kink 2) and size reduction stops. However, this does not suggest a completely dry particle, only that the mechanical structure is able to overcome the compression forces. Since the particle is hollow, solvent still remains inside the particle shell.

At this point the particles have not only obtained their final size but also their final morphology. Figure 5a features a particle obtained from the 10% PMMA-PS mixture. It has retained its sphericity but buckling is visible on the left hand side (side that was facing the acoustic waves) and as expected, it is hollow. Figure 5b features a 10% PMMA particle that is significantly more buckled. The inset picture exhibits the breath figure arrays. This morphology is due to the presence of condensing water on the particle surface during the skin formation. The different evaporation rates of water and THF result in a honeycomb or porous structure, whose order is determined by the size of the water droplets.

The time at which the radius reduction plateaus as well as the final size of the particle are very important properties for the spray dryer process. Different products, require particles to have specific sizes and morphology, therefore key results depicted in the above sections can be used to optimize production and characteristics of certain products.

4 Conclusion and Outlook

In this study acoustic levitation was used to study single droplets drying properties. These properties are a close match to those of single droplets undergoing spray drying therefore proving acoustic levitation to be a valid approach to model spray drying processes. PMMA and PS in two component systems with THF solvent or in a three component system (50-50 polymer mixture) were used to study solutions with large Peclet numbers (Pe ≥ 2), forming hollow particles with a rigid polymer shell.

The drying of a single droplet was found to undergo three distinct drying regimes. The first regime, was characterized by unhindered solvent diffusion to the droplet surface and further evaporation according to boundary layer theory. The parameters describing this regime are τ_1 and α_1. The former showed decrease with increasing polymer concentration, whereas the latter slight increase with increasing concentration. The start of the second regime was found to occur when the droplet surface is no longer saturated with solvent. From thereon, progressive skin formation occurs. Parameters characterizing this regime are τ_2 and α_2 and were both found to increase with increasing concentration. In the final regime, the particle retains its final size, structure and morphology. It was found that as polymer concentration increases the size reduction normalized by the initial droplet size decreases.

During the course of the experiments, particles often vibrated and rotated rapidly in the acoustic field. Optimisation of the levitator in future experiments can be achieved by introducing arranged transducers designed and programmed with accurate phase transition irregularities to limit particle vibration and spinning, especially in lower solution concentrations, however, this may create less representative spray drying conditions. Furthermore, incorporating vertical air circulation during the levitation will allow for a more accurate description of the complex heat, mass and momentum phenomena occurring in a spray dryer. Finally, radiation exposure of particles could be implemented to induce precise crosslinking (time-wise) to better define the size and size distribution of the particles formed. For example, combining the use of a photosensitive crosslinking agent with UV light exposure.

The results of this study are a valuable addition to the

little research of the fundamentals of a spray drying. A simple descriptive model was successfully used to characterise important physical phenomena occurring during the process. This information can be particularly useful in dynamic modelling, where intermediate states of the system cannot be guessed from initial and final conditions alone. The industrial relevance of this work can be traced to optimisation of process control of the spray drying process.

Conflicts of interest

There are no conflicts to declare.

Acknowledgements

We thank João T. Cabral and William N. Sharratt for their help and guidance throughout the reasearch and Róisín A. O'Connell for her assistance with SEM measurements.

Notes and references

1 *Spray Drying Equipment Market by Product Type, Application, Cycle Type, Drying Stage, Flow Type, Region - Global Forecast to 2025, ReportLinker, Accessed: 12 Dec 2020*.

2 E. M. Both, R. M. Boom and M. A. I. Schutyser, *Powder Technology*, 2020, **363**, 519–524.

3 J.-C. Lin and J. W. Gentry, *Aerosol science and technology*, 2003, **37**, 15–32.

4 W. A. Stein, *Chemie ingenieur technik*, 1973, **45**, 906–907.

5 A. B. D. Nandiyanto and K. Okuyama, *Advanced powder technology : the international journal of the Society of Powder Technology, Japan*, 2011, **22**, 1–19.

6 B. R. Bhandari, N. Datta, R. Crooks, T. Howes and S. Rigby, *Drying Technology*, 1997, **15**, 2509–2525.

7 W. T. Lee, F. S. Taip, M. N. Ibrahim and R. Kamil, *Empirical modeling and control for spray drying of orange juice powder*, 2011.

8 A. S. Mujumdar, L.-X. Huang and X. D. Chen, *Dairy science technology*, 2010, **90**, 211–224.

9 R. Vehring, *Pharmaceutical research*, 2007, **25**, 999–1022.

10 A. Ekdahl, D. Mudie, D. Malewski, G. Amidon and A. Goodwin, *Journal of pharmaceutical sciences*, 2019, **108**, 3657–3666.

11 B. Ali Al Zaitone and C. Tropea, *Chemical engineering science*, 2011, **66**, 3914–3921.

12 A. Marzo, A. Barnes and B. W. Drinkwater, *Review of scientific instruments*, 2017, **88**, 085105–085105.

13 E. Littringer, R. Paus, A. Mescher, H. Schroettner, P. Walzel and N. Urbanetz, *Powder technology*, 2013, **239**, 162–174.

14 R. Vehring, *Pharmaceutical research*, 2007, **25**, 999–1022.

15 R. Vehring, W. R. Foss and D. Lechuga-Ballesteros, *Journal of aerosol science*, 2007, **38**, 728–746.

16 M. Nuzzo, A. Millqvist-Fureby, J. Sloth and B. Bergenstahl, *Drying technology*, 2015, **33**, 757–767.

17 T. Watanabe, C. L. G., J. F. Douglas, T. Ono and J. T. Cabral, *Langmuir*, 2014, **30**, 2470–2479.

18 C. E. Udoh, V. Garbin and J. T. Cabral, *Langmuir*, 2016, **32**, 8131–8140.

19 A. F. 1932, *Dynamics of droplets*, Springer, Berlin; London, 2000.

20 R. B. .-R. B. Bird, *Transport phenomena*, Revised second ed. edn, 2007.

21 B. Al Zaitone and A. Lamprecht, *Colloids and surfaces, B, Biointerfaces*, 2013, **105**, 328–334.

22 F. K. A. Gregson, M. Ordoubadi, R. E. H. Miles, A. E. Haddrell, D. Barona, D. Lewis, T. Church, R. Vehring and J. P. Reid, *Physical chemistry chemical physics : PCCP*, 2019, **21**, 9709–9719.

23 W. N. Sharratt, A. Brooker, E. S. J. Robles and J. T. Cabral, 2018, **14**, 4453–4463.

24 K. Ozawa, E. Nishitani and M. Doi, *Japanese Journal of Applied Physics*, 2005, **44**, 4229–4234.

25 *Tetrahydrofuran Properties, GSI Environmental, Accessed: 17/Dec/2020*.

26 G. Meerdink, *Drying technology*, 1994, **12**, 981–982.

27 F. Meng, L. Luo, M. Doi and Z. Ouyang, *The European physical journal.E, Soft matter and biological physics*, 2016, **39**, 1–10.

28 X. D. Zhou, S. C. Zhang, W. Huebner, P. D. Ownby and H. Gu, *Journal of Materials Science*, 2001, **36**, 3759–3768.

29 Y. Rahimpour and H. Hamishehkar, *Advanced pharmaceutical bulletin*, 2012, **2**, 183–187.

Proof of Concept of Uncertainty Analysis and Sensitivity Analysis on Distributed Energy System Investment Models

Luke Whittington and Philip Zeeuw

Department of Chemical Engineering, Imperial College London, U.K

Abstract: An effective distributed energy system (DES) has been shown to be able to reduce the energy costs for given areas and buildings through effective design. Commercial buildings are one type of building that can benefit from the implementation of a DES due to their high energy consumption. The work in this paper expands on an existing integrated Technology Selection and Operation (TSO) optimisation model using DES. The model uses photovoltaic panels (PVs), batteries, combined heat and power units (CHPs), and absorption refrigeration chillers called AGOs. The aim is for the model to help decision makers find technologies that are attractive investments financially, as well environmentally sound. Data from a large UK retailer has been used to look at case studies for technology implementation and operation at 3 different stores of varying size. These results have then been compared to those from 2016. An important aspect for any investment however is the understanding of the uncertainty surrounding the investment and so a rigorous uncertainty analysis has been performed using Monte Carlo simulations as well as the Morris analysis. The results show that CHPs either alone or coupled to an AGO is the preferred investment, and have become more attractive since 2016. PVs and batteries on the other hand have become less attractive. CHPs, though chosen as the preferred investment by the deterministic model, show much higher uncertainties in their results due to them being heavily dependant on highly uncertain parameters.

1 Introduction

Climate change is undoubtedly one of the main challenges humanity is currently facing. The transition to renewable energy is a vital step in dealing with this issue, as highlighted by it being one of the UN's targets to reach by 2030 [1]. One of the pathways to achieving this is the introduction of distributed energy systems (DES), that is a system where the energy production is decentralised, and so closer to the energy consumer itself. They will typically rely on a number of small scale technologies, often using renewable energy. This shift from centralised to local energy production has happened for a number of reasons. With increasing energy costs along with better technology efficiency and pricing, energy security issues and distribution infrastructure constraints, DES has become an attractive investment for many. They allow for coupling of various technologies such as batteries, photovoltaics, combined heat and power units (CHPs), heat pumps, fuel cells, absorption chillers etc. These are just some of the technology options available when DES is implemented. DES are attractive to a variety of individuals and groups, whether it be business owners or infrastructure operators. When businesses and investors are looking at implementing a DES, an accurate assessment giving them the best option is paramount. Commercial organizations looking to invest in a DES often have a lot of choices when it comes to an investment portfolio. They often have several buildings that can be invested into as well as enough capital to make long-term investments, and so several types of technologies are available for them to invest in. However, there is potentially a lot on the line for people making the investment decisions in these organizations. Companies will often have different groups all wanting to use company money to invest in their department, and the various departments will often be judged on the success rate of their investments. This means that it is important for anyone suggesting in DES-investing has a good idea of the possible investment ideas as well as the likely outcomes of these investments and the risks involved in the investments. This will not only help make their case stronger when it comes to funding their investment strategies, but will also give them more confidence in the knowledge that they've chosen the correct strategy.

This paper will look at further developing the model presented in [2] and using it to find the optimal technology selection and operation for various scenarios and comparing them to results from previous years. Using the necessary data collected and given the parameters of the selected store, an optimal strategy for technology investment will be given by the model. This has then been coupled with various tools for measuring the uncertainty. This is a data driven approach and allows for the model and parameters to easily be updated as to provide accurate predictions for future scenarios and investments. The model and analysis tools have been constructed to provide key information regarding the financial, technical, and environmental understanding for an organisation's scenario and setting.

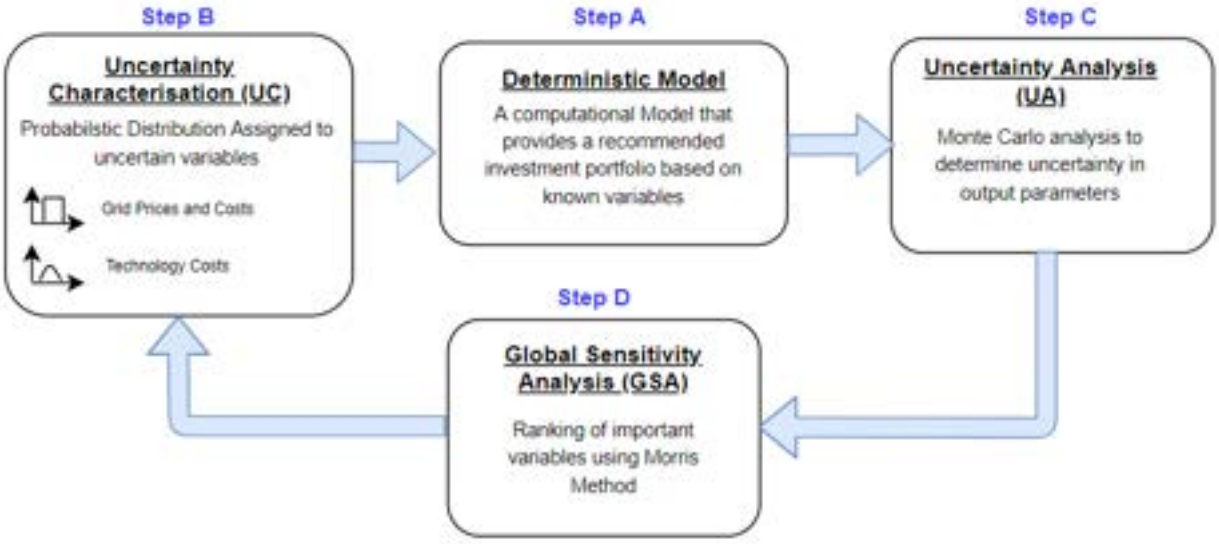

Figure 1: Workflow for Uncertainty Investigation in DES

2 Background

Extensive research has already been done in terms of designing DES and optimising building design to improve on a building's performance [3][4]. These papers highlight both the importance of designing an optimal DES and how buildings will operate better because of this. Numerous papers focus specifically on the combined heating and power [5] or combined cooling, heating and power [6] as they are useful choices especially for commercial organisations with large buildings.
Besides looking at the optimisation for the technology, the optimisation of the TSO model itself is of much relevance. It's not always the case of going for the same type of technology and operating it the same way. The optimal solution will vary based on a variety of factors as shown in [7]. Therefore, simply figuring out which technology is "best" becomes more difficult than just comparing their costs and efficiencies. A good model will be able to factor in all necessary information for the specific case study to provide the optimal solution. The optimal sizing when creating a DES is of key interest here. Previous work such as [8] have looked at simulating operational strategies for different sizes. Often the models will employ mixed-integer linear programming (MILP) [9]. Although significant research has been done in this field, many papers tend to focus specifically on one aspect of the DES, such as in [10] where they created an MILP to find the optimal size for residential CHP systems in Japan. This paper was different from previous deterministic-only papers as they had a rigorous sensitivity analysis regarding both various prices in Japan as well as policies regarding emissions. Other papers such as [11] focus on wind, PVs, diesel, and batteries instead of CHP and look at the optimal sizing needed to supply the necessary energy.
Using the previously mentioned papers, a gap has been identified for practical tools to identify optimal technology selection and sizing as well as operation that not only gives decision-makers easily obtained financial KPIs, but also tools for rigorous uncertainty analysis. The TSO modelling framework previously used by [2] has been expanded on and updated, as well as coupled with uncertainty analysis using Monte Carlo simulations and the Morris method to give the aforementioned decision-makers a clearer view regarding the uncertainty of the investments. Whereas [12] looks at much of the same in terms of effective design for a DES and the same methods for uncertainty analysis, it only focuses on one Swiss neighbourhood, while this paper will look at buildings in different parts of a country. This plays a major role as various technologies might be better suited for certain regions. A technology such as PVs will operate differently due to the difference in irradiance data and so the economic feasibility of the technology will be affected. Furthermore, there are price differences for the different regions in a country, and this has all been taken into account in the TSO model. The objective for this research project is to further improve the TSO model, and using this MILP, help commercial organisations in choos-

ing what types of technologies to invest in for different scenarios as well as understanding some of the uncertainty behind said investments. This includes finding a probable business-as-usual case that will show how the business will do both in terms of emissions and energy utilisation and cost for the selected time frame. The various scenario results will be analysed and examined to give organisations a better idea of the potential benefits the implementation of a DES can have. The model used in this paper builds on previous work but uses updated data regarding policies, energy pricing, as well as updated technology pricing and efficiency. This paper also goes further by reviewing some of the uncertainty associated with the selected investment portfolios found using the model and also comparing how the investment portfolios might have changed in the years since it was first created.

3 Methodology

The methodology used in this paper for uncertainty analysis of a TSO model is illustrated in figure 1. In step A a deterministic approach is used to find an investment portfolio. In step B, probability distribution functions (PDFs) are assigned to variables that are deemed uncertain in the model. In step C, Monte Carlo (MC) simulations are run to identify the uncertainty in the Key Performance Indicators (KPIs) that led to the specific investment portfolio in step A. Finally, in step D, the Morris method is used to rank the uncertain parameters in their effect on the KPIs.

3.1 Deterministic TSO Model

For the TSO model to determine the optimal solution for the various case studies there are a few steps that are taken. Firstly, a baseline is provided quantifying the energy costs as well as the carbon footprint of the store. This is the business-as-usual (BaU) scenario and is set as the worst case that the model will ever pick. Secondly, the model looks at the various selected technologies to install before then determining if and how the technologies can be used to find a scenario where the savings are the greatest compared with the baseline scenario. If no technology is economically feasible, the model will revert back to the baseline case.
To start off with, enough data for the model must be collected. This includes:

- Technology data
  - Here numerous types of different technologies were considered and four different ones were eventually chosen. These were: four types of PVs, four types of battery storage units, 28 types of CHP units. These CHP units could then be coupled with an AGO unit.
- Building data and parameters
  - Half-hourly profiles for demand of of electricity, heat, cooling and refrigeration.
  - Location, to access weather and irradiance data, as well as pricing of the electricity and gas in the given distribution network operator (DNO) area.
  - Area and size of the building to assess possible area for PV installation.
- Energy and carbon parameter projections
  - Carbon taxes, whether imposed by the government or an internal carbon tax imposed by the company itself.
  - Import and export prices for electricity for the given time frame.
  - Import prices for gas.
  - Carbon factor of grid electricity.

The model will then use this data to determine:

- Selected technology (only if it is better than the baseline scenario).
- The projected savings and capital investment, as well as other financial metrics such as internal rate of return (IRR), return on investment (ROI), payback period (PP), and discounted payback period (DPP).
- Carbon emissions as well as the carbon reduction.

The objective function used in the optimisation problem is set to minimise the overall cost for the selected time period.
The TSO model's objective is to find the optimal selection of technology and operational strategy for the energy generation and storage for the selected stores. The first step as previously mentioned is identifying a business-as-usual baseline. Here, no technology is implemented and all that is needed is the data regarding the demand and prices. Here it is assumed that the electricity is obtained from the grid, heat comes from the boiler using natural gas, and the refrigeration is obtained from an electric chiller. This option serves as a benchmark for the energy use and the cost of energy demand for the store. This solution is an option in all the other technology scenarios that are run and will be chosen if no technology is economically viable. The model will then solve for the optimum technology selection, comparing the minimum

cost of the energy over the chosen time period and comparing it to the baseline. Once the optimum combination is found, the various financial KPIs are calculated along with the savings in carbon emissions.

3.2 Uncertainty Characterisation

Uncertainty characterisation (UC) involves identifying the uncertain parameters in the model and assigning probability distribution functions (PDF) to their values. Each PDF must be made to best represent the type of uncertainty of the parameter. In this report, 13 types of parameters have been identified as having uncertainty and have been given PDFs as outlined in table 5. Table 1 shows the value of the uniform distributions used for energy cost and price, and gas cost at 1 January 2021 at midnight.

Table 1: Sample Distributions of Energy Carrier Prices

Uncertain Parameter	Uncertainty Representation
Energy Carier Prices	
Energy Cost	Uniform distribution [10.3,14.0]
Energy Price	Uniform distribution [2.99,4.04]
Gas Cost	Uniform distribution [2.03,2.75]

3.2.1 Technology Costs

The capital and maintenance costs for an energy storage, generation or distribution technology is subject to uncertainty because the costs calculated during the design stage may no longer be the cost in the implementation stage [13]. This paper follows the uncertainty distribution from Burhenne et al. [13], in which each variable takes a normal distribution. The mean is taken as the design stage prices, with a standard deviation of 7% of the mean.

3.2.2 Utility Costs and Demand

Electricity prices and costs are inherently uncertain in any predictions for the future. The deterministic model uses estimates from the large food retailer's internal analysts. This prediction into the future has increasing uncertainty as time goes on. The cost of buying electricity and gas, as well as the price of selling electricity back to the grid, have a cone of uncertainty. The initial uncertainty in 2021 is found by comparing estimates from the internal analysts at the large food retailer, and estimates by [14] [15]. An initial uncertainty of electricity of 15% was found, with an increase of 2% per year to accommodate for increasing uncertainty into the future. The cone of uncertainty subsequently obtained is shown in figure 2.

3.2.3 Technology Specifications

The technical performance of an energy technology might vary over time and function differently under real-world circumstances. PV technologies have been analysed by the food retailer to have negligible drop in effectiveness throughout its lifetime. For all other technologies, the efficiencies have been given a half normal distribution in accordance with the approach layed out in [16]. μ, the location parameter, is taken as the nominal value, with the scale parameter being equal to 5%.

Figure 2: Cone of Uncertainty for Electricity Costs

3.2.4 Carbon Tax

A carbon tax is implemented in the model as an amalgamation of a variety of different factors. Firstly, the UK government may implement a carbon tax on all businesses as they move towards net zero [17]. Secondly, the large food retailer has ambitions to become net zero sooner rather than later, and may therefore implement an internal carbon tax with which they assess all investments. The large food retailer may choose to go with an extra investment pool directed towards green investments, instead of an internal carbon tax. This, however, would effectively become an internal carbon tax, by making green investments when they otherwise may not be financially viable. With these different possible ways of a carbon tax being present in the investment, the distribution chosen is a uniform distribution with a large uncertainty.

3.3 Discount Rate

The large food retailer does not have internal discount rates used for many of the technologies. A uniform distribution centred at a 9% discount rate is chosen to assess all viable discount rates.

3.3.1 Emission Factor

The carbon emission factor relates to the amount of CO_2 being emitted for each unit of energy produced from an energy source. The emission factor of technologies used by the food retailer are assumed constant, as there are negligible variations in the carbon content of natural gas [12]. The carbon emission factor for the UK electricity grid are taken to be uncertain. Changes in politics, technology costs, and electricity prices may cause the grid emission factor to deviate from estimates. The Updated Energy Emissions Projections estimates the grid emission factor with an uncertainty of 8.5% [18]. A uniform distribution is used with this uncertainty.

3.4 Monte Carlo Analysis

To perform Monte Carlo sensitivity analysis, a deterministic model (section 3.1) and a framework for assigning probabilities to uncertain parameters (section 3.2) are required. A set of N samples are created randomly for all k uncertain variables. The resulting N x k matrix is used as an input into the deterministic model. During sample creation, it is important to consider correlations between variables. In this paper, none of the uncertain variables are deemed to have a correlation with each other, and therefore a random sampling of each PDF is possible. Once all N samples are created and the deterministic model has run N times, a N x 4 matrix stores the N samples for the 4 KPIs being analysed in the model.

$$y = \begin{bmatrix} y_{roi,1} & y_{irr,1} & y_{pp,1} & y_{dpp,1} \\ y_{roi,2} & y_{irr,2} & y_{pp,2} & y_{dpp,2} \\ \vdots & \vdots & \vdots & \vdots \\ y_{roi,n} & y_{irr,n} & y_{pp,n} & y_{dpp,n} \end{bmatrix} \quad (1)$$

3.5 Morris Rankings

The final part of the analysis is using the Morris method as outlined by [12] to rank the uncertain parameters in order of how much they affect the KPIs. The Morris method analysis is done with r iterations on the k parameters leading to r(k+1) Monte Carlo simulations being run for this method. This method ranks the parameters by calculating a metric μ^* that quantifies the effect on the output parameter depending on the size of the step change of the input parameter. By taking the average of the r values of the absolute $|\mu^*|$, a more accurate measurement can be taken. The Morris method is only qualitative and allows for parameters to be ranked, but not for any rigorous conclusions to be made about the exact quantitative effect on the KPIs.

3.6 Method Discussion

The methods provided here are meant to be used as an initial proof of concept for the probabilistic analysis of a TSO investment for a large food retailer. The Monte Carlo uncertainty analysis and the Morris sensitivity analysis are decision-supporting techniques, and not decision-making techniques [12]. To bring decision-making into this probabilistic model, optimization under uncertainty (OU^2) can be used. Although the methods outlined in this paper are not OU^2, they are synergistic with OU^2 and allow for a starting point for risk analysis.

3.7 Case Studies

Using the model described earlier and with the analysis methods developed a few case studies had to be chosen. In this instance it was chosen that the case studies would differ in terms of the location of the store as well as the technology that could be selected.

3.7.1 Store selection

Three different locations were chosen for the case studies. First a distribution centre in the South-West of England. Second, a relatively large supermarket in the North-West of England. Third, a relatively small supermarket in the East Midlands. The stores were chosen in different areas to account for the variances in electricity cost as well as the differences in weather for the different regions in the UK, specifically the differences in irradiance data. The stores chosen also differ greatly in size in order to get a significant difference both in the store's demand, but also the available space for PVs on the roof.

3.7.2 Technology Selection

When running the TSO model at the various stores, 4 different technology scenarios were chosen. Doing this would allow for the technologies to be compared against each other and seeing how they compare not just in terms of the financial KPIs, but also the carbon reduction. Doing this would also allow for the uncertainty to be calculated for the different technologies. The four technology scenarios chosen were as follows:

- PV and/or battery
- CHP
- CHP with or without AGO
- All of the technologies above

Table 2: Distribution Centre Determinstic Results 2021

	PVBAT	CHP	CHPAGO
Technology data	Simulation 1	Simulation 2	Simulation 3
Battery Technology	-	-	-
PV technology	Poly-Si	-	-
Number of panels	5257	-	-
Capacity (kWp)	1314	-	-
Investment cost (£)	£1.37 M	-	-
CHP Technology	-	ENER-G E770	ENER-G E530M AGO 150
Investment cost (£)		£1.09 M	£1.14 M
Total carbon reduction	0.33%	98.97%	95.12%
Total costs (£)	£1.37 M	£1.09 M	£1.14 M

3.8 Key Performance Indicators

3.8.1 Return On Investment (ROI):

The return on investment is a metric used to analyse the efficiency of an investment, or to compare the efficiencies of multiple investments [19]. Equation 2 shows how to calculate the ROI. A high ROI indicates a favourable investment, where large profit can be made on a minimal investment.

$$ROI = \frac{Value\,of\,Investment - Cost\,of\,Investment}{Cost\,of\,investment} \tag{2}$$

A minimum acceptable value of 0 is taken for the ROI. Any negative value of ROI indicates the investment will lose money. Any investment portfolio with a negative ROI is therefore not a worthwhile investment for the large food retailer. Although the ROI is a useful metric in comparing investments, it is sometimes overlooked because it does not account for how soon the investment will be beneficial to the company.

3.8.2 Internal Rate of Return:

The internal rate of return is a metric used to assess the profitability of a potential investment. The IRR represents the value of discount rate that would set the net present value of an investment to 0. IRR is the annual growth rate expected from an investment. Equation 3 shows how to calculate the IRR. An IRR higher than the used discount rate of 9% indicates a good potential investment portfolio.

$$0 = \sum_{t=1}^{T} \frac{C_t}{(1+IRR)^t} - C_o \tag{3}$$

Where C_o is the initial investment, C_t is the net cash flow in period t and t is the number of periods.

3.8.3 Payback Period

The payback period of an investment is the amount of time it takes before the initial cost of an investment is earned back [20]. The payback period is an easy metric used to compare investments based on how soon they will achieve positive results for a company. Payback period is often used in industry but has some major limitations. Many good investments may have longer payback periods due to their large initial investment, but the total payback over the lifespan of the investment (the ROI), may be large. A limitation of the payback period is that it does not account for the time value of money.

3.8.4 Discounted Payback Period

The discounted payback period is similar to the payback period, but it uses the discount rate to adjust the value of future income [21]. The adjusted cash flow value for t years after the initial investment is shown in equation 4

$$Discounted\,Cash\,Flow = \frac{Cash\,Flow}{(1+Discount\,Rate)^t} \tag{4}$$

The discounted payback period is a more valuable metric in assessing the effectiveness of an investment. However, due to the potential difficulties in choosing the correct discount rate, the payback period may still be used instead.

Table 3: Distribution Centre Determinstic Results 2016

	PVBAT	CHP	CHPAGO
Technology data	Simulation 1	Simulation 2	Simulation 3
Battery Technology	Lithium-ion	-	-
Capacity (kWel)	781	-	-
Investment cost (£)	£0.316	-	-
PV technology	Poly-Si	-	-
Number of panels	8051	-	-
Capacity (kWp)	1956	-	-
Investment cost (£)	£1.31 M	-	-
CHP Technology	-	ENER-G E770	ENER-G E530M AGO 150
Investment cost (£)		£0.851 M	£0.955 M
Total carbon reduction	29.92%	99.64%	95.68%
Total costs (£)	£1.63 M	£0.851 M	£0.955 M

4 Results and Discussions

4.1 Deterministic Results

The results from the deterministic model for the distribution centre in 2021 can be seen in table 2. The general trend among the results when comparing 2016 to 2021 investments, is a decrease in the attractiveness of PV and Battery investments and an increase for CHP and CHP coupled with AGO investment portfolios. Batteries have especially become less attractive as seen by them not being chosen in any of the simulations from 2021. PVs are also less favorable now and are only chosen in simulation 1 for 2 of the selected locations. CHP or CHP with AGO have on the other-hand become much more favorable and have been chosen in every simulation for 2021. Tables 2 and 3 show the technology chosen for the the distribution centre for the first 3 scenarios, as scenario 4 gave the exact same results in 2021 as scenario 3. The tables also give an overview over he capacity for the various technologies, with the CHP capacity being given in the name of the unit and the refrigeration capacity of the AGO being the number in their name.

4.2 Distribution Centre

4.2.1 Monte Carlo Results

CHP: The Monte Carlo analysis suggests that the deterministic model may underestimate the true value of the ROI and IRR. Figure 3 highlights the deterministic value of the ROI in orange, surrounded by the PDF of the ROI obtained using the Monte Carlo uncertainty analysis for the CHP investment portfolio. When comparing 2016 to 2021, the deterministic results show a 54% increase in ROI, showing that there has been an improvement in the investment. However, the Monte Carlo analysis suggests the improvement may be even larger. The lower bound of the 95% confidence interval increased by 252%. The Monte Carlo analysis therefore shows some limitations of using only a deterministic model.

CHP AGO: The increase in ROI and IRR for CHP AGO between 2016 and 2021 investment portfolios has an identical pattern to the CHP investment at the distribution centre. Comparing the PDFs from section 8.4 and section 8.10 shows the entire distribution has shifted upwards. The 95% confidence interval has shifted upwards by 1 for ROI.

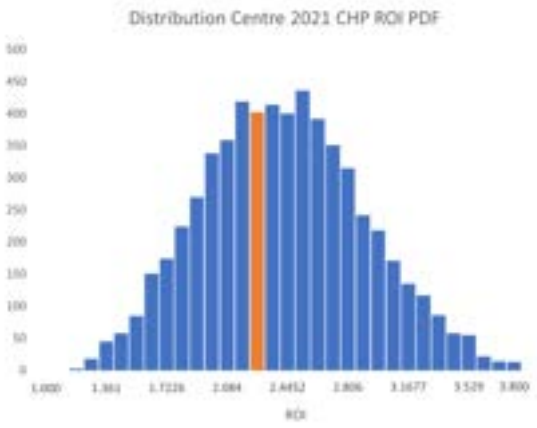

Figure 3: The Probability Distribution Function of the Return on Investment of the Distribution Centre in 2021

PVBat: The PVBat case study has a much narrower

confidence interval than CHP and CHP AGO, but a much lower ROI and IRR. The PVBat investment portfolio therefore shows the lowest amount of risk, but also the lowest benefits. This is likely due to PVBat being less dependent on volatile parameters, such as gas price. **Recommendation:** When comparing the CHP AGO investment portfolio to the CHP and PVBat investment portfolios, we see that the Monte Carlo analysis works as a decision-supporting mechanism. The deterministic model indicates that the CHP AGO has better returns on investment, and a faster discounted payback period, which is in agreement with the Monte Carlo confidence intervals. The value that Monte Carlo adds to this analysis, is the certainty with which the investment decision can be made, and knowledge of the risks associated with the investment. If more certainty is required for the investment, then the PVBat portfolio may still be chosen, even though it has a lower ROI and a longer payback period.

4.2.2 Morris Method Results

In table 4, the Morris rankings are shown for the ROI, IRR, and DPP for the CHP and PV Battery investment portfolios. Although some case studies deviated slightly from the rankings shown in table 4, most case studies have the exact same rankings and these will be discussed.

CHP and CHP AGO: The CHP and CHP AGO rankings show the CFE (Carbon factor of the UK electricity grid), gas price, and electricity cost have a relatively high impact on the ROI. These variables are inherently uncertain as they are predictions about the future. Therefore, it is difficult to reduce the uncertainty in the investments.

PVBat: Unlike the CHP rankings, The PVBat Morris rankings are topped mostly by factors that are not inherently uncertain. The maintenance cost of the solar panels is ranked highest. The reason for maintenance costs being highly impactful on the ROI is due to the investment strategy of the solar panels. After the large upfront cost that solar panels require, they work independently. The maintenance cost therefore becomes a large cost over the full lifespan of the system. While CHP units spend a lot of money on fuel, solar panels require no such continuous investment. By finding the best contractors, or buying in bulk to decrease certain costs, the large food retailer can increase the ROI by focusing on the key variables provided by the Morris ranking.

IRR and DPP: The Morris rankings for IRR and DPP are equivalent in the distribution centre and the small and large retail stores. The IRR rankings are discussed in section 4.3.2, the DPP rankings are discussed in section 4.4.2.

4.3 Large Retail Store

4.3.1 Monte Carlo Results

CHP: Similarly to the distribution centre, the large retail store has seen a large upwards shift of ROI and IRR between 2016 and 2021 investment portfolios.

PVBat: Unlike the distribution centre, where the PVBat investment portfolio became less attractive when comparing 2016 to 2021, the model has determined that the large retail store has no profitable PVBat investment available in 2021, while it was profitable in 2016. The likely cause of this is the increase in electricity prices between these years. Even with a large battery, it is unlikely that the PVBat system will be able to power the large store 24/7 due to intermittency issues. This means electricity must still be bought from the grid. In 2016 this was not a problem, but due to the increases in price the extra energy that must be bought is now more expensive.

Other: The deterministic model has determined that all other case studies are either identical to the CHP investment, or there is no investment at all. The Monte Carlo results are therefore equal to the Monte Carlo CHP results.

Figure 4: The Probability Distribution Function of the Return on Investment of the Small Store in 2021

Recommendation: As with the distribution centre, the Monte Carlo analysis works as a decision-supporting mechanism. The deterministic model provides the CHP investment portfolio as the optimal solution. The Monte

Table 4: Morris Rankings

	ROI		IRR		DPP	
Rank	CHP	PVBat	CHP	PVBat	CHP	PVBat
1	Discount Rate	Maintenance	CFE	Maintenance	Discount Rate	Discount Rate
2	CFE	Discount Rate	Gas Price	PV Inverter	Gas Price	Maintenance
3	Gas Price	PV Inverter	E Cost	PV BOS	E Cost	CAPEX
4	E Cost	PV BOS	E Price	CAPEX	Maintenance	PV Inverter
5	E Price	CAPEX	Carbon Tax	CFE	CAPEX	PV BOS
6	Carbon Tax	CFE	Maintenance	E Cost		E Cost
7	Maintenance	E Cost	CAPEX	E Price		
8	CAPEX	E Price		Carbon Tax		
		Carbon Tax				

Carlo analysis indicates that within the 95% confidence intervals the CHP investment is the most likely to have good returns for the large food retailer.

4.3.2 Morris Method Results

The Morris rankings for the ROI of the large retail store are equivalent to distribution centre in section 4.2.2.

The top variables of the Morris ranking for IRR can be seen in table 4. The main difference between the ROI and IRR rankings is the lack of the discount rate as a variable. This is because the discount rate is not a variable in the calculation for IRR. As with the ROI, the uncertainty in the IRR can be reduced by focusing on reducing the uncertainty of the top variables in the Morris rankings.

4.4 Small Retail Store

4.4.1 Monte Carlo Results

CHP:
Due to the large uncertainties provided by the uncertain variables noted in the Morris rankings for ROI, the 95% confidence interval for the ROI at the small retail store is very wide. Figure 4 shows the PDF of the investment portfolio. Highlighted in red are the possible outcomes with a negative return on investment. With a 5.9% chance of not breaking even, the large uncertainties mean the investment is much less attractive than the determinstic model makes it out to be. This is an increase in the investment option compared to 2016, where the deterministic model found no profitable investment portfolio for the CHP unit.

CHP AGO: The deterministic model indicates that there is no CHP AGO investment portfolio that is better than using just a CHP unit.

PVBat: The deterministic model in 2021 indicates a low ROI of 0.218 as can be seen in section 8.7. This decrease from 2016, where the ROI was 0.291, again indicates the fall to obscurity of PVBat. However, the 95% confidence interval is much more narrow than for the CHP investment, allowing for more certainty in the investment.

Recommendation: Unlike for the large store and the distribution centre, the Monte Carlo analysis acts a decision-making tool for the small retail store. The deterministic model indicates that a CHP investment will lead to larger gains for the food retailer. However, the uncertainty analysis indicates that there is a 5.9% chance of negative returns. The PVBat investment may have a lower expected return, but a higher chance of bringing positive returns.

4.4.2 Morris Method Results

The ROI and IRR rankings for the small retail store are similar to those in the distribution centre and large store and are discussed in section 4.2.2 and 4.3.2 respectively.

The discounted payback period Morris rankings can be seen in table 4. The discount rate is ranked highest for all investment types. To reduce uncertainty in the investment, the large food retailer is incentivised to analyse the technologies used and determine an accurate discount rate for their investment.

5 Conclusions

5.1 Monte Carlo

The Monte Carlo sensitivity analysis has been shown to be an extra decision-supporting mechanism that can aid the food retailer in the choosing of carbon reduction investments. For the small retail store, the analysis acts

as a decision-making mechanism, where the uncertainty in the deterministic investment portfolio makes the investment too high risk to be worth the slight possible increases in return on investment and internal rate of return.

5.2 Morris Method

The Morris method analysis may drive value creation for the retail store when actively paired with uncertainty characterisation. The higher on the list in the rankings, the more time and energy should be spent on decreasing the uncertainty of a parameter, or actively affecting the value of said parameter, such as for the maintenance costs.

6 Outlook

Further work can be done to improve the model and make it more accurate. Results from the Morris method indicate the most uncertain parameters and more time should be spent accurately forecasting these parameters. Additionally, the technology library can be either expanded or altered as new technologies come to the fore, and other technologies replaced if it is found that they are never chosen. Further work regarding the uncertainty analysis should also be done, such as implementing the Sobol method, which is a type of global sensitivity analysis. In addition to these changes the model is set up to be used for any selected store, not just the three chosen in this paper. The model can, as previously mentioned, be used for future studies, by just updating the necessary parameters.

7 Acknowledgments

Special thanks to Professor Nilay Shah and Dr. Salvador Acha for support and guidance in this research project. Thanks to Max Bird and Matthew Hart for technical help and supplying pricing forecasts, as well as all those who have previously helped in creating the optimisation model.

References

[1] (2020). "Ensure access to affordable, reliable, sustainable and modern energy," (visited on 12/21/2020).

[2] S. Acha, A. Mariaud, N. Shah, and C. N. Markides, "Optimal design and operation of distributed low-carbon energy technologies in commercial buildings," *Energy*, vol. 142, pp. 578–591, 2018, ISSN: 0360-5442.

[3] K. Amasyali and N. M. El-Gohary, "A review of data-driven building energy consumption prediction studies," *Renewable and Sustainable Energy Reviews*, vol. 81, pp. 1192–1205, 2018, ISSN: 1364-0321.

[4] A.-T. Nguyen, S. Reiter, and P. Rigo, "A review on simulation-based optimization methods applied to building performance analysis," *Applied Energy*, vol. 113, pp. 1043–1058, 2014, ISSN: 0306-2619.

[5] P. Ghadimi, S. Kara, and B. Kornfeld, "The optimal selection of on-site chp systems through integrated sizing and operational strategy," *Applied Energy*, vol. 126, pp. 38–46, 2014, ISSN: 0306-2619.

[6] H. Cho, P. J. Mago, R. Luck, and L. M. Chamra, "Evaluation of cchp systems performance based on operational cost, primary energy consumption, and carbon dioxide emission by utilizing an optimal operation scheme," *Applied Energy*, vol. 86, no. 12, pp. 2540–2549, 2009, ISSN: 0306-2619.

[7] C. N. Markides, "The role of pumped and waste heat technologies in a high-efficiency sustainable energy future for the uk," *Applied Thermal Engineering*, pp. 1–42, 12.

[8] W. El-Khattam, Y. G. Hegazy, and M. M. A. Salama, "An integrated distributed generation optimization model for distribution system planning," *IEEE Transactions on Power Systems*, vol. 20, no. 2, pp. 1158–1165, 2005. DOI: 10.1109/TPWRS.2005.846114.

[9] P. Mancarella, "Mes (multi-energy systems): An overview of concepts and evaluation models," *Energy*, vol. 65, pp. 1–17, 2014, ISSN: 0360-5442.

[10] H. Ren, W. Gao, and Y. Ruan, "Optimal sizing for residential chp system," *Applied Thermal Engineering*, vol. 28, no. 5, pp. 514–523, 2008, ISSN: 1359-4311.

[11] A. Malheiro, P. M. Castro, R. M. Lima, and A. Estanqueiro, "Integrated sizing and scheduling of wind/pv/diesel/battery isolated systems," *Renewable Energy*, vol. 83, pp. 646–657, 2015, ISSN: 0960-1481.

[12] G. Mavromatidis, K. Orehounig, and J. Carmeliet, "Uncertainty and global sensitivity analysis for the optimal design of distributed energy systems," *Applied Energy*, vol. 214, pp. 219–238, 2018, ISSN: 0306-2619.

[13] S. Burhenne, O. Tsvetkova, D. Jacob, G. P. Henze, and A. Wagner, "Uncertainty quantification for combined building performance and cost-benefit analyses," *Building and Environment*, vol. 62, pp. 143–154, 2013, ISSN: 0360-1323.

[14] N. Sönnichsen. (2020). "Projected wholesale price of gas in the united kingdom (uk) from 2019 to 2040," (visited on 12/21/2020).

[15] S. R. Department. (2016). "Uk: Projected prices of electricity 2020 to 2050," (visited on 12/21/2020).

[16] G. Giannakoudis, A. I. Papadopoulos, P. Seferlis, and S. Voutetakis, "Optimum design and operation under uncertainty of power systems using renewable energy sources and hydrogen storage," *International Journal of Hydrogen Energy*, vol. 35, no. 3, pp. 872–891, 2010, ISSN: 0360-3199.

[17] G. Bell. (2020). "Rishi sunak plans carbon emissions tax to help rebuild economy," (visited on 12/21/2020).

[18] E. Department for Business and I. Strategy. (2019). "Uk: Projected prices of electricity 2020 to 2050," (visited on 12/21/2020).

[19] J. Fernando. (2020). "Return on investment (roi)," (visited on 12/21/2020).

[20] J. Kagan. (2020). "Payback period," (visited on 12/21/2020).

[21] W. Kenton. (2020). "Discounted payback period," (visited on 12/21/2020).

Computational Modelling and Experimental Characterisation of the Fabrication of Tuneable Photonic Crystal pH Sensors

Rebecca L. Clancy[1], Andreas T. D. Richardson[1]

Imperial College London, Department of Chemical Engineering, South Kensington Campus, SW7 2AZ, U.K.

ARTICLE INFO

Keywords:
holographic pH sensor
photonic crystal
hologram
tuneable
finite-difference time-domain (FDTD)
computational electromagnetics

Abstract

H^+ (pH) sensitive, nanoparticle free holographic sensors were fabricated using a frequency tripled Q-smart 850 pulsed Nd:YAG laser of wavelength 355 nm and energy setting 100 mJ, to record holograms in the form of photonic crystals into polymeric hydrogel films. Films were fabricated with varying hydrogel composition, hydrogel thickness, number of laser pulses, grating geometry and recording tilt angle. Spectral responses and diffraction efficiencies were measured to determine sensor performance and tuneability. Spectrophotometric measurements illustrated shifts in diffraction peak wavelength in response to analytes with varying pH values from 3 to 9. Factors affecting sensor tuneability were found to be refractive index (as crosslinker density) and hydrogel thickness. 2D finite-difference time-domain simulations implemented in MATLAB of sensor writing and reading were used to compare experimental observations with theory, highlighting areas of ideal and non-ideal behaviour. Our findings may be used in the design and fabrication of reliable, sensitive pH sensors tailored to a variety of applications.

1. Introduction

Photonic crystals have a multitude of applications in physical, biological and chemical sensors used in pharmaceutical bioassays, medical diagnostics and food and water quality control [1]. The crystals can be tuned to manipulate light propagation through a medium [2], responding to chemical and physical stimuli.

The rise of the 'quantified self' movement [3] has seen opportunities for pH sensors to be used in wearable devices with uses such as monitoring wound healing [4, 5]. The development of an economic and mass producible method for non-invasive sensing will allow for easier treatment of patients [1]. The cheaper mass producibility of these holographic sensors over other optical sensors makes them desirable in point-of-care testing. However, commercial application of these sensors is still limited by issues with scalability and cost, and further research into their production and behaviour is required to produce reliable and user-friendly devices [6].

The present study concerns the fabrication of pH sensors in the form of H^+ sensitive holograms fabricated by laser-initiated polymerisation in a functionalised hydrogel medium. These sensors are amenable to miniaturisation, making them suitable for biomedical diagnostic applications such as targeted cancer and skin lesion treatment [7].

2. Background

Common methods for the fabrication of thin film photonic crystals include chemical vapour deposition [8] and molecular beam epitaxy [9], whilst another known method consists of using silver nanoparticles as the grating [10]. However, these methods are costly, slow and positionally inaccurate, making them unsuitable for scale up [2].

In contrast, laser induced photochemical patterning offers a cheaper, more rapid and scalable method to fabricate holographic sensors. It is used to form periodic, multi layered fringes of polymer in a hydrogel, an easily fabricated, miniaturisable medium, with tuneable physical characteristics. The hydrogel is made by free radical polymerisation of a polymer P1 consisting of a pH sensitive moiety, and the fringed grating is made by polymerisation of polymers P2 into P1.

On the exposure of P1 to incoherent UV light, free radical polymerisation occurs, forming a hydrophilic hydrogel structure capable of reversibly swelling in an aqueous solution. After addition of P2, the saturated hydrogel is irradiated using a Nd:YAG laser, as shown in fig. 1b. The transmitted beam is reflected back through the gel by a mirror, whereupon the interference of the incident and reflected beams leads to formation of a standing wave. Selective photo-polymerisation occurs at the antinodes, forming a fringe of P1 + P2 grating throughout the gel, illustrated in fig. 1a, of spacing $\lambda/2$. Unpolymerised P2 monomer is washed out, leaving layers of polymer with alternating refractivities which act as a Bragg mirror.

The operation of the sensor is based on the ability of the hydrogel to reversibly change its thickness by absorbing a fluid through a Donnan osmotic pressure increase, illustrated in fig. 2. The grating spacing changes as the fringes of P1 swell, whereas the rigidly polymerised P1 + P2 bands remain unchanged. This alters the periodicity, shifting the narrow band diffraction peak to longer wavelengths. This process is governed by Bragg's law:

$$n\lambda = 2d\sin\theta \tag{1}$$

where d is the fringe spacing, θ the incident white light

ORCID(s): 0000-0002-5466-7279 (A.T.D. Richardson)
[1] Authors contributed equally.

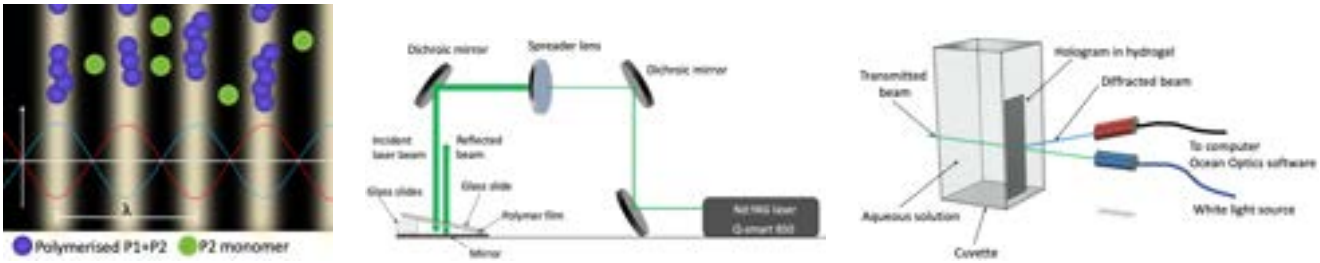

(a) Photopolymerisation occurring at the nodes of the standing wave formed by the interference of the incident and reflected wave.

(b) Overview of laser and lens setup, the hydrogel side placed facing down.

(c) Hydrogel submerged in aqueous solution in a cuvette, irradiated with white light.

Figure 1: Schematics of the hologram formation and the experimental setup.

angle, n the Bragg order and λ the diffracted wavelength.

In the case of the present pH sensors, amine groups in the photonic crystals are protonated at decreasing analyte pH values and deprotonated at increasing pH values, leading to the reversible swelling and deswelling of the hydrogel. To document this behaviour, a spectrophotometer and camera can be used to record the diffraction of a beam of white light as illustrated in fig. 1c.

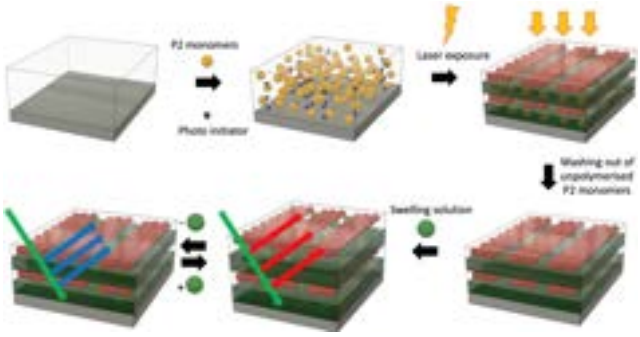

Figure 2: Formation of the hologram on laser exposure and reversible swelling of the gel upon a change in pH of the surrounding aqueous solution.

Previous work includes the study of the fabrication of photonic crystals via silver halide chemistry forming a silver nanoparticle grating. Simulations have been used to investigate size and nanoparticle (NP) distribution in the hydrogel [2, 11]. Increasing NP spacing causes a redshift in the narrow band diffraction peak and a decrease in diffraction efficiency. Increasing NP size yields stronger diffraction intensities but also a broad bandwidth and a redshift [2]. Optical measurements such as reflection spectra have been measured, and the effects of varying pH levels tested, confirming the predictions of the simulations. These conclusions provide an understanding of the structural fringe requirements to allow for a reliable and tuneable response. pH sensing range and sensor sensitivity can be altered by varying the concentration and nature of the ionisable comonomer in the polymer matrix [2].

Other works include the studying of the effects of factors such as ionic strength, temperature and hydrogel composition on gel swelling, response time and reversibility [12]. Low temperature sensitivity was found over a range of 20 °C to 45 °C. The swelling state of the film during exposure controls the spectral replay bandwidth, allowing for tuneability of the wavelengths across which the sensor operates. The ability of the sensors to measure pH levels in vivo was demonstrated in fermenting milk, showing reversibility of these sensors without any evidence of hysteresis [12].

This paper details a computational and experimental investigation of the behaviour of tuneable holographic pH sensors. In contrast to the majority of previous works, we utilise laser induced photochemical pattering for the fabrication of the photonic crystals. Sensor performance was characterised subject to varying conditions including polymer composition, film thickness and laser technique, all factors that have yet to be documented in the literature. To validate the experimental sensor performance, computational electromagnetics simulations of the optical behaviour and tuneability of the holographic sensor are performed.

2.1. Modelling

Computational modelling allows for performance comparisons to be drawn between a physical sensor and a digital counterpart. Models can also be used to make predictions regarding sensor performance under diverse conditions with greater ease and rapidity than repeated physical experimentation. The robustness of these predictions will depend on the strength of agreement between the computational model and the experimental results, as well as the range of applicability of parameters used and assumptions made during the modelling process.

Various aspects of both the fabrication and eventual utilisation of the holographic sensor may be modelled in order to better understand and characterise its performance. In the hologram recording step of the fabrication process, the interference between the incident and reflected laser beams may be modelled to determine the

location of the points of constructive and destructive interference within the electromagnetic field. These points control the photopolymerisation process occurring within the supporting hydrogel matrix through the formation of free radicals which initiate and propagate the polymerisation reactions. The normalised light intensity at each point in the hydrogel geometry can be considered a proxy for the degree of polymerisation, and used to determine the local refractive index.

A more precise representation of the polymer geometry may be derived from models of the photopolymerisation process that consider factors beyond light intensity. A simple approach employing reaction-diffusion kinetics solved in MATLAB has been demonstrated for a UV-curable resin [13]; the addition of thermomechanical modelling to the chemical kinetics permits the characterisation of thermal expansion and chemical shrinkage of the cured polymer [14]. A further enhancement of model quality is to consider the inherent stochasticity of the photopolymerisation approach [15]. Further validation studies are required to determine which of these diverse factors and phenomena contribute meaningfully to the resultant photopolymer geometry; it is important to balance the accuracy and complexity of a model with its practical usability as embodied by its computational cost.

The critical function in the sensor operation is the interaction of light with the Bragg stack. For a nanoparticle-based grating, finite-element modelling of the combined hydrogel has been demonstrated to illuminate the wave propagation characteristics, as well as determine the effect of varying parameters such as particle size, number of stacks, lattice spacing and defects [2, 11, 16]. Jiang et al. [17] further demonstrate a model of light interaction with a polymer-based lattice, using a finite-difference time-domain (FDTD) method implemented in MATLAB.

Finally, the crucial sensing property of the hydrogel matrix, embodied by its expansion and contraction on the reversible binding and dissociation of glucose, may also be modelled. Hydrogel swelling is reported to be sensitive to temperature, glucose, pH, ionic strength, light and electric fields [18] and thus a complex model incorporating these factors would seem to be required. However, under certain simplifying assumptions the overriding factor in swelling is the osmotic pressure [19]. Jiang et al. [17] employ a simplified approach by which the modelled geometry is uniformly scaled and the resultant diffraction behaviour observed qualitatively for a series of simulated light pulses.

Broadly, the eventual development of a general model for sensor performance under a diverse range of conditions will enable a rapid prototyping and development process and permit the selection of optimal parameters for a broad range of use cases. In the present work we shall restrict our computational analyses to the light-interaction processes of sensor writing and reading, basing our investigations on the established MATLAB implementation by Jiang et al. [17].

2.1.1. The finite-difference time-domain method

FDTD is one of a range of methods applicable to computational electrodynamics problems; importantly however, it is considered particularly simple, whilst still maintaining generality and robustness [20]. The method described by Yee [21] solves Maxwell's equations by discretising the electrical and magnetic fields in space and time. The fields are additionally offset from each other in space and time, permitting the use of central-difference approximations to the derivatives. 'Update' equations are formulated which allow the evaluation of the electric and magnetic fields at the next time step on the basis of the previous. The combination of these processes results in an iterative method whereby the electric and magnetic fields are successively evaluated until the desired duration is reached [22].

Maxwell's equations consist of Ampère's and Faraday's laws, which relate the magnetic and electrical fields, as well as Gauss's laws for the electric and magnetic fields, as follows [20–23]

$$\nabla \times \mathbf{H} = \mathbf{J} + \frac{\partial \mathbf{D}}{\partial t} \tag{2}$$

$$\nabla \times \mathbf{E} = -\frac{\partial \mathbf{B}}{\partial t} \tag{3}$$

$$\nabla \cdot \mathbf{D} = \rho_v \tag{4}$$

$$\nabla \cdot \mathbf{B} = 0 \tag{5}$$

$$\mathbf{D} = \epsilon \mathbf{E} \tag{6}$$

$$\mathbf{B} = \mu \mathbf{H} \tag{7}$$

where $\mathbf{H}$ is the magnetic field strength [$\mathrm{A\,m^{-1}}$], $\mathbf{J}$ is the current density [$\mathrm{A\,m^{-2}}$], $\mathbf{D}$ is the electric flux density [$\mathrm{C\,m^{-2}}$], $\mathbf{E}$ is the electric field, $\mathbf{B}$ is the magnetic flux density, ρ_v is the electric charge density [$\mathrm{C\,m^{-3}}$], ϵ is the permittivity, and μ is the permeability.

3. Materials and Methods

3.1. Equipment

Buffer and monomer solution preparation: A 100 ml measuring cylinder, a PX323/E Ohaus Pioneer Precision balance, a spatula, weighing boats, a Mettler Toledo LE438 pH sensor, a Fisherbrand Isotemp advanced stirrer, and Simax reagent glass bottles were used, purchased from MilliporeSigma.

Refractive index measurements: Forceps, Kern ORT 1RS Abbe Analogue Refractometer and a Stairville LED Gooseneck Lamp were used.

Diffraction efficiency measurements: Protective goggles, 5 mW 405 nm laser pointer and a Standard Photodiode Power Sensor (200 nm to 1100 nm, 50 mW) were used.

Hologram fabrication: Dichroic mirrors, an uncoated plano-concave lens, an analytikjena UVP Crosslinker, a Revlon handheld hairdryer, a frequency tripled Q-smart 850 pulsed Nd:YAG laser of wavelength 355 nm and energy 100 mJ, microscope slides, protective goggles and a single side polyester coated aluminium sheet were used. The output energy of the laser was maximised by using a delay time of 10 μs.

Optical characterisation: Plastic cuvettes, a glass cutter, and Ocean Optics Flame spectrometer in conjunction with Ocean Optics software on a computer, a Tungsten halogen light source, bifurcated optical fibres, an articulating base stage and a collimating lens were used.

Computational simulations: Code executed on the Research Computing Service and Department of Chemical Engineering Linux Cluster, both at Imperial College London. MATLAB R2020b, with Image Processing, Curve Fitting, Symbolic Math and Parallel Computing Toolboxes was used to develop code, based on work by Jiang et al. [17] implementing the FDTD method for TM^z polarisation [22].

3.2. Material

2-(dimethylamino)ethyl methacrylate (DMAEM), 3-(trimethoxysilyl) propyl methacrylate, acetone, 2-hydroxyethyl methacrylate (HEMA), ethylene glycol dimethacrylate (EGDMA), dimethyl sulfoxide (DMSO), methylene bisacrylamide (MBA), 2-hydroxy-2-methylpropiophenone (HMPP), ethylene glycol dimethacrylate (EGDMA), ethylene glycol, tris(hydroxymethyl)aminomethane (tris), methanol, acrylamide, glycerol 1,3-diglycerolate diacrylate (GDD), potassium chloride (KCl), hydrochloric acid (HCl), sodium hydroxide (NaOH), monochloroacetic acid, deionised (DI) water, ethanol, propan-2-ol, purchased from MilliporeSigma.

3.3. Methods

Silanisation of slides: To functionalise glass microscope slides, allowing for improved adherence of the polymer layer to the slide by covalent bond formation in a siloxane network (-Si-O-Si-) [24], clean slides were submerged in a silane solution of 3-(trimethoxysilyl) propylmethacrylate and acetone in a volume ratio of 1:50 at room temperature for 24 hours, rinsed with ethanol and excess solution wiped off.

Buffer solution preparation: Calculated amounts of KCl and monochloroacetic acid (for pH 3), and tris (for pH 7.06 through 9), were weighed out and dissolved in 80 ml of DI. They were then titrated with NaOH and HCl until they reached the desired pH values and made up to 100 ml.

Monomer solution preparation: P2 solution was made up of 8.3 % w/v acrylamide, 2 % v/v MBA/DMSO, 4.1 % v/v ethylene glycol, 31 % v/v GDD/MeOH, 0.8 % v/v triethanolamine, 20.7 % v/v DI, 0.2 % v/v HMPP. P1 solution consisted of HMPP, HEMA, EGDMA, DMAEM and propan-2-ol, in varying ratios determined by the EGDMA concentration selected.

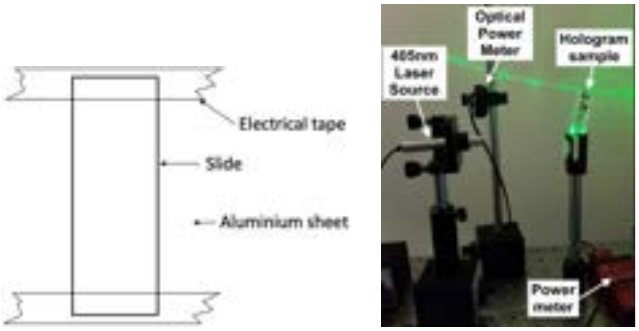

(a) Slide set down on parallel strips of electrical tape.

(b) Diffraction efficiency measurement.

Figure 3: Experimental setup details.

Polymerisation: 150 μl of P1 monomer solution was pipetted in a line onto the aluminium side of the polyester coated aluminium sheet, a silanised glass slide slowly lowered onto the solution droplet and exposed to UV light for 30 minutes at room temperature.

Variation of Hydrogel Thickness: Layers of electrical tape adhered to the aluminium sheet in parallel strips (see fig. 3a), were used to produce film thicknesses of 0.01 mm, 0.18 mm and 0.36 mm for 0, 1 and 2 layers of tape respectively.

Refractive index measurements: 150 μl of P1 solution was pipetted onto a non silanised glass slide, spread evenly and exposed to UV light for 30 minutes. The hydrogel was lifted off the glass by immersion in ethanol solution (50 vol% ethanol) for 30 minutes and placed in a refractometer for measurement.

Hologram fabrication: Once exposed, the slide was washed in warm water and dried. The polymer side of the slide was set on 150 μl of P2 monomer on an aluminium sheet for 10 minutes under red safe lighting, excess solution wiped off and blow dried at low heat for 2 minutes. The laser was set to 355 nm wavelength, 100 μs, and the number of pulses selected. The slide was placed on a mirror at 5° to the horizontal with the polymer side facing downwards, as seen in fig. 1b. To achieve the 5° angle, 3 glass slides were stacked up and the treated slide rested on top. Diffraction gratings were formed on laser exposure. To remove unpolymerised monomers in the grating, the slide was immersed in ethanol solution overnight.

Diffraction efficiency measurements: A slide containing a hologram was placed in the setup illustrated in fig. 3b. To avoid the zero-order diffraction beam from being diffracted directly back at the laser, the cuvette

was set at a slight angle. To achieve maximum reflection, a laser of wavelength closest to the Bragg peak for the respective grating was selected. The power of the zero (P_0) and first order (P) diffraction spots were measured and the diffraction efficiency calculated $\eta = P/P_0$.

Variation of tilt angle: The number of glass slides used to elevate the film being written was adjusted (see fig. 1b). Angles of 1.7°, 5°, 8.3° and 11.7° were reached with 1, 3, 5 and 7 slides respectively

Hologram geometry variation: The protocol was followed until laser exposure. The slide was cut into a square, the laser set to one pulse and centred on the slide, the position of the slide marked. The gel was exposed to one pulse, the slide was rotated 90° and exposed to a second pulse.

Optical measurements: The slide was cut into a strip at the point of the hologram and submerged in a cuvette filled with the desired buffer solution, the polymer side pointing into the solution. On irradiation with a white light source, the reflected light was measured with a spectrophotometer connected to the Ocean View software. On addition of a buffer solution, the spectrum was allowed to equilibrate, an overlay was taken, the buffer solution replaced with that of a different pH, the cuvette flushed three times with the new solution. The changing spectrum was allowed to equilibrate, and an overlay taken. Repeats were taken to ensure reliable results, a mean spectrum was calculated, and the standard deviation used to plot error bars.

The slide was removed and a white light spectrum captured for normalisation. The spectrophotometer used reached maximum intensity at certain points in the spectrum resulting in the saturation observed in fig. 5c. For the purpose of data normalisation this had no impact since the spectrophotometer was adjusted such that the hologram peaks occurred in the non-saturated region. We suggest future researchers use a spectrophotometer with a higher intensity limit.

A bifurcated cable and smartphone camera were used to record images of the colour of the replay wavelength observed (see fig. 5a). However, interference from the white light spectrum caused some of these to appear white, making it difficult to use as a basis for conclusions.

The values of the variables tested giving clear responses were determined and the Bragg peaks for this hologram were measured in the pH 7-9 range at increments of 0.25 to obtain the calibration curve shown in fig. 5b.

Data normalisation: Raw data were plotted as intensity vs. wavelength. Individual spectra were divided by the white light spectrum to give normalised values. Only spectra indicating clear trends have been included in this report.

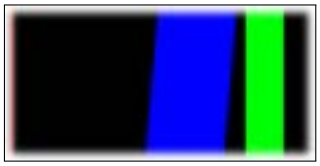

(a) Film writing setup schematic, showing: the planar source in red, film in blue, mirror in green, and PML boundary in white.

(b) Film reading: as in (a), with curved source. A representative recorded exposure intensity is overlaid on the film in white.

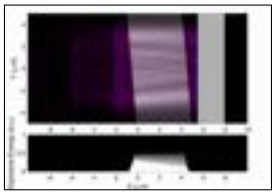

(c) Screenshot of grid during film writing.

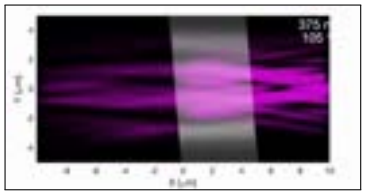

(d) Screenshot of grid during film reading, showing diffraction of pulse.

Figure 4: Details of simulation setups.

Film writing simulation: Objects including a planar source, mirror, perfectly-matched layer (PML) boundary [22] and film tilted to 5° (matching the experimental setup) were created in a 500 by 1000 pixel grid at 20 nm resolution, representing a total size of 10 μm by 20 μm, as illustrated in fig. 4a. The permittivity $\varepsilon = \varepsilon_0 \cdot \varepsilon_r$ was defined at each point on the basis of the refractive index n of each material: $n = \sqrt{\varepsilon_r \cdot \mu_r}$. The background was set to air, and assuming $\mu_r \approx 1$, permeability $\mu = \mu_0 \cdot \mu_r$ was constant throughout. A 355 nm pulse was defined at the source as a cosine function in the $\mathbf{J}_z$ field and allowed to traverse the medium and film, before being reflected at the mirror. The pulse duration and mirror position were set to cause the incident and diffracted waves to coincide within the film, where they interfered constructively and destructively. At each time step, the intensity of the electric field E_z was measured and summed, representing the exposure of the monomer to light and hence the degree of polymerisation. The final matrix of exposure intensity values was recorded as an image and passed to the film reading simulation.

Film reading simulation: A similar series of objects as in the film writing simulation was loaded (see fig. 4b). Notably, the refractive index (and hence, permittivity) at each point in the film was defined by interpolating between the values for the P1 and P2 solutions according to the relative intensity recorded at each point in the writing simulation. The background was set to water, to mirror the use of the physical sensor in aqueous solution, whilst the source was switched to a curved shape to focus the incoming beam on the centre of the film. A series of pulses, of wavelengths between 350 nm to 600 nm, were generated, and the intensity of the incident and diffracted beams was measured to calculate the diffraction efficiency $\eta = P/P_0$. From these data the spectral response of a given film was plotted, a first-

order Gaussian function was fitted, and the values of the peak wavelength μ and standard deviation σ were recovered.

4. Results and Discussion

4.1. Material selection

HEMA was chosen as the polymer backbone material due to its hydrophilic nature, allowing for substantial expansion in the buffer solution [25], as well as for its non-toxicity. Although other substances such as polyacrylamide are more hydrophilic at similar crosslinker densities, the grating formed would only adhere weakly on the slide and allow for less expansion.

The role of HMPP as the photoinitiator is to initiate the free radical reaction. While previous works picked DMPA for photopolymerisation, HMPP has been found to be more hydrophilic with a higher absorbance at the construction laser wavelength [26], giving it a higher mobility in the hydrogel during P2 polymerisation.

EGDMA was chosen as the crosslinker in P1. Whilst previous works have used GDM, EGDMA provided more reproducible peaks and faster peak movement. This is hypothesised to be because the additional alcohol group on GDM could allow for hydrogen bonding when the amine deprotonates at high pH values, causing interfering effects.

DMSO was chosen as the solvent in the P2 monomer solution due to its ability to act as a porogen within the P1 matrix, allowing for more P2 monomers to enter. It is also easily washed off following polymerisation.

A few factors play a role in determining the amount of crosslinker (EGDMA) used in the P1 and P2 monomer solutions. Crosslinker concentration directly controls the extent of polymerisation in the matrix, a determinant factor in the changing of the refractive index of the sensor upon swelling as well as the extent of film swelling. Increasing the difference between the refractive index of P1 and the P1 + P2 polymer leads to a brighter hologram.

MBA was chosen as the crosslinker in P2 and acrylamide as the polymer backbone, as they have different refractive indices to their P1 counterparts (EGDMA and HEMA respectively). Additionally, as P1 is more hydrophobic than P2, employing the more hydrophilic crosslinker MBA allows for more uptake of P2 monomers into the P1 matrix leading to a larger area of polymerisation. Propanol facilitates an increased P2 monomer uptake due to its high mobility in water and its high volatility allows it to be easily evaporated before laser exposure.

4.2. pH sensitive hologram fabrication

As the recording wavelength is outside of the visible range, a drying step is employed in the fabrication of the fringes. Recording in a shrunken state ensures that the replay wavelength will move towards the visible region on swelling of the film in an aqueous solution [27].

The initial spectral responses were tested at pH 3 and pH 9, mirroring previous work [12], which found that similar sensors exhibit a sigmoid shaped relationship between Bragg peak wavelength and pH, with a linear region approximately between pH 5-8 [12]. Considering the novelty of these sensors, this range was chosen to gain an understanding of their behaviour across a broad pH range, also yielding a Bragg shift large enough to easily detect. Whereas in point of care settings, spectrophotometers or mobile phone cameras can be employed to detect small wavelength shifts, in the present study a larger shift was desired to more easily determine trends.

The 7-9 pH range was chosen as it is representative of body conditions, and has been found to be the region in which the sensor behaves linearly [2]. This range also prevents other groups in the monomer solution from interfering with the protonation of DMAEM ($pK_a = 8.44$ [28]). To avoid different pH values giving the same replay wavelength, the sensors should be tuned to the linear range.

Figures 5a and 5b show the spectral response and the tuneable wavelength shift as a function of pH respectively. The former illustrates the sensitivity of the hologram, with an approximate wavelength shift of 5.5 nm per pH unit (representing a change of grating spacing of 2.25 nm per pH unit). A Henderson–Hasselbalch curve

$$\lambda = \lambda_0 + \frac{\Delta\lambda}{10^{(\mathrm{pH}-\mathrm{p}K_a)}+1} \tag{8}$$

was fitted [29], with $R^2 = 0.997$. The sensor was found to reliably detect even minor pH changes within the pH 7-9 range, with the apparent pK_a lying at 7.90 (95% CI: 7.78 to 8.03).

4.3. Incident light spectrum

The intensity of the incident white light spectrum in fig. 5c climbs steeply from the UV to the blue region, translating directly to the intensities of the replay wavelengths. This is an effect of the incident white light and is independent of the hologram tuneability so data is normalised before analysis.

4.4. Effects of crosslinker density

Figure 7a shows the positive relationship between film refractive index and crosslinker concentration. A fit following the form of the Lorentz–Lorenz relation [30]

$$R_M = \frac{n^2-1}{n^2+2}\frac{M_w}{\rho} \tag{9}$$

relating molar refractivity R_M to refractive index, molecular weight M_w and density was performed, with $R^2 = 0.978$. I hIncreased crosslinker density however leads to a trade-off between hologram brightness and spectral clarity as seen in fig. 6a. If applied in a system where a spectrophotometer is used to detect wavelength changes, sharp peaks and replay wavelength are

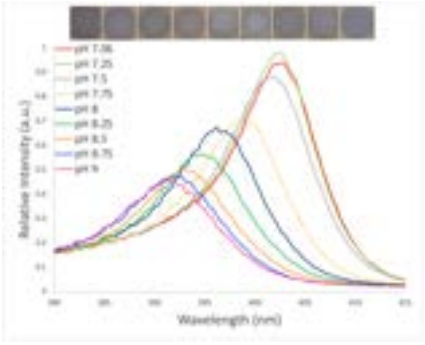

(a) Processed spectral responses, indicating an approximate peak wavelength shift of 5.5 nm per pH unit; colorimetric responses above (left to right) from pH 9 to pH 7.07.

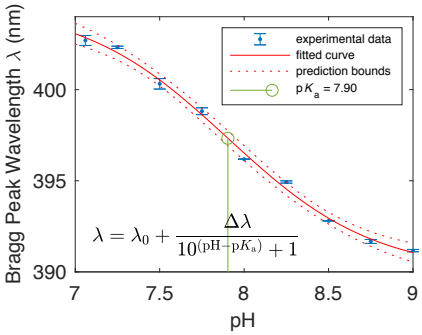

(b) Sigmoid calibration curve for Bragg peak wavelength as a function of pH, with a linear region between pH 7.5 and 8.5, showing sensitivity to small changes in pH.

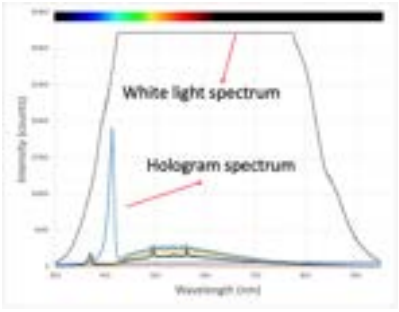

(c) Comparison between raw and white light (used for normalisation) spectra. At 470 nm the intensity is approximately eight times as intense as at 370 nm.

Figure 5: Spectral response of the sensor subject to changes in pH, showing processed data, the resultant calibration curve and details of the spectrum normalisation.

more important than a fractional increase in brightness, so the crosslinker density giving the highest refractive index is not necessarily the optimum.

Figure 6a shows the spectral response measured at pH 3 and pH 9, showing the tuneable nature of the replay wavelength as a function of crosslinker density. On a decrease in pH, the hydrogel expands due to the influx of hydrogen ions protonating the amine groups in the polymer, causing an increase in the lattice spacing of the grating and giving rise to a spectral shift.

Increasing crosslinker density resulted in slightly more intense and less sharp peaks, with 8 % giving a noisy spectrum showing peak splitting at pH 3. As density increases, the degree of swelling decreases due to increased grating rigidity. The increase in intensity is due to fact that as the difference in polymerisation strength between the strongly and weakly polymerised regions in the gel increases, the refractive index variation increases, creating a brighter hologram. The peak splitting may be caused by the non-uniform, Gaussian intensity distribution of the laser creating uneven fringes, resulting in the diffracted wavelength being non-monochromatic and giving rise to two peaks. This effect has also been observed in previous studies [31].

Conversely, at low crosslinker density of 2 %, the hydrogel cracked on polymerisation. 4 % was chosen as the concentration for the next steps, as it gave very sharp peaks, with an average peak shift of approximately 40 nm, representing a change in grating spacing of 20 nm.

4.5. Effects of film thickness

From fig. 6b it is clear that the replay wavelength is tuneable by altering hydrogel thickness, with an approximate average peak shift of 45 nm, corresponding to a change in grating spacing of 22.5 nm.

Although theory suggests that a perfectly uniform grating should produce narrower peaks at a greater number of fringes, the full widths at half maximum (FWHM) at pH 3 are 11.8 nm, 14.2 nm and 13.3 nm and at pH 9 are 8.2 nm, 12.5 nm and 9.1 nm for thicknesses of 0.01 mm, 0.18 mm and 0.36 mm respectively. This is likely caused by bulk diffusion dominating over surface diffusion in thicker films, leading to inhomogeneous swelling. These mass transfer effects also led to increased response time, which is a key parameter for sensor performance. The 0.01 mm thick film was taken for to the next stages of testing, as the sharper, thinner peaks associated with thinner films give a more distinct colorimetric response.

4.6. Effects of varying number of laser pulses

Previous works fabricated holograms using a single laser pulse in the writing stage. In this study, a trend of peak broadening was observed for increasing number of pulses (fig. 6c). This is likely due to imperfect alignment of the film between pulses, giving rise to out of phase reflection. The peak maxima show little variation, with an approximate peak shift of 30 nm (a grating spacing change of 15 nm), suggesting that replay wavelength is not tuneable as a function of number of laser pulses.

A positive correlation between number of laser pulses and diffraction efficiency was found, as illustrated in fig. 7b, which is consistent with expectations that increasing time of laser exposure increases the extent of polymerisation and thus diffraction efficiency of the grating. The contrast between the linear relationship observed at pH 3, and slightly non-linear relationship at pH 9 warrants further investigation. The range of 44 % to 49 % efficiency was higher than expected, as previous works involving similar sensors found much lower values. This promising property may be attributable to the P1 formulation.

These trends must be considered when designing a sensor: increasing the number of laser pulses results in a brighter hologram, however the trade-off against peak broadening makes it more difficult to observe colour changes with the naked eye. However, in a system

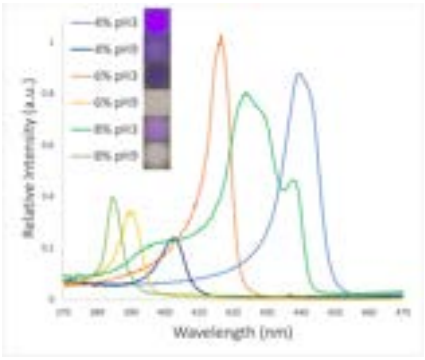

(a) varying crosslinker density: peak shift at pH 9 suggests potential for tunability.

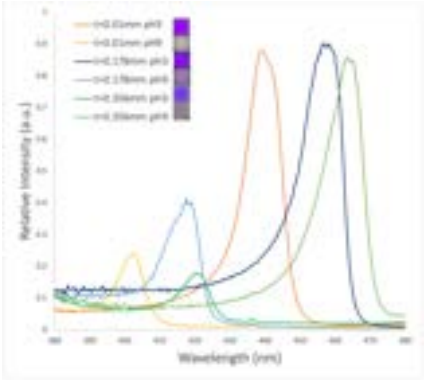

(b) varying thickness: similar peak shifts at both pH values indicate good tunability.

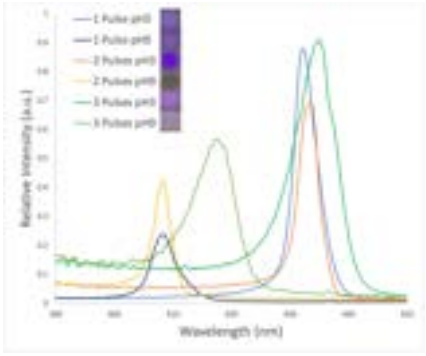

(c) varying laser pulses: minimal peak shift suggests little potential for tuning.

Figure 6: Spectral and colorimetric response at pH 3 and pH 9 of films subject to various changes in the fabrication process, illustrating the potential of these factors for tuning sensor replay wavelength.

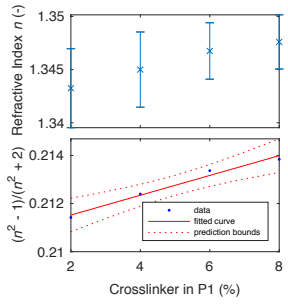

(a) refractive indices with varying crosslinker densities.

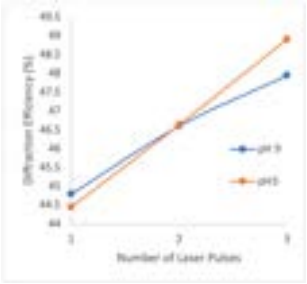

(b) diffraction efficiencies with varying number of laser pulses.

Figure 7: Refractive indices and diffraction efficiencies.

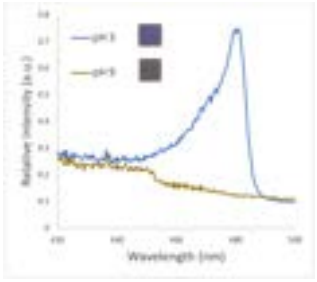

(a) varying grating geometry: a noisy spectrum with no visible peak at pH 9.

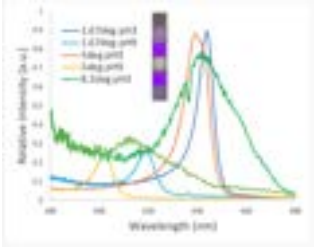

(b) varying tilt angle: no clear peak shift.

Figure 8: Spectral and colorimetric response at pH 3 and pH 9, suggesting that neither tilt angle or grating geometry play a role in replay wavelength tuneability.

where the wavelength change is detected with a spectrophotometer, brightness is a less important factor.

4.7. Effects of grating geometry

The lattice structured grating geometry did not produce a reliable hologram: the spectrum was noisy with broad peaks at pH 3, and barely visible peaks at pH 9 as seen in fig. 8a. This is attributable to the fact that this fabrication method gives rise to two competing gratings, with uneven swelling in multiple directions, highlighting the importance of uniform, distinct gratings in producing a reliable pH sensor.

4.8. Effects of varying tilt angle

There was no clear trend in the spectral response changes seen in fig. 8b when varying tilt angle, and there was insufficient evidence of tuneability. The main factor for consideration when selecting the tilt angle in hologram production is that of practicality. With increasing tilt angle, the spectrophotometer had to be angled accordingly. The largest practical angle tested was 5°. Broad and noisy peaks were observed at 8.3°, not ideal for a reliable pH sensor, and the spectrophotometer had to be set at a very steep angle, making it difficult to record the reflected light.

4.9. Simulation results

4.9.1. Grating expansion in reading

Spectral responses of a typical film, uniformly expanded between 100 % and 165 % of its original size, are presented in fig. 9a. Peak diffraction efficiencies in the range 0.35 to 0.45 were attained, comparing favourably with experimental results (e.g. fig. 3b).

A first-order Gaussian fit of the spectral response data was performed to determine the precise value of the diffraction peak μ and the standard deviation σ. A clear linear trend was observed in the value of the diffraction peak, highlighting the suitability of the grating expansion mechanism for sensing. In contrast, experimental results at varying pH (linked to expansion via the swelling process) showed a sigmoidal response (figs. 5a and 5b). This difference is attributable to saturation effects at high and low pH beyond which the physical film no longer swells or contracts. Considering the experimental shift of 5.5 nm per pH unit in the linear range together with the 226 nm peak shift observed for 65 % expansion in simulation (figs. 5a and 9a) we are

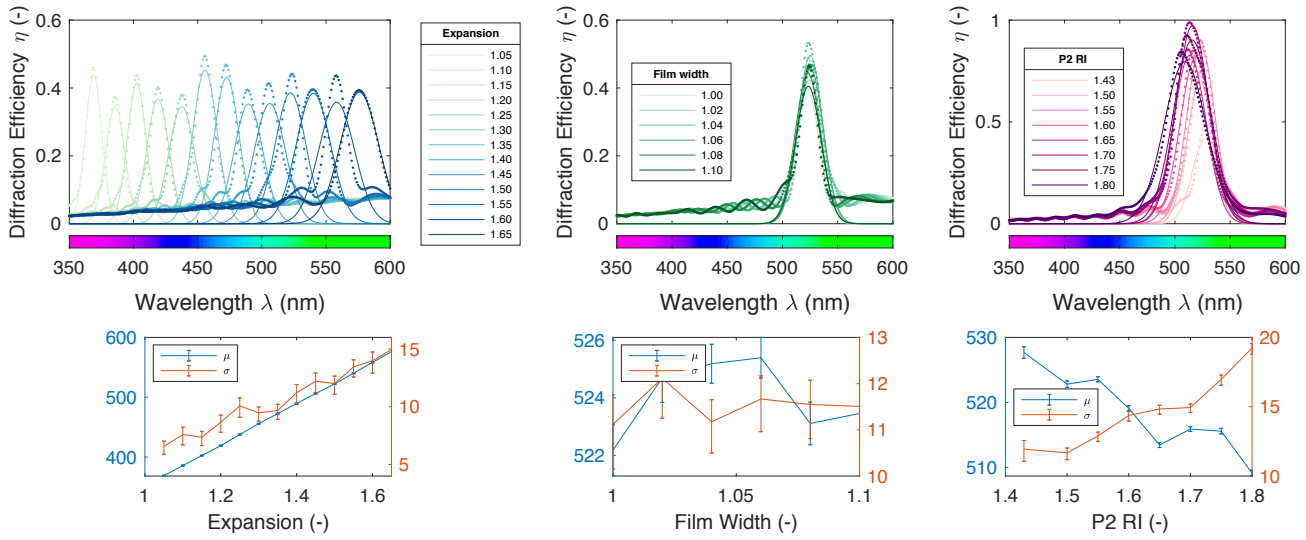

(a) varying film expansion during reading **(b)** varying relative film thickness **(c)** varying P2 refractive index

Figure 9: Diffraction efficiency spectral response plots, alongside parameters of the Gaussian fits (95% CI shown).

able to infer an approximate film expansion of 1.58 % per pH unit. This result provides a first approximation to the complex relationship between binding and hydrogel swelling.

The standard deviation of the Gaussian, corresponding to the width of the peak in the spectral response, also exhibited an overall increasing trend, though was not observed to be precisely linear. Notably, significant deviation from the Gaussian fit is observed at wavelengths far from the peak. The sinc-function form of the response curve is observed in theory for both wavelength and angular response of the Bragg grating [32], and demonstrates the closeness of the simulation to the analytical solution in theory. Although a much smoother spectral response curve is observed experimentally, multiple other factors are at play and thus it may be hidden by 'noise' due to reflection, absorption etc. The increasing baseline shown in the spectral response plot is likely due to the imperfect separation of the incident and diffracted beams during measurement of the diffraction efficiency. Thus, further investigations should be directed to refining the measurement of the individual pulses to improve the accuracy of the simulated diffraction efficiency measurement. In addition, the variation in peak height between spectra is unexpected and may be caused by numerical artefacts; a more robust measurement of diffraction efficiency may help tackle this.

4.9.2. Film thickness

A series of films of increasing relative thickness (baseline: 5 µm) were written with gratings and their spectral responses read, as shown in fig. 9b. The diffraction peaks observed remained close, with minimal change in peak width. Theory suggests that a wider film, written with a greater number of fringes, would result in stronger diffraction and hence a narrower peak, a trend contradicted in the experimental investigation, due to non-idealities unaccounted for in the simulation. However, the variation in μ and σ, though small in absolute terms, is noisy with large error bars and suggests that the small range of widths considered here (5 µm to 5.5 µm) is insufficient to elucidate a trend

Thicker films of the order of 10 µm (a reported physical film thickness [12]) were simulated, however numerical artefacts associated with the imaginary permittivity of the mirror were observed, causing the simulation to fail. In addition, to maintain a sufficiently small Δx to satisfy the Nyquist–Shannon sampling theorem [33], it was necessary to expand the simulation grid with a corresponding increase in computational cost. Further work is required to develop this investigation, and in particular should consider implications of the Courant–Friedrichs–Lewy condition and its associated number $S_c = c\Delta t/\Delta x \leq 1$, which strongly affects simulation stability [22].

4.9.3. P2 refractive index

A series of gratings were written for films with P2 RI values in the range 1.43 to 1.80 (P1 RI was kept constant at 1.37) and their spectral responses read, as shown in fig. 9c. As expected, the increased effective refractive index of the combined P1 + P2 film causes a small blueshift in the diffraction peak. This is consistent with experimental observation at pH 3 (fig. 6a) for increasing crosslinker concentration, which is proportional to refractive index (fig. 7a). Some deviations from this trend are however observed in the means of the Gaussian fits of the simulation data; the comparatively poorer quality of the fit relative to those in figs. 9a and 9b could be responsible, however the 95 % CI around the parameters remains small. Further investigation is required to determine the precise cause of deviations from the

overall decreasing trend in μ. Experimental observations at pH 9 are however inconsistent with modelling. As previously discussed, peak splitting is observed and may be responsible for this difference.

5. Conclusion

A photopolymerisation method was successfully used to fabricate a reliable, polymer based, nanoparticle free photonic crystal pH sensor of very high diffraction efficiency. The sensor was both experimentally tested and computationally modelled subject to variation in several factors affecting performance, with good overall agreement found between the two.

Effects of hydrogel thickness, crosslinker density in P1, tilt angle and number of laser pulses on sensor performance were studied using absorption spectra and diffraction efficiencies. Key trends identified include: increasing refractive index and decreasingly sharp peaks with increasing crosslinker density, peak broadening and increasing diffraction efficiency with increasing number of laser pulses, as well as peak broadening and an increase in Bragg shift on increasing film thickness.

Computational modelling revealed differences between ideal and physical responses, including saturation effects in film swelling and a switch from broadly ideal to non-ideal behaviour from pH 3 to 9 for spectral response with changing crosslinker concentration. Further investigation and analysis of these effects will permit the design of robust sensors.

The highlighted impacts of factors in the fabrication process on subsequent sensor performance can be used to design highly precise and tuneable pH sensors, considering the application of the sensor and the performance characteristics desired. Crosslinker density and hydrogel thickness were found to be the key factors in replay wavelength tuneability, whereas tilt angle, number of laser pulses and grating geometry did not show potential for tuning the colorimetric response.

With further development and research, the approach developed in this study exhibits potential for high resolution pH sensing, enabling applications including medical diagnostics in point of care and point of need settings, and quality control of consumer goods.

Acknowledgements

The authors thank Samuel Davies and Yunuen Montelongo for their help and guidance throughout this research project.

References

[1] A. K. Yetisen, PhD thesis, University of Cambridge, Cambridge, **2014**.
[2] C. P. Tsangarides et al., *RSC Adv.* **2014**, *4*, 10454–10461.
[3] M. Elsherif et al., *ACS Nano* **2018**, *12*, 5452–5462.
[4] E. M. Jones, C. A. Cochrane, S. L. Percival, *Advances in Wound Care* **2015**, *4*, 431–439.
[5] L. A. Schneider et al., *Archives of Dermatological Research* **2007**, *298*, 413–420.
[6] M. Zawadzka et al. in *Photonic Materials for Sensing, Biosensing and Display Devices*, *Vol. 229*, (Eds.: M. J. Serpe, Y. Kang, Q. M. Zhang), Series Title: Springer Series in Materials Science, Springer International Publishing, Cham, **2016**, pp. 315–359.
[7] A. Hendi et al., *International Journal of Nanomedicine* **2020**, *15*, 3887–3901.
[8] M. Scharrer et al., *Applied Physics Letters* **2005**, *86*, Publisher: American Institute of Physics, 151113.
[9] L. J. Martinez et al. in 2006 International Conference on Transparent Optical Networks, *Vol. 4*, 2006 International Conference on Transparent Optical Networks, ISSN: 2162-7339, **2006**, pp. 271–271.
[10] S. Hadlington, Cheap and colourful holographic sensors, Chemistry World, **2014**, https://www.chemistryworld.com/news/cheap-and-colourful-holographic-sensors/6999.article (visited on 13/10/2020).
[11] A. Breuer-Weil et al., *Nanoscale Research Letters* **2016**, *11*, 157.
[12] A. J. Marshall et al., *Analytical Chemistry* **2003**, *75*, 4423–4431.
[13] K. Taki, *Polymers* **2020**, *12*, 875.
[14] K. Gao et al. in Proceedings of the 2018 COMSOL Conference in Lausanne, COMSOL Conference, Lausanne, **2018**, p. 7.
[15] S. Sarkar, S. Lin-Gibson, *Advanced Theory and Simulations* **2018**, *1*, 1800028.
[16] N. Jiang et al., *Advanced Functional Materials* **2018**, *28*, 1702715.
[17] N. Jiang et al., 'Nanoparticle-Free Holographic Sensors'.
[18] J. Li, D. J. Mooney, *Nature reviews. Materials* **2016**, *1*, DOI 10.1038/natrevmats.2016.71.
[19] B. A. Mann, K. Kremer, C. Holm, *Macromolecular Symposia* **2006**, *237*, 90–107.
[20] A. F. Oskooi et al., *Computer Physics Communications* **2010**, *181*, 687–702.
[21] K. S. Yee, *IEEE Transactions on Antennas and Propagation* **1966**, *14*, Conference Name: IEEE Transactions on Antennas and Propagation, 302–307.
[22] J. B. Schneider, *Understanding the Finite-Difference Time-Domain Method*, **2010**.
[23] Y. Montelongo, PhD thesis, University of Cambridge, Cambridge, **2015**.
[24] H. Yuk et al., *Nature Materials* **2016**, *15*, 190–196.
[25] A. G. Mayes et al., *Analytical Chemistry* **1999**, *71*, 3390–3396.
[26] Sigma Aldrich, *Applications: free Radical Initiators*, Aldrich Polymer Products, **2019**, 19 pp.
[27] S. A. Benton, V. M. Bove, *Holographic imaging*, Wiley-Interscience, Hoboken, N.J, **2008**, 261 pp.
[28] K. S. Bose, R. H. Sarma, *Biochemical and Biophysical Research Communications* **1975**, *66*, 1173–1179.
[29] A. K. Yetisen et al., *Nano Letters* **2014**, *14*, Publisher: American Chemical Society, 3587–3593.
[30] D. W. v. Krevelen, K. t. Nijenhuis, *Properties of polymers: their correlation with chemical structure: their numerical estimation and prediction from additive group contributions*, 4th, completely rev. ed, Elsevier, Amsterdam, **2009**, 1004 pp.
[31] Y. Jiao, M. Liu in *Chemical Engineering Research: Reports of the 4th year research projects in the Department of Chemical Engineering at Imperial College London*, *Vol. 2*, **2020**, pp. 288–296.
[32] *Holographic Materials and Optical Systems*, (Eds.: I. Naydenova, D. Nazarova, T. Babeva), InTech, **2017**.
[33] C. Shannon, *Proceedings of the IRE* **1949**, *37*, 10–21.

Supplementary information

- Code used is available at https://doi.org/10.5281/zenodo.4331122
- Sample videos of reading and writing simulations are available at https://doi.org/10.5281/zenodo.4337561
- A video illustrating the fabrication and experimental characterisation of the sensors is available at https://doi.org/10.5281/zenodo.4333646

Pore Network Modelling of Diffusion in Rocks

Tanmayi Joishy and Florence Wade-Smith

Department of Chemical Engineering, Imperial College London, United Kingdom

Abstract

The effects of changing rock pore structure on the process of solute diffusion were investigated using two different models - a one dimensional (1D) Fickian model and a pore-scale model (PSM) for three rock samples: beadpack (BP); Bentheimer sandstone (BS); and Estaillades carbonate (EC). The PSM was built using pore network modelling (PNM). The models were used to simulate diffusion of carbon dioxide dissolved in water and diffusion rates were examined using breakthrough curves. Structural properties were extracted and effective diffusivity was determined where the values are 0.4094D for BP, 0.1019D for BS and 0.0313D for EC. Hence, the tortuosity values were found with BP having the smallest value of 0.78, BS with 2.4 and EC with 5.3. The diffusive behaviour is explained by these values in conjunction with the throat diameter, connectivity and porosity. The analysis was extended to the internal profiles of each sample to analyse pore-level behaviour. The PSM was found to be in good agreement with the Fickian model proving the potential of PNMs to model diffusive behaviour for both simple and more complex porous media. The Fickian model allows the extraction of useful parameters whilst the PSM reveals heterogeneities in the transport process. These findings are essential to understand the temporal and spatial evolution of the diffusive front in the context of residual CO_2 during capillary trapping for the purpose of carbon capture and storage (CCS).

Introduction

Across the globe, the importance of reducing atmospheric carbon dioxide concentration to meet global temperature targets is being realised. This has resulted in significant research in the field of Carbon Capture and Storage (CCS), particularly into the trapping characteristics of CO_2 in porous media. This is due to the potential contribution of this technology towards reducing anthropogenic emissions. Captured CO_2 is injected and stored in subsurface geological formations, displacing the brine that fills the pore space in these rocks. The research by Krevor et al. (2015) discusses the impact of capillary trapping in CO_2-brine systems on storage integrity and capacity. Observations have confirmed the stability of large masses, up to 10,000 tonnes, of residually trapped CO_2 for timescales of years. From this residual state, the CO_2 will slowly dissolve and diffuse into the continuum brine phase, thereby enhancing the storage capacity of the formation. It is essential that the behaviour of the dissolved CO_2 in rocks is understood, especially as rocks often have complex pore structures. As a result, understanding the microstructure of these rocks and consequently the effects on diffusion is critical to ensure the long-term storage security of CO_2.

Due to the complex nature of rocks, it is important to use modelling techniques. The simplest approach for the modelling of diffusivity in porous media is the one-dimensional (1D) Fickian model, which is a numerical method employing volume-averaging, treating the pore space as homogenous. An alternative approach which takes into account the heterogeneity of the pore space is the use of three-dimensional (3D) pore network models (PNMs). This is a well-established approach regarding the study of porous mediums, however the application with respect to the study of diffusivity has thus far been limited.

Pore network models can be constructed with limited microstructural information (Xiong et al. 2014), idealising the medium as a set of varying sized pore-bodies connected by throats through which transport occurs. A detailed analysis of pore network geometry is studied by Thomson et al. (2018) to compare porosity and PNMs for a variety of sandstone rocks and determine the permeability

through connected pore space. This finds throat geometry to be a key factor in order to understand fluid transport, thus, it is interesting to extend this analysis to alternative rock types which are present in sub-surface storage sites. Xiong et al. (2014) highlights the benefit of using PNMs to analyse the effects of heterogeneity within pore space structure on macroscopic transport coefficients. The growth in pore network modelling is emphasised by Blunt et al. (2013), where a range of imaging techniques are utilised to develop images of the rock structure hence allowing for the pore networks to be extracted. The work is considered an important step towards effective storage design and the key findings provide evidence that CO_2 can be trapped within the pore space. Therefore, this supports the use of pore space imaging for understanding multiphase processes in porous media. PNMs have successfully and efficiently shown to predict multiphase transport whilst accounting for the effect of microstructure. As a result, software has been continuously developed to improve the accessibility and extent of simulation for a wider range of physical structures and physical processes (Gostick et al. 2016).

In this paper, the Fickian model is used in combination with the pore-scale model (PSM) which is obtained using OpenPNM software. We will focus on three rock samples, namely the Beadpack (BP), Bentheimer sandstone (BS) and Estaillades carbonate (EC). This will enable us to analyse the impact of varying structural properties on solute diffusion in porous media and thus deduce whether PNM can be used to study the process of diffusion. The BS and EC are considered as outrocks but treated as analagous to sandstone and carbonate rocks that are often found in sub-surface storage sites.

Firstly, we will look at the diffusive transport at the macroscopic level and extract the effective diffusivity. Then we will investigate the effects of pore-scale heterogeneity by studying the evolution of the diffusive front for each sample. Finally, we aim to understand the microscopic structural effects by exploring the internal profile within each rock.

Methods & Materials

Image analysis and pore network simulations are carried out using Avizo and OpenPNM software. Firstly, 3D tiff images of each sample were used to build their individual pore networks. The simulations of the pore scale model were then carried out in Python to investigate the macroscopic transport characteristics. Secondly, the 1D Fickian model was implemented in MATLAB to determine effective diffusivity. The two models were then compared to understand the effect of heterogeneity within the rock samples. In this section, we outline the details of how this was carried out.

Image Analysis

In order to extract the required PNMs from micro-tomographic images, an image analysis workflow was employed, as shown in figure 1. The linear non-local means filter was chosen to remove any noise by using the entire image as a search window. The images were restricted to approximately 3mm in length due to the computational cost of comparing the neighbourhoods of all voxels to the neighbour of the current voxel in the entire image (Schlüter et al. 2014). In order to better distinguish between pores and throats, the implemented segmentation technique was the Otsu thresholding method. This entire process was carried out using Avizo software.

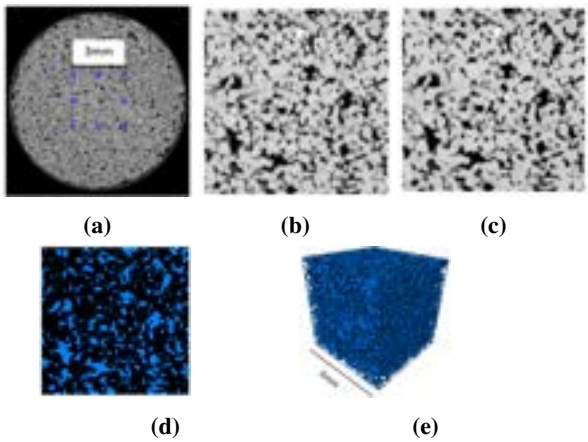

Figure 1: Workflow from X-ray microtomographic images to PNM for the Bentheimer sandstone using a voxel resolution of 9.9um: (a) Full 2D slice showing the defined cubic region of interest (ROI) of length 3mm, (b) 2D slice of ROI showing the raw image, (c) Result of (b) after the chosen filter is applied, (d) Segmentation of filtered image, (e) 3D image of segmented pore face used for PNM extraction.

The PNM is readily obtained using the SNOW network extraction algorithm. This requires the

input of a 3D tiff image which corresponds to figure 1e. The algorithm combines several methods, the details of which can be found in Gostick (2017). The 2D image for BS shown in figure 1c is also obtained for both BP and EC and the images for all three samples are shown in figure 2.

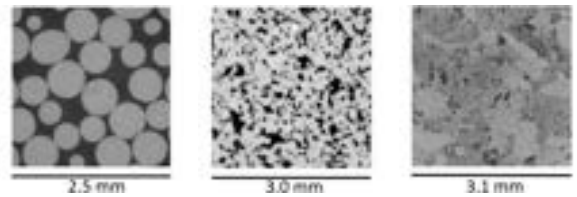

(a) BP **(b)** BS **(c)** EC

Figure 2: Filtered ROI for all three samples with their respective pore-scales, where the dark grey region represents the pore space, and light grey shows the rock.

Pore network models

Porous media can be considered as a distribution of variably sized voids which make up a system of pores. The distribution is dependant on the rock type and is specific to each sample. Each void is assumed to be spherical and has multiple neighbours connected by throats which act as potential pathways for mass transport. The throats are considered to be cylindrical and volume-less with each throat connecting exactly two pores, denoted by i and j. They allow mass transport via diffusion, which occurs due to a concentration gradient. The porosity, ϕ, of the rock is assigned entirely to the pores and is calculated,

$$\phi = \frac{V_v}{V_T} \tag{1}$$

where V_v is void volume and V_T is the total volume of the sample. The value of porosity is a structural property of the rock sample and is presented in table 1 with other properties that are extracted from the pore scale models.

Table 1: Properties of rock samples including the number of throats, N_t, number of pores, N_p, porosity and sample volume, V_T.

Sample	ϕ	N_p	N_t	V_T (mm^3)
BP	0.317	1400	2900	16.0
BS	0.238	3600	7500	28.1
EC	0.171	33700	47200	27.4

PSM implementation

The PSM was built using pore-network modelling. OpenPNM software is a customisable, open-source pore-network modelling package, written in Python, which is used to extract structural properties of the various porous samples. The modular structure of OpenPNM stores a variety of pre-written models, such as the geometry, phase, physics and algorithm modules which are all used in this work to achieve various objectives. The details of how these modules are implemented is displayed in code in the Supplementary Information. The physics module stores information about the different physical models used. The geometry module is specified to implement specific pore-scale geometrical models, containing information about the size of pores and throats in the network. The phases module is used to enable the prediction of thermophysical properties of the fluid, with the water class called in this work to study the diffusion of CO_2 dissolved in water. The algorithm module consists of a series of classes which enables transport simulations in the pore network. For this paper, the transient Fickian diffusion class has been used which allows the diffusion simulations to run using the appropriate algorithms. The fundamentals of these algorithms are based on the conservation of mass within the porous media and are contained in matrices which are solved in Python. To understand this, the mass balance equation for a solute in pore *i* is given by equation 2:

$$V_i \frac{dC_i}{dt} = \sum_j D A_{ij} \frac{C_j - C_i}{L_{ij}} \tag{2}$$

$$A_{ij} = \pi R_{ij}^2 \tag{3}$$

where *ij* refers to pore labels, D to the molecular diffusivity, A_{ij} is the cross-sectional area, shown in equation 3 where R_{ij} denotes the radius of a throat connecting two pores. C_j - C_i is the concentration difference between connected pores and L_{ij} is the characteristic length between pores *i* and *j*. The sum is taken over all throats connected to pore *i*, after which matrices are used to solve the mass balance at the pores to calculate the pore concentrations.

A set of conditions, namely the boundary and initial condition, is required to fully define the diffusive system. In this case the solute

concentration at the left boundary (where *x=0*) is set at an arbitrary value of 100 kgm^{-3} and the initial concentration (at *t=0*) is 0 kgm^{-3}. For comparison purposes, this is kept the same for each sample. The Crank-Nicolson time discretization scheme is used to perform transient simulations of transport phenomena and ensures that simulations are slow and 2^{nd} order accurate. The molecular diffusivity is manually inputted and a value of 2 $\times 10^{-9}$m^{2}s^{-1} is chosen and kept constant for all samples. This value is within the observed range of molecular diffusion coefficients for dissolved CO_2 (Zeebe 2011). Diffusion is the sole transport mechanism in this work, neither flow nor reaction are introduced or considered.

The pore network model for each of the porous media was then visualised in ParaView, an open-source data-analysis and visualisation application, for comparison.

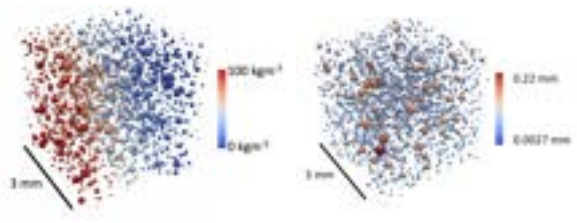

(a) Pore concentration **(b)** Pore diameter

Figure 3: Paraview images of BS showing a) the concentration front in the pores at a point in time mid-way through diffusion where the colour scale represents the concentration gradient and b) the pore diameter, shown by the corresponding colour scale. In both images the pore size is scaled by 1.25 pore diameter.

1D Fickian model

The 1D Fickian model was solved in MATLAB using Fick's 2^{nd} law, which assumes homogeneity across the samples:

$$\frac{\partial C}{\partial t} = D_e \frac{\partial^2 C}{\partial x^2} \tag{4}$$

where *C* is concentration, *t* is the time and *D* is the molecular diffusivity.

A volume-averaging method is employed which inevitably introduces aspects of uncertainty. The transport properties, in this case diffusivity, were treated as an adjustable parameter (Gostick et al. (2016)) in order to find a match between the PSM simulation results and the numerical results obtained from solving the Fickian model for each sample. The PSM was ran for a range of molecular diffusivities for each sample. This was then matched against the Fickian model where the inputted value for diffusivitiy was modified until the final adjusted diffusivity value which resulted in the most accurate overlap between the two results was taken as the sample's effective diffusivity. This was consequently used to calculate the tortuosity, shown in table 2, for each of the samples respectively:

$$\tau = \frac{D\phi}{D_e} \tag{5}$$

where τ refers to the tortuosity and D_e is the effective diffusivity.

In addition to the PSM and 1D Fickian model, a third model was briefly considered in this work. An analytic solution assuming unsteady diffusion in a semi-infinite slab was implemented. However, this considered a volume of solution at an interface that extended over a large distance. These assumptions were not validated and the model was unable to incorporate the microstructural details of the porous media. The agreement between the PSM and analytical solution was in poor thus this model was not incorporated or developed further.

Results

We study the details of the microscopic structure of porous media in order to understand the macroscopic diffusion through the rocks. We show the morphological properties extracted from the PSMs, as well as the computed effective diffusivity and tortuosity for all three samples. Additionally, we present the predicted transient concentration profiles at the outlet boundary. Finally, we discuss the ability of the Fickian model to accurately represent the PSM.

Microscopic structure

The pore-throat diameter distribution of the three samples is shown in figure 4, in the form of a histogram plot. Various statistical properties were calculated from data extracted from the PSMs, for example the mean throat diameter, $\overline{d}_t$, which is shown in table 2. BP has the largest throat diameter and range whereas EC has the smallest. All three distributions are positively skewed. The

relative standard deviation is calculated by dividing the standard deviation by the mean, finding EC to have the smallest value of 0.85. The mean pore diameters follows the same pattern as mean throat diameter with BP having a significantly larger value compared to EC.

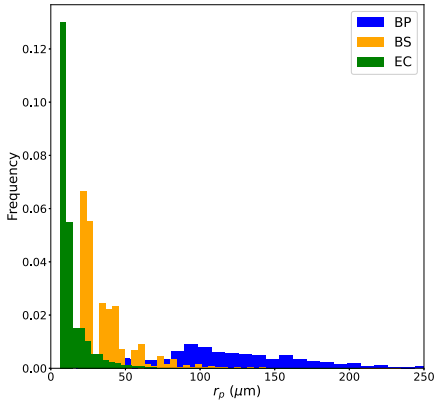

Figure 4: Distribution of throat diameter (μm) where the data for the histogram is sorted into 50 bins. The x axis is limited to 250 μm as the frequency of throats with a diameter greater than this was negligible.

From table 2 below, the tortuosity is seen to have the opposite trend compared to the mean pore and throat diameter, whereas the coordination number is similar for both BP and BS with a lower value for EC.

Table 2: Summary of microscopic properties showing the mean pore diameter, $\overline{d}_p$, mean throat diameter,$\overline{d}_t$, tortuosity, τ_p, and coordination number, N_C, for each rock sample.

Sample	$\overline{d}_p$ (μm)	$\overline{d}_t$ (μm)	D_e (m^2s^{-1})	τ	N_C
BP	61	103	0.4094D	0.78	3.9
BS	44	36	0.1019D	2.4	4.1
EC	15	13	0.0313D	5.3	2.8

Breakthrough curve analysis

The breakthrough curves shown in figure 5 are obtained from both the PSM and the Fickian model for each sample. The average concentration of the pores at the right boundary is measured, hence fixing position and observing concentration as a function of time. Effective diffusivity, D_e, shown in table 2, is obtained by the matching of the two models which is observed in the breakthrough curves by their close overlap. A trend can also be seen in the values for effective diffusivity, where D_e for BP is the largest; it is 4 times that of BS, which is 3 times the D_e of EC.

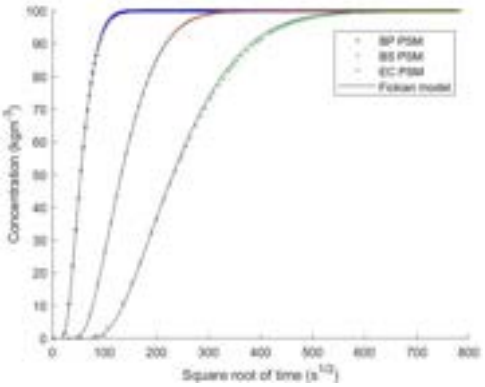

Figure 5: Breakthrough curves, showing the average concentration in the right boundary pores over time. The pore-scale model is displayed as coloured dots. The Fickian model is shown in black for all three samples.

For ease of visualisation, intermittent time values for the PSMs have been shown. Overall, it is apparent that each rock shows an almost exact agreement between the models, this is especially the case for BP which follows the same breakthrough curve for both models. The other two rocks show significant agreement between the models, however slight deviations are observed at the beginning; before the curve reaches 15 kgm^{-3} and 20 kgm^{-3} for BS and EC respectively. Additionally, EC shows similar deviations after a concentration of 47.5 kgm^{-3}, but still closely follows the same trend as the Fickian model. BP displays the fastest rate of diffusion and reaches full saturation by 180 $s^{1/2}$ whereas BS requires more time, only reaching 100 kgm^{-3} at 440 $s^{1/2}$. EC has a more gradual gradient and reaches complete saturation at 780 $s^{1/2}$. The samples follow the same pattern when considering the time taken to achieve a concentration of more than 0 kgm^{-3}, BP only takes 10 $s^{1/2}$ whereas EC requires 45 $s^{1/2}$, and BS is in between and needs 30 $s^{1/2}$.

Discussion

Microscopic structure

The different PSM simulations allow us to investigate the transport behaviour and details of microstructure and compare results between the

three samples. The histogram (figure 4) shows that EC has the narrowest throats which helps to explain why it exhibits the slowest rate of diffusion, as seen in figure 5. On the other hand, BP reaches 100 kgm^{-3} in the shortest time period, which can be partially attributed to BP having the largest mean throat diameter, allowing for faster rates of diffusion. Throats are understood to provide resistance between pores. Therefore, the analysis of the throat diameter is useful to understand the variation in pore concentration between the samples. The relative standard deviation is the largest for EC which supports the increased heterogeneity of the sample and can be visualised in the image of the sample in figure 2.

Currently, the parameters used within the model only consider one solute and its size is not considered a limiting factor. Hence, the effect of pore diameter is not considered important when considering transport processes in these porous media. This is due to the solute, CO_2 dissolved in water, having a diameter in the order of nanometres whereas the pores and throats considered are in the order of microns. However, if the analysis was extended to incorporate multiple solutes of varying size, the effect of the throat size distribution would have a more significant impact. A large solute would only be able to diffuse through throats with an accommodatingly large diameter, this would lead to changes in connectivity (Xiong et al. 2014). This allows for an interesting topic for further investigation. It is useful to note that in this work connectivity and coordination number are used interchangeably since varied solute size is not considered.

Studying the properties of the rock, shown in table 1, BP has the most simple and uniform microscopic structure; it has the fewest pores and throats. Additionally, the sample volume of BP is smaller due to the increased homogeneity which implies less volume is required to contain a sufficiently large number of representative pore sizes. This contributes to BP's faster breakthrough time. On the other hand, BS and EC are less uniform and have a wider pore-size distribution hence require a larger sample volume to contain the same representation. As BS and EC are comparable in length the differences in breakthrough time can be partially explained by their pore structure. They both have more pores and throats than BP with EC having the most, as well as smaller mean throat diameters where EC has the smallest. Furthermore, the effective diffusivity and tortuorsity, expressed in table 2 can help to understand the rate of diffusion. The values for tortuosity are inversely proportional to effective diffusivity, as shown in equation 5. The large D_e and small τ explain the fast rate for BP, visualised by the steep gradient. Tortuosity is a structural feature of the rocks which accounts for geometric factors since throats are not always straight and well connected. This affects the time taken for a solute to diffuse through the sample. EC shows the highest value of 5.3 for tortuosity which implies a longer time taken for diffusion to occur as the solute has to essentially diffuse over a larger distance. On the other hand, BP's low value of 0.78 indicates relatively straight throats physically and essentially a shorter diffusive pathway. Overall, the trend of decreasing rates of diffusion from BP to BS to EC are seen in the breakthrough curves.

Initially, the concentration throughout the pore space is 0 kgm^{-3}. Since the concentration at the right boundary is being measured in the breakthrough curve (figure 5), there is a delay for concentration to increase above 0 kgm^{-3} which corresponds to the time taken for the diffusive front to penetrate the entire pore space and reach the measured boundary. The trend in this time follows the pattern indicated by tortuosity; the time is shortest for BP, followed by BS and is the longest for EC.

Another contributing factor is the computed connectivity, shown in table 2, which corresponds to the average number of throats connected to each pore. This structural property shows BP and BS to have similar values where each pore is connected to approximately 4 neighbouring pores. Therefore, the difference in their breakthrough curves can be partly accounted for by their pore structure and porosity. A high porosity means more space is available for the movement of solutes. BP has the highest porosity value (table 1), this results in a higher probability of the solute finding a potential pathway and increases the likelihood of diffusion through the sample. Therefore, the slower rate of diffusion through BS can be understood by it's smaller porosity value than BP, despite having a similar connectivity. On the other hand, EC has a much lower N_C, where each pore is connected to 2.8 neighbouring pores on average resulting in fewer potential pathways for solute transport

compared to BP and BS. The porosity of EC is also lower than BS and BP. Due to the rock formation process, BS typically has one level of intragranular porosity whereas the porosity for EC is multi-scale leading to more complex transport behaviour. Porosity and connectivity both affect the path of the diffusive front so the slower rate of diffusion of EC can be further attributed to its low values.

These factors in combination with the throat geometry and effective diffusive are all jointly responsible for the diffusive behaviour seen in the breakthrough curves. Overall, the results from the curve are well explained by analysing the microscopic structure of the samples.

Internal profile

In addition to studying the concentration at the outlet pores over time, it is beneficial to study the internal profile by fixing time and analysing the concentration throughout every individual pore as a function of space. The number of pores are shown in table 1, and can be visualised by the number of data points in the internal profile figures below. Figure 6 shows that BP has the fewest pores, then BS (figure 7), followed by EC which has the most (figure 8). For each sample, eight time intervals are used and the times are arbitrarily selected to present the concentration profile in the porous media clearly. It is important to note that the time intervals for each of the samples are different and chosen to be relative to the various rates of diffusion. These same times are used to obtain the corresponding curves from the Fickian model. Generally, at early time intervals the concentration decreases significantly through the length of the rocks. The boundary condition (C=100 kgm^{-3} at x=0) and the initial condition, (C=0 kgm^{-3} at t=0), cause a high concentration gradient between the pores initially which leads to a steep gradient on the internal profile curves at low time intervals. At some locations on the right-hand side the pores remain at 0 kgm^{-3} where the diffusive front has not yet entirely penetrated the rock. With increasing time, the gradient becomes shallower as the average concentration throughout the pore space increases. This is due to the extent that the diffusive front has travelled. Finally, at the latest time, the sample is fully saturated as the concentration reaches 100 kgm^{-3} throughout the whole pore space. The internal profile is a good way to observe the diffusive front travelling through the porous media on a pore level. The degree of scattering represents the extent of heterogeneity within the individual samples, showing that pores at the same distance in the rock have a range of concentration values.

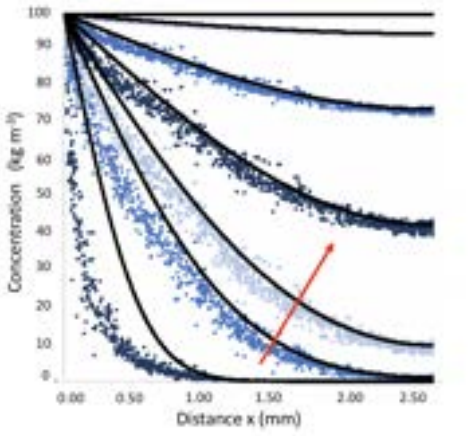

Figure 6: BP internal profile. The blue scatter shows the PSM concentration in the pores over the full length of the BP sample. Alternating shades of blue are used to distinguish between different times and the red arrow shows the direction of increasing time. The eight time intervals considered are: (0.01, 0.05, 0.1, 0.25, 0.5, 1, 5, and 10)$\times 10^4$s. The black lines show the Fickian model for the same time intervals.

The internal profile for BP shows that initially the concentration drops significantly within a very short distance from the boundary, where the concentration is set to 100 kgm^{-3}. At 100 s the concentration decreases to 0 kgm^{-3} in a distance of 1.25 mm into the sample, remaining at zero in the right half of the pores. At 500 s the concentration gradient remains high and the concentration reduces to zero in the boundary pores. At times greater than 500 s all the pores are partially saturated and pore concentration continues to increase for a fixed position but with a reduced driving force. The BP reaches full saturation by 80,000 s, explained by the low tortuosity of the BP as well as its relatively uniform pore space is reflected by the narrow scatter of points. This leads to a small range of concentration between the pores in a 2D slice at a given distance.

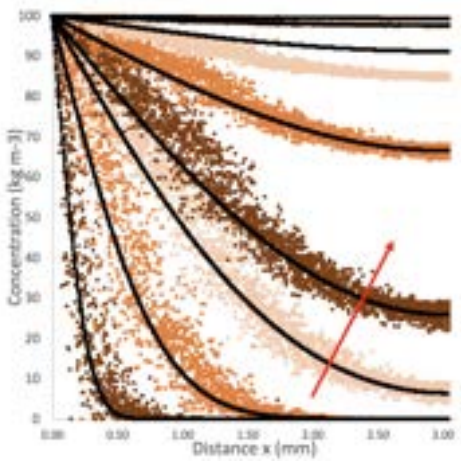

Figure 7: Analogous Internal Profile for BS: The eight time steps considered are: (0.01, 0.1, 0.5, 1, 2.5, 5.0, 7.5 and 10) $\times 10^4$s.

The concentration gradient follows the same trend for the three samples, although the diffusion rates vary between rock types. In BS at the first time interval (*t=100 s*), the concentration decreases to 0 kgm^{-3} within the first 1 mm into the rock. This is a shorter distance than observed in the BP which supports its faster diffusion rate. In BS, all the pores become partially saturated in times later than 1000 s and the pore space becomes fully saturated by 100,000 s. Compared to the internal profile for BP, BS shows an increased scatter. This is attributed to the increase in tortuosity which is more than 3 times larger for BS. Hence, the throats in BS deviate more from being straight connections between pores. Physically this means that as the diffusive front penetrates through the rock space, some of the solute travels much further whilst some only travels a short distance leading to a thick diffusive front. Therefore, it is useful to fix time and look at both the concentration range at a particular location and the range in location of a specified concentration. Quantitativly, the range at which the concentration is 30 kgm^{-3} is considered at the first time interval (t=100 for BP and BS), which can be seen to be in a number of pores ranging a distance of 0.25 mm in the BS. However, there is only one pore at this concentration in the BP. The degree of scattering increases further when looking from BS to EC, shown in figure 8 below, where the concentration is 30 kgm^{-3} over a width of 0.9 mm at the first time interval for EC (t= 1000s), representing a thicker diffusive front. Alternatively, this trend is supported by studying the concentration range in a 2D slice.

Furthermore, it is important to note that the scatter decreases at later times. This is due to the solute diffusing through the rock along a range of different paths and so at large times it is likely that the solute will have travelled approximately the same overall distance independent of which path it took. Hence, the thickness of the diffusive front decreases. This difference is most noticeable for EC due to its high tortuosity and heterogenous nature.

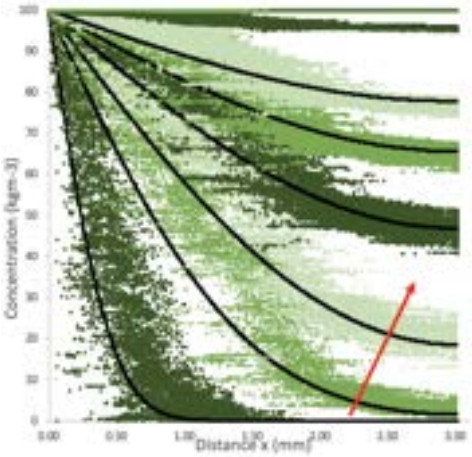

Figure 8: Analogous internal profile for EC: The times shown are (0.1, 1, 2.5, 5, 10, 20 and 40) $\times 10^4$s.

Comparing the internal profile of EC to that of BS and BP, it is immediately clear that there is a significantly larger number of pores, as well as a higher tortuosity. However, the same general trends observed in BS and BP can be seen with EC but with an increased time for the diffusive front to travel through the rock. For example, the time taken to reach full saturation is much higher for EC, around 400,000 s.

The difference between the internal profiles of BP, BS and EC support the trend observed in the breakthrough curves. The internal profile presents a good way to visualise the differences in microscopic structure between the different rock samples.

Comparison of Fickian and Pore Scale Models

It is useful to understand the equations that underpin the models incorporated in this work. Equation 2, used for the PSMs, is a simplification of equation 4 and is applied to the pores only. This is due to the assumption that mass transfer within throats is neglected and that there is

a linear gradient between the throats. This means that as soon as the solute reaches the entrance of a throat, at the next time step it has reached the other side of the throat with a linear gradient. This assumption eliminates the second order derivative in distance. However, the Fickian model does not make this assumption, and the second order derivative is still considered. If throats are sufficiently short, then the assumption to neglect mass transfer within throats is valid. The agreement of the breakthrough curves between both models supports this assumption and justifies the use of equation 2 as a simplification for Fick's 2^{nd} law of diffusion. It is important to look at both the breakthrough curves and internal profiles to understand if the models are able to fully capture the details of the microscopic structure. The incorporation of the matching technique used to find the effective diffusivity in the samples means that the Fickian model represents the PSM to a good level of accuracy. The PSM breakthrough curves for BS and EC show this good match, despite the complex nature of the pore space. Furthermore, the homogenous nature of the pore space in BP gives rise to the near exact agreement between models, since the Fickian model assumes homogeneity. Overall, the results from the breakthough curves indicate the diffusive process can be represented using the Fickian model.

As the concentration in the observed pores approaches the maximum of 100 kgm^{-3}, the diffusion rate slows down for all samples, visualised by the change in gradient. In particular, a significant amount of time is required to reach complete saturation once a concentration of 99 kgm^{-3} is achieved. This is captured in the shape of the breakthrough curves for both models. This result is anticipated as the Fickian model shows that the driving force for local diffusion is the concentration gradient. Therefore, when the concentration in the right pores is 99 kgm^{-3}, the driving force is considerably weaker so diffusion occurs at a much slower pace. For example, EC takes 240s$^{1/2}$ to reach 100 kgm^{-3} from this point. This is represented well by both the PSM and the Fickian model for all samples.

For the internal profile, the Fickian model is run for the same time intervals as the PSMs to assess the ability of Fick's law to accurately represent the transport within the pore space. The PSM is best represented by the Fickian model at intermediate times, for the BP this is 2,500s, BS is 10,000s, and EC is 50,000s. For BP, (figure 6), the Fickian model initially predicts the concentration gradient to be shallower, with the concentration higher throughout the first half of the pore space. This can be attributed to BP having a low number of pores and a narrow scatter which leaves little room for error in the Fickian model's ability to predict the diffusion at the pore scale. However, both models seem to agree the point at which concentration reaches 0 kgm^{-3}, implying that the Fickian model predicts the overall rate of diffusion well and that there is still a good agreement when considering average behaviour. At higher times the predictions of the Fickian model match the concentration profile of the PSM. This is because the diffusive front has had more time to diffuse through the sample therefore showing a more uniform and narrow front, this is especially the case after the halfway distance for each sample. The profile for BS (figure 7) shows a better match between the Fickian and PSM initially. However, as time reaches 50,000s the Fickian model over-predicts the concentration in the pore space for similar reasons to the under-prediction seen for the BP. There is a good match between the two models for the internal profile of EC. As the diffusive front is thick, the probability that the Fickian model will fit within the scatter increases since the Fickian model employs a volume-averaging method. EC is the least uniform and most tortuous but has a very large number of pores which leads to the Fickian model being a good match for average behaviour. However, unlike the PSM, the Fickian is not able to capture the details on an individual pore level. These findings provide significant evidence that there is the potential for pore network modelling to be used to study the diffusive process at a pore-scale, which has thus-far been a relatively unexplored field of study.

Conclusion

The breakthrough curves for the three rock samples follow the expected trends which are explained by differences in microstructure. The properties explored: porosity, throat diameter, connectivity, tortuosity, and effective diffusivity, were found to support the trends observed. The internal profiles present an increased scatter from BP to BS to EC, this is expected given the increased heterogenity

of the samples which can be observed from the images.

Overall, we have observed that there is a very strong agreement between the two models, reinforced by both the breakthrough curves as well as internal profiles. This is significant as it proves the potential of the pore-scale model to describe diffusion, from more simple porous media such as the beadpack to fairly complex porous media such as the Estaillades carbonate and proves the ability of pore network models to reflect the complexity in microstructure at a pore-scale.

The breakthrough and internal profile allow us to observe the concentration as a function of time and space respectively. This aids in the understanding of the temporal and spatial evolution of the diffusive front which is essential to understand when considering the residual CO_2 phase in capillary trapping. The Fickian model allows the extraction of useful parameters, such as the effective diffusivity, whilst the pore scale model reveals the heterogeneities in the transport properties that materialise as a result of the complexity of the pore space.

As this work is placed within an area of growing research, there is significant potential for future study. This work could be extended to investigate the effect of solute size on diffusion through the throats of pore network models. Large solutes are not able to diffuse through narrow throats so further investigation into the effects of connectivity would be required. This is particularly useful in order to understand transport in porous media beyond rocks, such as catalysts, where catalyst design depends significantly on solute and throat sizes. An important element of future model development is to study more complex processes, such as reaction and advection in combination with diffusion. These processes can be investigated in the context of CCS for long term geological stability. Hence, it would be additionally useful to look at the conditions in sub-surface storage sites and simulate a range of temperatures and pressures to study the transport processes at the pore scale.

Acknowledgements

The authors would like to express their gratitude to Paul-Ross Thomson and Nerine Joewondo for their invaluable support and guidance throughout this project.

References

Blunt, M. J., Bijeljic, B., Dong, H., Gharbi, O., Iglauer, S., Mostaghimi, P., Paluszny, A. & Pentland, C. (2013), 'Pore-scale imaging and modelling', *Advances in Water resources* **51**, 197–216.

Gostick, J., Aghighi, M., Hinebaugh, J., Tranter, T., Hoeh, M. A., Day, H., Spellacy, B., Sharqawy, M. H., Bazylak, A., Burns, A. et al. (2016), 'Openpnm: a pore network modeling package', *Computing in Science & Engineering* **18**(4), 60–74.

Gostick, J. T. (2017), 'Versatile and efficient pore network extraction method using marker-based watershed segmentation', *Physical Review E* **96**(2), 023307.

Krevor, S., Blunt, M. J., Benson, S. M., Pentland, C. H., Reynolds, C., Al-Menhali, A. & Niu, B. (2015), 'Capillary trapping for geologic carbon dioxide storage - from pore scale physics to field scale implications', *International Journal of Greenhouse Gas Control* **40**, 221–237.

Schlüter, S., Sheppard, A., Brown, K. & Wildenschild, D. (2014), 'Image processing of multiphase images obtained via x-ray microtomography: a review', *Water Resources Research* **50**(4), 3615–3639.

Thomson, P.-R., Aituar-Zhakupova, A. & Hier-Majumder, S. (2018), 'Image segmentation and analysis of pore network geometry in two natural sandstones', *Frontiers in Earth Science* **6**, 58.

Xiong, Q., Jivkov, A. P. & Yates, J. R. (2014), 'Discrete modelling of contaminant diffusion in porous media with sorption', *Microporous and Mesoporous Materials* **185**, 51–60.

Zeebe, R. E. (2011), 'On the molecular diffusion coefficients of dissolved co2, hco3-, and co32-and their dependence on isotopic mass', *Geochimica et Cosmochimica Acta* **75**(9), 2483–2498.

Optimizing COVID-19 vaccine supply chain network in England: A ChAdOx1 and BNT162b2 case study

Yichuan Zhu and Jiahao Ye
Department of Chemical Engineering, Imperial College London, U.K.

Abstract: The COVID-19 pandemic has urged the innovations of therapeutics and vaccines to mitigate its impact on human society. With imperative and substantial demand for vaccines, severe challenges arise in supply chain in terms of production, allocation, and storage. Here, we demonstrated a model-based, quantitative approach to simulate a four-echelon vaccine supply chain network in England using the GAMS software. An optimized supply chain network is first built from base case and then analyzed at three different studies: (1) weekly or daily transportations, (2) prioritization of target groups, and (3) multi-product vaccination strategies. The model investigates the effect of decision variables on total supply chain cost, vaccine availability and delivery time, to select the best immunization program for England. The results indicate resilience of the proposed supply chain in most scenarios, despite some bottlenecks have been found in regional and local storage capacities. We further found that ChAdOx1 vaccine has an absolute advantage in cost and storage complexity comparing with BNT162b2, but uncertainty holds for its time to approval. In ideal situations, a one-year vaccination strategy of targeting priority groups in the first 3 months under daily operation is recommended to maintain the reliability of supply chain and satisfy the demand in England.

1. Introduction

Coronavirus disease 2019 (COVID-19) has spread to the world with an unprecedented speed, causing one of the worst pandemics in the modern history. The mild symptom during its long incubation time has led to intensive transmission until the following acute respiratory distress or fatality. As of 5 December 2020, 66 million people were infected by COVID-19 with over 1.5 million deaths worldwide. Consequently, vaccine, as the most powerful technique to protect lives and mitigate infections, has been urgently demanded to achieve high immunization levels. Since the beginning of the outbreak, more than 300 pharmaceutical companies have started the innovation of COVID-19 vaccines at different paces, currently in preclinical or clinical stages.

Hitherto, over 355 million doses of vaccines have been ordered by the UK government from seven different companies to reduce the risk and promote fast vaccination for citizens (Armstrong, 2020). Amongst all these vaccine candidates, two of them are expected to be authorized and supplied first by the UK government. ChAdOx1 nCoV-19, one of the most promising vaccine developed by Oxford University and AstraZeneca, was ordered at the largest amount because of its advantageous cost based on adenovirus-vectored platform technology and proposed manufacturing facility in UK. Although there was a suspension of ChAdOx1 vaccine during its phase III clinical trial due to unexpected adverse effects, it is still considered a good candidate for vaccination in UK (Gov.uk, 2020). On the other hand, Pfizer/BioNTech's nucleoside-modified messenger RNA (mRNA) vaccine BNT162b2 has become the first vaccine that has been authorized for emergency use, with an announced efficiency of 90%. An expected 10 million doses of Pfizer vaccine will be delivered to UK by the end of 2020 which is enough to vaccinate 5 million people under prime-boost vaccination schedule (Alistair, 2020).

The imperative demand of vaccines leads to severe challenges in supply and distribution, which emphasizes the necessity of decision making. Vaccines require well-qualified and robust cold chain for storage and transportation, as inappropriate conducts may result in denaturation and wastage. For safe and efficacious delivery of vaccines in UK, protocols on each section of supply chain, including purchasing, storage, and distribution, need to follow the instructions from National Health Service (NHS) on a case-by-case basis (Hart, 2007). Similar to

Figure 1. ChAdOx1 vaccine supply chain network configuration. Red star represents AstraZeneca's manufacturing facility at Macclesfield. Numbers 1 to 9 show the centre of 9 regions in England. Blue dots represent local storage facilities at counties and unitary authorities

traditional vaccines, ChAdOx1 requires cold chain storage at temperatures between 2°C to 8°C which a slight modification on existing cold chain would be sufficient, yet the storage capacity needs to be improved to meet the demand. The major challenge for Pfizer vaccine is the requirement of a much stricter storage environment at a temperature below -70°C, as freezer temperatures instead of refrigerator could be hard to achieve in local pharmacies and hospitals. The Pfizer vaccines are proposed to be shipped in dry ice pack boxes with a storage time of 15 days, and an additional storage time up to 5 days could be achieved in normal refrigerated conditions (2°C to 8°C) once thawed (Pfizer, 2020). The short shelf life of mRNA vaccine would suggest using frequent operations and transportations to enable deliveries to recipients before they expire. Considering these two types of vaccines with different cold chain requirements, a conventional four-tier supply chain network was established and optimized on a mathematical model using the General Algebraic Modelling System (GAMS) for the techno-economic study of different vaccination strategies. The configuration of our proposed supply chain structure for ChAdOx1 vaccine is shown in Figure 1.

With a focus on ChAdOx1 and BNT162b2 vaccine, especially ChAdOx1 vaccine for our base case study, we simulated the supply chain for vaccine delivery in England after the approval of these vaccines and aim to investigate different supply strategies and their consequent effects to the overall supply chain performance. Real-world data for vaccines and vaccine supply chains are collected and imported to the model to analyze the bottleneck in the system. In this work, three comparative studies will be introduced with modifications of different transport intervals, targeting vaccination strategies and multi-product productions. To elucidate the supply chain performance, we focus on variations in vaccine availability, total deliver time and total system cost in different scenarios and how production plans are made available to meet the demands.

2. Literature Review

Pharmaceutical supply chain has been considered as one of the most important activities for efficacious delivery of vaccines. Many works have been done to investigate decision makings at each echelon of the supply chain. Production planning, inventory management and distribution are summarized as the major considerations. At the production stage, the uncertainty of vaccine demand makes it hard for manufacturers to plan their productions respectively, thus leads to a shortage in supply. Chick et al. (2008) showed that an optimum alignment of demand and supply could be achieved with a governmental contract which specifies the number of individuals to vaccinate. Arifoglu et al. (2012) also demonstrated the intervention methods by governments on both demand and supply side. To mitigate the risk of imbalanced market, UK government has closely involved in the immunization program and ranked the priority groups for vaccination which helps build a systematic vaccination schedule. Regarding inventory control, Shrestha, Wallace, and Meltzer (2010) studied potential shortages of inventory in stockpiling scenarios for pediatric vaccines in the United States. For storage facility design from scratch, the capacity of each node requires optimization for fluctuation on demands. In distribution and transportation, time is of the greatest importance. Geographical data and transport modes were required in specific cases, for example, a vaccination program in Montgomery County, studied by Aaby et al. (2006), to determine the actual time to delivery.

Mathematical modelling and GAMS were utilized as good simulation techniques for ordinary supply chains. Zamarripa et al. (2012) presented a Mixed Integer Linear Programming (MILP) model using GAMS with a case study on a proposed supply chain to minimize aggregated cost and accumulated delivery time. Game theory was also incorporated to manage uncertainties. Ramirez-Nafarrate, Lyon, Fowler, and Araz (2015) proposed a genetic algorithm with constraint relaxations which simultaneously optimize distribution locations and capacities. The advantages of the proposed

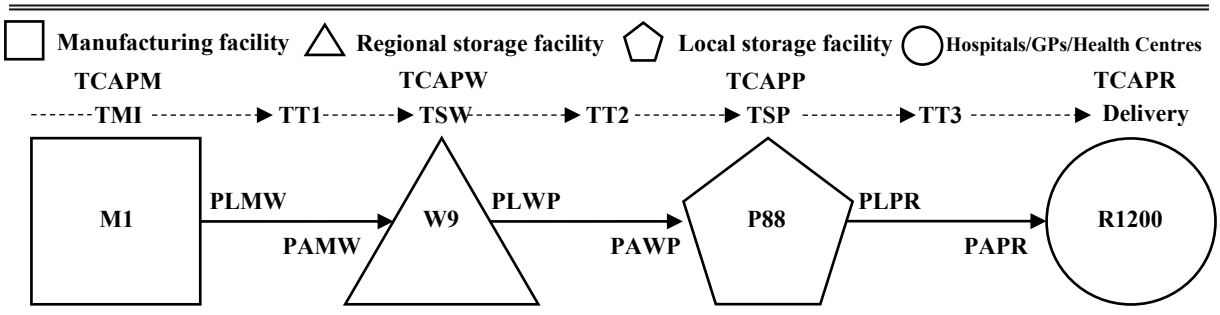

Figure 2. Vaccine distribution process. TCAPM, TCAPW, TCAPP, TCAPR are total capacities of the facilities. TMI represents the total time in manufacturing facility (including QC and fill-to-finish). TT1, TT2, TT3 represents transport time between manufacturing and regional stores, between regional and local stores, between local stores and hospitals, respectively. TSW and TSP represent the regional and local storage time. PLMW, PLWP, PLPR represent products leaving facilities. PAMW, PAWP, PAPR represent products arriving facilities.

algorithm were compared with the sequential approach on optimizations. For multi-product scenario, Pasandideh et al. (2015) designed a three-echelon supply chain with a bi-objective function on both cost minimization and demand satisfaction which runs on GAMS. The above-mentioned works provide detailed solution approach to optimize the supply chains with different structures. However, more considerations should be made in a vaccine supply chain.

Recent research works have been conducted on either pharmaceutical supply chain logistics or mathematical formulations of general supply chains. Only a few have been done to optimize the vaccine supply chain using mathematical simulation tools, especially for the most recent COVID-19 vaccine. Therefore, simulating COVID-19 vaccine supply chains using real-world data has great significance on the design of the actual supply chain. It could build an early landscape of how vaccines should be dispensed. And budgets at different scenarios could be estimated for future decision making.

3. Methods

3.1 Data and Assumptions

A four-tier distribution network was proposed in this work to model the COVID-19 vaccine's distribution process in England consisting of: (a) 1 manufacturing/national storage co-located facility, (b) 9 regional warehouse storage facilities, (c) 88 local storage facilities, (d) and 88 clusters of recipient locations (1200 hospitals/GP surgery /health centre facilities). A detailed workflow schematic is shown in Figure 2. The product flow starts from the manufacturing facility producing one batch of vaccine substances. Then, the vaccines are immediately filled into sterile vials and stored in freezers or refrigerators into co-located national stores awaiting collection by trucks and transferring to regional warehouses. After storing at regional warehouses, the vaccines are distributed to potential local stores via cold chain trucks. Each hospital or health centre is supplied by the closest local stores and receive daily vaccine doses via truck delivery again. The proposed four-tier network structure is illustrated in Figure 3.

Vaccine demand for each hospital was estimated based on the geographical population distribution of England, and the total demand for 18+ population has been estimated at 112 million doses (prime and boost included). The manufacturing facility was considered to operate centralized at a large scale, located at AstraZeneca Macclesfield site, UK. The formulation and fill-to-finish process is included in the TMI (total time in manufacturing facility). The operating and capital expenditure, lead time and production capacity information specific to ChAdOx1 and Pfizer/BioNTech mRNA vaccines was obtained from SuperPro Designer and presented in Table 1.

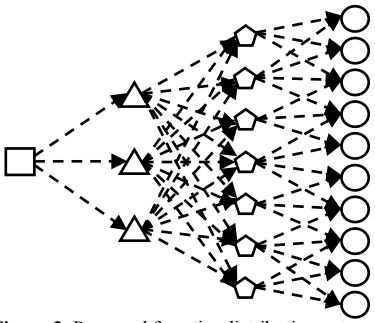

Figure 3. Proposed four-tier distribution network

Table 1. Vaccine production information

	ChAdOx1 Platform	mRNA Platform
Production scale [L]	2000	30
Duration of a batch [days]	30	2
Capacity [Doses year^{-1}]	581,096,436	365,290,000
CapEx+OpEx [$ year^{-1}]	57,686,000	615,847,000
Drug substance cost [$ dose^{-1}]	0.10	1.69
	Fill-to-finish	
CapEx+OpEx [$ year^{-1}]	307,369,000	
Cost per dose [$ dose^{-1}]	0.269	

The total investment of manufacturing facility is calculated by summing the CapEx and OpEx of manufacturing and liquid fill-to-finish process, resulted in 365,055,000 USD. The fill-to-finish process possesses a much higher capacity of 114,115,318 vials/year, assuming 10 doses per vial, which is capable of packing 2 times of ChAdOx1 vaccine production capacity, hence the liquid fill-to-finish process is not considered as a bottleneck in this case. The mRNA platform has advantages of a much smaller batch scale of 30 L and shorter lead time of 2 days which could enable agility and fast response in terms of vaccine supply. Despite having a smaller scale, mRNA platform showed a much higher drug substance cost (1.69 $ dose^{-1}) and only 62.9% annual production capability (3.65×108 doses) of ChAdOx1 annual capacity (5.81×108 doses).

With respect to transportation method, we considered ground transport only, with trucks as primary delivering vehicles, assuming a unit transport cost of 0.00040 $ dose^{-1}km^{-1}. Transport distance and time between facilities were calculated based on geographic coordinates and assumed a reasonable vehicle speed of 60 kmhr^{-1}. Real coordinates were implemented for manufacturing site, regional stores, and hospitals, whereas potential locations for local stores were chosen hypothetically and preferably close to 88 clusters of hospitals. The number of trucks required daily was obtained by summing all the connections established between echelons.

The number and capacity of facilities were obtained or calculated based on public-domain and industrial data, while locations and capacities for

local stores were selected based on geographical population distribution and vaccine demand from each recipient location. The storage time at each level/tier was assumed to be 2 days. This two-day storage allowance is chosen to buffer the potential scarcity in transportation vehicles, while still satisfies the 15 days delivery constraint for Pfizer/BioNTech vaccine.

In response to MHRA's recent authorization of Pfizer/BioNTech mRNA vaccine, this work also considers overseas supply of Pfizer vaccines in Belgium and air cargo import to UK. The manufacturing and logistics of vaccines are outsourced to Pfizer in Belgium. Therefore, for Pfizer mRNA vaccine, we consider the product flow starting at UK's airport, (assumed London Heathrow Airport) as the primary national store. Moreover, as UK government has ordered 40 million doses of Pfizer vaccine at an estimated cost of £588.4 million, an average cost of $19.61 per dose is considered as the vaccine production cost (Mullin, 2020). The stringent storage temperature below -70 °C for Pfizer vaccine also incurs a much more expensive storage cost, which consists of ultra-low temperature freezers and extra dry ice refilling cost.

3.2 Supply chain modelling - GAMS model

In this work, a mixed integer linear programming (MILP) model was developed in GAMS to investigate the optimal covid-19 supply chain network configuration under different vaccination strategies. The model sets, parameters and variables are summarized in supplementary information section.

Objective functions of the model:

$$min \sum_r \sum_t (DEFT_{rt} = D_r - \sum_p \sum_v PAPR_{vprt}) \qquad \text{Obj1}$$

The first objective function is to minimize the unsatisfied demand of vaccination in every recipient hospital. $DEFT_{RT}$ is a non-negative variable measuring deficit of daily vaccine demand D_r. When the overall vaccine deficit in all hospitals is minimized, the vaccine availability is maximized.

$$minCOST = CCM + CCWS + CCPS + CCRS + \sum_v CVWS_v + CVPS_v + CVRS_v + CVMT_v + TC_v \qquad \text{Obj2}$$

The second objective function is to minimize the total supply chain cost from manufacturing bulk vaccine substances to delivering packed vaccine doses to hospitals. The total cost includes CCM, the total capital cost of manufacturing facility, CCWS, CCPS, CCRS, the total capital cost of regional, local, and recipient storage respectively, and the sum of $CVWS_V$, $CVPS_V$, $CVRS_V$, the total variable cost of regional, local and recipient storage for each type of vaccines, and $CVMT_V$, TC_V which are total variable costs of manufacturing and transporting each vaccine.

$$minTTD = \sum_v TTA_v \; TTA_v = (TMI_v + TSW + TSP + TSR) \cdot \sum_p \sum_r \sum_t PAPR_{vprt} + \left(\sum_m \sum_w \sum_t PLMW_{vmwt} \cdot U1_{mw} + \sum_w \sum_p \sum_t PLWP_{vwpt} \cdot U2_{wp} + \sum_p \sum_r \sum_t PLPR_{vprt} \cdot U3_{pr}\right)/AS \qquad \text{Obj3}$$

The third objective is to minimize the TTD, the total time required for delivering all vaccines from manufacturing to hospitals, including the manufacturing time TMI_V, regional, local and recipient storage time (TSW, TSP, TSR) for every batch of vaccines arriving recipient locations ($PAPRV_{VPRT}$). The function also accounts for the exact distances travelled by vaccines between facilities at each level of the distribution network, $U1_{MW}$, $U2_{WP}$, $U3_{PR}$, which are then divided by AS, the average vehicle speed to calculate the total time spent during transportation. Optimization of this objective results in a network choosing the fastest route to deliver the vaccines.

In this work, a sequential optimization approach was adopted where the overall supply chain optimization was separated into sequential tasks. The first optimization is done to find the minimum deficit that can be achieved by the supply chain. Then, this value is plugged back as an additional constraint for minimizing total supply chain cost or total time to delivery, therefore both objectives can be optimized.

Model equality constraints:

Table 2. Cost Equations

$CCM = \sum_m E1_m \cdot CI_m$	E1
$CVMT_v = \sum_m \sum_t PINM_{vmt} \cdot CVM_m$	E2
$CCWS = \sum_w E2_w \cdot CIWS_w$	E3
$CVWS_v = \sum_w \sum_t TSW \cdot SCW_{vw} \cdot SW_{IN_{vwt}}$	E4
$CCPS = \sum_p E3_p \cdot CIPS_p$	E5
$CVPS_v = \sum_p \sum_t TSP \cdot SCP_{vp} \cdot SP_{IN_{vpt}}$	E6
$CCRS = \sum_r CIRS_r$	E7
$CVRS_v = \sum_r \sum_t TSR \cdot SCR_r \cdot SR_{IN_{vrt}}$	E8
$TC_v = 2 \cdot (\sum_{mwt} PLMW_{vmwt} \cdot U1_{mw} \cdot UTC + \sum_{wpt} PLWP_{vwpt} \cdot U2_{wp} \cdot UTC + \sum_{prt} PLPR_{vprt} \cdot U3_{pr} \cdot UTC)$	E9

It was assumed that manufacturing takes place centrally at AstraZeneca Macclesfield site. For Equation E1, E3, E5, the capital cost of manufacturing, regional, and local facility, CCM, CCWS, CCPS are incurred whenever there is a facility being established, which is indicated by the binary decision variables $E1_M$, $E2_W$, $E3_P$. The hospitals are already established and are potentially capable of storing the vaccines. The total variable costs ($CVMT_V$, $CVWS_V$, $CVPS_V$) are proportional to the quantity of vaccines through facilities (e.g.

$PINM_{VMT}$, $SWIN_{VWT}$, $SPIN_{VPT}$), multiplied by a unit variable manufacturing cost CVM_M or a unit storage cost (e.g. $TSW \cdot SCW_{VW}$).

The transport cost (TC_V) is calculated by multiplying total distance travelled to individual facilities by trucks with unit transport cost UTC (unit: \$ $km^{-1}dose^{-1}$). TC_V is also proportional to doses of vaccines delivered by trucks. In addition, the distance is counted twice in Equation 9 because total transport cost accounts for trucks departure and return trips.

Table 3. Mass Balance Equations

$PINM_{vmt} = SM_{OUT_{vmt+TMI}}$	$SW_{IN_{vwt}} = SW_{OUT_{vwt+TSW}}$	$SP_{IN_{vpt}} = SP_{OUT_{vpt+TSP}}$	E10
$PLMW_{vmwt} = PAMW_{vmwt+TT1}$	$PLWP_{vwpt} = PAWP_{vwpt+TT2}$	$PLPR_{vprt} = PAPR_{vprt+TT3}$	E11
$SW_{IN_{vwt}} = \sum_m PAMW_{vmwt}$	$SP_{IN_{vpt}} = \sum_w PAWP_{vwpt}$	$SR_{IN_{vrt}} = \sum_p PAPR_{vprt}$	E12
$SM_{OUT_{vmt}} = \sum_w PLMW_{vmwt}$	$SW_{OUT_{vwt}} = \sum_p PLWP_{vwpt}$	$SP_{OUT_{vpt}} = \sum_r PLPR_{vprt}$	E13

In Table 3, E10, $PINM_{VMT}$ implies the vaccine production schedule, i.e. the amount of vaccine products v ought to be produced in factory m at time point t. The inflow ($PINM_{vmt}$) and outflow of vaccines after a manufacturing lead time TMI ($SM_{OUTvmt+TMI}$) at manufacturing facility should be equal because of mass balance. In each storage facility, the inflow of products at time t must be equal to the outflow of vaccines at time t plus storage time. In addition, E11 the transportation balances indicate that the product leaving a facility to a lower tier facility at time t (e.g. $PLMW_{VMT}$) must equals the products arriving at the lower tier facility at time t plus a transport time ($PAMW_{VMT+TT1}$), for transportation between the national store and regional stores (TT1), between regional stores and local stores (TT2), and between local stores and recipients (TT3), respectively. For E12-13, vaccines inflow or outflow through a facility (e.g. SW_{IN}, SW_{OUT}) also equals the sum of vaccines arriving or leaving the facility (e.g. PAMW, PLWP).

Table 4. Capacity Equations

$CAPM_{mt} = E1_m \cdot TCAPM_m - \sum_{t-TMI}^{t-1} PINM_{vmt}$	E14
$CAPW_{wt} = E2_w \cdot TCAPW_w - \sum_{t-TSW}^{t-1} SW_{IN_{vwt}}$	E15
$CAPP_{pt} = E3_p \cdot TCAPP_p - \sum_{t-TSP}^{t-1} SP_{IN_{vpt}}$	E16
$CAPR_{rt} = E4_r \cdot TCAPR_r - \sum_{t-TSR}^{t-1} SR_{IN_{vrt}}$	E17

E14-17 depict the actual capacity of facility which is bounded by its corresponding total capacity and product flows. The continuous inflow of products would occupy part of the total capacity if the production batch/storage period is still in progress.

The optimization problem is also bounded by sets of inequality constraints. E18 depicts that product inflow cannot exceed the corresponding capacity of the facility. Constraint E19 and 21 depict that a match between facilities is only feasible when upper and lower level facilities are established, and product flows will only be established between existing facilities. E20 enforces the maximum and minimum product flows between established transportation connections. This is to prevent establishing transportation routes with extremely low/high throughput, and to enable efficient utilization of limited truck capacity.

Table 5. Model Inequality Constraints

$\sum_v PINM_{vmt} \le CAPM_{mt}, \sum_v SW_{IN_{vwt}} \le CAPW_{wt}, \sum_v SP_{IN_{vpt}} \le CAPP_{pt}, \sum_v SR_{IN_{vrt}} \le CAPR_{rt}$	E18
$X1_{mw} \le E1_m$, $X1_{mw} \le E2_w$, $X2_{wp} \le E2_w$, $X2_{wp} \le E3_p$, $X3_{pr} \le E3_p$, $X3_{pr} \le E4_r$	E19
$PLMW_{vmwt} \le S_{max} \cdot Y1_{vmwt}, PLWP_{vwpt} \le S_{max} \cdot Y2_{vwpt}, PLPR_{vprt} \le S_{max} \cdot Y3_{vprt}, PLMW_{vmwt} \ge S_{min} \cdot Y1_{vmwt}$, $PLWP_{vwpt} \ge S_{min} \cdot Y2_{vwpt}, PLPR_{vprt} \ge S_{min} \cdot Y3_{vprt}$	E20
$Y1_{vmwt} \le X1_{mw}, Y2_{vwpt} \le X2_{wp}, Y3_{vprt} \le X3_{pr}$	E21

The proposed MIP model was implemented in General Algebraic Modelling System (GAMS) version 32.2.0 and solved using CPLEX 12.10 solver.

3.3 Scenarios

Table 6 summarized all the scenarios simulated in this work, including variations on vaccine type, transport interval, local storage capacity and prioritization strategies. Scenarios are optimized with respect to vaccine availability, supply chain cost and total time to delivery.

Table 6. Scenarios summary

Scenario name	Vaccine	Transport interval	Storage capacity	Prioritization
Base Case	ChAdOx1	Daily	Standard	N/A
W1	ChAdOx1	Weekly	Standard	N/A
W2	ChAdOx1	Weekly	3.5× Standard	N/A
T1	ChAdOx1	Daily	Standard	1, 11*
T2	ChAdOx1	Daily	Standard	2, 10*
T3	ChAdOx1	Daily	Standard	3, 9*
T4	ChAdOx1	Daily	Standard	4, 8*
Multi-product	ChAdOx1 + BNT162b2	Daily	Standard	N/A

*Numbers represent the vaccination time for priority group and non-priority group within a year, unit in month.

4. Results

4.1 Base case analysis

In the base case scenario, a detailed study in storage capacity and budget was carried out under assumptions, considering ChAdOx1 vaccine as the only product available for supply. The base case introduces a vaccination strategy of an evenly distributed demand of COVID-19 vaccine assuming the entire vaccination program takes one year to complete. The vaccination is supposed to be done for all the populations above 18 years old in England, with each person demanding two doses. The total demand is aligned to 1200 existing hospitals and health care centres in England according to geographical population distribution and being clustered to 88 recipient location nodes. The model is running dynamically under a daily basis that transportations are made once per day, and the aim of this simulation is to find optimized capacities for each storage facilities in our proposed supply chain. After the first simulation with minimizing the vaccine deficit as the objective function, it is proven that the status-quo situation has sufficient capacity to operate the proposed vaccination strategy. On this basis, a sequential optimization is done to generate the fastest transportation strategies between echelons by minimizing the average time for each vaccine to delivery and cost of the overall supply chain system. At 100% availability of vaccines, the average capacities occupied in each local storage facilities are recorded and used in all other scenarios.

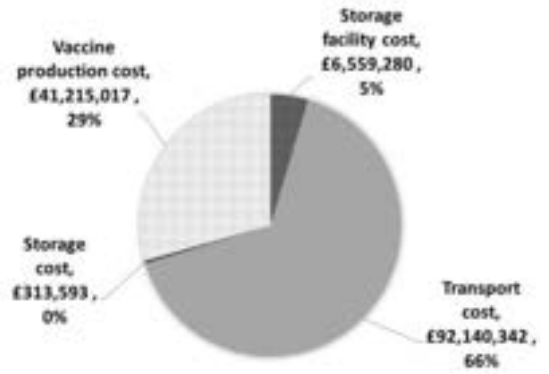

Figure 4. Cost composition of supply chain in base case, taken out manufacturing facility cost

At a total cost of $505,283,332.17 for operating the entire supply chain for a year, 72% is the fixed cost contributed by the annualized CapEx and OpEx for the newly implemented manufacturing facility for ChAdOx1 vaccine production. The composition of variable costings at optimized base case condition is shown in Figure 4, including production cost, inventory cost and distribution cost. As the cost of building the manufacturing facility is inevitable, it is suggested that a higher production capacity could lead to lower average manufacturing cost from economies of scale. More analysis is done from the storage and transport side in the supply chain. As Figure 4 shows, the contribution of each component of cost regardless of manufacturing facility cost demonstrates that transport cost should be the main consideration if we would like the total cost to be minimized. Vaccine production cost relates to the volume of raw material required; therefore, it is expected to be a fixed number in the case where 100% demand is met. On the other hand, the contributions of storage facility cost and electricity cost are very low, which will not be our main focus.

It is also worth notice that a few local storage facilities have optimized capacity of 0 which means that these facilities are not being utilized within the overall supply chain and can be removed. Although the local storage facility is designed to be at the centre of local government and counties, the model indicates that there would be very few demands in that local region and those demands could be addressed to another local facility nearby instead of using the proposed local facility. Moreover, shorter pathways exist between the echelons such that expected distributions are not selected in the case of cost minimization. Other results from the base case simulation including average distance travelled between the echelons and the total number of trips required are available for comparison in other scenarios.

The base case supply chain network benefits from its efficiently used storage capacities and 100% vaccine availability. Daily operations enable fast transportation between the nodes at shortest pathways such that the average lead time is reduced to a minimum of 6 days. Considering only one type of vaccine in the supply chain reduces the complexity of the distribution problem, which also benefits the health care worker from simpler operational procedures. In a view of overall supply chain management, the impact of human factor will be weakened if specialized training is conducted, and the risk of wastage and contamination could be minimized in this case as only one type of cold chain is utilized.

4.2 Transport interval

By changing the transportation interval from once per day to once per week, results have shown bottlenecks in storage facility capacities. Two scenarios are simulated to analyze the effect of changing the transport interval, where in scenario W1, same storage capacities from base case are used, and in scenario W2, local storage capacities are scaled up to 3.5 folds larger. As the minimum storage time in each node changes from 2 days to a week, the capacity needs to be magnified at the same ratio.

Results shown in Figure 5 indicate a fall in the vaccine availability from 100% to 21.4% and 74.1% as the transport interval is extended. The proposed vaccine demand could not be satisfied in either situation simulated in this section. For scenario W1, the restriction on local storage capacity limits the

number of vaccines delivered to recipient locations. The bottleneck is overcome in W2 by the magnification of local storage capacity, but still suffering from the limited capacity at its former echelon. The average distance travelled to deliver vaccines from manufacturing facility to regional stores is higher than that of in base case represents a cross-distribution due to the bottleneck. However, both scenarios have significant reductions in operational costs. Product cost is directly proportional to the quantity of vaccines produced therefore both scenarios require less budget in vaccine production, but it is not desirable in the case that government would like to vaccinate as many people as possible. A slight increase occurs in vaccine storage costs due to the extended storage time which leads to longer delivery time for vaccines. Transport costs have the most substantial difference because of the switch from daily to weekly transportation. There is a 13-fold reduction of transportation cost in scenario W1 comparing with the base case, partially attributes to the lower volume of product delivered, also because of the fewer number of trips needed for vaccine delivery.

In scenario W2, only a 2-fold reduction is observed as the availability rises. Because of the bottleneck on the existing capacity of regional storage facilities, the transportation will be done in a more tortuous way due to the shortage of inventory in several largely demanded regions like London. To satisfy the needs in those regions, transportation needs to be done from other regional stores to finally deliver to hospitals, and that longer travelling distance requires higher costs. Fewer number of trucks is required for transportation in a weekly basis, although the number is already in an acceptable range in the case of daily operation. Therefore, a trade-off has to be made between the cost of supply chain and the time for vaccines to be delivered.

The major issue in weekly transportation is that the model will have a slower response regarding fluctuations in demand to adjust the production. Demand forecast needs to be done at a longer time in advance which will be hard and uncertain. The supply deficit between the start of vaccine production and the time when recipient is vaccinated is also a drawback of this operation because earlier vaccination would have more positive externalities to the society. Governments would like to mitigate the pandemic at the fastest speed regardless of system costs, as pandemic-preventing measures like lockdown are causing an estimated loss of more than 1 billion pounds per day, even higher than the cost of building the entire supply chain (Islam, 2020). At a situation where costing is not a concern for UK government, strategies that enable faster vaccination is more preferred. In general, weekly transportation is favourable in the case that vaccine has a comparably long shelf life which does not require deliveries to be made within a half-month. However, to achieve a higher vaccine availability in real life, an upgrade of the existing cold chain is necessary to overcome the bottleneck at regional storage facilities in the case of weekly transportation. It is expected to see a more advantageous situation that both transport cost reduction and availability satisfaction could be optimized if the inventory shortage problem can be resolved.

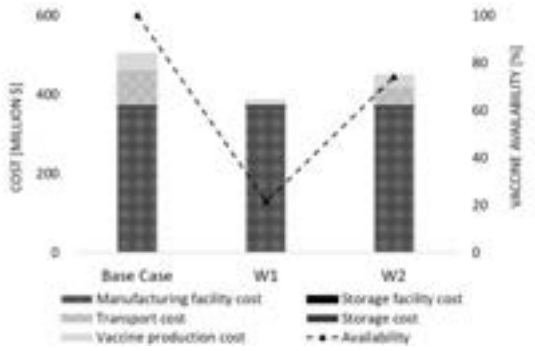

Figure 5. Cost compositions and availabilities in Base case, Scenario W1 and W2

4.3 Prioritizing vaccination strategies

To implement the vaccination plan at the highest return to the society, UK government has ranked nine priority groups for vaccination, advised by the Joint Committee on Vaccination and Immunization, aiming to give protection to high-risk citizens at the earliest stage (Gov.uk, 2020). Clear evidence suggested that risk of COVID-19 is correlated to age, and those over age of 65 years is considered to have the highest risk of severe illness. As one of the most important objectives for the vaccination program, minimizing the number of hospitalization and death can reduce extra burden on hospitals and preserve the functionality of the society. Therefore, in this study, the population is categorized into priority group and non-priority group, and time scales for vaccinating each group are assigned, respectively. Priority group includes health care workers and those over 65 years old, and non-priority group refers to the rest of the population. By separating the target groups, the vaccination progress can be visualized, and goals at each phase can be set for timely feedback. Meanwhile, efficiency in allocation of the resources can be improved and socioeconomic benefits are brought from this prioritizing immunization strategy (Hassan-Smith, Hanif and Khunti, 2020).

Using the age distribution at each geographical location, demands of vaccines were recalculated and addressed into our model. Four different vaccination strategies are considered, with the prioritized group being vaccinated within 1, 2, 3 or 4 months in phase I and the low priority group being vaccinated throughout the rest of the year, considered as phase II. This variation of time scales to vaccinate the priority group leads to fluctuation of demand and

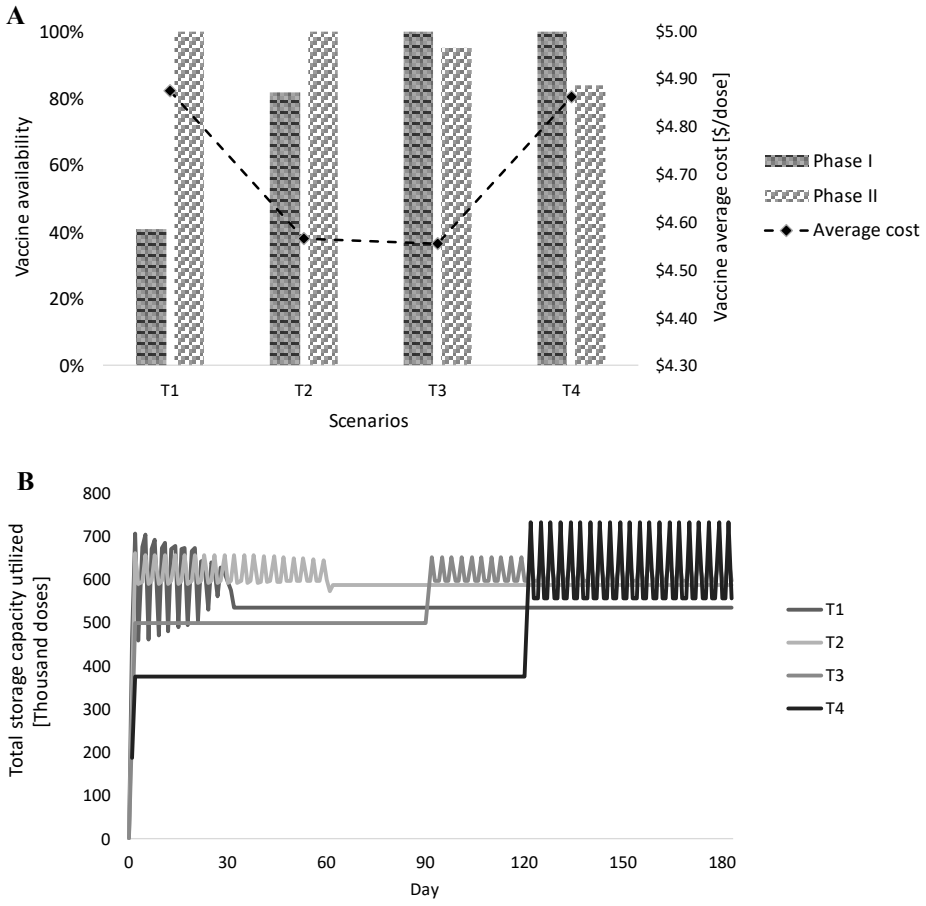

Figure 6. Supply chain results in different targeting vaccination scenarios T1 to T4. **(A),** vaccine availability and average vaccine cost in each scenario. Histogram shows the vaccine availabilities in phase I and phase II. Dotted line presents the change in average vaccine cost for delivery from T1 to T4, where optimum time for vaccinating priority group is between 2 months and 3 months. **(B),** total storage capacity occupied in local stores throughout the vaccination program T1 to T4 (only showing half of the year). Spikes denote that bottleneck exists at the vaccination period; sharper spikes indicate more serious bottleneck, for example, in phase I of T1 and phase II of T4

creates challenges for the resilience of supply chain. Ideally, it is beneficial to have an immunization program that even out the demand throughout the proposed period since less variation on demand could facilitate supply chain logistic stability. However, because of the difference in proportion of target groups in different regions, it is not feasible to control the constancy of demands. London has the lowest percentage of the population aged 65 years old and over, that is 11.3%, but in contrast, South West region has the highest of 21%. Thus, an urgent demand at phase I will lead to different shortages in vaccine inventory, and the purpose of simulations is to find the most feasible duration for vaccinating the prioritized group.

Result in Figure 6 A shows a robust supply chain structure that is capable of handling variation in demand between T2 and T3, with the best duration for phase I to be around 3 months (T3) where vaccine availabilities are considerably high in both phase I and phase II. The average cost for dispersing vaccine is also at the lowest. The requirement for phase I to be completed within 1 month restricted the vaccine availability in phase I to 41% due to the denser demand. A similar issue exists in T4 where availability in phase II is only 84%. As Figure 6B shows, the abrupt fluctuation in local storage capacities represent the barrier to achieve higher availability, and this barrier shifted from phase I to phase II between T2 and T3. From modelling results, it is found that bottlenecks exist at the local storage capacities in those counties and unitary authorities with larger proportion of old people. As the capacities are designed for normal vaccination without targeting different groups of population, the inventory shortage needs to be addressed if government decides to follow this vaccination strategy. Nonetheless, with different vaccine demands at phase II comparing with phase I, the capacity resources will be not used efficiently, provoking unavailing properties and additional operating costs. In general, vaccination strategy of targeting different population groups is an effective measure which is commonly used previously for influenza vaccines. To prevent deterioration of supply chain, schedule to shift between different phases needs to be determined prudently as more fluctuations of demand and vaccination phases will be considered in real-life.

4.4 Multi-products

To better capture the real-world activities in terms of vaccine development and approval, this scenario considers supply of MHRA recently authorized Pfizer/BioNTech's mRNA vaccine in combination with ChAdOx1 vaccine. It considers distribution of both vaccines within England but only ChAdOx1 being produced domestically. The BNT162b2 vaccines would be produced in Pfizer's Belgium manufacturing site and imported to England through air. Pfizer's manufacturing facility capital and operating cost are not included in the overall supply chain cost calculation since the production is outsourced overseas to Pfizer Belgium. Instead, the manufacturing cost is reflected in the vaccine procurement orders, with a 19.61$ per dose cost is assumed. Aforementioned assumptions of one-year vaccination plan and daily transportation remain unchanged. It is assumed that Pfizer/ BioNTech vaccines imported are stored in Pfizer tailored thermal shippers, which are capable of storing products under -70°C for 15 days. Therefore, the Pfizer vaccines will not be considered to occupy UK domestic storage capacity. Considering the lack of dry ice and ultra-low temperature freezer in the world, this scenario plans to vaccinate all priority group population (healthcare workers, 65+age population) in 3 months. With a protection rate of above 90%, the Pfizer vaccine roll-out could mitigate the high death rate among risk groups. After vaccinating high risk groups, we assume the ChAdOx1 vaccine would be approved in early 2021 and starts supplying the rest of the population in 9 months period. Based on Section 4.3 scenario T3, it is expected for ChAdOx1 vaccine supply in Phase II to experience a bottleneck at local store level. In this case, overseas supply of Pfizer vaccine is implemented as replenishments to address this bottleneck on local storage.

The supply chain cost per dose for both vaccines is shown in Figure 7 A. According to costing data mentioned in the Method section, the mRNA platform induces a significantly higher cost of vaccine substances than the adenoviral platform, therefore the supply chain decision is to choose ChAdOx1 vaccine whenever it is available. Although the supply chain cost of Pfizer vaccine is higher, it grants early availability of vaccines and enables fast vaccination of high priority groups. The majority of BNT162b2's supply chain cost incurred from overseas vaccine procurement, and notably its storage cost is higher than that for ChAdOx1. This could be explained by the far more stringent storage requirement for Pfizer's vaccine and the extra cost of dry ice replenishment. Ideally, this scenario could achieve 100% availability with a high protection rate on priority group population. It was further found that the sooner the ChAdOx1 vaccine is approved or authorized for emergency use, the lower the total supply chain cost would be. This is due to the lower

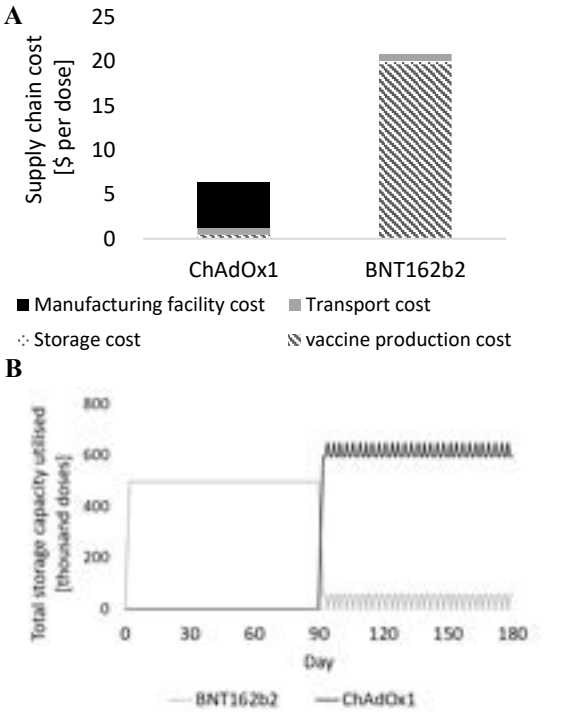

Figure 7. A, The total supply chain cost per dose for ChAdOx1 and BNT162b2 vaccine. **B**, The scenario considers Pfizer vaccine available and ChAdOx1 approved in 3 months (only half the year shown).

cost per dose of ChAdOx1 vaccine, and the economics of scale when producing more doses in the newly established manufacturing facility. In Figure 7 B, the total local storage capacity utilized for ChAdOx1 and BNT162b2 is shown. From previous study in scenario T3, a bottleneck is identified at local storage facility which restricted the vaccine availability in Phase II. In this case, scenario T3 can be improved with incorporation of Pfizer vaccine which satisfies the unmet demand from ChAdOx1, therefore achieving an overall vaccine availability of 100%. In general, although Pfizer vaccine has a much higher cost than ChAdOx1, the high efficacy and faster authorization accredits its use on high-risk groups at the earliest stage. After the approval of ChAdOx1, Pfizer vaccine could be an auxiliary to satisfy the demand during fluctuations or emergencies.

5. Conclusions

The research presented in this study outlined a model-based approach to optimize the COVID-19 vaccine supply chain network with respect to vaccine availability, total time to delivery and cost minimization objectives. Vaccine manufacturing and distribution activities were simulated in a MILP model, and data obtained was analyzed to identify any bottlenecks embedded in the proposed supply chain network. Manufacturing costs accounts for the dominant majority of overall supply chain cost. It was identified that the decrease of transportation frequency would result in bottlenecks at regional and local storage level. In case of prioritizing risk groups, the best performing scenario was T3 with

the highest vaccine availability and lowest variable cost. Introducing Pfizer's vaccine would result in higher supply chain cost but guarantee a higher vaccine availability. Further research should be carried out for Pfizer/BioNTech vaccine case to investigate the effect of overseas production and international air cargo uncertainties on vaccine delivery lead time. More data would be available in public domain as breakthroughs in ChAdOx1, Moderna as well as Imperial saRNA vaccine emerge. In addition, it would be worthwhile to conduct bottom-up data analysis regarding UK's local storage and hospitals capacities as well as introducing other promising vaccines into the supply chain network. With an expected expansion in total number of binary variables, the CPLEX solver would give a poorer performance, thus it is also necessary to explore new algorithms that could solve complex MIP problems.

Acknowledgements
The authors gratefully thank Dr. Dauda Ibrahim and Dr. Zoltán Kis (Imperial College London) for providing data, Wei Ooi, Rizqin Bin Rizal, Chen Tan and Thanat Wongwaisayawan (Imperial College London) for helpful discussion.

References

Arifoglu, K., Deo, S. and Iravani, S., 2012. Consumption Externality and Yield Uncertainty in the Influenza Vaccine Supply Chain: Interventions in Demand and Supply Sides. *SSRN Electronic Journal.*

Alistair Smout, E., 2020. UK Expects To Get 10 Million Doses Of Pfizer/Biontech Vaccine This Year. [online] Available at: <https://www.reuters.com/article/uk-health-coronavirus-vaccines-pfizer-br/uk-says-expects-to-receive-10-million-doses-of-pfizer-biontech-vaccine-this-year-idUKKBN27P1OT> [Accessed 13 December 2020].

Armstrong, M., 2020. Infographic: How Many Covid-19 Vaccine Doses Has The UK Secured?. [online] *Statista Infographics*. Available at: <https://www.statista.com/chart/23671/uk-procured-covid-vaccines-by-company/> [Accessed 5 December 2020].

Chick, S., Mamani, H. and Simchi-Levi, D., 2008. Supply Chain Coordination and Influenza Vaccination. *Operations Research*, 56(6), pp.1493-1506.

Hart, S., 2007. Immunisation Against Infectious Disease – Third edition. *Nursing Standard*, 21(35), pp.30-30.

Hassan-Smith, Z., Hanif, W. and Khunti, K., 2020. Who should be prioritised for COVID-19 vaccines? *The Lancet*, 396(10264), pp.1732-1733.

Islam, F., 2020. How Much Economic Damage Would A Circuit-Breaker Lockdown Do? [online] *BBC News*. Available at: <https://www.bbc.com/news/business-54543654> [Accessed 5 December 2020].

Pasandideh, S., Niaki, S. and Asadi, K., 2015. Optimizing a bi-objective multi-product multi-period three echelon supply chain network with warehouse reliability. *Expert Systems with Applications*, 42(5), pp.2615-2623.

Pfizer, 2020. Pfizer And Biontech To Submit Emergency Use Authorization Request Today To The U.S. FDA For COVID-19 Vaccine | *Pfizer*. [online] Available at: <https://www.pfizer.com/news/press-release/press-release-detail/pfizer-and-biontech-submit-emergency-use-authorization> [Accessed 5 December 2020].

Pfizer, 2020. COVID-19 Vaccine U.S. Distribution Fact Sheet | Pfizer. [online] Available at: <https://www.pfizer.com/news/hot-topics/covid_19_vaccine_u_s_distribution_fact_sheet> [Accessed 15 December 2020].

Gov.uk. 2020. Provisional Guidance Subject To MHRA Approval Of Each Vaccine. [online] *Gov. UK* Available at: <https://assets.publishing.service.gov.uk/government/uploads/system/uploads/attachment_data/file/943663/Greenbook_chapter_14a_v3.pdf> [Accessed 5 December 2020].

Ramirez-Nafarrate, A., Lyon, J., Fowler, J. and Araz, O., 2015. Point-of-Dispensing Location and Capacity Optimization via a Decision Support System. *Production and Operations Management*, 24(8), pp.1311-1328.

Mullin, G., 2020. Pfizer Covid vaccine could cost UK taxpayer £600million – ten times more than Oxford jab. [online] *The Sun*. Available at: https://www.thesun.co.uk/news/13169692/pfizer-covid-vaccine-cost-uk-600million-ten-oxford-jab/> [Accessed 5 December 2020].

Shrestha, S., Wallace, G. and Meltzer, M., 2010. Modeling the national pediatric vaccine stockpile: Supply shortages, health impacts and cost consequences. *Vaccine*, 28(38), pp.6318-6332.

Automatic Tuning of Adaptive PID Controllers using an Artificial Neural Network

Soleiman N. Anwary, Charles W. Rigby
Department of Process Systems Engineering, Imperial College London
{sna314, cwr17}@imperial.ac.uk

Abstract

— Process control is an integral part of any process system. It is present anywhere from large scale production processes to applications in robotic devices. Specifically, we are interested in systematic control of bioprocesses due to their presence in sustainable generation of fossil-fuel alternatives. These systems are highly non-linear and display stochastic behaviour which is not easily modelled, creating a disparity in the plant-wide dynamics and model dynamics [1]. In this paper we investigate a black-box optimisation method through the use of a surrogate model to approximate the system dynamics and tune PID controller parameters through a gradient descent optimisation algorithm. We show that PID tuning parameters can be optimised for linear and non-linear systems without the intervention of manual tuning methodologies such as Ziegler-Nichols or Cohen-Coon. We extended this concept to multiple linked controllers. In this case the surrogate model allowed communication between the PID controller nodes in the artificial neural network created. This multiple input and multiple output (MIMO) model is able to optimise PID controls for two different states of a system to various set point values for linear and non-linear systems so they reach stability at a steady state value given controllable system dynamics.

Key words: Black-box, artificial neural network, process control, PID, tuning, control, surrogate model, deep reinforcement learning, Q-learning, reinforcement learning, MIMO, optimisation

I. Introduction & Motivation

The topic of research considered in this paper covers a wide range of disciplines including process control, optimal control, black-box optimisation (BBO) and machine learning. Process feedback control dates back all the way to the third century BC. During this period Ktesibios of Alexandria employed a float valve to regulate the level in the water clocks used at that time [2]. Over the course of the subsequent centuries there was some development in process control, but it was not until the industrial revolution that process control became widely utilised. The digital revolution coupled with the work of Russian American scientist Nicolas Minorsky on a formal control law (today known as PID control) [3] allowed for the development of modern computational control technologies which are used almost universally today in all process systems.

Optimal control theory attempts to find a control law for a dynamical system that enables the system to optimally respond to changes and disturbances. Ensuring optimal control is not straightforward and historically a large amount of effort has gone into designing approaches to solve this problem. Many of the systems that arise in chemical engineering problems are non-linear in nature [4]. This poses a problem when considering the control of such systems, as there may not be an easily tractable analytical expression that describes their responses to variations in the operating conditions. In this paper we aimed to address this problem by producing an algorithm which can find the optimal PID parameters to control a black-box system which is, by definition, a priori unknown.

BBO methods are used in machine learning to find the minimum value of a real valued function that has no readily available analytical form. There are a wide variety of different BBO methods available including Genetic algorithms [5] and Particle Swarm algorithms [6].

The problem that we attempt to solve in the research paper can be described in its simplest form as follows: *how can the optimum parameters to tune a PID controller for a black-box process system be found in an automated and systematic way?* This is a vital problem to solve because an effectively tuned controller can provide a myriad of benefits in the operation of a process system. These benefits include but are not limited to ensuring product quality is maintained during operation by minimising the effects of process disturbances, establishing and maintaining process safety during operation and mitigating the effects of process start-up and shutdown. As the demands on the process industries grow over the coming years to serve an ever growing and increasingly affluent population, more energy and product wastage will occur in absolute terms. This highlights the importance of effective controller operation, and by extension controller tuning, as even small margins of unnecessary loss projected across time can lead to large unrealised profits for companies.

Methods such as Ziegler-Nichols [7] and Cohen-Coon tuning [8] have been traditionally used to tune process controllers. Today these methods are antiquated as they are time consuming and the controller parameters produced are generally not optimal. Currently in industry control engineers are increasingly

turning to computational methods to optimise their control systems. A significant number of these methods rely on a knowledge of the physical system which for chemical engineering applications is generally unrealistic as the processes are highly complex in nature. An example of a highly complex system that may benefit from BBO methods outside of chemical engineering is a neural network-based self-tuning PID controller for underwater vehicles [9]. Black-box optimisation methods can be exploited to provide a solution to this problem. In this research project we have considered a polynomial regression algorithm which approximates the true function by fitting a convex surrogate function. We can then apply a derivative based gradient descent to the surrogate function to arrive at the optimum point. To determine the effectiveness of this method requires us to consider the ease of implementation, the robustness of the method as well as how the dynamic system response is evaluated for the optimum tuning parameters.

The objectives of this research are primarily to have a robust algorithm which can be applied to determine the optimal control parameters for a wide range of systems. To do this we will consider a description of the proposed algorithm, an evaluation of the algorithmic solution and a discussion of its performance and finally considerations about potential future improvements.

II. Methods

We will now define explicitly, the exact form of the control system we used and how we set up the optimisation problem. We will then walk the reader through our algorithm which provides a solution to the problem for the single input single output case. Having arrived at a satisfactory solution for the preceding case we then consider the problem of multiple coupled controllers and how we can extend the functionality of the algorithm to tune both controllers simultaneously.

A. The Control System

Figure 1. is a representation of the feedback control loop. The value x_{ref} is the set point desired for the process variable x. The difference between the set point and the process variable gives the error signal which is passed into the PID feedback controller which evaluates the error producing a controller response u. The controller response u then passes into the black-box system which determines a new value for the process variable x. The value of the error is then recalculated and the process repeats. If the PID controller is tuned correctly the error signal should decay over time and ideally reach a steady state value of *zero*. The controller response u is determined using the following equation,

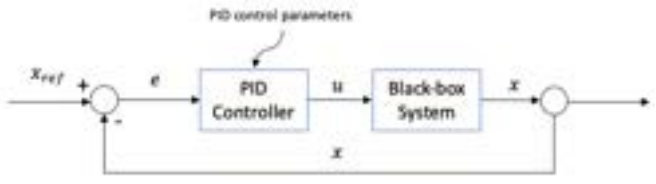

Fig. 1. PID controller feedback loop diagram for a black-box system.

$$u = \overbrace{k_p e(t)}^{\text{P}} + \overbrace{k_i \int_0^{\tau} e(\tau)d\tau}^{\text{I}} + \overbrace{k_d \frac{d}{dt} e(t)}^{\text{D}}. \quad (1)$$

Where P, I and D correspond to the proportional, integral and derivative terms respectively. The coefficients k_p, k_i and k_d are the tuning parameters as these are the values which can be changed to tune the controller response u for a given error. The black-box system shown in Figure 1. is the process system which we wish to tune. In reality we would perform experiments on this system to collect data about the system's dynamic response for a given step change and tuning parameters, $\mathbf{k} = [k_p, k_i, k_d]$. However, as this research is aimed at designing an algorithm to tune a wide variety of process systems, we instead simply define equations giving the change in the process variable for a given value of the process variable and a given controller response u. This allows us to test our algorithm on different systems, which is the main focus of this research. To ensure that the algorithm can tune the PID parameters for a wide variety of systems we used equations with both linear and non-linear dynamics for testing of the algorithm performance,

$$\dot{x} = 2x + u \text{ and } \dot{x} = x^2 + u. \quad (2)$$

B. The Optimisation Problem

The decision variables for the optimisation problem are the values of, $\mathbf{k} = [k_p, k_i, k_d]$. The different values for $\mathbf{k}$ give different dynamic responses for the control loop for a given black-box system. To determine which dynamic response is the best we define an objective cost function ϕ. This function must minimise the total error over time and penalise large controller response values to ensure the response is smooth. The form of the objective function we arrive at is the following,

$$\phi(x) = \sum_{i=0}^{N} (x_{ref} - x)_i^2 + p \sum_{i=0}^{N} u_i^2. \quad (3)$$

Where the first term is the square error summed over N discrete time steps and the second term in the equation is the square of the controller response multiplied by a penalty coefficient p. The second term is not essential for the minimisation, but it will help add greater curvature to the approximation of the function ϕ which becomes important for visualisation later. The greater the value of the penalty coefficient p the greater the added curvature. For our purposes we determined that $p = 2$ was sufficient.

C. The Algorithm

In this section we describe the steps the algorithm takes to find the value for the optimal control parameters $\mathbf{k}^*$. Please refer to Figure 2. for more details on the mechanics. The first step the algorithm takes is to define upper and lower bounds for the values of the control parameter $\mathbf{k}$. The lower bound on the parameter values is *zero* due to the way the control response function is defined. This means that if we define a 3D space for the possible values of k_p, k_i and k_d, with each dimension corresponding to a control parameter, that the space

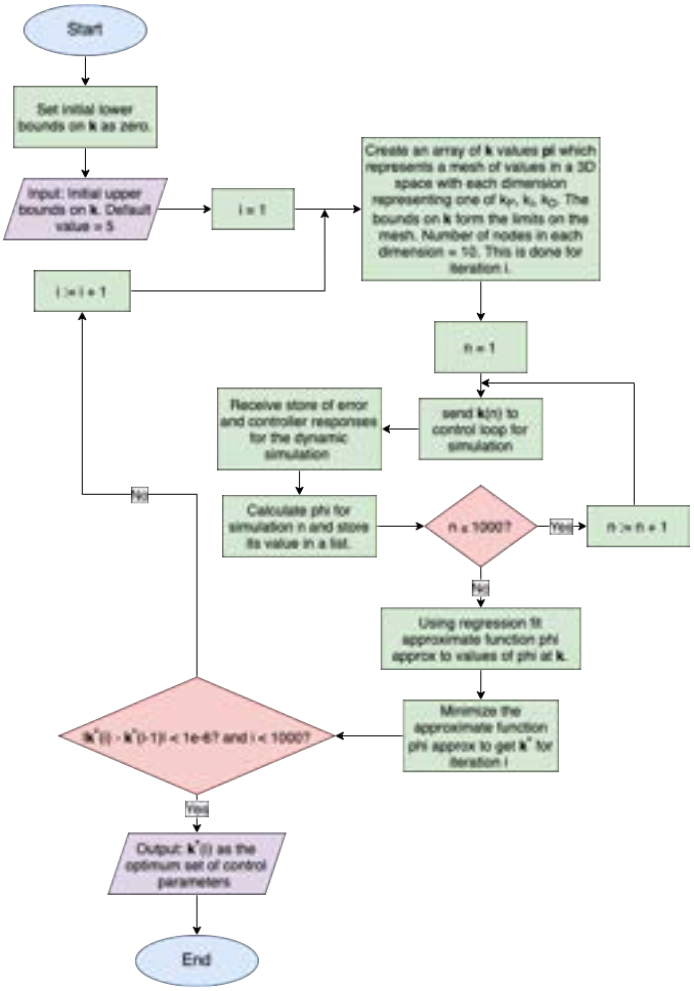

Fig. 2. Algorithm flowchart for the black-box optimisation model.

is restricted to the positive octant of the 3D region. The upper bound on the control parameters is defined such that an initial mesh of values can be produced in the 3D space. Note that the upper and lower bound values will be redefined as the algorithm iterates so it is not imperative that the upper bound constrains the problem such that the optimum value is in the initial region. The bounds are adjusted such that, if the optimal $\mathbf{k}^*$ generated is less than the bound size then the algorithm sets the lower bound to *zero* and expands the upper bound by the new bound size. This enforces the non-negativity constraint on $\mathbf{k}$ while generating a new sample space.

Once the bounds have been established for $\mathbf{k}$ the algorithm creates a low-resolution mesh of points within the 3D space defined by the bounds. Each point or node in the space defines a unique combination of k_p, k_i and k_d. The algorithm uses the number of points on each axis between the bounds as 10. The algorithm then performs a dynamic simulation for each node using the defined control system. For each simulation the value of the objective function is evaluated. Therefore, for every node in the 3D space we have a value for the objective function ϕ.

To perform a dynamical simulation the algorithm defines a total time for the dynamical simulation T and a discrete number of steps N. The simulation then proceeds by determining the initial value for the error, e_0, and storing it. The error is then passed into the controller which evaluates the controller response function as described earlier for $t = 0$ giving a value u_0 which is then stored. The black-box function is then used to evaluate a new value of x at time Dt, where $Dt = T/N$. This new value of x is used to calculate a new value for the error, which is again stored and the process loops until time equals T. The store of error and controller response values at the end of the simulation is used to calculate the value of ϕ for that simulation. As discrete time is used for the simulations a discrete version of the controller response function is used which is defined below,

$$u_n = k_p e_n + k_i \sum_{i=0}^{N} e_i + k_d \frac{e_n - e_{n-1}}{Dt}. \tag{4}$$

We can now use a regression technique to fit an approximate or surrogate function to the values of ϕ in the space. The method we use is the sequential least squares programming method from minimize in the scipy.optimize package. The approximate function we fit, ϕ_{approx}, is a convex quadratic function of the following form,

$$\phi_{approx}(k_p, k_i, k_d) = \mathbf{k} \cdot Q \cdot \mathbf{k}^T + \mathbf{c} \cdot \mathbf{k}^T, \tag{5}$$

Where,

$$\mathbf{c} = [c_1, c_2, c_3] \text{ and } Q = \begin{bmatrix} Q_1 & 0 & 0 \\ 0 & Q_2 & 0 \\ 0 & 0 & Q_3 \end{bmatrix}. \tag{6}$$

The parameters that we use to fit ϕ to ϕ_{approx} are the $\mathbf{c}$ and Q values. The reason that the off-diagonal terms in Q are zero is such that the approximate function retains its convexity and remains easily solvable to its global minimum. Once we have an analytical expression for ϕ_{approx} we can then minimise this function, again using minimize from scipy.optimize, to get the optimum values for $\mathbf{k}$ for the first iteration. With the optimum $\mathbf{k_1}^*$ values we can reset and tighten the bounds around $\mathbf{k}$ by a factor of 0.9 while preventing the bounds from going negative. With the new values for the bounds, we can define a tighter mesh in the positive octant with the same number of nodes as before. We then iterate the entire process until the optimum $\mathbf{k}^*$ values converge. The reason we set up the algorithm to iterate in this way is because each dynamic simulation for each unique value of $\mathbf{k}$ is computationally demanding and therefore, we want to minimise the required number of simulations to get to the optimum $\mathbf{k}^*$. In order to minimise the number of dynamic simulations we have the number of points on each axis, as specified earlier, as 10. This gives enough information to fit the approximate function to ϕ with a reasonable degree of accuracy. However, the accuracy of the fit is not high enough for us to conclude that the optimum $\mathbf{k}^* \approx \mathbf{k}^*_{approx}$ on the first iteration. Therefore, we must iteratively reduce the bounds, for the same number of points on each axis. This ensures as the number of iterations increases the resolution also increases

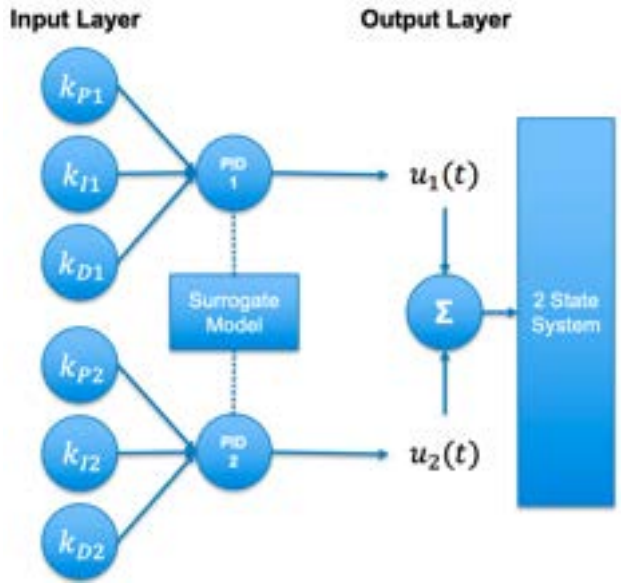

Fig. 3. High level view of the artificial neural network architecture for the multi input multi output control system algorithm.

eventually allowing us to approximate $\mathbf{k}^* \approx \mathbf{k}^*_{\mathbf{approx}}$ for a sufficient number of iterations.

D. Coupled Controllers with Multiple Inputs and Multiple Outputs (MIMO)

In a real process system, there will likely be cases where two or more controllers will be coupled. This means that it may be the case that the controllers act antagonistically and when the tuning parameters for one controller are optimised the other controllers may not be able to operate optimally. This is the problem of multiple input multiple output (MIMO) controller optimisation.

To extend our algorithm to the MIMO case we developed an artificial neural network, Figure 3, in which the two controllers tested were linked with a surrogate model function. The surrogate model function is the same form as Equation 6, where now $\mathbf{c}$ is a 1×6 vector and Q is a 6×6 diagonal matrix with off-diagonal elements equal to zero and diagonal elements Q_1 to Q_6.The objective function was ϕ_M, which was the sum of the square error signals from each controller over the simulation

$$\phi_M(x) = \sum_{i=0}^{N} (x_{ref,1} - x_1)_i^2 + (x_{ref,2} - x_2)_i^2. \tag{7}$$

In this research we were only able to test two controllers due to computational limitations caused by dimensionality issues. However, the functionality of the algorithm could easily be extended to n controllers given appropriate computational power. In the MIMO case we used the following equations to test two linked PID controllers and to evaluate the algorithms effectiveness. These equations are as follows,

$$\dot{x_1} = 2x_1 + x_2 + 2u_1 - u_2 \tag{8}$$

$$\dot{x_2} = x_1 + 2x_2 - 2u_1 + 2u_2. \tag{9}$$

III. Mathematical & Computational Aspects

We are addressing the problem of tuning parameter optimisation using a surrogate machine learning model. We are using a quadratic approximation to the actual dynamics of the system. For this problem to be solvable the surrogate model has to be convex and all the constraints must also be convex such that the problem overall is convex.

Definition III.1. *A function f: $\mathbb{R}^n \to \mathbb{R}$ is convex if and only if its domain is a convex set $\forall\ x, y \in \mathbb{R}^n$ and all $\lambda \in [0, 1]$*

$$f(\lambda x + (1-\lambda)y) \leq \lambda f(x) + (1-\lambda) f(y). \tag{10}$$

A multivariate quadratic function such as the surrogate model in Equation 5. is convex if and only if $Q \succcurlyeq 0$. This is important because it means that the quadratic coefficients of the surrogate model have to be constrained to non-negative values. So by defining Q to be a symmetric matrix and the constraining the quadratic term coefficients to be non-negative we ensure all eigenvalues of the matrix are positive and as such the matrix Q is positive semi-definite which keeps the optimisation problem convex. Most importantly, a convex system means any local minimum found is also a global minimum.

Another important concept in this project is controllability. For our algorithm to function the system must be inherently controllable to reach a steady state value.

Definition III.2. *A linear time-invariant system is controllable if and only if there exists an input function $\mathbf{u}(\mathbf{t})$ such that the system state goes from $\mathbf{x}(0) = 0$ to $\mathbf{x}(T) = \mathbf{x}^*$ for every $\mathbf{x}^*(t)$ where $0 < t < T$.*

More simply, for linear dynamical system, if the controllability matrix has full rank then the system is controllable [10], [11]. This is more complex for non-linear systems as they have to be first simplified through linearisation and then check controllability in small local time and also big global time [12].

IV. Results & Discussion

A. Optimisation of a 2D Control System

When optimising a control system we first have to segment the problem. The majority of dynamic systems are controllable using a P and I control system [13]. With this in mind, we pose the hypothesis: the algorithm should come to the conclusion that the majority of systems tested are PI-controllable. Indeed what we observed was that both linear and non-linear system dynamics were controllable and converged onto a set point. A number of set points were used to test model robustness and in each case the model presented a converging system

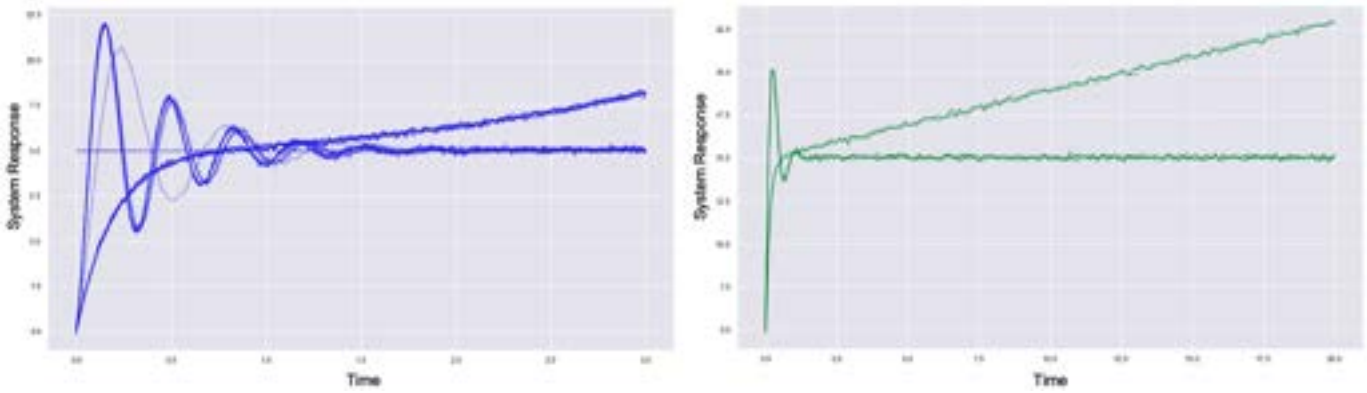

Fig. 4. The system responses shown are for the 2D case where we optimised only the tuning parameters k_p and k_i. The above two graphs show the system response history for each iteration that the algorithm runs for a linear (blue) and a non-linear (green) system, respectively. The system was run 40 iterations and samples at every 10^{th} iteration. We observe system stability being reached for each experiment.

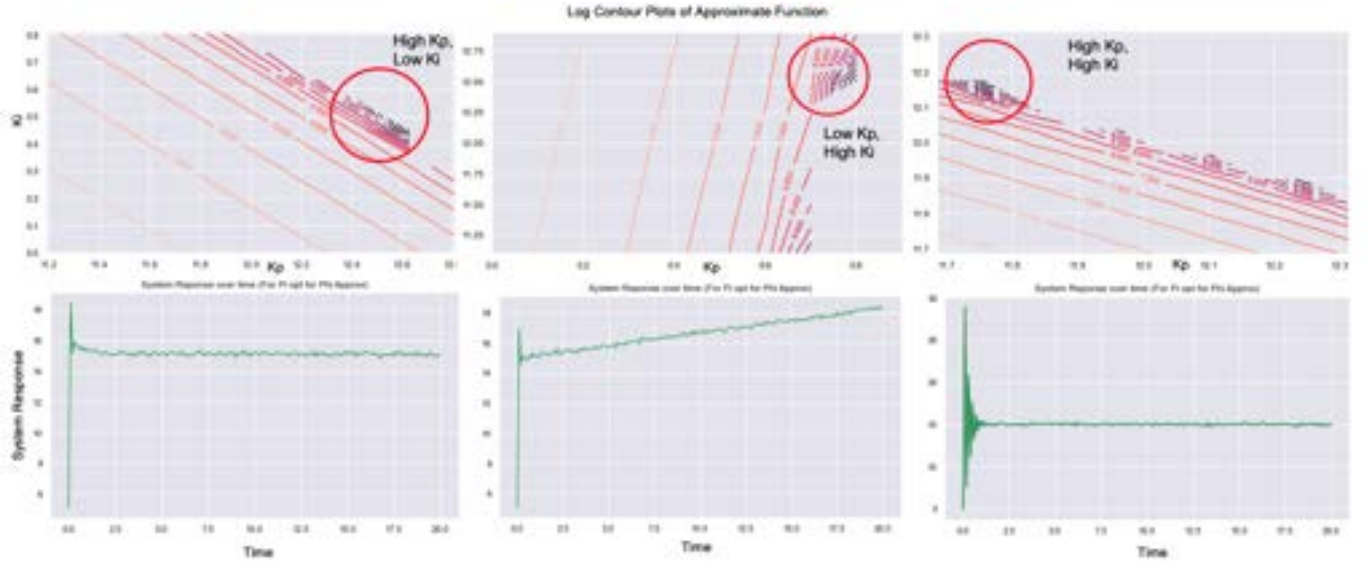

Fig. 5. The above figure shows log contour plots of the approximate function ϕ_{approx} for 3 different scenarios from left to right: a) system convergence, b) system divergence and c) oscillatory system response with convergence. Regions where the surrogate function estimates a minimum we see greater curvature and these regions are highlighted with a red circle and a corresponding annotation about the value of the tuning parameters. The experiments were conducted over linear system dynamics.

response. We can see Figure 4. shows system responses for the optimal set of tuning parameters, k_p and k_i as determined by the surrogate model optimisation. Several iterations of the model were plotted on the same axis to show how the algorithm parses through the mesh of tuning parameters generated. The darker lines represent later iterations and the latest updates to the optimal response. Equations (2) were used as benchmark dynamic systems to test the model performance. It is important to note the algorithm is designed to work on unknown system dynamics; the outputs of the system would be gathered and fed into the algorithm as an input. This would be used by the model to fit an approximate surrogate function and find the optimal tuning parameters. The cost function ϕ is evaluated at each iteration and plotted over the parameter vector space to visualise the surface. We do this in a 3D plot of k_p against k_i and ϕ in Figure 7. The value of ϕ is broken into percentiles and categorised in the plot using a continuous colour scale. It can be seen the cost function ϕ predicts the optimal value of $\mathbf{k}$ to be in the region with low k_i and high k_p values. The sample space in the parameter mesh is cubic and this is seen in the plot. The surrogate function ϕ_{approx} predicts the optimal $\mathbf{k}$ to be at $(5, 5)$. This is not completely consistent with what the cost function predicts. This may be because the surrogate model is sampled far more around that point and as such a greater weight is given for that set of values as the optimum $\mathbf{k}$. A higher density plot of ϕ was generated to test this and indeed the optimum predicted by the surrogate function moved closer to the darker red region where ϕ is minimised. Furthermore, while low values of the integral term are preferred - which controls how smooth the system response is - a *zero* value for k_i is not. Without any integral action the system response starts oscillating and often results in a steady state error. We

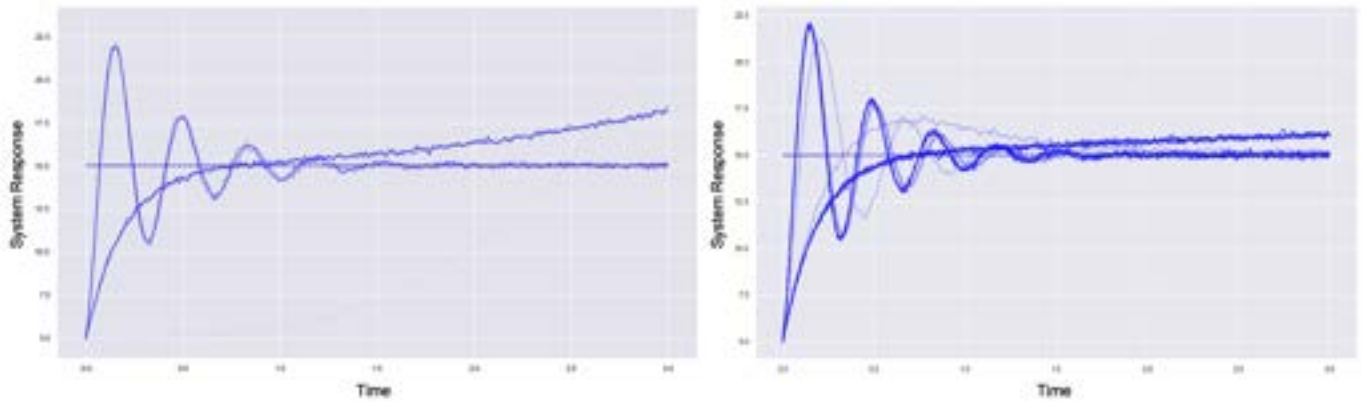

Fig. 6. The system responses shown are for the 3D case where we optimised the tuning parameters k_p, k_i and k_d. The above two graphs show the system response history for each iteration that the algorithm runs for a linear (blue) and a non-linear (green) system, respectively. The system was run 40 iterations and samples at every 10^{th} iteration. We observe system stability being reached at the steady state value of 15 for each experiment.

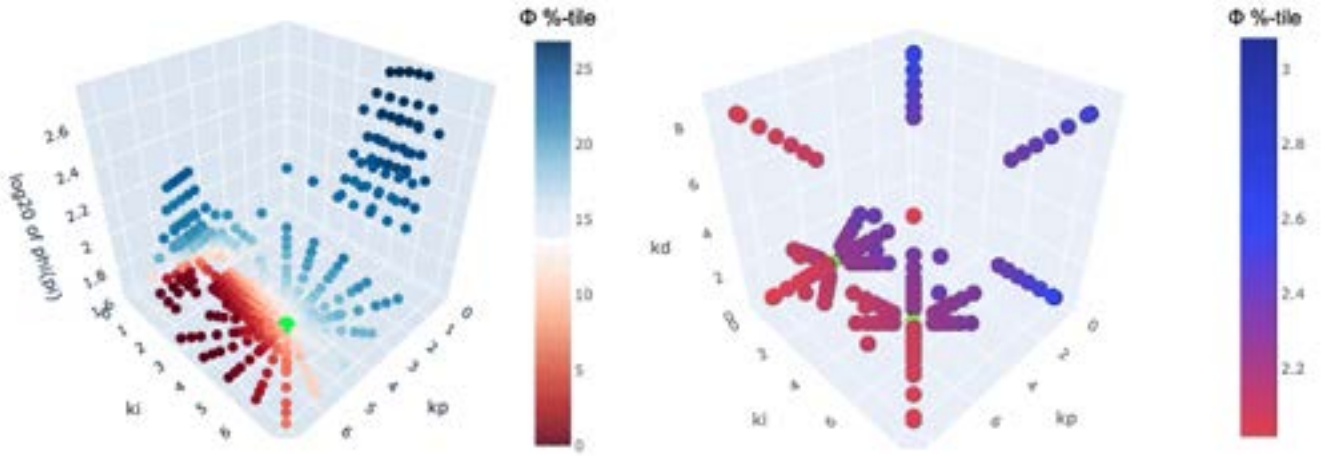

Fig. 7. a) The left 3D plot shows the behaviour of the cost function ϕ over the vector space of the tuning parameters for 20 iterations with a 10 samples per tuning parameter; this is specifically for the 2D optimisation of k_p and k_i only. The colour scale indicates the log value of ϕ as a percentile rank. The more red the points are, the closer the function is to *zero*. The green represents the optimum as determined by the surrogate model for this experiment. b) This is a 4D plot of the behaviour of ϕ function over the 3D vector space for k_p, k_i and k_d with the 4^{th} dimension being the log value of ϕ ranked as a percentile and visualised as colour. The colour scale is provided. The green dots represent where the approximate function places the optimum across 2 different iterations.

therefore suggest that a PI-control system is sufficient for most linear and non-linear systems with first order dynamics.

B. ϕ_{approx} vs. ϕ fit

We investigated the agreement between the surrogate function ϕ_{approx} and the cost function ϕ in Figure 5. and 7. Comparing the contours to the 3D scatter plot for ϕ in Figure 5. shows us that there is a large flat region before the surface shows curvature. This is seen in the contour plots. More specifically, there are three cases which were isolated for analysis: a) system convergence, b) divergence and c) fast oscillatory system response. In case a) we can see that the contour starts curving to a minimum which is in a region with a high k_p and low (and non-zero) k_i value. This is consistent with the predictions from the cost function alone. We can see the system reaches a steady state set point value preset at 15 for this experiment. Case b) presents a case where the contour is approaching a point which is in a region with low k_p and high k_i. It is clear that when the proportional gain is not large enough the system is not only slow to respond (large rise time) it is also unable to reach a steady state value and therefore stability. The final case is the last iteration of the experiment and shows that a possible system response is one with both k_p and k_i at the boundary of the active constraints set; here we observe large initial overshoot and initial oscillations which are brought about by the larger integral term compared to the other two cases.

C. Optimisation of a 3D Control System

We extended the PI-control parameter optimisation to the 3D case by also considering a derivative term, k_d. Figure 6. shows various system dynamics and how the model handled the optimisation to achieve a steady state system response for both linear and non-linear system dynamics. Once again we used several set point values to test the model and system

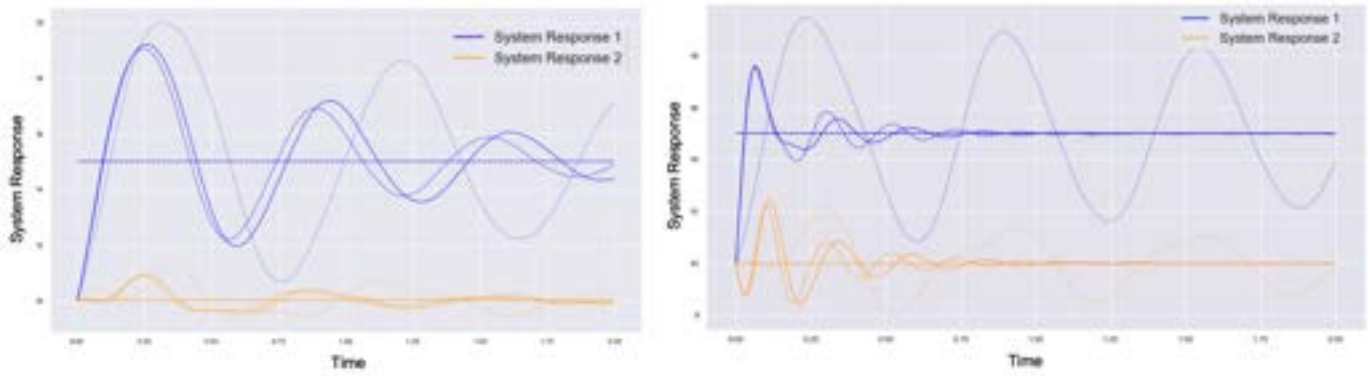

Fig. 8. The above shows the response curves for the MIMO system. The left graph is the response for the linear dynamic system and the right one is the graph for the non-linear dynamic system. We observe the history of the model as it iterates through various values of $\mathbf{k}$ to find the optimum.The orange and blue lines represent two different system states, each being controlled to a unique reference set point ($x_{ref,1} = 15$ and $x_{ref,2} = 10$). The simulations were carried out over 40 iterations with responses plotted at every 10^{th} iteration.

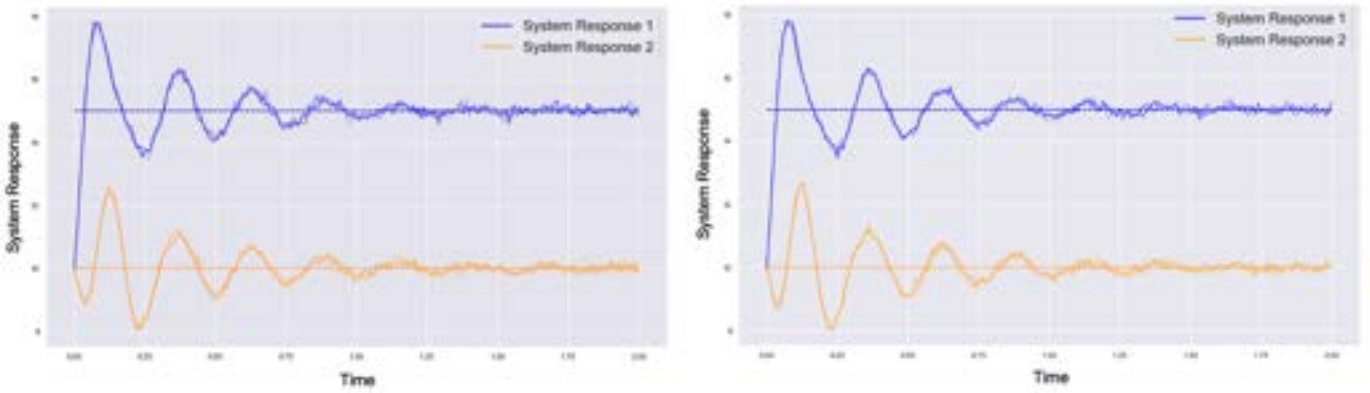

Fig. 9. The left graph is the MIMO response for the two different system states with added disturbance to the agent environment and noise to the controller. These graphs are plotted for the optimum $\mathbf{k}^*$ value. The responses were plotted for the same linear (left plot) and non-linear (right plot) systems as Figure 8.

response convergence. All tests showed the model successfully corrected for the step input error and brought the system back to the set point. There are several values of $\mathbf{k}$ which led to a sub-optimal response where the system slowly diverged from the set point. However, the last batch of iterations show that the most intensely coloured blue lines belong to the group of $\mathbf{k}$ solutions which yield a steady state system response. It was also important to understand how the cost function behaved across the parameter space. Figure 7. shows a 4D plot of the parameters k_p, k_i, k_d and the value of ϕ normalised as a percentile as the 4^{th} dimension which is shown as colour in this instance. We can see that once again a high value of k_p and low but non-zero values of k_i are preferred by the model for linear and simple non-linear dynamics. The parameter k_d is often very close to or is in fact *zero*. This reinforces the model's PI-control preference; it suggests that a proportional gain and a small integral error correction mode are sufficient to control most systems effectively. Furthermore, the surrogate approximate function ϕ_{approx} attempts to find optimal values for $\mathbf{k}$ in the region where the derivative term is zero, and the proportional and integral terms are equal because the model samples heavily in that region. This suggests that there is a compromise that has to be achieved for the surrogate model. It can either try to approximate the system dynamics in small local spaces which would improve the fit between ϕ and ϕ_{approx} or it can approximate the dynamics globally which means that ϕ_{approx} cannot be accurate across the whole domain. The model is designed to be memoryless - upon each iteration the model does not retain any state space variables describing the system or the tuning parameters which were used in the previous iteration prior to bound reduction. As a result, the approximate surrogate function inherently will not be able to approximate the system dynamics equally well over the entire space.

D. Multiple Input Multiple Output Control System (MIMO)

When designing the control algorithm it was important to consider use-case scenarios for its application. One such use-case is in biochemical processes. Biochemical processes utilise biological micro-organisms to produce chemical derivatives and high-value products otherwise too complicated to obtain through physical chemical modes. However, the complex interactions between the substrates in metabolic pathways and the culture fluid dynamics makes bioprocess control particu-

larly challenging to control [1]. System-wide or plant model dynamics cannot meaningfully be obtained for such processes and as such they must be treated as black-box models. Often there are multiple controlled variables such as pH, feed stock concentration, product concentration, temperature, pressure and flow rate. Many of these parameters are dependant on each other and as such a control system allowing communication between multiple controllers, which correct related system states is important. As such we have developed an artificial neural network (ANN) for multiple controllers which are linked to each other by a surrogate model function - in this case ϕ_{approx}. This surrogate model will allow the controllers to communicate and coordinate on the optimisation of the tuning parameters to reach system stability at a steady state value. A diagram is shown in Figure 3. The tuning parameters make up the weights of each distinct error term in the input layer, allowing the controllers to generate control functions as the output. With that in mind we tested the extended model on two controllers and applied it to both linear and non-linear systems as seen in equations (8) and (9). Figure 8. shows both system dynamics were brought to stability using the optimised tuning parameters. The history of how the model reached the optimal system response is shown. Upon addition of disturbance to the environment and noise to the controllers we optimised the tuning parameters and achieved stability at steady state for both the linear and non-linear system as is shown in Figure 9. This model can be, in theory, tested for n number of controllers and the optimisation algorithm will coordinate the controllers since the optimiser adjusts the weights of the proportional, integral and derivative terms for all controllers simultaneously. This makes the surrogate function a communication pathway to reach a globally optimal solution while exerting control on all system state variables.

V. Limitations & Complexities

1) Stochasticity: When developing this black-box optimisation model we added disturbance and noise to the system environment and control system itself, respectively. This was done to test the robustness of the algorithm to sudden and small changes and simulate a stochastic version of the model. A non-robust controller would explode the derivative term in response to the uneven characteristics of the system response if the tuning parameters are not optimised correctly. Interestingly, we saw that the model was able to bring linear and non-linear systems to stability but at the costs of removing the derivative term entirely. This may be because the derivative term, while reducing the initial overshoot of the system, would become too sensitive to disturbance and noise from the environment and controller, respectively. We used a frozen Gaussian probability density function (one where the mean and standard deviation is fixed for each random variable generated) to add the complexity of disturbance and noise as given by,

$$p(x) = \frac{1}{\sqrt{2\pi\sigma^2}} \exp\left\{-\frac{(x-\mu)^2}{2\sigma^2}\right\} \tag{11}$$

Where μ is the mean and σ is the standard deviation. A mean of $\mu = 0$ and standard deviation of $\sigma = 0.2$ were used.

2) Hyperparameter Optimisation: There were several hyperparameters which we did not yet optimise for in this model. These include the number of iterations the neural network needs to run to reach an optimum value, the size of the network itself, and the activation function for the optimisation. Black-box optimisation problems rapidly become computationally expensive. This is apparent when looking at the architecture of the ANN for the MIMO system. Each controller commands a set of six coefficients and three tuning parameters in the surrogate function and with a sample space as small as two samples per tuning parameter the space grows exponentially by $(2)^{n \cdot s}$ where n is the number of nodes (controllers) and s represents the dimensionality of the vector space, 3, in this case. As such we only tested the MIMO system using two controllers as we were running all simulations on a 2014 2.2 GHz quad-core i7 processor chip.

Currently, we are using a linear activation function in the PID controller i.e. the u control function. This means that the current neural network cannot stack several layers because irrespective of the number of layers in the neural network the activation of the output layer is simply going to be a linear combination of the input of the first layer [15]. This can be overcome by replacing the linear activation function with a non-linear function such as a Sigmoid function or a hyperbolic tangent function as shown below,

$$s(x) = \frac{1}{1+e^{-x}} \tag{12}$$

$$f(x) = \tanh(x) = \frac{1}{1+e^{-2x}}. \tag{13}$$

VI. Conclusion

Having performed all of the simulations we are able to draw some conclusions about both the algorithm and the general field. We hypothesised that as PI control was generally sufficient for most cases in the process industry it would likely be sufficient to control many of the black-box systems trialled on the algorithm. We determined that this was indeed the case as when the algorithm was trialled for simple PI control it returned k_p and k_i values which allowed the system to respond well to the given step changes.

To be successful it was also important for the algorithm to be able to determine optimum tuning parameters for a wide range of different system types. As seen in the results and discussion the algorithm was able to predict the optimum tuning parameters for both linear and non-linear black-box systems. This reflects positively on the algorithms robustness. However, to be able to formally define our algorithm as robust it would be necessary for us the test the algorithm on a very wide range of system dynamics. This unfortunately was not feasible for us to achieve as our time to produce this research was very limited, but it is something that we would wish to consider in future work in this area. For the algorithm to be of any

practical use it would have to be able to tune a number of linked controllers. In our testing the algorithm was able to tune two linked controllers. This functionality can be extended to any number of linked controllers. The constraining factor in our testing was the dimensionality of the problem with the increase in the number of controllers. The increase in the dimensionality of the problem simply made testing on any more than two linked controllers infeasible due to the increase in computation time. With access to HPC computers the algorithm would be able to effectively tune the parameters for any number of controllers. An interesting area for further research would be to look into methods of dimensionality reduction.

Perhaps the most important conclusion of this research is that the algorithm was successful in its primary objective which was to provide an automated and systematic way of tuning the control parameters for a black-box system. This is a particularly striking result as it demonstrates that with access to data about system responses and with no further knowledge of the actual system dynamics, it is possible to effectively find its optimum tuning parameters. This removes the need for any manual intervention using tuning methods, which in turn means that system operators need not be trained extensively in the methods by which control systems are tuned. It also means that any inefficiencies that arise from these tuning methods can be disregarded which would be beneficial in the operation of process systems due to more capable responses to disturbances and step changes that would be produced by the PID controllers.

VII. Outlook & Further Work

1) Non-linear Activation Function: As previously alluded to, it would be important to ascertain the model's behaviour with a non-linear activation function; this would be in pursuit of creating a better fit between the system dynamics and the approximate surrogate function globally across the entire sample domain.

2) Step Change Input: It would be interesting to train the neural net on a set of different disturbances and step input changes so that the model is able to handle large changes in the environment more effectively. This would involve prediction of optimal tuning parameters for specific step changes.

3) Gaussian Processes: In this paper we have explored the use of a convex quadratic function to approximate the system dynamics. However, studies have shown that using Gaussian processes (GPs) in place of a quadratic function can yield better results for global optimisation problems [16]. Gaussian Processes are a generalisation of the Gaussian probability distribution. While probability distributions can describe random variables, GPs (which are stochastic by definition) describe properties of functions over a finite space [17]. One of the reasons why GPs may be a better fit for this than a quadratic function might be because the presence of significant stochastic uncertainties in a system environment can lead to closed-loop performance and uncontrollability issues. GPs can be used to formulate nonlinear constraints for non-linear systems and thus improve control performance [14].

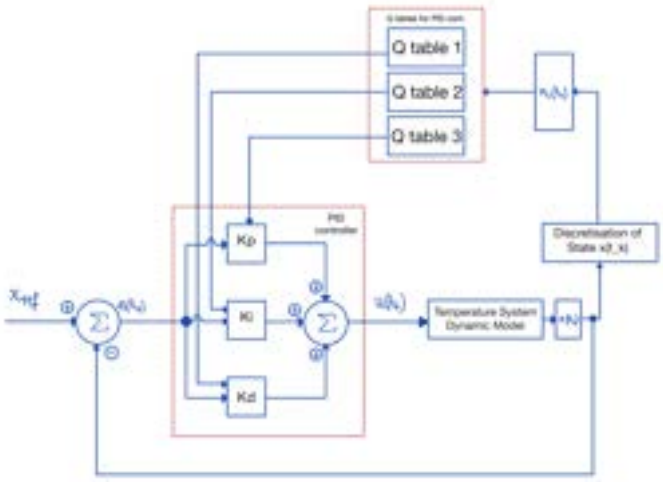

Fig. 10. Adaptive PID controller Q-learning architecture proposed for future work on this project.

4) Reinforcement Learning - Q-learning: Reinforcement learning (RL) is a branch of dynamic programming which has previously been applied to control systems by replacing PID controllers [18]. Ramanathan et. al. used Q-learning to control the fluid level in a non-linear conical tank and observed good performance [19]. A problem with replacing PID controllers with RL algorithms is that these algorithms heavily rely on the state space representation of the problem; that is, the architecture of the input, output and the system's dynamical equations. Research has emerged where RL/PID control hybrid algorithms have been proposed using techniques such as Discrete Action Reinforcement Learning Automata [20] to tune PID control parameters with a higher learning rate than RL algorithms alone. Actor-critic methods have also been proposed to optimally tune controllers [21] for wind turbines: the actor maps states to the PID tuning parameters and the critic evaluates the output of the actor [22], [23]. Quality learning (Q-learning) is being used in tuning single PID controllers [24] and recently experiments have shown they can be applied to multiple controllers [22]. Q-learning incorporates the importance of an agent's ability to both explore and exploit the environment's resources. It leverages the dynamic nature of policy rewards such that the process of controlling a system becomes dynamic; instead of having a static set of gains for a PID control systems in an attempt to control a dynamic environment, Q-learning changes the weights of tuning parameters dynamically to suit the particular disturbances sensed from the environment. This means a PID controller can directly control a system which is simple while allowing the Q-learning algorithm to dynamically adjust the control function to adapt to more complex and non-linear systems and situations. With this in mind, we created a simplistic Q-learning architecture schema for the control of a single PID controller as seen in Figure 10. This approach can be investigated more deeply to apply Q-learning RL/PID hybrid control algorithms to black-box dynamics of systems such as bioprocesses.

VIII. Acknowledgements

We would like to extend the warmest thanks to our research supervisors Professor Antonio Del Rio Chanona, Dr. Panos Petsagkourakis, and Ilya Orson Sandoval for their continued technical support and mentorship throughout the project.

References

[1] P. Petsagkourakis, I.O. Sandoval, E. Bradford, D. Zhang, E.A. del Rio-Chanona, *"Reinforcement learning for batch bioprocess optimization,"* Computers & Chemical Engineering, vol. 133, February 2020.

[2] W.Y. Svrcek, D.P. Mahoney, B.R. Young, *"A Brief History of Process Control and Process Simulation,"* in A Real Time Approach to Process Control, 3rd ed. Chichester, West Sussex, United Kingdom: John Wiley & Sons Inc. 2014 pp. 1-2.

[3] N. Minorsky, *"Directional Stability of Automatically Steered Bodies,"* Journal of the American Society for Navel Engineers, vol. 34, Issue 2, May 1922.

[4] H. Fatoorehchi, H. Abolghasemi, R. Zarghami, *"An Efficient Measure for Quantification of Nonlinearity in Chemical Engineering Processes Based on I/O Steady-state loci,"* Chemical Engineering Communications, vol. 202, May 2014.

[5] K. Deb, *"An Introduction to Genetic Algorithms,"* Sadhana, vol. 24, 1999.

[6] G. Lindfield & J. Penny, *"Chapter 3 – Particle Swarm Optimisation,"* in Introduction to Nature-Inspired Optimisation, Academic Press, 2017 pp. 49-68.

[7] J.G. Ziegler & N.B. Nichols, *"Optimum Settings for Automatic Controllers,"* Transactions of the ASME, vol. 64, 1942.

[8] G.H. Cohen & G.A. Coon, *"Theoretical considerations of retarded control,"* Trans. Amer. Soc. Mech. Eng. vol. 75, pp. 827-834, 1953.

[9] R. Hernández-Alvarado, et al., *"Neural Network-Based Self-Tuning PID Control for Underwater Vehicles,"* Sensors (Basel), vol. 16, September 2016.

[10] J. How, and E. Frazzoli, *16.30 Feedback Control Systems. Fall 2010.*, Massachusetts Institute of Technology: MIT OpenCourseWare, https://ocw.mit.edu.License:CreativeCommonsBY-NC-SA.

[11] J Klamka, *Controllability of Dynamical Systems*, 1st ed., 2009

[12] J. Coron, *Controllability of nonlinear systems*, University Pierre et Marie Curie, 2011

[13] K.J. Åström, R.M. Murray, *"15.7 Control Design in Common Application Fields,"* in Feedback Systems, 3rd ed. Princeton University Press, August 2017.

[14] E. Bradford, L. Imsland, *"Stochastic Nonlinear Model Predictive Control Using Guassian Processes,"* 2018 European Control Conference (ECC), Limassol, 2018, pp. 1027-1034, doi: 10.23919/ECC.2018.8550249.

[15] A. Sharma, *Understanding Activation Functions in Neural Networks*, The Theory of Everything, 2017.

[16] M.A. Osborne, R. Garnett, S.J. Roberts, *"Gaussian Processes for Global Optimisation,"* in 3rd International Conference on Learning and Intelligent Optimization, pp. 1-15, 2009.

[17] C. E. Rasmussen and C. K. I. Williams, *Gaussien Processes for Machine Learning*, MIT Press, 2006, pp.2-6

[18] Fernandez-Gauna, B., Ansoategui I., Etxeberria-Agiriano I., *Reinforcement learning of ball screw feed drive controllers*, Eng. Appl. Artif. Intell., 2014, **30**, pp.107-117

[19] Ramanathan, P., Mangla, K.K., Satpathy, S., *Smart controller for conical tank system using reinforcement learning algorithm*, Measurement, 2018, 116, pp. 422–428

[20] Howell, M.N., Frost, G.P., Gordon, T.J., et al.*Continuous action reinforcement learning applied to vehicle suspension control*, Mechatronics. (Oxf), 1997, 7, (3), pp. 263–276

[21] Sedighizadeh, M., Rezazadeh, A., *Adaptive PID controller based on reinforcement learning for wind turbine control*, International Scholarly and Scientific Research & Innovation, 2008, 2, (1), pp. 124–129

[22] Shi, Q., Lam, H. K., Xiao, B., and Tsai, S. H., *Adaptive PID controller based on Q-learning algorithm*, CAAI Transaction on Intelligence Technology,

[23] Mohammadi, S.M.A., Gharaveisi, A.A., Mashinchi, M., et al.: *New evolutionary methods for optimal design of PID controllers for AVR system*, 2009 IEEE Bucharest PowerTech, Bucharest, June 2009, pp. 1–8

[24] Watkins, C.J., Dayan, P., *Q-learning*, Mach. Learn., 1992, 8, (3–4), pp. 279–292

Wrong Way Behaviour of Packed Bed Reactors: Influence of Variable Velocity for a Gas-to-Liquid Reactor

Rajaram Ganesan, Varnaraj Khaitan
Department of Chemical Engineering, Imperial College London

Abstract Wrong way behaviour is a peculiar phenomenon that has been observed in a variety of different scenarios, whereby there is a transient temperature increase in the reactor when feed temperature is decreased. It has been modelled with various complexities but all models in literature assume constant velocity within the reactor. This work develops a two-phase model with velocity as a variable, accounting for gas contraction due to reaction and temperature dependent gas density. The model was implemented in gPROMS using Fischer-Tropsch conditions as a base. A sensitivity analysis was performed to see the impacts of crucial parameters, such as interfacial heat and mass transfer and heat of reaction, on the transient reactor response for step changes in feed temperature. This paper presents a novel extension of this to include transient responses to changes in feed velocity. Key findings are that even small step increases in feed velocity lead to significant transient temperature rises of the order of 100s of Kelvin, and accounting for variable velocity largely mitigates the magnitude of wrong way behaviour in contrast to constant velocity models. Sensitivities indicate complex, subtle interplays of heat and mass transfer as well as reveal insights on conversion and catalyst temperature profiles which can feed into design, operational and safety decisions. Future scope is wide, including accounting for radial effects, pressure drop as well as studying responses to simultaneous changes in feed velocity and temperatures.

Keywords: wrong way behaviour, transient, packed bed reactors, heat and mass transfer, variable velocity

Introduction

Wrong way behaviour is a term that describes a transient temperature rise in a reactor caused by a decrease in the feed temperature. The drop in feed temperature causes a decrease in reaction rate in the initial section of the reactor, leading to higher concentrations of the reactant downstream. Therefore, the reaction rate downstream increases, generating heat and causing a temperature peak before the cooler temperature wave reaches this section. The reaction rate subsequently downstream decreases and the reactor settles into a new, cooler steady state. This effect could potentially cause issues for start-up and reactor control, leading to catalyst damage and reactor runaway if the cool temperature wave cannot sufficiently mitigate the temperature peak.

Wrong way behaviour was predicted by Crider and Foss (1966)[1] whilst carrying out computations of transient behaviour in packed tubular reactors. They observed a decrease in transient temperature for a step increase in feed temperature. Subsequently, this behaviour was observed by various researchers, by Hoiberg et al.(1971)[2] for a packed bed reactor; by Van Doesburg and De Jong (1976)[3] whilst modelling the transient behaviour of the catalytic methanation of carbon dioxide; by Sharma and Hughes (1979)[4,5] whilst examining the behaviour of a fixed bed reactor for the oxidation of Carbon Monoxide; by Cavendish and Oh (1982)[6] in the context of the transient behaviour of catalytic converters.

Further to these observations, formal models were developed starting with Mehta et. Al (1981)[7] who modelled a simple one dimensional, single phase, pseudo-homogeneous plug flow reactor, providing insight into this behaviour and how different parameters affect it. In later work by Pinjala et Al. (1988)[8] the effects of axial dispersion of heat and mass to the model was introduced. They observed that dispersion decreases the magnitude of wrong way behaviour and prolongs the shift to a new steady state, thus conveying the importance of including dispersion effects in predictions of wrong way behaviour. However, this model was also incomplete as it neglected interfacial effects between the gas and solid catalyst because it assumed a single pseudo-homogeneous phase. A model taking these effects into account was developed by Chen and Luss (1989)[9]. They noted that the two-phase model was very similar to the pseudo-homogeneous model when a unique steady state exists for all feed temperatures whilst being less computationally costly. For multiple steady states, this also acted as a better model. This work was built upon by Quina et al. (2000)[10] who studied the dilution effect of the catalyst bed for both the heterogeneous and pseudo-homogeneous models, observing that increased heat capacity of the bed helped mitigate the magnitude of the transient temperature rise i.e. wrong way behaviour. Il'in and Luss (1992)[11] also built on Chen and Luss' work by introducing the concept of reactant adsorption on the solid catalyst, which was found to decrease the magnitude of wrong way behaviour.

All the aforementioned studies assume the idea of constant gas velocity within in the reactor at all times. In practice, this would not be the case as there would be two competing effects that would alter the gas velocity, namely the temperature effect and the velocity contraction effect. The first accounts for temperature dependent density of the gas. So for exothermic reactions, the temperature along the reactor would increase, leading to expansion of the gas phase and a subsequent increase in gas velocity. The second effect is contraction of gas as it is reacted away - into the liquid phase in the case of a gas-to-liquid (GTL) reaction. These effects will have an impact on the magnitude of wrong way behaviour and thus it is vital that they are modelled. Further, previous literature only explore transient behaviour in response to changes in feed temperature. However, from an operational perspective, changes in feed velocity are not uncommon for reasons ranging from upstream disturbances, start-ups or plant operator actions and thus warrant investigation. In lieu of this, the work firstly

aims to develop a two-phase model, derived for velocity as variable, in the context of a GTL reactor. Further, the sensitivity of this model will be examined to understand the role of various model parameters on the wrong way behaviour, when changes to feed temperature or velocity are made. Finally, model results will be contrasted to those obtained from the Chen and Luss' (1989)[9] constant velocity model to determine the significance of lifting the assumption of constant velocity.

Methods

The mass and energy balances derived for the gas phase as well as the solid catalyst are presented below in dimensionless form, followed by the boundary conditions used to solve them. Unless otherwise stated, x_T, θ and y refer to total concentration, temperature and mole fractions at *bulk* conditions.

$$\frac{\partial\left(u\cdot x_T\right)}{\partial z}=M_{\varepsilon}x_T\left[\frac{2}{\frac{\theta_s}{\theta}+1}\right]\left(y-y_s\right) \tag{1}$$

$$\begin{aligned}\frac{1}{Le}\frac{\partial\left(y\cdot x_T\right)}{\partial t}=&-\frac{\partial\left(u\cdot y\cdot x_T\right)}{\partial z}\\&-Mx_T\left[\frac{2}{\frac{\theta_s}{\theta}+1}\right]\left(y-y_s\right)\\&+\frac{1}{Pe_M}\frac{\partial}{\partial z}\left(x_T\frac{\partial y}{\partial z}\right)\end{aligned} \tag{2}$$

$$\begin{aligned}\frac{x_T}{Le}\frac{\partial\theta}{\partial t}=&-ux_T\frac{\partial\theta}{\partial z}+\frac{1}{Pe_H}\frac{\partial^2\theta}{\partial z^2}\\&-H\left(\theta-\theta_s\right)-U\left(\theta-\theta_w\right)\end{aligned} \tag{3}$$

$$\begin{aligned}M\left[\frac{2}{\frac{\theta_s}{\theta}+1}\right]\left(y-y_s\right)=&\\\eta_s y_s\frac{\theta}{\theta_s}\exp\left[\frac{1}{\theta_r}-\frac{1}{\theta_s}\right]&\end{aligned} \tag{4}$$

$$\begin{aligned}\left(1-\frac{1}{Le}\right)\frac{\partial\theta_s}{\partial t}=&H\left(\theta-\theta_s\right)\\&+\beta\eta_s y_s\frac{\theta}{\theta_s}\exp\left[\frac{1}{\theta_r}-\frac{1}{\theta_s}\right]\end{aligned} \tag{5}$$

$$\eta_s=\frac{3}{\varphi_s^2}\left(\frac{\varphi_s}{\tanh\left(\varphi_s\right)}-1\right) \tag{6}$$

$$\varphi_s^2=\varphi_0^2\exp\left[\frac{1}{\theta_r}-\frac{1}{\theta_s}\right] \tag{7}$$

Boundary conditions:

At $z=0$:

$$\begin{aligned}u_f x_{Tf}&=ux_T\\u_f x_{Tf}(1-y)&=-\frac{x_T}{Pe_M}\frac{\partial y}{\partial z}\\u_f x_{Tf}\left(\theta_f-\theta\right)&=-\frac{1}{Pe_M}\frac{\partial\theta}{\partial z}\end{aligned} \tag{8}$$

At $z=1$:

$$\begin{aligned}\frac{\partial\theta}{\partial z}&=0\\\frac{\partial y}{\partial z}&=0\end{aligned} \tag{9}$$

The following scalings and dimensionless groups were used to non-dimensionalise the model equations and boundary conditions.

Scaling equations:

$$\begin{aligned}x_T=\frac{C_T}{C_{T,\text{ref}}}=\frac{P/RT}{P/RT_{\text{ref}}}=\frac{\theta_r}{\theta};\therefore\left[x_{Tf}=\frac{C_{Tf}}{C_{T,\text{ref}}}=\frac{\theta_r}{\theta_f}\right]\\\theta=\frac{RT}{E};\therefore\left[\theta_r=\frac{RT_{\text{ref}}}{E}\right]\\y=\frac{y_A}{y_{Af}};\quad u=\frac{u'}{u_{f0}}\\z=\frac{z'}{L};\quad t=\frac{1}{Le}\frac{u_{f0}t'}{\varepsilon L}\end{aligned} \tag{10}$$

Dimensionless groups:

$$\begin{aligned}M&=3\frac{Lk_{mc}}{u_{f0}r_p}(1-\varepsilon)\\\varepsilon_A&=-y_{Af}\left(\frac{a+b-c}{a}\right)^{[12]}\\M_{\varepsilon}&=\varepsilon_A M\\U&=2\frac{Lh_w}{u_{f0}rC_{T,ref}c_{pf}}\\H&=\frac{Lh_f}{u_{f0}r_pC_{T,ref}c_{pf}}(1-\varepsilon)\\\beta&=\frac{R}{E}\frac{(-\Delta H)y_{Af}}{c_{pf}}\\Le&=1+\frac{(1-\varepsilon)\rho_s c_{ps}}{\varepsilon C_{T,ref}c_{pf}}\\Pe_M&=\frac{Lu_{f0}}{D_a}\\Pe_H&=\frac{Lu_{f0}C_{T,ref}C_{pf}}{\lambda_a}\\\varphi_0^2&=\frac{k\left(\theta_r\right)r_p^2}{D_e}=\frac{u_{f,0}r_p^2}{LD_e}\\\frac{k(\theta_r)}{k_0}&=\exp\left[-\frac{1}{\theta_r}\right]=\frac{u_{f0}}{Lk_0}\end{aligned} \tag{11}$$

This system of algebraic equations and partial derivatives were implemented as a distributed system, discretised and solved numerically in gPROMS using a backwards finite difference solver. Initialisation procedures were used to resolve most model instabilities, but where this was not feasible, the number of discretisations was adjusted to allow the model to run.

Key assumptions made when deriving the model are listed below:

1. Radial effects are neglected
2. Reaction rate is in steady state with respect to interfacial mass transfer
3. Intra-particle concentration gradient is in pseudo-steady state with respect to pellet temperature and

bulk conditions allowing the use of the isothermal effectiveness factor
4. c_p for both solid and fluid is constant
5. Pressure is constant with time and space
6. C_T is a function of temperature and pressure but is independent of composition and assumed to be at steady state.
7. Linear temperature gradient across the interfacial film between the fluid bulk and the catalyst particle surface
8. Liquid phase is neglected
9. Enthalpy of the gas going to/from particles goes into the liquid phase and can be neglected for the gas balances
10. u_f does not change with changes in feed concentration/temperature

Table 1 lists the values of dimensionless parameter values computed from the dimensional constants detailed in Table 2 in the Supplementary Information section. Unless otherwise specified, all analysis employs these values by default

Table 1: *Dimensionless constants calculated using the Equation 11*

Dimensionless Constant	Value
θ_r	0.05
ε_A	-0.3
M	0.774
M_ε	-0.15
H	31.1
U	0 (adiabatic, default) / 2.60
β	0.135
Le	261
Pe_M	4800
Pe_H	7795
ϕ_0^2	3.73

Results and Discussions

Wrong Way Example

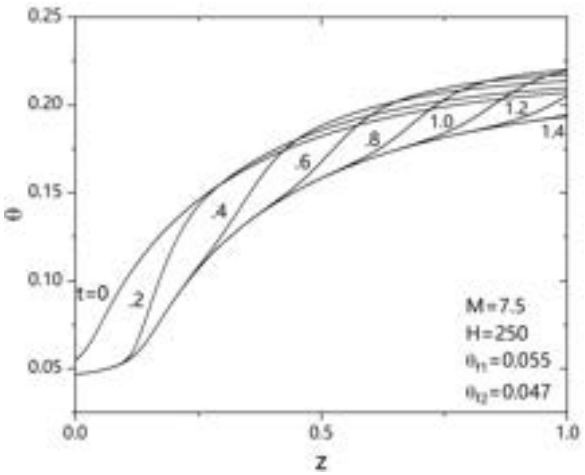

Figure 1: *An example of wrong way behaviour, shown by how θ varies through the reactor over time, for an adiabatically operated reactor for a step change in feed temperature from 0.055 to 0.047*

Figure 1 shows how the dimensionless temperature profile in the reactor changes with time when the dimensionless feed temperature is dropped from 0.055 to 0.047 (89 K) at $t = 0$. Wrong way behaviour is apparent here, with temperatures between $t = 0.2$ and $t = 1.2$ exceeding that of the steady state maximum temperature at $t = 0$, because of reasons discussed in the introduction. As time progresses, the temperature profile aligns to the final steady state profile, and deviations from it are pushed further downstream. This means the colder temperature front caused by the drop can is moving along the reactor.

Before examining the model's parametric sensitivities, an example instance of the model evaluated at default parameters is discussed to establish a baseline to build on.

Starting with temperatures, it is observed from Figure 2 that θ and θ_s are very similar, with their ratio being very close to unity, dipping to 0.95 at its lowest. This indicates that the dimensionless interfacial heat transfer coefficient, H has a value at which there is small limitation upon interfacial heat transfer. This impact of this limitation is evidenced by the dips observed in the ratio. The dips denote a zone of fast reaction in the reactor where heat is generated at the catalyst surface faster than it can be carried away, causing the ratio to drop. This manifests as a trough in the steady state profiles early in the reactor. The drop in feed temperature, however, causes additional dips transiently because of the increased reaction downstream caused by wrong way behaviour. At steady state, the downstream ratio returns to unity as the transient concentration rises dissipate, slowing heat generation by reaction, allowing the heat to be carried away.

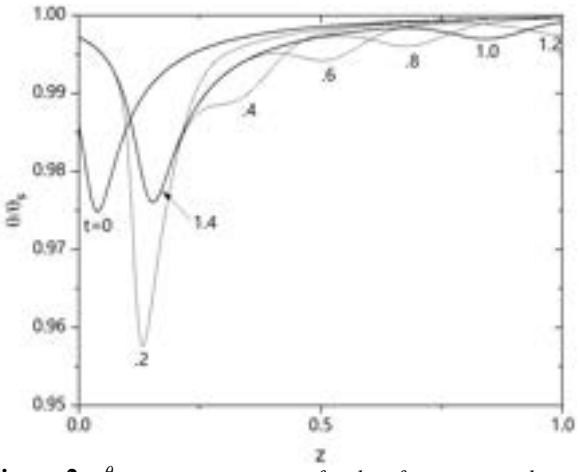

Figure 2: $\frac{\theta}{\theta_s}$ *against z over time for the aforementioned example*

The wrong way behaviour is evidenced in Figure 3 by the transient increase in the ratio of C to C_s, indicating higher bulk reactant concentrations downstream in the reactor as expected. The existence of wrong way behaviour implies that interfacial mass transfer coefficient, M is not totally limiting. If it was, the extra reactant downstream would not be transferred to the catalyst surface to react before the cool temperature wave reaches it. However, the C to C_s ratio reaches as high as 250 implying that mass transfer resistance is still significant although not limiting.

Perhaps the most important feature of the model is the velocity. Figure 4 shows how the velocity changes

through the reactor over time. It is evident that the temperature effect mentioned earlier dominates overall, seeing as the velocity increases significantly throughout the reactor. Notably, the velocity at the new steady state is higher than the initial steady state because concentration of the feed increases due to the temperature drop, meaning that overall molar flow rate increases and results in a higher velocity throughout the bed. This is a consequence of assuming that feed velocity remains constant when feed temperature is dropped (in practice, it would be adjusted to maintain molar flow rate). Conversely, upstream of the reactor, velocity contraction due to temperature drop dominates this increase in molar flow rate, causing velocity to be lower than at $t = 0$.

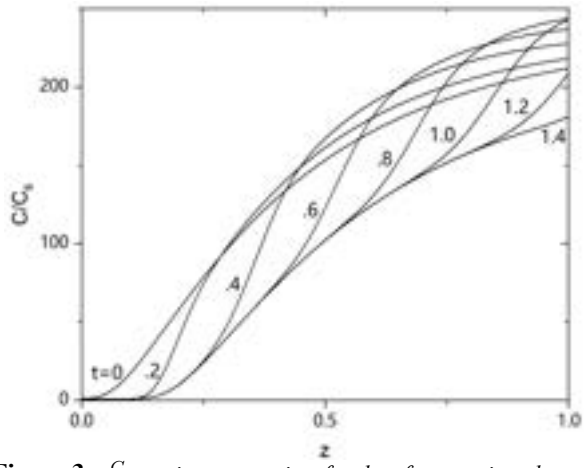

Figure 3: $\frac{C}{C_s}$ *against z over time for the aforementioned example*

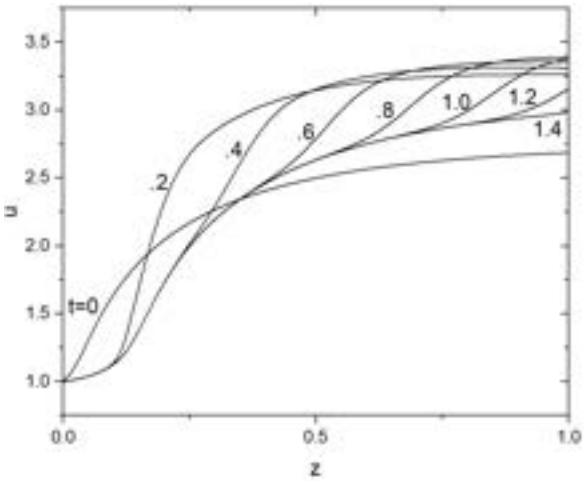

Figure 4: u *against z over time for the aforementioned example*

The Effects of Parameters

Dimensionless Heat Transfer Coefficient, H

Figure 5 is a master diagram showing the effect of different values of H (ranging from 25 to 250) on the magnitude wrong way behaviour when the feed temperature is dropped. It also displays the dependence of this magnitude on the size of the drop and the original and new feed temperatures between which it is dropped.

The solid lines represent maximal steady state temperature in the bed for any feed temperature specified on the x-axis. The dashed lines represent how the maximal transient temperature changes with the new feed temperature for a particular starting feed temperature. This starting feed temperature is represented by the intercepts of the dashed lines with the solid lines, and the temperature to which the feed is dropped from this starting point can be chosen on the x-axis. The y-axis represents the the maximal transient temperature across the bed relative to a reference (which is the steady state maximal temperature for a feed temperature of 0.05). For a given initial and final feed temperature, the magnitude of wrong-way behaviour is obtained by subtracting the y-axis value at the starting point from that at the new feed temperature, using the dashed line for the H value of interest.

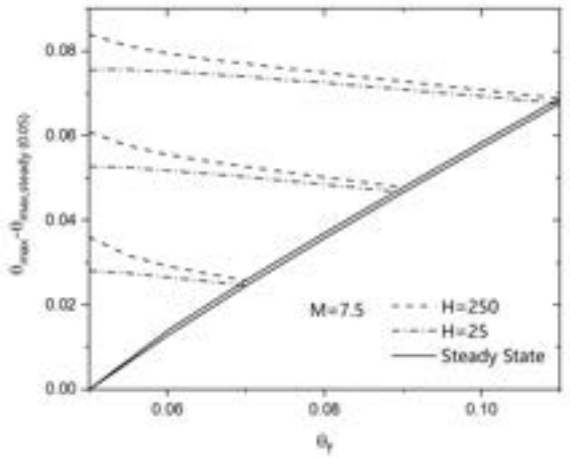

Figure 5: *Effect of H on wrong way behaviour for drops in feed temperature of various sizes*

The negatively sloped dashed lines verify the occurrence of wrong way behaviour because it signifies that the transient temperature for a feed temperature drop increases beyond the steady state maximum for the original feed temperature. Whereas if there was no wrong-way behaviour, the transient temperature would only decrease from the steady-state maximum and hence the maximal transient line would remain flat at the steady-state maximum value.

The continuously negative slope implies that wrong-way behaviour increases with the size of the drop. The larger the decrease in temperature, the larger the decrease in reaction rate early within the reactor. As a result, there is more concentration carried downstream and is reacted, causing larger transient temperature peaks.

Regarding the effect of H, a higher magnitude of wrong way behaviour occurs for $H = 250$ than for $H = 25$. Higher values of H imply less interfacial heat transfer limitations and therefore more heat released at the catalyst surface due to reaction is carried to the bulk, giving rise to increased magnitude of wrong way behaviour.

Dimensionless Mass Transfer Coefficient, M

Figure 6 is a master diagram similar to Figure 5, except it shows the effects of M on wrong way behaviour, varying from $M = 0.5$ to $M = 7.5$. For $M = 0.5$, there is no wrong way behaviour, due to the very high interfacial mass transfer limitations preventing the extra reactant concentration downstream caused by the temperature drop

from having an influence. Wrong way behaviour increases in magnitude with M. The reduction in mass transfer limitations means the extra reactant reaches the catalyst surface at a fast enough rate to react and generate heat before the cold temperature front approaches it. As with H, the larger the temperature drop, the greater the magnitude of wrong way behaviour.

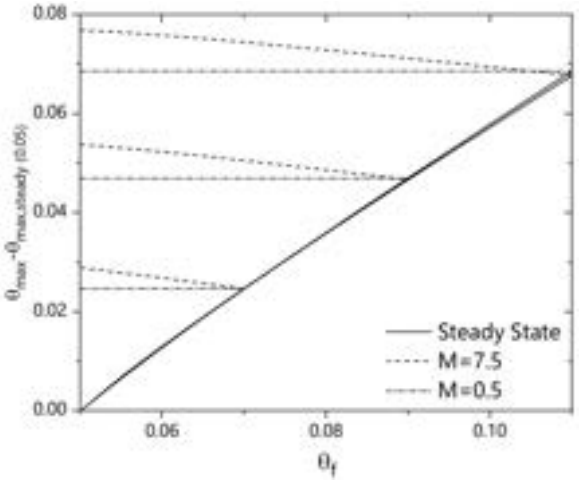

Figure 6: *Effect of M on wrong way behaviour for drops in feed temperature of various sizes*

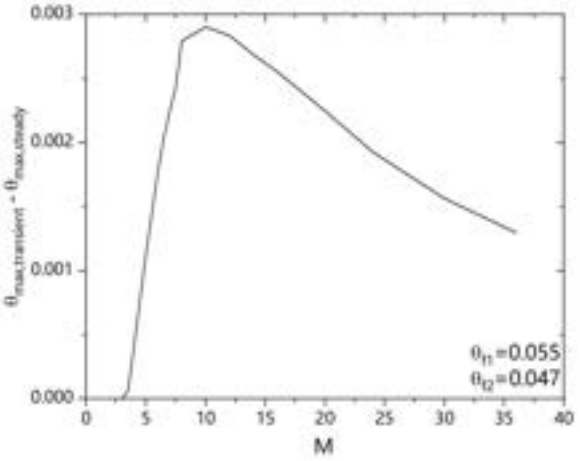

Figure 7: *The effect of M on the magnitude of wrong way behaviour for a feed temperature drop from 0.055 to 0.047*

Figure 7 represents how the magnitude of wrong way behaviour, defined as the difference between the maximal transient temperature and the maximal steady state temperature at the initial feed temperature, changes with M. Despite wrong way behaviour increasing for M up to 7.5, beyond this the magnitude of wrong way behaviour actually decreases as you increase beyond $M = 10$. This contradicts the fact that decreased mass transfer limitations should allow the increased concentration to be utilised. The concept of reaction zone comes into play here again. Increasing M reduces mass transfer limitations, meaning faster reaction. This leads to a sharpening reaction zone early in the reactor, where nearly all of the conversion happens. For sufficient M, the concentration at the end of the reactor is negligible. If this sharp zone is maintained even after the temperature drop, this means the concentration downstream is insensitive to the temperature drop, thus reducing the magnitude of wrong way behaviour as the reaction rate downstream does not increase as much.

Axial Mass (D_a) and Heat (λ_a) Dispersion Coefficients

The reactor system under consideration was initially modelled to include the axial dispersion of mass and heat, through the Peclet numbers for mass and heat respectively (Pe_M and Pe_H). The effects of varying these parameters on the magnitude of wrong way behaviour, for the same temperature drop as in the example discussed before, is presented in Figures 8 and 9. The y-axis conveys directly the magnitude of wrong way behaviour as defined before.

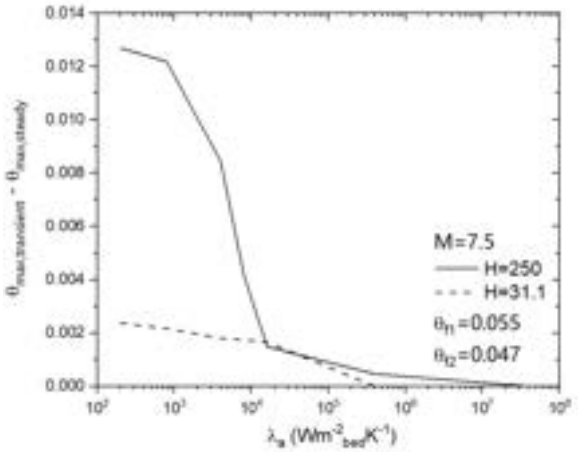

Figure 8: *Effect of varying λ_a on the magnitude of wrong way behaviour for a feed temperature drop from 0.055 to 0.047*

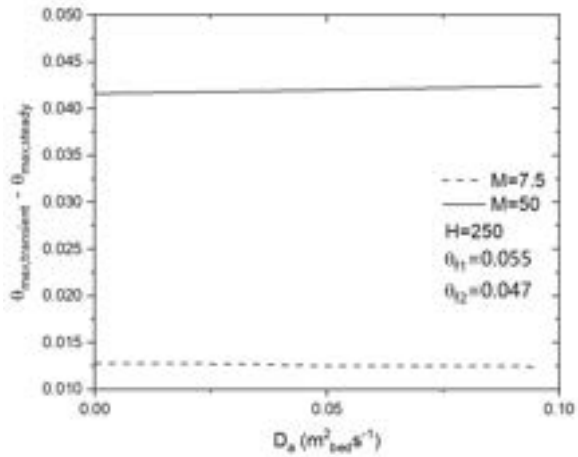

Figure 9: *Effect of varying D_a on the magnitude of wrong way behaviour for a feed temperature drop from 0.055 to 0.047*

Figure 8 shows that increasing the axial heat dispersion coefficient has a significant impact altering the magnitude of wrong way behaviour by about 300°C. Very high values of λ_a, i.e high dispersion, essentially simulates a large degree of mixing, making the reactor behave thermally similar to a continuously stirred tank reactor. In such a case any extra heat released due to drops in feed temperature is completely dissipated, suppressing wrong way behaviour. The reverse applies to very low values of heat dispersion. This is observed to a lesser extent at lower values of H. For example, when $H = 31.1$, whilst a similar trend is observed, the extent to which the wrong way behaviour is suppressed, as well its absolute magnitude, is significantly smaller for the same variations in λ_a. This is due to the fact that now wrong way behaviour is rather

limited by interfacial heat transfer. Thus, less heat is transferred to the bulk and there is less heat to be dispersed. Hence any change in dispersion has limited contribution.

In contrast, Figure 9 makes clear that axial mass dispersion has negligible impact on the magnitude of wrong way behaviour. Increasing mass dispersion, D_a, between 0 to 0.096 (i.e. varying Pe_M from infinity to 250) resulted only in about 3°C decrease in the magnitude of wrong way, for both $M = 0.$ and $M = 7.5$. This can be attributed to the fact at both values of M, interfacial mass transfer limitations are still quite significant. Hence while a higher M shifts the graph up, effects of mass dispersion does not overcome the interfacial limitations, unless operating very high values of M are modelled, where these limitations are negligible. However this is not feasible for the gPROMS model used here.

Feed Velocity, u'_f

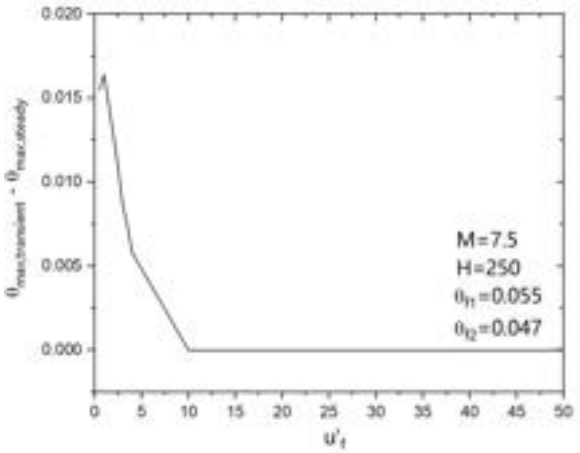

Figure 10: *Effect of varying u'_f on the magnitude of wrong way behaviour for a feed temperature drop from 0.055 to 0.047*

Employing the same method as in the preceding section, the dependence of wrong way behaviour on feed velocity is shown in Figure 10. It can be seen that at higher feed velocities, the magnitude of wrong way behaviour tends to zero for the same feed temperature drop. This is because the higher feed velocity translates to higher velocities in the bed and thus lower residence times of the reacting species. As a result, interfacial mass transfer is too slow to utilise the increased concentration downstream when feed temperature is dropped, mitigating the expected wrong way behaviour.

Having seen the effect of parameters like M and H on wrong way behaviour when the feed temperature is dropped (at constant feed velocities), Figures 11 and 12 are master diagrams that demonstrate the converse - the effect of parameters for step changes in feed velocity of different sizes and from different starting points at constant feed temperatures. This analysis is very practically relevant, as it is very possible for changes in feed velocity to take place in industrial settings due to plant operator actions or disturbances upstream to the reactor unit. Modelling this complexity, especially in the context of a variable velocity model, is unique to this paper, as literature is meagre for this aspect.

These master diagrams are similar to those presented in Figures 5 and 6, the difference being the y-axis is now the difference between maximal transient temperature relative to the steady state maximal temperature at the original feed velocity. This means the intercepts of the dashed lines now lie on the x-axis.

These master diagrams reaffirm that higher H increases wrong way behaviour, and that $M = 0.5$ gives no wrong behaviour whilst $M = 7.5$ does, in line with the discussions of the effect of interfacial heat and mass transfer earlier.

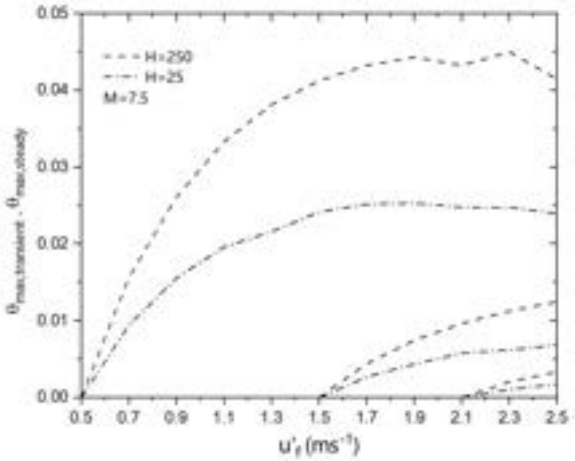

Figure 11: *Effect of H on wrong way behaviour for increases in feed velocity of various sizes*

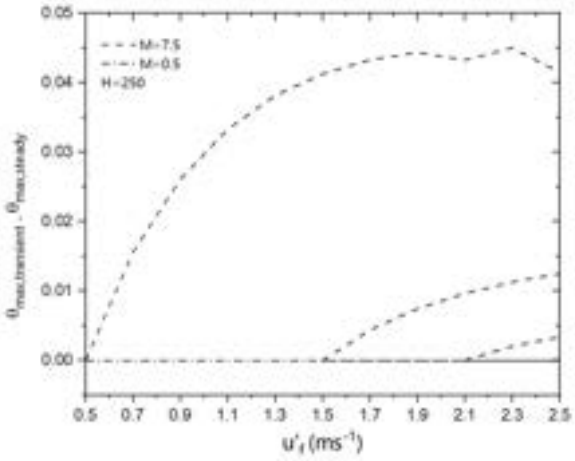

Figure 12: *Effect of M on wrong way behaviour for increases in feed velocity of various sizes*

More interestingly however, whilst Figure 10 shows that higher feed velocities tend to eliminate wrong-way behaviour, these plots reveal that when the feed velocity is suddenly stepped up, higher magnitudes of wrong-way behaviour result. When feed velocity is increased, velocity instantaneously increases throughout the reactor temporarily before settling to a new steady state. This is a result of the assumption that C_T is at steady state. As a result of increased u_f, concentration that was originally reacting upstream in the reactor is carried downstream of the reactor, where mass transfer (for $M = 7.5$) is fast enough to take advantage of the higher concentration resulting in more reaction and thus more heat i.e. more wrong way behaviour. To verify this, it was found that the temperature peak corresponding to wrong-way behaviour happens quickly and at a location downstream in the reactor.

Larger jumps in the feed velocity simply exaggerates this behaviour, especially if jumping from a smaller initial velocity, as more concentration is carried downstream. This result can be instructional to plant operators, suggesting that it may be wiser not to make sudden step-ups but rather slowly ramp it up, as even a small raise from 0.5 to 0.9 m s^{-1} can cause wrong way peaks of 400 K for example.

Thiele Modulus, ϕ_0

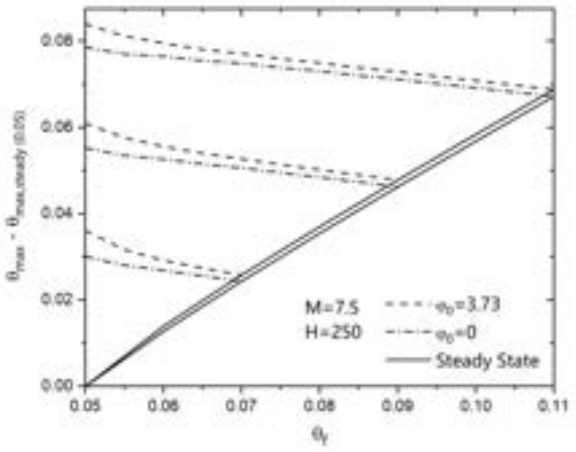

Figure 13: *Effect of pore diffusion limitations on wrong way behaviour for drops in feed temperature of various sizes*

The parameter ϕ_0 incorporates the effective diffusivity D_e and manipulating this reveals the interesting effect of intraparticle diffusional limitations on wrong way behaviour, as depicted in Figure 13, which again uses a similar presentation to Figures 5 and 6. Increasing ϕ_0 increases the diffusional limitation within the catalyst and $\phi_0 = 0$ signifies no limitation in turn leading to an isothermal effectiveness factor of 1. Logically, $\phi_0 = 0$ should yield higher wrong way behaviour as the catalyst effectiveness is as high as possible, leading to more reaction. Figure 13 shows that, for any initial feed temperature, varying ϕ_0 causes negligible impact for smaller drops in feed temperature, but for larger drops, $\phi_0 = 0$ actually yields smaller wrong way behaviour comparatively. This is because with no limitation, there is a very sharp reaction zone early in the reactor, which mitigates wrong way behaviour as discussed previously. Whereas with more diffusional limitations, this zone is less sharp. So, when the feed temperature is dropped, the resulting increased concentration is not immediately consumed, leaving higher concentrations available to react downstream, causing more wrong way behaviour.

Feed Fraction, y_{Af}

The feed fraction of reactant manifests itself in two different dimensionless numbers, β and ε_A. Manipulating both by the same proportion allows the effects of feed fraction to be observed. Figure 14 is a master diagram for feed fraction, similar to those presented for varying feed velocity. In general,it shows that increasing feed fraction increases the magnitude of wrong way behaviour. This is due to higher feed fraction leading to a less sharp reaction zone, increasing concentration sensitivity downstream in comparison to lower feed fraction. This is particularly the case for higher temperatures, as these temperatures will also allow fast reaction early in the bed.

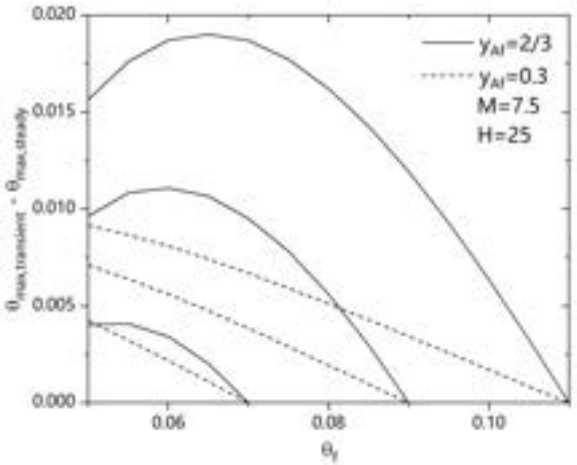

Figure 14: *The effect of feed fraction on wrong way behaviour for drops in feed temperature of various sizes*

Interestingly, for $y_{Af} = 2/3$, when dropped to lower θ_f values, the magnitude starts to decrease after a peak. This can potentially be explained by the fact the mass transfer limitations at $M = 7.5$ are unable to utilise any greater concentration increase. This, in combination with the assumption of constant feed velocity, which causes increased velocity, acts to start mitigating wrong way.

Heat of Reaction, ΔH

So far, it has been evident that the temperature effect on velocity has been dominating. This is due to the highly exothermic nature of the reaction, the parameter ΔH being set at 152 000 J mol^{-1}. It is therefore of interest to investigate the effect of ΔH on wrong way behaviour. Figure 15 shows this parameter's effect, scaled relative to the default value, on the magnitude of wrong way behaviour. The plot shows that decreasing the value actually increases the wrong way behaviour which seems counter-intuitive, given that lower ΔH is expected generated less heat. However, because there is less increase in velocity, the mitigating effect of increasing velocity on wrong way behaviour. Higher ΔH values leads to a net increase in wrong way behaviour. The peak in the curves for both feed fractions thus shows these competing effects at play. There comes a point, after which, ΔH is indeed too low to generate enough heat to cause significant wrong way behaviour, despite the continued reduction in velocity increase. This effect is further discussed in the Comparisons with Constant Velocity section.

Another effect to note is that for a higher feed fraction, the absolute magnitude of wrong way behaviour is highly affected. At lower values of ΔH, this is due to the increased contraction factor (negative expansion factor, ε_A). The greater gas contraction serves to mitigate the temperature effect more, increasing the time available for increased concentration to react downstream, thereby shifting the peak up. The peak also shifts left as the contraction is able to counteract the decreasing ΔH and cause larger wrong way behaviour despite lower heat of reaction.

At higher ΔH, the increased contraction factor is negated by the increased feed fraction causing more reaction, more heat generation and thus, a greater velocity increase. Alongside mass transfer limitations, this mitigates wrong way behaviour compared to a lower feed fraction.

As can be observed, there is a crossover point where the velocity increase due to higher feed fraction and effect of velocity contraction balance, shown by the intersection of the solid and dashed lines.

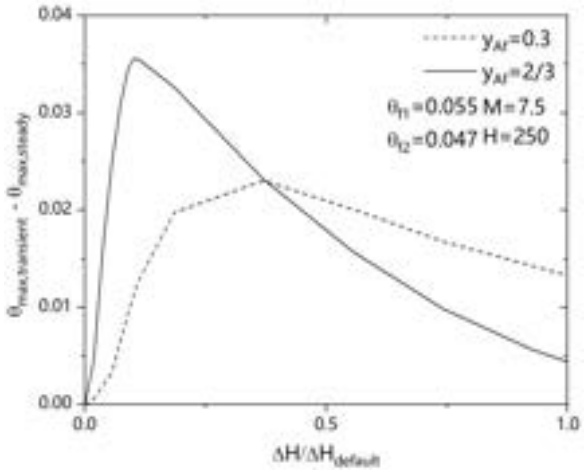

Figure 15: *The effect of ΔH, scaled relative to the default value, on the magnitude of wrong way behaviour for a temperature drop from 0.055 to 0.047*

Adiabatic vs Non-Adiabatic

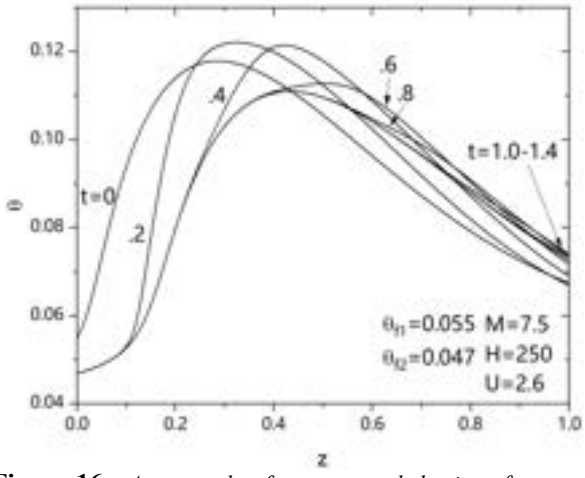

Figure 16: *An example of wrong way behaviour for a non-adiabatically operated reactor*

So far, only a purely adiabatic reactor has been examined. The temperature rises in the reactor observed so far are extreme, as shown in the example in Figure 1, rising to over $\theta = 0.2$ which corresponds to 2200 K. Practically, the reactor would have cooling and be run non-adiabatically. In Figure 16, we can see the temperature profile for a non-adiabatically operated reactor. This was run to the same specification as the wrong way example presented earlier, but for a non-adiabatic value of U. Early on in the reactor, there is a high reaction rate, generating vast quantities of heat, at a faster rate than the wall can remove it. Later on in the reactor, most reactant has been converted and thus reaction rate slows allowing the wall to remove heat faster than it can be generated.

Interestingly, there is still wrong way behaviour for the non-adiabatic reactor at these example specifications, implying that the extra heat is generated downstream in the reactor faster than the wall can mitigate it. However, when attempting the same temperature drops as in the master diagrams previously discussed, it was observed that there was no wrong way behaviour as the magnitudes were relatively small and able to be suppressed by heat removal at the wall. Sensitivities were carried out for non-adiabatic conditions and, in general, it was found that non-adiabatic conditions tended to mitigate wrong way behaviour, as expected due to the wall removing some of the heat generated.

Comparisons with Constant Velocity

It is vitally important to directly compare the wrong way behaviour for the existing constant velocity model to this variable velocity, in order to fully comprehend the effects of lifting this assumption.

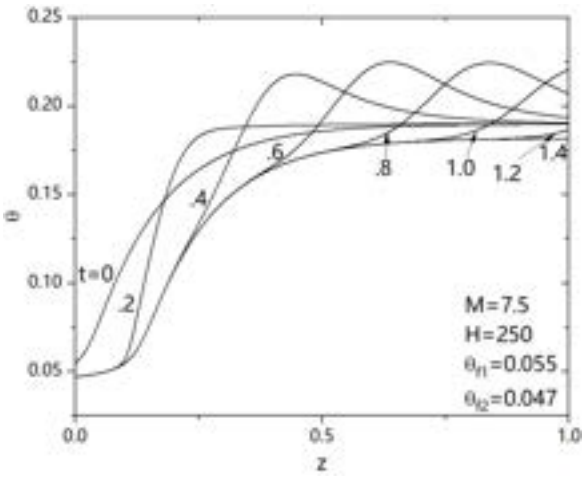

Figure 17: *A graph of dimensionless temperature over time against z for constant velocity for the same example as variable velocity*

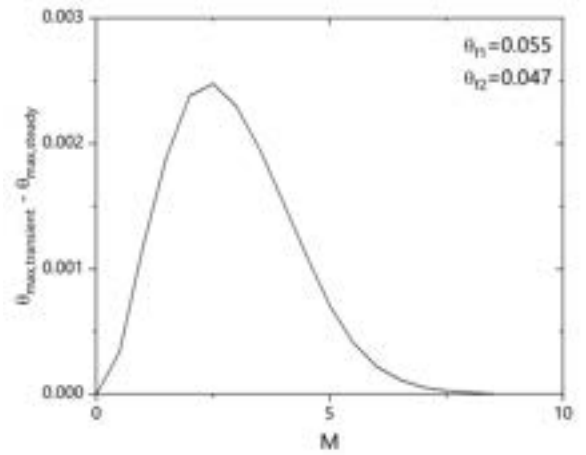

Figure 18: *The effect of M on the magnitude of wrong way behaviour in the constant velocity modelfor a feed temperature drop from 0.055 to 0.047*

Figure 17 shows how temperature changes for the same example as used for the variable velocity model. The key differences to note compared to Figure 1 are the peaks occur earlier in the reactor and are larger than for variable velocity. The peaks occur later in the variable velocity model because increasing velocity carries the extra reactant further in the reactor before it reacts. The peaks are

less tall for variable velocity as there is also less time for this extra reactant to react.

Figure 18 is similar to Figure 7, but plotted for the constant velocity model. There is still a peak, as before, thanks to the reaction zone concept discussed previously. However, this peak occurs for much lower values of M. This is because interfacial mass transfer does not need to be as fast to utilise the extra reactant, compared to increasing velocity. Another reason is that the reaction zone becomes very sharp for much lower M in the constant velocity model. Increasing velocity may serve to mitigate wrong way behaviour but also serves to make the reaction zone less sharp because the concentration is carried later into the reactor before it has time to react. Thus, faster mass transfer is needed to maintain the sharp reaction zone in the variable velocity model.

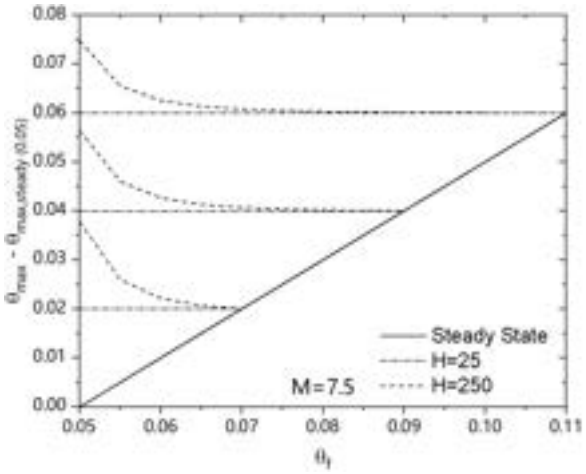

Figure 19: *Effect of M on wrong way behaviour for drops in feed temperature of various sizes for the constant velocity model*

Figure 19 is a master diagram for differing H.. Comparing this diagram to Figure 5, it can be observed that wrong way behaviour is lower in magnitude for $H = 25$ across all drops, and for $H = 250$, is smaller until the new feed temperature is below around 0.06. As previously explained, constant velocity removes the effect of reducing the sharpness of the reaction zone that variable velocity has. For $H = 25$, the interfacial heat transfer is not sufficient for the bulk to cool the catalyst surface and will not spread conversion along the reactor. This means a sharp reaction zone early in the reactor for a much wider range of temperatures, including to below $\theta_f = 0.05$. For $H = 250$, the faster interfacial heat transfer spreads conversion through the reactor but without the added effect of increasing velocity, this leads to lower concentration sensitivity downstream than for variable velocity. There does comes a new feed temperature, however, for higher H where the concentration downstream starts to become sensitive i.e. the reaction becomes more spread out across the reactor. At this point, constant velocity achieves greater wrong way as velocity does not increase to mitigate the effects of wrong way. The effect of H blunting the sharpness of the reaction zone so that concentration downstream is sensitive at higher temperatures also helps to explain the gradient increase in Figures 5 and 13.

Figure 20 shows the differences in wrong way behaviour for both constant and variable velocity models for fixed feed fractions and varying ΔH. One would expect for lower ΔH, when the reaction generates less heat, contraction would come into play for variable velocity, increasing the magnitude of wrong way behaviour compared to constant velocity for reasons explained before. However, it can be seen that for $y_{Af} = 0.3$, variable velocity always has lower magnitudes of wrong way behaviour. This is due to the contraction effect being too weak. When wrong way behaviour occurs, velocity increases transiently due to increased temperature, and for lower contraction this effect overpowers contraction, overall mitigating wrong way behaviour. For $y_{Af} = 2/3$ on the other hand, the contraction effect is strong enough at lower ΔH to overcome the increase in velocity caused by the wrong way behaviour temperature peaks, leading to overall increased wrong way behaviour relative to constant velocity. At higher ΔH, the contraction effect is outweighed by the temperature effect, meaning wrong way behaviour is smaller than for constant velocity.

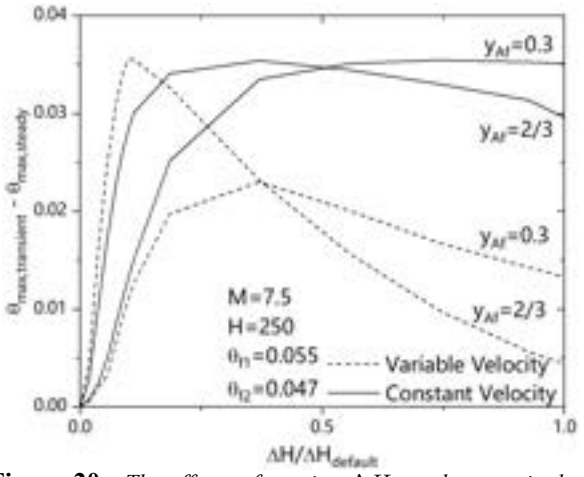

Figure 20: *The effects of varying ΔH on the magnitude of wrong way behaviour for varying feed fraction, comparing constant (solid lines) and variable velocity (dashed lines)*

Conclusions

This work presents a dynamic two-phase reactor model developed to account for variable velocity, which was successfully implemented into gPROMS Modelling Software. The model shows for a large range of parameters, the velocity expansion due to temperature dominates over velocity contraction due to reaction, serving to mitigate wrong way behaviour as opposed to constant velocity. However, there are exceptions for certain combinations of lower ΔH and higher contraction factors where velocity being a variable worsens wrong way behaviour. Sensitivities reveal interactions between heat and mass transfer parameters, which is expected due to their coupling via the reaction rate. Higher M values increase the magnitude of wrong way behaviour until such time as conversion is almost entirely in the early section of the reactor. Higher H acts to counter the latter effect. Increasing feed velocity also causes wrong way behaviour due to the same reasons as for a change in temperature.

Whilst the model provided consistent and explainable results, it is limited by certain assumptions. For example, assuming feed velocity remains constant for changes in feed temperature exaggerated the effects of variable

velocity, because it unduly increased velocity throughout the reactor instantaneously. In practice, feed temperature and velocity would be adjusted simultaneously to maintain molar flow and velocity in the reactor. Apart from lifting such assumptions, the model can also benefit from better initialisation procedures to enable model solution for more extreme parameters. There is potential to develop the model complexity to include radial effects, pressure drop or using more accurate equations of state in place of the ideal gas equation. On the whole, this model also has flexibility to be extended beyond Fischer-Tropsch GTL systems to a wider range of reactor/reaction systems by simple manipulation of parameters, making it a useful tool for industrialists.

Nomenclature

General Notation

ΔH	Heat of Reaction
a, b, c	Stoichometric Coefficents
C	Dimensionless Bulk Concentration ($= x_T y$)
C_s	Dimensionless Surface Concentration ($= x_{Ts} y_s$)
C_T	Total Concentration
c_{pf}	Specific Fluid Heat Capacity (Molar Basis)
c_{ps}	Specific Solid Heat Capacity (Mass Basis)
D_a	Axial Mass Dispersion Coefficient
D_e	Effective Diffusivity
E	Activation Energy
H	Dimensionless Interfacial Heat Transfer Coefficient
h_f	Interfacial Heat Transfer Coefficient
h_w	Wall Heat Transfer Coefficient
$k(\theta)$	Rate Constant at Temperature, θ
k_0	Pre-Exponential Factor
k_{mc}	Interfacial Mass Transfer Coefficient
L	Reactor Length
Le	Lewis number
M	Dimensionless Interfacial Mass Transfer Coefficient
M_ε	Defined by equation 11
P	Pressure
Pe_H	Peclet Number for Heat
Pe_M	Peclet Number for Mass
R	Ideal Gas Constant
r	Reactor Radius
r_p	Particle Radius
T	Temperature
t	Dimensionless Time
t'	Time
U	Dimensionless Wall Heat Transfer Coefficient
u	Dimensionless Velocity
u'	Velocity
u_{f0}	Reference Feed Velocity
x_T	Dimensionless Total Concentration
y	Dimensionless Mole Fraction
y_A	Reactant Mole Fraction
z	Dimensionless axial position
z'	Axial position in reactor

Greek Letters

β	Dimensionless Adiabatic Temperature Rise
η_s	Effectiveness Factor
λ_a	Axial Heat Dispersion Coefficient
ϕ_0	Thiele Modulus at $\theta = \theta_r$
ϕ_s	Thiele Modulus at $\theta = \theta_s$
ρ_s	Solid Density
θ	Dimensionless Temperature
ε	Bed Voidage
ε_A	Expansion Factor (Levenspiel, 1999)[12], negative value implies contraction

Subscripts

1	initial
2	final
f	feed, fluid
r, ref	reference
s	surface

References

[1] J.E. Crider and A.S. Foss. In: *AlChE* 12.3 (1966), pp. 514–522. DOI: https://doi.org/10.1002/aic.690120322.

[2] J.A. Doiberg, B.C. Lyche, and A.S. Foss. In: *AlChE* 17.6 (1971), pp. 1434–1447. DOI: https://doi.org/10.1002/aic.690170627.

[3] H. Van Doesburg and W.A. De Jong. In: *Chemical Engineering Science* 31 (1976), pp. 53–58. DOI: https://doi.org/10.1016/0009-2509(76)85008-7.

[4] C.S. Sharma and R. Hughes. In: *Chemical Engineering Science* 34 (1979), pp. 613–624. DOI: https://doi.org/10.1016/0009-2509(79)85106-4.

[5] C.S. Sharma and R. Hughes. In: *Chemical Engineering Science* 34 (1979), pp. 625–634. DOI: https://doi.org/10.1016/0009-2509(79)85107-6.

[6] S.H. Oh and J.C. Cavendish. In: *I.E.C. Prod. Res. Dev.* 21.1 (1982), pp. 29–37. DOI: https://doi.org/10.1021/i300005a006.

[7] P.S. Mehta, W.N. Sams, and D. Luss. In: *AlChE* 27.2 (1981), pp. 234–246. DOI: https://doi.org/10.1002/aic.690270210.

[8] V. Pinjala, Y.C. Chen, and D. Luss. In: *AlChE* 34.10 (1988), pp. 1663–1672. DOI: https://doi.org/10.1002/aic.690341010.

[9] Y.C. Chen and D. Luss. In: *AlChE* 35.7 (1989), pp. 1148–1656. DOI: https://doi.org/10.1002/aic.690350710.

[10] M.M.J. Quina and R.M. Quinta Ferreira. In: *Chemical Engineering Science* 55.7 (2000), pp. 3885–3897. DOI: https://doi.org/10.1016/S0009-2509(00)00029-4.

[11] A. Il'in and D. Luss. In: *AlChE* 38.10 (1992), pp. 1609–1617. DOI: https://doi.org/10.1002/aic.690381011.

[12] Octave Levenspiel. *Chemical Reaction Engineering*. 3rd Edition. John Wiley and Sons, 1999, p. 86. ISBN: 047125424X.

[13] J.Speight. "Gasification of Unconventional Feedstocks". In: Elsevier, 2014. Chap. 5, pp. 118–134.

[14] L. Nassr. "Simulation of Fischer-Tropsch Fixed-Bed Reactor in Different Reaction Media". MA thesis. Texas AM University, 2013.

[15] V. Govindarao and G. Froment. In: *Chemical Engineering Science* 41.3 (1986), pp. 533–539. DOI: https://doi.org/10.1002/aic.690381011.

[16] T.S. O'Donovan A.O. Odunsi and David A. Reay. In: *Applied Thermal Engineering* 93.3 (2015), pp. 1377–1393.

[17] NIST Standard Reference Database Number 69 NIST Chemistry WebBook. In:

[18] ThermoFischer Scientific. *Safety Data Sheet Iron (III) Oxide - Calcined Rev. 4*. 2019.

[19] B. Jager A.P. Steynberg R.L. Espinoza and A.C. Vosloo. In: *Applied Catalysis A: General* 186.1-2 (1999), pp. 41–54.

[20] Gerard P. laan and A. M. Beenackers. In: *Catalysis Reviews* 41.3-4 (1999), pp. 255–318.

[21] National Energy Technology Laboratory. *Syngas composition*. URL: https://www.netl.doe.gov/research/coal/energy-systems/gasification/gasifipedia/syngas-composition.

Optimisation of Monoclonal Antibody Purification Process via Data-Driven and Hybrid Modelling

Jiwon Kim and Seyoung Lee
Department of Chemical Engineering, Imperial College London, U.K.

Abstract
With ever increasing significance of monoclonal antibody (mAb) due to its versatility in biopharmaceutical industry, this project aims to investigate the potential of different computational algorithms in predicting the performance of protein A affinity chromatography process of Chinese Hamster Ovary (CHO) cell culture fluid containing mAbs and the process optimisation capacity of the proposed models was examined. Purely data-driven models with non-linear modelling capability, such as Support Vector Regression (SVR), Random Forest (RF) and Artificial Neural network (ANN), were trained on 80% of the data set and tested on 20% of the data set. Hyperparameters were tuned appropriately using grid search with k-fold cross validation. Additionally, in order to reduce the black-box effect of these models, hybrid model, whose parameters hold physical meanings, was developed by fitting the logistic function and determining the relationship between functional and process parameters via Multivariate Polynomial Regression (MPR). RF model demonstrated an accuracy of 98.17% with the strength in annual production estimation, whereas ANN showed an accuracy of 95.67% with the best understanding capability of the process. Despite a satisfactory accuracy of 94.57%, SVR was not recommended to be used in real-life process due to its poor computational efficiency. Hybrid model had an average fitting of higher than 99% with its strength in low computational requirement and exhibited acute insight towards the process. Overall, the optimisation result suggested a maximum of 14.8% increase in yield via altering the resin properties.

Keywords: Optimisation, Modelling, Monoclonal Antibody, Protein A affinity chromatography

1 Introduction

Since its first introduction in 1980's, monoclonal antibodies (mAbs) are one of the fastest growing classes of therapeutic compound [1] due to its efficacy in the treatment of cancer via the inactivation of tumour promoting agents [2] and reducing symptoms of various autoimmune diseases such as rheumatoid arthritis [3] by neutralising specific inflammatory mediators [4]. Reflecting its significance in treating incurable diseases, six out of the top ten best-selling pharmaceutical products were mAbs in 2018 [6]. Also, the efficacy of monoclonal antibody in treating infectious viral diseases such as the newly identified coronavirus, SARS-CoV-2 [5] is currently under clinical examination.

The production of mAbs is mainly based on the mammalian cell culture in the bioreactor during which many clones are genetically engineered to express the mAb of desired antibody specificity [8]. There are two main stages involved in the production of mAbs: upstream process (USP) and downstream process (DSP). In USP, the selected cell line is initially cultured in the series of inoculum trains before the sterilised production bioreactor is utilised for extensive cell growth, which typically operates in fed-batch mode. Whereas, in DSP, the mAbs from the culture fluid are purified to a permissible level for adequate human dosage by successive purification steps and viral inactivation.

End-to-end continuous processing via integration of USP and DSP is one of the most overarching challenges faced by biopharmaceutical industry as it can result in the reduction of processing time and the improvement in process economics [6]. Integrated continuous processing can reduce the average cost by 55% compared to conventional batch processing, considering both capital and operating expenses [7]. Despite a remarkable development in continuous process automation and control of USP, challenges still remain in DSP due to process immaturity and high cost involved as it accounts for more than 70% of the total manufacturing cost of mAb production [9]. Especially, the protein A affinity chromatography is the major bottleneck as it is the most expensive step in DSP, thereby urging the need for performance optimisation to establish robust process dynamics and reduce the cost associated.

Due to the high-resolution purification capability, the protein A affinity chromatography is commonly deployed at the initial stage of DSP. The culture fluid, containing mAbs and undesired impurities, from USP is loaded into the affinity chromatography column. The mAbs are bound to the pores of protein A resin particles, being immobilised for consequent washing and elution steps. Once unbound impurities are removed via washing, the bound mAbs are released from the column after the introduction of elution buffer. To retain the original column performance, various aseptic properties are restored in the regeneration step [8]. High cost of protein A resin (50-80% of total purification cost)[10] provides an initiative for further cost reduction by optimising the resin parameters along with various column performance parameters.

While process robustness and techno-economic efficiency are critical aspects of optimisation, special care should also be put into place with regards to regulatory purity requirements, such as host cell protein (HCP) level and mAb aggregate level. Especially, high HCP level poses a risk of product degradation and may even promote the development of immunogenic forms of the product, which would affect the safety of patient adversely. Acceptable level of residual HCP is traditionally set at 100 ng/mg therapeutic protein [11].

The optimisation strategy in bioprocessing should be based on the Quality-by-Design (QbD) framework to ensure product quality and consistency to meet the Quality Target Product Profile (QTPP) [6]. With respect to the Industry 4.0 initiatives, this emphasises the need for implementing a digital platform to establish in silico experimental environment through data-driven and hybrid modelling. It will enable easier, but more precise understanding on the relationship between Critical Process Parameters (CPP) and Critical Quality Attributes (CQA) during the implementation and execution of Design of Experiment (DoE). Hence, with the advancement in technology and computational capacity, the application of data-driven and hybrid modelling has come to an attention in the realm of bioprocess optimisation.

2 Background

The conventional modelling strategy for bioprocess, which is classified as kinetic and mathematical modelling, is based on the translation of fundamental process knowledge into mathematical equations and subsequent testing and fine tuning of the model with respect to experimental results are executed[12]. It has been widely exploited in optimising the affinity chromatography process and improving process knowledge along with its potential scale-up application. Pohar et al. developed a general rate mathematical model for the affinity chromatography system to determine new state-of-the art resin properties from experimentally determined breakthrough curves [8]. However, the process is laborious and lacks the flexibility of model structure as it is fixed by system knowledge. In response, data-oriented modelling has recently been introduced due to its capability of systematic, but less demanding process development even with limited process knowledge.

To exploit comparative advantages of both kinetic and data-driven modelling, hybrid modelling has been established. It consists of model structures that combine kinetic and data-driven submodels based on different knowledge sources [13]. The application of hybrid modelling in bioprocess has been highlighted owing to its potential in improving prediction quality and flexibility to select model complexity based on available data and knowledge [14].

In current practices, the optimisation of bioprocess is restricted by stochastic and complex nature of biological system. To tackle such challenge, the learning-based optimisation strategy via Machine Learning (ML) and Artificial Neural Network (ANN) has been proposed [15] [16]. Kotidis and Kontoravdi explored the potential of ANN and ML models in the prediction of protein glycosylation, in which the model was successful in simulating and predicting the glycoform distribution of four different recombinant proteins, despite its less computational demand [17]. Li and Yuan applied Support Vector Machines (SVM) to predict the key state variables in bioprocesses and the results suggested that for highly noisy training data, it outperforms the prediction ability of ANN [18].

However, since the black-box effect in ML and ANN models hinders the exploration of physical process, hybrid process models have been investigated to address such drawback [19]. Stosch et al. examined the integration of a parametric dynamic bioreactor with data-driven ANN model for E.coli fermentation to validate the efficiency of hybrid modelling in USP [14]. However, in spite of several applications of hybrid modelling in USP, its suitability to DSP operations has yet to be fully illustrated, especially with respect to chromatography optimisation and product purity [12].

The aforementioned knowledge gaps are present in relation to affinity chromatography process and its modelling strategies for process optimisation. This provides an initiative to investigate the potential of data-driven and hybrid modelling by ex-

amining their optimisation capacity and evaluating their relative suitability to the process.

3 Methodology

3.1 Data Acquisition

The data set regarding the experiment of protein A affinity chromatography of Chinese Hamster Ovary (CHO) cell culture broth containing the mAbs was kindly provided by Professor Andrej Pohar at National Institute of Chemistry, Slovenia

3.2 Data Exploration

The experiments were conducted at 5 different residence times (RT) (2, 4, 6, 8 and 10 minutes) and with 5 different protein A resins (*Eshmuno A, CaptivA PriMAB, POROS, MabCapture A* and *MabSelect SuRe LX*), resulting in total of 25 experiments. In each experiment, absorbance unit of UV light at 280 nm was recorded at 0.03 ml interval of total volume of liquid injected. This was the main target variable as it is directly linked to the concentration of mAb produced. Additionally, conductivity, buffer concentration, pressure, flow rate and temperature were recorded at 0.035ml interval of total volume of liquid fed. However, these were not carried over to further analysis as their variances were limited or did not play an active role in the loading step of the process. Conductivity was a noticeable metric as it exhibited a significant change throughout the process. Nevertheless, its behaviour was directly proportional to that of absorbance unit. Therefore, it was not extracted to avoid the co-linearity, thereby reducing the dimension of the analysis.

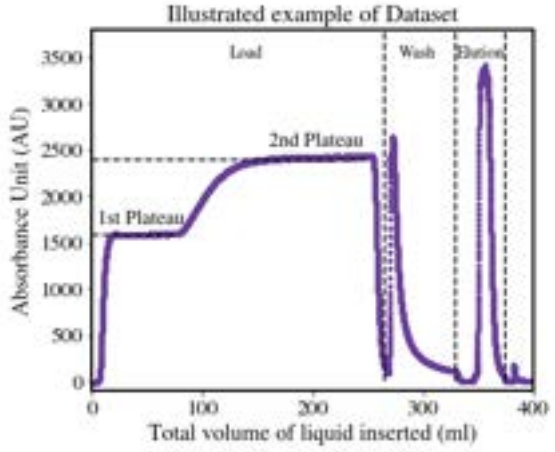

Figure 1: Exemplary Illustration of data set adapted by Pohar et al., 2018

In this project, the scope is limited to the loading step, based on the assumption that high binding concentration would lead to high yield of monoclonal antibodies after washing, elution and regeneration. Figure 1. illustrates an example of the data set of experiment with *CaptivA PriMAB* resin at the RT of 6 minutes. In the loading step, the first plateau represents the column breakthrough point, whereas the second plateau indicates the column saturation point.

3.3 Data Processing

Appropriate data wrangling was performed to ensure that the initial starting point of data set can reflect the actual starting point of the experiment and the same starting point was maintained throughout different experimental data sets. Moreover, since the variables of absorbance unit and the total volume of liquid injected do not represent the true physical quantity that is aimed to portray, these were converted to the concentration of mAb and time, respectively. The proportionality between absorbance unit and mAb concentration was identified as 15:1 as presented by Paul et al. in their research about analysis of mAb aggregates in mammalian cell culture supernatant [25].

After data processing, the data sets were collated with additional columns that provide information about the RT of the experiment and parameters of the resin used in the experiment (Equilibrium desorption constant (K_d), maximum binding capacity (Q_{max}), column void fraction (ϵ_c), particle porosity (ϵ_p), particle diameter (d_p) and parameter, taking pore diameter, antibody diameter and pore tortuosity into account(K_{fit})).

3.4 Data-driven ML model

In order to exploit the advantage of data-driven model, where it takes less effort and time to build a data-driven model [12], the data was first modelled using different ML models. Due to the apparent non-linear nature of the data set, models that respond well to the non-linearity were selected. For all models, training and test set were splitted into 8:2 ratio at random such that model can be trained on the training set and validated by the test set.

3.4.1 Support Vector Regression (SVR)

Support Vector Regression (SVR) is an extension of the classification method known as Support Vector Machine (SVM) which aims to find the hyperplane that separates the points with maximum margin[20]. In SVR, the main optimisation objective is focused on minimising the cost function

of data points outside the margin of ϵ [21]. Figure 2 portrays the simple example of linear kernel Support Vector, but in this analysis, non-linear kernels, rbf and polynomial, were used due to the non-linear nature of the process.

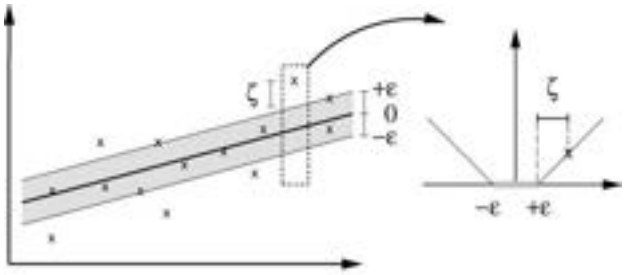

Figure 2: The soft margin loss setting for a linear SVM adapted by Schölkopf and Smola, 2002

In order to determine appropriate hyperparameters to find the most accurate model, grid search over different values of parameters with k-fold cross validation was carried out. In the case of SVR, the value of regularisation parameter(C) used to penalise the errors and ϵ, the margin in which the data points do not contribute towards the training loss function, are investigated in grid search thoroughly. To fit the model to the data set, an appropriate value of C should be selected to provide a good understanding of the shape of the non-linear curve and ϵ will result in error resistance from data fluctuation and prevent overfitting [26].

3.4.2 Random Forest (RF) Model

Decision Tree refers to the supervised ML algorithm, where at every node the data is continuously split to another subsequent nodes according to certain criteria until it reaches to the final decisions (leaves) [22]. The RF model is an ensemble model that utilises multiple randomised Decision Trees and makes prediction according to the average of the decision made by individual trees. The simplified RF algorithm is as follows [23][24]:

1. Draw n_{tree} samples from the training data set.
2. For each samples, grow a decision tree until the number specified in min_samples_leaf is reached. At each node, the best split is found either from all input features or a random subset of size max_features.
3. Predict the new data point by effectively aggregating the prediction of the trees. The number of trees is determined by n_estimators parameter in the model.

Despite the nature of RF model being piecewise linear, it is effective in describing the non-linear behaviour as it subdivides the input space into multiple independent regions where computation is more manageable. Therefore, given the apparent non-linearity of data, RF model is expected to predict to a degree of satisfaction. Moreover, although Decision Trees are known for its tendency to be overfitted, RF model prevents the overfitting effectively by aggregating the results of Decision Trees, thereby maintaining a good balance between fitness of the curve and the generalisation of the trend, which is critical in predictive modelling.

In order to use RF modelling algorithm, Random Forest Regressor in *scikit learn* was utilised. The data set was divided into training and test set of ratio 8:2 and the most appropriate hyperparameter was obtained using grid search with 5-fold cross validation of parameters: bootstrap, max_depth, max_features, min_samples_leaf, min_samples_split and n_estimators.

3.5 Artificial Neural Network (ANN) Model

Artificial Neural Network (ANN) is a computational modelling algorithm that replicates the working principle of biological neural network. In analogy with the neurons of human brain, ANN model consists of layers of nodes. The development of ANN model was carried out using *Tensorflow* package in Python.

The selected model was the sequential model provided by *keras* that consists of the normalisation layer fitted on the data set followed by multiple dense layers with ReLU activation function. The input layer contains nodes that are responsible for RT and resin parameters of interest and after subsequent processing through layers, single output of absorbance unit was obtained. To determine the loss at every epoch, Mean Absolute Error (MAE) was used and Adam optimiser was compiled with the model to improve model robustness at every training stage. The number of layers and nodes was determined by trial and error method such that there exists a balance between the accuracy of prediction and the computational efficiency. At every epoch, training and validation sets were sampled randomly at ratio of 8:2 and their losses were calculated separately to prevent overfitting. The training was completed after 100 epochs.

3.6 Hybrid Model

As illustrated in Figure 1, the loading step consists of two consecutive plateaus. Since the S-shaped plateaus resemble the logistic regression function,

the logistic function of the form shown in Equation 1 was fitted. The physical interpretation of functional parameters are summarised in Table 1.

$$f(x) = \frac{L}{1 + e^{-k(x-x_0)}} \quad (1)$$

Table 1: Physical interpretation of parameters of logistic function

Model	Accuracy
L	Maximum Yield
x_0	Time of surge
k	Gradient of surge
b	Systematic Error

The fitness of the function is evaluated by R-squared metrics and MAE. As one-to-one fitting of variables is only considered, R-squared metric was regarded to be sufficient enough to determine the function fitness and MAE was chosen over Mean Squared Error(MSE) and Root Mean Square Error(RMSE) as in some of the data sets, a series of anomaly was detected towards the end of the loading phase. Therefore, more robust error metrics were implemented.

As a consequence of fitting the logistic function into the data points, the functional parameters - L, k, x_0 and b - were determined. In order to scrutinise the relationship between functional parameters and process parameters, such as RT and resin parameters, the correlation metrics of Pearson correlation, Spearman's rho and Kendall's tau were calculated. Pearson correlation would determine the linear correlation between two parameters, thus, a pair of parameters with significant Pearson correlation could simply be fitted by the linear regression without computational effort. Spearman's rho and Kendall's tau determine the non-linear correlation between two variables in terms of the rank of variables.

After the correlation metrics were determined, the process parameters, demonstrating significant correlations to the functional parameters, were selected to model the functional parameters via Multivariate Linear Regression (MLR) and Multivariate Polynomial Regression (MPR).

The model is slightly inclined towards data-driven model in its core as the fitness of the logistic function is governed by the data. However, for the purpose of simplicity, this modelling approach is referred as 'hybrid model' in this paper, since its use of functional parameters with physical meaning aligns with the advantage of standard hybrid modelling. Therefore, it should be noted that this model does not integrate the kinetics and mathematics of the process as deeply as the hybrid models developed in other researches.

4 Results and Discussion

The programming implementation can be found in *https://github.com/SayYoungMan/bioprocessing_project*.

4.1 Support Vector Regression (SVR) Model

The training set was 5-fold cross-validated in grid search and the test set was used to determine the score of fitness subsequently. From the initial experiment comparing rbf kernel and polynomial kernel, rbf kernel outperformed polynomial kernel in terms of the computational efficiency and the modelling accuracy. Therefore, rbf kernel was used to model the data.

For hyperparameter optimisation, following parameter values were iterated and the pair of parameter values that provided the best score of 5-fold cross validation was determined.

Table 2: Hyperparameters and corresponding values used in Grid Search of SVR

Parameter	Values
C	[10, 100, 1000, 10000, 100000, 500000, 1000000]
ϵ	[0.001, 0.01, 0.1, 1, 10, 50, 100, 500]

The best set of parameters used in SVR was found to be C value of 10^6 and ϵ value of 50. This gave the accuracy of 93.42%. This suggests that there is a potential for further modelling with higher value of C by penalising the error more severely and aim to fit the curve more non-linearly. However, this comes with higher computational cost as the value of C increases, thus in practical settings, SVR might not be a feasible option for real-time modelling due to the necessity of high value of C. ϵ was optimised at the value of 50, which suggests that given the moderately fluctuating signal data, ϵ value of 50 showed a good coverage of these random errors. The failure to capture the initial stagnant behaviour at the level of 0 was also noticeable, but increased value of C would correct it. This result is demonstrated in Figure 3.

4.2 Random Forest (RF) Model

Similarly to SVR, the training data set was formed by 80% of the initial data set and 20% of it formed the test set to find out the fitness measure of the trained model. In order to tune the hyperparameters, 5-fold cross validation was implemented along with grid search with the following values of parameters.

Table 3: Hyperparameters and corresponding values used in Grid Search of RF

Parameter	Values
bootstrap	[True, False]
max_depth	[10, 20, 30, 40, 50, 60, 70, 80, 90, 100, 110]
max_features	['auto', 'sqrt']
min_samples_leaf	[1, 2, 4]
min_samples_split	[2, 5, 10]
n_estimators	[200, 400, 600, 800, 1000, 1200, 1400, 1600, 1800, 2000]

The determined parameters from the grid search were True bootstraping, 30 max_depth, 'sqrt' max_features, 1 min_samples_leaf, 5 min_samples_split and 1400 n_estimators. This model gave an accuracy of 99.95% in the test data set. The optimised number of tress (n_estimators) was calculated at the value of 1400, which comes at a cost of high computational effort. Therefore, it is advised to use lower number of trees to provide robust and efficient model, since the level of accuracy is high. The maximum depth of tree being optimised at the level of 30 portrays a good level of generalisation of the model. Using square root to reduce the number of features led to high level of accuracy as it generalised the shape of the curve appropriately. In order to visualise the prediction results, the model was used to predict the experiment of *CaptivA PriMAB* at the RT of 6 minutes.

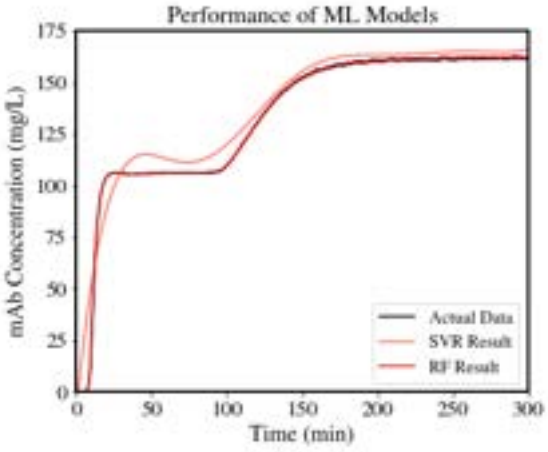

Figure 3: Prediction results of ML models

4.3 Artificial Neural Network (ANN) Model

From the trial and error, the model was optimised at the architecture of 3 hidden layers with 512, 256, 128 nodes progressively. The accuracy of the model on the test data set was 99.92%. As shown in Figure 4, there was no sign of overfitting to the training set, thereby showing a good understanding of general shape of the curve and robustness to the fluctuation. Each epoch took 15-28 seconds to train with 5ms/step on average, which is efficient enough to be utilised in the industry as a model to predict the real-life behaviour. Figure 5 demonstrates the prediction result of ANN model.

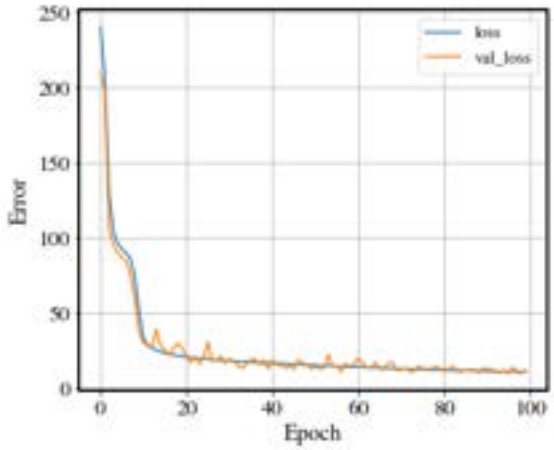

Figure 4: Train history of ANN model

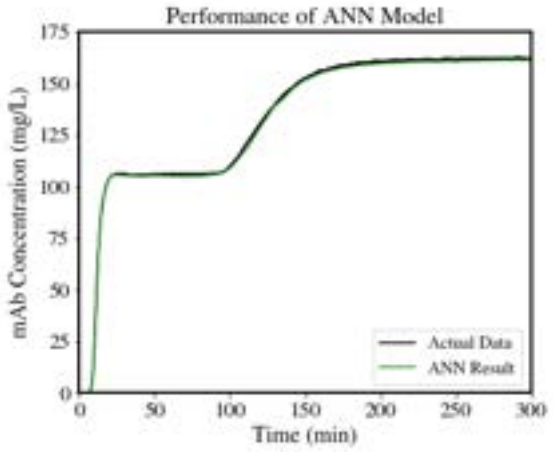

Figure 5: Prediction results of ANN model

Table 4: Accuracy of different data-driven models

Model	Accuracy
Random Forest	99.95%
SVR	93.42%
ANN	99.92%

4.4 Model Generalisation

The extremely high accuracy of RF and ANN model is due to the partial inclusion of every experiment in the training data set. Thus, it is easier for the models to predict the result as it can be simply derived from the training data. As a result, although the traditional method of train-validation-test split was executed, it still re-

sulted in slight overfitting of the model. This phenomenon is not desirable because the data set contains time-series data and the lack of number of experiments make process parameters appear to be discrete. Therefore, the generalisation of the model, that is the ability of the model to predict accurate results for unseen resin parameters, was doubted.

In order to approach this problem, all the data points from *CaptivA PriMAB* 6 minutes RT data set were excluded from the training set. The models were trained upon new training set and appropriate hyperparameters were identified and tuned to provide the best performance under this setting. The result can be found in Table 5 and Figure 6.

A slight decrease in accuracy of 1-4 percentage point (pp) was observed in both Random Forest and ANN model. In case of ANN, less number of layers used for computational efficiency and the generalisation provided robustness from the exclusion of data set, thereby providing remarkable understanding of overall shape, but slight deviation from the actual data. RF model had the highest accuracy with good prediction towards the end of the plateaus. This portrays the characteristic of RF model that constantly tries to re-adjust to the point of minimum error rather than trying to comprehend a general shape of the curve. Therefore, it showed the limits within the region of rapid change with scarce data points. SVR was least affected by the change because it was not initially overfitted as higher value of C to the point of overfitting could not be selected due to limited computational resources.

Table 5: Accuracy of revised models

Model	Accuracy
Random Forest	98.17%
SVR	94.57%
ANN	95.67%

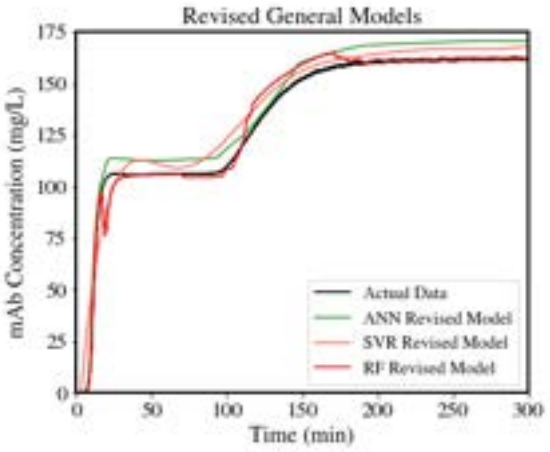

Figure 6: Revised Prediction results of models

4.5 Hybrid Model

As expected, the fitting of logistic function was successful with an average R-squared metric value of greater than 99%. Figure 7 shows the visualised example of the goodness of fit. The value of L was the most imperative parameter as it was directly related to the amount of production that needs to be optimised and the value of x_0 and b were also important as these were related to the duration of the cycle, which is indirectly linked to the annual production rate.

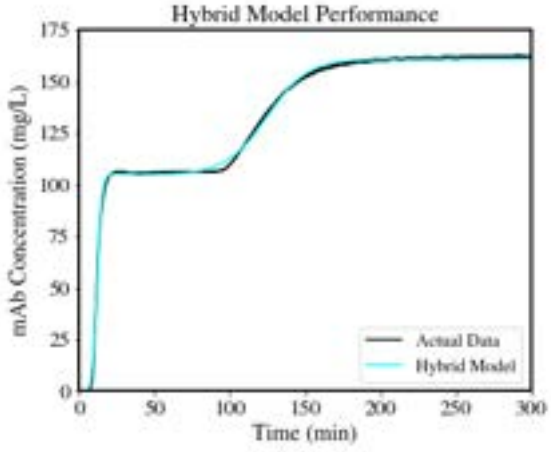

Figure 7: Performance result of Hybrid Model

Before proceeding to the mapping of relationship between functional and process parameters, their correlation was determined via correlation metrics and the key results are summarised in Table 6.

Table 6: Correlation metrics of statistically significant pairs

Process	Func.	Pearson	Spear	Kendall
RT	x0	0.997	0.980	0.912
RT	k	-0.894	-0.980	-0.912
Q_{max}	L	-0.273	-0.192	-0.124
ϵ_c	L	0.239	0.109	0.058
ϵ_p	L	-0.193	-0.302	-0.248
K_{fit}	L	0.343	0.514	0.394

x_0 and k were solely dependent on RT, which suggests that shorter RT is desired to make the annual production rate higher. However, shorter cycle is not desirable in terms of yield as the sufficient contact time is required for the mAbs to be bound to the resin particles. According to the analysis, RT did not show a significant correlation with L, which indicates that RT of 2 minutes was sufficient. K_{fit} showed the highest correlation with the value of L. This aligns with the theoretical explanation that the increase in K_{fit} causes an increase in effective diffusivity coefficient, which in turn leads to a decrease in transport resistance, making the adsorption of mAb

more efficient. Since K_{fit} describes the effect of specific resin-antibody pair, it is suggested to be most effective in describing the effectiveness of the resin. L was also found to be dependent on other resin parameters especially Q_{max}, ϵ_c and ϵ_p. However, their statistical significance was not proved due to high p-value ($p > 0.05$)

Based on the understanding that there is an element of co-linearity between resin parameters, the dimensionality reduction techniques such as Principal Component analysis (PCA) and Partial Least Squares (PLS) were initially performed. However, the results were not satisfactory as the regression between functional and process parameters resulted in the average accuracy of 64%. The accuracy metric was high in describing x_0 and k, but not for L and b. As x_0 and k were linearly dependent on the value of RT, it was described more accurately, but for more complex relationships, the dimensionality reduction failed to demonstrate its efficacy. This also suggests that the co-linearity in the resin parameters considered is not as significant as initially assumed.

Therefore, in order to decrease the dimensionality, from the values of the correlation metrics, some of the values that were proven to be trivial were manually removed from modelling. However, one should bear in mind that this would be a potential misdirection because in reality, all the physical parameters would cause a change in the process. For the purpose of the analysis, it was assumed that such exclusion can be effective within the range of data provided.

The modelling was then performed using Multivariate Polynomial Regression (MPR). Monotonic increase in accuracy was observed with an increase in degree polynomials as shown in Figure 8. Although the accuracy is maximised at higher degree, the data is likely to be overfitted, thus a careful balancing between overfitting and generalisation is again required.

Despite enormous potential and useful insight towards the process, current hybrid model bears the limitation in its core as it is only built upon a limited number of experiments. Therefore, its performance could be limited to certain values and range and the physical insight would likely be different in extreme conditions. For instance, at extremely short RT, L is most likely to be affected negatively. Thus, the model would be improved with the introduction of more experiments, while the data points for each experiment do not need to be as abundant as data-driven models.

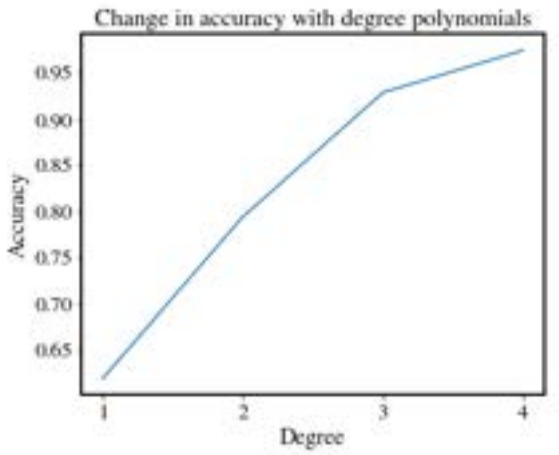

Figure 8: Accuracy of Functional Parameters with Degree Polynomial

4.6 Optimisation

The optimisation was performed via running the predictive models in the grid of data points, whose values vary within and slightly extended from the range used in the experiments. Consequently, the combination with the highest value of mAb concentration at total liquid volume of 250ml was selected. To evaluate the optimisation capacity of the models, the percentage increase from current production range is summarised in Table 7.

Table 7: Optimisation result of the models

Model	Yield (mg/L)	% Change
SVR	181.42	4.9 – 11.4
RF	176.81	2.3 – 8.6
ANN	181.96	5.3 – 11.8
Hybrid	186.95	8.1 – 14.8

Each model manifested a certain degree of optimisation capacity, implying the potential utilisation of these models to improve the process performance. Nevertheless, the result generated from RF model is most likely to be most accurate as it showed the best performance in predicting the final production yield, while others demonstrated slight over-prediction. Despite its robustness of data points within the experiment, Hybrid model was not as robust for the variation of process parameters, thus it bears a certain degree of inherent inaccuracy.

As emphasised in Section 4.5, the model prediction is solely based on the data provided in a certain range of parameter values. Therefore, the prediction of the data set outside the trained range might deviate from the actual phenomenon. Thus, further training with more combination of different process parameter values is recommended.

5 Conclusion

The optimisation result suggests that there is a room for further optimisation of real-life process up to 14.8% through the refinement of resin parameters along with various column performance parameters. Therefore, the proposed data-driven and hybrid models evince their potential towards the establishment of precise and robust optimisation platform for the affinity chromatography process in the pilot scale.

With respect to model utilisation, every model exhibited distinctive characteristics suggesting its specific use during the process. The strength of hybrid model lies in low computing power requirement and the provision of good insight into the process with high prediction accuracy. Therefore, it is recommended for a quick insight into the process. Despite failing to capture the general shape of the curve, the prediction ability of RF model at the plateaus was significant. As the production performance is measured at the point of column breakthrough and saturation, where the plateaus lie at in Figure 1, RF model would be suitable for estimating the mAb production rate. For ANN model, it is appropriate for the purpose of modelling progression of the whole cycle due to its good understanding of the curve. However, even with the rigidity with fair accuracy, the use of SVR model is not advised for modelling real-life process due to low computational efficiency.

6 Outlook

The scope of the analysis is focused on the DSP optimisation, highlighting the application of date-driven and hybrid modelling in the protein A affinity chromatography specifically. Despite the fact that the proposed models have demonstrated promising optimisation capability in the pilot scale, further studies should be carried out to examine its efficacy in the industrial scale production of mAbs. Upon scale-up, various design and process parameters are subject to change, implying the potential revamp in process characterisation. Thus, the optimisation strategy must be revised and modified accordingly.

Due to the time constraint, the techno-economic impact of the proposed optimisation models has yet to be established in this analysis. It is advised to examine the economic implication of each model as high cost of protein A affinity chromatography was the major bottleneck in DSP. In alignment with the industry 4.0 initiatives, the learning-based hybrid modelling has manifested its potentiality in developing a robust digital platform for continuous bioprocessing. On account of less complicated modelling capacity coupled with enhanced performance control, it would contribute to improving the economic potential of the mAb production. This leaves a room for further investigation to validate the techno-economic efficiency of data-driven and hybrid modelling.

Ultimately, the potential utilisation of data-driven and hybrid modelling in the mAb production targeted at SARS-CoV-2 virus remains to be explored to combat the unprecedented pandemic under the aim of wider, but more affordable vaccine distribution.

7 Acknowledgement

We would like to thank Professor Andrej Pohar at the Department of Catalysis and Chemical Reaction Engineering, National Institute of Chemistry, Slovenia for kindly providing the relevant data set for this project.

References

[1] K. Oxtoby. (2019). "How biologics have changed the rules for pharmaceutical industry", [Online]. Available: `https://www.chemistryworld.com/molecule-to-market/how-biologics-have-changed-the-rules-for-pharma/3010301.article` (visited on 12/01/2020).

[2] G. J. Weiner, "Building better monoclonal antibody-based therapeutics", *Nature Reviews Cancer*, vol. 15, no. 1, pp. 361–370, 2015.

[3] L. Bossaller and A. Rothe, "Monoclonal antibody treatments for rheumatoid arthritis", *Expert Opinion on Biological Therapy*, vol. 13, no. 9, pp. 1257–1272, 2013, ISSN: 1744-7682.

[4] N. Mahmud, D. Klipa, and N. Ahsan, "Antibody immunosuppressive therapy in solid-organ transplant part i", *mAbs*, vol. 2, no. 6, pp. 148–156, 2010.

[5] IAVI and Wellcome, "Expanding access to monoclonal antibody-based products", *IAVI*, 2020.

[6] M. M. Papathanasiou and C. Kontoravdi, "Engineering challenges in therapeutic protein product and process design", *Current Opinion in Chemical Engineering 2019*, vol. 27, pp. 81–88, 2019.

[7] J. Walther, R. Godawat, C. Hwang, Y. Abe, A. Sinclair, and K. Konstantinov, "The business impact of an integrated continuous biomanufacturing platform for recombinant protein production", *Journal of Biotechnology*, vol. 213, pp. 3–12, 2015.

[8] M. Grom, M. Kozorog, S. Caserman, A. Pohar, and B. Likozar, "Protein a affinity chromatography of chinese hamster ovary (cho) cell culture broths containing biopharmaceutical monoclonal antibody (mab): Experiments and mechanistic transport, binding and equilibrium modeling", *Journal of Chromatography B*, vol. 1083, pp. 44–56, 2018.

[9] B. Somasundaram, K. Pleitt, E. Shave, K. Baker, and L. H. L. Lua, "Progression of continuous downstream processing of monoclonal antibodies: Current trends and challenges", *Biotechnology and Bioengineering*, vol. 115, no. 12, pp. 2894–2907, 2018.

[10] B. Kelley, "Very large scale monoclonal antibody purification: The case for conventional unit operations", *Biotechnology Progress*, vol. 23, no. 5, pp. 995–1008, 2007.

[11] D. G. Bracewell, R. Francis, and C. M. Smales, "The future of host cell protein (hcp) identification during process development and manufacturing linked to a risk-based management for their control", *Biotechnology and Bioengineering*, vol. 112, no. 9, pp. 1727–1737, 2015.

[12] M. von Stosch, S. Davy, K. Francois, V. Galvanaukas, J.-M. Hamelink, A. Luebbert, M. Mayer, R. Oliveira, R. O'Kennedy, P. Rice, and J. Glassey, "Hybrid modeling for quality by design and pat – benefits and challenges of applications in biopharmaceutical industry", *Biotechnology Journal*, vol. 9, pp. 719–726, 2014.

[13] M. von Stosch, R. Oliveira, J. Oeres, and S. F. de Azevedo, "Hybrid semi-parametric modeling in process systems engineering: Past, present and future", *Computers & Chemical Engineering*, vol. 60, pp. 86–101, 2014.

[14] M. von Stosch, Jan-Martjin-Hamelink, and R. Oliveira, "Hybrid modeling as a qbd/pat tool in process development: An industrial e. coli case study", *Bioprocess Biosyst Eng.*, vol. 39, pp. 773–784, 2016.

[15] P.Petsagkourakis, I.O.Sandoval, E.Bradford, D.Zhang, and E. Rio-Chanona, "Reinforcement learning for batch bioprocess optimization", *Computers & Chemical Engineering*, vol. 133, 2020.

[16] Y. Sewsynker-Sukai, F. Faloye, and E. B. G. Kana, "Artificial neural networks: An efficient tool for modelling and optimization of biofuel production (a mini review)", *Biotechnology & Biotechnological Equipment*, vol. 31, no. 2, pp. 221–235, 2017.

[17] P. Kotidis and C. Kontoravdi, "Harnessing the potential of artificial neural networks for predicting protein glycosylation", *Metabolic Engineering Communications*, vol. 10, 2020.

[18] Y. Li and J. Yuan, "Prediction of key state variables using support vector machinesin bioprocesses", *Chemical Engineering & Technology*, vol. 29, pp. 313–319, 3 2006.

[19] A. Yang, E. Martin, and J. Morris, "Identification of semi-parametric hybrid process models", *Computers & Chemical Engineering*, vol. 35, pp. 63–70, 1 2011.

[20] W. S. Noble, "What is a support vector machine?", *Nature Biotechnology*, vol. 24, no. 12, pp. 1565–1567, 2006.

[21] A. J. SMOLA and B. SCHÖLKOPF, "A tutorial on support vector regression", *Statistics and Computing*, vol. 14, 199—222, 2004.

[22] X Oriant. (2017). "Decision trees for classification: A machine learning algorithm", [Online]. Available: `https://www.xoriant.com/blog/product-engineering/decision-trees-machine-learning-algorithm.html#:~:text=\%7C-,Blog,namely\%20decision\%20nodes\%20and\%20leaves` (visited on 12/13/2020).

[23] A. Liaw and M. Wiener, "Classification and regression by randomforest", *R News*, vol. 2/3, 18—22, 2002.

[24] scikit learn. (2020). "Randomforestregressor", [Online]. Available: `https://scikit-learn.org/stable/modules/generated/sklearn.ensemble.RandomForestRegressor.html` (visited on 12/15/2020).

[25] A. J. Paul, K. Schwab, and F. Hesse, "Direct analysis of mab aggregates in mammalian cell culture supernatant", *BioMed Central*, vol. 14, 99 2014.

[26] scikit learn. (2020). "Sklearn.svm.svr", [Online]. Available: `https://scikit-learn.org/stable/modules/generated/sklearn.svm.SVR.html` (visited on 12/15/2020).

A Scenario-based Analysis of Vaccine Stockpiling Uncertainty during COVID-19 pandemic

Rizqin Naim Bin Rizal and Wei Loon Ooi

Department of Chemical Engineering, Imperial College London, U.K.

Abstract

Vaccine supply chain is seen as the next step for the fight against COVID-19 as potential candidate vaccines has been identified. A steady supply of vaccine to the human population is important so that they can get vaccinated as soon as possible. Thus, it is imperative that the supply chain must be well equipped so that the best outcome may be achieved, and this requires planning ahead. Decision makers understand that producing vaccine stockpile before getting approval may have potential benefits. Some economic criteria might be investigated to measure the performance of the supply chain. In this paper, a mixed-integer programming (MIP) formulation is developed to simulate the vaccine supply chain in the UK with the integration of vaccine stockpile. Different amounts of stockpile is used to observe how well it can supply vaccines to potential patients. Two main objective functions were used to forecast the performance of the supply chain which are minimising total costs and maximising QALY benefits. Furthermore, a stockpile analysis was carried out to observe the benefits and loss of producing a vaccine stockpile and this corresponds to the probability of getting the approval of the vaccine.

Keywords: COVID-19, Vaccine supply chain, Vaccine stockpile, Mixed-integer programming, QALY benefit

1 Introduction

As vaccines usually have long manufacturing lead times, it is a usual practice for pharmaceutical companies to begin production before knowing the approval of vaccine by the Medicines and Healthcare Products Regulatory Agency (MHRA) and store the produced drug substance prior to fill-to-finish procedures. In the case of a vaccine rejection, it will obviously result in a large economic loss, but should it receive approval, the vaccines could be distributed through the supply chain to the recipients much faster than expected.

One of the major challenges of current vaccine supply chain is the preparation for sudden outbreaks [1]. The emergence of several potential candidates vaccine is a sign of encouragement in fighting against the spread of the coronavirus. As of November 2020, 3 vaccines, namely, Oxford/Astra Zeneca, Pfizer/BioNTech and Moderna has announced over 90% effectiveness in phase 3 clinical trials [2]. However, the vaccine still needs to be supplied to its potential patients in an orderly manner so that the vaccination programme is considered successful. Therefore, many studies simulate supply chain networks so that the optimal outcome is achieved and this could be put into practice.

This report outlines the development of General Algebraic Modelling System (GAMS) models to predict the scenarios between stockpiling and without stockpiling vaccines for an optimal outcome. More specifically, this paper looks further into the comparison between different benefits of minimizing total costs as well as maximising Quality-Adjusted life-years (QALY). Determining the difference between these benefits does not provide with enough information for decision making. As a result, this paper also presents a cost-based scenario analysis where a vaccine with stockpiling may or may not achieve approval and relating it to the probability of approval. Finally, these results may better impact the decision making process of stockpiling once the vaccine development is at an appropriate clinical phase. The decisions taken can be expressed as: whether to create a vaccine stockpile prior to vaccine approval, what and how much are the trade-off of minimising costs and maximising QALY benefit, how much vaccine stockpile to prepare considering the probability of approval and relevant cost incurred.

2 Background

This paper has been influenced by Stef Lemmens et al., in aspects of vaccine uncertainty and performance measures [3]. For **uncertainty**, we researched into vaccine stockpiling, whereas for **performance measures**, we looked into economic criteria and Quality-Adjusted life-years (QALY).

2.1 Vaccine Stockpiling

Historically, medical authorities such as the World Health Organisation (WHO) combat minor disruptions in seasonal outbreaks by actively maintaining a small stock level of vaccine, clearly insufficient to handle large disruptive outbreaks like the coronavirus outbreak. These stockpiles are used to a) Minimise total social costs, b) Minimise expected cases to a certain level, c) Maximise expected health benefits within certain cost range for stockpiling and d) Maximise available inventory for production capacity, according to Thompson et al. [4]. A few major risks to consider are tender procurement, outcomes of clinical trials and short shelf life.

Tender procurement plays a big role in the vaccine supply chain, as a lost tender will result in a large economic loss. Research by de Treville et al. investigates marginal value of time with tender risk and demand volatility, as well as incorporating the manufacturing lead time. According

to the paper, pharmaceutical companies may bid for a tender 10 months before delivery, and only receive any final answer regarding the tender 2 months before delivery [5]. Gatica et al. presents an optimisation-based approach to choose a final product and implementation strategy with differing clinical trials outcome probabilities including high success, target success, low success and failure scenarios [6] . Moreover, Anthony et al. predicted the COVID-19 vaccine production timelines for a range of vaccine portfolio of differing probability of success using JSON models by incorporating experts' predictions. The paper also utilises a Monte Carlo simulation to forecast the most probable vaccine platforms which will not be considered in this paper due to complexity reasons [7]. A research by Tsiakis et al investigates multi-product and multi-stage vaccine supply chain using Multi Integer Linear Programming (MILP) with an objective function of the minimisation of the total annualised cost of network [8].

2.2 Economic criteria

Research by Elisa et al. proposes an original mixed-integer non-linear programming (MINLP) cost-based model [9]. The paper also considered important factors including location management to support strategic and operating decisions to minimise costs for pharmaceutical companies. Even though this paper discusses interesting tactical decisions, these studies does not model for a high demand scenario to accommodate vaccinating the whole population of the UK. Research by King Hei Tsang created similar scenario-based stochastic MILP design model and analysed the financial risk by using expected NPV (eNPV) for a long time horizon [10]. The model also allows optimisation of investment and production strategy to maximise eNPV within constraints.

2.3 Quality-Adjusted life-years (QALY)

A common way to measure health benefits of a medication is via calculation of Quality-adjusted life-years (QALY) while Disability-adjusted life-years (DALY) is used to measure the amount of years taken away from perfect health as a result of a disease or condition. According to the WHO, QALY is defined to be measurement of equivalent healthy years lived, whereas DALY is defined to be the measurement of loss of health. Both metric represents the gap between the current pandemic situation and an ideal situation where the population lives to the standard life expectancy in perfect [11]. In this research, it can be assumed that QALY and DALY are the same and that any differences between the 2 metric is considered minor [12]. Previous literature by David et al., has discussed about the cost benefit analysis on the 3 months lockdown with an output of QALY benefits by using various strategies of suppression. From that paper, it has been concluded that it costs £30,000 to increase the life expectancy by one year, and 10 years of residual life expectancy has been lost on average for those who have died from COVID-19. This brings the QALY benefit per person vaccinated to be £300,000 [12].

3 Methods

To simulate the scenario of stockpiling, the GAMS software was employed in this research for the vaccine supply chain. Once a standard vaccine supply chain model was formulated, the stockpile scenario was integrated. The approach to this research can be divided into these categories: a) Modelling the standard vaccine supply chain problem based on data sources and current literature, b) Integrating the stockpile scenario into the standard vaccine supply chain model, c) Identifying the objective functions for the model, and d) Analysing the scenarios of stockpiling and without stockpiling.

3.1 Standard supply chain modelling

A general four-tier distribution network was taken as a starting point according to the research done by Kis et al [13]. Another extra level of fill-to-finish facility was added onto the supply chain model based on news by the UK government reserving manufacturing capacity for fill-to-finish production [14].

Figure 1: Supply chain structure

Figure 1 shows the four levels in the supply chain model, composed of 1 manufacturing facility, 1 fill-to-finish facility, 9 warehouses, 88 pharmacies and 88 recipients. The capital and variable costs of the facilities were taken from the simulation of the vaccine manufacturing of SuperPro Designer® Developed by Intelligen Inc. The demand and transportation cost were based off data from the Office of National Statistics (ONS) website, which is representative of the total population of UK, segregated into smaller regions throughout the country [15]. The candidate vaccine represented in this paper is the ChAdOx1 nCoV-19, thus 2 doses of vaccine, 4 weeks (28 days)apart is modelled for a vaccination timeline of 90 days to vaccinate the population of the UK [16].

The vaccine supply chain without stockpile scenario was implemented in GAMS with the related equations and

constraints which can be referred to Section 9, based on the standard supply chain model shown in Figure 1. The total time required including processing and transportation is 48 days post approval if no stockpiling decisions are put in place.

3.2 Stockpile-integrated supply chain modelling

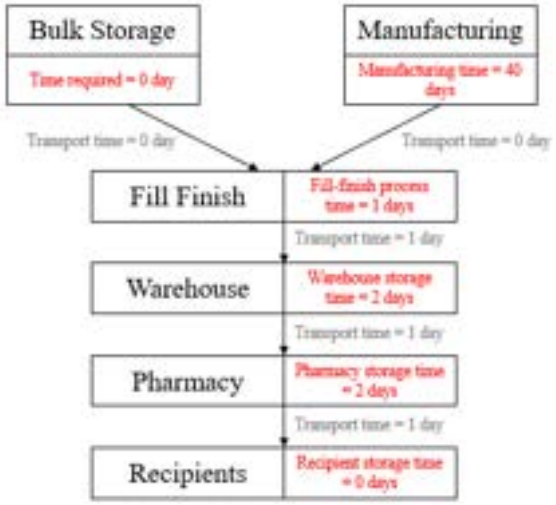

Figure 2: Supply chain structure overview for stockpiling scenario

Figure 2 shows the stockpile scenario, where another layer which is **Bulk Storage** was created in the supply chain to accommodate the storage of the vaccine prior approval. After receiving approval, the vaccines will be sent to fill-to-finish facilities to be converted into vials, ready to be transported to next levels in the supply chain.

The benefit of stockpiling scenario via bulk storage facility allows the vaccines to be received by the recipients much faster than the scenario without. By summing up the total transport and storage times, the vaccines will be received 8 days post approval, as compared to 48 days post approval for the scenario without stockpiling.

A range of stockpiling scenarios were used, which are 5 million doses, 10 million doses, 20 million doses and 30 million doses of vaccine. The reason that these values were used is because the total amount of vaccine required by the population is roughly 132m doses so a quarter of that value would be a good starting point as stockpile vaccines are targeted towards the earlier part of the vaccination program.

3.3 Optimisation Model Formulation - Objective functions

Three separate models have been created with differing objective functions which aims to:

1. **Minimise total costs**
2. **Maximise QALY benefit**
3. **Maximise QALY benefit with cost constraint**

The first objective function is to **minimise the total costs**, which is segmented into 2 distinct categories of total fixed costs (TFC) and total variable costs (TVC). The total fixed costs could be further broken down into the sum of capital/investment costs for all facilities including manufacturing, fill-to-finish, warehousing and pharmacy. Similarly, the total variable costs includes the storage and transport costs for all facilities, including the variable costs for manufacturing and fill-to-finish processes. The minimisation of total costs is represented by:

$$\min Cost = TFC + TVC \tag{1}$$

where TFC is denotes total fixed cost and TVC denotes total variable costs.

The second objective function is to **maximise QALY benefit** , which can be shown by:

$$\max \sum_{t} QB_t = Q_{pp} \cdot ceQ \cdot \frac{\sum_{vr} SR_IN_{vrt}}{2} \tag{2}$$

where QB_t denotes QALY benefit at time t, Q_{pp} denotes the QALY per person, ceQ denotes the cost effectiveness per QALY and SR_IN denotes the number of vaccinated people and is divided by two due to the second dose of vaccines.

After acquiring the maximised QALY, it was decided that a third objective function of **maximising QALY with cost constraint** was necessary as a method of pseudo bi-objective function optimisation in order to obtain a scenario where cost is minimised but with little QALY benefit sacrificed. The cost constraint was calculated by summing up the minimised cost and cost for maximising QALY benefit and dividing it by 2. Then, this value was entered into the model as cost constraint and simulated. This method was done repeatedly until there was a decrease in the QALY benefit. This point was then assumed to be the best possible point for a minimised cost and maximised QALY benefit. This method is similar to the Normal Constraint (NC) optimisation method, which approach was to transform the multiobjective function (minimising cost and maximising QALY benefit) into one single objective function in a reduced design space (maximising QALY with cost constraint) [17].

3.4 Stockpile Analysis

The next step of this study investigates whether manufacturing a bulk storage before the approval date is worthwhile for decision makers. Thus, in this section, the probability of obtaining the approval is taken into account as it is the deciding factor for companies. An expected value would correspond to the probability of approval and this can be a proxy to judge whether it is beneficial for vaccine pre-production. The main loss if rejection is obtained would be the cost invested in producing and storing the bulk storage before approval date. On the other hand, the main benefit of getting approval with a bulk storage is the amount of people that can be vaccinated more compared to a supply chain without stockpile. Accounting the vaccine efficacy and the probability of getting infected, the cost of

Table 1: Notation and data for cost benefit analysis

Symbol	Definition	Value	Unit
hr	hospitalisation rate	0.044	-
ccr	Critical care ratio	0.3	-
ifr	Infection fatality ratio	0.009	-
$ninc$	Non-ICU bed days for not critical condition	8	days
nic	Non-ICU bed days for critical condition	10	days
ic	ICU bed days for critical condition	6	days
ac_{NICU}	Average cost of non-ICU bed day	933	US$
ac_{ICU}	Average cost of ICU bed day	1152	US$
ac_{ELC}	Average cost of end-of-life care	232	US$

hospitalisation averted can be calculated with the candidates vaccinated.
Thus, the equation for the total cost of hospitalisation averted can be summarised below.

$$Cost_{hosp} = TVP \cdot E_v \cdot Z_{infection} \cdot Cost_{ht} \quad (3)$$

where TVP is the total number of people vaccinated, E_v is the efficacy of the vaccine, $Z_{infection}$ is the probability of infection, and $Cost_{ht}$ is the cost of hospitalisation for confirmed infections. $Cost_{ht}$ can be expressed in the following equation;

$$Cost_{ht} = \{hr \cdot [ccr \cdot (nic \cdot ac_{NICU} + ic \cdot ac_{ICU}) + (1 - ccr) \cdot ninc \cdot ac_{NICU}] + ifr \cdot ac_{ELC}\} \quad (4)$$

where the definitions and values for equation 4 are given in Table 1 [18].
The analysis can be summarised below which includes the probability of vaccination programme being approved to compare between the scenarios of rejection and approval by taking into account:

- the cost of bulk storage wasted for stockpiling if **rejected**
- the cost of hospitalisation averted if **approved**

As a result, an equation for expected value can be formulated by considering factors like costs and probability of approval. This can be simplified into equation 5:

$$E(X) = Cost_{hosp} \cdot Z - Cost_{Stockpile} \cdot (1 - Z) \quad (5)$$

where $E(X)$ is the expected value, $Cost_{hosp}$ represents the cost of hospitalisation averted if approved, $Cost_{Stockpile}$ represents the loss in the cost of stockpile loss if rejected and Z is the probability of vaccine approval.

4 Results and Discussion

In this section, the results of the model were analysed based on each of the scenario that were taken into attention. The amount of vaccine received was the main indicator as it can give a rough estimate of the amount of people getting vaccinated and this, in turn, would be proportional to the QALY benefit. Furthermore, the stockpile behaviour was also analysed as it was interesting how much of the vaccines in stockpile were distributed and at what rate. Lastly, the decision making strategy of taking a stockpile approach was also discussed here.

4.1 Stockpiling vs no-stockpiling scenario

Here, the comparison between the scenarios of stockpiling and no-stockpiling is discussed and deduced according to Figure 3 below.

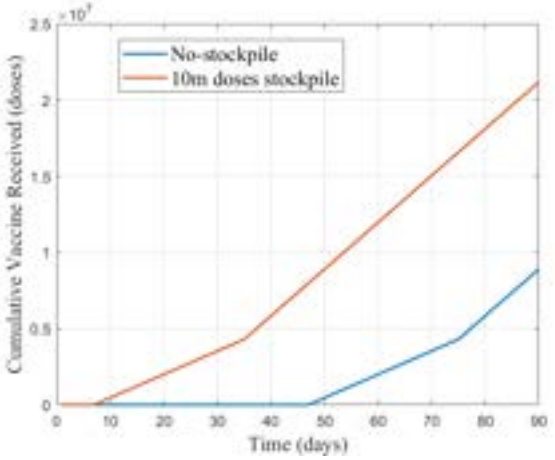

Figure 3: Cumulative doses of vaccine received vs time for no-stockpile and 10m doses vaccine stockpiling scenario

From Figure 3, the flow of vaccine from the bulk storage arrives at the recipients on day 8. Conversely, for the no-stockpiling scenario, the vaccine only arrives at the recipients 48 days after vaccine approval, taking into account the manufacturing time (40 days). It can be said that the stockpiling scenario is more desirable as it brings more benefits to the population in the way of an earlier vaccination process, thus potentially reducing the spread of the virus.
Over the course of 90 days, it is evident that the cumulative doses of vaccine received is clearly lower in the no-stockpile scenario (1.3m recipients) than the stockpiling scenario (2.1m recipients).
One interesting point to note in Figure 3 is the slight increase in gradient (representing the daily doses of vaccine received) on day 36 for the stockpile scenario. This can be explained by the increase in demand as recipients are required to take the second shot of vaccine 28 days after

their first (day 8 + 28 days = day 36). The same can be said about the no-stockpile scenario but on day 76.

4.2 Objective function - Minimising cost

Due to complex nature of the pharmaceutical industry, minimising cost is an important factor in maintaining the profitability of the companies. Based on assumptions and calculations from SuperPro Designer®, the capital costs for the supply chain are fixed at a total of **$940m**, which will remain constant for all scenarios in this paper. This was confirmed as the scenario where no stockpile was used, the model would just incur the capital costs as minimising it would translate to zero production of vaccine. However, this was not the case when the stockpile scenario was used as can be seen in Figure 4.

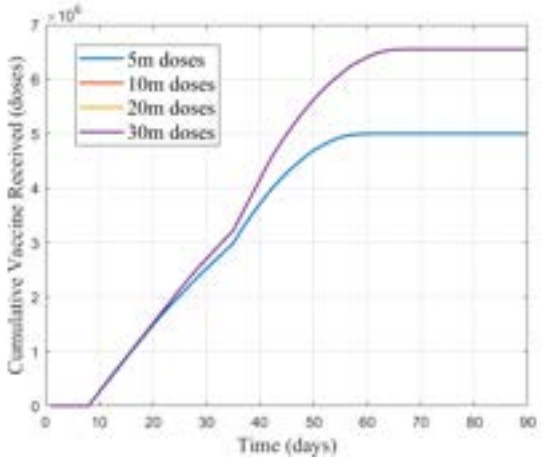

Figure 4: Cumulative doses of vaccine received vs time with objective function to minimise costs for various stockpiling scenarios

From Figure 4, it can be seen that by minimising cost, the stockpiling scenario of 10m, 20m and 30m vaccines has led to a maximum number of vaccine received of 6.5m doses after 90 days, whereas stockpiling scenario of 5m vaccines will supply 5m doses of vaccine to the recipients across 90 days. These numbers are well below the maximum vaccine doses of 22m vaccine recipients across 90 days calculated in the next section.

One explanation of such occurrence is that the model has identified that it would be much more costly to keep the vaccine in bulk storage than to distribute it to potential patients but only to a certain extent. This can be visualised in Figure 5.

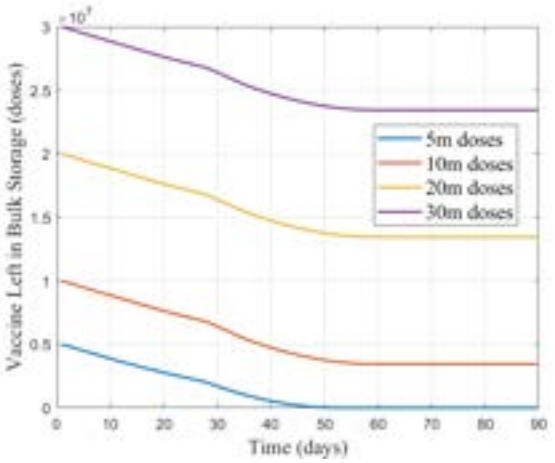

Figure 5: Doses of vaccine in bulk storage vs time

Figure 5 shows the doses of vaccine left in bulk storage, where in the case of 5m doses of vaccine stockpile, all of the doses were sent out to the recipients as it is much cheaper to do so than storing them in bulk storage. It is considered as vaccine wastage if the vaccines stored in the bulk storage are not used to vaccinate the population. For the scenario of 10m, 20m and 30m vaccine stockpile, the lines superimpose on each other in Figure 4, suggesting that after distributing 6.5m of vaccine doses, it is more costly to send out more vaccines than to store them. Thus, this leads to the plateauing of the cumulative doses of vaccine at 6.5m doses and storing any additional manufactured vaccines in bulk storage facilities as can be seen in Figure 4.
The relationship between each stockpiling scenario and the respective variable costs are noted in the Table 2.

Table 2: Variable cost for each scenarios, with objective function to minimise cost

Scenario	Variable Cost ($)
No stockpile	$0
5m doses stockpile	$8,273,000
10m doses stockpile	$17,659,200
15m doses stockpile	$36,539,200
20m doses stockpile	$55,419,200

From Table 2, it is evident that as the vaccine left in bulk storage increases, the variable cost increases due to increasing storage costs.

4.3 Objective function - Maximising QALY benefit

To gain the maximum number of the population vaccinated, we looked into the second objective function of maximising QALY benefit.

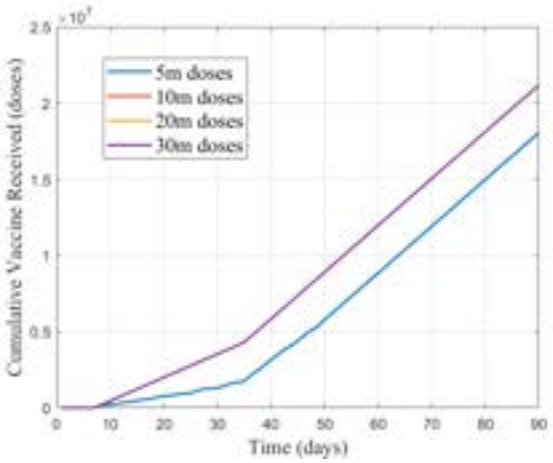

Figure 6: Cumulative doses of vaccine received vs time with objective function to maximise QALY benefit for various stockpiling scenarios

Without putting cost as a barrier, it can be observed from Figure 6 that for all of the stockpile scenarios, omitting the 5m doses vaccine stockpile, superimpose to similar numbers in terms of cumulative doses received by the recipients. The reasoning for this occurrence is the vaccine supply has met the total demand required and there are no deficit of vaccine doses. However, this is not the case for the 5m doses vaccine stockpile, as there is a deficit in vaccine and the supply does not meet the demand required. It is only until day 48 where the recipients receive vaccinations from manufactured vaccines after the approval date.
It can be deduced that there might be wastage in the number of vaccines produced or stored as there is no difference in the number of vaccines received for the cases of 10m, 20m and 30m doses of stockpile. With that in mind it was imperative to put a constraint in cost to reduce this wastage and to ensure that the vaccination programme would provide the best QALY benefit but with less wastage.

4.4 Objective function - Maximising QALY with cost constraint

In this section, an additional cost constraint was added to ensure a more appropriate economic and health outcome.

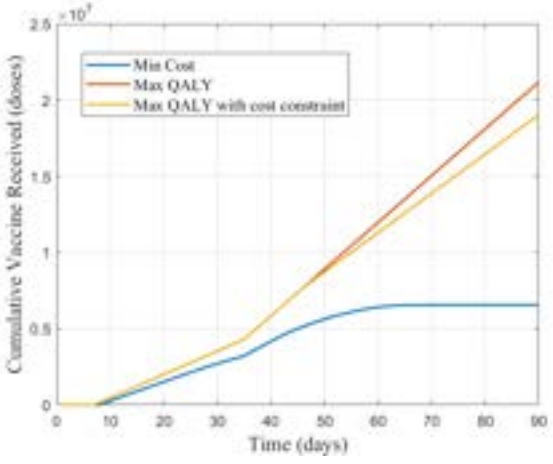

Figure 7: Scenario comparison for different objective functions for 10m doses stockpile

Table 3: Variable cost for different objective functions

Objective function	Variable Cost ($)
Mininising cost	$ 17,659,200
Maximising QALY benefit	$ 93,567,000
Maximising QALY benefit with cost constraint	$ 27,329,600

As seen from Figure 7, utilising the 10m dose vaccine stockpile scenario, the amount of doses of vaccine received has not changed significantly (2.1m doses less) between the maximised QALY scenario and the maximised scenario with a cost constraint but the cost savings as compared to the scenario of maximising QALY benefit is $66m. This can be calculated using variable cost from Table 3. This represents a cost saving of 70% based on scenario of maximising QALY benefit, which might potentially affect the profitability of the vaccine supplier.
Alternatively, for the scenario of minimising cost, there is a vast difference in vaccine received (15.5m doses less) as compared to the scenario of maximising QALY benefit. Even though variable cost of this scenario is about $76m less than the scenario of maximising QALY benefit, the drop in doses of vaccine received is too significant and will not be accepted as viable option.
Overall, it can be said that by maximising QALY benefit with cost constraint, a more desirable results can be obtained and will be studied in a greater detail in the next part of this section.

From Figure 8, it is observed that there is a much different trend for each stockpile amount as compared to the sole objective of maximising QALY benefit from Figure 6. The line representing the scenario without the stockpile is used as the benchmark for the stockpile scenarios.

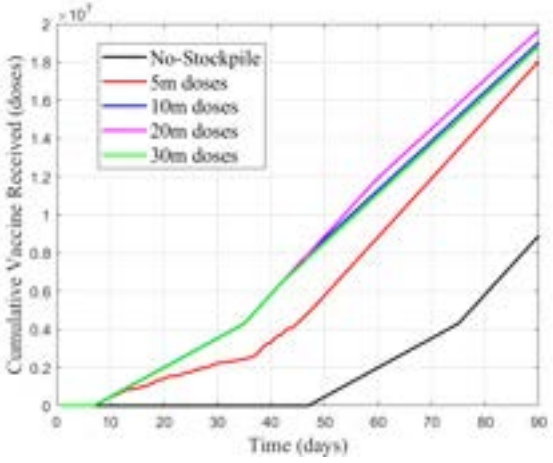

Figure 8: Cumulative doses of vaccine received vs time by maximising QALY benefit with optimum cost constraint for various stockpiling scenarios

Figure 8 shows that the scenario with a bulk storage of 20m doses supplies the most amount of vaccines to the recipient areas followed by 10m doses, 30m doses and 5m doses. Initially, it was thought that the scenario of 30m doses vaccine stockpile would supply the most to the recipient

areas but this was not the case here. One reason is that the constraint on the cost has been a limiting factor as there are more vaccine in bulk storage and as a result there would be more cost incurred to store 30m doses of vaccine. This would then decrease the amount of vaccine that could be manufactured or distributed after the date of approval.

The scenario which contains 20m doses of vaccine exhibited the most number of vaccines delivered since there are less costs on the storage of the 20m doses. There would then be extra funds as compared to the 30m doses of stockpile to manufacture more vaccines and distribute the ones in bulk storage. In the case where 10m doses of stockpile were used, it showed less vaccines received compared to 20m doses because it had less bulk storage vaccine but it has slightly more vaccines received compared to 30m doses since it has more funds to manufacture and distribute vaccine. Lastly, the scenario where 5m doses of vaccine that were kept in bulk storage had the least amount of vaccine received as the amount kept in stockpile were too little compared to the other scenarios.

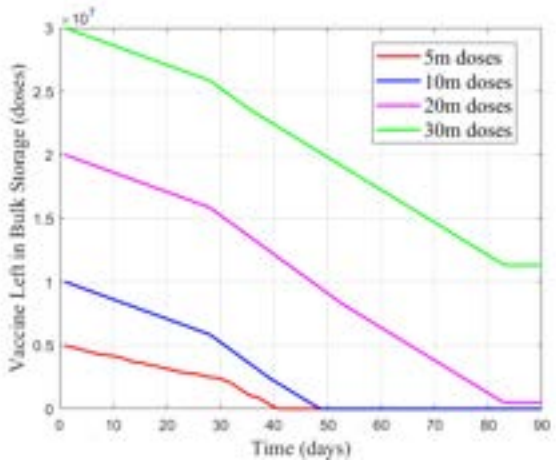

Figure 9: Doses left in vaccine bulk storage

It is also interesting to look into how the vaccine in bulk storage were distributed during this period by each of the different scenarios as shown in Figure 9. Here, it can be distinguished that more than 10m doses of vaccine stored in bulk storage were not distributed in the 30m vaccine stockpile scenario. The reason for this might be that the amount of vaccine in bulk storage is surplus to requirements or, on the other hand, the cost constraint has made it impossible for the rest of the vaccine in stockpile to be distributed to the recipients. This 10m doses of vaccine are considered wasted which could be used to treat potential patients.

There is much less vaccine wasted for the scenario of 20m vaccine doses stockpile as compared to the previous scenario but this can be still be seen as wasted vaccinations. The remaining two scenarios shows that vaccines stored in bulk storage was depleted after 48 days for the 10m doses stockpile scenario and 40 days for the 5m doses stockpile scenario.

Table 4: Variable cost for different stockpiling scenario with objective function to maximise QALY benefit with cost constraints

Scenario	Variable Cost ($)
No stockpile	$ 51,455,100
5m doses stockpile	$ 41,221,500
10m doses stockpile	$ 27,329,600
20m doses stockpile	$ 40,769,600
30m doses stockpile	$ 62,206,600

From Table 4, it can be seen that for the scenario of 5m doses vaccine stockpile and no stockpile, the lack of significant stockpile has led to a high variable cost as more vaccines have to be produced to achieve maximum QALY benefit. Conversely, for the scenario of 30m doses stockpile, an unnecessarily large amount of stockpile has not only led to extra bulk storage cost but also wastage in vaccine as well. The same reasoning could be used to explain the variable cost for the scenario of 20m doses stockpile but to a lesser severity. All things considered, the best scenario among the five is the scenario of 10m doses stockpile as it has proven not only to be the most economical in cost but also producing zero vaccine wastage.

4.5 Stockpile Analysis

Finally, this paper looks into the evaluation of each of the stockpile scenario before the the approval of the vaccine and whether it is worthwhile to start manufacturing in bulk. As mentioned in section 3.4, the benefits if approval is granted is the increase of cost of hospitalisation averted compared to the scenario without stockpile while the loss of rejection is the variable cost; i.e. cost of production and storage, and the capital cost of the stockpile facility.

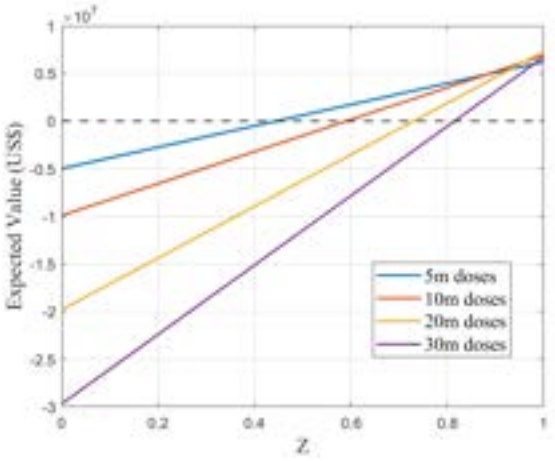

Figure 10: Graph of Expected Value vs Z

Figure 10 shows a graph of expected value against Z in which the probability of approval corresponded to the likely value of loss or gain. The dash line corresponds to the break-even expected value. It is observed that for the 5m and 10m stockpile scenario, there would be an expected loss for vaccine approval probability of below 0.446 and 0.591 respectively. These probabilities are known as the break-even probabilities. This trend where the break-even probability increases as the amount of stockpile increases is

also similar for the 20m and 30m stockpiles. The values of these are 0.731 and 0.816 respectively.

Thus, from these observations, it is clear that the rational decision for a low probability of vaccine approval is to stockpile a limited amount of vaccines.

Another thing to note here is that, as the amount of stockpile increases, the severity of expected value loss due to rejection would also increase. This means that there is an additional risk for an increased amount of stockpiling if a decision was made to stockpile before approval date. In contrast, a higher amount of stockpiling does not result to a significantly higher expected value or payback upon vaccine approval. From Figure 10, it can be observed that the gain in expected value tend to converge at a certain point for all scenarios of stockpiling. The stockpile amount which has the most gains is 20m followed by 10m, 30m and lastly 5m. As discussed in section 4.4, this is because the 20m stockpile is able to distribute the most amount of vaccine followed by 10m, 30m and 5m.

5 Conclusion

In summary, the 3 objective function models presented in this paper simulated different scenarios of vaccine stockpiling amount and has presented different health and economic impacts for the population. For the objective function of minimising cost, the QALY benefit produced is not satisfactory and for the objective function of maximising QALY benefit, the variable cost is too high. A 3rd objective function was introduced by maximising QALY benefit with cost constraint, which produced satisfactory results on both ends. It can be concluded that based on our assumptions and modelling, the 10m doses vaccine stockpile scenario (simulated to maximise QALY with cost constraint) provides the best solution to this uncertainty analysis as it manages to vaccinate 19m people (89% of maximum) within 90 days, and yet only spending $ 27,329,600 in variable costs (70% of cost savings). Furthermore, no wastage in vaccine bulk storage also proves that the vaccines stockpiled are managed appropriately and efficiently. Finally, this paper looked into the the relationship between the expected value and probability of vaccine approval for different vaccine stockpile scenarios. The scenario with 10m doses vaccine stockpile proved to be the best option with an acceptable risk and the expected value loss in case of vaccine rejection is much lower than the other stockpiling scenarios.

Ultimately, the decision of vaccine stockpiling and stockpiling amount is dependant on an array of drivers, including but not limited to: transport and storage capacity, demand, frequency of vaccination, vaccination timeline and etc. It is hoped that this research will aid companies as being a first approximation in deciding whether to stockpile or not. Further steps and limitations of this paper will be discussed in detail in the next section.

6 Limitations and Outlook

It is important to note that the assumptions applied in this model is not without its shortcomings so in this section the limitations of the model and the methodologies are discussed. After that, the outlook of this research is also studied to look into new avenues moving forward.

6.1 Accumulation of vaccine at different levels

In this model, an assumption is made where the input will be equal to the output at a specified time. It is also assumed that the number of vaccines produced is exactly the same as the demand and no deficit or surplus is considered. However, this may not be the case in reality as there may be an accumulation of vaccine if it is surplus to requirements or demand. The accumulation of the vaccine may incur more storage costs. Further research and optimisation can be taken to deal with such uncertainty.

6.2 Shelf life of vaccine

According to a press release by Moderna, the shelf life for its COVID-19 vaccine candidate can last up to 30 days with a refrigeration storage temperature of 2-8°C [19]. In the vaccine supply chain with a stockpile scenario, this has not been taken into account so it is quite reasonable to state that this model is limited by this. However, in this model, the distribution of vaccine from the bulk storage is done at a rate to satisfy demand and increase the QALY benefits. Nevertheless, it is imperative that future researches on similar topics must consider the shelf life of vaccines as the vaccine must be discarded when considered ineffective.

6.3 Timescale of vaccination period

In this model, a timescale of 90 days after approval has been chosen. However, a more complete approach would be to implement the vaccination programme across 365 days. The reason why 90 days was used instead of a full year is because the computing system was not capable of cope with the complexity of the equations. Thus, this has limited our results, where the full scale of the vaccination programme was not observed.

6.4 Metric for uncertainty analysis

The method that was used to analyse the risk of stockpile was based on the cost of hospitalisation averted and cost of the stockpile. This might be useful from the point of view of the government or economy but it does not provide any insights to private pharmaceutical companies whether it is beneficial for them. This might be the case but the coronavirus pandemic has impacted the economy especially the health sector. As in the case of NHS, there had to be an increase in capacity for the number of critical beds as the number of cases were soaring. As a result, the NHS is using all of its resources to curb this pandemic [20]. Although it might not be the only way to analyse the risk of stockpiling,

the cost of hospitalisation averted is a direct link with the number of people vaccinated in the supply chain.

6.5 Outlook

The approach that was taken in this paper can be further improved by looking into other avenues so that the model can be modified and gives a clearer picture of how stockpiling could work in a vaccine supply chain. One such way is by implementing new multi-objective function approaches such as back propagation (BP), and particle swarm optimisation (PSO), which was used in a paper by Sabegh et al., covering pharmaceutical supply chain for natural disaster response [21].

Since there is also an uncertainty regarding the development of stockpiling before the approval date, the Monte Carlo simulation could also be introduced in order to take into account the risk of stockpiling. Mangla et al. discusses in how this simulation was used to manage risks in operational networks in green supply chain [22]. An implementation of this technique in vaccine supply chain might prove useful especially in a time of a pandemic.

Other than that, it is also worth investigating the optimal time to produce the stockpile. As there is an uncertainty in when the approval date is given, it could be advantageous to look into this, together with the shelf life of the vaccine which could avoid potential wastage of any vaccine if it is manufactured beforehand.

There is also an opportunity here to investigate the effects of multi-product scenario for vaccine supply chain since there are different types of COVID-19 candidate vaccines such as the Pfizer/BioNTech and Moderna vaccines which uses mRNA technology as compared to the Oxford/Astra Zeneca vaccine which uses viral vectors in their vaccines. This would be an interesting study as these vaccines may have different manufacturing lead times while their total costs would also differ since they use different technologies.

7 Acknowledgement

The authors greatly acknowledge the support of Prof Benoit Chachuat and Dauda Ibrahim for the supervision on the project. We also acknowledge Prof Maria Papathanasiou and Prof Nilay Shah for the weekly research meeting for the insightful additions to the project. We acknowledge Zoltán Kis for providing information on capital and operating costs for the vaccine production model. Special thanks for Dauda Ibrahim again for the constant feedback on the GAMS model. We also thank Ye Jiahao and Zhu Yichuan for their skeleton supply chain model as a starting point.

8 References

[1] Duijzer, L. E., van Jaarsveld, W. and Dekker R., "Literature review: The Vaccine Supply Chain", *European Journal of Operational Research*, 2018.

[2] Binding, L. and Culbertson, A. (2020). "COVID-19 vaccines: How do the Moderna, Pfizer and Oxford coronavirus jab candidates compare?", [Online]. Available: `https://news.sky.com/story/covid-19-vaccines-how-do-the-moderna-and-pfizer-coronavirus-jab-candidates-compare-12134062`.

[3] Lemmens, S., Decouttere, C., Vandaele, N. and Bernuzzi, M., "A review of integrated supply chain network design models: Key issues for vaccine supply chains", *Chemical Engineering Research and Design*, 2016.

[4] K. M. Thompson and R. J. D. Tebbens, "Framework for Optimal Global Vaccine Stockpile Design for Vaccine-Preventable Diseases: Application to Measles and Cholera Vaccines as Contrasting Examples", *Society of Risk Analysis*, 2016.

[5] de Treville, S., Bicer, I., Chavez-Demoulin, V., Hagspiel, V., Schurhoff, N., Tasserit, C. and Wager, S., "Valuing Lead Time", *Journal of Operations Management*, 2014.

[6] Gatica, G., Papageorgiou, L. G. and Shah, N., "Capacity Planning under Uncertainty For The Pharmaceutical Industry", *IChemE*, 2003.

[7] McDonnell, A., Van Exan, R., Lloyd, S., Subramanian, L., Chalkidou, K., La Porta, A., Li, J., Maiza, E., Reader, D., Rosenberg, J., Scannell, J., Thomas, V., Weintraub, R. and Yadav, P., "COVID-19 Vaccine Predictions: Using Mathematical Modelling and Expert Opinions to Estimate Timelines and Probabilities of Success of COVID-19 Vaccines", *Center for Global Development*, 2020.

[8] Tsiakis, P., Shah, N. and Pantelides, C. C., "Design of Multi-echelon Supply Chain Networks under Demand Uncertainty", 2001.

[9] Gebennini, E., Gamberini, R. and Manzini, R., "An integrated production–distribution model for the dynamiclocation and allocation problem with safety stock optimization", *International Journal Production Economics*, 2009.

[10] Tsang, K. H., "Vaccine Supply Chain Optimisation", 2005.

[11] World Health Organisation, *The Global Burden of Disease concept*.

[12] Feng, X., Kim, D. D., Cohen, J. T., Neumann, P. J. and Ollendorf, D. A., "Using QALYs versus DALYs to measure cost-effectiveness: How much does it matter?", *International Journal of Technology Assessment in Health Care*, 2020.

[13] Kis, Z., Papathanasiou, M., Calvo-Serrano, R., Kontoravdi, C., and Shah, N., "A model-based quantification of the impact of new manufacturing technologies on developing country vaccine supply chain performance: A kenyan case study", *Journal of Advanced Manufacturing and Processing*, 2019.

[14] European Pharmaceutical Review. (2020). "UK government reserves Wockhardt production line to fill finish COVID-19 vaccines", [Online]. Available: https://www.europeanpharmaceuticalreview.com/news/125137/uk-government-reserves-wockhardt-production-line-to-fill-finish-covid-19-vaccines/#:~:text=The20UK\%20government\%20reserved\%20a,finish\%20of\%20COVID\%2D19\%20vaccines.&text=The\%20government\%20has\%20reserved\%20one,COVID\%2D19\%20in\%20the\%20UK..

[15] Office of National Statistics. (2020). "Estimates of the population for the UK, England and Wales, Scotland and Northern Ireland", [Online]. Available: https://www.ons.gov.uk/.

[16] Maheshi et al., "Safety and immunogenicity of ChAdOx1 nCoV-19 vaccine administered in a prime-boost regimen in young and old adults(COV002): a single-blind, randomised, controlled, phase 2/3 trial", *The Lancet*, 2020.

[17] Achille Messac, A. and Mattson, C. A., "normal constraint method with guarantee of even representation of complete pareto frontier",

[18] Zala, D., Mosweu, I., Critchlow, S., Romeo, R. and McCrone, P., "Costing the COVID-19 Pandemic: An Exploratory Economic Evaluation of Hypothetical Suppression Policy in the United Kingdom", 2020.

[19] Moderna. (2020). "Moderna Announces Longer Shelf Life for its COVID-19 Vaccine Candidate at Refrigerated Temperatures", [Online]. Available: https://investors.modernatx.com/news-releases/news-release-details/moderna-announces-longer-shelf-life-its-covid-19-vaccine#:~:text=Refrigeration\%20Storage\%3A\%20After\%20thawing\%2C\%20to,the\%206\%2Dmonth\%20shelf\%20life..

[20] Thorby, R., Tinson, A. and Kraindler, J. (2020). "COVID-19: Five Dimensions of Impact", [Online]. Available: https://www.health.org.uk/news-and-comment/blogs/covid-19-five-dimensions-of-impact.

[21] Sabegh, M. H. Z., Mohammadi, M. and Naderi ,B., "Multi-objective optimization considering quality concepts in a green healthcare supply chain for natural disaster response: neural network approaches", *International Journal of System Assurance Engineering and Management*, 2017.

[22] Mangla, S. K., Kumar, P. and Barua, M. K., "Monte Carlo Based Approach to Manage Risks in Operational Networks in Green Supply Chain", 2014.

Heat Integration for Cement Production with Reduced Carbon Impact using Direct Separation Reactors

Hiren H. Pandya[a] and Richard L. Woolley[a]

[a] *Department of Chemical Engineering, Imperial College London, SW7 2AZ, UK*

Abstract

Direct Separation Reactors (DSRs) are new vertically-heated reactors being developed to help to reduce the unavoidable CO_2 emissions attributable to the cement manufacturing process. A simulation of a pilot-scale 47 kt/year DSR plant was modelled on Aspen Plus V9, which showed that 4.9MW of excess heat is being produced. The flowrates were scaled-up to represent a 1 Mt/year process with 20 DSRs operating in parallel. A pinch analysis and subsequent heat integration around the reactors showed that considerable cost and CO_2 savings could be made by using a heat exchanger network to heat inlet streams that required heating. There was still 50MW of excess heat available after this, which was used to model raising steam for a Rankine cycle. This cycle could generate up to 12.9MW of electricity, or 9.6MW for scenarios with feasible heat exchanger areas. This was found to have a payback period of 5.5 years and saved a £7.6m in annual electricity costs. It was also found that a Rankine cycle with reheat could generate up to 15.6MW of electricity; a 20.6% increase from a single turbine cycle. These findings show that there are several opportunities for making cement plants with DSRs more economically and environmentally viable.

1. Introduction

The IPCC recommends an 80% reduction in CO_2 emissions by 2050, relative to 1990 levels [1]. Currently, the production of cement is responsible for 7% of global CO_2 emissions [2], with around 60% of these attributable to the calcination process and 40% to fuel combustion in the rotary kiln and indirect emissions caused by quarrying and transport [3]. Global cement production is centred in China (54%), India (8%), Vietnam and the US (each around 2%) [4].

Cement is needed to make concrete, which is necessary for the construction of buildings and other infrastructure [2]. Global cement production is forecast to increase by 12 to 23% from 2014 levels by 2050, driven by urbanisation and population growth [2]. As such, the decarbonisation of the cement production process is necessary to fulfil the IPCC's recommendations.

1.1 Cement Manufacturing Process

Ordinary Portland Cement (OPC) is the most common form of cement produced and used around the world [2]. It is produced by milling and crushing uncalcined raw meal, composed of a source of calcium carbonate such as limestone or chalk and a source of silica such as clay or shale in an approximately 80/20 split. This raw meal is either pre-calcined or calcined in a kiln at around 1500°C, followed by the addition of gypsum (which is used to moderate the setting time) at an amount of around 5% of the total mixture. In the usual OPC production method, hot combustion gases are contacted with the incoming meal in pre-heating cyclones, and then the heated meal is calcinated in the calciner [5].

The key reaction that occurs here is given by Equation 1.1.

$$CaCO_3 \leftrightarrow CaO + CO_2 \quad \text{(Eq. 1.1)}$$

After the kiln process, the hot mixture is air-cooled in order to solidify the clinker. Following this it is milled, and the end product is cement.

1.2 Carbon Capture and Storage (CCS) in the Cement Industry

As stated previously, approximately 60% of the CO_2 emissions from cement production are produced through the calcination reaction [6]. These are process emissions and are unavoidable, therefore carbon capture and storage (CCS) technologies are necessary to reduce these.

The CCS technologies most suitable for the cement industry include amine scrubbing, oxyfuel combustion and calcium looping, amongst others [3], [7]–[9].

Amine scrubbing is a post-combustion capture process and does not directly affect the cement manufacturing process. The flue gas is passed through an amine solution which captures CO_2. This solution, now rich in CO_2, is heated to reverse the reaction. It is the most well-developed and readily available technology; however it has issues regarding high cost and thermal energy requirements [7]–[9].

Oxyfuel combustion uses oxygen (as opposed to ambient air) as a combustion atmosphere, which produces a significantly higher concentration of CO_2 in the flue gases. This allows relatively simple CCS technologies to be used to capture these emissions [10]. In fact, these emissions can be immediately processed as they are close to pure CO_2 [10]. Unlike amine scrubbing, this technology requires difficult and expensive retrofitting of existing cement plants, so is mainly an option for new plants [3], [9]. Furthermore, there are increases in operating expenditure due to the cost of air separation [3], [9].

Calcium looping uses CaO as a regenerable sorbent to capture CO_2 in a carbonator. The reverse reaction, occurring in a calciner, produces a stream rich in CO_2 and regenerates the CaO [3]. There are potential energy savings from waste heat when this process is integrated with cement manufacture. Furthermore, only materials already present on a cement plant (such as CaO) are used in this process [8].

1.3 Direct Separation Reactors (DSRs)

Direct separation is a novel technology being developed to capture the unavoidable CO_2 emissions from cement production. The Australian company Calix Ltd is leading this research. The technology works by replacing the pre-calciner with a vertical externally-heated reactor, known as a Direct Separation Reactor (DSR), which allows limestone to be calcined without coming into contact with air or combustion gases, thus allowing close to pure CO_2 to be captured.

Figure 1.1 shows a schematic of the reactor. Solid material (raw meal) enters the top of the reactor and is calcined as it falls downwards. This calcination occurs because the reactor is externally heated using, for example, natural gas-fuelled burners around the outer wall. The calcined material is recovered at the bottom of the reactor. The calcination reaction releases CO_2, which flows counter-currently up the reactor. Since the solid material is heated externally, it does not come into contact with air or any combustion gases, so the CO_2 leaving the reactor is close to pure and can be directly captured [11]–[13].

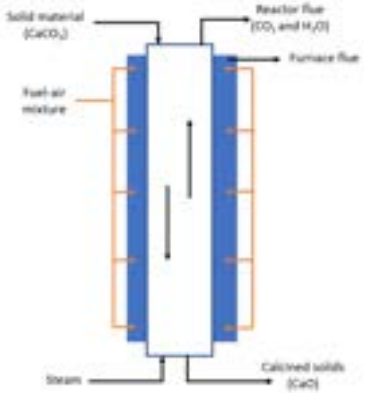

Figure 1.1: A direct separation reactor for cement production.

Note that steam can be injected at the bottom of the reactor in order to ensure a longer residence time of the solids and to reduce reactor temperatures. It also has a catalytic effect on the reaction [14]–[17]. Steam can be easily separated from the reactor flue gases, leaving a close to pure CO_2 stream.

The LEILAC (Low Emission Intensity Lime and Cement) project aims to construct a 240 t/day pilot reactor at the Heidelberg cement plant in Lixhe, Belgium, which will capture 95% of its process emissions. This constitutes about 60% of the plant's total emissions [11], [13].

Direct separation has several advantages over the other carbon capture technologies which could be implemented in the cement industry. Firstly, it is incredibly straightforward to retrofit older cement plants with this technology, as it only requires replacing the pre-calciner and requires no additional processes or chemicals [9]. Furthermore, direct separation can be used in conjunction with any number of other carbon capture technologies, such as amine scrubbing, and can use a variety of energy sources with a lower carbon footprint such as biomass [12]. This would allow further reductions in the carbon emissions from a cement plant [18]. Finally, it is believed that direct separation technology will be cheaper than many other potential carbon capture technologies as there are no additional capital or running costs (new CO_2 compression units will be needed but these are required for other forms of CCS anyway) [13].

2. Experimental

2.1 Aspen Simulation of DSR

A simulation of a 47kt/year cement plant using a single DSR was designed using the Aspen Plus V9 software. Figure 2.1 shows a diagram of the full plant which was modelled.

Raw meal, simulated as 79.2% $CaCO_3$, 13.2% SiO_2, 4.4% Al_2O_3, 1.9% Fe_2O_3 and the balance $MgCO_3$, at a flowrate of 2.2kg/s, is injected into the top of the DSR (Stage 1). The DSR consists of 12 separate stages, each modelled using a Gibbs reactor. A fuel-air stream is split to the individual stages to heat each separately. The heating is necessary to complete the calcination reaction. Hot steam is injected into the bottom of the reactor (Stage 12), for reasons noted previously. Cement clinker (primarily CaO) is released at the bottom of the reactor, where it passes through a rotary kiln, is cooled in a clinker cooler and is finally milled with the addition of gypsum ($CaSO_4$) to produce the final product of cement. Hot top gas rich in CO_2 is released from the top of the reactor and is separated from steam in a flash vessel. Subsequently, a pure stream of CO_2 is compressed and stored.

The conditions being used in the model, including flowrates and temperatures of each stream, were considered optimal at the time of writing. Particular interest was taken when deciding the temperature of the fuel-air stream. It was found, through sensitivity analyses, that preheating this stream to higher temperatures of around 500°C was the most energy efficient. Furthermore, it was found that using steam at 700°C and a flowrate of 1t/hour was the optimum.

Note that the system is not currently fully optimised and is undergoing further development.

In addition to the fuel-air stream, the raw meal, make-up air and steam-water streams need to be heated. To improve the energy efficiency of the plant, it was decided to heat these streams using some of the hot streams via a series of heat exchangers. This is discussed in detail in the next section.

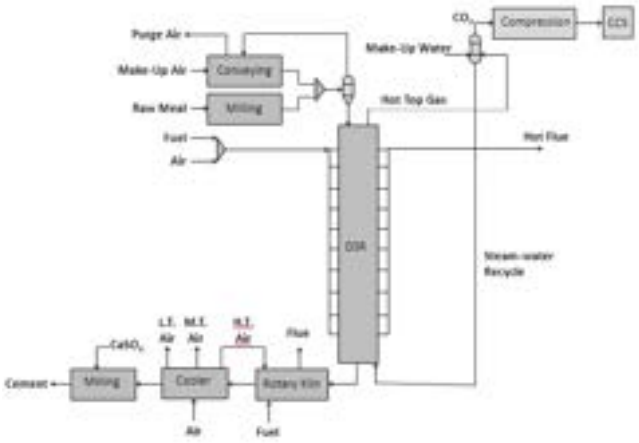

Figure 2.1: A full cement plant with DSR from which the Aspen Plus simulation was modelled.

2.2 Pinch Analysis

A pinch analysis for the system was conducted using the methodology as stipulated by Coulson & Richardson, 2005 and Kemp, 2007 [19], [20].

As can be seen by referencing Figure 2.1 with Table 2.1, the principal hot streams were streams 1, 2, 3 and 4. The main cold streams were streams 5, 6, 7 and 8. Note that the steam-water stream needed to be vaporised, and this was incorporated in the pinch analysis using the methods in Kemp [20]. It was decided to mix the medium temperature air stream from the cooler with the fuel-air stream to raise the temperature of the fuel-air stream from just above ambient to approximately 400°C. This allows for more efficient heat transfer than using heat exchangers. Table 2.1 shows the initial and desired temperatures of each stream.

Table 2.1: Hot and cold streams for the pinch analysis

Stream No.	Stream	Temperature (°C)	
		Initial	Final
1	Flue from burner	1200	100
2	Top gas from DSR	576	100
3	Low temp. air from cooler	169	100
4	Flue from rotary kiln	1200	100
5	Fuel-air	400	500
6	Make-up air	200	500
7	Steam-water	25	700
8	Raw meal	25	95

Note that there are no desired final temperatures for the hot streams (other than the top gas from the DSR); as much heat from them as necessary can be extracted. However, it was decided that the hot streams should be cooled to 100°C for the sake of conducting the pinch analysis. The top gas from the DSR should be cooled to 100°C for the condensation of water to occur. A minimum approach temperature of 10°C was used to conduct this analysis [19].

2.3 Aspen Simulation of Steam Rankine Cycle

Due to a large excess of heat from hot streams even after the heat integration via the pinch analysis, it was decided to model an ideal Rankine cycle with a single steam turbine. The model was produced on Aspen Plus V9. This would potentially improve overall efficiency by using waste heat to generate electricity (and so offset the net electrical requirements of the plant, and/or to sell to the grid).

The IAPWS-95 thermodynamic model was chosen to model this system as it provides one of the most accurate representations of the thermodynamic properties of water and steam over the range of conditions considered [21]. A flowsheet of the model can be seen in Appendix A.1.

From the results of the pinch analysis (section 3.2), it was apparent that three streams remain at elevated temperatures, namely the hot gas from the top of the reactor, the hot flue from the top of the burner and the flue from the rotary kiln. Since the hot top gas from the reactor contains the close to pure CO_2 which needs to be captured, it was not mixed with the other two streams and passed through its own heat exchanger, HX1. A mixture of the other two streams was passed through HX2. The hot stream outlet from HX1 was specified at 100°C to induce the condensation of water vapour in the stream. HX2 was initially specified with a hot outlet to cold inlet temperature difference of 10°C, since this would allow the highest amount of heat transfer from the hot stream without breaching the minimum approach temperature. This value was adjusted to find scenarios where the required heat exchanger areas were smaller. The turbine was specified with an outlet discharge pressure of 0.3 bar, which is amongst the minimum outlet pressure a turbine of this size can achieve based on industry data [22], [23]. The high-pressure water inlet pressure was to be specified to maximise turbine output, through sensitivity analysis on Aspen Plus and reference to an enthalpy-entropy diagram (Mollier chart, Appendix A.2). The steam flowrate was to be specified in a similar manner.

In order to simulate the process at typical production scale for cement (approximately 1 Mt/y) [24], the capacity was multiplied by around 20. This is further detailed in subsequent sections. The economic and CO_2 related implications of using a turbine system with the DSRs was also analysed.

2.4 Heat Exchangers Cost & Sizing

The heat exchangers were chosen to be shell and tube, due to being the most commonly used in the process industry and that they can be used over a wide range of temperatures and pressures [25]. Furthermore, costing data was readily available. Values for the air-air heat transfer coefficient (U) in a shell and tube heat exchanger, as well the flue gas–pressurised steam/water heat transfer coefficient used in the Rankine cycle are given in Appendix A.3. The calculation and assumptions used to calculate the value of U for HX2 in the Rankine cycle system can be found in Appendix A.4. These heat transfer values were used in conjunction with Equation 2.1:

$$Q = UA\Delta T_{LM} \text{ (Eq. 2.1)}$$

ΔT_{LM} is the log mean temperature difference of the four streams (hot inlet and outlet, cold inlet and outlet), and is defined in Equation A.5.1 (Appendix A.5)

From Equations 2.1 and A.5.1, an area, A, was found, and this was used to price the heat exchangers.

Pricing data for shell and tube heat exchangers was taken from Chemical Engineering Economics Appendix 1 [26] and [27] and [28] using the adjustment factors tabled in Appendix A.6.

Given the extremely high temperatures that the heat exchangers would be working at (>750°C in each case), a standard shell and tube heat exchanger material such as stainless steel would not be suitable [29]. Instead, Inconoy 800HT was chosen as the material of choice. The material factor for Inconoy 800HT was found by linearly scaling the $/kg costs for a reference material and the Inconoy 800HT.

Due to the limits of the costing graph in [26] and the typical sizes for shell and tube heat exchangers in [25], the maximum area for a heat exchanger that was considered was 11,500 ft^2 (1068m^2). Sensitivity of the cost/configuration of the heat exchanger network to the maximum allowable area and the heat exchanger lifetime was performed.

17 data points between areas of 9.3m^2 and 1021.9m^2 were taken from the costing graph in Garrett and used with Microsoft Excel's 'trendline' function to generate a function that directly linked the area (in m^2) to the cost, including the adjustment factors and exchange rates from Appendix A.6. The costs found for each scenario and configuration were then annualised and an annual maintenance cost of 2% of the initial capital investment [30] was used to calculate the total annual cost of the optimised/unoptimized heat integration scenarios.

The optimised and unoptimised scenarios refer to different configurations of a heat exchange network for a 20-tube DSR plant. More detail is given in section 3.3. Lastly, the performance of a heat exchange network in terms of both cost and overall CO_2 reduction was compared with two alternatives: gas and electrical heating (sections 3.7 and 3.8).

2.5 Efficiency Analysis and Further Opportunities

The Aspen model has assumed 100% isentropic and mechanical efficiency for the turbine and pump, and 100% efficient heat exchangers. In reality this is untrue and should be adjusted according to the best available technology, but allows an initial estimate of the viability of the process under ideal conditions to be found. The thermal efficiency of the Rankine cycle was calculated using Equation 2.3.

$$\eta_{thermal} = \frac{\dot{W}_{turbine}}{\dot{Q}_{in}} \text{ (Eq. 2.3)}$$

$\dot{W}_{turbine}$ is the total turbine outlet power and $\dot{Q}_{in}$ is the duty of all heat exchangers.

It is possible to improve this efficiency through modifications to the ideal Rankine cycle. A common modification is a Rankine cycle with reheat, whereby steam leaving the first turbine is reheated and passed through a second turbine in series (or through use of a two-stage turbine) [31], [32]. It was found that the hot outlet stream from HX2 was at high temperatures, so it was decided that this would be a suitable modification. This was modelled through modifications to the original Aspen simulation and is shown in Appendix A.7.

3. Results & Discussion

3.1 Baseline Performance of Aspen Model

The Aspen model for the DSR produces approximately 47kt/year of cement. Approximately 24 and 12 kt/year of CO_2 is produced from the DSR and burner flue respectively. That which is produced from the DSR can be captured and stored.

In order to heat the cold streams, a minimum of 2.4MW of heat is needed. If the hot streams were each cooled to 100°C, approximately 4.9MW of heat could be retrieved. This shows that there is a significant opportunity for heat integration using heat exchangers which could reduce the energy costs and carbon intensity of the heating processes considerably, and this is discussed in the following section.

It should be noted that the Aspen model only simulates a single, pilot scale DSR system producing 47kt of cement per year, whereas this figure is approximately 1Mt per year for an industrial scale cement plant [24]. Therefore, such a plant would require a number of DSR units to be operated in parallel, and in this case around 20. This would require approximately 48MW of heating with approximately 98MW of heat retrievable from the hot streams.

3.2 Evaluation of Heat Integration Opportunities

A proposed heat exchanger network is shown in Figure 3.1. This was devised after following the pinch analysis procedure detailed in section 2.2.

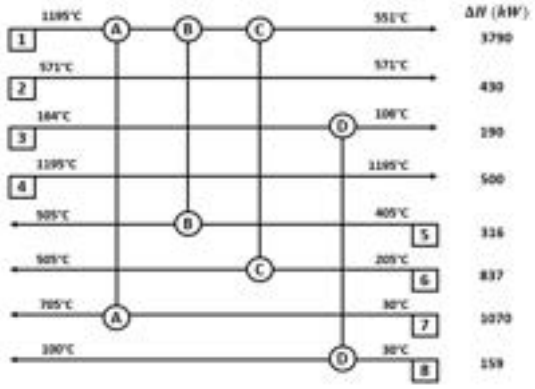

Figure 3.1: The proposed heat exchanger network

Table B.1.1 showing the duty for each heat exchanger can be found in Appendix B.1. Due to the large excess of heat in this system, it was found that there was no pinch point. Note that in Figure 3.1, streams 1, 2 and 4 are still at temperatures far higher than 100°C after the heat exchange has occurred. If each of these streams were cooled to 100°C, there would be approximately 2.5MW of excess heat available in the system for a single DSR, and 50MW for a parallel configuration of 20.

3.3 Heat Exchanger Costing & Sizing

As seen in Figure 3.1 there are four heat exchange incidences. However, the heat exchange between streams 3 and 8 (D) is based upon the hot air heating raw meal (a solid), and hence this was not sized or costed as a physical heat exchanger. Nevertheless, heat exchangers A, B, and C involve gas-gas and/or gas-liquid heat exchanges and the feasibility in terms of area and cost was considered. The pricing trendline discussed in section 2.4 is shown by Equation 3.1, where P is the price in GBP and A the area in m^2.

$$P = 41399A^{0.6877} \text{ (Eq 3.1)}$$

Using the data detailed in section 2.4, the area and cost of these heat exchangers per single DSR tube:

Table 3.1: Areas and Costs for HXs for different scenarios. Overall heat transfer coefficient values, U, are given in W/m²°C.

HX	U=10 Area (m²)	U=30 Area (m²)	U=50 Area (m²)
A	162	54	32
B	82	27	16
C	264	88	53

HX	U=10 Cost (£)	U=30 Cost (£)	U=50 Cost (£)
A	1,370,000	643,000	452,000
B	858,000	403,000	284,000
C	1,920,000	901,000	634,000

However, the desired outcome was to look at heat integration across a 20-tube DSR plant. There are multiple possible ways to arrange the heat integration; two extreme examples are shown in Figure 3.2 below:

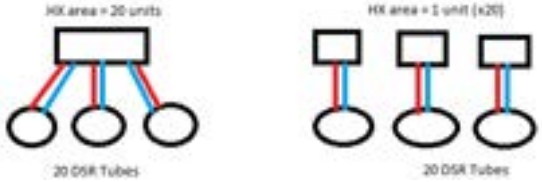

Figure 3.2: Schematic of possible HX configurations.

By examining the costing trendline in Equation 3.1 it was observed that it was always optimal to meet the required heat exchange area by allocating as much as possible of the area to one heat exchanger, as opposed to splitting it in any number of ways. Put simply, for a required heat exchange area of 1600m^2 it is more economical to have one heat exchanger of 1068m^2 and one of 532m^2 than two of 800m^2.

Table 3.2: Areas and costs for the optimised and non-optimised scenarios.

U = 50W/m²°C scenario

HX	Area required (m²)	No. of HXs	Layout	Total Cost (£)
A	647	1	1 x 647	3,550,000
B	329	1	1 x 329	2,230,000
C	1060	1	1 x 1060	4,980,000

Optimised cost for whole system = £10,800,000
Unoptimised cost = £27,400,000

U = 30W/m²°C scenario

HX	Area required (m²)	No. of HXs	Layout	Total Cost (£)
A	1079	1	1 x 1068 1 x 11	5,220,000
B	548	1	1 x 548	3,160,000
C	1762	2	1 x 1068 1 x 694	8,730,000

Optimised cost for whole system = £17,100,000
Unoptimised cost = £38,900,000

U = 10W/m²°C scenario

HX	Area required (m²)	No. HXs	Layout	Total Cost (£)
A	3236	3	3 x 1068 1 x 32	15,500,000
B	1643	2	1 x 1200 1 x 443	8,280,000
C	5287	5	4 x 1068 1 x 1015	24,900,000

Optimised cost for whole system = £48,600,000
Unoptimised cost = £82,900,000

It was found that for cases where the total surface area required for heat exchange exceeded the surface area that a single heat exchanger could provide, it was always optimal (in terms of cost) to have all bar one heat exchanger at the maximum permitted area. For the U = 30W/m^2°C optimised scenario, the average cost per kW of heat transfer was £385/kW which was compared with values from a heat integration example in industry [30] and was found to be similar. Assuming a lifetime of 20 years for the heat exchangers based off manufacturer data [33] and a conservative estimate compared to [34], as well as assuming an annual

maintenance cost of 2% of capital investment [30] the annualised cost for each of the scenarios could also be found:

Table 3.3: Annualised costs for the optimised and non-optimised scenarios.

Scenario	Optimised Annual Cost (£)	Non-optimised Annual Cost (£)
U=50W/m²°C	753,000	1,920,000
U=30W/m²°C	1,200,000	2,730,000
U=10W/m²°C	3,400,000	5,800,000

These annualised costs are useful to compare with the annual operating costs of alternative heating methods, as discussed in section 3.7. The sensitivity of the optimal heat exchange network price to the maximum shell and tube heat exchanger area was examined. In Table 3.4 the prices of the optimised scenarios for the various maximum heat exchanger area constraints are compared to the baseline scenario of $A_i \leq 1068m^2$ for U = 10W/m²K. The other U value scenarios show a similar trend but are generally less sensitive. U = 50W/m² is only affected in the $A_i \leq 600m^2$ scenario. This analysis assumes the pricing equation can be extrapolated:

Table 3.4: Sensitivity of annualised cost to max. HX area.

Max. A (m²)	Cost vs baseline	Optimised cost for whole system (£)
600	+19.3%	57,964,000
2000	-15.4%	41,100,000
4000	-26.8%	35,585,000
6000	-33.1%	32,517,000

The sensitivity of the annualised optimal heat exchange network cost to the life expectancy of the heat exchangers was also examined against the baseline annual cost for a 20-year life expectancy, for the U = 30W/m²°C scenario:

Table 3.5: Sensitivity of annualised cost to HX lifetime.

Lifetime (years)	Cost vs baseline	Optimised cost for whole system (£)
5	+213.5%	3,762,000
10	+71%.0	2,052,000
15	+23.5%	1,482,000
30	-24%	912,000

The same trend is applicable to the other U value scenarios. This is important to compare with the annualised costs for heating alternatives- if the HX lifetime were 5 years, gas heating becomes the cheapest heating method (see section 3.7).

3.4 Utilisation of Waste Heat by Rankine Cycle with Steam Turbine

To avoid damage to the turbine, it was decided that the outlet steam from the turbine should have a quality no less than 95% [35]. It should be noted that typical turbine outlet quality requirements can be higher. A scenario with an outlet quality of 1 is discussed in section 3.5. A sensitivity analysis was completed on Aspen Plus, whereby flowrate was varied with different turbine inlet pressures, and the maximum turbine power for each of these pressures was recorded. As can be seen from Figure 3.3, a pressure of 37 bar leads to the highest potential turbine power whilst maintaining outlet steam quality above 95%. This finding is corroborated with the use of a Mollier chart with an outlet pressure of 0.3 bar, as seen in Appendix A.2.

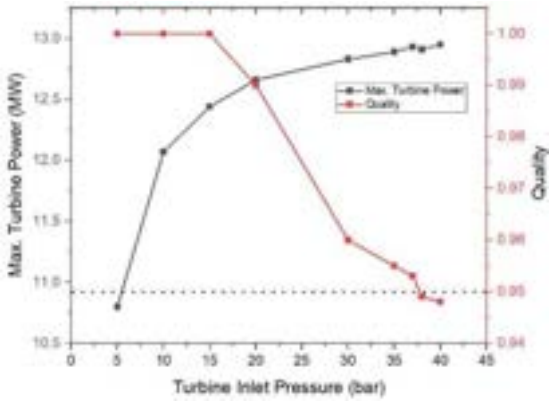

Figure 3.3: Maximum turbine power possible for various turbine inlet pressures. The dotted line indicates a quality of 95%.

From Figure 3.4, it can be seen that turbine power rapidly decreases with increasing flowrate, with a maximum of 12.93MW at 10.8 kg/s. Lower flowrates lead to temperature crossover errors from the heat exchangers, so were not considered. Quality decreases with flowrate, with only 10.8 kg/s meeting the minimum specification. These trends occur since the inlet temperature of steam to the turbine increases with decreasing flowrate, and a Mollier chart (Appendix A.2) shows how this leads to a greater change in enthalpy for the steam whilst passing through the turbine.

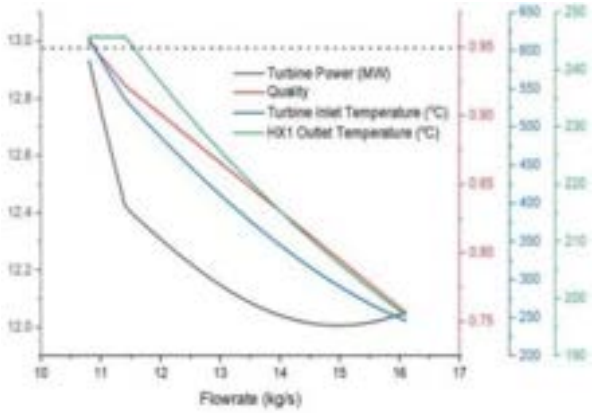

Figure 3.4: Turbine power, outlet quality, inlet temperature and HX1 outlet temperature over a range of flowrates, with a turbine inlet pressure of 37 bar. The dotted line indicates a quality of 95%.

The linear decrease in turbine power between 10.8 and 11.5 kg/s is due to the high-pressure water stream vaporising in HX1 between these flowrates, so the

temperature of the outlet stream from this heat exchanger remains constant throughout this range. Since the decrease in turbine inlet temperature with increasing flowrate slows at higher flowrates, there is a small increase in turbine power beyond 15 kg/s. Here, the increase in steam enthalpy at higher flowrates outweighs the decrease in enthalpy from being at lower temperatures.

It should be noted that this scenario considers an ideal situation with a completely efficient turbine and heat exchanger set-up. It therefore represents an estimate of the highest possible turbine power output possible for a single turbine in an ideal Rankine cycle.

3.5 Costing & Sizing for Rankine Cycle with Steam Turbine

It was found that using a hot outlet-cold inlet temperature difference of only 10°C for HX2 lead to infeasibly large areas and costs for this heat exchanger. This is due primarily to the very low overall heat transfer coefficients of steam-gas heat exchangers. From Figure 3.5 it can be seen how increasing the hot outlet- cold inlet temperature difference can drastically reduce the area required for HX2. Note, however, that the turbine power and quality of steam at the turbine outlet also decreases and breaches the allowed minimum of 95%.

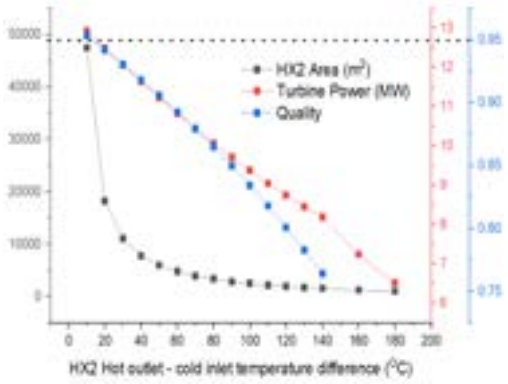

Figure 3.5: HX2 area, turbine power and quality against hot outlet to cold inlet temperature differences for HX2, for a steam flowrate of 10.8 kg/s, inlet pressure of 37 bar and overall heat transfer coefficient of 50 W/m²K. The dotted line represents a quality of 95%.

From Figures 3.3 and 3.4, it can be seen that reducing either the steam flowrate or turbine inlet pressure can increase the turbine outlet quality. These two parameters were therefore adjusted to find compromise solutions between turbine power output and heat exchanger areas whilst maintaining the minimum quality requirement. A number of possible solutions are given in Table 3.6.

A further opportunity for improving turbine outlet quality would be to increase the turbine outlet pressure. Figure B.2.1 in Appendix B.2 shows how this can, however, lead to a drastic decrease in turbine power.

To reach a quality of 95% a turbine outlet pressure of 4.1 bar is needed. Under these conditions, a turbine power of only 5.08MW is achievable with a HX2 area of 954m^2. This is for a flowrate of 10.8kg/s and inlet pressure of 37 bar, with a HX2 hot outlet-cold inlet temperature difference of 100°C. This turbine power is much lower than the previous scenarios with a similar HX2 area, so is therefore not recommended.

Table 3.6 gives several possible compromise solutions between turbine power output and cost, alongside Scenario 1 which gives an estimate of the highest possible turbine output (see section 3.4). Scenarios 2 and 4 use lower turbine inlet pressures whereas scenario 3 considers a lower steam flowrate. As expected, lower turbine power outputs correspond to lower total costs, except scenario 5. This scenario requires a much higher turbine output pressure of 4.1 bar, therefore would be suitable in a case where turbines capable of lower outlet pressures are unavailable, for instance. Scenario 4 represents a case when a turbine outlet quality higher than 95% is required (in this case the quality is 1). Notice how, generally, higher turbine power outputs require higher costs for the heat exchangers.

For the different Rankine cycle scenarios, the areas of HX1 and HX2 were calculated, and this was used to find the cost of each of them (shown in Table 3.6 as a combined value).

Table 3.6: Ideal Rankine cycle scenarios with feasible heat exchanger areas compared to the scenario with highest turbine output.

Scenario	Flowrate	Inlet Pressure	Outlet Pressure	HX2 hot out – cold in T difference	Turbine Power	Outlet Steam Quality	HX1 Area	HX2 Area	Total HX Cost
	kg/s	bar	bar	°C	MW	-	m²	m²	£
1	10.8	37	0.3	10	12.93	0.95	1400	48400	N/A
2	10.8	16	0.3	100	9.60	0.95	610	1930	2,560,000
3	6.3	37	0.3	220	7.48	0.95	670	1470	2,310,000
4	10.8	2	0.3	200	5.15	1	530	1090	1,913,000
5	10.8	37	4.1	100	5.08	0.95	670	1230	2,142,000

The pricing for the steam turbines as a single unit was taken from Chemical Engineering Economics Appendix 1 [26]. However, these values did not consider other factors when pricing the installation of a steam turbine system: the heat recovery steam generator (HRSG), piping, installation, etc. The sizing of the heat exchangers in Table 3.6 therefore provides an initial estimate for the sizing of the HRSG and most importantly proves its feasibility. Instead, the turbine system as a whole was priced using the conservative rule of thumb value of $5,000/kW [36], and 20% (average of 15-25% of total cost attributable to turbine unit) of this value roughly corroborated with the individually-calculated prices for the turbine units from [26].

Table 3.7: Turbine unit prices and overall system price

Scenario	Turbine unit price (Garrett) (£)	Turbine unit price (CHP) (£)	Turbine System cost (£)
1	N/A	N/A	N/A
2	7,359,000	7,295,000	36,475,000
3	5,724,000	5,681,000	28,405,000
4	4,497,000	3,914,000	19,570,000
5	4,456,000	3,861,000	19,304,000

Evidently the steam turbine should be looked at from an economic viewpoint. Using a steam turbine availability of 95% [37], the amount of a 1Mt/year plant's electricity demand that the turbine can provide can be calculated. Using the literature [29] value of 110kWh of electricity per tonne of OPC produced, the plant's electricity requirement was calculated (12.56MW). Therefore, key economic KPIs for each turbine scenario were found, using a turbine lifetime of 50 years [38] an operating cost of £0.0076/kWh [36], and a non-domestic electricity price of £0.0911 [39]. Further assumptions are detailed in Appendix B.3. The payback period for each scenario was 5.5 years; given that all costs are on a per kW basis, this is unsurprising. However, after the payback period, the amount of money spent on electricity annually is shown below for each scenario:

Table 3.8: Expenditure on electricity for turbine scenarios.

Scenario	Power (MW)	Annual expenditure on electricity (£)
1	N/A	N/A
2	9.60	2,362,000
3	7.48	4,054,000
4	5.15	5,913,000
5	5.08	5,969,000
No turbine	-	10,021,000

These savings are enough to exceed the annualised cost of implementing a heat exchange network.

3.6 Efficiency Analysis & Further Opportunities

The Aspen model used to develop the scenarios above considered an ideal Rankine cycle with a single steam turbine. For the optimum scenario (steam flowrate of 10.8 kg/s and inlet pressure of 37 bar, with HX2 hot outlet to cold inlet temperature difference of 10°C, i.e. scenario 1 from Table 3.6), a thermal efficiency of 35% was calculated. This is lower still for the other scenarios.

Through optimisation in Aspen Plus, it was found that an estimate for the maximum turbine output from a Rankine cycle with reheat was 15.6 MW. This occurs when the inlet and outlet pressures for the first turbine were 120 and 2.8 bar respectively, and steam flowrate 13.3 kg/s. This is a 20.6% increase in turbine output since more of the heat from the hot streams is being utilised. Further analysis is needed in terms of heat exchanger and turbine sizing and costing for this scenario, but initial results are promising.

3.7 Techno-Economic Analysis

The cost of creating a heat integration system was found in section 3.3, however this must be compared to the alternatives (electrical heating and gas heating) on a techno-economic basis. Firstly, the yearly duty for each of the three streams that required heating was found (for a 20-tube DSR plant), and from this the amount of energy (in kWh) was found. Based on electricity and gas prices, the annual cost could be found for the supply of energy. The price of electricity used was £0.0911/kWh [39] while the price of gas used was £0.0130/kWh [39]. The gas and electric heaters were priced as furnaces [26] (cost data for direct or indirect electric heaters could not be found for this scale) and their lifetime was assumed to be 30 years [40], and from this an annualised capital cost was combined with the operating cost:

Table 3.9: Annual Electricity and Gas demands and costs.

Stream	Duty (MW)	Electricity required per year (kWh)	Electricity cost per year (£)
7	21.32	186,782,700	17,016,000
5	6.32	55,386,300	5,046,000
6	16.74	146,658,200	13,361,000
Total			35,423,000

Total inc. equipment cost: £35,695,000

Stream	Duty (MW)	Gas heating required per year (kWh)	Gas cost per year (£)
7	21.32	186,782,700	2,428,000
5	6.32	55,386,300	720,000
6	16.74	146,658,200	1,907,000
Total			5,055,000

Total inc. equipment cost: £5,327,000

As seen in the results, gas heating is the cheaper method. However, both must be compared to the heat integration scenarios in which even the unoptimized, worst heat transfer coefficient value scenario has an annualised cost of around £5,800,000. This is more expensive than the annualised gas heating cost, but all

the other scenarios and configurations outperform gas heating on an economic basis.

3.8 Carbon Dioxide Reduction Potential

Given that the purpose of using a DSR for cement production is to reduce the amount of CO_2 emitted, it was considered important to also evaluate the reduction or increase in overall CO_2 emissions the suggested heat integration opportunities (heat exchanger network and steam turbine) would cause. As detailed in section 2.2, pre-heating of the steam-water, fuel-air, and make-up air streams was required. Sections 3.2 and 3.3 shows that this can be done via heat integration, however the alternatives are to use gas heating or electrical heating. Based on the heating duty requirements for the inlet streams, the amount of electricity or gas needed to achieve that duty was found, and hence the associated CO_2 emissions for both of those methods. For a 20-tube DSR plant, the following results were found:

Table 3.10: Annual CO_2 emissions for electrical and gas heating.

Method	CO_2 emitted per year (tonnes)
Electric	75,800
Gas	83,600

See Appendix B.4 for more detail on the energy requirements. This is based on a CO_2 emissions intensity of 0.195 $kgCO_2/kWh$ [41] for electricity generation and 0.215 $kgCO_2/kWh$ [42] for gas burning in the UK. Comparing the two sets of results, it is clear to see that using electrical heating has a lower carbon impact, although it should be noted that prior to 2019 (in the UK), the gas heating method would have had the lower carbon impact [42]. However as electrical power generation has shifted towards low-carbon methods, this has changed and will continue to do so.

To contextualise these results with regards to the project, they are compared against the amount of CO_2 that the Aspen model predicts a 1Mt/year DSR plant should capture: 473,600 tonnes per year. The amount of CO_2 that each heating method emits as a percentage of the amount of CO_2 that the DSR captures is shown in Table 3.11:

Table 3.11: Effective performance of CCS if electric/gas heating is used, for Aspen and LEILAC estimates.

Amount of CO_2 captured (tonnes)	Heat Integration	Electric	Gas
473,600 (Aspen)	0%	16.1%	17.7%
360,000 (LEILAC)	0%	21.1%	23.2%

It is also important to consider that this is the UK figure: in China, electric heating would emit 319,200 tonnes per year [43]. In Sweden, it would only be 17,100 tonnes [44]. Next, the CO_2 implications of integrating a steam turbine were examined. Using the value for carbon intensity of the UK's electrical grid [41], the amount of CO_2 emitted that was attributable to electricity usage in each turbine scenario was calculated and can be found in Appendix B.5. These values (between 5,000 and 13,000 t/year) are small relative to the amount of CO_2 that is avoided via creating a heat exchange network instead of using gas or electric heating. Therefore, on a purely environmental basis, it is recommended to prioritise the heat exchange network before the steam turbine.

4. Conclusions

Cement plants with DSRs produce a lot of excess heat from several sources. This reduces the energy efficiency of the process. It was found that there is a large excess of heat available (a total of 98MW if we were to cool each stream to 100°C, for a system of 20 DSRs in parallel). Therefore, a heat exchange network was designed, subject to heat exchange area constraints. It was found that the optimal configuration (on a cost basis) was highly dependent on the heat transfer coefficient. To give an idea of the approximate costs, using the middle U value of $30W/m^{2\circ}C$ the annualised cost was found to be £1,200,000. Heat integration was compared to the alternatives: gas or electrical heating, and was found to be more economical except in unoptimised low heat transfer coefficient scenarios. However, this annualised cost is highly sensitive to the heat exchanger lifetimes, and a shortened lifetime could render gas heating cheaper on an annualised basis. The impact on CO_2 emissions of alternatives to a heat exchange network was analysed, and it was found that gas heating of the inlet streams releases 18% of the amount of CO_2 that a 1Mt/year DSR plant captures, and electrical heating releases 16% in the UK (for China it is 67% and in Sweden just 3.6%). Excess heat still remained in the system after the heat exchanger network and can be used to raise steam for a steam Rankine cycle to generate electricity. An estimated maximum turbine power output of 12.93MW can be generated from an ideal Rankine cycle with a single turbine, when the turbine inlet and outlet pressures are 37 and 0.3 bar respectively and steam flowrate is at 10.8 kg/s. This scenario, however, leads to infeasibly high heat exchanger areas and costs, and should therefore not be implemented unless better heat-exchange technology is available. Instead, a number of compromise scenarios, with lower heat exchanger areas and costs, were produced, and these generate between 9.6 and 5.1MW of electricity. These systems require an initial expenditure between £36m and £19m, depending on the power output. They have a payback period of 5.5 years and save between £7.6m to £4m in electricity costs annually over their 50-year lifetime. They also offset between 5-13kt/year of CO_2, approximately 1.9% of the amount of CO_2 that the

DSRs capture annually. Due to the large hot outlet temperatures of the flue gases from HX2, it was decided that a Rankine cycle with reheat and a second turbine should be modelled, in order to utilise some of this excess heat. This configuration can generate up to 15.6MW of electricity (20.6% more than a Rankine cycle with only a single turbine), however more research is needed to optimise heat exchanger and turbine sizing and costs.

These findings show that there are a number of opportunities for making cement plants with DSRs more economically and environmentally efficient than previously thought, and shows that DSRs can be a viable alternative to the more traditional technologies used in the cement manufacturing industry at present.

Acknowledgments

We would like to express our gratitude to Dr. Justin G. Driver (Imperial College London) for his invaluable guidance and insights throughout the entirety of this project.

References

[1] J. Rogelj *et al.*, "Mitigation Pathways Compatible with 1.5°C in the Context of Sustainable Development," in *An IPCC Special Report on the impacts of global warming of 1.5°C above pre-industrial levels and related global greenhouse gas emission pathways*, Intergovernmental Panel on Climate Change, 2018, pp. 93–174.

[2] International Energy Agency, "Technology Roadmap Low-Carbon Transition in the Cement Industry," Paris, 2018.

[3] A. Bosoaga, O. Masek, and J. E. Oakey, "CO2 Capture Technologies for Cement Industry," in *Energy Procedia*, Feb. 2009, vol. 1, no. 1, pp. 133–140, doi: 10.1016/j.egypro.2009.01.020.

[4] U.S. Geological Survey, "Mineral Commodity Summaries," Jan. 2020.

[5] D. N. Huntzinger and T. D. Eatmon, "A life-cycle assessment of Portland cement manufacturing: comparing the traditional process with alternative technologies," *Journal of Cleaner Production*, vol. 17, no. 7, pp. 668–675, May 2009, doi: 10.1016/j.jclepro.2008.04.007.

[6] A. Naqi and J. G. Jang, "Recent progress in green cement technology utilizing low-carbon emission fuels and raw materials: A review," *Sustainability (Switzerland)*, vol. 11, no. 2. MDPI AG, Jan. 21, 2019, doi: 10.3390/su11020537.

[7] D. Leeson, N. mac Dowell, N. Shah, C. Petit, and P. S. Fennell, "A Techno-economic analysis and systematic review of carbon capture and storage (CCS) applied to the iron and steel, cement, oil refining and pulp and paper industries, as well as other high purity sources," *International Journal of Greenhouse Gas Control*, vol. 61, pp. 71–84, 2017, doi: 10.1016/j.ijggc.2017.03.020.

[8] J. Li, P. Tharakan, D. Macdonald, and X. Liang, "Technological, economic and financial prospects of carbon dioxide capture in the cement industry," *Energy Policy*, vol. 61, pp. 1377–1387, Oct. 2013, doi: 10.1016/j.enpol.2013.05.082.

[9] T. Hills, D. Leeson, N. Florin, and P. Fennell, "Carbon Capture in the Cement Industry: Technologies, Progress, and Retrofitting," *Environmental Science and Technology*, vol. 50, no. 1, pp. 368–377, Jan. 2016, doi: 10.1021/acs.est.5b03508.

[10] M. Schneider, M. Romer, M. Tschudin, and H. Bolio, "Sustainable cement production-present and future," *Cement and Concrete Research*, vol. 41, no. 7. Elsevier Ltd, pp. 642–650, 2011, doi: 10.1016/j.cemconres.2011.03.019.

[11] LEILAC, "The LEILAC pilot plant." https://www.project-leilac.eu/leilac-pilot-plant (accessed Dec. 02, 2020).

[12] P. Hodgson, M. Sceats, A. Vincent, D. Rennie, P. Fennel, and T. Hills, "Direct Separation Calcination Technology for Carbon Capture: Demonstrating a Low Cost Solution for the Lime and Cement Industries in the LEILAC Project," 2018. [Online]. Available: https://www.researchgate.net/publication/332876108.

[13] T. P. Hills, M. Sceats, D. Rennie, and P. Fennell, "LEILAC: Low Cost CO2 Capture for the Cement and Lime Industries," in *Energy Procedia*, 2017, vol. 114, pp. 6166–6170, doi: 10.1016/j.egypro.2017.03.1753.

[14] S. Ghosh, J. Kokot-Blamey, M. E. Boot-Handford, and P. S. Fennell, "Kinetics modeling, development, and comparison for the reaction of calcium oxide with steam," *Energy and Fuels*, vol. 33, no. 6, pp. 5505–5517, Jun. 2019, doi: 10.1021/acs.energyfuels.8b04383.

[15] F. Donat, N. H. Florin, E. J. Anthony, and P. S. Fennell, "Influence of high-temperature steam on the reactivity of CaO sorbent for CO 2 capture," *Environmental Science and Technology*, vol. 46, no. 2, pp. 1262–1269, Jan. 2012, doi: 10.1021/es202679w.

[16] M. Erans, S. A. Nabavi, and V. Manović, "Pilot-scale calcination of limestone in steam-rich gas for direct air capture," *Energy Conversion and Management: X*, vol. 1, Jan. 2019, doi: 10.1016/j.ecmx.2019.100007.

[17] M. Zhao *et al.*, "A novel calcium looping absorbent incorporated with polymorphic spacers for hydrogen production and CO2 capture," *Energy and Environmental Science*, vol. 7, no. 10, pp. 3291–3295, Oct. 2014, doi: 10.1039/c4ee01281j.

[18] S. A. Miller, V. M. John, S. A. Pacca, and A. Horvath, "Carbon dioxide reduction potential in the global cement industry by 2050," *Cement and Concrete Research*, vol. 114, pp. 115–124, Dec. 2018, doi: 10.1016/j.cemconres.2017.08.026.

[19] R. K. Sinnott, *Chemical Engineering Design*, 4th ed. Oxford: Elsevier Butterworth-Heinemann, 2005.

[20] I. C. Kemp, *Pinch Analysis and Process Integration*, 2nd ed. Oxford: Elsevier Ltd. , 2007.

[21] International Association for the Properties of Water and Steam, "Revised Release on the IAPWS Formulation 1995 for the Thermodynamic Properties of Ordinary Water Substance for General and Scientific Use," 2018.

[22] S. Zhou and A. Turnbull, "Steam Turbine Operating Conditions, Chemistry of Condensates, and Environment Assisted Cracking – A Critical Review," May 2002.

[23] Siemens, "Industrial steam turbines- the comprehensive Siemens product range from 2 to 250 megawatts," 2020.

[24] J. Oda, K. Akimoto, T. Tomoda, M. Nagashima, K. Wada, and F. Sano, "International comparisons of energy efficiency in power, steel, and cement industries," *Energy Policy*, vol. 44, pp. 118–129, May 2012, doi: 10.1016/j.enpol.2012.01.024.

[25] ESDU International plc., "ESDU 92013 Selection and costing of heat exchangers," 2006.

[26] D. E. Garrett, *Chemical Engineering Economics*, 1st ed. Dordrecht: Springer Netherlands, 1989.

[27] "Incoloy 800 supplier," *Steel Tubes India*, 2020. https://www.stindia.com/incoloy-alloy-800-800h-800ht-supplier.html (accessed Dec. 16, 2020).

[28] "Material Cost Data," *Massachusetts Institute of Technology*. Cambridge.

[29] M. S. Imbabi, C. Carrigan, and S. McKenna, "Trends and developments in green cement and concrete technology," *International Journal of Sustainable Built Environment*, vol. 1, no. 2. Elsevier B.V., pp. 194–216, 2012, doi: 10.1016/j.ijsbe.2013.05.001.

[30] R. Hackl and S. Harvey, "Identification, cost estimation and economic performance of common heat recovery systems for the chemical cluster in Stenungsund," 2013.

[31] J. R. Elliott and C. T. Lira, *Introductory Chemical Engineering Thermodynamics*, 2nd ed. Pearson Education, Inc., 2012.

[32] R. Kehlhofer, F. Hannemann, F. Stirnimann, and B. Rukes, *Combined-Cycle & Steam Turbine Power Plants*, 3rd ed. PennWell Corporation, 2009.

[33] "AVERAGE LIFE EXPECTANCIES," *CDW Engineering*, 2020. https://cdwengineering.com/average-life-expectancies/ (accessed Dec. 16, 2020).

[34] M. Adolfsson and S. Rashid, "Life Cycle Assessment and Life Cycle Cost of Heat Exchangers A Case for Inter Terminals Sweden AB Located in Port of Gothenburg," 2016.

[35] P. Apergi, "Power Generation from Waste Heat in cement plants - Application in Lafarge Volos plant," 2012.

[36] "Combined Heat and Power Technology Fact Sheet Series," Jul. 2016.

[37] K. Bolaji and O. Emeka, "Operation and Maintenance Schedule of a Steam Turbine Plant (A Case Study of Egbin Thermal Power Station)," 2014.

[38] Energy and Environmental Analysis, "Technology Characterization: Steam Turbines," Dec. 2008.

[39] "Energy Prices Non-Domestic Prices," *Department for Business, Energy & Industrial Strategy*. Department for Business, Energy & Industrial Strategy, Nov. 24, 2020.

[40] R. Patel and J. Singh, "Assess remaining life for heater tubes," *Hydrocarbon Processing*, Apr. 2019. .

[41] I. Staffell, M. Jansen, R. Green, R. Gross, T. Green, and P. McNally, "July to September 2020 Electric Insights Quarterly," 2020.

[42] I. Staffell, R. Green, R. Gross, T. Green, and G. Wilson, "October to December 2019 Electric Insights Quarterly," 2019.

[43] X. Li, K. Chalvatzis, and D. Pappas, *"China's electricity emission intensity in 2020 – an analysis at a provincial level"*. Aug. 2017

[44] A. Moro and L.Lonza, "*Electricity carbon intensity in European Member States: Impacts on GHG emissions of electric vehicles"*. Jul. 2017

Evaluating an Isoprene Producing Co-culture Model of *M. trichosporium* OB3b and *P. pastoris* using Dynamic Flux Balance Analysis

Hiu Lam Athena Wu, Stephen Tan
Department of Chemical Engineering, Imperial College London, U.K.

Abstract Biological synthesis of isoprene from a methane feedstock is potentially a more sustainable and selective production route for the valuable chemical. The present work refines an existing co-culture model of *Methylosinus trichosporium* OB3b and isoprene-producing *Pichia pastoris* by improving efficiency of the isoprene production phase as well as the microbial growth phase. Flux balance analysis provided an optimal cell density ratio for the production phase, while dynamic flux balance analysis elucidated the effects of NaCl inhibition, inoculation concentration and initial biomass ratio on the co-culture growth. Three key performance indicators were used to analyse the co-culture growth: matched-regime biomass ratio, peak methanol concentration and total biomass at specific time points. The optimal ratio for the production phase was calculated to be 1 *M. trichosporium* OB3b to 3.6 *P. pastoris*. The biomass ratio at the end of the growth phase was found to be affected only by the concentration of NaCl, and the peak methanol concentration was primarily affected by the initial biomass ratio. The total biomass at a specific time was affected by both the NaCl concentration and inoculation concentration. The most favourable growth conditions were found to be 153 mM and inoculation concentration of 0.1 gDW L^{-1} *M. trichosporium* and 0.2 gDW L^{-1} *P. pastoris*.

Keywords: *M. trichosporium* OB3b, *P. pastoris*, dynamic flux balance analysis, methane capture, isoprene, co-culture

1. Introduction

As the second largest contributor to anthropogenic greenhouse gas (GHG) emissions, methane accounts for 16% of the total 49 gigatons of carbon dioxide equivalent ($GtCO_2$-eq) emissions in 2010 [1]. Though appearing to pose a less imminent problem that the primary contributor, carbon dioxide (CO_2), in terms of absolute emission quantities, methane has a global warming potential (GWP) 25 times higher than that of CO_2 over a 100-year time scale [2]. Efforts have been made in utilising the potent greenhouse gas as an alternative carbon feedstock through chemical conversion to methanol, however the two-step process suffers from low conversion rates and moderate selectivity, as well as being highly energy intensive [3], [4].

Similar challenges are also found in the chemical synthesis of isoprene, a main component for producing synthetic rubber. Isoprene, also known as 2-methyl-1,3-butadiene, is mainly produced through extraction from the C5 liquid fraction of liquid petroleum pyrolysis. However, this petroleum-based process is subject to high energy requirements, high refining costs and low yields [5]. The current raw materials employed, namely petrochemicals and fossil fuel derivatives, are also unsustainable and contribute towards a carbon-intensive process [6], [7].

Compared to chemical routes, a biological conversion approach presents a less energy demanding, more selective and sustainable route towards methane capturing as well as isoprene synthesis. Methanotrophic bacteria, or methanotrophs, are capable of growing aerobically by utilising methane as their sole carbon and energy source. They possess a unique methane monooxygenase (MMO) enzyme which can catalyse the single-step conversion of methane to methanol at ambient temperatures and pressures [8]. On the other hand, the methylotrophic yeast *Pichia pastoris* has been widely employed in synthetic biology due to its ability to grow solely on methanol, well-established genetic engineering strategies and high productivities for expressing various recombinant products [9], [10]. A combined culture (co-culture) of these two species therefore introduces the possibility of an integrated bioprocess for direct isoprene synthesis from methane, which can offer the advantages of waste methane capturing, as well as an alternative synthesis route for isoprene with a reduced carbon footprint.

2. Background

The two most studied species of methanotrophs are *Methylosinus trichosporium* OB3b, and *Methyococcus capsulatus* [3]. In recent years, more research has been carried out to understand the methanol producing capacity of *Methylosinus trichosporium* OB3b, particularly about the inhibitory effect of organic compounds and salts (e.g. NaCl) on methanol dehydrogenase (MDH), a crucial enzyme in the methanol metabolism of the methanotroph [11]. This enzyme converts methanol to formaldehyde, which prevents the methanol produced from MMO being exported out of the methanotroph. The inhibition of this enzyme has thus allowed *M. trichosporium* OB3b to be an effective methanol exporting organism, with methanol production levels of 0.95 g L^{-1} at conversions over 60% reported [12]. High salt concentrations have also been found to increase the mass transfer coefficient ($k_L a$) of gaseous methane into the aqueous culture medium for the biomass, favouring methanol production [13]. However, studies have also reported that at NaCl concentrations of above 100mM, disruptive effects on the methanotroph's morphological structure have been observed [11], [14].

Pichia pastoris has been used to synthesise a wide variety of biomolecules, including proteins, lipases and albumins [10]. Notably, two recent studies have successfully engineered *Pichia* to produce the organic molecules isopentanol and lycopene [15], [16]. Lycopene is of particular interest as its synthesis route utilises a precursor known as dimethylallyl pyrophosphate (DMAPP). An enzyme known as isoprene synthase that is found in aspen leaves has been found to

synthesise isoprene from DMAPP, suggesting isoprene could potentially be produced from *Pichia* [17]. In previous unpublished work from Imperial College London Chemical Engineering laboratory, a co-culture model of *M. trichosporium* OB3b and *Pichia pastoris* was developed by simulating the integration of isoprene synthase gene into *Pichia*, allowing it to produce isoprene from DMAPP.

This present investigation is a further extension and refinement of the previous co-culture model. The co-culture model of methanotroph and *Pichia* was analysed using flux balance analysis (FBA) and its extension, dynamic-FBA (dFBA). These powerful modelling tools enabled the analysis of reaction fluxes through the genome-sale metabolic network of both organisms [18]. In particular, FBA is able to calculate the growth rate of an organism for a particular nutrient uptake rate (or vice versa) by optimising the fluxes through all metabolic pathways of the organism [18]. dFBA, on the other hand, incorporates the uptake and export reactions of the organism with a dynamic extracellular environment, allowing the metabolic activity of the organism to be simulated over a period of time where extracellular nutrients and metabolic by-products are changing in concentrations [19]. This allowed for the modelling of a dynamic culture without sacrificing insights into the intracellular metabolism of cells.

This study focuses on improving the two distinct phases of the previous co-culture model through two main objectives. The first was to elucidate the behaviour of both organisms during the growth phase (where both organisms are growing in cell density without isoprene production) by incorporating nutrient uptake kinetics and methane mass transfer limitations in the cell culture during the growth phase. The second was to provide a better estimate for the optimal cell density ratio during the production phase (during which biomass growth will be minimised and isoprene production maximised).

3. Methods

3.1 Co-culture model construction

Genome-scale metabolic models (GSMMs) of *Methylosinus trichosporium* OB3b (iMsOB3b) and *Pichia pastoris* (iMT1026 v3.0) were taken as .xml files in SBML format from Naizabekov and Lee (2020) and Tomàs-Gamisans *et al.* (2018) respectively [20], [21]. The models were imported into the COBRApy package version 0.20.0 running on Python version 3.8.5 and combined after tagging the metabolites and reactions in each GSMM with the corresponding suffix "_met" or "_pic".

To model an engineered *P. pastoris* transformed with the isoprene synthase gene for isoprene synthesis, the isoprene metabolite, synthesis reaction and exchange reactions between cellular compartments were added to the model according to standard procedure as stated in the COBRApy documentation [22]. Methanol-specific biomass and ATP maintenance reactions for *Pichia* were used (with the exception for simulations in the production phase, see section below). Full details about the additional reactions and modified reaction bounds can be found in Appendix I in the Supplementary Information document.

3.2 Optimising the production phase using FBA

In the production phase, *Pichia* expresses isoprene synthase, enabling the cell to start producing isoprene through dephosphorylation of dimethylallyl pyrophosphate (DMAPP). The co-culture is most efficient when the methanol export rate from the methanotroph is equal to the methanol uptake rate by the *Pichia* (Equation 1). To achieve this, the methanol fluxes (ν_{meoh}) as well as the ratio of biomass densities (X_{pic}/X_{met}) were calculated.

$$(X\nu_{\mathrm{meoh}})_{\mathrm{met}} = (X\nu_{\mathrm{meoh}})_{\mathrm{pic}} \quad (1)$$

The specific methanol export flux in *Methylosinus trichosporium* OB3b ($\nu_{\mathrm{meoh,met}}$) was estimated using a range of values from experiments in literature that maximised methanol production from the methanotroph.

The specific methanol uptake by *Pichia* ($\nu_{\mathrm{meoh,pic}}$) was calculated using FBA for an expected production level of isoprene. A reasonable production level was obtained by scaling the reported production level of another organic molecule (lycopene) in *Pichia*, as both organic molecules employ DMAPP as a precursor [16]. Isoprene production was scaled to be 8 times more than the final lycopene flux (Figure 4(c) in Bhataya *et al.*), according to the ratio of DMAPP precursors required to produce each molecule. This value was used to constrain the isoprene synthesis reaction (ISPS) in the co-culture model. The specific methanol flux for *Pichia* was then obtained by solving the co-culture model by minimising absolute value of the *Pichia* methanol uptake as the objective function. The default ATP maintenance value for *Pichia* in the iMT1026 v3.0 model was used (2.9 mmol gDW^{-1} h^{-1}) in carrying out these calculations. Although *Pichia* has been reported to have a lower ATP maintenance when growing on methanol, the use of a higher value here would be a way to account for energy used to maintain the viability of *Pichia* cells as they synthesise isoprene [21].

FBA was also used in a similar way to calculate the specific methanol uptake flux for the lycopene production reported in Bhataya *et al.* This was done to verify if the energetic requirements to produce isoprene and lycopene were similar enough to justify the aforementioned approach of scaling isoprene production by the amount of DMAPP precursor that the *Pichia* is expected to produce.

Lab-scale bioreactor yields of isoprene were taken from previous modelling experiments done in the Imperial College Chemical Engineering Laboratory (unpublished). The gPROMS model from previous work predicted that 26.8 moles of isoprene could be produced in a 5.5 L bioreactor with biomass concentration of 600 gDW m^{-3} in 200 days. Based on these values, an initial estimate of 1.692 mmol gDW^{-1} h^{-1} was obtained for the isoprene production level. An equivalent amount of lycopene based on the ratio of precursors was calculated to be 0.2115 mmol gDW^{-1} h^{-1}. Corresponding methanol uptakes were then obtained by solving the co-culture model.

3.3 Adapting the co-culture model to perform dFBA

Based on the approach outlined in Gomez *et al.* and the COBRApy documentation, the co-culture model was coupled with a dynamic extracellular system to model the growth phase of the organisms through dynamic flux balance analysis (dFBA) [22]. dFBA requires the nutrient uptake kinetics of both organisms. Methane uptake in *M. trichosporium* OB3b was found to follow Michaelis-Menten kinetics (Table 1), while methanol uptake in *P. pastoris* was reported to follow substrate inhibited growth (Equation 2) [23].

$$\mu_{pic} = \frac{0.146 S_{meoh}}{1.5 + S_{meoh} + {S_{meoh}}^2/8.86} \quad (2)$$

An additional correlation between the specific uptake rate of methanol ($\nu_{meoh,pic}$) and specific growth rate of *Pichia* (μ_{pic}) was determined using FBA and a linear regression package (sklearn, version 0.23.2) (Table 1).

Table 1: Kinetic uptake parameters for methane and methanol

Kinetic expression	Parameters	Sources
$\nu_{ch4} = \frac{\nu_{max} S_{ch4}}{K_m + S_{ch4}}$	ν_{max} = 8.28 mmol gDW^{-1} h^{-1} K_m = 0.018 mM	[24]
$\nu_{meoh} = \frac{\mu_{pic}}{Y_{X/S}} + m$	$1/Y_{X/S}$ = 77.05 mmol gDW^{-1} m = 0.088 mmol gDW^{-1} h^{-1}	[25]

Combining this correlation with Equation 2 allowed the specific methanol uptake to be correlated to the methanol concentration as required by dFBA.

To calculate the specific fluxes through each organism at each time point, lexicographic optimisation was used to ensure the fluxes of relevant reactions were maximised [26]. The objective functions were maximised in the following order: *M. trichosporium* OB3b growth, *P. pastoris* growth, methane exchange, methanol exchange. The methanotroph growth was ranked before *Pichia* growth to ensure that the dFBA would allocate methanol to the methanotroph. From these optimised fluxes, the specific nutrient fluxes were multiplied by the respective biomass growth rates to obtain the total flux, which was fed into an ODE solver to calculate the change in extracellular concentrations over time. The *solve_ivp* function was used to solve the system of ODEs using the BDF method as recommended by the COBRApy documentation [22].

Steady-state FBA was used as a complementary analysis tool to obtain the fluxes at time points of interest based on the extracellular concentrations as determined from the structured dFBA model.

The growth phase was modelled with a constant methane gas feed that served as a nutrient supply for the methanotroph. This resulted in an additional mass transfer term in the methane mass balance, as shown in Equation 3, which accounted for mass transfer limitations on how much dissolved methane could reasonably be provided to the methanotroph.

$$\frac{dS}{dt} = k_L a\,(S_{sat} - S) - v_{ch4} X_{met} \quad (3)$$

The process conditions of the growth phase were chosen to be 25^{o}C and 1.5 bar, where more methane could dissolve into solution compared to ambient conditions. Pressures above 1.5 bar could allow for even higher degrees of methane dissolution, but were deemed unsuitable for process safety considerations. The gas phase was assumed to be 50% methane.

3.4 Varying level of salt inhibition in dFBA

The inhibitory effect of NaCl on the MDH enzyme in the methanotroph was studied between 100 mM – 180mM, as Lee *at al.* reported that MDH was noticeably suppressed at these concentrations, which in turn suggests significant methanol export from the methanotroph [11]. Linear interpolation of the results from Lee *et al.* was used to estimate the relative MDH activity at intermediate salt concentrations. The relative activity of MDH was incorporated into dFBA by first solving the lexicographic optimisation at every time point. The methane uptake flux was bounded at the calculated value, and the MDH reaction flux was modified by the fractional relative enzyme activity. Lexicographic optimisation with these additional constraints was performed again to get the methanol export flux with a constrained MDH enzyme. Simulations for this investigation were carried out with 0.1 gDW L^{-1} initial biomass concentrations for each organism, initial methane concentration of 1.05 mM, and an initial methanol concentration of 1 mM.

As NaCl was the predominant salt in the nutrient medium, it was assumed to be the only salt that significantly affected the methane dissolution coefficient ($k_L a$). A sparged stirred tank bioreactor was also assumed, similar to that used in Kim *et al.*'s paper [13]. With these assumptions, the $k_L a$ value for different salt concentrations was calculated by linear interpolation of Kim *et al.*'s results.

3.5 Varying starting biomass ratio

The relative amounts of biomass used in simulations were between 0.1 gDW L^{-1} methanotroph : 0.1 gDW L^{-1} *Pichia* to 0.1 gDW L^{-1} methanotroph : 0.25 gDW L^{-1} *Pichia*, with the salt concentration held constant at 130mM NaCl and an initial methanol concentration of 1 mM. It seemed prudent to model scenarios with higher amounts of *Pichia*, as the desired biomass ratio at the end of the growth phase was 1 methanotroph : 3.6 *Pichia*. Concentrations higher than 0.25 gDW L^{-1} required a higher initial methanol concentration in the co-culture to support *Pichia* growth, and were not explored in this study since insights into the decoupled effect of the initial biomass ratio from the initial methanol concentration were preferred.

3.6 Varying starting biomass concentrations

The initial biomass concentrations were also varied to investigate if they have a significant effect on the co-culture growth. At a constant NaCl salt concentration of 100mM, the starting concentration of each species was varied between 0.04 gDW L^{-1} – 0.2 gDW L^{-1} while maintaining a 1 : 1 initial biomass ratio.

4. Results and Discussion

4.1 Optimal cell density ratio for the production phase

The optimal cell density calculated for isoprene production was 1 : 3.6 (methanotroph : *Pichia*). Although this isoprene production was scaled according to lycopene, both products utilise DMAPP as a precursor and thus activate similar metabolic pathways in *Pichia*. The energy demand on *Pichia* is therefore likely to be equivalent for the same mass of each product synthesised, although lycopene does undergo some additional aggregation and dehydration steps [16]. However, these reactions were found to add little impact to the energy demand on *Pichia*, as FBA results indicated that the specific methanol uptake to produce the same mass of lycopene was almost equivalent to the uptake calculated for isoprene. This led to the same biomass ratio as when isoprene was produced (see Table 2). The difference in the energetic requirements for both organic molecules did become more pronounced when the fluxes were scaled up to a production level of a 5.5 L bioreactor, but still did not affect the ratio much (row 3 in Table 2). Thus the *Pichia* can reasonably be expected to produce the scaled amount of isoprene and the corresponding methanol uptake was considered a good initial estimate to calculate the 1 : 3.6 ratio.

Table 2: Optimal biomass ratios for the production phase, calculated in different scenarios

Engineered *Pichia*	Met : *Pichia* ratio
Isoprene scaled from lycopene	1 : 3.6
Lycopene	1 : 3.6
Production scale isoprene	1 : 3.55
Recombinant proteins from literature	1 : 2.5 – 1 : 6.6

The validity of the calculated ratio was further strengthened by comparing against the range of cell density ratios calculated from uptake rates reported in literature. Methanol production by the methanotroph ranged from 1.43 – 2.67 mmol gDW^{-1} hr^{-1} [14], [27], [28] and methanol uptake by *Pichia* ranged from 0.41 – 0.56 mmol gDW^{-1} hr^{-1} [10], [23], [29], [30]. It should be noted that only the lower bounds of the *Pichia* methanol uptakes were taken, as the *Pichia* growth rate was desired to be as near zero as possible in the production phase in order to allocate the maximum amount of methanol in the *Pichia* for isoprene synthesis. Studies have shown that *Pichia* cells have a low death rate and thus do not require much nutrients for synthesising new cells [31],[32]. This led to a range of cell density ratios in literature from a lower bound of 1 : 2.5 to an upper bound of 1 : 6.6, depending on growth conditions of the organisms. The calculated 1 : 3.6 ratio, which accounts for the metabolic pathways for isoprene synthesis, falls nicely within these bounds and thus serves as a good initial estimate of the optimal cell density ratio for the production phase.

The high ratio of *Pichia* required is not surprising, as *Pichia* is known to take in and metabolise other carbon sources better than methanol. In one experiment, Pichia was reported to take in 8 times as much glycerol compared to methanol [33], which would allow for a methanotroph : *Pichia* ratio closer to 1 : 1. One reason for this decreased methanol uptake is that the metabolism of methanol in *Pichia* requires synthesising additional enzymes and peroxisomes, which limits the amount of methanol that can be metabolised [34]. In addition, high amounts of methanol is unfavourable to *Pichia* due to formaldehyde, a toxic substance for cells, being formed as part of the metabolism of methanol [35], [36]. This further suggests why more *Pichia* is needed to take in and utilise all the methanol exported by the methanotroph.

4.2 Regimes of biomass ratio during growth phase

For all in-silico growth phase simulations performed, the biomass ratio time profiles were found to demonstrate three regimes, each with distinctive features. For ease of reference, the regimes will be called the 'initial drop regime', the 'gradual increase regime' and the 'matched regime'.

In the 'initial drop regime', the biomass ratio initially dips slightly below the starting ratio (Figure 1(a)). This suggests the methanotroph is growing at a faster rate than the *Pichia*, which can be explained via the uptake kinetics of the nutrients. As observed from the Michaelis-Menten kinetic parameters in Table 1, the low K_m value for methane uptake (0.018 mM) suggests that even at relatively low methane concentrations (1 mM), the methane uptake is 98% of V_{max}, whereas a higher methanol concentration is required to achieve near-maximal uptake (2.7 mM). This leads to more methane being taken in by the methanotroph compared to *Pichia* at low nutrient concentrations, resulting in faster methanotroph growth.

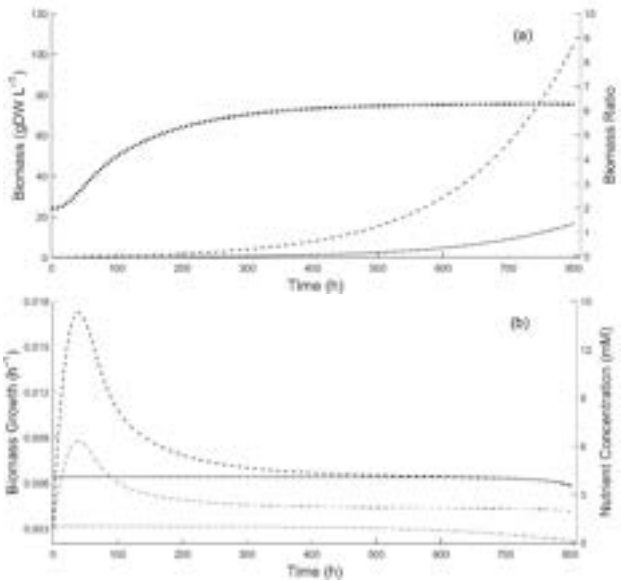

Figure 1: (a) Plot showing the ratio of Pichia biomass relative to 1 unit of methanotroph biomass (▪▪▪) over time with initial conditions as follows: 0.1 gDW L^{-1} methanotroph, 0.2 gDW L^{-1} Pichia, 0.1 mM methane, 1 mM methanol, and 165mM of NaCl. Also shown are actual amount of Pichia (---) and methanotroph (---) biomass. (b) Plot showing the extracellular methanol (thinner ---) and methane concentrations (thinner ---) for the same experiment, as well as the growth rates of Pichia (---) and methanotroph (---).

However, this initial growth regime does not persist for long. As the methanotroph growth rate is higher than *Pichia*, the total methanol exported by the methanotroph is greater than the total methanol uptake by the *Pichia*, leading to a rapid accumulation of methanol in the medium (see the first 50 hours of Figure 1(b)). Each *Pichia* cell is thus able to quickly increase its methanol uptake and grow faster, eventually surpassing the methanotroph growth. This causes the biomass ratio to start increasing in favour of *Pichia* and the 'gradual increase regime' begins. The methanol concentration

remains high for a while, as each methanotroph still exports more methanol than each *Pichia* is consuming due to *Pichia* having unfavourable kinetic parameters towards methanol, meaning that it will take in methanol more slowly compared to other nutrient sources like glycerol [33] . However, as the *Pichia* continues to grow more quickly than the methanotroph, the collective methanol demand from all *Pichia* cells eventually exceeds the total methanol export from all the methanotroph cells. This causes the methanol concentration to peak and then subsequently decrease. This leads to a suppressing effect on *Pichia* growth as its' specific methanol uptake (which is dependent on the extracellular methanol concentration) decreases. The biomass ratio starts to increase more slowly, but it does not decrease as the *Pichia* is still growing faster than the methanotroph.

The *Pichia* growth rate will continue to decrease as it demands more methanol than is added to the medium by the methanotroph, and the methanol concentration gradually decreases. Eventually, the *Pichia* growth rate slows to a point where the total methanol demand equals the total methanol export. At this 'matched regime', both the *Pichia* and methanotroph are growing at the same rate, and the biomass ratio does not change. As Figure 1(a) shows, this does not imply that both organisms stop growing but simply that they continue increasing in cell mass at the same rate. While it might appear unintuitive that the *Pichia* growth would slow to the same rate as the methanotroph, the *Pichia* growth is ultimately dependent on the amount of methanol provided by the methanotroph and so the growth rates will eventually be matched. This 'matched regime' is sustained for as long as there is sufficient dissolved methane to maintain the growth rate of the methanotroph. After a certain cell density, the methane demand from the methanotroph becomes greater than the rate of methane dissolution, and the co-culture is not able to sustain a steady ratio. Thus, the production phase should be started near the end of the matched regime, in order to ensure that the desired biomass ratio is still maintained while maximising the cell densities of the co-culture species.

4.3 Effect of NaCl concentration

Having identified the 1 : 3.6 (methanotroph : *Pichia*) optimal production phase ratio, effects of growth phase factors on attaining a production-ready biomass culture were then investigated. The effects of varying the different factors are discussed in the following sections by employing three key performance indicators which characterise the growth phase: the matched-regime biomass ratio, total biomass in the co-culture at *t* hours following inoculation, and peak methanol concentration in the media during growth. The standardised time point *t* for comparison between total biomass was chosen for most runs to be within the matched regime for each set of experiments.

Based on previously established correlations between NaCl concentrations and MDH activity in Lee *et al.* [11], the effects on the matched-regime biomass ratio, total co-culture biomass 160 hours after inoculation and peak methanol concentration were explored.

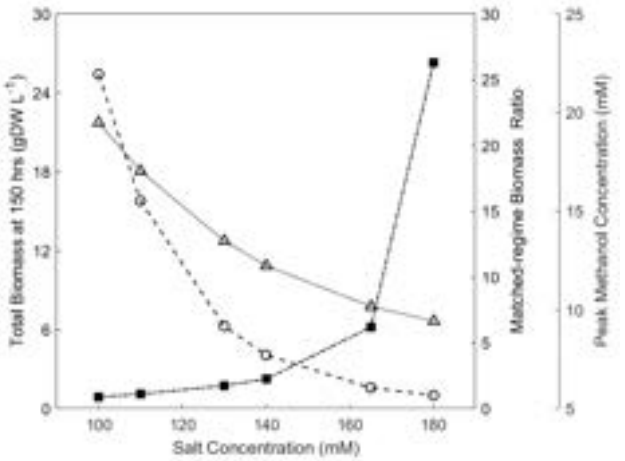

Figure 2: Effect of NaCl concentration on matched-regime biomass ratio (■), total biomass 160 hours from inoculation (○) and peak methanol concentration (△). Initial conditions of all simulations performed here were: 0.1 gDW L^{-1} methanotroph, 1 : 1 inoculation biomass ratio, 1.05 mM methane and 1 mM methanol.

As shown in Figure 2, the matched-regime biomass ratio increases with increasing NaCl concentrations. At high NaCl concentrations, more methanol is exported from the methanotroph due to the MDH enzyme being increasingly inhibited. This provides the *Pichia* with more methanol but leaves the methanotroph with less nutrients for growth. This effect on the methanol export capacity of the methanotroph thus contributes to a growth pattern where the methanotroph growth is suppressed while that of *Pichia* is encouraged, resulting in the observed increase in the matched-regime biomass ratio when the co-culture is grown under high NaCl concentrations.

The decreasing trend observed with total biomass can be explained by the total methanol export capacity of methanotrophs, which is affected by i) the specific methanol export from each individual methanotroph and ii) the total biomass content of methanotroph in the co-culture. With increasing salt concentrations, the specific methanol export of each methanotroph increases. However, the nutrients diverted away from the methanotroph leads to a slower increase in the amount of methanotroph in the co-culture. Overall, these two competing effects result in a net reduction in the overall methanol export capacity. Given that *Pichia* relies on the methanotroph for methanol to support its growth in this co-culture set-up, growth and total biomass of the co-culture is governed by the overall methanol export capacity and hence, growth of the methanotroph. As a result, total biomass decreases with increasing concentrations of NaCl.

The peak methanol concentration is influenced by both the overall methanol export capacity from the methanotroph, and the overall methanol consumption by the *Pichia*. As established above, increase in salt levels lead to a net reduction in methanol export capacity. When coupled with the relative abundance of *Pichia* under high salt concentrations, this results in an overall decrease in the extracellular methanol concentration, thereby decreasing the methanol peak.

All trends presented in Figure 2 were observed to exhibit a non-linear behaviour despite a linear correlation between the degree of MDH inhibition and the range of NaCl concentration

values investigated. This can be attributed to the exponential growth of the organisms, where a small change in the specific methanol export of each methanotroph would lead to a large effect on the KPIs when multiplied by the total amount of methanotroph and compounded over time.

It is also worth noting that above an NaCl concentration of 182 mM, MDH enzyme in the methanotroph exhibits less than 50% of its original activity, which would not allow the methanotroph to re-generate sufficient reducing power to support the activity of the pMMO enzyme in the absence of an exogenous source of reducing power (e.g. sodium formate). Thus, the upper limit of methanol export in the methanotroph is 50%, which is in line with the predictions of the previous co-culture model established at Imperial College London (unpublished).

4.4 Effect of inoculation biomass ratio

Another key growth phase parameter considered was the initial ratio of biomass to start growing the organisms from. Results from Figure 3 show that varying this ratio only has a significant effect on the peak methanol concentration, while the matched-regime biomass ratio and total biomass at 250 hours do not present a notable change.

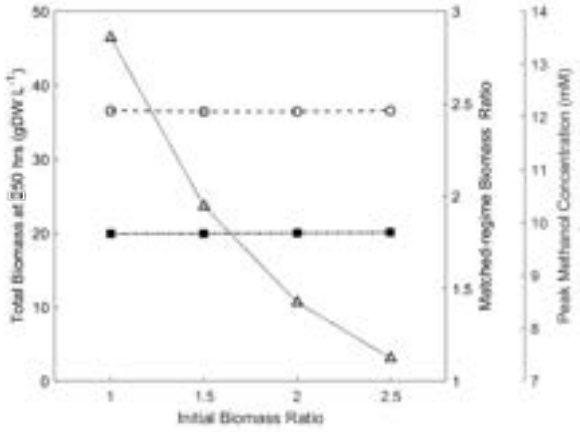

Figure 3: Effect of inoculation biomass ratio on matched-regime biomass ratio (■), total biomass 250 hours from inoculation (○) and the peak methanol concentration (△). Initial conditions of all simulations performed here were: 0.1 gDW L^{-1} methanotroph, 130mM NaCl, 1.05 mM methane and 1 mM methanol.

Since the inoculation biomass ratio does not influence the degree of MDH enzyme inhibition, the methanol allocation between the methanotroph and *Pichia* remains the same across the range of inoculation biomass ratios investigated. The methanotroph can thus be considered the controlling organism for overall co-culture growth since it contains the MDH enzyme. Starting with higher ratios therefore does not alter the matched-regime biomass ratio, as the *Pichia* growth rate would still reduce to that of the methanotroph during the gradual increase regime once its methanol consumption exceeds the production capacity of the methanotroph, as illustrated in Section 4.2.

The total amount of biomass at t = 250 hrs also does not vary with the inoculation biomass ratio, as the overall methanol export capacity was not affected. The peak methanol concentration, on the other hand, decreases at higher inoculation biomass ratios since more *Pichia* is available to take in methanol. At the same level of methanol export capacity, the bulk methanol uptake increases, thereby reducing the peak methanol concentration.

A decrease in the peak methanol concentration is favourable as previous studies have reported competitive inhibitory effects on the pMMO enzyme in the methanotroph at high concentrations of methanol [14]. As an initial estimate, it is recommended to keep the peak methanol concentration below 10mM, which corresponds to 40% pMMO relative activity. Thus, while biomass ratios greater than 1 : 2 are favourable, it is likely the pMMO enzyme is still inhibited to a certain degree. In order to quantify the impact of reduced pMMO activity on the growth phase, this effect is recommended to be incorporated into the co-culture model in the future and validated with laboratory experiments.

4.5 Recommended growth phase conditions for 1 : 3.6 ratio

To attain the optimal cell density of 1 : 3.6 during the matched-regime of the growth phase, an NaCl concentration of 153mM was required. This level of salt inhibition, however, is likely to induce disruptions to the methanotroph cell morphology. Studies have established that alternative combinations of NaCl and EDTA can be used to reduce the negative effects of associated with high NaCl concentrations [14], however their application to and effects on a methanotroph-Pichia co-culture are yet to be explored with further studies.

In addition to pMMO activity considerations as mentioned in Section 4.4, an inoculation biomass ratio of 1 : 2 was chosen due to favourable process economics with regards to raw material turnover. Considering potential scale-up applications for this bio-process, the amount of inoculation biomass required to start the growth phase at higher ratios can become significant, and since the total amount of biomass attained at time *t* would be the same, starting with the lowest ratio of 1 : 2 would be the most cost efficient as less biomass is required.

The end of the matched regime is reached at around 460 hours after inoculation (~19.2 days), at which the matched-regime biomass ratio attained was 1 : 3.65, with a total biomass concentration of 69.9 gDW L^{-1}, and a peak methanol concentration of 6.8 mM.

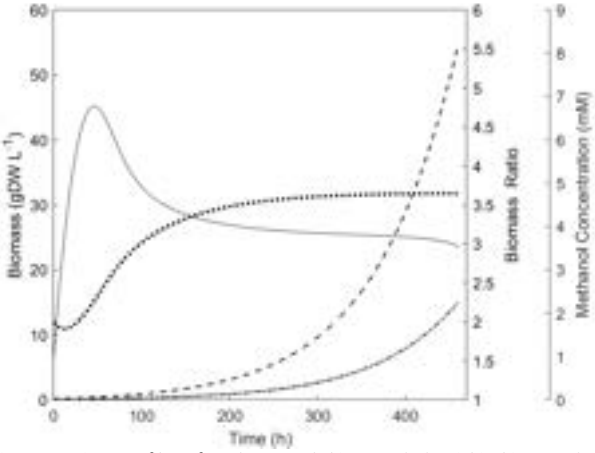

Figure 4: Time profiles of methanotroph biomass (---), Pichia biomass (---), biomass ratio (▪▪▪) and methanol concentration (—) for the recommended growth phase conditions of 1 : 2 inoculation biomass ratio and 153 mM NaCl. Initial conditions also included 0.1 gDW L^{-1} methanotroph, 1.05 mM methane and 1 mM methanol.

Table 3 below compares the choice of optimal growth phase conditions to two other experiments in which only one factor was varied. By comparing across the three runs, it is evident that although the salt concentration does have a slight effect on the peak methanol concentration, it is primarily affected and controlled at a level below 10mM by the inoculation biomass ratio. The two runs with different salt concentrations also reiterate the trends discussed in Section 4.3, where increasing the salt concentration to attain higher matched-regime biomass ratios comes at the expense of less total biomass being produced.

Table 3: Comparison between primary growth phase conditions and single parameter-altered cases

	1 : 2, 153 mM	1 : 2, 165 mM	1 : 1, 165 mM
Matched-regime biomass ratio	1 : 3.65	1 : 6.17	1 : 6.14
Total biomass (after 460 hrs)	69.9 gDW L^{-1}	13.9 gDW L^{-1}	13.8 gDW L^{-1}
Peak methanol concentration	6.8 mM	6.3 mM	10.2 mM

4.6 Effect of inoculation biomass concentration

Due to the governing effect of the methanotroph on overall co-culture growth, the inoculation biomass concentration was varied to investigate its effects on the matched-regime biomass ratio, total biomass 150 hrs from inoculation and peak methanol concentration, with results shown in Figure 5.

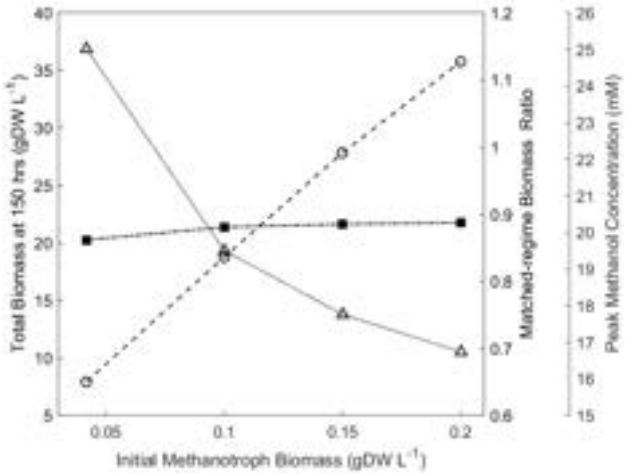

Figure 5: Effect of inoculation methanotroph concentration on matched-regime biomass ratio (■), total biomass 150 hours from inoculation (○) and the peak methanol concentration (△). Initial conditions of all simulations performed here were: 1 : 1 inoculation biomass ratio, 100 mM NaCl, 1.05 mM methane and 1 mM methanol.

As the inoculation biomass concentration does not influence the degree of MDH inhibition and nutrient split in the methanotroph, biomass ratio attained in the matched-regime remains unaffected. Total biomass present in the co-culture at 150 hours after inoculation, however, increases at higher inoculation concentrations. This can be attributed to an increase in the overall methanol export capacity from the methanotroph when the growth phase is initiated with higher amounts of biomass, despite each methanotroph having the same specific methanol export capacity. The co-culture is therefore able to attain higher cell densities.

Regardless of the inoculation biomass concentration, there appears to be a limit to the methanotroph biomass at the end of the matched regime. As discussed in Section 4.2, the biomass ratio exits the matched regime when the amount of dissolved methane in the system is insufficient to satisfy the total methane demand of the methanotroph. This was observed to occur when the dissolved methane concentration drops to 0.21 – 0.22 mM, with a corresponding total methanotroph biomass of 13.6 – 13.8 gDW L^{-1}. Further investigations are required to confirm whether other combinations with the same total methane demand would also lead to this phenomenon, or there are other factors that contribute to its specific occurrence at these parameter values.

Peak methanol concentrations were found to decrease with increasing inoculation biomass concentrations. With an increased methanol export capacity, more methanol accumulates during the initial period where growth of the *Pichia* lags behind that of the methanotroph. This in turn induces a higher specific methanol uptake rate in *Pichia* (as described by the uptake kinetics in Section 3.3) and encourages *Pichia* growth. When coupled with the increased initial amounts of *Pichia* at higher inoculation biomass concentrations, this results in a two-fold effect on methanol consumption rates which outweighs the increased methanol export, leading to a reduction in the peak methanol concentration.

4.7 Sensitivity Analysis of Model Parameters

The construction of the co-culture model required several parameters to be estimated. While a quantitative sensitivity analysis would provide valuable insights into the robustness of the reported results, time limitations made a comprehensive quantitative analysis infeasible. This paragraph will provide a qualitative discussion on the potential effects of parameters on the model results.

Firstly, the ATP maintenance reaction in the methanotroph model affects the total methane uptake by the methanotroph. Changing the default value of 3.5 mmol gDW^{-1} h^{-1} by ±20% leads to a ±2% change in the specific methane uptake of the methanotroph, which would affect the overall methanol export capacity of the methanotroph. A quantitative sensitivity analysis could be carried out to confirm how much the three KPIs are affected by this change in the methanol export capacity.

Secondly, the gas-liquid mass transfer coefficient for methane ($k_L a$) varies depending on the reactor configuration and the composition of the nutrient medium. Improving the mass transfer would result in more methane being able to dissolve into the aqueous medium, which would increase methanol export from the methanotroph and cause the co-culture growth to increase. However, the peak methanol concentration would inevitably be raised, and the balance of these two effects should be considered in future sensitivity analysis.

The uptake parameters for methane (K_m and V_{max}) could also change depending on the culture conditions, which would affect the methane import into the methanotroph. Similarly, the uptake parameters for *Pichia* ($Y_{X/S}$ and m) would also

influence the total methanol uptake, which would change the growth profiles over time and affect the three KPIs for the growth phase.

Finally, the ATP maintenance reaction in *Pichi*a and the methanol production rate were two key parameters in the production phase. The ATP maintenance value used in the *Pichia* model is fairly robust, given that extensive experimental results were used to validated the model [21]. On the other hand, the methanol production rate from the methanotroph differed between different experiments with different growth conditions, and thus this variance in the methanol production rate is a potential source of error for the calculated optimal cell density ratio in this paper.

5. Conclusions and Outlook

In this study, the optimal cell density ratio for isoprene production from the *M. trichosporium* OB3b and *P. pastoris* co-culture was evaluated based on precursor scaling and energetic requirement considerations, and both approaches confirmed a 1 : 3.6 (methanotroph : Pichia) ratio. Growth phase investigations that followed identified three distinct regimes for the biomass ratio, with a particular focus on the matched regime where a consistent biomass ratio can be maintained between the two species as they grow. Initiation of the production phase is recommended near the end of this matched regime in order to retain the targeted biomass ratio while maximising the co-culture cell density from growth.

The effects of NaCl concentration, inoculation biomass ratio and inoculation biomass concentration were discussed with respect to three key performance indicators (KPIs). In particular, the matched-regime biomass ratio was found to be solely influenced by the concentration of NaCl, while total biomass at *t* hours following inoculation were affected by both NaCl concentration and inoculation biomass concentration. Despite all three growth phase parameters having an effect on the peak methanol concentration, the inoculation biomass ratio was identified as the predominant factor that governs a low peak methanol concentration. Based on the deduced trends and considerations on pMMO enzyme deactivation, a salt concentration of 153 mM NaCl and inoculation biomass ratio of 1 : 2 were recommended for the growth phase.

The main findings in this study demonstrate the theoretical potential for a successful co-culture growth, but laboratory experiments will need to be carried out to quantify (i) the methanol production and uptake values that inform an optimum cell density ratio in the production phase, (ii) the exact amount of isoprene production from the co-culture in the production phase, (iii) the effects of changing growth parameters on the various key performance indicators (KPIs) of the growth phase. The findings in this paper provide an initial estimate for suitable ranges of variables to be tested with experiments in the laboratory.

Beyond the 'testing' phase of this first design-build-test-learn cycle, the co-culture model can be incorporated into a bioprocess model that would allow for a more holistic approximation of the physical and biological phenomenon that would be present in a bench or even pilot scale reactor. For example, the removal of isoprene through the gaseous exit stream would need to be considered. Additionally, the distribution of nutrients, cell crowding and competition for nutrients would have to be considered as well for a model to reasonably predict the actual level of isoprene production that could be achieved in bioreactors.

These bioprocess considerations will ultimately guide the design and optimisation of a bioreactor that would see a viable co-culture producing isoprene efficiently, which would set the grounds to assess the economic feasibility of the process. The aim is to achieve a sufficiently economical bioreactor that would be able to find commercial adoption and replacement of existing production methods for isoprene.

Nomenclature and Abbreviations

v_{meoh}	Specific methanol uptake	mmol gDW^{-1} h^{-1}
X	Mass density of biomass	gDW L^{-1}
μ	Specific growth rate	h^{-1}
v_{max}	Maximum rate of uptake	mmol gDW^{-1} h^{-1}
K_m	Michaelis constant	mM
S	Substrate concentration	mM
$Y_{X/S}$	Yield coefficient	gDW g(substrate)$^{-1}$
m	Maintenance coefficient	mmol gDW^{-1} h^{-1}
$k_L a$	Mass transfer coefficient	h^{-1}
$_{met}$	*M. trichosporium* subscript	
$_{pic}$	*P. pastoris* subscript	

DMAPP	Dimethylallyl pyrophosphate
ATP	Adenosine triphosphate
FBA	Flux balance analysis
dFBA	Dynamic flux balance analysis
ODE	Ordinary differential equation
MDH	Methanol dehydrogenase
pMMO	Particulate-form methane monooxygenase
KPI	Key Performance Indicator

Acknowledgements

The authors would like to acknowledge the help of Noah Sprent at Department of Chemical Engineering, Imperial College London. His previous modelling work in the department informed the scope of this present investigation and he provided much appreciated assistance with the modelling tools used and insights into our results.

Supplementary Information

A document containing detailed information regarding the co-culture model setup is included after the main report. The dFBA code for the co-culture model, as well as FBA code for calculating the optimal ratio, are available as jupyter notebook files separate to this document.

References

[1] O. Edenhofer, R. Pichs-Madruga, Y. Sokona, E. Farahani, and S. Kadner, 'IPCC, 2014: Summary for Policymakers', Intergovernmental Panel on Climate Change, 2014. [Online]. Available: https://www.ipcc.ch/site/assets/uploads/2018/02/ipcc_wg3_ar5_technical-summary.pdf.

[2] P. Forster *et al.*, 'Changes in Atmospheric Constituents and in Radiative Forcing', p. 106, 2007.

[3] C. E. Bjorck, P. D. Dobson, J. Pandhal, [1] Department of Chemical and Biological Engineering, University of Sheffield, Mappin Street, Sheffield S1 3JD, UK, and [2] The National Centre for Text Mining, Manchester Institute of Biotechnology, Princess Street, Manchester M1 7DN, UK, 'Biotechnological conversion of methane to methanol: evaluation of progress and potential', *AIMS Bioengineering*, vol. 5, no. 1, pp. 1–38, 2018, doi: 10.3934/bioeng.2018.1.1.

[4] I. Y. Hwang *et al.*, 'Batch Conversion of Methane to Methanol Using Methylosinus trichosporium OB3b as Biocatalyst', *Journal of Microbiology and Biotechnology*, vol. 25, no. 3, pp. 375–380, Mar. 2015, doi: 10.4014/jmb.1412.12007.

[5] G. O. Ezinkwo, V. F. Tretjakov, R. M. Talyshinky, A. M. Ilolov, and T. A. Mutombo, 'Overview of the Catalytic Production of Isoprene from different raw materials; Prospects of Isoprene production from bio-ethanol.', *Catalysis for Sustainable Energy*, vol. 1, Jan. 2013, doi: 10.2478/cse-2013-0006.

[6] J.-H. Kim *et al.*, 'Isoprene production by Escherichia coli through the exogenous mevalonate pathway with reduced formation of fermentation byproducts', *Microb Cell Fact*, vol. 15, no. 1, p. 214, Dec. 2016, doi: 10.1186/s12934-016-0612-6.

[7] X. Lv *et al.*, 'Enhanced isoprene biosynthesis in Saccharomyces cerevisiae by engineering of the native acetyl-CoA and mevalonic acid pathways with a push-pull-restrain strategy', *Journal of Biotechnology*, vol. 186, pp. 128–136, Sep. 2014, doi: 10.1016/j.jbiotec.2014.06.024.

[8] R. S. Hanson and T. E. Hanson, 'Methanotrophic bacteria.', *Microbiol Rev*, vol. 60, no. 2, pp. 439–471, Jun. 1996.

[9] D. A. Peña, B. Gasser, J. Zanghellini, M. G. Steiger, and D. Mattanovich, 'Metabolic engineering of Pichia pastoris', *Metabolic Engineering*, p. 14, 2018.

[10] N. K. Khatri and F. Hoffmann, 'Oxygen-limited control of methanol uptake for improved production of a single-chain antibody fragment with recombinant Pichia pastoris', *Appl Microbiol Biotechnol*, vol. 72, no. 3, pp. 492–498, Sep. 2006, doi: 10.1007/s00253-005-0306-1.

[11] S. G. Lee, J. H. Goo, H. G. Kim, J.-I. Oh, Y. M. Kim, and S. W. Kim, 'Optimization of methanol biosynthesis from methane using Methylosinus trichosporium OB3b', *Biotechnology Letters*, vol. 26, no. 11, pp. 947–950, Jun. 2004, doi: 10.1023/B:bile.0000025908.19252.63.

[12] C. Duan, M. Luo, and X. Xing, 'High-rate conversion of methane to methanol by Methylosinus trichosporium OB3b', *Bioresource Technology*, vol. 102, no. 15, pp. 7349–7353, Aug. 2011, doi: 10.1016/j.biortech.2011.04.096.

[13] K. Kim, J. Lee, K. Seo, M.-G. Kim, K.-S. Ha, and C. Kim, 'Enhancement of methane–water volumetric mass transfer coefficient by inhibiting bubble coalescence with electrolyte', *Journal of Industrial and Engineering Chemistry*, vol. 33, pp. 326–329, Jan. 2016, doi: 10.1016/j.jiec.2015.10.018.

[14] H. G. Kim, G. H. Han, and S. W. Kim, 'Optimization of lab scale methanol production by Methylosinus trichosporium OB3b', *Biotechnol Bioproc E*, vol. 15, no. 3, pp. 476–480, Jun. 2010, doi: 10.1007/s12257-010-0039-6.

[15] W. Siripong, C. Angela, S. Tanapongpipat, and W. Runguphan, 'Metabolic engineering of Pichia pastoris for production of isopentanol (3-Methyl-1-butanol)', *Enzyme and Microbial Technology*, vol. 138, p. 109557, Aug. 2020, doi: 10.1016/j.enzmictec.2020.109557.

[16] A. Bhataya, C. Schmidt-Dannert, and P. C. Lee, 'Metabolic engineering of Pichia pastoris X-33 for lycopene production', *Process Biochemistry*, vol. 44, no. 10, pp. 1095–1102, Oct. 2009, doi: 10.1016/j.procbio.2009.05.012.

[17] G. M. Silver and R. Fall, 'Characterization of Aspen Isoprene Synthase, an Enzyme Responsible for Leaf Isoprene Emission to the Atmosphere', *J. Biol. Chem.*, vol. 270, no. 22, pp. 13010–13016, Feb. 1995, doi: 10.1074/jbc.270.22.13010.

[18] J. D. Orth, I. Thiele, and B. Ø. Palsson, 'What is flux balance analysis?', *Nat Biotechnol*, vol. 28, no. 3, pp. 245–248, Mar. 2010, doi: 10.1038/nbt.1614.

[19] J. A. Gomez, K. Höffner, and P. I. Barton, 'DFBAlab: a fast and reliable MATLAB code for dynamic flux balance analysis', *BMC Bioinformatics*, vol. 15, no. 1, p. 409, Dec. 2014, doi: 10.1186/s12859-014-0409-8.

[20] S. Naizabekov and E. Y. Lee, 'Genome-Scale Metabolic Model Reconstruction and in Silico Investigations of Methane Metabolism in Methylosinus trichosporium OB3b', *Microorganisms*, vol. 8, no. 3, p. 437, Mar. 2020, doi: 10.3390/microorganisms8030437.

[21] M. Tomàs-Gamisans, P. Ferrer, and J. Albiol, 'Fine-tuning the *P. pastoris* iMT1026 genome-scale metabolic model for improved prediction of growth on methanol or glycerol as sole carbon sources', *Microb. Biotechnol.*, vol. 11, no. 1, pp. 224–237, Jan. 2018, doi: 10.1111/1751-7915.12871.

[22] 'Documentation for COBRApy — cobra 0.13.3 documentation'. https://cobrapy.readthedocs.io/en/latest/ (accessed Dec. 14, 2020).

[23] W. Zhang, M. A. Bevins, B. A. Plantz, L. A. Smith, and M. M. Meagher, 'Modeling Pichia pastoris growth on methanol and optimizing the production of a recombinant protein, the heavy-chain fragment C of botulinum neurotoxin, serotype A', *Biotechnol Bioeng*, vol. 70, no. 1, pp. 1–8, Oct. 2000, doi: 10.1002/1097-0290(20001005)70:1<1::aid-bit1>3.0.co;2-y.

[24] S. Lontoh, A. A. DiSpirito, and J. D. Semrau, 'Dichloromethane and trichloroethylene inhibition of methane oxidation by the membrane-associated methane monooxygenase of Methylosinus trichosporium OB3b', p. 8.

[25] H. W. Blanch and D. S. Clark, 'Biochemical Engineering', Taylor & Francis Group, 1997, p. 201.

[26] F. Scott, 'Simulation and optimization of dynamic flux balance analysis models using an interior point method reformulation', *Computers and Chemical Engineering*, p. 19, 2018.

[27] P. K. Mehta, S. Mishra, and T. K. Ghose, 'Methanol biosynthesis by covalently immobilized cells of Methylosinus trichosporium: Batch and continuous studies', p. 6, 1990.

[28] N. Pen, L. Soussan, M.-P. Belleville, J. Sanchez, C. Charmette, and D. Paolucci-Jeanjean, 'An innovative membrane bioreactor for methane biohydroxylation', *Bioresource Technology*, p. 11, 2014.

[29] J. Sinha *et al.*, 'Improved production of recombinant ovine interferon-tau by mut(+) strain of Pichia pastoris using an optimized methanol feed profile', *Biotechnol Prog*, vol. 19, no. 3, pp. 794–802, Jun. 2003, doi: 10.1021/bp025744q.

[30] A. E. Cunha *et al.*, 'Methanol induction optimization for scFv antibody fragment production in Pichia pastoris', *Biotechnol Bioeng*, vol. 86, no. 4, pp. 458–467, May 2004, doi: 10.1002/bit.20051.

[31] C. Rebnegger *et al.*, 'Pichia pastoris Exhibits High Viability and a Low Maintenance Energy Requirement at Near-Zero Specific Growth Rates', *Applied and Environmental Microbiology*, vol. 82, no. 15, p. 14, 2016.

[32] L. Paulová, P. Hyka, B. Branská, K. Melzoch, and K. Kovar, 'Use of a mixture of glucose and methanol as substrates for the production of recombinant trypsinogen in continuous cultures with Pichia pastoris Mut+', *Journal of Biotechnology*, vol. 157, no. 1, pp. 180–188, Jan. 2012, doi: 10.1016/j.jbiotec.2011.10.010.

[33] D. Zalai, C. Dietzsch, C. Herwig, and O. Spadiut, 'A dynamic fed batch strategy for a Pichia pastoris mixed feed system to increase process understanding', *Biotechnology Progress*, vol. 28, no. 3, pp. 878–886, 2012, doi: https://doi.org/10.1002/btpr.1551.

[34] A. Solà, P. Jouhten, H. Maaheimo, F. Sánchez-Ferrando, T. Szyperski, and P. Ferrer, 'Metabolic flux profiling of Pichia pastoris grown on glycerol/methanol mixtures in chemostat cultures at low and high dilution rates', *Microbiology,* vol. 153, no. 1, pp. 281–290, 2007, doi: 10.1099/mic.0.29263-0.

[35] E. Vartiainen, P. Blomberg, M. Ilmén, M. Andberg, M. Toivari, and M. Penttilä, 'Evaluation of synthetic formaldehyde and methanol assimilation pathways in Yarrowia lipolytica', *Fungal Biology and Biotechnology*, vol. 6, no. 1, p. 27, Dec. 2019, doi: 10.1186/s40694-019-0090-9.

[36] A. J. Sunga and J. M. Cregg, 'The Pichia pastoris formaldehyde dehydrogenase gene (FLD1) as a marker for selection of multicopy expression strains of P. pastoris', *Gene*, vol. 330, pp. 39–47, Apr. 2004, doi: 10.1016/j.gene.2003.12.015.

Nonsolvent-induced phase separation and breath figure arrays on a model polymer

Naomi Duru, Mingchuan Zheng

Department of Chemical Engineering, Imperial College London, South Kensington, SW7 2AZ, United Kingdom

Abstract

Nonsolvent-induced phase separation (NIPS) and breath figure arrays (BFA) can be used to impart surface structures on the film of a model polymer - poly(2,6-diphenyl-p-phenylene oxide) (PPPO). Polymer-solvent-nonsolvent ternary solutions (PPPO-DCM-heptane respectively) have been spin-coated to generate dry PPPO films that exhibit structures with hierarchical length scales, where the macro- and micro-structures formed on the film surface have been determined using optical and scanning electron microscopy (SEM). We report that the characteristic lengths of the macro-structures increase with initial concentration of PPPO in the ternary mixture and decrease with addition of heptane. SEM imaging reveals that micro-pores have been imparted by NIPS, and sizes of the micro-pores are reported to increase with heptane addition and decrease with greater initial concentration of PPPO in the solution. Solutions of PPPO and DCM with varying initial compositions have been drop-cast and dried in a humidity chamber at controlled relative humidity (RH) to induce BFA, where SEM imaging reveals the formation of micro-pores. Sizes of the micro-pores formed from BFA are found to increase with RH and decrease with higher starting concentration of PPPO. We conclude that NIPS and BFA are valid ways of imparting structures on polymer surfaces for industrial applications.

Keywords: polymer, demixing, porous materials, breath figure arrays, porosity

1. Introduction

Porous polymeric films have remarkable prospects for industrial applications, e.g. filtration, gas adsorption, membrane separation, energy storage, water treatments, and catalysis. [1, 2, 3, 4, 5, 6] In particular, their use as gas adsorbents have been of major interest; for example, they are vital in the detection or removal of matters in air, e.g. carbon dioxide, volatile organics, or microorganisms such as viruses. [7, 8, 9, 10] It is important therefore to study and employ techniques to control the porosity in designing porous polymeric materials. In this work, we have investigated the use of nonsolvent-induced phase separation (NIPS) and breath figure arrays (BFA) to impart porosity on a model polymer film - poly(2,6-diphenylphenylene oxide) (PPPO).

The molecular structure of PPPO monomers is shown in Figure 1. It is a thermally stable material patented by General Electric Company in 1969, where the initial application was cover sheets for extra-high voltage cables and other electric devices due to its low relative permittivity and dissipation factor. [11, 12, 13] The molecular weight (M_W) of PPPO ranges from 140-1450 kg/mol after synthesis. [14, 15, 16] The polydispersity index (M_W/M_N) ranges from 1.4 to 2.3. [14] Since its initial discovery, it was further developed by Akzo-Nobel for use as a porous polymer for gas adsorptions (such as in chromatography), given its thermal stability, insulating-nature, and good adsorption properties; it has since been used extensively for this purpose. [17, 18, 19, 20, 21, 22, 23, 24, 25] This of course makes PPPO an attractive candidate to be studied as a model polymer for gas adsorption. It has good solubility in most chlorinated and aromatic organic solvents. [13] Dicholoromethane (DCM) is a good solvent of PPPO and heptane a poor solvent, though DCM and heptane are miscible with each other. [26]

Non-solvent induced phase separation (NIPS) is a method for imparting porosity to polymeric materials. [27] The phase behaviour is exploited by adding a poor solvent to the polymer-solvent mixture until liquid-liquid demixing occurs, i.e. the ternary mixture crosses into a two-phase region. [1, 28, 29] In this study, the polymer is PPPO, the solvent DCM, and the nonsolvent heptane. Figure 2 explains NIPS through the use of a ternary phase diagram. The liquid-liquid phase boundary and the glass transition point of the system were mapped by O'Connell et al. under room temperature. [26] This system exhibits a Type I ternary diagram. [29, 30] Starting with a certain composition X in the single phase region, if the mixture is left to dry, the solvent and nonsolvent will evaporate and cross

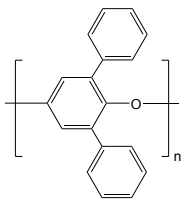

Figure 1: The molecular structure of poly(2,6-diphenylphenylene oxide) (PPPO)

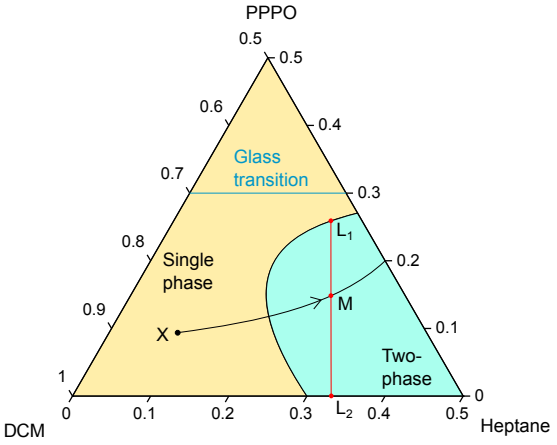

Figure 2: An illustration of NIPS through ternary diagram of the PPPO-DCM-heptane system, where PPPO is the polymer, DCM the solvent, and heptane the nonsolvent. Starting with composition X in the single phase region (yellow), if the mixture is left to dry, the solvent and nonsolvent will evaporate and cross into the two-phase region (blue), arriving at mixing point M. It would separate into two binodal phases whose compositions are L_1 (polymer-rich) and L_2 (polymer-poor). This process is known as phase inversion. [29, 30] Further evaporation would enable the mixture to cross the glass transition point. [31] Subsequent solidification would enable pores to be left at where the polymer-poor phase was. The liquid-liquid phase boundary of the PPPO-DCM-heptane mixture was mapped by O'Connell et al. under room temperature. [26]

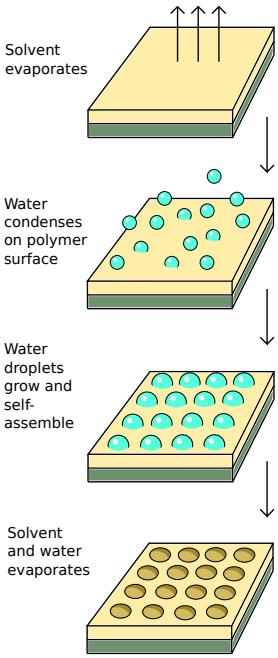

Figure 3: Schematic for BFA formation on polymer film. When a given polymer-solvent mixture is left to dry, endothermic evaporation of the solvent causes water content in the air above the film to condense on the surface. As dew appears, the water droplets grow in volume and self-assemble, occupying spaces on the polymer surface. When water and solvent both evaporate, the solidifed polymer film forms and where the water droplets were now become the pores.

into the two-phase region. As soon as the mixture enters the two phase region, demixing occurs and it separates into two liquid phases - one rich and one poor in polymer content. By tie-line construction shown here for point M along the drying curve, the composition of the polymer-rich phase would be L_1 and that of the polymer-poor phase L_2 and these phases would exist as an emulsion. This process is known as phase inversion. [29, 30] Further evaporation from the polymer-rich phase would cross the glass transition point, [31] and solidification would subsequently occur. The final structure is dictated by at this point by kinetic arrest; evaporation of the polymer-poor phase creates the resultant pores.

BFA is often considered a nature-inspired chemical engineering technique to impart porosity on polymer surfaces. It derives its name from the phenomenon where breathing on a cold surface generates water dew, in the form of fog. [32] Figure 3 is an illustration of how BFA works. For a given polymer-solvent mixture left to dry, evaporation of the solvent is endothermic and thus causes a reduction of temperature on the film surface. In this experiment, the polymer is PPPO and the solvent DCM. DCM is a highly volatile liquid at room conditions (boiling point around 40 °C at 1 atm [33]). Water contents in the air above the PPPO-DCM surface condense on the surface due to the reduction in temperature, where dew appears. The water droplets grow in volume and self-assemble, occupying spaces on the polymer surface. The solvent evaporates, and solidifed polymer film forms around the water droplets. When the film surface temperature returns to room temperature, the water evaporates, and where the water droplets were become the pores. These pores are usually circular in shape as it is energetically favourable for the water droplets to be spherical.

For industrial applications, there is a significant economic incentive to use NIPS and BFA for imparting porous structures. Compared to methods such as lithography, NIPS and BFA are inexpensive and considerably less time-consuming. With the favourable properties of PPPO for gas adsorption applications and the fact that the phase behaviour of the system PPPO-DCM- heptane has already been well-studied in literature, it is therefore highly relevant to investigate the use of NIPS and BFA for imparting porosity on PPPO films.

2. Experimental procedure

The materials used in this work consist of PPPO (M_N = 176 kg/mol, $M_W/M_N = 1.95$, $T_g = 228$ °C), [34] which was used as the model polymer, dichloromethane (DCM) (VWR Chemicals, 99.9%, $\rho = 1.33$ g cm^{-3}]), which was used as the solvent of PPPO, and heptane (VWR Chemicals, 99.8%, ρ = 0.67 g cm^{-3}), which was used as the nonsolvent.

Solutions of PPPO, DCM and heptane were prepared gravimetrically with varying compositions, displayed as black crosses on the ternary diagram in Figure 4. These solutions were spin-coated on an aluminosilicate wafer at 3000 rpm for 1 minute on a Laurell WS-400BZ-6NPP/Lite spin

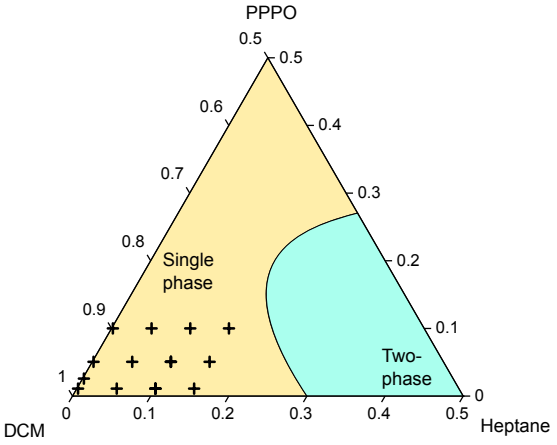

Figure 4: Compositions (by mass) of solutions of the PPPO-DCM-heptane system used for spin-coating are marked as black crosses on this ternary phase diagram. The single phase region is coloured yellow and the two-phase region blue, and the liquid-liquid phase boundary of the PPPO-DCM-heptane was mapped by O'Connell et al. under room temperature. [26]

coating machine, resulting in dried polymer films. Figure 5a illustrates this process. Since polymer materials synthesised through phase separation can exhibit hierarchical porous structures, [35] it was necessary to employ different analytic techniques in order to observe film structures at different length scales. Therefore, the resulting films were analysed through optical microscopy (Olympus BK14LED) to observe any structures imparted on the macro- level, whilst any micro-structures were analysed through scanning electron microscopy (SEM) (Zeiss Auriga FIB SEM).

For BFA, solutions of PPPO and DCM at varying compositions were prepared and drop-cast onto a glass slide in a humidity chamber (Coy Labs, Relative Humidity Chamber with an Electrotech Systems Microcontroller 5100, Figure 6). Figure 5b is a schematic of this process. The relative humidity (RH) was varied from 25% to 100% for concentrations of PPPO at 2.5%, 5% and 10%. The film surface was allowed to dry at room temperature and pressure in the chamber before removal therefrom to be placed in an oven for further drying. SEM was used to analyse films formed from samples employed in this method.

All films obtained were heated in an oven at 70 °C after their respective film formation processes, so that traces of water from the samples would be completely removed.

3. Results and discussions

3.1. Macro-structures imparted via NIPS

Figures 7 and 8 are the optical microscopy images at ×10 magnification of the films obtained by spin-coating samples of the PPPO-DCM-heptane mixture. Figure 7 contains images for films from spin-coating PPPO and DCM solutions without heptane at different initial concentrations of PPPO. Figure 8 contains images of films formed through spin-coating the PPPO-DCM-heptane ternary mixture at

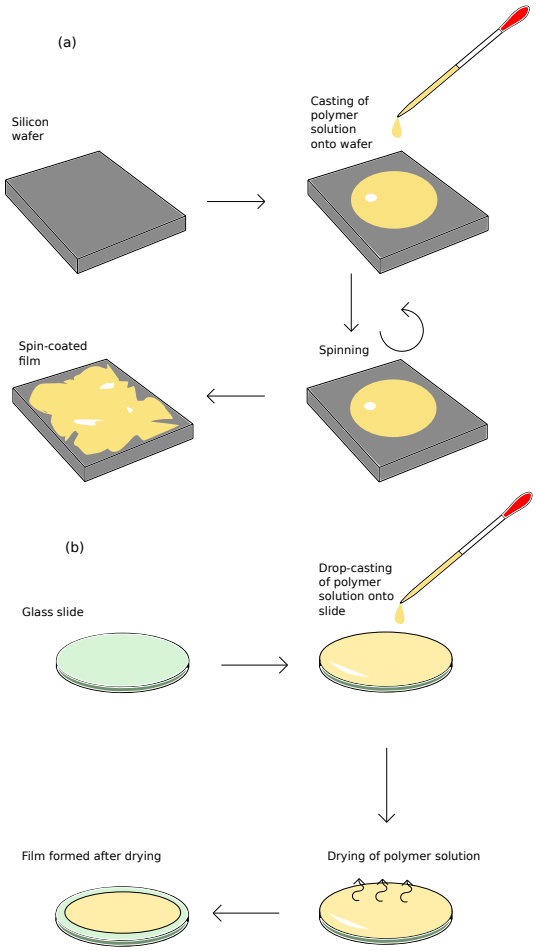

Figure 5: Techniques utilised in this study to impart surface structures on films of PPPO. (a) Spin coating, where droplets of a sample with desired composition of PPPO, DCM, and heptane are cast on an aluminosilicate wafer to be spun in a machine at 3000 rpm for 1 minute. (b) Drop-casting, where droplets of a sample with desired composition of PPPO and DCM are cast on a glass slide and allowed to dry. This process is to be carried out in a humidity chamber.

different compositions with varying initial concentrations of PPPO and heptane.

For both sets of images, macro-structures have been observed, and we divide the macro-structures into wrin-

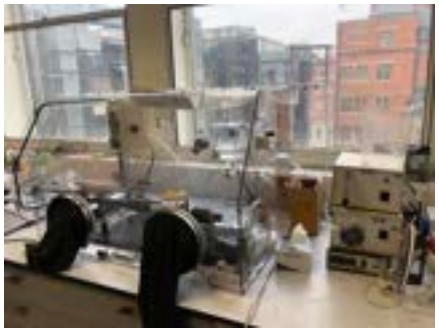

Figure 6: Photo of the relative humidity chamber used in this work (Coy Labs, Relative Humidity Chamber with an Electrotech Systems Microcontroller 5100).

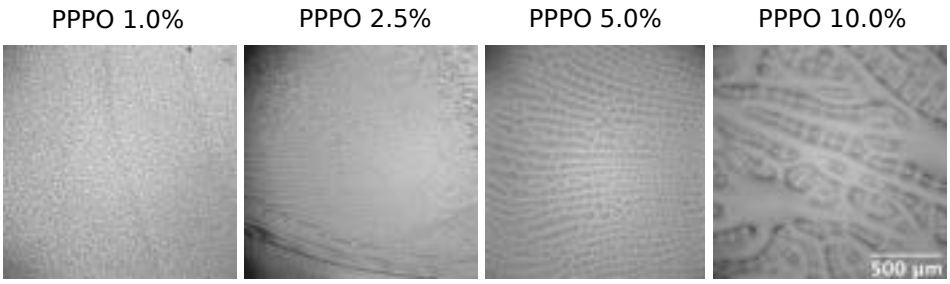

Figure 7: Optical microscopy images of films formed through spin-coating solutions of PPPO and DCM without heptane at varying initial PPPO concentrations.

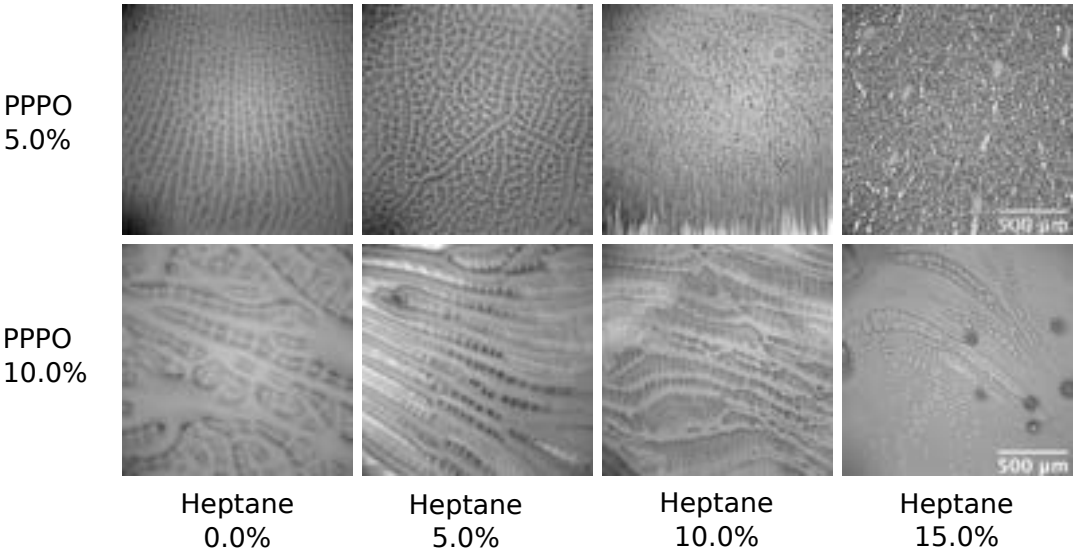

Figure 8: Optical microscopy images of films formed through spin-coating the (PPPO + DCM + heptane) solutions at different starting compositions, where the concentrations of PPPO and heptane have been varied.

klings and macrovoids between the wrinkles (also referred to as cells). [36] Characteristic length scales are needed to describe these wrinkles and macrovoids, so the wrinkle width is defined as the average distance between two adjacent wrinkles on the film, and the cell size is defined as the average cross-length of an individual macrovoid in between wrinkles. Figure 9 illustrates how these definitions work.

Figure 10 plots the characteristic wrinkle width and the cell size as analysed from images in Figure 7 against the initial concentration of PPPO. Figures 11a and 11b are plots of the average wrinkle widths and cell sizes as taken from Figure 8 with varying initial concentrations of PPPO and heptane. Below, we divide the discussions of wrinkle widths and macrovoids between wrinkles into Sections 3.1.1 and 3.1.2.

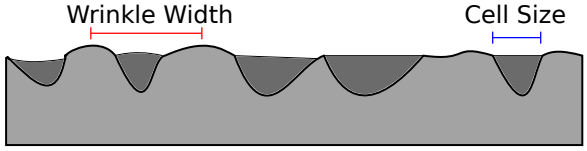

Figure 9: Definitions of the wrinkle width and cell size in this study.

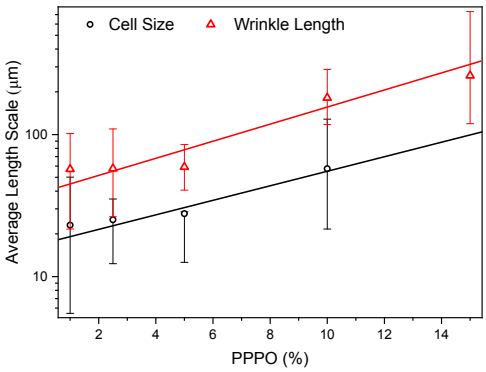

Figure 10: Effect of initial PPPO concentration on the average wrinkle width and cell size on the polymer film in a system of PPPO and DCM.

3.1.1. Wrinkling

As can be seen from Figure 7, for mixtures consisting only of PPPO and DCM without heptane, by adding PPPO to the initial mixture, there has been a transition of the macro-structure from a bicontinuous to a cellular pattern. The film also becomes thicker.

In Figure 10 we are able to observe that both the

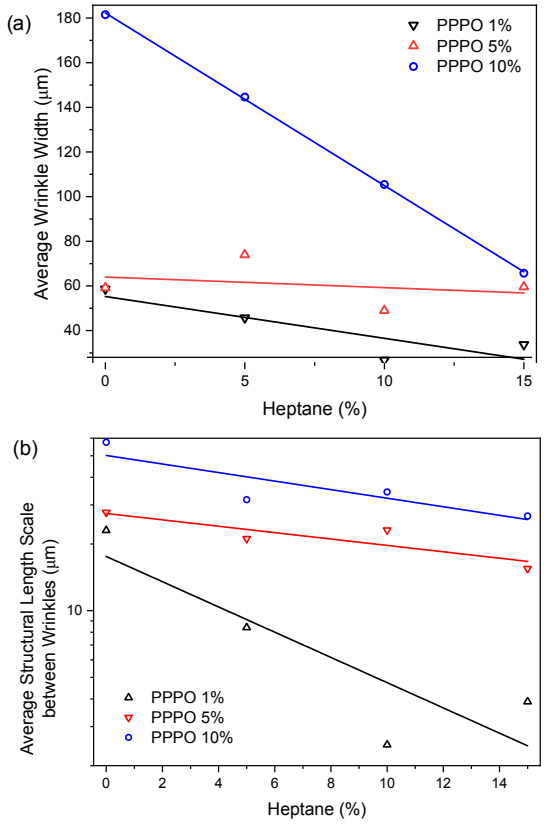

Figure 11: (a) Change in average wrinkle width on films formed via spin-coating the PPPO-DCM-heptane mixture with initial concentration of heptane for different initial concentrations of PPPO. (b) Change in average structural length scale between wrinkles on films formed via spin-coating the PPPO-DCM-heptane mixture with initial concentration of heptane for different initial concentrations of PPPO.

wrinkle width and cell size increase as the initial PPPO concentration increases. This increase in wrinkle width is attributed to the effect of a viscosity increase in the system. As a drop of polymer solution dries, it forms a gel-like skin on the surface of the drop, the solvent DCM then evaporates through the skin. This can be thought of as a bubble, with a lower pressure inside the bubble and a higher pressure outside of the bubble. This pressure is imparted on the polymer film in the form of wrinkles on its surface. As the PPPO concentration increases, the viscosity of the mixture increases. This leads to a thicker skin being formed on the surface of the bubble - one which is more resistant to mechanical buckling caused by the pressure differences either side of the bubble. A more resistant polymer film will therefore have less wrinkles, and result in larger distances between the wrinkles.

Figure 11a is a plot of change in wrinkle width on films formed via spin-coating the PPPO-DCM-heptane mixture with initial concentration of heptane for different initial concentrations of PPPO. With heptane added to PPPO and DCM, the positive trend between wrinkle width and PPPO concentration continues to hold: increasing PPPO initial concentration increases the final wrinkle width. On the other hand, Figure 11a indicates that an increased heptane initial concentration in the system will reduce the wrinkle width on the polymer film. Like before, we attribute this observation to the change of viscosity of the mixture. Since heptane is a less viscous liquid than DCM at ambient conditions (DCM = 0.413 cP at 25 °C, heptane = 0.3 cP at 25 °C [33, 37]), the addition of heptane reduces the overall viscosity of the polymer solution. This lowers the resistance of the film to mechanical instabilities caused by pressure differences during drying, reducing the widths of wrinkles.

3.1.2. Macrovoids between Wrinkles

In the absence of heptane, Figure 10 shows that the relationship between PPPO concentration and the structural length scales between wrinkles is synonymous with that of wrinkle width: increasing PPPO concentration enlarges the cell sizes. This again can be credited to the increase in viscosity: an increased viscosity generates a thicker film and reduces diffusive exchange between the solvent inside the bubble and the surrounding environment. As the solvent evaporates at slower rate, the solution has more time to coarsen or coalesce (which involves merging and subsequent evaporation of solvent in polymer poor phase, a process responsible for cell sizes in the film). Larger coarsening time scales generate larger macrovoids in the film, as the polymer poor phase bubbles have more time to coalesce before evaporation. At 15% PPPO the solution is so viscous that these bubbles cannot move throughout the film to merge; here, no cells are formed, hence the omission of their data point from Figure 10.

From Figure 8, it can be seen that the films hold the same basic macro-structure observed in the absence of heptane; however, a morphological transition from ordered, fairly uniform cells to a porous open structure occurs with the addition of heptane to the initial mixture. As such, the structural length scale of the surface pattern between wrinkles is a more appropriate description of the characteristic length than the cell size. At 10% heptane, holes begin to form in the film as shown at 5% PPPO, eventually permeating through the film at 15% heptane.

With heptane added to the mixture, Figure 11b is a plot of change in the average structural length scale between wrinkles on films formed via spin-coating the PPPO-DCM-heptane mixture with starting concentration of heptane for different initial concentrations of PPPO. Like before in Section 3.1.1, for the wrinkle width, the addition of heptane reduces the length scale on the polymer film: as can be seen from figure 11b, with more heptane added to the initial mixture, the average cell size decreases. The rationale for this follows an alternate reasoning: increased heptane concentration creates a starting composition closer to the two phase region on the ternary phase diagram (region in blue on Figure 4). This leads to an increased driving force for demixing such that the film enters the two phase region earlier during its drying process. Consequently, kinetic

arrest occurs sooner, as the film has less time to coarsen. This reduced time scale of coarsening in the polymer poor phase lead to smaller bubbles (and therefore length scales) being observed in the films, in agreement with [36].

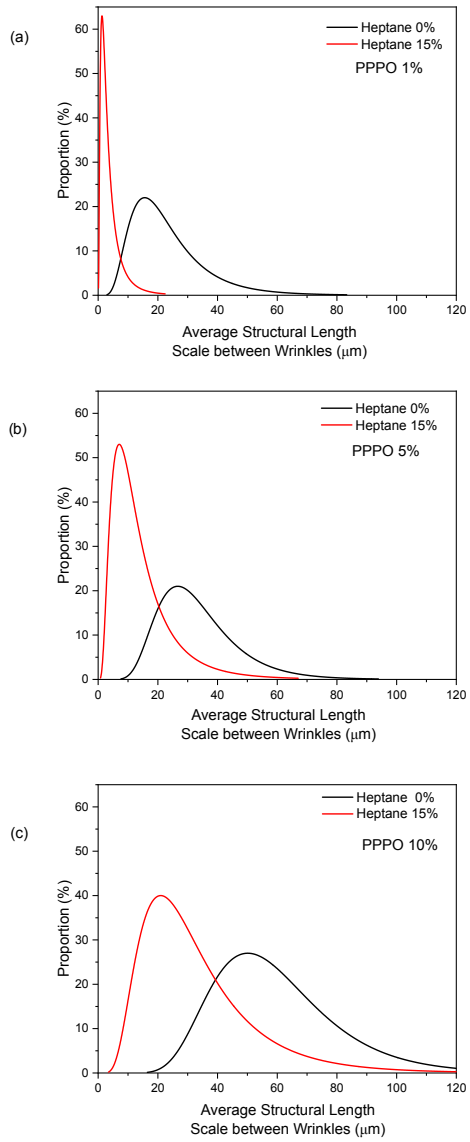

Figure 12: Graphs of the log-normal distributions (where the average and standard deviations are the input parameters) of the structural length scales between wrinkles for 0% and 15% initial heptane concentrations for (a) PPPO 1% (b) PPPO 5% (c) PPPO 10% initial concentrations.

Figure 12 shows graphs of the log-normal distributions (where the average and standard deviations are the input parameters) of the structural length scales between wrinkles for 0% and 15% initial heptane concentrations for different starting concentrations of PPPO. Here, it can be seen that the distribution of structural length scales between wrinkles narrows through an increased heptane concentration. This is because a reduced time scale for coarsening decreases the opportunity for polymer poor bubbles to naturally coagulate or remain dispersed amongst the polymer rich solution before evaporation and subsequent kinetic arrest. This narrowing occurs less strongly when the PPPO concentration is raised. Since more demixing occurs, the structural length scales between wrinkles become more distributed, the explanation being that a higher viscosity caused by an increased PPPO concentration lengthens the coarsening timescale. This counteracts the effect of heptane addition, which induces greater demixing, by providing more opportunities for the polymer poor phase bubbles to coagulate.

3.2. Micro-structures imparted via NIPS

Figure 13 shows the SEM images at ×1.5k magnification of the films formed by spin-coating samples of PPPO-DCM-heptane) mixtures with different starting concentrations of PPPO and heptane. Here, we are able to see that there are micro-pores, most of which circular in shape, imparted on the final polymer films. We have thus approximated these pores as circular in our analyses. In Figure 14a, the average area of the pores have been plotted against the initial concentration of heptane in the mixture for different initial concentrations of PPPO. The standard deviations of the pore areas are plotted in Figure 14b.

The graphs show that the sizes of the pores increase with addition of heptane to the PPPO-DCM mixture; on the other hand, the pores decrease in size with the addition of PPPO. These results seem to have been the total opposite of what have been observed for the macro-structure as described in Section 3.1. The standard deviation of the sizes of pores increase with the addition of heptane for 5% PPPO and decrease with the addition of PPPO. For 10% PPPO, though it might appear obvious as a decreasing trend with addition of heptane, due to the vertical scale being logarithmic, the change of standard deviation is too negligible to be meaningful.

We attribute this seemingly contradictory observation to the thermodynamics of the mixture, i.e. the ternary phase behaviour exhibited by PPPO, DCM, and heptane. Figure 15 provides an illustration through the use of ternary diagrams. Starting with the composition at point X (5% PPPO and 5% heptane) in Figure 15a, assuming that during drying, the mixture moves horizontally to the right into the two-phase region and at a certain point in time stops by the mixing point M. By the tie lines, it would separate into two liquids - L_1 for the polymer-rich phase and L_2 for the polymer-poor phase. The mixture would continue to dry, cross the glass transition, and solidify to form a porous surface just as illustrated before in Figure 2.

Then, in Figure 15b, starting again but with X at 5% PPPO and 10% heptane, again assuming horizontal movement into the two-phase region, after the same period of time, the ternary mixture would go deeper into the two-phase region, and we would expect composition M to move rightward as well. Due to the shape of the liquid-liquid phase boundary, the graphical distance $\overline{ML_1}$ relative to $\overline{ML_2}$ would be larger than it was in Figure 15a. The inverse lever arm rule states that in a ternary phase diagram, the

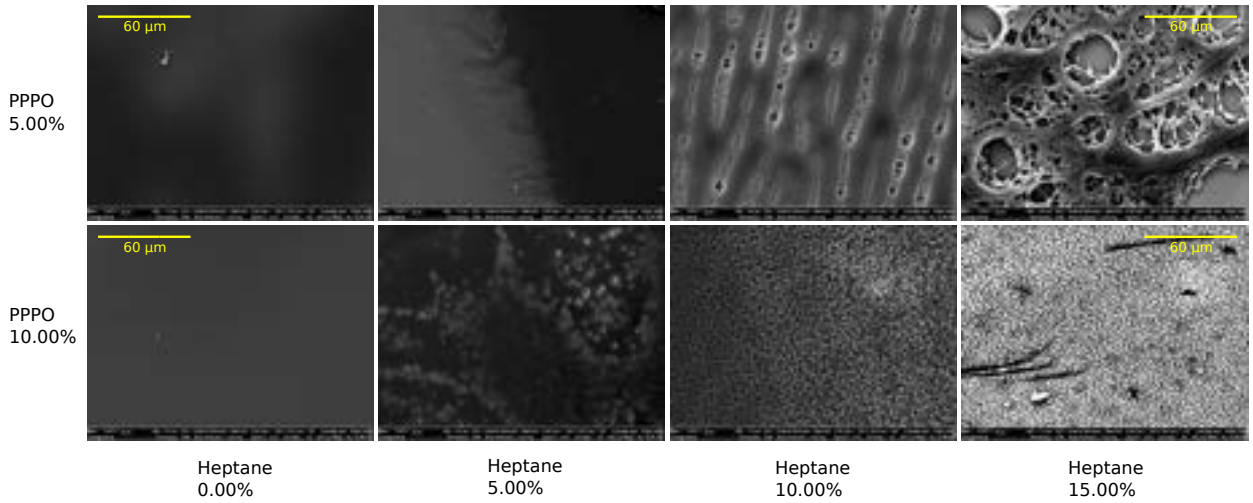

Figure 13: SEM images at ×1.5k magnification of the films formed by spin-coating samples of PPPO-DCM-heptane via spin-coating with different starting concentrations of heptane and PPPO.

amount of the polymer-rich phase relative to that of the polymer-poor phase is the reciprocal of their respective distances from the mixing point M; or, mathematically,

$$\frac{m_1}{m_2} = \frac{\overline{ML_2}}{\overline{ML_1}} \tag{1}$$

where m_1 is the mass of the polymer rich phase and m_2 the mass of the polymer poor phase. [29] Therefore, the mass of the polymer-rich phase would be smaller compared to that of the polymer-poor phase with an addition of heptane, giving rise to smaller pores after solvent and nonsolvent evaporate. Also, by going deeper into the two phase region, the effects of demixing would become more profound, giving rise to greater distributions of the sizes of the binodal phases, hence the increase of standard deviation of pore sizes with the addition of heptane.

If we change X to 10% PPPO and 5% heptane as in Figure 15c, because we are shifting the concentration of PPPO upwards, when horizontally entering the two-phase region, the mixing point M would also shift upwards. Again, by Equation 1, the mass of the polymer-rich phase would be smaller compared to that of the polymer-poor phase, making the pores in the final film smaller.

Since the scale is microscopic, we expect thermodynamics to play the most important role. Whereas before in Section 3.1, the observations have been explained from the perspective of fluid mechanics and convective heat and mass transfer, such that quantities like viscosity have a major effect, here in the microscopic length-scale they are expected to play minor roles. In other words, the macroscopic structures are mostly affected by the dynamic processes, the microscopic structures are predominantly influenced by equilibrium phenomena.

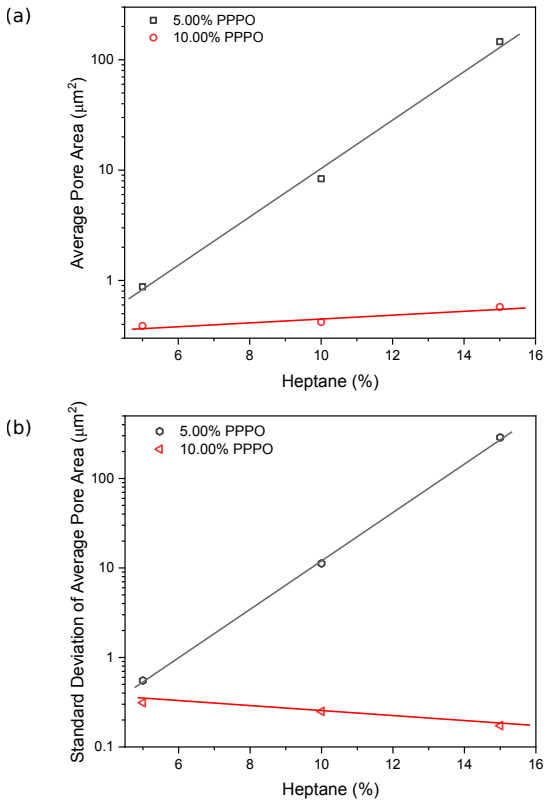

Figure 14: (a) Graph for the average area of the micro-pores as observed from SEM imaging against concentration of heptane at different PPPO concentrations. (b) Graph for the standard deviation of areas of micro-pores as observed from SEM imaging against concentration of heptane at different PPPO concentrations.

3.3. BFA

Figure 16 shows the SEM images at ×1.5k magnification of samples of PPPO and DCM solutions prepared at different initial concentrations of PPPO, drop-cast and dried in the humidity chamber under different RH. Formation of micro-pores are observed. The average pore area has been

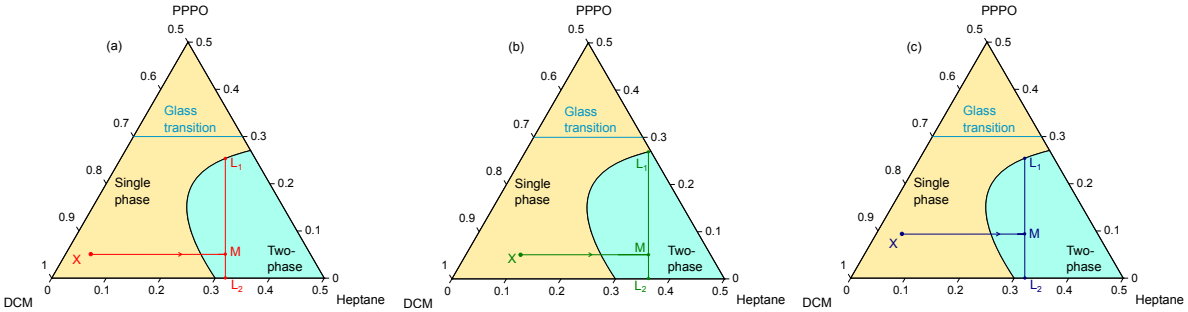

Figure 15: (a) Starting with X at 5% PPPO and 5% heptane, if the mixture moves horizontally rightward into the two-phase region, at M, it would separate into a polymer-rich phase with composition L_1 and a polymer-poor phase with composition L_2 (b) With X moved to 5% PPPO and 10% heptane, M would be expected to move rightwards. L_1 would be further from M compared to it was in (a). By the inverse lever arm rule, this means the polymer-poor phase has a greater mass. (c) With X moved to 10% PPPO and 5% heptane, M would be expected to shift upwards, and L_1 would be further away from M compared to it was in (a), resulting in a greater mass of the polymer-poor phase.

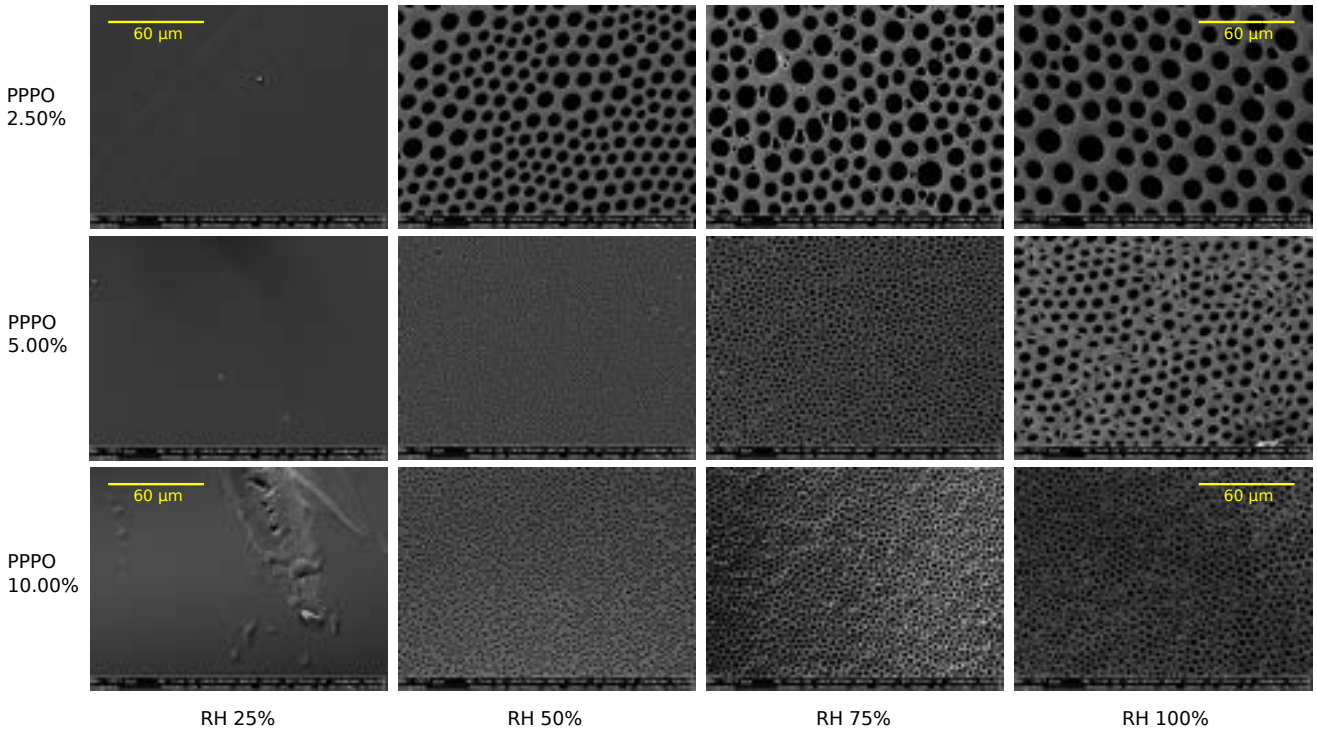

Figure 16: SEM images at ×1.5k magnification of films formed by drop-casting and drying solution samples of PPPO and DCM with different initial concentrations of PPPO and RH.

plotted in Figure 17 against RH and initial concentration of PPPO. Figure 17a shows that the pore sizes of the final PPPO film surface increase with higher RH. Figure 17b shows that the pore sizes decrease with increase of starting PPPO concentration.

To explain these observations, first, RH is a measure of how humid the air is relative to saturation at a given temperature. It is defined as [38]

$$RH = \frac{P_{H_2O}}{P^{sat}_{H_2O}} \tag{2}$$

where P_{H_2O} is the partial pressure of water in the air and $P^{sat}_{H_2O}$ is the saturation pressure of water at the given temperature. Thus, RH is directly proportional to the concentration of water in the air. The trends in Figure 17, therefore, can be interpreted as: the more water there is in the air above the PPPO film, the greater the sizes of the pores formed by BFA become. The following equation provides an explanation: [39]

$$R \propto (D\Delta p C_0 \delta^{-1} t)^{\frac{1}{3}} \tag{3}$$

where R is the radius of a water droplet, D the diffusive coefficient of water in air, ΔP the saturation pressure difference of water at the polymer-air interface, C_0 is the concentration of water in air, δ the characteristic length scale of the system which is related to the Schmidt number, and t the time. The sizes of the pores are directly proportional to C_0 and thus to the RH, because the more water there is in the air, the greater the driving force becomes for water vapour to diffuse onto the polymer film and condense.

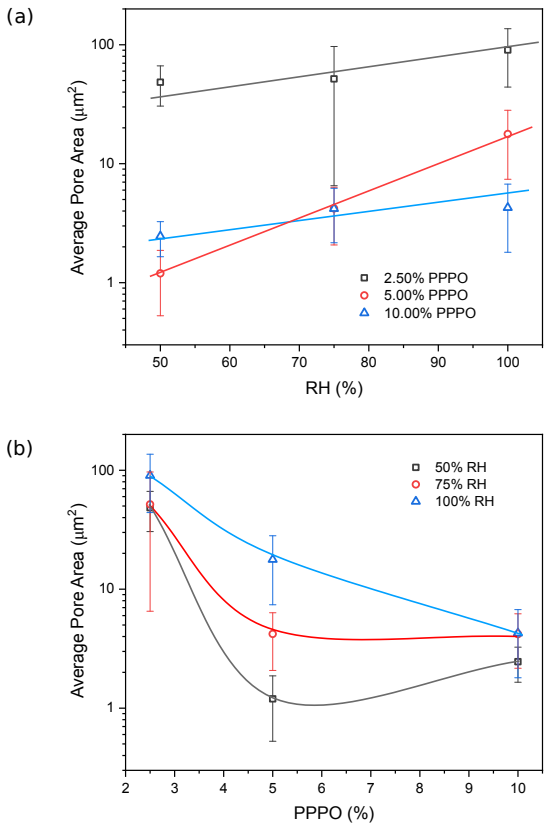

Figure 17: (a) Graph of the average area of the micro-pores imparted via BFA as observed from SEM imaging against RH (b) the average area of the micro-pores imparted via BFA as observed from SEM imaging against starting concentration of PPPO in the PPPO-DCM mixture. The error bars in (a) and (b) are the standard deviations of the areas of the pores. The two graphs represent the same set of data.

The observation that the pore sizes decrease with an increase in starting concentration of PPPO can be explained by the change in viscosity of the PPPO-DCM mixture. The more PPPO there is in the PPPO-DCM mixture, the more viscous this mixture becomes. This increases the resistance for coalescence of water droplets on the polymer solution surface, so it becomes harder for water droplets to grow in size. Also, a postulate states that a protective polymer shell may form around the water droplets. [40] So, with an increase of PPPO, this protective shell would be stronger, thus suppressing coalescence. Then, the more PPPO there is, the less DCM there is in the mixture. This decreases the amount of evaporation that would occur, which then decreases the surface temperature drop and thus the driving force for water to condense. It has also been suggested that vapour from the evaporating solvent lubricates the water droplets, making them bounce elastically without coalescence. [41] All these explanations lead to the same conclusion: having more PPPO in the starting solution would make the water droplets smaller and, consequently, the pores left by them after their evaporation smaller too.

4. Conclusions and outlook

Through spin-coating and drop-casting, macro- and micro-surface structures have been imparted on PPPO films as a result of wrinkling, NIPS, and BFA. Through optical microscopy, wrinkles and macrovoids have been observed on films obtained via NIPS on the macro-scale. Through SEM, micro-pores have been observed on films obtained via NIPS and BFA. Analyses of the images obtained from optical microscopy and SEM revealed the effects of starting PPPO and heptane concentrations, and RH on the final film wrinkle widths, sizes of the macrovoids, and sizes of the micro-pores.

For imparting surface structures on PPPO via NIPS through spin-coating, at the macro- level, a positive trend for both the wrinkle width and the macrovoid size has been observed as the starting PPPO concentration increases; the reverse is true for an increasing initial heptane concentration. The key parameters postulated to be influencing these results are the viscosity of the polymer film and driving force for demixing, both of which affect the coarsening time-scale and the subsequent final film structure. At the micro- level, an increase of starting PPPO concentration induces a decrease of pore sizes, whilst an increased initial heptane concentration would increase the pore sizes. Thermodynamics as shown through ternary phase diagrams have been hypothesised to dictate this effect, where relative amounts of the polymer-rich and -poor phases are postulated to determine the pore sizes.

For imparting surface structures on PPPO via NIPS through drop-casting in the humidity chamber, a greater RH would result in larger pores on the final PPPO film, postulated to be due to a higher driving force for water vapour diffusion onto the polymer film. A higher PPPO concentration decreases the pore sizes, which is postulated to be a result of a larger viscosity of the PPPO-DCM solution that increases the resistance of coalescence of water droplets.

To this end, for applications such as gas adsorption, we conclude that NIPS and BFA are valid ways of making porous polymeric films. The decision maker may find it necessary to tune the control variables such as the starting composition of the ternary mixture or the RH for their specific purposes.

Further research would seek to investigate the behaviour of film structure at ranges outside of the compositions studied in this work: primarily higher (over 15%) concentrations of both PPPO and heptane. It would also be beneficial to utilise analytic techniques to characterise the gas adsorption performance of the films obtained from this experiment. Methods such as dynamic vapour sorption (DVS) and gas chromatography (GC) can be employed for their abilities to rapidly collect information of the adsorption processes and high level of control and sensitivity.

Acknowledgements

We thank Roisin O'Connell for her supervisions. We thank Prof Joao Cabral for providing this research opportunity and his supervisions. We also thank Dr William Sharratt, Dr Gunjan Tyagi and Dr Luca Pellegrino for their support and help in the duration of this project.

Conflict of interest

The authors declare no conflict of interest.

References

[1] G. Guillen, Y. Pan, M. Li, E. Hoek, *Ind. Eng. Chem. Res.* 50 (2011) 3798–3817.
[2] C. Udoh, V. Garbin, J. Cabral, *Langmuir* 32 (2016) 8131–8140.
[3] T. Wanabe, C. Lopez, T. Ono, J. Cabral, *Langmuir* 30 (2014) 2470–2479.
[4] Q. Liu, Z. Tang, B. Ou, L. Liu, Z. Zhou, S. Shen, Y. Duan, *Mater. Chem. Phys.* 144 (2014) 213–225.
[5] R. Woodward, M. Kessler, S. Lima, R. Rinaldi, *Green Chem.* 20 (2018) 2374–2381.
[6] B. Ji, F. Shao, G. Hu, S. Zheng, Q. Zhang, Z. Xu, *J. Hazard. Mater.* 161 (2009) 81–87.
[7] D. Wales, J. Grand, V. Ting, R. Burke, K. Edler, C. Bowen, S. Mintova, A. Burrows, *Chem. Soc. Rev.* 44 (2015) 4290–4321.
[8] A. Ewing, A. Gabrienko, S. Semikolenov, K. Dubkov, S. Kazarian, *J. Phys. Chem. C* 119 (2015) 431–440.
[9] A. Ewing, S. Kazarian, *Supercritical Fluid Nanotechnology: Advances and Applications in Composites and Hybride Nanomaterials*, Taylor & Francis, 2015, Ch. 19, pp. 481–516.
[10] Y. Yang, X. Yang, W. Yang, S. Li, J. Xu, Y. Jiang, *RSC Adv.* 4 (2014) 42546–42553.
[11] A. Hay, *Macromolecules* 2 (1969) 107–108.
[12] A. Hay, N. Schenectady, Process of making poly-(2,6-diaryl-1,4-phenylene ethers) (Mar 1969).
[13] TENAX,* a new low-loss high-temperature resistant synthetic paper for EHV cables and other electrical equipment, Conference on Electrical Insulation & Dielectric Phenomena - Annual Report 1970, IEEE, 1970.
[14] P. Akers, G. Allen, M. Bethell, *Polymer* 9 (1968) 575–584.
[15] A. Shultz, *J. Polym. Sci., Part A-2: Polym. Phys.* 8 (1970) 883–891.
[16] W. Wrasidlo, *J. Polym. Sci., Part A-2: Polym. Phys.* 10 (1972) 1719–1729.
[17] R. Wijk, *J. Chromatogr. Sci.* 8 (1970) 418–420.
[18] S. Seshadri, J. Bozzelli, *Chemosphere* 12 (1983) 809–820.
[19] E. Pellizzari, J. Bunch, R. Berkley, J. McRae, *Anal. Lett.* 9 (1975) 45–63.
[20] R. Brown, C. Purnell, *J. Chromatogr. A* 178 (1979) 79–90.
[21] I. Maier, M. Fieber, *J. High. Resolut. Chromatogr.* 11 (1988) 566–576.
[22] K. Ventura, M. Dostal, J. Churacek, *J. Chromatogr. A* 642 (1993) 379–382.
[23] B. Alfeeli, V. Jain, R. Johnson, F. Beyer, J. Heflin, M. Agah, *Microchem. J.* 98 (2011) 240–245.
[24] H. Ghanbarian, B. Mirza, *J. Nanostructure Chem.* 8 (2019) 413–420.
[25] R. Brennan, R. Sandord, *Appl. Environ. Microbiol.* 68 (2002) 1464–1467.
[26] R. O'Connell, A. Porter, J. Higgins, J. Cabral, *Polymer* 180 (2019) 121652.
[27] L. Robeson, *Polymer Science: A Comprehensive Reference*, Elsevier, 2012, Ch. 8.13, pp. 325–347.
[28] E. Aram, S. Mehdipour-Ataei, *Int. J. Polym. Mater.* 65 (2015) 358–375.
[29] J. Seader, E. Henley, D. Roper, *Separation Process Principles: Chemical and Biochemical Operations*, Wiley, 2011, Ch. 8.3.1, pp. 313–316.
[30] J. Elliott, C. Lira, *Introductory Chemical Engineering Thermodynamics*, Prentice Hall, 1999, Ch. 12.3, pp. 430–431.
[31] J. Prausnitz, R. Lichtenthaler, E. de Azevedo, *Molecular Thermodynamics of Fluid-Phase Equilibria*, Prentice Hall, 1999, Ch. 8, pp. 417–503.
[32] A. Zhang, H. Bai, L. Li, *Chem. Rev.* 115 (2015) 98019868.
[33] Sigma-Aldrich, Dichloromethane.
URL `https://www.sigmaaldrich.com/chemistry/solvents/dichlorometh`
[34] R. Perry, D. Green, *Perry's Chemical Engineers' Handbook*, McGraw-Hill, 2008.
[35] X. Yang, L. Chen, Y. Li, J. Rooke, C. Sanchez, B. Su, *Chem. Soc. Rev.* 46 (2017) 481–558.
[36] A. Idris, Z. Man, A. Maulud, M. Khan, *Membranes* 7 (2017) 21.
[37] J. Dymond, H. Oye, *J. Phys. Chem. Ref. Data* 23 (1994) 41–53.
[38] D. Shallcross, *Handbook of Psychrometric Charts: Humidity Diagrams for Engineers*, Springer, 1997.
[39] D. Beysens, A. Steyer, P. Guenoun, D. Fritter, C. Knobler, *Phase Transit.* 31 (1991) 219–246.
[40] O. Pitois, B. Francois, *Eur. Phys. J. B* 8 (1999) 225–231.
[41] M. Srinivasarao, D. Collings, A. Philips, S. Patel, *Science* 292 (2001) 79–83.

Design of Novel RNA Thermometers for the Cold Shock Response in Bacterial Cells

Helen Ogbobi and Malinya Wijekoon

Department of Chemical Engineering, Imperial College London, U.K.

Abstract: RNA thermometers are biomolecular sensors capable of regulating gene expression at a translational level by changing conformation in response to a temperature shift. RNA thermometers that respond to cold shock could represent an invaluable tool for cell engineering applications in bioproduction. In this report, a cold shock inducible thermometer is designed for application in bacteria, with inspiration from the natural cspA cold shock thermometer. Through computational design, using RNAfold, a novel cold shock thermometer along with five variants were engineered, with primers designed for future testing *in vivo*. From these thermometers a maximum threshold temperature of 32℃ was obtained, with translation being permitted at or below this temperature. However above 32℃ translation was restricted due to a temperature dependent conformation change. Validation of the thermometers must be carried out through *in vivo* experimentation. Upon confirmation of the thermometers' behaviour in the natural system, further developments can be made to create a cold shock thermometer toolbox.

1 Introduction

Temperature is one of the various stimuli that can cause widespread physiological alterations within an organism. Cold shock is a thermal effect in which the organism experiences an extreme decline in temperature, whereas heat-shock refers to when the organism is subjected to high temperatures. At sub-physiological temperatures, there is potential for cells to suffer from a variety of cold stress related issues, including a decrease in membrane fluidity, changes in the structure of nucleic acids and reduced ribosome function (Phadtare & Severinov (2010)). To adapt to low temperatures, many organisms produce cold shock proteins (csps).

RNA thermometers (RNATs) contribute to the regulation of csp expression in bacteria at specific temperatures. RNATs are non-coding, gene expression regulatory elements that can control the translation of the associated mRNA strand in response to temperature. RNATs are located within the 5' Untranslated Region (5'UTR) of an mRNA strand. At a restrictive temperature, the 5'UTR forms a complex secondary structure which masks the translation initiation regions (TIR), making them unavailable for translation. The TIR consists of the ribosome binding site (RBS) and the start codon. At a permissive temperature, this secondary structure undergoes conformational rearrangement in which the start codon and RBS are fully accessible to the ribosome, allowing translation to occur (Somero (2018)).

RNATs prove to be powerful minimum sized genetic tools, effectively managing the expression of certain proteins at a specific temperature without the need for trans-acting regulator molecules or chemical inducers. Therefore, synthetic RNATs are widely applicable in research and biotechnology, for example as binary switches, biosensor components in large scale bioreactors and to study the function of essential genes which cannot be easily deleted or turned off. Furthermore, RNATs can be transferred between different bacterial and even amongst mammalian hosts without causing any adverse affects on the toxicity, the membrane permeability or the scale-up costs (Neupert & Bock (2009)). Cold shock RNATs allow protein expression at sub-physiological temperatures which, although leads to a lower rate of protein synthesis, can offer significant advantages in terms of increased protein solubility and slower proteolytic degradation, resulting in an increased expression of the target protein (EMBL (2020)). Additionally, low temperature protein synthesis allows a polypeptide to adopt a functionally active, specific conformational shape; vital in biosynthetic applications (Fakruddin et al. (2013)).

There has been a promising discovery of RNATs in bacteria. The expression of cold shock protein A (cspA), in *Escherichia coli (E.coli)*, is significantly enhanced due to the presence of an RNAT, which undergoes structural change upon a significant downward thermal shift (Yamanaka et al. (1999)).

This study aims at investigating the design of a novel cold shock responsive cis-acting RNA thermometer in bacterial cells. Structural understanding of the thermo-inducible nature of cspA mRNA was required as a starting point for the design of a simplified system, amenable for cell engineering. Different designs were considered, the folding of the structures analysed using computational tools. The insertion of these designs into genetic constructs was planned. These thermometers will undergo further testing, to be optimised for expression at desired temperatures *in vivo*. Ultimately, this cold shock RNAT can be utilised for protein expression at low temperatures for a range of applications in both bacterial and mammalian cells.

2 Background

2.1 *RNA Thermometers*

The two extreme thermal shifts which RNATs respond to are heat and cold shock. RNATs respond differently in each of these scenarios: during heat shock, the

hairpin structure essentially 'melts' into a relatively linear conformation, as the temperature increases. This melting process is known as the 'zipper' mechanism (Figure 1a). Alternatively during the 'switch' mechanism, the RNAT shifts from one configuration to another as the temperature changes (1b). The switch mechanism is adopted in both cold and heat shock RNATs. Whilst the structural tendencies differ in response to the two thermal shifts, in each case the start codon and RBS are exposed at each permissive temperature, respectively (Kortmann & Narberhaus (2012)).

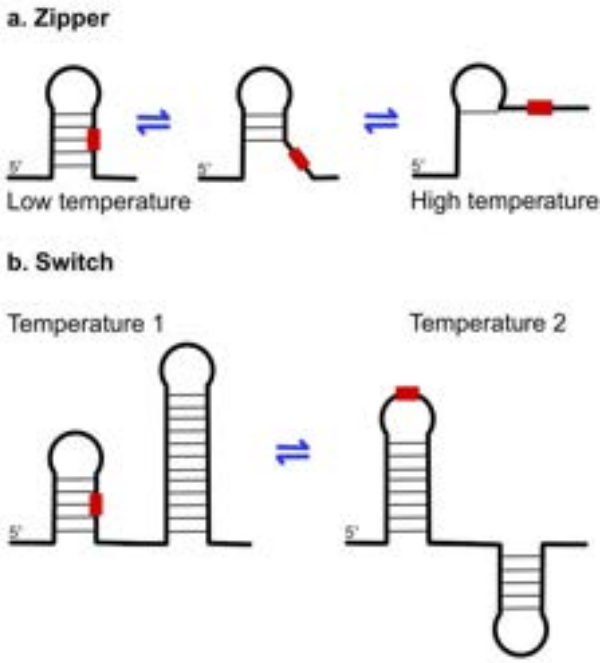

Figure 1: a. Increasing the temperature causes the hydrogen bonds between the nucleotides of the RNAT adopting the zipper mechanism to break. It will gradually melt, exposing the TIR, (illustrated by the red block) to allow translation. **b.** In the switch mechanism, there are two mutually exclusive structures which are adopted at specific temperatures. Notably, the structure at temperature 2 leaves the RBS sequence and start codon accessible to the ribosome.

Though most of the knowledge on the concept of RNATs is derived from bacteria, the presence of this genetic tool is not limited to this domain. In response to heat shock, the *Arabidopsis* plant experiences an enhanced expression of PIF7 (the bHLH transcription factor) at high temperatures and is repressed at colder conditions as a result of the zipper mechanism (Chung et al. (2020)). In mammals, there has only been one discovery of an RNAT; heat shock RNA 1 (HSR1) which adopts the zipper mechanism to regulate the expression of heat shock transcription factor, HSF1 (Choi et al. (2015)).

2.2 *Natural cold shock RNATs: Cold shock protein A*

The most notable example of a cold shock responding RNAT in nature is in the bacteria, *E. coli*. Though cspA is present at higher temperatures, there is a substantial increase in the expression of this protein as temperature decreases. This translational favouritism of cspA at lower temperatures is a result of the RNAT which employs the switch mechanism in response to cold shock. It has been found that following thermal shift down to 10℃ results in the cspA mRNA becoming more stable and less prone to degradation compared to the 37℃ structure (Giuliodori et al. (2010)).

In vivo dimethyl sulfate reactivity testing and temperature gradient gel electrophoresis revealed that the cspA 5'UTR undergoes a temperature-dependent structural change. Subsequently, chemical and enzymatic probing, using RNase V1 and RNases T1 and T2, at 10℃, 20℃ and 37℃ were carried out on the entire cspA mRNA. The cleavage patterns at 37℃ were radically different from the structures at 10℃ and 20℃. Based on the findings from the probing, two structural models of the full-length cspA sequence were constructed (Figure S1 and S2), and these structures were further validated by introducing mutations into the sequences(Giuliodori et al. (2010)).

A key region of the cspA secondary conformation is the pseudoknot - a structure formed when nucleotides within a hairpin loop of RNA, base pairs with a stretch of complementary nucleotides elsewhere in the RNA sequence (Brierley et al. (2007))). In the low temperature structure, the pseudoknot (base pairs between nucleotides 95-98 and 42-45) imposes constraints which exposes the Shine-Dalgarno (SD) sequence (the RBS in bacterial cells) and the start codon in an unstable helix (bases 141-181). However, as temperature increases, the stability of the pseudoknot decreases and new long-distance base pairings of regions of the 5'UTR with coding segments are energetically favoured, ultimately resulting in the TIR being 'hidden' from the ribosome in a double-stranded structure (bases 145-163 paired with bases 74-93). The existence of these structures has been analysed and validated using a variety of techniques, and the data obtained *in vitro* is fully compatible with the pattern of DMS reactivity *in vivo*, which suggests that the two structural models are likely to exist in the cell environmental (Giuliodori et al. (2010)). The nucleotides referred to in the this paragraph can be viewed in figure S1 and S2.

However, the switch mechanism of this natural cold shock RNAT is complex; it includes long distance interactions with the coding sequence of the cspA, as well as the binding of an S1 protein to aid the conformation change (Giuliodori et al. (2010)). There have been no attempts to devise synthetic cold shock RNATs following the 'switch' mechanism, that is applicable to any protein. Therefore, the two temperature dependent structures of cspA mRNA identified by Giuliodori et. al provided a starting point for this novel thermometer design.

2.3 *Synthetic heat shock RNAT in bacteria*

The design of novel cold shock RNATs is a concept that has not been greatly explored however, there have been several significant attempts to create novel

heat shock RNATs which provides valuable insight into the general design of these genetic controllers.

Waldminghaus, et al. designed heat shock responsive RNA thermometers, through a combination of computational design and in vivo screening. The researchers designed two thermosensitive RNA structures through the software programme SWITCH, which provides predictions of secondary structures of nucleic acids. Vienna RNA-fold was also utilised to give a prediction of the minimum energy of structure and further analysis of the secondary structure, allowing alteration and optimisation of the designs. The final structures were then analysed *in vivo*, with each RNAT inserted into a plasmid, and analysed via the Northern blot method (Waldminghaus et al. (2008))

Through a similar methodology, Bock, et al., were able to create simple, single stem-loop structured RNATs, optimised for enhanced gene expression at warmer conditions. In this experiment, twelve RNAT constructs were developed through the guidance of computational predictions. The constructs varied in thermal stability and amount of free energy held, achieving this by altering the following parameters: (i) the size of hairpin loop, (ii), the presence of mismatches and bulges, and (iii) the base content within the stem (Bock (2008)). The results of this research were further developed to create a 'genetic toolbox' of RNA thermometers of various sensitivity levels, suitable for use within a 29 to 37℃ temperature range (Sen et al. (2017)).

Building upon these various attempts to design synthetic RNA thermometers, Neupert and Bock presented guidance for the design of RNATs alongside methodologies for experimentation and optimisation of the thermometers. Though this paper, alongside the previous studies mentioned, are directly related to the heat shock response, the information from this research provides a solid foundation for the initial design of the cold shock RNATs (Neupert & Bock (2009)).

2.4 *Current low temperature protein expression technology*

One of the most widely used technologies in industry for foreign protein expression is the use of recombinant plasmids in an *E. coli*. host with T7 RNA polymerase; this system often gives high protein yield. (Briand et al. (2016)). This method has been adapted to produce proteins at lower temperatures to avoid the formation of inclusion bodies, improve protein folding and increase solubility of the protein.

The expression of recombinant protein (ß-galactosidase) at low temperatures by synthesising a cspA-lacZ fusion was investigated. The cspA promoter was chosen due to its temperature inducibility, as stated in section 2.2. It was found that alongside the promoter region and RBS, a sequence of 350 bp upstream of the cspA -35 box was necessary for temperature dependency. The recombinant plasmid successfully increased ß-galactosidase activity levels by five-fold upon a temperature decrease from 37℃ to 15-25℃ (Vasina & Baneyx (1996)).

Further work has been conducted into engineering low temperature expression systems for cold-adapted (psychrophilic) enzymes to ensure correct folding and structural integrity, with wide applicability in bio-catalysis and commercial value. (Bjerga et al. (2016)). For example, a system was constructed to express psychrophilic enzymes using a cspA promoter in combination with cold-active chaperonines and fusion partners to promote solubility. There were high expression levels for all candidate enzymes (Bjerga & Williamson (2015)).

E. coli based protein expression systems allow cultivation temperature to be decreased to approximately 18℃, however Miyake, et al. used cold-adapted bacterium, Shewanella sp. Strain Ac10, to construct a protein expression system which works at temperatures as low as 0℃, to supress the formation of inclusion bodies more effectively. With this system, 100mg/L of ß-lactamase and more than 10 mg/L of PepF and PepQ were obtained at 4℃; the highest obtained for a system using cold-adapted bacteria. This method offers an alternative to the commonly used *E. coli* T7 promoter system for low temperature protein expression (Miyake et al. (2007))

In comparison to *in vivo* methods, the cell-free protein synthesis process has a better scalability and is also faster and more cost-effective. It is possible that this system can be adapted for protein expression at sub-physiological temperatures (NewEnglandBioLabs (2020)).

CspA mRNA is being used extensively in the bioengineering industry for low temperature protein expression, however it is either used in its entirety or in combination with chaperonins or fusion agents. No attempts have been made to systematically explore which sections of the code are required for thermoinducibility. By understanding these key regions, a modular and easy-to-plug-in cold shock RNA thermometer can be engineered to produce a wide range of proteins. Furthermore, a novel thermometer can be varied to allow flexibility and tunability of the expression temperature.

3 Methodology

3.1 *Cold shock thermometer design*

The two conformations of cspA in *E. coli* (supplementary figure 6) were analysed in detail to determine the essential elements which resulted in temperature dependence. These sections were then used to computationally design a feasible cold shock RNAT. Modifications of this novel RNAT were engineered to explore the effects of secondary structure on the expression temperature and stability.

3.1.1 *Computational design of synthetic cold-shock thermometer*

The key principle of a cold shock RNA thermometer is that its functionality is dependent on the structural

accessibility of the SD site at different temperatures (Yamanaka et al. (1999)). This established the essential criterion for the design of the cold shock RNAT - the SD sequence must be accessible at low temperatures (10℃) but not at higher temperatures (37℃).

The software programme, RNAfold, was employed to sequentially analyse the cspA structures (supplementary figure 6), at specfic regions (such as the pseudoknot, TIR and at some of the coding segments), to pinpoint the key elements responsible for the conformational change with temperature. RNAfold utilises dynamic programming algorithms to predict the mathematical optimum of the minimum free energy (MFE), base pair probability, temperature dependency and overall secondary structure. The software makes predictions based on the minimum energy as these are the most biologically feasible structures, with the predicted values possessing an accuracy of 50-70% (Eddy (2004)).

RNAfold was used to experiment with thermometer design ideas that incorporated the identified essential areas. The predictions were computed by inputting the RNA sequence along with its associated dot-bracket notation (to implement specific base pair constraints and pair formations). In advanced folding options, the energy parameters to determine the secondary structure was selected to use the Turner model (Andronescu et al. (2010)), which were re-scaled at the chosen temperature. An iterative approach was used to modify and improve the designs until the essential criterion was met in final design thermometer.

3.1.2 *Computational design of thermometer variants*

Variations of the final RNAT were constructed, following guidance from Neupert and Bock. Stability alterations attempted included (i) the increase the hairpin loop size, (ii) the introduction of kinks into the stem and (iii) the increase of the stem length (Neupert & Bock (2009)). The sequences and dot-bracket notations were inputted into RNAfold to obtain structural predictions at 10℃ and 37℃. Variations in which the thermometer functionality was lost (due to a failure to meet the design criterion stated in section 3.1.1, were discounted as invalid. The structural predictions and values of the MFE of the variations accepted as functional were recorded and were further analysed using RNAfold to find the temperature at which the conformation change occurs.

3.1.3 *Design of controls*

To verify the reliability of the novel RNATs, the experimental results must be compared to that of a positive control which permits translation at all temperatures and a negative control which is always turned off. In the negative control, the TIR must be concealed within a double strand to prevent ribosome binding.

3.2 *Design of primers*

The optimally designed cold shock RNAT along with its variants were inserted into the P23118mRFP1 plasmid to clone the thermometer and test in bacterial cells. The original plasmid included a BBa_J23118 promoter followed by the RBS and then the red fluorescence protein (mRFP1). The plasmid also contained an AmpR gene alongside its promoter for Ampicillin resistance.

To insert the RNATs into the plasmid, the PCR amplification method was selected. Primers were designed to anneal to a region of the BBa_J23118 promoter and to a section of the RFP1 mRNA. Each primer contained a section of the thermometer in the overhangs (figure 2) and included a phosphorylated 5' end. Therefore, via PCR, the thermometer will be added between the promoter and RFP1. T4 DNA ligase will anneal the two ends of the thermometer to produce the final re-circularised construct (supplementary figure 7).

Figure 2: Cloning of the designed thermometer into a target plasmid using PCR amplification.

The region of base pairs annealing to the promoter and RFP1 must be long enough to ensure strong bonding during PCR. Furthermore, the melting temperature of the designed primers must be similar to ensure that they anneal to the plasmid at the same stage of the PCR process.

4 Results

4.1 *Novel cold shock thermometer sequence analysis*

From the cspA structural analysis to determine which elements were responsible for its thermal dependency, it was identified that a short section (bases 138 to 182) from the cold shock structure (Figure 3) included two hairpin loops (shown in table 2 as T1). Additionally, it was discovered that the secondary hairpin loop with the start codon and a short coding section of cspA was needed to maintain stability of the primary loop containing the SD sequence.

To ensure the SD sequence was single stranded in the loop of the primary hairpin, two bases were deleted from T1 (base positions 8 and 9), forming T2.

Another essential element was the 87-93 bases from the 37℃ cspA structure (Figure 3), as they will form complimentary base pairings with the SD sequence to form a double strand. This sequence (CCUUUAA) was inserted at the end of T2 to form T3.

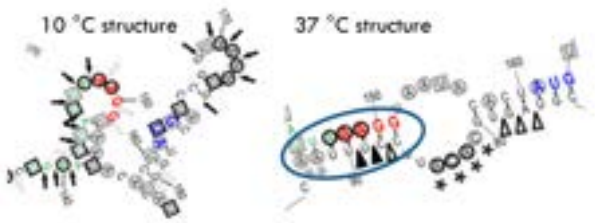

Figure 3: Close up of segments of the natural cspA structures at 10℃ and 37℃ which showed thermal dependence. The green section is the binding site of the S1 protein (not relevant for the synthetic RNATs), the SD sequence is in red whilst the start codon is highlighted in blue (Giuliodori et al. (2010)).

Simply, combining structural elements from the 10℃ and 37℃ cspA structures did not provide the desired change in shape. Therefore, an iterative approach of analysis of the RNAfold predictions and re-design was employed to ensure the final RNAT structure satisfied the design criterion. For example, a guanine nucleotide was added after the 5th base of T3, uracil was added after the 15th base, whilst the 45th base, cytosine, was substituted with a uracil nucleotide. T4 has been modified to ensure that the thermometer is 'in frame', producing T5.

4.2 *Novel cold shock thermometer structural analysis*

The synthetic cold shock thermometer (T5) undergoes a conformation change at 26℃ (T5's threshold temperature). At 37℃, the SD sequence and the start codon are 'hidden' in a double strand, unavailable for the ribosome to bind and initiate translation of the protein (Figure 5ai). However, at very low temperatures, below 26℃, the RBS occupies the loop of the shorter hairpin structure whereas the start codon is placed on a bulge in the longer hairpin (Figure 5aii). Therefore, the ribosome can access the sites to permit translation.

The ability of T5 to change shape relied on the stability and base-pair probabilities of specific regions of the sequence. For example, in the 10℃ structure, the AUGUA nucleotides in the first hairpin from the 5' direction forms complimentary pairs with the opposite UAUAU sequence, to keep the SD site in the hairpin loop and therefore available for the ribosome. As temperature increases, the MFE increases (Figure 5a) as the thermometer adopts the more energetically stable structure. Above 26℃, it becomes more energetically favourable for the AAGG sequence to bind with the UUCU code, effectively hiding it from the ribosome.

There is a fine interplay between the base pair probabilities and the forces of attraction of each of the mentioned sequences to bind to its complimentary code at certain temperatures. This interaction is determined by the more thermodynamically stable adoption of the structure. Therefore, each base sequence (as mentioned in above paragraph) was modified and engineered to ensure the attraction was at the right stability to allow temperature dependent shape change. Even small changes, for example, changing the sequence UUCC would mean the structure could not act as a cold shock thermometer. The third base was changed to a U as the G-U pairing was slightly weaker than a G-C, and therefore would reach a level of instability to allow temperature dependency.

The structural constraint input consisted of brackets which were used to ensure the secondary hairpin loop was always formed. However, there were no constraints on the primary hairpin loop, giving RNAfold the freedom to return the optimal secondary structure for that section of the thermometer where the SD sequence is hidden or exposed, at each temperature (Table 1) Each symbol dictates the behaviour of the corresponding base; the structural constraint sequence is the same length as the nucleotide sequence. The symbols represent:

- x : base must not pair
- . : no constraint at all
- () : matching brackets - base i pairs base j

4.3 *Variations of novel RNA thermometer*

Five variations (V1-V5) of T5 were obtained, shown in Table 2. V1-V4 have three bases added, increasing the size of the primary hairpin loop containing the SD site. V5 has six additional base, resulting in a larger size of the same loop and a small extension (increase by one base) of the stem immediately following this hairpin loop. The presence of these additional bases allows the structures to maintain their key thermo-regulation characteristic (shown in Figure 5).

The threshold temperature of V1-V3 occurs at 25℃ whilst V4 holds a threshold temperature of 26℃. These are very similar (if not equal) to the threshold temperature of T5. V5 had the highest recorded threshold temperature of 32℃.

From Figure 4, it is clear that for each of the variants, the MFE increases with temperature, following the trend observed for T5. The reflects the weakening of the hydrogen bonds between the bases within the stem of the structures as temperature increases. The MFE profile of T5 is always greater than that of the variants, indicating that the additional bases results in an increased level of stability. Increasing the size of the hairpin loop has a stabilising affect, as there are more phosphodiester bonds present.

As temperature increases, the MFE profiles of V1-V4 begin to align whereas the MFE value of V5 becomes closer to that of T5. Above the threshold temperatures for each of the thermometers, the bonds between bases of the hairpin break, opening the loop up and allowing the bases to bond to the complementary sequence (UUCU) on the opposing side. Simultaneously, beyond the threshold temperature, a bulge emerges in the middle of the stem of the high temperature structure RNAT. Neupert and Bock observed through experimentation that the presence of a bulge has a destabilising effect on the RNAT. As the size

Table 1: The structural constraints inputted into RNAfold and its prediction of the optimal secondary structure at various temperatures.

Temperature	Structural constraint
Input	.....((((x((x((.....)))))))).....
10℃	....(((((.....)))))..((((.((.((.....)))))))).....
37℃	.....(((((.....((((.((.((.....)))))))))))))....

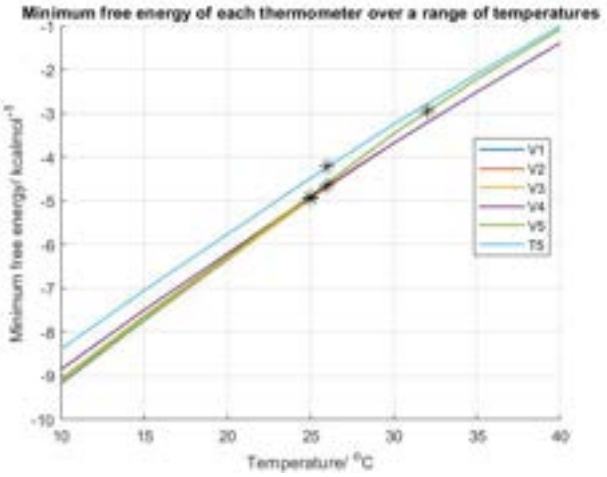

Figure 4: The graph illustrates the changing of minimum free energy for each structure upon temperature increase. The marked data points (*) indicate the temperature and free energy at which the structure undergoes a conformation change. The MFE data for V1-V4 are very similar therefore the lines align under the purple line as temeprature increases.

of the bulge becomes larger, this adverse affect increases. Thus, as V5 has a larger bulge than V1-V4, the MFE value of V5 begins to surpass the other variants beyond its threshold temperature (Neupert & Bock (2009))

Table 3 provides thermodynamic data for each of the thermometers obtained from RNAfold. Apart from the MFE structures, RNA can also fold into sub-optimal conformations, creating an ensemble (Moss, 2018). The free energy of the thermodynamic ensemble incorporates the MFE of the structure as shown in figure 5, as well as the energy of other possible sub-optimal structures. The free energy of thermodynamic ensemble is lower at 10℃ compared to 37℃ for all thermometers. This indicates that the low temperature structures are the most thermodynamically favourable structure as a result of a higher degree of stability. This is due to stronger hydrogen bonds and intramolecular attraction forces.

From the trend observed in Figure 4, as the temperature continues to increase beyond 37℃, the free energy may become close to 0 Kcal/mol meaning the high temperature structure becomes completely unstable, potentially exposes TIR and allows translation to occur again. This suggests that there is a temperature window in which the novel thermometer can operate effectively; well within the range at which low temperature protein expression can be carried out.

Additionally, at low temperatures, the MFE structure is much more frequent in the ensemble due to its higher stability, with V1 and V5 having the highest occurrence. The ensemble diversity (ED) metric measures the difference between the number of bases in the Boltzmann weighted conformations, averaged across the ensemble. A low ED, such as V1 at 10℃, indicates a single dominant conformation whereas a high ED suggest multiple diverse conformations and a lack of defined structure. With regards to this information, T5, V1 and V5 are most likely to occur *in vivo* out of the possible structures.

4.4 *Positive and Negative Controls*

Table 2 shows the sequences for the positive and negative controls. The positive control has a simple, linear secondary structure with the SD sequence. The negative control is an in-frame alteration of T3. The secondary structure produced from this sequence constricts the TIR in a double strand at all temperatures.

4.5 *Primer Design & Insertion into the Plasmid*

Table 4 shows the primers designed for each of the thermometers, respectively. Whilst the recommended base length of the primers was 40, only three of the primers designed followed this, with lengths varying between 49-47 bases. The highest temperature difference between a pair of primers was 3.7℃ – for the primers of V1 (F1, R1), V3 (F3, R3) and V4 (F4, R4).

The presence of an AUG codon in the thermometers, as outlined in section 4.2 causes some complications when inserting the thermometer into the plasmid. This start codon appears before the AUG for the RFP1. At low temperatures, once the ribosome attaches on to the SD sequence, translation will initiate when it comes across an AUG codon. It is essential to ensure that the section in between these start codons are kept in frame so that the mRFP1 is translated into the correct amino acids. However, this does mean that there will be a very short polypeptide sequence (Met-Ser-Gly-Lys-Met-Thr-Gly-Ser-Leu-Lys) attached to the start of the RFP1.

5 Discussion

The novel RNA thermometer, T5 and its variants (V1-V5), designed by computational means, are (in theory) capable of gene expression regulation in response to cold shock. These thermometers exhibit the essential structural features of cold shock RNATs in terms of accessibility of the SD sequence.

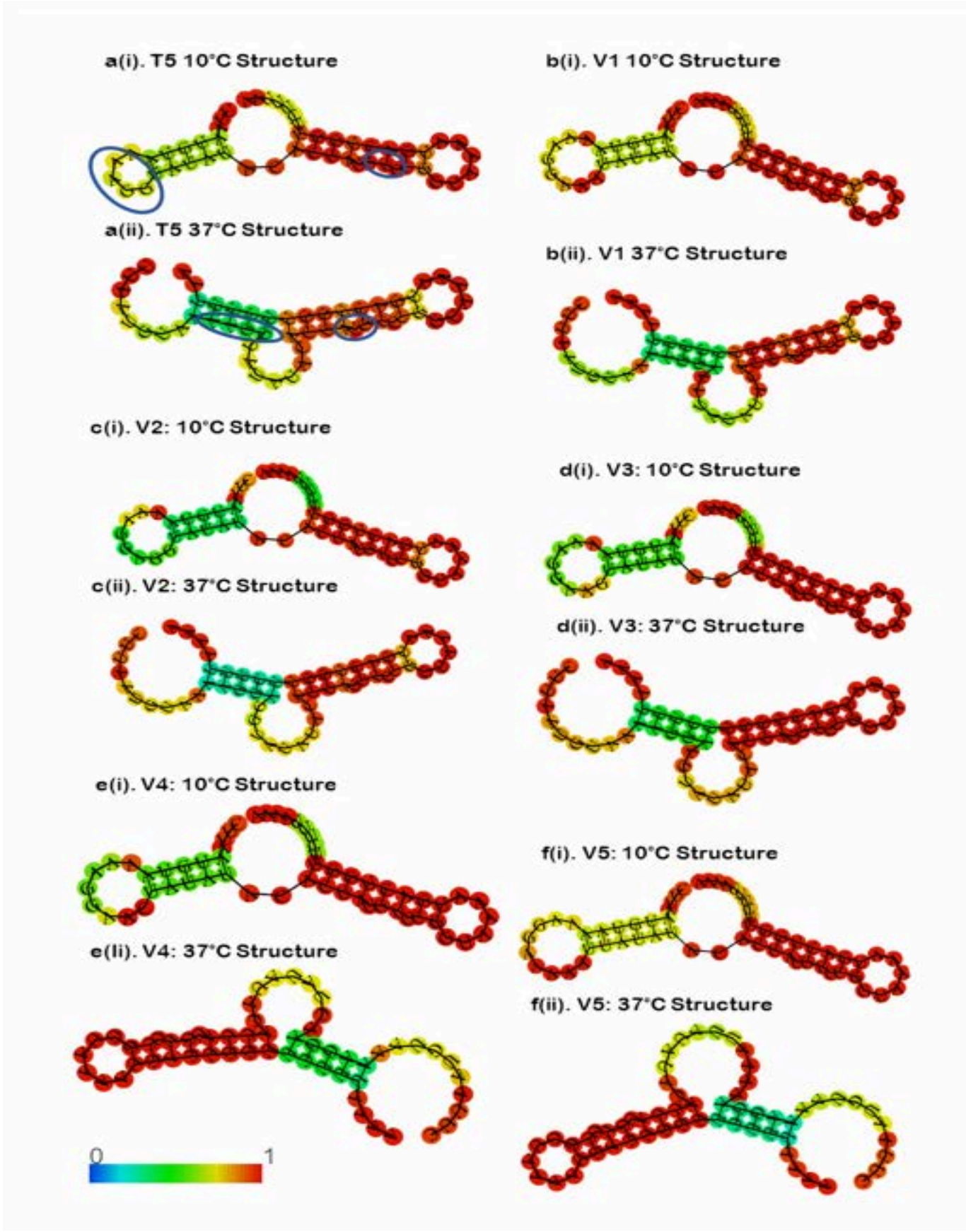

Figure 5: The secondary structures of T5 and variants V1-V5 predicted by RNAfold at 10℃ and 37℃. The areas circled in a(i) and a(ii) highlight the SD sequence and the start codon. The nucleotide colours reflect the base pair probabilities, as per the colour gradient shown.

Table 2: The RNAT sequences starting from the natural sequence to the final novel thermometer (T5), the 5 variants (V1-V5) and the controls. Red areas indicate the SD sequence and the start codon is shown in blue. The underlined nucleotides were added or modified. The triplet codons in green are the additions to the variants.

Thermometer Name	RNA sequence
T1	5' UUAAUUAUUAAAGGUAAUACACUAUGUCCGGUAAAAUGACUGGU 3'
T2	5' UUAAUUAAAAGGUAAUACACUAUGUCCGGUAAAAUGACUGGU 3'
T3	5' UUAAUUAAAAGGUAAUACACUAUGUCCGGUAAAAUGACUGGUCCUUUAA 3'
T4	5' UUAAUGUAAAAGGUAUAUACACUAUGUCCGGUAAAAUGACUGGUUCUUUAA 3'
T5	5' CUUAAUGUAAAAGGUAUAUACACUAUGUCCGGUAAAAUGACUGGUUCUUUAAAA 3'
V1	5' CUUAAUGUAAAAGGAAAUAUAUACACUAUGUCCGGUAAAAUGACUGGUUCUUUAAAA 3'
V2	5' CUUAAUGUAAAAGGAGGUAUAUACACUAUGUCCGGUAAAAUGACUGGUUCUUUAAAA 3'
V3	5' CUUAAUGUAAAAGGAAGUAUAUACACUAUGUCCGGUAAAAUGACUGGUUCUUUAAAA 3'
V4	5' CUUAAUGUAAAAGGAACUAUAUACACUAUGUCCGGUAAAAUGACUGGUUCUUUAAAA 3'
V5	5' CUUAAUGUAAAAGGAAAAAUUAUAUACACUAUGUCCGGUAAAAUGACUGGUUCUUUAAAA 3'
Negative control	5' CUUAAUGUAAAAGGUAUAUACACUAUGUCCGGUAAAAUGACUGGUCCUUUAAAA 3'
Positive control	5' UUAAUUAUUAAAGGUAAUACACUA 3'

Table 3: The thermodynamic data obtained from RNAfold for all 6 thermometer ensembles at 10℃ and 37℃

Thermometer Name	Free energy of the thermodynamic ensemble (kcal/mol)		Frequency of the MFE structure in the ensemble (%)		Ensemble diversity		Temperature threshold (℃)
Temperature (℃)	**10**	**37**	**10**	**37**	**10**	**37**	
T5	-8.87	-2.74	42.38	18.61	5.58	6.49	26
V1	-9.56	-3.02	50.83	22.30	5.01	7.08	25
V2	-9.88	-3.19	26.86	17.00	7.73	7.85	25
V3	-9.67	-3.06	39.12	21.07	7.22	7.24	25
V4	-9.33	-3.06	43.76	21.13	5.88	7.13	26
V5	-9.46	-2.94	50.83	15.79	5.19	7.69	32

Table 4: The forward (blue) and reverse (red) primers designed for the insertion of each thermometer into the plasmid via PCR

RNAT Name	Primer Name	Sequence	Length (Number of bases)	Melting Temperature (℃)
T5	F0	5' TCCGGTAAAATGACTGGTTCTTTAAAAATGGCTTCCTCC 3'	39	64.4
	R0	5' CATAGTGTATATACCTTTTACATTAAGACTAGTGCTAGCACAATACC 3'	47	61.5
V1	F1	5' ATGTCCGGTAAAATGACTGGTTCTTTAAAAATGGCTTCCT 3'	40	64.1
	R1	5' AGTGTATATATTTCCTTTTACATTAAGACTAGTGCTAGCACAAT 3'	44	60.4
V2	F2	5' GTCCGGTAAAATGACTGGTTCTTTAAAAATGGCTTCCTC 3'	39	63.7
	R2	5' ATAGTGTATATACCTCCTTTTACATTAAGACTAGTGCTAGCACA 3'	44	61.7
V3	F3	5' CTATGTCCGGTAAAATGACTGGTTCTTTAAAAATGGCTTCCTCC 3'	44	65.1
	R3	5' TGTATATACTTCCTTTTACATTAAGACTAGTGCTAGCACAATACC 3'	45	61.4
V4	F4	5' TGTCCGGTAAAATGACTGGTTCTTTAAAAATGGCTTCCTC 3'	40	64.4
	R4	5' TAGTGTATATAGTTCCTTTTACATTAAGACTAGTGCTAGCACAATA 3'	46	60.7
V5	F5	5' ATGTCCGGTAAAATGACTGGTTCTTTAAAAATGGCTTCCT 3'	40	64.1
	R5	5' AGTGTATATAATTTTTCCTTTTACATTAAGACTAGTGCTAGCACAA 3'	46	60.7

For each of the designs, at 37℃ the bases of the SD site bind to a complementary section of the same RNA strand further upstream, forming a double-stranded helix, leaving the SD sequence inaccessible to the ribosome and thus prevents translation. However, at 10℃, each design occupies an alternative structure in which the SD site has been released from the double strand, enabling the ribosome to access the sequence for translation. This is consistent with the structural behaviour of the natural cold shock RNAT in *E.coli.*

T5 and V1-V4, all correspond to a similar threshold temperature (25-26℃), demonstrating the addition of three bases to the SD hairpin loop will only increase the stability of the structure, the alteration neither improving nor hindering the thermometer functionality. Furthermore, the MFE profiles of V1-V4 are relatively close together, aligning between 20-25℃. This suggests that it is not the specific bases that affect the structure but the presence of the three extra bases in itself.

Whilst the results from RNAfold indicate that T5 and V1-V5, will operate as functional RNA thermometers, the programme only provides a prediction – thus it is not guaranteed that these results present the actual behaviour of the RNATs' in the natural *E.coli* system. RNAfold provides an understanding of structural stability in terms of the arrangement of bases, sequence length and constraint folding however, physiological factors (such as pH, enzymic activity and cellular interactions) must also be considered when evaluating the performance of the RNATs. Furthermore, RNAfold only provides a prediction of the MFE structure, however in an ensemble, sub-optimal conformations can occur. The likelihood of the MFE structure forming is predicted in table 3 but is not known precisely. Therefore, the structures must undergo further testing and analysis both *in vitro* and *in vivo*.

The primers designed in this study establishes the first step of this future testing phase, where the RNATs can be inserted into plasmids using PCR and transfected into bacterial cells for multiplication. Firstly, the functionality of the RNATs can be tested by observing the expression of the RFP1 under a microscope at chosen permissive and non-permissive temperatures. It is vital that results are compared with the positive and negative controls and 4-5 replicates are conducted. Secondly, the sensitivity of the thermometers to temperature change can be measured as well as the response time. Finally, chemical and enzymatic probing followed by point mutations can be utilised to visualise the configuration of the RNATs *in vivo*, and compare with the predicted structure. Upon the results of this experimentation, further improvements in the design can be made in terms of stability, allowing optimum efficiency of translational regulation and improved temperature sensitivity.

Additionally, another consideration factor is the presence of the AUG codon in the thermometer itself appearing before the start codon of the RFP1. As mentioned in section 4.5, this results in a chain of amino acids being formed before the actual polypeptide of the protein. Out of this short amino acid chain, only Lysine is positively charged and polar, and could potentially interfere with the formation of the secondary structure of the main polypeptide. Due to the short length and neutrality of the majority of the amino acids in this chain, it is highly unlikely that it could cause significant damage to the expression of RFP1, however this is a consideration that must be verified through laboratory experiments.

All of the designed thermometers operate within the range of 25-35℃, which is considered to be a feasible range in which low temperature protein expression is carried out. Despite the fact that proteins can be expressed at very low temperatures (below 15℃), where the stress cellular machinery would be activated and its natural cold shock response triggered, resulting in pathways and processes which could hinder the effectiveness of the thermometers. Furthermore, this temperature range is industrially relevant as translation at lower temperatures would require higher cooling and refrigerant costs. Therefore, having six thermometers that operate within this temperature range is the starting point for a cold shock RNAT toolbox. The RNATs (if proven to work as intended *in vivo*) were created to give the user the flexibility of choosing a thermometers for the expression of a specific protein, at a desired temperature. Upon modifications and research, more variants need to be created that operate around 20-25℃, which can be added to the library of cold shock thermometers.

The design of these novel thermometers sets the foundation for future designs of a library of cold shock RNATs for not only various bacterial species, but also in mammalian cells. The key difference between mammalian and bacterial RNA is the presence of a Kozak sequence (ACCAUGG) as opposed to the SD code being the site where the ribosome binds to (Li et al. (2017)). If this sequence can be incorporated into the novel cold shock thermometer in the place of the SD sequence, and verified experimentally, it would be possible to conduct low temperature protein expression in mammalian cells. This would have wide applications in the fields of biomedicine and gene therapy.

6 Conclusion

A novel cold shock RNA thermometer and five variations were successfully created *in silico* using RNAfold, deriving simple thermo-regulators from the utilisation of the natural cspA cold shock RNAT. Each design adopts the switch mechanism, exposing the SD sequence at low temperatures and concealing it in a double strand as the temperature increases. These RNATs have a threshold temperature within a range of 25-32℃, providing a wide range of viability of the thermometers. This allows the RNATs to be used as a template and tailored to fit the protein to be translated, whilst still achieving expression at the desired temperature. These synthetic cold shock RNATs provide a modular and minimum sized alternative to current low

temperature protein synthesis methods. It also offers the advantage of being the only thermo-regulatory expression system in cells that is controlled entirely by the action of RNA, without requiring the involvement of other molecules.

Future developments on this study could lead to the creation of a genetic toolbox for multiple organisms, providing a library of cold shock responding RNA thermometers with different sensitivities to effectively regulate gene expression. This will allow the temperature controlled translation of vital proteins to obtain precise conformations; highly useful in biotechnological, gene therapy and research applications.

References

Andronescu, M., Condon, A., Hoos, H., Mathews, D. & Murphy, K. (2010), 'Computational approaches for rna energy parameter estimation.', *Bioinformatics* **16**(12), 2304–2318.

Bjerga, G. E. K., Lale, R. & Williamson, A. L. (2016), 'Engineering low-temperature expression systems for heterologous production of cold-adapted enzymes.', *Bioengineered* **7**(1), 33–38.

Bjerga, G. E. K. & Williamson, A. L. (2015), 'Cold shock induction of recombinant arctic environmental genes.', *BMC Biotechnology* **15**(78).

Bock, R., K. D. . N. J. (2008), 'Design of simple synthetic rna thermometers for temperature-controlled gene expression in escherichia coli', *Nucleic Acids Research* **6**.

Briand, L., Marcion, G., A. Kriznik, A., Heydel, J., Artur, Y., Garrido, C., Seigneuric, R. & Neiers, F. (2016), 'A self-inducible heterologous protein expression system in escherichia coli', *Scientific Reports* **6**.

Brierley, I., Pennell, S. & Gilbert, R. (2007), 'Viral rna pseudoknots: versatile motifs in gene expression and replication', *Nature Reviews Microbiology* **5**.

Choi, D., Oh, H. J., Goh, C. J., Lee, K. & Hahn, Y. (2015), 'Heat shock rna 1, known as a eukaryotic temperature-sensing noncoding rna, is of bacterial origin', *Microbiol Biotechnol* .

Chung, B. Y. W., Balcerowicz, M., Antonio, M. D., Jaeger, K. E., Feng Geng, F., Franaszek, K., Marriott, P., Brierley, I., Firth, A. E. & Wigge, P. A. (2020), 'An rna thermoswitch regulates daytime growth in arabidopsis', *Nature Plants* .

Eddy, S. R. (2004), 'How do rna folding algorithms work?', *Nature Biotechnology* **22**(11).

EMBL, E. (2020), 'Protein expression e. coli - improving protein solubility.'.
URL: *https://www.embl.de/pepcore/pepcore_// services/protein_expression/ecoli/improving_protein// _solubility/index.html*

Fakruddin, M., Mazumdar, R. M., Mannan, K. S. B., Chowdhury, A. & Hossain, M. N. (2013), 'Critical factors affecting the success of cloning, expression, and mass production of enzymes by recombinant e.coli', *Biotechnology* .

Giuliodori, A. M., Pietro, F. D., Marzi, S., Masquida, B., Wagner, R., Romby, P., Gualerzi, C. O. & Pon, C. L. (2010), 'The cspa mrna is a thermosensor that modulates translation of the cold-shock protein cspa', *Molecular Cell* pp. 21–33.

Kortmann, J. & Narberhaus, F. (2012), 'Bacterial rna thermometers: molecular zippers and switches', *Nature Reviews Microbiology* .

Li, J., Liang, Q., Song, W. & Marchisio, M. A. (2017), 'Nucleotides upstream of the kozak sequence strongly influence gene expression in the yeast s. cerevisiae', *Journal of Biological Engineering* **11**(25).

Miyake, R., Kawamoto, J., Wei, Y.-L., Kitagawa, M., Kato, I., Kurihara, T. & Esaki, N. (2007), 'Construction of a low-temperature protein expression system using a cold-adapted bacterium, shewanella sp. strain ac10, as the host', *Applied and Environmental Microbiology* **73**(15), 4849–4856.

Neupert, J. & Bock, R. (2009), 'Designing and using synthetic rna thermometers for temperature-controlled gene expression in bacteria', *Nature Protocols* **36**(19), 1262–1273.

NewEnglandBioLabs (2020), 'Cell-free protein expression'.
URL: *https://international.neb.com/applications/protein-expression/cell-free-protein-expression*

Phadtare, S. & Severinov, K. (2010), 'Rna remodeling and gene regulation by cold shock proteins', *Landes Bioscience* .

Sen, S., Apurva, D., Satija, R. & Siegal, D. (2017), 'Design of a toolbox of rna thermometers', *American Chemical Society* **6**(8).

Somero, G. N. (2018), 'Rna thermosensors: how might animals exploit their regulatory potential?', *Journal of Experimental Biology* **221**.

Vasina, J. & Baneyx, F. (1996), 'Recombinant protein expression at low temperatures under the transcriptional control of the major escherichia coli cold shock promoter cspa', *Applied and environmental microbiology* **62**(4), 1444–1447.

Waldminghaus, T., Kortmann, J., Gesing, S. & Narberhaus, F. (2008), 'Generation of synthetic rna-based thermosensors', *Biological chemistry* **389**(10), 1319–1326.

Yamanaka, K., Mitta, M. & Masayori, I. (1999), 'Mutation analysis of the 5' untranslated region of the cold shock cspa mrna of escherichia coli', *Journal of Bacteriology* **181**(20), 6284–6291.

Synthesis and Optimisation of Novel Corn Starch Superhydrophobic $CaCO_3$ Films

Dhylan Mistry & Shav Vimalendiran

Department of Chemical Engineering, Imperial College London

Abstract

Nature is an inexhaustible source of inspiration; non-wetting lotus leaves have sparked considerable interest in the scientific community over the past decades. Superhydrophobic films have a wide range of industrial applications, but it is equally as important to mitigate environmental damage whenever pursuing these applications. Herein, we report the preparation of superhydrophobic composite coatings with an eco-friendly technique. The possibility of removing harmful solvents and non-bioderived polymers are investigated using precipitated calcium carbonate as the substrate (which can also be derived from eggshells), stearic acid as the surface modifying agent and corn starch as the binder. Following characterisation, the novel films show promising mechanical and superhydrophobic properties. An optimised formulation using corn starch with 50%w/w hydrophobic powder and 5.5%w/w stearic acid is presented as a statistically significant replacement for polyethylene/toluene films in terms of practical durability as well as superhydrophobicity (contact angle of 154.8° ± 4.7 ° vs 151.7 ° ± 1.5 ° for polyethylene/toluene and optimised formulation respectively).

I. Introduction

The origins of superhydrophobicity research are traced to Ollivier (1907) where perfect sphere beads of water were observed on toxic arsenic trioxide and soot surfaces. Hydrophobicity arises on a surface from a lack of attractive forces causing water to 'repel' off the surface (Chandler (2005)).The self cleaning and superhydrophobic 'lotus effect' has fascinated researchers; research in the area has been re-energised by the discovery that **low surface energy** from epicuticle wax crystals as well as **surface roughness** from papillae are fundamental to the phenomena. The growth in interest is also spurred by its applications particularly in acid- rain building protection, self-cleaning surfaces and rust protection (Latthe et al. (2019),Barati Darband et al. (2020)).

It is understood that low surface energy causes water droplets to bead up and potentially roll off. If the surface energy is high, water will spread out on the surface (e.g. glass) due to favourable interactions. The degree of hydrophobicity is characterised by the Water Contact Angle (WCA). An angle above 90° is hydrophobic and above 150° is superhydrophobic (Barati Darband et al. (2020),Bayer (2020)).

To minimise surface energy, silanated compounds, particularly fluoroalkylsilanes, gain the most attention due to the greatest minimisation in surface energy. Despite being very effective, their high cost and toxicity to the environment has incentivised researchers to seek alternatives. Hence, it was discovered that the roughened metallic surface of $CaCO_3$ develops superhydrophobicity when functionalised with surfactants (Demjén et al. (1997)). Fatty acids have been utilised due to commercial availability and reduced toxicity to the environment (Sheng et al. (2006),Hu & Deng (2010), Cao et al. (2016)).The carboxylic acid head (hydrophilic) chemisorbs onto the $CaCO_3$ surface seen in Figure 1, with the aliphatic tail orientated to provide surface hydrophobicity as well as physisorption from multiple layers of fatty acid (Kokkinis (2017)).

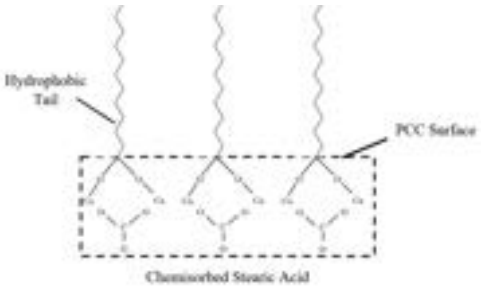

Figure 1: *Monolayer chemisorbed fatty acid functionalised $CaCO_3$*

To form a monolayer, ball milling, pestle and mortar milling as well as wet methods such as a hot aqueous slurry have been used (Cao et al. (2016),DeArmitt & Hancock (2003)). Pestle and mortar dry milling was used in this project due to simplicity, no solvent and restricted access to laboratory equipment for ball milling.

Stearic acid and Oleic acid, derived from sources such as cocoa butter and olives respectively, have been used as eco-surfactants and yielded successful SHP[1] using the mechanochemistry technique rather than the wasteful solvent approach (Deepika et al. (2013)). Stearic acid is one of the

[1]Superhydrophobic Powder

most suitable surfactants for calcium carbonate as it provides maximum surface coverage (Gilbert et al. (2001)). The powder was further optimised from hydrophobic to superhydrophobic with 2%w/w stearic acid (Shah & Ng (2016).). Superhydrophobicity can also be attributed to the hierarchical structure of $CaCO_3$ that provides surface roughness as seen by SEM imaging (Zhang et al. (2011)). The source of calcium carbonate has evolved from limestone and now can be derived from natural waste products such as eggshells (Seeharaj et al. (2019)), and seashells (Fang (2019)) enhancing sustainability.

Besides the superhydrophobicity of the powder, there was an additional challenge of producing a sustainable paint (binder solution) so that a homogeneous coating can be practically applied. Due to environmental concerns, starch has received a lot of attention; as a natural biodegradable biopolymer, it is a promising candidate to replace the petroleum-derived materials currently in use. Starch already boasts a wide range of uses in industry - it is used in cosmetics, textiles, pharmaceuticals and fuels amongst others (Kaur et al. (2012)). Amongst the candidates for petroleum replacement, starch is one of the most encouraging due to its diversity, film forming properties, availability, cost-effectiveness, and ease of handling (Dufresne & Castaño (2016), Cao et al. (2008)).

Starch has been obtained from various botanical sources; as a consequence of its numerous sources, starch itself is a diverse polymer with different shapes, sizes, structures and chemical properties (Smith (2001)). Starch contains two macro molecules: amylose (linear) and amylopectin (branched), with varying compositions allowing diverse physico-chemical properties of starch-based films. Corn Starch (Zea mays L.) was sourced with 28% w/w amylose content and a gelatinisation temperature of above 59.7 °C (Luchese et al. (2017)). Gelatinisation was essential to mitigate issues with cracking, hygroscopicity and non-continuous/inconsistent film formation (ZOBEL (1984)). Corn Starch was chosen as a starting point due to its low-cost and relatively high amylose content contributing to improved film flexibility, continuity and strength that occurs on cooling after gelatinisation (And & Han (2005)).

Starch repeating units feature three free OH groups on each glycoside ring, making the molecule strongly hydrophilic. The OH groups make starch a promising binder due to H bonding with glass. Despite improving the binding ability, various starch hydrophobic functionalisation processes were reviewed to counteract the inherent hydrophilicity which reduces the hydrophobicity of the coating (Wang et al. (2020)). Jiang et al. (2016) demonstrated short-chain amylose starch modification in ethanol solution using 2-Octen-1-yl Succinic Anhydride (OSA) to produce amphiphilic OSA-starch-nanoparticles (OSA-SNP's). The hydrophobicity of OSA-SNP's increased with the degree of substitution as the OH groups on starch molecules were replaced by hydrophobic OSA groups. Yu et al. (2019) formulated OSA-SNP powders which were pressed to obtain tablets; the starch modification had little effect on the particle size or morphology of starch, but increased the contact angle significantly, from 25.4° to 70.1°. The amphipathicity of modified starch polymers would increase the hydrophobicity of films over those that retained OH groups e.g. unmodified corn starch. The OSA-Corn starch films were created using a modified method as described by Shi & He (2012).

The addition of inorganic tetraethylorthosilicate (TEOS) can also improve hydrophobicity of starch based-films (Lima et al. (2017)) by the synergism of the components to form a starch-inorganic hybrid material. An adapted procedure was undertaken to prepare films by dip-coating with hydrolysis and condensation of TEOS in situ under a controlled pH, as demonstrated by Lima et al. (2017).

Water molecules can also act as a plasticiser for hydrophilic polymers. Wang et al. (2011) demonstrated how the addition of silica nanoparticles at 10% w/w corn starch not only increased shear strengths of starch-based binder but also increased the water resistance by 20.2%, something invaluable for industrial applications in humid environments. Starch films incorporating silica nanoparticles were also investigated.

Producing superhydrophobic coatings that not only have a high WCA but are more sustainable is still a trending topic. (Bayer (2020)). This year, water based PVA films have been produced (Gong et al. (2020)) with 160° WCA as well as nano-$CacO_3$ films using Ethanol as a solvent but with 107° WCA. (Syafiq et al. (2020)). There is limited research into using corn starch to develop superhydrophobic coatings. A recent superhydrophobic starch coating developed used expensive 80% amylose corn starch , PDMS, Montmorillonite and a multi-step application process involving spraying/curing(Chen et al. (2020)). Other superhydrophobic coatings developed utilise the developed SHP from $CaCO_3$ but use plastics such as Polyethylene and Polystyrene with a toluene solvent (Shah & Ng (2016)). Hence, there is a clear opportunity to combine the promising SHP with corn starch to produce superhydrophobic films.

i. Objectives

This project aims to investigate the feasibility of replacing the most recently optimised superhydrophobic coating using PE and Toluene (Fang (2019)) with starch to produce a stable, homogenous film thus reducing harmful solvents and plastics in the environment. Various starch coatings will be produced in order to optimise the formulation. The efficacy of hydrophobic starches (see introduction) will be explored and quantified. The proposed coating must be able to be dried at ambient conditions and be applied simply by dip-coating. The hydrophobic characteristics and durability of developed formulations will be compared and contrasted to the current formulation.

ii. Theory of Wetting Phenomena

Water contact angle (CA) is defined by the intersection of the three-phase boundary between solid, liquid and vapour. This is commonly described using Young's equation:

$$\gamma_{sv} = \gamma_{sl} + \gamma_{lv} cos\theta_i \quad (1)$$

Here, γ_{sv}, γ_{sl} and γ_{lv} denote the surface tensions of solid-vapour, solid liquid and liquid vapor respectively. θ_i denotes the 'equilibrium' CA on an *ideal* surface i.e. one that is smooth, inert, homogeneous and nonporous. Wenzel (1936) proposed an expression for the apparent equilibrium CA θ_w to account for surface roughness, as a function of roughness factor r_f

$$cos\theta_w = r_f cos\theta_i \quad (2)$$

This is valid when there is no gas trapped in between the droplet and crevices of the surface. When gas is trapped, the Cassie and Baxter model is used:

$$cos\theta_c = \sigma(1 + cos\theta_i) - 1 \quad (3)$$

Here the apparent CA (θ_c) is a function of the relative fractional area of solid in contact with air, σ, and θ_i (Cassie & Baxter (1944)). In this model, the more air trapped between the liquid-solid interface, the higher the contact angle.

However, static contact angle measurements alone aren't sufficient to fully characterise a surface as using the average static CA neglects the irregularities of a real surface. One static, metastable CA only designates an angle within the range of contact angles possible between the advancing, θ_A, and receding, θ_R, contact angles; reporting the dynamic contact angles are therefore important criteria to further characterize the hydrophobicity of our film surfaces (Gao & Mccarthy (2006)). Hysteresis is the term used to describe this range between advancing and receding contact angles; it originates from and can indicate the properties that cause a surface to differ from the ideal, such as surface inhomogeneity and roughness.

II. Method & Materials

i. Materials

Precipitated $CaCO_3$(PCC): Fisher Scientific (minimum assay 98%) containing calcite polymorph. **Stearic Acid:** $C_{17}H_{35}COOH$ from BDH Chemicals Ltd. as a GPR with a solubility of 0.57mg/l at 25°C Yalkowsky (2010). **DI Water:** used in all experiments. **Ethanol:** C_2H_5OH absolute (99.97% minimum assay) from VWR chemicals. Second most widely used industrial solvent due to lower toxicity than other alcohols and possibility for bio-derivation. **Toluene:** C_7H_8 as ACS reagent from VWR Chemicals (minimum assay 99.9%). Extremely flammable with a flashpoint of 4.4°C. **Corn Starch:** $(C_6H_{10}O_5)_n$ from Sainsbury's. Formula is the repeat unit for the α 1,4 linkages. **PE:** $(C_2H_4)_n$ as ACS reagent from BDH ltd. UK. **TEOS:** from Sigma-Aldrich (minimum assay 99%). **Hydrophobic fumed silica:** 'Aerosil ®R 972 treated with DDS' from Evonik, Germany. BET Surface Area of 90-130 m^2/g with d_p=16-20nm. **OSA:** (2-Octen-1-ylsuccinic anhydride) from Sigma-Aldrich (minimum assay 97%). **NaOH** ACS reagent from VWR Chemicals (minimum assay 99.6%). Utilised for pH adjustment in both TEOS (Lima et al. (2017)) and OSA (Shi & He (2012)) procedures.

ii. Formulation Methodology

Key	Formulation
A	PE+Toluene
B	5g Starch
Bb	5g starch,Drying at 60 °C, 700mBar
C	5g starch/0.286g silica
D	5g Starch/2gTEOS
E	5g OMS Powder

Table 1: *Formulation naming key. '**A-40-2.5**' for example corresponds to formulation A with 40%w/w hydrophobic powder and 2.5%w/w stearic acid.*

Functionalised Powder: prepared by addition of desired PCC:SA to a stainless steel pestle and mortar and milled for 10 mins to form hydrophobic powder (Fang (2019)).
Octenyl Modified Starch (OMS) Powder: 20g corn starch was suspended in 100ml of DI water, pH adjusted via addition of 3%w/w NaOH and stirred (MS-H280-Pro stirrer) at 25 °C for 10 mins. 3ml of OSA was diluted in 1:5 OSA to Ethanol mixture and mixed at 35 °C for 2 hrs. The mixture was filtered using 'Whatman ®Grade 1 (11 μm) filter paper and washed with 500ml distilled water. The residue was placed into glass petri dishes, dried in a vacuum oven at 60 °C, 700mbar for 24 hr and then shattered into powder. (Shi & He (2012), Song et al. (2010))
Paint formulations: Followed 2-step method presented by Tzouganatos (2015). This involved binder solution preparation followed by addition of hydrophobic powder. All formulated paints were dip coated onto Glass Microscopic Slides (1.0mm thick, 25mm x 75mm) to produce 4 samples. All samples, unless otherwise stated, were dried at ambient conditions in the fume-cupboard for 72 hrs.

A: 2%w/v of PE was dispersed in Toluene and heated under reflux at 90°C for 20 minutes. 40%w/w of 2.5% w/w SA functionalised powder was added and mixed for a further 25 minutes at 90°C.

B: 5 g of corn starch dispersed in 100ml 1:1 Ethanol:DI Water was covered with parafilm to avoid solvent loss and mixed at 70 °C for 20 minutes to achieve starch gelatinisation

(Ghasemlou et al. (2013), Fisher & Thompson (1997)). Temperature was maintained by both a thermometer as well as a temperature probe from the stirrer. Hydrophobic powder was rapidly added, recovered with parafilm and stirrer speed increased to mix for 5 minutes. **Bb** was an exception and had controlled drying (see table 1). **Adaptations for C and E** were 0.286g of nano-silica addition for C added with the 5g of cornstarch, and for E 5g of OMS replaced 5g of corn starch.

D: 5g of corn starch was dispersed in the same way as B for 20 minutes. The filmogenic solution was cooled to 40°C followed by a pH adjustment to 9 with NaOH. The pH was verified with 'Fisherbrand ®pH indicator sticks' and immediately followed by the slow addition of 2ml TEOS by syringe. The mixture was mixed for 1 hour at 40°C and the functionalised powder rapidly added. The mixture was left to mix for a further 10 minutes.

iii. Contact Angle Characterisation Methodology

Quantitative characterization of surface wettability was carried out through static CA measurement as well as sessile-droplet method for Hysteresis. Measurements were performed digitally on a ramé-hart advanced goniometer (590-u1). Accurate droplet volume dispensing was achieved using a ramé-hart Automated Dispensing System (100-22).

The dip-coated slides were placed onto the projection stage with sufficient backlight and the steel needle dropper was adjusted and focused in the frame before the stage was analysed using DROPimage Advanced software. For static CA measurements, a 10 μL droplet of DI water was placed on the surface and 100 measurements with a time interval of 0.01s were taken from the side profile. Measurements on each slide were performed in three locations to test surface homogeneity, and repeated for 2 separate slides to indicate reproducibility of the dip-coating method.

For the Sessile-droplet method, the needle was used to slowly dispense a droplet of 20 μL volume and inserted 2/3 into the centre of the droplet. The dispensed/withdrawn volume as a function of time can be described by a sawtooth function of amplitude $\pm 10\mu L$ and a period of 10s.[2] Changes in volume as well as measurements both took place at 0.25s intervals, and each reading was run for 25s to allow for two complete cycles to occur. Images were also taken at 0.25s intervals to qualitatively analyse results alongside measurements. This method was chosen to ensure that the droplet had a sufficient volume to obtain a volume-independent measurement of θ_A while minimising the effect of distortion of the droplet (and thereby the observed CA) due to the needle (Eral et al. (2012)). Dilated droplets formed the advancing CA, while contracted droplets should reach the receding angle. The sessile-drop method required many repeats of experiments on different locations to properly characterize the entire surface (Eral et al. (2012)). For this reason, we again collected hysteresis measurements in triplicate on 2 separate slides.

A python script was used to fit a polynomial of degree 6 to the hysteresis measurements and not any higher to avoid overfitting. For films with more variance, it was important to avoid a higher degree which accommodated outliers hence skewing the intrinsic property, θ_A, that was being determined. This degree was chosen by visually determining if overfitting was occurring. In Figure 2, the sharp troughs which are characteristic of pinning [3] witnessed while using this method are visible. Nonetheless, this data was used for θ_A plateaus.

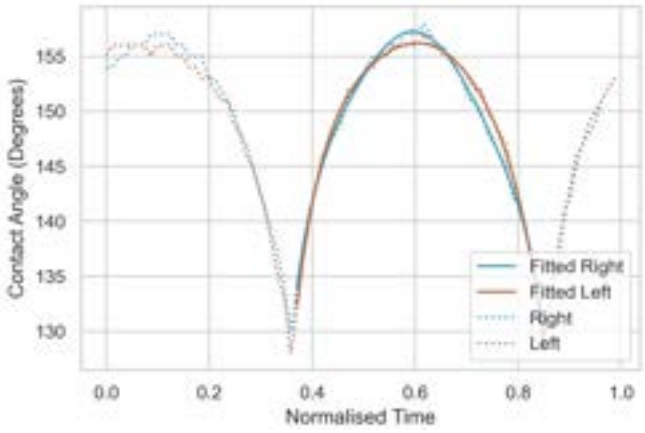

Figure 2: *B-50-5.5 slide hysteresis experiment showing Polynomial fitting*

iv. Statistical Analysis Methodology

The coefficient of determination (R^2) measured the fraction of the total variation in Y that is captured by the model. R^2 values were calculated to provide a quantitative measure of the polynomial's fit to the hysteresis data. In addition, the mean and standard deviation (SD) of static and advancing CA's were reported for each formulation. Comparison of the means amongst formulations were performed by one-way analysis of variance (ANOVA). ANOVA was used to evaluate whether there was any statistical evidence that the means of the sets of data differ using the F-distribution; therefore, the null hypothesis for this test was that all means were equal ($H_0 : \mu_A = \mu_B = ...$). During ANOVA, F-testing was conducted to test the underlying assumption of homoscedasticity as a preliminary step. If F > F crit the null hypothesis was rejected and at least one of the means is statistically different'. This 'omnibus' testing (assuming a significant result) was followed up by multiple pair-wise

[2] A sin-wave was not used in order to ensure that any observed plateaus (θ_A & θ_R) were a property of the droplet on the surface and not of the dispensing volume function.

[3] this phenomenon is explained further in the Results Section

category t-tests. The p-value was calculated to ascertain if there was a significant difference between specific individual groups. Statistical analysis between groups was primarily carried out on θ_A values as to not involve the uncertainty that is inherent from a metastable static droplet .

Non-paired, two-sample unequal/equal variance (depending on the result of an initial F-test) t-testing was then performed between slides within the *same* formulation to investigate the reproducibility of the dip-coating method. Factors that could affect these results include dipping speed, withdrawal speed, dipping angle etc.

The null hypothesis here was that the two population's of contact angles were the same ($H_0 : \mu_1 = \mu_2$). The Alternative H_1 was that they were different due to non-reproducibility of the dip coating method. The inherent bias of slide selection was mitigated in-lab by choosing random slides for analysis. If the p-value was found to be above the significance level $\alpha = 0.05$, the null hypothesis was not rejected and there was not sufficient evidence to conclude non-reproducibility via dip-coating and the variance of angles that were measured in data occurred by chance or some other factor.

v. Durability Testing Methodology

'DVS Advantage' was used for **DVS testing** to determine the hygroscopicity of the coatings. 50mg of the optimised formulation samples were used due to their hydrophobic nature. A step change from 0% RH to 90% RH was used and ran for 750 mins to determine percentage change in mass.

During **immersion testing** 2 slides of each formulation were placed into DI water in separate beakers. At 10 minute intervals up to 1 hour, the slides were taken out, dried with compressed nitrogen and static WCA recorded in triplicate.

Figure 3: *Stirrer causing surface mechanical abrasion*

The qualitative **mechanical abrasion method** tested physical robustness of prepared coatings on the glass substrate. The rotation speed of a 2cm stirrer bead was kept constant at 150rpm and the time for glass to be first seen recorded, as in Figure 3. This was repeated for 2 slides and the average determined. A 'Veho VMS-004 microscope camera' capable of 20-400x magnification was used to take images of the area of abrasion.

The **outdoor test** aimed to investigate the change in film characteristics due to rain droplets and higher RH than indoors (Syafiq et al. (2020)). 2 slides of each formulation had their static WCA measured before being placed outside on the window sill in SW7. Temperature and RH were monitored from BBC Weather for 5 days and the static WCA measured after being blown dry with compressed N_2.

III. Results & Discussion

i. Static WCA and Observations

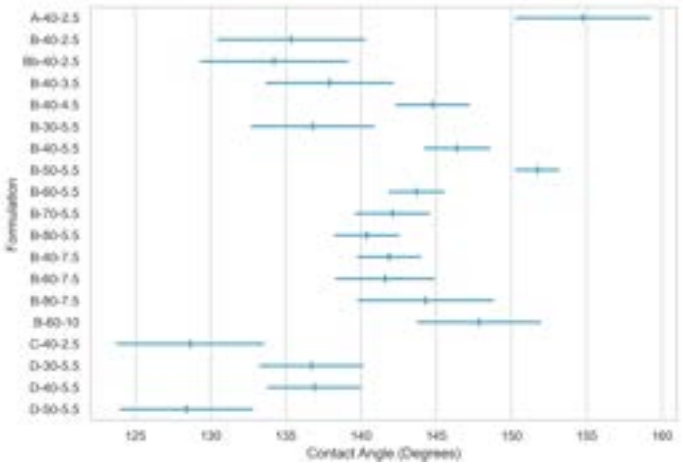

Figure 4: *Static WCA plot for produced formulations presenting mean & standard deviation. Films that exhibited absorption are omitted.*

Figure 4 presents a global view of collected static WCA's; from here it can be concluded that B-50-5.5 is the optimal formulation being statistically higher than all other starch based formulations (bar B-60-10 which exhibited inhomogeneous, powdery and unacceptable film properties). B-50-5.5 overlapped with A-40-2.5, showing comparable static water contact angles.

Figure 5: *Side by side comparison of A-40-2.5(left) B-50-5.5(right)*

Observations worth noting here were the failure of attempted starch modifications. It was hypothesised that OMS produced a more hydrophobic film (Jiang et al. (2016)) but exploratory experiments yielded observations of cracking and non-continuous film formation. It is postulated that the increased hydrophobicity of the particles interfered with the gelatinisation process of starch and therefore prohibited optimal dispersion of the OMS in 1:1 DI Water to Ethanol mixture. OMS was not able to be characterised as droplets were absorbed into the surface. TEOS films on the other hand showed improved film forming ability. However, TEOS and the other starch-inorganic hybrid nano-silica (Formulation C), exhibited sub-par hydrophobicity. It is possible that these inorganic silica particles, whether formed from TEOS (Lima et al. (2017)) in D or from silica nanoparticles in C interfered

Figure 6: *Bb-40-2.5 image at 25X magnification*

with the binding action of starch. 'Bb-40-2.5' was investigated to determine influence of drying rate on WCA. As seen in figure 4 there was a 1.5° reduction in static CA compared to the vacuum cupboard dried B-40-2.5 and crack formation was observed due to the increased drying rate as in Figure 6.

ii. Optimisation of Formulation B

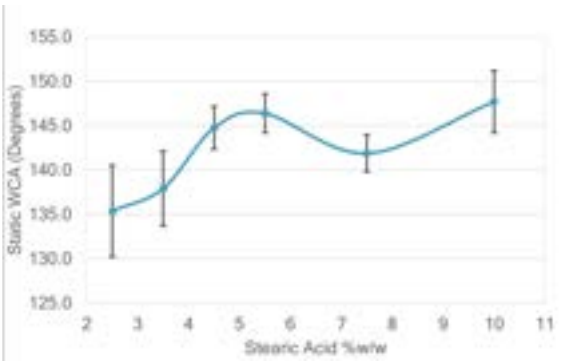

Figure 7: *The effect of increasing stearic acid %w/w for 40% w/w hydrophobic powder of formulation B*

As hydrophobic stearic acid (SA) %w/w was increased, a local maximum was observed; figure 7 shows that for 40% w/w SHP, the optimum stearic acid addition content in calcium carbonate was 5.5 % w/w with a water CA of 146.4° $\pm$ 2.2°. Beyond the optimum, the film became excessively powdery due to physisorbed SA SHP on the calcite surface resulting in a fluctuating WCA with a high SD. Therefore, the optimum was determined at 5.5%w/w to align with the objective of producing a homogeneous and continuous film. Pure stearic acid has a CA of 120° so it is expected that further increase in SA content will lead to a drop in CA.

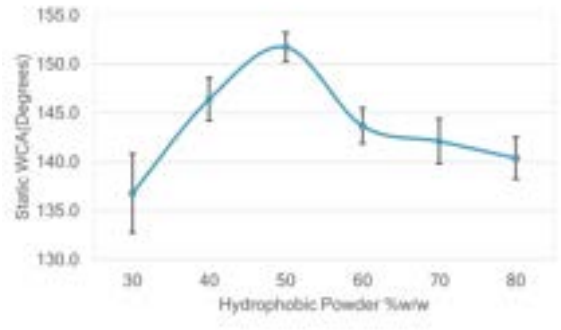

Figure 8: *The effect of increasing hydrophobic powder content for 5.5%w/w stearic acid of formulation B*

Figure 8 shows that for a SA weight % of 5.5, the optimum addition of SHP was 50%w/w with a WCA of 151.7 ° $\pm$ 1.5. Increasing SHP content improved hydrophobicity and viscosity for adhesion during dip coating. However, there was a compromise; as the binding solvent became more saturated there was a corresponding increase in in-homogenous film formation which featured pockets of non-bound powder. An optimum was therefore chosen to avoid this.

iii. Receding Contact Angle

Measuring θ_R using the sessile drop method led to considerable difficulty due to the rough surface topography of the samples. The droplet did not recede when water was withdrawn via the needle as the contact line remained pinned. This was ascribed to the local defect mechanism (Hong et al. (2011)); the presence of local defects that were considerably more wettable than the rest of the surface. Instead of receding, the withdrawal of the water caused a change of the droplet shape from a spherical cap to a conical one as demonstrated by figure 9. This effect was enhanced through the adhesion of water to the hydrophilic steel needle.

When even more water was withdrawn, the water snapped away from the needle. This indicated that the adhesion between the water and the films being analysed was higher than the cohesion between water molecules. Due to these reasons, θ_R could not be measured on any of our samples using this method.

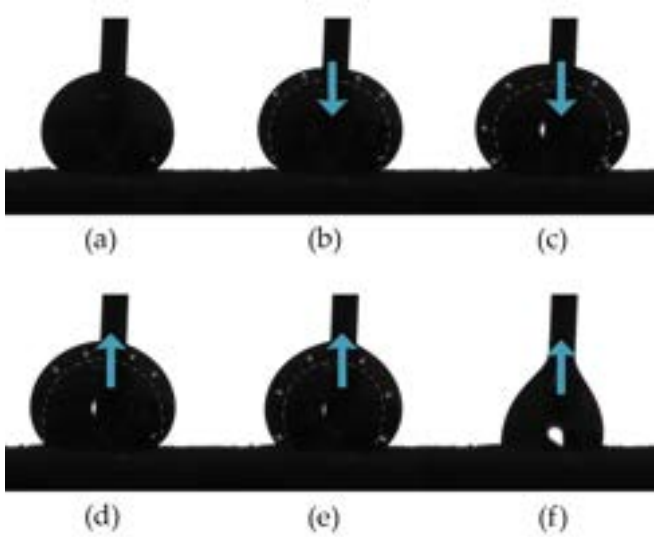

Figure 9: *Photograph sequence showing the sessile-droplet method with receding contact line pinning on a formulation C slide*[4]*: (a) The initial droplet volume (20μL); (b) Volume dispense increment before contact line advancement; (c) contact-line advancement due to volume increments dispensed into droplet; (d) reduction in droplet volume before droplet starts receding (with a pinned contact line); (e) A suction increment showing a receding contact line; (f) Further reduction in volume with a pinned contact line on slide surface showing the conical-esque shape.*

[4]Formulation C was chosen for figure 2 as the transition to a conical shape was more apparent and extreme on this film

iv. Statistical Analysis of θ_A

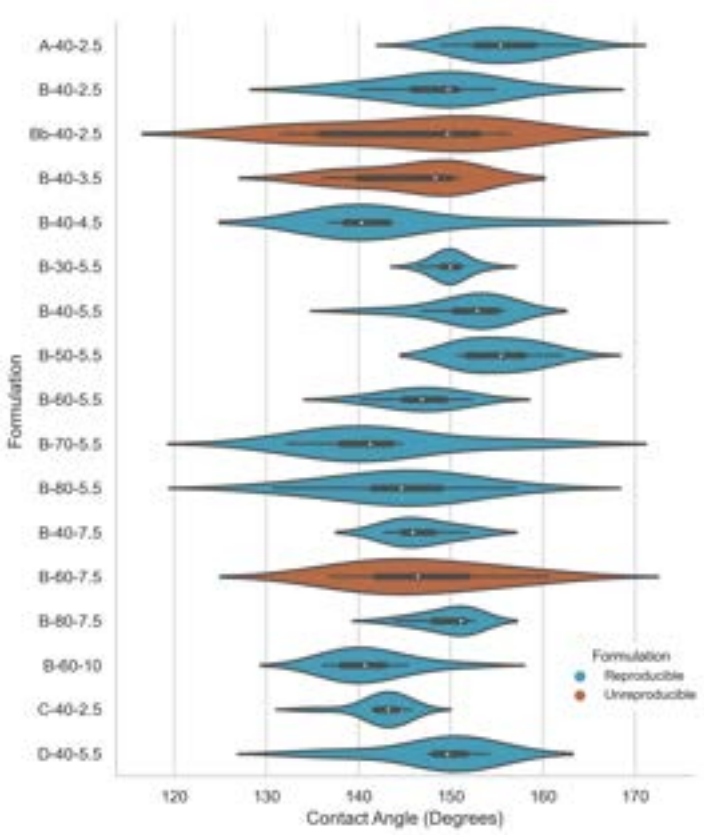

Figure 10: *Violin plot of θ_A for each formulation alongside box and whisker plots. Violin shape is a kernel density estimation of the underlying θ_A distribution.*

Figure 10 depicts the advancing contact angle measurements, which were all achieved with well fitting polynomials with a mean R^2 value of 0.99 from all experiments, indicating excellent goodness-of-fit.

During intra-formulation slide-to-slide analysis of θ_A, a P value of x can be understood as an x% likelihood that the difference in means was due to random chance. Conventionally, a P value $< \alpha = 0.05$ is significant in which case we rejected the null hypothesis, $H_0 : \mu_1 = \mu_2$. If the P value was greater than 0.05, we do not reject the null hypothesis and concluded no statistical significant difference between the two slides.

The only formulations that exhibited statistically significant differences between slides within the 95% confidence interval were Bb-40-2.5, B-40-3.5 & B-60-7.5 as shown in Figure 10 as 'unreproducible'. For the remaining formulations, it can be assumed that dip coating played an insignificant role in variance. Data can be safely grouped together and analysed as the remaining possible causes of formulation variance are chance and surface in-homogeneity. The interquartile range (IQR) for each formulations is presented in figure 10 and is an indicator of surface homogeneity for each film, with outliers accounted for. It was concluded that all reproducible films showed comparable surface homogeneity, attesting to the viability of a starch superhydrophobic films.

The null hypothesis *between* the starch-based film formulations was that of identical means ($H_0 : \mu_A = \mu_B = \mu_C = ...$). ANOVA was carried out on all starch-based films. With a calculated F-statistic and F crit of $4.560159 > 1.699042$ respectively, the null hypothesis was rejected and it was concluded that at least one of the formulations exhibited statistical difference. Since this was simply an 'omnibus' test, further t-testing was performed to investigate pair-wise statistical differences between formulations; namely B-50-5.5. B-50-5.5 was statistically different when compared to B-40-5.5 with a 95% likelihood, and statistically different to all other formulations with at *least* a 99.5% liklihood. B-50-5.5, the optimised formulation, therefore features statistically superior θ_A's to the other starch formulations.

Conversely, with a p-value of $0.6695104 > 0.05$, the null hypothesis $H_0 : \mu_{B-50-5.5} = \mu_{A-40-2.5}$ could not have been rejected. The measured θ_A's for B-50-5.5 and A-40-2.5 were *not* statistically different. This leads again to the conclusion that starch at 5.5% w/w SA and 50% w/w functionalised powder is a viable replacement for toluene and PE as presented by Khoo & Lim (2017). The films exhibited comparable super hydrophobic contact angles and surface homogeneities (IQR's) as shown in figure 10.

v. Durability Characterisation

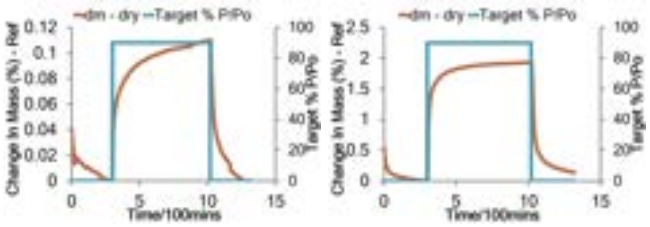

(a) *A-40-2.5* **(b)** *B-50-5.5*

Figure 11: *DVS Advance traces taken at 24.7 °C*

DVS experiments were completed allowing sufficient time for plateaus at 90% RH. It has been concluded that 'B-50-5.5' is 17.5x more hygroscopic than 'A-40-2.5'. It was promising however that 'B-50-5.5' is 8x less hygroscopic than native corn starch. The higher hygroscopicity is due to the inherent hydrophilicity of the hydroxyl groups on starch polymers. Smaller step changes can be used to determine a potential type ii isotherm (Rajabnezhad et al. (2020)).

Immersion tests studied the formulation's hydrophobic durability while the slides were in prolonged contact with water. From visual observations, upon immersion the surface became reflective (Figure 12) as a result of a pinned air layer,

characteristic of a superhydrophobic coating in the Cassie Baxter regime, as mentioned. When slides were removed, the surface appeared dry regardless of drying with compressed N_2.

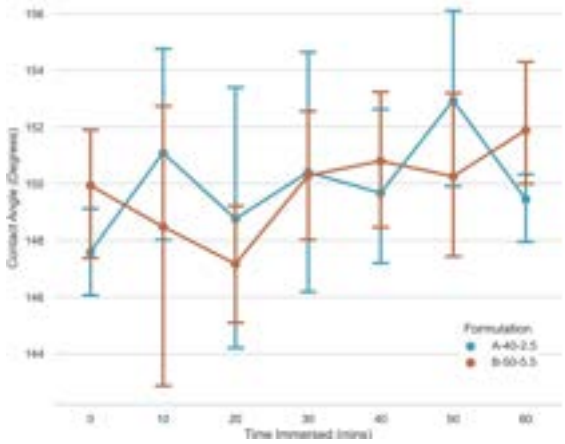

Figure 13: *Plot of Contact Angle as a function of time immersed in water for PE/Toluene and optimised formulation, showing standard deviation bars*

Figure 12: *Reflection on an A-40-2.5 slide resulting from pinned air layer*

Figure 13 demonstrates that there was no statistically significant drop in hydrophobicity for either of the slides due to an overlap in the standard deviation bars. In addition, the formulations show no statistical difference *between* each other at any time stamp. This further corroborates the conclusion that B-50-5.5 is a valid replacement for A in terms of super hydrophobicity and durability.

Nonetheless, a longer immersion time would be insightful as to the long-term effects of immersion. It can be concluded that both the B-50-5.5 and A-40-2.5 coatings show excellent hydrophobic durability up to 1 hour, with no statistically significant degradation, however long term experiments are required to examine if a plateau has truly been reached.

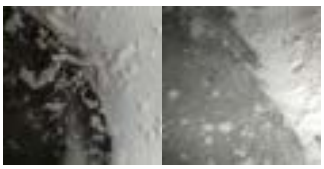

(a) *A-40-2.5* **(b)** *B-50-5.5*

Figure 14: *Images taken at 50X magnification*

The average time recorded during **Mechanical Abrasion Testing** for 2 slides of 'A-40-2.5' and 'B-50-7.5' was 5.1 seconds and 5.7 seconds respectively. The disparity of 0.6 seconds suggests durability is comparable. Figure 14 shows that A-40-2.5 formed a more coarse powder due to PE polymer grains.

During **outdoor testing** 2 Slides of A-40-2.5 and 2 slides of B-50-5.5 were placed on the windowsill from 02-Dec-2020 to 07-Dec-2020 in SW7, London, UK. The average temperature was 5 °C ± 3°C with an RH of 90%. Rain was recorded on 3 of the 5 days.

Description	μ_1	s_1	μ_2	s_2	t
A-40-2.5 (1)	152.8	3.9	147.6	1.9	2.0
A-40-2.5 (2)	150.1	1.1	149.7	1.1	0.4
B-50-5.5 (1)	151.8	2.9	146.5	3.6	1.9
B-50-5.5 (2)	151.6	1.8	150.9	2.5	0.4

Table 2: *1 is before and 2 is after the outdoor test. μ is the mean static WCA and s is the sample standard deviation*

A one-tailed t-test was used to test the hypothesis, at the 95% significance level that there was no statistical difference before and after the outdoor test. $H_0 : \mu_1 = \mu_2$ and $H_1 : \mu_1 > \mu_2$. $\nu = 4$ and so $t_c = 2.132$. Therefore, the null hypothesis was not rejected, and it was concluded that the integrity of both coatings was retained in outdoor conditions.

Figure 15: *A-40-2.5 and B-50-5.5 placed on windowsill at SW7, UK*

IV. Conclusion

This paper built on previous work done by Khoo & Lim (2017), Shah & Ng (2016) & Kokkinis (2017) by replacing the petrochemically derived materials with a biopolymer in corn starch. The modifications successfully produced comparable static and advancing contact angles to the PE/Toluene films in the optimised formulation:

Formulation	Static CA (°)	Adv. CA (°)
A-40-2.5	154.8 ± 4.7	156.0 ± 4.3
B-50-5.5	151.7 ± 1.5	155.3 ± 3.9

Table 3: *Table comparing Static and Advancing (θ_A) contact angles of previous and optimised formulations*

With comparable angles at a first glance, further statistical analysis on contact angles revealed stronger conclusions:

B-50-5.5 exhibited no statistical difference in either contact angle when compared to A-40-2.5 and therefore it was a viable option for sustainable development of superhydrophobic films. Durability-wise, the hygroscopicity of starch remained a limitation in DVS experiments. However, there was an insignificant change in hydrophobicity witnessed during the outdoor test; practically, the films had no degradation in integrity or hydrophobicity during this time. Immersion testing further attested to the practical integrity of the films, showing no statistical degradation of films. Mechanical durability is decreased to a limited degree, however. Additionally, starch *modifications* proved unsuccessful; OMS saw difficulty in continuous film formation and the hydrophobicity exhibited by TEOS was outmatched by the optimised formulation containing native corn starch. Globally, despite the hydrophilic properties of corn starch, there is sufficient evidence to conclude that starch is a promising eco-binder to eliminate PE/Tol in the production of superhydrophobic films using hydrophobic calcium carbonate powder.

V. Recommendations

The results of this exploratory investigation provide strong evidence for further targeted research into the incorporation of starch into superhydrophobic films. Logically, replacing the PCC used with eggshell waste as done by Khoo & Lim (2017) should be the next step to further improve the sustainability credentials of the novel films developed in this investigation. Attempts to reduce the ethanol used in the formulation protocol, and thereby reduce VOC offgassing during drying, will also help towards this goal. Additionally, a complete study of the hysteresis (namely θ_R) using sliding, captive bubble or evaporation methods (Eral et al. (2012)) should be undertaken to characterise the films further and further verify the optimised formulation presented here. To verify industrial applicability, characterisation using SEM, FTIR and TGA are required and investigations into alternative coating methods such as spin coating or bio-mineralisation (Tang et al. (2021) will provide further insight into the real-world practicality of these film. More broadly, further starch modifications should be investigated to dampen its hydrophilicity; this includes cross-linking of polymers to occupy hydroxyl groups and etherification/esterification using different materials with the objective of increasing hydrophobicity and decreasing apparent hygroscopicity (Wang et al. (2020)).

VI. Acknowledgements

We would like to express our sincere gratitude to **Dr Vikram A Karde** for his guidance throughout the project; **Dr Jerry Heng** for his kind assistance throughout the research; **Mr Ethan Errington** for assistance with training during unprecedented times.

References

And, Z. L. & Han, J. (2005), 'Film-forming characteristics of starches', *Journal of food science: an official publication of the Institute of Food Technologists.* **70**(1), E31–E36.

Barati Darband, G., Aliofkhazraei, M., Khorsand, S., Sokhanvar, S. & Kaboli, A. (2020), 'Science and engineering of superhydrophobic surfaces: Review of corrosion resistance, chemical and mechanical stability', *Arabian Journal of Chemistry* **13**(1), 1763–1802.

Bayer, I. S. (2020), 'Superhydrophobic coatings from ecofriendly materials and processes: A review', *Advanced Materials Interfaces* **7**(13), 2000095.

Cao, X., Chang, P. R. & Huneault, M. A. (2008), 'Preparation and properties of plasticized starch modified with poly(-caprolactone) based waterborne polyurethane', *Carbohydrate Polymers* **71**(1), 119 – 125.

Cao, Z., Daly, M., Clémence, L., Geever, L., Major, I., Higginbotham, C. & Devine, D. (2016), 'Chemical surface modification of calcium carbonate particles with stearic acid using different treating methods', *Applied Surface Science* **378**, 320–329.

Cassie, A. B. D. & Baxter, S. (1944), 'Wettability of porous surfaces', *Transactions of the Faraday Society* **40**, 546.

Chandler, D. (2005), 'Interfaces and the driving force of hydrophobic assembly', *Nature (London)* **437**(7059), 640–647.

Chen, Y., Liu, H., Yu, L., Duan, Q., Ji, Z. & Chen, L. (2020), 'Superhydrophobic modification on starch film using pdms and ball-milled mmt coating', *ACS Sustainable Chemistry Engineering* **8**(28), 10423–10430.

DeArmitt, C. & Hancock, M. (2003), *Particulate-Filled Polymer Composites*, pp. 357–424.

Deepika, Hait, S., Christopher, J., Chen, Y., Hodgson, P. & Tuli, D. (2013), 'Preparation and evaluation of hydrophobically modified core shell calcium carbonate structure by different capping agents', *Powder Technology* **235**, 581–589.

Demjén, Z., Pukánszky, B., Földes, E. & Nagy, J. (1997), 'Interaction of silane coupling agents with caco3', *Journal of Colloid and Interface Science* **190**(2), 427–436.

Dufresne, A. & Castaño, J. (2016), 'Polysaccharide nanomaterial reinforced starch nanocomposites: A review', *Starch - Stärke* **69**(1-2), 1500307.

Eral, H. B., Mannetje, D. J. C. M. Oh, J. M. (2012), 'Contact angle hysteresis: a review of fundamentals and applications', *Colloid and Polymer Science* **291**(2), 247–260.

Fang, H. (2019), Investigation of superhydrophobic coatings from different types of shell waste, Master's thesis, Imperial College London.

Fisher, D. K. & Thompson, D. B. (1997), 'Retrogradation of maize starch after thermal treatment within and above the gelatinization temperature range', *Cereal Chemistry Journal* **74**(3), 344–351.

Gao, L. & Mccarthy, T. J. (2006), 'Contact angle hysteresis explained', *Langmuir* **22**(14), 6234–6237.

Ghasemlou, M., Aliheidari, N., Fahmi, R., Shojaee-Aliabadi,

S., Keshavarz, B., Cran, M. J. & Khaksar, R. (2013), 'Physical, mechanical and barrier properties of corn starch films incorporated with plant essential oils', *Carbohydrate Polymers* **98**(1), 1117 – 1126.

Gilbert, M., Petiraksakul, P. & Mathieson, I. (2001), 'Characterisation of stearatestearic acid coated fillers', *Materials Science and Technology* **17**(11), 1472–1478.

Gong, X., Zhang, L., He, S., Jiang, S., Wang, W. & Wu, Y. (2020), 'Rewritable superhydrophobic coatings fabricated using water-soluble polyvinyl alcohol', *Materials Design* **196**, 109112.

Hong, S.-J., Chang, F.-M., Chou, T.-H., Chan, S. H., Sheng, Y.-J. & Tsao, H.-K. (2011), 'Anomalous contact angle hysteresis of a captive bubble: Advancing contact line pinning', *Langmuir* **27**(11), 6890–6896.

Hu, Z. & Deng, Y. (2010), 'Superhydrophobic surface fabricated from fatty acid-modified precipitated calcium carbonate', *Industrial Engineering Chemistry Research* **49**.

Jiang, S., Dai, L., Qin, Y., Xiong, L. & Sun, Q. (2016), 'Preparation and characterization of octenyl succinic anhydride modified taro starch nanoparticles', *Plos One* **11**(2).

Kaur, B., Ariffin, F., Bhat, R. & Karim, A. A. (2012), 'Progress in starch modification in the last decade', *Food Hydrocolloids* **26**(2), 398–404.

Khoo, J. Y. H. & Lim, J. V. (2017), 'A feasibility study on eggshells as a viable substitute for calcium carbonate in the fabrication of superhydrophobic coatings', p. 17–18.

Kokkinis, P. (2017), Durability of superhydrophobic coatings from recycled materials, Master's thesis, Imperial College London.

Latthe, S. S., Sutar, R. S., Kodag, V. S., Bhosale, A., Kumar, A. M., Kumar Sadasivuni, K., Xing, R. & Liu, S. (2019), 'Self – cleaning superhydrophobic coatings: Potential industrial applications', *Progress in Organic Coatings* **128**, 52 – 58.

Lima, K. O., Biduski, B., da Silva, W. M. F., Ferreira, S. M., Montenegro, L. M. P., Dias, A. R. G. & Bianchini, D. (2017), 'Incorporation of tetraethylorthosilicate (teos) in biodegradable films based on bean starch (phaseolus vulgaris)', *European Polymer Journal* **89**, 162 – 173.

Luchese, C. L., Spada, J. C. & Tessaro, I. C. (2017), 'Starch content affects physicochemical properties of corn and cassava starch-based films', *Industrial Crops and Products* **109**, 619–626.

Ollivier, H. (1907), *Annales de chimie et de physique*, Vol. 10, Masson.

Rajabnezhad, S., Ghafourian, T., Rajabi-Siahboomi, A., Missaghi, S., Naderi, M., Salvage, J. P. & Nokhodchi, A. (2020), 'Investigation of water vapour sorption mechanism of starch-based pharmaceutical excipients', *Carbohydrate Polymers* **238**, 116208.

Seeharaj, P., Sripako, K., Promta, P., Detsri, E. & Vittayakorn, N. (2019), 'Facile and eco-friendly fabrication of hierarchical superhydrophobic coating from eggshell biowaste', *International Journal of Applied Ceramic Technology* **16**(5), 1895–1903.

Shah & Ng, V. (2016), A simple production method for durable superhydrophobic calcium carbonate coatings, Master's thesis, Imperial College London.

Sheng, Y., Zhou, B., Wang, C., Zhao, X., Deng, Y. & Wang, Z. (2006), 'In situ preparation of hydrophobic caco3 in the presence of sodium oleate', *Applied Surface Science* **253**(4), 1983 – 1987.

Shi, S.-S. & He, G.-Q. (2012), 'Process optimization for cassava starch modified by octenyl succinic anhydride', *Procedia Engineering* **37**, 255–259.

Smith, A. M. (2001), 'The biosynthesis of starch granules', *Biomacromolecules* **2**(2), 335–341.

Song, X., Zhu, W., Li, Z. & Zhu, J. (2010), 'Characteristics and application of octenyl succinic anhydride modified waxy corn starch in sausage', *Starch - Stärke* **62**(12), 629–636.

Syafiq, A., Vengadaesvaran, B., Ahmed, U., Rahim, N. A., Pandey, A., Bushroa, A., Ramesh, K. & Ramesh, S. (2020), 'Facile synthesize of transparent hydrophobic nano- caco3 based coatings for self-cleaning and anti-fogging', *Materials Chemistry and Physics* **239**, 121913.

Tang, S., Chang, X., Li, M., Ge, T., Niu, S., Wang, D., Jiang, Y. & Sun, S. (2021), 'Fabrication of calcium carbonate coated-stainless steel mesh for efficient oil-water separation via bacterially induced biomineralization technique', *Chemical Engineering Journal* **405**, 126597.

Tzouganatos, I. (2015), Hydrophobic coatings from paper sludge ash, Master's thesis, Imperial College London.

Wang, X., Huang, L., Zhang, C., Deng, Y., Xie, P., Liu, L. & Cheng, J. (2020), 'Research advances in chemical modifications of starch for hydrophobicity and its applications: A review', *Carbohydrate Polymers* **240**, 116292.

Wang, Z., Gu, Z., Hong, Y., Cheng, L. & Li, Z. (2011), 'Bonding strength and water resistance of starch-based wood adhesive improved by silica nanoparticles', *Carbohydrate Polymers* **86**(1), 72–76.

Wenzel, R. N. (1936), 'Resistance of solid surfaces to wetting by water', *Industrial Engineering Chemistry* **28**(8), 988–994.

Yalkowsky, Samuel H. He, Y. J. P. (2010), *Handbook Of Aqueous Solubility Data*, CRC Press.

Yu, Z.-Y., Jiang, S.-W., Zheng, Z., Cao, X.-M., Hou, Z.-G., Xu, J.-J., Wang, H.-L., Jiang, S.-T. & Pan, L.-J. (2019), 'Preparation and properties of osa-modified taro starches and their application for stabilizing pickering emulsions', *International Journal of Biological Macromolecules* **137**, 277–285.

Zhang, H., Zeng, X., Gao, Y., Shi, F., Zhang, P. & Chen, J.-F. (2011), 'A facile method to prepare superhydrophobic coatings by calcium carbonate', *Industrial Engineering Chemistry Research* **50**(6), 3089–3094.

ZOBEL, H. F. (1984), Cchapter ix - gelatinization of starch and mechanical properties of starch pastes, *in* E. F. P. Roy L. Whistler, James N. Bemiller, ed., 'Starch: Chemistry and Technology (Second Edition)', second edition edn, Food Science and Technology, Academic Press, San Diego, pp. 285 – 309.

Process Plant Layout Optimisation and its Application to Flixborough (1974)

Sharada Joshi and Aghogho Otakoro
Department of Chemical Engineering, Imperial College London, U.K.

Abstract

This study builds upon previous work done on plant layout optimisation and investigates its applicability to a historical case study, using Flixborough (1974) as an example. The result of an existing tool which optimises process plant layout is validated against optimal layouts obtained in literature. Modifications are made to the tool to ensure more a robust performance and the cost of fatality constraints are further developed. The tool is used in a real-life case study to demonstrate its applicability - it has been successfully applied to a pilot study of the Nypro Plant at Flixborough, consisting of 11 units. The framework to account for incident frequencies has been implemented. It was found that the tool could not be applied to a full-scale study due to long computational times. Further work can be done to address limitations, such as the calculation of distances when large units are implemented, a betterment of the frequency framework used, and tackling the extensive computational times.

1 Introduction

1.1 Background

The spatial positioning of process equipment, office blocks and other administrative buildings or work centres should all be considered when determining the plant layout. This decision has a major impact on every aspect of the plant's lifetime, from the profitability of the plant to the functionality of the plant itself [1]. In order to achieve maximum plant efficiency, the layout of process units should complement the production process itself, whilst minimising operating and land costs, as well as material handling costs (which include the cost of piping). Generally, more spaced out units require more land and piping, which increases the operating and construction costs, thus affecting plant economics [1]. However, increasing the distance between units enhances safety and minimises the effects of an incident. This trade-off between safety and economic viability outlines the plant layout problem; careful consideration is required to tackle this multifaceted issue.

The importance of including safety considerations in the initial design stage of a plant is evident in the explosion of the Nypro Plant at Flixborough. The plant was built in 1938 and initially produced fertilizer. In 1964, the plant changed ownership, and by 1972 it had the capacity to produce around 70,000 tons/year of caprolactam, a raw material needed for the production of Nylon 6. However, the plant was operating below capacity, producing 47,000 tons/year of caprolactam [2]. At the time of the explosion in 1974, one of the reactors in the cyclohexane oxidation unit, Section 25A, was taken out of circulation and bypassed using a dog-leg connection pipe. Inadequate safety checks on this pipe led to its rupture, which subsequently led to a severe explosion. This resulted in 36 injuries and 28 fatalities, 18 of which came from the control room located near Section 25A [2]. The impact of this explosion was exacerbated by the lack of safety considerations in the layout of the plant; the Report of the Court of Inquiry states that loss of life could have been avoided had the control room been differently sited [3].

The incident occurred on a weekend, when 72 people were at the plant; the impact would have been much greater had it occurred on a normal working day, when approximately 550 people would have been expected to occupy the site [2]. Incidents such as these highlight the necessity to integrate plant layout considerations into the process design to achieve a safer design and help avoid or reduce the impact of any future incidents.

1.2 Literature Review

As previously discussed, a major factor leading to several accidents in process industries is inadequate plant layout [4]. Following incidents such as Flixborough and Bhopal, there have been numerous additions to legislation and industry practice [5]. Increasing awareness of hazards and concerns about safety, have led to numerous studies focusing on the integration of the process plant layout problem with quantitative methods to improve process plant safety early in the design process [6].

Use of mathematical modelling techniques to perform plant layout optimisations has become increasingly popular over the years as opposed to the use of engineering judgement alone [7]. Earlier methods involved

formulating layout optimisation as quadratic assignment problems (QAPs) which considered only equally sized units [8]. However as the chemical industry has advanced, the formulation of these problems has increased in complexity. This is due the increased number of design considerations that are now implemented to include components such as multiple floors and cost of business interruption - if an incident were to occur- and the inclusion of protection devices. Other studies have included potential injury cost to account for workers' safety, and land cost to account for cost of occupied land [9]. Other models, such as the construction-based approach, use iterative methods to solve reduced subproblems as a means of lowering computational times and to enable analysis of larger flowsheets [8]. Penteado considered the plant layout optimisation problem as a mixed integer nonlinear programming (MINLP) problem where piping cost, land cost, financial risk, and protection device cost were minimized [6]. Patsiatzis et al.[10] later developed a similar model but considered all process units to have a rectangular footprint rather than the circular footprint that Penteado had used. Building on early work which only took into account piping costs [11], they also incorporated the Dow Fire and Explosion Index (F&EI) into the mixed integer linear programming (MILP) model and used it to evaluate a process containing 7 process units as shown in Figure 1. Xu and Papageorgiou used the MILP formulations in this work as a basis for developing the construction-based approach, in which units are inserted into the model in an iterative manner to analyse larger flowsheets [8].

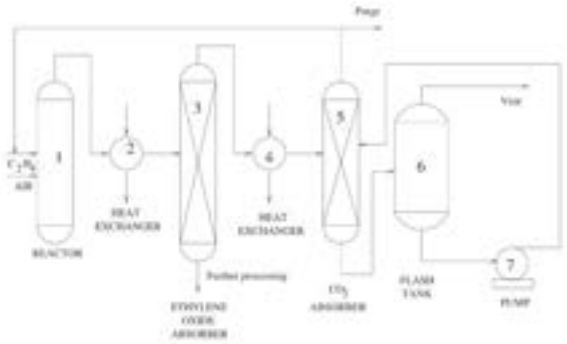

Figure 1: Flowsheet for the ethylene oxide plant [10]

Building on the work of Patsiatzis et al. [10], Tan [12] used the same ethylene oxide case study to develop a MILP model in Python which minimised the overall cost and also incorporated constraints related to the cost of land and the cost of fatality due to fire and explosion and chemical release. CPLEX, an optimisation software package, was used in conjuction with PuLP, a modelling library which leverages the use of Python, to solve the MILP's.

While Sadee made use of historical data to asses the effects of the blast at Flixborough [13], and Høiset et al. [14] applied computer modelling techniques to analyse the accident by creating a three dimensional simulation, very little work has been done on applying the developed MILP models to the incident. It is therefore necessary to determine whether these MILP models can be applied effectively to real production plants or incidents by gathering historical data.

1.3 Objectives

This study aims to validate the developed tool against literature to confirm that it has been formulated accurately. The study also aims to modify and further develop the cost of life constraints due to fire and explosion and chemical release (initially implemented by Tan [12]) to increase the robustness of the model and to ensure alignment with Dow's Chemical Exposure Index Guide (CEI) [15]. Finally, the study aims to explore the applicability of this model through the use of Flixborough (1974) as a case study.

This paper is laid out as follows: Section 2 details the model validation, modification to constraints and the approach followed to apply the model to Flixborough. The layouts obtained are presented and discussed in Section 3. Finally, Sections 4 and 5 conclude the study and highlight areas for future work. The nomenclature can be found in the Appendix.

2 Methodology

2.1 Model Validation

The layout problem considered involved the application of MILP to an ethylene oxide process as shown in Figure 1. In this case study, the objective function aims to minimise a combination of the piping cost, the maximum probable property damage cost and the cost of protection devices depending on the scenario considered (Equation 1). The constraints involved in the problem were equipment orientation constraints, non-overlapping constraints, distance constraints, area of exposure constraints and maximum probable property damage constraints as detailed in the work of Patsiatzis et al.[10], with a piecewise linear approximation used to calculate the value of the area of exposure (Equation 2).

$$\min \sum_i \sum_{j \neq i} C_{ij} \cdot D_{ij} + \sum_i \Omega_i + \sum_i \sum_{k \in K_i} P_{ik} \cdot Z_{ik} \quad (1)$$

$$V_i^e = C_i^p + \sum_{j \neq i} \left(C_j^p \cdot \psi_{ij} - \frac{C_j^p}{D_i^e} \cdot D_{ij}^{in} \right) \quad \forall i \in I_p \quad (2)$$

The implementation of this problem in Python, conducted in a previous research project [12], resulted in discrepancies in the optimal solution when compared with

literature (despite the same scenario setup, as shown in Table 1).

Table 1: Comparison of developed Python model developed by Tan [12] with literature, showing the total plant layout cost with and without protection devices

	Plant layout cost (USD)	
	With Protection Devices	Without Protection Devices
Tan [12]	292,964	445,300
Patsiatzis [10]	290,689	440,848

The first objective of this work was to achieve consistency with the literature. An excel spreadsheet was set up to verify the objective function resulting from the layout achieved by the optimiser (Appendix A.1). From performing a sensitivity analysis, it was realised that the code did not behave as expected. For example, increasing the land cost or the connection costs between the units had no effect on the objective function (it was expected that the units would be placed closer together as these costs were increased). An example of this behaviour can be seen in Figures 2 and 3 - a significant increase in the connection costs between units 1 and 2 had little effect on the plant layout (further examples can be viewed in Appendix A.2).

Thus, the code was amended to give the desired behaviour (Figure 4), by modifying equations, variables and control flow statements. In doing so, the objective function achieved matched the objective given in literature as shown in Table 2. The negligible difference in the objective has been attributed to the differences in the version of the CPLEX solver used, as this study made use of version 12.10, while the literature used version 6.5. As seen in Figures 1 and 5, there remains a difference in the optimal plant layout, as multiple layouts with the same objective function can exist [16].

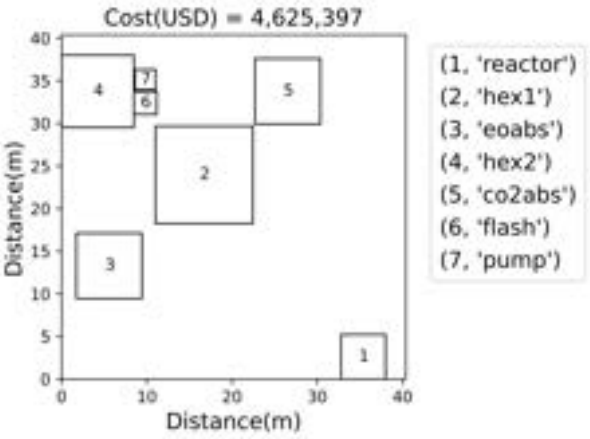

Figure 2: Plant layout generated by original model developed by Tan [12] with cost of connection between units 1 and 2 at 98.4 USD/m. Costs related to piping, land, MPPD and protection devices are considered

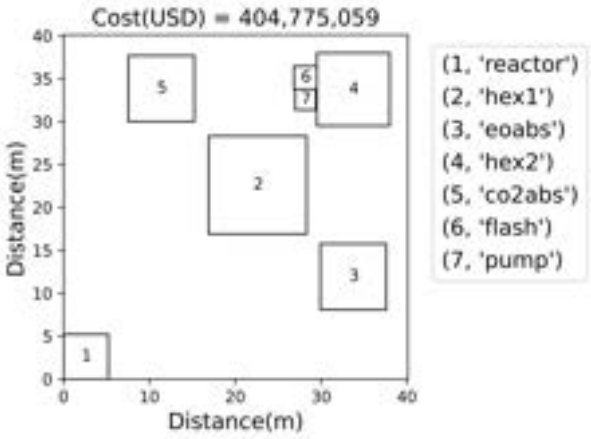

Figure 3: Effect on layout of increasing cost of connection between units 1 and 2 from 98.4 USD/m to 10,000,000 USD/m in the original model developed by Tan [12]. Costs related to piping, land, MPPD and protection devices are considered

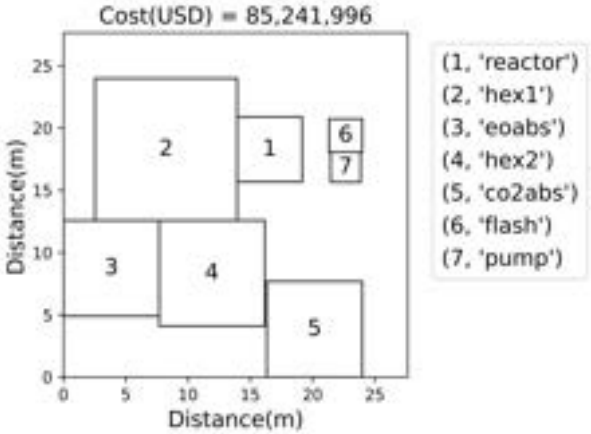

Figure 4: Effect on layout of increasing cost of connection between units 1 and 2 from 98.4 USD/m to 10,000,000 USD/m in the modified model. Costs related to piping, land, MPPD and protection devices are considered

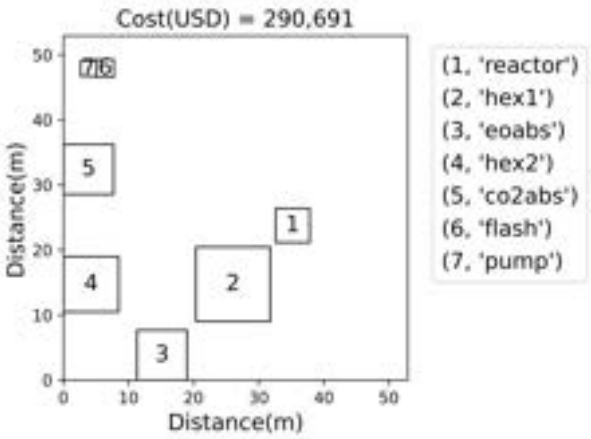

Figure 5: Optimal plant layout achieved using modified tool. Costs related to piping, MPPD and protection devices are considered

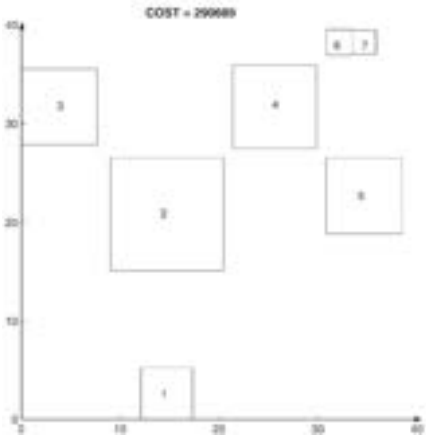

Figure 6: Optimal plant layout from literature [10]. Costs related to piping, MPPD and protection devices are considered

Table 2: Comparison of modified Python model with literature, showing the total plant layout cost with and without protection devices

	Plant layout cost (USD)	
	With Protection Devices	Without Protection Devices
Python	290,691	440,851
Patsiatzis [10]	290,689	440,848

Tan's model [12] built upon previous work [10] to include cost of fatality constraints due to fire and explosion and chemical exposure. The study assumed that an incident would always result in a fatality if the occupant was within the area of exposure of a pertinent unit (i.e. constant lethality up to the hazard distance). This paper modifies these constraints by making use of piecewise linear approximations as the impact of an incident decreases with distance in a nonlinear manner[17]. Equations 3 and 4 show the how this piecewise linear reduction was applied. The cost of fatality due to fire and explosion was then combined with the MPPD cost (Equation 5) which allowed the model to run efficiently.

This paper also modifies the calculations of the chemical exposure radius for each pertinent unit to ensure that they closely align with the Dow CEI system [15]. Although the MILP model can only approximate nonlinear constraints, it should be noted that this paper continues its use as the MILP model can guarantee that the calculated solutions are globally optimal, unlike a MINLP model [18].

In this study, the terms considered in the objective function were the total land cost, connection costs, MPPD costs, cost of protection devices and the cost of fatalities due to chemical release and fire and explosion. The resulting model will be a tool which enhances the use of process safety considerations in the initial design and layout stages of production plants.

$$V_i^{le} = OCC_i \cdot C^l + \sum_{j \neq i} \Bigg(OCC_j \cdot C^l \cdot \psi_{ij}^e - \frac{OCC_j \cdot C^l}{D_i^e} \cdot D_{ij}^{in} \Bigg) \quad \forall i \in I_p \tag{3}$$

$$V_i^{lc} = OCC_i \cdot C^l + \sum_{j \neq i} \Bigg(OCC_j \cdot C^l \cdot \psi_{ijh}^c - \frac{OCC_j \cdot C^l}{D_i^c} \cdot D_{ij}^{in} \Bigg) \quad \forall i \in I_p \tag{4}$$

$$V_i^e = OCC_i \cdot C^l + C_{pi} + \sum_{j \neq i} \Bigg(OCC_j \cdot C^l \cdot \psi_{ij}^e + C_{pj} \cdot \psi_{ij}^e - \frac{OCC_j \cdot C^l}{D_i^c} \cdot D_{ij}^{in} - \frac{C_{pj} \cdot D_{ij}^{in}}{D_i^e} \Bigg) \quad \forall i \in I_p \tag{5}$$

2.2 Application to Flixborough

2.2.1 Data collection & unit classification

In order to effectively apply this model to the Flixborough (1974) case study, a significant amount of data had to be gathered as shown in Table 3. Additionally, land cost, connectivity between blocks and the cost of these connections was determined. Unlike the ethylene oxide plant case study, where individual units (for example, the absorber) were implemented into the optimisation model, entire blocks (for example, the hydrogen plant) were considered to be units in the Flixborough case study. The main reason for this approach was to understand how the site at Flixborough should have been laid out if certain constraints were considered.

All major blocks in Flixborough were sized using the site plan shown in Figure 19 (Appendix B.1). The length and width of all major blocks in Figures 19 were measured using the scale provided on the map. The block dimensions were implemented into the code as the values of α and β.

All units were classed either as pertinent or non-pertinent using the definitions on pages 8-9 of Dow's F& EI guide [19]. The pertinent units were further classified depending on whether they were hazardous due to the risk posed by fire and explosion and/or due to chemical release. F&EI calculations were considered for the former, while CEI calculations were done for the latter using the procedures outlined in the respective Dow guides [19][15]. See Appendix B.6 for classification of all units. Note that for each pertinent unit, only the most hazardous compound present in the unit was considered for CEI calculations, as this enabled the evaluation of the worst-case

Table 3: Data needed as input into the Python model depending on unit type

	Unit type		
	Non-Pertinent	Pertinent (Fire and explosion)	Pertinent (chemical)
Unit dimensions	✓	✓	✓
Capital cost	✓	✓	✓
Occupancy	✓	✓	✓
Protection device configurations		✓	✓
Fire and explosion radius		✓	
Chemical exposure radius			✓

scenario should an incident occur. The most hazardous compound was determined by considering a combination of N_F, N_H and estimated inventory. Where data was not available, a compound known to be present on the plant was used instead.

2.2.2 Cost Estimation

Information relating to the majority of the blocks on the site was difficult to acquire and in most cases not available. In order to adequately estimate the capital cost of these blocks and to deduce the capacity of each unit at Flixborough, an adaptation of the Raschig Process, as detailed by Ritz [20], was assumed. A yearly output of 47,000 tons of caprolactam was used [2] as a starting point when estimating process capacities. It should be noted that reaction stoichiometry was assumed when calculating plant through-puts. A detailed list of reactions considered in this study is shown in Appendix B.4. Using information from the site plans, the aforementioned reactions and by applying engineering judgement, a simplified block diagram of the process was created (see Figure 22 in Appendix B.7).

Capital Cost Estimation The capital costs for the units were estimated using three main cost estimation methods. The capital costs of pertinent units were calculated using the Bridgewater method, shown in Equation 6, for plants that have predominantly liquid or solid phase handling processes [21]. The Timms correlation [21] was used for pertinent units that contained predominantly gas phase processes (Equation 7).

$$C = \begin{cases} 130,000N(\frac{Q}{s})^{0.30} & \text{if } Q < 60,000t/yr \\ 150N(\frac{Q}{s})^{0.675} & \text{else} \end{cases} \quad (6)$$

$$C = 8000NQ^{0.615} \quad (7)$$

The Conceptual Cost Estimating Manual [22] was used to estimate the capital costs of non-pertinent units.

All costs were quoted in terms of their equivalent cost in 1979 using *Chemical Engineering Plant Cost Index* (CEPCI) [23] [24] as the Flixborough plant was rebuilt and reopened in that year. A detailed list of all capital cost estimates used in this application and the CEPCI can be found in Appendix B.4.

Cost of connections The connectivity network between blocks is ambiguous in the site plans. Due to a lack of information available regarding the necessary connections between blocks, engineering judgement was exercised in order to determine the connectivity network. Figure 22 in Appendix B.7 helped in this regard. Four types of connections were considered: pipe, road, pavement and conveyor belt (see Appendix B.7 for the cost of connections).

Land cost and cost of protection devices Land cost was determined using average industrial land value estimates [25], with additional costs added for preparing the land. The Dow F&EI guide [19] was used to create a standard list of loss control features with corresponding loss control credit factors. Engineering judgement was applied to create and cost two lists of configurations which could be used on a plant or a storage tank.

Fire and explosion and chemical exposure The works at Flixborough employed 550 people [2]. This information was used to reasonably estimate the occupancy of each unit. Operating conditions for each pertinent unit were determined through research of similar processes documented in the literature. The procedure in Dow F&EI guide [19] was followed to determine the maximum probable property damage cost. The procedure in the Dow CEI guide [15] was followed to determine the exposure distance. In each case, the most hazardous compound present in a pertinent unit was selected to evaluate the worst-case scenario. Note that the areas of exposure have not been calculated for units which were not considered in the pilot study.

2.2.3 Additions to constraints

The approach to calculating the distance of fire and explosion exposure was modified in line with the Dow's F&EI guide [19]. It suggested that this distance, for large units, should be calculated from the outer edge of units, rather than from the centre. To take a conservative approach

and because of the linear nature of the model, the maximum distance to the edge of the units from the centre was added to the calculated distance of fire and explosion exposure. It should be noted that using this method, the distance of fire and explosion exposure would be overestimated for long, thin rectangular units. The distance of fire and explosion exposure is the diagonal distance between two units, whereas the tool calculates the rectilinear distance between units. To account for this discrepancy, the distance of fire and explosion exposure is multiplied by 1.414.

To create a more realistic model, a frequency framework was implemented to account for the number of incidents which could occur on a plant each year. Jung [9] used a frequency of $1 \times 10^{-5} yr^{-1}$ for each incident. Assuming ten of these incidents each year on a pertinent unit, a frequency of incident of $1 \times 10^{-4} yr^{-1}$ was used for all pertinent units. This was included in the costs of fatalities terms. To ensure the units in the objective function were constant, the cost of connections, land cost and the cost of protection devices were divided by the operating lifetime of the plant, assumed to be 25 years [26]. In practical terms, these terms would mean that the cost of purchasing land, protection devices and connections would be spread out evenly across 25 years.

2.2.4 Pilot Study

Due to size of the problem involved (18 pertinent units and 22 non-pertinent units), it was decided that a pilot study would be conducted (consisting of 11 units, 5 pertinent and 6 non-pertinent) to ensure that the code behaves as desired. The units considered for this lie in the immediate vicinity of Section 25A and are highlighted in Appendix B.1. It should be noted that the optimal layouts in this study have been obtained with the main office in a fixed position at the origin to reduce computational time.

3 Results & Discussion

3.1 Ethylene Oxide Case Study

Figure 7 shows the layout and objective function achieved when the modified model was applied to the ethylene oxide plant. As shown in Table 4, there is a 28.6% reduction in the objective function compared to that of the previous model, which demonstrates the effectiveness of the modifications made. Major reductions came from the land cost which reduced by 36% and the cost of fatality due to fire and explosion which also reduced significantly, primarily due to the piecewise linear approximation used. The reduction in land area and costs brings units closer together as seen in Figure 7. This was allowed by the model as the protection device configurations chosen have a lower loss control credit factor. A full cost break down and comparison can be seen in Table 5.

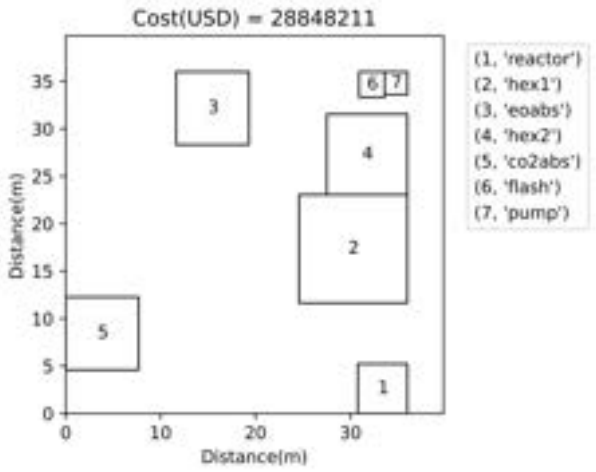

Figure 7: Layout of plant for improved EO model. All costs (i.e. connection costs, land cost, cost of protection devices, cost of maximum probable damage and costs of fatalities) are considered

Table 4: Comparison of modified Python model with literature, showing the total plant layout cost

	Plant layout cost (USD)	% difference
Developed Tool	28,848,211	-
Tan [12]	40,375,973	28.6

3.2 Flixborough Pilot Study

3.2.1 Scenario 1: Only connection costs considered

Figure 8 shows the optimal plant layout when only the connection costs are considered, as was the case in early work in this area [11]. In this scenario, the objective function (Equation 8) minimises the connection cost term, which results in connected units being placed next to each other on the plot. Section 25A is a stand-alone unit, which can be attributed to the fact that it is not connected to any other units. The warehouse, flaking plant, caprolactam plant and the ammonia sphere were all grouped together as expected as their connections costs were higher than that of all other units. The compact placement of connected units displays the same behaviour as that in literature [11]. As safety aspects are not considered, the trade-off described in section 1 does not exist in this scenario. Although this layout has limited relevance due to lack of safety considerations, it should be noted that the proximity of the main office, project office, control room and lab may be practical in reality.

$$\min \sum_{i} \sum_{j \neq i} C_{ij} \cdot D_{ij} \tag{8}$$

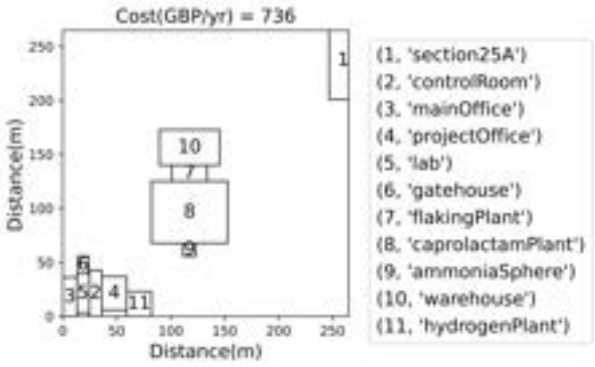

Figure 8: Optimal layout of plant section when only piping costs are considered

3.2.2 Scenario 2: Costs of fatalities not considered

Figure 9 shows the optimal layout when the costs of fatalities are not considered. The objective function for this scenario is shown in Equation 9. Contrary to expectations based off Patsiatzis' work [10], both pertinent and non-pertinent units are placed in the area of exposure of pertinent units. A possible explanation for this behaviour is the use of frequency of incidents, which is set to $1 \times 10^{-4} yr^{-1}$ for all pertinent units. This means the maximum probable property damage cost is significantly lower than the land cost even for a tightly packed layout. It should be noted that lowering the land cost does indeed move all units outside the pertinent units' areas of exposure as expected.

$$\min \sum_i \sum_{j \neq i} C_{ij} \cdot D_{ij} + \sum_i \Omega_i + \sum_i \sum_{k \in K_i} P_{ik} \cdot Z_{ik} + TLC \tag{9}$$

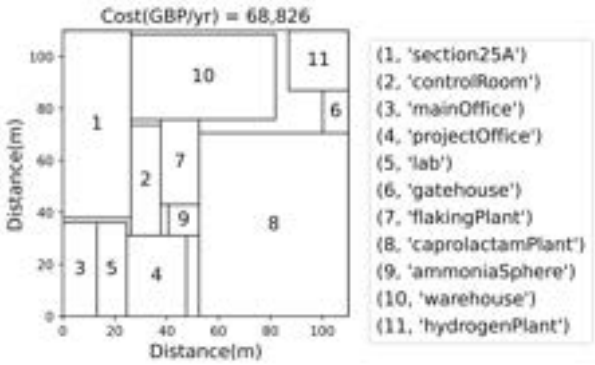

Figure 9: Optimal layout of plant section when all costs excluding the cost of fatalities are considered

3.2.3 Scenario 3: Land Cost not considered

Figure 10 shows the optimal layout when land constraints and costs were not considered in the optimisation. As a result, all units are placed outside the pertinent units' areas of exposure due to fire and explosion. The plot occupies the maximum available land area. The majority of the units still lie within the ammonia sphere's area of exposure due to chemical release despite being located as far away from it as possible. This is because the units are constrained to the plot of land available on site, the length of which is smaller than the exposure radius of the ammonia. The placement of the non-pertinent units exhibits practicality as the offices, lab and control room are located together, with the main office (which has the highest occupancy) being located outside both the explosion and chemical release radii of any pertinent unit. The ammonia sphere is the only major outlier in this plot which is expected as it has the largest chemical release radius - the large connection cost between the ammonia sphere and the caprolactam plant is outweighed by the higher cost of fatality associated with this. The objective function for this scenario is as shown in Equation 10.

$$\min \sum_i \sum_{j \neq i} C_{ij} \cdot D_{ij} + \sum_i \Omega_i + \sum_i \sum_{k \in K_i} P_{ik} \cdot Z_{ik} + \sum_i V_i^{lc} \tag{10}$$

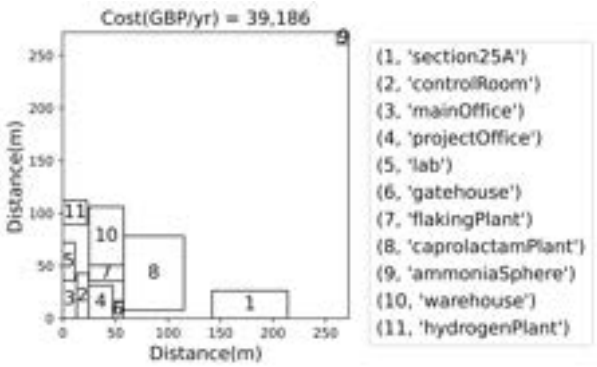

Figure 10: Optimal layout of plant section when all costs except land cost are considered

3.2.4 Scenario 4: All costs considered

Figure 11 shows the optimal layout when all costs are considered. The ammonia sphere is situated further away from other units due its area of chemical exposure. Despite this, all units fall within its release radius. The trade-off between additional land cost and piping is weighed up against the cost of fatality associated with being in the area of chemical exposure. In contrast, units are not situated within the pertinent units' area of exposure due to fire and explosion. This is attributed to distances involved in this case being relatively short. Scenario 4 shows a significant increase in the objective compared to Scenario 3, which is associated with the land cost. As a comparison, Section 25A was located approximately 100m away from the main office block at Flixborough, whereas the tool puts the distance between these units at 168m. The ammonia sphere at Flixborough was placed 276m away from the project office, while the tool places it 348m away (all

rectilinear distances). This result demonstrates the importance of assessing the area of exposure due to fire and explosion and chemical release to adequately place units. The objective function for this scenario is shown in Equation 11.

$$\min \sum_i \sum_{j \neq i} C_{ij} \cdot D_{ij} + \sum_i \Omega_i + \sum_i \sum_{k \in K_i} P_{ik} \cdot Z_{ik} + \sum_i V_i^{lc} + TLC \tag{11}$$

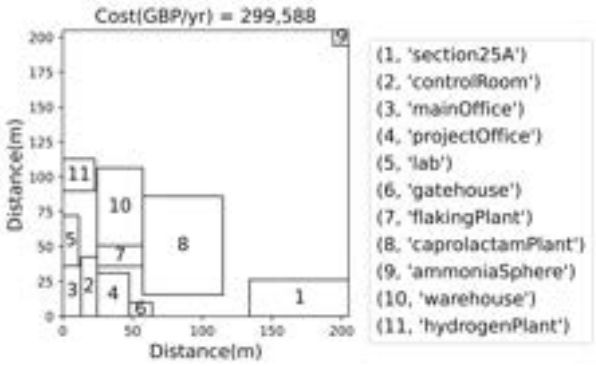

Figure 11: Optimal layout of plant section when all costs (i.e. connection costs, land cost, cost of protection devices, cost of maximum probable damage and costs of fatalities) are considered

The developed Python tool was not able to provide an optimal layout within a modest computational time when more units were considered. For example, running the model with 28 units did not yield a result, despite the run time exceeding two days. In fact, previous studies conducted highlight that this approach worked for only up to 11 units when the objective function contained the cost of connections term only [8]. The findings in this study agree with result in the literature when considering 5 pertinent units and 6 non-pertinent units. Adding another pertinent unit to the study does not yield a result in a modest computational time. However, it should be noted that the authors were able to add 4 further non-pertinent units despite there being more terms in the objective function.

3.3 Limitations

In order to apply the model to the Flixborough case study, all the data pertaining to the Flixborough plant had to be found. This was challenging as there was a lack of accurate information available. Furthermore, the authors were unable to access national archives which may have provided further insights. Thus, engineering judgement was used to estimate the data required for model inputs. Therefore, the accuracy of the application of this tool to a historical case study could be improved upon.

A major limitation when applying this model to more realistic scenarios is the method used to calculate the distance between units. Currently, the model calculates the rectilinear distance between units which includes half of the units' length or width. This method raised no major issues in the ethylene oxide plant due to the relatively small size of all the units considered. The shortcomings of this method became apparent when units with larger dimensions are implemented. Half of the units' length or width in this case forms a larger proportion of the total rectilinear distance between two units (compared to the physical space between them). This meant that in reality, many units were placed within areas of exposure due to fire and explosion and chemical release (which were calculated using diagonal distances) whereas the model believes that the unit is placed outside the exposure radii. An attempt to partly address this issue was made as described in Section 2.2.3.

Although data was collected and the methodology applied to most units present at Flixborough, this study was limited to a pilot study. The main reason for this was the large computational time involved when more units were added to the study. A potential solution to reduce this time was to increase the tolerance from 0, however this approach was discarded as the resulting layout would not be a true optimum (further, it would not be possible to deduce how the layout would differ if the optimum had been reached). To increase solution efficiency, one unit (the main office) was fixed in position. This has practical relevance, for example when deciding the placement of additional units in an already existing site. However, the problem of long computational times persisted when all terms in the objective function were considered. A possible cause of this is an increase in the number of symmetrical layouts which result in the same objective function [16]. Previous work in this area (Westerlund's study [27] for example) mentions the computational effort required in these complex problems. Therefore, a potential solution is to explore the implementation of symmetry breaking constraints as described in [27]. Further work can also be done which implements a different method as outlined in Section 1.2, to significantly reduce computational time and to scale-up the study [8].

4 Conclusion

In conclusion, the objectives of this study were achieved. The developed model has been successfully validated against literature. The negligible discrepancy which remains has been attributed to the differences in the versions of CPLEX solvers used. The constraints for cost of life due to fire and explosion and chemical release were successfully modified and resulted in greater robustness of the model and a closer alignment to Dow's CEI [15]. A 28.6% reduction from Tan's [12] objective function was achieved which demonstrates the model's ability to gen-

erate a better optimum solution.

The applicability of the improved model was shown in the Flixborough Pilot study. A full-scale study of Flixborough could not be conducted due to time limitations and the computational efforts required by the methodology implemented in the model. Nevertheless, a successful pilot study was run with 11 units. The results demonstrated the necessity of considering safety factors, such as costs of fatalities, when planning the layout of a plant. The model placed pertinent units further away from other units when all costs were considered, contrary to the site layout at Flixborough. The results also showed the model's ability to optimally place units given realistic data. The flexibility of the developed model is also shown in Section 3.2 where different combinations of safety considerations are implemented.

5 Outlook

The ethylene oxide plant case study could be advanced, by taking into account other constraints for example the maximum probable outage days and business interruption costs outlined in the F&EI guide [19].

To further develop the Flixborough case study and to expand the pilot study, the construction-based approach described in section 1 can be implemented and applied using the data collected in this work. The approach for calculating distances could be modified when applying this method to larger units due to the limitations discussed in section 3.3.

Finally, the frequency framework introduced in this study can be extended - fault tree analysis could be used to more accurately depict the frequency of events or incidents occurring on the different units.

Bibliography

[1] S. Jung, D. Ng, J.-H. Lee, R. Vazquez-Roman, and M. S. Mannan, "An approach for risk reduction (methodology) based on optimizing the facility layout and siting in toxic gas release scenarios," *Journal of Loss Prevention in the Process Industries*, vol. 23, no. 1, pp. 139–148, 2010, doi: 10.1016/j.jlp.2009.06.012.

[2] Aria, "Catastrophic explosion of a cyclohexane cloud june 1, 1974 flixborough united kingdom," 2008, accessed: 20/10/20. [Online]. Available: https://www.aria.developpement-durable.gouv.fr/wp-content/files_mf/FD_5611_flixborough_1974_ang.pdf

[3] D. of Employment, *Flixborough Disaster: Report of the Court of Inquiry*, 1975.

[4] F. I. Khan and S. A. Abbasi, "Major accidents in process industries and an analysis of causes and consequences," *Journal of loss prevention in the process industries*, vol. 12, no. 5, pp. 361–378, 1999, doi: 10.1016/s0950-4230(98)00062-x.

[5] T. Kerin, "The evolution of process safety standards and legislation following landmark events—what have we learnt?" *Process safety progress*, vol. 35, no. 2, pp. 165–170, Jun 2016, doi: 10.1002/prs.11762.

[6] F. D. Penteado and A. R. Ciric, "An minlp approach for safe process plant layout," 1996, doi:10.1021/ie9502547.

[7] J. Suardin, "The integration of dow's fire and explosion index into process design and optimization to achieve an inherently safer design," 2005, accessed: 1/11/2020. [Online]. Available: https://core.ac.uk/download/pdf/4271116.pdf

[8] G. Xu and L. G. Papageorgiou, "A construction-based approach to process plant layout using mixed-integer optimization," *Industrial engineering chemistry research*, vol. 46, no. 1, pp. 351–358, 2007, doi: 10.1021/ie060843k.

[9] S. Jung, "Facility siting and layout optimization based on process safety," Ph.D. dissertation, 2015, accessed: 30/10/20. [Online]. Available: http://hdl.handle.net/1969.1/ETD-TAMU-2010-12-8596

[10] D. I. Patsiatzis, G. Knight, and L. G. Papageorgiou, "An milp approach to safe process plant layout," *Chemical engineering research design*, vol. 82, no. 5, pp. 579–586, 2004, doi:10.1205/026387604323142612.

[11] L. G. Papageorgiou and G. E. Rotstein, "Continuous-domain mathematical models for optimal process plant layout," *Industrial engineering chemistry research*, vol. 37, no. 9, pp. 3631–3639, 1998, doi: 10.1021/ie980146v.

[12] Y. C. R. Tan, "Optimisation of process plant layout with shortcut hazard assessments," 2020.

[13] C. Sadee, D. Samuels, and T. O'Brien, "The characteristics of the explosion of cyclohexane at the nypro (uk) flixborough plant on 1st june 1974," *Journal of Occupational Accidents*, vol. 1, no. 3, pp. 203–230, 1977, doi: 10.1016/0376-6349(77)90001-3.

[14] T. S. K. M. S Høiset, B.H Hjertager, "Flixborough revisited — an explosion simulation approach," *Journal of Hazardous Materials*, vol. 77, no. 3, pp. 1–9, 2000, doi: 10.1016/S0304-3894(00)00197-7.

[15] "Dow's chemical exposure index guide, first edition," pp. 1–12, 1998. [Online]. Available: https://onlinelibrary.wiley.com/doi/abs/10.1002/97804709

[16] J. O. Ejeh, S. Liu, M. M. Chalchooghi, and L. G. Papageorgiou, "Optimization-based approach for process plant layout," *Industrial engineering chemistry research*, vol. 57, no. 31, pp. 10 482–10 490, 2018, doi: 10.1021/acs.iecr.8b00260.

[17] F. D. Alonso, E. G. Ferradás, J. F. S. Pérez, A. M. Aznar, J. R. Gimeno, and J. M. Alonso, "Characteristic overpressure–impulse–distance curves for vapour cloud explosions using the tno multi-energy model," *Journal of hazardous materials*, vol. 137, no. 2, pp. 734–741, 2006, doi: 10.1016/j.jhazmat.2006.04.005.

[18] I. Castillo, J. Westerlund, S. Emet, and T. Westerlund, "Optimization of block layout design problems with unequal areas: A comparison of milp and minlp optimization methods," *Computers chemical engineering*, vol. 30, no. 1, pp. 54–69, 2005, doi: 10.1016/j.compchemeng.2005.07.012.

[19] *Dow's fire and explosion index hazard classification guide, seventh edition*, 7th ed. Wiley, 1994, isbn:0470938188.

[20] J. Tinge, M. Groothaert, H. op het Veld, J. Ritz, H. Fuchs, H. Kieczka, and W. C. Moran, "Caprolactam," *Ullmann's Encyclopedia of Industrial Chemistry*, pp. 165–170, 2018, accessed 03/11/2020. [Online]. Available: https://onlinelibrary.wiley.com/doi/epdf/10.1002/14356007.a05_031.pub3?saml_referrer

[21] R. K. Sinnott, "Coulson and richardson's chemical engineering," vol. 6, no. 3, p. 248, 1999, isbn: 0750641428.

[22] J. S. Page, "Conceptual cost estimating manual," no. 2, p. 248, 1996.

[23] R. T. et al, "Analysis synthesis and design of chemical processes," 2018, accessed 01/11/2020. [Online]. Available: http://folk.ntnu.no/skoge/prost/proceedings/focapd_2004/pdffiles/papers/075_46.pdf

[24] S. Jenkins, "2019 chemical engineering plant cost index annual average," 2020, accessed: 07/11/2020. [Online]. Available: https://www.chemengonline.com/2019-chemical-engineering-plant-\\cost-index-annual-average/

[25] D. for Communities and L. Government, "Land value estimates for policy appraisal," 2015, accessed: 07/11/2020. [Online]. Available: https://assets.publishing.service.gov.uk/government/uploads/system/uploads/attachment_data/file/407155/February_2015_Land_value_publication_FINAL.pdf

[26] *National Research Council (US) Chemical Sciences Roundtable. Impact of Advances in Computing and Communications Technologies on Chemical Science and Technology: Report of a Workshop. Needs and New Directions in Computing for the Chemical Process Industries*, 5th ed. Washington (DC): National Academies Press (US), 1999, accessed: 05/11/2020. [Online]. Available: https://www.ncbi.nlm.nih.gov/books/NBK44989/

[27] L. G. Papageorgiou and J. Westerlunda, "Improved performace in process plant layout problems using symmetry-breaking constraints ," Tech. Rep., 2004, accessed 27/11/2020. [Online]. Available: http://folk.ntnu.no/skoge/prost/proceedings/focapd_2004/pdffiles/papers/075_46.pdf

[28] *Chemical Engineering Economics*. Springer, Dordrecht, 1989, isbn: 978-94-011-6546-4.

[29] G. D. Ulrich and P. T. Vasudevan, "Short-cut piping costs," 2006, accessed: 17/11/2020. [Online]. Available: http://docshare01.docshare.tips/files/25990/259908259.pdf

An assessment of the United Kingdom's carbon capture readiness for natural gas reciprocating engines

Christopher Brooker and Raaghav Chaudhry
Department of Chemical Engineering, Imperial College London, U.K.

Abstract

As the United Kingdom moves to become more dependent on renewable sources of energy for its electricity grid, the problem of intermittency has yet to be addressed fully. Reciprocating engines provide a good source of backup electricity. This paper sets out to find out, for a given electrical output, the required land footprint of a coastal carbon capture plant. A 30 wt% MEA solution was used in this post-combustion amine scrubbing carbon capture process to ensure a 90% CO_2 capture rate from the incoming flue gas. Aspen PLUS© was used to simulate a rate-based model of the reaction between monoethanolamine and carbon dioxide. The major pieces of process equipment were sized for a range of electrical outputs. These were then placed in a sensible layout in a scale model, and the land footprint was calculated from this. The relationship between the land footprint and the electrical output was non-linear. This non-linearity was due to the increasing areas of equipment being overshadowed by the substantially larger safety distances between components, which resulted in the sharp decrease in area per plant MW from $42\,m^2/(MW)$ at 100 MW to $13\,m^2/(MW)$ at 400 MW. The area/MW seems to converge towards $12\,m^2/(MW)$ at 800 MW plant sizes and higher as the number of large process units increases, notably the absorber and direct contact cooler, because of the 18.3 m limitations on their diameters.

Keywords: CO_2 capture, Post-combustion capture, Aspen Plus, Reciprocating Engines, Carbon Capture Readiness, Process modelling

Introduction

Background

The United Kingdom's ambition to reduce emissions to net-zero by 2050 makes it one of the first major economies to do so. As the United Kingdom moves further away from greenhouse gases, there is the ongoing problem of intermittency and energy security. This has critical implications for the supply of energy in the UK. As the production of electricity from renewable energy sources, such as wind and solar, is not always consistent, there will be drops in the overall production of electricity as seen in Figure 1. A way to approach this problem is by having energy production sites that use fossil fuels, which can "top-up" any decreases in electricity production (IEA 2019) to fulfil demand. The key problem with the use of these technologies is that CO_2 will be produced and emitted into the atmosphere. However, this can be overcome by designing and building a robust carbon capture and storage facility (CCS), which can remove most of the CO_2 that is produced.

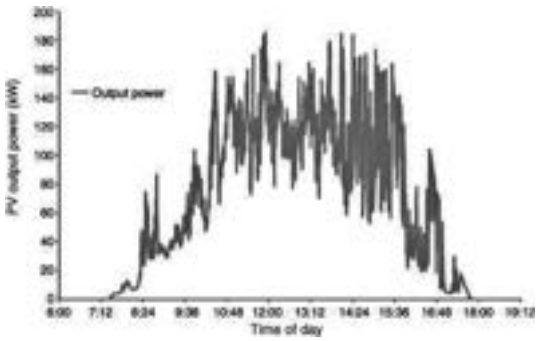

Figure 1: Solar PV output profile on a partly cloudy day at the DKASC in Alice Springs, Australia. Data found in Rowe et al. (2016)

The gaps in electrical production are likely to be supplied by natural gas engines. This is due to its fast start-up times. This would allow them to react to fluctuations in electricity production quickly. These can also integrate very well into the current electrical grid in the United Kingdom.

For compliance with Section 36 of the Electricity Act 1989, applications must demonstrate that there is "sufficient space available on or near the plant to accommodate carbon capture equipment" when it is "economically and technically viable" (Department for Business, Energy & Industrial Strategy 2018). This equipment must be sized correctly, so that the CCS system may process the emissions of the whole plant. These often remove between 80-90% of the CO_2 (Working Group III of the Intergovernmental Panel on Climate Change et al. 2005). However, merely sizing each unit is not enough for the overall land footprint, although it is a significant portion of it.

According to the IEA (2020), there are 20 operational and 3 under construction CCS plants across the world and 41 in various stages of development. This is a steady increase from 2016, which had 15 operational and 6 under construction CCS plants.

These plants often use post-combustion technology as it is well developed and is easier to retrofit a plant than using pre-combustion or oxy-fuel technologies. Within post-combustion technology, the most common type of capture technology used is amine scrubbing using monoethanolamine (MEA) solutions (Working Group III of the Intergovernmental Panel on Climate Change et al. 2005).

This source also states a fundamental problem in these processes is the flows of the chemical sorbents are often large and require large amounts of heat in order to be regenerated. Also, large gaseous flowrates are observed, due to the large presence of nitrogen and oxygen. This often comes at a high financial cost, which is often offset with a robust heat integration system.

There are other methods such as membrane separation and

distillation which can be used. However, these are often not implemented into larger-scale electricity production plants.

Literature Review

There are two main fuel types used in reciprocating engines, natural gas and oil. Both of these have their advantages and disadvantages, and the full details of these are outside the scope of this report. Natural gas is more commonly used when there are CHP applications (Agency 2016), and natural gas is also generally more favourable as it produces fewer emissions than oil, 181 t/(kWh) and 247 t/(kWh) respectively.

Although there is little data surrounding the land footprint for a CCS facility with reciprocating engines, there are papers regarding the land footprint for other technologies such as CCGT and IGCC (IEA 2020). However, this report by IEA fails to take into account different generation capacities and assumes a 500 MW production. Therefore the authors admit that there is some ambiguity surrounding the calculated net output of the plant. The report provides a reasonable estimate for this generation output, although, it would be inappropriate to assume that there is a linear correlation between generation output and area required for CCS.

Figure 2 illustrates the importance of land footprint for post-combustion, as 60% of land for CCGT with post-combustion capture and 5.5% of USCPF with post-combustion capture is the CCS facility.

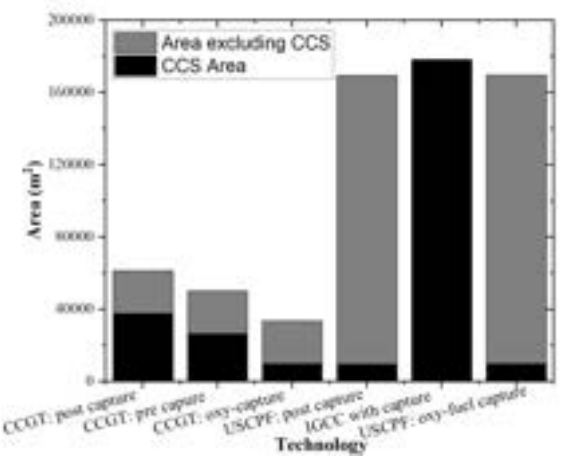

Figure 2: Data found in IEA Greenhouse Gas R&D Programme (IEA GHG), "CO_2 capture as a factor is power station investment decisions" 2006/8 (2006)

There is also some literature with regards, more specifically, to Section 36 of the Electricity Act 1989 (Florin & Fennell 2010). This paper looks more generally at technology types such as coal and CCGT. Many additional recommendations are made in this paper, such as an overall reduction in the land footprint for CCGT by 39%. Furthermore, Florin & Fennell (2010) states that it would be too simplistic to assume a linear correlation between electrical output and land footprint.

The common type of post-combustion absorption method is to use a 30 wt% solution of monoethanolamine (Chapel et al. 1999).

As stated in Rackley (2017), an operational advantage of using 30 wt% MEA is that there is "improved oxygen tolerance with low corrosivity". This allows for safer operation and reduced the frequency of maintenance requirements. However, a key disadvantage is that there is a higher solvent consumption compared to other technologies (Rackley 2017).

There are also many other technologies and methods that can be employed with regards to the mechanism of removing the CO_2. An alternative way is using different amine solvents, such as methyldiethanolamine (MDEA), or aqueous-carbonate based absorption.

Rackley explains how to choose an amine for amine-based absorption (Rackley 2017, p 116-117). With regards to the reaction rate, primary amines perform the best. On the contrary, with regards to regeneration and loading capacity, primary amines fair the worst. One can mix amines, such as MEA and MDEA. This can combine the benefits of each amine. However, this is not as often practised as 30 wt% MEA as previously stated.

Aqueous-carbonate based absorption involves using water to react with CO_2 and potassium carbonate (H_2CO_3) to form potassium bicarbonate ($KHCO_3$) (Rackley 2017, p. 119). The advantage of using this technology ahead of an amine-based absorption method, is the lower desportion energy requirement. This is between 0.9-1.6 GJ/(tCO_2) (Rackley 2017).

As stated in Foden (2018), the post-combustion capture area for a CCGT plant is 2.4 ha for a 500 MW plant. This means that the area requirement of the carbon capture process is approximately 48 m^2/(MW).

Aim and Novel Contribution

As seen in the Literature review section, there is currently no widely available carbon capture readiness report on reciprocating engines. The aim of this report is to fill this gap by finding the land footprint requirements for post-combustion carbon capture with natural gas reciprocating engines using 30 wt% MEA solution to ensure 90% CO_2 capture from the flue gas. An additional novelty is the design of the carbon capture amine scrubbing unit for various reciprocating engine plant sizes, rather than just one plant size stated in IEA (2020). With these findings, advice can be provided to UK legislation and Section 36 of the Electricity Act 1989 about the reciprocating engine carbon capture area requirements.

Source of Data and Key Assumptions

This process is assumed to be close to the coast. This means there was no need design a process to cool down the cooling water used, as the seawater can be used instead.

The initial emissions data for the reciprocating engine can be found in (U.S. Environmental Protection Agency Combined Heat and Power Partnership 2017, p 2-1.-2-27.). The data for a 9341 kW capacity engine has been used to determine the flue gas flowrates into the carbon capture palnt. The brand of the reciprocating engine that was used in this example was not expressly stated. However, during the work of this project, it was assumed to be WÄRTSILÄ© 34SG ENGINE (WÄRTSILÄ 2011). This created an emissions profile which was employed for the rest of the process. In the exhaust gas, the molar composition of the CO_2 post catalyst is 0.06 (2d.p.).

For the heat exchangers displayed in the block diagram (figure 3), the overall heat transfer coefficient and required surface area was found in Aspen PLUS V11©. As seen in Equation 1, U and ΔT_{lm} are assumed to be constant. Q is also assumed to increase linearly with increasing electrical output. As a result, A_s is also assumed to increase linearly.

$$Q = U \times A_s \times \Delta T_{lm} \tag{1}$$

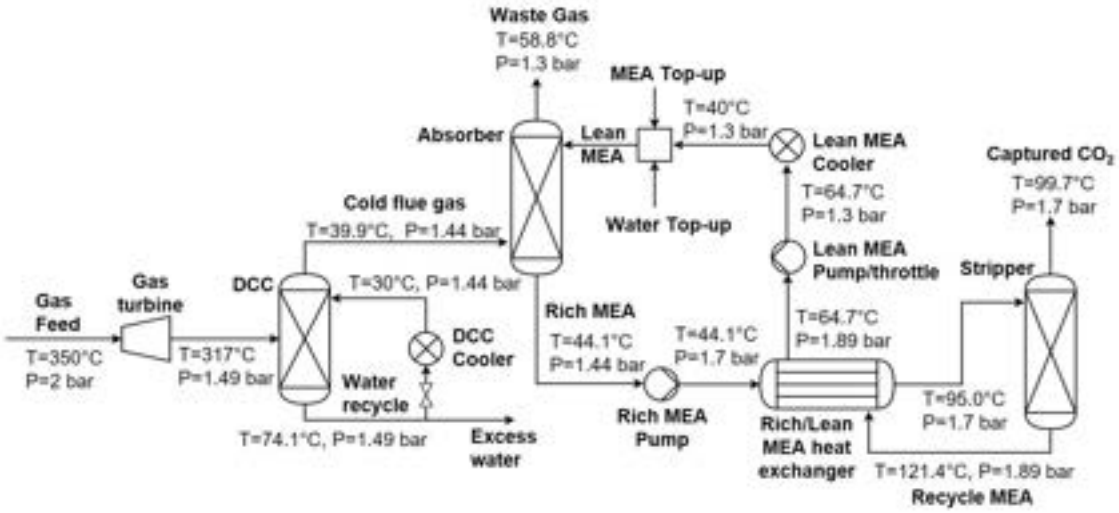

Figure 3: Amine scrubbing process block diagram

When sizing the heat exchangers throughout the process, it was decided that a fixed-tubesheet heat exchanger should be used. As stated in Mukherjee (1998), the maximum length of this type of heat exchanger was stated as 12 m and a maximum diameter of 3 m. Also, in Mukherjee (1998), the expected diameter of a tube within a shell-and-tube was stated to be 2 cm.

When sizing the pumps, as seen below, there are several assumed values. It was also assumed that the minor losses are negligible.

- Pipe Diameter (D) = 0.2 m
- Fanning friction (f) coefficient = 0.03
- Pipe length (L) is assumed to be the straight-line distance on the layout below
- The efficiency (η) = 80%

Amine degradation was another factor that should be considered. However, it was assumed that there was not enough oxygen in this system to justify an in-depth study of this phenomena.

Methods

Approach Summary

The method for designing a CCS process is set out in Foden (2018).

1. Establish a high-level design concept for the re-powered units.
2. Establish the likely CO_2 capture/storage requirement for the re-powered units using modelling.
3. Identify a preferred CO_2 capture technology for retrofit/integration to the re-powered units, and the likely impact of the preferred CO_2 capture technology on the performance of the re-powered units was modelled.
4. Establish the size of the main CO_2 capture plant/equipment using the above modelling
5. Preparation of an outline plot level plan to confirm that the CO_2 capture plant/equipment can be accommodated within the land currently available.

This method was rigorously followed. As this project was designed to provide a more general land footprint for varying electrical output, the additional steps in the method from Foden (2018) were not applicable, as they are site specific.

Flue Gas Composition

Emissions data was taken from U.S. Environmental Protection Agency Combined Heat and Power Partnership (2017) and used to find flowrates of the flue gas. The oxygen and nitrogen flowrates were missing from U.S. Environmental Protection Agency Combined Heat and Power Partnership (2017). As the natural gas flue can be assumed to be predominately methane (EIA 2020), the stoichiometric ratio between natural gas and oxygen was 2. The flowrates for CO_2 and volatile compounds (VOCs) were given, hence the flowrate of O_2 could be found. In this calculation, an excess of 5% of oxygen was used to ensure complete combustion. Given the flowrate of CO_2, the flowrate of H_2O could also be calculated. Finally, the flow of nitrogen was calculated, as air was being fed into the engine. The composition of air was assumed to be 79% and 21% N_2 and O_2 respectively. As there was a linear correlation for the flue gas flow against plant size, the values in Table 1 show the stream make-up in terms of molar flows per MW size of the reciprocating plant. The flue gas temperature leaving the engines was 350 °C with a high pressure of 2 bar. For this simulation, the trace amounts of NO_x (0.0004%), CO (0.002%) and VOC (0.002%) were ignored.

Table 1: Flue Gas Composition

Component	Molar flowrate ($kmol\,h^{-1}\,MW^{-1}$)	Mole fraction
H_2O	20.44	0.12
CO_2	10.22	0.06
N_2	128.79	0.76
O_2	10.20	0.06

Chemical Reactions and Reaction Kinetics

The reactions in this process can be seen in the mechanisms below (Luo & Wang 2017):

R1: Water dissociation:

$$2\,H_2O \rightleftharpoons H_3O^+ + OH^- \tag{2}$$

R2 Dissociation of CO_2:

$$CO_2 + 2\,H_2O \rightleftharpoons H_3O^+ + HCO_3{}^- \tag{3}$$

R3 Dissociation of carbonate:

$$HCO_3{}^- + H_2O \rightleftharpoons H_3O^+ + CO_3{}^{2-} \tag{4}$$

R4 Dissociation of the protonated amine:

$$MEAH^+ + H_2O \rightleftharpoons H_3O^+ + MEA \tag{5}$$

R5 carbonate formation:

$$MEACOO^- + H_2O \rightleftharpoons HCO_3{}^- + MEA \tag{6}$$

Equation 7 was used to calculate the equilibrium constants for the above chemical reactions, along with the specific correlations for each reaction stated in Table 2. K_J is the reaction equilibrium constant and C_1, C_2, C_3 and C_4 are the constants used to determine K_J.

$$\ln K_J = C_1 + \frac{C_2}{T} + C_3 \ln T + C_4\,T \tag{7}$$

Table 2: Correlations used to calculate the reaction equilibrium constant, K_J (Luo & Wang 2017)

Reaction	C_1	C_2	C_3	C_4
R1	132.8990	13445.90	22.4773	0
R2	231.4650	12092.10	36.7816	0
R3	216.0490	12431.70	35.4819	0
R4	4.9074	6166.12	0	0.00098482
R5	2.8898	3635.09	0	0

Aspen Simulation

The amine scrubbing process using a 30 wt% MEA solvent was simulated in Aspen PLUS V11©. The flowsheet for the model can be seen in Figure 3, where 90% of the CO_2 in the flue gas was captured in the absorber and then released in the stripper, where it would be further treated before storage. Simulations were run for 5 different plant sizes; 100, 200, 400, 650 and 800 MW. The electrolyte NTRL equation of state model (ElectNRTL) was used, as there were significant flowrates of charged compounds. A rate-based calculation model was used for the absorber and stripper columns to correctly model the mass transfer reactions occurring in this process. The direct contact cooler (DCC) was modelled in the following equilibrium based method as set out in Queiroz et al. (2012). Design specs and sensitivity analysis were run to further optimise the 3 column design parameters to ensure a 90% CO_2 recovery from the flue gas. A pressure drop of 0.01 bar per stage was also implemented.

Sulzer BX structured packing was used in the absorber column, contrarily, 1.5 in or 25 mm IMTP random packing was used in the stripper column. The DCC, however, used 1.5 in or 25 mm pall metal rings packing, as this follows a similar pilot process run by Cousins et al. (2012).

MEA and water losses were observed in both the waste gas and the captured CO_2 stream. Therefore, an input was required to make up these water and MEA flowrates in the system. This was conducted by topped-up the recycle lean MEA stream with MEA and Water top-ups, as seen in Figure 3.

Sizing of Columns

The absorber and stripper column diameters were sized according to Chapel et al. (1999) in meters (m). These values were used as the initial diameters in the Aspen model simulation. The equation used for the absorber was:

$$D_A = A \times \sqrt{\frac{(te/d)}{\%CO_2}} \tag{8}$$

The equation for the stripper column was:

$$D_S = 0.13 \times \sqrt{\frac{te}{d}} \tag{9}$$

Where:

A = 0.56 at 3% CO_2 to 0.62 for 13% CO_2

te/d = tonne/day CO_2 recovered

$\%CO_2$ = volume % CO_2 in flue gas before cooling, wet basis

Having calculated these initial diameters, the columns were simulated in Aspen and further changes were made to these dimensions to ensure a maximum column flooding of 80%.

The direct contact cooler column (DCC) was sized having completed initial calculated using the equations from Olander (1961). Design specs in Aspen determined the flowrate for the 30 °C water circulation requirements for cooling the flue gas to 40 °C, as well as the column diameter for this cooling process. A flooding of 80% was also used here.

Sizing of Heat Exchangers

The Rich/Lean MEA heat exchanger was designed to be a shell-and-tube counter-current heat exchanger, due to its safety and limited leakage in comparison to other types of exchangers. This uses the heat from the hot recycle MEA stream to heat up the Rich MEA stream to 95 °C.

The DCC and Lean MEA coolers were designed to be a counter-current heat exchanger, using 20 °C cooling water.

The length for the Rich/Lean MEA heat exchanger and the 2 coolers were fixed at 12 m. Given the diameter of the tubes also being fixed, the number of tubes in the shell must be adjusted using the equation below:

$$\text{Surface Area} = n \times \pi \times \text{diameter} \times \text{Length} \tag{10}$$

The heat exchangers that were used in this are assumed to be shell and tube heat exchangers, as they are the most widely used and still allow for good heat exchange whilst minimising leakage.

Sizing of Pumps

After the initial values below are found:

- Pipe Diameter (D)
- Pipe Length (L)
- Entry and Exit Pressures (P_1 and P_2)
- Entry and Exit elevation (z_1 and z_2)
- Specific gravity of the material (s_g)
- Friction Factor (f)
- Volumetric Flow rate (Q)
- Pump Efficiency (η)

These variables were inputted into the equations below (and also found in Brown (2003)):

$$v = \frac{Q}{A} \tag{11}$$

$$\frac{P_1}{s_g} + \frac{v^2}{2g} + z_1 + \varepsilon_p = \frac{P_2}{s_g} + \frac{v^2}{2g} + z_2 + hf \tag{12}$$

$$hf = f(\frac{L}{D})(\frac{v^2}{2g}) \tag{13}$$

$$\varepsilon_p = f(\frac{L}{D})(\frac{v^2}{2g}) - (\frac{P_1 - P_2}{s_g}) + (z_2 - z_1) \tag{14}$$

$$\text{Power} = \frac{s_g \cdot Q \cdot \varepsilon_p}{\eta} \tag{15}$$

Safety considerations

The safety distance for each process unit could be found in *Lees' loss prevention in the process industries : hazard identification, assessment, and control* (2005) and the process environment for amine scrubbing falls under "Zone 2". The source states that for a process to fall under "zone 2" it must be "A zone in which a flammable atmosphere is not likely to occur in normal operation and if it occurs only exist for a short time". These were added to the already sized process units to find the overall spacing requirements between process units.

When calculating the land footprint of the carbon capture plant, careful consideration was given to the safety radii of each process unit. No piece of process equipment should fall into the safety radius of another piece of equipment. Although, safety radii may overlap provided the first condition is not violated.

Table 3: Take from *Lees' loss prevention in the process industries : hazard identification, assessment, and control* (2005)

Liquid temperature (°C)	Safety Radius (m)
>100	6
100-200	20
200>	30

Plant Layout and Land Footprint Calculation

The overall layout of the plant was designed to reduce the land footprint within the relevant safety considerations. However, to ensure ease of operations, process units that were placed near each other and in a systematic way as shown in figure 3. This would also ensure that the layout of any piping network would be more simplistic, therefore reducing the overall cost of the plant.

The land footprint was then calculated by creating a 2D scale model of the plant, followed by surrounding the perimeter of the plant with a rectangle. The area of this rectangle was represented in the results as the total carbon capture land footprint. In this model, the Rich/Lean MEA heat exchanger, the Lean MEA heat exchanger and the DCC cooler were all represented as a rectangle. This was because they were horizontal cylinders. The DCC, absorber and stripper columns were represented as circles as they were vertical cylinders.

Results and Discussions

Absorber and Stripper diameter equation validation

The equations from Chapel et al. (1999) were used to determine the absorber and stripper diameters. As these were generalised equations which could be used for any column and packing type, further validation was conducted to ensure Equations 8 and 9 could be successfully implemented. Using Sinnott et al. (2005) and Perry et al. (2008), the diameters were determined using first principles, and the results showed that the diameters calculated from this method were 0.1 m smaller than the Chapel et al. (1999) method. This validated the use of Equations 8 and 9 for finding the initial absorber and stripper diameters.

CO_2 Loading

The flowrate of the 30 wt% MEA solution had to be initially determined to achieve a 90% CO_2 capture in the absorber. The model was first run using a 0.5 ratio of moles of CO_2:MEA. However, this was not enough to meet the requirements, as the waste gas leaving the absorber had a composition of greater than 10% CO_2. This was due to the high flowrates of MEACOO- and MEAH+ leaving the bottom of the stripper, as not all the CO_2 absorbed was able to be extracted in the stripper. Hence, a greater CO_2:MEA ratio was required. Studies showed that a typical carbon capture process used a CO_2:MEA molar ratio ranging from 0.15 - 0.35 (Bui et al. (2018)). The lower the ratio, the greater the absorption of CO_2 from the flue gas. However, the volume of water circulating around the system was much higher. This meant a greater reboiler duty was required to ensure the captured CO_2 could be released in the distillate of the stripper. Other studies have highlighted that a ratio of 0.3 was better, as this can further reduce the reboiler duty (Sakwattanapong et al. (2005)). Sensitivity analysis were conducted on the model, which showed that the optimum ratio for the moles of CO_2:MEA was 0.25, as anything lower required a much larger reboiler duty for 90% CO_2 extraction.

Reboiler Duty

The Aspen model was optimised to ensure a 90% carbon capture from the incoming flue gas. It was necessary for the reboiler duty to remain between the recommended duty of 3.6-4.0 GJ/(tCO_2

absorbed) for a 90% CO_2 extraction using a 30 wt% MEA solution stated by Bui et al. (2018). Due to the low concentration of CO_2 in the flue gas, 6 mole%, the simulation struggled to obtain a 90% CO_2 extraction at the lower end of this reboiler duty range. Previous studies have shown a reboiler duty of 3.98 $GJ/(tCO_2)$ for 600 MW CCGT natural gas power plant with has a slightly higher CO_2 composition of 8 mole% in its flue gas (Soltani et al. (2017)). Other studies working on natural gas CCGT carbon capture have also shown a range from 3.3 - 4.2 $GJ/(tCO_2)$ for the reboiler duty, with lower CO_2 compositions from 3 - 6 mole% having even higher reboiler duties (Sakwattanapong et al. (2005)). Sakwattanapong et al. (2005) also shows how the CO_2 loading plays an integral role in determining the reboiler duty. The paper shows how a lean CO_2 loading of 0.25 has a greater range of reboiler duties from 4.4 to 5.4 $GJ/(tCO_2)$. However, for this study, all process models were optimised to the upper limit of 4.0 $GJ/(tCO_2)$ as stated by Bui et al. (2018).

Model Optimisation

The DCC, absorber and stripper parameters were optimised by conducting sensitivity analysis. Table 4 shows the main optimised column parameters. The sensitivities ran on the column heights and number of stages showed a logarithmic trend. The diameters for these columns were increased from initial estimates to ensure the column operated at a maximum flooding of 80%. The change in diameter created no difference in the CO_2 capture rate. This can be seen particularly with the absorber column, which increased by 0.65 m, compared to no change in the stripper diameter. This change in the absorber is due to the column operating at pressures higher than atmospheric. The absorber column pressure was set to 1.3 bar in the top stage, and the top stage in the stripper was set to 1.7 bar. Higher pressures were explored in the stripper column as this should, in theory, increase the amount of CO_2 released from MEA. However, higher pressures showed marginal changes, about a 0.08% increase in CO_2 released per 0.1 bar increase in pressure. The maximum possible top stage pressure in the stripper column was 2 bar, as higher pressures meant the temperature of the stripper bottoms was above 125 °C. The temperature cannot be so high for the lean MEA recycle stream, as solvent degradation would be observed.

Table 4: Optimised Column Parameters

Absorber no. of stages	15	Absorber height	25 m
Stripper no. of stages	20	Stripper height	21 m
DCC no. of stages	6	DCC height	10 m

Different types of packing for the columns was also explored. A paper from Arachchige & Melaaen (2012) stated that Sulzer BX Gauze packing was the best available structured packing for the absorber due to the large large surface area of the packing, closely followed by Flexipac-1Y and Mellapak-350Y. Further simulations showed that either of these packings could be used as minimal changes were seen to the CO_2 absorption rate.

Model Limitations

The Aspen model further showed that although a 90% CO_2 recovery was attained, a lot of water was leaving the system with the CO_2 in the stripper distillate. The stream had a 30% mass fraction of water, which was a surprisingly large amount of water vapour in this stream. A large amount of water vapour leaving in this matter means a lot of reboiler heat was being used to vapourise the water, and therefore a larger reboiler duty would be required to extract the same amount of CO_2. A possible explanation could be the low lean CO_2 loading ratio used, as the lower the ratio, the greater the water circulating around the system. However, as discussed in the section above, a ratio of 0.25 was necessary to capture 90% of the incoming CO_2 in the flue gas.

Additionally, different reaction equations and kinetics were explored. The same reactions were stated by Tong et al. (2012) with different thermodynamic kinetic constants. The different rate constants made no difference to the model simulation. Furthermore, Zhang et al. (2009) and Lim et al. (2013) modelled the reactions slightly differently. The carbonate formation reaction (R5) and dissociation of carbonate (R2) were slightly altered. These reactions were also no longer equilibrium reactions, with the forward and backward rates of reaction being different. Running the process using these different reactions and kinetics showcased a slight increase in the CO_2 recovery in the stripper, a 0.5% increase. However, the initial issue regarding the high water flowrates leaving the stripper remained the same. Hence, the reason behind the high water flowrate out of the stripper must be due to the combined limitations of 4.0 $GJ/(tCO_2)$ for the reboiler duty and the 90% extraction of CO_2 being possibly only at a lean MEA stream ratio of 0.25 moles of CO_2:MEA. When increasing the reboiler duty, it became easier for the CO_2 to be released from its MEACOO- carbamate state, hence reducing the overall water distillate flowrate. At reboiler duties of 5 $GJ/(tCO_2)$, the water flowrate reduced by as much as 46%.

Another limitation was that the pure CO_2 composition of the gas stream leaving the final flash after being recovered from the stripper distillate was only 96.5% by mass. This should be 99%, as this was the requirement for CO_2 storage. Further separation of water is required and should be investigated. Also, a CO_2 compression train was required to pressurise the CO_2 to greater than 130 bar for transportation to the storage site. This was not modelled in this simulation and should be further investigated to ensure an accurate carbon capture plant size and plant heat requirements can be obtained.

Sizing of process units

Figure 4 shows that a square root relationship between the diameter of a given unit and electrical output. This was expected as the area of each unit should increase linearly with electrical output. Therefore, the diameters should increase in a square root fashion. It was interesting to notice how the increase in the absorber and DCC diameters were far greater than the stripper's. In fact, at 800 MW, the absorber diameter is almost double the stripper. This can be explained by the liquid to gas flows ratio within each column. As the absorber has the recycled lean MEA solution as well as the large flue gas flowrate, a much greater volume is required and therefore a larger diameter. On the other hand, the stripper has a similar liquid flowrate to the absorber (recycled lean MEA solution). However, the majority of the gas flowrate is cut down to only 90% of the CO_2 entering the absorber and trace amounts of N_2 and O_2. The DCC column would always remain greater than the absorber as it contains a higher liquid flowrate, due to the high water recirculating flowrate to cool down the hot flue gas.

As stated in Equation 8, there was a square root relationship between the flow of CO_2 and the diameter of the absorber column. The flow of CO_2 was also directly proportional to the electrical output. However, the maximum diameter for a column constraint, which was 18.3 m, has to be applied at larger electric outputs (Fluor 2017). This was illustrated in Figure 4. This problem was overcome in the plant layout by having multiple smaller columns, which would have the same area as the original larger column.

For the Absorber, it exceeds the 18.3 m at approximately 660 MW. Therefore, after this value, there must be two or more absorber columns. For the DCC, it exceeds the 18.3 m at approximately 440 MW. Therefore, after this value, there must be two or more DCC columns. Within the stated range of electrical output, there was no need to have more than one stripper column.

There was a similar problem with regards to the maximum diameter with the heat exchangers. As previously stated, the maximum diameter of the heat exchangers was 3 m. Each heat exchanger exceeds this value at varying points. The Rich/Lean MEA heat exchanger exceeds this limit at approximately 660 M. Overall, only two of these heat exchangers are ever needed. The Lean MEA heat exchanger exceeds the limit at approximately 440 M. Overall, only two of these heat exchangers were ever needed as the largest power plant modelled was 800 MW. The DCC cooler exceeds the limit earliest out of the three heat exchangers. It exceeds this limit at approximately 180 MW. Overall, 1, 2, 3, 4 and 5 heat exchangers were required in the 100, 200, 400, 650, 800 MW plants respectively.

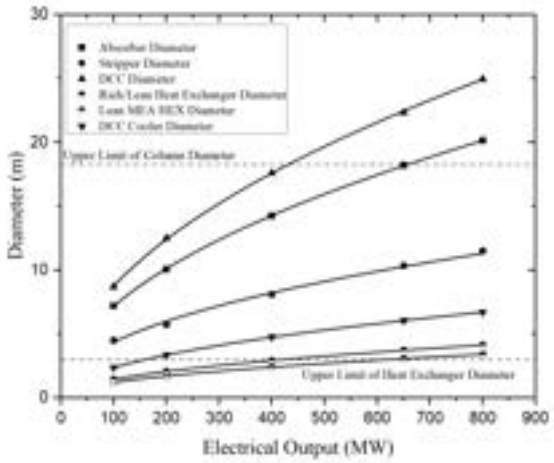

Figure 4: Illustrates how the diameters of the major process units change with increasing electrical output.

The limitations, as stated above, have a large impact on the overall land footprint of the plant, because each process unit must have a sufficient safety radius. This, in turn, has an impact on the layout of the plant and then on the land footprint.

There are other pieces of process equipment for which dimensions can be found, for example, the pump after the absorber and the flash column at the end of the process. These pieces of process equipment are not deemed to have a large enough land footprint to warrant a full sizing. However, the key pieces of information of the pump, notably heads and power are calculated and can be found in Figure 5.

Pump Sizing

For the Rich MEA Pump, it was unsurprising that increasing the electrical output has caused an increase in the electrical penalty. However, the Lean MEA Pump showed a very different behaviour. The lean MEA pump should actually be a throttle up to a plant size of 620 MW. After this, a pump was required. This was due to the lean MEA throttle being responsible for the drop in the pressure of the MEA solution from 1.89 bar when leaving the stripper to 1.3 bar before it enters the absorber. However, a pump is required to transport the fluid from the absorber to the stripper, as well as to the top of the absorber. This requires a unique balance between the pumping power required from the stripper to the absorber to overcome the frictional loses, as well as the power produced from decreasing the pressure. Between 100-400 MW, the electrical power required decreases. After 400 MW the electrical power required begins to increase. This is due to the fact that the volumetric flowrate has increased, so the power being produced from the pressure drop is no longer sufficient to pump the large volume of lean MEA and therefore after a plant size of 620 MW, an energy penalty would be incurred by installing a pump rather than a throttle. As to be expected, the head increases for each pump with increasing electrical power in a quadratic manner.

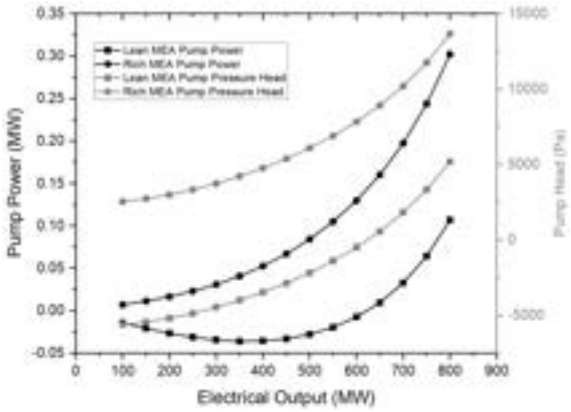

Figure 5: Illustrates how the power and pressure head of the two key pumps change with varying electrical output.

Heat integration considerations

Pump power requirements highlight an important aspect of the total power usage of a carbon capture plant. The power requirements for the gas turbine and the reboiler in the stripper are linear relationships, unlike the pump powers. The gas turbine has a net power of -54 kW per plant MW while reducing the flue gas pressure from 2 to 1.49 bar, whereas the reboiler requires 449.6 kW per plant MW. This power requirement for the reboiler is very large, and heat integration should be explored further. Due to time restraints, a proper heat integration for the reboiler was not conducted. The flue gas was cooled from 313 °C after leaving the gas turbine requires a large amount of cooling water reduce the temperature down to 40 °C. Therefore, there is an opportunity to utilise the energy from the hot flue gas. However, the flue gas cannot be used to heat the reboiler fully. A heat exchanger network would be required where some of the energy comes from the hot flue gas and the remaining from the reciprocating engines plant in the form of a CHP. This would, in turn, decrease the overall diameter of the DCC as a lower temperature flue gas would require

a smaller water recirculation flowrate and therefore decrease the land footprint from the DCC and the DCC cooler. Also, this increases the overall output of the reciprocating engines plant as the carbon capture energy demand decreases.

Plant Layout and Land Footprint

The generic layout of the plant can be found in Figure 6. This layout was replicated in all electrical outputs. This was done as it would facilitate easier operations in the plant if process units that were connected on the block diagram in Figure 3 were also close in the layout.

Table 5: Key for the components in Figure 6

Serial	Name of process unit
C1	Absorber
C2	Stripper
C3	DCC
H1	Rich/Lean MEA Heat Exchanger
H2	Lean MEA cooler
H3	DCC Cooler

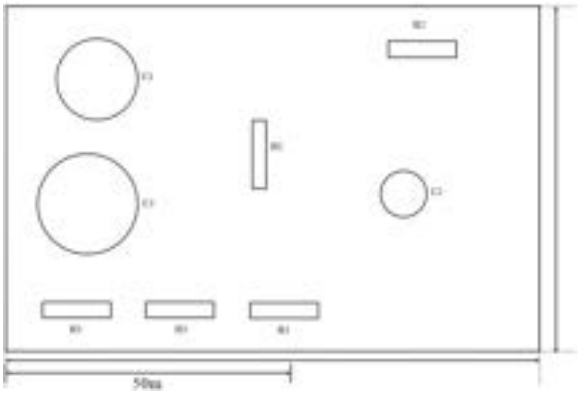

Figure 6: Land Footprint for a 400 MW plant

Although Figure 6 was the general basis in which all plants are based off, there are significant variations to the layout at 650 and 800 MW. At 650 MW a second DCC is required. At 800 MW a second absorber was required. These extra columns, predictably, have a large impact on the overall layout of the plant. However, the generic principles and placement of the process unit remains the same.

Figure 7 shows a trend which follows a statement that was said in Florin & Fennell (2010) in that the land footprint of a carbon capture plant cannot be approximated to a linear relationship.

It was interesting to notice how the area per plant MW decreases from $42\,\mathrm{m}^2/(\mathrm{MW})$ at 100 MW to $13\,\mathrm{m}^2/(\mathrm{MW})$ at 400 MW . In this range, only the number of DCC coolers changes. This showed how an increase of 2.5 m diameter of the stripper and the diameters of the DCC and absorber columns nearly doubled, the area per power plant MW decreases by a quarter. This highlights the fact from Figure 7 that the majority of the land footprint is comprised of safety distances between components and if the number of components stayed the same, the area per MW would continue to decrease for large plants and eventually reach a plateau. However, due to the limitations for the specific process equipment, a considerable rise in the area can be seen between 400 and 650 MW due to the addition of a DCC. Furthermore, the rise from 650 MW to 800 MW was due to an additional absorber. These additional components seem to stop the area per MW decreasing below $12.5\,\mathrm{m}^2/(\mathrm{MW})$. If these sizing limits did not exist, the land footprint would have decreased well below $10\,\mathrm{m}^2/(\mathrm{MW})$, possibly even lower than $5\,\mathrm{m}^2/(\mathrm{MW})$ for a large reciprocating engine plant.

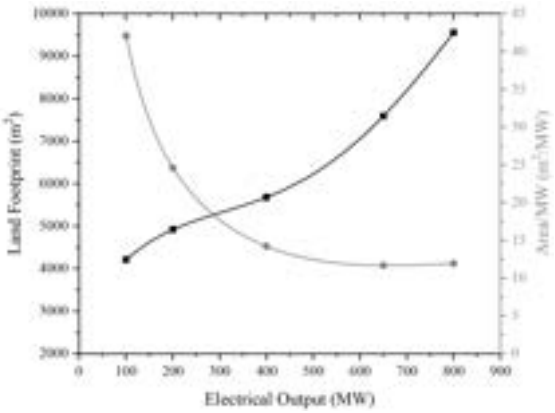

Figure 7: Shows how varying electrical output has an effect on the overall land footprint of the carbon capture plant from reciprocating engines.

As a rigorous plant optimisation method was not carried out, the values for the land footprint may require further revisions. However, as the layout follows a sensible logic, it is likely to be close to an optimal value.

As seen in Figure 6, there was a significant amount of land that was empty, predominately due to the safety radii. The layouts here are not optimised. The layouts are designed to ensure that process equipment should be near each other, whilst also minimising the land footprint. Further rigorous optimisation should be looked into to maybe further reduce the actual plant land footprint by utilising the empty space better.

Within the context of Figure 4, it was clear why there was a sharp increase in the land footprint requirements past 400 MW. This was due to multiple columns being used as previously discussed. These multiples of process units have such a large impact as they disrupt the general layout of the plant. Another factor was also that the safety radii constitutes a larger percentage of the overall size of the process unit when small units are used. These factors in tandem cause a large increase in land footprint.

These plant sizes only contain the 6 most crucial elements in a carbon capture plant, as shown in Table 5. An important structure missed out was the reboiler. It was expected that this kettle heat exchanger would have a noticeable impact on the land footprint and should be investigated further. Small plant equipment, such as the pumps, flash units and gas turbines at the start of the process to reduce the incoming flue gas pressure were not considered in the design. Each component was thought to have a small area and hence make a small impact on the land footprint. However, incorporating all these components together could cause a greater change than initially expected.

Furthermore, the results calculated are significantly smaller

than the proposed size found in the literature review. Foden (2018) states that a carbon capture area of $48\,m^2/(MW)$ is required for a 500 MW CCGT plant. This does include some additional large pieces of equipment which were not calculated in this study, such as the CO_2 compression equipment, admin buildings and storage tanks for the MEA and water top-up. Also, a substantial pieces of equipment were left out. The un/loading storage, electric power and steam, and cooling and utilities facilities. All these missing pieces of equipment accounted for nearly half the space requirement for the 500 MW plant in Foden (2018). This also explains the reasons behind a smaller carbon capture area than proposed for a CCGT with post-combustion storage in (Florin & Fennell 2010). Additionally, it was unclear on the exact carbon capture layout and the number of key components used in the design, for example the number of absorbers and DCC units. As seen from Figure 6, it was clear that a large increase in area was due to the additional units used in design. This could be another factor in the larger areas observed, apart from not sizing some critical large cooling equipment.

Also, the land availability around the power plant's location would play a key role in sizing the carbon capture facility. Each carbon capture facility would be unique. This model assumes that any terrain is available. However, some sites may not have the luxury of having a perfect rectangular area, and so some components may be unable to be placed next to each other. For example, if the land available had a small width, the components would have to be placed in a single file line causing the carbon capture facility land footprint to increase substantially. Therefore, this study provides a general overview of the area required for a carbon capture plant and plant sizing should be carried out for each unique site to optimise the layout of the available land at the specific plant site.

Cooling Requirement Considerations

Cooling requirements for the use of cooling water in heat exchangers can have a significant impact on the carbon capture area. However, within this plant, it has not been sized, due to the original assumption of a coastal plant area. If the plant in question is near the coast, cooling towers are not required. Although it was assumed that this plant was close the coast, it would be sensible and appropriate to suggest a land footprint for a plant which may not have this luxury. A series of cooling towers, which use air to cool the water, are commonly used to generate the cooling water plant requirements at temperatures of $20\,^{\circ}C$. These often take up much of the land surrounding them.

The CCR report for the 2500 MW CCGT plant as found in Sangster (2017), and had a cooling land footprint of approximately $0.457\,km^2$, giving a land footprint per MW of $18.3\,m^2/(MW)$.

This value should be treated with a large amount of scepticism. The value stated is simply for reference and it may not be appropriate to generalise. The electrical output for this plant is very high and so generalising down to 800 MW may not be appropriate. However, if this can be generalised, it would shift the Area/MW plant up by $18.3\,m^2/(MW)$. Meaning the graph would level off at 30.3 rather than $12\,m^2/(MW)$.

Conclusion

This paper has presented how the layout of a post-combustion carbon capture plant should be carried out when attached to reciprocating engines. In turn, it has been found that the relationship between Electrical Plant Output and Land Footprint is non-linear. This non-linearity is due to the increasing areas of equipment being marginal changes compared to the substantially larger safety distances between components which resulted in the sharp decrease from $42\,m^2/(MW)$ at 100 MW to $13\,m^2/(MW)$ at 400 MW. The area/MW seems to converge towards $12\,m^2/(MW)$ at 800 MW plant sizes and higher due to the number of large process units, the absorber and DCC, increases because of the limitations on the dimensions of process units. One key assumption that the plant facility was coastal can cause significant changes to the carbon capture area requirements. Further studies have shown how over half a typical carbon capture layout is occupied by air coolers to meet the high cooling water demands from the DCC and lean MEA coolers.

Outlook

As seen from the section regarding the high cooling requirements, it is essential for a rigorous modelling for the area required for cooling to be looked into. When providing a carbon capture process plant area, it is important to note not all plants are in a coastal location and the cooling space required will be substantial - at least accounting for half the overall area. Furthermore to ensure a proper and accurate overall carbon capture plant size, other process equipment, such as the reboiler, should also be sized.

There is much scope for further research in this area. One area, in particular, is that the layout of the plant is not optimised. This, in itself, is a very complex problem. Within this problem, there is also scope to research for a more rigorous model for safety distances from *Lees' loss prevention in the process industries : hazard identification, assessment, and control* (2005).

The model that has been presented is a 2D ("bird's eye view") way. This could be taken further by using a 3D model, including the heights of different process units. This research would provide a more holistic view of the process and would allow for further research to be done on environmental outcomes of the process.
As the 800 MW has 5 DCC coolers due to unit size limitations, the use of other heat exchangers, apart from shell and tube, should be further explored to reduce the land footprint requirements. Plate heat exchangers could be a good starting point, as these are more compact and therefore take up less space. It would be important to find the unit size limitations for these heat exchangers as well.

Finally, a robust heat integration method should be explored to heat up the steam in the reboiler. This would reduce the energy penalty a plant faces by incorporating a carbon capture process.

Acknowledgements

We would like to thank Justin Driver for his advice and guidance during this project, particularly with Aspen Plus.

References

Agency, U. E. P. (2016), 'Combined heat and power technology fact sheets series: Reciprocating engines'.
URL: *https://www.energy.gov/sites/prod/files/2016/09/f33/CHP-Recip %20Engines.pdf*
Date Accessed 11/11/2020

Arachchige, U. S. P. R. & Melaaen, M. C. (2012), Selection of packing material for gas absorption.

Brown, G. O. (2003), The history of the darcy-weisbach equation for pipe flow resistance, *in* 'Environmental and Water Resources History', pp. 34–43.

Bui, M., Adjiman, C. S., Bardow, A., Anthony, E. J., Boston, A., Brown, S., Fennell, P. S., Fuss, S., Galindo, Amparo and, H. L. A., Hallett,

J. P., Herzog, H. J., Jackson, G., Kemper, J., Krevor, S., Maitland, G. C., Matuszewski, M., Metcalfe, I. S., Petit, C., Puxty, G., Reimer, J., Reiner, D. M., Rubin, E. S., Scott, S. A., Shah, N., Smit, B., Trusler, J. P. M., Webley, P., Wilcox, J. & Mac Dowell, N. (2018), 'Carbon capture and storage (ccs): The way forward.', *Energy Environmental Science 11.5 (2018): 1062-176.* .

Chapel, D. G., Mariz, C. L. & Ernest, J. (1999), Recovery of CO_2 from flue gases: Commercial trends.

Cousins, A., Cottrell, A., Lawson, A., Huang, S. & Feron, P. H. (2012), 'Model verification and evaluation of the rich-split process modification at an australian-based post combustion co 2 capture pilot plant', *Greenhouse Gases: Science and Technology* **2**(5), 329–345.

Department for Business, Energy & Industrial Strategy (2018), 'Consents and planning applications for national energy infrastructure projects'.
URL: *https://www.gov.uk/guidance /consents-and-planning-applications-for-national-energy-infrastructure-projectscarbon-capture-readiness-ccr*
Date Accessed: 11/11/2020

EIA (2020), 'Natural gas explained'.
URL: *https://www.eia.gov/energyexplained/natural-gas/*
date accessed 14/12/2020

Florin, N. & Fennell, P. (2010), Assessment of the validity of —Approximate minimum land footprint for some types of CO2 capture plant‖ provided as a guide to the Environment Agency assessment of Carbon Capture Readiness in DECC's CCR Guide for Applications under Section 36 of the Electricity Act 1989 , Technical report, Imperial College London.

Fluor (2017), 'Fluor Econamine FG Plus^{SM}'.
URL: *web.archive.org/web/20180130163806/http://www.fluor.com:80/about-fluor/corporate-information/technologies/fluor-econamine-fg-plus*
date accessed 13/12/2020

Foden, A. (2018), The drax power (generating stations) order; carbon capture readiness statement, Technical report, WSP UK Limited.

IEA (2019), 'Natural gas-fired reciprocating engines are being deployed more to balance renewables'.

IEA (2020), 'World large-scale ccus facilities operating and in development, 2010-2020'.
URL: *https://www.iea.org/data-and-statistics/charts/world-large-scale-ccus-facilities-operating-and-in-development-2010-2020*
Date Accessed 11/11/2020

IEA Greenhouse Gas R&D Programme (IEA GHG), "CO_2 capture as a factor is power station investment decisions" 2006/8 (2006), CO_2 capture as a factor in power station investment decisions, Technical report, IEA.

Lees' loss prevention in the process industries : hazard identification, assessment, and control (2005), 3rd ed. edn, Elsevier Butterworth-Heinemann, Amsterdam ; London.

Lim, Y., Kim, J., Jung, J., Lee, C. S. & Han, C. (2013), 'Modeling and simulation of co2 capture process for coal- based power plant using amine solvent in south korea', *Energy procedia, 2013, Vol.37, p.1855-1862* .

Luo, X. & Wang, M. (2017), 'Improving prediction accuracy of a rate-based model of an mea-based carbon capture process for large-scale commercial deployment', *Engineering (Beijing, China)* **3**(2), 232–243.

Mukherjee, R. (1998), 'Effectively design shell-and-tube heat exchangers', *Chemical Engineering Progress* **94**, 21–37.

Olander, D. (1961), 'Design of direct contact cooler-condensers', *Industrial and engineering chemistry* **53**(2), 121–126.

Perry, R. H., Green, D. W. & ProQuest (2008), *Perry's Chemical Engineers' Handbook*, 8th ed. edn, New York: McGraw-Hill.

Queiroz, J. A., Rodrigues, V. M., Matos, H. A. & Martins, F. (2012), 'Modeling of existing cooling towers in aspen plus using an equilibrium stage method', *Energy conversion and management* **64**, 473–481.

Rackley, Stephen A., a. (2017), *Carbon capture and storage*, second edition. edn.

Rowe, D., Sayeef, S. & Platt, G. (2016), Chapter 7 - intermittency: It's the short-term that matters, *in* F. P. Sioshansi, ed., 'Future of Utilities Utilities of the Future', Academic Press, Boston, pp. 129 – 150.
URL: *http://www.sciencedirect.com/science/article/pii/B9780128042496000075*
Date Accessed 16/12/2020

Sakwattanapong, R., Aroonwilas, A. & Veawab, A. (2005), 'Behavior of reboiler heat duty for co2 capture plants using regenerable single and blended alkanolamines', *Industrial engineering chemistry research,2005-06-08, Vol.44 (12),p.4465-4473* .

Sangster, M. (2017), The Eggborough CCGT (Generating Station) Order Land within and adjacent to the Eggborough Power Station site, Goole, East Yorkshire DN14 0BS, Technical report, Eggborough Power Limited.

Sinnott, R. K., Coulson, J. M. & Richardson, J. F. (2005), *Chemical Engineering Design*, 4th ed. edn, Oxford : Elsevier Butterworth-Heinemann.

Soltani, S., Fennell, P. & Mac Dowell, N. (2017), 'A parametric study of co2 capture from gas-fired power plants using monoethanolamine (mea)', *International Journal of Greenhouse Gas Control. Volume 63 (2017); Pp 321-328: 321-328.* .

Tong, D., Trusler, J. M., Maitland, G. C., Gibbins, J. & Fennell, P. S. (2012), 'Solubility of carbon dioxide in aqueous solution of monoethanolamine or 2-amino-2-methyl-1-propanol: Experimental measurements and modelling', *International journal of greenhouse gas control, 2012-01, Vol.6, p.37-47* .

U.S. Environmental Protection Agency Combined Heat and Power Partnership (2017), 'Catalog of chp technologies'.
URL: *https://www.epa.gov/sites /production/files/2015-07/documents/catalog_of_chp_technologies.pdf*
date accessed 16/11/2020

WÄRTSILÄ (2011), 'WÄRTSILÄ 34SG ENGINE TECHNOLOGY'.
URL: *http://www.gastopowerjournal.com /documents/34SG_ET_082011.pdf*
date accessed 16/11/2020

Working Group III of the Intergovernmental Panel on Climate Change, Metz, B., Davidson, O., de Coninck, H., Loos, M. & Meyer, L. (2005), *Carbon Dioxide Capture and Storage*, Cambridge University Press.

Zhang, Y., Chen, H., Chen, C.-C., Plaza, J. M., Dugas, R. & Rochelle, G. T. (2009), 'Rate-based process modeling study of co2 capture with aqueous monoethanolamine solution', *Industrial engineering chemistry research, 2009-10-21, Vol.48 (20), p.9233-9246* .

Decarbonisation of the UK Residential Sector using Spatial Agent Characterisation

Yu Shan Koh and Zong Hao Lee
Department of Chemical Engineering, Imperial College London, U.K.

Abstract

Decarbonising the residential sector is important to reduce UK's greenhouse gas emissions. For emissions reduction policies to be effective, a better understanding of consumers behaviour and characteristics is required. This paper presents a spatial agent characterisation approach that clusters energy density, heat demand per capita and GDP per capita at a 1km^2 resolution to define spatial agents' objectives when adopting heating technologies. Spatial agent clustering is done using Jenks Optimization Method and DBSCAN (Density-Based Spatial Clustering of Applications with Noise). The agents' objectives for importance of types of cost when adopting heating technologies are then determined. Results show a range of characteristics for the spatial agents, each with a different preference for types of cost based on their income level and energy consumption. The spatial agents results can be readily used in MUSE (ModUlar energy systems Simulation Environment), which is an Integrated Assessment Model that utilises agent-based modelling.

1 Introduction

The UK has committed to achieving a net-zero greenhouse gas (GHG) emissions goal by 2050 [14]. Although the GHG emission has been reduced by 43% in 2018 relative to 1990 levels [41], the wide gap towards achieving the net-zero goal requires aggressive decarbonisation [40]. Currently, 23% of the UK's GHG emissions originate from the residential sector [13]. This is partly due to the face that the UK has one of the oldest housing stock in Europe [20], where the old dwellings tend to have poor thermal insulation. As a result, the heating consumption in the residential sector accounts for 78% of the overall residential energy consumption [14]. Therefore, decarbonisation of the residential sector, especially for heating technologies, is a crucial step to achieve the UK's net zero target.

When deciding on decarbonisation pathways low-carbon heating technology, a strong determining factor for mass adoption is the resident's household income [28]. This is because any radical shift in cleaner heating technologies may be felt most acutely among low-income households as heating cost makes up a high proportion of their income [16]. The cost gap between cheap heating technologies, which are often the most polluting, and cleaner alternatives influences the heating technologies uptake [47]. It is therefore vital to assess the relationship between economic factors, energy consumption, and geographical location to understand the residents' investment decision-making.

This paper aims to characterise spatial groups of residents who share a similar behaviour, also known as spatial agents, in the residential sector by examining the agents' heat energy consumption and financial status in high resolution (1km x 1 km). A comprehensive understanding of these agents is required to examine their investment behaviour in low-carbon technologies adoption before deploying a large-scale commercialisation of low-carbon technologies. Therefore, spatial agents with a range of attributes are defined to assess their investment behaviour based on their respective objectives. The defined spatial agents can then be readily integrated in MUSE [1] (ModUlar energy systems Simulation Environment) to outline the heating technology investment behaviour of the agents in future research.

This paper is structured as follows. Section 2 describes the literature review of the work that has been done to evaluate decarbonisation pathways in the residential sector. Section 3 explores the methods for clustering and agent characterisation. Section 4 describes the characteristics of the spatial agents. Finally, Section 5 outlines the conclusion, limitations and outlook of this paper.

2 Literature Review

2 .1 Factors affecting investment in low carbon technology

Energy density (ED), covering both heating and cooling demand density, influences the overall energy investment costs [45]. Extensive research has been carried out on evaluating energy density spatially in energy system models. When evaluating where district energy network could be expanded, Finney et al.[18] used a Geographical Information System (GIS) spatial model to map existing and emerging heat sources and sinks in Sheffield, England. Similarly, Nielsen et al. [39] mapped the heat density and associated costs to determine the economic feasibility of deploying district heating in Denmark. The results show that implementation of heating technologies are dependent on spatial heat densities. Jalil-Vega [24] also developed a linear opti-

[1] MUSE is a bottom-up technologically rich Integrated Assessment Model (IAM) of energy systems that simulate real-world decisions of investors by modelling the investment and operational decisions specific to each sector.

misation model to evaluate the most cost-effective heat decarbonisation pathways to meet the heat density demand in UK cities.

Heat density per capita (HDpc) is not a common metric used in evaluating energy transition. Instead, it is used as an intermediate step to calculate heat density [37]. This presents a gap in knowledge because considering energy use per capita provides a more accurate understanding of the energy performance [19]. Platten, Mangold and Mjörnell [51] found that considering only energy density without population count when assessing heating technologies puts an unfair burden on low-income households who generally have a low energy per capita. These households need to bear the costs of retrofitting projects within their area, even if they account for a disproportionately small amount of the overall energy density as compared to the higher-income households. Therefore, to alleviate this unjust burden on low-income households, this paper recognises the importance of incorporating HDpc when considering decarbonisation pathways.

To ensure energy policies are more inclusive to low-income households, Gross Domestic Product per capita (GDPpc) should also be included in the analysis. While there exist many studies on the correlation between GDPpc (i.e income per capita) and energy demand [30] [46], studies that relate spatial data for GDPpc and energy consumption are rarely undertaken due to the lack of availability of spatial income data [36]. Therefore, this paper uses spatial GDPpc data as a proxy for income per capita to capture the effect of income on overall energy consumption.

The studies outlined above emphasise the importance of assessing ED, HDpc and GDPpc on a spatial basis when deciding on the complementary heating technologies. However, spatial resolution also plays a key role when determining decarbonisation pathways in energy system modelling [43]. Jalil-Vega [24] found that analysing heat networks at a higher resolution helped determine which zones would benefit more or faster from heat networks, which allows for more cost-effective energy planning. The results showed that there were up to around 50% difference in heat technology uptake when considering different resolutions. The studies aforementioned were done at resolutions lower than what was done in this paper. For studies that have been done at high resolution, the scope has been limited to small-scale studies [37].

It is clear that for high resolution spatial analysis, current literature is limited to small-scale analysis and does not assess ED, HDpc and GDPpc together. This paper aims to bridge the gap by linking high resolution spatial analysis of heat demand and GDP together for the entire United Kingdom to highlight suitable decarbonisation pathways.

2 .2 Clustering techniques

To perform pattern grouping in energy data, clustering is one of the most commonly used techniques to segment consumers with similar energy consumption [22]. Insights into the characteristics of cluster are useful to improve heat network management and the accuracy load forecasting [3]. For energy data clustering, most research point towards K-means clustering [1]. The limitations of K-means are shown in Table 1. To overcome its limitations, other classification method and clustering method have been reviewed in this paper.

Jenks Natural Breaks, also known as Jenks optimization is one of the most widely used method in spatial analysis[9]. Jenks optimization classifies data into different classes according to predefined number of breaks [25]. Ref. [6] found that Jenks optimization has a high accuracy and good adaptability on spatial analysis. Jenks optimization differs slightly from K-means in which K-means only minimise Euclidean distance within clusters, but Jenks optimization also maximises the deviation between clusters [29]. This feature, known as goodness of variance fit is particularly useful to classify values in heavily-skewed distribution. [31].

Classification method alone is not sufficient to consider the combined effect of different attributes on investment behaviour, so another clustering method is explored to fill in this gap. Density Based Spatial Clustering of Applications with Noise (DBSCAN) was found to outperform K-means because of its ability to exclude noise points and discover clusters of arbitrary shape [56]. Besides, DBSCAN does not require pre-defined number of clusters, therefore reducing human bias[55]. The main benefits of DBSCAN to the data used in this paper are its ability to separate clusters of high density from low density data points, and its robustness to outliers.

It appears that multi-dimensional clustering methods are not popular as of today. 3D clustering could be used to combine multiple feature in a single procedure. For this reason, in this paper, three attributes are investigated in a 3D space using DBSCAN to identify the neighbouring points that fall within a sphere due to its proximity which indicates similarity in characteristics. Different from the common approaches that use 1D clustering, usually either only energy demand or socio-economic index, this paper aims to combine three indices in a 3D DBSCAN clustering to create investors' spatial profiles in a 1km^2 resolution.

2 .3 Agent Characterisation

Agent-based modeling (ABM) is a model that simulates the interactions between agents that have a set of attributes, and describes their decicision-making based on a set of rules. [5].

Although there are studies that apply ABM in modelling energy consumption in the residential sector [58], most work do not consider the spatial components in the ABM. Spatial ABM is more commonly used in the other industries [35]. This highlights a gap in current studies because utilising spatial data in ABM models allows understanding of the interactions between agents depending on their specific lo-

Clustering Method	Features	Examples of References
K-means	Sensitive to the number of clusters specified[55]	Segmentation of heat consumption intensity to characterise building behaviour at urban scale [21]
	Only minimises distance within cluster [1]	Classification of spatio-temporal electricity demand profiles at urban scale [21]
	Does not work well with outliers	Classification of heat exchange station based on the smart meter recordings [50]
	Only clusters spherical shape data	
Jenks Natural Breaks	Depends on the number of breaks specified	GIS approach on classification of geothermal potential[54]
	Minimises distance within cluster and maximises the deviation between cluster [29]	Default classification method on mapping software[10]
	Performs well in heavily-skewed data[31]	Differentiation of ecosystem bundles for landscape planning [32]
DBSCAN	Number of clusters need not be specified [55]	Disaggregation of electrical meter data to identify distinct groups of loads[11]
	Separate high density data points from low density data points	Clustering West Nile Virus spatio-temporal data
	Handles outliers efficiently[7]	
	Can identify arbitrary shape data [56]	

Table 1: Comparison of clustering methods and their used applications

cation [8]. Ref. [49] found that considering spatial components in ABM reduces spatial agglomeration effects that alters the interactions among the agents, which subsequently influences the agents' decision-making process. Therefore, to address this gap, this paper characterises spatial agent based on the output from spatial clustering methods.

To address the gaps mentioned above, this paper aims to assess three attributes (ED, HDpc GDPpc) together at high resolution 1km and apply clustering method to create spatial agents that represent different investment behaviour across different locations in the UK. These defined spatial agents input can be readily integrated in Agent-based models for future research.

3 Methodology

This paper presents two approaches to analyse decarbonisation pathways in the UK residential sector: (1) High resolution spatial clustering method with GIS approach to assess the ED, HDpc and the wealth of residents; (2) Agent characterisation to define spatial agents' objectives and investment behaviour. The combination of these approaches assesses the spatial agents' energy consumption behaviour and their financial status, and provides data for to project the future heating technology investment.

3 .1 Spatial Clustering

3 .1.1 Data Collection

Three attributes — GDP per capita, energy density and heat demand per capita — are chosen to analyse the UK residents' energy consumption and their financial status, which influences their adoption of low-carbon heating technology infrastructure. Datasets used in this paper (cite diego) contain values of attributes in 1km^2 resolution and accounts for 84.2% of the UK's area and 99.8% of UK population.

3 .1.2 Clustering Methods

Clustering is a data analysis tool for grouping objects with similar characteristics, which has been widely used in the energy sector to assess spatio-temporal electricity demand [52]. In this paper, "band" refers to the bound of a cluster. In this paper, Jenks optimization method is performed on ED and HDpc individually to aggregate spatial areas with similar characteristics. It determines the optimal breakpoints to classify values into classes by minimising the variance within classes, while maximising the differences between between classes' mean, as defined in Eq. Prior to classification, the Elbow Method is used to determine the optimal number of clusters. The Elbow Method aims to minimise the sum of squared errors (SSE), which are the distances between each data point and its cluster's mean, as shown in Eq.1 [48] and 2[57]. The optimal number of clusters are determined from the 'knee' of the plot, which is the point where further increase in clusters do not have a significant impact on the SSE.

$$S_k = \sum_{r=1}^{k} \frac{1}{n_r} D_r) \tag{1}$$

$$D_r = \sum_{i=1}^{n_r - 1} \sum_{i=1}^{n_r} ||d_i - d_i||^2 \tag{2}$$

where S_k is the sum of squares, k is the cluster number, n_r is the total members' points in the cluster r, and D_r is the sum of squared distances between d_i and d_j.

Firstly, Jenks optimization method is applied to the clustering on ED and HDpc, while the clusters on GDPpc are determined from (Diego Moya, personal communication, November 2, 2020). However, Jenks optimization method cannot be used directly on the HDpc data due to the presence of outliers, which results in a heavily skewed dataset. To overcome this limitation, since most of the data points (99.75%) are below the mean value, Jenks optimization method is only applied on values below the mean of 23 MWh/cap-yr to obtain HDpc bands. The values above the mean value are considered as one cluster. Each 1 km^2 grid that falls within the bands are assigned to its respective band. The shapefiles (a geospatial vector data) containing geographical coordinates and its corresponding attributes values and bands were overlapped. The overlapped grids that belong to the same band in every attribute are aggregated to form the spatial agents used in this study, and the results are displayed in QGIS 3.16.0 software [2].

The clusters from Jenks optimization method is a result of clustering the attributes independently, which leads to a large number of unique spatial agents. To reduce the number of agents and consider the relationships between the three attributes, Density-Based Spatial Clustering of Applications with Noise (DBSCAN), a density-based clustering algorithm, is chosen to perform clustering on the cluster results from Jenks optimization method based on the proximity of mean values of the three attributes in a 3D space. DBSCAN measures the number of objects in a given space, groups dense regions into a group, and label points in low density regions as noise points [17]. It is fast and reliable in handling large spatial data [59] compared to other hierarchical and partitioning clustering methods because the algorithm does not require manual input of number of clusters prior to clustering [42]. Thus, DBSCAN is the most suitable to cluster the 3D spatial data in this paper. The DBSCAN algorithm is explained in Appendix 7 .1.

DBSCAN requires input information on these parameters [26]:
1. Epsilon (Eps): Radius of the cluster or a Eps-neighborhood
2. $MinPts$: Minimum number of points to form a cluster

DBSCAN algorithm divides a dataset into groups of high and low density regions based on the rules stated in Appendix 7 .1. In summary, DBSCAN creates a sphere of radius = Eps around every data point. DBSCAN then classifies them into core object, border object and noise. If the circle around a point contains at at least $MinPts$ number of points, the data point is considered as core object. If the number of points is less than $MinPts$, the data point is classified as border object. If the data point is neither core object nor border object, then it is treated as noise. The DBSCAN algorithm repeats the process until all points have been visited.

For the initial input parameters, the heuristic suggests $MinPtsln(n)$ where n is the number of data points [4]. Eps is determined from the 'knee' in the K-Nearest Neighbour (KNN) plot of average distance between each point and its nearest 'k' number of neighbouring points, where k = $MinPts$ [17] in Figure 9.

To account for the differences in magnitude of the 3 attributes, DBSCAN is performed on scaled values, that is calculated using Eq. 3 [15]. The DBSCAN algorithm explores each point in the 3D model and groups data points together if the points fall within the radius equal to Eps and meet a specified density threshold [38]. This procedure allows identification of clusters of arbitrary shapes in 3D space. DBSCAN clustering technique is applied the second time on the clusters that contains >25% high population size. To meet the input criteria of MUSE, clusters with less than 5% population were combined with the closest Eps-neighbor to form the spatial agents.

$$z = \frac{x - \mu}{\sigma} \tag{3}$$

where z is the scaled value or known as Z Score, x is the attribute value, μ is the mean of the data and σ is the standard deviation of the data.

3 .2 Agent Characterisation

3 .2.1 Agent Definition

In this paper, spatial agents are defined at a 1 km^2 resolution, based on the three attributes: GDPpc, HDpc, ED. Each agent represents different type of UK residents, and its characteristics can be integrated into ABM to simulate the decision-making of different agents under different scenarios. [27]

3 .2.2 Objectives

Financial concern is the most important factor to a homeowner's decision when adopting heating technologies [23][34]. Considering the financial aspects of agents when evaluating the feasibility of implementing low-carbon technologies is crucial to ensure that the benefits of the energy transition are realised by both the lower and higher-income households [30]. In this paper, financial aspects will first be taken into account to assess the relative importance of different types of cost for each agent depending on their financial status, before further characterising the agents based on their energy consumption.

Since the spatial agents prioritises objectives based on economic metrics, the GDPpc of UK residents are segmented into low, medium and high income brackets. The commonly used threshold in the UK for low income is at 60% of the national median income [23], whereas the high income threshold is at 1.5 times the median income [53]. Medium

[2] Quantum Geographical Information System (QGIS) is a free and open-source platform for analysing and editing spatial data.

income levels are considered to be the income between the low and high income thresholds. Each income bracket prioritises a different set of objectives in its decision-making process.

The following objectives were chosen to determine an agent's decision making process:
1. Capital cost: The ability to pay the immediate expenses, in this case, the upfront installation cost, highly depends on the agents' availability of savings and capital. [23]
2. Equivalent Annual Cost (EAC): The annualised cost over the lifetime of an asset in addition to the annual maintenance cost determines the attractiveness of a long-term investment.
3. Operating cost: The expenses related to using the technology asset, such as fuel cost and service cost.

Generally, the higher the income levels, the greater the likelihood of investing in energy technologies [34]. While there are no studies to quantify the percentage of importance for each cost based on the household income, work has been done to indicate the general preferences of cost for each income level. Lower income households tend to prioritise capital cost and operating cost because they are likely not to have the savings to pay for the initial capital cost [2] and the savings from operating cost helps them cover other living costs [44]. On the contrary, higher income households do not see upfront capital cost as a barrier to adopt heating technologies, and therefore prioritise EAC over capital cost and operating cost when making investments [12].

Therefore, each agent has its preferences for each type of objective depending on the proportion of people belonging in low, medium, and high income brackets. For each agent, the percentage of importance WS for each objective j is calculated as follows:

$$WS_{j,n} = \sum_{i \,\epsilon\, i} w_{i,n}\, obj_{j,i} \tag{4}$$

where income level $i \,\epsilon\, \{low, medium, high\}$,
j ϵ $\{capital\ cost, EAC, operating\ cost\}$,
$w_{i,n}$ = % of population of i in agent n,
$obj_{j,i}$ = importance of objective j to i.

The agents are characterised based on the parameters investigated in this paper, i.e percentage of importance of each objective, size of population that belongs in the agent, ED, HDpc and GDPpc. The importance of each objective informs the decision strategy of each agent. Finally, the data is prepared to be implemented in MUSE for future research on modelling the heating technology investment behaviour of these agents, as shown in Appendix 10 and 11.

Table 2: Importance of types of cost to each income segment

Income level	Low	Medium	High
GDP per capita (£/ capita)	0 - 16410	16411 - 41025	> 41025
Importance of Capital cost	50%	25%	0%
Importance of EAC	0%	75%	100%
Importance of Operating cost	50%	0%	0%

4 Results and Discussion

4 .0.1 Attributes Band Results

From the Elbow Method, the optimal number of clusters is determined using a line graph of sum of squared error (SSE) plotted against number of clusters (k), as shown in 8 The k for ED and HDpc are chosen at 4 and 6 respectively. Using these results, Jenks optimization determined the band for ED and HDpc, as shown in Table 3 and Table 4.

Table 3: Band results for energy density (MWh/km^2-yr) using Jenks Optimization method

Band	Minimum	Maximum	Population (%)
1	1	6371	20.4
2	6371	20394	29.0
3	20394	44319	38.9
4	44319	130890	11.6

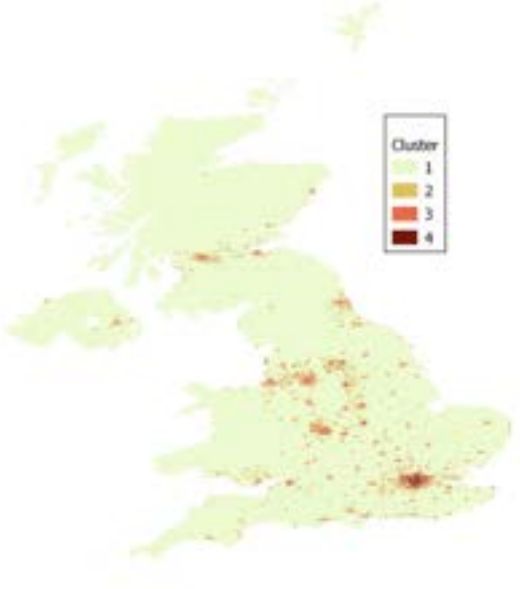

Figure 1: Energy density band in the residential sector across UK.

In Figure 1, a declining trend in ED is observed as the residents live further away from the cities. Clusters with high ED (Band 3 and 4) that account for approximately half of UK population resides in the cities, for instance, London and Manchester. The area coverage in Band 3 and 4 shows that these regions are densely populated. As the deployment of centralised heating systems such as

district heating largely depends on how many consumers agree to connect to a heat network [33], these areas will benefit the most from these technologies due to its high resident connectivity as well as the number of residents that can benefit from this. On the other hand, the residents belonging to Band 1 occupy 93% of area but only account for 20% of the UK population. For the short-term planning to arrive at UK's climate goal, this analysis reveals that it is not the utmost priority to invest in new low-carbon technology in areas with Band 1 because of their low energy consumption and low population density.

Table 4: Band results for heat density per capita (MWh/cap-year) using Jenks Optimization method

Band	Minimum	Maximum	Population(%)
1	7	11	32.4
2	11	12	37.3
3	12	14	22.5
4	14	16	6.5
5	16	23	1.0
6	23	Inf	0.3

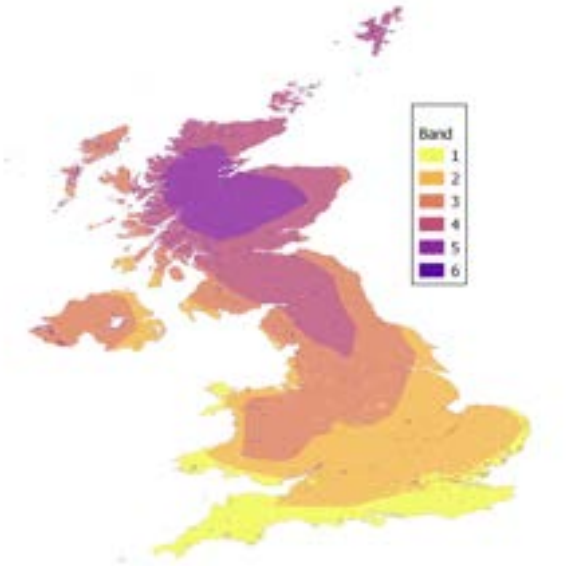

Figure 2: Heat demand per capita band in the residential sector across UK.

The most apparent trend in Figure 2 shows that HDpc increases as it progresses up North of UK. The clusters that belong to high HDpc (Band 4, 5 and 6) are not only found in the Northern regions but also along the coastline of the UK. This is attributed to the weather condition variability across the UK. These regions experience colder temperatures and higher average wind speed, so residents living in these areas require more heat to warm their houses. However, these residents only account for only 7.8% of the population, as shown in Table 4. Approximately 70% of the UK population belong to the low HDpc clusters (Band 1 and 2) and they are mainly found in the South of the UK.
The trend difference shown in the HDpc and ED maps is expected because HDpc considers the heat demand for each resident irrespective of the area population density that these residents live in. This shows that the insights on clusters' energy consumption behaviour and coverage area is dependent on the energy metric chosen. Therefore, this reinforces the idea that assessing multiple attributes when characterising agents will provide a more holistic understanding during energy policy making.

4 .0.2 DBSCAN Clustering Results

136 agents are obtained after each 1km^2 grid is assigned to its cluster using the band results from Jenks optimization. The detailed information can be found in supplementary material. DBSCAN 3D clustering is performed on the 3 attributes of these 136 agents. Using ln(n) $\approx$ 3 in the K-Nearest Neighbour approach 7 .1, Eps is found to be 0.35. The results show 10 agents with 2 agents accounting for 28% and 38% of UK population respectively. To reduce the size of these 2 agents, the same clustering technique is applied again on these two clusters individually to form a total of 18 clusters. Finally, spatial agents with less than 5% of the UK population are combined with its nearest neighbour, resulting in 9 final spatial clusters.

4 .0.3 Financial Objectives of Spatial Agents

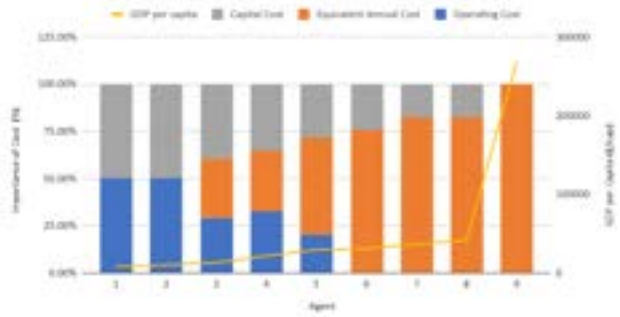

Figure 3: Relationship between income level and importance of cost to each agent. This suggests that financial objectives vary based on income level. As the proportion of medium and high income households belonging to an agent increases, the agent will be more likely to prioritise EAC when making energy-related investments. An opposite trend is observed in capital cost. The values can be found in Appendix. 7 .3

Table 5: Composition of income bracket in each agent

Agent	Low (%)	Medium (%)	High (%)	Population (%)
1	100.0	0.0	0.0	18.3
2	100.0	0.0	0.0	22.1
3	58.0	42.0	0.0	8.0
4	65.0	9.9	25.1	6.1
5	40.	31.9	27.2	14.1
6	0.0	98.2	1.8	5.5
7	0.0	70.8	29.2	8.8
8	0.0	70.0	30.0	10.8
9	0.0	0.0	100.0	5.8

The narratives of all 9 spatial agents are described in Appendix . 6. Table 5 shows the population of low,

medium and high income percentage in each agent as well as the importance of cost to the corresponding spatial agent.

Appendix. 12 shows the distribution of the 9 agents across the UK. Since this paper focuses on segmenting agents based on their financial status, this figure describes the location of each agent, ordered from the lowest to the highest GDPpc.

Figure 4: Geographics of Spatial 1 and 2

Agent 1 and 2 who account for the largest population (40.4%) are the low-income agents, and they deem capital cost and operating cost equally important, as shown in Fig. 3. Their above-average HDpc usage could suggest that their income is a barrier to install new energy-efficienct technology. To meet their high heat demand in a cost-effective way, they will most likely choose natural gas boiler as their preferred heating technology because it is affordable and widely available. However, considering that natural gas boilers use fossil fuel as a fuel source, the uptake of this technology will come at the expense of environmental pollution. Economic incentives such as subsidies need to be provided to these low-income agents to lower the cost barrier of adopting low-carbon heating technologies. This is especially the case for Agent 2 because it belongs in the low-income threshold but it uses higher than average HDpc and ED. It will be challenging to introduce decarbonisation pathways to these agents through large-scale heating energy retrofitting projects since they live in small clusters scattered across the country.

Figure 5: Geographics of Spatial 7 and 8

Upper-middle class agents who earn above the average income, Agents 7 and 8, are generally more inclined to live at the edges surrounding a city instead of living near the the city centre. EAC (82%) has a greater importance than capital cost (18%) to both of these agents, while operating cost is not their concern. This is because these agents live comfortably and can easily cover their monthly expenses. Due to the insignificance of operating cost to these agents, they tend to use above-average ED. This presents an opportunity to increase the uptake of low-carbon heating technologies for these agents, especially for Agent 7, since they consume more energy and have a higher willingness to pay for heating technologies that can provide them cost savings in the long run even if the initial capital cost is relatively high.

Figure 6: Geographics of Spatial 3, 4 and 6

Generally, as the residents' income increases, they live closer to the centre of cities, as characterised by Agent 3, 4 and 6. These agents mostly consist of medium-income households that belong to the working-class community. Agent 6 represents the working class in London, in which 98% of them fall under the medium-income group. This working class agent typically have the savings to pay for upfront capital cost, so they prioritise more on the

EAC relative to capital cost instead. This explains the relative importance of EAC and capital cost at a scale of 75% and 25% respectively. Agent 6 only resides in London, a densely populated city, and therefore uses the highest average ED among all agents. However, these individuals require the least HDpc. This could be due to the higher efficiency heating technologies in the city and the relatively warmer weather in London. Besides, this working-class agent could have better knowledge in energy-saving measures that results in the least HDpc. Therefore, Agent 6 might be more willing to adopt future clean heating technologies.

Agent 4 behaves in a very similar way to Agent 6 in terms of high ED and low HDpc, but Agent 4 is found across major city centres in the UK, such as Liverpool and Edinburgh. The results of Agent 4 and 6 show that people who live in the cities generally have high ED and low HDpc. Agent 3 predominantly resides at the edge of London and is scattered across the UK. Agents 3 and 4 perceive all types of cost as equal important factors to consider. Agent 3 is dominated by low and medium income group but Agent 4 is a mix of low (65.0%) and high (25.1%) income group. The heterogeneity of the income level in Agent 4 would make it difficult for decarbonisation policies to implement a income-targeted policy for this agent.

Figure 7: Geographics of Spatial 5 and 9

The highest income agent (Agent 9) and the average-income agent (Agent 5) that account for 19% of the overall UK population do not live in major cities, but instead are most widely spread out across the country. These agents have high HDpc and low ED due to their dispersed location, including rural areas. Agent 5 has a strong preference for EAC (51%), while agent 9 perceives EAC as the only determining financial factor. Although this might suggest that they could be the most receptive towards new, clean heating technologies, their low population densities might pose a challenge for policy-makers to introduce centralised decarbonisation pathways for these agents.

5 Conclusions

This paper presents a novel way of characterising high resolution spatial agents in the UK residential sector. Spatial data on energy density, heat demand per capita, and GDP per capita are clustered to group spatial agents with unique characteristics. The agents are segmented based on their income level, which determines the relative importance of annual cost, equivalent annual cost (EAC) and operating costs for heating technologies. The results of the spatial agent characterisation provides an understanding of the location of the agents, their associated attributes and their cost preferences.

From our spatial clustering of agents, our results showed the characteristics of spatial agents at a 1km ^{2} resolution. Specifically, our results highlighted that upper-middle class agent (Agent 7) that lived near the edges surrounding a city is the most promising spatial agent to adopt decarbonisation pathways. This agent mainly prioritises EAC and has an above-average energy density and heat demand per capita usage. This suggests that they have the means to afford clean new or retrofit heating technologies that often have a higher upfront capital cost, and are more willing to adopt these technologies if it provides cost savings in the long-run. Therefore, prioritising decarbonisation in the energy consumption of these agents will result in anincrease in uptake of low-carbon heating technologies.

Additionally, introducing low-carbon technologies among low-income agents might be a challenge, especially for the low-income agent that has above-average energy density and heat demand per capita (Agent 2). Capital cost and operating cost are major barriers for decarbonisation for this agent. They do not have the savings to afford efficient heating technologies, and their widely dispersed homes across the country also poses an additional challenge for large-scale commercialisation of low-carbon technologies. Financial incentives such as energy subsidies will be needed to support this agent.

The authors would like to highlight the limitations of this paper:
i) The importance of cost to income-specific group of agents is assumed, as shown in 7 .3, is based on the general trend stated in Section 3 .2.2. The overall importance of cost to each agent, which ultimately determines the feasibility of heating technology retrofitting project is dependent on these key assumptions. Thus, further research can be done to accurately quantify the importance of types of cost for different income groups by collecting empirical data through large-scale surveys. This will provide a more precise agent characterisation to be included in ABM models.

ii) Since each agent might contain a mix of income groups with different proportions, the overall importance of a type

of cost to an agent is assumed to be proportional to the size of each income group within the agent. This might lead to a higher percentage of deviation from the actual overall importance of cost to the agent because individual deviations of low, medium and high income from the actual importance of cost are all included in the analysis. To overcome this limitation, future research could set an additional constraint during 3D clustering of attributes so that each spatial agent only belongs to one income bracket.

iii) This paper uses GDPpc as a proxy for income per capita. Since income data is private and confidential, it is unlikely for high-resolution data of income per capita to be publicly available for future research. Instead, this paper chooses GDPpc as the closest resemblance of income per capita. This limitation is difficult to overcome, but it should still be noted that this assumption might not fully reflect the actual income per capita. A comparison of the other attributes can be done using UK National Statistics of the Lower and Middle Super Output Areas (LLSOAs) to validate the results.

The results from this paper assist future agent-based modelling research to assess spatial agents with multiple attributes in MUSE. Other parameters such as technical reliability of the heating technology and the agents' environmental concern can be investigated to further characterise the agents. Besides, the results support future policies for residential heat technology projects based on spatial agents segmentation. To ensure decarbonisation policies in the residential sector are effective and inclusive, there is a pressing need for further studies to be done in spatial agent characterisation to help UK achieve its net-zero carbon goal.

6 Acknowledgement

The authors would like to thank Diego Moya for his support and guidance throughout this research.

References

[1] Ahmadi-Karvigh, Simin, Ali Ghahramani, Burcin Becerik-Gerber and Lucio Soibelman [2018], 'Real-time activity recognition for energy efficiency in buildings', *Applied energy* **211**, 146–160.

[2] Ameli, Nadia and Nicola Brandt [2015], 'Determinants of households' investment in energy efficiency and renewables: evidence from the oecd survey on household environmental behaviour and attitudes', *Environmental Research Letters* **10**(4), 044015.

[3] Beckel, Christian, Leyna Sadamori and Silvia Santini [2012], Towards automatic classification of private households using electricity consumption data, *in* 'Proceedings of the Fourth ACM Workshop on Embedded Sensing Systems for Energy-Efficiency in Buildings', BuildSys '12, Association for Computing Machinery, New York, NY, USA, p. 169–176.
URL: *https://doi.org/10.1145/2422531.2422562*

[4] Birant, Derya and Alp Kut [2007], 'St-dbscan: An algorithm for clustering spatial–temporal data', *Data & knowledge engineering* **60**(1), 208–221.

[5] Bonabeau, Eric [2002], 'Agent-based modeling: Methods and techniques for simulating human systems', *Proceedings of the national academy of sciences* **99**(suppl 3), 7280–7287.

[6] Chen, Jian, Shengtian Yang, Hongwei Li, Bin Zhang and Junrong Lv [2013], 'Research on geographical environment unit division based on the method of natural breaks (jenks)', *Int. Arch. Photogramm. Remote Sens. Spat. Inf. Sci* **3**, 47–50.

[7] Chimwayi, KB and J Anuradha [2018], 'Clustering west nile virus spatio-temporal data using st-dbscan', *Procedia computer science* **132**, 1218–1227.

[8] Crooks, Andrew, Nicolas Malleson, Ed Manley and Alison Heppenstall [2018], *Agent-based modelling and geographical information systems: a practical primer*, SAGE Publications Limited.

[9] Danielaini, Titih Titisari, Basant Maheshwari and Dharmappa Hagare [2018], 'Defining rural–urban interfaces for understanding eco-hydrological processes in west java, indonesia: Part i. development of methodology to delineate peri-urban areas', *Ecohydrology & Hydrobiology* **18**(1), 22–36.

[10] De Smith, Michael John, Michael F Goodchild and Paul Longley [2007], *Geospatial analysis: a comprehensive guide to principles, techniques and software tools*, Troubador publishing ltd.

[11] Deb, Chirag, Mario Frei, Johannes Hofer and Arno Schlueter [2019], 'Automated load disaggregation for residences with electrical resistance heating', *Energy and Buildings* **182**, 61–74.

[12] DECC, UK [2013], 'Home owners' willingness to take up more efficient heating systems', *London, UK: Department of Energy and Climate Change* .

[13] Department for Business, Energy Industrial Strategy [n.d.*a*], *ANNEX: 1990 - 2015 UK GREENHOUSE GAS EMISSIONS, FINAL FIGURES BY END USER*.

[14] Department for Business, Energy Industrial Strategy [n.d.*b*], 'Energy consumption in the uk'.

[15] DeVore, Greggory R [2017], 'Computing the z score and centiles for cross-sectional analysis: a practical approach', *Journal of Ultrasound in Medicine* **36**(3), 459–473.

[16] Ekins, Paul and Matthew Lockwood [2011], 'Tackling fuel poverty during the transition to a low-carbon economy'.

[17] Ester, Martin, Hans-Peter Kriegel, Jörg Sander, Xiaowei Xu et al. [1996], A density-based algorithm for discovering clusters in large spatial databases with noise., *in* 'Kdd', Vol. 96, pp. 226–231.

[18] Finney, Karen N, Vida N Sharifi, Jim Swithenbank, Andy Nolan, Simon White and Simon Ogden [2012], 'Developments to an existing city-wide district energy network–part i: Identification of potential expansions using heat mapping', *Energy Conversion and Management* **62**, 165–175.

[19] Fokaides, Paris A, Kyriacos Polycarpou and Soteris Kalogirou [2017], 'The impact of the implementation of the european energy performance of buildings directive on the european building stock: The case of the cyprus land development corporation', *Energy Policy* **111**, 1–8.

[20] for Communities, Department and Local Government [n.d.], *English Housing Survey*.

[21] Gianniou, Panagiota, Xiufeng Liu, Alfred Heller, Per Sieverts Nielsen and Carsten Rode [2018], 'Clustering-based analysis for residential district heating data', *Energy conversion and management* **165**, 840–850.

[22] Guha, Sudipto, Rajeev Rastogi and Kyuseok Shim [1998], 'Cure: An efficient clustering algorithm for large databases', *SIGMOD Rec.* **27**(2), 73–84.
URL: *https://doi.org/10.1145/276305.276312*

[23] *How low income is measured in households below average income* [2016].
URL: *https://www.gov.uk/government/publications/how-low-income-is-measured/text-only-how-low-income-is-measured*

[24] Jalil Vega, Francisca Alejandra [2018], 'Development of a systems approach for studying decarbonisation pathways of heat demand in the uk'.

[25] Jenks, George F [1967], 'The data model concept in statistical mapping', *International yearbook of cartography* **7**, 186–190.

[26] Karami, Amin and Ronnie Johansson [2014], 'Choosing dbscan parameters automatically using differential evolution', *International Journal of Computer Applications* **91**(7), 1–11.

[27] Karimi, Mohammad Javad and Sadegh Vaez-Zadeh [2020], 'An agent-based model for electric energy policy assessment', *Electric Power Systems Research* p. 106903.

[28] Kastner, Ingo and Paul C Stern [2015], 'Examining the decision-making processes behind household energy investments: A review', *Energy Research & Social Science* **10**, 72–89.

[29] Khan, Fouad [2012], 'An initial seed selection algorithm for k-means clustering of georeferenced data to improve replicability of cluster assignments for mapping application', *Applied Soft Computing* **12**(11), 3698–3700.

[30] Lekavičius, V, V Bobinaitė, A Galinis and A Pažėraitė [2020], 'Distributional impacts of investment subsidies for residential energy technologies', *Renewable and Sustainable Energy Reviews* **130**, 109961.

[31] Lin, Yue [2013], 'A comparison study on natural and head/tail breaks involving digital elevation models'.

[32] Liu, Yanxu, Tong Li, Wenwu Zhao, Shuai Wang and Bojie Fu [2019], 'Landscape functional zoning at a county level based on ecosystem services bundle: Methods comparison and management indication', *Journal of environmental management* **249**, 109315.

[33] Ltd, Element Energy [n.d.], 'Research on district heating and local approaches to heat decarbonisation'.

[34] Mahapatra, Krushna and Leif Gustavsson [2008], 'An adopter-centric approach to analyze the diffusion patterns of innovative residential heating systems in sweden', *Energy Policy* **36**(2), 577–590.

[35] Manley, Ed and Tao Cheng [2018], 'Exploring the role of spatial cognition in predicting urban traffic flow through agent-based modelling', *Transportation Research Part A: Policy and Practice* **109**, 14–23.

[36] März, Steven [2018], 'Assessing the fuel poverty vulnerability of urban neighbourhoods using a spatial multi-criteria decision analysis for the german city of oberhausen', *Renewable and Sustainable Energy Reviews* **82**, 1701–1711.

[37] Meha, Drilon, Tomislav Novosel and Neven Duic [2020], 'Bottom-up and top-down heat demand mapping methods for small municipalities, case gllogoc', *Energy* p. 117429.

[38] Micheletti, Natan, Marj Tonini and Stuart N Lane [2017], 'Geomorphological activity at a rock glacier front detected with a 3d density-based clustering algorithm', *Geomorphology* **278**, 287–297.

[39] Nielsen, Steffen and Bernd Möller [2013], 'Gis based analysis of future district heating potential in denmark', *Energy* **57**, 458–468.

[40] on Climate Change, Committee [2019], *Net Zero: The UK's contribution to stopping global warming*, Committee on Climate Change.

[41] on Climate Change, Committee [n.d.], *Reducing UK emissions: 2018 Progress Report to Parliament*.
URL: *https://www.theccc.org.uk/publication/reducing-uk-emissions-2018-progress-report-to-parliament/*

[42] PERAFÁN-LÓPEZ, Juan Carlos and Julián SIERRA-PÉREZ [2020], 'An unsupervised pattern recognition methodology based on factor analysis and a genetic-dbscan algorithm to infer operational conditions from strain measurements in structural applications', *Chinese Journal of Aeronautics* .

[43] Pfenninger, Stefan, Adam Hawkes and James Keirstead [2014], 'Energy systems modeling for twenty-first century energy challenges', *Renewable and Sustainable Energy Reviews* **33**, 74–86.

[44] Preston, Ian, Vicki White, Katharine Blacklaws and D Hirsh [2014], 'Fuel and poverty', *A Rapid Evidence Assessment for the Joseph Rowntree Foundation. Centre for Sustainable Energy. Reg charity* **298740**.

[45] Sachs, Julia, Diego Moya, Sara Giarola and Adam Hawkes [2019], 'Clustered spatially and temporally resolved global heat and cooling energy demand in the residential sector', *Applied Energy* **250**, 48–62.

[46] Santin, Olivia Guerra, Laure Itard and Henk Visscher [2009], 'The effect of occupancy and building characteristics on energy use for space and water heating in dutch residential stock', *Energy and buildings* **41**(11), 1223–1232.

[47] Tian, Shanjun and Shiyan Chang [2020], 'An agent-based model of household energy consumption', *Journal of Cleaner Production* **242**, 118378.

[48] Tibshirani, Robert, Guenther Walther and Trevor Hastie [2001], 'Estimating the number of clusters in a data set via the gap statistic', *Journal of the Royal Statistical Society: Series B (Statistical Methodology)* **63**(2), 411–423.

[49] Tsekeris, Theodore and Klimis Vogiatzoglou [2011], 'Spatial agent-based modeling of household and firm location with endogenous transport costs', *NETNOMICS: Economic Research and Electronic Networking* **12**(2), 77–98.

[50] Tureczek, Alexander Martin, Per Sieverts Nielsen, Henrik Madsen and Adam Brun [2019], 'Clustering district heat exchange stations using smart meter consumption data', *Energy and buildings* **182**, 144–158.

[51] von Platten, Jenny, Mikael Mangold and Kristina Mjörnell [2020], 'A matter of metrics? how analysing per capita energy use changes the face of energy efficient housing in sweden and reveals injustices in the energy transition', *Energy Research & Social Science* **70**, 101807.

[52] Voulis, Nina, Martijn Warnier and Frances MT Brazier [2018], 'Understanding spatio-temporal electricity demand at different urban scales: A data-driven approach', *Applied Energy* **230**, 1157–1171.

[53] *Wage levels* [2020].
URL: *https://data.oecd.org/earnwage/wage-levels.htm*

[54] Yalcin, Mustafa and Fatmagul Kilic Gul [2017], 'A gis-based multi criteria decision analysis approach for exploring geothermal resources: Akarcay basin (afyonkarahisar)', *Geothermics* **67**, 18–28.

[55] Zambelli, Antoine E [2016], 'A data-driven approach to estimating the number of clusters in hierarchical clustering', *F1000Research* **5**.

[56] Zhan, Sicheng and Adrian Chong [2020], 'Building occupancy and energy consumption: Case studies across building types', *Energy and Built Environment* .

[57] Zhang, Yaqian, Jacek Mańdziuk, Chai Hiok Quek and Boon Wooi Goh [2017], 'Curvature-based method for determining the number of clusters', *Information Sciences* **415**, 414–428.

[58] Zhang, Zhihui, Rui Jing, Jian Lin, Xiaonan Wang, Koen H van Dam, Meng Wang, Chao Meng, Shan Xie and Yingru Zhao [2020], 'Combining agent-based residential demand modeling with design optimization for integrated energy systems planning and operation', *Applied Energy* **263**, 114623.

[59] Zhou, Aoying, Shuigeng Zhou, Jing Cao, Ye Fan and Yunfa Hu [2000], 'Approaches for scaling dbscan algorithm to large spatial databases', *Journal of computer science and technology* **15**(6), 509–526.

Modelling Density and Viscosity of Partially Carbonated Aqueous 2-Amino-2-Methyl-1-Propanol and Piperazine for CO_2 Capture

Marissa Adila Binti Husin and Vikneswaran Sathasivam

Department of Chemical Engineering, Imperial College London, U.K.

Abstract

Piperazine (PZ) and 2-amino-2-methyl-1-propanol (AMP) are among the amines that are being considered to optimise and improve the existing carbon capture, utilisation and storage technologies (CCUS). In this work, density and viscosity of carbon-loaded and unloaded PZ and AMP solutions were correlated based on existing experimental data as a function of temperature, composition and CO_2-loading for a range of industrial temperatures between 298.15K - 333.15K. Polynomial, Vogel-Fulcher-Tammann(VFT) and Redlich-Kister equations were the main equations used as basis of the models, achieving an average deviation of 0.1% and 2.0% for density and viscosity respectively.

KEYWORDS— AMP, PZ, CSS, Redlich-Kister, VFT

1 Introduction

The effect of climate change is more imminent now than before as extreme temperatures, hydrological change, floods and droughts around the globe are becoming a norm [1]. The Intergovernmental Panel on Climate Change (IPCC) in its Special Report on limiting global warming to 1.5°C addressed the importance of carbon capture, utilisation and storage (CCUS) technology in achieving climate goals [2]. This is due to the global power demand which is currently heavily dependent on fossil fuel and therefore, requires a transition time to clean energy, as well as hard-to-abate carbon-intensive industries such as iron and steel production [3]. Therefore, there has been a need to find a feasible CCUS technology that can be introduced in existing power plant as a transitional step to combat the inevitable climate change [4].

It has been identified that amine-based CO_2 capture technology is suitable to be used in capturing CO_2 from flue gas in a process called postcombustion CO_2 capture (PCC). This technology is advantageous based on two main reasons: the ease of installing amine-based PCC in existing plants and the reversible reaction between amine and CO_2 by using temperature variations in the absorbing and stripping columns [5]. The main limitation of PCC is the high energy demand in separating CO_2 [6]. This contributes to thermal degradation of amine solvent, thus reducing availability for amine to be recovered and recycled which would increase the material cost required in CCUS. Primary amine groups are generally stable and the added steric hindrance protects the amine from thermal degradation [7].

Therefore, two additional amines have been an interest of study which are 2-amino-2-methyl-1-propanol (AMP) and piperazine (PZ). These amines exhibit significant desirable properties such as rapid CO_2 absorption kinetics and low heat demand in recovery [8] for AMP, as well as high solubility of CO_2 in aqueous solution for PZ due to the presence of two amine groups within its cyclic molecule, thus providing higher alkalinity per molecule. These properties could overcome the shortcomings of the current choice of amine such as MEA, and consequently establishing a more optimised CCUS technology [9, 10].

2 Background

Designing large scale absorption column for PCC begins with the knowledge of physical properties of the amine solutions in detail. Physical properties such as density and viscosity of this system are vital for sizing and material utilisation purposes. However, with a large number of possible combinations of properties and blends available, it is impossible to identify this efficiently through experimental methods. Therefore, this has become the main driver in establishing empirical correlations of physical properties for initial design purposes. Lack of predictability in these properties may cause safety issues such as unforeseen temperature peaks due to the exothermic absorption of CO_2 with amine solution which may cause the current process design to be infeasible for this spike in process conditions [11].

There are many researches that have correlated densities and viscosities of unloaded aqueous solution of AMP and PZ but further improvements to these models could be made to increase robustness and ease of usage of models. Previous studies include Chan et al. [12] who incorporated the Redlich-Kister equation to model density of AMP at each temperature without universal model, Muhammad et al. [13] who managed to acquire surface tension, refractive index, density and viscosity for lower mole fraction of aqueous PZ as well as other various studies on vapour-liquid equilibrium data and liquid heat capacities [14][15][16].

While there are empirical formulations established

for other CO_2-loaded amines such as MEA, DEA and MDEA, density and viscosity of CO_2-loaded PZ and AMP were least analysed [17]. This work was conducted to bridge this knowledge gap by formulating models to accurately represent the density and viscosity of both CO_2-loaded and unloaded AMP and PZ solutions as a function of temperature, composition in terms of mole and mass as well as CO_2-loading.

3 Methods

3.1 Data Collection and Processing

Experimental data sets were essential to test and validate the reliability of models proposed. The experimental data sets which characterised the density and viscosity of PZ and AMP were primarily collected from published research papers through Google Scholar and DETHERMA.

Extra validation steps were conducted to ensure the reliability of the data collected. Methods of data measurement stated in each literature were analysed and experimental data would only be collected for measurements with low percentage of uncertainties, which could be summarised in Table 1 and Table 2.

The experimental data collected were further processed to remove any existing systematic errors originated from a particular source, as well as anomalies which could cause unnecessary large deviations and increase complexity of modelling. A box plot method was utilised to investigate the deviation of a particular data from the median. Anomalies were detected using the 1.5 IQR rule and removed from this study. Comparing data from several sources into this study was advantageous in ensuring both the reliability of data sets and robustness of models obtained.

Standardised notations were used throughout the research to distinguish the components involved, where: i = 1, 2, 3 which translated to 1 ≡ H_2O, 2 ≡ AMP, 3 ≡ PZ. The composition terms used in this research, specifically mass fraction (w_i) and mole fraction (x_i) were composition in the CO_2-free solution of amine as this supports practicality in industrial practices. Mass fraction of amine is defined as $w_i = m_i/(m_1 + m_i)$ where m is mass in kg, and mole fraction is defined as $x_i = n_i/(n_1 + n_i)$ where n is number of moles in mol.

It was found that a fair amount experimental data were reported in molality, and it was essential that standardised units of measurements were used throughout the research. Therefore, a conversion equation was applied to covert the molality as follows:

$$w_i = \frac{MW_i M_i}{MW_i M_i + 1000} \tag{1}$$

Where MW_i is the mass fraction in kg mol^{-1} and M_i is the molalility in mol $kg_{H_2O}^{-1}$. The units of the rest of terms were standardised as follows: $\alpha \equiv mol_{CO_2}$ mol_{amine}^{-1}, temperature ≡ K, viscosity ≡ mPas, density ≡ kg m^{-3}.

3.2 Optimisation Tools

Optimisation was executed using the add-in solver function on Microsoft Excel. The solver function utilised the Generalized Reduced Gradient (GRG) nonlinear algorithm which was reported by Lasdon et al. [39] to achieve the set target for an objective function by varying defined parameters. The least-square optimisation technique was incorporated into this function where sum square of the differences between the experimental and the calculated values were minimised. This optimisation techniques were incorporated in obtaining all models formed across the pure, binary and ternary systems.

The add-in regression tool on Microsoft Excel was utilised to perform multiple linear regressions in order to investigate the temperature dependence of the physical properties. Combination of parameters were chosen on the basis of highest coefficient of determination, R^2 value which indicated a close fit to the regression line produced.

Statistical measurements of Average Absolute Relative Deviation (AARD) and Maximum Absolute Relative Deviation (MARD) were used as key measurements to assess the accuracy of models obtained. These statistical measurements could be defined as follows:

$$\Delta_{AARD,X} = \frac{1}{N}\sum_{i=1}^{N}\frac{|X_{exp,i} - X_{calc,i}|}{X_{exp,i}} \times 100\% \tag{2}$$

$$\Delta_{MARD,X} = \max\left(\frac{1}{N}\sum_{i=1}^{N}\frac{|X_{exp,i} - X_{calc,i}|}{X_{exp,i}} \times 100\%\right) \tag{3}$$

Where X is the physical property investigated and N is the number of experimental data considered in the model. The low values of AARD and MARD signifies a good fit of model to the experimental data.

4 Results & Discussion

4.1 Pure Amine System

Correlations for the densities of pure liquid amine were obtained by fitting experimental data extracted from previous researches into a temperature-dependent quadratic equation that takes the form as follows:

$$\rho_i = A + B\left(\frac{T}{T_o}\right) + C\left(\frac{T}{T_o}\right)^2 \tag{4}$$

Table 1: Sources used to obtain density data

Source	Equipment	T (K)	Uncertainty
AMP			
Aguila-Hernández et al. [18]	Anton Paar DMA 45 Densimeter	313.15 - 333.15	0.04 %
Álvarez et al. [19]	Anton Paar DSA 5000 Densimeter	298.15 - 323.15	0.05 %
Braun et al. [20]	Mettler PE3600 Densimeter	299.15 - 313.15	0.10 %
Chan et al. [12]	Anton Paar DMA 45 Densimeter	298.15 - 353.15	0.03 %
Henni et al. [21]	Anton Paar DMA 4500 Densimeter	298.15 - 343.15	0.05 %
Karunarathne et al. [22]	Anton Paar DMA 4500 Densimeter	293.15 - 343.15	0.05 %
Khan et al. [23]	Not specified	298.15 - 313.15	0.50 %
Li et al. [24]	25-mL Gay-Lussac Pycnometer	303.15 - 353.15	0.50 %
Mandal et al. [25]	25-mL Gay-Lussac Pycnometer	293.15 - 323.15	0.04 %
Stec et al. [26]	Kyoto Electronics KEM DA-645 Densimeter	293.15 - 333.15	0.05 %
Muhammad et al. [13]	Anton Paar DMA 5000 Densimeter	298.15 - 333.15	0.01 %
Rebolledo-Libreros and Trejo [27]	Kyoto Electronics KEM DA-645 Densimeter	303.15 - 343.15	0.01 %
Samanta and Bandyopadhyay [28]	25-mL Gay-Lussac Pycnometer	298.15 - 333.15	0.05 %
Shojaeian and Haghtalab [29]	Anton Paar DMA-58 Densimeter	293.15 - 343.15	0.20 %
Welsh and Davis [30]	25-mL Gay-Lussac Pycnometer	313.15 - 333.15	0.50 %
Xu et al. [31]	Calibrated 25-mL Pycnometer Bottles	293.15 - 333.15	0.10 %
Zhang et al. [32]	Anton Paar DMA 5000 densimeter	293.15 - 363.15	0.02 %
PZ			
Derks et al. [33]	Anton Paar DMA 58 Densimeter	293.15 - 323.15	0.01 %
Freeman and Rochelle [34]	Mettler-Toledo DE 40 Densimeter	293.15 - 333.15	0.10 %
Liu et al. [35]	Anton Paar DMA 4500 Densimeter	283.15 - 323.15	0.05 %
Murshid et al. [36]	Anton Paar DMA 5000 Densimeter	298.15 - 333.15	0.03 %
Samanta and Bandyopadhyay [28]	25-mL Gay-Lussac Pycnometer	298.15 - 333.15	0.05 %
Stec et al. [26]	Kyoto Electronics KEM DA-645 Densimeter	293.15 - 333.15	0.05 %
Sun et al. [37]	25-mL Gay-Lussac Pycnometer	303.15 - 313.15	0.05 %

Where ρ_i is the density of pure component, T is the corresponding temperature of substance whereas A, B and C are parameters to be obtained through optimisation. As experimental data were within the range of 293.15K - 313.15K, the value of T_o = 298.15K was deemed suitable to scale the temperatures incorporated into further calculations in the study, thus making the equation dimensionless resulting in lower margin of computational error when performing iterations using the Solver function to obtain suitable parameters for the respective density models.

The equation was further tested with polynomials of higher and lower orders by observing the resulted AARD and MARD after validating with experimental data. It was found that Eqn 4 was sufficient for pure density calculations supported by the low AARD and MARD of calculated densities produced while requiring small number of parameters.

While this method was proven sufficient for the water and pure liquid AMP systems, a different approach was needed to calculate the pure liquid density of PZ due to the lack of experimental data available. This setback stemmed from the high melting temperature PZ at T = 379.15K [40].

The absorption of CO_2 by amine solution is typically conducted at low temperatures of 293.15 K - 333.15K. This is supported through previous literature data by Rashid et al. [41], who have experimentally proven that the efficiency of CO_2 absorption is inversely proportional to operating temperature due to decrease mobility of CO_2 at low temperature, therefore modelling the density of PZ at high temperatures would not give practical benefits to the study.

To overcome this setback, a group contribution approach was used to calculate the pseudo pure liquid PZ density utilising Eqn 4 and the structural similarities observed between piperazine, piperidine and cyclohexane molecules.

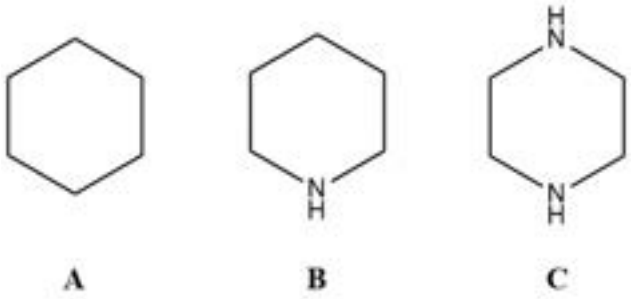

Figure 1: Comparison of molecular structures between amines: **A**, Cyclohexane ; **B**, Piperidine ; **C**, Piperazine

An approximation of pseudo pure liquid PZ density was obtained by first formulating density models of pure liquid cyclohexane and piperidine. These two models were validated by experimental data obtained from past literatures to assess its accuracy and reliability, obtaining AARD values of 0.03% and 0.05% respectively. The contribution of the amine group on the density of molecules could then be obtained and this

Table 2: Sources used to obtain viscosity data

Source	Equipment	T (K)	Uncertainty
AMP			
Álvarez et al. [19]	Schott-Geräte AVS 350 Ubbelohde Viscometer	298.15 - 323.15	0.05 %
Braun et al. [20]	Brookfields LVT Viscometer	299.15 - 313.15	1.00 %
Henni et al. [21]	Cannon-Ubbelohde Viscometers	298.15 - 343.15	0.03 %
Karunarathne et al. [22]	Anton Paar Physica MCR 101 Rheometer	293.15 - 343.15	1.00 %
Khan et al. [23]	Ostwald Viscometer	298.15 - 313.15	1.00 %
Li and Lie [38]	Cannon-Fenske Routine Viscometer	303.15 - 353.15	1.00 %
Liu et al. [35]	iVisc Capillary Viscometer	303.15 - 343.15	1.00 %
Mandal et al. [25]	Ostwald Viscometer	293.15 - 323.15	0.03 %
Murshid et al. [36]	Ubbelohde Viscometer	298.15 - 333.15	1.00 %
Rebolledo-Libreros and Trejo [27]	CannonFenske Viscometer	303.15 - 343.15	0.30 %
Samanta and Bandyopadhyay [28]	Ostwald Viscometer	298.15 - 333.15	1.00 %
Welsh & Davis	Cannon-Fenske Capillary Viscometer	313.15 - 333.15	0.50 %
Xu et al. [31]	Cannon-Fenske Routine Viscometer	293.15 - 349.15	1.00 %
PZ			
Derks et al. [33]	PSL Ubbelohde Viscometer	293.15 - 323.15	1.00%
Freeman and Rochelle [34]	Anton Paar Physica MCR 300 Rheometer	293.15 - 333.15	1.00 %
Liu et al. [35]	Anton Paar Physica MCR 100 Rheometer	283.15 - 323.15	1.00 %
Murshid et al. [36]	PSL Ubbelohde Viscometer	298.15 - 333.15	0.10 %
Samanta and Bandyopadhyay [28]	Ostwald Viscometer	298.15 - 333.15	1.00 %
Sun et al. [37]	Canno-Fenske Routine Viscometer	303.15 - 313.15	1.00 %

contribution was added to the density of cyclohexane to obtain the density of pure liquid PZ as follows:

$$\rho_{NH} = \rho_{Piperidine} - \rho_{Cyclohexane} \tag{5}$$

$$\rho_{PZ} = \rho_{Cyclohexane} + 2 \cdot \rho_{NH} \tag{6}$$

Models to approximate the viscosities of pure liquid amines were obtained through a similar optimisation method as density where comparison with experimental data was conducted to minimise the sum square of residuals, but utilising the Vogel-Fulcher-Tammann (VFT) as it demonstrated a more accurate temperature dependency of viscosity as follows:

$$ln(\eta) = A + \frac{B}{(T/T_o) + C} \tag{7}$$

Similarly, a group contribution method was used to obtain the pseudo pure liquid viscosities of PZ within the range of temperature defined for this investigation, using the following equations:

$$ln(\eta_{NH}) = ln(\eta_{Piperidine}) - ln(\eta_{Cyclohexane}) \tag{8}$$

$$ln(\eta_{PZ}) = ln(\eta_{Cyclohexane}) + 2 \cdot ln(\eta_{NH}) \tag{9}$$

Due to the non-linearity nature of the VFT equation, parameter C was kept constant at C = -0.00183 to enable implementation of simple addition rules in performing group contribution calculations. Comparing the models obtained for piperidine and cyclohexane with experimental data, the AARD achieved were 1.72% and 0.86% respectively, which provided good indications on the goodness of fit of the viscosity model proposed for PZ.

Table 3 shows the corresponding parameters for density and viscosity models of AMP and PZ obtained from the optimisation conducted, which were used in developing models in Section 4.2 and 4.3. The low deviations reported suggested that the models proposed provided a good fit on the density and viscosity of pure components.

Table 3: *Parameters obtained for Eqn 4 and 7 to calculate pure density and viscosity of water and liquid amines, along with its respective AARD and MARD*

	A	B	C	AARD	MARD
Density					
AMP	1048.2	-	-117.84	0.07%	0.16%
PZ	1243.0	-324.59	21.539	-	-
Viscosity					
AMP	-5.1332	4.0421	-0.59952	1.35%	2.72%
PZ	-5.5921	6.2577	-0.00183	-	-

4.2 H_2O-Amine System

The density of CO_2-free aqueous amine solution was calculated using the excess molar volume approach. Molar volume of substances in the solution could be derived from pure liquid density as follows:

$$\overline{V_i} = \frac{MW_i}{\rho_i} \tag{10}$$

Where $\overline{V_i}$ is the molar volume of substances is m^3 mol^{-1}, MW_i is the molar mass and ρ_i is the pure density of substances which could be calculated using Eqn 4 and variables in Table 3 for pure amine. Density of water was calculated using the correlation developed by **?**] as below:

$$\rho_1 = 0.79484 + 0.48906\left(\frac{T}{T_o}\right) - 0.28679\left(\frac{T}{T_o}\right)^2 \quad (11)$$

Using the molar volumes of substances obtained, the density of binary mixture consisting of water and amine could be related to excess molar volume of substance in the following form:

$$\rho_o = \frac{x_1 M_1 + x_i M_i}{\overline{V^E} + x_1\overline{V_1} + x_i\overline{V_i}} \quad (12)$$

Where ρ_o is the density of aqueous amine, x_i is the mole fraction of substances in the solution and $\overline{V^E}$ is the excess molar volume of solution. A model for $\overline{V^E}$ was developed using the Redlich-Kister expansion as a function of mole fractions as follows:

$$\overline{V^E} = x_1 x_i[A_1 + A_2(x_1 - x_i) + A_3(x_1 - x_i)^2] \quad (13)$$

An isothermal multiple linear regression analysis was conducted to assess the number of terms sufficient to model the changes of density with concentration, and it was observed that 2 composition terms were enough to achieve accurate predictions. The A_j leading terms were expanded to assess the model's dependency on temperature, and a linear dependence on temperature observed a good correlation to the experimental data and therefore, A_j was modelled as follows:

$$A_j = a_j + b_j\left(\frac{T}{T_o}\right) \quad (14)$$

Further optimisation was conducted to reduce the number of parameters in the model without compromising the goodness of fit. The final optimised models removed the total dependency on the second composition term for AMP, whereas as a constant was sufficient for A_3 in the PZ binary system. The final parameters obtained are summarised in Table 4 along with AARD and MARD of each model.

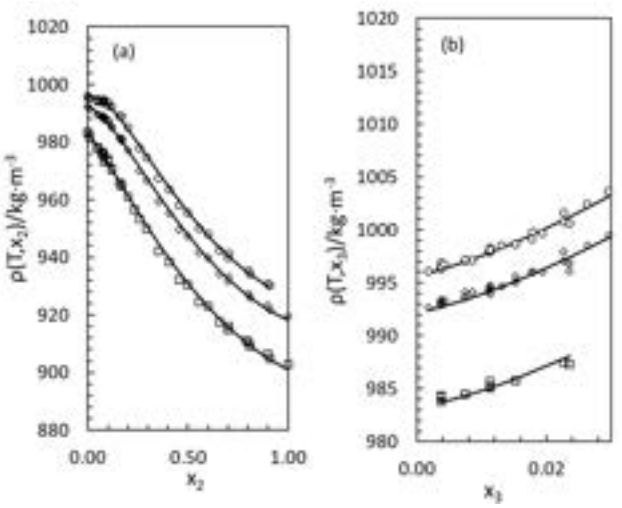

Figure 2: Unloaded density of experimental values compared to empirical correlation at various temperature for (a) AMP and (b) PZ : ○, T = 303.15 K; ◇, T = 313.15 K; □, T = 333.15 K. Lines were calculated using parameters from Table 4

Across all data sets tested, $\overline{V^E}$ exhibited negative values which suggested that effective packing caused the deviation of densities from its ideal value.This was contributed by the formation of hydrogen bonding among unlike molecules, thus strengthening the intermolecular forces that contributed to a more compact packing [22].

While the goodness of fit was well represented by the low deviations achieved, it is worth noting that a limitation was faced when modelling the density for PZ as there were limited experimental data available, specifically only for mole fractions below $x_3 = 0.03$. More experimental data would be required to validate if the model proposed would give accurate approximation for a wider range of amine compositions, however accurate predictions could be achieved within the composition range tested owing to its low AARD value of 0.04%.

A similar concept was applied in calculating the viscosity of the amine solution, where the viscosity of solution could be approximated using the viscosity of pure substances with its respective mole fraction as follows:

$$ln(\eta_o) = x_1 ln(\eta_1) + x_i ln(\eta_i) + x_1 x_j ln(\eta^*_{1i}) \quad (15)$$

Where η_o is the calculated viscosity of an amine solution, η_i represents the pure density of amine which could be calculated through Eqn 7 and parameters in Table 3 and η^*_{1i} describes the non-ideal viscosity term of mixture. The viscosity of water in this question was approximated using the IAPWS-95 equation recommended with AARD values of 0.1%, which takes the form of expression as follows [42]:

$$ln(\eta_1) = -3.6957 + \frac{1.9011}{(T/T_o) - 0.4689} \quad (16)$$

The term η^*_{1i} describes any deviation occured in the viscosity of solution from its ideal value. This term was modelled using the Redlich-Kister expansion with a quadratic polynomial form on mole fractions upon performing a multiple linear regression analysis, resulting in a correlation of the following expression:

$$x_1 x_j ln(\eta^*_{1i}) = x_1 x_i [A_1 + A_2(x_1 - x_i) + A_3(x_1 - x_i)^2] \quad (17)$$

The temperature dependence for the leading A_j terms were tested and it was found that expanding the term as a function of reciprocal of absolute temperature $(1/T)$ was proven most fitting demonstrated through the significant low AARD obtained as compared to a direct dependence on T. As similar temperature dependence of viscosity was observed in the frequently used VFT equation to calculate $ln(\eta)$, this then supported the reliability of the temperature dependence chosen to model $ln(\eta^*_{1i})$. Therefore, A_j was expanded as follows:

$$A_j = a_j + b_j \left(\frac{T}{T_o}\right) + c_j \left(\frac{T}{T_o}\right)^2 \quad (18)$$

The resulting parameters obtained through least square optimisation are presented in Table 4 along with their respective AARD and MARD values, which supported a strong goodness of fit of the models obtained in characterising the viscosity of amine solution which was validated by experimental data as observed in Fig 3

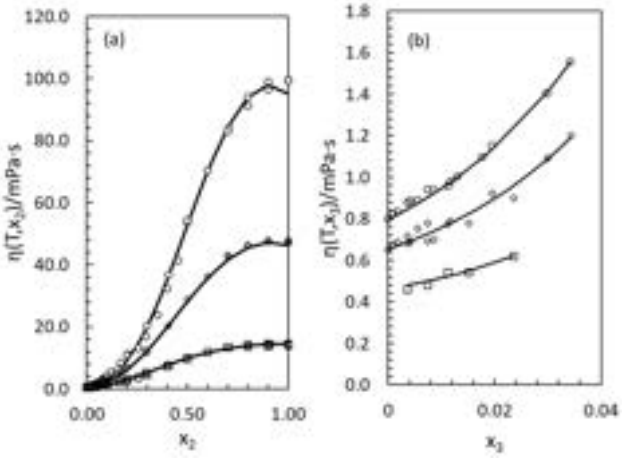

Figure 3: Unloaded viscosity of experimental values compared to empirical correlation at various temperature for (a) AMP and (b) PZ : ○, T = 303.15 K; ◇, T = 313.15 K; □, T = 333.15 K. Lines were calculated using parameters from Table 4

It could be observed that the AMP binary system required a significantly higher number of parameters as compared to the model obtained for PZ, which were 8 and 3 respectively. This was due to the limited number of experimental data available for PZ and therefore, the model could only be obtained for a low range of molar compositions.

However, similar initial curvature could be observed between both AMP and PZ binary systems which suggests that a similar trend of viscosity could be obtained for PZ at higher compositions as observed for AMP. This could be validated by obtaining additional experimental data to further establish a complete model of viscosity for PZ solution.

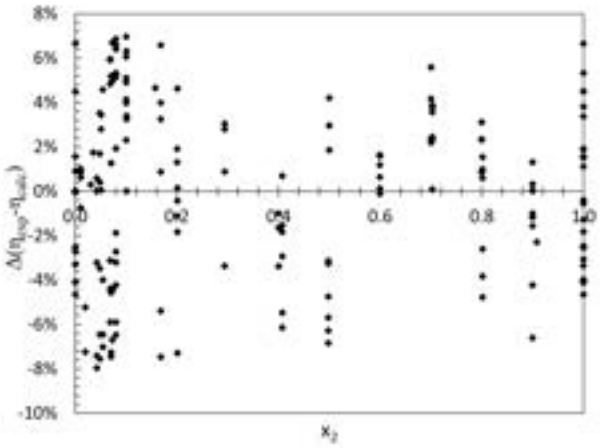

Figure 4: Percentage deviation of experimental viscosities (η_{exp}) of unloaded aqueous AMP solutions from values (η_{calc}) calculated using parameters from Table 4

Another noticeable observation was that both systems exhibited large MARD values. A deviation graph was plotted to examine this finding and as shown in Fig 4, the high deviations mainly occured at $x_2 \leqslant 0.1$. This was caused by the sensitivity of measuring equipment which was on average at 1% and as a result, caused large proportion of absolute deviations at smaller η measured. However, the absolute deviation within this range was reported at values below 0.1 mPas which still supports the excellent fit of the model.

4.3 H_2O-Amine-CO_2 System

The relationships between density of the ternary amine system, ρ with temperature, mass fraction and carbon loading were identified by plotting a graph of of density against a single variable while keeping the other 2 constant. It was apparent that plotting the objective variable as ρ/ρ_o eliminates the temperature dependence of the data. This similar approach was adopted by Freeman and Rochelle [34], which allowed the analysis to solely focus on the effects of mass fraction, w_i and carbon loading, α on density.

The outcome of the analysis exhibited a linear dependence of ρ/ρ_o on α, where the gradient is a quadratic function with respect to w_i achieving a 4-term non-linear equation. This equation was validated against experimental data which enabled the removal of two less-contributing terms without impacting the goodness of fit. The final model was obtained as follows:

Table 4: *Parameters obtained for Eqn 13 and 17 to calculate the density and viscosity of binary systems, along with its respective AARD and MARD*

	a_1	b_1	c_1	a_2	b_2	c_2	a_3	b_3	c_3	AARD %	MARD %
Density											
AMP	-0.00523	-0.00085	-	-0.00806	0.00519	-	-	-	-	0.08	0.38
PZ	0.05345	-0.02848	-	-0.13336	0.01703	-	0.08321	-	-	0.04	0.13
Viscosity											
AMP	-14.714	22.351	-	92.145	-198.28	110.28	200.13	-430.72	233.85	3.32	7.95
PZ	48.093	-	-	-	-	-	-118.55	87.636	-	1.83	6.84

$$\frac{\rho}{\rho_o} = 1 + d\alpha w_i \tag{19}$$

Where d is the parameter to be varied in the optimisation work. A plot comparing experimental data and data generated by the model as a linear function of αw_i could be observed in Fig 5.

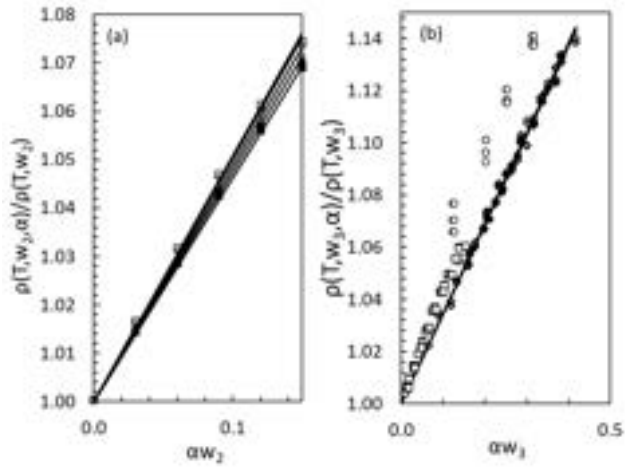

Figure 5: Loaded density of experimental values compared to empirical correlation at various temperature for **(a) AMP** :○, T = 293.15 K; ▫, T = 298.15 K; ⋄, T = 303.15 K; △, T = 313.15 K; •, T = 323.15 K; ■, T = 333.15 K and at various mass fraction for **(b) PZ**: ○, w_3 = 0.15; ⋄, w_3 = 0.15 - 0.63; ▫, w_3 = 0.63. Lines were calculated using parameters from Table 4

The equation was regressed for mass fractions within of range 0.30 - 0.51 for industrial relevance as extreme high and low concentrations of amine is unlikely to be utilised in industrial systems [34]. It was observed that a good fit was achieved for this range supported by the low AARD value of 0.17%.

The robustness of the correlation was further tested by plotting the experimental data outside of the aforementioned range of mass fractions. It could be observed that density with $w = 0.63$ and below $w = 0.15$ exhibited an average deviation of 2.65% and 0.53%. This analysis suggested that the model could be utilised in obtaining a close approximation of density for mass concentration below the range of study, while concentration higher than the range would require a different model.

Limited experimental data was available for the AMP ternary system and therefore, the model proposed could only be validated with mass fraction of $w = 0.30$. An analysis on this data set revealed that there was a more significant temperature dependence of density and therefore, the d term was expanded as follows:

$$d = d_1 + d_2 T \tag{20}$$

Incorporating the additional temperature term significantly reduced the AARD value to 0.07% supporting the good fit of the model. Similar trend was observed for the PZ ternary system at low and high composition of amine, which suggested temperature dependence would be more significant at high and low concentrations of amine in the ternary system and should be incorporated when modelling densities within these ranges.

Table 5: *Parameters obtained for Eqn 19 and 20 to calculate the density of ternary systems, along with its respective AARD and MARD*

	d_1	d_2	AARD %	MARD %
AMP	0.89623	0.00130	0.07	0.16
PZ	0.34447	-	0.17	0.47

The amine-H_2O-CO_2 systems for viscosity were not as straightforward as they depend on temperature, mass fraction and carbon loading. To remove temperature dependence $\eta_{loaded}/\eta_{water}$ was calculated from the experimental values. This ratio was then correlated with modified VFT Eqn 21. Experimental data obtained for PZ were regressed by keeping the mass fraction constant to find the optimal correlation for A and B from Eqn 21. A reasonable correlation could not be established as there were only 4 data set for AMP viscosity.

$$ln\left(\frac{\eta}{\eta_{water}}\right) = A + \frac{B}{C + T/T_o} \tag{21}$$

The best correlation found through this method required 7 parameters as seen in Eqn 22 and Eqn 23. Moreover, at low ($w_2 = 0.15$) and high ($w_2 = 0.63$) mass fraction proposed, the model did not fit. As seen in Fig 7 where the percentage deviation was the lowest at mid range values of αw_3. The same model was then used to fit the AMP data sets.

$$A = a_1 + a_2 w_3 + a_3 w_3^2 + a_4 \alpha + a_5 \alpha^2 \tag{22}$$

Table 6: *Parameters obtained for Eqn 22 and 23 to calculate the viscosity of ternary systems, along with its respective AARD and MARD*

	a_1	a_2	a_3	a_4	a_5	b_1	b_2	AARD %	MARD %
AMP	-0.02230	1.9126	1.3227	0.80238	0.28743	1.6880	1.1511	0.27	0.40
PZ	-2.2326	11.951	-28.064	1.7086	-0.81625	-1.7162	29.703	1.74	6.99

$$B = b_1 w_3 + b_2 w_3^2 \tag{23}$$

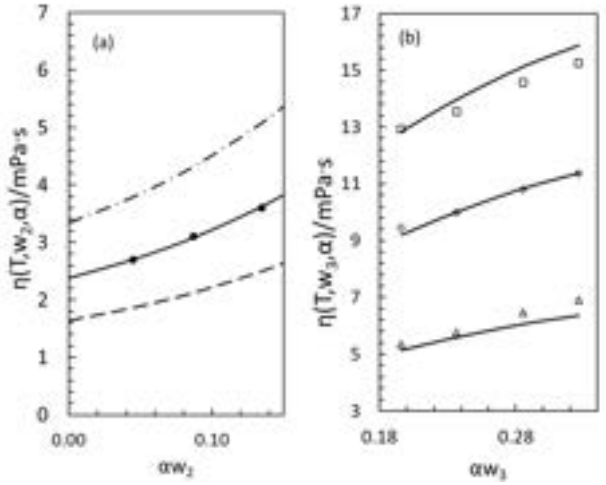

Figure 6: Loaded viscosity of experimental values compared to empirical correlation at mass fraction of w_2 = 0.3 for **(a) AMP** and at various temperature for **(b) PZ**: □, T = 303.15 K; ◇, T = 313.15 K; △, T = 333.15 K. Lines were calculated using parameters from Table 4

Table 6 summarises the values of these parameters for both PZ and AMP. AMP observed the lowest AARD and MARD value compared to PZ. However, this model was only suitable for mass fraction of w_2 = 0.3 and could be extended for a wider temperature range. This relationship could be seen in figure 6 where the correlation for constant mass fraction at different temperature was plotted.

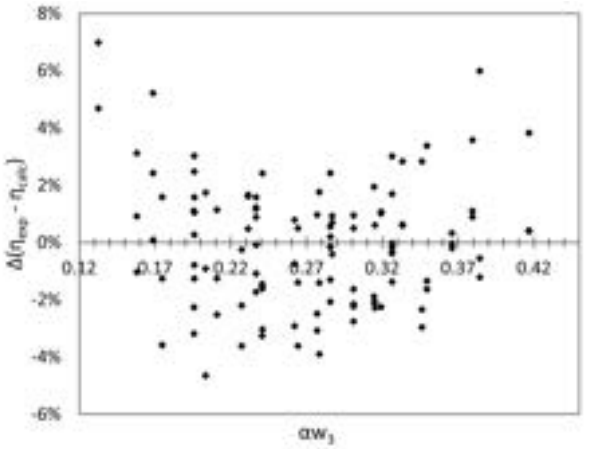

Figure 7: Percentage deviation of experimental viscosities (η_{exp}) of loaded aqueous PZ solutions from values (η_{calc}) calculated using parameters from Table 6

Overall the correlation obtained showed a good fit but viscosity values at two extremes were complex to model. This was due to the formation of carbamate and bicarbonate ions [43]. The formation of these ions creates a more complex chemical interaction which can notably increase the viscosity of the solution. For example, model presented by Freeman and Rochelle [34] for PZ only worked well within amine mass fraction range from 0.30 to 0.46. Therefore, a generic model requires understanding of these interactions.

5 Conclusions

Experimental data obtained from literature review provided the framework which allowed model of equations to be obtained to predict the density and viscosity of amine solutions. Empirical correlations to model the density and viscosity of the CO_2-loaded and unloaded AMP and PZ solutions as a function of temperature, composition and CO_2-loading were achieved using polynomial, VFT and Redlich-Kister equations. The models obtained were of high accuracy with an average AARD values of 0.1% for density and 2.0% for viscosity which suggested that the models obtained provided a good fit to the measured data. Overall this work unifies existing research on AMP and PZ to provide an insight to improve the modelling of these molecules in order to design a better optimised CCUS plants.

6 References

[1] N. W. Arnell, J. A. Lowe, A. J. Challinor, and T. J. Osborn, "Global and regional impacts of climate change at different levels of global temperature increase," *Climatic Change*, vol. 155, no. 3, pp. 377–391, Aug. 2019. [Online]. Available: https://doi.org/10.1007/s10584-019-02464-z

[2] "Global Warming of 1.5 ºC —." [Online]. Available: https://www.ipcc.ch/sr15/

[3] M. Crippa, G. Oreggioni, M. Muntean, E. Schaaf, E. Lo Vullo, E. Solazzo, F. Monforti, J. Oliver, and E. Vignati, *EDGAR booklet 2019*, Oct. 2019.

[4] J. P. Gouveia, J. Seixas, M. Labriet, P. Fortes, and M. Gargiulo, "Prospective scenarios for the adoption of CCS technologies in the Iberian Peninsula," *Sustainable Energy Technologies and Assessments*, vol. 2, pp. 31 – 41, 2013. [Online]. Available: http://www.sciencedirect.com/science/article/pii/S2213138813000234

[5] B. Dutcher, M. Fan, and A. G. Russell, "Amine-Based CO2 Capture Technology Development from the Beginning of 2013—A Review," *ACS Applied Materials & Interfaces*, vol. 7, no. 4, pp. 2137–2148, 2015, _eprint: https://doi.org/10.1021/am507465f. [Online]. Available: https://doi.org/10.1021/am507465f

[6] B. Xue, Y. Yu, J. Chen, X. Luo, and M. Wang, "A comparative study of MEA and DEA for post-combustion CO2 capture with different process configurations," *International Journal of Coal Science & Technology*, vol. 4, no. 1, pp. 15–24, Mar. 2017. [Online]. Available: https://doi.org/10.1007/s40789-016-0149-7

[7] Q. Huang, J. Thompson, L. Lampe, J. Selegue, and K. Liu, "Thermal Degradation Comparison of Amino Acid Salts, Alkanolamines and Diamines in CO2 Capture," *Energy Procedia*, vol. 63, pp. 1882–1889, 2014.

[8] A. Wilk, L. Więcław-Solny, D. Śpiewak, T. Spietz, and H. Kierzkowska-Pawlak, "A Selection of Amine Sorbents for CO2 Capture from Flue Gases," *Chemical and Process Engineering*, vol. 36, 2015.

[9] S. Kadiwala, A. V. Rayer, and A. Henni, "High pressure solubility of carbon dioxide (CO2) in aqueous piperazine solutions," *Fluid Phase Equilibria*, vol. 292, no. 1, pp. 20 – 28, 2010. [Online]. Available: http://www.sciencedirect.com/science/article/pii/S0378381210000233

[10] S. K. Dash, A. N. Samanta, and S. S. Bandyopadhyay, "Solubility of carbon dioxide in aqueous solution of 2-amino-2-methyl-1-propanol and piperazine," *Fluid Phase Equilibria*, vol. 307, no. 2, pp. 166 – 174, 2011. [Online]. Available: http://www.sciencedirect.com/science/article/pii/S0378381211002408

[11] H. Rashid, N. Hasan, M. Nor, and M. Iskandar, "Temperature Peak Analysis and Its Effect on Absorption Column for CO2 Capture Process at Different Operating Conditions," *Chemical Product and Process Modeling*, vol. 9, 2014.

[12] C. Chan, Y. Maham, A. E. Mather, and C. Mathonat, "Densities and volumetric properties of the aqueous solutions of 2-amino-

2-methyl-1-propanol, n-butyldiethanolamine and n-propylethanolamine at temperatures from 298.15 to 353.15 K," *Fluid Phase Equilibria*, vol. 198, no. 2, pp. 239 – 250, 2002. [Online]. Available: http://www.sciencedirect.com/science/article/pii/S0378381201007683

[13] A. Muhammad, M. I. A. Mutalib, T. Murugesan, and A. Shafeeq, "Thermophysical Properties of Aqueous Piperazine and Aqueous (N-Methyldiethanolamine + Piperazine) Solutions at Temperatures (298.15 to 338.15) K," *Journal of Chemical & Engineering Data*, vol. 54, no. 8, pp. 2317–2321, Aug. 2009, publisher: American Chemical Society. [Online]. Available: https://doi.org/10.1021/je9000069

[14] Patil Mayurkumar, Vaidya Prakash, and Kenig Eugeny, "Bench-scale study for co2 capture using amp/pz/water mixtures," *Chemical Engineering Transactions*, vol. 69, pp. 163–168, Oct. 2018. [Online]. Available: https://doi.org/10.3303/CET1869028

[15] Y.-R. Chen, A. R. Caparanga, A. N. Soriano, and M.-H. Li, "Liquid heat capacity of the solvent system (piperazine+2-amino-2-methyl-1-propanol+water)," *The Journal of Chemical Thermodynamics*, vol. 42, no. 4, pp. 518 – 523, 2010. [Online]. Available: http://www.sciencedirect.com/science/article/pii/S0021961409002729

[16] A. Hartono, M. Saeed, A. F. Ciftja, and H. F. Svendsen, "Binary and ternary VLE of the 2-amino-2-methyl-1-propanol (AMP)/piperazine (Pz)/water system," *Chemical Engineering Science*, vol. 91, pp. 151 – 161, 2013. [Online]. Available: http://www.sciencedirect.com/science/article/pii/S0009250913000213

[17] R. H. Weiland, J. C. Dingman, D. B. Cronin, and G. J. Browning, "Density and Viscosity of Some Partially Carbonated Aqueous Alkanolamine Solutions and Their Blends," *Journal of Chemical & Engineering Data*, vol. 43, no. 3, pp. 378–382, 1998, _eprint: https://doi.org/10.1021/je9702044. [Online]. Available: https://doi.org/10.1021/je9702044

[18] J. Aguila-Hernández, R. Gómez-Quintana, F. Murrieta-Guevara, A. Romero-Martínez, and A. Trejo, "Liquid Density of Aqueous Blended Alkanolamines and N-Methylpyrrolidone as a Function of Concentration and Temperature," *Journal of Chemical & Engineering Data*, vol. 46, no. 4, pp. 861–867, 2001, _eprint: https://doi.org/10.1021/je0002944. [Online]. Available: https://doi.org/10.1021/je0002944

[19] E. Álvarez, D. Gómez-Díaz, M. D. La Rubia, and J. M. Navaza, "Densities and Viscosities of Aqueous Ternary Mixtures of 2-(Methylamino)ethanol and 2-(Ethylamino)ethanol with Diethanolamine, Triethanolamine, N-Methyldiethanolamine, or 2-Amino-1-methyl-1-propanol from 298.15 to 323.15 K," *Journal of Chemical & Engineering Data*, vol. 51, no. 3, pp. 955–962, May 2006, publisher: American Chemical Society. [Online]. Available: https://doi.org/10.1021/je050463q

[20] N. O. Braun, U. Persson, and H. T. Karlsson, "Densities and Viscosities of Mono(ethylene glycol) + 2-Amino-2-methyl-1-propanol + Water," *Journal of Chemical & Engineering Data*, vol. 46, no. 4, pp. 805–808, 2001, _eprint: https://doi.org/10.1021/je010004z. [Online]. Available: https://doi.org/10.1021/je010004z

[21] A. Henni, J. J. Hromek, P. Tontiwachwuthikul, and A. Chakma, "Volumetric Properties and Viscosities for Aqueous AMP Solutions from 25 °C to 70 °C," *Journal of Chemical & Engineering Data*, vol. 48, no. 3, pp. 551–556, 2003, _eprint: https://doi.org/10.1021/je0201119. [Online]. Available: https://doi.org/10.1021/je0201119

[22] S. S. Karunarathne, D. A. Eimer, and L. E. Øi, "Density, viscosity and free energy of activation for viscous flow of CO2 loaded 2-amino-2-methyl-1-propanol (AMP), monoethanol amine (MEA) and H2O mixtures," *Journal of Molecular Liquids*, vol. 311, p. 113286, 2020. [Online]. Available: http://www.sciencedirect.com/science/article/pii/S0167732219367005

[23] A. A. Khan, G. N. Halder, and A. K. Saha, "Comparing CO2 removal characteristics of aqueous solutions of monoethanolamine, 2-amino-2-methyl-1-propanol, methyldiethanolamine and piperazine through absorption process," *International Journal of Greenhouse Gas Control*, vol. 50, pp. 179 – 189, 2016. [Online]. Available: http://www.sciencedirect.com/science/article/pii/S1750583616302201

[24] G. Li, H. Chi, Y. Guo, W. Fang, and S. Hu, "Excess Molar Volume along with Viscosity and Refractive Index for Binary Systems of Tricyclo[5.2.1.02.6]decane with Five Cycloalkanes," *Journal of Chemical & Engineering Data*, vol. 58, no. 11, pp. 3078–3086, 2013, _eprint: https://doi.org/10.1021/je400529k. [Online]. Available: https://doi.org/10.1021/je400529k

[25] B. P. Mandal, M. Kundu, and S. S. Bandyopadhyay, "Density and Viscosity of Aqueous Solutions of (N-Methyldiethanolamine + Monoethanolamine), (N-Methyldiethanolamine + Diethanolamine), (2-Amino-2-methyl-1-propanol + Monoethanolamine), and (2-Amino-2-methyl-1-propanol + Diethanolamine)," *Journal of Chemical & Engineering Data*, vol. 48, no. 3, pp. 703–707, 2003, _eprint: https://doi.org/10.1021/je020206a. [Online]. Available: https://doi.org/10.1021/je020206a

[26] M. Stec, T. Spietz, L. Więcław-Solny, A. Tatarczuk, A. Wilk, and A. Sobolewski, "Density of unloaded and CO2-loaded aqueous solutions of piperazine and 2-amino-2-methyl-1-propanol and their mixtures from 293.15 to 333.15 K," *Physics and Chemistry of Liquids*, vol. 54, no. 4, pp. 475–486, 2016, publisher: Taylor & Francis _eprint: https://doi.org/10.1080/00319104.2015.1115328. [Online]. Available: https://doi.org/10.1080/00319104.2015.1115328

[27] M. E. Rebolledo-Libreros and A. Trejo, "Density and Viscosity of Aqueous Blends of Three Alkanolamines: N-Methyldiethanolamine, Diethanolamine, and 2-Amino-2-methyl-1-propanol in the Range of (303 to 343) K," *Journal of Chemical & Engineering Data*, vol. 51, no. 2, pp. 702–707, 2006, _eprint: https://doi.org/10.1021/je050462y. [Online]. Available: https://doi.org/10.1021/je050462y

[28] A. Samanta and S. S. Bandyopadhyay, "Density and Viscosity of Aqueous Solutions of Piperazine and (2-Amino-2-methyl-1-propanol + Piperazine) from 298 to 333 K," *Journal of Chemical & Engineering Data*, vol. 51, no. 2, pp. 467–470, 2006, _eprint: https://doi.org/10.1021/je050378i. [Online]. Available: https://doi.org/10.1021/je050378i

[29] A. Shojaeian and A. Haghtalab, "Solubility and density of carbon dioxide in different aqueous alkanolamine solutions blended with 1-butyl-3-methylimidazolium acetate ionic liquid at high pressure," *Journal of Molecular Liquids*, vol. 187, pp. 218 – 225, 2013. [Online]. Available: http://www.sciencedirect.com/science/article/pii/S0167732213002481

[30] L. M. Welsh and R. A. Davis, "Density and Viscosity of Aqueous Blends of N-Methyldiethanolamine and 2-Amino-2-methyl-1-propanol," *Journal of Chemical & Engineering Data*, vol. 40, no. 1, pp. 257–259, 1995, _eprint: https://doi.org/10.1021/je00017a055. [Online]. Available: https://doi.org/10.1021/je00017a055

[31] S. Xu, F. D. Otto, and A. E. Mather, "Physical properties of aqueous AMP solutions," *Journal of Chemical & Engineering Data*, vol. 36, no. 1, pp. 71–75, 1991, _eprint: https://doi.org/10.1021/je00001a021. [Online]. Available: https://doi.org/10.1021/je00001a021

[32] K. Zhang, B. Hawrylak, R. Palepu, and P. R. Tremaine, "Thermodynamics of aqueous amines: excess molar heat capacities, volumes, and expansibilities of water+ methyldiethanolamine (MDEA) and water + 2-amino-2-methyl-1-propanol (AMP)," *The Journal of Chemical Thermodynamics*, vol. 34, no. 5, pp. 679 – 710, 2002. [Online]. Available: http://www.sciencedirect.com/science/article/pii/S0021961402909377

[33] P. W. Derks, K. J. Hogendoorn, and G. F. Versteeg, "Solubility of N2O in and Density, Viscosity, and Surface Tension of Aqueous Piperazine Solutions," *Journal of Chemical & Engineering Data*, vol. 50, no. 6, pp. 1947–1950, 2005, _eprint: https://doi.org/10.1021/je050202g. [Online]. Available: https://doi.org/10.1021/je050202g

[34] S. A. Freeman and G. T. Rochelle, "Density and Viscosity of Aqueous (Piperazine + Carbon Dioxide) Solutions," *Journal of Chemical & Engineering Data*, vol. 56, no. 3, pp. 574–581, 2011, _eprint: https://doi.org/10.1021/je1012263. [Online]. Available: https://doi.org/10.1021/je1012263

[35] J. Liu, S. Wang, A. Hartono, H. F. Svendsen, and C. Chen, "Solubility of N2O in and Density and Viscosity of Aqueous Solutions of Piperazine, Ammonia, and Their Mixtures from (283.15 to 323.15) K," *Journal of Chemical & Engineering Data*, vol. 57, no. 9, pp. 2387–2393, 2012, _eprint: https://doi.org/10.1021/je300102d. [Online]. Available: https://doi.org/10.1021/je300102d

[36] G. Murshid, A. Shariff, M. Bustam, and F. Ahmad, "Volumetric Properties, Viscosities and Refractive Indices of Aqueous Solutions of 2-Amino-2-methyl-1-propanol (AMP)," *Research Journal of Chemistry and Environment*, vol. 17, pp. 22–31, 2013.

[37] T. F. Sun, P. J. Kortbeek, N. J. Trappeniers, and S. N. Biswas, "Acoustic and Thermodynamic Properties of Benzene and Cyclohexane as a Function of Pressure and Temperature," *Physics and Chemistry of Liquids*, vol. 16, no. 3, pp. 163–178, 1987, publisher: Taylor & Francis _eprint: https://doi.org/10.1080/00319108708078516. [Online]. Available: https://doi.org/10.1080/00319108708078516

[38] M.-H. Li and Y.-C. Lie, "Densities and Viscosities of Solutions of Monoethanolamine + N-methyldiethanolamine + Water and Monoethanolamine + 2-Amino-2-methyl-1-propanol + Water," *Journal of Chemical & Engineering Data*, vol. 39, no. 3, pp. 444–447, 1994, _eprint: https://doi.org/10.1021/je00015a009. [Online]. Available: https://doi.org/10.1021/je00015a009

[39] L. S. Lasdon, A. D. Waren, A. Jain, and M. Ratner, "Design and Testing of a Generalized Reduced Gradient Code for Nonlinear Programming," *ACM Trans. Math. Softw.*, vol. 4, no. 1, pp. 34–50, Mar. 1978, place: New York, NY, USA Publisher: Association for Computing Machinery. [Online]. Available: https://doi.org/10.1145/355769.355773

[40] "Piperazine." [Online]. Available: https://pubchem.ncbi.nlm.nih.gov/compound/Piperazine#section=Melting-Point

[41] H. Rashid, N. Hasan, M. Nor, and M. Iskandar, "Temperature peak analysis and its effect on absorption column for co2 capture process at different operating conditions," *Chemical Product and Process Modeling*, vol. 9, 01 2014.

[42] W. Wagner and A. Pruß, "The IAPWS Formulation 1995 for the Thermodynamic Properties of Ordinary Water Substance for General and Scientific Use," *Journal of Physical and Chemical Reference Data*, vol. 31, 2002.

[43] H. Svensson, C. Hulteberg, and H. T. Karlsson, "Precipitation of AMP Carbamate in CO2 Absorption Process," *Energy Procedia*, vol. 63, pp. 750 – 757, 2014. [Online]. Available: http://www.sciencedirect.com/science/article/pii/S1876610214018980

Agent-Based Modelling of The Steelmaking Industry in India:
Assessment of Preferential Pathways towards Sustainable Development

Miguel Lema Botelho, Rou Jing Tan

Abstract

This paper investigates the preferential pathways to meet projected steel demand in Maharashtra, India, whilst achieving decarbonisation of the steelmaking industry in the region. To achieve this objective, an agent-based modelling approach with the ModUlar energy systems Simulation Environment (MUSE) is used. Three main production routes are analysed: Blast Furnace/Basic Oxygen Furnace, Electric Arc Furnace and Hydrogen Direct Reduction. Various configurations for each of these routes are considered to account for different fuel types, electricity sources, levels of scrap usage and the option to import hydrogen or generate it on-site through an electrolyser. Three options were considered for the electricity sources: cogeneration, harnessing electricity from the grid in India or from a source with a mix of variable renewable electricity and gas. The last option was only explored for the Hydrogen Direct Reduction process, given that its CO_2 mitigation potential is limited when cogeneration is used or when electricity is harnessed directly from the grid, due to the high emissions grid factor in India. Results show that the implementation of carbon prices is crucial to drive the adoption of Hydrogen Direct Reduction process. However, significant decarbonisation can only be achieved through a combination of high carbon prices and access to a low cost and low CO_2 intensive source, such as variable renewable electricity and gas, to power the Hydrogen Direct Reduction process. However, it is found that this will lead to a considerably higher energy consumption. Therefore, a key area of focus to achieve decarbonisation will be ensuring the required energy supply, with an emphasis placed on supporting the growth of variable renewable electricity availability. Decarbonisation of the steelmaking industry will inevitably lead to higher costs of steel production. Therefore, effective policy efforts and favourable market condition, such as the increasing global demand for carbon-free steel, will be key factors to enable the sustainable development of steelmaking industry in this region. Additionally, Hydrogen Direct Reduction was shown to be a better long-term investment than Electric Arc Furnace, which was not adopted in any of the scenarios despite the latter having a lower capital and operating costs.

Keywords - Hydrogen, Steel Production in India, Decarbonisation, Hydrogen Direct Reduction (H-DR), Agent-based Modelling

1. Introduction

In 2019, the iron and steel sector alone contributed to 7% of the total global CO_2 emissions[1]. This sector is also the largest industrial consumer of coal, which globally provides 75% of its energy demand [1]. Global crude steel production reached approximately 1870 Mt in 2019, up by 3.4% compared to 2018, and is projected to increase in the future [2]. This presents the challenge of how to keep with rising steel demand whilst decarbonising the sector. As the second largest steel producing country in the world [2], India will be instrumental in the global steel industry transition. This sector plays a key role in India's economy, accounting for 2% of GDP, but it also accounts for 7% of total CO_2 emissions in the country [3]. In fact, India's steel industry is much more energy and emissions intensive when compared to international benchmarks [4]. This stems from factors such as the heavy reliance on coal for directly reduced iron (DRI) furnaces and the relatively low share of scrap in the sector's total metallic inputs (23%), when compared to the global average (32%) [4]. Steel demand in India is expected to increase by almost five-fold in the next 30 years, driven by both economic growth and infrastructure development [5]. It is predicted that this would lead CO_2 emissions to triple by 2050, in case action is not taken [6]. As a result, decarbonisation of the steel industry has become an important area of focus for the Indian government, as it strives towards meeting its emission targets outlined in the Paris Agreement [7]. The Indian government has already rolled out several policies aimed at improving energy efficiency and environmental performance. These include the coal tax, the Perform Achieve Trade (PAT) Scheme to reduce energy consumption by promoting energy efficiency, and the National Resource Efficiency Policy [8]. However, there are currently no taxes directly applicable to CO_2 emissions [5].

Some of the decarbonisation strategies that could be pursued in India's steel making industry include:

- **Improving energy efficiency:** Steel production is energy intensive. It is important that players in this sector adopt industry best practices and implement the required energy management systems to ensure efficient use and recovery of energy throughout the steelmaking process.
- **BF/BOF efficiency programs, examples:**
  1) optimizing the blast furnace (BF) burden mix by maximizing the iron content in raw materials to decrease the usage of coal as a reductant
  2) using coke oven gas in the BF as an energy source [9].
- **Increasing share of scrap-based EAF:** Steel production through the secondary route requires around one-eight of the energy of that produced from iron ore [4]. However, the potential of increasing the share of Electric Arc Furnace (EAF) based steel production is limited due to the scrap availability required to fulfil the input requirements, as well as the continuous demand for high quality virgin steel.
- **Maintaining existing processes but with Carbon Capture and Storage (CCS)**
- **Switching to alternative fuels and reductants**
- **Deployment of alternative production methods. Some examples include:**

1) Smelting reduction
2) Bioenergy with CCS (bio-CCS)
3) Electrowinning
4) Top gas recycling blast furnace (TGRBF/BOF) with CCS and biomass
5) Directly Reduced Iron (DRI) and EAF using hydrogen as a reductant (H-DR)

In the short term, CO_2 emissions reductions can be achieved by promoting energy efficiency and secondary production routes. However, to achieve deep CO_2 emissions cuts in the long term, fundamental changes in the steelmaking processes are required. H-DR is believed to be one of the most promising technologies to achieve this goal, where favorable market conditions and environmental policy will play a key role.

This study follows an agent-based modelling approach with MUSE (ModUlar energy systems Simulation Environment) to conduct an assessment of the preferential pathways to meet projected steel demand by 2050, whilst decarbonising the steelmaking sector. The scope of this study is concentrated in Maharashtra, India. This region is studied due to it being an industrial hub [10], with BF/BOF accounting for 100% of steel production capacity[11]. Therefore, there presents a high decarbonisation potential.

2. Literature Review

There are various studies in scientific literature where techno-economic models are used to outline preferential pathways to meet the projected steel demand, whilst achieving decarbonisation. Upon assessing previous work, it was found that the majority of these studies were carried out for Sweden and Germany. Fischedick et. al [12] identified the H-DR process as the most economically and environmentally attractive production route for Germany's steel industry in the long-term through a multi-criteria analysis, when comparing it to other alternative production methods. Toktarova et al. [13] conducted a techno-economic evaluation of Sweden's steel industry, with the conclusion that large-scale adoption of H-DR could result in almost completely fossil-free steel production, thereby achieving carbon neutrality in sector by 2045. In fact, it is predicted that Sweden will be marketing fossil-free steel as early as in 2026 due to the Hydrogen Breakthrough Ironmaking Technology (HYBRIT) projects currently taking place [14].

The techno-economic aspects of hydrogen direct reduction have been studied in existing literature. However, there is limited information regarding knowledge development and learning curves since there are only a small number of R&D projects and hydrogen reduction technology is not widespread enough yet [15]. Vogl et al. outlined a potential process design for the H-DR process and corresponding operational parameters, energy consumption, and economic performance, as well as considerations around scrap variability[16]. However, there is a lack of information in scientific literature when it comes to other possible configurations of the H-DR process, such as having the option for co-generation.

Although several studies mentioned H-DR as the most promising technology for the steel industry transition, it is important to note that the conditions under which case studies for countries such as Sweden and Germany were conducted do not accurately reflect the reality of other major steel producing countries, such as India. These include country specific factors such the grid emissions intensity, projected steel demand, as well as the policy and regulatory environment. On the other hand, a large part of the CO_2 mitigation achieved through the H-DR process depends on the energy mix employed, especially considering its high electricity consumption. Therefore, a high emissions grid factor, such as the one observed in India, could potentially lead to a different outlook than the one obtained in the case studies for Germany and Sweden. For these reasons, a case study specific to India is required.

The Energy and Resources Institute published a report on India's steel sector roadmap highlighting different strategies to achieve decarbonisation, with results showing that the large-scale adoption of H-DR could lead to a 94% reduction in CO_2 emissions, assuming hydrogen production is emissions free [5]. However, the findings from this study present an overly optimistic view with limited implementation considerations. There are also gaps when it comes to considerations around scrap availability, and the option to have different configurations for each production method. These factors were accounted for in this study. The International Energy Agency argued that in order to achieve deep emission cuts with the adoption of H-DR in India, this process would have to be fully powered by variable renewable electricity (VRE)[4]. The option to harness VRE to power the H-DR process is explored in this study as well.

Diego et al. [11] set out an agent-based methodology integrated in MUSE (ModUlar energy systems Simulation Environment) to model and assess the opportunities for fuel-switching within the iron-steel industry in Maharashtra, India. This study also highlighted the advantages of using Agent-Based Integrated Assessment Model (AB-IAM) such as MUSE over conventional IAMs.

This study follows an agent-based model integrated in MUSE and aims to give a holistic overview of the challenges and opportunities for the adoption of alternative production routes to achieve decarbonisation in the steelmaking industry in Maharashtra, India. The authors believe that this study will be of interest to the policy-makers and investors in India.

3. Methodology

3.1. MUSE Modelling

The ModUlar energy systems Simulation Environment (MUSE) was utilised to achieve the objectives of this study. MUSE was chosen due to its ability to focus on an investor's motivations to favour a particular production pathway, while employing an iterative market clearing algorithm (MCA) that simulates a real-world environment to connect all parts of the model in achieving a partial equilibrium. The total investment decision is made considering the estimated future demand, estimated future installed capacity and the technologies' utilisation factor. The agents then rank the available configurations based on the chosen investment objectives, and invests into potential new assets preferentially, until the demand gap is

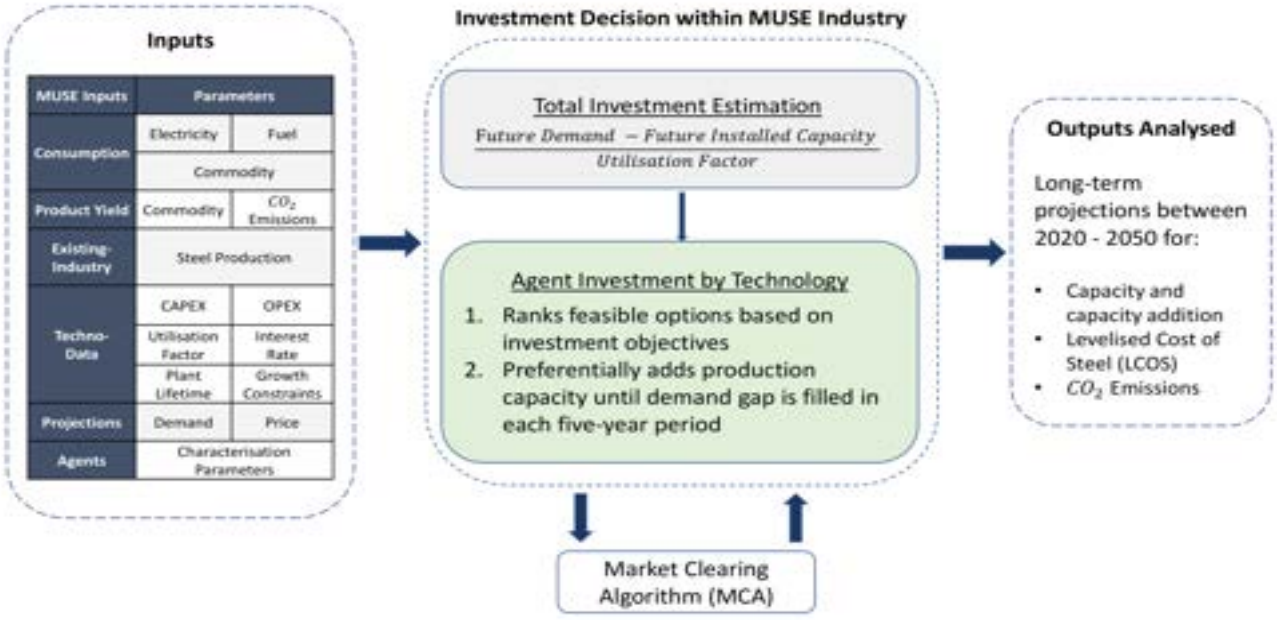

Fig. 1: MUSE Model Framework [11], [17]

filled in each five-year period. Hence, this approach leads to a more realistic long-term decision-making process both in terms of investment and operational feasibility. Figure 1 shows a visual representation of the framework followed in the MUSE model.

Techno-economic data, consumption and product yield inputs were obtained from literature sources (refer to Section 8). Existing industry steel production and demand projections in the region considered were obtained from [11].

A single-agent approach was employed with the main investment objective of minimising the levelised cost of steel (LCOS). This is due to the cost objective being a distinctive feature of the industrial investors in this sector. The LCOS metric also allows for the consideration of all inputs and their inter-dependencies. This includes factors such as capital, fuel and emission costs, thus presenting a more comprehensive overview of the modelled scenarios.

For each simulation, the MUSE model generates long-term projection outputs for each asset across each 5-year time segment between 2020 and 2050. The most relevant outputs for this study were determined to be capacity & capacity additions, levelised cost of steel (LCOS), CO_2 emissions and energy consumption.

3.2. *Sources of electricity*

Different configurations were considered for each production route depending on the source of electricity used. These include electricity generated on-site through a Combined heat and power (CHP) unit, electricity harnessed from the grid in India and a combination of variable renewable electricity with natural gas (VREg). All relevant techno-economic data are available in Section 8.

3.2.1. CHP: The first option considered was to generate electricity on site through a CHP system, also known as cogeneration. The Combined-cycle gas turbines (CCGT) were selected for this case, as they are favored in process industry applications due to their high electrical efficiency. The emissions factor for this option was estimated to be 0.45 tCO_2/MWh [18].

3.2.2. Grid: The option to import electricity from the grid in India was also considered. The emissions grid factor in India was estimated to be 0.82 tCO_2/MWh [19]. This high value is driven by the large proportion of coal in the power generation sector mix, which was 73% in 2018 [20]. Despite the projected growth in the share of renewables on top of potential efficiency improvements, it is unrealistic to expect significant decarbonisation within India's power generation sector in the short to medium term. For these reasons, the CO_2 mitigation potential of H-DR is limited, given its significant electricity consumption coupled with the high grid emissions intensity in India. Therefore, the option of utilising electricity from a low carbon intensity source to power the H-DR process was examined.

3.2.3. VREg: An alternative approach to using grid electricity is to harness variable renewable electricity (VRE) directly. By 2035, Solar Photovoltaics (PV) generation is expected to achieve levelised costs of around USD 20/MWh and wind around USD 30/MWh in certain locations in India. These regions possess the highest capacity factors, wind speeds and irradiation potential that allow such techo-economic advancements to be possible [4]. Given the low cost of electricity and very low CO_2 intensity, having VRE as the main power source for H-DR processes has considerable potential in driving this production route. Additional factors such as higher carbon taxes could then increase the cost competitiveness of this route

even further. However, there are undoubtedly implementation challenges associated with the variability of VRE due to intermittencies of its sources. This could be tackled either from the supply side (e.g through the use of hydrogen or battery electricity storage), or from the demand side (e.g tolerance of a certain degree of ramping or periods of ceasing production), where additional costs would have to be considered [4]. In this particular study, a combination of VRE and natural gas was chosen to fulfill the demand gap (VREg), and to ensure a more stable process operation condition. This would still result in an associated low cost and low CO_2 intensity of the electricity, whilst ensuring operational feasibility. The estimated emissions factor is 0.09 tCO_2/MWh in 2035, which is a very significant decrease compared to all other options.

3.3. Production routes and corresponding configurations

This section presents the 3 production routes and the respective configurations considered. All relevant techno-economic data are available in Section 8.

3.3.1. BF/BOF: In this production route, iron ore is reduced in the blast furnace (BF) and refined to crude steel in the basic oxygen furnace (BOF). The main reducing agent, coke, alongside the typical fuels employed: coal, natural gas and heavy fuel oil, contributes to a large amount of CO_2 emissions. This is currently the main production method in the region of focus, accounting for nearly 100% of total steel production. A total of six configurations were considered to account for different fuel types and sources of electricity used, as shown in Table I.

Table I: BF/BOF Configurations

Fuel Type	Electricity Source	
	Imported	Generated
Coal	bof_coal_eim	bof_coal_egen
Gas	bof_NG_eim	bof_NG_egen
Fuel Oil	bof_fo_eim	bof_fo_egen

3.3.2. EAF: The Electric Arc Furnace (EAF) process primarily employs scrap to produce steel. This production method involves the melting of scrap metal in an electric arc with heat emitted by electrodes, leading to a high electricity consumption. This secondary steelmaking production route had already been presented in various case studies as a competitive alternative to the BF/BOF process in terms of both economic performance and CO_2 abatement potential. However, there are limitations for its adoption coming from scrap availability and the continuous demand for high quality virgin steel. Through the consideration of the current proportion of steel production in Maharashtra compared to the whole of India, as well as the current % of steel produced with EAF in the country, the maximum limit on scrap-based production configuration capacities were calculated and subsequently accounted for in the model by limiting the maximum capacity additions. As shown in Table II, two configurations were considered to account for different electricity sources.

3.3.3. H-DR: The base configuration for the H-DR process in this study is shown in Figure 2. Utilising hydrogen as the reducing agent, the iron ore is reduced directly in the shaft, and compacted to hot briquetted iron (HBI), which is then melted and converted to liquid steel in an electric arc furnace (EAF).

Table II: EAF Configurations

Electricity Source	
Imported	Generated
EAF_eim	EAF_egen

In order to account for the operational flexibility with the usage of scrap in the H-DR process, two options were considered – 100% hot briquetted iron (HBI) and 50% scrap/ 50% HBI. Similarly to the EAF, the scrap-based H-DR configurations had capacity addition limitations to account for the scrap availability as well. The option to import hydrogen or to produce it on-site with an electrolyser was also considered. In the cases where hydrogen is imported, it is exclusively referring to "green" hydrogen, which is obtained from a VREg electricity source. The possibility to use electricity from different sources was also considered when formulating the configurations. These include importing electricity from the grid or from the VREg mix, as well as generating electricity on site. A total of eight configurations were considered, as shown in Table III. One important point to note is the source of the imported electricity depends on the scenario considered to distinct between either the grid or VREg mix.

Table III: H-DR Configurations

Hydrogen Source	Scrap Usage	Electricity Source	
		Imported*	Generated
Imported	0	hdr1_him_eim	hdr1_him_eg
	50%	hdr2_him_eim	hdr2_him_eg
Generated	0	hdr1_hg_eim	hdr1_hg_eg
	50%	hdr2_hg_eim	hdr2_hg_eg

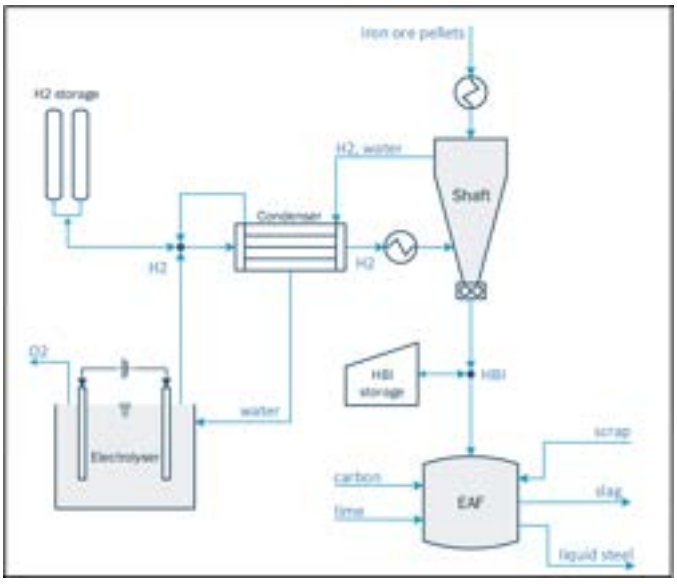

Fig. 2: HDR Process Diagram [16]

3.4. Scenario Modelling

A total of 6 scenarios were considered with the aim of understanding the impact of various factors such as potential carbon prices imposed by the Indian government, and having the H-DR process to be powered by VREg sources. The scenarios considered are as follows:

- Base Case
- Scenario 1 – Implementation of moderate carbon taxes
- Scenario 2 – Implementation of high carbon taxes
- Base Case VREg
- Scenario 3 – VREg powered H-DR, Implementation of moderate carbon taxes
- Scenario 4 – VREg powered H-DR, Implementation of high carbon taxes

All stated scenarios are modelled with current projections for the various techno-economic factors considered, such as the price of commodity and energy inputs, grid emissions intensity and technology efficiencies. The carbon taxes utilised are shown in Table IV.

Table IV: Carbon Prices Implemented

Carbon prices (USD / ton CO_2)	2020	2050
Moderate	10	50
High	10	80

4. RESULTS AND DISCUSSION

As mentioned in Section 3.4, a range of different outputs from each simulation was analysed. The breakdown of the production capacity additions for each of the scenarios from 2020 to 2050 is outlined from Figure 5 to Figure 10. This was done to understand which configurations are favored in each of the scenarios.

In order to compare the decarbonisation potential of each of the production pathways, the trends of CO_2 emissions for the different scenarios are presented in Figure 4. Figure 3 shows the values of LCOS for each of the scenarios considered.

Table V provides a summary of the outcomes for the different scenarios in terms of H-DR capacity in 2050, decarbonisation potential, and the final LCOS value.

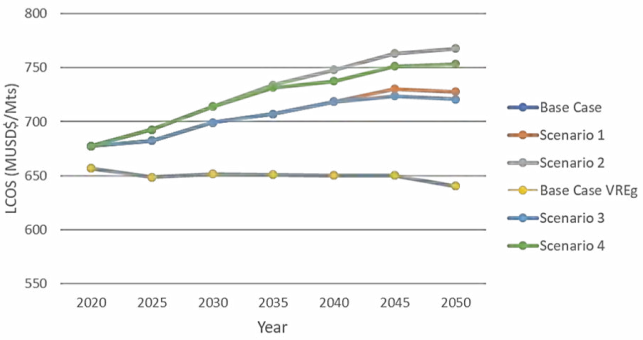

Fig. 3: LCOS Trend Comparison between Scenarios

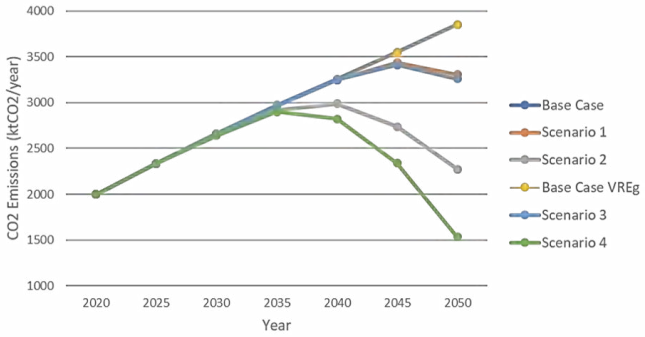

Fig. 4: CO_2 Emissions Trend Comparison between Scenarios

4.1. Base Case and Base Case VREg

For the base case, the BF/BOF route corresponded to 100% of all production capacity, as shown in Figure 5. The same result was observed in the base case VREg (Figure 6). These scenarios also yielded the same results in terms of total CO_2 emissions (Figure 4), LCOS (Figure 3) and the share of the different configurations in the production capacity. This indicates that having the option for the H-DR process to harness electricity from a VREg source alone is not sufficient to drive its adoption.

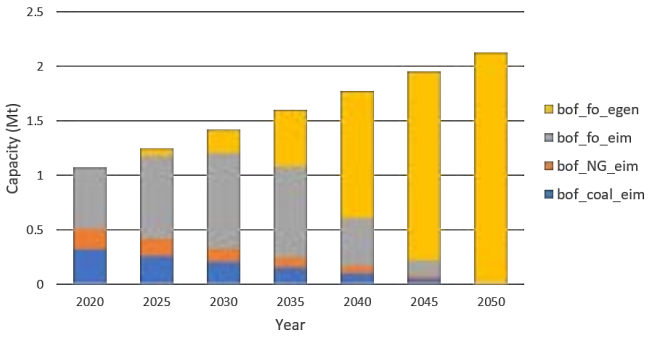

Fig. 5: Base Case Capacity Additions from 2020 to 2050

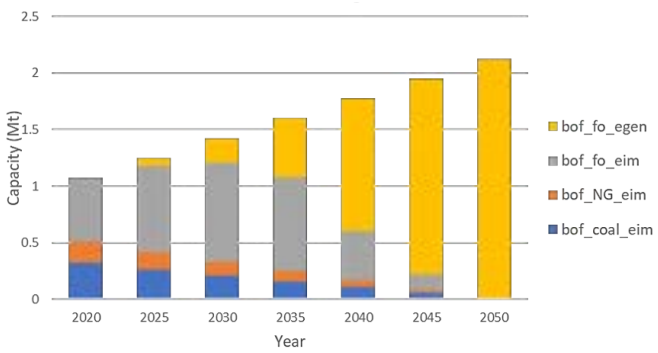

Fig. 6: Base Case VREg Capacity Additions from 2020 to 2050

4.2. Scenario 1 vs Scenario 2 - effect of carbon taxes (moderate/high)

Both of these scenarios accounted for the same current projections but with different levels of carbon taxes. For

Table V: Results Summary

Scenarios	Total % of H-DR in 2050	% change of CO2 in 2050 compared to 2020	Comparison with Base Case	
			Reduction in total CO_2 emissions	% Change in LCOS in 2050
Base Case	0.00%	92.72%	-	-
Scenario 1	22.98%	65.37%	-3.28%	13.6%
Scenario 2	65.40%	13.69%	-13.29%	19.8%
Base Case VREg	0.00%	92.72%	0.00%	0.0%
Scenario 3	23.79%	63.09%	-3.64%	12.5%
Scenario 4	74.6%	-23.26%	-19.67%	17.6%

scenario 1, implementation of moderate carbon prices led to H-DR being first adopted in 2035, and amounting to 22.98% of total capacity in 2050, with hdr2_hg_eg being the most favoured configuration (Figure 7). For scenario 2, the implementation of high carbon prices led to a H-DR adoption as early as 2030. There is now a much larger proportion of total H-DR capacity in 2050 (65.4%), with the most favoured configuration being hdr2_hg_eg (Figure 8). This signifies that the implementation of carbon prices is crucial to drive the adoption of H-DR. However, the CO_2 mitigation potential in both of these scenarios is still limited. Scenario 1 resulted in a 65.27% increase in CO_2 emissions in 2050 relative to 2020, while scenario 2 resulted in an increase of 13.69% (Table V). This is because hdr2_hg_eg still generates a relatively high CO_2 emissions from the usage of the CHP system. Therefore, this proves a need to further explore the option of powering the H-DR process with a VREg source. In terms of the LCOS, as shown in Figure 3, scenario 2 led to a higher LCOS compared to that of scenario 1, which is expected due to the higher carbon prices imposed.

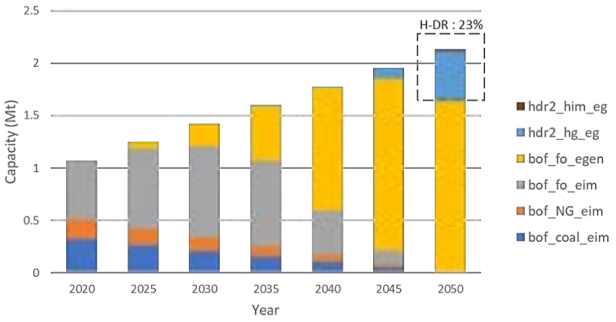

Fig. 7: Scenario 1 (moderate carbon taxes) Capacity Additions from 2020 to 2050

4.3. Scenario 1 vs Scenario 3 - effect of moderate carbon taxes and VREg

Scenario 3 considered current projections, moderate carbon taxes, and for H-DR to harness electricity from a VREg source. As seen in Figure 9, in this scenario H-DR was first adopted in 2035, and amounts to 23.79% of total capacity in 2050, which is slightly higher than the 22.98% observed in scenario 1. This share difference was due to the hdr2_him_eim configuration being invested in 2040. The drivers behind this situation was a combination of carbon taxes and the projected decrease in the prices of electricity from VREg sources, as a result of

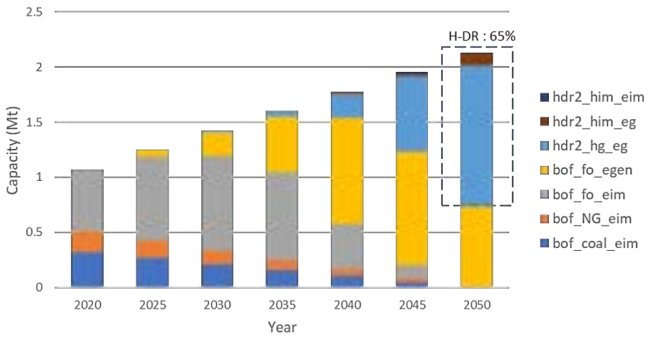

Fig. 8: Scenario 2 (high carbon taxes) Capacity Additions from 2020 to 2050

lower wind and solar power generation costs. As shown in Figure 3, the LCOS values for scenarios 1 and 3 are the same until 2040, with scenario 3 registering a lower LCOS after that year. From Table V, it is observed that scenario 3 led to an increase of 63.09% in CO_2 emissions in 2050 relative to 2020. Despite the availability of a low-cost and low CO_2 intensive electricity source (VREg) in this scenario, coupled with the presence of moderate carbon taxes, the CO_2 mitigation potential is still limited due hdr2_hg_egen being the most favoured H-DR configuration. This suggests that if higher carbon prices were introduced, the VREg route could potentially be favoured and therefore lead to a considerably higher reduction in CO_2 emissions.

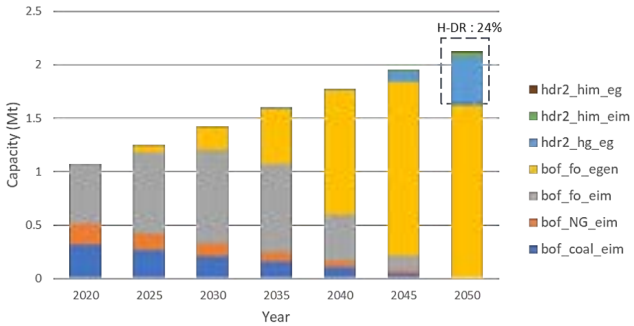

Fig. 9: Scenario 3 (moderate carbon taxes and VREg) Capacity Additions from 2020 to 2050

4.4. Scenario 4 - effect of high carbon taxes and VREg

Scenario 4 accounted for current projections, high carbon taxes and the option for H-DR to harness electricity from a

VREg source. As seen in Figure 10, in this scenario H-DR was first adopted in 2030, and amounts to 74.6% of total capacity in 2050, which is the highest out of all scenarios considered. One key observation is that scenario 4 is also the only scenario that led to successful decarbonisation with a 23.3% reduction in CO_2 emissions in 2050 relative to 2020 (Table V). This was driven by the large share of the H-DR configuration with electricity harnessed from a VREg source (74.6% total capacity in 2050). Therefore, when comparing scenarios 4 and 3 it can be concluded that the effect of VREg is only intensified when high carbon taxes are present. On another note, even though the same level of carbon taxes was implemented in scenarios 2 and 4, scenario 4 resulted in a lower LCOS (Figure 3). This was due to the low cost and low CO_2 intensive electricity associated with the VREg source present in scenario 4.

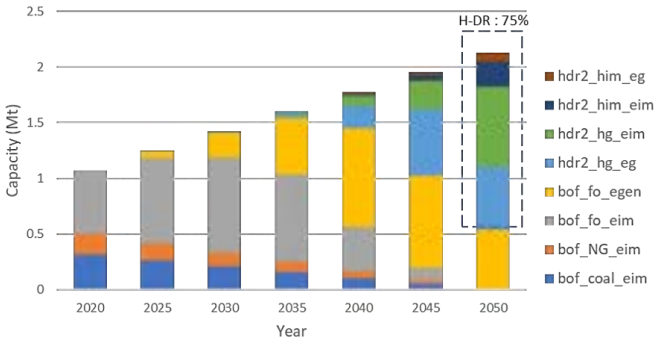

Fig. 10: Scenario 4 (high carbon taxes and VREg) Capacity Additions from 2020 to 2050

Figures 11 and 12 show the breakdown of energy consumption by source from 2020 to 2050, for the base case and for scenario 4, respectively. It is observed that scenario 4 led to a considerably higher energy consumption than the base case over time, resulting in 9.05 PJ/MTsteel in 2050, which is 84% higher than the base case (4.92 PJ/MT steel in 2050). This is driven by the high energy demand coming from the H-DR processes. However, as discussed previously, scenario 4 achieves decarbonisation, which is chacaracterised by a shift from sources such as fuel oil to VREg. Therefore, a key area of focus to achieve the observed outcome in scenario 4 will be to ensure the required energy supply, with an emphasis placed on supporting the growth of VREg availability.

It is clear that decarbonisation of the sector will inevitably lead to a high levelised cost of steel (Figure 3). This brings the question of whether the steel manufactured in this scenario would be able to compete against lower priced options on the market. India rolled out the Domestically Manufactured Iron and Steel Products Policy in 2017 [8], which essentially supports domestically manufactured iron and steel products by giving them a preference over international competitors when it comes to government procurement contracts. This will be an important enabling factor for the sustainable development of the steelmaking industry. However, the key driver will the growing demand for carbon-friendly steel products worldwide. This is a trend that has already been observed in various industries, such the auto industry where manufacturers such as Volkswagen or Toyota are now aiming eliminate carbon emissions completely from their entire value chains, including their suppliers, and taking on a full life cycle perspective [9]. For these reasons, despite the higher LCOS associated with decarbonising the steelmaking industry, this production pathway becomes attractive not just from an environmental, but also economic perspective.

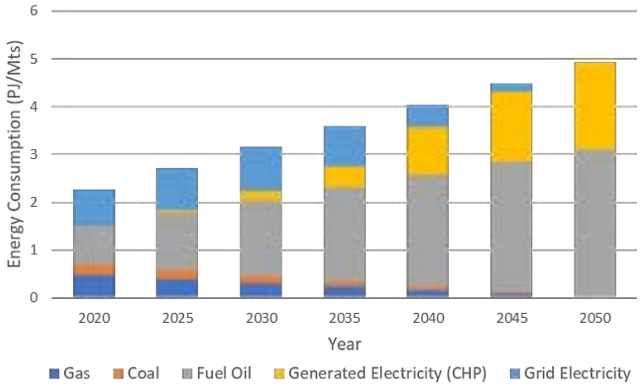

Fig. 11: Base Case Energy Consumption from 2020 to 2050

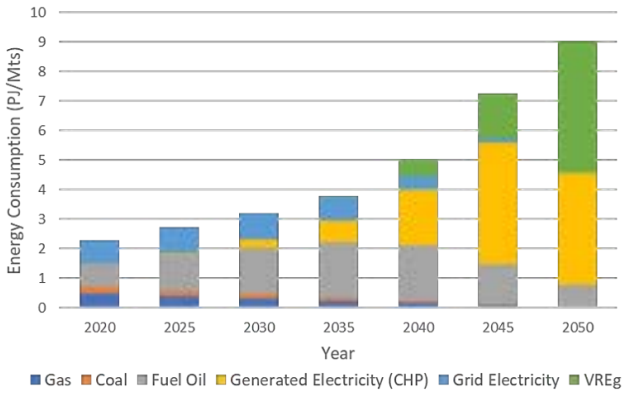

Fig. 12: Scenario 4 (high carbon taxes and VREg) Energy Consumption from 2020 to 2050

4.5. EAF vs H-DR

None of the different scenarios modelled resulted in the adoption of the EAF production route. As discussed previously, the fact that in both base cases the BF/BOF route corresponded to approximately 100% of production capacity shows that carbon prices are required to favour other alternative routes. All the H-DR configurations adopted in the scenarios with carbon taxes are less CO_2 intensive than the alternative EAF route. Therefore, it can be concluded that in the presence of carbon taxes, the H-DR production route becomes more cost competitive than the EAF, despite having higher values for CAPEX and OPEX. This is intensified in scenario 4 where high carbon taxes were implemented alongside having the VREg option for the H-DR process. On another note, H-DR configurations with cogeneration or with an operation running on 50% scrap significantly contributed to the cost

competitiveness of this route. For these reasons, it is concluded that H-DR is a better long-term investment than EAF.

4.6. Sensitivity Analysis

Sensitivity analysis was performed on factors other than carbon prices that could potentially impact the share of production capacity for the different configurations. This analysis was mainly conducted for scenarios 1 and 3, since it could be logically inferred that the high carbon prices implemented in scenarios 2 and 4 would outweigh the impact caused by a change in the other factors studied. Given the fact that across all scenarios the H-DR process was the only alternative route that is favoured, the aim of this analysis was to identify other drivers for its adoption. Therefore, the factors studied include a decrease in hydrogen and electricity prices, as well as improvements in electrolyser efficiencies.

4.6.1. Decrease in hydrogen prices: For this case, the forecasted hydrogen prices were decreased by 10, 30 and 50% for scenarios 1 and 3, with the summarised capacity share of each configuration in 2050 shown at Table VI and VII. This was done to understand whether having lower hydrogen prices would favour the H-DR configurations where hydrogen is imported rather than produced on site. For scenario 1, it was found that a decrease in hydrogen prices resulted in no significant change at all. For scenario 3, a reduction of 50% led to a considerably higher adoption of hdr2_him_eim in 2050, increasing from 0.6% in the original scenario to 16.9%. However, it is important to note that such a steep reduction in hydrogen prices is highly unlikely, especially when the costs associated with storage and transportation are taken into consideration.

Table VI: Scenario 1 - Capacity Share of Each Configuration in 2050

Scenario 1, % Decrease in Hydrogen Prices				
Configurations	0%	-10%	-30%	-50%
bof_coal_eim	0.0%	0.0%	0.0%	0.0%
bof_NG_eim	0.0%	0.0%	0.0%	0.0%
bof_fo_eim	0.0%	0.0%	0.0%	0.0%
bof_fo_egen	77.0%	77.0%	77.8%	76.2%
hdr2_hg_eg	22.2%	22.2%	21.4%	20.9%
hdr2_him_eim	0.8%	0.8%	0.8%	2.5%
hdr2_him_eg	100.0%	100.0%	0.0%	0.4%

Table VII: Scenario 3 - Capacity Share of Each Configuration in 2050

Scenario 3, % Decrease in Hydrogen Prices				
Configurations	0%	-10%	-30%	-50%
bof_coal_eim	0.0%	0.0%	0.0%	0.0%
bof_NG_eim	0.0%	0.0%	0.0%	0.0%
bof_fo_eim	0.0%	0.0%	0.0%	0.0%
bof_fo_egen	76.2%	74.1%	73.7%	37.3%
hdr2_hg_eg	20.9%	12.8%	12.8%	3.5%
hdr2_him_eim	2.5%	12.7%	12.7%	58.4%
hdr2_him_eg	0.4%	0.4%	0.8%	0.8%

4.6.2. Improvements in electrolyser efficiency: For this case, the impact of improvements in electrolyser efficiency was studied for both scenarios 1 and 3 by decreasing the corresponding electrolyser CAPEX by 10, 30 and 50%. The rationale behind this was to understand whether the adoption of the H-DR configurations where hydrogen is imported is driven by lower hydrogen prices or the high electrolyser CAPEX. It was found that a decrease in electrolyser CAPEX up to 50% resulted in no change for both scenarios considered. Therefore, it can be inferred that hydrogen prices is the most influential factors out of the two.

4.6.3. Decrease in electricity prices: For this case, the forecasted electricity prices for scenarios 1 and 3 were decreased by 10, 30 and 50% (Table VIII and IX). This was done to understand the level of impact that low electricity prices have on H-DR adoption. A decrease of 10 and 30% did not result in any significant change for both scenarios. However, when electricity prices were decreased by 50%, distinct results were observed across the two scenarios. For scenario 3, this led to a considerably higher adoption of H-DR, which is characterised by a higher share of the hdr2_hg_eim configuration. However, for scenario 1 this actually led to BF/BOF making up a larger proportion of the capacity in 2050 (96%) than previously (77%). There was a 10-year delay in the adoption of H-DR (2045 instead of 2035), and most of the capacity prior to this was filled up by the BF/BOF route. This shows that a steep decrease in electricity prices favours the BF/BOF route initially, as the electricity cost savings outweighed the costs associated with carbon taxes. Hence, solely decreasing electricity prices is not a reasonable way to promote the adoption of H-DR.

Table VIII: Scenario 1 - Capacity Share of Each Configuration in 2050

Scenario 1, % Decrease in Electricity Prices				
Configurations	0%	-10%	-30%	-50%
bof_coal_eim	0.0%	0.0%	0.0%	0.0%
bof_NG_eim	0.0%	0.0%	0.0%	0.0%
bof_fo_eim	0.0%	0.0%	0.0%	0.0%
bof_fo_egen	77.0%	77.0%	76.6%	96.0%
hdr2_hg_eg	22.2%	22.2%	22.2%	2.4%
hdr2_him_eg	0.8%	0.8%	0.8%	0.8%

Table IX: Scenario 3 - Capacity Share of Each Configuration in 2050

Scenario 3, % Decrease in VREg Electricity Price				
Configurations	0%	-10%	-30%	-50%
bof_coal_eim	0.00%	0.00%	0.00%	0.00%
bof_NG_eim	0.00%	0.00%	0.00%	0.00%
bof_fo_eim	0.00%	0.00%	0.00%	0.00%
bof_fo_egen	76.21%	77.73%	57.38%	32.81%
hdr2_hg_eim	0.00%	0.41%	13.54%	59.96%
hdr2_hg_eg	20.93%	21.46%	16.34%	2.23%
hdr2_him_eg	0.40%	0.41%	0.40%	0.00%
hdr2_him_eim	2.47%	2.53%	12.35%	5.00%

5. CONCLUSION

This study carried out an agent-based modelling approach using the ModUlar energy systems Simulation Environment

(MUSE) to outline preferential production pathways in meeting steel demand by 2050, whilst achieving decarbonisation within the sector. The scope of this study was concentrated in Maharashtra, India, with the three production routes considered being Blast Furnace/Basic Oxygen Furnace (BF/BOF), Electric Arc Furnace (EAF) and Hydrogen Direct Reduction (H-DR). Multiple configurations were considered for each of the production routes to account for different fuel types, electricity sources, levels of scrap usage and the option to import hydrogen or generate it on-site through an electrolyser. Three options were considered for the electricity: cogeneration, harnessing electricity from the grid in India and harnessing electricity from a variable renewable electricity and gas (VREg) source. The last option was only explored for the H-DR process, given that its CO_2 mitigation potential is considerably limited when a a Combined heat and power (CHP) system is used or when electricity is harnessed directly from the grid, due to the high emissions grid factor. Several scenarios were modelled to reflect differing levels of implemented carbon taxes and the option to power the H-DR process with the VREg source. The outputs for each scenario were then analysed. These include the share of capacity taken by each configuration, resulting % change in CO_2 emissions in 2050 relative to 2020, and resulting levelised cost of steel (LCOS). The different scenarios were then compared based on these values to derive key insights.

Results show that the implementation of carbon prices is crucial to drive the adoption of H-DR. However, as observed in scenarios 1, 2 and 3, the CO_2 mitigation potential is limited due to hdr2_hg_eg being the most favoured H-DR configuration, which still resulted in relatively high CO_2 emissions attributed to the CHP system. Scenario 4, where a high carbon tax was implemented alongside the powering of H-DR processes with a VREg source, was the only one where decarbonisation was achieved, with a 23.3% reduction in CO_2 emissions compared to 2020. This was driven by the large production capacity of the H-DR configuration powered by a VREg source in this scenario. Therefore, it is concluded that a combination of high carbon prices and access to a low cost and low CO_2 intensive power source (e.g VREg) is the key driver for H-DR adoption and decarbonisation. Given that scenario 4 results in a considerably higher energy consumption (84% higher than base case for 2050), a key area of focus to achieve decarbonisation will be ensuring the required energy supply, with an emphasis placed on supporting the growth of VREg availability.

Decarbonisation of the steelmaking sector will inevitably lead to a high levelised cost of steel, as observed in scenario 4. For this reason, the price competitiveness of steel produced in this scenario was explored. It is concluded that policies in India such as the Domestically Manufactured Iron and Steel Products Policy, as well as the growing global demand for carbon-friendly steel products will be key factors to enable the sustainable development of this sector.

In addition, H-DR proved to be a better long-term investment than EAF, which was not adopted in any of the scenarios modelled despite having lower capital and operating costs than H-DR. This could be attributed to two main reasons. Firstly, all the H-DR configurations adopted in the scenarios with carbon taxes are less CO_2 intensive than the alternative EAF route. Secondly, H-DR configurations such as the ones with cogeneration or with an operation running on 50% scrap significantly contribute to the cost competitiveness of this route.

Sensitivity analysis was conducted on scenarios 1 and 3 to identify other drivers for H-DR adoption. These include a decrease in hydrogen and electricity prices, as well as improvements in electrolyser efficiencies. Regarding hydrogen prices, only a decrease of 50% had a significant impact in scenario 3, which led to the capacity of hdr2_him_eim configuration in 2050 to increase from 0.6% to 16.9%. No change was observed when improvements in electrolyser efficiencies were analysed. Regarding electricity prices, only a 50% decrease resulted in significant changes. For scenario 3, this led to a considerably higher adoption of H-DR, which was characterised by a higher share of the hdr2_hg_eim configuration. However, for scenario 1 there was a substantial increase in the BF/BOF capacity proportions in 2050 (96%) than previously (77%).

6. Outlook

Overall, this study concludes that decarbonisation of the steelmaking industry in the Maharashtra region can only be achieved through a combination of carbon prices and having the option to power the H-DR process with a low cost and low CO_2 intensive electricity source. The VREg source was considered due to the projected decrease in the cost of power generation from solar and wind sources in India. This brought up the issue of the variability caused by intermittency, which was accounted for by adding natural gas to the mix, which can be used to fulfil the demand gap. Given the impact observed of having the option to power the H-DR process with a VREg source, further research needs to be conducted to better assess its implementation feasibility. This includes accounting for factors such as battery and hydrogen storage, transportation, infrastructure required, and the additional costs associated. The approach followed in this project can also be used as a basis for expanding the analysis to the steelmaking industry in other regions in India. However, the small pool of India specific literature and information was a limiting factor for this study. This led to a part of the techno-economic data for the different production configurations reflecting either worldwide values or values from plants in different countries. There is also limited information on the H-DR process regarding knowledge development and learning curves since there are only a small number of R&D projects and hydrogen reduction technology is not widespread enough yet [15]. Therefore, more accurate future projections of techno-economic values for the H-DR process are required to better assess its potential. This study aims to give a holistic overview of the challenges and opportunities for decarbonisation in the steelmaking industry in Maharashtra, India. In order to continue these efforts, it is essential to take a full life cycle approach (LCA) to assist with policy making. This LCA approach would consider the potential impact from all the stages associated with resource extraction, manufacturing, product use and end of-life (reuse,

recycling or disposal). Worldsteel has been collecting life cycle inventory data from its member companies worldwide and launched the Worldsteel Life Cycle Inventory (LCI) methodology [21]. This could be used as a basis to conduct the LCA.

7. Acknowledgements

The authors would like to express their gratitude to Dr. Sara Giarola from the Sustainable Gas Institute (SGI) for her support and guidance throughout this project.

8. Supplementary Material

The supplementary material for this paper can be found by clicking here.

References

[1] "Tracking industry 2020 – analysis." [Online]. Available: https://www.iea.org/reports/tracking-industry-2020

[2] "Global crude steel output increases by 3.4% in 2019," January 2020. [Online]. Available: http://www.worldsteel.org/media-centre/press-releases/2020/Global-crude-steel-output-increases-by-3.4--in-2019.html

[3] P. Pal, H. Gupta, and D. Kapur, "Carbon mitigation potential of indian steel industry," *Mitigation and Adaptation Strategies for Global Change*, vol. 21, no. 3, pp. 391–402, 2016, iD: Pal2016. [Online]. Available: https://doi.org/10.1007/s11027-014-9605-0

[4] "Iron and steel technology roadmap – analysis," 2020. [Online]. Available: https://www.iea.org/reports/iron-and-steel-technology-roadmap

[5] W. Hall, T. Spencer, and S. Kumar, "Towards a low carbon steel sector," Tech. Rep., 2020. [Online]. Available: https://www.teriin.org/sites/default/files/2020-03/Towards%20a%20Low%20Carbon%20Steel%20Sector%20Report.pdf

[6] "Carbon emissions by india's steel sector to triple by 2050," 2020. [Online]. Available: https://www.bloomberg.com/news/articles/2020-02-04/carbon-emissions-by-india-s-steel-sector-to-triple-by-2050

[7] "The road from paris: India's progress towards its climate pledge," 2020. [Online]. Available: https://www.nrdc.org/resources/road-paris-indias-progress-towards-its-climate-pledge#:~:text=The%20Road%20From%20Paris%3A%20India's%20Progress%20Towards%20Its%20Climate%20Pledge,-Share&text=India%20is%20on%20track%20to,non%2Dfossil%20fuels%20by%202030

[15] D. Kushnir, T. Hansen, V. Vogl, and M. Åhman, "Adopting hydrogen direct reduction for the swedish steel industry: A technological innovation system (tis) study," *Journal of Cleaner Production*, vol. 242, p. 118185, January 1, 2020. [Online]. Available: http://www.sciencedirect.com/science/article/pii/S0959652619330550

[8] "Annual report 2018-19," Tech. Rep., 2019. [Online]. Available: https://steel.gov.in/annual-reports

[9] C. Hoffmann, M. V. Hoey, and B. Zeumer, "Decarbonization challenge for steel," June 3, 2020. [Online]. Available: https://www.mckinsey.com/industries/metals-and-mining/our-insights/decarbonization-challenge-for-steel

[10] I. B. E. Foundation, "Information about maharashtra: Industries, exports, economy infrastructure growth," 2020. [Online]. Available: https://www.ibef.org/states/maharashtra.aspx

[11] D. Moya, S. Budinis, S. Giarola, and A. Hawkes, "Agent-based scenarios comparison for assessing fuel-switching investment in long-term energy transitions of the india's industry sector," *Applied Energy*, vol. 274, p. 115295, 2020. [Online]. Available: http://www.sciencedirect.com/science/article/pii/S0306261920308072

[12] M. Fischedick, J. Marzinkowski, P. Winzer, and M. Weigel, "Techno-economic evaluation of innovative steel production technologies," *Journal of Cleaner Production*, vol. 84, pp. 563–580, December 1, 2014. [Online]. Available: http://www.sciencedirect.com/science/article/pii/S095965261400540X

[13] A. Toktarova, I. Karlsson, J. Rootzén, L. Göransson, M. Odenberger, and F. Johnsson, "Pathways for low-carbon transition of the steel industry—a swedish case study," *Energies*, vol. 13, no. 15, p. 3840, Jul 2020. [Online]. Available: http://dx.doi.org/10.3390/en13153840

[14] LKAB, "Hybrit – towards fossil-free steel," October 27, 2020. [Online]. Available: https://www.lkab.com/en/about-lkab/technological-and-process-development/research-collaborations/hybrit--for-fossil-free-steel/

[16] V. Vogl, M. Åhman, and L. J. Nilsson, "Assessment of hydrogen direct reduction for fossil-free steelmaking," *Journal of Cleaner Production*, vol. 203, pp. 736–745, December 1, 2018. [Online]. Available: http://www.sciencedirect.com/science/article/pii/S0959652618326301

[17] S. Luh, S. Budinis, S. Giarola, T. J. Schmidt, and A. Hawkes, "Long-term development of the industrial sector – case study about electrification, fuel switching, and ccs in the usa," *Computers Chemical Engineering*, vol. 133, p. 106602, February 2, 2020. [Online]. Available: http://www.sciencedirect.com/science/article/pii/S0098135418313644

[18] "Combined heat and power," 2010. [Online]. Available: https://iea-etsap.org/E-TechDS/PDF/E04-CHP-GS-gct_ADfinal.pdf

[19] K. Takahashi and M. Louhisuo, "Iges list of grid emission factors," vol. 10.9, p. 5, 2020. [Online]. Available: https://www.iges.or.jp/en/pub/list-grid-emission-factor/en

[20] "Brown to green: the g20 transition towards a net-zero emissions economy 2019." [Online]. Available: https://www.odi.org/publications/11501-brown-green-g20-transition-towards-net-zero-emissions-economy-2019

[21] W. Association, "Lifecycle assessment in the steel industry," 2017. [Online]. Available: https://www.worldsteel.org/zh/dam/jcr:22f5ed93-0311-4f8a-a90c-b9ac424a3d01/LCA%2520position%2520paper.pdf

A CATALYST DESIGN STUDY FOR THE CATALYTIC CONVERSION OF ETHANOL TO BUTADIENE
Research Project

Robin BARREYRE

Department of Chemical Engineering, Imperial College London, U.K.

Abstract

Replacement of hydrocarbon raw material in the production of butanol and butadiene is highly advanced. Guerbet reaction and Lebedev reaction are respectively producing those molecules. To maximize the yield of reactions, different catalysts have been used at different process conditions.

Introduction

Gasolines and petroleum molecules are the most often produced from fossil fuel. They are either distilled or synthetise. Both butadiene and butanol are mostly produced from steam cracking compounds, so from hydrocarbons.

But some reactions are using renewable biomass to synthetise those molecules. Our approach is to care about those synthesis which are the Guerbet reaction and the Lebedev reaction. By gathering literature's information, we expect to find the ideal process conditions to run these reactions.

The Guerbet reaction has been known for more than a century but is actually a big research area with the new challenges nowadays. Indeed, this reaction uses ethanol to synthetise biggest alcohol compounds as butanol.

The Lebedev reaction also known a resurgence of interest for a reaction discovered in 1928 by using $ZnO\text{-}Al_2O_3$ catalysts. In fact, as the Guerbet reaction, this process is using ethanol to form butadiene.

Butadiene and butanol are two crucial compounds of the chemical industry. Butadiene is produced to create rubbers or resins when butanol is mainly produced for varnish as a solvent.

Background

The main objective of the project is to gather information from several publications for both reactions.

Guerbet Reaction

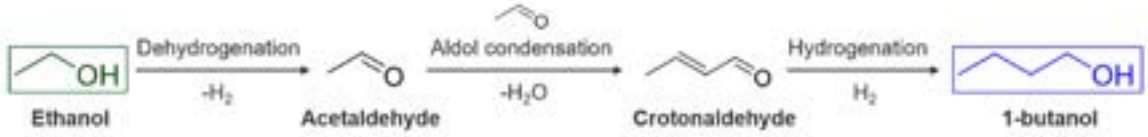

Figure 1 – reaction network of the Guerbet reaction

These are the steps of the Guerbet coupling of ethanol to 1-butanol. First, ethanol is dehydrogenated to an acetaldehyde. Then, the action of a strong base on the aldehyde to form an enolate allows the aldolization of aldehyde. The aldol is quickly dehydrated in the basic or acidic environment by condensation and resulting a crotonaldehyde. Finally, the crotonaldehyde is hydrogenated to give 1-butanol.

Catalyst role

Two types of catalysts can be used for this process, we will discuss separately: Homogeneous and heterogeneous catalysts. Each type of catalyst has its own specificity and process conditions, but also its inconvenient.

Heterogeneous

Concerning heterogeneous catalysts, the reaction is on the surface of the solid catalyst. Metal nanoparticles are supported on an inactive surface, those nanoparticles

play the role of active particles by adsorption of gas on their surface.

Hence, basic and acid environments are replaced by the basicity or the acidity of sites (2). Depending the number of acid and basic sites on the catalyst, the reaction will be efficient or not. The Guerbet reaction improves by the implement of weak acid sites and strong base sites (3). Indeed, weak acid sites are related to the dehydration of the aldol (3). Strong basic sites are involved in both dehydrogenation of ethanol (2, 3) and even in the aldol condensation as well (4). In fact, the combination of weak acid sites and strong basic sites allows a good selectivity of butanol coupled with a conversion of ethanol.

For those types of catalysts, the combination of several metals is the key to improve the reaction. In fact, copper allows ethanol dehydrogenation to acetaldehyde (3) due to the contribution of strong acid sites (2) and the quantity of weak acid sites (3). Copper is known as a Lewis acid due to its electron-deficiency. Besides, copper plays on the quantity of basic sites, becoming lower (2, 3). At the same time, the number of strong basic sites is getting higher by combination of copper and nickel (3).

On the other hand, the addition of a metal oxide to cooper is increasing the strength of basic sites (3) then catalyse dehydration and the aldol condensation (2). In fact, as a metal oxide, it is a weak base. But a too important concentration of acid sites is bad for the selectivity of the reaction as it improves the formation of other products as 1,1-diethoxy.

The addition of both acid and basic sites inside catalysts favours the formation of butanol but it must be in a certain range of concentrations.

Table 1 – Heterogeneous catalysts used on different literatures and the yield for the Guerbet reaction

Reference	Catalyst used	Selectivity	Conversion	Yield
(2)	5Cu-Mn/HSAG	33.0%	27.0%	8.9%
(3)	2.5Cu2.5Ni-Mn/HSAG	30.0%	39.0%	11.7%
(4)	CuNi-PMO	62.5%	47.3%	21.9%
(5)	Cu10Ni10 - PMO	39.3%	56.5%	22.2%

In the literature, the used of copper seems to be recorded everywhere as known for a great catalyst for both hydrogenation and dehydrogenation reaction rates. For the same reasons, nickel is commonly used for those reactions (5). Both combined are supposed to increase the selectivity of butanol (3), reason why it is used in the literature.

The use of a high surface-area graphite (HSAG) (2, 3) does not seem necessary even though carbon improves as inert surface the number of centres. Another method uses porous metal oxide (PMO) (4,5) as surface of the active phase of the catalyst with great results and seems to be a true counterweight to HSAG for a relatively new technology but twice more efficient in term of yield. In fact, both HSAG catalysts studied there (table 1) show yields around 10 % versus 20% for PMO catalysts.

Table 2 – Process conditions for Guerbet reaction and a heterogeneous catalyst

Reference	Catalyst used	T	Pressure	Yield
(2)	5Cu-Mn/G	230 °C	50 bar	8.9%
(3)	2.5Cu2.5Ni-Mn/HSAG	230°C	50 bar	11.7%
(4)	CuNi-PMO	320°C	70 bar	21.9%
(5)	Cu10Ni10 - PMO	320°C	80 bar	22.2%

Porous Metal Oxyde (PMO) beard catalysts proceed at larger temperatures than HSAG beard catalysts. Despite this difference, the yield's gain appears to be important compared to utilities cost, but a deepest technical and economic analysis would allow to choose. Moreover, the number of impacts on the surface by a gas increases in function of the pressure. So, the process pressure must be important, about 50 to 80 bar.

Also, according to these data, it appears that a combined copper and nickel catalyst on PMO surface is the more efficient couple to process the Guerbet reaction. By operating at 320 °C and about 70 bar, we can achieve a yield of 22 %, which is quite reasonable according to the difficulty to achieve strong selectivity.

Homogeneous

Homogeneous catalysts are in the solution, under the same phase than the solvent. Hence, there is more contact between reactive molecules and catalyst molecules. It is the reason of choosing this type of catalysis, having a gain in term of number of molecular reactions, so a greater efficiency.

Besides, the reaction happens in the solvent, the environment must be basic by addition of a base. Indeed, both dehydrogenation and aldol condensation require basic environment. The literature agrees to suggest sodium ethoxide EtONa as base for its characteristics as a strong base (pKa = 15.5). Compared to other common bases, both selectivity and conversion are boosted by the used of EtONa (1, 7) for a base which is simple to synthetize at industrial scale.

Despite true convenience to use heterogeneous catalysts, both selectivity and conversions stay low and present a downside for their use. The work on homogeneous catalysts shows an increase on selectivity on conversion, so on yield.

On heterogeneous catalysts, the metal-based is supported by ligands that promote the Guerbet reaction. From the literature, two metal-base appeared very often: Ruthenium-base and Manganese-base.

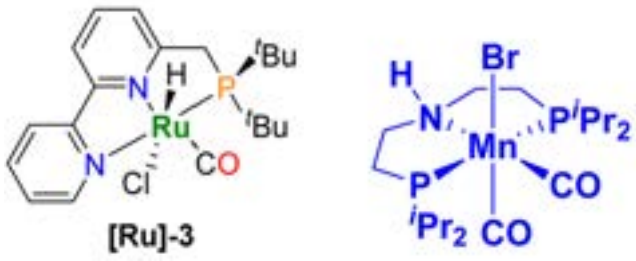

Figure 2 – Homogeneous catalysts: Pincer Ruthenium Catalyst (7) and Pincer Manganese Catalyst (1)

Table 3 – Homogeneous catalysts used on different literatures and the yield for the Guerbet reaction

Reference	Catalyst used	Selectivity	Conversion	Yield
(1)	$[HN(CH_2CH_2PPh_2)2]Mn(CO)_2Br$	72.0%	47.0%	33.8%
(6)	$[RuCl(\eta^6\text{-}p\text{-cymene})C(PPh_2)_2]Cl$	93.6%	22.1%	20.7%
(7)	RuHCl(tBuPNP)(CO)	60.3%	73.4%	35.8%
(8)	Mn Catalyst	92.0%	11.2%	9.8%
(8)	Mn Catalyst	28.6%	87.0%	22.7%

Yield of butanol using the Guerbet reaction is boosting using homogeneous catalysts (Table 3). Both selectivity of butanol and conversion of ethanol improve significantly. Both ruthenium-based and manganese-based catalysts offer great yield depending on the ligands and the geometry of the catalyst. It must be known that it seems difficult to obtain both enormous selectivity of butanol (around 90%) with a great conversion of ethanol. It is the reason why each of these catalysts are interesting. Depending on the objective and the process, we will have to choose between selectivity and conversion to maximize the target.

Table 4 - Process conditions for Guerbet reaction and a homogeneous catalyst

Reference	Catalyst used	T	Base concentration	Yield
(1)	$[HN(CH_2CH_2PPh_2)2]Mn(CO)_2Br$	150 °C	5% mol	33.8%
(6)	$[RuCl(\eta^6\text{-}p\text{-cymene})C(PPh_2)_2]Cl$	150 °C	25% mol	20.7%
(7)	RuHCl(tBuPNP)(CO)	110 °C	20% mol	35.8%
(8)	Mn Catalyst	160 °C	6% mol	9.8%
(8)	Mn Catalyst	160 °C	6% mol	22.7%

Those catalysts allow to decrease the hard conditions we were forced to run with heterogeneous catalysts. Indeed, the temperature falls from about 50%. Moreover, the process is running at the atmospheric pressure. Those two parameters allow both gain of CAPEX and utilities.

The concentration of the base has been also studied to optimize the process. In function of the catalyst, the base concentration has been fixed for each publication to optimize the process. It appears to be an important parameter but without being able to give a correlation between molar concentration and yield or metal-based catalyst.

Nevertheless, the homogeneous catalyst processes stay nowadays rare due to the complexity and the cost to separate the catalyst from the product. For the biggest industrial applications, catalysts are always in a heterogenous phase. Besides, the scarcity coupled to the difficulty of extraction of the ruthenium (10) could be an impediment to the implement of ruthenium catalysts in favour of manganese's.

Finally, despite a well-known utilization of heterogeneous catalysts on industrial plants, new processes using homogeneous phases made strong efforts to obtain a true efficiency to perform the Guerbet reaction when heterogeneous processes reach a ceil. Also, we will choose rather a homogeneous manganese-based catalyst, operating at 150 °C with a NaOEt concentration of 5% in mol to achieve the reaction of ethanol to 1-butanol.

Lebedev Reaction

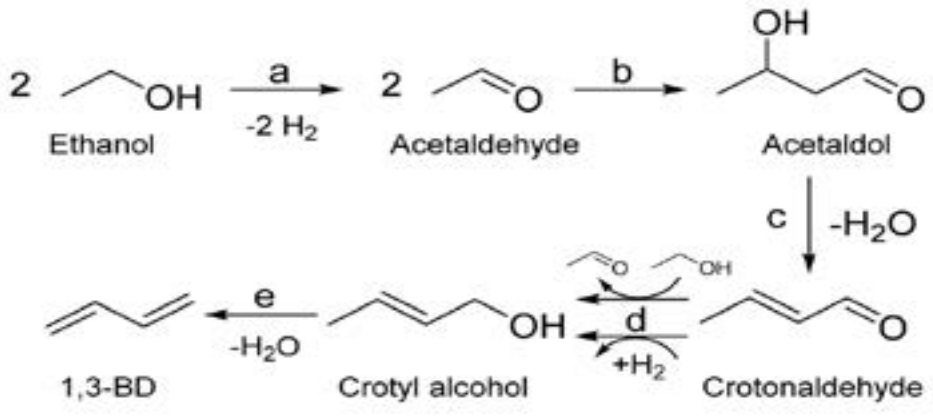

Figure 3 – reaction network of the Lebedev reaction

These are the steps of the Lebedev coupling of ethanol to butadiene. First, ethanol is dehydrogenated to an acetaldehyde (a). Then, the action of a strong base on the aldehyde to form an enolate allows the aldolization of aldehyde (b). The aldol is quickly dehydrated in the basic environment by aldol condensation (c) and resulting a crotonaldehyde. The crotonaldehyde is hydrogenated to give 1-butanol (d) in a reaction called Meerwein–Ponndorf–Verley (MPV) reduction, which is dehydrated to afford butadiene (e).

Catalyst role

The Lebedev reaction is realised with heterogeneous catalysts. Their performances are good enough to not look at the complexity of potential homogeneous catalysts that could replace the first ones.

As well as for the Guerbet reaction, acid/base properties of the catalysts will be extremely important to achieve the reaction. So, pair of basic and sites catalyse the aldol condensation step (13, 14) and the ethanol dehydrogenation step (12), while the dehydration of ethanol happens on acid sites (13). Besides, literature has shown that the Meerwein–Ponndorf–Verley reduction happens on acid sites because of their contribution to transfer hydrides.

Literature has also shown that limited amount of strong basic sites and an intermediate number of acidic sites give the best couple to maximize the Lebedev reaction (14).

Magnesium oxide (MgO) (14) or ZrO2 (15) are used to obtain basic sites. Other publications offer to use HfO2 coupled with ZnO as basic sites carriers. Alkili metals (Na, K and Li) can be added to the solution to increase the basicity (13).

Silicon dioxide (SiO2) is the most used to obtain acid sites (9, 11, 14, 15). As we saw in the previous part, copper can be used to increase the number of weak acid sites (12).

Table 5 - Catalysts used on different literatures and the yield for the Lebedev reaction

Reference	Catalyst used	Selectivity	Conversion	Yield
(11)	HfO2-ZnO-SiO_2	50.0%	97.7%	48.9%
(12)	CuTaSiBEA	73.0%	88.0%	64.2%
(13)	1.2-K-ZrZn-MgO-SiO_2	57.8%	44%	37.2%
(15)	2Ag-4ZrO2-SiO_2	71.3%	55.2%	39.4%
(16)	MgO–SiO_2	68.0%	32.0%	21.76%

Most publications (Table 5) are using SiO2 coupled with another oxide. Among those catalysts, the conversion of 98% of ethanol by using HfO2-ZnO-SiO2 (11) is interesting despite a lower butadiene selectivity. The selectivity obtained with 2Ag-4ZrO2-SiO2 (15) is important.

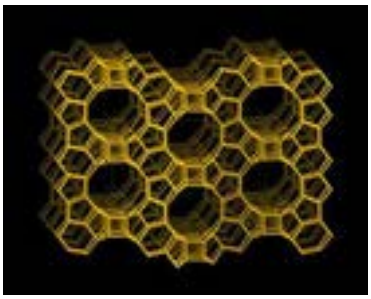

Figure 4 – BEA zeolithe structure (18)

But one publication is using a more efficient catalyst: CuTaSiBEA zeolites (13). This catalyst is a zeolite in beta form whose we add Si and Ta (1 wt. %). Among metals we could add to the zeolite, copper appeared to be the most efficient one in term of selectivity of butadiene and conversion of ethanol compared to silver and zinc. This catalyst is far more efficient in term of both selectivity and conversion than generally used catalysts and appears to be the future for Lebedev reactions.

Table 6 - Process conditions for Lebedev reaction

Reference	Catalyst used	T	WHSV	Yield
(11)	HfO2-ZnO-SiO_2	360 °C	1.12 h^{-1}	48.9%
(12)	CuTaSiBEA	325 °C	0.5 h^{-1}	64.2%
(13)	1.2-K-ZrZn-MgO-SiO_2	375 °C	0.31 h^{-1}	37.2%
(15)	2Ag-4ZrO2-SiO_2	320 °C	0.31 h^{-1}	39.4%
(16)	MgO–SiO_2	325 °C	0.3 h^{-1}	21.76%

To compare process conditions for the Lebedev reaction (Table 6), temperature and WHSV were the most unambiguous parameters. Each of the studied processed at the atmospheric pressure. WHSV for Weight hourly space velocity compares the charge stock weight per hour and the catalyst weight loaded in the reactor. So, biggest WHSV, biggest the production is (9). Most catalysts allow productions around 0.3 to 0.5 h^{-1} even the best catalyst CuTaSiBEA. The great WHSV of HfO2-ZnO-SiO2 coupled with its high ethanol conversion allows it to be a great catalyst in term of production rates.

In term of temperatures, the range is quite tightened between 320 and 375 °C in function of the publication. It is a reasonable temperature for the industry

even if it can put problems in term of CAPEX.

Finally, despite a great production rate by using HfO2-ZnO-SiO2 as catalyst, CuTaSiBEA zeolite is the most efficient catalyst for a temperature around 325°C. Besides, the cost of zeolites is cheap (17) coupled with temperature equivalent and a better yield, it appears as the best compromise.

Conclusion

Both Guerbet reaction and Lebedev reactions have been reconsidered in the past few years to answer the environmental issue and the necessity to replace fossil fuel compounds by biomass. In order to achieve this, publications have been made to give operation parameter to these reactions. After analysis of both reaction's catalysts and parameters, heterogeneous catalysts stay a safe bet as largely expend on industrial plants for large scales of production, which concerned productions of butanol and butadiene that are commodity for all chemistry. Nevertheless, homogeneous catalysts are very efficient to product butanol with the Guerbet reaction such as the manganese-based catalysts that operate at low temperatures and pressures. Concerning the Lebedev reaction, the new zeolite catalysts are extremely efficient in term of both selectivity of butadiene and conversion of ethanol for process temperatures around 325 °C.

References

(1) Catalytic Upgrading of Ethanol to n-Butanol via Manganese-Mediated Guerbet Reaction. Naveen V. Kulkarni, William W. Brennessel, and William D. Jones. *ACS Catalysis* 2018 *8* (2), 997-1002. DOI: 10.1021/acscatal.7b03653.

(2) Continuous Catalytic Condensation of Ethanol into 1-Butanol: The Role of Metallic Oxides (M = MgO, BaO, ZnO, and MnO) in Cu-M/Graphite Catalysts, Cristina Lopez-Olmos, María V. Morales, Antonio Guerrero-Ruiz, and Inmaculada Rodríguez-Ramos. *Industrial & Engineering Chemistry Research* 2020 *59* (38), 16626-16636. DOI: 10.1021/acs.iecr.0c04113.

(3) C. Lopez-Olmos, et al. « Optimization of Cu-Ni-Mn-catalysts for the conversion of ethanol to butanol ». *Catalysis Today*, vol. 357, novembre 2020, p. 132-42.

(4) Xi, X.-Y.; Sun, Z.-H.; Cao, H.-T.; Pei, Y.-T.; ten Brink, G.H.; Deuss, P.J.; Barta, K.; Heeres, H.J. Catalyst Performance Studies on the Guerbet Reaction in a Continuous Flow Reactor Using Mono- and Bi-Metallic Cu-Ni Porous Metal Oxides. *Catalysts* 2020, *10*, 996

(5) *ACS Sustainable Chem. Eng.* 2017, 5, 2, 1738–1746. Publication Date: December 12, 2016. https://doi.org/10.1021/acssuschemeng.6b02494.

(6) Dr. George R. M. Dowson, et al. « Catalytic Conversion of Ethanol into an Advanced Biofuel: Unprecedented Selectivity for n-Butanol ». *Angewandte Chemie International Edition*, vol. 52, no 34, juillet 2013, https://doi.org/10.1002/anie.201303723.

(7) *J. Am. Chem. Soc.* 2016, 138, 29, 9077–9080. Publication Date: July 11, 2016. https://doi.org/10.1021/jacs.6b05433.

(8) *J. Am. Chem. Soc.* 2017, 139, 34, 11941–11948. Publication Date: August 18, 2017.

https://doi.org/10.1021/jacs.7b05939.
(9) *Catal. Sci. Technol.,* 2020, 10, 4860.
(10) https://www.lelementarium.fr/element-fiche/ruthenium/
(11) G.M. Cabello González, et al. « Ethanol conversion into 1,3-butadiene over a mixed Hf-Zn catalyst: Effect of reaction conditions and water content in ethanol ». *Fuel Processing Technology*, vol. 193, October 2019, p. 263-72.
(12) *ACS Sustainable Chem. Eng.* 2017, 5, 3, 2075–2083. Publication Date: January 10, 2017. https://doi.org/10.1021/acssuschemeng.6b01728.
(13) Simoní Da Ros, et al. « Ethanol to 1,3-Butadiene Conversion by using ZrZn-Containing MgO/SiO2 Systems Prepared by Co-precipitation and Effect of Catalyst Acidity Modification ». *ChemCatChem*, vol. 8, no 14, July 2016, p. 2376-86, https://doi.org/10.1002/cctc.201600331.
(14) Carlo Angelici, et al. « Influence of acid–base properties on the Lebedev ethanol-to-butadiene process catalyzed by SiO2–MgO materials ». *Catalysis Science and Technology*, no 5, 2015, https://doi.org/10.1039/C5CY00200A.
(15) Vitaly L. Sushkevich, et al. « Design of a Metal-Promoted Oxide Catalyst for the Selective Synthesis of Butadiene from Ethanol ». *ChemSusChem*, vol. 7, no 9, September 2014, p. 2527-36, https://doi.org/10.1002/cssc.201402346.
(16) Lewandowski, M, Babu, GS, Vezzoli, M, Jones, MD, Owen, RE, Mattia, D, Plucinski, P, Mikolajska, E, Ochenduszko, A & Apperley, DC 2014, 'Investigations into the conversion of ethanol to 1,3-butadiene using MgO: SiO2 supported catalysts', *Catalysis Communications*, vol. 49, pp. 25-28. https://doi.org/10.1016/j.catcom.2014.02.003.
(17) Claire Bernardon. Les zéolithes comme catalyseurs ”verts” pour la synthèse organique : de leur synthèse à façon à leurs applications en chimie organique. Catalyse. Université de Strasbourg, 2016. Français. NNT : 2016STRAF017. fftel-01427286f.
(18) https://europe.iza-structure.org/IZA-SC/framework.php?STC=BEA

Kinematic Parameters Examination for Process Modelling of Protein Crystallisation

Matthew Lai and Isaac Furlonge
Department of Chemical Engineering, Imperial College London, U.K.

Abstract

Quality and quantity of crystals alter with different operating conditions, initial composition and equipment setup. The associated trials are lengthy and costly, obstructing the scale-up development for protein crystallisation processes. A crystallisation process model framework can serve as a prediction tool for crystal quantity and quality under various scenarios. Successful estimations of lysozyme's nucleation and growth kinetic parameters by the model framework is the main objective of this study. The three stages of iteration trails are initial trail, iteration and verification with literature justified guesses and bounds. The crystal sizes obtained from estimation have good agreement with experimental crystal sizes. This is further proven when the median crystal diameter is fixed for the iterative process. There is still room for improvement with deviation spotted from the concentration time graphs regarding induction time, final concentration, and the emergence of double peaks in CSD for some runs. The consideration of shear induced secondary nucleation has minimal effect on concentration time graph and CSD. In order to test the validity of parameter estimation under various scenarios, experiment sets with varying cooling profiles, and varying volume and initial concentration were used.

Keywords: Process Modelling, Protein Crystallisation, Scale-up, Parameter Estimation

1. Introduction

The major challenge in the pharmaceutical industry is providing a reliable, time and cost-effective manufacturing process, with a large global demand and substantial health sector contribution towards protein-based drugs. A crystallisation purification step that removes impurities is what 90% of active pharmaceutical ingredients (APIs) would be go forward at some stage of their production. Crystallisation is the preferred method over traditional chromatography purification as requirements of packing materials has made scaling up in chromatography method considerably more expensive even though it can reach a higher protein purity.[1] In large-scale bio-separation industry, crystallisation purification method was widely used, separating specific proteins from mixtures.

Parameters ranging from physical factors (temperature, pressure, magnetic field), chemical factors (precipitants concentration, pH, buffer type) and biochemical factors can influence crystallisation. This can cause variation in the quality and quantity of crystal obtained, as nucleation and growth rates of crystals are affected by alterations of phase diagrams of proteins in the presence of different supersaturation condition.[2] Uncertainty of quality of the protein crystals formed are the main challenge in terms of laboratory to industrial size scaling up and the transition of batch to continuous process. The quality of pharmaceutical crystals can be determined by the following six criteria: purity, yield, chirality, size, polymorphism and morphology; and the latter three can affect the bioavailability in addition to performance level.[3]

There are limited successful protein crystallisation studies despite the importance of protein crystallisation. Multiple trial and errors are required, as protein compounds have a fragile structure and possess weak interactions, thus obtaining a suitable crystallisation conditions in terms of pH and temperature would not be an easy feat.[4] There are gaps in the description and prediction for quality of crystals and crystal size distribution (CSD) obtained with a lack in both classical and two-step mechanisms which define the growth and nucleation process of protein crystallisation.

Overall, the progress of scaling up protein crystallisation process was hindered by costly and time-consuming trial and error procedures. For pharmaceutical development, it is highly desirable to model crystallisation process, as a tool to estimate kinetic parameters and predict crystal quality for example crystal size distribution (CSD). In developing a reliable process model, the correctness of the parameter estimation and the legitimacy of the assumptions for modelling are

integral. In this study, complete model formulation which includes the strategy of iteration were used. In order to achieve this parameter estimation of kinetics, gCRYSTALS software packaged was utilized. The kinetics of crystal growth, primary and secondary nucleation were examined and estimated within the limits of the data used.

The focus of this report is to derive a parameter estimation framework using gCRYSTALS to estimate the kinetic parameters of the crystal growth models and primary nucleation of lysozyme. This will then be an ideal basis suited for large scale up of protein crystallisation as opposed to laborious and time-consuming empirical methods. Furthermore, the computational results, thermophysical properties and approach of the iteration of parameter estimation will be examined.

Figure 1: Research scope involving the major steps of crystallisation process

2. Background

2.1. The importance of modelling

Before the modelling software was developed, the scale up process of crystallisation was done empirically. This resulted in many experiments since a myriad of variables were involved (e.g. temperature, pH) where each variable must be selected and determined from inherent knowledge on the molecular interactions of small -scale laboratory experimental runs. This is then transitioned to industrial scale processes.

For the empirical scale up of this procedure, screening phase (2 – 10 μL), batch mode (1 mL, 10 mL in stirred tank crystalliser), semi-batch mode (10 mL – 1 L in tubular crystalliser) and continuous mode (MSMPR), were scaled up where their operational limits were examined. Key considerations include solubility, polymorphism, buffer solubility and operating conditions at the following: screening phase, effect of agitation on crystallisation process at batch mode, seeding and agglomeration at semi-batch mode, process control, monitoring and integration at continuous mode.

Although this procedure is still common today, it has many disadvantages. It is very laborious and time consuming (has a high residence time) and produces low quality crystals. For example, the crystals can be either show very high coefficient of discrepancies, too large or undersized.[5] This further justifies why a crystal growth model for scale-up processes are needed.

Figure 2: Predictive crystallisation process model capturing parameters requirement[6]

For this to be achieved, the model must be able to accurately estimate the kinetic parameters and crystal size distribution that reflects the real system of crystallisation. Specification of equipment, mechanism of crystallisation and process and operating conditions are all variables that result in product quality. Since many parameters are involved, the process model is dissected as shown in Figure 2. This aids in simplifying the entire process for clearer understanding.

2.2. Parameter Estimation

Mathematical modelling of protein crystallisation involves a function of many parameters. These parameters include activation energy, growth rate constant, nucleation rate, coefficients of solubility and super saturation order. Parameter estimation has an integral role since most of these parameters are unknown. Experimental data is generated by using the results from simulation of different techniques of optimisation. Crystal size distribution (CSD) and concentration are the experimental data that are used to develop our crystal modelling framework.

Data from literature were used as a starting point for the parameter estimation. The input data were constrained by reasonable bounds, which were chosen by from literature. This region of the objective function will then be minimised in an attempt to produce a function of the model framework that is similar to that of the experimental data. To further clarify, this function represents the variation of the experimental data and model framework. In order to describe lysozyme's nucleation and growth, the parameter values estimated are kinetic constants of primary nucleation, secondary nucleation and growth.[7]

3. Experimental Methods

3.1. Theory and Mathematical Models

3.1.1. Solubility

Solubility shows the equilibrium between the rate of crystallisation and dissolution. The end concentration is the solubility as the system reaches equilibrium. Nucleation will be generated if concentration of protein supersedes the super-solubility line. When calculating supersaturation, accurate prediction of solubility is required when it comes to modelling. The prediction of solubility plays a crucial role in the crystallisation model as it governs the aspects of crystallisation, such as growth and nucleation.

Achieving equilibrium state takes a large amount of time as the accurate measurement of solubility is affected by the prolonged agitation. This experimental difficulty emphasises the importance of the prediction of solubility. By fitting a polynomial equation using the experimental data of solubility, a model of empirical solubility is obtained. It must be noted that this however may not have much substantial meaning.

To forecast the differences in solubility with respect to temperature, vant' Hoff equation[8] can be used utilising the first principle approach. Equation below describes solubility assuming that the solvent and solute would produce a solution that is ideal (activity coefficient = 1):

$$\ln(x) = \left(\frac{1}{T_f} - \frac{1}{T}\right)\frac{\Delta H_f}{R}$$

Vant' Hoff equation can be then further simplified when fitting to a real system where A and B are solubility constant:

$$\ln(x) = \frac{A}{T} + B$$

On the other hand, a polynomial equation can empirically express the temperature requirement of solubility where A, B, C and D are polynomial coefficients[9]:

$$-RTln(x) = A + BT + CT^2 + DT^3$$

In the gCRYSTAL program, there were three expressions in which solubility can be shown: vant' Hoff, hybrid form (polynomial/exponential) and a generic polynomial.

3.1.2. Supersaturation

The key factor that leads to crystallisation is supersaturation. This is the variance between the equilibrium and current chemical potential. The zone of supersaturation is present when the change in chemical potential, $\Delta\mu_i$ is a positive number.

Dynamic mixture composition, x_i, makes it problematic when taking record of the chemical potential. Taking that into consideration, an expression for supersaturation with respect to concentration of solution is as follows[10]:

$$\mu_i(T, P, x_i) = \left(\frac{\partial G}{\partial n_i}\right)_{T,P,N_{j,j\neq i}}$$

$$\Delta\mu = \frac{c}{c^*} = 1 - \frac{\Delta c}{c^*} = S - 1 = \sigma$$

Supersaturation is also linked to nucleation rate and crystal growth which are key kinetic parameters to note. Increased supersaturation will result in increased nucleation and growth rate. However, it can produce unwanted CSD if both kinetic parameters are too high. To control the size of crystals produced and omit the undesirable products, the level of supersaturation must be kept within the preferred range.

3.1.3. Nucleation model

The two categories for nucleation are primary and secondary. The formation of first crystals in a system that has no initial crystals is primary nucleation. This can either be homogeneous or heterogeneous. Supersaturation is a main contribution to homogeneous nucleation. The occurrence of other insoluble materials (e.g. dust, impurities) drives heterogeneous nucleation.[11]

Secondary nucleation is the birth of nuclei with the existence of crystals. Collision is the main source of secondary nucleation, where this can occur from crystals-to-impeller (CI), crystals-to-wall (CW), crystals-to-crystals (CC) collisions. Aggregation, attrition, abrasion and breakage are all different types of collision. (Figure 3)

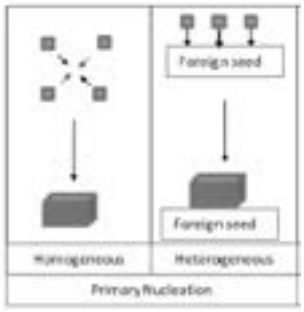

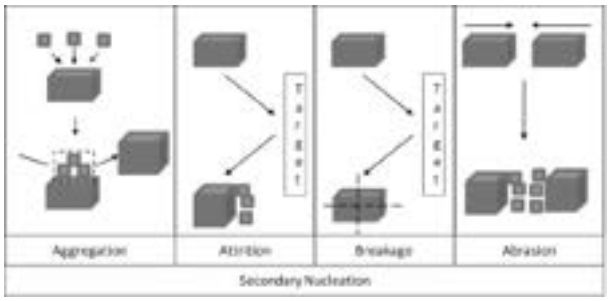

Figure 3: Schematic diagram of primary and secondary nucleation phenomena[12]

Mullin's Classical Kinetics can describe primary nucleation:

$$J_{prim} = A_0 \exp\left(-\frac{16\pi(\alpha\sigma)^3 v_0^2}{3k^3T^3(lnS)^2}\right)$$

This however assumes spherical nucleus formation and isotropic interfacial surface tension. Therefore, these properties are not directionally dependent which are limitations for the first principle expression. Crystallisation in industry often uses an empirical expression of the Power law for better performance. This equation was chosen to represent primary nucleation kinetics in this study.

$$J_{prim} = \exp(lnk_n)\left(\frac{\Delta_c}{\rho_c}\right)^n \exp\left(-\frac{E_{A,n}}{RT}\right)$$

Evans' models have CI and CC collision expressions[13], and an empirical expression of secondary nucleation is also available. The following are the respective equations:

$$J_{sec_{ci}} = k_{n_{ci}}\sigma^{nci}\frac{N_Q}{N_P}k_v\rho_c\epsilon\int_{L_{minct}}^{\infty} nL^3dt$$

$$J_{sec_{cc}} = k_{n_{cc}}\sigma^{ncc}\rho_c\epsilon^{\frac{5}{4}}L^{-4}\int_{L_{mincc}}^{\infty} nL^0dL$$

$$J_{sec_{cc}} = k_n\left(\frac{\Delta c}{\rho_c}\right)^n \exp\left(-\frac{E_{A,n}}{RT}\right)\epsilon^a\psi^b$$

Mermsann's equation is used for gCRYSTAL, in a designated form that requires inputs of surface shape factor and solubility factors which adds on secondary nucleation rate constant.[30]

$$B = K_N E_k f_c x(\sigma)$$

3.1.4. Crystal Growth Model

Crystals will grow after achieving nucleation where diffusion and surface-reaction are the two control mechanisms for crystal growth rate (G). Mixing velocity and growth rate both increased for diffusion-controlled growth, until it became a surface reaction. This occurred as the controlling element was now the inclusion of solute into the lattice. Diffusion is the limiting factor of growth rate in a non-agitated system and becomes surface reaction rate driven as impeller speed and velocity increases. Equation for a single crystal growth with both components considered:

$$\frac{dM}{dt} = \left[\frac{A}{\frac{1}{k}+\frac{1}{\kappa}}\right](c - c_i)$$

Assuming spherical particle behaviour:

$$\frac{dL}{dt} = G(L) = \left[\frac{2\phi_A/\phi_v\rho}{\frac{1}{k}+\frac{1}{\kappa}}\right]\Delta c$$

A two-step kinetics model can be used to portray crystal growth, in a form of first principal model made by Mersmann. Step 1, diffusion-controlled mass transfer step, is defined as:

$$G(L) = k_d(L)\left[\frac{C_{bulk} - C_{int}(L)}{\rho_{crys}}\right]$$

Step 2, surface integration step, is defined as:

$$G(L) = k_g \exp\left(-\frac{E_{A,g}}{RT}\right)\left[\frac{C_{int}(L) - C_{sat}}{\rho_{crys}}\right]^g$$

A power law kinetics model which is semi-empirical is often used as it takes the least variables in consideration. The scarce experimental data for protein crystallisation favours the power law kinetics model. Power law kinetics can be an expression for crystal growth showing an empirical correlation. This equation was chosen to represent growth kinetics in this study.

$$G(L) = k_g \exp\left(-\frac{E_{A,g}}{RT}\right)\left(\frac{\Delta c}{\rho_c}\right)^g$$

3.2. Methodology

3.2.1. Material and Experimental Setup

Material and arrangement of the employed data are studied for possible help in the explanation of variation of results from the model simulation before proceeding into model formulation. Table 1 summarises all key materials and setups for the respective experiments.

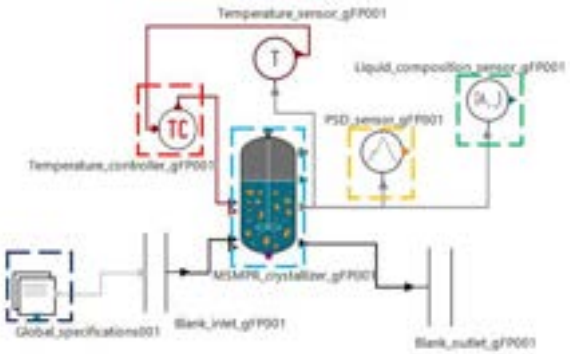

Figure 4: Protein crystallisation Ffowsheet in gCRYSTAL, [black]: Global specification, thermophysical properties specified, [red]: temperature controller, control the crystallisation temperature, [blue]: MSMPR crystalliser, initial conditions and crystallisation mechanisms are specified

[orange]: PSD sensor, measure CSD, [green]: composition sensor, measure the concentration of lysozyme

The temperature controller (TC) is kept within the desired temperature for thermostatic crystallisation experiments, where cooling profiles for cooling crystallisation experiments are created. The liquid composition and particle size distribution (PSD) sensors are used to attain the CSD and concentration respectively. (Figure 4)

3.2.2. Modelling formulation

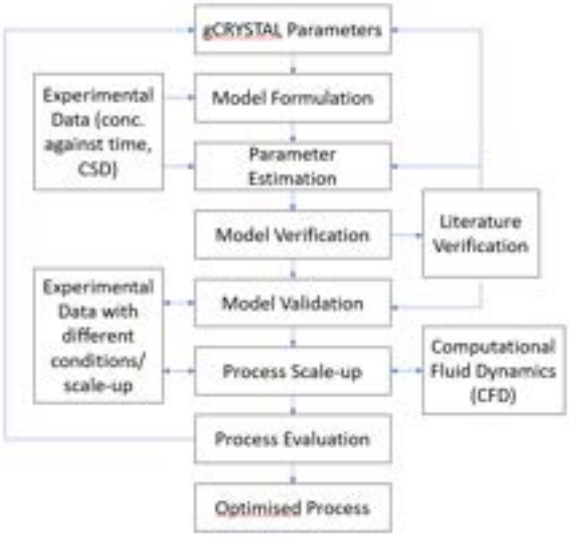

Figure 5: Crystallisation process workflow with use of gCRYSTAL

Detailed diagnosis could be made for the instances of validation and verification for the model (Figure 5). Both liquid phase components and lysozyme crystals required inputs of specific heat capacity and density coefficients. The data of specific heat capacity and density were plotted with temperature on the x-axis. By using gCRYSTAL, the data points are fitted with the trendline and the coefficients of the polynomials are noted. It should be made known that temperature has no effect on the density of lysozyme.

Since lysozyme is denatured at 75^{o}C, the coefficient of the specific heat is estimated between the range of 0^{o}C to 75^{o}C. [14]

For the enthalpy of crystallisation of lysozyme crystals, an enthalpy of -13.2 kcal/mol is attained after inputting the w/v of NaCl and initial concentration of lysozyme. A value of -15.1 kcal/mol was used as the number calculated from vant' Hoff's equation. Conversion to J/kg is completed to fit the format in gCRYSTAL.[15]

Protein solubility can be expressed as a function of precipitant/salt concentration, pH and temperature. There are two methods that can be used to aid in crystallisation (increase in supersaturation), that is, increasing both the temperature and concentration of salt.

Kinetics estimated can be significantly varied by the change in nucleation and growth rate. This is because supersaturation is based on solubility. Changing pH, salt concentration and temperature affects this. Solubility data was obtained from various literature sources before they were used in gPROMS.

Two different literature sources with comparable conditions of pH 4.5 and 5% (w/v) NaCl, have produced polynomial coefficients that are comparable.[16,17]

A third order polynomial is used to represent the solubility data. With the aid of Python (Figure 6), conversion from mg/ml to kg solute / kg liquid is required to fit the solubility input unit in gCRYSTAL.

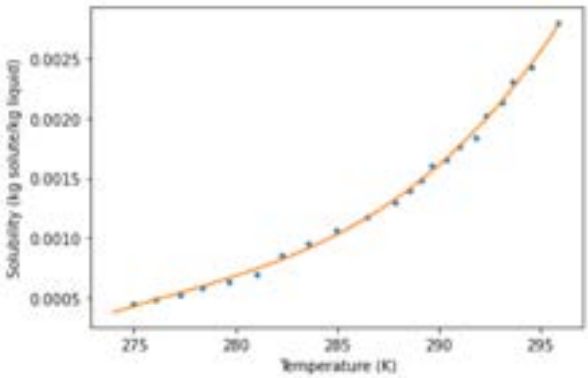

Figure 6: Fitting solubility data of literature into a polynomial using Python

3.2.3. Iteration Strategy

Deduction of the impacts of each kinetic parameter regarding the model is done by development of a flowsheet that recognises the substantial impact that boundaries and initial guesses have towards the estimation of parameters. The parameter estimation strategy can be categorised to three main parts, initial trial, iteration step, and verification step.

Initial trial uses literature's initial guess (Table 3). All kinetics bounds were relaxed until no error output is obtained by the software. Its goal is that the model runs without giving error and knowing the range of the valid initial guesses. The iteration step iteratively alters the initial guesses and constricts the kinetics bounds, with possible implementations of an alternative mechanism as a model comparison. This aims to estimate kinetics within a reasonable range and investigate sensitivity of the kinetics. Finally, the verification step implements PSD quantity (i.e. D_{50}) data into

the experimental data, where possible relaxation of bounds gives the estimated kinetics a reasonable particle size distribution (PSD).

4. Results and Discussion

4.1. Parameter estimation for cooling protein crystallisation

Table 4 & 5 records all iteration results for this section. Initial trial, trial #1, utilised the literature initial guesses with relaxation of boundaries. Although the model can run without no errors arising, the CSD obtained has a median at 48-68 μm range as the nucleation activation energy has a high upper bound with the relaxed boundaries.

Trials #2, #3 and #4 are performed to review the sensitivity of primary nucleation rate constant toward the CSD, with initial guesses of primary nucleation rate constant of 10, 20 and 40 respectively. Increasing primary nucleation rate constant gives increasing crystal sizes as expected.

Comparing to trial #4, trial #5 regresses the boundary of supersaturation ratios from [1-10] to [1-5]. Smaller CSD median values were obtained and this was an expected result with the experiment being less saturated. Trial #6 changes the initial growth rate constant and corresponding boundary from 3 μm/min and [0-10] μm/min to 2 μm/min and [0-5] μm/min. The CSD median values yielded were greater than trial #5. The initial guess of primary nucleation activation energy is upped to 5000 J/mol with a larger boundary of [0 – 20000] J/mol for trial #7. The CSD obtained is similar to CSD for the ones on trial #5, showing that primary nucleation activation energy has a small effect towards CSD. Trial #8 was a comparison to trial #2, with rate constant boundaries relaxing from [0-50] to [0-100]. This adds a similar change to that for trial #6 where the CSD is minimally affected. Trial #9 further narrows the initial growth rate constant and corresponding boundary with 1 μm/min and [0-2] μm/min as the conditions. The CSD median values are lower than the ones obtained in both trial #5 and trial #6, as the growth rate constant is smaller.

The objective functions for all trials are at 5 x 10^7, where the amount of initial drop of concentration were greatly exaggerated for the first 1000s. This was the main deviation from experimental values.

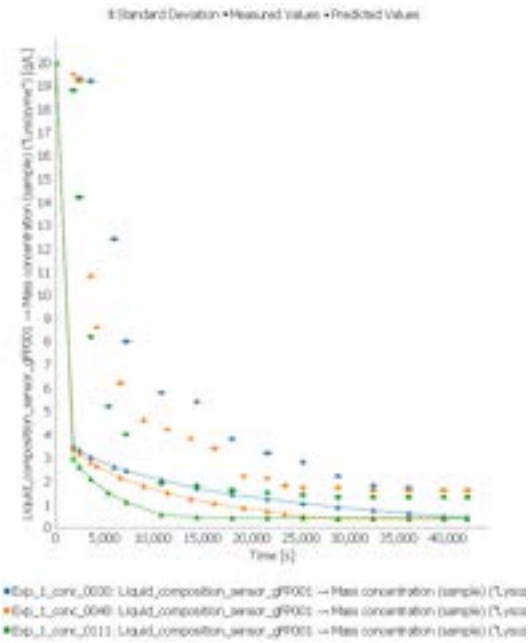

Figure 7: Lysozyme concentration as a function of time plot for trail #9

For some CSD distributions, double peaks were observed with ranges of [5-10] μm and [15-25] μm respectively, where the latter peak has a greater volume fraction. This means that the median diameter would be leaning closer to the [15-25] μm peak.

4.2. Parameter estimation for cooling protein crystallisation with the fixation of median crystal size

Table 6 records all iteration results for this section. Finding the differences between estimated kinetic parameters and published literature range is the reasoning behind performing iterations with fixed median crystal sizes. Inclusion of CSD data into gCRYSTAL was completed with the aim to get similar crystal sizes. It would reach the desired crystal size for the prediction if the median diameter is fixed. In gCRYSTAL, the median diameter D_{50} value at the end of the batch is inputted. The parameter estimator would push all kinetic parameters in order to fulfil the desired D_{50} size.

The experimental CSD are as shown in the diagram. The cooling rates, 0.048 C/minand 0.030 C/min, give D_{50} ranges at 10-20 μm. The cooling rate 0.111 C/min gives D_{50} ranges at 25-35 μm, Runs with D_{50} values at 5-30 μm are completed. (Figure 8)

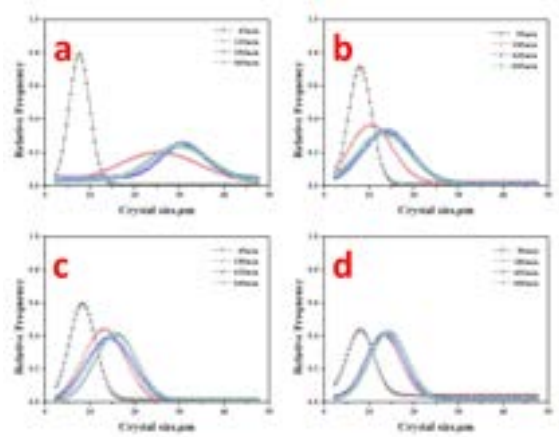

Figure 8: Experimental CSD at a) 0.111 C/min, b) 0.048 C/min, c) 0.030 C/min, d) 0 C/min[21]

Good fits were obtained when D_{50} was at 10-25 μm. Runs at 15 and 20 μm results have the least deviation between the set D_{50} value and D_{50} value obtained from the optimiser, that is, in 10^{-2}. An abnormal growth rate bounds in [0-100] μm/min resulting in 31.22 μm/min is the only run at 5 μm that does not give errors on the estimation process, indicating that it is unlikely the median crystal size would be at 5 μm. Runs at 30 μm has failed to reach the set D_{50} value, maximising at 27.4 μm. This again indicates that it is unlikely the median crystal size would be at 30 μm. (Figure 9)

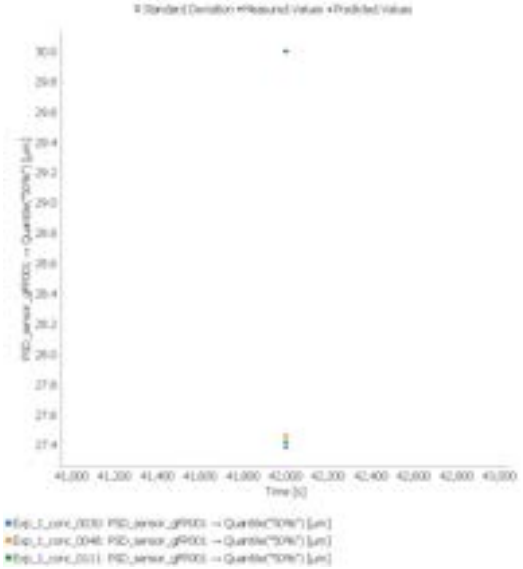

Figure 9: 50% quantile / median value of PSD at the end of experiment (42000 s) for D_{50} value at 30 μm

4.3. Parameter estimation for cooling protein crystallisation with the consideration of secondary nucleation effects

Tables 7, 8 & 9 record all iteration results for this section. Shear induced secondary nucleation is included in the model for possible improvements in CSD and objective functions. Initial guess of secondary nucleation rate constant is at -35(ln) with a boundary of [-50, 0](ln). Initial guess of the solubility factor is at 0.414 with a boundary [0,1]. The other two parameters for Mersmann kinetics, surface shape factor and number of entities are fixed at pi and 1 respectively. The rate constant is set to be greater than the literature value which is to test the sensitivity of second nucleation kinetics towards the growth and CSD model.

For trial #3 where the supersaturation ratio bounds are narrowed from [0,10] to [0,5](all growth and primary nucleation parameters), the initial and boundary numbers were the same. Growth and primary nucleation parameters with and without secondary nucleation influences do not differ much. The largest deviations are from trial #3 where there are boundary changes, and trial #2 which fewer steps of iterations were completed before estimating the results. This gives a smaller secondary nucleation rate constant and solubility factor.

When comparing CSD distributions with and without secondary nucleation influences, trials #2 and #6 has shown a left shift on CSD. Trials #3, #5, #7 and #9 has shown a right shift on CSD. Trial #2 as mentioned above has a less reliable estimation of parameters. For trial #6, double peaks are spotted and omitting the smaller peak at [1-10] μm would increase the CSD. A right shift instead of a left would be observed(Figure 10). The magnitude of increase in median diameter is small despite a rate constant close to the lower limit (-50).

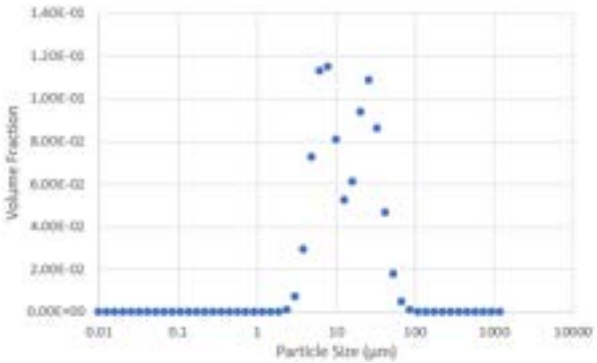

Figure 10: Volume fraction against particle graphs indicates the CSD for trail #6

The problem of exaggerated amount predicted for initial drop of concentration persists together with little changes for growth in primary nucleation parameters and CSD in secondary nucleation influence. This suggests that secondary nucleation plays a minor role for this set of experiment.

4.4. Parameter estimation for thermostatic protein crystallisation with differing volumes

Table 10 & 11 records all iteration results for this section. In order to test the validity of parameter estimation under different scenarios, a new set of experiment is introduced with different volumes and initial mass concentrations. CSD data are incorporated forcing the desired predicted crystal size. The experimental CSD for experiment 1 and 2 gives D_{50} range 10-20 μm and 15-25 μm. (Figure 11)

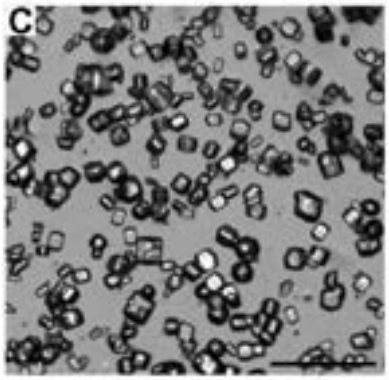

Figure 11: Lysozyme crystals under microscope (scale bar is 100 μm)[22]

Good CSD fits are obtained for the investigated D_{50} range at 5-25 μm where the maximum deviation out of all runs is ± 0.026 μm. For concentration-time graph, comparing parameter estimation values to experimental values, experiment 1 has a longer time taken for initial concentration drop and experiment 2 has a shorter time taken for initial concentration drop. Both experiments have dropped to 3.5 g/L at 42000s for parameter estimation which is lower than the experimental values. The objective functions for all runs are at the range of 1.5 x 10^7 to 2 x 10^7. For runs at 5, 10 and 15 μm, growth rate constant reaches the maximum of boundary at 10 μm/min. (Figure 12)

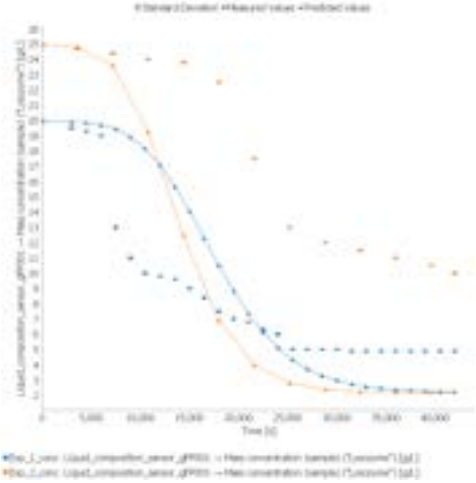

Figure 12: Lysozyme concentration as a function of time plot for D_{50} value at 15 μm

Shear induced secondary nucleation is again included in the model, with Mersmann kinetics parameters having initial guesses and boundaries. As the same as part 3, there are little changes for CSD graph and concentration time graph, suggesting that secondary nucleation plays a minor role for this set of experiment.

5. Conclusion

The motivation of this study it to estimate the kinetic parameters of lysozyme's nucleation and growth models by building a parameter estimation model. Valid thermophysical properties, thorough built for bounds & initial guesses iterations and sensitivity analysis for the estimated parameters were done to complete the objective which was to achieve the set CSD and remove kinetic parameter estimation that has a small effect.

For crystal size distribution (CSD), boundaries and initial guesses of primary nucleation rate constant has the most influence followed by growth rate constant. Activation energy of crystal growth parameter has regressed to 0 J/mol regardless changes on other parameters.

It was found that the predicted crystal sizes are comparable to experimental size range. A slight overestimation for CSD is spotted, thereby the median diameter of D_{50} is incorporated to estimate kinetic parameters that would obtain an experimental size range similar to the published literature range. The iteration achieved good agreement for D_{50} at 10-25 μm coinciding with the experimental D_{50} values. However the difference in D_{50} values between 0.111 C/min and other cooling rates were not obtained in the estimation results.

Shear induced secondary nucleation is included in the model for possible improvements in CSD and objective functions. There were little changes for CSD graph and concentration time graph despite a large rate constant close to the lower limit (-50). As such, this suggest that secondary nucleation plays a minor role for this set of experiment.

The magnitude of initial drop of concentration is exaggerated for the first 1000s, together with double peaks observed on some CSD distributions. This served as the two factors that caused deviations of parameter estimation results to experimental data.

A new set of experiment was introduced to test the validity of parameter estimation under

different scenarios. The predicted crystal sizes are comparable to experimental size range. A better fit for concentration time graph was obtained and compared to the cooling experiments. However, the expected time for the initial drop on concentration and terminal mass concentration were the two main deviations that caused difference between parameter estimations and experimental data. Shear induced secondary nucleation was included in the model, but no significant effects were observed.

6. Outlook

This study has rigorously gone through the first three steps of the workflow: model formulation, parameter estimation and model verification. Further experimental data are vital to proceed further in the workflow with optimised processes through developments on estimated kinetics. Hydrodynamics and thermodynamics factors are considered in model building to obtain reliable and accurate kinetics.

A series of experiments would be demanded to achieve this goal, with involvements on three main areas: fluid motion (impeller diameter effects, speed and crystalliser type), secondary nucleation (seeding, attrition, agglomeration and breakage) and measurement of predictive solubility and control of supersaturation. Aspen+ and HYSYS are prrocess simulators that can be utlized to support the prediction of thermodynamic properties. Computational fluid dynamics (CFD) would be useful to better comprehend the fluid mechanics, mixing effect and investigating polymorphism using quality control tools.

A plethora of advantages would be obtained on the employment of the continuous processing mode. These include a high throughput, added convenience of scale-up in series, the eradication of intermediate storage and steady production. Despite the added benefits of using the continuous processing mode, the pharmaceutical industry has been adamant to follow the tenets incorporated owing to the high initial investment required to purchase and outfit new equipment and the copious amount of control and design expected from the process of continuous crystallisation.[3]

The refinement of both the control and design can be achieved by utilizing a modelling framework. In this context, once there are adequate capabilities of predictive for the projected kinetics, continuous multistage crystallisation can be accomplished. Figure 13 below depicts the workings of the continuous multistage crystallisation in gCRYSTAL.

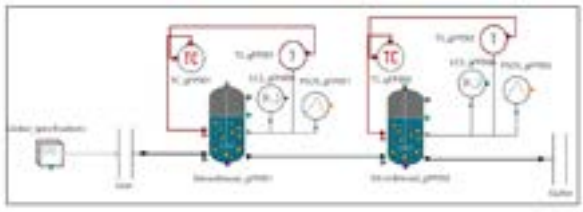

Figure 13: Continuous multistage process implementation

Decreasing storage lifespan of the dried product caused by solvent inclusion, is one of the consequences of agglomeration; a common problem in pharmaceutical crystallisation.[18] Low solubility of lysozyme creates lengthy residence time of crystallising lysozyme which increases the tendency of agglomerates formation.[19] It has led to over-measurement of crystal size distributions for particle size analysers e.g. Malvern Instrument. Smoluchowski's kinetics, Mumtaz's kinetics and Power Law kinetics are kernels that can be incorporated in gCRYSTAL as the agglomeration mechanism. Better estimation and objective function with the desired experimental crystal size can be achieved after considering agglomeration kinetics[20].

Evaporative crystallisation and heterogeneous seed crystallisation are other experiments that could be incorporated in gCRYSTAL.

7. Acknowledgements

We, the authors, would like to express our heartfelt gratitude to our research supervisor, Jerry Heng, at Imperial College London, for his guidance and motivation throughout this project. Our sincere thanks to Ian Rosbottom, our PhD advisor, who dedicated his time to teach us and assist us in troubleshooting gCRYSTALS. We would also like to thank Hamish Mitchell who participated in our weekly meetings and gave us meaningful suggestions.

8. References

1. Franzreb, M., Müller, E. & Vajda, J. *Cost Estimation for Protein A Chromatography An In Silico Approach to MAb Purification Strategy*.

2. McPherson, A. & Gavira, J. A. Introduction to protein crystallization. *Acta Crystallographica Section F:Structural Biology Communications* (2014)

3. Su, Q., Nagy, Z. K. & Rielly, C. D. Pharmaceutical crystallisation processes from batch to continuous operation using MSMPR stages: Modelling, design,

and control. *Chem. Eng. Process. Process Intensif.* (2015)
4. Carpenter, E. P., Beis, K., Cameron, A. D. & Iwata, S. Overcoming the challenges of membrane protein crystallography. *Current Opinion in Structural Biology* vol. 18 581–586 (2008).
5. Kougoulos, E. Predictive modelling of organic crystallization processes. (2005).
6. Bermingham, S. K. S. K. *et al.* A design procedure and predictive models for solution crystallisation processes. in *Proceedings 5th International Conference on Foundations of Computer-Aided Process Design* (2000).
7. Lillacci, G. & Khammash, M. Parameter estimation and model selection in computational biology. *PLoS Comput. Biol.* (2010)
8. Mullin, J. W. Solutions and solubility. in *Crystallization* (2001).
9. Kresheck, G. C. *et al.* The Effect of D20 on the Thermal Stability of Proteins. Thermodynamic Parameters for the Transfer of Model Compounds from H20 to D201,2.
10. Baillon, F., Espitalier, F., Cogné, C., Peczalski, R. & Louisnard, O. Crystallization and freezing processes assisted by power ultrasound. in *Power Ultrasonics: Applications of High-Intensity Ultrasound* (2015).
11. Doran, P. M. *Bioprocess engineering principles: Second edition*. *Bioprocess Engineering Principles: Second Edition* (2012)
12. Vedantam, S. & Ranade, V. V. Crystallization: Key thermodynamic, kinetic and hydrodynamic aspects. *Sadhana - Acad. Proc. Eng. Sci.* (2013)
13. Evans, T. W., Sarofim, A. F. & Margolis, G. Models of secondary nucleation attributable to crystal-crystallizer and crystal-crystal collisions. *AIChE J.* (1974)
14. Schön, A., Clarkson, B. R., Jaime, M. & Freire, E. Temperature stability of proteins: Analysis of irreversible denaturation using isothermal calorimetry. *Proteins Struct. Funct. Bioinforma.* (2017)
15. Schall, C. A., Arnold, E. & Wiencek, J. M. Enthalpy of crystallization of hen egg-white lysozyme. *J. Cryst. Growth* (1996)
16. Forsythe, E. L., Judge, R. A. & Pusey, M. L. Tetragonal chicken egg white lysozyme solubility in sodium chloride solutions. *J. Chem. Eng. Data* (1999)
17. Cacioppo, E. & Pusey, M. L. The solubility of the tetragonal form of hen egg white lysozyme from pH 4.0 to 5.4. *J. Cryst. Growth* (1991)
18. Savjani, K. T., Gajjar, A. K. & Savjani, J. K. Drug Solubility: Importance and Enhancement Techniques. *ISRN Pharm.* (2012)
19. Oliva, J. A., Wu, W. L., Greene, M. R., Pal, K. & Nagy, Z. K. Continuous Spherical Crystallization of Lysozyme in an Oscillatory Baffled Crystallizer Using Emulsion Solvent Diffusion in Droplets. *Cryst. Growth Des.* (2020)
20. Su, Q., Rielly, C. D., Powell, K. A. & Nagy, Z. K. Mathematical modelling and experimental validation of a novel periodic flow crystallization using MSMPR crystallizers. *AIChE J.* (2017)
21. Tang, X. H., Liu, J. J., Zhang, Y. & Wang, X. Z. Study on the influence of lysozyme crystallization conditions on crystal properties in crystallizers of varied sizes when temperature is the manipulated variable. *J. Cryst. Growth* (2018)
22. Smejkal, B. *et al.* Protein crystallization in stirred systems-scale-up via the maximum local energy dissipation. *Biotechnol. Bioeng.* (2013)
23. Darcy, P. A. & Wiencek, J. M. Estimating lysozyme crystallization growth rates and solubility from isothermal microcalorimetry. *Acta Crystallogr. Sect. D Biol. Crystallogr.* (1998)
24. Gómez, J., Hilser, V. J., Xie, D. & Freire, E. The heat capacity of proteins. *Proteins Struct. Funct. Bioinforma.* (1995)
25. Imaizumi, S., Matsuda, T. & Hatta, I. Measurement of dynamic specific heat capacity of lysozyme crystals. *J. Phys. Soc. Japan* (1979)
26. Leung, A. K. W., Park, M. M. V. & Borhani, D. W. An improved method for protein crystal density measurements. *J. Appl. Crystallogr.* (1999)
27. Perry, R. H. & Green, D. W. *Perry's Chemical Engineers' Handbook, 8th Edition*. *Journal of Chemical Information and Modeling* (2013).
28. Steele, W. V., Chirico, R. D., Cowell, A. B., Knipmeyer, S. E. & Nguyen, A. Thermodynamic properties and ideal-gas enthalpies of formation for 2-aminoisobutyric acid (2-methylalanine), acetic acid, (4-methyl-3-penten-2-one), 4-methylpent-1-ene, 2,2'-bis(phenylthio)propane, and glycidyl phenyl ether (1,2-epoxy-3-phenoxypropane). *J. Chem. Eng. Data* **42**, 1052–1066 (1997).
29. Navarro, C. A., Sierra, C. A. & Ochoa-Puentes, C. Evaluation of sodium acetate trihydrate-urea des as a benign reaction media for the Biginelli reaction. Unexpected synthesis of methylenebis(3-hydroxy-5,5-dimethylcyclohex-2-enones), hexahydroxanthene-1,8-diones and hexahydroacridine-1,8-diones. *RSC Adv.* **6**, 65355–65365 (2016).
30. Agrawal S.G., A.H.J. Paterson, Secondary Nucleation: Mechanism and Models. *Chemical Engineering Communications* (2015)

Application of a CHO cell Genome-Scale Metabolic Model for Bioprocess Optimisation

Wei Yang Lee[1] and Yihan Zhang[1]

[1] *Department of Chemical Engineering, Imperial College London, U.K.*

Abstract Chinese Hamster Ovary (CHO) cells are the most important host cells for producing Immunoglobulin G (IgG) in the biopharmaceutical industry. Flux Balance Analysis (FBA) has been a useful tool for performing computational analysis of under-determined cell metabolism model. This technique would create comprehensive flow maps across metabolic networks, which would enable researchers to obtain deeper insights into cell metabolism. Despite FBA has been widely used in many applications, it often overestimates the reaction fluxes for large genome-scale metabolic networks due to the large degree of freedom arising from the complexity of the cell. In this study, the predictive performance of FBA was evaluated, using the experimental data obtained from the Kotidis et al.[1]. Additional constraints such as availability constraints for carbon and nitrogen were added within the flux balance analysis framework to significantly reduce the flux variability, resulting in improved accuracy of biomass growth rate prediction. Furthermore, parsimonious enzyme usaged FBA was incorporated into our study to force the cells to use the carbon sources and enzymes more efficiently under the growth pressure. Although our results demonstrated that pFBA does not improve our model's predicting power, but it significantly reduces the net flux in the network. The objective functions of biomass growth and IgG production rate are utterly opposite, resulting in the low specific productivity of IgG. To address these issues, we demonstrated the bi-level programming to couple the biomass growth rate and the IgG production by conducting the genetic intervention, which includes up-regulating, down-regulating and knock out reaction fluxes. The genetic intervention was presented to identify necessary reactions and genes that satisfy the coupled objectives of biomass formation and IgG production.

Introduction

Monoclonal Antibodies (mAbs) play an important role in the novel treatment of cancers and autoimmune diseases. Typically, monoclonal antibodies are manufactured by conducting genetic engineering to harness a host cell to produce the therapeutic protein. In particular, Chinese Hamster Ovary (CHO) cells are the most dominant host cell in the production of IgG in biopharmaceutical industries[2] due to their potential to produce non-immunogenic antibodies[3,4]. However, CHO cells are not naturally designed to produce therapeutic proteins, the specific production rate is relatively low. Despite CHO cells are being commonly used as a host over the decades, the complexity of CHO metabolism network rendered with a huge challenge in optimising IgG productivity[5]. Therefore, it is apparent that there is a need to enhance the modelling approach for the metabolism description of CHO cell line.

Flux balance analysis is a constraint-based modelling approach to compute the metabolic network based on the stoichiometry of the metabolic reactions without the need for kinetic data. The prediction of FBA is based on the assumption that cells evolve optimally in response to changes in their environment due to evolutionary pressures. Several in silico analysis have been carried out to study the CHO cell physiology including flux balance analysis and genome-scale modelling[6–8]. Though FBA has been widely used to study CHO cells metabolism at genome-scale, it still has hindrance in predicting fluxes due to a large number of unknown variables that emerge from the complexity of the metabolic network, the inaccurate and incomplete construction and analysis of the genome-scale model, as well as limited knowledge on the definition of a biologically relevant objective function[9]. Additionally, even when FBA was given a well-curated network, the experimental growth rates still do not always match the predictions from FBA. As a result, experimental flux data is often incorporated into FBA to constrain the solution towards the experimentally observed behaviours. Extracellular flux such as carbon source and oxygen uptakes rates as well as by-product secretion rates are often set as the constraints for the FBA approached. However, these data are still not sufficient to ensure a single solution. Although several studies have been carried out to incorporate other 'omics' datasets into constraint-based models to improve flux estimations, it is very difficult to quantify these datasets with the current cellular physiology[10,11].

In this work, a novel method called carbon constraint FBA (ccFBA) is applied to estimate intracellular fluxes in the CHO metabolic network[5]. This method simultaneously considers the elemental balance of carbon throughout the network and the reaction fluxes associated with the carbon. By adding additional constraints on the carbon availability in the model under studied physiological conditions, ccFBA can improve the intracellular flux predictions by reducing the flux variability. Besides carbon, the nitrogen elemental balance was also considered as nitrogen is one of the most abundant elements in the cells. Furthermore, the parsimonious enzyme usage Flux Balance Analysis (pFBA) was employed to further reduce the flux variability[12]. This optimisation method assumes the cell is using a minimum amount of enzymes to reach

a maximised objective, which leads to minimisation of total fluxes in the cell. Although the FBA approaches in predicting protein production has been proven helpful, prediction of IgG is still difficult as the production of IgG from the CHO is an antagonistic function to the production of biomass. This result in FBA is no longer suitable in predicting the fluxes of biomass and IgG simultaneously. Only one of them can be maximised under a Flux Balance Analysis while the other one is suppressed to zero flux to reach a feasible solution. To accomplish the goal mentioned above, the two objective functions of maximising IgG productivity and maximising biomass growth rate are now coupled to carry out bi-level optimisation. This method arises from the fact that some flux of IgG would be produced as a by-product when the biomass is being produced. Therefore, biomass production is selected as the main objective function in the bi-level optimisation.

Methods

Cell Lines and Media

A CHO suspension cell line provided by the previous work of Kotidis et al.[1] was used to perform the biomass and IgG production prediction study. The data were taken from a fed-batch process of CHO where the CHO cells were seeded at 2 million cells/mL and cultured in CD-CHO medium (Invitrogen, UK). Culture aliquots were collected daily for analysis. Cell concentration and viability were determined with the Viability and Cell Count assay on NucleoCounter NC-250TM. Concentrations of the proteins and nutrients were quantified using the BLItz system (Pall ForteBio Europe, Portsmouth, UK).

Viable Cell Density and Integral viable cell concentration

A Gaussian frequency distribution of cell diameter/ volume can be assumed[13]. Therefore, mean cell volume can be used as a reliable population descriptor. The integral of viable cell concentration was calculated as follows:

$$\mathrm{IVCC}_1 = \frac{0.5\,(X_1 + X_0)}{t_1 - t_0} + \mathrm{IVCC}_0 \qquad (1)$$

where X_1 and X_0 are the viable cell density at final and initial time points, respectively. t_1 and t_0 are the time at final and initial time points, respectively. IVCC_1 and IVCC_0 are the IVCC at final and initial time points, respectively.

To predict the cell behaviour of CHO cell culture under the experimental condition by Kotidis et al.[1], uptake and secretion rate of nutrients and products have to be consistent with the experimental values of the specific metabolic flux. The specific metabolic flux rate was calculated as follows:

$$\mathrm{q} = \frac{[\mathrm{met}]_1 - [\mathrm{met}]_0}{\mathrm{IVCC}_1 - \mathrm{IVCC}_0} \qquad (2)$$

where $[\mathrm{met}]_1$ and $[\mathrm{met}]_0$ are the final and initial metabolites concentrations, respectively, IVCC_1 and IVCC_0 are the IVCC at final and initial time points, respectively.

Genome scale model

Genome-scale metabolic models (GEMs) are mainly used to characterise gene-protein-reaction (GPR) interactions for whole metabolic genes in a cell computationally. It allows for the prediction of growth capabilities and auxotrophies across a cell species. In this study, iCHO1766[14] was used to ensure all the data related to the stoichiometry of cell metabolism are all up to date. The whole model and the reference data for genes, reactions and metabolites are available in the BiGG database. iCHO1766 is the most updated and well-curated CHO genome-scale metabolic model. The model contains 6,663 reactions, 1,766 genes and 4,456 metabolites. The large number of genes and reactions has made the iCHO1766 a large genome-scale network, leading to an under-determined metabolic system. Thus, Flux Balance Analysis is employed to illustrate CHO cell metabolism under the current medium condition.

Flux Balance Analysis & Flux Variability Analysis

Metabolic fluxes through CHO metabolic network were determined using the Flux Balance Analysis (FBA) which constraints are enforced by the stoichiometric ratio in the metabolic network. In FBA, the fluxes through the metabolic network can be found by solving the equation $\mathbf{S}.\mathbf{v} = 0$. Generally,$\mathbf{S}$ matrix generated by CHO cell can be notably under-determined due to the large genome-scale model of CHO. Thus, an objective function is required to be fixed in the constraint-based model to solve the system of linear equation in matrix form. The objective function can be the maximisation of biomass production or minimisation of nutrient uptake rate. Using the matrix representation, the problem of optimisation can be formulated as follows:

$$\begin{aligned} max \quad & \mathbf{c}^T \cdot \mathbf{v} \\ s.t. \quad & S \cdot \mathbf{v} = 0 \\ & \mathbf{v_{min}} \leq \mathbf{v} \leq \mathbf{v_{max}} \end{aligned} \qquad (3)$$

Where $\mathbf{c}^T$ is a vector that represents the objective function to be maximised as a linear equation of fluxes and v is the vector of all metabolic fluxes. $\mathbf{v_{min}}$ and $\mathbf{v_{max}}$ indicate the upper bound and the lower bound of the fluxes. They are primarily used to identify the constraint for biomass growth rate, the irreversibility of reactions or the continuous uptake from the environment. $\mathbf{S}$ is the stoichiometric matrix representing the stoichiometry of reactions in the metabolic network. To replicate the growth morphology of CHO cells in various culture media, the biomass reactions were optimised while at the same time limiting the rate of uptake/secretion of all essential nutrients and amino acids at experimental data. To obtain the optimal solution in the under-determined CHO genome-scale model, we imposed constraints on the exchange

reactions using the experimental flux values. We calculated the upper bounds and lower bounds values of exchange reactions using the specific metabolic flux rate calculation by Eqn 2. For the exchange reactions in which its bound values were not measured experimentally, its lower bound value is set at 0 whereas its upper bound values are set as 1000. This results in the remaining exchange reactions are only allowed for secretion. Additionally, intracellular reactions are required to be unconstrained, which means their bounds were set to arbitrarily large values according to their reversibility properties. Flux Variability Analysis (FVA) was employed to reduce the arbitrarily large bounds of intracellular. FVA makes use the basic formulation shown in Eqn 3, to find the maximum and minimum possible fluxes for each reaction in the metabolic network under the specific feed condition by iterating over all reactions.

Elemental Constraint FBA

The results produced by FBA often cannot match the experimental data because of the existence of redundancy and plasticity in cellular metabolism. Additionally, FBA assigns arbitrarily large bounds for intracellular fluxes, which results in many folds higher number of atoms passing through the network than those that are available to the cell via its surroundings. To increase the robustness of the solutions from FBA, the model was further constrained. An additional constraint which takes account of the amount of uptake different element was added to the permissible fluxes through intracellular reactions. The new elemental constraints is defined in Eqn 4.

$$v_j{}^{bnds} = \frac{N^{TOT}}{N_j} \tag{4}$$

where $v_j{}^{bnds}$ is the elemental constraints of reaction j, N^{TOT} stands for the total amount of the specific element available in the environment and N_j represents the number of atoms participating in reaction j. Based on the definition of elemental constraints, the reduction of the feasible region depends on both amount of atoms available in the environment and the number of atoms involved in the reaction. Carbon and nitrogen are good considerations of the additional constraints due to their large cellular demand and limited availability via the medium.

By imposing the carbon or nitrogen availability constraint on a constraint-based model, the flux variability can be greatly reduced and eventually improving the accuracy of flux predictions in CHO cells. In order to carry out the ccFBA and ncFBA, it is important to include all the carbon and nitrogen sources, as well as their comprehensive chemical formulation into the framework. The experimental uptake and secretion rates for major carbon sources such as glucose and lactate need to be fed into the constraint-based model. Besides, certain compounds in the cells would potentially act as co-factor pair, such as ATP/ADP or $NAD^+/NADH$, in which their carbon and nitrogen atoms do not participate in the reaction. Therefore, it is important to skip the co-factor pairs when predicting the allowable carbon or nitrogen flux through biochemical reactions. The ccFBA and ncFNA were carried out in this work following the algorithm proposed by Lularevic et al.[5]. The algorithm is available on GitHub and the steps of the algorithm are detailed in the Lularevic et al.[5].

Parsimonious Enzyme Usage FBA

Parsimonious Enzyme Usage Flux Balance Analysis (pFBA) is a bi-level optimisation problem, in which the net metabolic flux through all gene-associated reactions in the network is minimised and followed by applying FBA to optimise the cell growth using the flux ranges obtained from the net flux minimisation. This method is mainly based on a hypothesis that cells use the carbon sources and enzyme more rapidly and efficiently under the growth pressure. pFBA begins with classifying the genes and proteins into five classes which are essential class, pFBA optima, metabolically less efficient(MLE), enzymatically less efficient (ELE) and pFBA no-flux. In pFBA, essential and pFBA optima are upregulated as they contribute the most to the optimal growth. In contrast, ELE, MLE and pFBA no-flux are down-regulated or removed to save resources for improving growth rate. Here, the pFBA optima were computed for CHO cells, using the experimentally measured metabolites uptake rates.

Genetic Engineering

Besides altering cell medium condition, medium composition and feed strategy, genetic engineering provides an alternative way to improve cellular performance of increasing IgG production. This can be achieved by regulating different genes and knocking out reactions that are not necessary for IgG production and cell growth. This makes the model into a bi-level optimisation problem, which involves several binary variables that were used to define genetic knock-outs and reaction regulations in the cell. In our work, the bi-level optimisation algorithms consist of two optimisation problem which is the growth rate and IgG production. In the algorithm, the IgG production is chosen to be the upper-outer optimisation as this aligns with the goal of this experiment which is to maximise the IgG production. Meanwhile, the cell growth rate is selected as the lower-inner optimisation objective function. The formulation of genetic engineering is shown in Table 1. However, bi-level optimisation gave a very large non-linearity and strong duality theorem was used to convert it into a mixed-integer linear programming (MILP) problem which is easier to implement and faster to solve in GAMS32.2 using CPLEX solver.

Results

Phases split

Growth rate of CHO cells could be approximated by Eqn 5

$$N_x = N_{x,0}e^{\mu t} \tag{5}$$

Table 1: Genetic engineering formulation

Outer Objective	Max IgG production rate	
Outer constraints	each reaction can only be intervened once	$y_j^{up} + y_j^{KO} + y_j^{down} \leq 1$
Outer constraints	total number of interventions (k) k	$\sum_j y_j^{up} + y_j^{KO} + y_j^{down} = k$
Inner Optimisation	Inner Objective	Max Biomass growth rate
	Stoichiometry	$\sum S_{ij} v_j = 0$
	Knock out reaction upper bound	$v_j \leq UB_j(1 - y^{KO})$
	Knock out reaction lower bound	$v_j \geq LB_j(1 - y^{KO})$
	Upper bounds	$v_j \geq (LB_j + (UB_j - LB_j)e_{up})y_j^{up} + LB_j(1 - y_j^{up})$
	Lower Bounds	$v_j \leq (UB_j - (UB_j - LB_j)e_{down})y_j^{down} + UB_j(1 - y_j^{down})$
$i \in$ metabolites, $j \in$ reactions, $y_j \in \{0, 1\}$		

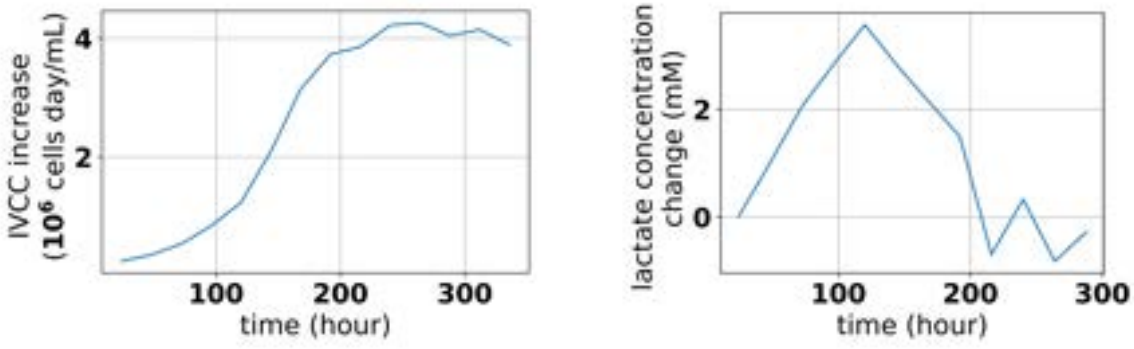

(a) *Experimental growth rate of Feed 3*

(b) *Change in lactate concentration of Feed 3*

Figure 1: *Phase split depends on both biomass growth rate and lactate flux. Figure 1(a) shows that the growth rate of CHO cells slows down at 210 hour in feed 3, which indicates a potential phase transition from exponential phase to stationary phase. Figure 1(b) shows that the lactate flux for feed 3 decreases and even get negative when the cell grows above 200 hours. These are both the evidence of a phase transition in CHO cell behaviour.*

where N_x is the number of viable cells in the medium, $N_{x,0}$ is the number of viable cells in the medium at the initial time, t is culture duration and μ is the growth rate of biomass. The specific growth rate could be estimated by fitting the experimental increase in integral viable cell concentration (IVCC) against culture duration using the form of Eqn 5.

The experimental data of the first 48 hours were not used as the cells were initially in metabolic adaptation period right after inoculation[15]. As shown in Figure 1(a), cell growth rate varies over the whole culture period. The analysis shows that from day 2 to 5, the growth rate can be accurately described by an exponential growth rate of approximately 0.021 h^{-1}, whereas day 6 to 8, the cell growth rate decreases slightly to approximately 0.017 h^{-1}. Subsequently, the cell growth significantly slows down to approximately 0.007 h^{-1} from day 8 to 14.

Despite a much slower biomass growth rate, it is important to note that the lactate concentration drops significantly during the stationary phase. As shown in Figure 1, on day 9, lactate flux tends to be negative which indicates CHO cell growth has entered the stationary phase. Therefore, cell culture growth could be divided into 3 phases which are early exponential phase, late exponential phase and stationary phase accordingly.

Computational prediction in CHO performance

The results of FBA are shown in Figure 2(a). Unfortunately, the accuracy of prediction is not adequate to be applied in genetic engineering. Flux balance analysis with an objective "maximising biomass growth rate" could overestimate biomass growth rate with arbitrarily large intracellular flux upper bounds[16].

Elemental constraints could effectively constrain the intracellular fluxes in exponential-phase cell growth, which were not appropriately constrained by arbitrary bounds from FVA. As shown in Table 2, nitrogen constrained FBA shows a weaker ability in constraining enzymatic reactions than carbon-constrained FBA. It is convincing that the demand for the elements in interest passed a specific reaction is one of the key factors determining the ability to constrain that specific reaction.

After the introduction of carbon constraints, an upper bound for biomass growth rate is applied to the model, which significantly improved the accuracy of prediction as shown in Figure 2(b). Especially for late exponential phase, the percentage difference between computational results and experimental results decreases dramatically from 161% to 113%. Accuracy could be further improved by applying ncFBA as shown in Figure 2(c). But in contrast to the reduction of intracellular reaction fluxes, ncFBA showed a much better ability in constraining biomass growth rate. Thus the combination of both elemental con-

Table 2: *Elemental constraints can effectively constrain intracellular fluxes. Here are 6 examples of intracellular fluxes of important enzymatic reactions in different pathways. The comparison between the upper bounds of these reactions can illustrate the impact of introducing elemental constraints.*

enzymatic reactions	upper bound of FVA	upper bound of ccFBA	upper bound of ncFBA
Hexokinase	40.74	2.23	32.14
Phosphofructokinase	40.74	2.23	32.14
Pyruvate kinase	40.92	4.45	33.32
Acetyl-CoA carboxylase	40.60	4.45	32.00
Vitamin D3 25-hydroxylase	0.15	0.12	0.12
Fatty-acid–CoA ligase	20.30	0.67	16.00
Glutamine synthetase	40.60	2.67	1.61

straints was then used for the prediction of biomass growth rate, but Figure 2(d) showed no further improvement in the accuracy.

Yeo et al.[9] stated the enhancement of prediction accuracy by applying pFBA. pFBA is then applied to elemental-constrained FBA model to see if there are any more accurate computational results. However, Figure 2(e) shows no further improvement in computational results, though the reduction in flux variability compared to basic flux balance analysis is observed. This is mainly due to pFBA's lack of ability to describe the intrinsic biomass growth and products secretion restriction in mammalian cell. Nevertheless, the net flux which is the inner objective of a pFBA optimisation problem has been decreased significantly as shown in Figure 2(f).

Minimisation of nutrient uptake rate

However, the stationary phase prediction had no improvement by implementing the elemental constraint method. The percentage difference between experimental IgG production rate and computational IgG production rate remains at 77% as shown in Figure 2. During stationary phase, CHO cell culture shifts to six times higher energy use efficiency coupled with lactate consumption[17]. Compared to exponential growth phase which is characterised by high-flux glycolysis and glutaminolysis pathway, the stationary phase has lower fluxes in glycolysis pathway[15] and higher fluxes in TCA cycle[18]. Selvarasu et al.[19] also showed a significant decrease in lipid and nucleotide pathways fluxes compared to exponential phase. This suggests that the activities of these pathways significantly slow down during stationary phase. However, the mechanism of transitions between the exponential phase and stationary phase is still unknown due to the complexity of mammalian cell metabolic network[15].

Figure 1(a) shows a significant slowdown in cell growth rate, this makes biomass objective function (BOF) inappropriate to accurately predict cell performance. The results also show a large gap between the real growth rate and prediction as shown in Figure 4(a). The IgG production rate was also applied as an objective of FBA. However, Figure 3 shows a gradual decline in experimental IgG productivity, therefore IgG production rate cannot be used as an objective of FBA either. The result of IgG objective function is shown in Figure 4(b).

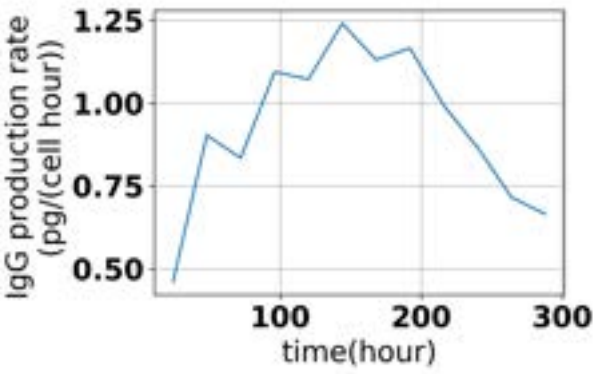

Figure 3: *IgG production rate time evolution*

Chen et al.[20] indicate an alternative way to choose a cellular objective function which is minimising nutrient uptake rate for flux balance analysis. In this project, glucose, lactate, histidine, threonine, valine, methionine, lysine, isoleucine, phenylalanine uptake rates were used as the objective function for CHO cell growth in stationary phase. The results are illustrated in Figure 4. Predictions of histidine, threonine, methionine and phenylalanine uptake rates are within the experimental range of the specific nutrient uptake rate.

Genetic engineering

The optimisation of genetic engineering model was performed in GAMS 32.2. The formulation involves k values which is the total number of genetic interventions. For the different scenario of genetic interventions, the optimisation loops with different values of k from 10 to 70 by steps of 10 and two iterations for each value of k. In total, 14 scenarios were tested for each phase in feed 3. The up-regulation and down-regulation factors were set as 0.7 and 0.3, respectively since Pandey et al.[21] states, these parameter sets can generate the best description of cell culture.

GAMS shows that intervened reactions mainly

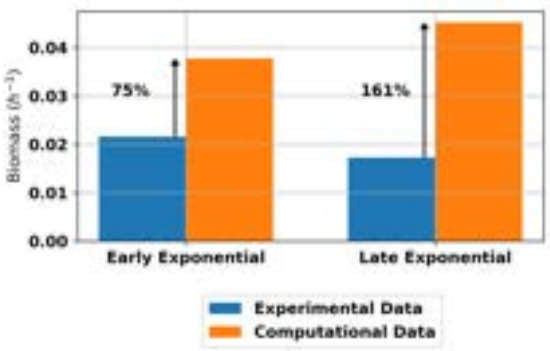

(a) *Flux balance analysis results*

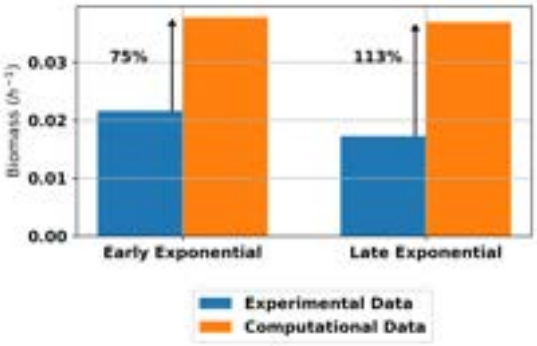

(b) *Carbon constrained flux balance analysis results*

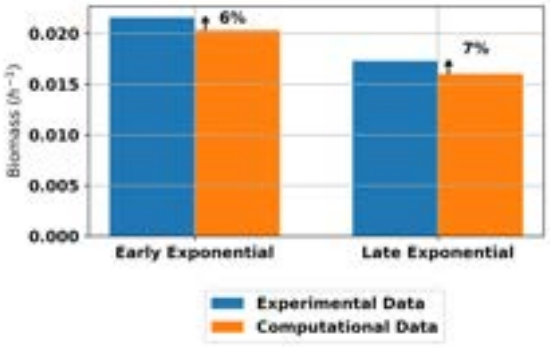

(c) *Nitrogen constrained flux balance analysis results*

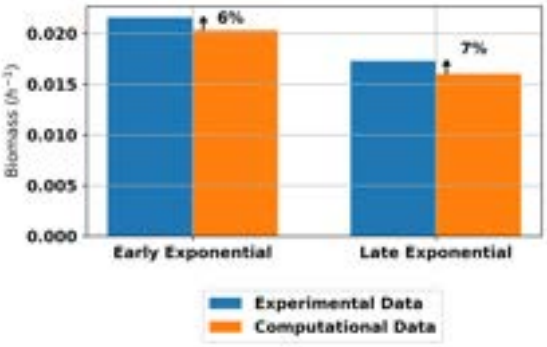

(d) *Nitrogen & carbon consrained flux balance analysis results*

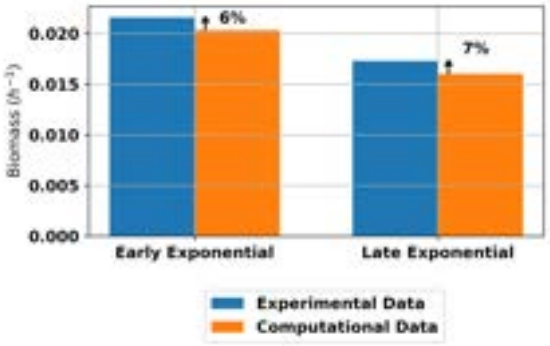

(e) *Parsimonious enzyme usage flux balance analysis results*

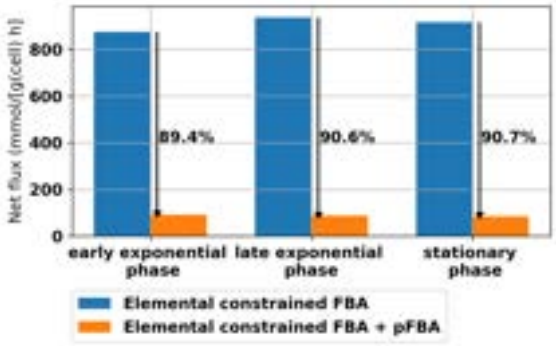

(f) *The computational net flux of cell growth before and after applying pFBA*

Figure 2: The computational results of iCHO1766 GEM after applying different constraint-based optimisation methods.

belong to glycolysis, oxidative phosphorylation, protein production, endoplasmic reticular transport (also known as secretory), extracellular transport, urea cycle/amino group metabolism, purine catabolism and miscellaneous pathways. For example, Table 3 shows one of the scenarios tested in this project. This scenario included 10 genetic interventions (7 up regulations and 3 knock-outs), and metabolic pathways involved are extracellular transport, oxidative phosphorylation and urea cycle/amino group metabolism pathways. In fact, for other scenarios, the reactions and pathways involved in genetic engineering are similar. However, Figure 5 shows the Pareto front of wild-type and mutant CHO cell in all 3 growth phases. The current scenarios cannot show any observable increase in IgG production rate.

Discussion

Elemental constrained FBA

In this study, different constraint-based metabolic modelling approaches were applied to improve the predicting accuracy of the metabolic model. The effect of the implementation of carbon and nitrogen availability constraints on the steady-state flux predictions in the metabolic models of CHO were investigated in this project, though other elements such as hydrogen and oxygen were considered and phased out. The results demonstrated that both nitrogen-constrained network and carbon-constrained network were able to increase the accuracy of flux predictions for biomass production

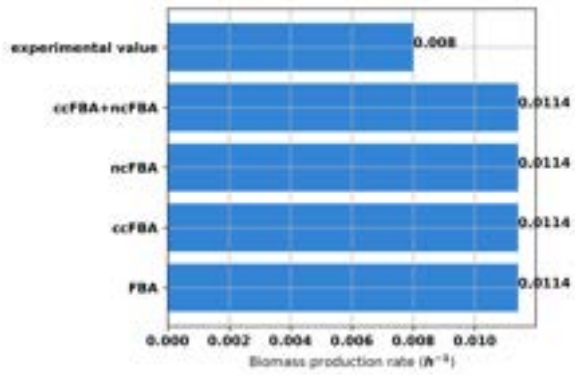

(a) *Use biomass growth rate as cellular objective*

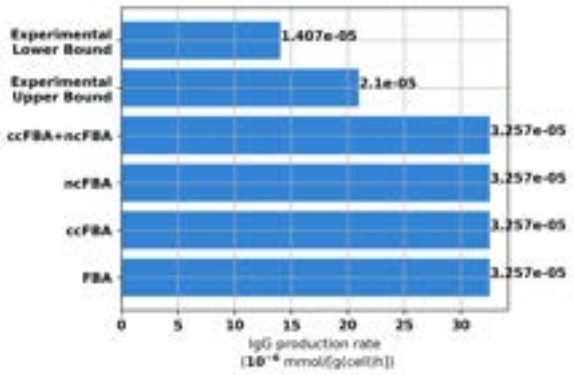

(b) *Use IgG production rate as cellular objective*

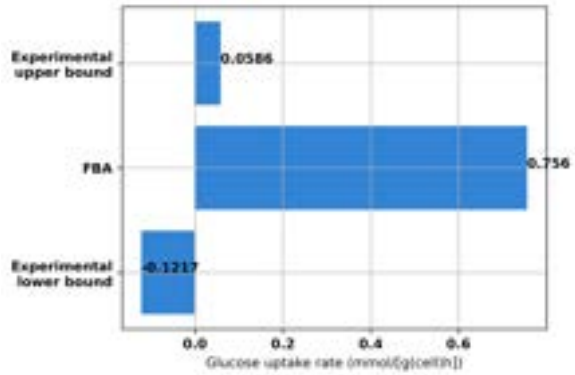

(c) *Use glucose uptake rate as cellular objective*

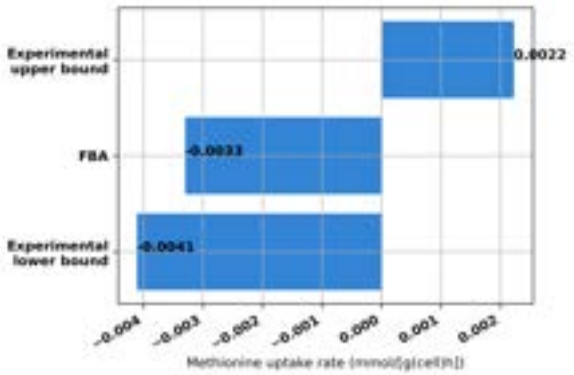

(d) *Use methionine uptake rate as cellular objective*

Figure 4: *The results from different method when using different conventional cellular objectives for prediction of CHO cell performance in stationary phase. Figure 4(a) indicates large overestimations in CHO cell growth in stationary phase when using conventional BOF. Figure 4(b) indicates large overestimations in IgG production in stationary phase when using conventional IgG production rate objective function. Figure 4(c) & 4(d) show results of using minimisation of glucose uptake rate and methionine uptake rate as cellular objective for feed 3 stationary phase.*

Table 3: *Scenario 1 of mutant CHO cell in early exponential phase*

Reactions	Genetic intervention	Pathways
Choline uniport forward reaction	Up regulation	Extracellular transport
Bicarbonate transport forward reaction	Up regulation	Extracellular transport
ATP synthase backward reaction	Up regulation	Extracellular transport
Cytochrome c oxidase backward reaction	Up regulation	Oxidative phosphorylation
Ubiquinol-10 cytochrome c reductase backward reaction	Up regulation	Oxidative Phosphorylation
HCO_3 equilibration reaction backward reaction	Up regulation	Urea cycle/amino group metabolism
Inorganic diphosphatase production	Up regulation	Oxidative phosphorylation
Inorganic diphosphatase consumption	Knock out	Oxidative phosphorylation
Cytochrome c oxidase forward reaction	Knock out	Oxidative phosphorylation
mitochondrial NADH dehydrogenase forward reaction	Knock out	Oxidative phosphorylation

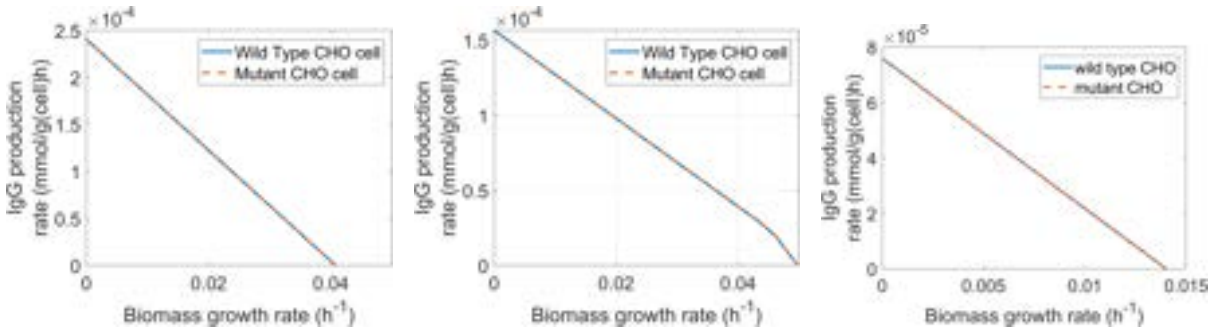

(a) *Early exponential phase Pareto front* (b) *Late exponential phase Pareto front* (c) *Stationary phase Pareto front*

Figure 5: *Pareto fronts of different phases in feed3 including the production of IgG by wild-type CHO cell and mutant CHO cell.*

by reducing the flux variability. In particular, nitrogen constrained network showed a higher accuracy of flux prediction than that of the carbon-constraint network, but a greater solution space reduction by the carbon-constraint network than that of the nitrogen-constraint network. This can be attributed to the total amount of carbon and nitrogen atom in the medium provided and the different demands by each reaction. According to the algorithms, it is evident that there is more carbon atom in the medium due to the majority of the culture nutrients are occupied by amino acids, glucose and lactate which mainly consist of carbon atoms. As ccFBA and ncFBA are based on the hypothesis that the constraint for each intracellular reaction change according to the total number and reaction demands of carbon and nitrogen atoms, it can be concluded that the combination of both methods will generate a much more realistic prediction in intracellular fluxes, biomass growth and product secretion rates.

Parsimonious enzyme usage FBA (pFBA)

Various studies have shown that the production of large quantities of protein and enzyme could disrupt the normal growth functions of a cell[22]. 'Protein burden' is the term that is used to describe the cost to a cell of producing a protein, as measured by the associated growth-rate depression. The results of these studies indicate the cells are expected to adjust the gene expression level as needed for growth under growth selective pressure. In other words, genes and proteins associated with functional reactions in the optimum pathways are expected to be unregulated, thereby maximising the defined growth rates. On the other hand, genes and proteins associated with reactions within the less efficient pathways should be down-regulated to reduce the maintenance demand on cells. An in silico approach was conducted by Lewis et al.[23] to compute the maximal growth rate of the E.coli genome-scale models using pFBA. Moreover, they applied pFBA to the omics dataset to identify the correlation between the changes in genome-scale gene expression levels and optimal growth predictions from computational analysis during the complex adaptation process. Based on their results, it is apparent that pFBA optima and essential genes are significantly up-regulated whereas the rest are not, especially ELE and MLE. Consequently, It can be concluded that the up-regulation of the pFBA optima and the down-regulation of less efficient classes can lead to an improved growth rate. Despite the pFBA can significantly reduce the flux variability, it is still not an ideal tool for computational analysis of mammalian cell metabolism; particularly owing to its lack of ability to replicate the intrinsic restriction on growth capacity and by-product secretion in mammalian cell culture[9].

Stationary phase cellular objective

The decrease in IgG production shown in Figure 3 and biomass growth rate shown in Figure 1(a) implied that the cellular objective for stationary phase cell growth is no longer maximising IgG production or maximising biomass growth. In the stationary phase, the lower flux of glycolysis pathway and higher flux through the TCA cycle indicates that the metabolism shifts to more efficient use of substrates and energy[15]. The mechanism of phase transition is still unknown, while the observation made by Carinhas et al.[24] indicates the phase transition is a substantial suppression in both metabolite transport and metabolism. A potential suppression factor could be implemented in GEM to manipulate the change in glycolysis pathway and TCA cycle. As the suppression factor determination should be based on experimental intracellular fluxes of glycolysis pathway and TCA cycle during the whole culture duration but this proposed method is not investigated in this project due to lack of experimental information. The potential cellular objective for stationary phase is the minimisation of the nutrient uptake rate. Computational results of several essential amino acid uptake fluxes by 'minimisation of nutrient uptake rate' well lay within the experimental bounds which confirms the validity of this approach.

Genetic engineering

The Pareto fronts of both wild type and mutant CHO cell overlap which indicates no observable improvement by genetic intervention. Few reasons caused these issues. One of the reasons is gene and pathway redundancy as there could be more than one gene encoding for the reactions(s) associated with the genetic intervention, or there is an alternative pathway that can compensate for the changes in the expression level of the gene. Additionally, mammalian cells possess a large number of genes and proteins compared to microbial cells. This makes it difficult for the researchers to determine how the cell reacts to the changes in reactions in CHO cells and how the cell chooses the metabolic pathways to compensate for any reaction knock out. Several studies have shown that the application of growth-coupled production on microbial cells is able to improve its productivity of desired metabolites. This could be done by coupling the desired metabolites and the cell growth so that the growth of the cell can drive the production. Nonetheless, this approach cannot be applied to protein production as the metabolites need to be simple enough in order for it to stoichiometrically couple to growth. Another reason that it is difficult to apply growth coupled production on the mammalian cells like CHO is that our knowledge of the many regulatory mechanisms that are taking place in cells to cause them to respond to various conditions and changes is still limited[25]. For example, we still have no full understanding of the function of many annotated genes in CHO cells. In many cases, the annotation is derived from embryonic development, which does not properly state their actual functions and characteristics. Consequently, genetic engineering of CHO cells would continue to be slow, laborious and incapable of addressing most of the complex mammalian cells as long as no precise functional annotation for all the genes present in CHO cells is available[26].

Conclusion

With a predicted increase of CHO presence in the biopharmaceutical industry, a comprehensive understanding of the CHO metabolisms becomes necessary. Herein, we have demonstrated the flux balance analysis to compute the metabolic fluxes of the CHO models given the set of upper and lower bounds. Besides, we showed that both carbon and nitrogen constraint FBA were able to improve our model's flux predicting power where the latter showed a better result in agreement with the experimental data. Although there were no noticeable changes in the accuracy of flux prediction when pFBA was applied. Nonetheless, a significant reduction in net flux was still observed. Several studies on the application of pFBA on microbial cells have been proved successful. Therefore, further optimisation of the pFBA is possible if further analysis is to be performed.

For stationary phase, the method for CHO cell prediction is different due to the different CHO cell culture behaviour during stationary phase. Both time evolution of biomass growth and IgG productivity during the whole culture duration implies the conventional objective function of FBA is not appropriate to describe stationary phase metabolism. The high energy and substrates usage efficiency implies that minimisation of nutrient uptake rate from the medium is a potential cellular objective for CHO cell in stationary phase. The computational results of several metabolites uptake show agreement with the experimental bounds. However, the agreement between the computational intracellular fluxes should be compared with experimental data for intracellular fluxes in future work.

In regards to genetic engineering, the current genetic engineering model with purely up and down-regulation and knock out cannot give any further improvement in mutant CHO cell IgG productivity. Due to the complexity of mammalian cell metabolism network, for all scenarios obtained in this project, a small number of genetic interventions will not change the overall CHO cell performance in IgG productivity.

Outlook

The mechanism of phase transition from exponential phase to stationary phase is still not well known. The change in CHO cell culture behaviour during the stationary phase can be described as higher energy and substrates usage efficiency. Understanding the mechanism of phase transition is essential for modelling the stationary phase CHO cell growth behaviour. Thus, further investigation has to be made to have a deeper understanding of the mechanism of phase transition and the reason behind the fact of higher energy and substrate efficiency during stationary phase.

Due to time constraints, genetic engineering results were not successful. Different algorithms should be investigated for genetic engineering model. The formulation involved in this project is shown in Table 1, but there are several potential combinations of objectives that haven't be tested in this project. Huang et al.[7] stated different objective combinations that can be potentially used to predict mutant CHO cell performance. This project mainly explored the effect of the total number of genetic interventions in mutant cell performance, but there are several other parameters such as up-regulation factor and down-regulation factor, which were used to manipulate the flux bounds of up or down-regulated reactions, which also have significant impacts on IgG production and biomass growth of mutant CHO cell.

Current genetic engineering model can only describe the intervention of one growth phase. However, the genetic intervention has to be applied at the beginning of CHO cell culture. Genetic intervention model should have the ability to optimise the whole culture duration for IgG production based on a computational model which is able to describe the whole CHO cell culture duration. Antoniewicz et al.[27] state C-13 dynamic metabolic flux analysis (DMFA) is able to predict the time evolution of CHO cell and identify the metabolic shift in a fed-batch process which is helpful for a whole culture duration optimisation. Thus, C-13 DMFA should be investigated further.

Genetic engineering results would need experimental validation. Under the same feed condition and medium condition, how different in reality the mutant CHO cells will perform from wild-type CHO cells including nutrient uptake rate, intracellular fluxes, biomass growth rate and IgG secretion rate. It is essential to monitor the change in glycolysis, oxidative phosphorylation, protein production, endoplasmic reticular transport (also known as secretory), extracellular transport, urea cycle/amino group metabolism, purine catabolism and miscellaneous pathways. Based on the results, these pathways should be paid extra attention as these pathways frequently appeared in all scenarios generated by GAMS.

Other genetic interventions should be considered. Pandey et al.[21] indicate the impacts of knock-out, up and down regulations on IgG productivity. Introduction of one or several trans-genes into CHO cell culture can also potentially improve CHO cell performance by One of the candidates is the heterologous expression of the transcription factor X-box binding protein-1 (XBP-1) which can lead to increasing flux in endoplasmic reticular transport pathway and increasing IgG productivity[28].

Acknowledgements

We would like to express our great appreciation to Mr Thanasis Antonakoudis for his constructive suggestions and experimental data for our research work. We would like to offer our appreciation to Mr James Morrissey for his generous advice in presentation preparation.

Supplementary Information

The code could be found in https://github.com/yz12117/FYRP

iCHO 1766 GeM is provided by http://bigg.ucsd.edu/

search?query=iCHO.

Experimental data is provided by Kotidis et al.[1]

References

[1] Pavlos Kotidis et al. 'Constrained global sensitivity analysis for bioprocess design space identification'. In: *Computers & Chemical Engineering* 125 (2019), pp. 558–568.

[2] Gary Walsh. 'BioPharmaceutical benchmarks 2018'. In: *Nature Biotechnology* 36.12 (2018), pp. 1136–1145.

[3] Yuzhou Fan et al. 'Amino acid and glucose metabolism in fed-batch CHO cell culture affects antibody production and glycosylation'. In: *Biotechnology and bioengineering* 112.3 (2015), pp. 521–535.

[4] Jong Kwang Hong et al. 'Towards next generation CHO cell line development and engineering by systems approaches'. In: *Current opinion in chemical engineering* 22 (2018), pp. 1–10.

[5] Maximilian Lularevic et al. 'Improving the accuracy of flux balance analysis through the implementation of carbon availability constraints for intracellular reactions'. In: *Biotechnology and bioengineering* 116.9 (2019), pp. 2339–2352.

[6] X Yu Lawrence et al. 'What can mathematical modelling say about CHO metabolism and protein glycosylation?' In: *The AAPS journal* 15 (2017), pp. 212–221.

[7] Seongkyu Yoon Zhuangrong Huang Dong-Yup Lee. 'Quantitative intracellular flux modeling and applications in biotherapeutic development and production using CHO cell cultures'. In: *Biotechnology and Bioengineering* 114.12 (2017), pp. 2717–2728.

[8] Sarantos Kyriakopoulos et al. 'Kinetic modeling of mammalian cell culture bioprocessing: the quest to advance biomanufacturing'. In: *Biotechnology journal* 13.3 (2018), p. 1700229.

[9] Hock Chuan Yeo et al. 'Enzyme capacity-based genome scale modelling of CHO cells'. In: *Metabolic Engineering* (2020).

[10] Jennifer L. Reed. 'Shrinking the Metabolic Solution Space Using Experimental Datasets'. In: *PLoS Computational Biology* 8.8 (2012).

[11] C H Schilling R Mahadevan. 'The effects of alternate optimal solutions in constraint-based genome-scale metabolic models'. In: *Metabolic Engineering* 5.4 (2003).

[12] Cyrielle Calmels et al. 'Applications of a genome-scale model in tandem with enzyme assay for identification of metabolic signature of high and low CHO cell producer'. In: *Metabolic engineering communications* 9 (2019), e00097.

[13] 'Metabolic phenotyping of CHO cells varying in cellular biomass accumulation and maintenance during fed-batch culture'. In: *Biotechnology and Bioengineering* 115.3 ().

[14] Hooman Hefzi et al. 'A consensus genome-scale reconstruction of Chinese hamster ovary cell metabolism'. In: *Cell Systems* 3.5 (2016), pp. 434–443.

[15] Xiao Pan et al. 'Metabolic characterization of a CHO cell size increase phase in fed-batch cultures'. In: *Applied microbiology and biotechnology* 101.22 (2017), pp. 8101–8113.

[16] Carlos Eduardo García Sánchez Rodrigo Gonzalo and Torres Sáez. 'Comparison and Analysis of Objective Functionss in Flux Balance Analysis'. In: *Biotechnology progress* 30.5 (2014), pp. 985–991.

[17] Verónica S Martínez et al. 'Flux balance analysis of CHO cells before and after a metabolic switch from lactate production to consumption'. In: *Biotechnology and bioengineering* 110.2 (2013), pp. 660–666.

[18] Neelanjan Sengupta, Steven T Rose and John A Morgan. 'Metabolic flux analysis of CHO cell metabolism in the late non-growth phase'. In: *Biotechnology and bioengineering* 108.1 (2011), pp. 82–92.

[19] Suresh Selvarasu et al. 'Combined in silico modeling and metabolomics analysis to characterize fed-batch CHO cell culture'. In: *Biotechnology and bioengineering* 109.6 (2012), pp. 1415–1429.

[20] Yiqun Chen et al. 'An unconventional uptake rate objective function approach enhances applicability of genome-scale models for mammalian cells'. In: *NPJ systems biology and applications* 5.1 (2019), pp. 1–11.

[21] Vikash Pandey et al. 'TEX-FBA: A constraint-based method for integrating gene expression, thermodynamics, and metabolomics data into genome-scale metabolic models'. In: *bioRxiv* (2019), p. 536235.

[22] C. G. Kurland & Henjiang Dong. 'Bacterial growth inhibition by overproduction of protein'. In: *Molecular Microbiology* 21 (1996), pp. 1–4.

[23] Nathan E Lewis et al. 'Omic data from evolved E. coli are consistent with computed optimal growth from genome-scale models'. In: *Molecular systems biology* 6.1 (2010), p. 390.

[24] Nuno Carinhas et al. 'Metabolic signatures of GS-CHO cell clones associated with butyrate treatment and culture phase transition'. In: *Biotechnology and bioengineering* 110.12 (2013), pp. 3244–3257.

[25] Anis Hamdi. 'Key Challenges in Designing CHO Chassis Platforms'. In: *Processes* 8 (2020).

[26] Takuya Matsumoto. 'Engineering metabolic pathways in Escherichia coli for constructing a "microbial chassis" for biochemical production'. In: *Bioresource Technology* 245 (2017).

[27] Maciek R Antoniewicz. 'Methods and advances in metabolic flux analysis: a mini-review'. In: *Journal of industrial microbiology & biotechnology* 42.3 (2015), pp. 317–325.

[28] Eric Becker et al. 'An XBP-1 dependent bottleneck in production of IgG subtype antibodies in chemically defined serum-free Chinese hamster ovary (CHO) fed-batch processes'. In: *Journal of biotechnology* 135.2 (2008), pp. 217–223.

Identifying novel mixtures as working fluids in Organic Rankine Cycles through an improved computer-aided molecular and process design algorithm

Jun Hong Leong and Kuan Yang Tan
Department of Chemical Engineering, Imperial College London, U.K.

Abstract The success of Organic Rankine Cycles (ORC) hinges on the choice of working fluid which is challenging due to the many options available. Conventionally, pure working fluids are used even though mixtures have been shown to perform equally well as the use of mixtures render the problem combinatorial. While CAMPD algorithms are key to identifying the optimum mixture as working fluid, the ORC primal problem is often restricted to a small design space as it easily becomes intractable. In this paper, we focus on solution of the primal problem through a series of feasibility tests using the SAFT-γ Mie Equation of State. Our tests discard infeasible mixtures, reduces the solution space, and enables a good initial guess to the primal problem. Tests were shown to reduce CPU time by 77% and achieve better convergence to a local optimum. Through an automated algorithm developed, 1100 unique mixtures were evaluated. Novel mixtures identified were found to perform better than pure fluids by as much as 45%. The optimal mixtures typically consist of alkanes, alkenes, and short chain ethers. High performing pure fluids were also found to be good components in mixtures. The robust algorithm can then be extended to include the full CAMPD framework with an expanded design space.

1. Introduction

With increasing efforts to combat the perennial problem of climate change, there is a need for green technologies that are able to recover energy from new or existing sources while remaining economically viable. Organic Rankine Cycles (ORC) present as a potential solution to address this problem, given its ability to generate power from low grade heat sources such as solar,[1] geothermal[2] and even industrial waste heat.[3] ORC operate similarly to traditional steam power cycles but differ in the use of organic compounds instead of water as the working fluid. This difference in working fluid allow ORC to operate at conditions otherwise unsuitable for water and facilitates the recovery of heat at lower temperatures ranging from 100-350 °C for power generation.[4]

Where ORC truly triumphs is not just in its simplicity,[5] but also the ability to accommodate a diverse design space due to its compatibility with a large pool of working fluids. Although pure components are most commonly used, mixtures have been shown to significantly improve performance due to non-isothermal phase change in evaporation and condensation.[6] This 'temperature-glide' allows the temperature profiles of the heat source and cooling medium to be matched, reducing exergy losses.[7]

In the design of ORC, key challenges stem from the selection of appropriate working fluid and the optimisation of process conditions in order to maximise the overall efficiency. However, the two challenges are interlinked and have mutual dependence on each other. This added complexity originates from the fundamental design in ORC since the heat source for recovery dictates both the process conditions and the thermophysical properties of the working fluid. To that end, the use of Computer-aided Molecular and Process Design (CAMPD) in the context of ORC promises a reduction in the time and effort in obtaining the optimum working fluid compared to the conventional strategy of trial and error. This is achieved by designing the desired working fluid based on the required thermophysical properties and the process design.[8] The inherent value of CAMPD to ORC applications forms the motivation of this study.

2. Background

2.1. Computer-aided molecular and process design

In seeking process optimality, the presence of numerous decision variables and constraints on process structure, operating conditions, and molecular design together with the complex interactions amongst them make it a particularly challenging problem. One variable cannot be solved without knowledge of the other *a priori*. As such, the unique requirements of this conundrum calls for a method enabling all variables to be optimised simultaneously. Gani & Brignole[9] first developed a concept known as computer-aided molecular design (CAMD) where optimal molecules are determined *in silico*, given a set of molecular feasibility constraints. Based on the optimal molecules designed, process conditions were then identified. However, the criteria defining the optimal molecule can often be elusive with no guarantee of an optimal process design. This led to the development of CAMPD where molecule and process design are now optimised simultaneously.

CAMPD consist of both continuous and discrete decision variables – process conditions being the former while variables such as the number of functional groups in a given molecule and cycle topology[10] as the latter. Consequently, this problem belongs to the class of mixed integer non-linear programs. Typical solution strategies involve decomposing the problem into a nonlinear program (NLP) and a mixed integer linear program commonly known as the primal problem and master problem respectively. This can then be solved using the Outer Approximation (OA)[10] algorithm. In the ORC context, the primal problem optimises process conditions for a specific working fluid and provides an input to the master problem to generate a new working fluid. This continues until the termination criteria is satisfied.[11]

The ORC process is one area where CAMPD can be applied and is modelled through a series of mass and energy balances with process constraints. The objective function most commonly used are performance indicators relating to economic or thermodynamic performance. However, CAMPD problems are significantly more complex and poses a numerical challenge to solve. Firstly,

the design space is enlarged with an increased number of variables and constraints to satisfy. Secondly, the combinatorial nature of the problem due to the presence of discrete decision variables renders the problem potentially intractable. Finally, the use of complex Equations of State (EoS) such as SAFT-γ Mie (SGM) makes the problem highly non-linear and non-convex. In addition, identifying a feasible point to be an initial guess is not known *a priori* and poses yet another barrier to solution of the problem from a numerical perspective. Developing a robust algorithm capable of coping with these challenges is hence a key priority for successful solution of the CAMPD problem.[12]

2.2. Pure fluids and mixtures

There has been extensive research on the identification of optimal pure working fluids in ORC, and on the applications of ORC. Papadopoulos *et al.*[13] first used a CAMD approach to generate a candidate list of pure fluids, using Group Contribution (GC) methods and cubic equations of state to determine thermodynamic properties. These were then evaluated using heuristic-based targets. White *et al.*[14] optimised thermodynamic performance of ORC using the SAFT-γ Mie (SGM) EoS and validated GC transport property prediction methods.

As most studies utilised a restricted design space in the selection of working fluids to avoid an intractable problem, Bowskill *et al.*[12] implemented the concept of feasibility tests into CAMPD for the design of pure working fluids. This permits the use of a larger design space, as feasibility tests will first eliminate infeasible working fluids and allow the OA algorithm to converge quickly towards the local optimum.

While studies on ORCs using pure working fluids are more mature and extensive, the use of mixtures as working fluids in ORCs is relatively novel and uncharted. Gianfronco *et al*.[15] first demonstrated the merits of using a multi-component, non-azeotropic mixture for tailoring ORC to specific applications; Papadopulos *et al.* pioneered the first CAMPD optimisation framework for binary mixtures, extending a multi-objective optimisation framework from pure fluids[16] to binary mixtures.[17] Oyewunmi & Markides[18] used n-pentane/n-hexane and R-245fa/R-227ea mixtures to show improved cycle and performance efficiency from the temperature-glide effect where the evaporation and condensation temperatures varies continuously with composition.

However, most of the work on mixtures is limited to an even smaller design space, due to the increased combinatorial complexity given by additional degrees of freedom in the mixture composition and the different permutations of components compared to single pure working fluids. Consequently, optimisations are largely based on a pre-defined set of fluid permutations.[19] It was only recently when Schilling *et al.*[20] used a 1-stage Continuous-Molecular Targeting Computer-Aided mixture and blend design method to identify optimal working fluid mixtures from several million possible combinations, whilst simultaneously optimising the process and equipment.

One other notable ORC process design for mixtures is the work of Sarkis & Robert[11] where feasibility tests in the spirit of Bowskill *et al.*[12] was developed for mixtures to be implemented before solution of the primal problem. While this approach for mixtures can be considered novel, the design space was extremely limited as only 10 arbitrary mixture combinations were evaluated. In addition, a large portion of infeasible solution remained in the primal problem even after implementation of the feasibility tests. The lack of active research in this area presents an opportunity to seek new ways of expanding the design space in CAMPD and harness the potential of mixtures as an ORC working fluid.

2.3. Motivation and objectives

This paper is an extension to the work of Bowskill *et al.*[12] and Sarkis & Robert.[11] Bowskill *et al.*[12] incorporated feasibility tests in the CAMPD OA framework to generate a list of candidate pure working fluids for an ORC process, while Sarkis & Robert adapted this for binary mixtures by using the top performing working fluids from the work of Bowskill *et al.* [12] to form binary mixtures.

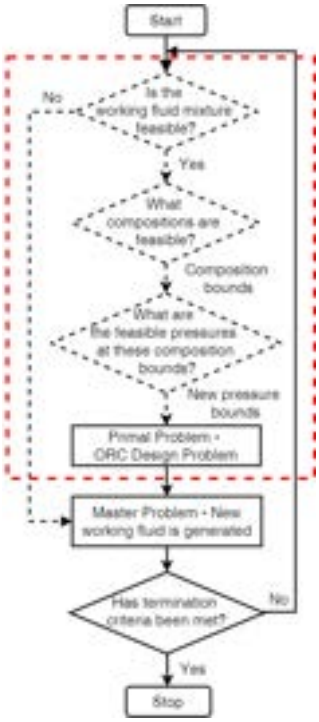

Figure 1: Refined OA algorithm with improved feasibility tests for mixtures. The focus (outlined in red) is to allow an expanded design space whilst maintaining robust solution of the ORC Design Problem.

This study aims to further develop the CAMPD OA framework by improving on the feasibility tests for binary mixtures. In doing so, a more robust OA algorithm can be developed and will facilitate the expansion of the design space. This can be seen in Fig. 1 where the focus of the study is in red, with the dotted diamonds representing the feasibility tests to be implemented sequentially.

To that end, we aim for a more accurate determination of the feasible solution space by tightening process bounds on mixture composition and pressure through implementation of our feasibility tests. An initialisation problem to obtain a good initial guess to the SGM EoS used for thermodynamic property prediction will also be implemented to aid solution of the primal problem. This will subsequently be validated by automating the proposed algorithm in order to enlarge the design space and allow evaluation of multiple combinations of

mixtures in the primal problem. An assessment can then be made on how feasibility tests aid algorithm robustness, whilst discovering novel mixtures as working fluids.

3. Methodology

3.1. ORC primal problem formulation

The ORC problem is formulated in gPROMS as

$$\begin{aligned} &\min_{\boldsymbol{x}} f(\boldsymbol{x}, \boldsymbol{n_1}, \boldsymbol{n_2}) \\ &s.t. \boldsymbol{h}(\boldsymbol{x}, \boldsymbol{n_1}, \boldsymbol{n_2}) = 0 \\ &\boldsymbol{g}(\boldsymbol{x}, \boldsymbol{n_1}, \boldsymbol{n_2}) \leq 0 \\ &\boldsymbol{x} \in \boldsymbol{X} \\ &\boldsymbol{n_1}, \boldsymbol{n_2} \in \boldsymbol{N} \end{aligned} \quad (1)$$

where the vector $\boldsymbol{X}$ represents the set of continuous process variables such as temperature and pressure. The vector $\boldsymbol{N}$ consists of all the pure components obtained in the work of Bowskill *et al.*[12] The vector of non-negative discrete variables $\boldsymbol{n_1}, \boldsymbol{n_2}$ corresponds to the functional groups of the two pure components used.

The set of equality constraints represent the energy conservation and continuity equations and all other thermodynamic states within the ORC model. The set of inequality constraints represent the process conditions imposed on the ORC operation, such as temperature and pressure bounds.

No molecular feasibility constraints are needed, given that the vector $\boldsymbol{N}$ consists of chemically feasible components, although they may be identified as infeasible pure working fluids for ORC by Bowskill *et al.*[12]

The objective function used in the primal problem is the net power generation, $\dot{W}_{net}$ where

$$\dot{W}_{net} = |\dot{W}_{turbine}| - |\dot{W}_{pump}| \quad (2)$$

The composition of component 1, working fluid mass flowrate $\dot{m}_{wf}$, extent of superheating ΔT_{extent}, condenser operating pressure P_1 and evaporator operating pressure P_2 are decision variables used to maximise $\dot{W}_{net}$ within gPROMS to obtain candidate mixtures as potential working fluids.

3.2. ORC process model

The ORC model consists of a condenser, pump, evaporator, and turbine as shown in Fig. 2 with assumptions adopted from Schilling *et al.*[21] and Bowskill *et al.*[12] for low grade heat and geothermal applications. The working fluid leaving the condenser (state 1, Fig. 3) is first compressed from P_1 to P_2 (state 2, Fig. 3) with an adiabatic pump of isentropic efficiency η_p. Thereafter, it is heated in the evaporator minimally until its dew point at P_2 (state 2b, Fig 3) into a single phase vapour, with the possibility of superheating allowed by ΔT_{extent} (state 3, Fig. 3). The superheated vapour is then expanded inside an adiabatic turbine of isentropic efficiency η_t where work is extracted in the form of power generation (state 4, Fig. 3). It is then cooled to its bubble point at pressure P_1 in the condenser into a single phase liquid, with no sub-cooling allowed. Both condensation and evaporation are assumed to be isobaric and the ORC operates at two pressure regimes. State 1 and 4 operate at pressure P_1, while state 2 and 3 operate at pressure P_2.

The power generation from the pump and turbine is

$$\dot{W} = \eta \frac{\dot{m}}{MW_{mix}} (h_{in} - h_{out}) \quad (3)$$

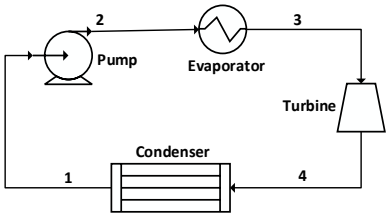

Figure 2: Flowsheet of the ORC model used

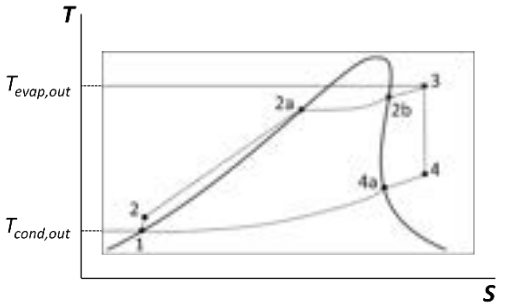

Figure 3: Temperature-entropy diagram of a mixture in an ORC displaying non-isothermal phase change behaviour. Vapour fraction at the outlet of the evaporator (state 3) is 1 to prevent damage in the turbine.

The ORC model is constrained by absolute temperature and pressure bounds. In the evaporator, the maximum temperature, T^U is dependent on the temperature of heat source T_{hs} and the pinch point for minimum temperature approach ΔT_{min}, such that

$$T_{evap,out} \leq T^U \quad (4)$$

$$T^U = T_{hs} - \Delta T_{min} \quad (5)$$

A similar constraint on the minimum temperature is imposed on the condenser where cooling water is used.

$$T_{cond,out} \geq T^L \quad (6)$$

$$T^L = T_{cw} + \Delta T_{min} \quad (7)$$

To account for the non-isothermal phase change behaviour in mixtures, an approach proposed by Sarkis & Robert[11] was used, where interior pinch point constraints in the vapour-liquid equilibrium (VLE) region were enforced.

The pressure bounds for the ORC, $[P^L, P^U]$ is set between 1 bar and 50 bar to prevent operation at sub-atmospheric conditions and at extremely high pressures which will invariably increase the cost of process equipment. It is also desired for the ORC to operate at sub-critical pressures of the working fluid where

$$P_{cond} \geq P_r^L P_{c,mix} \quad (8)$$

$$P_{evap} \leq P_r^U P_{c,mix} \quad (9)$$

Both P_r^L and P_r^U are reduced pressure factors between 0 and 1 to enforce sub-critical operation.

As the SGM EoS used does not have an existing routine to estimate the critical pressure, the critical pressure of the mixture, $P_{c,mix}$ is approximated as a linear combination of the critical pressure of the pure components[11] such that

$$P_{c,mix} = z_1 P_c(\boldsymbol{n_1}) + (1 - z_1) P_c(\boldsymbol{n_2}) \quad (10)$$

where $z_1 \in [0,1]$ and is the composition of component 1 in the mixture. Further details on approximating $P_c(\boldsymbol{n_1}, \boldsymbol{n_2})$ can be found in Section 3.3.

3.3. Thermophysical properties

SGM was used to determine the thermodynamic properties of the working fluid (binary mixture) as it is

most suited for use in the CAMPD algorithm. Unlike other EoS, SGM utilises a group contribution (GC) approach which is able to determine the properties of a component or mixture just from knowledge of its constituent functional groups.[22] In addition, the parameters used in SGM are typically regressed below the critical point and well-suited for sub-critical use[23] which is enforced in our ORC process model. Finally, the SGM framework has been extensively applied in not just ORC applications[12,14] but across a wide spectrum of applications including CAMPD for solvent design in separation processes,[25] phase behaviour of aqueous mixtures[26], and in CO_2 capture.[27]

As SGM is unable to estimate the melting points of pure components T_m in gPROMS, they were estimated using a GC correlation proposed by Hukkerikar *et al.*[28] Here, the correlation constant, $T_{m,0}$ and first order group contributions, C_i are used.

$$\exp\left(\frac{T_m}{T_{m,0}}\right) = \sum_{i=1}^{q} N_i C_i \quad (11)$$

Finally, the critical pressure of pure components, $P_{c,pure}$ is estimated by identifying the point which satisfies the following conditions when temperature and pressure is allowed to vary independently.

$$\mu^{vapour}(T,P) = \mu^{liquid}(T,P) \quad (12)$$

$$\frac{v^{vapour}(T,P)}{v^{liquid}(T,P)} \leq 1+\varepsilon \quad (13)$$

where μ is the chemical potential, v is the vapour or liquid specific volume and ε is a user-defined tolerance.

3.3.1. Chemical design space

As mentioned in Section 3.1, pure components obtained from the work of Bowskill *et al.*[12] are used to form arbitrary combinations of mixtures. Although all of these pure components satisfy molecular constraints, some are infeasible in the ORC process. In this study, feasible and infeasible components exclusively refer to the feasibility of the working fluid in an ORC.

A total of 50 feasible and 2605 infeasible pure components were used to arbitrarily form 1100 unique binary mixtures. These molecules consist of any combination of the following 9 functional groups: $-CH_3$, $-CH_2-$, -eO-, -cO-, -COO-, -CH=, -COOH, $-CH_2OH$ and $=CH_2$. -eO- corresponds to an end chain ether group where it is between a $-CH_3$ and $-CH_2$ group. -cO- corresponds to a central ether group where it is between two $-CH_2-$ groups.

3.4. Feasibility tests

To aid algorithm robustness, several improvements are made to the feasibility tests proposed by Sarkis & Robert.[11] Test 0 enforces sub-critical operation required by the ORC model. Test 1 ensures that the mixture is capable of a phase change within the temperature range of $[T^L, T^U]$. Test 2 has been reformulated for mixtures to better define feasibility bounds on composition and pressure. This is essential as the ORC model implicitly assumes the possibility of forming a single phase vapour in the evaporator and a single phase liquid in the condenser. A mixture that violates this is infeasible and will cause a numerical failure in the primal problem.

3.4.1. Test 0: Absolute process bounds

While the temperature and pressure bounds of $[T^L, T^U]$ and $[P^L, P^U]$ have been specified for a general ORC model, tighter process bounds unique to each binary mixture are desired to achieve a smaller solution space. The absolute lower bound on temperature can be updated by comparing the melting points of the pure components with T^L. This is possible as the binary mixture has a depressed melting point relative to its pure components.[29] The updated lower bound, $T^{L0}_{\boldsymbol{n_1},\boldsymbol{n_2}}$ is defined as

$$T^{L0}_{\boldsymbol{n_1},\boldsymbol{n_2}} = \max\{T^L, \{\max[T_m(\boldsymbol{n_1}), T_m(\boldsymbol{n_2})] + \Delta T_{min}\}\} \quad (14)$$

To enforce sub-critical operation, the maximum and minimum reduced pressure factors, P_r^L and P_r^U defined in Eqn. (6) and (7) are used to specify $P^{L0}_{\boldsymbol{n_1},\boldsymbol{n_2}}$ and $P^{U0}_{\boldsymbol{n_1},\boldsymbol{n_2}}$ where

$$P^{L0}_{\boldsymbol{n_1},\boldsymbol{n_2}} = \max\{P^L, P_r^L \min[P_c(\boldsymbol{n_1}), P_c(\boldsymbol{n_2})]\} \quad (15)$$

$$P^{U0}_{\boldsymbol{n_1},\boldsymbol{n_2}} = \min\{P^U, P_r^U \max[P_c(\boldsymbol{n_1}), P_c(\boldsymbol{n_2})]\} \quad (16)$$

Consequently, the updated absolute process bounds are now $\left[T^{L0}_{\boldsymbol{n_1},\boldsymbol{n_2}}, T^U\right]$ and $\left[P^{L0}_{\boldsymbol{n_1},\boldsymbol{n_2}}, P^{U0}_{\boldsymbol{n_1},\boldsymbol{n_2}}\right]$, where T^U is left unconstrained to allow superheating in the evaporator. Two further constraints are enforced in Test 0 to ensure the new process bounds are feasible.

$$T^{L0}_{\boldsymbol{n_1},\boldsymbol{n_2}} - T^U \leq 0 \quad (17)$$

$$P^{L0}_{\boldsymbol{n_1},\boldsymbol{n_2}} - P^{U0}_{\boldsymbol{n_1},\boldsymbol{n_2}} \leq 0 \quad (18)$$

3.4.2. Test 1: Saturation behaviour

For a simple binary mixture, the bubble and dew temperature is bound between the saturation temperature of its constituent pure components as seen in Fig. 4. As the mixture is required to undergo a phase change within the condenser and evaporator, Test 1 seeks to identify if this is possible by looking at the boundaries of the pure components. The minimum and maximum saturation temperature, $T^{sat,min}_{\boldsymbol{n_1},\boldsymbol{n_2}}$ and $T^{sat,max}_{\boldsymbol{n_1},\boldsymbol{n_2}}$ is defined as

$$T^{sat,min}_{\boldsymbol{n_1},\boldsymbol{n_2}} = \min\left\{T^{sat}\left(P^{L0}_{\boldsymbol{n_1},\boldsymbol{n_2}}, \boldsymbol{n_1}\right), T^{sat}\left(P^{L0}_{\boldsymbol{n_1},\boldsymbol{n_2}}, \boldsymbol{n_2}\right)\right\} \quad (19)$$

$$T^{sat,max}_{\boldsymbol{n_1},\boldsymbol{n_2}} = \max\left\{T^{sat}\left(P^{U0}_{\boldsymbol{n_1},\boldsymbol{n_2}}, \boldsymbol{n_1}\right), T^{sat}\left(P^{U0}_{\boldsymbol{n_1},\boldsymbol{n_2}}, \boldsymbol{n_2}\right)\right\} \quad (20)$$

Furthermore, we enforce the following constraints

$$T^{sat,min}_{\boldsymbol{n_1},\boldsymbol{n_2}} - T^U \leq 0 \quad (21)$$

$$T^{L0}_{\boldsymbol{n_1},\boldsymbol{n_2}} - T^{sat,max}_{\boldsymbol{n_1},\boldsymbol{n_2}} \leq 0 \quad (22)$$

Eqn. (21) and (22) ensure that a liquid and vapour can be formed within the temperature range of $[T^{L0}_{\boldsymbol{n_1},\boldsymbol{n_2}}, T^U]$ respectively. Both constraints must be satisfied for a mixture to pass Test 1. Otherwise, it will be considered infeasible and discarded.

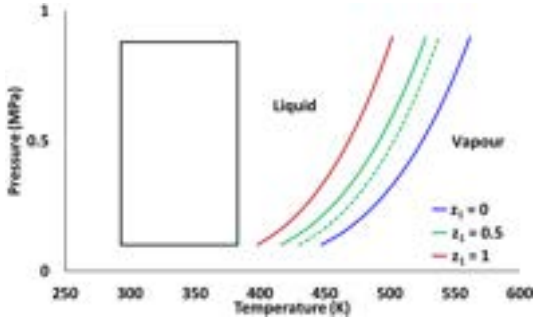

Figure 4: Generalised case of a binary mixture containing two infeasible pure components. The solid green line corresponds to the bubble curve, and the dotted green line corresponds to the dew curve. There is no overlap of the VLE region with the operating region (in black).

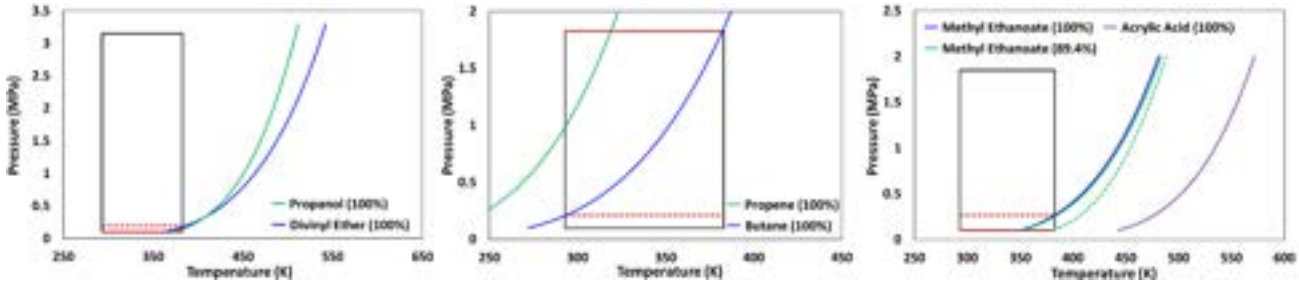

(a) (b) (c)

Figure 5: Pressure temperature graph of a) propanol & divinyl ether (feasible-feasible), b) propene & butane (feasible-feasible), and c) methyl ethanoate & acrylic acid (feasible-infeasible) with the absolute process bounds (in black). In all three cases, Test 2 has identified the feasible composition bounds and tightened the pressure bounds (in red). The minimum feasible composition in Fig. 5c is 89.4% methyl ethanoate.

As feasible and infeasible pure components are used to form binary mixtures, there is a possibility of an infeasible-infeasible combination. This should be avoided and is demonstrated in Fig. 4 where the saturation curves of both pure components (red and blue lines) do not intersect the operating region (in black). Consequently, phase change in the binary mixture is not possible. Hence, Test 1 is a powerful tool to eliminate the infeasible-infeasible mixture combination. This is important as infeasible mixtures will cause a numerical failure in the primal problem.

3.4.3. Test 2: Composition and pressure bounds

The final outcome of Test 2 is to pass tighter feasible bounds on composition and pressure to the initialisation problem and primal problem to enhance algorithm robustness. This is achieved through a better initial guess to the primal problem which decreases CPU time and prevents numerical failure.

As the bubble and dew temperatures of a binary mixture are a function of both composition and pressure, the following constraints must be satisfied for the mixture to be feasible in the primal problem.

$$T^{L0}_{\boldsymbol{n_1},\boldsymbol{n_2}} - T_{bubble}(P_1, \boldsymbol{z}) \leq 0 \quad (23)$$

$$T_{dew}(P_2, \boldsymbol{z}) - T^U \leq 0 \quad (24)$$

$$P_1 - P_2 + \Delta P \leq 0 \quad (25)$$

$$P_1, P_2 \in \left[P^{L0}_{\boldsymbol{n_1},\boldsymbol{n_2}}, P^{U0}_{\boldsymbol{n_1},\boldsymbol{n_2}}\right] \quad (26)$$

Eqn. (23) and (24) ensures that a single phase liquid and single phase vapour can be formed at $T^{L0}_{\boldsymbol{n_1},\boldsymbol{n_2}}$ and T^U respectively. The vector $\boldsymbol{z}$ consists of the composition of component 1 and 2 in the mixture.

Eqn. (25) ensures that the pump outlet pressure, P_2 (state 2 and 3) is always larger than the pump inlet pressure, P_1 (state 1 and 4) which is assumed in the primal problem. ΔP is a non-negative user-defined parameter.

Finally, Eqn. (26) enforces that P_1, P_2 must be within the updated pressure bounds obtained in Test 0. The following objective function is then used with Eqn. (23) – (26) to obtain the feasible composition bounds $[x^{L2}_{\boldsymbol{n_1}}, x^{U2}_{\boldsymbol{n_1}}]$ with respect to component 1 in a binary mixture.

$$x^{L2}_{\boldsymbol{n_1}} = \min_{\boldsymbol{z},P_1,P_2} x_{\boldsymbol{n_1}} \quad (27)$$

$$x^{U2}_{\boldsymbol{n_1}} = \max_{\boldsymbol{z},P_1,P_2} x_{\boldsymbol{n_1}} \quad (28)$$

Similarly, for the tightened bounds on pressure

$$P^{L2}_{\boldsymbol{n_1},\boldsymbol{n_2}} = \min_{\boldsymbol{z},P_1,P_2} P_1 \quad (29)$$

$$P^{U2}_{\boldsymbol{n_1},\boldsymbol{n_2}} = \max_{\boldsymbol{z},P_1,P_2} P_2 \quad (30)$$

The new bounds $[x^{L2}_{\boldsymbol{n_1}}, x^{U2}_{\boldsymbol{n_1}}]$ and $[P^{L2}_{\boldsymbol{n_1},\boldsymbol{n_2}}, P^{U2}_{\boldsymbol{n_1},\boldsymbol{n_2}}]$ obtained reduces the solution space significantly as seen in Fig. 5. Fig. 5a illustrates a propanol & divinyl ether mixture where the feasible composition range is [0,1]. Test 2 has significantly reduced the upper bound on pressure from 3.2 MPa to 0.2 MPa. This is possible as both the saturation curves of propanol and divinyl ether will not be in the operating region at pressures above 0.2 MPa. Similarly in Fig. 5c, the feasible composition range for a methyl ethanoate & acrylic acid mixture has been identified by Test 2 to be [0.894, 1]. The upper pressure bound has also been reduced from 1.9 MPa to 0.3 MPa.

The final pressure bound obtained in Test 2, $[P^{L2}_{\boldsymbol{n_1},\boldsymbol{n_2}}, P^{U2}_{\boldsymbol{n_1},\boldsymbol{n_2}}]$ is passed on to the initialisation problem formulated in order to solve the SGM and obtain a good initial guess to the primal problem.

Thereafter, the set of variables from the output of the initialisation problem and the updated bounds $[x^{L2}_{\boldsymbol{n_1}}, x^{U2}_{\boldsymbol{n_1}}]$ and $[P^{L2}_{\boldsymbol{n_1},\boldsymbol{n_2}}, P^{U2}_{\boldsymbol{n_1},\boldsymbol{n_2}}]$ are passed on to the primal problem.

3.5. Implementation

The refined algorithm for mixtures outlined in Fig. 1 is automated using C++ in Microsoft Visual Studio 2019. Implementation of feasibility tests, initialisation problem and primal problem is executed sequentially via the gO:RUN function and gPROMS Modelbuilder. A total of 1100 combinations of binary mixtures were evaluated, with each evaluation taking approximately 2 minutes.

3.6. Process specifications

This study utilises similar process conditions as Bowskill *et al.*[12] to ensure that the feasibility of components used from their work remains valid for ORC.

Table 1: Summary of operating specifications used in the ORC model

Parameter	Symbol	Units	Value
Critical pressure tolerance	ε	-	0.21
Heat capacity (heat source)	$c_{p,hs}$	kJ kg^{-1} K^{-1}	4.2
Heat capacity (cooling water)	$c_{p,cw}$	kJ kg^{-1} K^{-1}	4.19
Inlet temp. (cooling water)	$T_{in,cw}$	K	283
Inlet temp. (heat source)	$T_{in,hs}$	K	393
Isentropic efficiency (pump)	η_p	-	0.9
Isentropic efficiency (turbine)	η_t	-	0.8
Mass flowrate (cooling water)	$\dot{m}_{cw}$	kg s^{-1}	100
Mass flowrate (heat source)	$\dot{m}_{hs}$	kg s^{-1}	66
Min. absolute pressure	P^L	bar	1
Max. absolute pressure	P^U	bar	50
Min. reduced pressure factor	P_r^L	-	10^{-5}
Max. reduced pressure factor	P_r^U	-	0.8
Min. pressure difference	ΔP	bar	0.01
Min. absolute temperature	T^L	K	293
Max. absolute temperature	T^U	K	383
Min. temperature approach	ΔT_{min}	K	10

Table 2: Evaluation of the primal problem with and without composition and pressure bounds obtained in Test 2 for mixtures 1) butane & decane, 2) butane & octane, 3) 1,4-pentadiene & 2-methoxyethyl allyl ether, 4) But-1-ene & 3-butoxyprop-1-ene, 5) 1,4-pentadiene & decane. *O* represents an optimal solution, *F* represents a failed optimization result, *N* represents the number of iterations required for optimization, and *t* is the CPU time (s). The stationarity condition measures the proximity to a local optimum. The feasibility condition is the sum of all violated bounds and constraints.

No.	Without Test 2						With tightened composition and pressure bounds from Test 2					
	Status	N	t (s)	$\dot{W}_{net}$ (MW)	Stationarity Condition	Feasibility Condition	Status	N	t (s)	$\dot{W}_{net}$ (MW)	Stationarity Condition	Feasibility Condition
1	O	151	452	0.9336	2.294	0	O	44	85	0.9342	8.113×10^{-5}	0
2	F	391	732	-	1.467	6845.564	O	34	75	1.0302	8.085×10^{-5}	0
3	O	51	182	1.0360	1.741	0	O	32	80	1.0362	6.979×10^{-5}	0
4	O	186	475	1.0403	9.280	0	O	39	93	1.0409	8.567×10^{-5}	0
5	F	90	33	-	0.003	273.601	O	47	119	0.9654	4.573×10^{-5}	0

4. Results and discussion

4.1. Impact of feasibility tests

Across the solution of 1100 unique binary mixtures in the primal problem, Test 0 was found to reduce the upper bound on pressure by an average of 40 – 60%. Thereafter, 300 infeasible-infeasible mixtures were eliminated in Test 1, with the remaining mixtures comprising of 460 feasible-feasible (FF) and 340 feasible-infeasible (FIF) combinations. This shows that Test 1 is capable of significantly reducing the solution space by eliminating infeasible mixtures. Accordingly, this translates to a reduction in computational cost of about 30%. This may be an underestimate, since infeasible solutions typically require significantly longer CPU time before the primal problem terminates due to a numerical failure. In addition, Test 1 is extremely efficient as only the saturation bounds of the problem are examined and a mixture is typically analysed within 5 seconds in our study.

To quantify the impact of Test 2, five feasible-infeasible mixtures were evaluated in the primal problem with and without the tightened composition and pressure bounds. The mid-point of the composition and pressure bounds were used as an initial guess to the optimisation of the objective function, $\dot{W}_{net}$ in both cases. The feasibility and stationarity tolerance is set to 0 and 10^{-5} respectively.

It is important to note that the feasible composition bounds obtained in this study are vastly different to those obtained in the work of Sarkis & Robert.[11] A continuous range of feasible composition can now be obtained compared to discrete composition intervals of 0.1 previously. Crucially, Test 2 has now been reformulated to better satisfy the key requirements and assumptions defined in the ORC model. This will be addressed in greater detail in the case study. Table 2 illustrates the benefit from a tighter composition and pressure bound with the implementation of Test 2. This allows a significant reduction in CPU time and iterations required. In all five mixtures, the iterations required for convergence to an optimal is reduced by an average of 65% and up to 91%. The optimisation time has also been greatly reduced, by an average of 77% and up to 90%.

By tightening process bounds, Test 2 is also able to eliminate the likelihood of numerical failure in the primal problem. An example can be seen in mixtures 2 and 5, where the sequential quadratic programming (SQP) solver failed when the composition and pressure bounds were not tightened. This is most likely due to an infeasible initial guess in the optimisation problem, evident from their non-zero feasibility condition which is the sum of all the violated bounds and constraints. This is augmented by the penalty function within the SQP solver which will cause the objective function to become trivially small. While the solver does have the ability to recover from an infeasible starting point, it will result in unnecessarily long computational times with no certainty of a successful optimal solution. Suppose the infeasible initial guess can be avoided or the SQP solver recovers and obtains a feasible solution, there is no guarantee still that the solution has converged to a local optimum. This can be seen from the significantly larger stationarity value than the set tolerance of 10^{-5} in mixtures 1, 3 and 4. The stationarity value gives indication of the proximity to a local optimum through the Lagrange function. It is highly likely that the algorithm did not terminate due to optimality, but because no better solution can be found. In such cases, the algorithm will still terminate as long as the feasibility tolerance is not violated.

Contrasting this with the solutions obtained using the composition and pressure bounds given by Test 2, it is evident that the algorithm terminated due to optimality. Stationarity values are in the magnitudes of 10^{-5} along with a trivial feasibility condition. This highlights the importance of a good initial guess to the primal problem and the value of Test 2 to a robust CAMPD algorithm.

4.1.1. Case study: Butane & Decane mixture

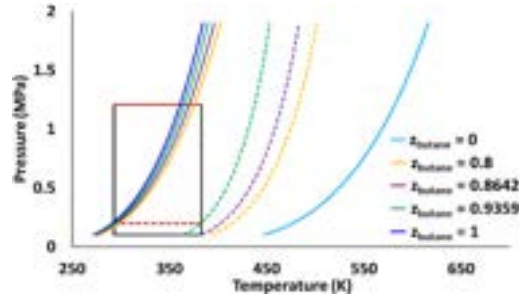

(a)

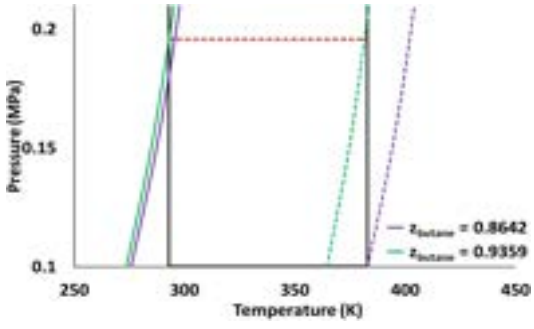

(b)

Figure 6: Bubble (solid) and dew (dashed) curve of a butane & decane mixture. Fig. 6b magnifies Fig. 6a at the lower pressure bound.

Table 3: Comparison of the performance of feasible-feasible mixtures and the optimal compositions with their pure component counterparts

Pure Working Fluid			Top Working Feasible- Feasible Fluid Mixtures			
Functional Groups	**Name**	$\dot{W}_{net}$ **(MW)**	**Rank**	**Name (Component 1, 2)**	$\dot{W}_{net}$ **(MW)**	**Optimal** z_1
1 CH_3, 1 CH_2, 1 CH=, 1 CH_2=	But-1-ene	0.856	1	Butane & Hex-1-ene	1.236	0.50
2 CH_3, 2 CH_2	Butane	0.853	2	MEE & EPE	1.234	0.57
2 CH_3, 1 CH_2, 1 eO	Methyl ethyl ether (MEE)	0.852	3	Hex-1,5-diene & Butane	1.234	0.53
2 CH_3, 1 COO	Ethyl methanoate	0.572	4	Butane & 3-ethoxy-prop-1-ene	1.232	0.52
1 CH_3, 2 CH_2, 1 cO, 1 CH=, 1 CH_2=	3-ethoxy-prop-1-ene	0.418	5	Butane & EPE	1.230	0.51
2 CH_2, 2 CH=, 2 CH_2=	Hex-1,5-diene	0.395	6	Hex-1,5-diene & But-1-ene	1.229	0.51
1 CH_3, 3 CH_2, 1 CH=, 1 CH_2=	Hex-1-ene	0.373	7	But-1-ene & Hex-1-ene	1.223	0.54
2 CH_3, 3 CH_3, 1 cO	Ethyl propyl ether (EPE)	0.353	8	MEE & Hex-1,5-diene	1.222	0.57
			9	But-1-ene & Ethyl methanoate	1.220	0.61
			10	MEE & Hex-1-ene	1.215	0.59

Table 4: Comparison of the performance of feasible-infeasible mixtures and the optimal compositions with their pure component counterparts

Pure Feasible Working Fluid			Top Working Feasible – Infeasible Fluid Mixtures			
Functional Groups	**Name**	$\dot{W}_{net}$ **(MW)**	**Rank**	**Name (Component 1, 2)**	$\dot{W}_{net}$ **(MW)**	**Optimal** z_1
1 CH_3, 1 CH_2, 1 CH=, 1 CH_2=	But-1-ene	0.856	1	But-1-ene & Allyl butyl ether	1.041	0.95
2 CH_3, 2 CH_2	Butane	0.853	2	Pent-1,4-diene & 2-methoxy ethyl allyl ether	1.038	0.93
1 CH_2, 2 CH=, 2CH_2	Pent-1,4-diene	0.848	3	Butane & Octane	1.030	0.95
Pure Infeasible Working Fluid			4	Butane & 4-methoxyethoxy-1-butene	1.026	0.94
2 CH_3, 8 CH_2	Decane	-	5	Pent-1,4-diene & 3-(2-ethoxyethoxy)-1-propene	0.981	0.97
2 CH_3, 6 CH_2	Octane	-	6	Pent-1,4-diene & Decane	0.966	0.98
1 CH_3, 4 CH_2, 1 cO, 1 CH=,1 CH_2=	Allyl butyl ether	-	7	Pent-1,4-diene & 1-hydroxy-but-3-ene	0.963	0.90
1 CH_2, 1 CH=, 1 CH_2, 1 COH	1-hydroxy-but-3-ene	-	8	Pent-1,4-diene & 1-hydroxy-ethyl propyl ether	0.953	0.93
1 CH_3, 3 CH_2,1 eO, 1 cO, 1 CH=, 1 CH_2=	4-methoxyethoxy-1-butene	-	9	Pent-1,4-diene & Allyl butyl ether	0.944	0.97
1 CH_3, 2 CH_2, 1 cO, 1 COOH	1-hydroxy-ethyl propyl ether	-	10	Butane & Decane	0.934	0.99
1 CH_3, 4 CH_2, 1 eO, 1 cO, 1 CH=, 1 CH_2=	3-(2-ethoxyethoxy)-1-propene	-				

The constraints given by Eqn. (23) – (26) implemented in Test 2 is examined in greater detail in this section, using a feasible-infeasible mixture as an example.

Sarkis & Robert[11] first reported that a mixture of butane & decane is feasible when $z_{butane} \in [0.8,1]$. However, the constraints proposed in their work can only ensure that the mixture is in VLE. This is insufficient as the evaporator demands a single phase vapour at the outlet, where that the vapour fraction is 1.

Similarly, a single phase liquid needs to be formed at the outlet of the condenser. This is only guaranteed if Eqn. (23) and (24) is satisfied where both the bubble and dew curve at a particular composition will intersect the vertical temperature bounds (in black) as seen in Fig. 6.

This is evident in Fig. 6a, where the dew curve of the mixture at $z_{butane} = 0.8$ lies outside the temperature bounds. Consequently, no single phase vapour can be formed in the evaporator at the specified process bound. Evaluating this composition in the primal problem will thus lead to an infeasible solution.

Marginally satisfying Eqn. (23) and (24) yields a lower bound on composition with $z_{butane} = 0.8642$ where formation of a single phase vapour is now possible at the minimum absolute pressure of 0.1 MPa. From Fig. 6b, a single phase liquid can be formed at pressures larger than 0.18 MPa. This presents a second problem. Within the temperature range, the bubble pressure will always be larger than the dew pressure at this composition. This violates the requirements of our ORC model where the condenser is required to operate at a lower pressure regime compared to the evaporator. This is because a pump is connected between the outlet of the condenser and the inlet of the evaporator

To avoid such scenarios from occurring, a third constraint is imposed to guarantee that the pump outlet pressure (P_2) is always larger than the pump inlet pressure (P_1). This is given by Eqn. (25). Implementing all the reformulated constraints in Test 2 will give a new bound on the feasible composition of a butane & decane mixture where $z_{butane} \in [0.9359,1]$. Accordingly, the new bounds on pressure can be obtained from the same constraints used. This is seen from Fig. 6b, where the lower bound on pressure has been increased to 0.196 MPa, represented by the dotted red line. At this pressure, the bubble curve at the minimum feasible composition just contacts the lower temperature bounds while the corresponding dew curve cuts the upper temperature bound at a slightly higher pressure, indicating that the constraint given by Eqn. (25) is active.

4.2. Expansion of design space

In this section, we conduct an evaluation of the mixtures used in the solution of the primal problem.

4.2.1. Performance of mixtures relative to pure fluids

From Tables 3 and 4, it can be seen that performance improves when a pure feasible component is mixed with

another, regardless of the latter's feasibility. Specifically, the improvement in performance of FF mixtures (42 – 45% increase in $\dot{W}_{net}$ generated) was markedly greater than in FIF mixtures (11-22% increase in $\dot{W}_{net}$ generated). This improvement in performance is attributed to the 'temperature-glide' present in mixtures where the evaporation and condensation temperatures vary continuously due to changes in vapor and liquid composition.[20] This allows temperature profiles of heating and cooling sources to be matched, reducing exergy losses.[15] Other possible explanations could be related to the changes in thermodynamic properties. However, the lack of experimental data and literature available[30] in this area makes it inherently difficult to evaluate the differences in thermodynamic performance.

Thus, while the performance of mixtures has been found to perform better than their pure counterparts in this specific ORC model used, it remains difficult to conclude that this extends to all ORC applications. Indeed, there have been multiple studies asserting that pure components are not necessarily inferior to mixtures as working fluids in ORC.[30] Li *et al.* studied 18 different zeotropic mixtures and concluded that mixtures only outperform pure fluids in very specific scenarios yet typically fares worse in techno-economic considerations.[31] This coincides with the findings of Wu *et al.* where they found that mixtures require a significantly larger heat transfer area[32] which drives the costs of process equipment up.

Consequently, the use of pure fluids and mixtures should be considered on a case-by-case basis depending on the type of application. While this study has used the net power generation as an objective function, it is highly possible that the top working fluids will change should a different metric be used for comparison. This also implies the importance of selecting a suitable objective function for optimisation based on techno-economic requirements.

4.2.2. Effect of composition on net power generation

It is noteworthy that most FF binary mixtures have an optimal composition of approximately 50%. This suggests that having near equimolar compositions in FF mixtures improves thermodynamic performance. One possible explanation could be the change in intermolecular attractions between the two components, which are factors that influence the phase behaviour and heat transfer within the evaporator and condenser. Further investigation is required to ascertain this hypothesis, as existing literature in this area is scarce. For FIF mixtures, the top fluids have a composition of at least 90% in the feasible component, suggesting that the addition of a small amount of an infeasible component improves the performance of the binary mixture.

While there is no clear trend on the effect of composition on the objective function $\dot{W}_{net}$, the same cannot be said should a costing model be introduced. As mentioned above, mixtures have been shown to require a larger heat transfer area and thus higher capital costs due to larger evaporator and condenser sizing. This is due to a decrease in heat transfer coefficients compared to their pure component counterparts.[30]

4.2.3. Selection of components in binary mixtures

For FF and FIF mixtures, all the top candidates contain at least one feasible and high performing pure component. These are usually low in molecular weight and have few functional groups. Furthermore, alkanes, alkenes, and short chain ethers are shown to be high performing – both as a pure component individually and as part of a binary mixture. All these observations are in good agreement with the existing literature.[12,20,24]

For FIF mixtures, there is a variety of infeasible components appearing in the list of high performing FIF mixtures, indicating no clear trend in the selection of infeasible components. Further extensive studies need to be conducted to better determine if a relationship exists between the infeasible pure components that will form a high performing FIF mixture.

However, for the feasible components in FIF mixtures, only three of the top performing feasible pure working fluids (pent-1,4-diene, butane, but-1-ene) are shown to be high-performing when combined with an infeasible component. Interestingly, while butane and but-1-ene appeared in the list of top performing working fluids in both FF and FIF mixtures, pent-1,4-diene does not appear in the list for FF mixtures.

Notably, pent-1,4-diene was one of the top performing fluids in a case study of Bowskill *et al.*[12] and was also selected in a multi-objective optimisation based on thermodynamic properties in the work of Papadopoulos *et al.*[16] This suggests that some of the heuristics used for selecting working fluids might be applicable in the selection of components for binary mixtures.

We conclude this section by providing a heuristic for selecting components in mixtures based on our study:

1) One of the components should be a high performing pure working fluid in a binary mixture.
2) Alkanes, alkenes, and short-chain ethers are generally good choices as feasible components for both FF and FIF binary mixtures.

4.3. Algorithm limitations

4.3.1. Estimation of critical pressure

As the SGM EoS does not have an existing routine to predict the critical point,[23] the critical pressure for a pure component, $P_{c,pure}$ was estimated to be the pressure at which the vapour-liquid molar volume ratio is 1.21. Consequently, $P_{c,pure}$ determined in this study is a crude estimate of its experimental value.

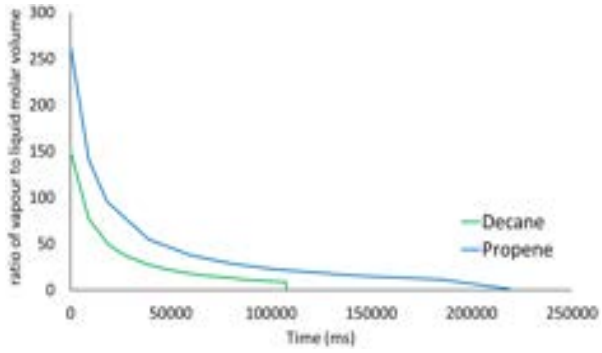

Figure 7: Comparison of vapour-liquid molar ratio evaluated by gPROMS for decane and propene. Evaluation is complete when the ratio is at least 1.21. There is a kink present in the curve for decane at the end.

Furthermore, the ability to evaluate this ratio within gPROMS is limited and highly molecule-dependent. This is seen in Fig. 7 where the decrease in ratio for propene is smoother and without the kink observed in decane.

Consequently, this translates to a more inaccurate estimation of critical pressure for decane. This inaccuracy is further made worse in the estimation of the critical pressure of a mixture $P_{c,mix}$, as it is taken to be the linear combination of its two corresponding $P_{c,pure}$. Should $P_{c,mix}$ be an overestimate of its experimental value, the ORC operation is no longer guaranteed to be sub-critical even with its reduced pressure factor P_r^U. Conversely, an underestimate risks reducing the design space and a loss of potential solutions. This motivates the need for a more robust method to determine the critical pressure using an appropriate EoS.

4.3.2. Non-convex and non-linear primal problem

As the primal problem is highly non-convex and non-linear, it is extremely dependent on the initial guess for an optimal local solution to be found. Despite reducing the search space to only consist of the feasible compositions, the algorithm has been found to terminate sub-optimally, as no better solution can be found. This can be seen from Table 5, where an initial composition (normalised) guess of 0.1, 0.3 and 0.9 resulted in solutions with a stationarity condition significantly larger than the specified tolerance of 10^{-5}. The best local optimum was obtained with the objective function $\dot{W}_{net} = 0.9342$, corresponding to a normalised composition of 0.865.

It is important to mention that restarting the primal problem using the solution obtained from the previous optimisation (which terminated due to no improvement) as an initial guess has not shown to improve the convergence at all. In our studies, the primal problem will still terminate yet again due to no improvement.

More importantly, the optimal solution obtained has been shown to be dependent on the initial guess where there is an 8% deviation from the minimum and maximum $\dot{W}_{net}$ in the butane-decane mixture.

Table 5: Values of the optimal solution for different initial guesses of composition (normalised) for a binary mixture of butane and decane. The feasible composition bounds are [0.936, 1].

Initial Guess	Status	$\dot{W}_{net}$ (MW)	Stationarity	Feasibility
0.1	Optimal	0.8573	4.409	0
0.3	Optimal	0.8859	2.125	0
0.5	Optimal	0.9342	5.486×10^{-5}	0
0.7	Optimal	0.9314	6.131×10^{-5}	0
0.9	Optimal	0.9317	9.616	0

As such, for candidate mixtures highlighted to be high performing, it is recommended that multiple initial guesses are used for further evaluation in the primal problem to verify the local optimum obtained. This will allow comparisons between multiple local optima and hopefully enable a solution closer to the global optimum.

4.3.3. Discontinuities in the feasibility region

Instances of failure in the primal problem has also been recorded, even when the candidate mixture is deemed feasible by Test 2 and had its composition and pressure bounds tightened. This usually manifests in a SQP failure, or a trivially small objective function. The reason this might happen may be due to the disjointed feasibility regions present in the pressure bounds. It is important to note once again that bubble and dew pressures in a mixture are a function of both temperature and composition. When obtaining the pressure bounds in Test 2, the minimum and maximum pressure are evaluated across the entire feasible composition range to give $[P^{L2}_{n_1,n_2}, P^{U2}_{n_1,n_2}]$. However, the pressure bounds at a specific isopleth are only a subset of $[P^{L2}_{n_1,n_2}, P^{U2}_{n_1,n_2}]$. (The feasible composition range comprises of multiple isopleths in a temperature-pressure diagram.) Therefore, there exist a pressure within $[P^{L2}_{n_1,n_2}, P^{U2}_{n_1,n_2}]$ which is infeasible for a specific composition. These represents infeasible solutions, which might be encountered during solution of the primal problem. Consequently, the SQP solver may not be able to recover from this due to the penalty function imposed and thus terminates with a numerical failure. One way to mitigate this is to implement Test 2 directly within the primal problem such that pressure bounds can be continuously updated for a given temperature and composition.

Although there are significant improvements made, VLE may still not be guaranteed since the pressure bounds are a function of composition. Given that the ORC model requires a mixture to coexist in VLE across the entire specified condition, the absence of VLE is sufficient to cause a numerical failure. This occurrence is not uncommon in the CAMPD context.[10] Furthermore, discontinuities are typically present in the differential and algebraic equations used to describe phase behaviour[33] and further amplifies the numerical challenge which cripples the solver in most cases. To address this problem, Kamath *et al.*[34] proposes the use of complementarity constraints to relax the VLE condition imposed when single phase flow is encountered in discontinuities.

5. Conclusion

In this study, we have shown that feasibility tests are instrumental in the construction of a full CAMPD algorithm. Specifically, our formulated feasibility tests mitigate the problem of non-linearity and non-convexity by making the ORC primal problem more tractable. We have achieved at least a 30% reduction in computational cost as Test 1 has eliminated more than 300 infeasible combinations from our list of 1100 candidate mixtures. By tightening the composition bounds in Test 2, and the pressure bounds in both Tests 0 and 2, the search space has been significantly reduced to contain only the feasible regions. This has shown to aid the solution of the primal problem by avoiding an initial guess at an infeasible point (resulting in a numerical failure), and to achieve a convergence significantly closer to a local optima.

From the 800 binary mixtures evaluated in the primal problem, it was found that they performed better than their corresponding pure components. This was observed in both FF and FIF mixtures and is attributed to their non-isothermal phase change behaviour. Although no clear trend was seen in the effect of mixture composition on $\dot{W}_{net}$, we found that high performing pure fluids are typically good components in binary mixtures. This was found to be especially so for alkanes, alkenes, and short chain ethers.

The successful automated implementation of the feasibility tests, together with the solution of the primal problem further validates the possibility of increasing the design space. This proof of concept can be extended to now include the master problem and certainly paves the way forward to a full CAMPD OA algorithm.

6. Future work

To further improve the existing implementation, an additional test on azeotropic composition is proposed to be developed. As mentioned above, binary mixtures exhibit better performance than their pure component counterparts due to the non-isothermal phase change. However, this will no longer be the case in an azeotropic composition as the mixture will now behave as a pure fluid. While the net power generation from an azeotropic mixture is expected to decrease, it is possible that the thermal efficiency will increase similar to a pure fluid due to the reduced demand in heat transfer area.[32] This is in agreement with Oyewunmi *et al.*[36] who concluded that azeotropes reduce capital costs in the evaporator and condenser. As such, further research should be conducted to ascertain the effect of azeotropes in ORCs.

In addition, having developed a robust algorithm less prone to numerical failures, a higher fidelity model can now be implemented to obtain a more realistic representation of the ORC process. Different ORC and cycle topologies are recommended to be investigated for mixtures, such as the inclusion of regenerators, turbine bleeding, or reheating.[35] The heating and cooling sources can also be varied to obtain different groups of working fluids suitable for the recovery of low, medium, and high grade heat. Existing literature have shown that fluids containing CH=CH bonds are optimal for medium or high-grade (250/350 °C) heat sources.[24]

7. Acknowledgements

We gratefully acknowledge the support given by David Bowskill and Lauren Lee throughout the course of this research. Their expertise and insight were immensely valuable and crucial to its successful outcome

8. References

[1] Aboelwafa, O., Fateen, S. K., Soliman, A. & Ismail, I. M. (2018). *Renewable and Sustainable Energy Reviews.* 82 868-885.

[2] Ahmadi, A., El Haj Assad, M., Jamali, D. H., Kumar, R., Li, Z. X., Salameh, T., Al-Shabi, M. & Ehyaei, M. A. (2020). *Journal of Cleaner Production.* 274 122950.

[3] Al-Bahadly, I. (2019). *Energy Conversion: Current Technologies and Future Trends.*

[4] Zhang, X., Wu, L., Wang, X. & Ju, G. (2016). *Applied Thermal Engineering.* 106 1427-1439.

[5] Ziviani, D., Beyene, A. & Venturini, M. (2014). *Applied Energy.* 121 79-95.

[6] Schilling, J., Entrup, M., Hopp, M., Gross, J. & Bardow, A. (2021a) *Renewable and Sustainable Energy Reviews.* 135 110179.

[7] Bamorovat Abadi, G. & Kim, K. C. (2017a). *Renewable and Sustainable Energy Reviews.* 73 1000-1013.

[8] Churi, N. & Achenie, L. E. K. (1996). *Industrial & Engineering Chemistry Research.* 35 (10), 3788-3794.

[9] Gani, R. & Brignole, E. A. (1983). *Fluid Phase Equilibria.* 13 331-340.

[10] Gopinath, S., Jackson, G., Galindo, A. & Adjiman, C. S. (2016). *AIChE Journal.* 62 (9), 3484-3504.

[11] Sarkis, M. & Robert, N. (2019) Towards the Development of a Computer Aided Molecular and Process Design Framework for Mixtures as Organic Rankine Cycles Working Fluids.

[12] Bowskill, D. H., Tropp, U. E., Gopinath, S., Jackson, G., Galindo, A. & Adjiman, C. S. (2020). *Molecular Systems Design & Engineering.* 5 (2), 493-510.

[13] Papadopoulos, A. I., Stijepovic, M. & Linke, P. (2010a). *Applied Thermal Engineering.* 30 (6), 760-769.

[14] White, M. T., Oyewunmi, O. A., Haslam, A. J. & Markides, C. N. (2017a). *Energy Conversion and Management.* 150 851-869.

[15] Angelino, G. & Colonna di Paliano, P. (1998). *Energy.* 23 (6), 449-463.

[16] Papadopoulos, A. I., Stijepovic, M. & Linke, P. (2010b). *Applied Thermal Engineering.* 30 (6), 760-769.

[17] Papadopoulos, A. I., Stijepovic, M., Linke, P., Seferlis, P. & Voutetakis, S. (2013). *Industrial & Engineering Chemistry Research.* 52 (34), 12116-12133.

[18] Oyewunmi, O. A. & Markides, C. N. (2016). *Energies.* 9 (6), 448.

[19] Molina-Thierry, D. & Flores-Tlacuahuac, A. (2015). *Industrial & Engineering Chemistry Research.* 54 (13), 3367-3383.

[20] Schilling, J., Entrup, M., Hopp, M., Gross, J. & Bardow, A. (2021b). *Renewable and Sustainable Energy Reviews.* 135 110179.

[21] Schilling, J., Tillmanns, D., Lampe, M., Hopp, M., Gross, J. & Bardow, A. (2017). *Molecular Systems Design & Engineering.* 2 (3), 301-320.

[22] Haslam, A. J., González-Pérez, A., Di Lecce, S., Khalit, S. H., Perdomo, F. A., Kournopoulos, S., Kohns, M., Lindeboom, T., Wehbe, M., Febra, S., Jackson, G., Adjiman, C. S. & Galindo, A. (2020). *Journal of Chemical & Engineering Data.* 65 (12), 5862-5890.

[23] Kiselev, S. B. & Ely, J. F. (1999). *Industrial & Engineering Chemistry Research.* 38 (12), 4993-5004.

[24] White, M. T., Oyewunmi, O. A., Haslam, A. J. & Markides, C. N. (2017b). *Energy Conversion and Management.* 150 851-869.

[25] Gopinath, S., Galindo, A., Jackson, G. & Adjiman, C. S. (2016). *Computer Aided Chemical Engineering.* 38 73-78.

[26] Sadeqzadeh, M., Papaioannou, V., Dufal, S., Adjiman, C. S., Jackson, G. & Galindo, A. (2016). *Fluid Phase Equilibria.* 407 39-57.

[27] Kazepidis, P., Papadopoulos, A. I., Seferlis, P., Perdomo, F. A., Galindo, A., Jackson, G. & Adjiman, C. S. (2019). *Computer Aided Chemical Engineering.* 46 463-468.

[28] Hukkerikar, A. S., Sarup, B., Ten Kate, A., Abildskov, J., Sin, G. & Gani, R. (2012). *Fluid Phase Equilibria.* 321 25-43.

[29] Ge, X. & Wang, X. (2009). *Industrial & Engineering Chemistry Research.* 48 (4), 2229-2235.

[30] Bamorovat Abadi, G. & Kim, K. C. (2017b). *Renewable and Sustainable Energy Reviews.* 73 1000-1013.

[31] Li, Y., Du, M., Wu, C., Wu, S. & Liu, C. (2014) *Energy.* 77 509-519.

[32] Wu, Y., Zhu, Y. & Yu, L. (2016). *Applied Thermal Engineering.* 96 57-63.

[33] Majer, C., Marquardt, W. & Gilles, E. D. (1995). *Computers & Chemical Engineering.* 19 507-512.

[34] Kamath, R. S., Biegler, L. T. & Grossmann, I. E. (2010). *Computers & Chemical Engineering.* 34 (12), 2085-2096.

[35] Schilling, J., Horend, C. & Bardow, A. (2020). *AIChE Journal.* 66 (5), e16903.

[36] Oyewunmi, O., Kirmse, C. & Markides, C. (2016) Heat Exchanger Analysis of Azeotrope Mixtures in Organic Rankine Cycles.

Literature Review and Experimental Design in Producing Rigid Polyurethane Foam for Sportswear Clothing

Lay Ping Tan and Ming Jiun Ngu

Department of Chemical Engineering, Imperial College London, U.K.

Abstract The main objective of this study is to produce a rigid polyurethane foam (PUF) to be incorporated in sportswear clothing, rendering support and protection while not neglecting its aesthetic value. The density of PUF ideally lower than 1.3 gcm^{-3} and compressive strength around 0.5 – 5 MPa are the main conditions to be satisfied. Hence, this study takes a holistic approach in identifying the potential chemicals and outlining the feasible experiment steps. As a continuation from the study in the previous year, polyethylene glycol (PEG) is analysed to suggest potential improvements. The average OH values and the number average molecular weight should be taken into considerations in selecting the suitable polyols and in deciding the blend of the main polyols. The study on the effect of cross-linker and the use of polyols with higher functionality are gradually introduced in the experimental planning. Cost-effective and green raw materials such as starch, glycerol and polycaprolactone triol (PCLt) are suggested to promote cross-linking in the polymer matrix. Modification of the conventional PUF into an auxetic foam can be employed to improve the shock absorbing performance. Other alternatives to improve the foam compressive strength include the impregnation of PUF with shear thickening fluid (STF) and the sandwich-structured composite made of warp-knitted spacer fabrics (WKSF) and PUF.

Keywords: *polyurethane foam (PUF), polyethylene glycol (PEG), starch, polycaprolactone triol (PCLt)*

Introduction

Polymer foams were first discovered during the 1930s, with polystyrene foam being the first invented polymer foam (Sivertsen, 2007). Polymer foam (also known as porous polymer material) has a distinctive microcellular structure resulting from the controlled entrapment of gas during the polymerization process. As compared to the solid polymer, polymer foam received higher popularity for being a good thermal insulator, lightweight and most importantly it has high specific strength (Drobny, 2014).

One of the more commonly found polymers is polyurethane (PU). It was first discovered by Dr Otto at the start of World War II as a substitute for rubber and as a protective coating layer for metals and woods (Sivertsen, 2007). With the advancement of technology, polyurethane foam (PUF) with different properties was progressively being introduced in the furniture and automotive industries. PUF is formed via polyaddition of polyfunctional isocyanate with polyol while the foaming process is usually conducted via one-shot process, where the base chemicals, catalyst and blowing agents are directly mixed. The properties of the foam can be altered easily by modifying the raw materials together with the inclusion of additives such as cross-linking agents, fillers, surfactants and chain extenders (David *et al.*, 2010). These enable different PUF to be produced, ranging from soft elastomers to rigid thermoplastics. Consequently, broader applications of PUF are introduced in industries such as adhesives, textile fibres and scaffolds in biomaterials (Kausar, Zulfiqar and Sarwar, 2013).

Viscoelastic property of PUF was initially used to provide a cushioning effect to the astronauts during take-off and landing (Geddes, 2016). This was then adapted in car racing cockpits as noise and vibration harshness foam (NVH) and as the padded foam in the drivers' helmet. Furthermore, in contact sports such as lacrosse and American football, PUF is usually found in the protective helmets as a shock absorber and could be modified easily to give personal protection to other parts of the body. In terms of impact absorbance, other material like polyethylene foam fails to compete with PUF as it tends to rebound energy quickly and thus fails to provide the necessary protection (Romano, 2019). Moreover, as compared to silicone-based polymer foam, which is also a great impact absorbance material, PUF is more suitable to be incorporated in garments. This is because silicone is relatively heavier which could be a potential hindrance to the wearer besides resulting in sagging of the garments.

On the contrary, there is a growing environmental concern on the disposal methods for the non-biodegradable polymer wastes. These wastes are normally burned through incineration or dumped in landfills which lead to emissions of harmful greenhouse gases. Hence, the use of green and bio-based polymers such as synthetic polymers and natural polymers in PUF has been proven to alleviate the disposal issue. Polycaprolactone triol (PCLt) and polyethylene glycol (PEG) are classified as the synthetic polymers, both having microorganism-susceptible functional groups. The natural polymer is inherently biodegradable, with starch considered as one of the most promising materials due to its natural abundance and low cost (Dae-Hyun *et al.*, 2007).

With the highly versatile traits and the simplicity of the foaming process, PUF becomes the material that many have sought after across major end-user industries. Generally, the growth in the polymer foam market has an upward rising trend and among all the available polymers, PUF has been registered to occupy the largest share in the global market during the forecast period (Markets, 2020). The global PU market size is valued at UD 74.01 billion in 2020 and is estimated to reach USD 105.2 billion by 2025, registering a CAGR of 7.0% (Grand Review Research, 2019). Meanwhile for the bio-based PUF, slow market growth is recorded as compared to other bio-polymers due to the complicated technology and high manufacturing cost both of which could be solved through

more favourable government policies and technology advancement.

In these respects, this research aims to produce a rigid, lightweight and sustainable PUF that exhibits an excellent shock absorbance performance while not neglecting its aesthetics. The manufacture of PUF that satisfies both fashion and functional use in the sportswear industry will be discussed further in this report.

Polymer Foaming Process

Polyurethane foaming is normally done in a one-shot or two-shot method. For one-shot method, all materials are mixed homogeneously before being poured into a mould, whereas in two-shot method, all materials except isocyanates are mixed well before the addition of isocyanate (Kim and Kim, 2008). Polymer foaming can be done in several stages: (a) mixing of raw materials with additives; (b) creaming period, when the activity of blowing agent is promoted by the temperature rise from exothermic reaction; (c) rising period, when the gas generated raises the foam until a sufficient rigidity is obtained; (d) curing period, when the hardening of the polymer through cross-linking occurs (Marciano, Rojas and Williams, 1982). Batch foaming, foam injection moulding and foam extrusion moulding are the commonly used processing techniques.

Blowing and gelling are the two main reactions involved in foam synthesis. The blowing reaction occurs when isocyanate groups react with water yielding polyurea and CO_2 which expands the trapped air bubbles within the foam. The gelling reaction arises from (i) the formation of urethane bonds between isocyanates groups and hydroxyl groups and (ii) the formation of biuret bonds between urea groups and isocyanates groups. Additives are added to ensure a good balance between gelling and blowing reactions. This enables the gas to be effectively sealed within foams to cause cell nucleation. The cells merge and grow thus expanding in cell diameter. In the case of large numbers of cells formed, the volume of foam gradually increases which causes the cell skin to become thinner, resulting in an unstable foam. Thus surfactants are added to stabilise the foam (Jin *et al.*, 2019).

The foam cell size depends on the overall viscosity of the mixture. At low viscosity, foams with larger cell size and uniform cell size distribution are produced, resulting in a flexible foam. Whereas at very high viscosity, the bubble formation and growth are greatly suppressed which reduces the cell size, limiting the foam expansion (Septevani *et al.*, 2015). The plasticizer can be added to reduce the overall viscosity of the mixture, thus producing a less rigid foam.

PUF behaviour can be classified into rigid, semi-rigid and flexible, depending on their cell geometry such as closed cells or open cells. Closed cell structure has bubbles of air separated from each other by the polymer matrix which enables its compressibility property. On the contrary, open cell structure has interconnected pores which allow passage of fluid within foam and thus improves the breathability and moisture vapour transmission of the foam. Rigid PUF with a closed cell structure exhibits the desirable properties such as low density, low thermal conductivity, and high strength-to-weight ratio, which make it suitable for automotive and sportswear protective gears application. Flexible PUF with an open cell structure is instead used in bedding and acoustic insulation application (Altan, 2016).

Variables

Polyol

Short-chain polyols are usually the additives to enhance reactivity and functionality of the main polyol used. On the other hand, long-chain polyols are conventionally used to react with the isocyanate groups to form urethane bonds. Long-chain polyols mainly form the soft segment while contributing to the hard segment through the urethane bond formation. A longer soft segment produces a more elastomeric foam where it plays an important role in shock absorbing application.

The main factors that define the properties of PUF formed are the chemical structure, equivalent weight (E) and functionality(f) of the polyol used. The relationship between E and f is described in Equation 1**.** To produce a rigid foam, the range of OH value for the main polyol should be within 350 – 800 mg KOH/g and the number average molecular weight (M_n) should be within 300 – 1000 $gmol^{-1}$ (Furtwengler and Avérous, 2018). The formulated blends of polyols with the aforementioned OH values and M_n are often used in preparing a rigid PUF as they exhibit better physical properties at low temperature due to their lower tendency to crystallize (Thirumal *et al.*, 2009).

$$Equivalent\ Weight\ (E) = \frac{Number\ Average\ Molecular\ Weight(M_n)}{Functionality\ (f)} \quad (1)$$

High overall functionality (3.0 -8.0) of polyol in the system increases the cross-linking density thus enhances its mechanical property. For example, the addition of sorbitol and pentaerythritol into palm oil increases the overall OH value and consequently exhibits a 10% increase in compressive strength of the foam panel (Furtwengler and Avérous, 2018). Deviation from the optimal ranges often results in semi-rigid or soft foam.

Polyester polyol and polyether polyol are the two commercially used chemicals for PUF. Polyester polyols are derived from diacids and di- or tri-functional polyols to form ester bonds. This ester bond formed has a lower resistance towards hydrolysis which deteriorates the mechanical properties of PUF. The introduction of carbodiimides and other additives could address this issue. Besides, the use of vegetable oil (triglyceride) as the bio-based polyesters are encouraged to phase out petroleum-derived polyol. However, due to the lack of hydroxyl group in its crude form, a series of reactions such as epoxidation, ring-opening reaction, transesterification, hydroxylation, etc are required to modify its chemical structure, leading to its high cost.

Polyether polyols are synthesised via ring-opening anionic polymerization of oxiranes and are usually conducted in a catalysed batch process. Different oxiranes such as propylene oxide or butylene oxide have been used for different purposes and to increase bio-based content in polyol, more biobased oxiranes can be used. Overall, by having higher stability towards hydrolysis and ageing, polyether polyol is more widely used as compared to polyester polyol.

The ease of reproduction of the foaming process and the accessibility of materials in the market are emphasized in selecting the suitable polyol.

Isocyanate group

Isocyanates contribute to the hard segment in the polymer where its chemical structure (aliphatic versus aromatic) affects its properties. The most important commercial aromatic isocyanates are methylene diphenyl diisocyanate (MDI) and toluene diisocyanate (TDI), which are often used to produce thermoplastic elastomers and foams. Commercially found aliphatic isocyanates are hydrogenated MDI (HMDI) and hexamethylene diisocyanate (HDI). In contrast to aromatic isocyanates, PUF made of aliphatic isocyanates are UV-stable and less susceptible to oxidative discolouration, thus they are normally preferred in exterior coatings application (Polymerdatabase, 2020). Aromatic isocyanates provide a higher cross-linking density due to the presence of the aromatic rings, where a significant increase in glass transition temperature (T_g) and compression strength were observed (Javni, Zhang and Petrović, 2003). On top of that, aromatic isocyanates are cheaper than aliphatic isocyanates in the market.

The R value is defined as the molar ratio of the cyanate groups (-NCO) to the hydroxyl groups (-OH). The molar ratio of each chemical is obtained by dividing the mass of chemical used by its equivalent weight (Equation 1). The hard segments are mainly contributed by the urethane bonds which are formed in the gelling reaction. Additional bonds such as allophanates, biurets and isocyanurates are formed as the side reactions at higher R value, which improve the cross-linking density of the polymer matrix. The isocyanurate bonds are formed via trimerization process which is useful to improve the thermal stability of the foam. This is consistent with the findings of Park *et al.* where the ratio of the isocyanurate ring absorbance to urethane group increases with higher R value (Park *et al.*, 2013).

The foam density was observed to decrease with increasing R value. Higher isocyanate content enables more isocyanates available to react with water to form carbodiimide bonds and carbon dioxide gas, thus resulting in additional foaming which decreases the foam density. The foam compressive strength was reported to increase with R value, however there is an adverse effect beyond a maximal point as shown in the study of Abdel *et al.*, where beyond a maximal R value of 1.1, compressibility strength decreases (Abdel Hakim *et al.*, 2011). The decrease in compressive strength is due to the excessive cross-linking which causes the foam to be brittle (Modesti and Lorenzetti, 2001).

Chain extender and Cross-linking Agent

Short-chain polyols and polyamines are classified as chain extenders and cross-linking agents based on their respective functionality. Chain extenders are low molecular weight compounds with the functionality of two. The commonly used chain extenders are 1,4-butanediol (BDO) and 1,5-pentanediol (PDO). Cross-linking agents are compounds of functionality greater than two, such as glycerol and triethanolamine.

Both additives contribute towards the hard segments by increasing the intermolecular interaction. Covalent and hydrogen bonds are usually formed between the additives and NCO-terminated prepolymers. When a diol is added, it reacts to form urethane bond (Equation 2) while urea bond will be formed when a diamine is used instead (Equation 3).

$$-NCO + -OH \rightarrow -NHCOO- \quad (2)$$

$$-NCO + -NH_2 \rightarrow -NHCONH- \quad (3)$$

The presence of urea groups enables hydrogen bonding to form, thus increases its crystallinity and produces a hard foam. According to Delpech *et al.*, ethylene diamine group exhibits brittleness at lower NCO/OH ratio as compared to hydrazine. This is because the diamine group enhances the miscibility between phases and also enables a higher probability of hydrogen bond formation as compared to a diol group (Delpech and Coutinho, 2000). The results found by Ramesh *et al.* agree upon the use of diamine group instead of diol as it exhibits better strength and hardness (Ramesh, Rajalingam and Radhakrishnan, 1991). However, it is not easy to handle the use of diamine group due to its higher volatility.

The gradual addition of chain extenders and cross-linking agents increases foam T_g value, which is an indication of an increase in cross-linking density. Molecular motion is restricted due to the increase in hard segment content and short-chain three-dimensional network. However, the trend changes with T_g decreases when excessive additives are added due to the plasticization effect. Extensive coalescence of cells is observed at very low viscosity which leads to less stable foams (Septevani *et al.*, 2015).

Besides, chain extenders and cross-linking agents in excess will compete with polyols in reacting with isocyanate groups. This causes excess heat to be generated due to the exothermic bond formation. Consequently, it increases the internal gas pressure that leads to the breakdown of the cell walls which results in a poor-quality foam. Furthermore, it was proven that the excessive use of chain extenders would cause a reduction in density and mechanical strength of foam (Thirumal *et al.*, 2009). It was similarly observed in the study of Hakim *et al.* that excess addition of cross-linking agents produces a more brittle foam (Abdel Hakim *et al.*, 2011).

Blowing agent

There are two main types of blowing agent. Physical blowing agents are typically the volatile solvents which vaporise to cause cell nucleation and the process is usually endothermic. On the other hand, chemical blowing agents are the compounds that involve in the chemical reaction to produce CO_2, where the gaseous formed causes foam expansion. This is typically an exothermic reaction. Hydrochlorofluorocarbons and cyclopentane are the commonly used physical blowing agents while water is the preferred chemical blowing agent due to its low cost. Water reacts with the diisocyanate to form polyurea and CO_2 with the evolution of heat. There is an observed increase in the overall reaction kinetics of polyurethane foaming when water content increases which is possibly due to the increase in reaction temperature. Polyurea formed reacts further with the isocyanate to form biuret bonds which contribute to the higher compressive strength. This process is greatly accelerated when the water content increases (Hyung CHOE *et al.*, 2004).

A good foam is a foam with smaller cell size, narrow cell distribution, low foam density and high cell density. Smaller cell size can be achieved with the use of water as the blowing agent whereas cyclopentane generally gives a non-uniform cellular structure and a lower compressive strength foam (Kurańska *et al.*, 2018). Hence water as the cheap and better blowing agent is widely used. Besides, higher water content reduces the viscosity of the polymer matrix by increasing its free volume fraction. The higher number of nucleating agents further promotes the nucleation rate in relation to polymer solidification. This produces a foam with thicker foam core and thinner skin (Barzegari and Rodrigue, 2009). However, beyond an optimal point, an adverse effect is observed where its compressive strength starts to decrease (Thirumal *et al.*, 2008). Hence an optimal water content is required to produce the desired PUF.

Catalyst

Catalyst is used to increase the overall kinetic rate, enable the reaction to be conducted at a lower temperature, shorten the curing time, and lower the curing temperature. The two common types of catalyst are tertiary amines and organometallic catalysts. Generally, a metal catalyst is preferred due to its lower volatility characteristics as compared to amine catalyst. It enhances isocyanate-hydroxyl reaction via complex formation where the positive metal centre interacts with the electron-rich oxygen atom of both NCO and OH groups to form an intermediate complex. The further rearrangement of the complex subsequently forms the urethane bond (Sharmin and Zafar, 2012).

The difference in cell morphology and the decrease in cell size are observed when catalyst concentration increases (Hyung CHOE *et al.*, 2004). A proper adjustment of catalyst type and concentration is crucial in controlling the overall polymer expansion as it determines the balance between gelling and blowing. If the gelling process has not proceeded well to retain the gas, it will result in rapid evolution of gas which will consequently cause the expanding foam to collapse.

Mould Temperature

Cell morphology is highly dependent on the mould temperature. When a molten polymer is added into a relatively cold mould, rapid solidification occurs resulting in insufficient cell nucleation and growth. On the contrary, a higher temperature of the core promotes local cell growth further away from the mould walls. This gives rise to an increase in skin thickness (Barzegari and Rodrigue, 2009). This is consistent with the study done by Jackovich *et al.*, where the average density of foam was found to decrease as mould temperature increases. The result observed is due to the decrease in polymer viscosity and the reduction in packing effect from the wall. However, the decrease in foam density is insignificant after reaching a threshold temperature.

Besides, it is also observed that mechanical properties improve significantly when the temperature increases. This might be associated with the change in the chemical reaction of the system which changes polymer properties as well as the change in pressure inside closed cells of the foam (Jackovich *et al.*, 2005).

Surfactant

A surfactant reduces the viscosity of the foaming system to promote bubble generation during mixing. It also helps to lower the surface tension between the cells to prevent cell coalescence, resulting in a uniform distribution of smaller cells (Luo *et al.*, 2018). For a free-rise foam, foam volume was found to increase up to seven times with the addition of a surfactant (Helbig *et al.*, 2015).

Table 1 Molar composition of the formulations reproduced from the results last year (Iylia Ismail and Swee Kee Hoo, 2019).

PUF	Feature	BDO (1,4-butanediol)	PDO (1,5-pentanediol)	PEG600 (polyethylene glycol)	PEG8000 (polyethylene glycol)	TDI (toluene diisocyanate)	MDI (methylene diphenyl diisocyanate)	R value	Compressive strength (MPa)
A	Hard	0	2	0	0	1.05	1.05	1.05	10.7
B	Hard	1	0	0	0	1.05	0	1.05	10.6
C	Hard	0	1	0	0	1.05	0	1.05	9.90
D	Soft	0.99	0	1	0	1.90	0	0.95	0.01
E	Soft	0.33	0	1	0.23	1.85	0	1.18	0.65
F	Soft	0.99	0	1	0.23	2.30	0	1.03	0.75

Flaws Identification from the Last Year's Report

The PUFs produced last year did not reach the desired rigidity and aesthetic values. The foams also failed to retain their shape after being compressed.

There has been an inconsistency in the R value used which varies from 0.95 till 1.18 as shown in Table 1. The extremely low compressive modulus in PUF D is suspected due to its low R value. R value of 0.95 implies that isocyanates were underreacted thus resulting in a relatively soft foam. Hence, several optimal R values, preferably larger than 1 should be fixed. The mass of isocyanates required could then be calculated.

PEG 8000 (M_n = 8000 $gmol^{-1}$) was mixed with PEG 600 (M_n = 600 $gmol^{-1}$) in PUF E and F to further soften the hard foam formed. However, the blended polyol accounted for the number average molecular weight (M_n) of 1984 $gmol^{-1}$ and average OH values of 147 mg KOH/g which fall out of the range of a rigid foam. Both average M_n and OH values of the blended polyol should be considered as PEG of higher M_n offers a lower OH value, which is consistent with the study of Furtwengler *et al.* where the OH value decreased from 410 to 190 mg KOH/g with the increase of PEG M_n from 400 to 1000 $gmol^{-1}$ (Furtwengler and Avérous, 2018).

Irregular cell sizes and rough surface were observed in the foam produced last year. The SEM image analysis could be done to study the cell size and its distribution more thoroughly. Besides, a surfactant can be added to solve this irregularity. It was noticed that the mixing and curing of the foam were conducted under room temperature. A higher temperature might be more favourable for both gelling and blowing processes.

Furthermore, the demoulding process of a rigid foam from a hard mould tends to destroy the foam. This could be solved by using a demoulding agent or replacing the mould with more flexible silicone material. On top of that, diorganopolysiloxane which is a silicone-bonded group is often used as a mould releasing agent for PUF (Cekada *et al.*, 1964).

Formulations & Experimental Steps

First Generation

Isocyanate group used will be toluene diisocyanates (TDI), as the result obtained from the previous year (Iylia Ismail and Swee Kee Hoo, 2019) has proven its ability in producing foam with the desired rigidity. TDI exhibits the highest compressive strength, followed by methylene diphenyl diisocyanate (MDI) and hexamethylene diisocyanate (HDI) (Kwon *et al.*, 2007). Similarly, 1,4-butanediol (BDO) as the chain extender is being used as a continuation of previous study. Bis[2 -(N,N dimethyl-amino) ethyl] ether was previously added as a catalyst, however, dibutyltin dilaurate (DBTL) is more suitable here due to its higher foaming efficiency and ability to accelerate biuret and isocyanurate reactions (Takamtsu, 1999).

An optimal range of polyol M_n to produce a rigid PUF is between 300–1000 $gmol^{-1}$ while the range of OH value should fall within 350 – 800 mg KOH/g (Furtwengler and Avérous, 2018). The results found in the study of Heiss *et al.* further consolidate the use of a PEG with very low M_n will give rise to a foam which is too hard and brittle. Hence, the use of PEG 200 is ruled out (Heiss *et al.*, 1954). PEG 600 in the findings of Swee Kee *et al.* resulted in a relatively soft foam even with the use of chain extender. Thus, PEG 300 is suggested here as its OH values and M_n fall within the optimal range of a rigid foam. In the scenario when a soft foam is created despite using PEG 300, a further increase in chain extender content or a blend of PEG 200 can be considered. However, in the case when a too rigid foam is produced, a blending of polyol between PEG 300 and PEG 600 could be done instead to obtain a softer foam. The M_n and OH value of the polyol blend with reference to Table 3 should fall within the optimal ranges as suggested by Furtwengler *et al.* to produce a rigid foam.

A range of R value between 0.9 to 1.3 (Equation 4) can be used to obtain the mass of TDI required for the known amount of polyol used as suggested in Table 2. Trials run to find the optimal values are crucial because the excess blowing agent (water) used will result in a decrease in compressive strength while excessive use of the catalyst will disrupt the balance between gelling and blowing.

$$R\ value = \frac{\frac{TDI\ (g) \times 2}{174}}{\frac{H20\ (g) \times 2}{18} + \frac{PEG\ (g) \times 2}{(M_n\ of\ PEG)} + \frac{BDO(g) \times 2}{90}} \quad (4)$$

Table 2 Composition of the ingredients used in the first generation.

Ingredients	Parts Per 100 Parts Polyol (Php)	Reference
Water	0.5 – 1.0	(Abdel Hakim *et al.*, 2011)
Dibutyltin dilaurate (DBTL)	0.50 – 0.75	(Li *et al.*, 2017)
1,4-butanediol (BDO)	5 – 15	(Iylia Ismail and Swee Kee Hoo, 2019)
Silicone oil	1.0 – 2.5	(Abdel Hakim *et al.*, 2011)

Table 3 Hydroxyl value and number average molecular mass of PEG.

PEG	Hydroxyl Value (mg KOH/g)	Number Average Molecular Mass, M_n ($gmol^{-1}$)
PEG 600	178 – 197	570 – 630
PEG 300	356 – 394	285 – 315
PEG 200	535 – 590	190 – 210

Preparation for First Generation

All chemicals can be obtained from Sigma-Aldrich. Materials are separated into 2 parts, Part A and Part B following the two-shot method. Part A are polyols, water, silicone oil and catalyst while Part B is isocyanate group. Part B is poured into a mixing tank containing Part A and

the mixture are continuously stirred under the ambient condition for 5-10 s. The mixture is then poured to fill up half of the mould to allow rising to occur. Preparation and mixing are to be done in the fume chamber as the chemicals used are toxic. Curing under room temperature is expected to take around 24 h before it is ready for characterisation. Mixing and curing can be done under a higher temperature to increase the reaction rate.

Second Generation

Cross-linking agents can be considered if the foam produced in the first generation fails to achieve the required rigidity. Starch is often added as a polyol or a cross-linking agent as it has more than two hydroxyl groups per repeating anhydroglucose unit (Dae-Hyun *et al.*, 2007). Owing to its complete biodegradability, its abundance in nature and its very low cost, starch is a promising candidate for sustainable polymer foaming. However, the hydrophilic property of starch will increase the foam water absorption capacity, which is undesirable in the sportswear application. A study from Koenig and Huang showed that this limitation could be overcome by (i) the blending of starch with hydrophobic synthetic polymers or (ii) the addition of plasticised starch which has its hydrogen bonds between starch molecules cleaved or destructurised (Koenig and Huang, 1995).

On the other hand, glycerol is also a biodegradable and low toxic additive. Being a short-chain molecule with three hydroxyl groups, it is a great solvent for the polymer which enhances the miscibility of the mixture with water. The viscosity of starch increases with increasing temperature and cross-linking density, which is undesirable for bubble growth. Hence with the addition of glycerol, besides acting as a cross-linker, it is also a plasticiser and flexibiliser in the starch-based polymer which helps to reduce the overall viscosity of mixture (ScienceDirect, 2020). This is consistent with the findings of Thuy *et al.* where increasing the glycerol content up to 20 w/w% yielded a relatively softer foam, where at 50 w/w% the foam became friable (Thuy, Vuong and Duc, 2020).

In the study of Dae Hyun *et al.*, it was found that the addition of starch and glycerol in the mixture enhanced the rigidity, impact resistance and compressive strength (Dae-Hyun *et al.*, 2007). However, the foam produced in his study failed to achieve our desired compressive strength, possibly due to the use of PEG with M_n of 8818 $gmol^{-1}$. Hence, the use of lower M_n PEG is expected to increase compressive strength.

To start off, PEG 300 can be used in conjunction with starch and glycerol as the cross-linker. Similar chemicals and steps could be adapted from the previous generation while varying R ratio between 0.9 to 1.3 (Equation 5). A mass ratio of PEG: glycerol: BDO is fixed at 8: 1: 1 in all trial runs while the starch weight percentage in this polyol mixture is varied between 10 w/w % to 40 w/w %. In the case when the foam fails to display the required rigidity, PEG of lower M_n can be used to replace PEG 300 and similarly if the foam were to be too rigid, higher M_n PEG can be employed instead.

Preparation for Second Generation

The following steps are adapted from the study done by Dae Hyun *et al.* (Dae-Hyun *et al.*, 2007). All the materials suggested can be obtained from Sigma-Aldrich. Polyols (PEG, corn starch containing 25-30% amylose content, glycerol and BDO) are mixed and heated to 100 °C under a continuous stirring for 1 h to fully gelatinized starch. The gelatinisation of starch will result in greater starch dispersion which leads to higher compressibility strength of the blend (Kim, Choi and Park, 2000). The mixture is then cooled to 40°C. DBTL and water within the range allowed are added and stirred for 1 min, before TDI is added. The remaining steps from the previous generation can be followed.

Soluble starch (100% amylose content) can be employed instead of corn starch to carry out the mixing at a lower temperature. The operating details can be found in the third-generation analysis. The temperature treatment for starch varies with its amylose content. In gelatinization, corn starch requires higher temperature treatment to break down the granular structure due to its significantly higher content of amylopectin. Amylopectin is a highly branched and bigger molecule as compared to amylose. Thus it requires more energy to unfold amylopectin double helices during gelatinisation (Ratnayake and Jackson, 2006). Despite the high processing temperature, amylopectin molecules have a higher tendency to be cross-linked (Wongsagonsup *et al.*, 2014). This together with the cost of material should be factored in when selecting the suitable starch.

$$R\ value\ = \frac{\frac{TDI\ (g) \times 2}{174}}{\frac{H20\ (g) \times 2}{18} + \frac{PEG\ (g) \times 2}{(M_n \text{ of } PEG)} + \frac{Starch(g) \times 3}{162} + \frac{Glycerol(g) \times 3}{92}} \quad (5)$$

Third Generation

This generation mainly aims to study the effect of triol polyol to produce a rigid foam. Polycaprolactone triol (PCLt) is commonly used for its biodegradability due to its low melting point (~60 °C), which is the conventional temperature used during composting (Jiang and Zhang, 2013). Triol functional group of PCLt enables more urethane bonds to be formed, thus giving rise to harder segments. Moreover, PCLt (M_n = 300 $gmol^{-1}$) has OH values between 304 -583 mg KOH/g which falls into the optimal OH value range of a rigid foam.

The study done by Roberta et al. has proven that the foam made of PCLt and hexamethylene diisocyanate (HDI) has the desirable mechanical performance, registering 0.96 MPa of compressive strength at the starch composition of 20% by weight (Roberta Alfani, Salvatore Iannace, 1997). To further improve on its compressive strength, TDI is suggested to replace HDI. This is because TDI has the aromatic rings which contribute to the hard segments while HDI has aliphatic chains which behave more like the soft segments (Kwon *et al.*, 2007).

To start off, PCLt and starch are used while similar steps and chemicals with proposed compositions could be

adapted from Table 2 except for BDO. The triol functionality of PCLt enables sufficient formation of urethane bonds without the contribution from BDO. Starch weight percentage in polyol mixture is varied between 10 w/w % to 40 w/w % and R value between 0.9 to 1.3 is varied using Equation 6. In the scenario when the foam is too rigid, PEG 200 could be added as a plasticizer due to its lower viscosity. Besides, it is also more miscible with starch due to its hydrophilicity property. Consequently, it increases the mobility of starch chains thus enhances the foam flexibility (Kim, Choi and Park, 2000). On the other hand, BDO could be added if a soft foam is produced.

$$R\ value = \frac{\frac{TDI\ (g) \times 2}{174}}{\frac{H20\ (g) \times 2}{18} + \frac{PCLt\ (g) \times 3}{300} + \frac{Starch\ (g) \times 3}{162}} \quad (6)$$

Preparation for Third Generation

The following steps are adapted from the study done by Roberta *et al.* (Roberta Alfani, Salvatore Iannace, 1997). All the materials suggested can be obtained from Sigma-Aldrich. Soluble starch containing 100% amylose content (Sigma, 2020) and PCLt are mixed at 55 °C and stirred for 5 min before silicone oil, water and DBTL are added subsequently. TDI is then added and stirred for a few seconds until the liquid starts to whiten. The mixture is then quickly poured to fill up half of the mould and is stored in the oven for 1 h at 55°C to enable reaction completion. It is then cured under room temperature for 24 h before it is ready for characterisation.

Characterization methods

PUF with a density lower than silicone or more specifically lower than 1.3 g cm^{-3} is desired. The conventional way of determining density can be adopted where the volume and weight of the foam are measured. Otherwise, the density could be more accurately measured by using a pycnometer. PUF can be cut into several specimens to measure the average density.

Foam compressive strength between 0.5 to 5.0 MPa is desired. Lloyds instruments universal testing machine (EZ50) with the compression mode could be used to determine the maximum stress each foam could withstand. Ballistic tests could also be conducted to estimate the impact energy absorbed by the foam at different ball launch speeds which is a replication of the high-risk sports (Rouhani *et al.*, 2019).

Thermal-physiological comfort of the PUF can be assessed based on its air permeability. This can be analysed by the means of electronic high differential pressure method. The wettability properties of the PUF surface is a measure of its hydrophobicity. Imagine processing technique like a drop analyser test is used to determine the contact angle between the PUF surface and a water droplet.

Contact angle surface analysis can be requested at https://imperiallondon.sharepoint.com/sites/foe/ChemicalEngineering/ServiceReq/SitePages/Home.aspx .

When different chemicals are used, scanning electron microscope (SEM) can be used to study foam morphology which includes the cell size distribution and skin thickness. Cell size could affect both the water absorption ability and density of PUF. When cell size is larger, broken and interconnected, it tends to have a higher water absorption ability. On the other hand, smaller cell size increases foam density and uneven cell structure might lead to degradation in mechanical properties (Thirumal *et al.*, 2008).

Recommendations

Auxetic Material

Auxetic materials are becoming more popular for their high tolerance to indentation and resilience to fracture properties. Having a negative Poisson ratio (NPR) allows them to expand laterally in one or many perpendicular directions when extended axially. In simpler term, it becomes thicker when it is being stretched, hence rendering them resistance to impact (Nallavan, 2020). This is consistent with the study done by Foster *et al.* which shows that the helmet containing auxetic foam in replacement for conventional foam has lower severity indices under impact test (Foster *et al.*, 2018).

The multi-axial expansion and double curvature traits provide extra comforts and have great mechanical properties. Under impact loading test, there is an even distribution of stress over the surface which consequently leads to the bottom layers of the auxetic material to experience smaller impact. However, for non-auxetic material, it exhibits greater stress in the centre. This implies that the energy is not attenuated, thus the wearer is more prone to receive the energy upon impact (Yang, Vora and Chang, 2018).

Auxetic PUF is considered as it can be manufactured from the conventional flexible PUF via the thermal-mechanical process. As proposed by Lakes et al, triaxial compression is exerted on PUF to partially buckle the cell struts and induce re-entrant morphology. Under compression state, heating above the softening temperature of the polymer is conducted which is then followed by cooling to fix the structure. Different auxetic properties could be achieved depending on the type of PUF and the process parameters including temperature, compression ratio and time (Li and Zeng, 2016).

Shear Thickening Fluid (STF)

STF is a concentrated colloidal silica suspension which changes from a honey-like liquid to a solid material almost instantly and reversibly upon impact. This is due to large increase in apparent viscosity above a critical shear rate. Due to the large energy absorption during phase transition and its recyclability, STF is a suitable impact absorbing material in body armour and personal protection equipment in sports.

STF is normally encapsulated either in a rigid body or in a soft body foam which provides a 3-D shape to the STF. Encapsulation is necessary to prevent the leakage of STF due to its liquid state at rest. Besides, ethylene

glycol (EG) is the main carrier fluid in STF which is very sensitive to the change in humidity due to its hydrophilic property. By encapsulating STF, it eliminates the humidity issue associated with EG.

A vacuum pump could be used to create pressure difference for STF to infiltrate the foam. The STF-foam is then coated with silicone to prevent the leakage and evaporation of STF (Soutrenon and Michaud, 2014).

Warp-knitted Spacer Fabrics (WKSF)

Warp-knitted spacer fabric (WKSF) is a 3-D knitted fabric which comprises two independent fabric layers connected with pile yarns. Under compression, the pile yarns act as a linear spring to distribute the surface pressure and to provide a great cushioning effect (Miao and Ge, 2008). Compressive strength of spacer fabric is closely related to the type of spacer yarn used and its cross-thread density. Generally, a coarser yarn and lower cross-thread density result in a greater energy absorption ability (Velosa *et al.*, 2012).

The space between the two outer layers also enhances the air permeability and breathability, which are the desired properties in the sportswear industry to provide the thermal-physiological comfort (Xiaohua, Hong and Xunwei, 2008). On top of that, WSKF is a recyclable material and has a lower cost as compared to PUF. These factors drive the trend of WSKF in replacing the conventional PUF in automobile cushioning textiles such as dashboard covers and car seat padding.

WKSF can be treated with a shear thickening fluid to offer extra energy absorption and damping properties (Wardiningsih, Troynikov and Fuss, 2015). The leakage issue of STF can be solved by encapsulating the fabrics with a heat-sealed polyethylene film (Lee, Wetzel and Wagner, 2003).

Moreover, the integration of WKSF in PUF offers enhanced compressive strength through the formation of a sandwich-structured composite. The incorporation of WKSF in PUF was found to improve its compressive strength by 107% as compared to PUF alone and it also achieved a maximum energy absorption of 90% (Wang *et al.*, 2019). The composite consists of two faces of spacer fabrics separated by a foam core. The composite is produced by impregnating WKSF with PUF via reaction injection moulding method (Helbig *et al.*, 2015). The recyclability and biodegradability of the composite are highly dependent on the raw materials employed in manufacturing WSKF and PUF.

Conclusion

This study is to design viable experiments and to investigate the various factors involved to produce a rigid and lightweight polyurethane foam (PUF). To be incorporated in sportswear clothing, the foam density lower than 1.3 g cm^{-3} is favoured. Shock absorbance performance could be associated with the foam compressive strength, which ideally falls between 0.5 to 5.0 MPa.

The general approach of the experimental planning is to improve on the PUF properties derived from polyethylene glycol (PEG) which was produced in the previous year. Hence, PEG is incorporated in the first generation as the main polyol. Optimal ranges of average OH values (350 -800 mg KOH/g) and number average molecular weight (300 – 1000 $gmol^{-1}$) are required to produce a rigid PUF. Such conditions should be taken into considerations in selecting the suitable polyol and in deciding the blend of the main polyols.

To further improve from the first generation, the role of cross-linkers can be studied in the second generation. Starch and glycerol are suggested to promote extra bond formations and thus increases its rigidity and compressive strength. On the other hand, the third generation explores the effect of triols on foam rigidity. Polycaprolactone triol (PCLt) could improve the cross-linking density with its triol functionality. The use of PCLt which is a biodegradable polymer enables a greener and more sustainable polymer foaming.

A relatively smooth foam surface with regular cell sizes is desired to improve its aesthetic values. Thus, a surfactant is suggested to address the irregularity of cell size. Impact resistance property could be enhanced by the modifications of a conventional PUF into an auxetic foam due to its negative Poisson ratio (NPR). The impregnation of PUF with shear thickening fluid (STF) and the sandwich-structured composite made of warp-knitted spacer fabrics (WKSF) and PUF can be considered too to improve the foam compressive strength.

Acknowledgements

The authors would like to offer gratitude to Kiren Passi for the inspirations for this research.

References

Abdel Hakim, A. A. *et al.* (2011) 'Preparation and characterization of rigid polyurethane foam prepared from sugar-cane bagasse polyol', *Materials Chemistry and Physics*. Elsevier B.V., 129(1–2), pp. 301–307. doi: 10.1016/j.matchemphys.2011.04.008.

Altan, M. (2016) 'Thermoplastic Foams: Processing, Manufacturing, and Characterization', *Intech*, (tourism).

Barzegari, M. R. and Rodrigue, D. (2009) 'The effect of injection molding conditions on the morphology of polymer structural foams', *Polymer Engineering & Science*, 49(5), pp. 949–959. doi: 10.1002/pen.21283.

Cekada, J. *et al.* (1964) *Plastic Mold Releases*.

Dae-Hyun, K. *et al.* (2007) 'Structural, Thermal, and Mechanical Properties of Polyurethane Foams Prepared with Starch as the Main Component of Polyols', *Fibers and Polymers*, 8(2), pp. 155–162.

David, J. *et al.* (2010) 'Development of novel environmental friendly polyurethane foams', *Environmental Chemistry Letters*, 8(4), pp. 381–385. doi: 10.1007/s10311-009-0236-8.

Delpech, M. C. and Coutinho, F. M. B. (2000)

'Waterborne anionic polyurethanes and poly(urethane-urea)s: Influence of the chain extender on mechanical and adhesive properties', *Polymer Testing*. Elsevier Science Ltd, 19(8), pp. 939–952. doi: 10.1016/S0142-9418(99)00066-5.

Drobny, J. G. (2014) *Polymeric Foam - an overview | ScienceDirect Topics*. Available at: https://www.sciencedirect.com/topics/engineering/polymeric-foam (Accessed: 30 October 2020).

Foster, L. *et al.* (2018) 'Application of auxetic foam in sports helmets', *Applied Sciences (Switzerland)*, 8(3), pp. 1–12. doi: 10.3390/app8030354.

Furtwengler, P. and Avérous, L. (2018) 'Renewable polyols for advanced polyurethane foams from diverse biomass resources', *Polymer Chemistry*. Royal Society of Chemistry, pp. 4258–4287. doi: 10.1039/c8py00827b.

Geddes, D. (2016) *PU Foams in Sport and Leisure Applications - Technical Foam Services*. Available at: https://tinyurl.com/yyjsbhcw (Accessed: 2 November 2020).

Grand Review Research (2019) *Polyurethane Market Size Worth $105.2 Billion By 2025*. Available at: https://www.grandviewresearch.com/press-release/global-polyurethane-pu-market (Accessed: 30 October 2020).

Heiss, H. L. *et al.* (1954) 'Preparation of Polymers from Diisocyanates and Polyols', *Industrial & Engineering Chemistry*, 46(7), pp. 1498–1503. doi: 10.1021/ie50535a052.

Helbig, F. *et al.* (2015) 'Flexible Spacer Fabrics for Reinforcement of Rigid', (July), pp. 19–24.

Hyung CHOE, K. *et al.* (2004) 'Properties of Rigid Polyurethane Foams with Blowing Agents and Catalysts', *Polymer Journal*, 36(5), pp. 368–373. doi: 10.1295/polymj.36.368.

Iylia Ismail and Swee Kee Hoo (2019) 'Designing polyurethane foams aimed at sportswear market', *Department of Chemical Engineering, Imperial College London, U.K.*

Jackovich, D. *et al.* (2005) 'Temperature and Mold Size Effects on Physical and Mechanical Properties of a Polyurethane Foam', *Journal of Cellular Plastics*. Sage PublicationsSage CA: Thousand Oaks, CA, 41(2), pp. 153–168. doi: 10.1177/0021955X05051739.

Javni, I., Zhang, W. and Petrović, Z. S. (2003) 'Effect of different isocyanates on the properties of soy-based polyurethanes', *Journal of Applied Polymer Science*, 88(13), pp. 2912–2916. doi: 10.1002/app.11966.

Jiang, L. and Zhang, J. (2013) 'Biodegradable Polymers and Polymer Blends', in *Handbook of Biopolymers and Biodegradable Plastics: Properties, Processing and Applications*. Elsevier Inc., pp. 109–128. doi: 10.1016/B978-1-4557-2834-3.00006-9.

Jin, F. L. *et al.* (2019) 'Recent trends of foaming in polymer processing: A review', *Polymers*. MDPI AG. doi: 10.3390/polym11060953.

Kausar, A., Zulfiqar, S. and Sarwar, M. I. (2013) 'High performance segmented polyurethanes derived from a new aromatic diisocyanate and polyol', *Polymer Degradation and Stability*, 98(1), pp. 368–376. doi: 10.1016/j.polymdegradstab.2012.09.004.

Kim, C. H., Choi, E. J. and Park, J. K. (2000) 'Effect of PEG molecular weight on the tensile toughness of starch/PCL/PEG blends', *Journal of Applied Polymer Science*, 77(9), pp. 2049–2056. doi: 10.1002/1097-4628(20000829)77:9<2049::AID-APP22>3.0.CO;2-C.

Kim, S. H. and Kim, B. K. (2008) 'Effect of Isocyanate Index on the Properties of Rigid Polyurethane Foams Blown by HFC 365mfc', 16(5), pp. 467–472.

Koenig, M. F. and Huang, S. J. (1995) 'Biodegradable blends and composites of polycaprolactone and starch derivatives', *Polymer*, 36(9), pp. 1877–1882. doi: 10.1016/0032-3861(95)90934-T.

Kurańska, M. *et al.* (2018) 'The influence of blowing agents type on foaming process and properties of rigid polyurethane foams*)', 672(10). doi: 10.14314/polimery.2018.10.2.

Kwon, O.-J. *et al.* (2007) 'Characterization of Polyurethane Foam Prepared by Using Starch as Polyol Oh-Jin', *Journal of Applied Polymer Science*, 116(5), pp. 2658–2667. doi: 10.1002/app.

Lee, Y. S., Wetzel, E. D. and Wagner, N. J. (2003) 'The ballistic impact characteristics of Kevlar woven fabrics impregnated with a colloidal shear thickening fluid', 8, pp. 2825–2833.

Li, J. *et al.* (2017) 'The Use of Lignin as Cross-linker for Polyurethane Foam for Potential Application in Adsorbing Materials', 12, pp. 8653–8671.

Li, Y. and Zeng, C. (2016) 'On the successful fabrication of auxetic polyurethane foams: Materials requirement, processing strategy and conversion mechanism', *Polymer*. Elsevier Ltd, 87, pp. 98–107. doi: 10.1016/j.polymer.2016.01.076.

Luo, Y. *et al.* (2018) 'Effect of crosslinking agent on properties and morphology of water-blown semirigid polyurethane foam', *Journal of Applied Polymer Science*, 135(42), pp. 1–11. doi: 10.1002/app.46753.

Marciano, J. H., Rojas, A. J. and Williams, R. J. J. (1982) 'Curing kinetics of a rigid polyurethane foam formulation', *Polymer*, 23(10), pp. 1489–1492. doi: 10.1016/0032-3861(82)90250-6.

Markets, M. (2020) *Polymer Foam Market Global Forecast to 2025*. Available at: https://tinyurl.com/y6zze5bg (Accessed: 31 October 2020).

Miao, X. H. and Ge, M. Q. (2008) 'The compression behaviour of warp knitted spacer fabric', *Fibres and Textiles in Eastern Europe*, 16(1), pp. 90–92.

Modesti, M. and Lorenzetti, A. (2001) 'Experimental method for evaluating isocyanate conversion and trimer formation in polyisocyanate-polyurethane foams', *European Polymer Journal*, 37(5), pp. 949–954. doi: 10.1016/S0014-3057(00)00209-3.

Nallavan, G. (2020) 'Impact of recent developments in fabrication of auxetic materials on safety and protection in sport', *AIP Conference Proceedings*, 2271(September). doi: 10.1063/5.0024805.

Park, D. H. *et al.* (2013) 'Effects of isocyanate index and environmentally-friendly blowing agents on the morphological, mechanical, and thermal insulating properties of polyisocyanurate-polyurethane foams', *Macromolecular Research*, 21(8), pp. 852–859. doi: 10.1007/s13233-013-1106-6.

Polymerdatabase (2020) *Properties of Polyurethane*. Available at: https://polymerdatabase.com/polymer classes/Polyurethane type.html (Accessed: 4 November 2020).

Ramesh, S., Rajalingam, P. and Radhakrishnan, G. (1991) 'Chain-extended polyurethanes—Synthesis and characterization', *Polymer International*, 25(4), pp. 253–256. doi: 10.1002/pi.4990250409.

Ratnayake, W. S. and Jackson, D. S. (2006) 'Gelatinization and solubility of corn starch during heating in excess water: New insights', *Journal of Agricultural and Food Chemistry*, 54(10), pp. 3712–3716. doi: 10.1021/jf0529114.

Roberta Alfani, Salvatore Iannace, L. N. (1997) 'Synthesis and Characterization of Starch-Based Polyurethane Foams'. Available at: https://pubs.acs.org/sharingguidelines.

Romano, G. (2019) *Polyurethane vs Polyethylene Foam: What's the Difference Between Them?* Available at: https://tinyurl.com/yywotf9a (Accessed: 30 October 2020).

Rouhani, H. *et al.* (2019) 'The Effectiveness of Protective Headgear in Attenuating Ball-to-Forehead Impacts in Water Polo', *Frontiers in Sports and Active Living | www.frontiersin.org*, 1(2). doi: 10.3389/fspor.2019.00002.

ScienceDirect (2020) *Glycerol - an overview*. Available at: https://tinyurl.com/y44mb2sh (Accessed: 19 November 2020).

Septevani, A. A. *et al.* (2015) 'A systematic study substituting polyether polyol with palm kernel oil based polyester polyol in rigid polyurethane foam', *Industrial Crops and Products*. Elsevier, 66, pp. 16–26. doi: 10.1016/j.indcrop.2014.11.053.

Sharmin, E. and Zafar, F. (2012) 'Polyurethane: An Introduction', *Polyurethane*, pp. 3–16. doi: 10.5772/51663.

Sigma (2020) *sigma-aldrich.com*. Available at: https://tinyurl.com/yxqsuurb (Accessed: 20 November 2020).

Sivertsen, K. (2007) *POLYMER FOAMS 3.063 Polymer Physics Spring 2007*.

Soutrenon, M. and Michaud, V. (2014) 'Impact properties of shear thickening fluid impregnated foams', *Smart Materials and Structures*, 23(3). doi: 10.1088/0964-1726/23/3/035022.

Takamtsu, F. M. & K. (1999) 'Effects of Amine Catalysts on Structure of Polyurethane Foams', *Elastomer*, 34, pp. 285–291.

Thirumal, M. *et al.* (2008) 'Effect of foam density on the properties of water blown rigid polyurethane foam', *Journal of Applied Polymer Science*, 108(3), pp. 1810–1817. doi: 10.1002/app.27712.

Thirumal, M. *et al.* (2009) *Morphological and Thermal Properties of Rigid Polyurethane Foam: Effect of Chain Extender, Polyol and Blowing Agent*, *Cellular Polymers*.

Thuy, N. T., Vuong, T. Q. and Duc, V. M. (2020) 'Effects of glycerol and NCO/OH on rigid polyurethane foam based on bio-polyol of rubber seed oil using water as blowing agent', *Vietnam Journal of Chemistry*, 58(3), pp. 392–397. doi: 10.1002/vjch.202000008.

Velosa, J. C. *et al.* (2012) 'Mechanical behavior of novel sandwich composite panels based on 3D-knitted spacer fabrics', *Journal of Reinforced Plastics and Composites*, 31(2), pp. 95–105. doi: 10.1177/0731684411431354.

Wang, H. *et al.* (2019) 'Spacer fabric/flexible polyurethane foam composite sandwiches: Structural design and quasi-static compressive, bursting and dynamic impact performances', *Journal of Sandwich Structures and Materials*. doi: 10.1177/1099636219859629.

Wardiningsih, W., Troynikov, O. and Fuss, F. K. (2015) 'Energy absorption and performance relevant to thermal wear comfort evaluation of existing impact protective pad and materials intended for impact protective pad', *Procedia Engineering*. Elsevier B.V., 112(December), pp. 122–127. doi: 10.1016/j.proeng.2015.07.186.

Wongsagonsup, R. *et al.* (2014) 'Effect of cross-linking on physicochemical properties of tapioca starch and its application in soup product', *Carbohydrate Polymers*. Elsevier Ltd., 101(1), pp. 656–665. doi: 10.1016/j.carbpol.2013.09.100.

Xiaohua, Y., Hong, H. and Xunwei, F. (2008) 'Development of the warp knitted spacer fabrics for cushion applications', *Journal of Industrial Textiles*, 37(3), pp. 213–223. doi: 10.1177/1528083707081592.

Yang, C., Vora, H. D. and Chang, Y. (2018) 'Behavior of auxetic structures under compression and impact forces', *Smart Materials and Structures*. IOP Publishing, 27(2). doi: 10.1088/1361-665X/aaa3cf.

Mathematical Modelling of Targeted Thrombolysis by a Multifunctional Nanomedicine: Effects of Clot Length and Coarseness on Recanalization Time

Michael Pratt and Jonathan Reading

Department of Chemical Engineering, Imperial College London, United Kingdom

Abstract

Acute ischaemic strokes occur when an artery to the brain is occluded by a blood clot. The use of thrombolytic agents, such as tissue plasminogen activator (tPA), is a common treatment method however this can sometimes be ineffective and is limited by the risk of intracerebral haemorrhage (ICH). Previous works have developed a 1D mathematical model for intravenous thrombolysis using free tPA and established a functional activated-platelet-sensitive nanocarrier for the targeted delivery of tPA. This paper presents the unification of these works with the development of a computational model for targeted thrombolysis using a multifunctional nanomedicine. The effect of clot length and coarseness on recanalization time, spatial and temporal concentrations of fibrinolytic species were investigated for a clot in the middle cerebral artery (MCA). It was found that clot lysis time increased with increasing clot length for both models. The nano-particle model exhibited that increased coarseness lead to decreased recanalization time for finer clots. However, for very coarse clots a slower rate of dissolution at the clot front resulted in increased complete recanalization time. The results present a lower recanalization time of nano-particles compared to free tPA and the minimisation of ICH effects.

1 Background

Acute ischaemic stroke (AIS) is one of the leading causes of death and disability in the world [1]. It is the most common type of stroke and occurs when a cerebral artery is occluded with a blood clot, diminishing or halting blood supply to the brain. Ischaemic strokes can be treated via thrombolysis, whereby a fibrinolytic agent is intravenously administered to patients to dissolve the blood clot and restore cerebral blood flow [2]. The use of fibrinolytic agents is limited due to safety concerns regarding the possibility of severe side effects such as intracerebral haemorrhage (ICH) [3]. There are numerous available thrombolytic agents however alteplase, a recombinant tissue plasminogen activator (tPA), is currently the most common agent because its high fibrin specificity somewhat mitigates haemorrhagic complications[4]. Furthermore, the effectiveness of thrombolytic treatment is dependent on many properties such as clot specificity (location, size and composition) and drug dosage regimens [5, 6, 7]. Current thrombolytic therapy involves intravenous infusion of tPA at 0.9mg/kg distributed as a 10% initial 1-minute bolus followed by continuous 1-hour infusion of the remaining 90% [8]. This continuous infusion and high dosage are required to maintain sufficiently high tPA concentrations due to its short half-life [9].

A number of studies have been undertaken to investigate the optimum dosage of tPA for AIS using mathematical models considering the previous approved dosage for treating AIS was determined based on clinical outcomes, such as Rankin Scale and NIHSS [8, 10, 11]. Piebalgs et al. proposed a mathematical model evaluating clot lysis patterns for a given therapeutic regimen in a patient-specific geometry reconstructed from CT scans. Three dose levels were explored by coupling a 3D thrombolysis model with a compartmental model for clots of two distinct fibrin conformations (coarse and fine) and concluded shorter recanalization times for coarse clots with a higher dosage [6]. Gu et al. developed a less computationally intense 1D model based on Piebalgs findings and reported clot lysis performance of 12 dosage regimens based on the degradation of fibrin binding sites [5]. Another 3D-compartmental coupled study [7] further investigated lysis performance for varying clot length and position in the middle cerebral arteries (MCA) however it is advantageous to

investigate performance of regimens on varying clot lengths and conformation for a less computationally intense 1D model.

To minimise ICH and off-targets of thrombolysis from current treatments, various efforts have been made that allow for thrombus-targeted delivery and controlled local release of thrombolytic drugs. Attempts have been made to improve the half-life of tPA by PEGylation or encapsulation in order to achieve sufficient drug accumulation for effective clot specificity and breakdown [12, 13, 14]. Poly(lactic-co-glycolic acid)-based, shear-active nanotherapeutics [15] and the use of magnetically-activated nanomotors [16] have been explored however these systems would be difficult to implement in a clinical setting. Other investigations have focused on characteristics of the thrombus site [17, 18, 19] of which GPIIb-IIIa ($\alpha_{IIb}\beta_3$) integrins on activated platelets are most attractive. Normally, $\alpha_{IIb}\beta_3$ integrins are inactive on resting platelets however become abundantly expressed and activated (40,000-80,000 per platelet) on the platelet surface when thrombus formation occurs [20, 21]. In this vein, Huang et al. reported an activated-platelet-sensitive nanoparticle using PEGylated liposome coated with a conformationally-constrained, cyclic RGD (cRGD) peptide [22]. This nanoparticle is a promising candidate for targeted thrombolytic therapy with minimal side effects due to its higher specificity and affinity for $\alpha_{IIb}\beta_3$ integrins compared to linear RGD structures [12].

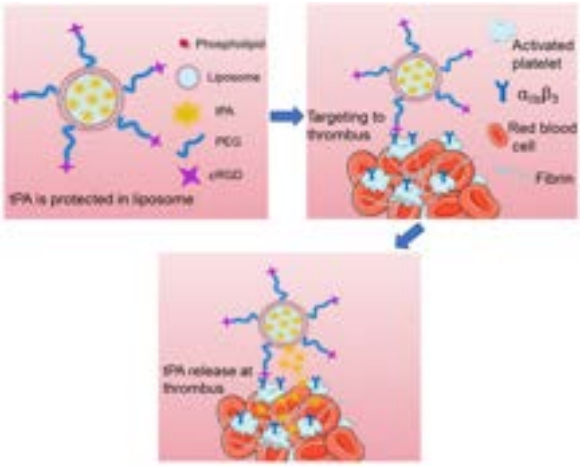

Figure 1: Schematic showing targeted drug delivery using nano-particles [12]

2 Introduction

In this study, we present a less computationally intensive mathematical modelling framework for simulation of thrombolytic therapy for the treatment of AIS. This is achieved through the use and development of the Gu et al. multiscale model [5]. The model includes (i) the systemic circulation and effects of tPA on plasma proteins (systemic pharmacokinetics and pharmacodynamics (PKPD)) and (ii) clot lysis at the clot site (local PD). This paper has produced computational simulations for thrombolytic treatment in ischaemic stroke by varying clot conformation and size for a fully occluding clot in the M1 segment of the middle cerebral artery of an 80kg man. Various dosage regimens proposed in the works of Gu et al. [5] are explored for each parameter, one at a time, in the 1D model. The effectiveness of the lysis treatment is measured by the lysis completion time. The risk of ICH is monitored by the plasma concentration of fibrinogen in accordance with Vandelli et al. findings [23]. Furthermore, this study explores the development of the 1D model described above to account for encapsulated tPA in arginine–glycine–aspartic acid (RGD)-coated nanoparticles as described in Huang et al. [22]. The model reflects changes in (i) the removal of systemic PKPD model, (ii) nanomedicine transport and (iii) addition of selective targeting of activated platelets and triggered tPA release at the clot site. The nanoparticle performance is compared to free tPA equivalent dose for varying clot conformation and size. Once validated, this computational model can be further used for efficient optimisation of nanoparticle dosage for other varying clot parameters.

3 Methods

3.1 Overview of Existing Computational Model

The compartmental model was used to simulate the movement of tPA through the body (pharmacodynamics) and the body's biological response to tPA (pharmacokinetics) and consists of two compartments, the central compartment, and the peripheral compartment. The tPA is administered intravenously into the central compartment, which contains six fibrinolytic proteins (plasmin (PLS), plasminogen (PLG), fibrinogen (FBG), $\alpha 2$ – antiplasmin (AP), $\alpha 2$ – macroglobulin (MG) and plasminogen activator inhibitor type 1 (PAI)) and characterises the plasma. The peripheral compartment consists of tissues where drug distribution is much slower. The drug (tPA) is exchanged between the central and peripheral compartment whilst the fibrinolytic proteins are assumed to remain only in the compartmental model as the plasma concentrations of these species are expected to change insignificantly.

The compartmental model was then used to solve the temporal concentrations of tPA and the six fibrinolytic proteins for different tPA dosage regimens which were then inputted into the local pharmacodynamics model.

In the local pharmacodynamics model, blood flow, species transport and clot dissolution were modelled to be 1D and unidirectional. In this study, treating the blood clot as a porous medium, the volumetric flowrate of blood was calculated using Darcy's law and the temporal and spatial variations of the proteins and tPA in the free phase were resolved using the 1D convection-diffusion-reaction equations. Temporal concentrations for bound phase species were resolved using the rate equations for bound phase reactions and extent of clot lysis was determined.

3.2 Modelling Strategy

The model developed by Gu et al. was used as a foundation for the development of the nano-particle model however, the compartmental model did not need to be included as tPA is now encapsulated within the nano-particles and the systemic effects of tPA are therefore negligible. In this study initial and inlet concentrations are specified by the user in the local pharmacokinetic-pharmacodynamic model. Similar to the previous study, the blood flowrate was calculated using Darcy's law, convection-diffusion-reaction equations were used to determine temporal and spatial concentrations and bound phase rate equations were used to resolve temporal and spatial concentrations for the bound species. A schematic of the modelling strategy is outlines in section A.4 of the supplementary materials.

3.3 Nano-Particle Model

3.3.1 Clot Properties

The key difference between the model developed in this study compared to the model presented in *Pharmaceutics* [5], is the use of encapsulated tPA within nano-particles for targeted thrombolysis. In this model, the clot is simplified to consist of a network of fibrin fibres with activated platelets uniformly distributed throughout. Integrins are present on the surface of activated platelets and react with the nano-particles to release tPA. To account for the presence of platelets, the total initial volume fraction of the clot and the void fraction were calculated using the following equations:

$$\Phi_{tot,0} = \Phi_{p,0} + \Phi_{f,0} \tag{1}$$

$$\epsilon_{tot,0} = 1 - \Phi_{tot,0} \tag{2}$$

Where $\Phi_{p,0}$ and $\Phi_{f,0}$ represent the initial volume fraction occupied by activated platelets and fibrin respectively. The initial concentrations of activated platelets and integrins were determined using the following equations:

$$C_{PLT,0} = \frac{P_{max}\Phi_{p,0}}{N_{AV}} \tag{3}$$

$$C_{INT,tot,0} = N_{INT}C_{PLT} \tag{4}$$

Where P_{max} is the maximum packing density for platelets, N_{AV} is Avogadro's number, and N_{INT} is the number of integrins per platelet. Platelets are assumed to be fixed in the space occupied by the clot and remain fixed in place as the clot breaks down.

3.3.2 Flow, Transport and Clot Lysis

The volumetric flowrate of the blood, Q, was calculated using Darcy's law for flow through a porous medium:

$$Q = \frac{k_{clot}}{\mu}\Delta P_x \tag{5}$$

Where μ is the fluid viscosity, ΔP_x is the pressure drop across the clot and k_{clot} is the clot permeability. To account for the presence of activated platelets, the definition for the permeability constant, k_{clot} was adjusted:

$$\frac{1}{k_{clot}} = \frac{1}{k_p} + \frac{1}{k_f} \tag{6}$$

$$\frac{1}{k_p} = \frac{150\Phi_p^2}{S_p^2 D_p^2(1-\Phi_p)^3} \tag{7}$$

$$\frac{1}{k_f} = \frac{16\Phi_f^{1.5}(1+56\Phi_f^3)}{R_f^2} \tag{8}$$

Where k_p and k_f are the permeability constants for platelets and fibrin respectively, S_p is the sphericity, R_f is the fibrin fibre radius, and D_p is the platelet diameter.

Flow velocity was then calculated from the volumetric flowrate and used in the convection-diffusion-reaction equations to resolve temporal and spatial concentrations of the plasma proteins and tPA.

$$\frac{\partial C_i}{\partial t} = -U\frac{\partial C_i}{\partial x} + D_i\frac{\partial^2 C_i}{\partial x^2} + R_i \tag{9}$$

Where C_i and R_i are the concentration and reaction source terms of species i. Whilst the convection-diffusion-reaction equations remained unchanged

from previous work [5], the introduction of nano-particles into the 1D model required consideration of a further five free species and reaction terms. It is expected that the reaction of nano-particles with integrins is a highly complex mechanism and consequently is not comprehensively understood [22]. For the sake of simplicity, the interactions were modelled by the following four reactions. A summary of the nano-particle reactions can be found in Table 1.

Table 1: Nano-particle Release Mechanism

No.	Reaction
1	$NP + INT \rightleftharpoons NP^{INT}$
2	$NP^{INT} \longrightarrow v_{rel}tPA + NP^{INT}_{empty}$
3	$NP_{empty} + INT \rightleftharpoons NP^{INT}_{empty}$
4	$NP \rightleftharpoons v_{rel}tPA + NP_{empty}$

Reaction 1 represents the adsorption and desorption of the nano-particles to and from the integrin binding sites. The destabilised integrin-nano-particle complex then releases tPA via reaction 2 where v_{rel} is equal to the moles of tPA per mole of NP. It is assumed that each nano-particle releases all of its encapsulated tPA. The empty nano-particles (NP_{empty}) continue to bind to integrins (reaction 3) which reduces the number of available integrin binding sites. Finally, reaction 4 accounts for drug leakage via diffusion.

The number of bound species considered remains unchanged from previous studies [6] as does the clot lysis model. The temporal concentrations of bound species were resolved using the rate equations:

$$\frac{\partial n_j}{\partial t} = R_j^{clot} \tag{10}$$

Where n_j and R_j^{clot} are the concentrations and reaction source terms of bound species j. To monitor the breakdown of the clot, extent of lysis was calculated and once the value exceeded the critical extent of lysis, $E_{L,crit}$, the thrombus was considered to be broken down. Details of all model equations used can be found in section A.5 of the supplementary material.

3.4 Implementation of Mathematical Model and Simulation Details

3.4.1 Numerical Procedures

The mathematical model detailed above was implemented in MATLAB R2020b. Unlike the previous study,the boundary conditions were specified by the user as the inlet and initial concentrations due to the exclusion of the compartmental model in this study. The partial differential equations were then solved numerically by approximating derivatives with finite differences and employing the backward Euler method for time integration. For a detailed description of the discretisation and integration techniques, refer to Gu [5].

3.4.2 Existing Model Simulations

The existing 1D model was first investigated before the development of the model to include nano-particles. Clot length L_{clot} and fibrin fibre radius R_f were varied to investigate the effect of changing clot length and conformation on the recanalization time for all dosage regimens devised in previous work [5].

Table 2: Different values of L_{clot} and R_f studied

R_f **[nm]**	L_{clot} **[mm]**
50	2.5
75	5.0
100	7.5
125	10.0
150	-

After collecting data, it was decided that the following dosage regimens would be discussed in this paper:

Table 3: List of dosage regimens discussed in this report.

Regimen	Description
1	10 % as bolus + 90% as continuous over 1 h
9	50% as bolus + 50% as continuous over 1h
12	10% as bolus + 60% as continuous over 30 min + 30% as continuous over 1 h

All regimens used a tPA dosage of 0.9 mg/kg. For details of all dosage regimens refer to Gu [5].

3.4.3 Nano-Particle Model Simulations

Due to the exclusion of a compartmental model, dosage regimens could not be investigated for the nano-particle model. Instead, the output temporal concentration profile of tPA from regimen 1 in the previous study was used to calculate an equivalent dosage. This equivalent dosage was calculated as the maximum of the tPA profile. From this, the inlet nano-particle concentration was calculated using the following equation:

$$C_{NP,x_0} = \frac{C_{tPA}}{v_{rel}} \tag{11}$$

Clot length and coarseness shown in Table 2 were also investigated for the nano-particle model and then compared with the free tPA model. Sensitivity analysis was also carried out to analyse how platelet volume fraction, fibrin volume fraction, and pressure drop across the clot affected the recanalization time.

Table 4: List of parameters and their values used in work

Parameter	Definition	Values
L_{clot}	Length of clot	5mm
d_{clot}	Clot position	5mm
D_A	Diameter of occluded artery	3mm
ΔP_x	Pressure drop	60mmHg/cm
μ	Viscosity	0.0037 Pas
R_{f0}	Fibrin fibre radius	100nm
Φ_{p0}	Platelet vol. fraction	0.3
Φ_{f0}	Fibrin vol. fraction	0.05
N_{INT}	No. of integrins per platelet	8×10^{-4}
S_p	Sphericity	1
D_{p0}	Platelet diameter	$2\mu M$
$C_{tPA,0}$	Initial and inlet tPA Concentration	5×10^{-5}
$C_{PLG,0}$	Initial and inlet PLG concentration	2.2 $2\mu M$
$C_{FBG,0}$	Initial and inlet FBG concentration	8 $2\mu M$
$C_{PLS,0}$	Initial and inlet PLS concentration	0 $2\mu M$
$C_{AP,0}$	Initial and inlet AP concentration	1 $2\mu M$
$C_{MG,0}$	Initial and inlet MG concentration	3 $2\mu M$
$C_{PAI,0}$	Initial and inlet PAI concentration	$5 \cdot 10^{-4} \mu M$

4 Results and Discussions

4.1 Temporal and Spatial Variation of Nano-Particle Model

Distributions of free phase nano-particles, empty nano-particles (due to leakage of tPA), bound nano-particles to integrins on activated platelets and empty bound nano-particles are shown in Figure 2. Figure 2a shows the nano-particle concentration increase from the inlet at a constant rate defined by the resistance of the blood clot against blood flow. Nano-particles reach the clot at time 7.13 min and begin to bind to integrins on the platelet surface. The concentration of nano-particles bound to integrins increases gradually as the nano-particles disperse through the clot. Once the nano-particles have bound to integrins, tPA is released leaving behind the empty, integrin-bound nano-particles. This species concentration increases from the front of the clot towards the rear over time. Figure 2d exhibits the leakage of tPA from nano-particles resulting in empty nano-particles before and throughout the clot at 0.005 m. This release of tPA is insignificant when compared to therapeutic levels (Figure 3a).

Concentration of tPA differs from that reported by Gu because of the encapsulation of tPA within the nano-particles [5]. This tPA only gets released in therapeutic quantities once it has reached the clot at length 0.005 m following the binding of nano-particles to integrins. There exists insignificant concentrations of tPA before the 0.005 m clot due to the effect of tPA leakage from the nano-particles. During clot lysis, the released tPA slowly penetrates into the clot, creating a band of high tPA concentration near the progressing clot front as dissolution occurs which increases in intensity due to the accumulation of excess, transported tPA and of tPA released from nano-particles binding with integrins on platelets present further into the clot.

Before the nano-particles reach the clot, there is a homogenous distribution of the total binding sites within the clot. When the amount of tPA at the clot front reaches therapeutic levels due to release from nano-particles, the clot starts to degrade progressing to the rear of the clot at 0.01 m until complete dissolution of the clot occurs at 24 min. There exists a delay in the dissolution of the clot front at length 0.005 m. The front of the clot reaches full dissolution at 16.38 min compared to the 15.25 min complete dissolution time of the clot at space 5.3mm. These results differ from the works explored by Gu and can be explained by the introduction of the nano-particles. The comparably slow rate of dissolution begins to manifest once the binding sites of the clot decrease to 10 μM and the localised volume fraction of the clot at the front reduces. Before this point the concentration of binding sites steadily decreases from the front to the rear of the clot. Later in time the clot effectively becomes coarser at 0.005 m region and therefore tPA transport through this point in space is faster than the time needed for tPA adsorption. Piebalgs concluded that coarse clots exhibited little deviation of extent of lysis (function of n_{tot}) over space with free tPA therefore alluding to high transport rates of tPA throughout the clot and therefore no progression of a clot breakdown front. This effect is exacerbated in this model by the absence of free tPA reaching the front of the clot

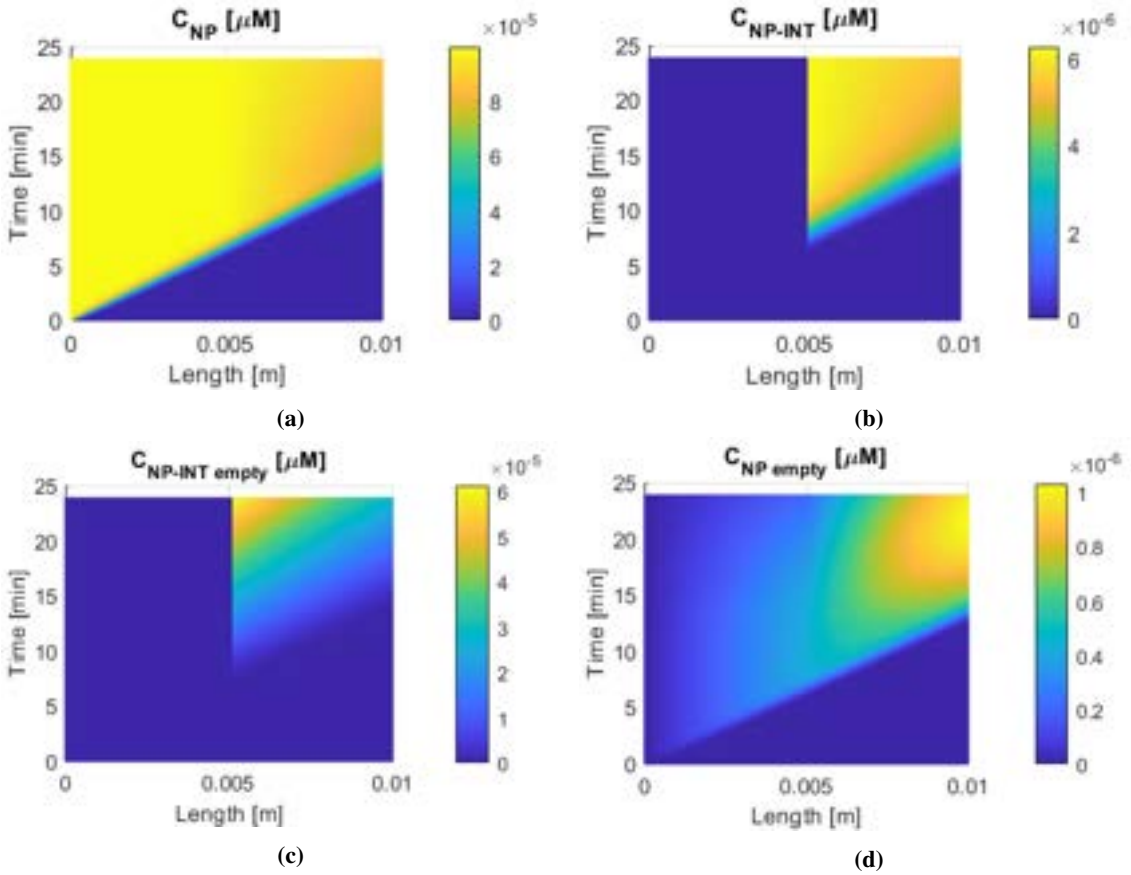

Figure 2: Temporal and spatial concentrations of nano-particle species. Each map shows variations of concentration in time (vertical axis) and space (horizontal axis). (a) Nano-particles, (b) Nano-particles bound to Integrins, (c) Empty Nano-particles bound to Integrins following release of tPA, (d) Empty Nano-particles

due to nano-particle encapsulation. Furthermore, this low dissolution rate could mean that for certain clot properties and dosages there is a risk of incomplete clot dissolution.

4.2 Nano-Particle Model Sensitivity

The unexpected slower dissolution rate at the front of the clot was further investigated by varying the fibrin fibre radius which has the effect of changing the clot coarseness. Figure 4a shows that a clot with lower fibrin fibre radius of 50 nm yielded results similar to Gu with the dissolution of clot progressing from the front to the rear with no visibly slower clot front dissolution rate [5]. However, Figures 4b and 4c show that for coarser clots (clots with larger fibrin radii) there is a significant increase in time taken for the front of the clot to be broken down. As discussed in Section 4.1, lower concentrations of binding sites has the effect of reducing the local resistance of the clot at this point in space. Lowering the resistance allows for increased flowrate of species through the clot therefore increasing the rate of tPA transport. Moreover, there is low tPA concentration at the front of the clot (Figure 3a). The concentration directly drives the rate of tPA adsorption onto fibrin in the clot and therefore a low tPA concentration results in a low adsorption rate. Therefore, the longer dissolution time can be attributed to the rate of tPA transport through the clot exceeding the rate of tPA adsorption at clot front which ultimately leads to the break down of the clot.

In testing this hypothesis further, the pressure drop across the blood clot and the initial volume fractions of platelets and fibrin within the clot were varied. The results can be seen in the Supplementary Materials. The effects were as expected with increased pressure drop resulting in increasingly higher dissolution rates for the clot front. This is because increased pressure drop enhances transport rate of tPA (and all species) because of a higher blood flowrate through the clot. Similarly, a lower initial volume fraction of fibrin and platelets also increased the dissolution rate at the clot front. Lower volume fraction results in a clot with lower resistance and therefore the rate of tPA transport is significantly higher than the rate of tPA adsorption at the clot front.

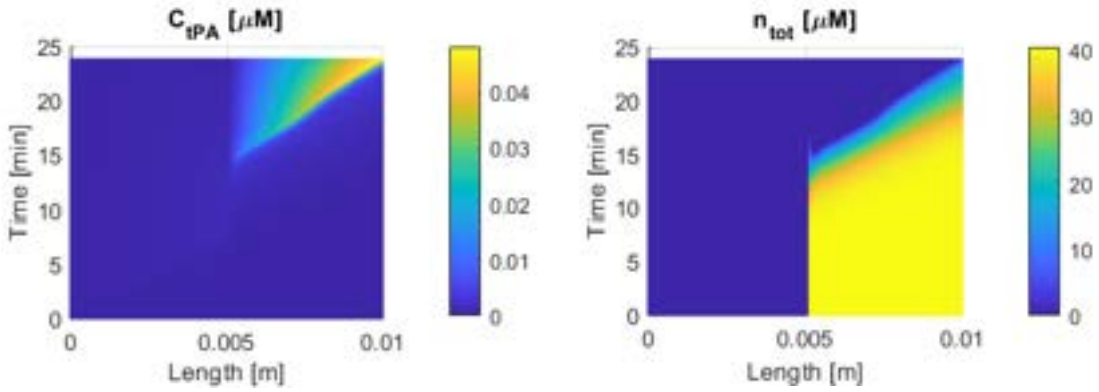

(a) (b)

Figure 3: Temporal and spatial concentrations of free tPA (a) and the total concentration of binding sites (n_{tot}) in the clot (b).

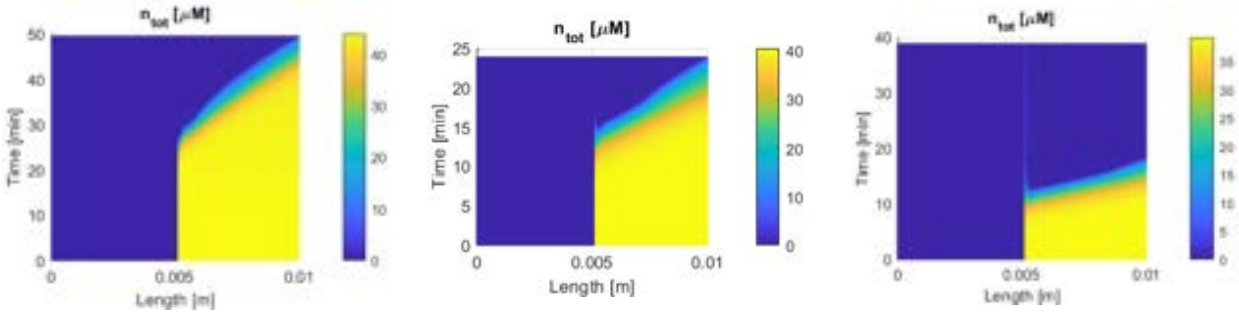

(a) (b) (c)

Figure 4: Temporal and spatial concentrations for total concentration of binding sites (n_{tot}) in the clot. Fibrin fibre radius (R_{f0}) is varied for the clot with (a) R_{f0} of 50 nm, (b) R_{f0} of 100 nm and (c) R_{f0} of 150 nm.

4.3 Effect of Clot Coarseness on Recanalization Time

From Figure 5, it can be seen that Regimens 1, 9 and 12 all follow a similar trend as the fibre radius increases and the clot gets increasingly more coarse. As a result, the general trend shows a steep decrease in recanalization time for smaller fibre radii and then the curve gets increasingly less steep as fibre radius increases. This can be explained through the resistance equation in which an R_{f0} squared term appears in the denominator, therefore, variations in smaller values of R_{f0} have a much greater impact on the resistance and consequently recanalization time in comparison to larger values of R_{f0}.

For a fibrin fibre radius of 50 nm, the recanalization time for the nano-medicine model was significantly lower than the free tPA model. This can be attributed to the nano-particle equivalent dosage estimation and the tPA release mechanism.

The equivalent dosage used in the nano – model was calculated as a maximum from the tPA concentration profile outputted from the compartmental model for regimen 1, and, consequently, is likely to provide a consistently higher concentration of tPA at the clot than the free tPA models resulting in a smaller recanalization time. The nano-particle model also makes the assumption that when nano-particles react with integrins, all contained tPA is released immediately. In reality however, the tPA released from the nano-particles is a function of time and follows a release curve [22] and recanalization time would be greater. The trend observed for the nano-particle model is similar to the free tPA model from 50nm to 116.5nm however beyond 116.5nm, the recanalization time begins to increase. This is because as the clot gets more coarse, resistance decreases and flow velocity therefore increases. As a result of this, the convection term in the convection-diffusion-reaction equation dominates the tPA reaction term and tPA passes through the clot before reacting with and breaking down the clot front. As a result, the front of the clot takes considerably longer to break down than the rest of the clot resulting in the higher clot lysis times.

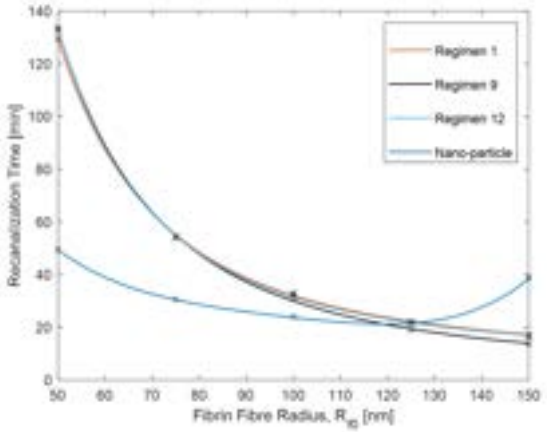

Figure 5: Effect of Varying Fibrin Fibre Radius on Recanalization Time

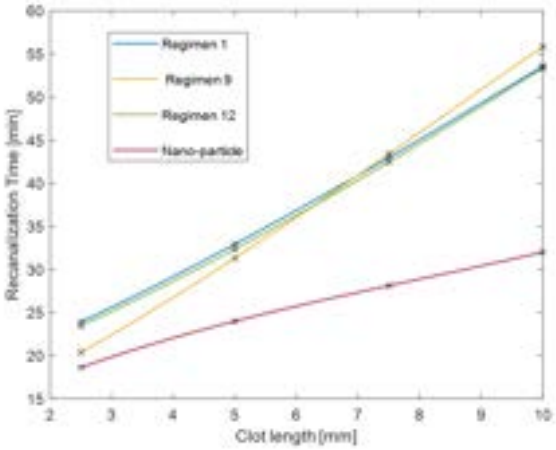

Figure 6: Effect of Varying Clot Length on Recanalization Time

4.4 Effect of Clot Length on Recanalisation Time

The effect of varying the length of the clot on the recanalization time was investigated for regimens 1, 9 and 12 of the free tPA model and for a 0.028g equivalent nano-particle dosage for the nano-particle model. Figure 6 above shows the outcome of these simulations. The three regimens from the free tPA model all follow a very similar trend however, the nano-particle model differs significantly.

Looking at the three free-tPA model simulations, it is seen that regimen 9 is more effective than regimens 1 and 12 for smaller clots but as the clot length increases, regimen 9 becomes less effective, eventually taking greater amounts of time to break down the clot than the other two regimens. For regimen 9, 50% of the dosage is delivered as a bolus and then 50% is delivered continuously over the next 60 minutes as opposed to regimens 1 and 12 where, in both cases the initial bolus is only 10% and the remaining tPA is delivered over the next 60 and 90 minutes respectively. Regimen 9 is more effective for smaller clots as the initial bolus results in high levels of tPA which break down a significant section of the clot in a short amount of time and the low tPA levels provided by the continuous delivery of the remaining 50%, despite the low clot lysis rate, are enough to break the remainder of the clot down in a short amount of time. However, as the length increases, the 50% bolus does not have enough of a significant effect for the majority of the clot to be broken down, and the effect of the low clot lysis rate, after the initial spike in tPA, on the recanalization time is exacerbated.

Regimens 1 and 12 follow a very similar trend which can be expected as the regimens themselves are similar. Regimen 12 proves to be slightly more effective than regimen 1 at all clot lengths studied which is unusual as regimen 1 provides a higher level of tPA over the first hour of drug delivery. It is therefore concluded, that higher dosages of tPA do not always result in lower lysis times due to the reaction of tPA with plasminogen activator inhibitor type 1 (PAI) and that there exists an optimal tPA concentration [5].

The data collected from the nano-particle model shows that the nano-particle drug was significantly more effective than the free tPA which is unexpected as the delay due to the additional tPA release mechanism should increase the total recanalization time. As mentioned in section 4.3, the dosage of nano-particles used in the nano-particle model is likely to result in a greater local concentration of tPA at the clot in comparison to the free tPA model hence why recanalization time is lower. Furthermore, the model doesn't include a tPA release function and assumes that the nano-particles are either full or empty, when in reality the process is likely to follow a release curve. [22].

4.5 Nano-Particle Dosage Considerations

As discussed in Section 4.3, the dosage of nano-particles was chosen to release a concentration of tPA equivalent to the maximum concentration at the output of Gu's compartmental model for dosage regimens 1 [5]. Following this, the effects of nano-particle dosages on recanalization time and concentration of total fibrin binding sites were investigated. The low (Figure 7a) and high (7c) dosages reflect equivalent tPA release of Regimens 2 and 3 of Gu et al. study respectively. Increased nano-particle dosage decreases time for recanalisation by 0.74 min (comparing low

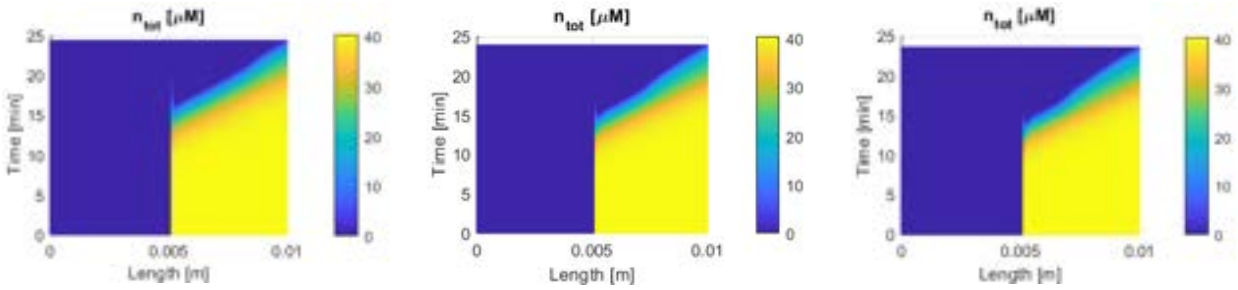

(a) (b) (c)

Figure 7: Temporal and spatial concentrations for total concentration of binding sites (n_{tot}) in the clot. Dosage is varied with tPA equivalent dosage of (a) 0.01876 μM, (b) 0.028177 μM and (c) 0.03751 μM

and high dosages) whereas Gu reported a change of 2.92 min for free tPA. For higher dosages, the effect of lower dissolution rate at the front of the clot is diminished which would reduce the risk of incomplete clot dissolution without the risk of ICH due to the encapsulation of tPA. Dosage is an important factor when considering recurrent strokes make a large proportion of all strokes [24] and rate of re-occlusion is as high as 30% for free tPA treatments [25].

5 Conclusion

In conclusion, a mathematical model that simulates the selective thrombolysis of blood clots via an activated-platelet-sensitive nano-particle was successfully developed to be used to evaluate the therapeutic efficacy and suitability of nano-particles for treatment. The model incorporates the targeted delivery and release of tPA at the blood clot site and 1D progression of clot lysis whilst minimising undesirable effects associated with typical fibrinolysis treatments (ICH). Furthermore, the results for various clot lengths and coarseness support previous studies that clot size and coarseness has a significant impact on recanalization time. Sensitivity analysis was conducted and it was found that increased clot coarseness results in slower rates of dissolution at the clot front. Moreover, the model produced insight into potential incomplete thrombolysis risk of nano-particle use for coarser clots and the effects of nano-particle dosage is worth investigation in the future to mitigate these risks. The model can be further improved by the inclusion of a mobility function for platelets to capture more realistic platelet transport from the clot following clot dissolution. In addition, the model can be extended through effective modelling of a nano-particle release mechanism rate in order to evaluate the unexpected low recanalization time.

6 Acknowledgements

The authors would like to thank Miss Emily Manchester for contributions to model debugging. The authors would also like to thank Dr. Boram Gu for assistance and access to the mathematical model of previous works.

References

[1] A. Bivard, L. Lin, and M.W. Parsonsb. Review of stroke thrombolytics. *Stroke*, 15:90–98, 2013.

[2] A.V. Alexandrov, W.S. Burgin, A.M. Demchuk, A. El-Mitwalli, and J.C. Grotta. Speed of intracranial clot lysis with intravenous tissue plasminogen activator therapy: sonographic classification and short-term improvement. *Circulation*, 103:2897–2902, 2001.

[3] O. Adeoye, R. Hornung, P. Khatri, and D. Kleindorfer. Recombinant tissue-type plasminogen activator use for ischemic stroke in the united states: a doubling of treatment rates over the course of 5 years. *Stroke*, 42:1952–1955, 2011.

[4] N.A Peters and C.A. Paciullo. Alteplase for the treatment of pulmonary embolism: A review. *Adv. Emerg. Nurs.*, 37:258–272, 2015.

[5] B. Gu, A. Piebalgs, Y. Huang, C. Longstaff, A.D. Hughes, R. Chen, S.A. Thom, and X.Y. Xu. Mathematical modelling of intravenous thrombolysis in acute ischaemic stroke: Effects of dose regimens on levels of fibrinolytic proteins and clot lysis time. *Pharmaceutics*, 11:111, 2019.

[6] A. Piebalgs, B. Gu, D. Roi, K. Lobotesis, S.A. Thom, and X.Y. Xu. Computational simulations of thrombolytic therapy in acute ischaemic stroke. *Scientific Reports*, 8:15810, 2018.

[7] B. Gu, A. Piebalgs, Y. Huang, D. Roi,

K. Lobotesis, C. Longstaff, A.D. Hughes, S.A. Chen, R.and Thom, and X.Y. Xu. Computational simulations of thrombolysis in acute stroke: Effect of clot size and location on recanalisation. *Medical Engineering and Physics*, 73:9–17, 2019.

[8] NINDS rtPA Stroke Study Group. Tissue plasminogen activator for acute ischemic stroke. *New England Journal of Medicine*, 333:1581–1587, 1995.

[9] E. Tanswell, P.and Seifried, P.C. Su, W. Feuerer, and D.C. Rijken. Pharmacokinetics and systemic effects of tissue-type plasminogen activator in normal subjects. *Clinical Pharmacology Therapeutics*, 46:155–162, 1989.

[10] N. Logallo, C.E. Kvistad, A. Nacu, H. Naess, U Waje-Andreassen, Asmuss, et al. The norwegian tenecteplase stroke trial (nor-test): randomised controlled trial of tenecteplase vs. alteplase in acute ischaemic stroke. *BMC Neurol*, 14:106, 2014.

[11] B.C.V. Campbell, P.J. Mitchell, L. Churilov, N. Yassi, T.J. Kleinig, R.J. Dowling, et al. Tenecteplase versus alteplase before thrombectomy for ischemic stroke. *New England Journal of Medicine*, 378:1573–1582, 2018.

[12] G. Huang, Z. Zhou, R. Srinivasan, M.S. Penn, K. Kottke-Marchant, R.E. Marchant, and A.S. Gupta. Affinity manipulation of surface-conjugated rgd peptide to modulate binding of liposomes to activated platelets. *Biomaterials*, 29:1676–1685, 2008.

[13] J. Kim, J. Kim, J. Park, Y. Byunb, and C. Kim. The use of pegylated liposomes to prolong circulation lifetimes of tissue plasminogen activator. *Biomaterials*, 30:5751–5756, 2009.

[14] S. Jin, Y. Wang, H. Zhu, Y. Wang, S. Zhao, M. Zhao, J. Liu, J. Wu, W. Gao, and S. Peng. Nanosized aspirin-arg-gly-asp-val: Delivery of aspirin to thrombus by the target carrier arg-gly-asp-val tetrapeptide. *ACS Nano*, 7:7664–7673, 2013.

[15] N. Korin, M. Kanapathipillai, B.D. Matthews, M. Crescente, A. Brill, T. Mammoto, K. Ghosh, S. Jurek, S.A. Bencherif, D. Bhatta, et al. Shear-activated nanotherapeutics for drug targeting to obstructed blood vessels. *Science*, 337:738–742, 2012.

[16] R. Cheng, W. Huang, L. Huang, B. Yang, L. Mao, K. Jin, Q. ZhuGe, and Y. Zhao. Acceleration of tissue plasminogen activator-mediated thrombolysis by magnetically powered nanomotors. *ACS Nano*, 8:7746–7754, 2014.

[17] S.T. Gunawan, K. Kempe, J. Bonnard, T.and Cui, K. Alt, L.S. Law, X. Wang, et al. Multifunctional thrombin-activatable polymer capsules for specific targeting to activated platelets. *Advanced Materials*, 27:5153–5157, 2015.

[18] J.N. Marsh, A. Senpan, G. Hu, M.J. Scott, P.J. Gaffney, P.A. Wickline, and G.M. Lanza. Fibrin-targeted perfluorocarbon nanoparticles for targeted thrombolysis. *Nanomedicine*, 2:533–543, 2007.

[19] G. Lippi, C. Mattiuzzi, and E.J. Favaloro. Novel and emerging therapies: Thrombus-targeted fibrinolysis. *Semin Thromb Hemost*, 39:48–58, 2013.

[20] J. Sánchez-Cortés and M. Mrksich. The platelet integrin iib3 binds to the rgd and agd motifs in fibrinogen. *Chem Biol*, 16:990–1000, 2009.

[21] M. Schwarz, G. Meade, P. Stoll, J. Ylanne, N. Bassler, Y.C. Chen, et al. Conformation-specific blockade of the integrin gpiib/iiia: a novel antiplatelet strategy that selectively targets activated platelets. *Circ Res*, 99:25–33, 2006.

[22] Y. Huang, L. Yu, J. Ren, B. Gu, C. Longstaff, A.D. Hughes, S.A. Thom, X.Y. Xu, and R. Chen. An activated-platelet-sensitive nanocarrier enables targeted delivery of tissue plasminogen activator for effective thrombolytic therapy. *Journal of Controlled Release*, 300:1–12, 2019.

[23] L. Vandelli, M. Marietta, M. Gambini, M. Cavazzuti, T. Trenti, M.A. Cenci, et al. Fibrinogen decrease after intravenous thrombolysis in ischemic stroke patients is a risk factor for intracerebral hemorrhage. *Journal of Stroke and Cerebrovascular Diseases*, 24: 394–400, 2015.

[24] R. Oza, K. Rundell, and M. Garcellano. Recurrent ischemic stroke: Strategies for prevention. *American Family Physician*, 96:436–440, 2017.

[25] A.V. Alexandrov and J.C. Grotta. Arterial reocclusion in stroke patients treated with intravenous tissue plasminogen activator. *Neurology*, 59:862–867, 2002.

Depot Optimisation for Vehicle Fleet Electrification

Layla Mehmet and Lucia Rodriguez

Department of Chemical Engineering, Imperial College London, U.K.

Abstract

Adoption of electric vehicles has increased dramatically in recent years due to the deepening of the global energy crisis, advances in battery technology and emission mitigation growing in importance. The optimal scheduling of electric vehicles is essential to effectively manage the increased stress placed on the power grid due to the large-scale penetration of electric vehicles. To address this challenge, this paper presents an overview of an optimisation model which proposes a smart charging solution for EV fleets. The model is a Mixed Integer Linear Program (MILP) formulated in Python and solved using CPLEX, which minimises electrical consumption and carbon costs, as well as a state of charge (SOC) penalty. The model is tested on the Birchmere depot and a scenario analysis that explores the impact of various parameters such as carbon tax, variable electricity tariffs and photo-voltaic (PV) power generation on the performance of the system is conducted. The optimal charging strategy reduces peak grid demand by 96% to facilitate feasible operation at the depot given grid limitations. The results show high grid response to a variable electrical price tariff, but minimal sensitivity to changes in carbon taxing. Despite variability in performance, PV installation supplemented with battery storage is found to be the most efficient operational change achieving a carbon output reduction of 14% and an average running cost of £0.124/kWh including tax.

Keywords: *Electric Vehicles, Smart Charging, MILP, Optimisation*

I. Introduction

1.1. Background

With the advent of stricter regulations related to emissions, energy resource limitations and the financial crisis, the world has unleashed a global race to electrify transportation. Negative consequences of the continuously increasing output of emissions can be observed both on the local and global scales and reducing the use of fossil fuels is a commonly agreed upon measure to target this issue.

The transport sector was the largest-emitting sector of the UK economy at 126 MtCO_2e in 2017, representing 28% of the UK greenhouse gas (GHG) emissions [**1**]. Appropriate energy policy must be adopted to reduce emissions in the transportation sector [**2**] and EVs play an essential role in the low-carbon transition [**3**]. Commercial fleets are a critical starting point to introduce electric vehicles (EVs) since they will reduce air pollution in densely populated areas and are a key technology to contribute to greenhouse gas (GHG) emission reductions objectives. GHG emissions of EVs are 17-30% lower than that of petrol and diesel vehicles over the entire vehicle life cycle, and these could be cut by at least 73% by 2050 since the carbon intensity of the EU energy mix is predicted to decrease [**4**].

Policymakers are striving to phase out the sales of internal combustion vehicles and to push the automobile market towards lower emissions by including fuel economy regulations, financial incentives and city access restrictions [**5**]. The United Kingdom is committed to a target of net zero emissions by 2050, proposing a ban on the sale of all polluting vehicles by 2035 [**6**]. In London, the Ultra-low emission zone (ULEZ) launched in 2019 introduced notable financial penalties for the operation of heavy-polluting vehicles and by 2021, the ULEZ will cover a wider area of London, including the Royal Borough of Greenwich – the case study that is analysed in this paper [**7**]. This acknowledges the urgent need to move towards cleaner fuelled vehicles and will further incentivise the uptake of EVs.

Another factor that is driving the electric vehicle market is the technological innovation and progress within the sector. Battery technology is improving at an escalating rate and average battery density is rising at 4-5% per year. The price of the lithium-ion battery has fallen by 87% from 2010 and 2019 and will continue to fall due to the exploitation of new manufacturing techniques [**8**].
In addition, the expansion of electric vehicles is also due to the significant introduction of intermittent, renewable energy resources into the electricity grid. As renewable generation becomes more important, electricity system decision makers are looking to increase storage capacity [**9**], and EVs appear to be a low-cost energy storage resource for the grid, capable of providing further flexibility to support power systems operations.
Following government intervention and technological advances, electric vehicles are expanding significantly. In Europe, EV sales increased by 44% in 2019, the highest rate since 2016, and some countries like the United Kingdom reported triple-digit growth [**10**]. This is aligned with the global EV forecast, which predicts a compound annual growth rate of 29% achieved over the next ten years [**5**].

1.2. Motivation

As a result of the increasing number of EVs, balancing electricity demand and supply will be essential to minimise the pressure placed on the electricity grid. Scheduling EVs is a valuable technique to mitigate night peak problems and to shift grid demand [**11**]. Smart charging enables the control of charging and discharging and encourages charging at periods of low electricity demand. With smart charging, EVs could support real-time balancing of the grids by adjusting their charging levels and adapting their charging patterns to flatten peak demand [**12**]. In the present paper, an optimal charging scheduling strategy is proposed to mitigate carbon emissions and to minimise total electricity consumption, and hence reduce the overall cost of the Royal Borough of Greenwich's (RBG) current fleet. Of notable interest to this discussion is the formulation and the design choices made in the development of the EVs model.

1.3. Relevant Literature

The surge in EVs has led many research groups in both academia and industry to conduct work on EV optimal charging strategies. The work is divided into two areas depending on whether it affects the power grid or individual users [**13**]. In 1983, Heydt researched the impact of EV deployment on loads and proposed different ways to alleviate peak loading with off-peak recharging, and the shift of peak loads to off-peak periods [**14**]. Kristoffersen et al. introduced a framework for optimising electric drive vehicles and discharging given driving patterns of the vehicle fleet and changes in electricity spot prices [**15**]. In a different study, Kaur et al proposed a two-level hierarchical control mechanism to generate an optimal scheduling policy for charging and discharging of EVs using MILP to minimise the frequency deviations at the grid level while supporting bi-directional vehicle-to-grid capabilities [**16**]. However, some methods did not present a simple and effective way to formulate and solve the optimal charging problem of EV fleets.

1.4. Focus of this Study

The present paper describes the optimisation model being applied to the RBG fleet and explores the RBG's ambition to electrify their commercial fleet, in line with the wider council's carbon neutral aims. This potential is explored using modelling and optimisation to understand how EV utilisation can be increased, whilst considering grid capacity and spatial constraints at the depot. Real-world data from the commercial organisation is used in order to assess which options are most viable and cost-effective to decarbonise logistic centres. The carbon mitigation potential and the cost-benefit that the different solutions can provide to this energy intensive fleet is also identified. Finally, alternative on-site generation options, such as photo-voltaic cells (PV) and energy storage are explored, in order to supply enough electrical power for charging at the depot.
The remaining sections of the paper are structured as follows: Section II describes in detail the optimisation formulation developed for the RBG. A case study is developed in Section III and the different baseline model and scenarios

are presented. Section IV presents results and discussion of the baseline model and of the different scenarios analysed. Finally, section V and VI conclude the paper, highlighting important findings and suggesting opportunities for future work.

II. Optimisation Formulation for Fleet Scheduling

An optimisation model of fleet charging schedules with battery and PV that uses mixed-integer linear programming (MILP) has been developed to minimise the cost function. The objective function is subject to constraints to control the feasible region. The MILP problem is formulated in Python and solved with IBM ILOG CPLEX Optimisation Studio IDE 12.10.0.

2.1. Multi-Objective Function

$$\min_{\varepsilon, P^{grid}} \sum_{k}^{n} (w_1 \varepsilon_k + w_2 P_k^{grid} (C_k^{elec} + I_k C^{CO_2})) \quad (1)$$

A weighted sum of the largest deviation below a specified SOC threshold at each hourly time step plus the total electrical consumption and carbon cost. w_1 represents the artificial SOC penalty cost (£/%-hr) which is heavily weighted against w_2 to ensure enough power is drawn. The objective function is normalised as follows to run the simulation results:

$$\alpha_{\mathrm{k}} = w_2 (C_k^{elec} + I_k C^{CO_2}) \quad (2)$$

The value of w_1 is adjusted such that:

$$\frac{w_1}{mean(\alpha_{\mathrm{k}})} = constant \quad (3)$$

for all scenarios. Hence, the objective function becomes:

$$J = min \sum_{k}^{n} (w_1 \varepsilon_k + \alpha_{\mathrm{k}} P_k^{grid}) \quad (4)$$

2.2. Constraints

Initial condition (i.e. k=0) of EV SOC:

$$x_{i,k} = x_i^{init} \quad \forall i \in EV,\ k = 0 \quad (5)$$

Initial condition of plug-in matrix:

$$A_{i,j,k} = A_{i,j}^{init} \quad \forall i \in EV,\ j \in Plg,\ k = 0 \quad (6)$$

In one timestep, the increase in EV SOC is at most equal to the maximum power flow from a connected plug minus the predicted discharge from driving:

$$x_{i,k} \leq x_{i,k-1} + \sum_{j \in Plg} \frac{(A_{i,j,k-1} P_j^{ch})}{CAP_i} - \frac{dis_{i,k-1}}{CAP_i} \quad \forall i \in EV,\ k \in [1 \dots N] \quad (7)$$

In one timestep, the drop in EV SOC is at most equal to the discharged power from driving:

$$x_{i,k} \geq x_{i,k-1} - \frac{dis_{i,k-1}}{CAP_i} \quad \forall i \in EV,\ k \in [1 \dots N] \quad (8)$$

If an EV is predicted to arrive at a given time step, the values in the row of the plug-in matrix associated with that EV can increase from 0 to 1; otherwise values in that row must not increase (i.e. vehicles can only plug in when they arrive):

$$A_{i,j,k+1} - A_{i,j,k} \leq \gamma_{k,i} \quad \forall i \in EV, j \in Plg,\ k \in [0 \dots N-2] \quad (9)$$

If an EV is predicted to depart at a given time step, the values in the row of the plug-in matrix associated with that EV can decrease from 1 to 0; otherwise values in that row must not decrease (i.e. vehicles can only plug out when they depart):

$$A_{i,j,k} - A_{i,j,k+1} \leq \phi_{k,i} \quad \forall i \in EV, j \in Plg,\ k \in [0 \dots N-2] \quad (10)$$

If a vehicle is away from the depot, the values in the row of the plug-in matrix associated with that vehicle must be 0 (i.e. if the vehicle leaves the depot, it cannot still be using a plug at the depot):

$$A_{i,j,k+1} \leq 1 - \phi_{k,i} \quad i \in EVs, j \in Plg,\ k \in [0 \dots N-2] \quad (11)$$

The number of 1s in a column of the plug-in matrix must be less than the number of plugs of the type associated with that column (i.e. there can't be more EVs using a certain plug type than there are plugs of that type):

$$\sum_{i \in EV} A_{i,j,k+1} \leq nlpg_j \quad \forall j \in Plg,\ k \in [0 \dots N-2] \quad (12)$$

The number of 1s in a row of the plug-in matrix must be at most 1 (i.e. an EV can't be plugged into 2 plugs):

$$\sum_{j \in Plg} A_{i,j,k} \leq 1 \quad \forall i \in EV,\ k \in [1 \dots N-1] \quad (13)$$

Power drawn by each EV:

$$P_i^{EV} \geq [(x_{i,k-1} - x_{i,k})\ CAP_i] \quad \forall i \in EV,\ k \in [0 \dots N-1] \quad (14)$$

The power drawn from the grid must be equal to the stationary battery charge minus the stationary battery discharge, plus the power drawn by the EVs:

$$P_k^{grid} = P_k^{bat^+} - P_k^{bat^-} + PV_k^{gen} + \sum_{i \in EV} P_i^{EV} \quad \forall k \in [0 \dots N-1] \quad (15)$$

The change in the SOC of the stationary battery is given in terms of the charge, discharge and an efficiency value:

$$SOC_{k+1}^{bat} = SOC_k^{bat} + \frac{P_k^{bat^+} \eta^{bat}}{CAP^{bat}} - \frac{P_k^{bat^-}}{\eta^{bat} CAP^{bat}} \quad \forall k \in [0 \dots N] \quad (16)$$

Initial stationary battery charge:

$$SOC_k^{bat} = SOC^{init} \quad \forall k = 0 \quad (17)$$

The penalty variable must be greater than the largest drop of an EV SOC below a threshold (given by λ).

$$\varepsilon_k \geq \lambda - x_{i,k+1} \quad \forall i \in EV,\ k \in 0 \dots N \quad (18)$$

III. Case Study: Birchmere vehicle depot

3.1. Fleet Composition

Although the current RBG integrates a mixed fleet of roughly 550 vehicles, only 469 are selected to appear in this study. The vehicles selected satisfy the following requirements:

Year of viability (*when EV equivalents are available on the market*), must be between 2020 and 2023. This leads to the exclusion of the gully vehicle, tractor, small RCV and Gritter HCV.

Vehicle type quantity: Vehicles in the depot present in small quantities are neglected since they would not have a significant effect on the model. These include: PEOS Specialist Vehicle (small tipper), Specialist HGV, Graffitti HGV (large custom van), Large sweeper, Small sweeper, Tail lift van.

Table 1: *Current Fleet Composition*

Vehicle Type	Amount	Battery Cap. (kW)	Dist. travelled (km)
S. Van	60	40.0	50.1
M. Van	74	75.0	20.0
L. Van	98	43.0	39.8
D. Van	10	11.5	9.0
T. Van	101	15.4	20.0
Car	9	62.0	36.8
Coach	77	92.0	10.0
L. RCV	41	170.0	20.0

Note that 'S.' denotes 'small', 'M.' denotes 'medium', 'L.' denotes 'large', 'D.' denotes 'dropside' and 'T.' denotes 'tipper'.

On average, all fleet vehicles travel a relatively short distance on a daily basis. This means that EV range is not an issue for the fleet since current EVs are able to travel up to 300km on a single charge.

3.2. Baseline Model

The baseline model presents a working charging strategy with the use of an optimisation model which minimises the SOC penalty on the system and overall electricity cost. A fixed electricity

price of £0.145/kW is assumed and no carbon tax or PV is applied. The simulation is run over a 5-day interval to allow for substantial grid loads and carbon outputs and to account for day to day disparities with respect to electricity cost and carbon emissions. The state of charge (SOC) penalty threshold is set at 50% and a penalty cost of £1,000/%-hr is applied to ensure that EV SOC is maintained above 0 for the entirety of the run whilst also ensuring the model is flexible enough for reductions in grid load. The maximum grid capacity limit is set at 120kWh to match that of the Birchmere depot. The model is implemented with 469 "fast" chargers available for use, each with a charging speed of 7kW.

3.3. Scenario description

Once the baseline model has been developed, the following scenarios are applied in order to explore the functionality of the optimisation model:

1. Minimise electricity price - *Variable electricity tariff, no carbon tax and £937/%-hr SOC penalty*
2. Minimise carbon output - *Fixed electricity tariff, £20/tonne carbon tax and £1,023/%-hr SOC penalty*
3. Multi-objective Optimisation - *Variable electricity tariff, £20/tonne carbon tax, £960/%-hr SOC penalty*
4. Multi-objective Optimisation with PV Installation - *Variable electricity tariff, £20/tonne carbon tax, £960/%-hr SOC penalty and 500 PV panels (817.5m^2) with storage*

IV. Results

4.1. Overview

The main function of the optimisation is to exploit cost metrics such as electricity price, carbon tax and SOC penalty in order to increase efficiency of the charging system and reduce carbon output subject to EV charging requirements and power grid limitations. There are three main objectives:

1. Reduce Power Demand
2. Reduce Running Cost
3. Reduce Carbon Output

The primary objective is explored in the baseline model and the secondary objective is the main focus of scenario 1 - where a variable electricity tariff will replace the fixed electricity tariff used in the baseline model. The tertiary objective will be explored in scenario 2 with the application of a carbon tax at £20/tonne. Scenario 3 will be a multi-objective study on all three objectives and finally, in scenario 4, photovoltaic installation will be applied to the depot to see if further improvements can be made. The main metrics used to assess performance are the total grid power, unit running cost (electrical consumption and carbon cost), carbon intensity and total carbon output. The SOC penalty cost is adjusted in each scenario to ensure that EVs have enough power to sustain their trips. Since it is an artificial cost with the functionality of a constraint, it is not considered a metric of performance.

4.2. Baseline Model

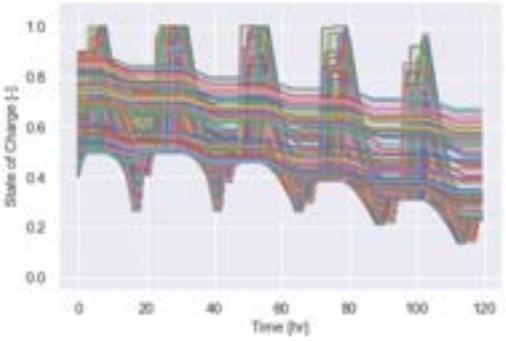

Figure 1: *State of Charge of EVs*

Figure 1 demonstrates the SOC of all the EVs throughout the five day simulation. The SOC initially increases as EVs are plugged into the grid giving rise to peaks in the early hours of the morning. At 9hrs EVs are expected to plug out of the system and leave the depot to carry out their trips; during this period the SOC will start to drop below 50% at which point a penalty is

incurred. Upon return to the depot, EVs will gradually charge back up again overnight where a small number of EVs such as small vans will need to charge to 100% in accordance with the fact that they travel the largest distance. In order to minimise penalty costs, EV SOC is maintained between 50-100% when at the depot where EVs such as coaches will not need to charge to full capacity as they only need enough power to sustain a 10km journey.

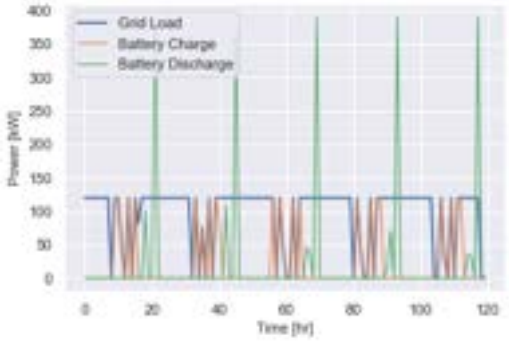

Figure 2: *Baseline power profile*

Figure 2 demonstrates the grid load as well as battery charge and discharge power. The power demand is driven purely by the minimum charging requirements of EVs based on their trips (e.g. expected distance travelled). The long flat peaks at 120kWh are an indication that most of the power is drawn outside of working hours when EVs are present in the depot and plugged into the grid. The sharp intermittent peaks in grid load whilst EVs are away occur when battery storage facilities are charging up in preparation for the return of EVs. Once EVs return to the depot a combination of grid power and the discharging battery power is used to quickly charge up the vehicles in order to mitigate heavy SOC penalty costs.

The baseline model has effectively implemented a smart charging solution to reducing peak demand from 3.3MW (simultaneous charging of all EVs - dumb charging) to just 120kW (smart charging) satisfying the power grid limitations at the Birchmere depot. The total grid load over the 5-day interval is at 11.5MWh (80% of the total grid capacity available) resulting in a total running expense of £1,671. The carbon output is relatively high at 2,017kg, resulting in a carbon emission rate of 0.174kg/kWh.

4.3. Scenario 1: Minimising Electricity Price

A variable electricity tariff is applied to drive the unit price of electricity of the system down. In order to make the optimisation comparable to the baseline model, a SOC penalty cost of £937/% is applied to ensure that the weighting of the electricity price relative to that of the SOC penalty is identical to that of the baseline scenario. Figure 3 shows the resulting grid load response when optimised with respect to electricity price. As expected, the total grid load is reduced at times where electricity price is on a rise as seen by the decreasing number of peaks during working hours. At this point savings are made with respect to running costs as less power is drawn from the grid. The remaining sharp peaks occur when electricity price is both decreasing and under £0.18/kWh. It should be noted that flat grid load peaks are still observed at peak electricity price as they are necessary to ensure that the SOC requirements of the EVs are met in order to avoid the heavy SOC penalty charge.

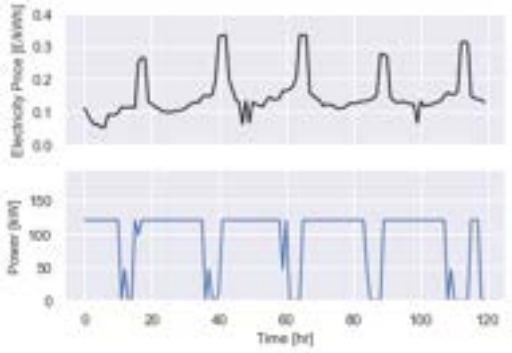

Figure 3: *Grid response to variable elec. tariff*

A power reduction of 2% is achieved yielding an overall cost reduction of 8% from the baseline model. As a result, the average unit price of electricity is reduced from £0.145/kWh to £0.136/kWh. Additionally, due to the relatively large decrease in grid load, the overall carbon output is reduced by 3.7% resulting in a carbon emission rate of 0.171kg/kWh.

4.4. Scenario 2: Minimising CO_2 emissions

The following optimisation model minimises the cost of carbon using real time carbon emissions data to reduce the total carbon output of the system, as well as the carbon intensity. This is achieved by encouraging smarter charging where EVs only draw from the grid at times of low carbon intensity. A fixed electricity tariff of £0.145/kWh is assumed for comparability to the baseline model and a carbon tax of £20/tonne is assumed in line with current tax rates [**17**].

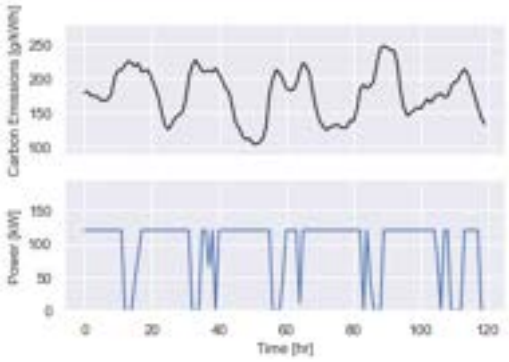

Figure 4: *Grid response to carbon emissions*

Figure 4 demonstrates the change in grid load at £20/tonne. When compared to the baseline model (Figure 2), there is evidently a change in the times at which power is drawn as seen by the dip in grid load demand at 40hrs and 64hrs where carbon emissions peak. This is indicative of a smarter charging system where EVs only draw from the grid when carbon emissions are low, resulting in a lower average carbon intensity. The total grid requirement for the optimisation is 11.5MWh, resulting in carbon emissions of 1,966kg. Whilst the decrease in grid load is only minor (0.2%), there is a 2% decrease in carbon relative to the baseline resulting in an improved carbon emissions rate of 0.170kg/kWh, similar to the system applied in scenario 1. However, the running cost for this simulation is expectedly higher once the cost of carbon is incorporated, resulting in a unit running cost of £0.149/kWh.

4.5. Scenario 3: Multi-Objective Optimisation

The following scenario explores the interplay between objectives 2 and 3 in a multi-objective optimisation minimising with respect to varying electricity price and carbon emissions. When a carbon tax of £20/tonne is applied a carbon intensity of 0.171kg/kWh and a decrease in carbon output of 3.8% relative to the baseline model is observed, similar to savings made in scenario 1, minimising for electricity price. Additionally, the running cost of electricity is also identical to scenario 1 at £0.136/kWh; however, due to the additional cost of carbon, the overall running cost is slightly higher at £0.139/kWh. The results suggest that the carbon cost function bears little weighting in the optimisation model. Since the overall carbon cost is just 2.5% of the total running cost (£1,571), this result is expected. Figure 5 demonstrates the grid load profile for the multi-objective optimisation which is almost identical to Figure 3 for the electricity price optimisation. It is clear that the carbon tax is not high enough to substantially influence the grid load profile.

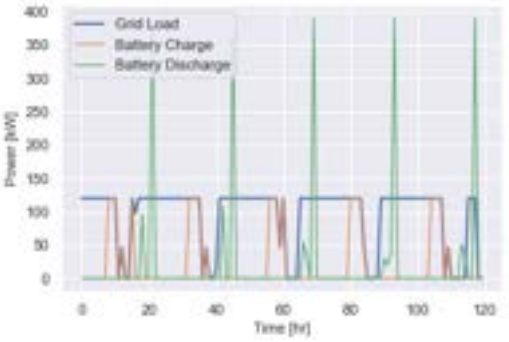

Figure 5: *Multi-objective power profile*

A carbon tax sensitivity analysis is applied to see if a higher carbon tax can increase the weighting of the carbon cost relative to the electricity cost in the objective function in order to bring about a larger reduction in carbon emissions. The SOC penalty is adjusted as such to ensure that the relative weighting between the running costs and the SOC penalty remains constant so that the average SOC of the vehicles is maintained at sufficient levels. Table 2 indicates the relative savings when a range of carbon taxes are

Table 2: *Carbon tax sensitivity analysis*

	Carbon Tax £/kg					
Operational Changes	0	20	40	60	80	100
Grid Load Savings (%)	2.0	2.1	2.1	2.6	1.9	2.1
Carbon Output Savings (%)	3.7	3.8	3.7	4.3	3.5	3.8
Carbon Intensity (kg/kWh)	0.171	0.171	0.171	0.171	0.171	0.171
Running cost (£/kWh)	0.136	0.139	0.142	0.146	0.150	0.153

applied in a multi-objective optimisation, where a carbon tax of £0/tonne represents the singular objective optimisation which minimises with respect to electricity price only. The changes observed with respect to grid load and carbon output are very subtle, where any changes in carbon output mirror the changes in grid load, suggesting that they are a direct result of decreasing power rather than smarter charging. This observation can be reaffirmed by the fact that the carbon intensity of each run, is constant at 0.171kg/kWh. Whilst the unit price of electricity remains at £0.136/kWh, the increase in carbon tax results in an increased running cost where a carbon tax at £100/tonne results in an 11% increase in the total running cost.

4.6. Scenario 4: Photo-voltaic Cells

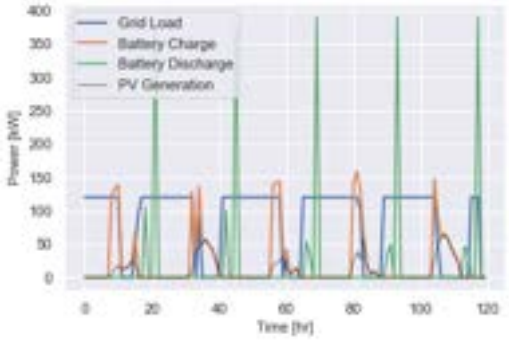

Figure 6: *Multi-objective power profile with PV generation and storage*

PV is introduced with battery storage in order to alleviate grid load, particularly at times of peak demand where the grid load is at maximum grid capacity (120kW). Since a substantial portion of PV generation occurs during working hours, when EVs are outside the depot, PV installation alongside battery storage facilities are implemented to ensure that energy is not wasted. Figure 6 demonstrates the grid profile when the multi-objective optimisation is applied with PV. The flat peaks observed whilst EVs are charging at the depot are much thinner, indicating that a significant level of savings are made with respect to grid load. It is important to note that PV generation often coincides with the time at which electricity price and carbon emissions are peaking, therefore substituting grid load requirements with generated PV power yields substantial savings and is by far the smartest means of charging. The total grid load requirement is reduced by 11.5% to 10.2MWh and the carbon output is reduced by 14.3% to 1,721kg. It should be noted however, that this simulation runs on day 300 of the year (autumn), hence, it is not representative of a full working year. As there is a significant level of uncertainty surrounding PV generational capacity, the simulation is run on three additional days of the year. Table 3 demonstrates the variability in operational behaviour with respect to seasonal changes where day 30 (winter) demonstrates the worst case scenario with a minimum PV generation of 731kWh once again giving rise to substantial grid load savings of 8.4% and carbon savings of 11.3%. Despite high variability in PV generation throughout the year, it is clear that PV is without a doubt one of the most effective means of improving operational behaviour within the depot both with respect to carbon mitigation and cost reduction.

Table 3: *Seasonal changes in a multi-objective optimisation with PV*

	Simulation Start Day			
Operational Changes	30	120	210	300
PV Generation (kWh)	731	1704	2885	1125
Grid load Savings (%)	8.4	14.8	23.7	11.5
Carbon Output Savings (%)	11.3	18.8	28.2	14.3
Carbon Intensity (kg/kWh)	0.169	0.166	0.164	0.168
Running Cost (£/kWh)	0.134	0.0937	0.114	0.124

V. Conclusion

This work has proposed an effective smart charging strategy for EV fleets with the use of a multi-objective optimisation model employing real-time data on electricity price and carbon emissions. The model has been tested on the Birchmere depot with a sample size of 469 EVs. The optimal charging strategy reduces peak power grid demand by 96% to facilitate feasible operation under the 120kW power grid limit at the depot. A sensitivity analysis on the models response to changes in carbon tax is carried out, however, the smart charging solution is not substantially affected, demonstrating a relatively stable model with respect to changes in carbon taxing policy. A multi-objective optimisation formulation with photo-voltaic installation supplemented with battery storage has been proven to be the most efficient operational system achieving a carbon output reduction of 14% and an average running cost of £0.124/kWh including tax.

VI. Future Work

To further reduce the maximum power required at the RBG depot and manage demand effectively without placing additional strain on the power supply, off-site charging could be investigated. This option would also overcome space constraints since not all vehicles would have to be charged at the depot. Off-site charging would be based on the destination of RBG vehicles, dwell times and the availability or potential for deployment of charging infrastructure. Moreover, implementing V2G technology would also help ease the strain on the power grid since the battery charge from the vehicle could be used to provide additional supply during peak demand, and this could be further inspected.

Furthermore, a regenerative hydrogen fuel cell (RHFC) system could also be explored as a potential option for electric energy storage. Although hydrogen storage has a lower round-trip efficiency than lithium ion batteries, it provides more energy dispatched from storage for the same quantity of manufacturing energy input, it has a high energy density and a low rate of self-discharge [**18**].

VII. Acknowledgements

We would like to express our sincere gratitude to Edward J O'Dwyer for his continuous support, feedback, and insight he gave us throughout the project.

Nomenclature

P^{bat+}	Stationary battery charging power
P^{bat-}	Stationary battery discharging power
P^{grid}	Power drawn from grid
α	Unit running cost
η^{bat}	Charging efficiency of stationary battery
γ	Arrival of EV at depot
λ	EV SOC Penalty Threshold
ϕ	Departure of EV from depot
ε	EV low SOC penalty variable
A	Plug-in matrix
A^{init}	Plug-in matrix at time k=0
C^{CO_2}	Carbon price
C^{elec}	Electricity price
CAP	Energy capacity of an EV's battery

CAP^{bat}	Energy capacity of stationary battery
dis	EV battery discharge at each time step
EV	Set of all EVs
I	Carbon Intensity
i	Specific EV from set EV
j	Specific plug type from set Plg
k	Time step
$nplg$	Number of plugs of given type
P^{ch}	Maximum charging power of given plug type
P^{EV}	Power drawn by EVs
Plg	Set of all plug types
PV^{gen}	PV generation
SOC^{bat}	Stationary battery SOC
SOC^{init}	Stationary battery SOC at time k=0
w_1	SOC Penalty Weight
w_2	Carbon and Electricity Cost Weight
x	EV State of Charge
x^{init}	EV SOC at time k=0

References

[1] Hirst, D., 2020. [online] House of Commons Library. Available at: https://commonslibrary.parliament.uk/research-briefings/cbp-7480/ [Accessed 2 December 2020].

[2] H.C. Ong, T.M.I. Mahlia, H.H. Masjuki, "A review on energy pattern and policy for transportation sector in Malaysia" *Renewable and Sustainable Energy Reviews,* Volume 16, Issue 1, 2012, Pages 532-542,[online] Available at: https://doi.org/10.1016/j.rser.2011.08.019

[3] E. Daramy-Williams, J. Anable, S. Grant-Muller, "A systematic review of the evidence on plug-in electric vehicle user experience" *Transportation Research Part D: Transport and Environment,* 71, 2019, pp.22-36 Available at: https://doi.org/10.1016/j.trd.2019.01.008

[4] European Environment Agency. 2020. *EEA Report Confirms: Electric Cars Are Better For Climate And Air Quality.* [online] Available at: https://www.eea.europa.eu/highlights/eea-report-confirms-electric-cars/ [Accessed 2 December 2020].

[5] Deloitte Insights. 2020. *Electric Vehicles.* [online] Available at: https://www2.deloitte.com/us/en/insights/focus/future-of-mobility/electric-vehicle-trends-2030.html [Accessed 6 December 2020].

[6] GOV.UK. 2020. *Government Takes Historic Step Towards Net-Zero With End Of Sale Of New Petrol And Diesel Cars By 2030.* [online] Available at: https://www.gov.uk/government/news/government-takes-historic-step-towards-net-zero-with-end-of-sale- of-new-petrol-and-diesel-cars-by-2030#:~:text=The%20UK%20has%20taken%20another,in%20the%20UK%20by%202030. [Accessed 7 December 2020].

[7] Matters, T., 2020. *ULEZ Expansion.* [online] Transport for London. Available at: https://tfl.gov.uk/modes/driving/ultra-low-emission-zone/ulez-expansion [Accessed 6 December 2020].

[8] BloombergNEF. 2020. *BNEF EVO Report 2020 | Bloombergnef | Bloomberg Finance LP.* [online] Available at: https://about.bnef.com/electric-vehicle-outlook/ [Accessed 5 December 2020].

[9] S. o. California, Sept. 2010. "Assembly bill 2514: Energy storage systems"

[10] Gersdorf, T., Hertzke, P., Schaufuss, P. and Schenk, S., 2020. *McKinsey Electric Vehicle Index: Europe Cushions A Global Plunge In EV Sales.* [online] Available at: https://www.mckinsey.com/industries/automotive-and-assembly/our-insights/mckinsey-electric-vehicle-index-europe-cushions-a-global-plunge-in-ev-sales [Accessed 9 December 2020].

[11] T.Zhang, H. Pota, C.-C. Chu and R. Gadh, 2018, 'Real-time renewable energy incentive system for electric vehicles using prioritization and cryptocurrency', *Appl. Energy,* vol.226, pp. 582-594.

[12] Irena.org. 2020. [online] Available at: https://www.irena.org/-/media/Files/IRENA/Agency/Publication/2019/Sep/IRENA_EV_Smart_Charging_2019.pdf?la=en&hash=E77FAB7422226D29931E8469698C709EFC13EDB2#:~:text=Smart%20charging%20means%20adapting%20the,EVs%20while%20meeting%20mobility%20needs [Accessed 6 December 2020].

[13] F. Kong, X. Liu et al., 2017, "Sustainable transportation with electric vehicles", *Foundations and Trends,* vol. 2, no. 1, pp. 1-132.

[14] G. Heydt, 2007, 'The impact of electric vehicle deployment on load management strategies'. *IEEE Transactions on Power Apparatus and Systems,* no. 5, pp. 1253-1259.

[15] T. Kristoffersen, K. Capion, and P. Meibom, 2010, 'Optimal charging of electric drive vehicles in a market environment', *Applied Energy.*

[16] K. Kaur, N. Kumar and M. Singh, 2018, 'Coordinated Power Control of Electric Vehicles for Grid Frequency Support: MILP-Based Hierarchical Control Design', *IEEE Transactions on Smart Grid,* vol.10.

[17] Hirst, D., 2018. *Carbon Price Floor (CPF) And The Price Support Mechanism.* House of Commons Library, pp.7,8.

[18] A. Pellow, M., J. M. Emmott, C., J. Barnhartd, C. and M. Bensonaef, S., 2015. Hydrogen or batteries for grid storage? A net energy analysis. *Energy Environmental Science,* (7).

Process Design and Techno-Economic Assessment for Biofuel Production of Excreted Octanol from Genetically Engineered Cyanobacteria

Marie Jones and Noah Van Surell
Department of Chemical Engineering, Imperial College London, U.K.

Abstract
Biofuels are attractive substitutes for liquid fossil fuels, especially to decarbonise transportation. Microalgae appear as a promising production platform for biofuels, due to their ability to convert CO_2 into chemicals with high energy content. The fuel properties of octanol, excreted from genetically engineered cyanobacteria *Synechocystis sp.* PCC 6803, enable direct combustion in motor engines. The continuous production of bio-octanol and its subsequent recovery by liquid-liquid extraction with hexadecane was modelled using Aspen Plus. With flue gas from a 500 MW coal-fired power plant, concentrations of up to 1.44 g/L of algae and 1.2 g/L of octanol were achieved. The process could ultimately avoid the emission of 330 tonnes of CO_2-equivalent per annum. Despite the clear positive environmental impact of the technology, the economics of the process are not favourable unless the biomass side-products are recovered. A subsidy of £0.95 per litre of bio-octanol was found to provide the necessary financial incentive for investment in microbial fuel production. Moreover, future technological improvements and green policies for biofuel production should accelerate the path to net zero.
Keywords: *Process simulation, Excreted biofuels, Octanol production, Microalgae, Techno-economic, Sustainability*

1 | Introduction

Signed in 2015, the Paris Agreement on Climate Change acknowledged the vital necessity to keep the increase in global average temperatures to well below 2°C above pre-industrial levels. The recent announcements of the UK's Ten Point Plan for a Green Industrial Revolution [1] and the European Green Deal [2] embody their commitment to drastically reduce their greenhouse gas emissions. Over 70% of the global yearly CO_2 emissions originate from transportation, heating and electricity generation [3]. Alongside wind and solar energy, biofuels are expected to play a key role in the transition to clean energy sources; offering an interesting alternative to liquid fossil fuels for sectors where decarbonisation proves to be challenging, especially aviation [4].

Intensive research in the last decade has led to a shift in biofuel production from edible biomass to agricultural and biological wastes [5]. Despite the improvement in alleviating the unethical competition between food and bioenergy crops, the significant environmental impact of land and water usage results in the necessity for a more sustainable feedstock [4]. Microalgae appear as a promising production platform for the third generation of biofuels, due to their ability to remove CO_2 from the atmosphere and to secrete higher energy content chemicals [6]. However, tremendous efforts from both science and policy are still required to make this technology economically viable [7].

In this study, the production of bio-octanol from genetically engineered cyanobacteria and its subsequent recovery by liquid-liquid extraction was simulated with Aspen Plus for the first time in published literature. A techno-economic assessment was performed to evaluate the economic potential of this novel process and its sensitivity to bio-fuel mandating policies. This study provides accurate estimates of the biomass and biofuel yields achievable with flue gas from a 500MW coal-fired power plant. It offers a benchmark for further investigations on the microbial production of excreted octanol, which is receiving increasing interest from the scientific community due to its promising use as a drop-in fuel.

2 | Background

Bioethanol is currently the most widely used biofuel and is found in all petroleum fuels distributed in the EU and the UK [8]. However, the high oxygen content, low carbon chain length and poor lubricity of ethanol limits the maximum blend concentrations to 10 vol% in order to avoid excessive engine wear and stress [8]. Alcohols of longer chain length have thus been increasingly studied and octanol was found to have diesel-like fuel properties [9]. Its energy content, lubricity, viscosity and thermodynamic properties make it a direct diesel replacement, alleviating the necessity of transforming existing vehicles and distribution infrastructures [10].

Octanol, as opposed to butanol and ethanol, does not accumulate substantially in any known organism and can therefore only be produced by genetically engineered microbes. Previous studies have reported the synthesis of 1-octanol by extending the 1-butanol pathway; via the process of reverse beta-oxidation and by modifying pathways linked to amino-acid and fatty-acid metabolisms [11]. Akhtar et al. performed fatty-acid chain elongation with fatty acyl ACP intermediates to produce 62 mg/L of octanol in *E.coli* and demonstrated that it can be exclusively excreted into the culture media via a naturally occurring efflux pump mechanism [9]. Yunus and Jones reported the first synthetic route for octanol biosynthesis in cyanobacteria [10]. By implementing the elongated fatty-acid metabolism pathway in *Synechocystis sp.* PCC 6803, a 15-fold improvement in the titer of excreted octanol was achieved.

The growth conditions and kinetics of *Synechocystis sp.* PCC 6803 have been extensively studied due to the cyanobacteria's ability to efficiently capture CO_2 and convert it into valuable fuels. The simplicity of both culture conditions and genetic manipulation as well as its short doubling time compared to other microalgae make *Synechocystis sp.* PCC 6803 an interesting choice for industrial biotechnology [12]. The main parameters influencing biomass growth are culture density, temperature, mixing rate, pH, supply rates of CO_2 and nutrients, light intensity and growth inhibition due to produced

chemicals [13]. Wagner et al. proposed a mathematical model successfully capturing the effects of light intensity and temperature on the growth rate of *Synechocystis sp.* PCC 6803 [8].

Continuous microalgae cultivation has been studied in 3 main types of photobioreactor (PBR) systems: open raceway ponds, tubular PBR and flat panel PBR [14]. Despite being inexpensive and easy to build, the risks of contamination, the low biomass productivity and the large water uptake of open ponds make them less attractive than closed-systems for microbial fuel production [15]. Flat-panel PBR are a promising configuration which was shown to achieve the highest average photosynthetic efficiency, areal and volumetric productivities [14]. However, due to the novelty of this technology, large scale flat-panel PBR are 43% more expensive than well-established tubular PBR [15].

The large-scale cultivation of microalgae to produce biofuels and high-value compounds is still considered to be in its infancy. Nevertheless, a few cultivation plants using flue gas as a carbon source are in commercial operation, including the "Hanging Gardens" facility in Brandenburg (Germany) which utilises the flue gas from a nearby coal-fired power station to grow cyanobacteria in a 48000 L closed system PBR [16]; and the Algafarm in Portugal which produces microalgae in 1300 m^3 tubular photobioreactor using flue gas from a cement factory as feedstock [17].

The purification of the end-product has been significantly facilitated thanks to the natural excretion of octanol in the cell medium, as opposed to the energy-intensive extraction by cell lysis and isolation of biofuels contained in the internal cellular compartments [9]. Despite this major improvement, the downstream processing of biofuels remains an important technical and economic barrier to commercialisation. Different technologies, including distillation, gas stripping, pervaporation, membrane separation, adsorption and liquid-liquid extraction have been investigated for the integrated recovery of ethanol and butanol from the fermentation broth [18]. Modelling and simulation of those processes has found that ionic liquid extraction was the most energy efficient separation technology for excreted butanol [8]. However, similar studies must still be carried out for the production of bio-octanol.

The economic feasibility of biofuel production from microalgae has been assessed in multiple studies and for different techno-economic scenarios. The consensus is that large-scale algal production could become profitable given favourable market conditions and political measures [7],[19]. In addition to process intensification, environmental policy promoting greener transportation fuels could indeed lead to a market expansion and rise in selling price for octanol. In 2018, the octanol market size was £160 million and current projections expect the market to reach £230 million by 2025, due to the increasing demand for biofuels [20]. The valorisation of the biomass by-product could also help reduce biofuel production costs [8].

3 | Method

3.1 Process modelling

The production of octanol by genetically engineered cyanobacteria and its subsequent recovery was modelled in Aspen Plus V11 using the thermodynamic method based on the NRTL equation of state. The algae was modelled as a solid with the molecular formula $C_{106}H_{263}O_{110}N_{16}P$. The solid enthalpy and Gibbs energy of formation, as well as the solid heat capacity polynomial coefficients and molar volume were retrieved from published literature [21],[22]. The process, shown in Figure 3.1, consists of 3 stages: (1) a culture medium preparation section where nutrients are mixed with water enriched in dissolved CO_2 following mass transfer between flue gas and water in a counter-current packed tower; (2) a cultivation stage with a photobioreactor (PBR) in which biomass, later harvested by a filter, and octanol are produced; and (3) an octanol recovery process where the alcohol is extracted from the aqueous phase with a solvent and distilled to reach the required purity for usage as drop-in fuel [23]. To account for pressure drops in the system, the feed to the PBR, the liquid outlet of the filter and the water and solvent recycle streams are passed through pumps. The PBR is assumed to be inoculated with 1g/year of microalgae.

3.1.1 Growth kinetics and octanol production

The production of biomass is governed by the equation: $106\,CO_2 + 16\,NO_3^- + HPO_4^{2-} + 122\,H_2O + 18\,H^+ \longrightarrow C_{106}H_{263}O_{110}N_{16}P + 138\,O_2$ [24]. The kinetics of microalgae growth were assumed to follow a Monod model [25]:

$$\frac{dX}{dt} = \mu \cdot X \tag{3.1}$$

where X is biomass concentration (g/L) and μ is biomass specific growth rate (h^{-1}). Cyanobacteria decay was not modelled since it has been shown to become prevalent only at reaction temperatures above 34°C, which will not be studied in this project [8].

Previous studies have found that combined CO_2 and nutrient concentrations, temperature and light intensity are the main factors influencing cyanobacterial growth rate [7]. In this study, CO_2 and nutrients, including phosphorus and nitrogen sources, were assumed to be supplied in excess, thus biomass growth is only a function of temperature and incidence light, which are considered as two independent factors. The rate can thus be expressed as the product of two distinct functions of light intensity $k(Irr)$ and temperature $k(T)$ [25]:

$$\mu = \mu_{\max} \cdot k(Irr) \cdot k(T) \tag{3.2}$$

where μ_{max} is the maximum biomass specific growth rate (g/L).

The Aiba model is used to simulate the effect of light intensity on cyanobacteria growth [8]:

$$k(Irr) = \frac{1}{Irr + k_s + \frac{Irr^2}{k_i}} \tag{3.3}$$

where k_s is the photosaturation constant (μE) and k_i is the photoinhibition constant (μE).

Temperature determines the activation of biochemical enzymes involved in the process of cellular reproduc-

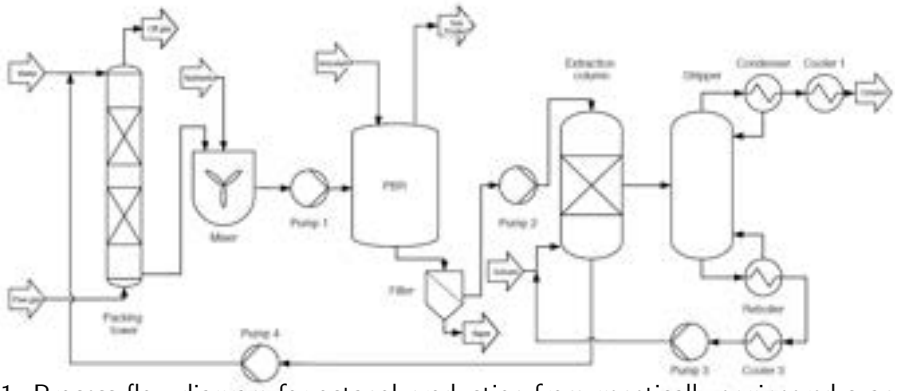

Figure 3.1: Process flow diagram for octanol production from genetically engineered cyanobacteria

tion [26]. The thermal effects on bacterial growth rate can be simulated with the Arrhenius equation, although the model was not developed to predict the possible negative impact of high temperature on enzymatic activity [25]:

$$k(T) = \mathrm{A_g} \cdot exp\left[-\frac{\mathrm{Ea_g}}{\mathrm{R}}\left(\frac{1}{T} - \frac{1}{\mathrm{T_g}}\right)\right] \qquad (3.4)$$

where A_g is the pre-exponentional factor, Ea_g is the algae growth activation energy (kJ/mol) and T_g is the reference temperature for algae growth (K).

The parameters μ_{max}, A_g and Ea_g were determined by fitting the model to published data for the growth of cyanobacteria *Synechocysystis* PCC 6803 [13]. The constants k_s and k_i were obtained from unpublished experimental data at a constant temperature of 30°C [27]. The values obtained are provided in the Supplementary Information.

Octanol production follows the stoichiometric equation: $8\,CO_2 + 9\,H_2O \longrightarrow C_8H_{18}O + 13\,O_2$. Experiments conducted under controlled conditions showed that the average ratio of octanol production to biomass growth is 0.83 [27].

3.1.2 Algae cultivation conditions

It was chosen to simulate the growth of *Synechocysystis* PCC 6803 in a tubular photobioreactor due to the commercially proven suitability of this technology [28]. In horizontal tubular PBR made of stacked layers of glass tubing, the algal culture is circulated by a centrifugal pump under turbulent regime to allow good mixing. The pressure drop ΔP in the tubular reactor can be calculated in Pa for any flow velocity v in m/s as follows:

$$\Delta \mathrm{P} = \zeta \cdot \frac{\rho}{2} \cdot \mathrm{v}^2 \qquad (3.5)$$

where ζ is given by the glass tube manufacturer as 1.96 for the 5.5m long tubes and 0.252 for the U-bends, and ρ is the algae culture density approximated to 1 g/cm^3 [28]. The tubular photobioreactor's operation resembles a plug flow reactor and was modelled with the Aspen block for a PFR [26]. The transmissivity of the glass tubes were taken as 60% to calculate the heating energy of the solar radiation [29].

Photoautotrophic production of excreted octanol from genetically engineered cyanobacteria is best performed in a country with good solar irradiation and temperatures generally comprised within the range for optimum microalgae growth. Andalusia in Spain was found as a suitable location. Light irradiance and air temperature data were retrieved and clustered, with the *kmeans* algorithm available in MATLAB, into four typical time periods as shown in Figure 3.2 [30]. Assuming that no growth can occur with zero solar irradiance, corresponding to night-time, the process could typically be operated for 4246 hours per year.

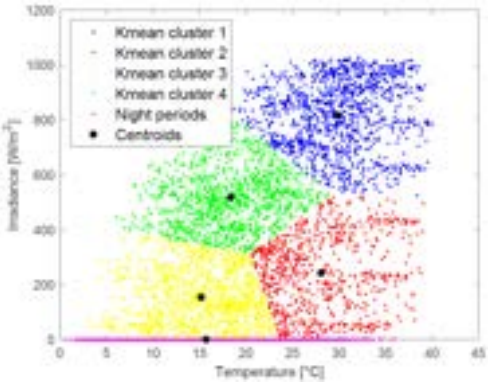

Figure 3.2: Graphical representation of the K-means clustering as a function of temperature and solar irradiance

Fuel gas from a coal-fired power plant was selected as the carbon source for microalgae growth. Its typical composition was taken as 12-14 vol% CO_2, 8-10 vol% H_2O, 3-5 vol% O_2 and 72-77 vol% N_2, assuming that SO_x and NO_x were efficiently removed by pollution control technologies [31]. The amount of flue gas feed was based on the Los Barrios thermal power plant in Cadiz, which is representative of a 500 MW coal-fired power plant delivering electricity to 1.5 million inhabitants [32]. The PBR feed also contains two fertilisers: sodium nitrate and monosodium phosphate, which were added in stoichiometric proportions [33]. For simulation simplicity, these chemical species were modelled as HNO_3 and H_2PO_4.

3.1.3 Octanol recovery

Unlike most microbial biofuel production processes, the genetically engineered cyanobacteria *Synechocysystis* PCC 6803 excretes octanol directly into the culture medium, thus avoiding costly microalgae harvesting and dewatering, and cell lysis steps [5]. The PBR out-

let stream is passed through a low energy centrifugal separator to retain all the solid algae from the liquid phase. The wet algae, containing 0.1% of the liquid outlet stream, is collected and multiple biomass recovery options are evaluated.

The octanol present in the aqueous phase is then recovered by counter-current Liquid-Liquid Extraction. Hexadecane was selected as solvent due to its proven low toxicity towards microalgae, since water from the extractor is recycled to the cultivation stage [34]. The 10-stage extraction unit is operated at the cultivation temperature. The water stream is then recycled to the cultivation stage. Due to the negligible amounts of nutrients in the spent medium and an organic load assumed to be below the legal thresholds for water discharge in the sea, wastewater treatment was not considered in this simulation [33]. The octanol-rich solvent is then fed to a stripper, modelled using an Aspen-built RadFrac column containing 10 theoretical stages, with the molar reflux ratio set at 1.1. The polishing step was optimised to reach an octanol purity above 99%. The product stream is cooled to ambient temperature before storage and transportation. The regenerated solvent is cooled down to cultivation temperature prior to recycling to the extraction column.

3.2 Techno-economic assessment

3.2.1 Capital and operating cost estimation

The capital costs for equipment were estimated following equipment sizing. The cost estimates found in literature were adjusted using the ratio of Chemical Engineering Plant Cost Index (CEPCI) for the reference year and 2020 [35]. Prices given in foreign currencies were converted to GBP at the exchange rate of November 2020. Table 3.1 summarises the design equations for economic evaluation of the equipment.

Carbon dioxide from the flue gas was captured in a gas-liquid contactor whose inlet area was estimated from engineering studies performed by Carbon Engineering Ltd [36]. The cost for the PBR was obtained from a quote by SCHOTT AG for a complete system including glass tubes, connectors and the metallic frame [28]. The PBR is fitted with electrical heaters, with an electrical efficiency of 100%, to maintain a constant growth temperature during colder periods. The size and costs of the centrifugal separator were approximated from the PHOTOFUEL project [33]. The costs for the single-stage centrifugal pumps and the static mixer are derived from a correlation proposed by Towler and Sinnott [37]. The cost of storage tanks were estimated through scaling of industrial data [38].

The coolers and the condenser were modelled as shell-and-tube heat exchangers operating with 12.7°C deep water from the Western Mediterranean Sea as cooling fluid [39]. The kettle reboiler is operated with steam diverted from power station steam cycle at 280°C. The heat exchange areas are computed with the logarithmic mean temperature difference of the two fluids, assuming a constant temperature for the cooling/heating medium. This assumption is a reasonable hypothesis since the working fluid flow rates can be tuned to prevent large temperature variation. The overall heat transfer coefficient is evaluated by Aspen Plus to be 0.85 $kW.m^2.K^1$. The heat exchanger costs were estimated through a correlation, developed by Couper et al., where f_d is the type factor, f_m the material factor, f_p the pressure factor and C_b a function of the heat transfer area [38].

Table 3.1: Design equations for equipment costing

Equipment	Cost equation	Unit
Packed tower	$15800(A_{inlet})$	m^2
Static mixer	$570+1170(F)^{0.4}$	L/s
Photobioreactor	$2.4(V_R)$	L
Electrical heaters	$0.0103(P)$	kW
Filter	$7467(P)$	kW
Columns	$17640(D)^{1.066}(H)^{0.802}$	m
Heat exchangers	$1.827 f_d f_m f_p C_b(A)$	m^2
Pumps	$8000+240(F)^{0.9}$	L/s
Storage tanks	$470(V)$	m^3

In order to calculate other fixed capital costs the Factorial Method was implemented [37]. This method equates the total fixed capital costs of the plant to the total purchased equipment cost multiplied by the installation or Lang Factor. A value of 3.63 was chosen as this corresponds to a mixed fluids-solids processing system. The method also equates individual Direct and Indirect Capital Costs as factors of the total purchased equipment cost. Individual costing calculations and values can be found in the Supplementary Information.

The utilities and chemical prices used in this study are also reported in the Supplementary Information. Cooling water is brine which is assumed to be obtained for free through connections to the cooling system of the power-plant. Flue gas is also a free feedstock. Electricity is mostly used for electrical heating of the PBR, cultivation harvesting by the separator and medium circulation. The electrical power required to circulate the cultivation medium was determined based on the pressure drop in the system, assuming a pumping efficiency of 70% [28]. For plants consuming over 500 MWh/year, industrial electrical prices equal 7.09 pence per KWh [40]. CO_2 emission factor for the electricity from the average mix of Spain in 2019 is taken as 0.19 tCO_2-eq/MWh [41].

3.2.2 Financing & Financial Assumptions

Reflecting the average lifespan of a glass-tubular PBR, the lifetime of the plant has been assumed to be 30 years with a constant year on year depreciation [28]. The project is approximated to a European Green and Renewable Energy firm operating in the 2019 financial year. As such the Stern School of Business recommends a debt to equity ratio of 1.09 with financing covered by 52% debt and 48% equity [42]. With the advent of the EU Green Bond Standard and other green financing solutions unlocked by the new EU budget, the debt is to be covered by Green bonds with a maturity of 20 years and an annual interest rate of 0.875% [43]. In addition, a corporate tax rate of 25% is incorporated, reflecting the plant's location in Andalucía [44]

In order to generate key performance indicators

(KPIs) for the project the equity rate is calculated using the Capital Asset Pricing Model (CAPM). The equity rate r_e can be expressed as a function of the risk-free rate r_f and the risk premium r_p:

$$r_e = r_f + (\beta \cdot r_p) \tag{3.6}$$

where β refers to the beta coefficient. The risk-free rate is defined as the rate of return on short-term US Treasury bills, backed by the US government which enables its risk-free nature. The risk premium is associated with the excess in returns earned by investing in the stock market when compared with the risk-free rate. As of October 2020 in Spain the risk-free rate and risk premium were -0.62% and 8.19% respectively [45]. The beta coefficient used was 0.88 indicating the Green and Renewable Energy sector has a systemic risk lower than the market [42].

Using the equity rate, the weighted average cost of capital (WACC) can be calculated by:

$$WACC = \left(\frac{E}{D+E}\right) \cdot K_E + \left(\frac{D}{D+E}\right) \cdot K_D \cdot (1-t) \tag{3.7}$$

which takes into account the companies debt (D) and Equity (E) financing as well as the associated cost of equity (K_E), cost of debt (K_D) and corporate tax rate (t).

Due to the project's inherent green nature, it is assumed that financial support can be acquired via carbon credits implemented by the EU's Emission Trading Scheme (ETS), as well as renewable energy subsidies from the Spanish Government and the EU. The process utilised to generate bio-octanol requires a constant feed of CO_2 from flue gas. Accounting for CO_2 emissions from electricity consumption, the process will still produce negative net carbon dioxide emissions. Under the EU's ETS, CO_2 emissions are a tradable commodity with an incentive for higher polluting firms to pay others for carbon credits. These credits are in the form of a European Union Allowance (EUA) which gives the holder the right to emit one tonne of carbon dioxide. As of November 2020 the price of one EUA is €28 [46]. The European Commission's Green Deal which is committed to carbon neutrality by 2050, has indicated that the price of EUA's will continue to increase to €50-€60 or approximately £50 by 2030 [47]. Given the longevity of the plant, this figure was used when calculating how many carbon credits could be sold on an annual basis. In 2011 EU subsidies for bioethanol were estimated to be €0.21 per litre, which when adjusted for inflation and exchange rates, equals £0.21 per litre [48]. This figure was used when estimating potential EU subsidies for octanol production.

4 | Results and Discussion

This section contains a presentation and discussion of the process simulation from both a technical and economical point of view.

4.1 Process simulation

4.1.1 Algae growth and octanol recovery

The baseline simulation scenario was constructed for a flue gas feed of 2.7 ktonnes/year of CO_2-equivalent at 150°C. The water feed to the gas-liquid contactor, assumed to be at 20°C, was adjusted to 20 tonnes/hour, in order to achieve a dissolution rate of 5.3 g of CO_2 per kg of water. This corresponds to 30% of the CO_2 from the flue gas being dissolved in water. Due to the heat transfer phenomenon between the hot flue gas and water during the CO_2 dissolution step, no cooling nor heating is necessary for the CO_2-rich aqueous stream to reach the desired operating temperature of the photobioreactor (PBR), thus avoiding costly additional equipment and energy requirements.

The PBR is operated at the inlet temperature of the feed, which must be comprised between the optimum range of operating conditions, i.e between 30°C and 34°C [8]. The tubular reactor is modelled as 5.5 meter long glass tubes with an outside diameter of 65 mm, connected together with U-bends to achieve a total PBR volume of 29 m^3. This configuration results in an algae residence time of 36 minutes, which corresponds to the trade-off between high oxygen concentration and growth rate. Despite not being including in the developed kinetic model for cyanobacteria growth, the accumulation of O_2 in the PBR can indeed inhibit and led to up to 30% loss of biomass productivity with oxygen concentrations above 30 mg/L [49]. To avoid oxygen build-up and thus growth inhibition, frequent degassing is required, thus limiting the length of the tubular PBR [50].

At the outlet stream of the PBR, 99.5% of the CO_2 dissolved in water was found to have been converted to biomass and octanol. This is coherent with the results obtained by Weissman and Tillett, reporting that microalgae could convert more than 99% of CO_2 in solution [51]. The simulation resulted in an algae concentration of 1.44 g/L, which is coherent with the optical density reported for the experimental growth of *Synechocystis* PCC 6803 [27]. The microalgae converted carbon dioxide into octanol via the elongated fatty-acid metabolic pathway, with each kilogram of biomass fixing 2.26 kg of CO_2. The simulated fixation efficiency is above the average value of 1.83 $kg_{CO_2}/kg_{biomass}$ [52]. The improved fixation of CO_2 could be explained by the limitations of the kinetic model which does not account for oxygen inhibition and the risk of toxicity of the produced organic compound on the microalgae cells [49]. Another reason for the discrepancy lies in the fact that the kinetics were derived for a cyanobacteria which was genetically engineered to maximise the uptake of CO_2 for the production of excreted octanol [13].

Following filtration, the octanol titer in aqueous solution was found to be 1.2 g/L. Although the maximum reported concentration for octanol produced by genetically engineered *Synechocystis* PCC 6803 is 905 mg/L, the simulation result is deemed feasible when no product is lost through volatilisation [10]. The selectivity of cO_2 towards octanol is limited by the toxicity of the alcohol.

The concentration of octanol in the PBR must not exceed the threshold which would lead to cyanobacteria growth inhibition [10].

A solvent-to-octanol mole ratio of 3.5 resulted in almost complete recovery of the octanol into the hexadecane solvent. Indeed, only 1 g per year of octanol would remain in the water stream to be recycled to the gas-air contactor. Very little hexadecane was found to dissolve in the aqueous solution and the mass fraction of solvent is less than the maximum acceptable limit for microalgae growth of 0.05% [53]. The octanol-rich solvent at cultivation temperature was further distilled in a RadFrac column where 98.8% of the octanol is stripped from the hexadecane solvent. The lean solvent can be recycled to the extraction column with the addition of a make up, corresponding to 10 wt% of the fresh solvent, to account for a purge system avoiding octanol build up during liquid-liquid extraction.

With a yearly flue gas feed of 7900 tonnes, the baseline process can thus yield up to 104 tonnes per year of octanol with a purity of 98.8%, in addition to 125 tonnes per year of wet biomass with a dry algae content of 60 wt%. Detailed stream tables for the baseline process simulated with Aspen Plus can be found in the Supplementary Information. Furthermore, it should be noted that the model, simulating clean flue gas, does not take into account the potential contamination of the algae by toxic compounds present in some flue gas. Nonetheless, studies have found that the growth of cyanobacteria was not negatively impacted by NO_X and CO at their typical concentrations in flue gas [54]. Moreover, once the carbon capture industry is well developed, it would be interesting to consider operating the process with pure CO_2 to avoid any contamination.

4.1.2 Energy balance

The photosynthetic efficiency (PE) of phototropic growth was calculated as the energy stored as biomass and octanol per unit of light absorbed, assuming an algae combustion enthalpy of 23.6 kJ/g of dry biomass [55]. With a yearly irradiance of 6883 $MJ.m^{-2}.year^{-1}$, PE for algae growth only was found to be 22.5%, which is coherent with the reported maximum PE under ideal outdoor conditions [55]. The value increased to 52% when accounting for the energy contained in octanol. Taking the energy content of octanol as 49.6 MJ/kg, the baseline process indeed yields 2032 $MJ.m^{-2}.year^{-1}$ in a PBR of 1904 m^2 [9].

Furthermore, it should be noted that the solar radiance had a limited impact on the cyanobacteria growth rate. The hourly production of biomass and octanol for the four different typical time periods, assuming a constant reaction temperature, varied by less than 0.05%. This result is coherent with the Aiba model which predicts a wide optimal range for light intensity [8]. However, the model does not account for the internal variations of light intensities in the photobioreactor [29]. The PBR configuration and operation thus need to be optimised on a case-by-case basis to maximise the photosynthetic efficiency.

Despite the limited effects of light intensity on algae growth, clustering the weather data provides an insight into the heating requirements for the cultivation stage. The energy provided to the PBR by the sun was calculated for each typical time period to determine the energy requirements to maintain the culture medium at 30°C, accounting for the heat transfer by convection from the ambient air. It was found that external heating was required only for the colder and less sunny time periods, corresponding to winter months. The heating requirements for the PBR account for 44% of the electricity consumed by the cultivation stage, amounting to 596 MWh/year. The circulation pumps and the filter account for 43% and 13% respectively. Heat in the form of steam is supplied to the reboiler at a rate of 0.9 MWh/kg of octanol produced. The estimated energy requirement for the process, excluding the cooling duty, represents less than 1% of the energy contained in the octanol product, thus highlighting the immense potential of microbial biofuels. Wagner et al. had found that the break-even butanol concentration, in terms of energy, was 3.7 g/L for LLE with ionic liquid [8]. Due to the higher energy content of octanol and the non necessity of a two-stage extraction process and a polishing step to obtain high purity alcohols, the octanol process is most likely to be less energy intensive for the same microalgae. Further developments in the model would have to be performed to confirm this hypothesis. The energy requirements for the cooling system, as well as the pumping power of the cooling sea water and the heating demand for the steam, were indeed not included in this study. Finally, the feasibility of heat integration could be explored, especially between the kettle reboiler and the solvent cooler.

4.2 Process sensitivity analysis

4.2.1 CO_2 dissolution

The mass flowrate and the temperature of the water feed were varied from 5-35 tonnes/hr and 15-30°C respectively, to measure their impact on the rate of CO_2 dissolution and the production of octanol. The nutrients feed was automatically adjusted to the amount of CO_2 dissolved and the reaction temperature was that of the inlet feed to the PBR. It was found that the lower the water temperature, the more CO_2 dissolved, which is coherent with experimental and modelling results showing that the solubility of CO_2 decreases with increasing temperature [56]. For constant water feed temperatures, the concentration of octanol at the PBR outlet initially triples when the flowrate is increased to 20 tonnes/hr, followed by a slower linear increase of 0.01 g/L of octanol per tonne of extra water. This trend attests that, although the amount of CO_2 dissolved in water increases linearly with the flowrate, the concentration of octanol which can be achieved at the PBR outlet reaches a plateau, which could be explained by the reduced residence time of the reactants in the PBR of constant volume. It was also observed that, without additional cooling of the flue gas feed, the reactor feed temperature is above the acceptable growth conditions of 34°C for water flowrates below 17 tonnes/hr at 20°C.

Moreover, increasing the water flowrate leads to a greater pressure drop in the PBR thus higher energy requirements for the circulation pump, as well as for the

filter. The energy usages of the cultivation and harvesting stages per kg of octanol produced were plotted as a function of achieved octanol concentration. Figure 4.1 shows that the maximum octanol concentration is achieved for a colder water flow and that the energy requirements for a given octanol concentration increase with water temperature. To reach the same octanol concentration, the water flowrate and thus the pumping and filtration power are higher for a higher water feed temperature due to the reduced solubility of CO_2 [56].

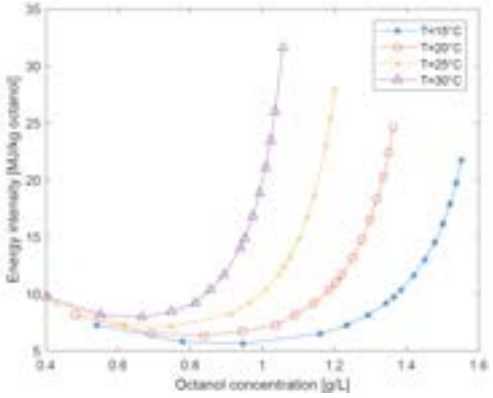

Figure 4.1: Cultivation energy as a function of octanol concentration for different water feed temperatures

Figure 4.1 suggest that there is an optimum octanol concentration, associated with water feed flowrate, to minimise the energy requirement of the circulation and filtration systems. The energy intensity, although initially high due to the low amount of CO_2 dissolved and thus available for biomass growth, then decreases until a plateau of octanol concentration is reached. Passed this point, the energy intensity increases exponentially, attesting to the significant additional power required to marginally increase the octanol concentration. There thus exists a trade-off water flowrate between the octanol concentration and the energy required to pump and filter the culture medium.

The amount of dissolved CO_2 in water, available for conversion to biomass and octanol, also determines the process's ability to alleviate the global warming potential of the flue gas. In the baseline process scenario, 450 tonnes per year of CO_2 are captured from the flue gas. The electricity supply for the pumping, filter and heating systems is responsible for 113 tonnes of CO_2 equivalent emitted per year. The simulated microalgae process is thus able to prevent the emission of over 300 tonnes of CO_2 every year. The embedded emissions in the process were found to represent less than 3% of the total emissions due to the plant's construction and operation, and could thus be neglected [57]. Although the combustion of octanol in engines will emit the CO_2 captured by the process, biofuels are a carbon neutral source of energy which, in contrast to fossil fuels, does not emit additional CO_2 into the atmosphere.

4.2.2 Solvent usage

Hexadecane, despite being recycled at over 90%, is the most expensive chemical involved in the process. It is essential to optimise its usage in liquid-liquid extraction to reduce operating costs. The achieved purity of the octanol product was investigated for different mass ratios of solvent to octanol. It was found that purity sharply rose with an increasing ratio up to 98.5% purity, corresponding to a ratio of 2 kg of solvent per kg of octanol extracted. To reach the required purity of 99%, the ratio must be above 3, thereby confirming that the solvent feed simulated in the baseline process is optimal.

4.3 Capital and operating costs

When calculating CAPEX and OPEX for this plant process, pricing for revenue and costs often varied significantly depending on the source. As a result, it was decided to maintain a conservative view when formulating the profitability of the process. The small scale of the plant further hinders the process's potential profitability. Combining these factors results in a project that is unable to break-even during it's 30 year lifespan. Further sensitivity analysis will provide potential solutions for financial feasibility.

Total equipment costs were priced at £339,000, which when combined with a Lang factor of 3.63 generate a Total Fixed Capital of £1.23 million. A working capital totalling 11.3% of this value is incorporated into the initial financing [42]. This renders a Total Capital Cost of £1.369 million split £714,000 and £655,000 between debt and equity respectively; saddled with a loan interest rate of 0.875% and equity rate of 6.59%. Due to operating costs narrowly outstripping revenues, the plant is unable to payback its initial financing during its 30 year operating history. Sales of octanol and algae total £113,000 and £163,000 each, equalling an annual revenue stream of £277,000. Algae pricing is extremely varied due to its wide applicability. Subsidies of £26,000 and carbon crediting of 17,000 a year increase the total annual revenue to £320,000.

Fixed operating costs include labour, maintenance, insurance and plant overheads. Due to the plant's small size, labour costs represent the salaries of two workers and a plant supervisor, totalling £89,000 annually [33]. Maintenance and insurance are taken as 5% and 1% of the Total Fixed Capital respectively with plant overheads equalling 50% of labour costs [37]. Raw materials cost add an additional £45,000 and utilities equal £43,000 annually. Hence, with fixed costs, variable costs and depreciation aggregating to £207,000, £88,000 and £41,000 respectively, total cost of sales amounts to £336,000. Coupled with the total revenue, the plant exhibits an annual gross profit of -£16,000.

4.4 Strategies for economic feasibility

4.4.1 Options for algae recovery

With a production rate of 104 tonnes of octanol per year, the financial model predicts octanol sales are unable to counter the operating and maintenance costs needed to run the plant. As a result, a new revenue stream is required. Approximately 125 tonnes of dry algae are required to produce 104 tonnes of octanol. Selling this biomass is a necessity if there is to be any chance of making this process financially viable. Besides energy the algae market is split into three additional segments; Cosmetics/Pharmaceuticals, Food and Chemicals. These market segments decrease in value but increase in volume. Diversifying algae recovery is critical as selling it all to one sector may instigate a

price slump due to oversupply.

The cosmetic industry provides the highest potential returns for algal revenues with a variety of algal byproducts used in high end skincare products. Market research firm Kline estimates the market size for these byproducts to be £300 million in the EU in 2013. Many of the byproducts used in skincare such as cartenoids, omega-3 fatty acids and sterols are also used in the pharmaceutical industry [58]. These marine natural products (MNPs) currently represent a niche corner of the £700 billion global pharmaceutical market. However, with increasing demand from the WHO for new antibiotics and other drugs, this niche market is expected to expand [59].

Health capsules currently dominate 75% of the algae food market with the remainder used as food additives in pasta, bread and yoghurt. Algal health capsules have a market volume of up to 10,000 tonnes of dry matter per year and an average turnover of £900 million a year [60]. While whole microalgae biomass sells for £35 per kg, certain byproducts sell for a lot more [59]. β-Carotene can sell upwards of £1850 per kg, omega-3 PUFA for £30,000 and polyunsaturated fatty acids for £45,000 per kg [61]. However, the largest obstacle to the expansion of the algal food market are stringent food safety regulations, with EC regulation 258/97 applying to the European market. Until some of these barriers are lowered, the commercial viability of this market is questionable. Instead a common alternative to food, is incorporating algae into animal feed. For example in 1999, 1000 tonnes of microalgae were used for aquaculture costing up to £75 per kg [62].

Fertilisers are a viable alternative due to algae's rich nitrogen and phosphorous content. This is greatly utilised in India where cyanobacteria are increasing annual rice yield by 22% [59]. This is a result of cyanobacteria containing a variety of growth promoters from bioactive polysaccharides to IAA growth hormones. The microalgal biostiumulants market was worth £375 million in Europe in 2013. Biotech firm Soley sell microalgae soil fertilisers for approximately £15 per kg [59]. However for this study algae was priced at £1.3 per kg, mirroring the pricing of Spanish firm Agroplasma S.A [59]. In relation to the figures provided above this price is evidently low. However this matches with the conservative values used to estimate the profitability of the process. In addition, further expenses may be necessary to treat algal salinity before it can be utilised as a fertiliser.

4.4.2 Sensitivity to bio-fuel mandating policies

With a current subsidy of £0.21 per litre or 19% of octanol sell price, the plant process is economically infeasible. The EU-2020 climate policy mandates that biofuels account for a minimum 7% share in transportation with the global biofuel share set to rise to 15% by 2065 [63]. The biofuel industry is currently in it's infancy. In order to nurture and grow, it is in dire need of frequent cash injections. This study argues that the biofuel industry will follow a similar template that the solar industry has taken over the last 20 years, where solar energy costs have declined by 82% between 2010-2019 [64]. This achievement was only made possible by massive state backed subsidies and tax brakes that artificially propped and stabilised the industry long enough for technological advances and mass production to cut costs. While China was at the forefront of solar advancements, the EU can do the same with the biofuel market.

To do so, co-ordinated government financial support is required. Therefore this study performed a sensitivity analysis to estimate the amount of support required to artificially protect the industry from market forces that would otherwise tear it down. Note that performing a sensitivity analysis on subsidies can be used as a proxy for alternative government support such as tax brakes as they both artificially inflate profitability.

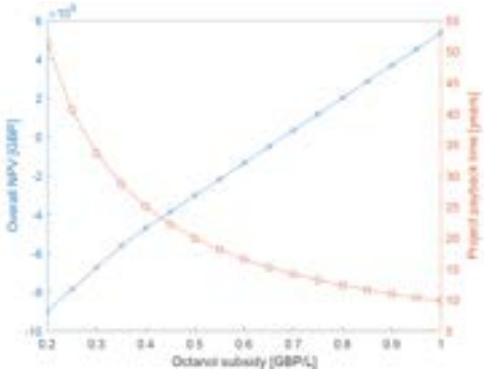

Figure 4.2: NPV and Project Payback as a function of Octanol Subsidy Pricing

As displayed in Figure 4.2, the current subsidy of £0.21 per litre of octanol equates to an overall NPV of £-874,000 with a payback period just shy of 49 years. Given the plants 30 year lifespan, investors will never be able to recoup their losses. A subsidy of £0.68 per litre of octanol is required to break even with an associated pay-back time of 14.6 years. This corresponds to an increase in annual subsidy support from £26,400 to £85,400.

However, this study recommends an annual cash injection of £119,000 which equates to a subsidy of £0.95 per litre of octanol in order to cement the financial viability of the process. Note that this value is more than the break-even point with an NPV of £453,000. This is necessary to boost investor confidence and make a persuasive argument to invest in the plant rather than the bond market or other safer, low return alternatives. Moreover, this increases the return on equity (ROE) to 3.9% which matches the average ROE of Green and Renewable Energy firms in Europe in 2019 [42].

Nevertheless, this study is aware that a subsidy of £0.95 per litre of octanol, may not be politically acceptable. It is therefore expected that some of the additional funding will be covered by rising octanol prices, lower costs due to economies of scale and additional revenue from algae byproducts. As a result, a lower subsidy may be sufficient to guarantee profitability in the industry.

5 | Conclusion

This study argues that the large-scale production of bio-octanol by genetically engineered cyanobacteria is a feasible and replicable pathway for renewable and green energy. However, technological success does not equate

with commercial feasibility and many barriers remain to ensure the process's long term viability.

The process simulation results tend to encourage the application of innovative process design methodologies to industrial scale production of biofuels by microalgae. Whilst the techno-economic evaluation performed in this study proves that incentives for financial investments and political measures are required to develop the microbial fuel industry.

Although the utilisation of Aspen Plus has underscored the technological feasibility of the process, computer models are prone to limitations and further development of this study should primarily include pilot plant experiments. Moreover, the expected positive environmental impact of this process must be validated by a Life Cycle Analysis which would provide added weight to the argument that this technology should be an integral part of the EU's new Green Policy. The investigation of environmental impact of biofuel production from microalgae has already commenced under the EU's Horizon 2020 Photofuel project.

6 | Acknowledgements

The authors would like to express their gratitude to Dr Dongda Zhang from the University of Manchester, Daniel Rodriguez Vallejo and Zhixuan Wang from Imperial College London for their generous support and guidance on kinetic modelling and process simulation.

References

[1] *The ten point plan for a green industrial revolution*, GOV.UK, Nov. 2020. [Online]. Available: https://www.gov.uk/government/publications/the-ten-point-plan-for-a-green-industrial-revolution.

[2] *A european green deal*, European Commission, Text, Dec. 2019. [Online]. Available: https://ec.europa.eu/info/strategy/priorities-2019-2024/european-green-deal/actions-being-taken-eu_en.

[3] H. Ritchie and M. Roser, *Emissions by sector*, Our World in Data, 2016. [Online]. Available: https://ourworldindata.org/emissions-by-sector.

[4] H. A. Alalwan, A. H. Alminshid, and H. A. S. Aljaafari, "Promising evolution of biofuel generations. subject review", *Renewable Energy Focus*, vol. 28, pp. 127–139, Mar. 1, 2019. DOI: 10.1016/j.ref.2018.12.006.

[5] V. Piemonte, L. Di Paola, G. Iaquaniello, and M. Prisciandaro, "Biodiesel production from microalgae: Ionic liquid process simulation", *Journal of Cleaner Production*, Special Volume: Process Integration for Cleaner Production, vol. 111, pp. 62–68, Jan. 16, 2016. DOI: 10.1016/j.jclepro.2015.07.089.

[6] J. Trivedi, M. Aila, D. P. Bangwal, S. Kaul, and M. O. Garg, "Algae based biorefinery—how to make sense?", *Renewable and Sustainable Energy Reviews*, vol. 47, pp. 295–307, Jul. 1, 2015. DOI: 10.1016/j.rser.2015.03.052.

[7] B. Patel, B. Tamburic, F. W. Zemichael, P. Dechatiwongse, and K. Hellgardt, *Algal biofuels: A credible prospective?*, ISRN Renewable Energy, Review Article, Dec. 31, 2012. DOI: https://doi.org/10.5402/2012/631574. [Online]. Available: https://www.hindawi.com/journals/isrn/2012/631574/.

[8] J. L. Wagner, D. Lee-Lane, M. Monaghan, M. Sharifzadeh, and K. Hellgardt, "Recovery of excreted n-butanol from genetically engineered cyanobacteria cultures: Process modelling to quantify energy and economic costs of different separation technologies", *Algal Research*, vol. 37, pp. 92–102, Jan. 2019. DOI: 10.1016/j.algal.2018.11.008.

[9] Kalim Akhtar, Hariharan Dandapania, Kati Thiel, and Patrik R. Jones, "Microbial production of 1-octanol: A naturally excreted biofuel with diesel-like properties", *Metabolic Engineering Communications*, vol. 2, pp. 1–5, Dec. 1, 2015. DOI: 10.1016/j.meteno.2014.11.001.

[10] I. S. Yunus and P. R. Jones, "Photosynthesis-dependent biosynthesis of medium chain-length fatty acids and alcohols", *Metabolic Engineering*, vol. 49, pp. 59–68, Sep. 1, 2018. DOI: 10.1016/j.ymben.2018.07.015.

[11] F. Kremer, L. M. Blank, P. R. Jones, and M. K. Akhtar, "A comparison of the microbial production and combustion characteristics of three alcohol biofuels: Ethanol, 1-butanol, and 1-octanol", *Frontiers in Bioengineering and Biotechnology*, vol. 3, 2015. DOI: 10.3389/fbioe.2015.00112.

[12] A. Cordara, A. Re, C. Pagliano, P. V. Alphen, R. Pirone, G. Saracco, F. B. d. Santos, K. Hellingwerf, and N. Vasile, "Analysis of the light intensity dependence of the growth of synechocystis and of the light distribution in a photobioreactor energized by 635 nm light", *PeerJ*, vol. 6, e5256, Jul. 27, 2018. DOI: 10.7717/peerj.5256.

[13] T. Zavřel, M. A. Sinetova, D. Búzová, P. Literáková, and J. Červený, "Characterization of a model cyanobacterium synechocystis sp. PCC 6803 autotrophic growth in a flat-panel photobioreactor", *Engineering in Life Sciences*, vol. 15, no. 1, pp. 122–132, 2015. DOI: 10.1002/elsc.201300165.

[14] J. H. de Vree, R. Bosma, M. Janssen, M. J. Barbosa, and R. H. Wijffels, "Comparison of four outdoor pilot-scale photobioreactors", *Biotechnology for Biofuels*, vol. 8, no. 1, p. 215, Dec. 18, 2015. DOI: 10.1186/s13068-015-0400-2.

[15] N.-H. Norsker, M. J. Barbosa, M. H. Vermuë, and R. H. Wijffels, "Microalgal production — a close look at the economics", *Biotechnology Advances*, vol. 29, no. 1, pp. 24–27, Jan. 1, 2011. DOI: 10.1016/j.biotechadv.2010.08.005.

[16] A. K. Vuppaladadiyam, J. G. Yao, N. Florin, A. George, X. Wang, L. Labeeuw, Y. Jiang, R. W. Davis, A. Abbas, P. Ralph, P. S. Fennell, and M. Zhao, "Impact of flue gas compounds on microalgae and mechanisms for carbon assimilation and utilization", *ChemSusChem*, vol. 11, no. 2, pp. 334–355, 2018. DOI: https://doi.org/10.1002/cssc.201701611.

[17] A4F, *ALGAFARM - SECIL / ALLMICROALGAE | a4f*. [Online]. Available: https://a4f.pt/en/projects/algafarm.

[18] L. M. Vane, "Separation technologies for the recovery and dehydration of alcohols from fermentation broths", *Biofuels, Bioproducts and Biorefining*, vol. 2, no. 6, pp. 553–588, 2008. DOI: 10.1002/bbb.108.

[19] V. Amanor-Boadu, P. H. Pfromm, and R. Nelson, "Economic feasibility of algal biodiesel under alternative public policies", *Renewable Energy*, Renewable Energy for Sustainable Development and Decarbonisation, vol. 67, pp. 136–142, Jul. 1, 2014. DOI: 10.1016/j.renene.2013.11.029.

[20] "Global 1-octanol market report, history and forecast 2014-2025, breakdown data by manufacturers, key regions, types and application", DataIntelo, 2018. [Online]. Available: https://dataintelo.com/report/1-octanol-market/.

[21] N. Schneider, T. J. Fortin, R. Span, and M. Gerber, "Thermophysical properties of the marine microalgae nannochloropsis salina", *Fuel Processing Technology*, vol. 152, pp. 390–398, Nov. 1, 2016. DOI: 10.1016/j.fuproc.2016.06.039.

[22] M. Popovic, "Thermodynamic properties of microorganisms: Determination and analysis of enthalpy, entropy, and gibbs free energy of biomass, cells and colonies of 32 microorganism species", *Heliyon*, vol. 5, no. 6, e01950, Jun. 1, 2019. DOI: 10.1016/j.heliyon.2019.e01950.

[23] B. Rajesh Kumar, S. Saravanan, D. Rana, V. Anish, and A. Nagendran, "Effect of a sustainable biofuel – n-octanol – on the combustion, performance and emissions of a DI diesel engine under naturally aspirated and exhaust gas recirculation (EGR) modes", *Energy Conversion and Management*, vol. 118, pp. 275–286, Jun. 15, 2016. DOI: 10.1016/j.enconman.2016.04.001.

[24] U. von Gunten, "Water and waster water treatment course", EPFL, Nov. 2019.

[25] Q. Béchet, A. Shilton, and B. Guieysse, "Modeling the effects of light and temperature on algae growth: State of the art and critical assessment for productivity prediction during outdoor cultivation", *Biotechnology Advances*, vol. 31, no. 8, pp. 1648–1663, Dec. 1, 2013. DOI: 10.1016/j.biotechadv.2013.08.014.

[26] Zhang, P.Dechatiwongse, E.A.del Rio-Chanona, G.C.Maitland, K.Hellgardt, and V.S.Vassiliadis, "Modelling of light and temperature influences on cyanobacterial growth and biohydrogen production", *Algal Research*, vol. 9, pp. 263–274, May 1, 2015. DOI: 10.1016/j.algal.2015.03.015.

[27] Z. Wang, *Continuous growth and productivity of octanol strain of synechocystis sp. PCC6803*, 2020.

[28] *Tubular glass photobioreactors*, SCHOTT AG. [Online]. Available: https://www.schott.com/tubing/english/special_glass/industry_environment/pbr.html.

[29] T. H. Mehlitz, "Temperature influence and heat management requirements of microalgae cultivation in photobioreactors", PhD thesis, Faculty of California Polytech-

nic State University, 2009. [Online]. Available: https://digitalcommons.calpoly.edu/cgi/viewcontent.cgi?article=1061&context=theses.
[30] I. PINEDO, *Daily radiation*, EU Science Hub - European Commission, Text, May 10, 2019. [Online]. Available: https://ec.europa.eu/jrc/en/PVGIS/tools/daily-radiation.
[31] C. Song, W. Pan, S. T. Srimat, J. Zheng, Y. Li, Y.-H. Wang, B.-Q. Xu, and Q.-M. Zhu, "Tri-reforming of methane over ni catalysts for CO2 conversion to syngas with desired h2/CO ratios using flue gas of power plants without CO2 separation", in *Studies in Surface Science and Catalysis*, ser. Carbon Dioxide Utilization for Global Sustainability, S.-E. Park, J.-S. Chang, and K.-W. Lee, Eds., vol. 153, Elsevier, Jan. 1, 2004, pp. 315–322. DOI: 10.1016/S0167-2991(04)80270-2.
[32] "Report on the coal-fired power plants in spain", International Institute for Law and the Environment (IIDMA), Jan. 2016. [Online]. Available: http://archivo-es.greenpeace.org/espana/Global/espana/2015/Report/cambio-climatico/PITFALLS%20OF%20COAL_FINAL.pdf.
[33] Benjamin Ruff and F. Fosse, "Financial evaluation - PHOTOFUEL", IFP Energies nouvelles, Nov. 4, 2019. [Online]. Available: http://www.photofuel.eu/uploads/files/photofuel-d6.4_biocatalytic_butanol_production_costs.pdf.
[34] K. Miazek, L. Kratky, R. Sulc, T. Jirout, M. Aguedo, A. Richel, and D. Goffin, "Effect of organic solvents on microalgae growth, metabolism and industrial bioproduct extraction: A review", *International Journal of Molecular Sciences*, vol. 18, no. 7, Jul. 4, 2017. DOI: 10.3390/ijms18071429.
[35] *Chemical engineering plant cost index*, Chemical Engineering. [Online]. Available: https://www.chemengonline.com/pci.
[36] G. Holmes and D. W. Keith, "An air–liquid contactor for large-scale capture of CO_2 from air", *Philosophical Transactions of the Royal Society A: Mathematical, Physical and Engineering Sciences*, vol. 370, no. 1974, pp. 4380–4403, Sep. 13, 2012. DOI: 10.1098/rsta.2012.0137.
[37] G. P. Towler and R. K. Sinnott, *Chemical engineering design: principles, practice, and economics of plant and process design*, 2nd ed. Boston, MA: Butterworth-Heinemann, 2013, 1303 pp., ISBN: 9780080966595.
[38] J. R. Couper, W. R. Penney, J. R. Fair, and S. M. Walas, Eds., *Chemical process equipment: selection and design*, 2nd, Boston: Gulf Professional Publishing, 2005, ISBN: 9780123725066. DOI: 10.1016/B978-0-12-372506-6.00019-8.
[39] *Mediterranean sea water masses: Vertical distribution I*, GRID-Arenda, 2013. [Online]. Available: https://www.grida.no/resources/5885.
[40] *International industrial energy prices*, GOV.UK. [Online]. Available: https://www.gov.uk/government/statistical-data-sets/international-industrial-energy-prices.
[41] "CO2 emissions of electricity generation in spain", Red Eléctrica de España, May 2020.
[42] A. Damodaran, *Useful data sets*. [Online]. Available: http://people.stern.nyu.edu/adamodar/New_Home_Page/dataarchived.html#region.
[43] *0.875% EUR bond 2019/2029*, BASF, Feb. 28, 2019. [Online]. Available: https://www.basf.com/global/en/investors/creditor-relations/basf-bonds/bonds-in-detail/0-875-EUR-Bond-2019-2029.html.
[44] *Corporate tax rates table - KPMG global*, KPMG, Nov. 11, 2020. [Online]. Available: https://home.kpmg/xx/en/home/services/tax/tax-tools-and-resources/tax-rates-online/corporate-tax-rates-table.html.
[45] *ES - market risk premia*, Fenebris. [Online]. Available: http://www.market-risk-premia.com/es.html.
[46] *Carbon price viewer*, Ember. [Online]. Available: https://ember-climate.org/data/carbon-price-viewer/.
[47] A. Nordeng, "Refinitiv carbon market survey 2020", Refinitiv, May 6, 2020. [Online]. Available: https://www.refinitiv.com/content/dam/marketing/en_us/documents/gated/reports/global-carbon-market-emission-trading-system-review-2020.pdf.
[48] C. Charles, I. Gerasimchuk, R. Bridle, T. Moerenhout, E. Asmelash, and T. Laan, "Biofuels—at what cost? a review of costs and benefits of EU biofuel policies", International Institute for Sustainable Development, Apr. 2013. [Online]. Available: https://www.iisd.org/gsi/sites/default/files/biofuels_subsidies_eu_review.pdf.
[49] E. Sforza, M. Pastore, S. M. Franke, and E. Barbera, "Modeling the oxygen inhibition in microalgae: An experimental approach based on photorespirometry", *New Biotechnology*, vol. 59, pp. 26–32, Nov. 25, 2020. DOI: 10.1016/j.nbt.2020.06.003.
[50] C. A. d. Fonseca e Sousa, "Oxygen accumulation in photobioreactors", OCLC: 931586824, PhD thesis, Wageningen University, May 21, 2013, 121 pp.
[51] W. Kim, J. M. Park, G. H. Gim, S.-H. Jeong, C. M. Kang, D.-J. Kim, and S. W. Kim, "Optimization of culture conditions and comparison of biomass productivity of three green algae", *Bioprocess and Biosystems Engineering*, vol. 35, no. 1, pp. 19–27, Jan. 1, 2012. DOI: 10.1007/s00449-011-0612-1.
[52] X. Chai and X. Zhao, "Enhanced removal of carbon dioxide and alleviation of dissolved oxygen accumulation in photobioreactor with bubble tank", *Bioresource Technology*, vol. 116, pp. 360–365, Jul. 1, 2012. DOI: 10.1016/j.biortech.2012.03.105.
[53] Y. Okumura, J. Koyama, H. Takaku, and H. Satoh, "Influence of organic solvents on the growth of marine microalgae", *Archives of Environmental Contamination and Toxicology*, vol. 41, no. 2, pp. 123–128, Aug. 1, 2001. DOI: 10.1007/s002440010229. [Online]. Available: https://doi.org/10.1007/s002440010229.
[54] J. Doucha, F. Straka, and K. Lívanský, "Utilization of flue gas for cultivation of microalgae chlorella sp.) in an outdoor open thin-layer photobioreactor", *Journal of Applied Phycology*, vol. 17, no. 5, pp. 403–412, Oct. 1, 2005. DOI: 10.1007/s10811-005-8701-7.
[55] M. Janssen, J. Tramper, L. R. Mur, and R. H. Wijffels, "Enclosed outdoor photobioreactors: Light regime, photosynthetic efficiency, scale-up, and future prospects", *Biotechnology and Bioengineering*, vol. 81, no. 2, pp. 193–210, 2003. DOI: https://doi.org/10.1002/bit.10468.
[56] J. J. Carroll, J. D. Slupsky, and A. E. Mather, "The solubility of carbon dioxide in water at low pressure", *Journal of Physical and Chemical Reference Data*, vol. 20, no. 6, pp. 1201–1209, Nov. 1, 1991. DOI: 10.1063/1.555900.
[57] T. M. Mata, M. Cameira, F. Marques, E. Santos, S. Badenes, L. Costa, V. V. Vieira, N. S. Caetano, and A. A. Martins, "Carbon footprint of microalgae production in photobioreactor", *Energy Procedia*, 5th International Conference on Energy and Environment Research, ICEER 2018, 23-27 July 2018, Prague, Czech Republic, vol. 153, pp. 432–437, Oct. 1, 2018. DOI: 10.1016/j.egypro.2018.10.039.
[58] M. I. Khan, J. H. Shin, and J. D. Kim, "The promising future of microalgae: Current status, challenges, and optimization of a sustainable and renewable industry for biofuels, feed, and other products", *Microbial Cell Factories*, vol. 17, Mar. 5, 2018. DOI: 10.1186/s12934-018-0879-x.
[59] M. van der Voort, E. Vulsteke, and C. Visser, "Macro-economics of algae products", Swansea, Public Output report of the EnAlgae project, Jun. 2015, p. 47.
[60] O. Pulz and W. Gross, "Valuable products from biotechnology of microalgae", *Applied Microbiology and Biotechnology*, vol. 65, no. 6, pp. 635–648, Nov. 1, 2004. DOI: 10.1007/s00253-004-1647-x.
[61] J. N. Rosenberg, G. A. Oyler, L. Wilkinson, and M. J. Betenbaugh, "A green light for engineered algae: Redirecting metabolism to fuel a biotechnology revolution", *Current Opinion in Biotechnology*, vol. 19, no. 5, pp. 430–436, Oct. 2008. DOI: 10.1016/j.copbio.2008.07.008.
[62] P. Coutteau and P. Sorgeloos, "The use of algal substitutes and the requirement for live algae in the hatchery and nursery rearing of bivalve molluscs: An international survey", *Journal of Shellfish Research*, vol. 11, no. 2, pp. 467–476, 1992. [Online]. Available: http://www.vliz.be/en/imis?module=ref&refid=2726&printversion=1&dropIMIStitle=1.
[63] S. J. Okullo, F. Reynès, and M. W. Hofkes, "(bio-)fuel mandating and the green paradox", *Energy Economics*, p. 105 014, Nov. 11, 2020. DOI: 10.1016/j.eneco.2020.105014.
[64] M. Taylor, P. Ralon, H. Anuta, and S. Al-Zoghoul, "Renewable power generation costs in 2019", IRENA, Abu Dhabi, 2020. [Online]. Available: /publications/2020/Jun/Renewable-Power-Costs-in-2019.
[65] M. A. García-Rubio, A. Ruiz-Villaverde, and F. González-Gómez, "Urban water tariffs in spain: What needs to be done?", *Water*, vol. 7, no. 4, pp. 1456–1479, Apr. 2015. DOI: 10.3390/w7041456.
[66] *Hexadecane product*, www.alibaba.com, 2020. [Online]. Available: //www.alibaba.com/product-detail/Hexadecane-N-Hexadecane_60371911420.html.
[67] *China reliable manufacturer octanol*, www.alibaba.com, 2020. [Online]. Available: //www.alibaba.com/product-detail/China-Reliable-Manufacturer-Octanol-Isooctyl-Alcohol_60769171164.html.
[68] *International industrial energy prices*, GOV.UK, May 2020. [Online]. Available: https://www.gov.uk/government/statistical-data-sets/international-industrial-energy-prices.

Imperial College London

Department of Chemical Engineering

Retrofitting of the UK Gas Grid for Hydrogen Delivery

Authors:
Deborah Abraham, Onalethata Diane

Abstract

Decarbonisation of the heat sector is fundamental to the UK's pathway towards a net zero greenhouse gas emissions target by 2050 and future energy security. This target cannot be achieved with continued natural gas use in the gas network, as the domestic heat sector has had the slowest progress in reducing emissions, compared to the power sector. This is demonstrated by only a 1.8% reduction in household emissions between 2018 to 2019, compared to 8.4% in the power sector. Injection of hydrogen into the gas grid has been presented as a low carbon solution to this problem, and is at the forefront of interest with various projects undertaking this work, such as Hydeploy in the UK, and Germany's conversion. In this study, a techno-economic analysis is conducted to consider how the UK gas grid can be retrofitted to ensure compatibility and safe transport of 100 vol% hydrogen to meet domestic and commercial gas demand. As part of this study, the infrastructure challenges associated with this transition were highlighted, the most important of which was the issue of hydrogen embrittlement within steel transmission pipeline. Different scenarios were synthesised, including use of an unmodified gas grid with more frequent maintenance, use of oxygen inhibitors to solve embrittlement issues, and localised hydrogen production via electrolysis. Results show that these scenarios are viable and more cost-effective compared to building a new hydrogen transmission pipeline. All scenarios were found to be far more expensive than natural gas use due to retrofitting expenses. An analysis on emissions reduction was conducted to indicate which scenario would be more desirable to the UK's emissions target. Conclusions indicated producing and distributing green hydrogen would reduce emissions by 98%, making it the best scenario for the UK's emission strategy.

1 Introduction

Currently, the UK National Grid is responsible for providing gas to 22.6 million houses in the UK [1], having transported 878Twh of energy in 2019 alone [2]. Natural gas consists primarily of methane and other hydrocarbons, with varying contents of other impurities including CO_2 and water vapour. This results in large levels of greenhouse emissions from household usage alone, accounting for 15% of the UK's total emissions [3]. The recently amended Climate Change Act 2008 states an increase from 80% to a 100% reduction in emissions target by 2050 [4]. The heat sector has only undergone a 16.7% reduction in greenhouse gas emissions since 1990 [5]. Decarbonisation of this sector would aid in reaching this target.

Research into alternative fuels that could replace natural gas in the gas grid has highlighted hydrogen as an important energy carrier to achieve decarbonisation goals. Hydrogen, when used as a fuel, produces water vapour only. Therefore replacing natural gas with hydrogen will avoid CO_2 emissions. Not only is hydrogen a low carbon energy carrier, its high energy density also makes it a valuable fuel, which has resulted in it being currently used in the transport sector via hydrogen fuel cell technology [6].

Despite Brexit, the UK is still subject to EU climate change agreements [7]. On 8 July 2020 the European Commission proposed an EU hydrogen strategy under the 'European Green Deal'. This will promote the production of clean hydrogen in Europe as a key investment priority and an avenue for economic growth, which will contribute to recovery from the economic effects of COVID-19 [8]. However, ensuring the large scale deployment of hydrogen will require complementary assets such as a distribution infrastructure, which would be capital intensive. Instead, the existing gas grid consisting of an extensive network of pipelines buried underground which covers long distances with limited losses, makes it an excellent choice for delivering the growing quantities of hydrogen to be produced in the future.

Hydrogen has different chemical and physical properties from natural gas, therefore retrofitting of the gas grid will be required to ensure suitability for hydrogen transport. Research states that the transmission network is able to transport a hydrogen-natural gas blend of up to 15-20 vol% with no significant safety issues or retrofitting needed [9]. Numerous projects worldwide have carried out this analysis, for example, HyDeploy was the first in the UK to inject a 20vol% hydrogen mixture into a gas network, deeming the current pipelines and structure as suitable to transport this gas mixture [10]. This would only result in a 7% reduction in emissions from the heat sector.[11].

However, this was done for a private gas network for Keele university.

Other studies have considered the injection of pure hydrogen into the gas grids. Dodds and Demoullin [1] made a technical assessment on the feasibility of the current pipelines for hydrogen transport. They discovered that an entirely new transmission network would need to be built due to incompatibility of the pipeline materials with hydrogen. An estimate was made for the cost of conversion but a full techno-economic analysis was not provided. Jamie Speirs, et.al, [12] came to the same conclusion as Dodds and Demoullin, but included costs of new infrastructure. However no costs of retrofitting existing gas infrastructure were presented. The H21 Leeds City Gate project [13] did a techno-economic analysis of converting natural gas infrastructure to 100% hydrogen use, but this was done for a limited conversion area (city of Leeds). This project aims to undertake this analysis for the whole of the UK.

This project will fill the gaps in literature left by these studies by providing an in-depth techno-economic analysis into retrofitting the gas grid to deliver enough hydrogen to meet gas demand in all distribution zones in the UK. The engineering feasibility of the grid will be assessed and unlike in literature where one method is explored, different scenarios for how retrofitting the gas grid can be done will be explored and compared on their economic value, technical feasibility and possible limitations. The motives behind how each scenario was selected will be explored in the next section.

2 Methodology

The first logical step was to assess the technical feasibility of using the current grid to transport hydrogen. The UK gas grid is made up of a national transmission network (NTS) and a distribution system. The NTS is made primarily from a medium strength (X52) and a higher strength steel (X70) which transports gas at high pressures ranging from 70 bar to 94 bar [1].The distribution system is made up of different materials which include 47% lower strength steel, 8% iron and the remainder, polyethylene [14]. This system operates at a lower pressure; 7-30 bar. The high-pressure gas from the NTS, which is maintained via compressor stations, needs to be fed through pressure reduction stations before going into the distribution network that delivers gas to the 13 distribution zones in the UK. The entire grid structure must be examined to decide which parts need to be altered and retrofitted, and those that are suitable for use without modification.

2.1 Infrastructure Challenges

2.1.1 Low-Pressure Distribution Network

Research states that polyethylene pipes are suitable for hydrogen delivery at the low pressures of the distribution network, as they are insusceptible to hydrogen embrittlement. There still remains uncertainty about whether the iron and steel pipes will be suitable at lower pressures, as the threshold pressure at which hydrogen embrittlement will be induced varies with pipeline microstructure[1]. However, an Iron Mains Replacement Programme (IMRP) is currently in effect to replace all iron pipes surrounding buildings in the distribution network by 2032, due to safety implications [15]. Therefore, part of this network will already be prepared for hydrogen conversion, leaving a requirement to replace only the remaining 5% of iron pipes and all steel pipes post-IMRP. A cost of £300000 per km of pipeline was used, which was taken from the UK government hydrogen supply paper.[14]

2.1.2 High-Pressure Transmission Network

Conversely, hydrogen embrittlement would be a significant issue if the high strength steel pipelines were to transport hydrogen at high pressures. This could result in a loss of material ductility and ultimately, premature failure [16]. Therefore, either a new high pressure transmission line would have to be built parallel to the existing one, or more realistically, a different way needs to be found to transport hydrogen over long distances. This is further discussed in Section 2.4.

2.1.3 Compressor and Pressure Reduction Stations

Presently, the compressors used in the gas grid are centrifugal compressors. These are not ideal for compressing hydrogen because to achieve the same compression ratio as with natural gas, they would need to operate at tip speeds three times faster, owing to hydrogen's smaller molecule size[17]. Therefore the compressors will need to be replaced with reciprocating ones, as these are more preferable for hydrogen compression and can achieve higher pressures[18]. Due to hydrogen's smaller density, it has a volumetric flow velocity of approximately three times that of natural gas[19]. This results in a requirement for more powerful turbines in the compressor stations to deliver this higher volumetric flow.

There are currently 24 compressor stations with operating powers of up to 27MW [20],the power would therefore need to be tripled for hydrogen delivery [21]. The following equation was used for the costing of compressors [14];

$$Cost(£mn) = 0.3114 * size(MW) + 1.3869 \quad (1)$$

As for the pressure reduction stations, there is not enough evidence in literature which suggests that they would not be compatible with hydrogen, so only small remedial work would be needed [1].

2.1.4 Storage

The natural gas sites in the UK [22] are shown below in Table 1:

Storage Site	Location	Space ($10^9 m^3$)	Type
Aldborough	East Yorkshire	0.20	Salt Cavern
Holford	Cheshire	0.20	Salt Cavern
Hornsea	East Yorkshire	0.24	Salt Cavern
Holehouse Farm	Cheshire	0.02	Salt Cavern
Humbly Grove	Hampshire	0.30	Depleted Field
Hatfield Moor	South Yorkshire	0.07	Depleted Field
Hill Top Farm	Cheshire	0.06	Salt Cavern
Stublach	Cheshire	0.22	Salt Cavern

Table 1: UK Natural Gas Storage Sites

The total storage capacity amounts to 1.31 billion m^3. Salt caverns are commonly used for several gases, including hydrogen. The HyGeo project in France plans to convert salt caverns used for propane storage into 1.5Gwh hydrogen storage ready for 2024 [23]. However, depleted fields have been stated unsuitable for hydrogen storage due to contamination by hydrocarbons, sulphur compounds and other residual contaminants[14]. This leaves 0.94 billion m^3 of storage capacity that can be re-purposed to store hydrogen.

2.2 Gas interchangeability

The second step was to consider to what extent hydrogen could be a good substitute for natural gas in terms of pipeline energy delivery rate. The flowrate of gas through a pipe is described by:

Natural gas has a higher heating value (HHV) which is almost 3 times as much as that of hydrogen; ($40MJ/Nm^3$ compared with $13MJ/Nm^3$). Therefore, in order to deliver the same amount of energy using hydrogen as with natural gas, one would need a volumetric flowrate of hydrogen which is 3 times higher. As explained in 2.1.3, the smaller mass density of hydrogen already accounts for this. This means that using the same pressure drop, but higher powered compressors, the same amount of energy can be delivered using hydrogen. Because of this different volumetric energy content, the non-domestic gas meters will need to be replaced with hydrogen-specific meters.

2.2.1 Linepack flexibility

The gas grid linepack is the amount of gas contained in the pipelines at any point in time. This acts as an inherent storage feature of the pipelines which can be varied by adjusting the pressure to meet changes in supply or demand. Unfortunately, because hydrogen has a lower mass density and compressibility than natural gas, the linepack for a 100% hydrogen grid would be reduced to 17% and 26% of the natural gas grid, for the NTS and low pressure network respectively [11]. In order to account for this, additional pipeline will be added to the grid as part of the retrofitting needed.

2.3 KPI Selection and Key Assumptions

In order to provide a thorough techno-economic analysis, the following key performance indicators were selected; levelised cost of gas delivered, as it provides an effective cost comparison to the current natural gas usage, net-present value and internal rate of return. Emissions saved compared to using natural gas was also included to conclude whether the scenarios were worth their costs for the decarbonisation effects they would have.

- The techno-economic assessment was carried out from 2030 to 2050 to match the IMRP and allow time for strategy adoption. A discount rate of 3% was assumed, as well as an inflation assumption of 2%.
- A consistent natural gas demand projection from 2030 to 2050 was used for all scenarios based on a pathway to decarbonisation paper [24]. This was in Twh, and hydrogen was assumed to replace all this demand.
- End-use appliances which would need to be replaced, including domestic gas meters, boilers and cookers, were not considered as part of the retrofitting, and only major components of the grid were considered.
- A learning rate of 0.98% was assumed for compressors [25]
- Electrolysis plant operation hours were assumed constant and to be operating all hours of the year except for maintenance, as constant electricity supply was assumed.

2.4 Scenarios Considered

Taking into account all the considerations discussed in 2.1 and 2.2, scenarios were considered for retrofitting of the gas grid to transport 100% hydrogen in a safe way. Since the distribution system is sufficient for use with minimal retrofitting, the main challenge was to find an option for a suitable high pressure transmission system.

The first option considered was building a new hydrogen NTS, parallel to the existing one, made of lower strength steel. Research conveys that steel grades lower than X52 do not experience hydrogen embrittlement and mechanical fracture behaviour remains ductile, although fracture toughness would decrease with pressure by up to 50% [26]. However, this would not only be costly, but also unrealistic due to the way National Grid Plc operates as a regulated monopoly in the UK. It would be highly unlikely that National Grid would disregard their investment in the current network and construct one on top of it, as it could be detrimental to economic profits. Therefore, this scenario was not investigated further.

Another option is to use the current NTS without modification, but to include more rigorous pipeline integrity management systems (PIMS). The extra maintenance costs would then be added to the operational cost of the grid.[27][28]. Although Germany is currently retrofitting high-strength steel pipelines

to convert to hydrogen transmission pipes [29], there is limited research that would indicate whether the current transmission network is plausible for use with hydrogen. However this scenario was considered, as if plausible, it could be cost effective in comparison to other scenarios.

It may be possible to use coatings or oxide layers which would provide a physical barrier between hydrogen and the steel pipelines. This is a well-developed industrial process [30], but this would require excavating the existing pipes, which would be costly and unfeasible. Another method to create this barrier is use of gas inhibitors such as oxygen and sulphur dioxide which work by preventing the adsorption of hydrogen to the pipeline. A study by Michler et.al[31] has shown that small concentrations of O_2 (10^{-2} -10^{-3} vol%) are sufficient to prevent hydrogen embrittlement almost completely. This was selected as a scenario to assess its economic feasibility for application to the UK gas grid.

As research points to a new NTS being required, whereas the distribution network can be successfully retrofitted, another option was to replace the NTS with hydrogen production plants to transmit hydrogen into the distribution network injection points. How this can potentially be done is explored in Section 2.4.1.

2.4.1 Scenario 1: Localised Hydrogen Production

In this scenario, hydrogen production plants will replace the NTS by delivering hydrogen straight to the local distribution network, which will then be transported to meet demand.

The method of hydrogen production is important and can aid or slow down the emissions target. A greener method than the commonly used steam methane reformation is electrolysis which produces less emissions, offering growing potential for future implementation. Polymer electrolyte membrane (PEM) electrolysis was chosen, (being more efficient in adapting to renewable electricity fluctuations, over alkaline electrolysis which has higher maintenance costs) [32]. PEM Electrolysis is projected to decrease in costs by 75% in 2050, due to larger plants becoming available in the future which benefit from other economies of scale [14].

Import	**UK Destination**	**Capacity (10^9 m^3)**
IUK	East Anglia & North Thames	25.5
BBL	South East	14.2
Vesterled	Scotland	14.2
Langled	North East & East Midlands	26.3

Table 2: Hydrogen Import Capacities

There are current initiatives to produce green hydrogen on a large scale, such as the 1 Gigawatt Electolysis Plant, which will be constructed from 2025-2030 in the Netherlands [33]. However, due to large capacities being needed to replace natural gas demand, the production scenario was supplemented with hydrogen imports to make it more applicable to the UK [34], where the destinations of the imports in Table 2 were applied to the demand in the corresponding local distribution zone.

To produce the lowest emissions possible, the type of electricity that fuels the process will need to be renewable or greener. Thus this scenario was split into two sub scenarios for a comparison on emissions saved; one in which the electricity will be supplied from the electricity grid, producing 'blue' or 'grey' hydrogen, and the other in which a selection of renewable or carbon-neutral energy plants would be constructed and connected to the electrolysis plants.

a) Electricity Grid Connection

Overall costs included in the analysis are the capital costs and operating costs for the electrolysis plants, which include water, electricity and maintenance costs, and the costs for the extra distribution pipeline.

Firstly, the required electrolyser capacity was calculated based on demand, as literature states a 55Mwh plant is needed to produce one tonne of hydrogen [19]. This was calculated to size the PEM plants for each LDZ, from which a capital cost was derived based on the electolyser cost per kwh [14]. Electricity costs for this sub scenario were taken from an average UK price from reliable Ofgem reports [35].

The required length of pipeline was estimated via the distance from where the hydrogen plants have potential to be located, to the LDZ offtake points. This was done by considering hydrogen clusters that have potential to produce large quantities of green hydrogen in the situated LDZ. These included Southampton, Bristol and South Wales, the Thames Estuary, Aberdeen and Grangemouth, Teeside and Liverpool[24]. The length of pipeline was converted into a capital cost [14] and then added to the distribution network steel/iron pipeline replacement costs to calculate total pipeline CAPEX.

b) Connection to blend of Green Electricity
The same methodology used in **a)** was used here. However, electricity for running the PEM electrolysers was obtained from new onshore wind farms, solar, biomass and nuclear plants, instead of the electricity grid. The proportions of these green energy technologies were taken from a system transformation scenario in which net zero is reached by 2050 through revolutionising the electricity sector [36].

2.4.2 Scenario 2: Using the NTS with gas inhibitors

In order for hydrogen embrittlement to take place, the hydrogen molecules are first disassociated, then absorb to the surface of the steel. An O_2 inhibitor would form a thin oxide layer on the pipeline interior,

preventing H_2 from further disassociation[31]. Oxygen inhibitors were chosen for this scenario as they require significantly less quantity per kg of hydrogen compared to other inhibitors such as SO_2 or CO [27]. Pressure swing adsorption (PSA) plants placed after the NTS offtakes would be needed to purify the hydrogen to over 99% [37]. These operate at 20-40 bar, so they will need to deliver the hydrogen to pressure reduction stations for entry into the lower pressure network.

The table below gives the relevant parameters for use of the oxygen inhibitors;

Parameter	Amount
Inhibitor quantity($kg_{inhibitor}/kg_{H_2}$)	0.0024
Inhibitor price(£/$kg_{inhibitor}$)	0.054
Lifetime of PSA plant(years)	20
Energy demand of PSA plant(kWh/kg_{H_2})	2.46
Hydrogen recovery rate for PSA plant(%)	93
Maintenance for PSA plant	4%
Capital cost for PSA plant(£/kWh)	827

Table 3: Cost parameters using Oxygen inhibitors [27][38]

An in depth-cost analysis was made for this scenario, which included the inhibitor costs required for hydrogen demand and costs of the PSA plants. The PSA costs were modelled according to the cost for CO_2 capture using standard commercial zeolite 13x, which according to Meindersmaet et al, is appropriate for use in this scenario. [27] The methodology for calculating the cost of retrofitting the distribution network is the same as Scenario 1. The following table gives the overall costs included in the analysis;

Component	Capex	O&M
NTS Pipelines	X	✓
Distribution network pipelines	✓	✓
Compressor Stations	✓	✓
O_2 inhibitors	X	✓
PSA purification plants	✓	✓

Table 4: Cost analysis for using O_2 inhibitors

2.4.3 Scenario 3: Using the NTS with no modifications

As proposed by Cerniauskas et.al [27], a scenario was considered where 5% of CAPEX extra maintenance was added to the operating costs. The NTS pipelines remain unchanged and the other retrofitting costs are as described in Scenario 1.

3 Results and Discussion

The following table shows the core retrofitting activities performed on the distribution network as well as the cost of replacing compressors. These are all included in each scenario considered.

Retrofitting Activity	Total CAPEX
Replacing low pressure distribution network pipelines- incl labour	£11.3 billion
Replacing non-domestic gas meters	£622.7 million
Additional pipelines -linepack purposes	£3.4 billion
Replacing district governers	£133.5 million
Replacing compressors on the NTS- incl labour	£149.2 million
Total	**£15.6 billion**

Table 5: Cost for core retrofitting activities. (The retrofitting costs for meters, district governers and additional pipelines were taken from the UK government hydrogen supply chain project[14])

3.1 Levelised cost of gas delivered

The results indicate that localised production of hydrogen would cost the most, (over 100 times as much as natural gas delivery, which is only £0.01/kWh). Use of an oxygen inhibitor would only cost 5 times as much using natural gas. Each scenario is further discussed below;

Figure 3.1: Levelised cost of gas delivered for each scenario

3.2 NPV and IRR

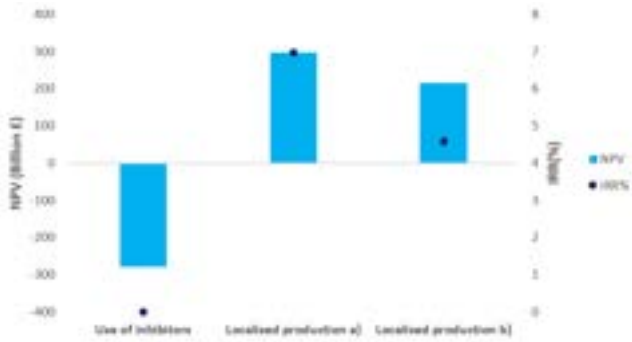

Figure 3.2: NPV and IRR results for each scenario

To calculate the NPV and IRR of the scenarios, cash inflows were accounted for. For the inhibitor cost scenario, these include revenue from the NTS grid entry and exit capacity fees, distribution and provision of storage capacity as well as metering services to households. For the scenarios dealing with hydrogen production, the revenue streams mentioned above (excluding the NTS grid fees) were considered, but an additional source of revenue was the sale of the hydrogen produced at retail prices.

Figure 3.2 shows that the inhibitor scenario is not economically viable under the parameters considered, as the NPV is negative. This is because of the large costs incurred as a result of the novel requirement for hydrogen purification for this scenario as discussed in Section 3.4. Furthermore, the compounded annual growth rate (CAGR) of the inflows (-1.67%) is larger than that of the cash outflows(1%), suggesting that the inflows are falling at a much faster rate than can be offset by the reduction in projected outflows during the lifetime of the project. Section 3.5 delves deeper into pricing options which would render this scenario economically feasible.

For the hydrogen production scenarios, both show a strong positive NPV with rates of return of 7% and

5%, owing to the strong revenue stream generated from the sale of the hydrogen produced.

3.3 Scenario 1: Localised Hydrogen Production

The levelised cost for this scenario was the highest compared to scenarios utilising the NTS, as shown in Figure 3.1. This is because of the large capital and operating costs associated with the electrolysis plants. As shown in Figure 3.3, the capital costs for the electrolysers were extremely large, making retrofitting of pipelines, gas meters and district Governors practically insignificant in comparison.

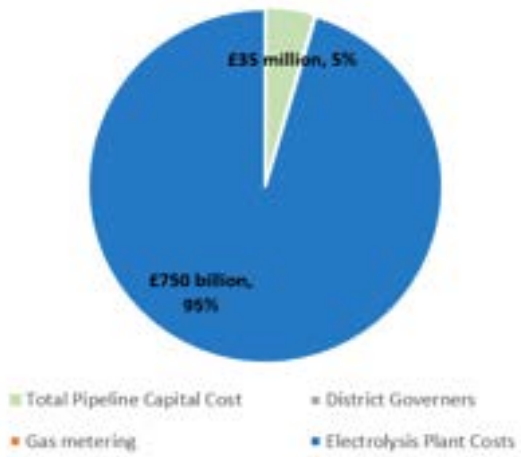

Figure 3.3: Breakdown of capital cost contribution to the Localised Hydrogen production scenario

However, it is important to note that this value for constructing an electrolysis plant is for 2030; if this was done in 2050, due to technological advancement the electrolyser would cost £300/kw [14], it would be far less costly - around £332.8 billion, which would give a levelised cost of £1.08 per kwh.

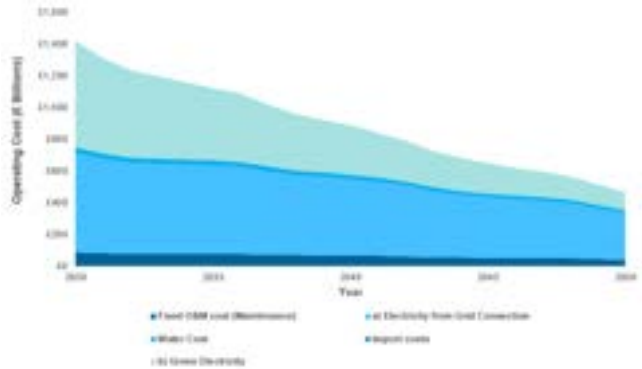

Figure 3.4: Localised Hydrogen Production OPEX: Electricity Grid Connection vs Green Electricity

The levelised cost for the subscenario in which electricity is supplied by green energy production, is higher than that in which it is supplied by the electricity grid, as displayed in Figure 3.1. This is because capital, operating and maintenance costs associated with building wind, biomass, solar and nuclear plants would be far more expensive than electricity grid connection. This is presented in Figure 3.4, where the operating costs alone for the green energy generation technologies are comparable to the cost of electricity from the grid, without including capital costs.

When comparing the levelised cost of hydrogen results with values found in literature, they agree as the Petroleum Economist predicts an LCOE between $2.50 and $10 per kg for green Hydrogen [39]. The value for green hydrogen found being £3.64 per kwh, or £5.25 per kg, lies within the range predicted.

The NPV values for this scenario, displayed in Figure 3.2, are largely positive due to the associated revenues being greater than the operating and capital costs. These included revenue from a gas bill, which is projected to be three times as much in comparison to distributing natural gas [40], to account for the higher levelised cost of hydrogen. Again the trend of the first subscenario being more economically viable than the second is demonstrated here, with a higher NPV, which is due to cheaper electricity costs although the same amount of revenue is generated.

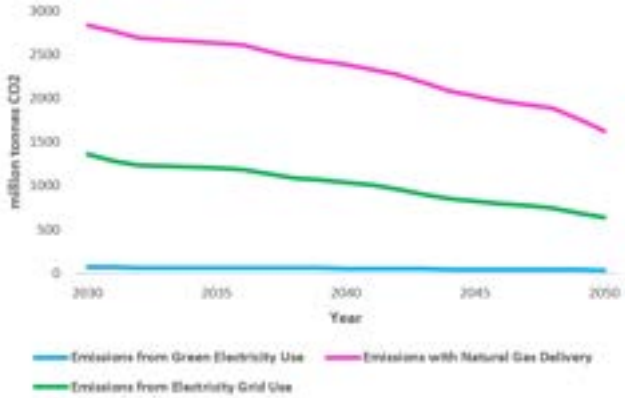

Figure 3.5: Total Emissions Comparison

Although comparing this scenario with continuing the use of natural gas in the grid, there are high costs involved and the levelised cost is magnitudes greater, emissions would be reduced drastically which benefits the movement to a 100% reduction in emissions. This is shown above in Figure 3.5, where emissions are reduced by 56% and 98% for grey/blue hydrogen and green respectively.

Carbon tax is projected to increase linearly from £70 in 2030 to £200 in 2050 [41]. Including this in the levelised cost of natural gas gives £0.39/kwh. Therefore to make the levelised cost for this equal to the green hydrogen scenario and thus make it economically viable, it would require a constant carbon tax of £958/tonne CO_2, which is out of the projected range.

3.4 Scenario 2: Use of inhibitors

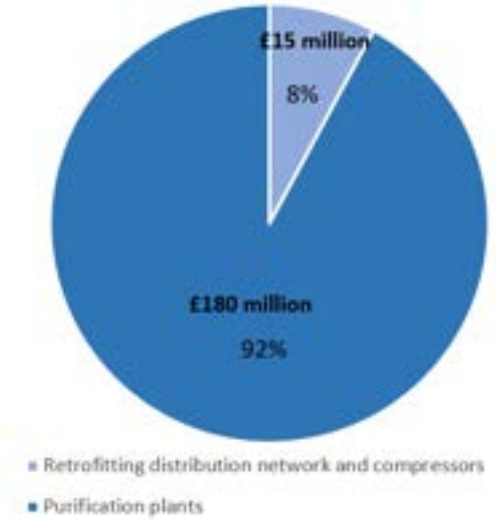

Figure 3.6: Inhibitor scenario CAPEX structure

Figure 3.6 shows the CAPEX cost structure of the inhibitor scenario. Evidently, the majority of costs incurred are due to purifying the hydrogen to make it appropriate for end-use.

The CAPEX from this analysis was compared with the cost of building new hydrogen transmission pipelines, which was calculated to be £305 billion. This means that although it is a costly scenario, it still provides a cost competitive alternative to building a new NTS. Research has been made into ways of reducing the PSA costs such as increasing adsorber working capacity or increasing the number of steps in the process such as adsorber bed pressure equalisation [42], but this was beyond the scope of this project, and can be considered for future versions of this research.

Figure 3.7 shows the operating cost projection for the project lifetime. Evidently, these costs are dominated by the operation and maintainance of the purification plants, followed by upkeep of the storage salt caverns and distribution network.

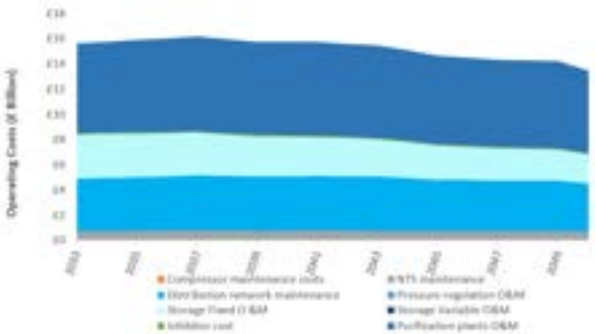

Figure 3.7: Inhibitor scenario operating expenses breakdown

3.5 Sensitivity Analysis

3.5.1 Scenario 1: Localised Hydrogen Production

A sensitivity analysis was carried out on major parameters that appeared to have the biggest impact on capital or operating costs. These were the demand projection, electricity costs and electrolysis plant capital cost.

a) Sensitivity to demand: Due to uncertainties involved in predicting gas demand in the future, as it depends on government sustainability strategy, the sensitivity of the LCOE results to varying demand projections was investigated. Gas demand projections published by the National Grid [36] were inputted into the model:

- Steady State Progression: Gas demand remains high due to large focus on supply security and short-term thinking on emissions
- Slow Progression: Focuses on long-term change and a slow environmental strategy, giving a slow decrease in gas demand
- Two Degrees: Large effort and focus on environmental sustainability, with a faster decline in gas demand due to a shift to greener resources

Results for this are shown in Figures 3.8 and 3.9.

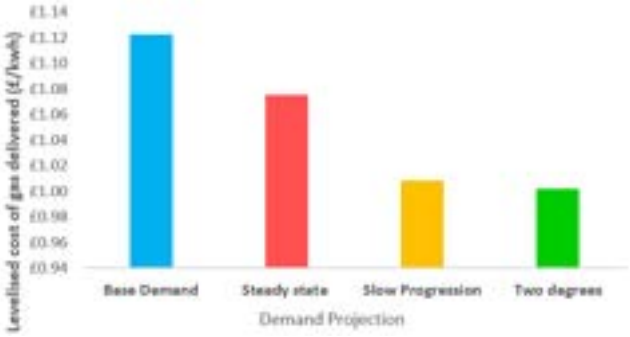

Figure 3.8: Scenario 1a: Sensitivity to Demand

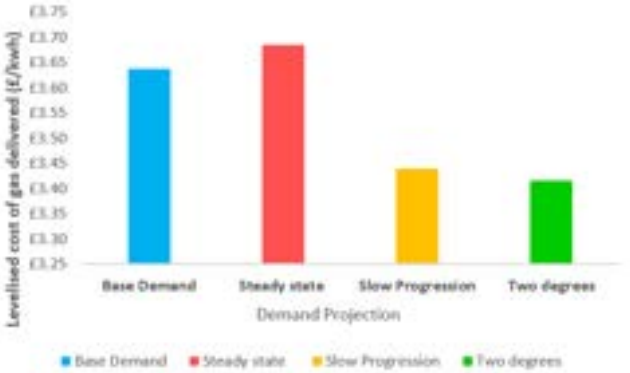

Figure 3.9: Scenario 1b: Sensitivity to Demand

The steady state progression, having an insignificant decrease in gas demand in the observed time frame, therefore had the least decrease in levelised cost in Figure 3.8 and actually increased the value in 3.9. This is due to the costs increase in the first subscenario not offsetting the demand increase from the base projection. Therefore the denominator in the levelised cost calculation, which includes demand, increases more than the numerator increases from costs, thus decreasing the value. This is the reverse for subscenario b, in which costs are so high that a small increase has a bigger impact than an increase in demand, thus resulting in a higher levelised cost. For both subscenarios, the slow progression and two degrees have an expected larger decrease in LCOE due

to a significant decrease in demand. Therefore, shifting public focus to environmental sustainability would not only have a positive impact on global emissions, but also decrease costs for hydrogen transport.

b) Sensitivity to Varying Electricity Prices and Plant CAPEX Future electricity prices also have associated uncertainties in their prediction as they vary based on the state of the economy and other factors; therefore a sensitivity analysis was carried out with varying prices from the norma scenario. The electrolysis capital costs also depend on more investment in PEM electrolyser technology and increasing their efficiency, thus there will also be uncertainties. Results are displayed below in Figure 3.10:

Figure 3.10: Scenario 1: Sensitivity to Electricity Price

Varying the electricity price by ±30% resulted in an approximate 20% change in levelised cost. Due to the large electricity requirement for the electrolysers, majority of costs are attributed to this. Therefore, varying the electricity price would have a significant impact on this value. The figure also shows the levelised cost is not sensitive to the capital costs. As operating costs are much greater than the capital costs, varying capital costs will not have a significant effect.

3.5.2 Scenario 2: Use of inhibitors

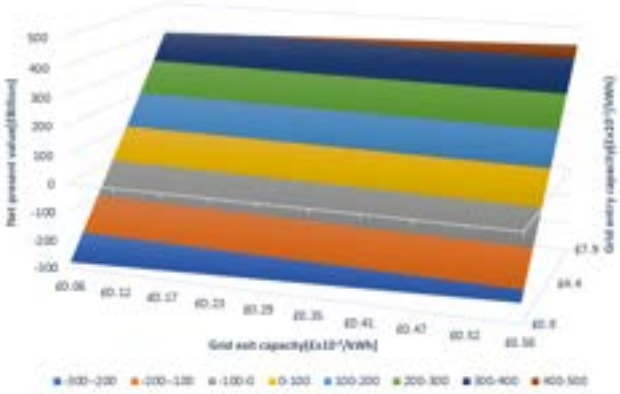

Figure 3.11: Scenario 2: Influence of Grid Capacity Fees on NPV

A big uncertainty in the techno-economic analysis was grid capacity fees in transporting hydrogen. The fees used yielded a negative NPV in Figure 3.2. Therefore a sensitivity analysis was performed which helped determine the prices needed to break-even.
Figure 3.11 shows that the scenario becomes viable starting at grid entry prices of £0.0351/kwh and a grid exit capacity price of £0.0041/kwh. This is an increase of 1100% and 2013% respectively, which would only be plausible with significant subsidies and government policies in place.

4 Conclusion and Outlook

To conclude, results from the techno-economic analysis indicate that the NTS with no modification scenario, if plausible, would be the most cost effective scenario, due to the lowest levelised cost of hydrogen delivered. However, more research needs to be published that would label the NTS as compatible with hydrogen, as currently this scenario would not be technically feasible - frequent maintenance would be needed which is undesirable. Conversely, the NTS with inhibitor scenario is not economically feasible, based on its negative NPV and high costs. Literature did not give a quantitative analysis on emissions for the PSA plants, but evidently these would be high due to high pressure and energy requirements. Therefore, both NTS scenarios are not recommended by this study.

Results also showed that the most expensive scenarios are the local hydrogen production options explored, with levelised costs of hydrogen delivered of greater magnitude than natural gas, and an unrealistic carbon price needed to make them comparable. These levelised costs were found sensitive to gas demand projections, therefore they could become far cheaper based on societal focus and strategy on decarbonisation targets. Emissions are also reduced by 56% or 98% depending on the electricity source. Therefore, although high investment would be needed, the localised production scenarios are strongly recommended due to their potential to accelerate efforts towards the 100% emissions reductions 2050 target.

To strengthen this research, there have been a growing number of optimisation models and improvements in spatio-temporal resolutions which can be used to highlight all operational issues arising from the transition to 100% hydrogen. This will give a more detailed view on retrofitting requirements, and lead to a more robust techno-economic analysis. Conducting a Monte Carlo analysis could also produce a probability distribution and a better range of the results. The sensitivity analysis did not include all parameters that could have affected the results, so a Monte Carlo analysis would solve this issue. Furthermore, conducting a UK region level analysis could give greater focus and shift to the emissions target. Scotland, Wales and Northern England are geographically more suitable to producing green hydrogen due to greater renewables capacity, so this close analysis could make this study more applicable to the UK. Lastly, an analysis on safety implications with hydrogen use in homes will strengthen the applicability of this project.

References

[1] S. D. P. Dodds, "Conversion of the uk gas system to transport hydrogen", 2013. [Online]. Available: http://www.sciencedirect.com/science/article/pii/S0360319913006800.

[2] DUKES, *Chapter 4 natural gas*, 2016. [Online]. Available: https://assets.publishing.service.gov.uk/government/uploads/system/uploads/attachment_data/file/912021/DUKES_2020_Chapter_4.pdf.

[3] BEIS, "2018 uk greenhouse gas emissions", 2018. [Online]. Available: https://assets.publishing.service.gov.uk/government/uploads/system/uploads/attachment_data/file/863325/2018-final-emissions-statistics-summary.pdf.

[4] T. N. Archives, *The climate change act 2008 (2050 target amendment) order 2019*, 2019. [Online]. Available: https://www.legislation.gov.uk/ukdsi/2019/9780111187654.

[5] BEIS, "2019 uk provisional greenhouse gas emissions: Summary", 2019. [Online]. Available: https://assets.publishing.service.gov.uk/government/uploads/system/uploads/attachment_data/file/875482/2019_UK_greenhouse_gas_emissions_provisional_figures_statistical_summary.pdf.

[6] S. S. et al, "Hydrogen: A sustainable fuel for future of the transport sector", 2015. [Online]. Available: http://www.sciencedirect.com/science/article/pii/S1364032115006127.

[7] DExEU, *International agreements if the uk leaves the eu without a deal*, 2019. [Online]. Available: https://www.gov.uk/government/publications/international-agreements-if-the-uk-leaves-the-eu-without-a-deal/international-agreements-if-the-uk-leaves-the-eu-without-a-deal.

[8] E. Commission, *Eu hydrogen strategy*, 2020. [Online]. Available: https://ec.europa.eu/energy/topics/energy-system-integration/hydrogen_en#eu-hydrogen-strategy.

[9] S. S. C. J. Quarton, "Power-to-gas for injection into the gas grid", *Renewable and Sustainable Energy Reviews*, vol. 98, 2018. [Online]. Available: http://www.sciencedirect.com/science/article/pii/S1364032118306531.

[10] *Hydrogen is vital to tackling climate change*, 2020. [Online]. Available: https://hydeploy.co.uk/.

[11] C. J. Quarton and S. Samsatli, "Should we inject hydrogen into gas grids?", *Applied Energy*, vol. 275, 2020. [Online]. Available: http://www.sciencedirect.com/science/article/pii/S030626192030684X.

[12] J. S. et al, "A greener gas grid: What are the options", *Energy Policy*, vol. 118, pp. 291–297, 2018. [Online]. Available: http://www.sciencedirect.com/science/article/pii/S0301421518302027.

[13] H21, "H21 leeds city gate", [Online]. Available: https://www.northerngasnetworks.co.uk/wp-content/uploads/2017/04/H21-Report-Interactive-PDF-July-2016.compressed.pdf.

[14] BEIS, "Hydrogen supply chain evidence base", 2018. [Online]. Available: https://assets.publishing.service.gov.uk/government/uploads/system/uploads/attachment_data/file/760479/H2_supply_chain_evidence_-_publication_version.pdf.

[15] HSE, *Enforcement policy for the iron mains risk reduction programme 2013 - 2021*, 2013. [Online]. Available: https://www.hse.gov.uk/gas/supply/mainsreplacement/enforcement-policy-2013-2021.htm.

[16] Y. W. e. a. X. Li, "Effect of pre-strain on hydrogen embrittlement of high strength steels", 2014. [Online]. Available: http://www.sciencedirect.com/science/article/pii/S0921509314009526.

[17] A. Brown, *Hydrogen transport*, 2019. [Online]. Available: https://www.thechemicalengineer.com/features/hydrogen-transport/.

[18] B. C. C. e. a. van der Zwaan, "The cost of pipelining climate change mitigation: An overview of the economics of ch4, co2 and h2 transportation", 2011. [Online]. Available: http://www.sciencedirect.com/science/article/pii/S030626191100314X.

[19] C. Findlay, "What's your purpose? reusing gas infrastructure for hydrogen transportation", 2020. [Online]. Available: https://www.siemens-energy.com/global/en/news/magazine/2020/repurposing-natural-gas-infrastructure-for-hydrogen.html.

[20] S. C. et al, "Options of natural gas pipeline reassignment for hydrogen: Cost assessment for a germany case study", 2020. [Online]. Available: http://www.sciencedirect.com/science/article/pii/S0360319920307023.

[21] M. E. Tools, *Compressor power requirement*. [Online]. Available: https://myengineeringtools.com/Compressors/Tools_Compressor_Power.html.

[22] DUKES, *Gas storage sites and import/export facilities in the united kingdom*, 2019. [Online]. Available: https://www.gov.uk/government/statistics/natural-gas-chapter-4-digest-of-united-kingdom-energy-statistics-dukes.

[23] E. Bellini, "Hydrogen storage in salt caverns in france", 2020. [Online]. Available: https://www.pv-magazine.com/2020/07/30/hydrogen-storage-in-salt-caverns-in-france/.

[24] K. O'Neill, *Pathways to net zero: Decarbonising the gas networks in great britain*, 2019. [Online]. Available: https://www.northerngasnetworks.co.uk/wp-content/uploads/2019/11/Navigant-Pathways-to-Net-Zero-2-min.pdf.

[25] N. K. et al, "Using learning curves on energy-efficient technologies to estimate future energy savings and emission reduction potentials in the u.s. iron and steel industry", Tech. Rep., 2015. [Online]. Available: https://www.osti.gov/servlets/purl/1372638.

[26] HSE, "Injecting hydrogen into the gas network - a literature search", 2015. [Online]. Available: https://www.hse.gov.uk/research/rrpdf/rr1047.pdf.

[27] S. C. et al, "Options of natural gas pipeline reassignment for hydrogen: Cost assessment for a germany case study", 2020. [Online]. Available: http://www.sciencedirect.com/science/article/pii/S0360319920307023.

[28] NaturalHy, "Using the existing natural gas system for hydrogen", 2004. [Online]. Available: https://www.fwg-gross-bieberau.de/fileadmin/user_upload/Erneuerbare_Energie/Naturalhy_Brochure.pdf.

[29] H. B. et al, *Energy transition with hydrogen pipes*. [Online]. Available: https://www.mannesmann-linepipe.com/fileadmin/footage/MEDIA/gesellschaften/smlp/Documents/Energy_transition_with_hydrogen_pipes_Mannesmann_H2ready_and_the_changeover_of_existing_Gasunie_natural_gas_networks.pdf.

[30] B. J. Grainger S., "Chapter 5: Electrodeposited coatings. engineering coatings - design and applications", 1998. [Online]. Available: www.scopus.com.

[31] T. M. et al, "Assessing the effect of low oxygen concentrations in gaseous hydrogen embrittlement of din 1.4301 and 1.1200 steels at high gas pressures", 2012. [Online]. Available: http://dx.doi.org/10.1016/j.corsci.2012.08.015.

[32] C. Richner, *Electrolyzer overview: Lowering the cost of hydrogen and distributing its production*, 2020. [Online]. Available: https://pv-magazine-usa.com/2020/03/26/electrolyzer-overview-lowering-the-cost-of-hydrogen-and-distributing-its-productionhydrogen-industry-overview-lowering-the-cost-and-distributing-production/.

[33] S. Delta, *Start of initiative for construction of 1 gw electrolysis plant for green hydrogen in zeeland*, 2019. [Online]. Available: https://www.smartdeltaresources.com/en/news/start-of-initiative-for-construction-of-1-gw-electrolysis-plant-for-green-hydrogen-in-zeeland.

[34] E. UK, *Gas supplies*, 2019. [Online]. Available: https://www.energy-uk.org.uk/our-work/generation/gas-generation/gas-supplies.html.

[35] Ofgem, *All wholesale electricity charts and indicators*, 2020. [Online]. Available: https://www.ofgem.gov.uk/data-portal/all-charts/policy-area/electricity-wholesale-markets.

[36] N. G. ESO, *Future energy scenarios*, 2020. [Online]. Available: https://www.nationalgrideso.com/document/173821/download.

[37] W. L. et al, "Experimental analysis of membrane and pressure swing adsorption (psa) for the hydrogen separation from natural gas", 2017. [Online]. Available: http://www.sciencedirect.com/science/article/pii/S0959652617317274.

[38] M. T. Ho, *Techno-economic modelling of carbon capture systems for australian industrial sources*, 2007.

[39] J. Peatie and D. Powell, "Levelised costs will settle the blue-green debate", 2020. [Online]. Available: https://www.ehn.org/natural-gas-vs-renewables-2640991454.html.

[40] P. Homewood, *Hydrogen future would triple energy bills*, 2020. [Online]. Available: https://notalotofpeopleknowthat.wordpress.com/2020/10/16/hydrogen-future-would-triple-energy-bills/.

[41] DECC, "Guidance on estimating carbon values beyond 2050: An interim approach", 2020. [Online]. Available: https://assets.publishing.service.gov.uk/government/uploads/system/uploads/attachment_data/file/48108/1_20100120165619_e___carbonvaluesbeyond2050.pdf.

[42] M. T. H. et al, "Reducing the cost of co2 capture from flue gases using pressure swing adsorption", 2008. [Online]. Available: http://dx.doi.org/10.1021/ie070831e.

2

Crystallisation Behaviour and the Effects of Cooling Rate & Sample Volume of Sodium Dodecyl Sulfate in Aqueous Solution

Alessia Borys
Department of Chemical Engineering, Imperial College London, U.K.

Abstract

The temperature of crystallisation and growth of different polymorphs were investigated using different sample volumes, 0.5 μl, 5 μl and 20 μl, and cooling rates, 0.5°C/min, 1.0°C/min, 5.0°C/min and 10°C/min. A concentration of 20 wt.% sodium dodecyl sulfate, SDS in aqueous solution was used and studied with optical microscopy and FT-IR spectroscopy. The cooling rates 5.0°C/min and 10°C/min showed no sign of crystallisation for the investigated temperature range of 25°C to -5°C. The temperature of crystallisation for the cooling rate of 0.5°C/min had a greater range and a lower average than 1.0°C/min in both 0.5 μl and 5 μl. Polymorphs in 0.5 μl started as platelet-like structures in both cooling rates (0.5°C/min and 1.0°C/min) and needles appeared at lower temperatures (0.5°C/min having a larger percentage than 1.0°C/min). Pure crystals were found for one experiment in the form of needles (cooling rate of 0.5°C/min and sample volume 0.5 μl). Confirmed hydrates/polymorphs with IR-spectrum were hemihydrate/needles, monohydrate/hexagonal platelets. Potential hydrates/polymorphs were dihydrate/square platelets, and an undefined hydrate/mix of different hydrates was a grain-like structure found in the sample volume of 5 μl. Due to time constraints and limited access to laboratories because of the pandemic many findings did not reach the threshold for statistical significance, they do however warrant further investigation as they have the possibility of furthering our understanding of SDS and its crystallisation behaviour.

Introduction

Surfactants are molecules that generally have an alkyl chain with 8-22 carbons (the tail) as well as a functional group, usually referred to as the headgroup. The carbon chain is hydrophobic, and the headgroup is hydrophilic, thus giving the molecule an amphiphilic structure [1]. The amphiphilic structure makes the molecule behave in a certain way when dissolved in a solvent, i.e., aqueous solution, the hydrophobic carbon chain breaks hydrogen bonds between water molecules causing some of the surfactant molecules to go to the interface (surface) of the solution, where they form a thin layer and position themselves with their hydrophobic group towards the air. This behaviour makes the surface tension of the water decrease [2]. Another key attribute is that when surfactants reach a specific concentration, critical micelle concentration (CMC) they start to form micelles, see figure 1. Important to note is that only surfactants with one alkyl group form spherical micelles, whereas surfactants with two tails form planar micelles (bilayers) [1].

Figure 1. Formed micelle from surfactant with one tail-group.

Surfactants named emulsifiers and surface treatment agents are able to increase the solubility of different mixed solutions, i.e., water and oil, therefore making it possible to wash away the oil, making them great detergents [3]. In the case of sodium dodecyl sulphate, SDS, see figure 2 for structure, it is a common ingredient in many household products, primarily detergents and other cleaning agents but are also being used in drug-delivery [4].

Figure 2. Chemical structure of sodium dodecyl sulphate, SDS.

Nucleation and crystal growth are the two steps in the crystallisation of a surfactant. The first step of phase transition is nucleation, where a new structure is formed within the liquid phase as molecules self-assemble into a cluster. What then follows is additional growth of these clusters into crystals [5]. A crystals morphology is its overall shape and structure. When a compound is able to form different solid structures, it is referred to as polymorphism, this means that the chemical structure is the same, but the crystal structure is not. The polymorphs have different properties, e.g., melting point, solubility, chemical and physical abilities [6].

The importance of studying crystallisation lies in its increasingly widespread use in many industries, from fertilisers and detergents to food and pharmaceuticals. To know more about a products crystallisation is to better understand its properties and application, resulting in a more stable final product [6]. Commercial SDS solids appear to be in different crystal forms, a mixture instead of one homogenous morphology. This is possibly because the crystallisation process is not yet very well understood and is thought of as a somewhat random

process. However, a high purity in terms of crystal form should be sought after to have a more reliable product.

Previous studies have been conducted of the crystallisation of SDS and determined the existence of a few different hydrates; the monohydrate, hemihydrate, 1/8 hydrate, dihydrate and anhydrous. Some hydrates have been assigned their own crystal structures, but not all, the monohydrate has been ascribed the crystal structure of hexagonal platelets and the hemihydrate to needle-structures [7]. The dihydrate has been deemed the most stable form but has not yet been assigned a crystal structure [8]. The different hydrates have also been identified by their IR-spectrum, so although some do not have a recognisable crystal structure, there are different ways of categorising them.

Past papers report on the crystallisation temperature (induction temperature) with varying results. In a study using temperature-programmed milli-scale batch crystallisation, $T_{crystal}$ was determined to be 15.10°C, 20wt.% SDS in water and had a cooling rate of 0.5°C/min [9]. Another study that made use of 20 wt.% SDS in water with varying cooling rates, determined with optical microscopy, that the crystallisation occurred at 2.2°C (0.5°C/min), -0.6°C (1.0°C/min), -2.9°C (5°C/min) and -3.6°C (10°C/min) [7]. A study using differential scanning calorimetry found that for 20 wt.% SDS in water and a cooling rate of 1.0°C/min that $T_{crystal} \approx 12$°C [10]. Other studies looked at the morphology of the crystal lattice, and one observed that they seemed to form a platelet-like structure [11], while another study agreed, they also found that at lower temperatures needle-like structures appeared [12].

In this paper, the crystallisation of SDS has been studied to investigate the role of *rate of cooling* and *sample volume* on crystallisation, the formation of different polymorphs, and the kinetics of growth. This was done with IR-spectroscopy, and optical microscopy of an SDS concentration of 20 wt.% in water, the linear cooling rates that were studied were 0.5°C/min, 1.0°C/min, 5.0°C/min, 10°C/min of the temperature interval of 25°C to -5°C. Sample volumes that were studied: 0.5 μl, 5 μl and 20 μl.

Experimental section

Materials and methods. Throughout this project, an SDS concentration of 20wt.% together with deionised water (Centra ELGA filtration system) was used. SDS had been purchased from Sigma-Aldrich (ACS reagent grade, ≥ 99.0% purity). The sample was made at least 12 hours before use and was discarded after one week. Before use, the solution was filtered through a 0.2 μm PTFE syringe filter. See figure 3 for the experimental setup.

Optical microscopy. Optical microscopy was done with *Hyperion Bruker*, 10x objective lens was used together with *Linkam temperature stage* to regulate the temperature, 0.1±°C stability and accuracy. A small drop of solution, circa 0.1 mm in diameter, was placed on circular CaF_2 plates that were then sealed with spacer (~10 μm). The drop was cooled from 25°C to -5°C with the cooling rates: 0.5°C/min, 1.0°C/min, 5.0°C/min and 10°C/min. A new drop was used for each experiment on clean plates, and each cooling rate was replicated at least three times. The same experiment was repeated with a bulk sample volume of 5 μl and 20 μl.

IR-spectroscopy. The IR spectra were measured with *Bruker Tensor 27* FT-IR spectrometer, integrated with *Hyperion* microscope. Microscope assisted (15x cassegrain optics) spectrum was acquired in transmission mode. *Linkam temperature stage* to regulate the temperature, 0.1±°C stability and accuracy. With parameters set at 64-32 scans/min, resolution: 4 cm^{-1}, spectral range: 3900-900 cm^{-1}, absorbance mode and single channel. The sample was sandwiched between two IR-transparent CaF_2 plates (with spacer). The same cooling rates were used for optical microscopy, 0.5°C/min, 1.0°C/min, 5.0°C/min, 10°C/min, each was repeated at least three times. Sample volumes investigated were 0.5 μl and 5μl. All spectra were processed with post acquisitional spectral processing, baseline correction and *Savitsky–Golay* smoothening.

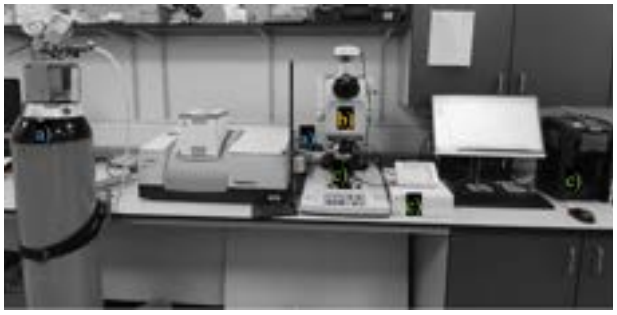

Figure 3. Experimental set up for both optical microscopy and IR-spectroscopy. a) nitrogen gas to inhibit condensation, b) microscope, Hyperion Bruker, c) Linkam temperature stage.

Troubleshooting. The experiment had to be adjusted and changed, along with the project aim due to unforeseen occurrences, such as condensation on the CaF_2 plates during cooling. To prevent this condensation, nitrogen gas was brought in to flow over the sample during the experiment.

The rates 5°C/min and 10°C/min were excluded from the project as they did not produce any crystals above -3°C.

On occasion no crystal growth was seen at all for the entire temperature range (25°C to -5°C), this for different cooling rates, the behaviour was accredited to the small sample volume, and a bulk volume was decided to be investigated and added to the project objective.

Conversely, when crystals were found before the cooling was initiated at ~20°C it was thought to be due to the cold temperature of the laboratory. This

was solved by placing heaters in the room and making sure the temperature remained constant and above 22°C.

The kinetics of growth was experimented with, but only one experiment was successful, 0.5 μl, 1.0°C/min, and therefore it was not included in this paper. Due to time constraints, this was not investigated further. Moving forward, alternative techniques for observing growth kinetics would be needed.

Results

Cooling rates 5.0°C/min and 10°C/min. The two faster cooling rates did not have any crystallisation in our temperature range of 25°C to -5°C. Multiple experiments were done with the same results.

Induction temperature. Table 1 shows the induction temperature, the temperature at which the sample starts to crystallise, $T_{crystal}$ / induction temperature for different cooling rates and sample volume, as well as the different shapes of the crystals.

Table 1. Relationship between cooling rate, volume, time of crystallisation and morphology. Morphology description in table: p = platelets, n = needles, s = sand/grainy appearance Letter in bracket symbolise that the morphology was present but was in minority.

$T_{crystal}$	Volume [μl]	Rate [$°C/min$]	Morphology Start	Morphology Overall
8	0.5	0.5	p	p n
-1	0.5	0.5	p	p
13	0.5	0.5	p	p n
4	0.5	0.5	p	p
1	0.5	0.5	n	n
5	5	0.5	s	s
12	5	0.5	s	s p
10	0.5	1	p	p
10	0.5	1	p	p (n)
12	0.5	1	p	p (n)
8.5	0.5	1	p	p (n)
14	5	1	s	s
13	5	1	s	s p

For the cooling rate of 1.0°C/min, sample volume 0.5 μl, the crystallisation started between temperature 8.5°C and 12°C with a *mean temperature of 10.1°C,* at cooling rate 0.5°C/min and same sample volume (0.5 μl) the crystallisation occurred between temperatures -1°C and 13°C with a *mean temperature of 5°C.* The mean difference was 4.9°C between the two rates.

A t-test was run to compare the two groups; however, the mean difference was not statistically significant (t = -1.9631, df = 4.6401, p = 0.1113), a p-value of 0.05 was chosen as the threshold of significance. Figure 4 shows this in a box plot chart, where it becomes clear that the range of crystallisation temperature is a lot larger for cooling rate 0.5°C/min than that of 1.0°C/min. The t-test was chosen to compare the mean difference of induction temperature between the two cooling rates. The data met the parametric assumption of the t-test, having a normal distribution.

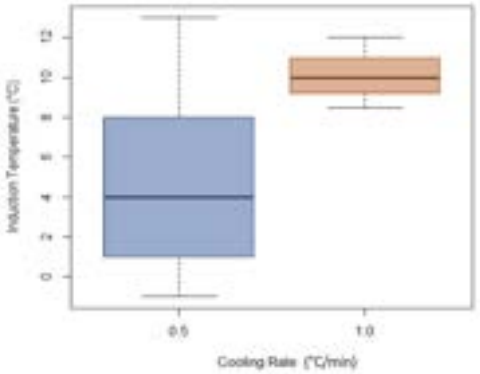

Figure 4. Box plot chart with regards to the induction temperatures for the two rates, 0.5°C/min and 1.0°C/min, sample volume of 0.5 µl.

At bulk volume of 5 μl and cooling rate 1.0°C/min $T_{crystal}$ was between 13°C and 14°C, and for 0.5°C/min it was between 5°C and 12°C.

Morphology. Note that *platelets* when used, named in this section does not apply to one specific hydrate unless specified. All images have the same scale-marker unless stated otherwise, see figure 7 for more information. See figure 5 for a general description of hexagonal platelets and needles.

The morphology varied at different cooling rates and sample volumes, see table 1 for an overview. 1.0°C/min, 0.5 μl, predominantly showed platelets at induction temperature and occasionally displayed needles at lower temperatures, but always in the minority, see figure 6. 0.5°C/min, 0.5 μl, showed a lot of variance, but would, for the most part, have platelets at induction temperature, and have a larger quantity of needles at lower temperatures in comparison to 1.0°C/min, see figure 6. One important thing to note is that the platelets were of different geometry and structure and may not be ascribed to the same hydrate. Some were close to circular others bigger and of irregular shape, some hexagonal and a few nearly perfect squares. Both cooling rates had a mixed morphology when the cooling ramp was completed, with different platelets and, or needles.

On one instance 0.5°C/min produced pure crystals, needle structures appeared at induction temperature and continued to grow throughout the cooling ramp, not showing any signs of platelets or other crystal structures forming, see figure 7.

a) *b)*

Figure 5. a) hexagonal platelet, b) needle structure

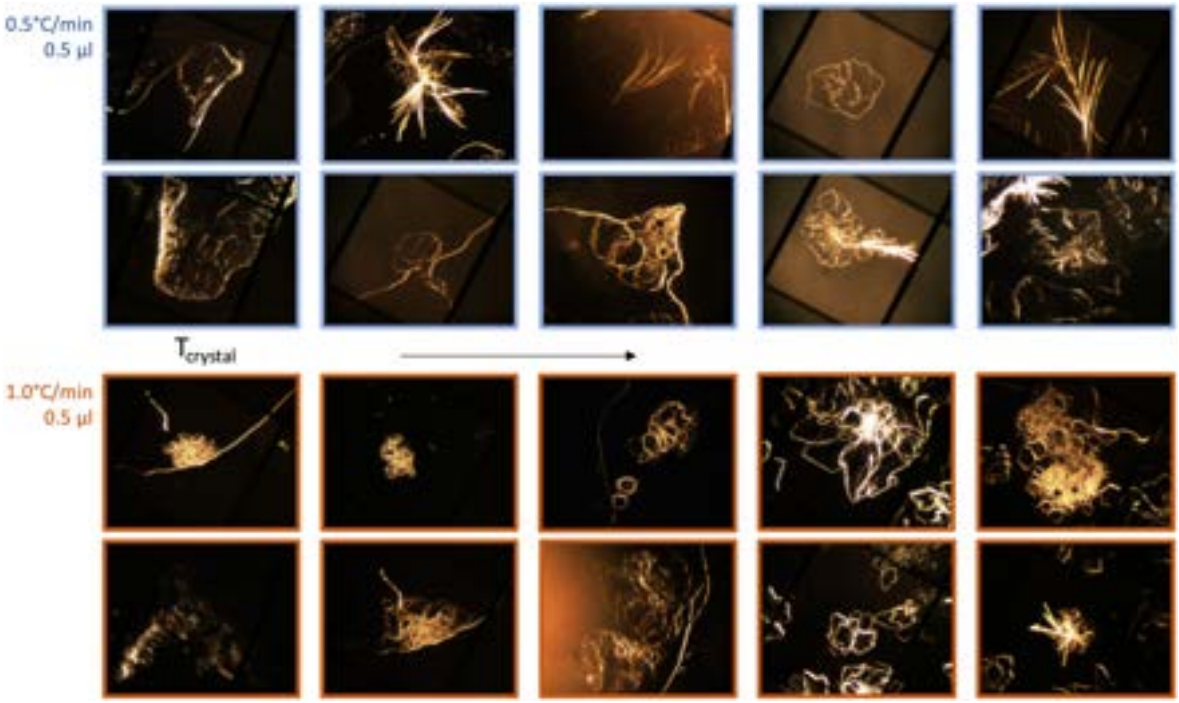

Figure 6. Optical microscopy of crystal structures at different temperatures as the sample cools with a cooling rate of 0.5°C/min (top two rows, blue) and 1.0°C/min (bottom two rows, orange), sample volume of 0.5 µl. From left to right, left: at temperature of crystallisation, moving to the right as it cools, images vertical of each other are of the same temperature. Note that these images are not all from the same sample but have been chosen based on how well they represent the general behaviour. Larger version in supplementary information.

After the cooling ramp the sample was held isothermally at -5°C to see if other structures would develop, they did not.

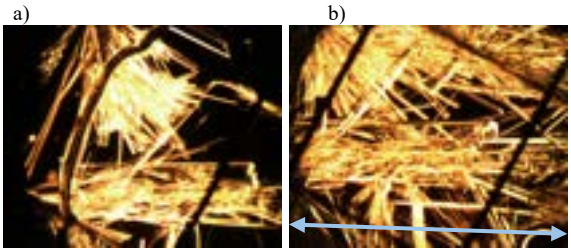

Figure 7. Needles forming in a sample of 0.5 µl and a cooling rate of 0.5°C/min. a) at a temperature of 8.2°C, b) at a temperature of -5°C. No other crystal structure was present at any temperature. The length across the image, marked by the blue arrow is of 0.01mm, no images have been cropped unless stated otherwise and therefore are all of the same length across.

At bulk volume, 5 μl, both cooling rates would start to appear more viscous and look more and more like sand/gel before finally crystallising, see figure 8. The developed crystals were very small compared to the micro sample volume (0.5 μl) and had a similar appearance to grains of sand, and both cooling rates shared this behaviour. For both repeats with the cooling rate 1.0°C/min, the same thing happened (grain), although for one experiment small square platelets appeared at a lower temperature. The cooling rate 0.5°C/min formed larger crystals for one of the experiments, these grew from a small seed until finally growing so large they grew out of frame, see figure 9. These big crystals were larger than the ones in the sample volume of 0.5 μl and only showcased platelets throughout the entire

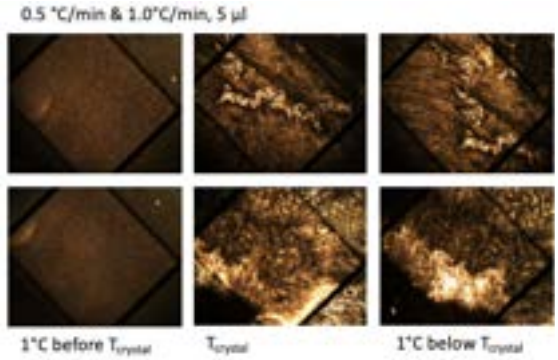

Figure 8. Optical microscopy of sample-volume 5 µl as it starts to crystallise. Row 1 – cooling rate of 1.0°C/min, row 2 – cooling rate of 0.5°C/min.

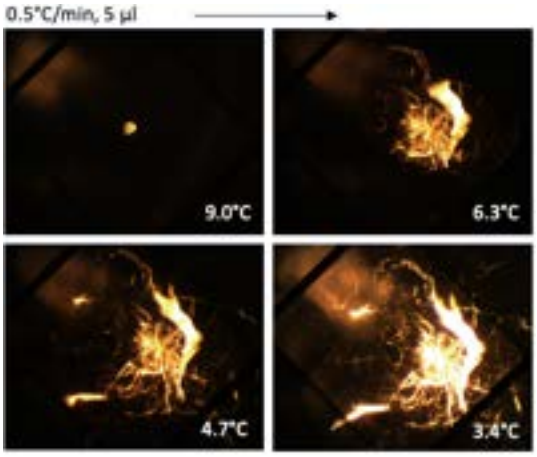

Figure 9. Optical microscopy of sample volume 5 µl as a larger crystal is formed and grows as it cools with a cooling rate of 0.5°C/min.

cooling ramp, these platelets were of a close to circular geometry.

A larger bulk sample was used as well, 20 μl, this behaved very similarly to 5 μl for both rates, for the cooling rate 1.0°C/min very small crystals appeared and when 0.5°C/min was investigated larger crystals would form, see figure 10. The large crystals were similar in geometry for both volumes, almost circular although they did not grow in the same manner, in 5 μl they covered a greater surface area, and in 20 μl they grew more on top of each other, overlapping.

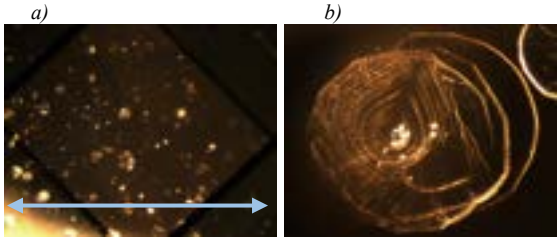

Figure 10. Optical microscopy of bulk-sample (20 µl). a) 1.0°C/min at 1.5°C, b) 0.5°C/min at 0°C. Blue arrow for scale, length = 0.01mm.

IR-spectrum. The spectrum shown in this section has been chosen based on how well they represent our findings; an extended version can be found in the supplementary information (SI). The spectrum, figure 11, have highlighted regions to easier refer to the bands of interest, the images included with the spectrum is of the structure that the measurement is taken from. All spectrums have been processed with post acquisitional spectral processing, baseline correction and *Savitzky–Golay* smoothening.

The hemihydrate (SDS · ½ H_2O) was confirmed to be the needle structure in sample volume 0.5 μl, see figure 6 and 7, as they coincide with the characteristics found in the literature of the IR-spectrum. The spectrum taken of the needle structure, seen in figure 11 a) at cooling rate 0.5°C/min was also found in the cooling rate of 1.0°C/min (sample volume 0.5 μl), the δCH_3 region (green) has a strong peak, the $v_{as}OSO_3^-$ band (darker blue) has strong peaks with a wide split of approximately 65 cm^{-1} as well as two strong singlets in the $v_sOSO_3^-$ region (lighter blue).

Some of the platelet structures in sample volume 0.5 μl were confirmed to be the monohydrate (SDS · H_2O), these platelets appeared to be of hexagonal geometry. The spectrum in figure 11 b), cooling rate 1.0°C/min (0.5 μl), displays the defining features of one of these hexagonal platelets (monohydrate), the strong singlet in the δCH_3 region (green) followed by a weak doublet (1398 – 1394 cm^{-1}), the $v_{as}OSO_3^-$ band (darker blue) has strong peaks with a wide split of approximately 45 cm^{-1} (smaller than for the hemihydrate) as well as one sharp peak and one strong singlet in the $v_sOSO_3^-$ region (lighter blue). This was also seen for the cooling rate, 0.5°C/min (0.5 μl).

Some of the polymorphs that appeared to be platelets had an IR-spectrum that indicated that they could be the dihydrate (SDS · 2 H_2O) as they share the IR-spectrum characteristics found in the literature. As seen in figure 11 c), light-green line: cooling rate 0.5°C/min (0.5 μl), dark-green line: 1.0°C/min (0.5 μl) and blue line: cooling rate 1.0°C/min (5 μl), for the spectrum that display the strong peak in the δCH_3 region (green) followed by a weak peak, the $v_{as}OSO_3^-$ band (darker blue) has a very strong unresolved peak as well as three strong singlets in the $v_sOSO_3^-$ region (lighter blue) [8]. The most reoccuring crystal shape for this spectrum was a platelet with square geometry, see figure 12 for a closer look at this shape, note that these are of a different scale to previous images. These square platelets were for the most part rather small but did vary in size. They appeared both in the micro sample volume of 0.5 μl, both cooling rates, and the bulk of 5 μl (only cooling rate 1.0°C/min).

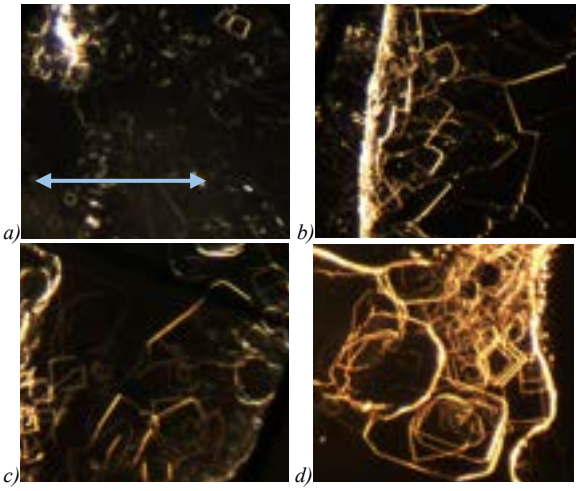

*Figure 12. Zoomed in versions of images displaying square crystal structures with sharp edges, referred to as the dihydrate in this paper. **a)** bulk volume of 5 µl with matching spectrum in figure 11 c), cooling rate 1.0°C/min, **b)** cooling rate 1.0°C/min, sample volume 0.5 µl, **c)** cooling rate 0.5°C/min, sample volume 0.5 µl, **d)** cooling rate 0.5°C/min, sample volume 0.5 µl. Important to note is that these images are **not** of the same scale as the others shown throughout the paper. Blue arrow for scale, length = 0.005 mm. Larger version in supplementary information.*

A final polymorph that has been referred to as grain or sand (see figure 8) in this paper show signs of being either a mix of different hydrates or an undefined one (see figure 11 d)). The spectrum in figure 11 d) (sample volume 5 μl) had a cooling rate of 0.5°C/min, the same spectrum and morphology did however also appear for the cooling rate of 1.0°C/min. The spectrum has an unresolved band in the $v_{as}OSO_3^-$ region (darker blue), similarly to the dihydrate, although slightly more resolved, it is potentially a different hydrate altogether other than the three discussed in this paper as it also appears to show signs of being a triple peak which is not like other hydrates we have seen.

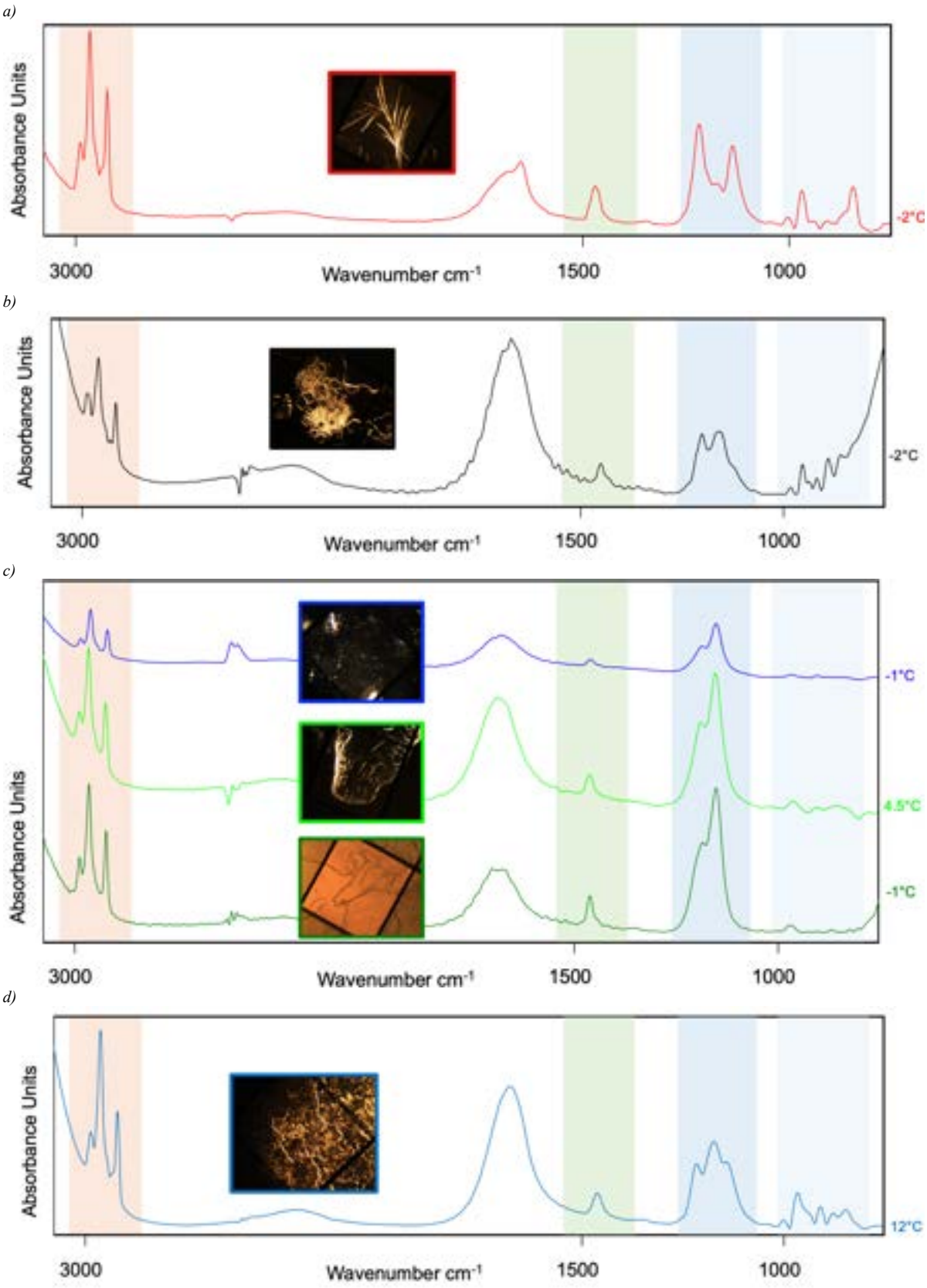

Figure 11. a) IR-spectrum of the hemihydrate, needles. Sample volume 0.5 µl and cooling rate 0.5°C/min, b) IR-spectrum of the monohydrate, hexagonal platelets. Sample volume 0.5 µl and cooling rate 1.0°C/min, c) . IR-spectrum of the potential dihydrate, small squares. Blue, top line: sample volume 5 µl and cooling rate 1.0°C/min, light-green middle line: sample volume 0.5 µl and cooling rate 0.5°C/min, dark-green bottom line: sample volume 0.5 µl and cooling rate 1.0°C/min.
d) IR-spectrum of the unidentified, grain hydrate. Sample volume 5 µl and cooling rate 0.5°C/min.
The framed images are the crystals of which the spectrum is taken of the temperature displayed to the right of the graph. Highlighted areas refer to specific bonds of interests.

Table 2. Average and median shift (8°C) for the sample volume of 0.5 µl and cooling rates 0.5°C/min and 1.0°C/min. Average shift: from micellar solution to crystallised, median shift: from micellar solution to solution at 8°C.
*Band 1: the two larger peaks (in the orange band in spectrum figures), $v_{as}(CH_2)$ and $v_s(CH_2)$, circa 2920 cm^{-1} and 2850 cm^{-1} respectively. Band 2: peak in the highlighted green region in spectrum figures, $\delta(CH_3)$ circa 1470 cm^{-1}. Band 3: the two more prominent peaks in the darker blue region in the spectrum figures, $v_{as}(OSO_3^-)$ circa 1270 - 1200cm^{-1}. Numbers marked in **bold** indicate that they are the larger shift compared to the other cooling rate. The shift was calculated as seen in equation 1. Extended version of table in supplementary information.*

AVERAGE SHIFT

	band 1		band 2	band 3	
0.5°C/MIN	3.5367	1.6733	**5.2233**	**14.4033**	3.3933
1.0°C/MIN	**4.0467**	**2.6000**	1.5367	10.1333	**4.5167**

AVERAGE MEDIAN SHIFT (8°C)

	band 1		band 2	band 3	
0.5°C/MIN	**5.6733**	1.3800	1.2633	**14.7300**	**6.3267**
1.0°C/MIN	4.0467	**2.5300**	**2.1767**	10.3067	2.9933

For the sample volume of 0.5 μl the average shift of the areas of interest, see figure 11 for areas highlighted, average shift meaning the shift of the peaks as they go from micellar solution to crystallised. It was discovered that the cooling rate of 1.0°C/min had an overall slightly larger shift than 0.5°C/min, see table 2. The median shift, meaning the shift of the peaks as they go from micellar solution to 8°C (the median), was also investigated and found that the cooling rate 0.5°C/min had a larger shift than 1.0°C/min, which shows that 0.5°C/min started its shift earlier, see table 2.
The average shift in wavenumber was calculated as seen in equation 1, $Shift_{average,n,i}$ = the average shift of a specific cooling rate $[cm^{-1}]$.

$$Shift_{average,n,i} = \frac{\sum_n |band_i|}{n} \qquad (1)$$

$|band_i|$ = the shift of band $i = 1$, 2 or 3,
n = number of repeats per cooling rate. The shift was calculated at each cooling rate and peak. The absolute value was summed and divided by the number of repeats for each rate. Example, cooling rate 0.5°C/min, 3 repeats ($n = 3$), band 2 ($i = 2$)

Discussion

Induction temperature of micro-volume, 0.5 μl. The induction mean temperature for the cooling rate 0.5°C/min (0.5 μl) was lower than that of 1.0°C/min (0.5 μl), this does not coincide with the literature, where at lower cooling rates the induction temperature increases [7] [11]. This experiment saw the opposite happen; the lower cooling rate, 0.5°C/min had a lower average induction temperature than the faster, 1.0°C/min. $T_{crystal}$ also had a much larger range for the slower cooling rate, 0.5°C/min, a finding that can be ascribed to the randomness of the crystallisation process, although, this randomness can also be due to a lack of understanding of other underlying phenomena. A theory regarding the lower $T_{crystal}$ is that by lowering the cooling rate the molecules have more time to rearrange into stable structures that favour remaining in liquid form or liquid crystals and therefore the induction temperature is lower. This theory is possibly reinforced by the discovery of the larger, earlier (median, 8°C) shift for the slower cooling rate of 0.5°C/min and the lower average induction temperature. Alternatively, there was something wrong with the experimental conditions, the sample, randomness in the process or other unknowns, and the data should be discarded. As seen in the t-test that was run to compare the two groups, the mean difference, was not statistically significant (t = -1.9631, df = 4.6401, p = 0.1113), see figure 4. While the data met the parametric assumption of normality, the homogeneity of variance and sample size was lacking. This was due to time restrictions brought about by the pandemic, which was made worse as some samples had to be discarded due to experimental error. It was felt that the t-test was still appropriate as it is robust against small deviations from parametric assumptions. The test did not meet the threshold for statistical significance (p=0.05). However, it is likely that this was due to the aforementioned small sample size. More tests are certainly warranted to explore this effect further.

Induction temperature, bulk- vs micro volume. There is a clear difference between the crystallising behaviour between the bulk volumes of 5 μl, 20 μl and the micro volume of 0.5 μl. The nucleation of the bulk volume propagates all over, making the induction temperature higher than that of the smaller volume, this could be explained if the limiting step to crystallisation in a very small volume is nucleation. On a few occasions, no crystallisation occurred at all when the sample volume 0.5 μl was cooled at different rates. If nucleation is the limiting step this makes sense as no crystal can form without a nucleation event. This phenomenon was never observed with larger

sample-volumes. Whereas for a larger volume, 5 μl or 20 μl, the rate-limiting step is crystal growth, as the probability of a nucleation event goes up with volume [13]. With increased sample-volume (5 μl, 20 μl) the range of $T_{crystal}$ decreased for both cooling rates, although it is important to note that the number of samples was smaller than that of the 0.5 μl volume. Therefor this would also have to be investigated further with a larger number of samples.

Morphology and hydrates, micro volume. Platelets and needles were the most reoccurring crystal shapes for both cooling rates (0.5°C/min and 1.0°C/min) in sample volume 0.5 μl, see table 1. For the cooling rate of 1.0°C/min (0.5 μl), platelets were the first to appear at $T_{crystal}$, as it cooled needles started to appear although in the minority. For the same sample volume (0.5 μl) but cooling rate 0.5°C/min the same thing happened, platelets appeared first and needles at lower temperatures, however, needles were of a higher percentage than for 1.0°C/min. In a few instances for 0.5°C/min needles were the only morphology to appear, this indicates a form of stability as there is no mix of different polymorphs, they were pure crystals. After taking a closer look at the different crystals that have been referred to as platelets in the result section, it appears as if they cannot be labelled as the same structure, as neither the geometry nor size is the same. This is also confirmed with the IR-spectrum. It would not be implausible to find different polymorphs as there are still SDS-hydrates that have not been assigned a crystal structure [14] [7]. With regard to identifying hydrates in our samples, both needles and platelets have previously been assigned to different hydrates. Hexagonal platelets are ascribed to the monohydrate ($SDS \cdot H_2O$) and needles to the hemihydrate ($SDS \cdot 12\ H_2O$), the IR-spectrum taken of some of the platelets and the needles also coincide with the ones in the literature, see figure 11 a) and b) [12].

Morphology and hydrates, bulk volumes. For the bulk volume (5 μl) the crystallisation started with a sand-like texture that then turned into grain-like crystals of very small size compared to those of sample volume 0.5 μl. As the sample grew larger, it also grew taller and thicker, which made it harder to distinguish between different crystal structures as it was only possible to observe the crystals on the surface. The larger bulk-sample of 20 μl behaved much like 5 μl, very small crystals and predominantly platelet-like structures. Another observation of the bulk volumes, 5 μl and 20 μl, was that the crystals tended to be smaller and of a greater number per area unit than 0.5 μl, this could be ascribed to the larger sample-volume having more nucleation sites and the crystals forming are fighting for space to grow, resulting in them being very small and closely packed. For the cooling rate of 0.5°C/min, for both bulk volumes (5 μl, 20 μl), it had much larger crystal structures growing that would eventually grow so large that they grew out of frame, these were larger than those of the micro volume (0.5 μl). A larger sample volume either produces much larger crystal structures or very small ones.

IR-spectrum, dihydrate. As discussed, the IR-spectrum did confirm that not all platelets belonged to the same hydrate, found in sample volume 0.5 μl as well as 5 μl and with both cooling rates, have the characteristics of the dihydrate's spectrum found in the literature [8]. A question that arises is if the spectrum isn't of a micellar solution or partly, as it does share some features with the spectrum of a micellar solution, especially in the unsplit $\nu_{as}(OSO_3^-)$ region. After spectrum analysis, it was determined that it was fully crystallised as it did not have the distinguishing shoulder at circa 2860 cm^{-1} of a solution in a partially micellar state, as well as general shift [15]. The crystal structures of the cooling rate of 0.5°C/min (0.5 μl) shared the same geometry, close to a *perfect* square. These squares were not very large, see figure 12, but did vary in size and would generally grow to fill a larger surface area while also stacking on top of each other. The surfaces of the squares are smooth, depicting that the general crystallographic orientation is well preserved as it grows [5]. For the cooling rate of 1.0°C/min (0.5 μl) the crystal structure is more of an irregular geometry, although showing signs of sharp edges and arguably a common seed structure, perhaps a faster cooling rate does not allow enough time to rearrange to form more ordered crystal structures. The majority of the crystal structures forming with the spectrum of the dihydrate had a square geometry, as seen in figure 12. Another key thing to note is that this hydrate/structure only appeared at lower temperatures, most often between 3°C to -1°C.

IR-spectrum, grain-structure, 5 μl. The IR-spectrum also confirmed the suspicion of another hydrate, brought about by the grain structure found in sample volume 5 μl of both cooling rates. The spectrum also indicated that it could be a mixture of polymorphs as the spectrum shares characteristics with both the dihydrate and the monohydrate. As the occurrence of a mix of polymorph was common, it would not be unlikely for it to be a combination of different hydrates. The thickness of the sample also goes up with volume, lowering the resolution, making it hard to differentiate between structures.

Conclusions

In a sample volume of 0.5 μl the cooling rate 0.5°C/min had an average temperature of crystallisation at a lower temperature than 1.0°C/min, the range of $T_{crystal}$ was also rather large. The morphological characteristics observed were also different for each cooling rate, both began

crystallisation with platelets with the appearance of needles at lower temperatures, 0.5°C/min having a higher percentage of needles than 1.0°C/min. The growth of pure crystals in the form of needles appeared for the cooling rate of 0.5°C/min in one of the experiments, displaying a form of stability.

An earlier shift in the IR-spectrum for 0.5°C/min was observed. Surprisingly, it crystalised at lower temperatures, which suggests an earlier ordering of molecules that are able to remain in a liquid phase.

As the sample volume increased so did the temperature of crystallisation for both cooling rates. The crystal morphology changed as well, having either very small or very large crystals forming, the larger ones belonging to the rate 0.5°C/min and predominantly small crystals forming for the cooling rate of 1.0°C/min. This applies to both bulk volumes investigated, 5 μl and 20 μl.

Confirmed polymorphs in our samples were the hemihydrate and monohydrate, needles and hexagonal platelets respectively.

The IR-spectra suggested that the dihydrate may have also been present. These spectra were associated with a square crystal structure and were most frequently seen at the cooling rate of 0.5°C/min (sample volume 0.5 μl). Also, they only appeared at lower temperatures (between 3°C and -1°C).

The grain-like crystal structure in the larger sample volume (5 μl) was determined to be either a mix of hydrates or an undefined structure; as it displays characteristics from both the dihydrate and monohydrate, or neither.

Many of the effects we observed, hinted at new insights into the crystallisation behaviour of SDS. Unfortunately, due to the pandemic limiting lab time, sample sizes were smaller than we would have liked. But from these preliminary findings, it is clear that this is an exciting avenue of research and more work is needed.

Acknowledgements

I would like to thank Dr Gunjan Tyagi for her generous support and great advice as well as Professor João Cabral for providing additional insights.

Supplementary Information

Supplementary information can be found in the file labelled *supplementary information*. The file contains further IR-spectrum as well as images taken with optical microscopy and more extensive data tables.

References

[1] Y. Nakama, “Chapter 15 Surfactants,” in *Cosmetic Science and Technology: Theoretical Principles and Applications*, Elsevier, 2017, pp. 231-244.

[2] M. Sagir, M. Mushtaq, M. Tahir, M. Tahir and A. Shaik, “Chapter 1 Surfactants,” in *Surfactants for Enhanced Oil Recovery Applications*, Springer, Cham, 2020, pp. 1-11.

[3] S. Paria, “Surfactant-enhanced remediation of organic contaminated soil and water,” *Advances in Colloid and Interface Science,* vol. 138, no. 1, pp. 24-58, 2008.

[4] M. Sammalkorpi, M. Karttunen and M. Haataja, "Structural Properties of Ionic Detergent Aggregates: A Large-Scale Molecular Dynamics Study of Sodium Dodecyl Sulfate," *The Journal of Physical Chemistry,* vol. 111, no. 40, pp. 11722-11733, 2007.

[5] T. H. Zhang and X. Y. Liu, "13 Controlled Colloidal Assembly Experimental Modeling of Crystallization," in *Handbook of Crystal Growth*, Elsevier, 2015, pp. 561-594.

[6] V. Sreepriya and V. V. Ranade, “Crystallization: Key thermodynamic, kinetic and hydrodynamic aspects,” *Sadhana,* no. 38, p. 1287–1337, 2013.

[7] R. M. Miller, O. Ces, N. J. Brooks, E. S. J. Robles and J. T. Cabral, “Crystallization of Sodium Dodecyl Sulfate-Water Micellar Solutions under Linear Cooling,” *Crystal Growth & Design,* vol. 17, no. 5, pp. 2428-2437, 2017.

[8] R. P. Sperline, "Infrared Spectroscopic Study of the Crystalline Phases of Sodium Dodecyl Sulfate," *Langmuir,* vol. 13, no. 14, pp. 3715-3726, 1997.

[9] L. A. Smith, K. J. Roberts, D. Machin and G. McLeod, “An examination of the solution phase and nucleation properties of sodium, potassium and rubidium dodecyl sulphates,” *Journal of Crystal Growth,* vol. 226, no. 1, pp. 158-167, 2001.

[10] E. Summerton, G. Zimbitas, M. Britton and S. Bakalis, "Crystallisation of sodium dodecyl sulfate and the corresponding effect of 1-dodecanol addition," *Journal of Crystal Growth,* vol. 455, pp. 111-116, 2016.

[11] L. Smith, A. Duncan, G. Thomson, K. Roberts, D. Machin and G. McLeod, “Crystallisation of sodium dodecyl sulphate from aqueous solution: phase identification, crystal morphology, surface chemistry and kinetic interface roughening,” *Journal of Crystal Growth,* vol. 263, no. 1-4, pp. 480-490, 2004.

[12] R. M. Miller, A. S. Poulos, E. S. J. Robles, N. J. Brooks, O. Ces and J. T. Cabral, "Isothermal Crystallization Kinetics of Sodium Dodecyl Sulfate–Water Micellar Solutions," *Crystal Growth & Design,* vol. 16, no. 6, pp. 3379-3388, 2016.

[13] A. McPhersona and Y. G. Kuznetsova, "Mechanisms, kinetics, impurities and defects: consequences in macromolecular crystallization," *Acta Crystallographica Section F,* vol. F70, pp. 384-403, 2014.

[14] T. Lee, K. L. Yeh, J. X. You, Y. C. Fan, Y. S. Cheng and D. E. Pratama, "Reproducible Crystallization of Sodium Dodecyl Sulfate·1/8 Hydrate by Evaporation, Antisolvent Addition, and Cooling," *ACS Omega,* vol. 5, no. 2, pp. 1068-1079, 2020.

[15] T. Kawai, H. Kamio, T. Kondo and K. Kon-No, "Effects of Concentration and Temperature on SDS Monolayers at the Air−Solution Interface Studied by Infrared External Reflection Spectroscopy," *The Journal of Physical Chemistry,* vol. 109, no. 10, pp. 4497-4500, 2005.

Atomistic simulation of pH-responsive PLP-NDA

By Darshil Dholakia, Mathusan Kandiah
Department of Chemical Engineering, Imperial College London, UK

Abstract

A new class of pseudopeptides derived from the poly (L-lysine *iso*-phthalamide) backbone have provided promising experimental results as drug carriers to facilitate intracellular drug delivery. Studies found that grafting 10-carbon long hydrophobic side chains onto the backbone, to form PLP-NDA, significantly increased both the hemolytic activity and intracellular delivery of therapeutics. In this study, molecular dynamics (MD) software was utilised to investigate the interactions between variants of PLP-NDA and the membrane. The grafting ratio, the spatial distribution and the side chain length were considered as variables. Increasing the grafting ratio from 20% to 80% showed greater membrane thinning by a factor of 2.04. Altering the sequence of NDA grafts on the backbone from spread to skew caused 1.29 times more thinning. Finally, increasing the side chain length from 5 carbons to 20 carbons led to a 2.43 times deeper thinning effect. The results from experimental studies and the observations made in computational MD go hand in hand to further our knowledge and understanding of the mechanisms underpinning drug delivery.

Key Words: *pH-responsive, comb-like pseudopeptide, block and random polymers, simulation, membrane thinning, Van der Waals*

1 Introduction

To this day, intracellular drug delivery is a key matter of research in the pharmaceutical sector, with new insights advancing the field over the past few decades. With the introduction of MD, a more robust approach could pave the way for a new perspective, with possibilities for elucidating the specific mechanisms of these deliveries and the membrane interactions at play in these processes. With these concepts understood, researchers can rationally design their delivery vehicles and therapeutic agents to optimise the transport of hydrophilic, membrane-impermeable molecules into target cells.

In previous work, interest has been focused on the development of pH-responsive vehicles with the ability to undergo a conformational change once transitioning from the extracellular pH to the intracellular endosomal pH. Experimental work conducted by Kopytynski et al focused on pseudopeptides with a poly(L-lysine *iso*-phthalamide) (PLP) backbone grafted with phenylalanine at a stoichiometric ratio of 50%, PP50.[8] This focus was motivated by previous demonstrations of the polymer's potential to deliver trehalose to human erythrocytes at acidic extracellular pH for cryopreservation purposes. The report concluded that the polymer could facilitate the delivery of different sized payloads varying in terms of their chemical and physical properties.

However, the intracellular trehalose delivery efficiency achieved by using PP50 was limited to a maximum of 35% and high incubation times made it less ideal for applications in therapeutics.[3] Chen et al, inspired by naturally existing membrane proteins covalently attached to long-chain fatty acids, reported a class of pH-responsive, membrane-anchoring, comb-like pseudopeptides with significant endosomolytic activity.[4] This new polymer PLP-NDA, shown in Figure 1a consisted of hydrophobic decylamine (NDA) chains grafted onto the a PLP backbone to form a "comb-like" architecture to enhance polymer-membrane interaction. The hemolytic activity was found to be a function of the number of NDA side-chain moieties; the polymer with the highest grafting ratio, PLP-NDA18, exhibited superior membrane-disruptive activity at endosomal pH. These alkyl side chains increase the hydrophobicity of the copolymer, which is known to enhance penetration into the hydrophobic core of the lipid bilayer.[3,18] Spatial distribution of grafted moieties were investigated to look at how the distribution of the different monomers, throughout the copolymer chain, can influence their effectiveness.[15,18] The studies found that random copolymers, whereby the grafted monomer units are randomly distributed and spread out, were more effective with membrane interactions when compared to the block polymers, where all the grafted monomers are skewed to one side of the chain. This work can be used to investigate how the arrangement of

(a) **(b)**

Figure 1: **(a)** Poly(L-lysine *iso*-phthalamide) monomer unit and alkyl-grafted monomer unit. R = OH indicates the ungrafted monomer unit, PLP. R=$NH(CH_2)_nCH_3$ refers to the grafted unit, with 'n' number of CH_2 . The polymers when varying pendant chain length in this paper include PLP-NDA (n=9), PLP-PA (n=4) and PLP-IA (n=19)] **(b)** PLP-NDA20 (20% grafted) 3D structure

monomer units impacts the polymer's overall interaction ability, to ultimately penetrate and thin the membrane.

Previous computational studies have explored the suitability of protonated copolymers, namely PLP with and without phyenylalanine-grafted side chains, for the membrane penetration process and compare them to their deprotonated counterparts.[20] A measure considered to examine such effects was the free energy change upon reaching the lipid core. It was reported that the protonated forms incurred reduced energetic penalties than their deprotonated counterparts to reach the bilayer core. These results informed this study's decision to only investigate protonated copolymers. Additionally, a computational modelling approach centered around investigating polymers made up of a large number of repeat units will provide interesting insights into how larger polymers interact with lipids in the human body; this will allow valid comparisons to be made between computational and experimental results obtained.[2,20]

2 Methods

Molecular dynamics simulations were performed using GROMACS v.5.1.4.[13] The systems were visualised using Pymol[19] and VMD 1.9.3.[7] The simulation models were parametrised by united atom forcefield GROMOS 54a7. All expensive jobs were submitted to the high-performance cluster at Imperial College London.[10] The simulations were carried out by following MD tutorials assembled by Justin Lemkul.[9] To analyse the membrane thickness, a grid-based membrane analysis tool, Gridmat-MD was utilised.[1] All graphs shown were plotted using MATLAB R2020b.[12]

2.1 Preparation of Polymers

2.1.1 Formation of topologies

This project explores the mechanism by which drug delivery occurs using the derivatives of an endosomolytic pseudopeptide, PLP-NDA, through a model dioleoylphosphocholine (DOPC) membrane. The grafting ratio, spatial distribution of the grafts and the NDA sidechain lengths were varied to produce 8 derivatives. Initially, for each polymer, a SMILES code was submitted to Cactus that translated the code to a 'protein databank' (pdb) file format.[21] The pdb files could then be submitted to Automated Topology Builder (ATB) from which united atom pdb and 'include topology' (itp) file templates were obtained.[11] United atom interatomic potentials treat the hydrogen and carbon atoms in methyl groups and methylene bridges as one interaction centre; making accurate charge determination, explained later, simpler.

2.1.2 Fragmentation

To input accurate static charges for each atom type in the polymer template itp files, fragmentation of the polymer was carried out. This involved submitting separate fragment pdb files into ATB to be processed up till the 'DFT Hessian QM (QM2)' stage for accurate charge determination. The need for fragmenting the pseudopeptide arose due to the default size limit of 40 atoms to reach the final processing stage. The different fragments submitted to ATB are shown in figure 2.

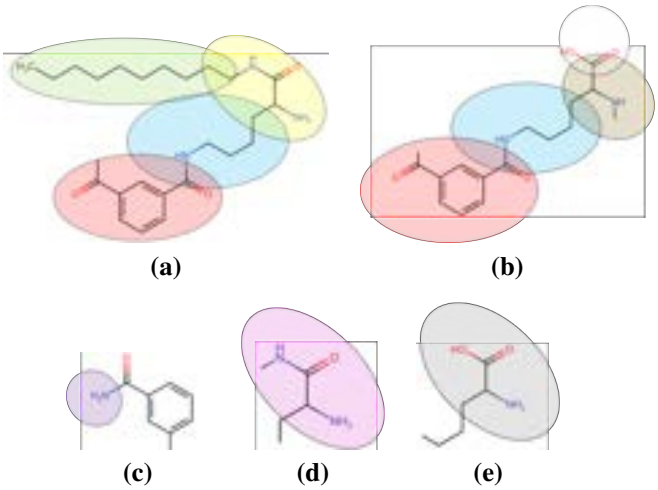

Figure 2: **(a)** PLP-NDA unit fragments **(b)** PLP unit fragments **(c)** Start NH_2 capping group fragment **(d)** PLP-NDA unit end NH_2 capping group fragment **(e)** PLP unit end NH_2 capping group fragment

2.1.3 Different structures of polymers

The approach taken in this report aims to formulate a computational understanding of the effects of hydrophobicity on the membrane-destabilising ability of PLP-NDA. Differing degrees of hydrophobicity were achieved by varying the grafting ratio, NDA side-chain length and the spatial distribution of NDA pendants on the PLP backbone, resulting in skewed and spread polymers as shown in figures 3b and 3c. This was done to explore the existence of any relationship between spatial distribution of grafts and membrane thinning.

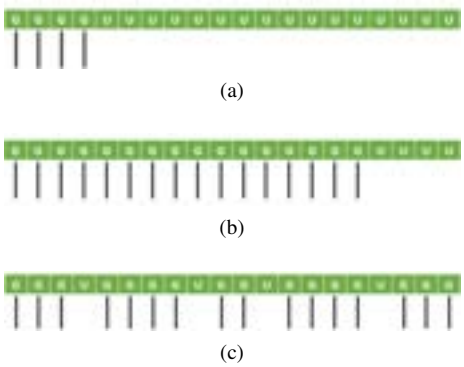

Figure 3: Structures of **(a)** PLP-NDA20 skew **(b)** PLP-NDA80 skew **(c)** PLP-NDA80 spread. The green squares containing 'G' with a protruding black line are the grafted PLP-NDA monomer units and the ones containing 'U' with no black line are the ungrafted PLP unit

2.1.4 Polymer Coiling

To avoid unnecessarily expensive computational load, the linear 20-mer pseudopeptides were coiled, as the linear structure would require too large a box to fit around. Further, the coiled polymer represented more closely an energy minimised structure as, upon equilibration, these lengthy polymers have been observed to form globule-like structures. The coiling was achieved using Pymol's 'scramble unfixed atoms' functionality.

2.2 Polymer Insertion

The box within which the polymer was confined had dimensions of 6.5691nm x 6.8178nm x 6.8585nm. The insertion of the polymer into a 'GROMACS' (gro) coordinate file, which had a solvated DOPC bilayer contained in a box of size 6.5104nm x 6.5104nm x 8.2937nm, was achieved by using 'gmx insert-molecules' with the option -replace SOL to ensure replacement of only water molecules by the polymer. Figure 4 shows the final polymer-bilayer system, excluding solvent molecules for clarity, visualised on VMD 1.9.3.

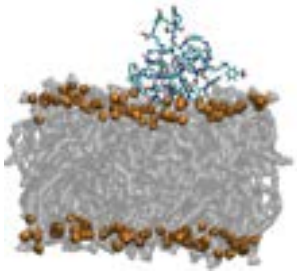

Figure 4: The simulated system containing the 128 DOPC molecules, 64 on each leaflets, and the polymer. The orange spheres represent the phosphorus atoms in each DOPC molecule and the grey area in between represents the hydrophobic core of the bilayer

2.3 100 ns Simulation

The time step for the 100 ns simulation was chosen to be 2 fs. The system was subjected to 500 ps of NVT and 500 ps of NPT equilibration before the 100 ns production run using md.mdp. The simulations were performed at 320K using the v-rescale thermostat with a coupling constant of 0.1 ps and at constant pressure using the Parrinello-Rahman barostat with a coupling constant of 2 ps and compressibility of 4×10^{-5} bar^{-1}.[14,17] The LINCS algorithm was used to constrain all bonds.[6] Short-range nonbonded interactions were computed using a cutoff of 1.4 nm, and the long-range electrostatic interactions were computed using the particle mesh Ewald (PME) method with 0.16 nm for the Fourier spacing.[5]

2.4 Data points

2.4.1 Van der Waals interactions

To obtain Van der Waals interaction evolution plots, an 'energygrps' option was added to the previous md.mdp file, whereby the residue names of both the polymer in question and the lipid bilayer were used as the option's argument. After running gmx mdrun with the -rerun option to ensure a less computationally expensive run, gmx energy was used on the output binary energy (edr) file from the previous step to get the Van der Waals evolution plot by selecting the 'LJ-SR' option (Lennard-Jones Short Range). The data was plotted with a 100-frame moving average.

2.4.2 Hydrogen Bonding

To analyse the evolution of the number of hydrogen bonds formed between the polymers of interest and the bilayer, the 'gmx hbond' functionality was utilised. The 2 different types of hydrogen bonds that were observed between polymers and bilayer are shown in Figure 5. The 3D images were obtained from PyMOL.

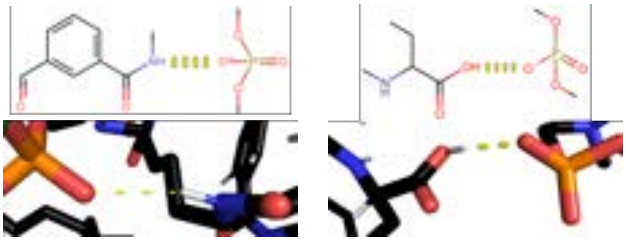

(a) **(b)**

Figure 5: Hydrogen bonds between **(a)** PLP backbone NH amine group and the DOPC phosphate group **(b)** Ungrafted unit carboxyl group and the DOPC phospate group

2.4.3 Membrane Thickness

Upon completion of the 100 ns simulation, the data obtained could then be analysed via Gridmat-MD. This is a Perl script designed to extract data on the apparent thickness of the lipid bilayer on a singular frame basis, meaning it was only possible to extract the thickness data at a specific point in time during the 100 ns. Gridmat-MD determines the membrane thickness by calculating the distance between the phosphorus atoms of opposing DOPC leaflets. All membrane thinning data was averaged over 10 frames; these were selected based on the frames that exhibited the strongest vdW interactions from one simulation run.

3 Results and discussion

3.1 Van der Waals interactions

The independent variables chosen for this study all revolve around altering polymer hydrophobicity; a greater proportion of or longer NDA sidechains will lead to increased hydrophobicity, thus enhancing PLP-NDA-bilayer contact. This increased contact between membrane-disruptive PLP-NDA and the DOPC bilayer has been found to induce membrane thinning. Analysis of the intermolecular interactions serves as a possible pathway to understanding the key driving force behind such effects. As such, a key focus of this study was Van der Waals (vdW) interactions between the pseudo-peptides and the DOPC bilayer. Figure 6 illustrates the development of the Lennard-Jones (LJ) potential over the length of the 100 ns simulation for a range of polymers.

3.1.1 Varying grafting ratio

As can be seen from Figure 6a, both PLP-NDA20- and PLP-NDA80-bilayer systems experienced a drop in LJ potential along the reaction timeline. This signifies the increase in system stability for both polymers as the vdW attractions are constantly decreasing. Based on the data, it can also be seen that PLP-NDA80 experienced stronger vdW interactions than PLP-NDA20, indicated by the former's lower moving average over the 100 ns. PLP-NDA80's LJ potential was significantly lower than that of PLP-NDA20 between the 40 ns – 80 ns window; the former with a mean value of -681 kJ/mol within this window, compared to the latter's -559 kJ/mol.

Further, from figure 6a, large fluctuations in LJ potential values for both polymers can be observed between the 2 repeats conducted; visualised by plotting continuous error areas. This indicates the highly chaotic nature of MD simulations, hence the importance of carrying out further repeats to obtain reliable results. Moreover, significant amount of overlap between the continuous error areas of PLP-NDA20 and PLP-NDA80 highlights the result's lack of reliability, thus revealing the need for conducting further analysis to notice definitive trends.

3.1.2 Hydrogen bonding

As such, the evolution of hydrogen bonding was analysed as shown in figure 7.

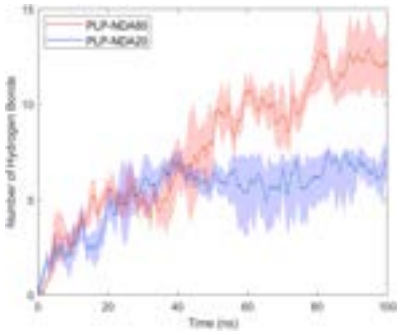

Figure 7: Moving average of the number of hydrogen bonds between polymer and membrane for PLP-NDA80 (red) and PLP-NDA20 (blue)

Figure 7 displays the strong divergence between the number of hydrogen bonds formed with PLP-NDA20 and PLP-NDA80 after the 40 ns point. The gradient for a linear line of best fit in the window of 40 ns – 100 ns for PLP-NDA20 and PLP-NDA80 would be 4.43×10^{-4} and 0.0011, respectively. The slope for PLP-NDA80 is 2.5 times that of its lower grafting counterpart, quantifying the sharper increase in the number of hydrogen bonds formed between PLP-NDA80 and the bilayer. This is in agreement with figure 6a which also shows noticeable divergence in polymer-bilayer interactions between PLP-NDA20 and PLP-NDA80 after the 40 ns mark.

3.1.3 Varying spatial distribution of grafts

To explore the effect of concentrated hydrophobicity achieved by developing polymers with varied spatial distribution of grafts, PLP-NDA80 skew and PLP-NDA80 spread were simulated. An 80% degree of grafting was chosen based on the results from previous section, whereby a higher grafting ratio correlated to stronger bilayer interaction. Clear deviation can be noted between the LJ potentials of the skew and spread polymers post 2 ns from figure 6b. More specifically, both potential profiles seem to plateau past the 80 ns point; PLP-NDA80 skew had a lower mean LJ potential of -700 kJ/mol in this window, whereas PLP-NDA80 spread experienced a mean LJ potential of -506 kJ/mol. A larger degree of interactions with the bilayer were observed due to heightened local levels of hydrophobicity in the PLP-NDA80 skew polymer.

However, large fluctuations in data were visualised using continuous error areas, especially for PLP-NDA80 spread, thus signifying the lack of reliability. This exposes the need for further repeats to be carried out.

3.1.4 Varying pendant chain carbon lengths

The carbon chain length of the grafted chains plays a crucial role in the overall effectiveness of the overall polymer. An optimal length would provide enough membrane anchoring potential, enhancing the polymer-membrane binding ability and facilitating the insertion of the polymer into the bilayer surface. The polymers constructed were PLP-PA, PLP-NDA

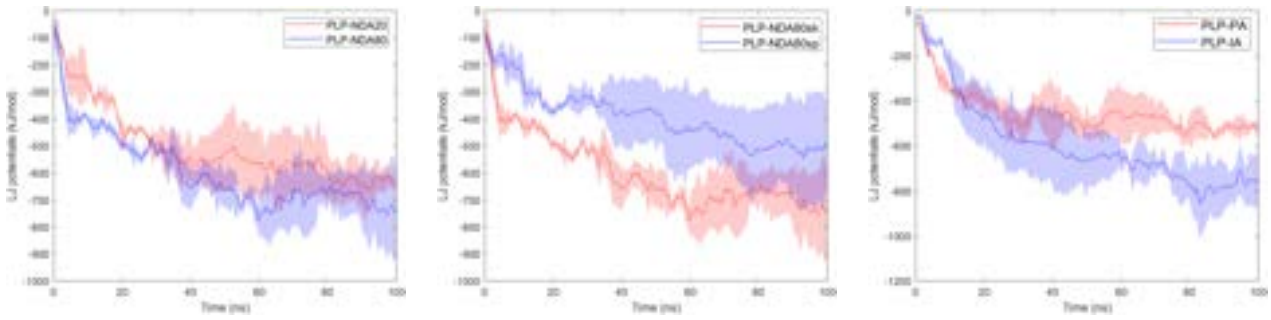

(a) **(b)** **(c)**

Figure 6: Van der Waal interactions between polymer and membrane for varying **(a)** grafting ratio **(b)** spatial distribution of grafts **(c)** pendant carbon chain length

and PLP-IA (carbon chain lengths of 5C, 10C and 20C respectively), and each were skewed with 20% grafting.

From figure 6c, it can be concluded that past the 15 ns simulation time, PLP-IA exhibited superior performance, illustrated by the steeper decline in the moving average of the LJ potential. Gradient analysis of a linear line of best fit post 15 ns revealed PLP-IA's slope was nearly 2.5 times greater than that of PLP-PA; the former with –0.0591 and the latter with -0.0251. The PLP-PA moving average could reach LJ potentials as low as -856 kJ/mol as opposed to the lowest levels reached by PLP-IA of -552 kJ/mol, further demonstrating the superiority in performance. The large fluctuations, again highlight the need to conduct further repeats.

3.2 Extent of membrane thinning

Membrane thinning is thought to be the preliminary stage to endocytosis. The contact area induces membrane curvature, which is known to increase the passive permeability of the membrane to these therapeutics to facilitate the cross-membrane drug delivery.[23] Not only is there membrane thinning, but there is an observable membrane thickening effect seen in all the membrane thickness plots, in a radius around the point of polymer contact. This is best seen in the below figure 8. This is too minor to address in full but good insight nonetheless into what seems to be a very early look at possible endocytosis. Looking at the relative effectiveness of the polymers in question with respect to the extent of membrane thinning observed over the course of a simulation can provide insight into the polymers' effectiveness in drug delivery.

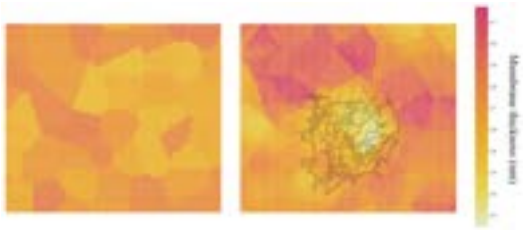

Figure 8: Visualisation of the membrane thickness without PLP-NDA20 (left) and with PLP-NDA20 (right)

3.2.1 Varying polymer grafting ratio

The extent of membrane thinning between the two polymers of differing grafting ratios are shown in the figure 9a and 9b. It shows that the higher grafting ratio polymer PLP-NDA80 has a greater membrane thinning effect compared to the PLP-NDA20, by a factor of 2.04. This shows that a higher degree of grafting leads to better membrane contact and binding and consequently, improved membrane thinning. Chen et al observed the same trend from 3-18% grafting of PLP-NDA in their study; a continuous rise in intracellular delivery ability, positively correlating with the extent of grafting.[3] Looking at the graphs, the effective width of membrane thinning is also higher for the 80% grafted polymer. This could be due to the larger size of the polymer impacting a greater radius around the point of contact on the membrane.

3.2.2 Varying spatial distribution of grafts

Structural isomerism of pH-responsive membrane-thinning polymers and their impact on effective permeability of the membrane have been investigated. Thus, looking into how the spatial distribution of these grafts affect membrane thinning ability for PLP-NDA may give useful insights. In Figure 9b and 9c, the skewed copolymer induces greater membrane thinning ability by a factor of 1.29. As expected, the difference is much less than that of changing the polymer grafting ratio as isomerism theoretically does not affect polymer-to-bilayer contacts in terms of membrane anchors formed for binding, whereas 12 more possible pendant chains, each providing another anchoring point into the membrane, is a significant difference.

These findings reaffirm the hypotheses behind several studies, namely Oda et al and Baulin et al, whereby it was postulated that altering copolymer configurations between block and random induce a varied degree of membrane activity.[16,22] However, Baulin et al results are not aligned with ones of this study. They concluded that copolymers with balanced hydrophobicity are better able to mimic "pore-forming" proteins as they can stick to membrane surfaces for longer; whereas, due to the additional localisation effect in block polymers,

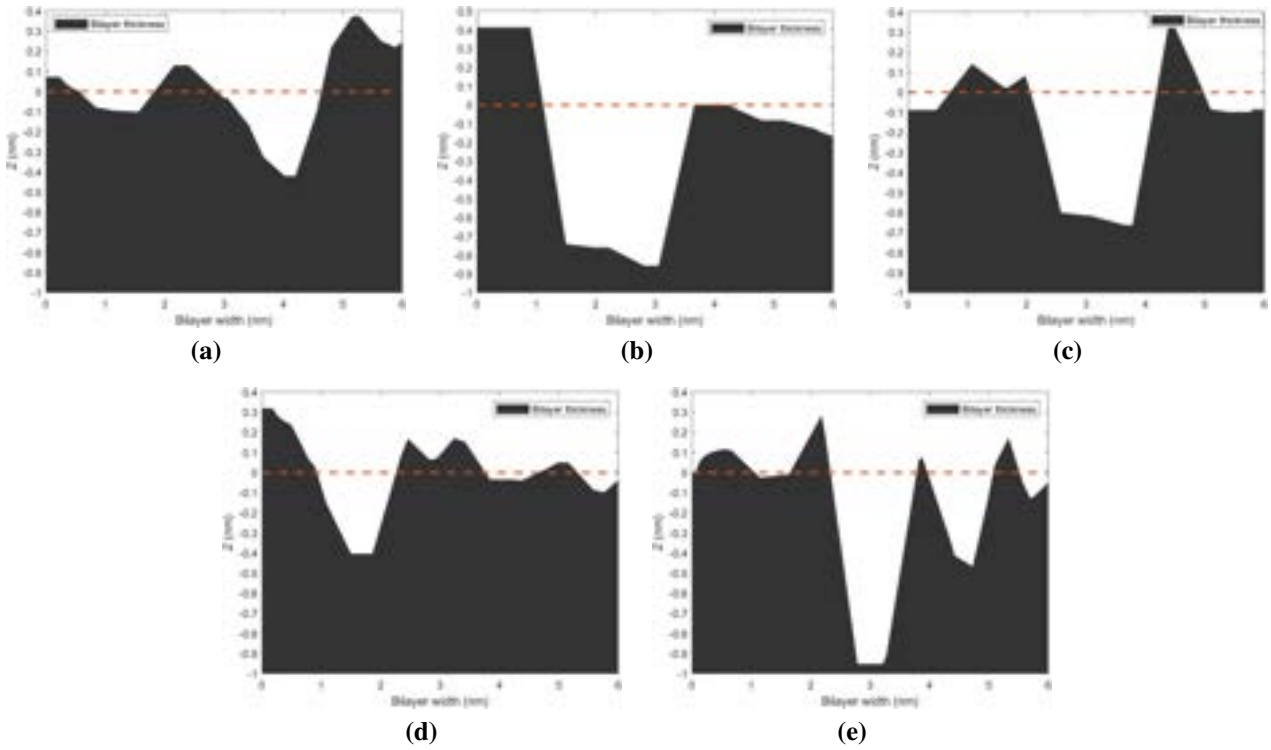

Figure 9: Cross section membrane thickness for **(a)** PLP-NDA20sk **(b)** PLP-NDA80sk **(c)** PLP-NDA80sp **(d)** PLP-PA **(e)** PLP-IA

they exhibited reduced translocation abilities. It can be said however, due to the coarse graining approach adopted by Baulin et al, longer time frames could be simulated, whereas, the all-atom approach used in this investigation hampered its ability to carry out longer simulations which could be the reason for the divergence in results.

3.2.3 Varying pendant chain carbon lengths

Along with grafting ratio, the pendant side chain carbon length is known to be another important property of these polymers which affects intracellular delivery of therapeutics. The PLP-IA penetrates the membrane significantly less than the PLP-PA by a factor of 2.43. This supports the idea that the increase in carbon side chain length forms these longer anchors from the polymer which are used to stabilise the polymer on the membrane, to undergo endocytosis. The study of Chen et al supports this but only so far. The increased effectiveness from 5C to 10C is expected, however the results for polymers, with longer than 10C sidechains, are contradictory as the experimental study showed a significantly lower relative effectiveness of the polymer. This was theorised to be because of polymer aggregation of these longer carbon chain polymers.[3]

3.3 Polymer Unwinding

The mechanism by which the membrane thinning occurs can start to be elucidated through these computational methods. Looking at figure 10a, the polymer is initially in its equilibrium coiled state. However, once contact is initiated with the membrane, a slight conformational change is apparent as the polymer appears to partially unwind and distribute over the surface of the membrane. This distributed contact is what appears to lead to the preliminary stage of membrane thinning. Although there is observable membrane interaction, the polymer does not completely unwind and does not form strong interactions with the membrane. Instead, it can be postulated that the polymer uncoiling is hindered by the intramolecular bonds formed within the polymer. These bonds hold the polymer together and keep the interior of the polymer coil from in-

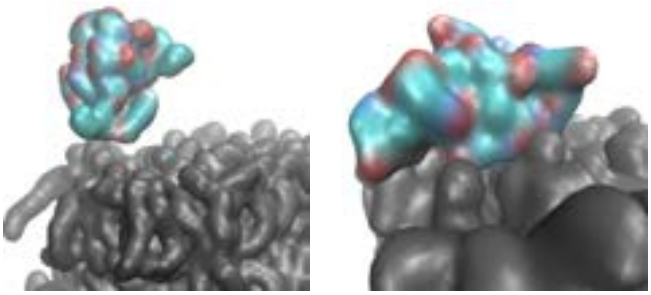

Figure 10: **(a)** Polymer equilibrium, coiled structure before membrane contact **(b)** unwound polymer structure upon membrane contact

teracting with the membrane, reducing the polymers effective hydrophobicity. Due to this effective decrease, the hydrophobicity of the PLP-IA is lower than the limit at which polymer aggregation becomes significant, hence why it continues the trend of improved membrane thinning in these simulations.

These 100 ns simulations are orders of magnitude less than the actual time frame over which these therapeutics have their effect. Over longer times frames like those in experimental studies, polymers have time to uncoil, thereby increasing their effective hydrophobicity and, in the case of PLP-IA, exceeding the limit at which polymer aggregation becomes significant, leading to the drop in polymer effectiveness during the experimental studies.

4 Conclusion

In this study, a computational look at a promising class of new polymers, namely PLP-NDA and its variants, provided key insights into their effectiveness as drug carriers, in particular the polymer-membrane interactions upon extracellular approach. The effect of grafting ratio, spatial distribution of the grafts and the pendant grafted sidechain lengths were varied to observe their effects on polymer effectiveness with respect to their abilities to thin the DOPC bilayer. Increasing the grafting ratio of these hydrophobic side chains provided more membrane anchors for the polymer, leading to better membrane thinning. Previous experimental studies observed the same trend from 3-18%.[3] Membrane interaction was significantly better with the longer carbon chain lengths due to each chain introducing more hydrophobicity for the polymer, allowing it to penetrate the membrane more deeply into the hydrophobic core. However, this is contradictory to previous studies, whereby carbon chains longer than 10C caused polymer aggregation, hampering the membrane thinning effect; longer MD simulations could reaffirm this finding, as a 100 ns simulation is very short in relation to the overall process of cross-membrane transport.[3] Changing the spatial distribution of the grafts to a 'spread' formation made the polymer less effective, theorised to be because of the less localised hydrophobicity, leading to membrane thinning over a wider area instead of concentrated in a smaller region. Contradictory studies exist that report higher effectiveness for the 'random' copolymers, however, the difference in results is thought to be down to the length of simulations carried out.[15,22] Not only does this study show great potential for the use of MD in this field, but these ideas can be developed to advance the knowledge required to build a comprehensive understanding of the mechanisms guiding the process of drug delivery.

Acknowledgements

The authors thank Dr. Rongjun Chen and Nicole Henry for their help with the theory and background. The authors also thank Thomas Nok Hin Cheng for his help with HPC setups, fragmentation and overall guidance. We thank the Imperial College High-Performance Computing Service for providing computational resources.

References

[1] William J Allen, Justin A Lemkul, and David R Bevan. "GridMAT-MD: a grid-based membrane analysis tool for use with molecular dynamics". In: *Journal of computational chemistry* 30.12 (2009), pp. 1952–1958.

[2] Rongjun Chen et al. "Synthesis and pH-responsive properties of pseudo-peptides containing hydrophobic amino acid grafts". In: *Journal of Materials Chemistry* 19.24 (2009), pp. 4217–4224.

[3] Siyuan Chen et al. "Comb-Like Pseudopeptides Enable Very Rapid and Efficient Intracellular Trehalose Delivery for Enhanced Cryopreservation of Erythrocytes". In: *ACS Applied Materials & Interfaces* (2020).

[4] Siyuan Chen et al. "Membrane-anchoring, comb-like pseudopeptides for efficient, pH-mediated membrane destabilization and intracellular delivery". In: *ACS Applied Materials & Interfaces* 9.9 (2017), pp. 8021–8029.

[5] Tom Darden, Darrin York, and Lee Pedersen. "Particle mesh Ewald: An N· log (N) method for Ewald sums in large systems". In: *The Journal of chemical physics* 98.12 (1993), pp. 10089–10092.

[6] Berk Hess et al. "LINCS: a linear constraint solver for molecular simulations". In: *Journal of computational chemistry* 18.12 (1997), pp. 1463–1472.

[7] William Humphrey, Andrew Dalke, and Klaus Schulten. "VMD – Visual Molecular Dynamics". In: *Journal of Molecular Graphics* 14 (1996), pp. 33–38.

[8] Michal Kopytynski et al. "A Versatile Polymer-Based Platform for Intracellular Delivery of Macromolecules". In: *Advanced Therapeutics* 3.2 (2020), p. 1900169.

[9] Justin Lemkul. "From proteins to perturbed Hamiltonians: A suite of tutorials for the GROMACS-2018 molecular simulation package [article v1. 0]". In: *Living Journal of Computational Molecular Science* 1.1 (2018), p. 5068.

[10] Imperial College London. *High Performance Computing (HPC)*. `http://www.imperial.ac.uk/admin-services/ict/self-service/research-support/hpc/`. [Online; accessed October-2020].

[11] Alpeshkumar K Malde et al. "An automated force field topology builder (ATB) and repository: version 1.0". In: *Journal of chemical theory and computation* 7.12 (2011), pp. 4026–4037.

[12] MathWorks. *MATLAB Graphics*. English. Version R2020b. MathWorks. 265 pp.

[13] E. Lindahl B. Hess M.J. Abraham D. van der Spoel. *GROMACS Reference Manual*. English. Version 2018. The GROMACS Deveopment Team. 270 pp.

[14] Shuichi Nosé and ML Klein. "Constant pressure molecular dynamics for molecular systems". In: *Molecular Physics* 50.5 (1983), pp. 1055–1076.

[15] Yukari Oda et al. "Block versus random amphiphilic copolymers as antibacterial agents". In: *Biomacromolecules* 12.10 (2011), pp. 3581–3591.

[16] Yukari Oda et al. "Block versus random amphiphilic copolymers as antibacterial agents". In: *Biomacromolecules* 12.10 (2011), pp. 3581–3591.

[17] Michele Parrinello and Aneesur Rahman. "Polymorphic transitions in single crystals: A new molecular dynamics method". In: *Journal of Applied physics* 52.12 (1981), pp. 7182–7190.

[18] Sivaramakrishnan Ramadurai et al. "Dynamic studies of the interaction of a pH responsive, amphiphilic polymer with a DOPC lipid membrane". In: *Soft Matter* 13.20 (2017), pp. 3690–3700.

[19] Schrödinger, LLC. "The PyMOL Molecular Graphics System, Version 1.8". 2015.

[20] Shuzhe Wang and Fernando Bresme. "Simulation Studies on the Lipid Interaction and Conformation of Novel Drug-Delivery Pseudopeptidic Polymers". In: *The Journal of Physical Chemistry B* 121.39 (2017), pp. 9113–9125.

[21] David Weininger. "SMILES, a chemical language and information system. 1. Introduction to methodology and encoding rules". In: *Journal of chemical information and computer sciences* 28.1 (1988), pp. 31–36.

[22] Marco Werner, Jens-Uwe Sommer, and Vladimir A Baulin. "Homo-polymers with balanced hydrophobicity translocate through lipid bilayers and enhance local solvent permeability". In: *Soft Matter* 8.46 (2012), pp. 11714–11722.

[23] Semen O Yesylevskyy, Timothée Rivel, and Christophe Ramseyer. "The influence of curvature on the properties of the plasma membrane. Insights from atomistic molecular dynamics simulations". In: *Scientific reports* 7.1 (2017), pp. 1–13.

INVESTIGATION INTO THE DECOMPOSITION TECHNIQUES EMPLOYED IN OPTIMISING A CHIMERIC ANTIGEN RECEPTOR T-CELL THERAPY SUPPLY CHAIN

Mingzhe Feng & Henrico Yuwono
Department of Chemical Engineering, Imperial College London, U.K.

Abstract

The promising results of Chimeric Antigen Receptor T-Cell therapy as a treatment for B-Cell Lymphoma is spurring the development of an optimised autologous supply chain system. The combinatorial explosion which stems from the enlarged problem size and high number of binary variables calls for solving methods that would help optimise this increasingly intractable MILP problem. Decomposition is one of many approaches which could overcome said challenge by sub-dividing the major problem into smaller, less computationally demanding sub-problems. Three decomposition variants were investigated, namely: decomposed models with and without time constraints, i.e. the deadline regarding therapy turnover, as well as Lagrangian Decomposition. The removal of time constraints yielded better, faster solutions than the original problem whereas the enforcement of time constraints and Lagrangian Decomposition provided worse, slower results than the original problem. Several limitations leading to sub-optimality have been identified in the model including uneven sub-problems in terms of function, code structure and solver interpretation. This prompts further work, which is suggested to focus on functional decomposition, community structure detection and temporal decomposition.

Keywords: Chimeric Antigen Receptors T-Cell Therapy, Autologous MILP Supply Chain, Combinatorial Explosion, Decomposition, Lagrangian Decomposition.

1 Introduction

The recent emergence of Chimeric Antigen Receptor (CAR) T-Cell therapy as a promising immunotherapy treatment for B-Cell Lymphoma has raised several challenges for its mass adoption in the drug market (Papathanasiou et al. 2020). Two of which revolve around the scale-up of the supply chain model, more specifically: the autologous nature of the therapy and scheduling complexities. Firstly, the autologous nature of CAR T-Cell therapy means that every therapy is catered specifically towards each patient. Therapy starts when a tissue sample is taken from said patient, modified and returned back to the same patient. This creates an interesting supply chain model whereby the production (or modification) of the patient's tissue cells can only begin once it has reached the manufacturing facility, as this is required to be returned to the corresponding patient. In other words, this supply chain lacks the traditional stock of materials and heavily enforces the traceability of each sample, such that no sample is returned to a different patient (Nwosu 2020). This also implies that demand cannot be simply forecasted in advance as the nature of patient health is unpredictable.

Secondly, the aforementioned complexities in the supply chain are compounded by discrete scheduling decisions in the form of integer variables (Stefansson et al. 2011). This coupled with the model's long discretized time interval makes for a large optimisation problem which is computationally expensive (Floudas & Lin 2005). This is a common problem in supply chain models as they contain many binary decision variables, which are utilized for assignment, scheduling as well as other specific functions to the model itself. These decisions tend to grow combinatorially as more choices are introduced into the model. In this case, as the demand for therapies (i.e. number of patients) increase, a combinatorial explosion of decisions is observed, resulting in sub-optimal solutions and eventually an intractable problem to solve. Therefore, methods - in which the problem size can be either reduced or broken down into separate components - are necessary to reduce computational demand and improve tractability.

One method in which such difficult optimisation problems can be overcome is through decomposition. This problem-solving approach subdivides a major problem into smaller sub-problems. Computationally, this could allow large intractable problems to be broken down into less complex sub-problems and be successfully optimised either in parallel or in sequence (del Rio-Chanona et al. 2016). Multiple decomposition methods exist which could be applied to solve Mixed Integer Linear Programming (MILP) models, such as the Lagrangian Decomposition (LD) method whereby complicating variables are dualised and removed from the constraint set (Visweswaran 2009).

This then creates a separable objective function which can be split into two sub-problems, each with their own corresponding set of constraints. Thus, two smaller sub-problems have been created and would theoretically be less computationally demanding than the original complex problem. However, one drawback to be wary of in this approach is that for each set of

copy constraints introduced, one Lagrange multiplier must be added; the calculation and iteration of these multipliers could be time consuming.

1.1 Model Structure

As such, this paper modified a CAR T-Cell therapy supply chain in the form of an MILP model. The model simulated a random normal distribution of patient demand within a time period allocated to one of four random Leukapheresis Sites (LS). After one day of sample extraction, the sample was transferred to one of six Manufacturing Facilities (MF) either using a one- or two-day delivery method. The samples were then modified in the MF for seven days and afterwards checked for quality using in-house Quality Control sites (QC), which take a further seven days. As quality control was in-house, transport time and cost from MF to QC were set to 0. Finally, the modified samples were sent back to Hospitals (H), which correspond to the same leukapheresis sites from which the samples entered from, again, using one- or two-day delivery option. For example, if a sample originated from LS 4, the therapy had to be returned to H 4 and this is done to simulate the minimal travel capabilities of last-stage cancer patients. A simplified diagram of the supply chain can be seen in Figure 1.1 below.

The model decided (as binary variables) which MF to build (constrained to two), when to allocate the samples to those MF and which transport mode to choose between nodes whilst minimising cost and turnaround time (which has been constrained to the maximum 17 days). The full mathematical model can be found in Section 7.1.

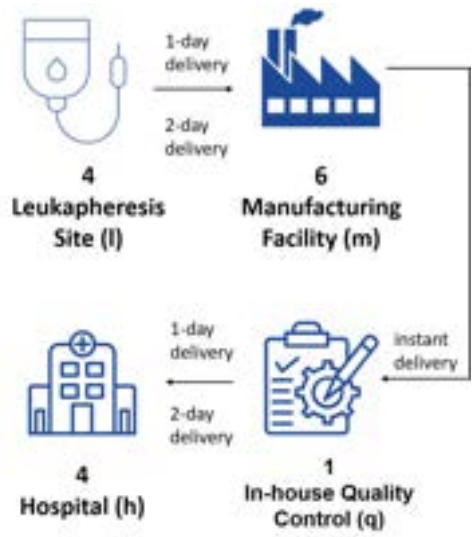

Figure 1.1: CAR T-Cell therapy supply chain diagram.

In the base case for this model, 50 patients were introduced and randomly distributed across 130 days. This resulted in 2,420,752 decision variables, of which 702,060 were binary, and 3,263,154 constraints. The introduction of one extra patient results in 14,040 additional binary variables into the supply chain, thus creating $2^{14,040}$ more combinations, further worsening the combinatorial explosion of the model and rendering it more intractable.

It is evident from the scale and nature of the problem, decomposition methods are a useful way to deal with this combinatorial explosion as well as allowing room for investigation in the scaling up of therapy demand and supply. Ultimately, this paper aims to implement a variety of decomposition methods to the CAR T-Cell therapy supply chain to minimise computational demands and allow further scale-up.

2 Decomposition Methods

The decomposition strategy implemented in this paper consisted of breaking down the supply chain spatially (Kheirabadi et al. 2019) into two separate sub-problems (upstream and downstream). Separating upstream from downstream provided 2 sub-problems of equal nodes, namely LS & MF in sub-problem 1 (SP1) and QC & H sub-problem 2 (SP2). Moreover, this gave a reasonably even distribution of mass balance constraints between the two sub-problems as shown in Figure 2.1 below. Variables INC to INH were associated with mass balances flowing into and out of each node, wherein the two sub-problems were linked by Constraint 37.

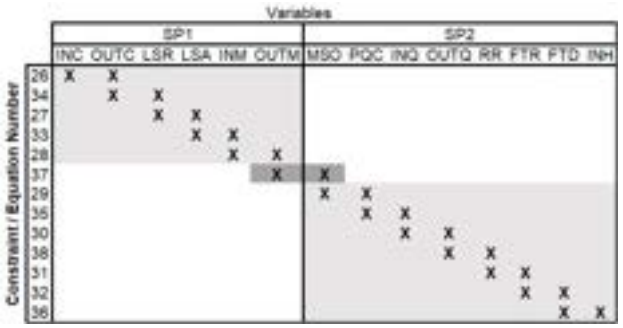

Figure 2.1: Decomposition separation matrix

SP1 focused around allocating therapies and transport costs between LS and MF as well as calculating manufacturing capacity and costs as shown in Figure 2.2 below.

$$\begin{aligned} min \quad & TOTCOST1 = \sum\nolimits_{p \in P} (TC1_p + CTM_p) \\ & TC1_p, CTM_p \in R, \quad TOTCOST1 : R \to R \end{aligned} \tag{1}$$

Where $TC1_p$ was the transport cost between LS and MF for therapy p and CTM_p was the total manufacturing cost per therapy p.

Figure 2.2: SP1 flow diagram

SP2 focused around the remainder of the supply chain which included quality control costs and transport costs between the MF to QC (in-house) to H as shown in Figure 2.3 below.

$$\begin{aligned} min \quad & TOTCOST2 = \sum\nolimits_{p \in P} (TC2_p + CQC_p) \\ & TC2_p, CQC_p \in R, \quad TOTCOST2 : R \to R \end{aligned} \tag{2}$$

Where $TC2_p$ was the transport cost between MF to QC (in-house) to H for therapy p and CQC_p was the quality control cost per therapy p.

Figure 2.3: SP2 flow diagram

Sequential decomposition was necessary in solving both sub-problems as information needed to be carried forward from SP1 to SP2. This information revolved around the outlet flow rate of therapies from MF. Otherwise, SP2 could not be properly initialised and thus there would be no flow of therapies throughout this sub-problem, resulting in a zero cost objective function. As a result, the variable OUTM (flow of therapies out of MF) was parameterised from SP1 into SP2 to allow for initialisation (Kheirabadi et al. 2019). The variables E1 (whether or not a MF is established) and Y1 (whether or not transport mode j is taken between LS and MF) were also parameterised into SP2 as these were binary variables which were a part of the conflicting constraints in the model (constraints that contain variables that appear in more than one sub-problem). These could not be iterated through the Lagrangian decomposition method due to their binary nature which resulted in a failure to converge.

This left the decomposition model with one conflicting constraint (the total return time of therapy p) as it contained STT_p, the start time of therapy p (variable from SP1) and CTT_p, the completion time of therapy p (variable from SP2).

$$\begin{aligned} CTT_p - STT_p \leq 17 \quad \forall p \\ CTT_p, STT_p \in R \end{aligned} \tag{3}$$

Three different investigations were conducted in dealing with this conflicting constraint and their performances against the original model were evaluated. Small-scale problem sizes were investigated first with the introduction of one patient into the model and thereafter increased incrementally for scale-up.

2.1 Unconstrained Time Method

For this decomposition method, all equations regarding the time constraints (Equations 94 - 97 and 124 - 126) in Sections 7.1.8 and 7.3.9 in each sub-problem were removed. The Lagrange multipliers in the objective functions were set to zero (in Equations 68 and 98) and the program ran without iteration.

2.2 Manually Constrained Time Method

In this methodology, time constraints were manually added into both sub-problems in which a dummy variable, $TIMEATOUTM_p$ was introduced into SP1. This variable recorded the time at which therapy p left the manufacturing site and the difference between $TIMEATOUTM_p$ and STT_p was constrained to a maximum of 9 days (Equations 96 and 97). Furthermore, all other time constraints in both sub-problems were active in this case. The Lagrange multiplier in both objective functions (from Equations 68 and 98) were set to zero and the program ran without iteration.

$$\begin{aligned} TIMATOUTM_p - STT_p \leq 9 \quad \forall p \\ TIMEATOUT_p, STT_p \in R \end{aligned} \tag{4}$$

A block diagram shows the flow of information between both sub-problems in Figure 2.4 below.

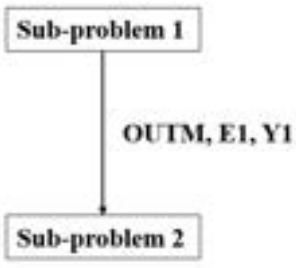

Figure 2.4: Block diagram for the flow of information in both the unconstrained time and manually constrained time case.

2.3 Lagrangian Decomposition Method

Lagrangian decomposition methods are an effective way to solve constrained optimisation problems whereby the objective functions and constraints are combined into a reformulated objective function. Considering the equality constrained problem:

$$\begin{aligned} \min_{x} \quad & F = f(x) \\ x \in R^n \quad & f : R^n \to R \end{aligned} \tag{5}$$

This can be transported into a separable problem with vector variables x_i and number of subsystems NS:

$$\min \quad F = \sum_{i=1}^{NS} f_i(x_i) \tag{6}$$

subject to:

$$h_i(x) = 0 \tag{7}$$

The Lagrangian function for the above optimisation problem is given by:

$$L = \sum_{i=1}^{NS} f_i(x_i) + \sum_{i=1}^{NS} \lambda_i^T h_i(x) \tag{8}$$

where the equality constraints are relaxed through the introduction of a Lagrange multiplier (known as Lagrangian relaxation).

In the case where strong duality holds (Boyd et al. 2004), the solution to the original optimisation problem exists on the saddle point of the Lagrangian function with respect to the Lagrange multipliers (dual variables) and original problem variables (primal variables).

$$\max_{\lambda} \min_{x} L = \min F \tag{9}$$

The solution approach consists of updating both primal and dual variables until convergence is reached such that the equality constraint is satisfied (i.e. $h_i(x) = 0$). For most non-convex problems, there exists a duality gap between the primal and dual problem, therefore a quadratic penalty term - weighted by a penalty parameter - is introduced to remove the duality gap between problems (Puerner 2018). In this case, as the optimisation problem is MILP and thus convex, the Lagrangian function provides a sufficient condition for which convergence is reached without the need to add a quadratic penalty term.

In the context of this optimisation problem, Constraint 97 underwent Lagrangian relaxation into the objective function of SP1, $\lambda_{p1}(TIMEATOUTM_p - STT_p)$ along with the deactivation of Constraint 96. For SP2, Constraints 124 and 126 were deactivated, whilst a Lagrangian term of $\lambda_{p2}(CTT_p - 17)$ was introduced into the objective function. The Lagrange multipliers here served as a penalty parameter in which it penalised the objective function for taking a longer time to return the therapy. The multipliers were continuously updated with a gradient step parameter (α) where $\lambda_{p,k+1} = \lambda_{p,k} + \alpha * h(x)$ until convergence was reached and the time constraint was satisfied. The resulting objective functions for sub-problems 1 and 2 are shown as Equations 68 and 98 respectively in Sections 7.2.7 and 7.3.8. The algorithm is as follows, as summarised in Figure 2.5:

For every patient p, while $CTT_p - STT_p > 17$:

1. Determine $TIMEATOUTM_p$ in SP1.
2. Carry forward $OUTM_p$, $E1_m$, $Y1_{p,l,m,j,t}$ as parameters into SP2.
3. Determine CTT_p in SP2.
4. Update λ_{p1} by $\lambda_{p1,k+1} = \alpha(TIMEATOUTM_p - STT_p) + \lambda_{p1,k}$.
5. Update λ_{p2} by $\lambda_{p2,k+1} = \alpha(CTT_p - 17) + \lambda_{p2,k}$.

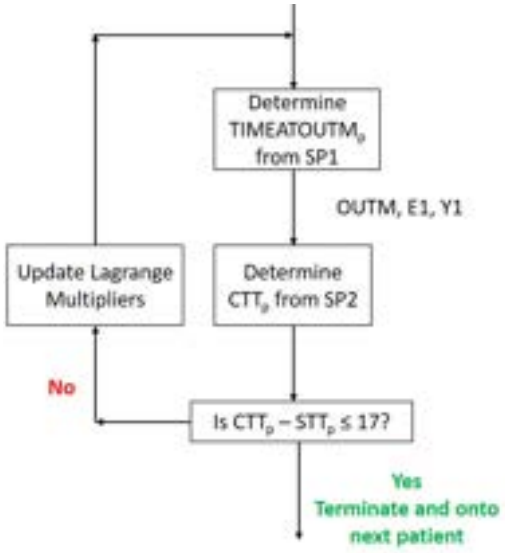

Figure 2.5: Block diagram of the Lagrangian decomposition.

This choice of decomposition algorithm was due to the need to maintain linearity in the objective function. Other decomposition algorithms such as the Augmented Lagrangian decomposition algorithm, Bertsekas' algorithm and the SALA algorithm were considered but not implemented since they introduce a squared non-linear term in the objective function (Puerner 2018). As the decomposed model could only execute properly in GLPK (discussed further below), this solver is not able to solve objective functions containing quadratic terms, and thus provides reason to have a linear Lagrangian relaxation of the time constraints mentioned above.

3 Results and Discussion

3.1 Model Validation

The original model from GAMS was transferred into Pyomo (Python) as this allowed greater flexibility in writing advanced scripts for the decomposition algorithm (Hart et al. 2011). Table 1 below compares the original problem in Pyomo with the one in GAMS, both of which ran in the Imperial College London Chemical Engineering cluster.

Table 1: Model validation

	GAMS Model	Python (Pyomo) Model
Parameters	50 Patients 4 LS 6 MF 4 QC (in-house only) 4 H 130 days	50 Patients 4 LS 6 MF 1 QC (in-house only) 4 H 130 days
Objective Function	$ 5,038,180.94	$ 5,038,179.80
Objective Function per patient	$ 100,763.62	$ 100,763.60
Solver	CPLEX	
Time taken	92.6 seconds	Solver Time: 95.1 seconds Program time: 115.0 seconds

To test the validity of the program transfer, the Pyomo model ran using identical input parameters as the GAMS model. The GAMS model used 4 QC nodes but only the in-house QC node was enabled for all manufacturing facilities to simulate in-house quality control. This is similarly done with the Pyomo model whereby only 1 QC node was set-up which simulates the same in-house quality control for all manufacturing sites. Hence, it is worth noting that this reduction in nodes would affect computational time. Ultimately, the Pyomo model yielded similar results to the original GAMS model within reasonable extent as seen in Table 1 above.

It should also be noted that the allocation of hardware in the cluster may not be exactly identical between the models. Hence, the time taken to solve them may not represent a fair comparison between both models. For reference, the two models were sent to the cluster with a symmetric multiprocessing (SMP) requirement of 8-12.

3.2 Decomposition

CPLEX, Gurobi and GLPK were initially used to solve the decomposition model, but it was discovered that both CPLEX and Gurobi considered the model infeasible. This was because after solving SP1, the values attained for OUTM were found to be non-binary with non-precise values for CPLEX and Gurobi. Thus, when OUTM was parameterised and carried forward into SP2, values for all consequent mass balances resulted in an infeasible solution. GLPK, on the other hand, was discovered to properly converge and solve both sub-problems at low patient numbers.

The non-convergence of OUTM from CPLEX and Gurobi were surprising as these are considered to be much more effective integer solvers than GLPK. However, it can be hypothesised that the structure of this decomposition strategy affected the ability for both CPLEX and Gurobi to correctly produce valid values for OUTM. All three solvers use primal/dual simplex and/or barrier interior methods when solving for any MILP via linear relaxation. This provides a lower bound to the problem and afterwards, a form of branch and bound method is applied to find a feasible solution to the problem (Mittelmann 2007). In particular, this results in the approximation of the variable OUTM for both CPLEX and Gurobi.

Moreover, OUTM did not hold very much importance in calculating the objective function value as well as having no forward linking variable in SP1, due to the cut-off point (end of SP1, beginning of SP2). Therefore, both CPLEX and Gurobi may have valued computational speed over precision in the approximation of OUTM, which resulted in non-integer values. Whereas GLPK prioritised precision, enabling it to solve SP2 feasibly.

Results from each decomposed method were compared to the original problem in terms of both program time and objective function. All instances of the model (decomposed and original versions) were run on the same personal computer using the solver GLPK. For all comparisons, the time-scale for each decomposed method and the original problem were reduced to 90 days in the interest of time.

3.2.1 Unconstrained Time Method

In the unconstrained time decomposed case, both program time and objective function were compared to the original model for up to a number of 6 patients. The program was found to be incapable of running more than 7 patients. It was suspected that the GLPK solver in SP1 ran into issues with Constraint 80, which resulted in the program not being able to find a solution at a higher number of patients.

Program Time

Figure 3.1: Program time comparison between Original and Decomposed formulation.

As shown in Figure 3.1 above, when time constraints were inactive, between patients 1 and 3, the decomposed program ran approximately the same as the original program, and with higher patient numbers it ran faster. This shows that for a very small sample size of patients (1-3), the marginal gap

in program time between the two cases is much less due to the smaller difference in the number of possible binary decisions. In increasing the patient number past 3, it is observed that the difference in number of binary decisions between the two cases allowed for a noticeable increase in computational speed for the decomposed case.

One would argue that the difference in program times between the two cases should increase when patient number increases, as the introduction of more binary decisions would result in a more effective decomposition when breaking down the problem. However this was not observed to be the case as SP1 took most of the computational stress when solving compared to SP2, evidenced in Table 2 below:

Table 2: Optimiser time (s) for the unconstrained time case.

Patient No.	Original	SP1	SP2
1	0.4	0.2	0.1
2	1.8	0.8	0.1
3	5.2	3.1	0.1
4	9.2	3.2	0.3
5	14.2	5.1	0.5
6	21.1	14.3	0.8

Table 2 shows that SP1 required most of the computational demand as it took much longer to solve than SP2. Because of this, the difference in program time between the two cases did not shrink. Note that "Optimiser time" in Table 2 is not equivalent to "Program time" in Figure 3.1; optimiser time records the time it takes for GLPK to solve each (sub-)problem, whilst program time records the time taken for the whole Python code to run, this includes reading and importing data as well as the optimiser time itself.

Objective Function

Figure 3.2: Objective function value comparison between Original and Decomposed formulation.

Furthermore, the decomposition method for the unconstrained time case showed to be very accurate in its objective function (total cost) value when compared to the original problem. A difference of 0% was observed between the two cases for all number of patients studied. This shows that the parameterisation of OUTM, E1 and Y1 into SP2 did not worsen the optimal value of total cost as both cases produced the same solution. It is suspected, however, that at higher patient numbers, a greater disparity of optimal cost would be exhibited between the two cases, with the decomposed case giving a higher objective function. This would be due to the parameterisation of variables into SP2 yielding a sub-optimal solution for the whole problem as the problem size increases.

3.2.2 Manually Constrained Time Method

The time constrained method was able to solve the model for up to 8 patients, but was unable to run 9 patients or more. Similar to Section 3.2.1, the GLPK solver encountered issues with Constraint 80 whereby SP1 could not solve at higher patient numbers. Interestingly, a substantial gap in both program time and objective function is observed when the seventh patient was introduced in the model.

Program Time

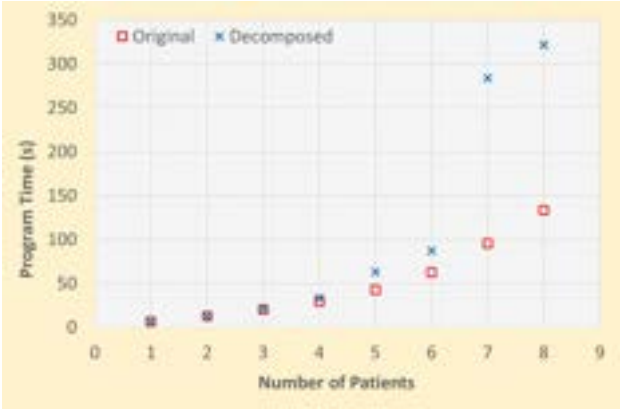

Figure 3.3: Program time comparison between original and manually constrained formulation.

In terms of program time, the decomposed model performed similar to the original problem when up to four patients were introduced. Afterwards, every patient introduced took much longer to solve (especially after the introduction of the seventh patient) under the same circumstances as shown in Figure 3.3.

While the trend of increasing problem size yielding much longer solving time is expected due to the nature of the binary variables (Stefansson et al. 2011), the immense jump from the sixth to the seventh patient, on the other hand, is surprising. The initial hypothesis of the cause could be the overcapacity of one manufacturing facility, forcing the model to build a second factory and hence compute more assignment combinations per patient. However, this possibility has been ruled out because a simple mass

balance analysis was conducted and it was found that the manufacturing facility would still be able to accommodate the seventh patient within that time period.

Instead, this result could have been caused by the instability of the model. To further elaborate, in some cases, when random patients were admitted into the model within one day of each other, this made the model unsolvable. When the difference in admission day was then increased to at least two, the model would solve as intended. This highlights the instability of the model created on Pyomo and could have been caused by a mismatch between the code structure and the solver's interpretation of the program as more details will be discussed in Section 3.3.

Table 3: Optimiser time (s) for the manually constrained time method.

Patient No.	Original	SP1	SP2
1	0.6	0.3	0
2	1.4	1.2	0.1
3	3.3	4.1	0.2
4	6.8	10.8	0.3
5	14.5	34.9	0.5
6	29.0	53.4	0.8
7	56.1	243.3	1.1
8	88.6	276.1	1.6

Upon closer inspection on the optimiser time of each sub-problem in Table 3 above, a similar pattern emerges whereby SP1 took significantly longer to solve than SP2. This provides useful insight into the original model itself, in which much of the computational demand came from the upstream section, more specifically the manufacturing facilities of the supply chain.

Objective Function

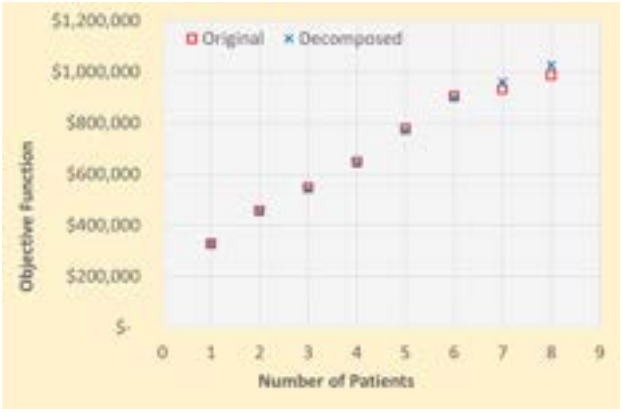

Figure 3.4: Objective function comparison between original and manually constrained formulation.

From Figure 3.4 above, it is observed that, up to the introduction of the sixth patient, the objective function values between the two programs are very similar. However, slight, yet noticeable deviations beyond patient 6 suggests that the decomposed case provided sub-optimal solutions which could be attributed to the parameterisation of binary variables OUTM, E1 and Y1 from SP1 into SP2, as previously discussed in Section 3.2.1. When problem size increases, parameterisation would be expected to yield sub-optimal solutions due to the rigidity of available choices in SP2, evidenced from patients 7 and 8.

3.2.3 Lagrangian Decomposition Method

The Lagrangian Decomposition method managed to run for up to 6 patients. A gradient step (α) value of 200 was found to be effective in allowing the algorithm to converge.

Program Time

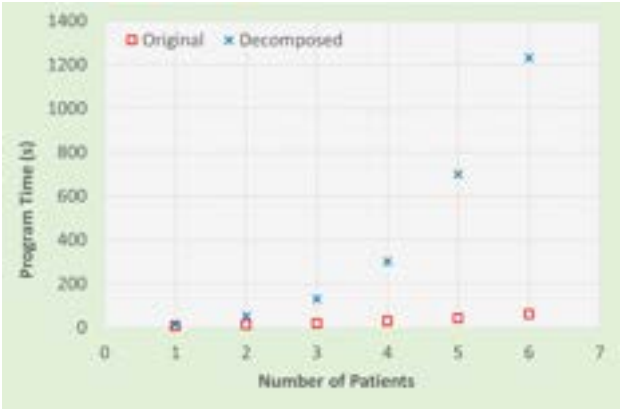

Figure 3.5: Program time comparison between original and Lagrangian Decomposition method.

As shown in Figure 3.5 above, the Lagrangian Decomposition method performs considerably worse than the original formulation. The difference in performance between the two cases grew larger as number of patients increased. This is an unsurprising result as this method required the iteration of both sub-problems until the therapy return time for each patient was no greater than 17 days. As seen from the unconstrained time method, despite the decomposed program having a faster run time than the original program, the difference between the two was not significant enough to allow for a faster run time when an iterative process (i.e. Lagrangian Decomposition) was introduced.

Table 4: Number of iterations for each patient number.

Patient No.	Total Iterations	Mean Iterations per Patient
1	2	2.0
2	6	3.0
3	6	2.0
4	12	3.0
5	15	3.0
6	17	2.8

In Table 4 it is observed that as patient number increased, total iterations within the program also increased in a proportional fashion, with the mean

number of iterations per patient being between 2 or 3. The introduction of additional patients compounded the number of iterations for the decomposed case, which explains the increasing difference of program time between that and the original case shown in Figure 3.5.

Objective Function

Figure 3.6: Objective function comparison between original and Lagrangian Decomposition method.

As seen in Figure 3.6 above, the objective function value was seen to be similar in both cases with minor deviations in the decomposed case. These deviations occurred in all patient numbers whereas for the manually constrained method, it only occurred as the number of patients were increased. Therefore, this suggests that there are inherently some inaccuracies in the Lagrangian Decomposition objective function value. One reason for this occurrence could be that the iterations themselves caused a build up of rounding errors in the final optimised value which differed slightly than the one from the original solver. These inaccuracies are small however, and do not affect the general interpretation of results.

When the program ran 6 patients, a greater deviation occurred between the decomposed and the original model in its objective function. This indicates sub-optimality for the decomposed case which was identified through the large size difference in the total cost value between the two cases. This would imply that the Lagrangian Decomposition method yielded less accurate results in the objective function for all patients and produced a sub-optimal solution sooner, with a greater optimality gap compared to the manually constrained time method. However, this cannot be said for certain as more patients need to be sampled in order to come to this conclusion with reliable confidence.

3.3 Further Discussion

Overall, it is evident that as patient number rises and time is constrained, the difference in program time and objective function between the decomposed methods and the original model widened. The main bottleneck in solving the decomposed problems have also been identified to be SP1. This could be due to the uneven decomposition of the model in terms of function. More specifically, in SP1, the solver would have to solve for scheduling, assignment, and routing problems simultaneously by choosing which MF to build, which MF to send the therapies to, and also which transport mode to choose from. On the other hand, SP2, only had to optimise routing the therapies from MF to H resulting in substantially greater computational demand in SP1 than in SP2.

Furthermore, a limitation of this decomposition strategy was highlighted whereby at several instances the model yielded local optima instead of global optima when solved using personal PCs. The global optima were identified when the model was solved using the same cluster mentioned in Section 1. For example, in the manually constrained model when 6 patients were introduced, the cluster was able to obtain an objective function 0.6% lower than personal PCs as the cluster chose to build MF 1 instead of MF 4 in the personal PC's case. This limitation is hypothesised to have originated from one structural and two technical sources.

Structurally, this limitation could have been caused by the sequencing and parameterisation of SP1 into SP2. This caused each sub-problem to be solved independently which could have resulted in sub-optimal solutions for the entire model. This is evidenced in a paper by Kinable (2014), whereby the School Bus Routing Problem was decomposed into assignment and routing sub-problems. These sub-problems were solved independently and resulted in sub-optimal solutions. This sub-optimality was mitigated by the use of heuristics but was still unable to be completely eliminated. Therefore, a different structural decomposition approach could be explored to minimise the optimality gap seen in the CAR T-Cell supply chain model.

The two hypothesised technical sources of limitations were the use of an elementary solver, GLPK, as well as a mismatch in specifications between the model generated and the solver utilised. GLPK is an open-source solver which is known to be sufficient in solving relatively smaller scale problems than the one used in this paper. However, commercial solvers such as Gurobi and CPLEX have been known to be much better at solving harder models and at a much faster pace. For instance, as benchmarked by Mittelmann (2018), GLPK could only solve 2 MILP problems, while both Gurobi and CPLEX were able to solve all 86 available MILP problems. This is compounded by the possible mismatch between the model specification and solver used as the code was generated generically in Pyomo. These two complications could be mitigated in the future by scripting the code exclusively on platforms offered by

commercial solvers, minimising the mismatch between the code structure and the solver's interpretation.

Despite the limitations above, the decomposed model serves as a good starting point for further development due to the success in solving the unconstrained time case. However, as this supply chain deals with cancer patients (with many of them being in the final stages of the disease), a few days can make a significant difference in the effectiveness of treatment.

4 Conclusions

In conclusion, this investigation has come up with several spatial decomposition methods that were able to solve the CAR T-Cell therapy supply chain optimisation at low patient numbers. These involve the removal of time constraints, manual introduction of time constraints at each sub-problem and the implementation of Lagrangian Decomposition. When time was completely unconstrained, the decomposition method successfully solved the supply chain at a faster pace than the original model whilst resulting in near identical objective function values. When time constraints were introduced into the decomposition model however, the time taken to solve said model increased whilst slight deviations from the optimal objective function were observed. This prolonged time-to-solve is further compounded when Lagrangian multipliers were introduced in the Lagrangian Decomposition method due to the iterations required to optimise the multiplier.

Ultimately, the first sub-problem was found to be the bottleneck for all these variants of decomposition. Furthermore, the performance of this paper's model could have been limited by the choice of solver as well as a mismatch between the code structure and the solver's interpretation of the program. Consequently, this only allowed the model to solve for fewer patient numbers. Hence, future work could focus on further decomposing the first sub-problem and to decompose the model temporally instead of spatially.

5 Outlook

First of all, further decomposing sub-problem 1 could help minimise the bottleneck of the model. This is because SP1 still contains scheduling, assignment, and routing problems altogether as mentioned earlier in Section 3.3. One possible method to eliminate this bottleneck is to decompose by problem function. As such has been done by Chaieb et al. (2019), whereby a home health care scheduling problem has been decomposed into assignment, grouping and routing problems each with their own dedicated solving techniques. Chaieb et al. (2019) was able to obtain better solutions than the undecomposed problem and this approach has been applied to solve a real-life problem in the Zealand Company.

As mentioned in Section 3.3, however, if the sub-problems were to be solved independently of each other, it could lead to sub-optimal solutions. Interestingly, the design of sequencing which sub-problem to solve for first could be explored, as done by Takeda & Papalambros (2012), whom utilised the coupling strengths between sub-problems and minimised the optimality gap.

Alternatively, constructing optimal sub-problems can be facilitated by the use of community structure detection as done by del Rio-Chanona et al. (2016), in which optimal partitions can either be found with minimal couplings in between or not identified altogether. However, the utilisation of this method is more ideally suited towards dense cluster groups with sparse connections between these clusters (del Rio-Chanona et al. 2016). Thus, this method can potentially be used to cluster a large group of patients who enter the model within a short time period, which is similar to the temporal decomposition discussed further below.

Another potential use of community structure detection can also be to cluster treatments geographically, which would allow for reducing transport costs as well as the time taken for each therapy treatment as seen in Figure 5.1 below. This requires each partition to be sufficiently dense enough in allowing manufacturing capacity to stay high, preventing costs from becoming too large. However it should be noted that the demand for patients is random in the CAR T-Cell supply chain and difficulties could arise in fulfilling the partition requirement.

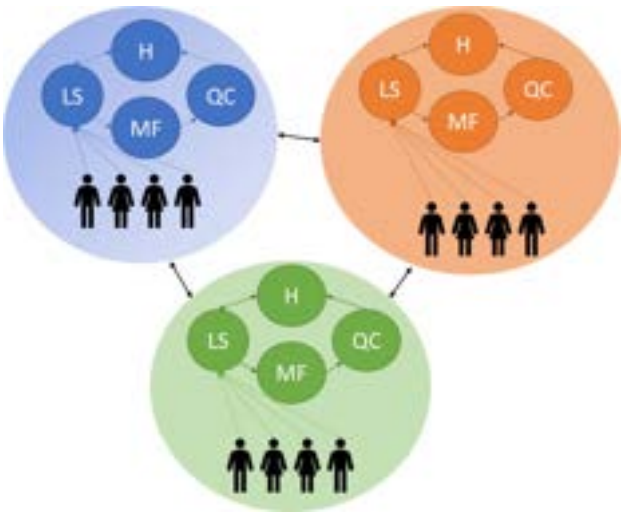

Figure 5.1: Community structure detection of geographically partitioning therapy treatments.

Finally, temporal decomposition is the

segmentation of the original problem by time periods, for example, for a 150 day time span, one can break this down into 3 sub-problems each spanning over 50 days. However, one potential complication to this method is the linking of ongoing samples between time periods. More specifically, if a patient's treatment spans over two sub-problems, this would require information to be passed from the previous time period to the next by the use of tracking constraints and some reformulations of other constraints (Sousa et al. 2011), such as the manufacturing mass balance (Equation 80). This temporal decomposition approach has proven to produce high quality solutions in some cases for Sousa et al. (2011) whilst also providing promising results when demand is uncertain - which is very applicable to the real-life scale up of the CAR T-Cell therapy supply chain.

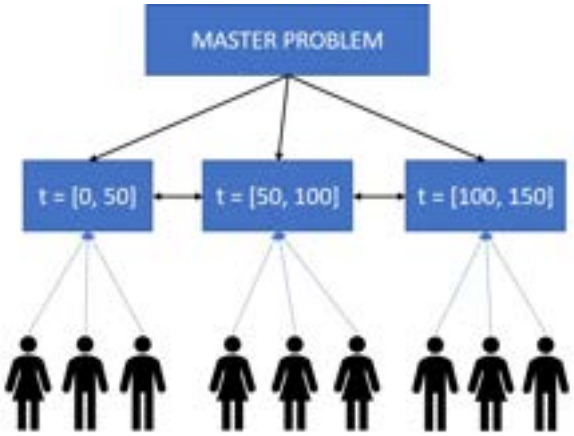

Figure 5.2: Temporal decomposition depiction showing patient allocation between different time segments.

6 Acknowledgements

First, we would like to thank our supervisors Dr. Antonio del Rio Chanona, Dr. Maria Papathanasiou and Dr. Andrea Bernadi for providing us with an extremely exciting research project and giving us deep insights into the workings of this field. We would like to especially thank Damien van de Berg for his patience in answering our questions and his contribution to the refining of our model. Also, we are very grateful to Miriam Sarkis for her wonderful support and feedback on our work.

References

Boyd, S., Boyd, S. P. & Vandenberghe, L. (2004), *Convex optimization*, Cambridge university press.

Chaieb, M., Jemai, J. & Mellouli, K. (2019), 'A decomposition - construction approach for solving the home health care scheduling problem', *Health care management science* **23**(2), 264–286.

del Rio-Chanona, E. A., Fiorelli, F. & Vassiliadis, V. S. (2016), 'Automated structure detection for distributed process optimization', *Computers & Chemical Engineering* **89**, 135–148.

Floudas, C. A. & Lin, X. (2005), 'Mixed integer linear programming in process scheduling: Modeling, algorithms, and applications', *Annals of operations research* **139**(1), 131–162.

Hart, W. E., Watson, J.-P. & Woodruff, D. L. (2011), 'Pyomo: modeling and solving mathematical programs in python', *Mathematical programming computation* **3**(3), 219–260.

Kheirabadi, M., Naderi, B., Arshadikhamseh, A. & Roshanaei, V. (2019), 'A mixed-integer program and a lagrangian-based decomposition algorithm for the supply chain network design with quantity discount and transportation modes', *Expert Systems with Applications* **137**, 504–516.

Kinable, J. (2014), 'Decomposition approaches for optimization problems'.

Mittelmann, H. D. (2007), Recent benchmarks of optimization software, *in* '22nd Euorpean Conference on Operational Research'.

Mittelmann, H. D. (2018), Latest benchmark results - informs annual conference, *in* 'INFORMS Annual Conference'.

Nwosu, C. P. (2020), 'Investigation of novel supply chain networks for chimeric antigen receptor t-cell therapy'.

Papathanasiou, M., Stamatis, C., Lakelin, M., Farid, S., Titchener-Hooker, N. & Shah, N. (2020), 'Autologous car t-cell therapies supply chain: challenges and opportunities?'.

Puerner, J. (2018), 'Decomposition methods in optimization of chemical processes'.

Sousa, R. T., Liu, S., Papageorgiou, L. G. & Shah, N. (2011), 'Global supply chain planning for pharmaceuticals', *Chemical engineering research design* **89**(11), 2396–2409.

Stefansson, H., Sigmarsdottir, S., Jensson, P. & Shah, N. (2011), 'Discrete and continuous time representations and mathematical models for large production scheduling problems: A case study from the pharmaceutical industry', *European journal of operational research* **215**(2), 383–392.

Takeda, N. & Papalambros, P. Y. (2012), 'A heuristic sequencing procedure for sequential solution of decomposed optimal design problems', *Structural and multidisciplinary optimization* **45**(1), 1–20.

Visweswaran, V. (2009), *Decomposition techniques for MILP: lagrangian relaxationDecomposition Techniques for MILP: Lagrangian Relaxation*, Springer US, Boston, MA, pp. 632–638.
URL: *https://doi.org/10.1007/978-0-387-74759-0*$_1$14

CFD modeling of immiscible liquid-liquid dispersion in a stirred vessel

Yuyi Liu[1] and Licheng Huang[1]

[1]Department of Chemical Engineering, Imperial College London, U.K.

December 2020

Abstract

In this paper we formulate a stirred tank mixing case with water and oil acting as two phases, using a pitched blade impeller. Direct Numerical Simulation is employed with hybrid front-tracking and level-set method to capture complex interfacial deformation, rupture, and droplet coalescence, as well as change in topology. With a relatively small surface tension and density difference between water and oil, the interface reaches the impeller blades with an azimuthal-symmetry shape under high Reynolds number. As the rotation rate increases, this shape is stretched thinner by the torque generated by the impeller and breaks before reaching the impeller due to Rayleigh-Plateau instability. During the mixing stage, there is a consistent trend of increasing interfacial area and decreasing lowest interface position as the rotation rate increases, which shows a sign of more efficient mixing. Additionally, an increase in vertical clearance height gives more compact vortical structure above the impeller, leading to higher local homogeneity, while an increase in horizontal clearance reduces mixing efficiency by increasing potential dead zone below the impeller.

Keywords: Stirred vessel, Mixing, Emulsification, Front-tracking, CFD, Fluids Structure Interaction, Droplet size distribution

1 Introduction

Emulsification is the process of dispersing two or more immiscible liquids together to form a semistable mixture. One or more phases are dispersed as small droplets in the other continuous phases. This liquid-liquid dispersion process is of tremendous importance to study droplet size distribution (DSD) so as to determine the mass and heat transfer rates through interfacial areas in many industrial applications whether chemical, petroleum, bio-pharmaceutical, paint or in food applications.

Given the broad range of applications, there have been numerous studies within the fluid mechanics mixing which have focused on liquids' hydrodynamic characteristics and DSD. Naeeni *et al.* [1, 2] demonstrated that an increase in agitation speed was found to decrease mean droplet diameter and increase the homogeneity of the system. A wider droplet size distribution profile was achieved at higher oil volume fractions with almost no significant change in droplet size. Increasing the viscosity of the oil phase resulted in poor mixing, with a gradual shift towards smaller droplets and narrower droplet size distribution. The shape of the droplets changed from sphere to spheroid with an increase in agitation speed. An increase in droplet deformation rate was also observed with an increase in the oil phase viscosity and a decrease in the interfacial tension between the two immiscible liquids. Zhou *et al.* [3] showed non-linear relationship between mean droplet diameter and maximum stable droplet size in a stirred tank equipped with a Rushton turbine. Uddin *et al.* [4, 5] studied liquid-liquid dispersion patterns from no dispersion area to partially dispersed and finally fully dispersed one with a '+' shaped flat blade. The transition of dispersion regimes was accelerated along with the increase in rotational speed, ratio of dispersion phase volume to continuous one, density of dispersion phase, impeller diameter, vessel diameter, and the decrease of the impeller depth.

Apart from above laboratory results, numerical simulations were applied to model dispersion patterns through computational fluid dynamics (CFD). Naeeni *et al.* [1] have performed a CFD

study, coupled with a population balance method (PBM) in order to obtain the DSD of their mixing configuration. Using an Eulerian multiphase approach and a standard $k-\epsilon$ turbulent model, their CFD results agree with experimental observations within error region. For an advanced simulation of emulsion, Heath *et al.* [6] coupled PBM with transport equations to model flocculation of high molecular weight polymers in a slurry system.

However, few of these methods actually capture the characteristics of highly deforming interfaces with complex topology changes, which is crucial to heat and mass transfer through interfacial area. Moreover, the motion of aforementioned studies is driven by a Rushton or a flat-blade turbine rather than a pitched-blade impeller, which is more widely used in industrial mixing. As a result, these studies are unable to analyse the rich and complex vortical stuctures of the mixing pattern. In this paper, liquid-liquid dispersion is studied in a stirred vessel via three-dimensional (3D) direct numerical simulations by coupling Direct-Forcing Methods for the impeller from Fadlun *et al.* [7] with a front-tracking technique for the interface from Shin *et al.* [8]. The results elucidate the transition of dispersion regimes and the dispersion patterns depending on mechanical configurations, i.e. impeller speeds, aspect ratios, which is ratio of vessel to impeller diameter, and vertical clearance heights.

The rest of this article is organised as follows. Section 2 describes the configuration, sets out the governing equations, and summarizes the computational methods. Section 3 presents results of effects of key parameters on emulsification process: the mechanisms of liquid-liquid dispersion is described, followed by analyses of interfacial area and position and droplet behaviour. Finally, Section 4 summarizes the findings and provides outlook for future studies.

2 Methodology

The mixing tank, shown in Figure 1, modeled in this study consists of a flat-bottom cylindrical tank with two different internal diameters of 8.5 cm (see Figure 1 (a)) and 12.75 cm (see Figure 1 (b)). The cylinder height was set to be 17.2 cm to ensure enough vertical travel distance for oil droplets during the mixing process. It is filled with half oil at the top and the other half water at the bottom, so the oil-water interface is set at a fixed height of 8.6 cm. A pitched blade impeller with diameter of 5 cm, height of 1 cm, thickness of 0.2 cm and blade inclined angle at $45°$ was immersed in water phase with variable vertical clearance heights, C, from its center to the tank bottom of 3.5 cm, 5 cm and 6.5 cm and rotated at different frequencies f at 10 Hz, 15 Hz and 20 Hz. The chosen frequency starts at 10 Hz due to the threshold of emulsification from Kahouadji *et al.* [9].

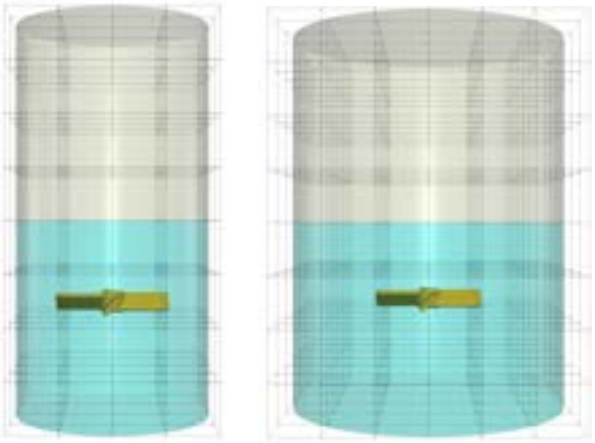

(a) (b)

Figure 1: Schematic illustration of the computational domain: a cylindrical mixing vessel with top half oil and bottom half water. A pitched-blade impeller is immersed in the water phase. The domain is of size $8.6\times8.6\times17.2$ cm^3, and divided into $4\times4\times8$ subdomains. The Cartesian structured grid per subdomain is 32^3, which gives a global structured mesh grid of $128\times128\times256$, (a); The domain is of size $12.9\times12.9\times17.2$ cm^3, and divided into $6\times6\times8$ subdomains, giving a global structured mesh grid of $192\times192\times256$, (b).

The characteristic length, velocity, and pressure scales are the impeller diameter, D_i, blade tip speed, $\pi f D_i$, and $\rho(\pi f D_i)^2$, respectively that determine the Reynolds, Froude, and Weber numbers given by:

$$Re = \frac{\rho\pi f D_i^2}{\mu} \tag{1}$$

$$Fr = \frac{\pi^2 f^2 D_i}{g} \tag{2}$$

$$We = \frac{\rho\pi^2 f^2 D_i^3}{\sigma} \tag{3}$$

Navier-Stokes equations are applied as follows, assuming incompressible and immiscible viscous fluids in a 3D Cartesian domain $\boldsymbol{x} = (x, y, z) \in [0, 8.6]^2 \times [0, 17.2]$ or $[0, 12.9]^2 \times [0, 17.2]$ cm depending on the tank diameter which is slightly greater than the tank dimensions in order to avoid calculation mistakes on boundary conditions:

$$\nabla \cdot \boldsymbol{u} = 0 \tag{4}$$

$$\rho(\frac{\partial \boldsymbol{u}}{\partial t} + \boldsymbol{u}\cdot\nabla\boldsymbol{u}) = -\nabla p + \nabla\cdot\mu(\nabla\boldsymbol{u} + \nabla\boldsymbol{u}^T) + \rho\boldsymbol{g} + \boldsymbol{F} + \boldsymbol{F_{fsi}} \quad (5)$$

where $\boldsymbol{u}$ is the fluid velocity, t the time, p the pressure, $\boldsymbol{g}$ the gravitational acceleration, $\boldsymbol{F}$ the local surface tension, and $\boldsymbol{F_{fsi}}$ the solid-fluid interaction force. $\boldsymbol{F}$ is described by the hybrid formulation from Shin *et al.* [8, 10].

$$\boldsymbol{F} = \sigma\kappa_H\nabla I \quad (6)$$

where σ, the surface tension coefficient, is assumed to be constant and I, the indicator function, is 0 in one phase and 1 in the other phase. Numerically I is resolved with a sharp but smooth transition across 3 to 4 grid cells and generated using a vector distance function computed directly from the interface geometry from Shin *et al.* [11, 12]. κ_H is twice the mean interface curvature field calculated on the Eulerian grid using:

$$\kappa_H = \frac{\boldsymbol{F}_L\cdot\boldsymbol{G}}{\sigma\boldsymbol{G}\cdot\boldsymbol{G}} \quad (7)$$

where

$$\boldsymbol{F}_L = \int_{\Gamma(t)} \sigma\kappa_f\boldsymbol{n}_f\delta_f(\boldsymbol{x}-\boldsymbol{x}_f)\,ds \quad (8)$$

$$\boldsymbol{G} = \int_{\Gamma(t)} \boldsymbol{n}_f\delta_f(\boldsymbol{x}-\boldsymbol{x}_f)\,ds \quad (9)$$

Here $\boldsymbol{x}_f$ is a parameterisation of the interface, $\Gamma(t)$, and $\delta_f(\boldsymbol{x}-\boldsymbol{x}_f)$ is a Dirac distribution that is non-zero only when $\boldsymbol{x}=\boldsymbol{x}_f$. $\boldsymbol{n}_f$ is the unit normal vector to the interface and ds is the length of the interface element. κ_f is twice the mean interface curvature calculated on the Lagrangian interface structure. The geometric information corresponding to the unit normal, $\boldsymbol{n}_f$, and length of the interface element, ds, in $\boldsymbol{G}$ are computed directly from the Lagrangian interface and then distributed onto an Eulerian grid using the discrete delta function. The details follow Peskin *et al.* [13] well-known immersed boundary approach using our procedure for calculating the force and constructing the function field $\boldsymbol{G}$.

The Lagrangian elements of the interface are advected by integrating

$$\frac{d\boldsymbol{x}_f}{dt} = \boldsymbol{V} \quad (10)$$

with a second-order Runge-Kutta method where the interface velocity, $\boldsymbol{V}$, is interpolated from the Eulerian velocity. Incorporating the complex geometry of the impeller and its rotation requires the implementation of the so-called Direct Forcing Method from Fadlun *et al.* [7], which is done by incorporating a fluid-solid interaction force $\boldsymbol{F_{fsi}}$ in Equation (5). This force is defined numerically using the latest step of the temporal integration of Equation (5).

$$\rho\frac{\boldsymbol{u}^{n+1}-\boldsymbol{u}^n}{\triangle t} = \text{local}^n + \boldsymbol{F}^n_{\boldsymbol{fsi}} \quad (11)$$

where 'local' stands for the right-hand-side terms of Equation (5) that contain the convective, pressure gradient, viscous, gravitational, and surface tension force terms. Here, the superscripts denote the discrete temporal step in the computation.

In the solid part of the domain corresponding to the impeller, $\boldsymbol{F}^n_{\boldsymbol{fsi}}$ the forced rotational motion $\boldsymbol{V}^{n+1}$ is enforced:

$$\boldsymbol{u}^{n+1} = \boldsymbol{V}^{n+1} = 2\pi f((y-y_0), -(x-x_0)) \quad (12)$$

where $(x_0, y_0) = (4.3, 4.3)$ or $(6.45, 6.45)$ depending on the tank diameter are the position of the impeller center. Hence $\boldsymbol{F_{fsi}}$ is

$$\boldsymbol{F}^n_{\boldsymbol{fsi}} = \rho\frac{\boldsymbol{V}^{n+1}-\boldsymbol{u}^n}{\triangle t} - \text{local}^n \quad (13)$$

The no-slip condition is applied for the velocity and the interface at the edge of the impeller parts where we impose a solid rotating motion and axial free-slip condition $\partial\boldsymbol{u}/\partial z = 0$. The computational domain is a rectangular parallelepiped where the entire domain is discretized by a uniform fixed 3D finite-difference mesh and has a standard staggered MAC cell arrangement from Harlow *et al.* [14]. The velocity components u, v, and w are defined on the corresponding cell faces while the scalar variables (pressure p, and the distance function ϕ) are located at the cell centers. All spatial derivatives are approximated by standard second-order centred differences. The velocity field is solved by a parallel generalized minimal residual (GMRES) method from Saad, Y. [15] and the pressure field by a modified parallel 3D Vcycle multigrid solver based on the work of Kwak *et al.* [16] and described in Shin *et al.* [8]. Parallelisation is achieved using an algebraic domain decomposition where communication across processes is handled by Message Passing Interface (MPI) protocols.

The chosen pitched-blade turbine is built using a combination of primitive geometric objects (planes, cylinders, and rectangular blocks) where each object is defined by a static distance function $\varphi(x, y, z)$, positive in the fluid and negative in the solid. The resulting shape corresponds to

the iso-value $\varphi(x, y, z) = 0$. Details on how to construct similar complex objects are described in Kahouadji *et al.* [17].

For Equation (5), (11), and (13), we use the single-field formulation for the density ρ and viscosity μ:

$$\rho(\boldsymbol{x}, t) = \rho_o + (\rho_w - \rho_o)\mathcal{H}(\boldsymbol{x}, t) \tag{14}$$

$$\mu(\boldsymbol{x}, t) = \mu_o + (\mu_w - \mu_o)\mathcal{H}(\boldsymbol{x}, t) \tag{15}$$

where the subscripts o and w designate the oil and water phases. The indicator function, $\mathcal{H}$, is essentially a numerical Heaviside function, ideally 0 in the oil phase and 1 in the water phase. $\mathcal{H}$ is resolved with a sharp but smooth transition across 3 to 4 grid cells and is generated using a vector distance function $\varphi(x)$, positive for the water phase and negative for the oil phase, and is computed directly from the interface geometry from Shin *et al.* [12]. Oil and water phases are of constant physical properties at $20°$C, as shown in Table 1.

Table 1: Fluids physical properties from Ibara, R. J. [18]

Property	Oil	Water
Density ρ (kg/m^3)	950	1000
Interfacial tension γ (mN/m)	35	
Viscosity μ (mPa $\cdot$ s)	10	1

3 Results and Discussions

3.1 Process overview

The whole process is a combination of several complex dynamics. After a period of quasi-flat free surface, the interface starts to deform and accelerates towards the impeller. Once it reaches the impeller, it is ruptured by the impeller and liquid-liquid dispersion starts. Both impeller downward pushing force and buoyancy are applied to ligaments and droplets and then, the number of droplets is large enough to initiate coalescence. We believe a kinetic equilibrium between droplets generation and coalescence will be reached eventually in this process.

The clearance is set at a relatively low profile to generate more interface deformation and increase travel distance of the interface before reaching the impeller, as shown in Figure 2 and 3.

At the first 1.5 cycles of rotation, the free surface remains quasi-flat. Although there is no baffles in the tank, little azimuthal motion at the free surface can be observed due to the interfacial stress between water and oil. As the oil phase has a viscosity ten times higher than water, shear velocity is suppressed. The flow trajectories show that a relatively stable state is maintained, with two primary vortices forming above and below each blade tip, as shown in Figure 2 (a), (b), and (c).

From $t = 1 \times T$, the vortex below the impeller starts to vanish due to a higher velocity of the vortex above the blade tip. This difference of velocity starts to create distinctive Kelvin-Helmholtz vortices at the interface of two vortices, and merge at the bottom of the tank at $t = 2 \times T$, as shown in Figure 2 (d) and (e). As these two counter rotating vortices spread, smaller secondary vortices are generated by the impeller and the interaction between vortices and between vortex and tank wall, as shown in figure 2 (f), (g) and (h). At this moment, the stable state is totally disturbed and the system stars to behave turbulently.

The free surface starts to deform significantly at $t = 4 \times T$. At this moment the velocity of water near the surface and the pressure difference between water and oil is high enough to deform it, forming an azimuthal, periodic pattern with a wave count of 4, corresponding to the number of impeller blades. As the impeller rotating, the vortices above the blades spread and rise to lift the interface around the tank wall, while the center is pulled downwards due to low pressure created by the impeller. As there is no baffle in the tank, the azimuthal speed generated by the impeller will therefore exert a torque on the free surface as it travels down. Instead of a 'reverse bell' shape, the interface deforms downwards with a helical shape with 4 rotating curtains, as shown in figure 3. This phenomenon is also observed by Kubitschek *et al.* [19] when applying big torque and downward force towards a viscous fluid: oil phase in our case.

The free surface deformation is accelerated as it approaches the impeller and reaches the impeller at $t = 6 \times T$, as shown in figure 2 (i) and (p). Now the free surface is very close to the low-pressure zone created at the blade tips and thus, gets stretched radially along the blade, as shown in Figure 2. As it travels towards the blade tips, force exerted on the surface increases dramatically and the surface is further stretched. The first rupture of the surfaces occurs around $t = 6.5 \times T$ where the blade tip cuts through the curtain, creates a shear force much larger than the surface tension between two fluids, and the first droplet

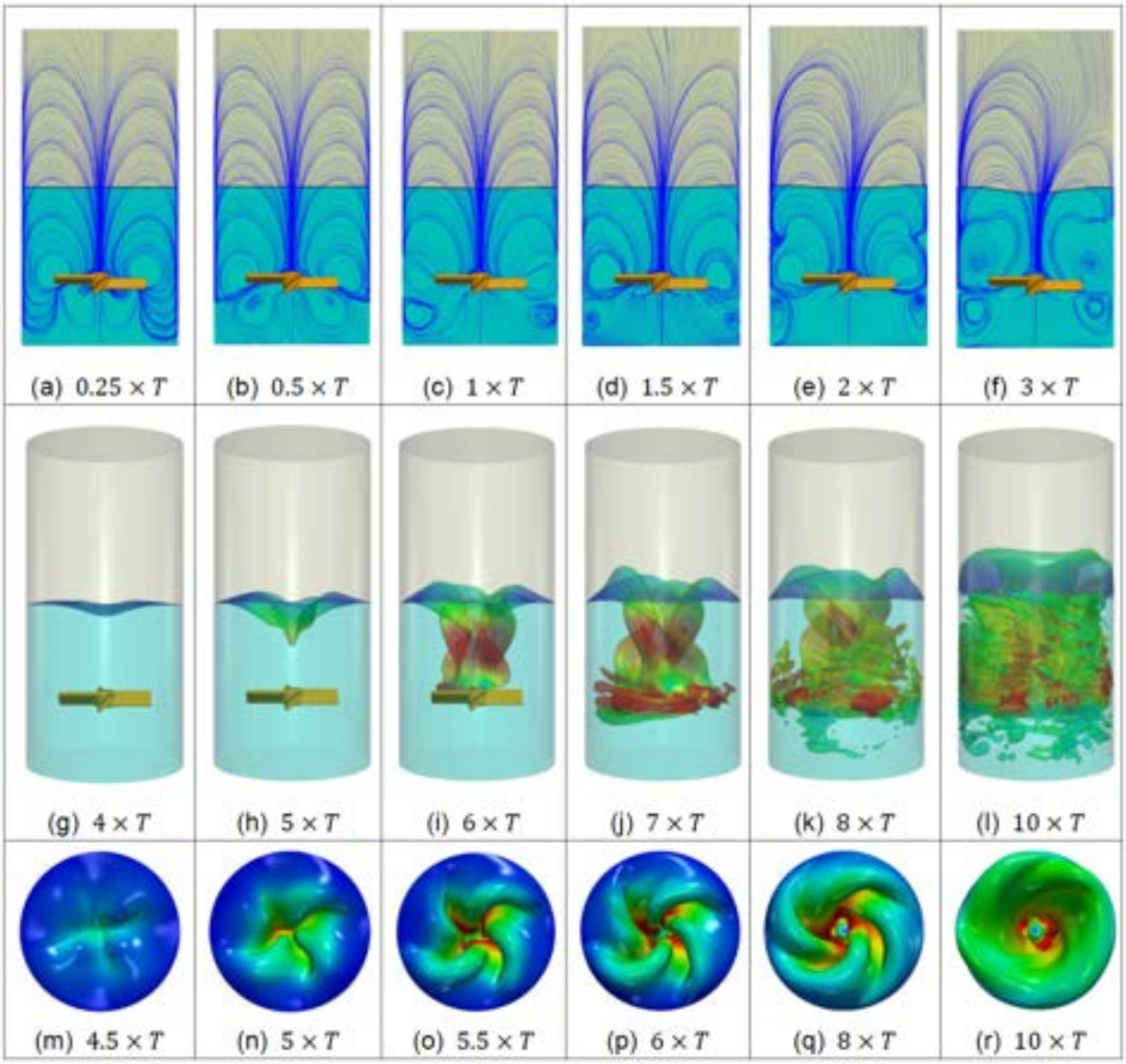

Figure 2: Spatio-temporal evolution of the flow of two phases, vortical structure, and top-view interface shapes colored with velocity magnitude. The vertical clearance is set at 3.5 cm and the impeller speed is set at 10 Hz. Dimensionless numbers are $Re = 78540$, $Fr = 5.03$, $We = 3524$.

formed is also exerted with a large radial momentum to make it a long ligament.

The long ligaments are given large radial speed by the impeller to travel towards tank wall quickly. The ligaments hit the wall right after their formation as the aspect ratio in this case is relatively low. Kinetic energy inside these ligaments is still high enough to rupture the interface as they hit the wall This causes the primal ligaments to break down, and some secondary ligaments float back to the free surface due to buoyancy and upflow is created by decomposition of impeller radial speed on the tank wall, while some of them are pushed downwards due to bottom vortex. Apart from some small droplets created by stretching of the ligaments near the impeller, most of the droplets are created when the ligaments travelling downwards have lost too much momentum to maintain the shape, and collapse into several smaller droplets due to Rayleigh-Plateau instability after $t = 8 \times T$. At this moment surface tension is greater than the shear stress around the droplet and thus, spherical and teardrop-shaped droplets are formed at the bottom quarter of the tank.

The system losses its azimuthal symmetry right after first interface rupture, and the upper faces of impeller blades are fully covered with oil after $t = 8 \times T$ as shown in Figure 2 (k) and (q). Although higher fluid viscosity leads to a larger energy requirement for powering the impeller, more ligaments will be produced at this moment. It is

noticeable that although ligament generating rate is increased, the increasing rate of overall interfacial area will still decrease gradually, as shown in Figure 4 (a), this is due to the size of the tank and more coalescence when number of droplets is increasing. We believe a steady state will eventually be reached where we have a constant interfacial area of this process. After $t = 9 \times T$ the characterizing helical shape of the free surface in the center is almost vanished, and a 'reverse bell' shape of the interface is observed, as shown in Figure 2 (l) and (r).

3.2 Free surface shape before and after reaching the impeller

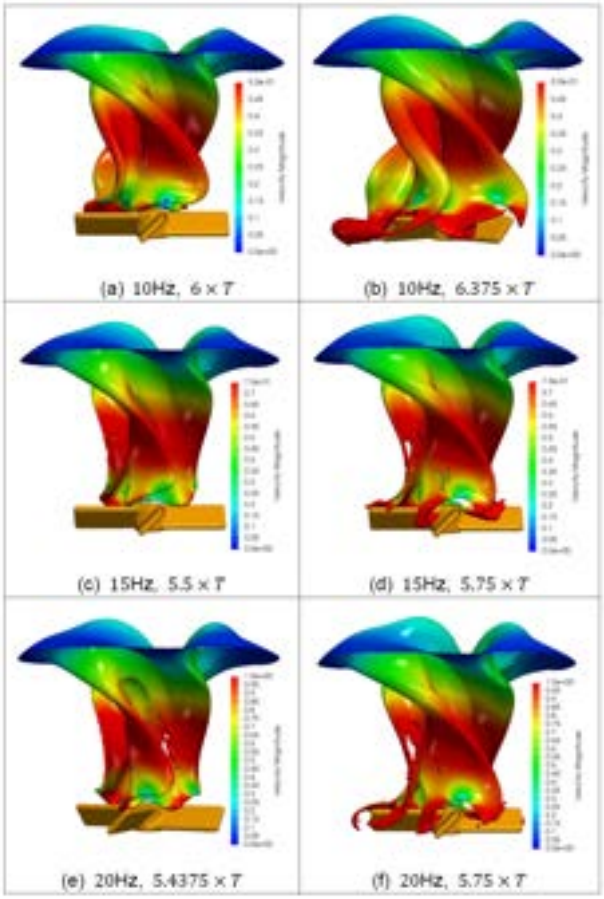

Figure 3: Shape of the free surface before/after reaching the impeller at 10 Hz, (a), (b); 15 Hz, (c), (d); 20 Hz, (e), (f). Velocity profile region is set at $[0, 0.5]$, $[0, 0.75]$, $[0, 1]$ ms^{-1}, with $(Re,\ Fr,\ We)$ = $(78540,\ 5.03,\ 3524)$, $(117810,\ 11.32,\ 7931)$, $(157800,\ 20.12,\ 14100)$ respectively.

In this section we focus on the shape of the free surface before and after reaching the impeller at different impeller speeds. Vertical clearance of the impeller is set at 3.5 cm and impeller speed is 10 Hz, 15 Hz and 20 Hz respectively. The helical shape of the free surface has a velocity profile that increase dramatically while it travels down the tank, as shown in Figure 3. Furthermore, the thickness of the curtain created by impeller rotation is highly affected by rotational speed. Higher impeller speed always refers to a higher radial and axial velocity and more turbulent system, and shear stress applied to the curtain is thus higher. This creates a thinner curtain that may break before reaching the impeller due to more turbulence and instability, as shown in Figure 3 (d), (e) and (f).

The free surface reaches the impeller with more rotations at a lower frequency due to longer time requirement, as described in Figure 3 (a), (c) and (e), thus a larger azimuthal distortion of the curtain is observed. As it deforms and stretches, the velocity profile shows a pattern of higher velocity in the middle of the deformation region and some 'low velocity spots' when the rotation curtains approach the impeller blades. This is due to blockage of the impeller blades underneath to cancel out the velocity in z direction. The rest of the curtain is further stretched by direct force from impeller blades, high pressure zone below each blade and centrifugal force. This stretches the curtain from impeller hub towards the blade tip to a limit where the curtain is eventually ruptured at the blade tip.

It is also noticeable that at higher impeller speed, pressure difference between front and back of each blade is high enough to rupture the interface before it reaching the impeller, as shown in Figure 3 (d) and (f). Difference of the time taken for the interface reaching the impeller between 15 and 20 Hz is smaller than that between 10 and 15 Hz, and this may imply that at higher impeller speed, the time taken for kinetic energy delivery and interface deformation is constrained by configurations, such as aspect ratio and vertical clearance of the impeller. This may also imply it is essential to apply higher resolution for this degree of turbulence as thinner curtains can be simulated more distinctly when mesh density is high enough to capture their characteristics.

3.3 Droplet behaviors and interface movements

In this section we study the relationship between impeller speed and interfacial area created by impeller agitation, movement of droplets (represented by lowest interfacial position in z direction) and droplet size distribution (DSD) after a period of agitation. The vertical clearance is set at a higher profile of 5 cm for the emulsification process to start earlier, and agitation speed is set

at 10 Hz, 15 Hz, and 20 Hz. Plots of these data are shown in Figure 4.

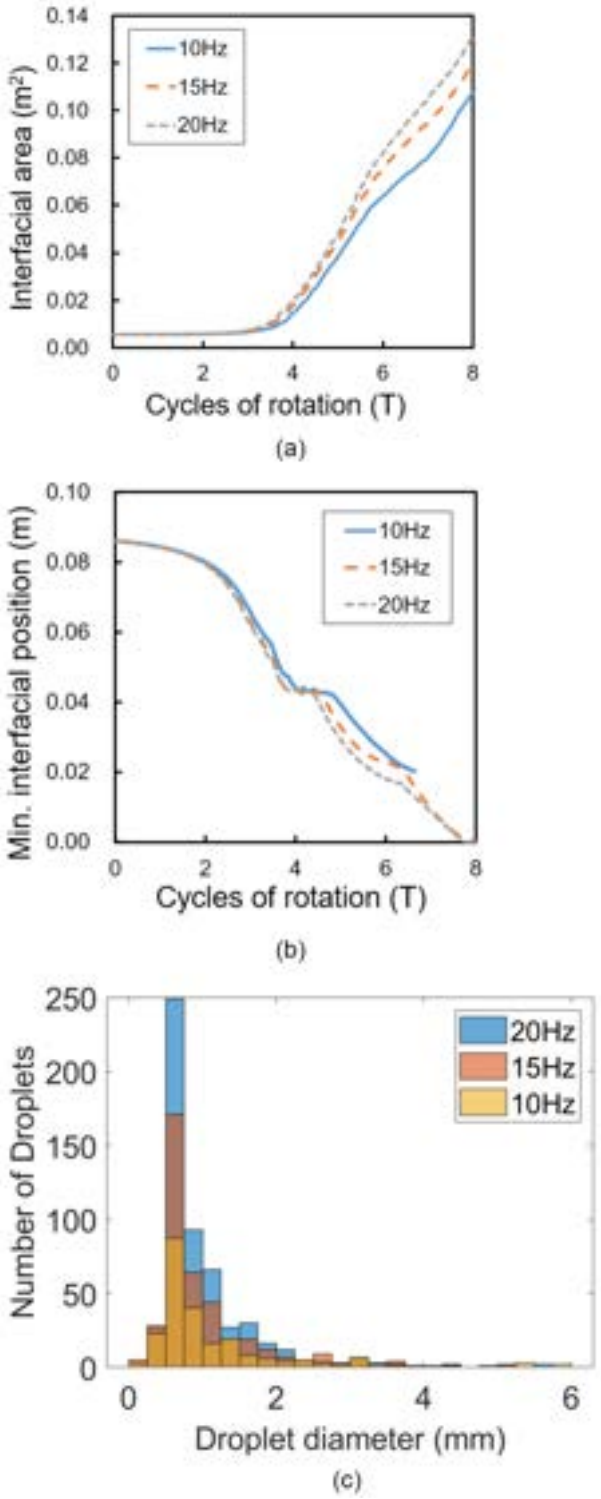

Figure 4: Droplet behaviors and interface movements: Interfacial area, (a); Lowest interfacial position, (b); Droplet size distribution(DSD), (c) at $t = 8 \times T$ at 10 Hz, 15 Hz, and 20 Hz with (Re, Fr, We) = (78540, 5.03, 3524), (117810, 11.32, 7931), (157800, 20.12, 14100) respectively.

From Figure 4(a), the interfacial area is kept at a constant value between $t = 0 \times T$ and $t = 2.5 \times T$ when the free surface is quasi-flat. A slight increase between $t = 2.5 \times T$ and $t = 3.5 \times T$ is then observed due to significant deformation of the free surface towards the impeller. Until this moment there is no droplet formed.

At $t = 3.5 \times T$ the free surface is close enough to the impeller to be further accelerated and deformed, and it reaches the impeller at $t = 4 \times T$. This is also shown in Figure 4(b) where the interface reaches the impeller and lowest interface position in z direction fluctuates due to absence of axial speed before the ligaments reach the tank wall. After $t = 4 \times T$ the ligaments and droplets are produced with absence of the coalescence due to low droplet density. As a result, the interfacial area increases dramatically between $t = 3.5 \times T$ and $t = 5.5 \times T$. Increasing rate of interfacial area starts to decrease gradually after $t = 5.5 \times T$ as rate of coalescence is increasing while the droplet density increases. In this case, we believe a steady state of interfacial area will be achieved while a dynamic equilibrium between coalescence and droplet generation is achieved.

The acceleration of the interface deformation can also be found in Figure 4(b) between $t = 0 \times T$ and $t = 4 \times T$. After the ligaments hit the tank wall, its radial velocity is redirected into a pair of opposite axial velocity due to momentum conservation. Droplets traveling downwards is further tracked and shown in this figure. Droplets which initially at the lowest position may lose momentum quickly because of size, shape, position in tank, etc. This makes it rise again due to buoyancy and no longer be the lowest one. In this case the algorithm tracks another droplet instead. This can be seen at around $t = 6.5 \times T$ where there is a small spike in the plot, showing a switch of tracing target. As there is a parasitic interface appears at the bottom of the tank by numerical error in 10Hz case at $t = 6.65 \times T$, we truncated the plot after it and removed that droplet from calculations of interfacial area and DSD.

Droplets inside the bulk are counted and measured by a python code detecting the topology of each separate interface, and their equivalent spherical diameters are calculated. A histogram is plotted in Figure 4(c) for a better view of their size distribution. At $t = 8 \times T$, we detected 242, 404 and 555 separate droplets/ligaments at impeller speed of 10 Hz, 15 Hz and 20 Hz respectively. Droplet number increases dramatically while increasing impeller speed and mean droplet size decrease slowly due to less coalescence and higher power input. The mean diameters of these droplets are 1.45 mm, 1.12 mm and 1.07 mm, with a median around 0.75 mm for all

three cases. About 35%, 42% and 45% of the droplets have a diameter close to median droplet size and this refers to a better homogeneity while increasing the impeller speed. Some of the remained ligaments have larger sizes and lie on the right of the main spike. Outliers are mainly droplets coalescing around the tank wall, forming a layer of oil inside the water phase.

These plots show a consistent trend of increase in interfacial area, decrease in lowest interface position at the same number of cycles when agitating speed increases. This is a sign of more efficient mixing. We have also observed that changing magnitude of these benchmarking variables between 10 and 15 Hz is higher than that between 15 and 20 Hz, as we described in Section 3.2. This may also implies the mixing efficiency is reaching a plateau when increasing the impeller speed. Thus, we should keep a balance between power consumption and mixing efficiency when considering industrial applications.

3.4 Varying horizontal and vertical clearance

Both horizontal and vertical clearances of the impeller may have huge impacts on vortical structure and kinetic energy distribution in the mixing tank, as well as the interface behavior. In this section horizontal clearance is studied by varying the aspect ratio of the tank and vertical clearances are studied via three different heights of the impeller from tank bottom. Impeller speed is set at 10 Hz and for constant dimensionless numbers.

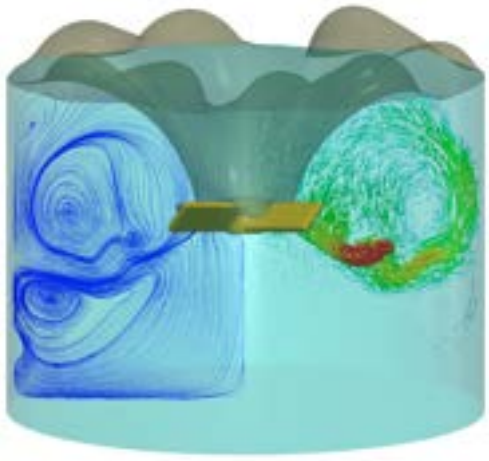

Figure 5: Moment of interface ($t = 5.375 \times T$) reaches the impeller for larger aspect ratio: $D_t/D_i = 2.55$, with (Re, Fr, We) = $(78540, 5.03, 3524)$. All velocity vectors are scaled and colored by its magnitude, with a range of [0, 0.6] ms^{-1}.

Figure 5 shows the vortical structure and velocity profile of a tank that has a larger aspect ratio, D_t/D_i. The vertical clearance is kept at 5cm for a comparison to Figure 6(b). As tank diameter increases, overall volume increases and therefore, power input per unit volume decreases. The vortex above the impeller is larger than the one with smaller aspect ratio, thus the axial velocity is lower. This explains a longer time requirement for the interface to reach the impeller. At larger aspect ratio, radial speed generated by impeller rotation may also be insufficient. This makes ligaments reaching the wall with a lower momentum, and more of them may float back to the free surface. As the bottom vortex always forms close to the tank wall, and most of the droplets flow along the streamlines, this shows a large potential dead zone below the impeller.

For three different vertical clearances, C, the time taken for the interface to reach the impeller is recorded with corresponding vortical structure and velocity field, as shown in Figure 6. As velocity produced by the impeller is mainly radial, downflow of the water only occur at the tank wall when radial velocity decomposes. It is also shown in this figure that the velocity of the upper vortex is significantly higher than the lower one, which leads to a larger portion of oil ligaments travelling back to the free surface. The size of the upper vortex depends on the impeller clearance and for a lower clearance, upper vortex is significantly larger and thus, average kinetic energy inside it is relatively low. Therefore, axial velocity generated by the vortex is lower, and this explains the difference in time taken for the interface to reach the impeller, as noted in Figure 6. For a higher clearance, as the interface reaches the impeller very quickly, the radial velocity may have limited effects on the interface and thus, degree of radial distortion of the interface is smaller, as shown in Figure 6(c).

We have also recorded the behavior of the system $3 \times T$ after the interface reaches the impeller. As shown in Figure 6 (d), (e) and (f), most of the droplets are travelling along the streamline. This shows the importance of vortical structure in the system as it may affect the mixing quality. The vortex below the impeller reaches the tank bottom at a lower clearance, and this implies less dead zone below the impeller as droplets are easier to travel towards the bottom. For a higher clearance, droplet produced may concentrate at the middle of the tank, and a smaller vortex also implies a better circulation of the oil ligaments so that they can be re-ruptured by the impeller and achieve a

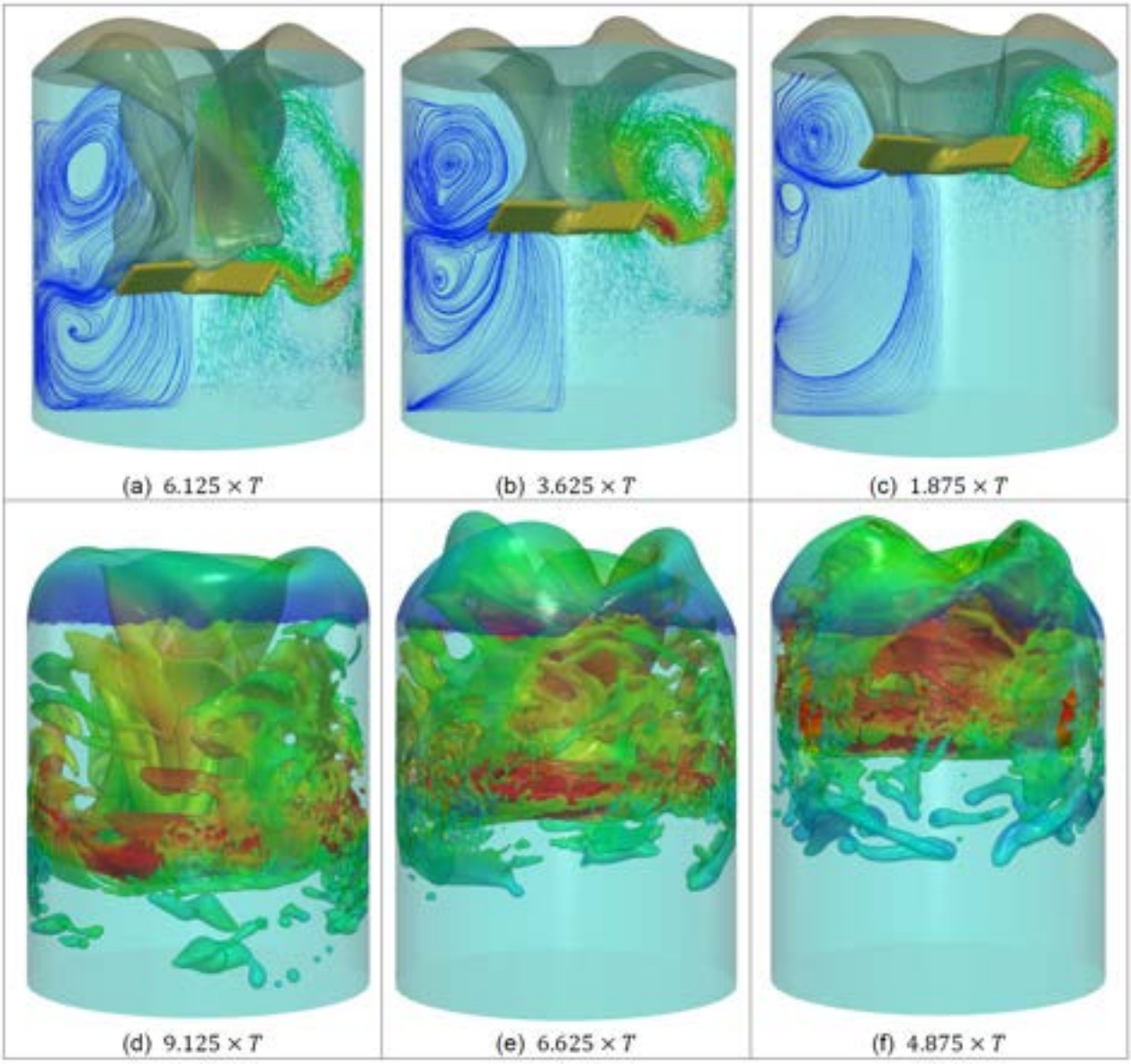

Figure 6: Moment of interface reaches the impeller and $3 \times T$ after, showing streamlines, velocity vector and pressure profile for: $C = 3.5$ cm, (a), (d); $C = 5.0$ cm, (b), (e); and $C = 6.5$ cm, (c), (f), with (Re, Fr, We) = (78540, 5.03, 3524). All velocity vectors and interface are scaled and colored by velocity magnitude, with a range of [0, 0.6] ms^{-1}.

higher homogeneity locally.

It is also noticeable that in all cases we studied, oil only covers the upper surface of the impeller, this means axial velocity produced by the impeller may not be applied to the droplets and thus, most of the droplets are moving radially after detaching from the impeller.

4 Conclusion and perspectives

This paper studies numerically the complex dynamics of liquid-liquid mixing using a pitched blade impeller and investigates on key parameters that affect mixing pattern. We have shown the vortical structure at different stages of the emulsification process and studied droplet behavior as they travel along these streamlines. We discover a helical-shaped interface distortion which is also found in Kubitschek *et al.* [19], and the thickness of these helical curtains increases as impeller speed decreases. We have also found an increase in interfacial area and droplet count at the same number of cycles as impeller speed increases, showing a better homogeneity of the system. Vertical and horizontal clearances also play key roles in efficient mixing as they affect vortical structure, local homogeneity and energy input per unit volume significantly. Therefore, for an emulsification process, a smaller aspect ratio is recommended while vertical clearance depends on the position of discharge. It is observed that changing magnitude of these benchmarking vari-

ables between 10 and 15 Hz is higher than that between 15 and 20 Hz. This implies the mixing efficiency is reaching a plateau when increasing the impeller speed. During the simulation we discover an insufficiency in mesh density after interface reaches the impeller. This could also be an explanation of the above observation as it is hard to have a correct prediction of turbulence under this mesh density. Future studies may focus on simulations with higher mesh density for better interface prediction. Variation of viscosity ratio, density ratio, surface tension and switching to Non-Newtonian fluid between two phases may also be studied to reach a generalized relationship of these parameters towards efficient emulsification. Furthermore, different types of impeller may also be studied for both axial and radial flow patterns and implement of baffles shall be considered as well.

Acknowledgements

We gratefully acknowledge the technical support from Dr. Lyes Kahouadji and Prof. Omar K. Matar for numerical simulation discussions. The numerical simulations were performed with code BLUE from Shin *et al.* [8] and run using the high-performance computing resources provided by the Research Computing Service (RCS) of Imperial College London and visualisations have been generated by Paraview.

References

[1] Naeeni SK, Pakzad L. Droplet size distribution and mixing hydrodynamics in a liquid–liquid stirred tank by CFD modeling. International Journal of Multiphase Flow 120. 2019.

[2] Naeeni SK, Pakzad L. Experimental and numerical investigation on mixing of dilute oil in water dispersions in a stirred tank. Chemical Engineering Research Design. 2019:493–509.

[3] Zhou G, Kresta SM. Correlation of mean drop size and minimum drop size with the turbulence energy dissipation and the flow in an agitated tank. Chem Eng Sci 53. 1998:2063–2079.

[4] Horiuchi S, Uddin MA, Kato Y, Kikuchi N. Liquid/liquid Mixing Pattern in a Mechanically-stirred Vessel. ISIJ International. 2014:82–86.

[5] Tanaka R, Uddin MA, Kato Y. Flow Characteristics Related to Liquid/liquid Mixing Pattern in an Impeller-stirred Vessel. ISIJ International. 2018:620–626.

[6] Heath AR, Koh PT. Combined population balance and CFD modelling of particle and aggregation by polymeric flocculant. Third International Conference on CFD in the Minerals and Process Industries CSIRO Melbourne, Australia. 2003:339–344.

[7] Fadlun EA, Verzicco R, Orlandi P, Mohd-Yusof J. Combined immersed-boundary finite-difference methods for three-dimensional complex flow simulations. Journal of Computational Physics 161. 2000:35–60.

[8] Shin S, Chergui J, Juric D. A solver for massively parallel direct numerical simulation of three-dimensional multiphase flows. Journal of Mechanical Science and Technology 31 (4). 2017:1739–1751.

[9] Kahouadji L, Batchvarov A, Amores CRC, Shin S, Chergui J, Juric D, et al. The transition to aeration in two-phase mixing in stirred vessels. 2020. Available from: `arxiv.org/abs/2011.08689`.

[10] Shin S, Chergui J, Juric D, Kahouadji L, Matar O, Craster RV. A hybrid interface tracking - level set technique for multiphase flow with soluble surfactant. J Comp Phys 359. 2018:409–435.

[11] Shin S. Computation of the curvature field in numerical simulation of multiphase flow. J Comp Phys 222. 2007:872–878.

[12] Shin S, Chergui J. A hybrid interface method for three-dimensional multiphase flows based on front tracking and level set techniques. Int J Numer Meth Fluids 60. 2009:753–778.

[13] Peskin CS. Numerical analysis of blood flow in the heart. J Comp Phys 25. 1977:220–252.

[14] Harlow FH, Welch JE. Numerical calculation of time dependent viscous incompressible flow of fluid with free surface. Phys Fluids 8. 1965:2182–2189.

[15] Saad Y. Iterative Methods for Sparse Linear Systems. 2nd Edition, Society for Industrial and Applied Mathematics. 2003.

[16] Kwak DY, Lee JS. Multigrid algorithm for the cell-centered finite difference method ii: Discontinuous coefficient case. Wiley InterScience. 2004. Available from: `www.interscience.com`.

[17] Kahouadji L, Nowak E, Kovalchuk N, Shin S, Chergui J, Juric D, et al. Simulation of immiscible liquid-liquid flows in complex microchannel geometries using a front-tracking scheme. Microfluidics and Nanofluidics 22, 126. 2018.

[18] Ibara RJ. Horizontal and low-inclination oil-water flow investigations using laser-based diagnostic techniques. Imperial College London, PhD Thesis. 2017.

[19] Kubitschek JP, Weidman PD. Helical instability of a rotating viscous liquid jet. Department of Mechanical Engineering, University of Colorado, Boulder, Colorado 80309-0427, USA. 2007.

COMPARATIVE ASSESSMENT OF POLYNOMIAL OPTIMISATION SOLVERS

Maxim Boghii and Janusshan Sivanesakanthan
Department of Chemical Engineering, Imperial College London, U.K.

Polynomial optimisation problems (POPs) are often encountered in many chemical engineering areas such as pooling and blending, multiproduct plant scheduling and wastewater treatment. Current state-of-the-art solvers frequently fail to find global optima for many instances, causing potential losses due to local solutions being implemented. Recently, a new technique was introduced which reformulates POPs as Quadratically Constrained Quadratic Problems before using GUROBI to find the global optimum of the resulting problem. This paper analyses and compares the effectiveness of this reformulation approach with other novel polynomial optimisation algorithms, mainly RAPOSa, suggesting improvements to it. The performance is tested on 59 instances of POPs from the MINLP and DS-TS Libraries. The Reformulation approach demonstrates very good performance when solving problems from the MINLP Library, especially pooling and wastewater treatment instances, some of which were previously unsolved. At the same time, it fails to solve several problems from the DS-TS library which include many high-order multilinear terms. Several areas for improvement were suggested including the development of new monomial decomposition techniques and pre-processing strategies. However, the reformulation approach shows promising results and could potentially be integrated within current state-of-the-art solvers to tackle specific instances of POPs.

1. INTRODUCTION

Computational optimisation is a convenient and effective method used in industriy to achieve solutions during the decision-making process. The chemical engineering industry often uses optimisation to enhance equipment and systems. Due to the nature of these problems, they are often formulated as multivariate polynomial programs with polynomial constraints. Generally, these programs are constructed to maximise either yield or profit whilst adhering to constraints such as design equations and process restrictions. Examples include pooling and blending process, water treatment networks and power distribution networks. As a wide range of industries work with nonlinear problems, considerable efforts and resources have been put into ensuring global optimality is reached.

Multivariate polynomial programs are a type of mixed-integer nonlinear program (MINLP) which are represented as (Linderoth & Luedtke, 2016):

$$\min \quad f(\mathbf{x},\mathbf{y}) \tag{1.1}$$

$$\begin{aligned} \text{s.t.} \quad & g_r(\mathbf{x},\mathbf{y}) \le 0, && r = 1,\ldots,R_i \\ & h_r(\mathbf{x},\mathbf{y}) = 0, && r = R_{i+1},\ldots,R \\ & L_i \le x_i \le U_i, && i = 1,\ldots,n \\ & L_j \le y_j \le U_j, && j = 1,\ldots,m \end{aligned}$$

The function f represents the objective function which is a function of continuous variables x_i and integer variables y_i, which are components of the vectors **x** and **y.** The objective function is subject to inequality constraints represented by the functions g_r and equality constraints represented by the functions h_r. The problem is also constrained by the variable bounds present on x_i and y_i. The problem can be considered a polynomial optimisation programme (POP) when the function f, g and h are polynomials of the following form:

$$c_1 a_1(x,y) + \ldots + c_k a_k(x,y) ; \quad c_k \in \mathbb{R},\ k=1,\ldots,K \tag{1.2}$$

$$a_k(x,y) = x_1^{d1,j}\ldots x_n^{dn,j}\ \ y_1^{d1,j}\ldots y_n^{dn,j} ; \quad d_j \in \mathbb{Z}^+ \ \forall\ n,k \tag{1.3}$$

Chemical Engineering problems are often nonlinear in nature with many local minima. Inefficient optimisation could lead to a global solution not being found therefore local optima being used in designs and processes (Karia, 2020). This could also result in significant losses in yields and profits. Therefore, it is critical to develop global solvers that are both efficient and widely applicable.

Algorithms for global optimisation can be grouped into 4 different groups:

1. **Incomplete methods:** Algorithm attempts to find global solutions using search methods; however, there is no guarantee that one will be found.
2. **Asymptotically complete methods:** This method finds local optima at distributed starting points; the method will

find a global solution if given infinite time.

3. **Complete methods:** Tolerances must be set for these algorithms which are then used to find a guaranteed global solution in limited time.
4. **Rigorous methods:** Very similar to a complete method however there is error control.

(Adjiman , 2020)

Global solutions are difficult to find especially for polynomial problems which can be incredibly complex. A possible solution is to reformulate the problem as a quadratically constrained quadratic program (QCQP). QCQPs are a subset of MINLPs, with objective and constraint functions that are quadratic with continuous and discrete variables. T.Karia, C.Adjiman and B.Chachaut have developed a technique to reformulate POPs as QCQPs to be solved with commercial solvers. In this paper, we aim to analyse and compare the effectiveness of this POP to QCQP reformulation against other novel polynomial optimisation algorithms, suggesting areas for further improvement.

This paper is structured as follows: Chapter 2 provides information on global optimisation algorithms and POP to QCQP reformulation. Chapter 3 describes the methodology employed to solve and analyse all POPs considered in this paper. Chapter 4 provides detailed analysis on the effectiveness of the solvers considered and compares its performances. Chapter 5 concludes the research done in the paper and gives an outlook for further research to be done in this area.

2. BACKGROUND

2.1 Spatial branch-and-bound algorithms

The spatial branch-and-bound(sBB) technique is at the root of all the current state-of-the-art global optimality solvers. It uses the principle of 'divide and conquer' to partition the feasible region into smaller parts, finding the optimum solution in those until the global optimum of the original problem is determined. The following steps are common in most sBB algorithms (Belotti, et al., 2013):

- Obtaining an upper bound (UB) of the global optimum by finding a feasible solution to the optimisation problem (usually a local minimum).
- Building a convex relaxation for the optimisation problem and solving it to obtain a lower bound (LB) to the global optimum.
- Partitioning the feasible set into smaller parts.
- Repeating the steps above for the smaller parts
- Accelerating the convergence of the problem by employing various domain reduction strategies or pre-processing techniques.

The procedure described above allows sBB algorithms to find a global solution to the optimisation problem within specified tolerances and within finite time. The diagram below is an example of a branch-and-bound tree.

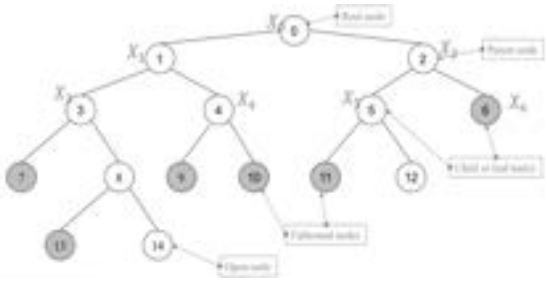

Figure 1. Branch-and-bound tree with the labels showing different parts of the tree (Adjiman , 2020)

The branch-and-bound tree is made of nodes which are either fathomed or incumbent nodes. A fathomed node is one that does not have to be branched further; this could be due to a node being infeasible or the node having a feasible solution worse than the current incumbent. The incumbent node represents the current best objective value; however, this node can be fathomed as it could represent a value that is feasible for the relaxed problem and not the actual problem.

For a minimisation problem the objective value of the incumbent node is known as the upper bound. During the branch and bound a valid lower bound is also found for the problem, once the gap between the upper and lower bound is equal to or less than the set tolerance the problem has been solved (GUROBI, 2020).

2.1.1 Advances to branch-and-bound

In the field of optimisation there have been many advances to the branch-and-bound process. The most significant of these advances are presolves and parallelism (GUROBI, 2020)

Presolve is a set of problem reductions that are usually started before the branch-and-bound process. This method decreases the size and complexity of the problem to obtain a start point for the branch-and-bound problem. This considerably decreases the CPU time of the problem as it very similar to warm-start optimisation.

Figure 2. Branch-and-bound tree with the labels showing different parts of the tree (GUROBI, 2020).

Parallelism is a method used by many commercial solvers which allows simultaneous processing of nodes. As each active node can be processed individually, multiple nodes can be kept active to be processed. However, this method is only applicable when past the root node and is only effective after a few branches down the tree.

2.2 MIPOP to QCQP Reformulation (POP2QCQP)

A novel approach to tackle MIPOPs has been recently proposed (Karia, 2020) which takes advantage of the superior performance of GUROBI when solving QCQPs (Mittelman, 2020). A quadratisation approach is used to reformulate MIPOPs as QCQPs and the performance and efficiency advantage of GUROBI over other state-of-the-art solvers is exploited to obtain solutions to the original problems. This method of solving MIPOPs demonstrated better performance than BARON, ANTIGONE and SCIP on a test set containing problems from MINLPLib and randomly generated MIPOPs. Additionally, it solved several unsolved instances from MINLPLib (Karia, 2020). To illustrate this, the following type of MIPOPs is considered:

$$\min \quad f(\boldsymbol{x},\boldsymbol{y}) \qquad (2.2.1)$$

$$\text{s.t.} \quad g_r(\boldsymbol{x},\boldsymbol{y}) \le 0, \quad r=1,\dots,R_i$$
$$h_r(\boldsymbol{x},\boldsymbol{y}) = 0 \quad r=R_{i+1},\dots,R$$
$$\boldsymbol{x} \in [\boldsymbol{x}^L, \boldsymbol{x}^U] \subset \mathbb{R}^{nx}$$
$$\boldsymbol{y} \in \{\boldsymbol{y}^L, \dots, \boldsymbol{y}^U\} \subset \mathbb{Z}^{ny}$$

where $\boldsymbol{x}$ and $\boldsymbol{y}$ represent the continuous and integer variables respectively, while $f(\boldsymbol{x},\boldsymbol{y})$, $g(\boldsymbol{x},\boldsymbol{y})$ and $h(\boldsymbol{x},\boldsymbol{y})$ are all polynomial functions.

The reformulation algorithm is based on the idea that any polynomial term can be transformed into a quadratic term by introducing additional variables. This is done by creating a list $\mathbb{B}$ containing all the monomials of $\boldsymbol{x}$ and $\boldsymbol{y}$ with the following properties (Rumschinski, et al., 2010):

- For every monomial q in the objective function and constraints equations, there exists $b_1, b_2 \in \mathbb{B}$ such that $q = b_1 b_2$
- For every monomial $q \in \mathbb{B}$ of degree >1, there exists $b_1, b_2 \in \mathbb{B}$ such that $q = b_1 b_2$
- $1 \in \mathbb{B}$

Therefore, from (2.2.1) the functions $f(\boldsymbol{x},\boldsymbol{y})$, $g_r(\boldsymbol{x},\boldsymbol{y})$ and $h_r(\boldsymbol{x},\boldsymbol{y})$ could be written in the form:

$$g_r(\boldsymbol{x},\boldsymbol{y}) = \xi^T \boldsymbol{Q}_r \xi \,, \; r = 0,\dots,R$$

Where the vector ξ represents all the monomials in set $\mathbb{B}$, while $\boldsymbol{Q}_r$ are suitable symmetric matrices to be determined during the reformulation step. Additionally, constraints need to be added to represent high-order monomials in terms of lower-order monomials. This is done by adding the following equality:

$$\xi^T \boldsymbol{R}_j \xi = 0, \; j = 0,\dots,n_d$$

Where $\boldsymbol{R}_j$ are suitable symmetric matrices while n_d represents the number of such decompositions. Finally, the bounds on variables in ξ should be specified in another constraint as: $\mathbf{A}\xi \le 0$ where $\mathbf{A}$ is a suitable real matrix.

Overall, the reformulation of (2.2.1) has the following form:

$$\min \quad \xi^T \boldsymbol{Q}_0 \xi \qquad (2.2.2)$$

$$\text{s.t.} \quad \xi^T \boldsymbol{Q}_r \xi <= 0, \; r = 0,\dots,R_i$$
$$\xi^T \boldsymbol{Q}_r \xi = 0, \quad r = R_{i+1},\dots,R$$
$$\xi^T \boldsymbol{R}_j \xi = 0, \quad j = 0,\dots,n_d$$
$$\mathbf{A}\xi \le 0, \qquad \xi_1 = 1$$

2.3 Reformulation – Linearisation Technique (RLT)

As it can be deduced from the name, this method consists of two parts, Reformulation and Linearisation, and it was initially formulated to solver bilinear problems, however later

adapted for polynomial problems (Sherali & Tuncbilek, 1992) of the following form:

$$\min \quad f(\boldsymbol{x}) \qquad (2.3.1)$$

$$\text{s.t.} \quad g_r(\boldsymbol{x}) \le 0, \quad r=1,\ldots,R_i$$
$$h_r(\boldsymbol{x}) = 0 \quad r=R_{i+1},\ldots,R$$
$$L_i \le x_i \le U_i \quad i=1,\ldots,n$$

Where $f(\boldsymbol{x})$, $gr(\boldsymbol{x})$ and $hr(\boldsymbol{x})$ are polynomials of degree $j \in I$.

The reformulation part involves generating bound factor inequality constraints and combining them with the original constraints to obtain a reformulation of the original problem. These are of the form:

$$x_i - L_i \ge 0 \text{ , } i=1,2,\ldots,n \qquad (2.3.2a)$$
$$U_i - x_i \ge 0 \text{ , } i=1,2,\ldots,n \qquad (2.3.2b)$$

The linearisation part consists of introducing the RLT variables $X_{j,k},\ldots$ to substitute the nonlinear terms. In this case:

$$X_{j,k},\ldots = x_i * x_j * \ldots, \; 1 \le j \le k \le n \qquad (2.3.3)$$

The RLT algorithm firstly obtains a linear relaxation of (2.3.1) by substituting all nonlinear variables using RLT variables (2.3.3) and constraints in (2.3.2) are appended to make the linear relaxation tighter. At this stage, constraints (2.3.3) are not added to the problem so we can solve the reformulation to obtain a lower bound for (2.3.1). If this solution also satisfies (2.3.3), then it is feasible to (2.3.1). This principle is used in a branch-and-bound algorithm which exploits the violations of (2.3.3) to converge to a global solution.

However, one significant drawback is the remarkable increase in problem size. To overcome this, several techniques are used such as: J-Sets (Dalkiran & Sherali, 2013), Semidefinite Programming (SDP) (Sherali, et al., 2012a), Reduced RLT and NLP Solvers (Sherali, et al., 2012b), reducing the size of the problems. Furthermore, RLT-POS, a global optimisation solver was designed specifically for polynomial optimisation problems, which incorporated some of these techniques (Dalkiran & Sherali, 2016). Its performance was compared with several state-of-the-art solvers such as BARON, COUENNE or SparsePOP and it demonstrated better performance for some of problems from the randomly generated test set.

Very recently, Reformulation Algorithm for Polynomial Optimisation – Santiago (RAPOSa) was developed (Gonzalez-Rodriguez, et al., 2020), which is also based on RLT and includes some of the improvements mentioned above. The main advantage of RAPOSa is the use of a local NLP solver at some of the nodes of the branch and bound tree to decrease the upper bound faster. Its performance has also been tested on randomly generated polynomial problems and MINLP Lib instances, showing better results than state-of-the-art solvers in some cases. However, both RLT-POS and RAPOSa can only solve problems with continuous variables.

2.4 Other methods

Several other algorithms have been developed to solve MIPOPs, these are briefly presented below:

An Adaptive, Multivariate partitioning algorithm was developed (Nagarajan, et al., 2019) which is based on the idea of piecewise polyhedral relaxation. This involves partitioning the domain in the most promising regions and constructing a series of sub-envelopes. Additionally, domain reduction strategies are implemented as part of pre-processing. These include piecewise relaxation and sequential bound-tightening techniques. This algorithm was tested on several Pooling and Blending problems from the MINLPLib and demonstrated better performance than state-of-the-art solvers on some instances. It also managed to reach global optimum and reduce the bound gaps for previously unsolved problems.

The Bernstein polynomial approach (Patil, et al., 2012) was used to develop a sBB-type MIPOP solver. This method reformulates a multivariate polynomial as a Bernstein polynomial, resulting in an easier problem that can be solved in a branch-and-bound algorithm. A Bernstein polynomial is defined as follows:

$$B_n(x) = \sum_{\nu=0}^{n} \beta_\nu b_{\nu,n}(x)$$

where:

$$b_{\nu,n}(x) = \binom{n}{\nu} x^\nu (1-x)^{n-\nu}, \quad \nu = 0,\ldots,n,$$

Several enhancements were added to the original Bernstein global optimization algorithm (Patil & Nataraj, 2014) such as a modified subdivision procedure, a vectorized Bernstein cut-off test and a new branching rule for the de-

cision variables. The performance of the resulting algorithm was reported to be better than several state-of-the-art solvers on a set of 19 test problems.

Finally, Monomial-wise optimal separable underestimators were proposed to solve polynomial optimisation problems (Buchheim & D'Ambrosio, 2017). Instead of the usual convex relaxations in the branch and bound algorithm, this used separable underestimators of the polynomial objective functions to compute lower bounds of the optimum solution, increasing the rate at which the sBB tree converges and increasing the robustness of the algorithm, especially with dense problems. However, this approach is only applicable to box-constrained MIPOPs. The algorithm outperformed standard global optimisation solvers while performing better in the case of dense polynomial objective functions.

Although these methods show very promising results, they have not yet been implemented in any openly available software, therefore a more detailed and thorough analysis was not possible and is beyond the scope of this paper.

3. METHODS

3.1 Implementation

This paper applies the QCQP reformulation to a set of problems which are then solved using GUROBI's MIP solver. GUROBI's MIP solver requires a programme with quadratic constraints in the form of a .lp file. To acquire the QCQP Reformulation, the approach built by Tanuj Karia and Dr Benoît Chachuat was employed. This approach referenced in (Karia, 2020) uses Python v3.7 and a MC++ framework to convert a POP problem in a .gms format to a QCQP in .lp format. The process of file conversion can be shown by the figure below (Karia, 2020):

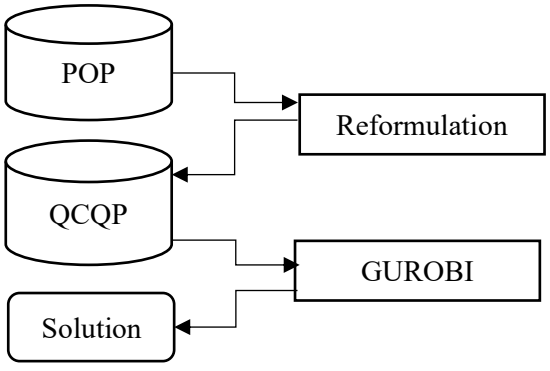

Figure 3. A flowchart showing the process needed to complete the POP2QCQP reformulation +GUROBI method

As previous research has been done comparing the reformulation approach to state-of-the-art solvers such as BARON, ANTIGONE and SCIP (Karia, 2020) this paper compares the reformulation approach to novel Polynomial optimisation algorithms. Amongst the several possibilities described in Section 2, RAPOSa was chosen for this paper mainly due to its public availability and strong performance shown by González-Rodríguez et al., where it outperformed BARON and ANTIGONE on a chosen test set. RAPOSa also has a choice of linear and non-linear solvers to use. GUROBI was used as a linear solver (to solve the linearised problem and obtain suitable lower bounds at each iteration of the branch-and-bound tree) and IPOPT was used as a non-linear solver, as this combination was proved to perform the best. (Gonzalez-Rodriguez, et al., 2020).

Fair comparison of both solvers was ensured by using the same machine to test both solvers. In addition, all problems were solved with the following conditions:

- Absolute Tolerance: $1e^{-9}$
- Relative Tolerance: $1e^{-4}$
- Feasibility Tolerance: $1e^{-5}$
- Time Limit: 3600s

3.2 Testing Environment

RAPOSa is currently limited as it does not have the capability to solve problems with integer or binary variables. Therefore, all problems considered in this paper were POPs with only continuous variables. This limitation did restrict the applications that were chosen for the problem set; however, to efficiently test the solvers, problem sizes ranging from 2 to 11,000 variables and constraints were considered. In addition to application-based problems, randomly generated problems were also considered in the test set. The test set contains 59 problems, of which some have not been solved to global optimality.

3.2.1 MINLP library

The MINLP library possesses a range of problems that vary by application and computational complexity. Chemical engineering optimisation problems were mainly obtained from this library. A total of 48 problems were collected for the test set with applications such as catalytic cracking, pooling and wastewater systems. The problems were very large and had up

to 11,000 variables and constraints. The problems in this test set whilst large did not have a high complexity, as the constraints did not contain many high-order multilinear terms. (Vigerske, 2020)

3.2.2 DS-TS library

The DS-TS library introduced by Dalkiran and Sherali, 2016 consists of randomly generated problems. The problems are much smaller than those from the MINLP library however, the constraints are much more complex. RAPOSa has been tested using instances from this library, and outperformed all commercial solvers tested. 11 problems were selected from the DS-TS set, most of which are of a high degree and low number of variables and constraints. This combination is the opposite to that seen in the MINLP library therefore allowing us to effectively test both solvers. (Dalkiran & Sherali, 2016).

3.3 Performance analysis methods

The effectiveness of solvers can be assessed with many different metrics. This paper focuses on 4 different metrics: the number of instances solved, the CPU time, the number of iterations per second and the bound gap.

Performance profiles were produced using the CPU time metric where the number of instances solved before a specific time was found and plotted. This allows us to compare both solvers simultaneously as all instances were tested on the same machine.

The number of iterations per second and the bound gap can be recorded from the output of the solver which displays all information necessary for these metrics.

Shifted geometric mean (SGM) was also used in analysis of the solvers. This technique reduces the effect of outlier on the data. SGM also shows the correlation of the data as low values represent data that has fewer outlier and stronger correlations. The equation for SGM is shown below (Mittelman, 2020):

$$SGM = \exp\left(\frac{\sum_1^n \ln(\max(0, v_i + s_h))}{n}\right) - s_h$$

n = number of problems
v_i = performance metric
s_h = shifter parameter (3.3.1)

4. Results & Discussion

Table 1. Performance metrics for all instances when solved with the POP2QCQP reformulation method and RAPOSa

Full Test Set

	POP2QCQP Reformulation	RAPOSa
Mean Relative Gap	6.73	12
Iterations per second	9195	251
Percentage of instances solved	63.8%	53.4%
SGM	92.1	184.6

Table 2. Performance metrics for all instances from the MINLP Library when solved with the POP2QCQP reformulation method and RAPOSa

MINLP Library

	POP2QCQP Reformulation	RAPOSa
Mean Relative Gap	1.45	17.9
Iterations per second	10302	299.5
Percentage of instances solved	66.7%	48.9%
SGM	83.9	238.2

Table 3. Performance metrics for all instances from the DS-TS Library when solved with the POP2QCQP reformulation method and RAPOSa

DS-TS Library

	POP2QCQP Reformulation	RAPOSa
Mean Relative Gap	22.6	0.29
Iterations per second	4469	46.3
Percentage of instances solved	54.5%	72.7%
SGM	136.2	58.9

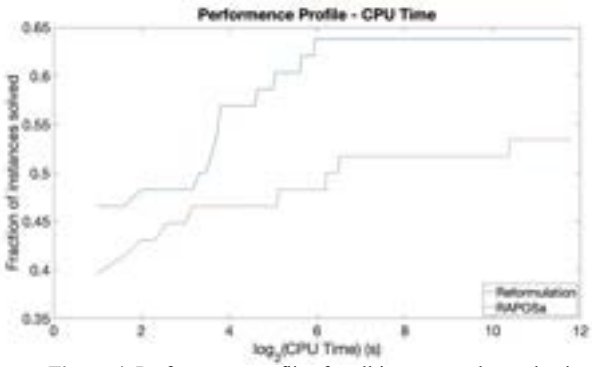

Figure 4. Performance profiles for all instances when solved with the reformulation method and RAPOSa

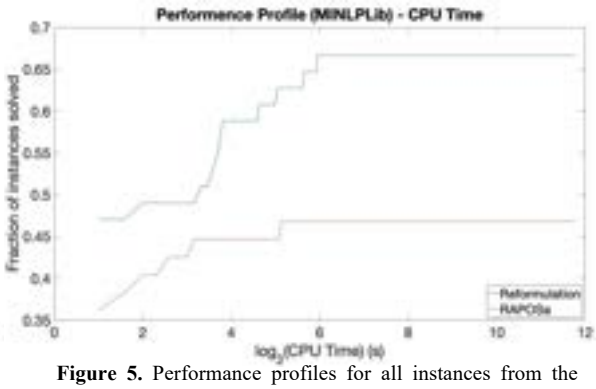

Figure 5. Performance profiles for all instances from the MINLP library when solved with the reformulation method and RAPOSa

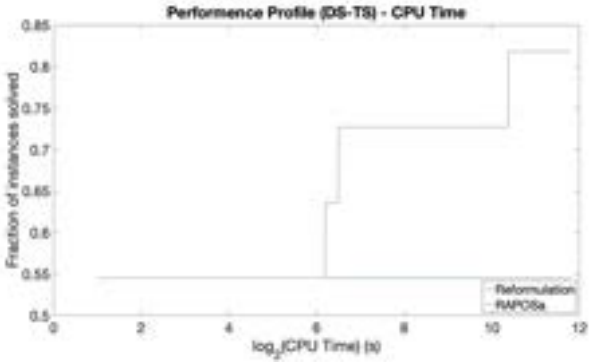

Figure 6. Performance profiles for all instances from the DS-TS library when solved with the reformulation method and RAPOSa

As explained previously, in this section the performance of the POP2QCQP Reformulation+GUROBI approach is compared to that of RAPOSa for a chosen set of test problems. It is worth noting that the time taken to reformulate the polynomial optimisation problems as QCQP was not considered as it was observed to be negligible even for large instances.

Firstly, the performance profiles presented in Figure 4 above clearly demonstrate the overall superior performance of the POP2QCQP Reformulation method over RAPOSa within 1h of operation. GUROBI solved roughly 64% of the problems to global optimality, while RAPOSa only 53%. Additionally, most problems were solved within the first 100 seconds, where the Reformulation is also superior, and only very few of them were solved later indicating that most instances were either too easy or too difficult. The shifted geometric mean also proves the superiority of the POP2QCQP reformulation, having a value of 92.1 compared to 184.6 of RAPOSa. The mean relative gap between upper and lower bounds is almost twice higher for RAPOSa, showing that even for problems that were not solved to optimality, the Reformulation method was closer to the solution on average, having a smaller gap between upper and lower bounds.

The POP2QCQP Reformulation approach demonstrates exceptional performance with problems from the wastewater and pooling classes, often improving the known bounds or solving previously unsolved instances. These classes are particularly important because these are some applications of POPs in Chemical Engineering, demonstrating the benefits of using this approach. This is mainly due to the absence of many high-order multilinear terms, resulting in relatively few auxiliary variables being added to the problem during reformulation and the exceptional effectiveness of GUROBI when solving this type of problems.

For a more detailed analysis, we need to consider the problems from MINLP Lib and the randomly generated DS-TS library separately.

4.2 MINLP Library and DS-TS Library

For the instances in the MINLP Library, which consists of real-life applications of optimisation problems, GUROBI solves a bigger proportion of the problems (0.667) than RAPOSa (0.489)

and is better at closing the gap between upper and lower bounds for the problems where it fails to find a global optimum. On average, the relative gap between upper and lower bound is 1.45 for the POP2QCQP reformulation and 17.9 for RAPOSa. Additionally, RAPOSa often gets stuck on a set of upper and lower bounds within the first few seconds and fails to find better bounds afterwards. However, RAPOSa is much more effective when solving problems from the DS-TS library. The POP2QCQP reformulation approach often fails to find a feasible solution to provide an upper bound, while RAPOSa is very good at closing the gap even for the problems that it does not manage to solve within 1 hour. The mean relative gap is 22.6 and 0.29 for POP2QCQP reformulation and RAPOSa respectively.

Unlike the two metrics discussed above, the number of iterations per second is much lower for RAPOSa for both libraries. This metric essentially shows how quickly the algorithm can find a new set of bounds each time it goes through the problem. It represents how easy it is to find a feasible solution (upper bound) and/or solve a relaxation of the problem (lower bound). The reason behind the lower figures of RAPOSa is the addition of much more constraints and variables as part of the reformulation strategy it employs compared to MC++ Reformulation as described in 2.3. The problem size increases significantly, making it much harder for RAPOSa to solve for the Upper and Lower bound, even with the enhancements that try to prevent this in place.

These results are in line with the observations made by Gonzalez-Rodriguez et al. who proved that RAPOSa shows better performance than most state-of-the-art solvers on instances from the DS-TS library, while its performance was worse for problems from the MINLP Lib. Additionally, it was demonstrated that the MC++ reformulation method performed worse than state-of-the-art solvers on a test set of randomly generated problems, while being better on instances from MINLP Lib (Karia, 2020).

The main reasons for this difference between the two libraries are the size and density of the problems. The problems in the MINLP Library have very many variables and constraints, while being relatively sparse. This essentially means that there are many non-zero terms when the optimisation problem is represented in a matrix form as described in 2.2. The POP2QCQP Reformulation Method seems to be more efficient at tackling these kinds of problems, while it struggles when the problems become denser. At the same time, problems in the DS-TS Library have much fewer variables and constraints, while being much denser, containing many high-order multilinear terms. In these conditions, RAPOSa is much more effective than POP2QCQP reformulation

This could be explained by the fact that in the RAPOSa algorithm, the number of additional constraints generated is increasing very quickly with the number of variables and constraints of the optimisation problem. Therefore, for the MINLP Library instances, the size of the problem is increased immensely so RAPOSa is very slow at finding new sets of upper and lower bounds, its performance being relatively bad. At the same time, the POP2QCQP Reformulation demonstrates incredible results as the monomial decomposition is very efficient since there aren't that many high-order multilinear terms. Although RAPOSa is still iterating slower than the Reformulation method for the DS-TS instances, it can build very tight lower bounds and solve for upper bounds efficiently as the size of the problems is much smaller. It can improve on the bounds within few iterations due to the novel approach it takes at finding upper and lower bounds within its branch and bound tree, as explained in 2.3. For the POP2QCQP Reformulation method, we cannot know what exactly within the algorithm is causing such a loss of efficiency since a detailed description of GUROBI is not publicly available, it being a commercial solver. However, we believe GUROBI is significantly slowed down by the dense optimisation problems and higher degree polynomials due to the significant number of auxiliary variables introduced in such problems caused by inefficient monomial decomposition. GUROBI is thus unable to find tight lower bounds and feasible upper bounds due to this increase in problem size and complexity.

5. Conclusion & Outlook

The aim of this paper was to analyse and compare the performance of the POP2QCQP Reformulation method with other novel polynomial optimisation algorithms, highlighting advantages and disadvantages, and suggesting improvements for the POP2QCQP Reformulation algorithm. Amongst several alternatives, RLT-

based RAPOSa was chosen for the detailed comparison due to its public availability and promising claimed results. The tests were done on a set consisting of instances from two libraries: MINLP Lib and DS-TS. The former contains mostly real-life applications of optimisation problems, while the latter has only randomly generated polynomial optimisation problems.

Results showed that POP2QCQP Reformulation performs much better on instances from MINLP Lib, managing to find the optimum solutions more often and quicker on average. Moreover, it was able to solve previously unsolved problems and showed incredible performance on pooling and wastewater treatment problems, which is significant as these are some of the important Chemical Engineering applications. At the same time, RAPOSa was much more effective with instances from the DS-TS library. It managed to solve a larger proportion of problems and was much better at closing the gap for the ones not solved by either algorithm. The analysis demonstrated that the POP2QCQP Reformulation algorithm is very effective with large problems, containing many variables and constraints, but is very slow when the problems are dense, containing many high order multilinear terms, even when there are very few variables and constraints. This is likely due to the addition of many auxiliary variables during the reformulation. RAPOSa, on the other hand, showed worse performance with the big problems due to the enormous number of additional constraints it was adding while solving them. This was also reflected in the number of iterations per second, RAPOSa falling behind significantly at this parameter.

Moving forward, it is important to find pathways that reduce the number of auxiliary variables introduced during the POP2QCQP reformulation, although finding the smallest number of monomials is a NP-hard problem (Rodriguez-Heck, 2019). Other state-of-the-art algorithms, such as BARON or ANTIGONE could be used instead of GUROBI to solve the reformulated QCQP problems specifically for dense instances.

Several pre-processing strategies should also be investigated for the POP2QCQP Reformulation algorithm such as warm-starting or constraint propagation. In addition to this, other Polynomial Optimisation algorithms need to be tested and suitable enhancements adapted, such as the modified Bernstein polynomial approach, the adaptive, multivariate partitioning algorithm or the monomial-wise optimal separable underestimators as described in 2.4, while the run time and the number of threads should also be increased to unveil the full potential of the algorithms. As this study only considered continuous problems, due to inability of RAPOSa to tackle integer variables, MIPOPs need to be tested with either RAPOSa when this feature is available or with the other novel MIPOP algorithms described above.

Bibliography

Adjiman , C., 2020. *CE4-06A Advanced Process Optimisation.* London : Imperial College London.

Belotti, P. et al., 2013. *Mixed-Integer Nonlinear Optimisation.* s.l.:s.n.

Buchheim, C. & D'Ambrosio, C., 2017. Monomial-wise optimal separable underestimators for mixed-integer polynomial optimization. *Journal of Global Optimization,* pp. 759-786.

Dalkiran, E. & Sherali, H., 2013. Theoretical filtering of RLT bound-factor constraints for solving polynomial programming problems to global optimality. In: *Journal of Global Optimization.* s.l.:s.n., p. 1147–1172.

Dalkiran, E. & Sherali, H. D., 2016. RLT-POS: Reformulation - Linearization Technique-based optimization software for solving polynomial programming 87 problems. *Mathematical Programming Computation,* pp. 337-375.

Gonzalez-Rodriguez, B. et al., 2020. *Computational advances in polynomial optimization: RAPOSa, a freely available global solver,* Santiago: s.n.

GUROBI, 2020. *Mixed-Integer Programming (MIP) - A Primer On The Basics - Gurobi.* [Online]
Available at: https://www.gurobi.com/resource/mip-basics/
[Accessed 15 December 2020].

Karia, T., 2020. *State-of-the-art deterministic global optimisation,* s.l.: s.n.

Linderoth, J. & Luedtke, J., 2016. *Mixed Integer Nonlinear Programming.* [Online] Available at: https://www.ima.umn.edu/materals/2015-2016/ND8.1-12.16/25419/Luedtke-minlp.pdf [Accessed 15 December 2020].

Mittelman, H., 2020. *Non-Convex QPLIB Benchmark,* s.l.: s.n.

Nagarajan, H. et al., 2019. An adaptive, multivariate partitioning algorithm for global optimization of nonconvex programs. *Journal of Global Optimization,* pp. 639-675.

Patil, B. & Nataraj, P., 2014. An Improved Bernstein Global Optimization Algorithm for MINLP Problems with Application in Process Industry. *Mathematics and Computer Science,* pp. 357-377.

Patil, B., Nataraj, P. & Bhatiya, S., 2012. Global Optimization of mixed-integer nonlinear (polynomial) programming problems: the Bernstein polynomial approach. *Computing,* pp. 325-343.

Rodriguez-Heck, E., 2019. *Linear and quadratic reformulations of nonlinear optimization problems in binary variables,* Liege: University of Liege.

Rumschinski, P., Borchers, S., Bosio, S. & Weismant, R., 2010. Set base dynamical parameter estimation and model invalidation for biochemical reaction networks. In: *BMC Systems Biology.* s.l.:s.n., p. 69.

Sherali, H., Dalkiran, E. & Desai, J., 2012a. Enhancing RLT-based relaxations for polynomial programming problems via a new class of v-semidefinite cuts. In: *Computational Optimization and Applications.* s.l.:s.n., p. 483–506.

Sherali, H., Dalkiran, E. & Liberti, L., 2012b. Reduced RLT representations for nonconvex poly-nomial programming problems. In: *Journal of Global Optimization.* s.l.:s.n., p. 447–469.

Sherali, H. D. & Tuncbilek, C. H., 1992. A global optimization algorithm for polynomial programming problems using a Reformulation-Linearization Technique. In: *Journal of Global Optimization.* s.l.:s.n., p. 225–249.

Vigerske, S., 2020. *MINLPLIB: A Library of Mixed-Integer And Continuous Nonlinear Programming Instances.* [Online] Available at: www.minlp.org [Accessed 15 December 2020].

Framework for a Machine Learning Approach to Cancer Classification with IgG Glycome Profiles

Authors: Vanessa Tang, Alessandro Tonus

Supervisor: Cleo Kontoravdi

Department of Chemical Engineering, Faculty of Engineering, Imperial College London

Abstract

Detecting cancer at an early stage improves prognosis, therefore there has been strong motivation for researching biomarker diagnostic methods, such as using N-glycans. However current technology demands in-depth understanding of glycosylation processes, limiting diagnostic applicability; machine learning has the potential to overcome this with a computational approach. We propose a framework for the development of a cancer classification model. Using input data such as glycan profiles and patient information, two classifiers are developed; a support vector machine and an artificial neural network, with optimised structures and hyperparameters. A two-tailed t-test is used on the accuracy metrics, $F1$ score and *recall*, to identify the best-performing classifier. The framework was tested with a set of dummy data generated using the results of a colorectal cancer study to demonstrate its functionality. This study showcases the potential of a machine learning approach for using glycan biomarkers to diagnose cancer.

Keywords: Glycosylation, N-Glycan, Cancer, Machine Learning, Framework.

1 Introduction and Background

Cancer Research UK predicts that 1 in 2 people in the the United Kingdom will get cancer in their life time.[1] When compared to countries with similar healthcare systems (including Australia, Canada, Norway, Denmark, Ireland and New Zealand), the UK appears to lag behind on cancer survival, incidence and mortality rates.[2] The NHS Long Term Plan makes the commitment to detect 75% of cases at an early stage by 2028,[3] as detecting and treating cancer early can significantly improve prognosis. In order to achieve this, there needs to be an innovative approach to diagnostics.[4] Other factors such as inaccuracy of diagnosis, high cost and perceived risk of radiation exposure for certain screening methods further fuel the need for the development and validation of non-invasive biomarkers.[5]

Studies have observed aberrant alterations in serum and IgG glycosylation being closely related to pathological conditions such as cancer.[6,7,8] Glycosylation is a post-translational modification of proteins involving a highly complex network of reactions. It plays an important role in biological processes such as host pathogen interactions, immune responses and in inflammation.[9] There have been promising findings in discovering potential blood-based biomarkers such as N-glycans and glycoproteins for detecting cancer.[5,10,11]

The screening for biomarkers has specific requirements including sensitivity (the ability of a test to correctly identify patients with a disease) and specificity (the ability of a test to correctly identify people without the disease).[12] One of the limitations of current methods for screening glycan-based biomarkers and glycan

data analysis is the need for considerable expertise in the field.[9]

Machine learning (ML) methods have become a popular tool for the medical research community[13] because of their self-learning capability for modelling complex patterns and relationships from input data without the need of explicit programming. Through employing various statistical, probabilistic and optimisation tools, ML eliminates the need to understand complex biological processes. Previous research into cancer applications of ML focused on modelling the progression, recurrence and survival rate with the integration of information such as histological, clinical, population-based and patients' personal data.[14,15,16,17] More recently, neural networks and deep learning have been adopted, mainly using images as inputs,[18,19] for cancer classification, or analysing biomarkers for risk assessment. ML has also been used in glycosylation-related studies, such as using artificial neural networks (ANN) to predict glycosites or glycan distribution profiles.[20] There have been no attempts to utilise machine learning to understand the relationship between glycan profiles, patient data and cancer diagnosis.

Therefore, we are proposing a machine learning framework to develop an optimised classifier model to identify individuals with cancer, using algorithm input features such as glycan profiles and personal data. The framework development is presented as a methodology, and its application is shown through an experiment using a dummy dataset.

2 Framework Development

We intended to build a machine learning model based on Vučković et al.[21] Colorectal cancer research – the largest of its kind, collecting the IgG glycome profile for 24 N-glycans on 760 Colorectal cancer patients and 538 matching healthy controls, as well as BMI, sex and age. Due to delays and operational difficulties, the full dataset could not be obtained. Instead, the results reported from the study were used to generate an artificial dataset, which was then used to develop a framework that can be applied to the patient data to obtain a fully optimised classifier.

The framework was developed and tested using Python, incorporating machine learning best practice with the latest tools and methods available for ML and model optimisation.

2.1 Framework Overview

The overall framework involves various steps (Figure 2.1). The dataset containing both input variables and cancer markers is split into a training and a test set, and the cancer markers are isolated from the input variables. Then, the latter are processed to prepare them to be imported into the classifier models. The training set is used to optimise both an artificial neural network (ANN) and a support vector machine (SVM), using k-fold cross validation performance as an optimisation metric. The best performing model for each is then evaluated on the test set for comparison. In order to estimate an average and standard deviation for performance, the test set is split into five separate subsets, and the classifiers are evaluated on each. A two-tailed t-test is then performed to understand if either model is performing better than the other.

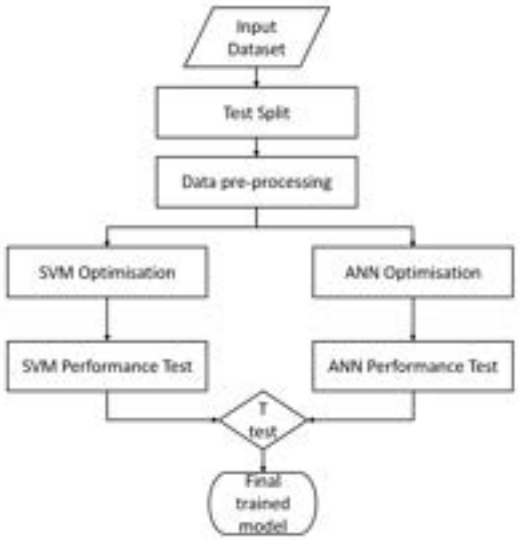

Figure 2.1: *Overview diagram of the proposed framework, showcasing the internal data flow and processes, as well as decision points*

2.2 Input Data and Test Split

While a specific dataset was used during the development of this framework, the methodology and corresponding code proposed can generalise to any input patient set.

The dataset is imported as a CSV or Excel file, with features as columns, and samples as rows. The cancer marker column is then isolated as the output feature, while all feature-containing columns are extracted as input variables.

In order to enable an unbiased evaluation of classifier performance on data that was not used for training, a train-test split was implemented. Train-validation-test split is not used at this stage because the training set generated during preprocessing is being subdivided further during the model training and optimisation stage instead; a validation set serves a similar purpose to that of a test set, but is instead used to optimise parameters.[22] A test split ratio of 0.2 was used during framework development based on initial testing.

It would be possible to incorporate data importing and splitting with the optimisation algorithms, but the proposed method is to perform the split separately and export results into a separate file. The optimisation algorithm would re-sample with each iteration, so a unified code would lead to the use of a different dataset each time, making it challenging to compare performance of the optimised models.

2.3 Data pre-processing

For the purpose of preprocessing the train and test input sets before feeding them into the predictive model, a unified feature processing function was created.

All numerical features are scaled with the SKLearn MinMaxScaler function to maximise training speed of the models.[23] The function is fit to all numerical feature columns, using the entire dataset, extracting the minimum and maximum value that appears in each. Then, Eq. 1 is used to transform all the data, applying it column-wise, in order to ensure consistent scaling between 0 and 1 for every feature.

$$x_{scaled} = \frac{x - x_{min}}{x_{max} - x_{min}} \tag{1}$$

Categorical features are encoded using OneHotEncoding to map them to arrays of binary variables,[24] allowing them to be used as inputs for the classifier models. This is necessary because they can only process numbers as inputs. The encoder is fit on the entire dataset, for each of the categorical columns, to recognise unique categories and add a binary variable for each to an array (Figure 2.2). Then, it is used to process the training and test input sets, producing encoded features that are appended to the scaled numerical ones.

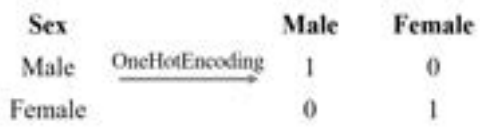

Figure 2.2: *Sample application of OneHotEncoding; two categories for patient sex (male and female), are mapped to binary variables within an array*

Principal Component Analysis (PCA) was considered as an optional preprocessing step to reduce the dimensionality of numerical inputs and consequently the computing power required by the model. It was not, however, enabled in the main framework, as the artificially generated data would offer limited insight.

In previous literature, PCA was widely used in medicine as a preprocessing step for image classification neural networks,[25] and with combined biomarker and patient data for hepatitis C classification.[26] It has, however, never been proposed as a preprocessing step for cancer classification with biomarkers. PCA could be used to investigate the effect of feature reduction on the accuracy of the neural network. The scaled numerical features would be projected into a smaller feature space of lower dimensions. The principal components to use as inputs would be selected to be the ones with greatest contribution to the variance in the data.[27]

This could be used after the initial optimisation of the models to investigate neural network performance with reduced information, by gradually feeding in fewer principal components. The potential benefit would be reducing the input size, allowing for reduced structure complexity, training time and computational power required for the model.

2.4 Classifier model optimisation

To develop a classification model, SVM and ANN are investigated, as both machine learning approaches have shown success in applications with proteomic profiles in previous studies.[28,29]

Hyperparameters for both are optimised using the Hyperopt and Hyperas Python libraries. A distinctive aspect of the proposed framework is the use of a tree-structured Parzen estimator algorithm, which was shown to outperform other approaches in previous literature.[30] This reduces the number of iterations compared to the more widely used brute force and grid search approaches, by taking into account previous runs in the optimisation steps taken; for example, it

would stop exploring in a direction that worsens performance, while other common algorithms would not.

k-fold cross-validation is the resampling procedure proposed to evaluate model performance during optimisation. The training set is divided into k different parts (referred to as k folds). During each optimisation iteration, one fold is held out as the validation set on which model performance is evaluated and recorded, after training with the remainder of the data. This process is repeated k times until all the parts have been used as the validation set once, then the performance metric is averaged for comparison in the optimisation algorithm. By training k different models, averaging the accuracy of the k iterations gives a less biased understanding of the algorithm performance. It overcomes the situation where the accuracy from a single evaluation was a result of chance or a biased validation set.[31]

2.4.1 Support Vector Machine

Support vector machines are a supervised learning method that uses a single mathematical function in multiple dimensions (kernel function) to create a boundary that best separates the possible output classes. They are often used for classification tasks because of their efficiency.[32] SVMs were modelled through the SciKitLearn library in python.

The model is optimised with respect to the type of kernel used, kernel-specific parameters, and the regularisation hyperparameter C (Table 1).

The kernel determines what type of function is used by the model to perform the classification. The structures considered were linear, polynomial, and radial basis function (rbf), commonly used for classification tasks.[32] The linear kernel is the simplest one, but cannot deal well with non-linearity; when applying the framework, the presence of strong cross-correlations within the input variables could not be described well with it, while the other two could handle non-linearity better, and would be expected to be the optimal choices. The only kernel-specific parameter to optimise is the polynomial degree, and for the framework proposed this is achieved through specifying "options" from second to fourth degree. This range was chosen based on initial experimentation yielding good results with the dummy dataset using lower degree polynomials. When applying the framework to the real patient measurements, this could need to be adjusted if better results are achieved with higher order polynomials.

The hyperparameter C is used to prevent model overfitting, and contrast noise in the data. The framework investigates a log-spaced range between 0 and 1, with a lower value being better for noisy observations.[33]

Table 1: Summary of SVM optimisation choices

Choice	Alternatives
Kernel	linear, polynomial, rbf
Polynomial Degree	2, 3, 4
C	Log range (0 – 1)

2.4.2 Artificial Neural Network

The ANN model used is a multi-layer perceptron (MLP). A MLP consists of fully connected sequential layers of nodes – an input layer for the input features of a sample; a variable number of hidden layers, which process the inputs through an activation function tied to each node present in it; and an output layer, which outputs the probability of a sample belonging to each of the possible classes. The internal parameters that determine the output of each node, known as weights, are adjusted through a mini-batch backpropagation training algorithm.[34] ANNs were modelled through the Keras and TensorFlow libraries, and a SciKitLearn wrapper was used to enable the reading of the ANN model as an optimisation input.

The ANN is optimised with respect to the number of hidden layers, number of neurons, activation function, and dropout rate in each layer, as well as learning rate and batch size. The optimisation criterion is the averaged model performance in a 5-fold cross-validation with the training set (Table 2).

This criterion does not optimise for learning speed, as it was deemed less critical with respect to the aim of the model. The number of epochs (number of passes of the entire training set the algorithm has completed) was kept at 50, in order to obtain an accurate model without excessive computation time. This number was chosen based on when well-performing models would plateau in their validation accuracy.

The number of layers was set as a binary choice between two and three, after initial experimentation with the ANN model showed good

performance with two layers. For each of them, the number of neurons was a choice between values around the number of features in the input size, a common starting point for iteratively finding the optimal amount (Table 2).[35] The activation function alternatives were chosen to be Rectified Linear Unit (ReLu), Hyperbolic Tangent (TanH) and Sigmoid, which have been shown to be highly performing in classification tasks.[36] The output layer was kept fixed to 2 neurons with a SoftMax activation function. This is standard practice for classification tasks, and causes the model to output a probability for each class (cancer and control in this case), with the activation function ensuring they sum up to 1.[37]

Table 2: Summary of ANN optimisation choices. Alternatives separated by a comma denote discrete choices, while ranges are specified

Choice	Alternatives
No. Layers	Two, Three
No. Neurons	8, 16, 24, 32
Activation Fn.	relu, sigmoid, tanh
Dropout Rate	Linear range (0 – 0.3)
Learning Rate	0.005, 0.001, 0.0001
Batch Size	32, 64

Dropout layers were included in the model in order to prevent overfitting. A dropout layer causes the model to ignore the output of a certain fraction of the neurons in a layer during a training iteration, making it harder to overly adapt to noise in the training data.[38] The range to be tested was limited in order to avoid instability during the execution of the code, which was observed to appear with higher maximum dropout rate values.

An Adaptive Moment Algorithm (ADAM) is used as the training optimiser for the ANN, because of its efficiency and low memory requirement, especially crucial when training hundreds of different models with k-fold validation.[39] The learning rate was specified to determine the initial size of the changes the model would make with each training iteration. Options were given in differing orders of magnitude around the preset value of 0.001, which was observed to perform well. The choices could not be logarithmically spaced because a value of 0.01 was observed to cause excessive instability during code execution. Batch size options were specified based on the recommended values proposed in the TensorFlow user pages.[40]

2.5 Comparison metrics and final model selection

To evaluate and compare the optimised models, to choose the final candidate, a confusion matrix is applied to the predictions of the same test set. A confusion matrix reports True Positives (TP), True Negatives (TN), False Positives (FP) and False Negatives (FN) predicted.

The metrics used to compare the two models are *precision* and *recall*. *Precision* is the fraction of correct output labels (i.e. cancer patient) out of the total number of model output labels for a given class (Eq. 2), and *recall*, also known as sensitivity, is the fraction of correct output labels out of the total actual labels for a given class (Eq. 3). In the ML model, there is a trade-off in the metrics chosen to maximise – the higher the *recall* the lower the precision, or vice versa. Therefore taking more metrics into consideration, $F1$ score is used, which represents the harmonic mean between *precision* and *recall* values (Eq. 4), widely used in classification problems.[41]

$$precision = \frac{TP}{TP + FP} \tag{2}$$

$$recall = \frac{TP}{TP + FN} \tag{3}$$

$$F1 = 2\frac{precision \times recall}{precision + recall} \tag{4}$$

To ensure that apparent differences between the scores are not the result of chance, a two-tailed t-test is used to evaluate the differences in the means of two set of accuracy scores. This statistical test is appropriate as sample populations are independent and there is no information on whether the mean of ANN's $F1$ score or *recall* is likely to be greater than that of SVM's or vice versa. Test statistics T and standard deviation S_D can be calculated using Eq. 5 and 6, and be compared to p value found on the Student t-distribution table, with $n-1$ degrees of freedom. If $|T| > p$, the null hypothesis will be rejected, meaning that there is statistical significance to conclude that one model being more accurate than the other. In case the null hypothesis is not rejected, the final model would be the one which requires less computational power, the support vector machine.

In order to perform the test, multiple performance samples are necessary. To achieve this, the test dataset is split into a number of equal

subsets that gives an appropriate sample size. By doing this, independent test samples are obtained; trained model performance can be evaluated against each of them, allowing an estimation of the standard deviation, as well as enabling the use of the t-test.

$$T = \frac{\bar{D}}{S_D/\sqrt{n}} \approx t_{n-1} \tag{5}$$

$$S_D = \sqrt{\frac{1}{n-1}\sum_{i=1}^{n}(D_i - \bar{D})^2} \tag{6}$$

3 Experiment

3.1 Dataset Generation

Due to the lack of information on the skewness or glycan distribution profile of Vučković et al's dataset, the assumption of normal distribution was made. Therefore in order to generate normally distributed profiles, the reported median, first and third quartile values from the real dataset need to be transformed. Wan et al's approximation methods in the estimation of the sample mean and standard deviation (Eq. 7 and 8) were used,[42] as they are an improvement from the state of the art method by Hozo et al[43] for data that is not normally distributed.

$$\bar{X} \approx \frac{q_1 + m + q_3}{3} \tag{7}$$

$$S \approx \frac{q_3 - q_1}{\eta(n)} \tag{8}$$

$\eta(n)$ in Eq 8 converges to approximately 1.35 when n is large (i.e. >50), therefore Equation 8 can be simplified to Eq 9.

$$S \approx \frac{q_3 - q_1}{1.35} \tag{9}$$

The calculated mean and standard deviation is input into the SobolGSA Software developed by Imperial Professors S. Kucherenko and O. Zaccheus.[44] Given a limited understanding of the real dataset, complex relationships between features and data points, as well as patient information, could not be replicated.

3.2 Discussion

The generated dataset includes 1023 samples for both the cancer and healthy classes. Each sample reports the relative presence of the 24 N-glycans highlighted in the colorectal cancer study, as well as a binary marker for the class, with cancer patients encoded as 1, and controls as 0. It is fed into the framework to build two optimised models.

SVM Optimiser: The optimisation resulted in the hyperparameters shown in Table 3. The low degree polynomial function could imply limited non-linearity present in the dataset, therefore a radial-based function is not needed. C-value is less than 1 which indicates high levels of noise and variance.

Table 3: Optimised hyperparameters for the support vector machine classifier

Function	Degree	Log parameter C
Polynomial	2	0.592

ANN Optimiser: The optimised model has three layers with the attributes shown in Table 4, an optimal learning rate at 0.001, and batch size of 64. The small number of layers could be an indication of the lack of complex correlations in the dataset.

Table 4: Optimised structure and parameters of the artificial neural network classifier

Layer	No. of Neurons	Activation Function	Dropout Rate
1	24	sigmoid	28.2%
2	8	tanh	11.9%
Output	2	softmax	n/a

The learning curve (Fig 3.1) shows the comparative performance between the train and test data. The model appears to be a reasonable fit with the plots continue to increase with experience. Train accuracy increases overtime and stabilises around 70–75%, whereas test accuracy increases sharply during the first 20 epoch to about 80%. There is a 10% difference in accuracy after 50 epochs as a result of the presence of dropout to prevent overfitting the data. Due to the disabling of neurons, those nodes are temporarily removed from the network, along with its incoming and outgoing connections,[38] therefore the subsequent layers are attempting to construct a model based on incomplete representations. Therefore, it is more difficult for the network to build an accurate model, resulting in lower training accuracy. During the testing stage when all the information is available, the network naturally performs better.

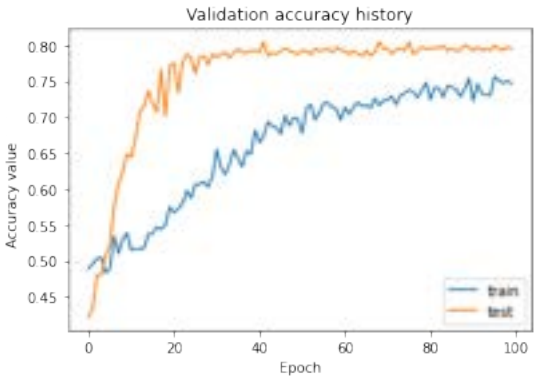

Figure 3.1: *Validation accuracy history plot of $F1$ score against the number of passes the ML algorithm has completed, for the train (blue line) and test sets (orange line) from the optimised artificial neural network classifier. Train set is the data used to train the model, while the test set is used to evaluate it*

Model performance: $F1$ score and *recall* vary around 80% for both the SVM and ANN models. The limited accuracy is a result of simple correlations within the dummy dataset. Accuracy might be higher if a real set of data is used. With additional features such as age and BMI in the real data, accuracy should increase.

Recall scores are higher than $F1$ scores implies that both models captures a higher proportion of cancer cases, leading to a higher false positive rate than false negative rate. In this context this is acceptable as it may be more preferable to "flag" a patient as having cancer than to "miss" any patients with cancer. While this incurs mental stress on the in fact healthy individual, the estimated lifetime burden for false negative result is much higher than false positive result.

Table 5: $F1$ score and *recall* for SVM and ANN optimised models with variance from the 5 subsets

	ANN	SVM
$F1$	$79.4\% \pm 4.5\%$	$80.9\% \pm 3.6\%$
recall	$82.1\% \pm 3.5\%$	$83.5\% \pm 4.7\%$

Model Comparison: The test dataset was split into 5 equal subsets of 82 samples, in order to ensure a balanced representation of cancer patients in each. Increasing the number of subsets leads to an increase in the standard deviation of model performance.

The statistical t-test was performed for both accuracy measurements, $F1$ and *recall*, with results shown in Table 6. In both comparisons T value is less than critical value, therefore the null hypothesis cannot be rejected – meaning that there is no significant statistical differences between the accuracy of the two models. In this respect, there is no preferences on which model to use. Therefore, one would choose the model with higher computational efficiency, which in this case is the SVM.

Table 6: Summary of the t-test used to compare the model performance

	$F1$	*recall*
T statistics	1.465	1.100
p value	2.776	2.776
null hypothesis	Not rejected	Not rejected

4 Conclusion

In this paper, we propose a framework for the development of a machine learning approach to cancer classification with N-glycan data. The input dataset contains both numerical and categorical features, which are preprocessed through MinMax scaling and OneHotEncoding respectively. The ML framework automates the model development process through optimising the structure and selected hyperparameters for SVM and ANN, using a Tree-structured Parzen algorithm to improve optimisation efficiency. Each iteration is evaluated through k-fold validation, and the outputs are two fully optimised classifiers, one for each type. A k-fold test split is then used to estimate the variance of trained model performance. Finally a t-test is used on both $F1$ score and *recall*, the chosen accuracy metrics, to compare the two models and choose the best performing one.

The proposed framework was tested with a dummy dataset, generated from the results of a colorectal cancer study. There was no significant statistically significant difference in classification performance between the optimised models, therefore the SVM was the optimal classifier, given its lower computational power demand.

5 Outlook

Moving forward, the approach could be refined by investigating input feature selection methods. This could allow a simpler model structure by decreasing the number of inputs that need to be processed, positively impacting processing speed as well. This could be achieved with PCA,

as discussed in Section 2.3, autoencoder neural networks, or with a genetic algorithm applied to ANN development, all of which have shown success for this application in previous literature.[45,46] Then, further analysis of false positives and false negatives could offer an insight into what features are confusing the model, and give a better understanding of the applicability of it as a diagnostic tool.

After delineating a comprehensive framework, it should then be applied to the patient dataset,[21] finally incorporating patient features and glycan profiles. This would provide an insight into what glycan measurements and patient features strongly influence the output, and allow the models to be used to their full potential, if there are complex correlations within the inputs. After applying the framework, a finalised classifier could then be extracted.

The next key step in the evaluation of this approach is applying it on more patient datasets. Putting it to test with different sets, either from other geographical areas, or different types of cancer, would have major implications for the potential uses of the classifier as a diagnostic tool. Successful testing with more cancer types would open opportunities for the development of a non-invasive test, which would only require a blood sample, and could be used as a routine check for cancer.

Acknowledgements

We thank Pavlos Kotidis (Department of Chemical Engineering, Imperial College London), for his support throughout the course of this project.

References

[1] Cancer Statistics for the UK, 2015.

[2] Arnold M, Rutherford M, Lam F, Bray F, Ervik M, and Soerjomataram I. ICBP SURVMARK-2 online tool, 2019.

[3] NHS. Interim NHS People Plan. Technical report, NHS, 6 2019.

[4] Cancer Research UK. Delivering on the Conservative Party Manifesto cancer commitments - Cancer Research UK representation to the Comprehensive Spending Review 2020. Technical report, Cancer Research, 9 2020.

[5] Abrha G Gebrehiwot, Daniel Seifu Melka, Yimenashu Mamo Kassaye, Tufa Gemechu, Wajana Lako, Hiroshi Hinou, and Shin-Ichiro Nishimura. Exploring serum and immunoglobulin G N-glycome as diagnostic biomarkers for early detection of breast cancer in Ethiopian women. *BMC Cancer*, 19, 2019.

[6] Salomé S. Pinho and Celso A. Reis. Glycosylation in cancer: Mechanisms and clinical implications, 9 2015.

[7] Maja N. Christiansen, Jenny Chik, Ling Lee, Merrina Anugraham, Jodie L. Abrahams, and Nicolle H. Packer. Cell surface protein glycosylation in cancer. *PROTEOMICS*, 14(4-5):525–546, 3 2014.

[8] Xingchen Pang, Hongjiao Li, Feng Guan, and Xiang Li. Multiple roles of glycans in hematological malignancies, 9 2018.

[9] Muchena J. Kailemia, Dayoung Park, and Carlito B. Lebrilla. Glycans and glycoproteins as specific biomarkers for cancer, 9 2017.

[10] Celso A. Reis, Hugo Osorio, Luisa Silva, Catarina Gomes, and Leonor David. Alterations in glycosylation as biomarkers for cancer detection, 4 2010.

[11] Sureyya Ozcan, Donald A. Barkauskas, L. Renee Ruhaak, Javier Torres, Cara L. Cooke, Hyun Joo An, Serenus Hua, Cynthia C. Williams, Lauren M. Dimapasoc, Jae Han Kim, Margarita Camorlinga-Ponce, David Rocke, Carlito B. Lebrilla, and Jay V. Solnick. Serum glycan signatures of gastric cancer. *Cancer Prevention Research*, 7(2):226–235, 2 2014.

[12] Amelia Swift, Roberta Heale, and Alison Twycross. What are sensitivity and specificity? *Evidence-Based Nursing*, 23(1):2–4, 1 2020.

[13] Konstantina Kourou, Themis P. Exarchos, Konstantinos P. Exarchos, Michalis V. Karamouzis, and Dimitrios I. Fotiadis. Machine learning applications in cancer prognosis and prediction, 1 2015.

[14] D. V. Cicchetti. Neural networks and diagnosis in the clinical laboratory: State of the art, 1992.

[15] ALISTAIR J. COCHRAN. Prediction of Outcome for Patients with Cutaneous Melanoma. *Pigment Cell Research*, 10(3):162–167, 6 1997.

[16] Igor Kononenko. Machine learning for medical diagnosis: History, state of the art and perspective. *Artificial Intelligence in Medicine*, 23(1):89–109, 8 2001.

[17] Kanghee Park, Amna Ali, Dokyoon Kim, Yeolwoo An, Minkoo Kim, and Hyunjung Shin. Robust predictive model for evaluating breast cancer survivability. *Engineering Applications of Artificial Intelligence*, 26(9):2194–2205, 10 2013.

[18] Jinsa Kuruvilla and K. Gunavathi. Lung cancer classification using neural networks for CT images. *Computer Methods and Programs in Biomedicine*, 113(1):202–209, 1 2014.

[19] Natalia Antropova, Benjamin Q. Huynh, and Maryellen L. Giger. A deep feature fusion methodology for breast cancer diagnosis demonstrated on three imaging modality datasets. *Medical Physics*, 44(10):5162–5171, 10 2017.

[20] Pavlos Kotidis and Cleo Kontoravdi. Harnessing the potential of artificial neural networks for predicting protein glycosylation. *Metabolic Engineering Communications*, 10:e00131, 6 2020.

[21] Frano Vučković, Evropi Theodoratou, Kujtim Thaçi, Maria Timofeeva, Aleksandar Vojta, Jerko Štambuk, Maja Pučić-Baković, Pauline M. Rudd, Lovorka Derek, Dražen Servis, Annika Wennerström, Susan M. Farrington, Markus Perola, Yurii Aulchenko, Malcolm G. Dunlop, Harry Campbell, and Gordan Lauc. IgG glycome in colorectal cancer. *Clinical Cancer Research*, 22(12):3078–3086, 6 2016.

[22] Davide Anguita, Luca Ghelardoni, Alessandro Ghio, Luca Oneto, and Sandro Ridella. The 'K' in K-fold Cross Validation. In *European Symposium on Artificial Neural Networks*. ESANN, 2012.

[23] Sergey Ioffe and Christian Szegedy. Batch normalization: Accelerating deep network training by reducing internal covariate shift. In *32nd International Conference on Machine Learning, ICML 2015*, volume 1, pages 448–456. International Machine Learning Society (IMLS), 2 2015.

[24] Patricio Cerda, Gaël Varoquaux, and Balázs Kégl. Similarity encoding for learning with dirty categorical variables. *Machine Learning*, 107(8-10):1477–1494, 9 2018.

[25] Vinod Kumar, Jainy Sachdeva, Indra Gupta, Niranjan Khandelwal, and Chirag Kamal Ahuja. Classification of brain tumors using PCA-ANN. In *Proceedings of the 2011 World Congress on Information and Communication Technologies, WICT 2011*, pages 1079–1083, 2011.

[26] Tahseen A Jilani, Huda Yasin, and Madiha Mohammad Yasin. PCA-ANN for Classification of Hepatitis-C Patients. *International Journal of Computer Applications*, 14(7):975–8887, 2011.

[27] Louis Ferré. Selection of components in principal component analysis: A comparison of methods. *Computational Statistics and Data Analysis*, 19(6):669–682, 6 1995.

[28] Stefka Tyanova, Reidar Albrechtsen, Paulina Kronqvist, Juergen Cox, Matthias Mann, and Tamar Geiger. Proteomic maps of breast cancer subtypes. *Nature Communications*, 7(1):1–11, 1 2016.

[29] Terence C W Poon, Tai-Tung Yip, Anthony T C Chan, Christine Yip, Victor Yip, Tony S K Mok, Conrad C Y Lee, Thomas W T Leung, Stephen K W Ho, and Philip J Johnson. Comprehensive Proteomic Profiling Identifies Serum Proteomic Signatures for Detection of Hepatocellular Carcinoma and Its Subtypes. *Clinical Chemistry*, 49(5):752–760, 5 2003.

[30] James Bergstra, Rémi Bardenet, Yoshua Bengio, and Balázs Kégl. Algorithms for Hyper-Parameter Optimization. Technical report, ational Science and Engineering Research Council of Canada, 2011.

[31] Juan Diego Rodríguez, Aritz Pérez, and Jose Antonio Lozano. Sensitivity Analysis of k-Fold Cross Validation in Prediction Error Estimation. *IEEE Transactions on Pattern Analysis and Machine Intelligence*, 32(3):569–575, 2010.

[32] E. A. Zanaty. Support Vector Machines (SVMs) versus Multilayer Perception (MLP) in data classification. *Egyptian Informatics Journal*, 13(3):177–183, 11 2012.

[33] Shizhong Liao and Lei Jia. Simultaneous tuning of hyperparameter and parameter for support vector machines. In *Lecture Notes in Computer Science (including subseries Lecture Notes in Artificial Intelligence and Lecture Notes in Bioinformatics)*, volume 4426 LNAI, pages 162–172. Springer Verlag, 2007.

[34] Marco Gori. Deep Architectures. In *Machine Learning*, pages 236–338. Elsevier, 1 2018.

[35] Tijana Vujičić, Tripo Matijević, and Zoran Ševarac. Comparative Analysis of Methods for Determining Number of Hidden Neurons in Artificial Neural Network. Technical report, Central European Conference on Information and Intelligent Systems, 2016.

[36] Bekir Karlik and A Vehbi Olgac. Performance Analysis of Various Activation Functions in Generalized MLP Architectures of Neural Networks . *International Journal of Artificial Intelligence And Expert Systems*, 1(4), 2013.

[37] Bolin Gao and Lacra Pavel. On the Properties of the Softmax Function with Application in Game Theory and Reinforcement Learning. *arXiv*, 4 2017.

[38] Nitish Srivastava, Geoffrey Hinton, Alex Krizhevsky, and Ruslan Salakhutdinov. Dropout: A Simple Way to Prevent Neural Networks from Overfitting. *Journal of Machine Learning Research*, 15:1929–1958, 2014.

[39] Diederik P Kingma and Jimmy Lei Ba. ADAM: A METHOD FOR STOCHASTIC OPTIMIZATION. Technical report, ICLR, 2015.

[40] tf.keras.Sequential | TensorFlow Core v2.3.1.

[41] M Hossin and Sulaiman. A REVIEW ON EVALUATION METRICS FOR DATA CLASSIFICATION EVALUATIONS. *International Journal of Data Mining & Knowledge Management Process (IJDKP)*, 5(2), 2015.

[42] Xiang Wan, Wenqian Wang, Jiming Liu, and Tiejun Tong. Estimating the sample mean and standard deviation from the sample size, median, range and/or interquartile range. *BMC Medical Research Methodology*, 14(1):135, 12 2014.

[43] Stela Pudar Hozo, Benjamin Djulbegovic, and Iztok Hozo. Estimating the mean and variance from the median, range, and the size of a sample. *BMC Medical Research Methodology*, 5(1):13, 4 2005.

[44] Kucherenko S. and Zaccheus O. SobolGSA Software | Research groups | Imperial College London.

[45] Kai Han, Yunhe Wang, Chao Zhang, Chao Li, and Chao Xu. Autoencoder Inspired Unsupervised Feature Selection. In *ICASSP, IEEE International Conference on Acoustics, Speech and Signal Processing - Proceedings*, volume 2018-April, pages 2941–2945. Institute of Electrical and Electronics Engineers Inc., 9 2018.

[46] Dong Ling Tong and Robert Mintram. Genetic Algorithm-Neural Network (GANN): a study of neural network activation functions and depth of genetic algorithm search applied to feature selection. *Springer*, 2010.

Supporting Information

All datasets and codes are available on a GitHub repository, available at: github.com/PK1617/CancerGlycans

404

Heuristic Methods to Improve and Expand the SAFT-γ Mie Database via Analysis of ^{13}C NMR Spectroscopy

Yuting Wu and Beom Seok Kang
Department of Chemical Engineering, Imperial College London, U.K.

Abstract
The SAFT-γ Mie Equation of State (EoS) provides strong predictive capabilities of phase behaviour and bulk properties. The quality of prediction from the SAFT-γ Mie can be advanced via expansions and improvements of the database. ^{13}C Nuclear Magnetic Resonance (NMR) Spectroscopy is a powerful technique to detect intramolecular interactions. The chemical shift term in ^{13}C NMR spectra represents the intensity of shielding and deshielding around the nucleus of interest, which indicates the quantum electronic correlation effect. Empirically, the chemical shift of a carbon is a sum of additive parameters from its neighbouring groups, and the parameters indicate the nature of the group. With considerations of group-contribution effect, the chemical shift analysis is carried out to determine the comparative level of optimisation of the SAFT parameters of each group. Among the groups of interest: carboxyl, hydroxyl, and amine, it is concluded that carboxyl has the lowest level of optimisation, and therefore it is highly recommended to further optimise its SAFT parameters. Moreover, the heuristic method to determine the priority for the higher-order groups to develop is presented. It is concluded that second-order groups should be considered prior to other higher-order groups. Amine is the most recommended group of interest to develop the related second-order groups.

1. Introduction

Physical and thermodynamic properties of the compounds or mixtures are essential for the process engineering designs. The increasing demands and complexity of newly designated process decisions creates a gap between the existing scarce availability and the actual need of experimental data of interest in science and industry [1]. It is possible to obtain the desired properties from new experimental measurements; however, these are expensive and time-consuming. Therefore, predictions or estimations of the required physical property fill the gap and can also be used to describe the thermodynamic systems.

Group-contribution methods are powerful tools for predicting the thermophysical properties of pure compounds and mixture [2]. Several group contribution methods are established substantially [3]. Over the last centuries, various models have been constructed according to the properties of interest and availability of the experimental data set. Group contribution methods can be divided into different levels.

The most fundamental one, zeroth level, the properties of a molecule are usually determined by the elemental contributions [4]. For example, molecular weight can be evaluated accurately. In this level, no detailed information on the molecular structure is known. The next level considers the bond connectivity between different atoms. Benson (1965) [5] introduced a bond contribution concept and critical properties for single molecules can be estimated. Marrero and Pardillo (1999) [6] adopted an advanced bond contribution approach to estimate the boiling point that depends on bond connectivity not only atoms, but also group of atoms. In general, it was quite accurate, but this method failed which had large errors due to the increase complexity in polyfunctional compounds.

The most commonly used group contribution methods are based on the concept of treating molecules as combinations of several functional groups. The determination of functional group depends on the comparisons between the initial postulation of groups and the experimental data accompanied by efficient statistical techniques. Lydersen (1955) [7]developed a group contribution method to estimate critical properties successfully. Joback (1984,1987) [8] [9] re-evaluated Lydersen's work by adding several new functional groups and determined new parameters. The modelling of intramolecular interactions between the selected functional groups (proximity effect) are more challengeable, the presence of a particular functional group can modify the local environment and properties of a neighbouring group [2]. Therefore, inaccurate selections of groups may bring possible errors towards prediction. Constantinou and Gani (1994) [10] developed an advanced group contribution method based on the UNIFAC groups and also introduced higher order groups. Estimations are performed at two levels: first-order groups as the most basic level, and second-order groups with the first-order groups as building blocks. By adopting secondary groups, more accurate prediction is obtained. These new features gave a certain level of flexibility and overcame limitations of using the 'lower order' groups. Vijande, Pineiro, and Legido (2001) [11] proposed a method that considers the proximity effect by introducing mutual perturbations parameters for different functional groups. Thus, the proximity effect between neighbouring functional groups are successfully considered and described quantitatively.

However, the problem was raised from indefinite group selection methods, since there is no theoretical basis [2].

Hence, Wu and Sandler (1991) [2] introduced a theoretical approach for the identification of functional groups. Intramolecular and intermolecular interactions are investigated based on the electrostatic charge/electrostatic force and molecular geometry. Quantum mechanical ab initio molecular orbital calculations are done for defining the groups. The newly defined groups are considered as approximately electroneutral and relatively small; therefore, the charges do not change in different systems and transferability of groups remain. The groups defined in this approach, the mixture prediction quality increased substantially.

Nuclear Magnetic Resonance (NMR) spectroscopy allows investigation of compounds at quantum level, providing the information on both the structure and the dynamics [12]. Usually, the structure of molecule can be identified by utilising the NMR technique. Using ^{13}C NMR,

chemical shift from spectra allows to find the constitutional functional groups. After the observation of the chemical shift phenomena, Ramsey [13] discovered that the original difference for ^{13}C chemical shift arises from the electronic motions around the nucleus. The actual magnetic field experienced by nucleus will be modified by an additional magnetic field which was induced by the orbiting electrons. The shielding/deshielding concept is directly related to the electron density distribution within a molecule [14]. As more electrons surround the nucleus in motion, the extent of shielding will be greater. This terminology can be act as a theoretical basis for the identification of groups.

In SAFT-γ Mie group contribution approach, the selected groups are modelled as heteronuclear fused spheres which make up the molecular chain [15]. Each sphere gives a specific contribution towards the properties of molecules. The characteristics of functional groups are assumed to be independent of the molecular environment, therefore the functional groups' properties are transferable in different compounds [10]. For example, a CH_2 group in pentane will be treated in the same way as the CH_2 group in octane. Under this concept, the properties can be estimated in a quick way with a certain level of accuracy at a relatively low computational cost. Current SAFT-γ Mie equation of state (EoS) employ the criteria of identification for first-order group by Marrero and Gani (2001) [16] as building blocks for the molecules of interest [17]. Moreover, Hutacharoen et al. [18], adopted the group identification process by Wu and Sandler [2] for n-alkan-1-ols, the higher-order group CH_2OH is found to predict the pure component data more accurately than OH. This suggests that the higher-order groups may result in a more precise prediction. The origin for this achievement is due to the certain inclusion of electronic correlation effect between existing groups [2].

Current SAFT-γ Mie database constitutes 58 groups and is continuously expanding due to the growing attention and interest [17]. Enlarging the size of the database is always recommended since it not only allows the prediction of wider variety of molecules, but also it would improve the overall quality of predictions if higher-order groups are used.

Hence, the main aim of this work is to suggest the possible ways to improve the quality and accuracy of predictions by considering the chemical shift effect. Two means of improving the database will be discussed: improvement by optimising the existing groups' parameters for SAFT-γ Mie, and enlargement by introducing new higher-order groups. To achieve this, the sophisticated intramolecular effect will be correlated with current quality of estimation for certain groups.

2. Theory

2.1. Nuclear Magnetic Resonance (NMR)

Electrons and many nuclei have intrinsic spin angular moment which give rise to a magnetic moment and result in them behaving like bar magnets under an external magnetic field [19]. Figure 1 illustrates the nuclear motion in the absence/presence of external magnet field [20].

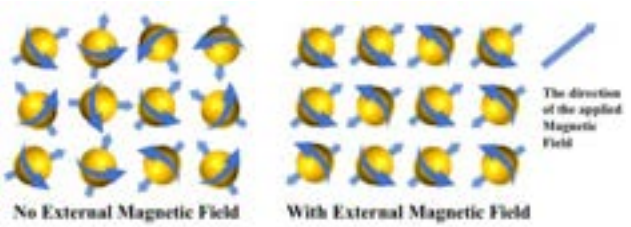

Figure 1. Illustration of nuclear spinning without/with external magnetic field. Yellow spheres represent the nuclei or electrons, and light blue arrows illustrate their centre axis of spinning [20].

The magnetic moment of an atom can be determined by its nuclear constitution. Usually, any odd and even combinations of protons and neutrons can generate magnetic moments and a half integer nuclear spin quantum number [19]. As a result, ^1H,^{13}C, and ^{15}N are usually used in this technique. Since the carbon-containing molecules are the major compounds of interest in the industry, ^{13}C NMR spectroscopy is investigated. For ^{13}C, there exists two spin states due to its magnetic moment, and the energies of these spin states depend on their orientation with respect to an applied magnetic field. When the electromagnetic radiation of the appropriate frequency is applied, the lower energy spin state absorbs the energy and resonant transitions can take place between two states [19]. This can be used to generate a signal, forming a peak in the resultant NMR spectrum.

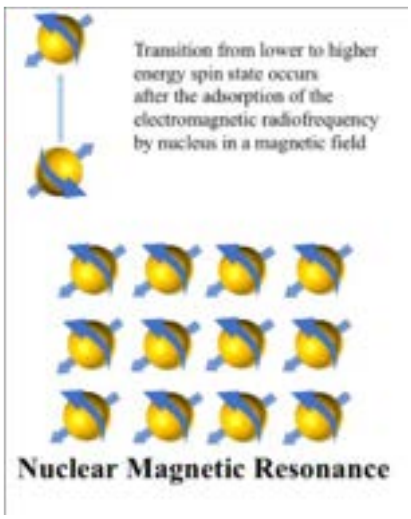

Figure 2. Nuclear magnetic resonance: when the transition from low energy to high energy spin state occurs after the adsorption of electromagnetic radiofrequency [20].

The most important features for NMR are the spin-spin coupling constant and the chemical shift. The splitting effect of the peak can be observed from the spectra and this can be explained by spin-spin coupling constants, which describe the interactions between the spinning nuclei. This phenomenon occurs frequently in ^1H NMR. However, due to the low natural abundance of ^{13}C, the possibility for having ^{13}Cs together is very low, so this can be neglected. Chemical shift (symbolised as δ) is defined as:

$$\delta=\frac{v-v^{\circ}}{v^{\circ}}\times 10^6 \text{ (ppm)} \qquad (1)$$

where v is the resonance frequency of interest and v° is the resonance frequency of a reference molecule. This δ scale

is independent to the applied field. The reference molecule typically used is $Si(CH_3)_4$, tetramethylsilane (TMS).

Since the first observation of the chemical shift [21] [22] [23] [24] [25] [26] [27] [28] , a lot of chemists devoted themselves to scientific investigations and exploited the phenomena as a powerful technique to identify the molecular environment. Grant et al. [23] developed a purely empirical relationship by linear regression analysis of the experiment shift data. Patterns were observed that the chemical shift can be described as a set of additive parameters. The additivity rule is given by:

$$\delta_C = K + n_\alpha A_\alpha + n_\beta B_\beta + n_\gamma C_\gamma + n_\delta D_\delta + n_\varepsilon E_\varepsilon + \sum S \quad (2)$$

where K is a constant given by the chemical shift of methane (-2.3ppm) [29], n_α, n_β, n_γ, n_δ, and n_ε represent the number of substituents having additive chemical shift parameters (in ppm) of A_α, B_β, C_γ, D_δ, and E_ε respectively and S is a branching effect parameter (in ppm). The chemical shift parameters for alkane are presented in Table 1. The notations α, β, γ, δ and ε indicate the position with respect to the target nucleus (or atom), e.g., α is a position with one chemical bond in between, and the carbon at α position will get affected by the A_α chemical shift parameter, etc. Graphical representation of the positional notations is shown in Figure 3.

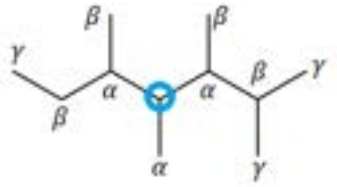

Figure 3. Illustration of a molecule with notations for each carbon. The notations are made with respect to the target atom of interest (blue circle).

Chemical Shift Parameters (ppm)				
A_α	B_β	C_γ	D_δ	E_ε
9.1	9.4	-2.5free rotation -6.5 eclipsed -0.4 anti	0.3	0.1

Table 1. Table of additive chemical shift parameters of carbon atoms in an alkane [29].

The original correlations were derived from alkanes initially [23], but similar trends were attainable from other organic compounds. Any organic compound can be described as a substituted molecule from parent molecule (alkane, alkene, etc) [29]. The parameters consider both the steric effect of molecular geometry and the distinct nature of the neighbouring substituents at different positions with respect to the carbon of interest. Since the conformational dependencies of the α and β substituent effects have not been investigated theoretically, usually these substituent effects are assumed to be independent of conformational arrangement [30]. The substituent γ effect is well studied which can be explained in terms of sterically induced polarization of the electrons of the C-H bond and conformation of the molecule. Moreover, the δ and ε position parameters are usually very small and thus can be neglected.

As Ramsey [13] mentioned, the circulating electrons around the nucleus induces an extra magnetic field. The actual magnetic field experienced by each nucleus contains both the applied and the induced magnetic field. The actual strength of magnetic field affects the energy difference between various spin states and the resulting chemical shift for a particular nucleus. Therefore, the actual nuclear resonance frequency is sensitive to the molecular environment of the nucleus. Moreover, shielding/deshielding concepts describe the local electronic distribution and it depends on the details of the local environment (proximity effect). In general, electron donating groups can increase the electron density at the nucleus, which shield the nucleus. Electron withdrawing groups result in strongly deshielded nuclei's large chemical shifts. Hence the shielding concepts are directly related to the chemical shift. By arranging the resonance condition in NMR [29] (Equations 3 and 4), the chemical shift thus can be expressed in terms of shielding constant (Equation 5). The equations are given by:

$$\Delta E = h\nu = \gamma_N \hbar B_{local} \quad (3)$$

$$\nu = \frac{\gamma_N B_{local}}{2\pi} = \frac{\gamma_N B_0(1-\sigma)}{2\pi} \quad (4)$$

$$\delta = \frac{(\sigma^o - \sigma)}{(1-\sigma^o)} \times 10^6 (ppm) \quad (5)$$

where ν is Larmor precession frequency (resonance frequency/NMR frequency), γ_N is nuclear magnetogyric ratio that its value depends on the identity of the nucleus and is determined empirically (the constant of proportionality), B_{local} and B_0 are magnitude of local and applied magnetic field strength respectively, σ is shielding constant of the nucleus, which is a dimensionless quantity, and σ^o is the shielding constant of a nucleus in a reference molecule.

From the theoretical approach, detailed analysis based on nuclear shielding are carried out based on semi-empirical and quantum chemical (ab initio) levels [31]. From using ab initio methods, the chemical shifts can be calculated from the corresponding wave functions [14]. It requires detailed knowledge of molecular orbitals. Linear combinations of perturbation-dependent atomic orbitals approximations are adopted to construct molecular orbitals in external magnetic field. The degree of accuracy for a particular ab initio method depends on the electron correlation effects and the gauge-independence problem [32]. In a semi-empirical method, the density functional theory is utilised to develop the equations based on the electron density. Both methods require intensive computational inputs and quantum chemical knowledge. The increasing complexity of large molecules increases the computational details and time substantially [33]. Therefore, it is necessary to exercise these methods with care and complement details further in the future. Despite the fascinating interpretations of theoretical approach, the actual applications limit to small molecules at current level. As a result, the fast and accurate empirical models continue to be a useful and active method for the prediction of chemical shift.

2.2. SAFT-γ Mie Equation of State

Statistical Associating Fluid Theory (SAFT) EoS adopts the model that considers molecules as linear chains of segments [15] [34]. Since the development of the SAFT EoS in

the 1980s, original SAFT model has been extended [17]. Different advanced versions of SAFT appeared, which are more accurate and realistic for scientific and engineering purpose. In this study, SAFT-γ Mie is used. Within the Wertheim's first order thermodynamic perturbation (TPT1) theory [35] [36] [37] [38], the heteronuclear molecular model can be developed by an equation of state via various relevant parameters which include the identities of the heteronuclear segments making up the molecules. In SAFT, the total Helmholtz free energy, A, of fluid is expressed as a summation of different contributions [15] [39] [40]:

$$\frac{A}{Nk_BT} = \frac{A^{ideal}}{Nk_BT} + \frac{A^{monomer}}{Nk_BT} + \frac{A^{association}}{Nk_BT} + \frac{A^{chain}}{Nk_BT} \qquad (6)$$

where N is the total number of molecules, k_B is Boltzmann's constant, T is the absolute temperature of the system, and A^{ideal}, $A^{monomer}$, A^{chain} and $A^{association}$ are the ideal gas, monomer, chain interaction and association contribution to the total Helmholtz free energy, A, respectively.

SAFT-γ Mie takes a group contribution approach, which the heteronuclear fused spheres make up the molecular chain and each sphere gives a specific contribution towards the total Helmholtz free energy, and subsequently the properties of the molecules.

The fused spheres interact via Mie potentials [41] of variable repulsive and attractive range. The interaction energy between two fused segments k and l can be expressed as following:

$$\Phi_{kl}^{Mie}(r_{kl}) = C_{kl}\varepsilon_{kl}\left[\left(\frac{\sigma_{kl}}{r_{kl}}\right)^{\lambda_{kl}^r} - \left(\frac{\sigma_{kl}}{r_{kl}}\right)^{\lambda_{kl}^a}\right] \qquad (7)$$

$$C_{kl} = \frac{\lambda_{kl}^r}{\lambda_{kl}^r - \lambda_{kl}^a}\left(\frac{\lambda_{kl}^r}{\lambda_{kl}^a}\right)^{\frac{\lambda_{kl}^a}{\lambda_{kl}^r - \lambda_{kl}^a}} \qquad (8)$$

where r_{kl} is the centre-to-centre separation of two segments, σ_{kl} is the segment diameter, ε_{kl} is the depth of the potential well, λ_{kl}^r and λ_{kl}^a are the repulsive and attractive exponents of the interaction between the segments respectively, and C_{kl} is a prefactor to ensure minimal interaction is $-\varepsilon_{kl}$.

Current group contribution method adopts a simplified representation of molecular structure which allows transferability. The fused heteronuclear molecules are broken down into several functional groups (monomer segments), where each functional group's characteristic is assumed to be independent of the molecular environment that the group stays. With this assumption, the properties can be estimated in a quick way with a certain level of accuracy and relatively low computational requirements.

The distinct parameters are estimated from appropriate experimental data using computational optimisation. The parameters that describe each functional group in the SAFT-γ Mie EoS are obtained by regression to pure-component vapor-liquid equilibrium data [15], i.e., vapor pressures (p_{vap}), and saturated liquid densities (ρ_{satliq}), as well as single-phase liquid density data (ρ_{liq}) for different temperatures and pressures. The unlike segment properties are obtained by means of combing rules and regression to experimental data [15].

Figure 4. Illustration of applying fused heteronuclear model to n-heptane. With the typical approach, the molecule can be devided into two methyl (CH_3) groups (orange spheres) and five methylene (CH_2) groups (green spheres) [42].

The performance of the SAFT-γ Mie prediction can be quantified by obtaining percentage average absolute deviation (%AAD) with respect to experimental data. The %AAD of a specific property *X* (%AADX) is given as:

$$\%AADX = \frac{1}{n_X}\sum_{i=1}^{n_X}\left|\frac{X_i^{exp} - X_i^{calc}}{X_i^{exp}}\right| \qquad (9)$$

where n_X is the total number of data points available of a property *X*, X_i^{exp} is the ith experimental value, and X_i^{calc} is the calculated (predicted) value for the same property at the same conditions with the ith experimental point. A low %AAD generally indicates high accuracy and reliability of corresponding groups' parameter sets.

3. Methods

According to the shielding/deshielding concept from NMR, the difference in the chemical shifts of various atoms originate from the difference in local electronic distributions around each nucleus, which can relate to the proximity/neighbouring effects that the presence of a particular functional group can modify the local environment and properties of its neighbouring groups. Also, the empirical additive relationships elucidate that the chemical shift of a carbon atom depends on the neighbouring atoms or groups, and these are assumed to be functioning mutually independent. Thus, the presence of a dissimilar heteronuclear atom or group as a neighbour will result in different extents of interaction and electronic correlation effects. When the electronic distribution over an atom is the same in different molecules or when the arrangement of atoms is completely synchronous in systems, the atomic contribution towards total energy and properties will be same [43]. Therefore, the deviation in the electronic interaction would result in the modification of the potential energy profile between the segments. Our analysis will be based on postulating that the electronic interaction will significantly affect the performance of current group contribution approach in SAFT-γ Mie.

Hence, a higher chemical shift, which indicates more sophisticated electronic correlation effects, with respect to a reference parent molecule will lead to lower accuracy of predictions of thermophysical properties. From this, a negative correlation between %AAD and chemical shift can be postulated.

The ^{13}C NMR spectra data used in this research are obtained from SpectraBase [44]. However, for the compounds without experimental ^{13}C NMR spectra data, the empirical additivity rule is applied to obtain the predicted chemical

shift values. Chemical shift values are all with respect to TMS and solvent are consistent in same family, these allow to minimise the external influence or variations towards the chemical shift [45]. As discussed before, there are two ways that can possibly improve the quality of predictions. The first way is to optimise the existing SAFT group parameters in the database. The second way is to develop new higher-order groups. We will discuss the both, in considerations of the chemical shift deviation, but using different term of defining it.

In this research, a "first-order group" is defined as the most basic functional group that could be used in the group contribution theory, such as CH_3, CH_2, OH and COOH. A "higher-order group" is defined as the combination of two or more first-order groups, such as CH_2OH and $CHOHNH_2$.

3.1. Optimisation for the existing groups

The estimation of SAFT parameters is done by minimising an objective function via computational process. However, since estimation does not give the exact minimum point, the estimation process requires continuous optimisation of the parameters. We define "the level of optimisation" of a group as the closeness of the group's SAFT parameters to the minimum. The level of optimisation of parameters is not easily measurable. It is very difficult to ascertain whether a group's parameters set is optimised to the same level as other groups'. In this work, the chemical shift term will be used to determine the comparative level of optimisation.

The existing SAFT-γ Mie model parameters for methyl (CH_3) and methylene (CH_2) group gave remarkably accurate predictions for unbranched alkane molecules from ethane to n-decane. The n-alkane family can be divided into the methyl and methylene functional groups according to current group contribution approach. Using the groups as building blocks, Papaioannou et al. [15] had reported average %AAD of 1.55% for vapour pressure, 0.59% for saturated liquid density and 0.59% for single phase liquid density, for n-alkane molecules from ethane to n-decane. Although higher order groups can also be developed, at this stage CH_3 and CH_2 are sufficient to describe the linear alkane family.

The molecules that will be discussed are substituted linear alkanes. The substituent effect is described as the replacement of a hydrogen atom by a different functional group or atom. The main functional group modifies the electronic environment of the nearest methyl or methylene group. The reference chemical shift data will be obtained from ^{13}C NMR spectra of parent alkane. For each carbon at child molecules, the deviation of the carbons' chemical shifts from corresponding parent molecules' carbons will be obtained. The chemical shift deviation would show the proximity effect from the functional groups, which would contain the information of the nature of the groups and the sensitivity for different neighbouring positions [29]. An example that illustrates the identification of the parent alkane and the positioning method is shown in Figure 5. The relative term is used in this study to examine the extent of changes in molecular environment with respect to the reference atom. Percentage relative chemical shift deviation at position # (%RCSD#) is defined as:

$$\%RCSD_{\#}=\frac{\left|\delta_{\#}^{child}-\delta_{\#}^{parent}\right|}{\delta_{\#}^{parent}}\times 100\ (\%) \qquad (10)$$

where $\delta_{\#}^{child}$ and $\delta_{\#}^{parent}$ are the chemical shifts of the carbons at position #, of the child molecule and the parent molecule, respectively.

To consider all the effects that a functional group would give to the molecules of interest, the term that would consider all the chemical shift deviation effects throughout the molecule should be used. Therefore, an average percentage relative chemical shift deviation will be used, where the average relative chemical shift deviation is obtained by averaging the relative chemical shift deviation among all carbons to examine the effect of a functional group towards the whole molecule.

According to our postulations, theoretically, a positive correlation is expected to exist between the average percentage relative chemical shift deviation and the %AAD, if every SAFT group parameters are optimised to the same level. The level of optimisation will be examined by comparing the result to the theory.

Figure 5. A simple representation for the identification of the parent alkane and positioning order for linear substituted alkane, for 1-pentanol, pentylamine and hexanoic acid. They all have the same parent alkane, pentane. Acknowledging that both SAFT-γ Mie and additivity rule considers carboxyl group (COOH) as a separate group, the carbon inside carboxyl group (COOH) of carboxylic acid molecules will not be included in the carbon chain length counts nor in the relative chemical shift deviation calculations. Position 1 denotes the first neighbouring carbon atom of the functional group, similarly, position 2 represent the second neighbouring carbon atom and so on. In these cases, OH, NH_2, COOH are the main functional groups. A_{α}, B_{β}, C_{γ}, D_{δ}, and E_{ε} represent the other carbon position notation with respect to the functional group.

3.2. Introducing higher-order groups

The second way to improve the quality of prediction is introducing and developing new higher-order groups. Adding new higher-order groups to the database is always beneficial, but estimating the parameters takes lots of time and effort. Therefore, it is required to determine the priorities of higher-order groups to be developed.

The effectiveness of making higher-order groups in terms of the chemical shift effect would be discussed in this section. Comparison between empirical parameters with respect to parent alkane gives an initial indication for the needs of defining new groups. The parameters will be obtained either from literature or by calculating manually. The three groups of interest will be considered primarily in this research: amine (NH_2), carboxyl (COOH), and hydroxyl (OH). In this study, we will examine only the molecules with a linear carbon chain with a functional group at an end of the chain, to remove any possible uncertainties that could come from using branched molecules or polyfunctional molecules.

4. Results

4.1. SAFT Parameters Optimisation Suggestions

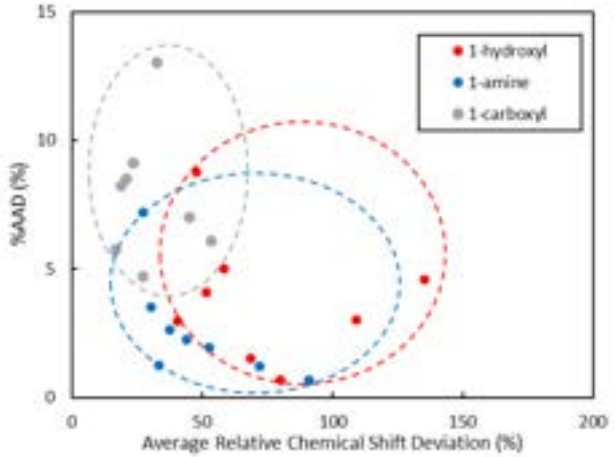

Figure 6. Plots of the percentage average absolute deviation (%AAD) of vapour pressure (p_{vap}) prediction using the SAFT-γ Mie EoS against the ^{13}C NMR average percentage relative shift deviation, of 1-hydroxyl molecules (red circles), 1-amine molecules (blue circles) and 1-carboxyl molecules (grey circles). Each point represents a molecule, from $CH_3(CH2)_2Y$ to $CH_3(CH_2)_9Y$, where Y is group of interest. Dotted lines are the guide-lines showing the clustered area of each group.

Figure 6 is a graph of %AAD against average relative chemical shift deviation. For each group, a cluster of data points can be observed on the figure, which is marked with a dotted-line circle.

The range of %AAD shows the level of optimisation of parameters. Moreover, the % average relative shift deviation is clustered within a certain range for each group. The molecules plotted on Figure 6 are all unbranched linear carbon chain molecules from $CH_3(CH_2)_2Y$ to $CH_3(CH_2)_9Y$, with the groups of interest placed at the end of each carbon chain, where Y is a group of interest. The analysis is done for CH_3CH_2Y molecules as well, but they had significantly high % average relative shift deviations due to the low reference chemical shifts of the parent alkane, ethane. Hence, for a clear visualisation of the cluster regions, the ethane-based molecules were removed from the graph. The significantly high relative chemical shift deviation of ethane-based molecules is shown as in Figure 7.

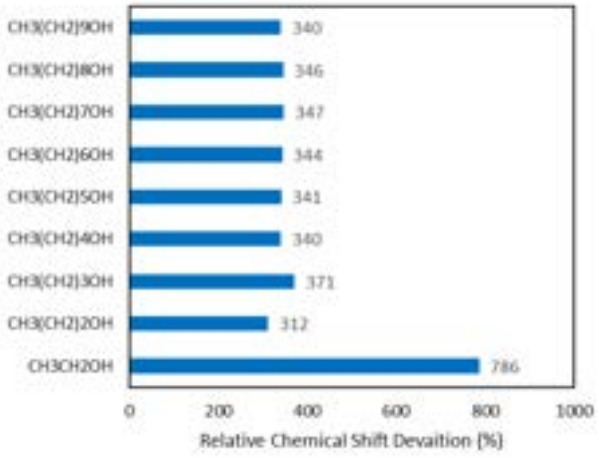

Figure 7. Bar chart of the relative chemical shift deviation of the nearest carbon 1-hydroxyl molecules from CH_3CH_2OH to $CH_3(CH_2)_9OH$.

Group	Chemical Shift Parameter (ppm)				
	A_α	B_β	C_γ	D_δ	E_ε
OH	48.3	10.2	-5.8	0.3	-
COOH	21.5	2	-2.5	0.6	0.5
NH_2	29	11.4	-4.6	0.6	0.5

Table 2. ^{13}C NMR Chemical shift parameters for different functional group towards different neighbouring carbons [29].

A_α, B_β, C_γ, D_δ, and E_ε parameters represent the strength of a functional group towards different neighbouring carbons. However, in most of the cases, δ and ε are negligibly small. Accordingly, only the first three carbons would have a meaningful chemical shift deviation, while the others will have chemical shift deviation of around zero. Therefore, for unbranched linear carbon chain molecules with a chain length larger than or equal to three (when the functional group is at the end of molecule), the sum of chemical shift effect from one group is about the same with the sum of its α, β and γ chemical shift parameters.

Furthermore, a shorter-chained molecule will have a higher average relative chemical shift deviation, and as the chain gets longer, the average relative chemical shift deviation will converge to zero. The convergence explains the clustering of data points in terms of relative chemical shift deviation. The sum of chemical shift parameters is different for each group, which leads to the data points of molecules with a certain group getting clustered within certain area.

Although Figure 6 plots the %AAD of vapour pressure, this pattern also appears on that of saturated vapour density and saturated liquid density which can be found in the section D of supplementary information.

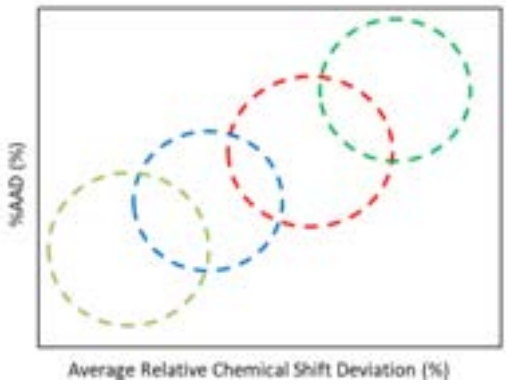

Figure 8. Illustration of the expected trend between the percentage average absolute deviation (%AAD), and the average relative chemical shift deviation of different molecules. The coloured dotted lines are the area where the clusters of data are positioned for each group, where different colours represent different groups.

As explained previously, a positive correlation is expected between average relative chemical shift deviation and %AAD, if every groups have the same level of optimisation for their SAFT parameters. Therefore, the clusters of data points of different groups are expected to appear as shown in Figure 8.

As shown on Table 2, the sum of the absolute value of chemical shift parameters of hydroxyl (OH) group is the highest among the groups of interest, and carboxyl (COOH) has that of the lowest. As a result, as shown on Figure 6 by

the cluster regions, hydroxyl group had the right-most cluster region, and carboxyl group had the left-most cluster region.

According to the sum of the chemical shift effects from each group, the expected trend is hydroxyl (OH) group having the highest %AAD in general, followed by amine (NH_2) and carboxyl group (COOH). However, for vapour pressure, carboxyl group had the highest AAD in general as shown on Figure 6, followed by hydroxyl and amine group. Therefore, carboxyl is the group that is "out of expectation". This suggests that carboxyl group's SAFT parameters are not optimised as enough as other groups' parameters.

The analysis and graph plotting are done with %AAD of saturated vapour density and saturated liquid density, and the resultant graphs are provided in supplementary information section. To consider the %AAD of each group with a more objective standard, the average %AADs of each property for each family are obtained as shown in Table 3.

Family	Mean-%AAD (%)		
	p_{vap}	ρ_{satliq}	ρ_{satvap}
1-hydroxyl	3.69	2.49	6.97
1-amine	2.40	1.19	8.10
1-carboxyl	9.52	0.94	10.09*

Table 3. Mean Percentage Average Absolute Deviation (Mean %AAD) of vapour pressure (p_{vap}), saturated liquid density (ρ_{satliq}), and saturated vapour density (ρ_{satvap}) by families, from CH_3CH_2Y to $CH_3(CH_2)_9Y$, where Y is the group of interest. For 1-carboxyl, the saturated vapour density data are only available from heptanoic acid ($CH_3(CH_2)_5COOH$) to undecanoic acid ($CH_3(CH_2)_9COOH$), and the red star is used as the indication of this.

The average %AAD of saturated liquid density of each family is in the right order of what is expected: carboxyl the lowest, and hydroxyl the highest. However, that of saturated vapour density is in the opposite order of what is expected: carboxyl the highest, and hydroxyl the lowest.

Theoretically, carboxyl is expected to have the lowest average mean-%AAD for any property, but it has the highest average %AAD on saturated vapour density and vapour pressure. Although it has the lowest average %AAD on saturated liquid density, the unexpectedly high mean-%AADs on saturated vapour density and vapour pressure indicate that carboxyl group requires further optimisation of SAFT parameters.

Using the same approach, the level of optimisation can be compared between different groups by analysing their %AAD and their average relative chemical shift deviation simultaneously. For example, because hydroxyl group's chemical shift parameters are higher than that of amine group, even after the same level of optimisation, hydroxyl group is expected to have a generally higher average %AAD compared to amine group. However, if a group (carboxyl in this case) is "out of expectation" and has an unexpectedly high %AAD considering its chemical shift deviation, this means the group's level of optimisation of SAFT parameters is generally lower than the other groups, and hence further optimisation is needed.

To make comparisons, "benchmark/reference groups" would be required. Benchmark groups should be highly optimised to give sufficiently accurate predictions. Using these groups' mean-%AAD values as the standards, the groups that require further SAFT parameters optimisation can be determined by comparisons.

We recommend amine (-NH_2) group and hydroxyl (-OH) group as the possible benchmark groups. They have considerably low %AADs for the properties we examined: vapour pressure, saturated liquid density, saturated vapour density. By comparing a group with the two benchmark groups, it will be able to determine the proper position of the group's cluster region, and the predicted order of mean-%AADs. This will suggest whether the group would require further optimisation of SAFT parameters or not.

4.2. Higher-order Groups Suggestions

From molecular approach, using higher-order groups are expected to be more representative for distinct molecular environment. Thus, more accurate predictions are obtainable by using higher-order groups rather than first-order groups. Usually, introducing a new higher-order group is done when the existing corresponding first-order groups do not give sufficiently good predictions for some molecules even after the optimisation of the SAFT parameters. One of the reasons of inaccurate predictions could be due to a significant electronic correlation between two first-order groups.

In this study, we will define a "second-order group" as a higher-order group that consists of two first-order groups. There are two main reasons why only the second-order groups would be considered. First, a higher-order group with too many first-order groups inside will lose transferability [16]. This kind of group would have a limited number of molecules that will benefit from defining such group. Second, the A_α parameter is often the largest contributing chemical shift parameter. The explanation for the significance of this would be provided later in this section.

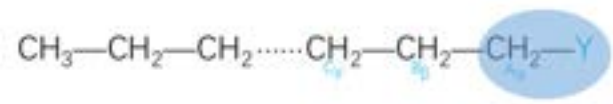

Figure 9. Simple illustration of a second-order group, CH_2Y (blue oval), in a molecule. The symbols below each carbon (light blue) are the chemical shift parameters that the carbons will be affected by.

We will primarily consider the CH_2-Y second-order group, where Y is a group of interest. After defining and developing the second-order group CH_2Y, the electronic correlation effect represented by A_α parameter of group Y will stay inside the newly defined second-order group. However, the other chemical shift effects, such as B_β, will remain. As a result, the only chemical shift effect that will disappear by defining the second-order group would be A_α chemical shift. Similarly, the benefit from developing CH_2CH_2Y would be the removal of chemical shift effects from A_α and B_β parameters.

However, as shown in Table 3, the highest chemical shift parameter for most of the groups is the A_α parameter. Also, there often exists a significant difference between A_α parameter and B_β parameter. Therefore, removing B_β

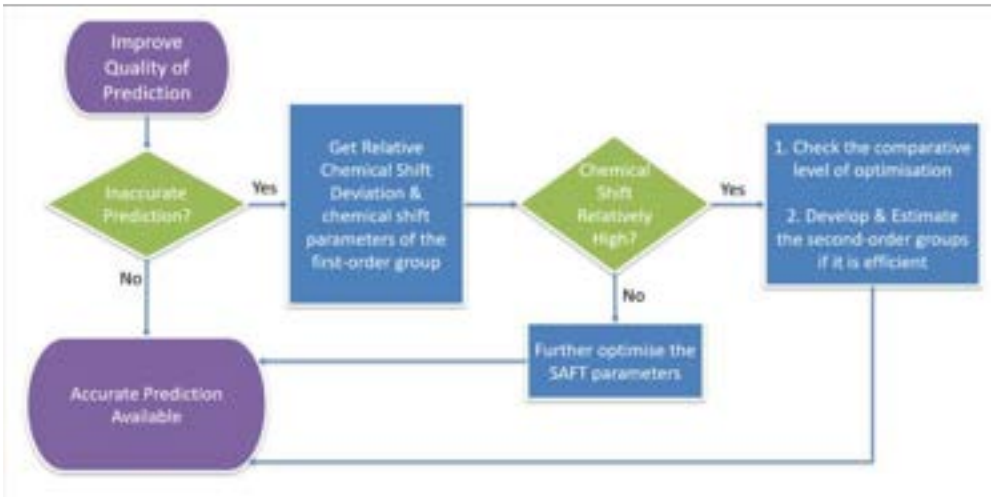

Figure 10. An overall flowchart of the heuristic method suggested in this work, to improve the SAFT-**γ** Mie database.

parameter will not be as efficient as removing A_α parameter, which gives less motivation of developing higher-order groups than second-order groups.

Therefore, for efficiency, it is recommended to develop second-order groups prior to developing any other higher-order groups. Unless a functional group has a considerably high B_β parameter, it would be inefficient to develop third-order groups or higher.

Accordingly, for development of the new second-order groups, only A_α parameters will be compared between different groups. Among the groups of interest, the group with the highest α parameter is hydroxyl group (OH). Hence, it is recommended the most to develop the second-order groups that contain hydroxyl group inside. However, the current SAFT-γ Mie database already provides some hydroxyl second-order groups such as CH_2OH and CHOH [18]. The next recommended group would be amine group, as it has the second highest α parameter among the groups of interest. Second-order groups, such as CH_2NH_2, $CHNH_2$, etc., can be defined in the future to improve the accuracy of prediction of some molecules, especially those with high relative chemical shift deviation. For carboxyl group, this process is recommended the least, and it is more recommended to optimise the parameters before defining related second-order groups.

The groups with high A_α chemical shift parameters should be prioritised to define and estimate related second-order groups. However, this only applies when the first-order groups are optimised to the same level. If one is considered to be not as optimised as other groups, it is more recommended to optimise the group than to develop second-order groups.

4.3. General Heuristic Method

Combining the two approaches introduced, a general heuristic method is proposed as following.

First, one should decide the group of interest and the linear carbon chain molecules (molecules of interest) that contain the group. The %AAD of each property for the molecules should be calculated to determine the accuracy of prediction. Then, the ^{13}C NMR spectra data for the molecules of interest and corresponding parent alkane molecules should be collected in order to obtain the average relative chemical shift deviation of the molecules and the chemical shift parameters of the group of interest. By this, it would be able to compare %AAD and average relative chemical shift deviation simultaneously with other groups.

The comparative level of optimisation of the group can be obtained at this stage. If the level of optimisation is lower than other groups, a further optimisation process of the group's SAFT parameters would be recommended. However, if the group's SAFT parameters are already highly optimised, then the group's A_α chemical shift parameter should be compared to determine the effectiveness of defining the second-order groups that contain the group of interest.

Finally, if it is decided that defining the second-order groups will effectively improve the quality of prediction, the A_α chemical shift parameter of the group of interest can be compared with that of other groups', to determine the priority for developing second-order groups.

The flowchart of the general heuristic method is shown in Figure 10.

5. Conclusion and Discussion

A study of connecting ^{13}C NMR spectroscopy with SAFT-γ Mie equation of state (EoS) was done to improve the quality of prediction. The chemical shift in ^{13}C NMR spectroscopy was investigated by empirical approach. It was postulated that the proximity effect and electronic correlation is observable via the chemical shift. This had naturally led to using the chemical shift to determine the nature of functional groups and the sensitivity of neighbouring carbons towards the effect.

From this approach, a high chemical shift effect of a functional group means the group is affecting its neighbouring carbons largely. Therefore, this would cause an unexpectedly high intensity of interaction, which would cause an inaccuracy of prediction of thermophysical properties using SAFT-γ Mie EoS. As a result of this effect, a negative correlation between the accuracy of prediction and the chemical shift effect was expected. To quantify the accuracy of prediction, percentage average absolute deviation (%AAD) was obtained for each thermophysical property for each molecule. Also, to determine the chemical shift effect specifically from the functional groups, the chemical shift deviation term was defined and obtained. Since high %AAD means a low accuracy of prediction, resultantly, a positive correlation was expected between %AAD and chemical shift deviation.

Utilising this to improve the quality of prediction using SAFT-γ Mie EoS, two heuristic methods were introduced. The methods were followed with the groups of interest: carboxyl (COOH), hydroxyl (OH), and amine (NH_2). As a result of applying the heuristic methods to the linear carbon chain molecules with a group of interest at their ends of the chain, two suggestions were made according to each heuristic method.

The first heuristic method was a method to determine the level of optimisation comparatively. The expectation is that %AAD should have a positive correlation with chemical shift deviation. Therefore, by comparing the %AAD of different groups, if a group has an unexpectedly high %AAD, it will mean that the group would require further optimisation of its SAFT parameters. To examine the groups of interest, the graph of %AAD against the average relative chemical shift deviation was plotted, and a cluster of data points was observable for each group. The general position of the groups on the graph was shown by the region of the clusters. To analyse this with a more objective measure, mean-%AAD of each property (vapour pressure, saturated liquid density, saturated vapour density) for each group was obtained. The mean-%AAD values were compared simultaneously with the average relative chemical shift deviation to find out the data that were "out of expectation". Carboxyl group had unexpectedly high mean-%AAD on vapour pressure and saturated vapour density, and therefore it was able to conclude that carboxyl is the group that is recommended the most among the groups of interest, to further optimise the SAFT parameters. Moreover, for comparative determination, the need of "benchmark/reference groups" was mooted, which are supposed to have highly optimised SAFT parameters. The recommended benchmark groups were amine and hydroxyl, since they had considerably low %AAD and were optimised continuously over years.

The second heuristic method was made to give suggestions on the selection process of defining new second-order groups. In this research, a second-order group means a group that is consisted of two first-order groups. This process was done by comparisons too, where the A_α chemical shift parameters from the groups of interest were compared. From qualitative analysis, it was discovered that defining second-order groups would only result in removing the chemical shift effect of α position of carbon with respect to the functional group. Also, a higher-order groups with more than two first-order groups inside were considered to be not transferable and inefficient. Due to these considerations, it was concluded that the functional group with a relatively higher A_α chemical shift parameter should be considered with a higher priority to develop corresponding second-order groups. Among the groups of interest, although hydroxyl had the highest A_α chemical shift parameter, since it already had the second-order groups in the database such as CH_2OH and CHOH, amine was recommended as the next group to develop its second-order groups such as CH_2NH_2 and $CHNH_2$.

However, the direct linkage between the chemical shift and quality of estimation remains a challenge due to the uncertainties of the level of optimisation processes for obtaining model parameters. Due to absence of higher order groups in current SAFT-γ Mie database, qualitative analysis and possible suggestions were carried out at this stage only.

The study of NMR is still an active area especially at the quantum chemical level which may provide a more theoretical based guidance for the group selection. In this study, solvent, temperature, steric phase state and conformational effects towards the chemical shift are not considered [31]. Therefore, the ^{13}C NMR analysis may not be accurate enough. Similarly, it is also possible to interpret molecular environment through different spectra (Ramen, Infrared) in combinations NMRs for different atoms.

On the other hand, the prediction of thermophysical properties using SAFT was done only for vapour pressure, saturated liquid density, and saturated vapour density. Further research can be done with more various properties, and this would give much broader information for comparison. Molecules with linear carbon chain with 2 to 10 carbons (except the C inside the COOH group, for carboxyl molecules) were taken into account only, due to the quality issue on predicting the thermophysical properties of branched molecules. Moreover, indistinguishing isomers are not addressed in this work.

This research had suggested two heuristic methods that would aid to make qualitative interpretation on some factors that could significantly affect the accuracy of predictions using SAFT-γ Mie equation of state (EoS). Although the approach might not tell everything about the group contribution theory, it will offer a useful guide to some key decisions.

6. References

[1] J. M. P. J. P. O. Bruce E. Poling, The Properties of Gases and Liquids, Fifth Edition-McGraw-Hill Professional, 2000.

[2] S. S. Wu HS, "Use of ab initio quantum mechanics calculations in group contribution methods. 1. Theory and the basis for group identifications," Industrial & engineering chemistry research, vol. 30, no. 5, pp. 881-889, 1991.

[3] Z. Kolská, M. Zábranský and A. Rando, "Group Contribution Methods for Estimation of Selected Physico-Chemical Properties of Organic Compounds," in Thermodynamics - Fundamentals and Its Application in Science, Ricardo Morales-Rodriguez, IntechOpen, 2012.

[4] E. Baum, Chemical Property Estimation: Theory and Application, CRC Press, 2018.

[5] B. SW，, "III-Bond energies," Journal of Chemical Education, vol. 42, no. 9, p. 502, 1965.

[6] E. P.-F. J Marrero-Morejón, " Estimation of pure compoundproperties using group-interaction contributions," AIChE Journal, vol. 45, p. 615–621, 1999.

[7] A. L. Lydersen and Engineering Experiment Station, Estimation of critical properties of organic compounds by the method of group contibutions, Madison University of Wisconsin , 1955.

[8] K. G. Joback, "A unified approach to physical property estimation using multivariate statistical techniques," Massachusetts Institute of Technology, 1984.

[9] K. Joback and R. Reid, "Estimation of Pure-Component Properties from Group-Contributions," Chemical Engineering Communications, vol. 57, no. 1-6, pp. 233-243, 1987.

[10] L. Constantinou and R. Gani, New Group Contribution Method for Estimating Properties of Pure Compounds, AIChE Journal October 1994 Vol. 40, No. 10, 1994.

[11] J. Vijande, M. M. Pineiro and J. L. Legido, Group-Contribution Method for the Molecular Parameters of the PC-SAFT Equation of State Taking into Account the Proximity Effect. Application to Nonassociated Compounds, Ind. Eng. Chem. Res. 2010, 49, 9394–9406, 2010.

[12] B. Plainchont, P. Berruyer, J.-N. Dumez, S. Jannin and P. Giraudeau, Dynamic Nuclear Polarization Opens New Perspectives for NMR Spectroscopy in Analytical Chemistry, Analytical Chemistry 2018 90 (6), 3639-3650, 2018.

[13] N. Ramsey, “Magnetic shielding of nuclei in molecules,” Physical Review, vol. 78, pp. 699-703, 1950.

[14] F. J. C., “Calculations of Chemical Shieldings: Theory and Applications,” Wiley Periodicals, Concepts Magnetic Resonance Part A 20A, pp. 42-69, 2004.

[15] T. L. C. A. C. S. A. G. J. E. A. M. A. G. Papaioannou Vasileios, “Group contribution methodology based on the statistical associating fluid theory for heteronuclear molecules formed from Mie segments,” he Journal of chemical physics, vol. 140, no. 054107, 2014.

[16] J. Marrero and Rafiqul Gani, Group-contribution based estimation of pure component properties, Fluid Phase Equilibria 183–184 (2001) 183–208, 2001.

[17] “Expanding the Applications of the SAFT- Mie Group-Contribution Equation of State: Prediction of Thermodynamic Properties and Phase Behaviour of Mixtures,” Department of Chemical Engineering, Centre for Process Systems Engineering, Imperial College London, London, 2020.

[18] D. S. P. V. S. R. A. C. J. G. G. A. Hutacharoen P, “Predicting the Solvation of Organic Compounds in Aqueous Environments: From Alkanes and Alcohols to Pharmaceuticals,” Industrial & Engineering Chemistry Research, vol. 56, no. 38, pp. 10856-10876, 2017.

[19] J. d. P. J. K. Peter Atkins, “Atkins’ Physical Chemistry,” Oxford University Press, 2018, pp. 488-529.

[20] A. T. V. E. K. B. Ioannis P. Gerothanassis, “Nuclear Magnetic Resonance (NMR) Spectroscopy: BASIC Principles And Phenomena, and their applications to chemistry, Biology and Medicine,” Chemistry Education : Research And Practice In Europe, vol. 3, no. 2, pp. 229-252, 2002.

[21] Y. F. C. Proctor W. G., “The Dependence of a Nuclear Magnetic Resonance Frequency upon Chemical Compound,” Phys. Rev., vol. 77, no. 5, p. 717, 1950.

[22] D. W.C., “Dependence of the 19F Nuclear Resonance Position on Chemical Compound,” Phys. Rev., vol. 77, p. 736, 1950.

[23] P. E. Grant D.M., “Carbon-13 magnetic resonance. II. Chemical shift data for the alkanes,” Journal of the American Chemical Society, vol. 86, no. 15, pp. 2984-2990, 1964.

[24] G. D. M. Dalling D. K., “Carbon-13 magnetic resonance. IX. Methylcyclohexanes,” Journal of the American Chemical Society, vol. 89, no. 25, pp. 6612-6622, 1967.

[25] G. D. Litchman WM, “Carbon-13 magnetic resonance. XI. Structural and electronic effect on the carbon-13 nuclear magnetic resonance spectra of the halogen-substituted methanes,” Journal of the American Chemical Society, vol. 90, no. 6, pp. 1400-1407, 1968.

[26] Z. B. Somayajulu GR, “Effect of nonbonded interactions on the carbon-13 chemical shifts and diamagnetic susceptibilities of halomethanes,” Journal of Magnetic Resonance , vol. 30, no. 1, pp. 51-58, 1969.

[27] G. D. P. E. Dalling DK, “Carbon-13 magnetic resonance. XXIII. Methyldecalins,” Journal of the American Chemical Society, vol. 95, no. 11, pp. 3718-3724, 1973.

[28] J. P. Smith DH, “Prediction of carbon-13 nuclear magnetic resonance chemical shifts,” Journal of the American Chemical Society, vol. 100, no. 11, pp. 3316-3321, 1978.

[29] W. V. E. Breitmaier, Carbon-13 NMR Spectroscopy- High-Resolution Methods and Applications in Organic Chemistry and Biochemistry, Gordon & Breach Science Pub , 1987.

[30] S. H. Y. Michael Barfield, “Ab Initio IGLO Studies of the Conformational Dependencies of alpha-, beta-, and gamma-Substituent Effects in the 13C NMR Spectra of Aliphatic and Alicyclic Hydrocarbons,” J. Am. Chem. Soc, vol. 112, pp. 4747-4758, 1990.

[31] R. S. Prigogine I, Advances in Chemical Physics, Vol.123, Wiley, 2002.

[32] J. Vaara, “Theory and computation of nuclear magnetic resonance parameters,” The Journal of Physical Chemistry, vol. 9, p. 5399–5418, 2007.

[33] S. R. W. Widdifield Cory M., “Understanding Chemical Shielding Tensors Using Group Theory, MO Analysis, and Modern Density-Functional Theory,” Concepts in Magnetic Resonance Part A, vol. 34, pp. 91-123, 2009.

[34] P. V. S. M. P. T. C. A. A. C. J. G. G. A. Dufal S, “Prediction of thermodynamic properties and phase behavior of fluids and mixtures with the SAFT-γ Mie group-contribution equation of state,” Journal of Chemical & Engineering Data, vol. 59, no. 10, pp. 3272-3288, 2014.

[35] W. M.S., “ Fluids with highly directional attractive forces. IV. Equilibrium polymerization,” Journal of statistical physics, vol. 42, pp. 477-492, 1986.

[36] W. MS, “Fluids with highly directional attractive forces. I. Statistical thermodynamics,” Journal of statistical physics, vol. 35, pp. 19-34, 1984.

[37] W. MS, “Fluids with highly directional attractive forces. II. Thermodynamic perturbation theory and integral equations,” Journal of statistical physics, vol. 35, pp. 35-47, 1984.

[38] W. MS, “Fluids with highly directional attractive forces. III. Multiple attraction sites,” Journal of statistical physics, vol. 42, pp. 459-476, 1986.

[39] G. K. J. G. R. M. Chapman WG, “. SAFT: Equation-of-state solution model for associating fluids,” Fluid Phase Equilibria, vol. 52, pp. 31-38, 1989.

[40] G. K. J. G. R. M. Chapman WG, “New reference equation of state for associating liquids,” Industrial & engineering chemistry research, vol. 19, no. 8, pp. 1709-1721, 1990.

[41] M. G., “Zur kinetischen Theorie der einatomigen Körper,” Annalen der Physik, vol. 316, no. 8, pp. 657-697, 1903.

[42] N. C. f. B. Information., “"PubChem Compound Summary for CID 8900, Heptane" PubChem,,” [Online]. Available: https://pubchem.ncbi.nlm.nih.gov/compound/Heptane. [Accessed 14 12 2020].

[43] M. T. C. J. R. C. a. C. C. Richard F. W. Bader, “Properties of atoms in molecules: atomic volumes,” Journal of the American Chemical Society, vol. 109, no. 26, pp. 7968-7979 , 1987.

[44] J. W. &. Sons, “SpectraBase,” 8 12 2020. [Online]. Available: https://spectrabase.com/.

[45] J. C. Facelli, “Chemical shift tensors: Theory and application to molecular structural problems,” Progress in Nuclear Magnetic Resonance Spectroscopy, vol. 58, pp. 176-201, 2011.

[46] W. G. M. E. P. J. Linstrom, “NIST Chemistry WebBook, NIST Standard Reference Database Number 69 (National Institutes of Standards and Technology WebBook, Gaithersburg MD, 20899,” [Online]. Available: http://webbook.nist.gov/.

[47] L. J. G.M. Wilson, “Critical Constants Tc, Pc, Estimation Based on Zero,First and Second Order Methods,” in AIChE Spring Meeting, New Orleans, LA, 1996.

[48] R. G. Jorge Marrero, “Group-contribution based estimation of pure component properties,” Fluid Phase Equilibria, Vols. 183-184, pp. 183-208, 2001.

[49] C. d. D. Jameson, “Theoretical and physical aspects of nuclear shielding,” Nuclear Magnetic Resonance an Specialist Periodical Reports, The Royal Chemical Society, pp. 68-93, 2009.

[50] C.J. Jameson, Isotope effects on chemical shifts and coupling constants, in: D.M. Grant, R.K. Harris (Eds.), Encyclopedia of Magnetic Resonance, Chichester: John Wiley & Sons, 1996.

[51] G.-V. A. J. G. Davies LA, “Describing the properties of chains of segments interacting via soft-core potentials of variable range with the SAFT-VR approach,” International journal of thermophysics, vol. 19, pp. 675-686, 1998.

[52] A. C. J. G. G. A. Lymperiadis A, “A generalisation of the SAFT-γ group contribution method for groups comprising multiple spherical segments,” Fluid Phase Equilibria, vol. 274, pp. 85-104, 2008 .

Computational Investigation on Lipid-Polymer Interactions and Intracellular Delivery for Novel Pseudopeptic Polymers

Yuxin Liu and Nicolas Yiakoumi

Department of Chemical Engineering, Imperial College London, South Kensington Campus, London, SW7 2AZ, United Kingdom

Abstract: The pharmaceutical industry has been utilizing pseudopeptides to coat viral-mimicking liposomal systems. Pseudopeptides constructed by a poly(L-lysine isophthalamide) backbone are potential drug delivery candidates due to their membrane lysis ability at different pH. A computational analysis was carried out on 16-mer polymer chains with L-phenylalanine grafted side chain at different grafting ratios, to gain a deeper understanding of these polymer species. The investigation seeks to analyse the interactions of these polymers with a dipalmitoyl phosphatidylcholine (DPPC) lipid bilayer used as a model for the liposomal membrane. 75% L-phenylalanine grafted side chain on the PLP backbone (PP75) created the strongest polymer-membrane interactions after 150 ns of all atom molecular dynamic simulation, causing a 48% reduction in membrane thickness, with the highest area per lipid value of 0.96 (nm^2) observed and an average of 4.93 Hydrogen bonds formed between the polymer and DPPC. Umbrella sampling technique was used to pull calcein, a hydrophilic drug, towards the DPPC in two separate configurations to mimic the polymers' drug releasing and loading capabilities. Protonated PP75 16-mer outperforms PP50 in inducing drug release and loading into the DPPC membrane as it requires a smaller potential mean force difference to push calcein from its stabilised position to a location 1nm away from the DPPC centre.

1. Introduction

The administration of drugs and vaccines is a huge and vital market for pharmaceutical companies but has proven challenging over the years. This sector has greatly benefited from the general use of synthetic polymers up to this date[1]. The range of synthetic polymers used in this sector spans from poly(ethylene glycol) (PEG)[2], used by the pharma industry in plasticizers, up to Poly(amino acids)[3–7] used for the formation of micelles and liposomes. Recent advancements in modern technology, have enabled the pharmaceutical industry to utilize liposomal nanocontainers to replace the viral envelope that has been traditionally being used for RNA transfer into organisms[8]. Messenger RNA (mRNA) and short interfering RNA (siRNA) have shown to cure triple negative breast cancer, demonstrating the importance and potential success of these molecules[9]. Polymers have been used by the research community in this field to coat the liposome. The function of these polymers is to mimic the viral spikes, present on the virus cell, so as to enable interactions with the human cell membrane and allow the liposomal structure to undergo endocytosis[10]. Despite continuous advancements in this field, the efficient transport and delivery of the payload encapsulated inside the liposomal nanocontainer to intracellular sites, such as the cytoplasm still poses a significant challenge to the scientific community[11].

Researches have been looking into non-viral vectors as opposed to the much more promising viral ones due to safety concerns and impending struggles of scaling up such systems. The development of multifunctional liposomes with efficient cytoplasmic drug delivery is currently high in demand. Research has been carried in obtaining pH-sensitive liposomal systems by coating the surface of the liposome with fusogenic peptides, to better mimic the release mechanism of the drug payload into the cytoplasm by the liposome system[12]. Recently a group of biocompatible pseudopeptides has emerged, that effectively mimics both the structure and pH-responsive metastabilizing ability of influenza viral peptides. This parent pseudopeptide is poly(l-lysine iso-phthalamide) (PLP)[13,14]. Using the parent pseudopeptide, polymers of different grafting ratios can be constructed. PP50 refers to a polymer that has 50% stoichiometric degree of substitution with L-phenylalanine on the PLP backbone.

There is limited research concerning computational molecular dynamics simulations in this sector, as this is an emerging field, influenced heavily by the advancements of computational capabilities made possible by the scientific and software community. Sivaramakrishnan Ramadurai et al have investigated computationally the effect of the PP50 polymer with 1,2-dioleoyl-sn-glycero-3-phosphocholine phospholipid bilayer (DOPC) membrane at different pH to model the polymer's ability to become protonated and deprotonated with changing pH[15]. Shuzhe Wang and Fernando Bresme analysed and evaluated free energy changes upon polymer permeation through a dipalmitoyl phosphatidylcholine (DPPC) lipid bilayer membrane using both protonated and deprotonated monomers to create 5-mer polymers of 0% and 100% grafting ratios[16]. Gullia Rocci and Luca Monticelli carried out a research on polymer nanoparticles interactions with a phospholipid membrane to look into membrane thinning and insertion mechanisms[17].

The computational investigation carried out in this paper, seeks to achieve an analysis for the PLP polymers with different grafting ratios and a linear backbone. The goal was to examine and identify the

best grafting ratio to be used for efficient drug release, inducing endocytosis and optimizing the drug loading procedure. Building on Shuzhe Wang and Fernando Bresme work[16], the polymers to be used in this investigation contained a 16 monomer linear backbone chain, formulated solely from either the protonated or the deprotonated monomers. Continuing the work carried out by Siyuan Chen and Rongjun Chen[10], this investigation explores and compares different grafting ratios using the available monomers to obtain the optimal ratio to coat the virus mimicking liposome system. This paper tries to understand and explain the observed results, by postulating the possible mechanisms of polymer-membrane interactions along with obtaining the optimal grafting ratio for drug loading and release.

2. Methods

2.1 Building biological system. Prior to carrying out all-atom molecular dynamic simulations, all the molecular structures used in this research were manually constructed. This was implemented to ensure the recognition and interpretation of set structures by the computational software GROMACS[18] used in this research. Figure 1(a) displays the monomer structures used to construct the 16-mer pseudopeptides investigated in this research paper.

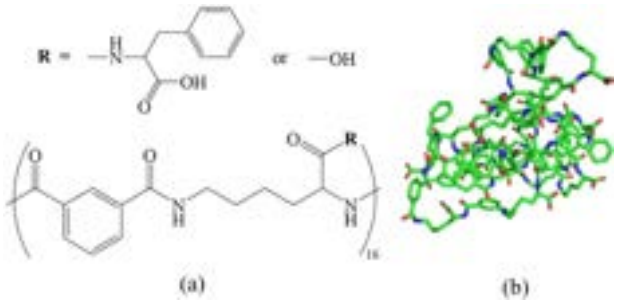

Figure 1: Chemical structure (a) of the grafted and un-grafted monomers used to create the 16-mer polymers, containing L-phenylalanine and Hydroxyl R side groups on the poly (L-lysine iso-phthalamide) (PLP) backbone respectively & (b) simulated globulated PP50 in aqueous environment, where green, red and blue represent Carbon, Oxygen & Nitrogen atoms respectively.

The ungrafted monomer is made up by a poly (L-lysine iso-phthalamide) (PLP) backbone[10]. PP0, PP25, PP50, PP75 & PP100 represent the polymers that are 0%, 25%, 50%, 75% & 100% grafted with L-phenylalanine on the PLP backbone, respectively. The correct configuration of the monomer structures was acquired from CACTUS[19] and was then submitted to the ATB[20] for the topology generation with united all-atom GROMOS 54A7 forcefield[21]. Partial charges of individual atoms were calculated using Density Functional Theory (DFT)[22]. Due to the large number of atoms, polymers were broken up into fragments to ensure efficient DFT calculations. Dipalmitoyl phosphatidylcholine (DPPC) was chosen for this investigation as an appropriate bilipid system to mimic liposomal cell membrane, due to its abundance in biological membranes[23–25]. The topology and configuration of the 128-lipid DPPC membrane used in in this computational research was downloaded from reference[26]. All polymer-membrane systems are solvated with water molecules.

2.2 Simulation parameters. The time step for all the simulations carried out in this experiment was chosen at 1 fs. All simulations were allowed to equilibrate for 500 ps for both NVT (constant number, volume, temperature) and NPT (constant number, pressure, temperature), before proceeding with the execution of the molecular dynamics (MD) run. The LINCS algorithm was used to constrain all bonds[27]. A Verlet cut off-scheme was used, that allowed for buffered neighbour searching and a Particle Mesh Ewald (PME) coulomb type was applied for long range electrostatics[28]. Temperature of 310 K was chosen for all simulations to effectively mimic the average cell membrane temperature. For the deprotonated polymers, sodium ions were used to neutralize the charge of the system. This was done by replacing some of the water molecules present in the system, as GROMACS cannot perform molecular dynamic simulations of charged systems.

Prior to commencing the polymer-membrane interactions, it was observed that the linear backbone structure obtained was computationally demanding. Therefore, the globalization function within PyMOL[29] was used to turn the linearly created backbone polymers into globular ones as seen in Figure 1(b)[29]. The newly formulated globular polymers outputted from PyMOL[29] were equilibrated for 500 ps in both NVT and NPT before proceeding with an MD run of 200 ns in total. The radius of gyration for each of the globulated 16-mer polymers was plotted to ensure that the structures used in further work for the polymer-membrane interactions were the stabilised ones. This ensured that the simulations mimicked the biological system as closely as possible. The plots for the radius of gyration for each of the different grafting ratios can be found in the Supporting Document.

In obtaining the polymer-membrane interactions, the polymer was always placed 0.02 nm from the membrane's upper leaflet. This was done to prevent atom overlapping. If the polymer was placed further away, a larger MD run would be required to ensure measurable interactions between the polymer and the membrane. All simulations in this experiment were carried by Imperial College's High-Performance Computing (HPC)[30] system.

2.3 Membrane thickness. To observe the membrane thickness resulting from the polymer-DPPC interactions, a brand-new software was developed to quantify the localised membrane thickness. The software was written in Python script. It utilized the membrane topology to identify the positions of each phosholipid headgroup and classified

them into either the upper or lower leaflet depending on their vertical position. Once the upper and lower leaflet were categorized, the software separated the membrane (top-view) into 36 equal cells and then calculated the average vertical position of the upper and lower leaflet in each of those 36 cells. The average vertical position of the lower leaflet was then subtracted from the average vertical position of the upper leaflet to obtain the average thickness of the DPPC in each of the 36 cells assigned by the Python code. The script then outputted a 6x6 matrix with the average thickness in each cell, at different time intervals. The matrix was plotted on a 6x6 map, to visually represent the DPPC thickness.

2.4 Area per lipid. Area per lipid was calculated in this investigation using FATSLiM[31].The FATSLiM in-build code identifies the phosphorous groups located in the phospholipid membrane, using the topology file (.gro). Using this information, FATSLiM identifies the area per lipid within the biological membrane system automatically and exports the values in a .csv format.

2.5 Umbrella Sampling. To examine the processes of drug-loading and drug-release, Umbrella Sampling (US) was applied to calculate the Potential Mean Force (PMF). Calcein ($C_{30}H_{26}N_2O_{13}$) is selected as the tested drug molecule, as it is widely used experimentally to measure membrane leakage[32]. The hydrophilic drug molecule is relatively small, that allowed for computational resource conservation. In this experiment, a single Calcein molecule is pulled vertically from the water phase, towards both the outer DPPC layer and inner DPPC layer to simulate drug loading and drug release, respectively. The aforementioned DPPC has been priorly simulated using the setup stated in Section 2.2, where the polymer has already been interacting with outer DPPC layer to form the polymer-membrane system. The pulling rate is set at 0.01 nm ps^{-1} and the harmonic constrain force is 1000 KJ/mol/nm^2. Each configuration from the pulling trajectory is 0.02 nm apart along the reaction coordinate. Each configuration is equilibrated for 100 ps with NPT before progressing with an MD run of 10 ns in total. PMF profile is then constructed using the weighted histogram analysis method (WHAM)[33].

3. Results

3.1 Effect of different grafting ratio on membrane-polymer interactions. As stated, the primal investigation of this research was to identify the best polymer grafting ratio to be used on the virus-mimicking system, for endocytosis optimization of the drug payload into the liposome, along with the facilitation of drug release. As observed from Figure 2 we can detect that protonated PP25, PP50 & PP75 all demonstrated membrane thinning to different extents due to the polymer-DPPC interactions. Protonated PP0 can be seen to exhibit membrane insertion, whereas protonated PP100 is seen to have the smallest interaction with the DPPC membrane. This can be explained and justified down to two main reasons. The first and main one, has to do with the structure of the molecules themselves. As explained previously the ungrafted monomer, seen in Figure 1(a), used to construct PP0 is much smaller and less bulky. Even though both monomers contain an amide and a carboxyl group that allows them to polymerize using amide bonds, the linear 16-mer structure of PP0 has no side group branching. Upon globulation of the linear structures, the two nitrogen end groups in PP0, are more accessible to interact with the DPPC membrane and allow for strong interactions. Over a larger time-span, since these groups are hydrogen bond (H-bond) donors, formation of Hydrogen bonds (H-bonds) with the hydrophilic part of the DPPC is observed, as oxygen atoms present in the phospholipid heads are H-bond acceptors. As seen by Figure 2(a), the nitrogen end group in PP0 is readily accessible and can form hydrogen bonds with a multitude of phospholipid heads.This allows for the membrane insertion of this specific end group as time progresses.

Table 1: Average number of Hydrogen bonds formed between the 16-mer protonated polymers and the DPPC membrane for different grafting ratios across the first 50 ns of the simulation.

Polymer	Average number of Hydrogen bonds
PP0	3.31
PP25	2.84
PP50	4.88
PP75	4.93
PP100	1.93

Table 1 verifies the relatively strong interaction of PP0 with the DPPC with an average of 3.31 H-bonds formed in the first 50 ns. Unfortunately, the rest of the molecule is too bulky and cannot unravel and interact with the membrane in the simulation time of this experiment (150 ns) and therefore membrane thinning is not observed. In comparison, PP100 statistically has the highest number of H-bond donors as grafted monomers contain one more H-bond donor when compared with the ungrafted ones. PP100 can theoretically form the largest number of interactions with the DPPC based on molecular dynamic statistics if an infinite simulation time was allowed. For the simulation time tested, the groups that can interact with the membrane in PP100 are blocked by the extra side groups present in the monomer structure and are not readily available to interact with the membrane, displaying only an average of 1.93 H-bonds formed as seen by Table 1. The second reason has to do with the placement of the molecule. Molecules were obtained and placed on the same position with respect to the DPPC membrane with no rotation to any axis prior to placement. It can

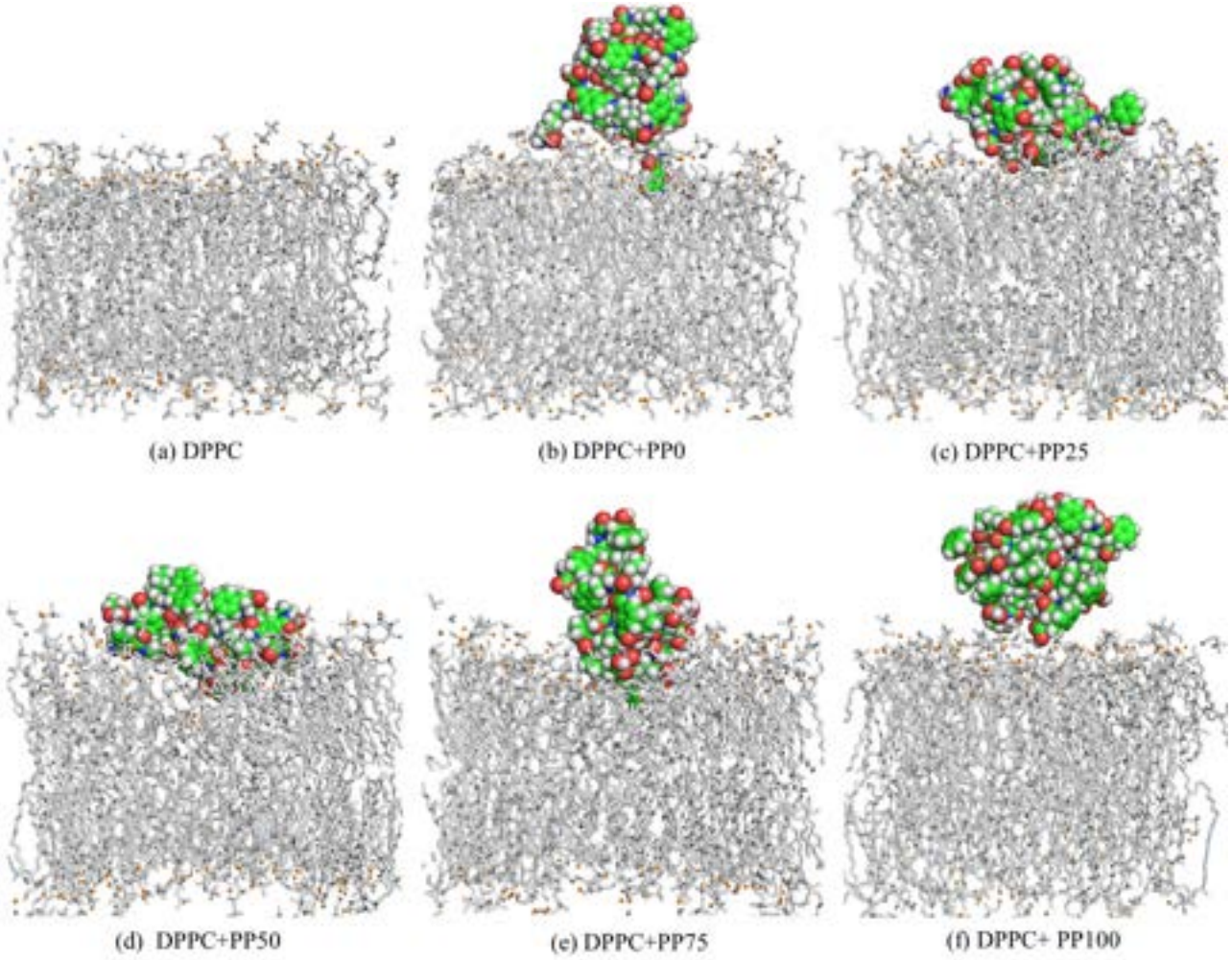

Figure 2: Side-view DPPC-polymer interaction at time t=100 ns for all the grafting ratios tested, using all atom molecular dynamic simulation. Green, red, blue and white spheres represent Carbon, Oxygen, Nitrogen & Hydrogen atoms respectively. Grey represents DPPC lipids and orange dots represent Phosphorous atoms on lipid head groups.

therefore be postulated that the limited interactions between PP100 and the membrane can be attributed to the fact that the H-bond donor groups are not placed in a location that allows them to readily interact with the membrane. PP50 and PP75 were chosen to be further investigated in this research as they displayed the strongest polymer-membrane interactions. This can be verified as both molecules formed the largest number of H-bonds, 4.88 & 4.93 respectively compared to 2.84 for PP25, in the first 50 ns of the simulation, as seen in Table 1. Results for the deprotonated 16-mer polymers, can be found in the Supporting Document, were also obtained but are not discussed in this investigation.

3.2 Effect of different grafting ratio on membrane thinning. In the case of PP25, PP50 & PP75 as mentioned previously, membrane thinning was detected to different extents. As seen by Figure 2, we can visually see that PP75 caused the greatest degree of thinning to the membrane, whereas PP25 generated the least. This observed response can again be attributed to the structure of these polymers. All three aforementioned polymers contain both the grafted and the ungrafted monomer in different compositions. Therefore, all aforesaid grafting ratios contain H-bond donors such us -NH & -OH at different compositions. The grafted monomer contains one more H-bond donor compared to the ungrafted one as mentioned in section 3.1. It is therefore more likely for a molecule with a higher composition in the grafted monomer to obtain a stable globular structure that contains more H-bond donors that are available and can allign with H-bond acceptors to form H-bonds and interact strongly with the DPPC membrane.

Table 2: Number of individual atoms found in the polymer (C, H, N & O) that are 0.03 nm from the upper leaflet of DPPC. These are the atoms in DPPC's close vicinity, that can interact with the bilayer.

Polymer	Number of atoms
PP50 t=50 ns	149
PP50 t=100 ns	273
PP75 t=50 ns	216
PP75 t=100 ns	355

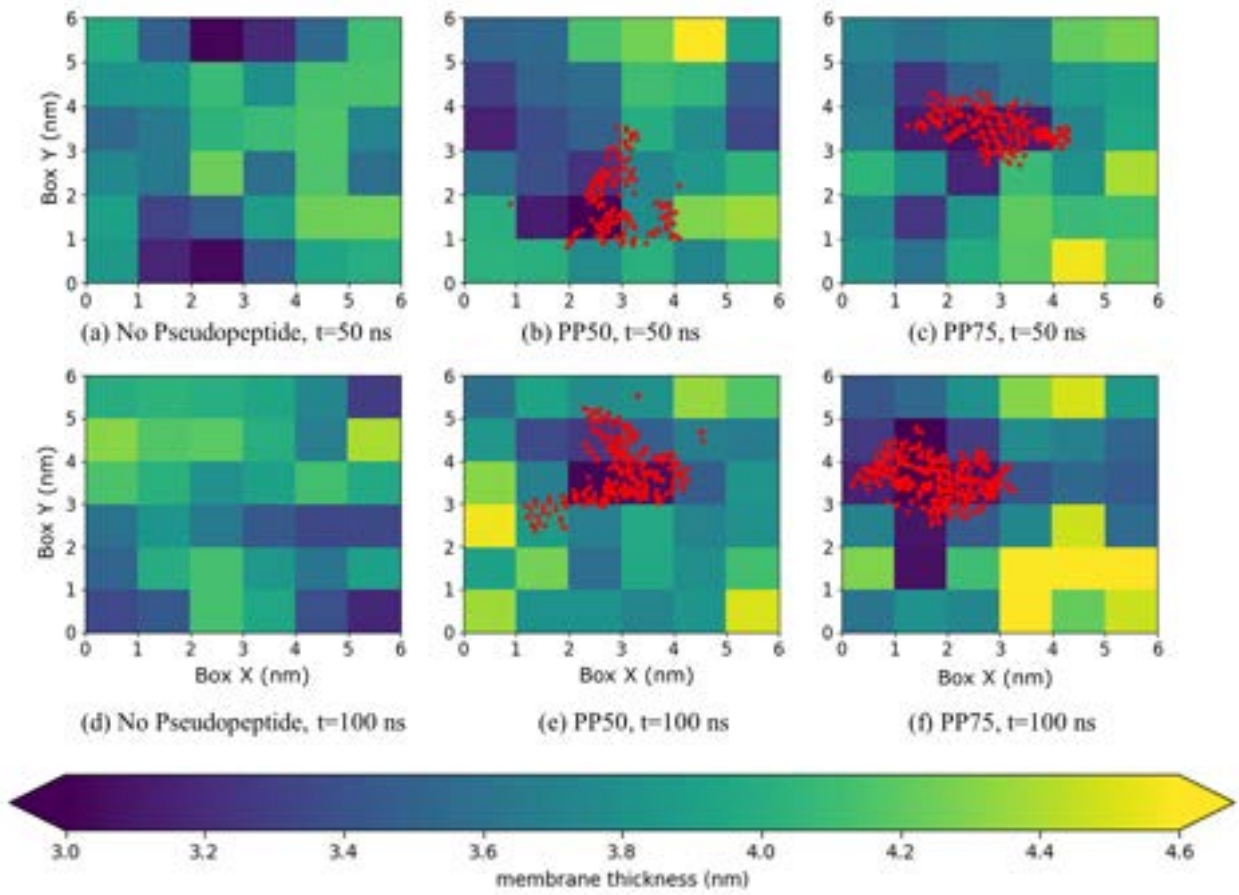

Figure 3: Top-view of DPPC thickness across the 6 nm $\times$ 6 nm membrane box used, for DPPC oscillating on its own and for PP50 & PP75 interacting with the DPPC at time t=50 ns & t=100 ns. The red dots represent individual atoms of the polymer (Carbon, Hydrogen, Nitrogen & Oxygen) that are 0.03 nm from the upper leaflet of DPPC. These are the atoms in DPPC's close vicinity that can interact with the phospholipid membrane.

The reason membrane thinning is observed in PP75, opposed to membrane insertion seen in PP0 is associated with the branching present in these compound molecules. The groups associated with H-bond formation are not seen to be branching out of the globular structure. They are incorporated uniformly within the molecule, as opposed to PP0. This allows for H-bond formation across the whole molecule, as opposed to a singular area. A multitude of H-bonds can be formed across the molecule, causing lateral pulling of phospholipids towards the H-bond donors providing us with the appropriate membrane curvature. From Figure 3 it is evident that the polymer that achieved the largest degree of membrane thinning, with no rotation along any axis prior to placement was PP75. In PP75 the atoms that can interact with the DPPC as seen by the red dots in Figure 3, found in the membrane's close vicinity, are numerously greater and denser when compared to PP50 as seen by Table 2. PP75 created the largest degree of membrane thinning over the largest area in the DPPC. PP75 forced 4 cells of the DPPC to a thickness value less than 3 nm at time t=50 ns. Thickness values obtained were compared to the average DPPC thickness of 4.2 nm, found computationally in this experiment, prior to any polymer addition. The average DPPC thickness is aligned with experimental results[34]. Cells of membrane thickness less than 3 nm were increased from 4 to 6 at time t=100 ns with the lowest thickness, 2.19 nm, resulting in a 48% membrane thickness reduction, obtained in the cell with x and y coordinates of 1-2 nm and 3-4 nm, respectively. PP50 exhibited a much milder DPPC interaction with only 1 cell having a thickness less than 3 nm at time t=50 ns. This number increased to 2 cells at time t=100 ns with the lowest thickness, 2.64 nm resulting in a 37% thickness reduction, observed in the cell with x and y coordinates of 2-3 nm and 3-4 nm.

3.3 Effect of different grafting ratio on area per lipid. Area per lipid (APL), gives us a quantitative measure for the structure and functions of bio membranes[35]. It displays the distortion extent of the lipids in the DPPC membrane, caused by the addition of the polymer. The more a lipid is distorted, the more area it occupies as it is no longer structurally packed in the membrane bilayer, resulting in higher area per lipid values. It is therefore expected to observe high area per lipid values in positions of membrane distortion, caused by the polymer-membrane

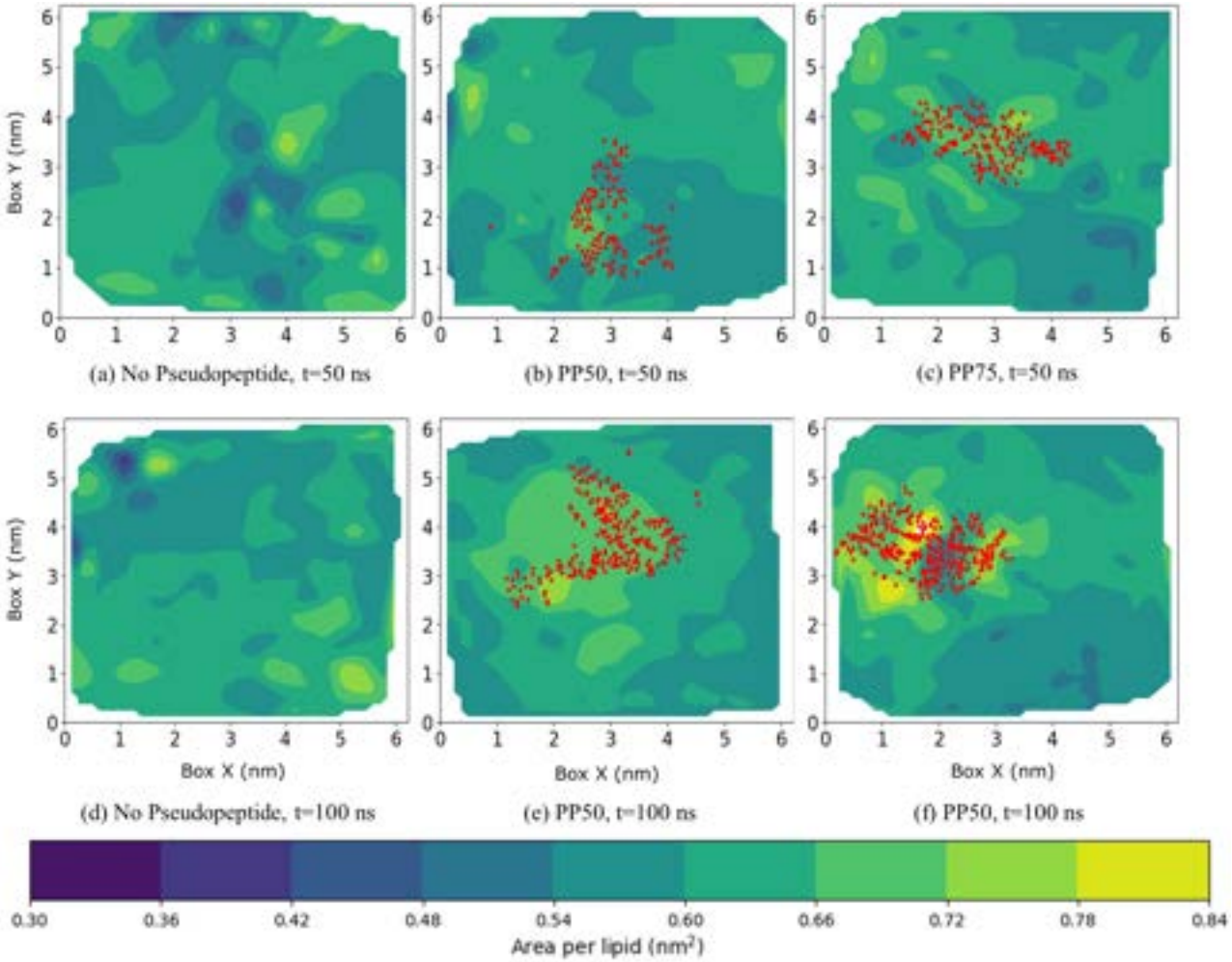

Figure 4: Top-view of area per lipid (nm^2) across the DPPC as a result of the interaction of the different grafting ratios for the protonated 16-mer polymer chains depicted at time t=50 ns & t=100 ns. Area per lipid for the DPPC with no polymer is depicted to act as reference. Red dots represent individual polymer atoms (Carbon, Hydrogen, Nitrogen & Oxygen) that are 0.03 nm from the upper leaflet of the DPPC. These are the atoms in DPPC's close vicinity that can interact with the bilayer.

interactions. It is found experimentally[36] that the average area per lipid value for a DPPC membrane is 0.567 at 320 K[35]. Since the investigation was run at 310 K, this value can be used as a control measure. PP75 displayed the highest area per lipid at t=100 ns with a value of 0.96 (nm^2), a 69 % increase from the control value, located at x=1.8 nm and y=4.0 nm. This verifies the strong interactions between PP75 and the DPPC membrane, as the location of observed highest area per lipid coincides with the location for lowest membrane thickness detected. PP50 adhered to show high area per lipid values as well, in the designated locations of heavy membrane polymer interactions that resulted to membrane thinning.

3.4 Analysis of PMF to mimic drug release.

After the initial analysis, it was identified from Figures 3 & 4 that PP50 and PP75 were the polymers that showed substantial membrane-polymer interactions. Due to the time-frame available for this investigation, a potential mean force was only applied to the protonated PP50 & PP75 polymer-membrane systems. The behaviour observed from Figure 6 for both polymers, shows the presence of three regions that the calcein molecule is exposed to and can interact with, displayed in Figure 5. The first region encountered by the calcein molecule is the water region, far away from the DPPC. Here calcein is unable to interact with the DPPC and interaction with the water region is negligible, resulting in a free energy value of zero. As calcein starts to move towards the DPPC it enters the second region, the 'lipid-water' region. Here the interactions between the calcein molecule and lipid head groups are energetically favourable, leading to negative PMF values, for both grafting ratios tested. Since calcein was chosen to model a hydrophilic drug[32], interaction with the hydrophilic heads of the DPPC is expected, as the drug molecule is pulled towards the membrane interface. This is observed for PP75 & PP50, as seen by Figure 6. Once calcein has reached the DPPC interface, it will start to interact with the third and final section, the 'lipid region'. Here calcein interacts with the lipophilic tail region inside the DPPC, where interactions are unfavourable resulting in a monotonic increase of free energy for both grafting ratios tested.

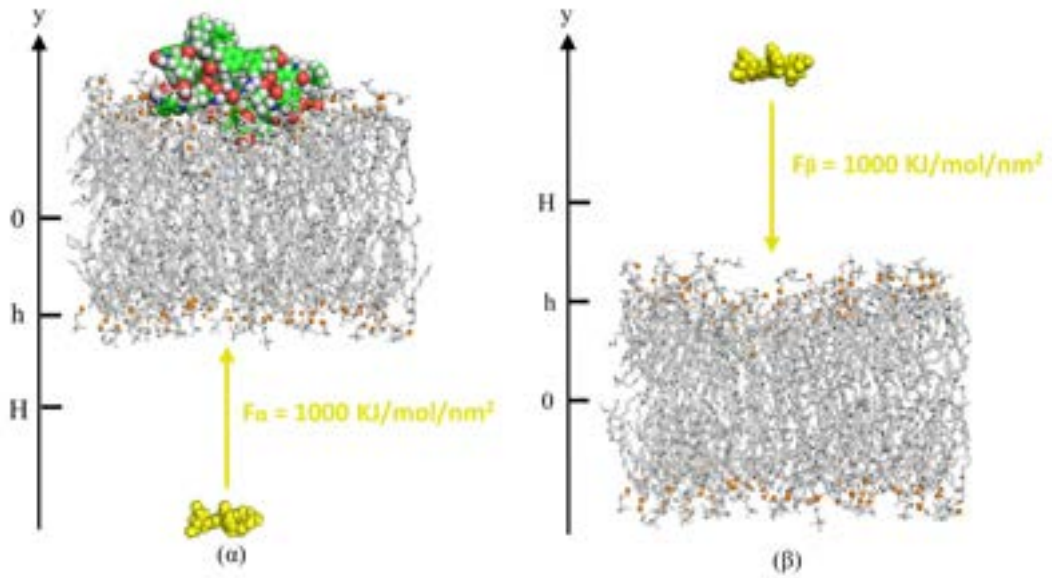

Figure 5: Umbrella Sampling simulations of (α) single calcein molecule pulled towards the lower layer of DPPC mimicking drug release and (β) single calcein molecule pulled towards the upper layer of DPPC imitating drug loading. Pulling force for both cases is 1000 $KJ/mol/nm^2$. DPPC center is at y=0, lipid-water phase is between y=h and y=H, water phase is at $|y|>$ H.

It is observed that for PP75, the calcein free energy minimum is formed closer to the DPPC center compared to PP50. This is attributed to the polymer-membrane interaction. PP75 interacts more heavily with the DPPC resulting in higher membrane distortion supported with higher area per lipid values as seen in Figure 4(c)(f). This allows the drug molecule to naturally approach the membrane and stabilize in a position closer to the DPPC center as seen in Figure 6 where calcein achieved an energy minimum of 2.5 nm from the DPPC center compared to 2.76 nm observed for PP50. PP75 displayed a lower free energy minimum of -31.4 kJ/mol compared with -25.7 kJ/mol for PP50, seen by Table 3 . This shows that there is a stronger calcein-DPPC interaction with PP75.

Table 3: PMF values, in kJ/mol, recorded at different positions for the drug releasing α and loading β simulations: min corresponds to the minimum PMF obtained, max is the observed maximum PMF at postion y=-1 nm and Δ is difference between the observed maximum and minimum obtained.

PMF	PP50α	PP75α	PP50β	PP75β
min	-25.7	-31.4	-27.5	-45.2
max	46.1	9.5	99.4	1.5
Δ	71.8	40.9	126.9	46.7

This can be attributed to the uneven membrane profile created by PP75. The two end groups in PP75 create strong interactions on either side forcing the phospholipids to be tightly packed in the middle, forming a region of low area per lipid as seen at x=2.1 nm and y=3.5 nm in Figure 4(f). This region, packed with hydrophilic head groups allows for strong interactions with the calcein molecule resulting in a more stable interaction depicted by a lower free energy value. It is observed that lower minima lead to lower observed maxima for both polymers. In order to quantify drug release, one should look at the difference between the recorded maximum and minimum found in Table 3. The difference between the two values identifies the energy required for drug release. This is the energy required to push the molecule from its stabilised from, (minimum) observed on the lower side of the membrane, to a position of 1 nm from the DPPC center (observed maximum). PP75 has a lower free energy difference of 40.9 kJ/mol compared to 71.8 kJ/mol for PP50. This shows that PP75 facilitates calcein drug release opposed to PP50 and agrees with the experimental results obtained from[10]. In both cases, the energies required to reach the bilayer center were positive. Therefore, it is unlikely to observe such transition naturally due to the high energy barrier required for both molecules[16]. This is anticipated, since lipid bilayers, including DPPC, are composed of mainly fatty acids that represent a lipophilic barrier through which hydrophilic molecules are unable to naturally diffuse.

3.5 Analysis of PMF to mimic drug loading. In order to identify which polymer optimizes drug loading into the liposome, calcein was placed at the top of the DPPC. Unfortunately, in this configuration both the drug molecule and the polymer are located on the same side of the DPPC. Given the small cross sectional area of DPPC that was used in this investigation, it is impossible to run drug loading simulation without overlapping with the polymer. It was therefore decided to remove the polymer and observe the DPPC response. It was observed that after 90 ns, membrane thinning detec-

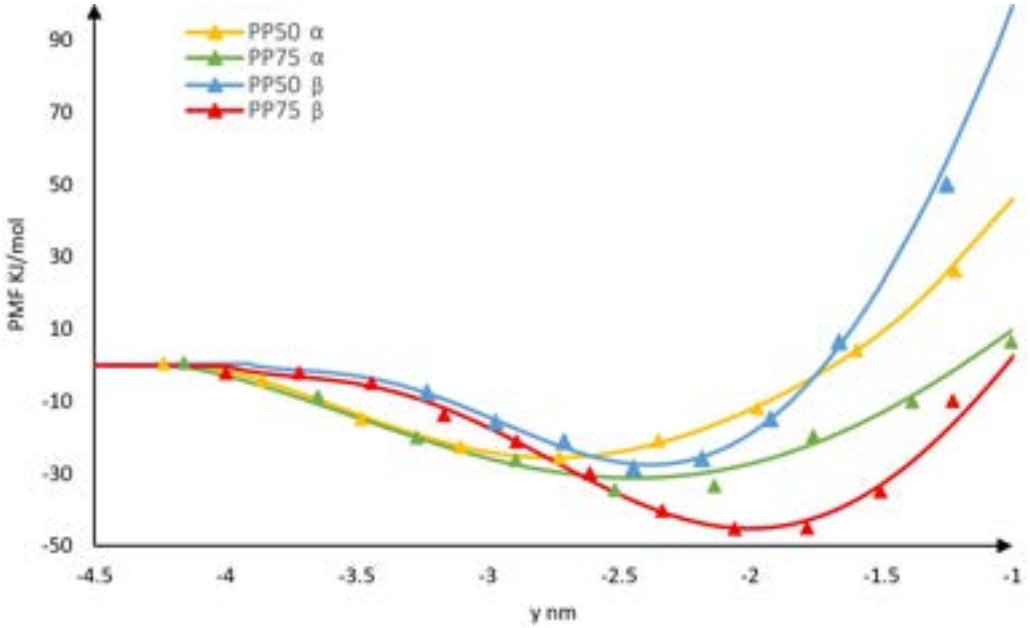

Figure 6: PMF profiles obtained from the pulling of a single calcein drug molecule towards the DPPC, using Umbrella sampling (US), in both drug releasing α and drug loading β simulations.

ted by the initial membrane-polymer interaction is not reversed, as the average membrane thickness remained unchanged after polymer removal (analysis can be found in the Supporting Document). This observation can be explained by the work done by Neha Shafique and Kiley E. Kennedy[37] focusing on the dynamics of DPPC. It was found that between 305 K and 310 K the DPPC is in a transition region between a lipid and a gel phase. The gel phase is still technically fluid but has less fluidity. Therefore, thinning caused by the polymer is not faded quickly, and we consider removing the polymer an appropriate approximation. As seen from Figure 6, a similar pattern for the free energy graphs of both PP50 & PP75 was observed. This is anticipated as the hydrophilic calcein still interacts with the same three regions of 'water', 'water-lipid' & 'lipid' in the same order, as mentioned in section 3.4. Favourable interactions with the 'water-lipid' region result in negative free energy values with a monotonic increase upon the movement of the drug molecule into the lipophilic lipid region. PP75 stabilizes again closer to the DPPC center, at -2.00 nm, with a lower free energy value, -45.2 kJ/mol, when compared to the PP50, -2.45 nm & -27.5 kJ/mol displayed in Figure 6. When compared with the drug releasing simulation it can be observed that both PP50 & PP75 form their stabilised form in a position closer to the DPPC. This can be justified by distorted phospholipids in the DPPC, resulting from protonated polymer-membrane interactions that create a 'hole' closer to the DPPC center where calcein can be inserted and stabilised with strong interactions formed with a multitude of phospholipid heads.

The energy difference between minima and observed maxima was calculated from Table 3 at 46.7 kJ/mol & 126.9 kJ/mol for PP75 and PP50, accordingly. This information establishes PP75 as a better polymer to be used for drug loaing compared to PP50. The large energy difference can be attributed to polymer-membrane interactions. As mentioned in Figure 4 PP75 obtains higher APL causing a greater lipid distortion. Since lipids are more heavily distorted for PP75, it enables calcein to experience fewer interactions with the lipids inside the lipohillic region when moving towards the center of the DPPC. This requires less energy compared to PP50 that experiences heavier interactions with the 'lipid' region as phospholipids are more tightly packed.

4. Conclusion

In this study, a computational foundation was set for analysing the DPPC membrane interactions for a novel class of polymers, polylysine isophthalamide (PLP) with and without L-phenylalanine-grafted side chains at different compositions. Analysis of these polymers was carried out to explain the membrane-lipid interactions and identify the optimal composition for drug release and loading. 75% L-phenylalanine grafted side chain on the PLP backbone (PP75), formed the strongest interactions with the DPPC from all the grafting ratios tested. It formed the largest number of average hydrogen bonds, created the greatest degree of membrane thinning and achieved the highest area per lipid values. PP75 outperformed PP50 both in the drug release and drug loading simulations of calcein with the DPPC. It achieved a lower PMF value for both simulations at a position closer to the DPPC centre along with a smaller energy requirement between the observed minima and maxima. This correlated well with the experimental results in similar papers[10]. It is there-

fore deduced that for optimizing both the drug loading and drug release of a single hydrophilic drug like calcein, the 16-mer PP75 protonated polymer should be used due to its increased performance over the 16-mer PP50 protonated polymer.

Further studies building on this research would incorporate the results obtained in the computational simulations of this investigation to verify further experimental work on biological membranes. The primary investigation would be to achieve a computational comparison between the membrane thinning effect, observed by the DPPC when exposed to the polymer, and membrane permeation. In the research community it has been proven experimentally that membrane thinning leads to increased membrane permeability[38]. This would allow researchers to obtain quantitative results for diffusion coefficients of different molecules in the DPPC-PLP system. In addition, Ernest Awoonor-Williams and Christopher N.Rowley's[39] computational work investigated the trajectory of oxygen molecules crossing the DPPC bilayer. Diffusivity and PMF values were quoted for water and oxygen molecules across the membrane as well. The PMF result for water came in line with the results obtained for calcein. Creating and modelling a solubility-diffusion model like this, will enhance the understanding of cross-membrane motion mechanisms and aid with designs that depict drug molecules moving in a controlled single direction either via endocytosis or exocytosis. In order for such design to be achieved, passive transport would be required, as in this investigation a constant force was used to pull the drug molecule. Calcein leakage through passive transport can be facilitated via the addition of cholesterol[10] or via increasing the number of calcein molecules to allow the formation of a concentration gradient. However such changes will increase the number of atoms present in the model. To achieve such designs with increased complexity, a coarse grain model would be required. Coarse-grain modelling approximates all atom simulations and allows results to be obtained much faster, allowing for simulating larger and more complicated systems. This would therefore require coarse-grain model validation for the tested polymers.

Acknowledgements

We thank Imperial College London for providing a High Performance Computing service. We acknowledge the guidance and technical support provided from Nikki Henry and Nok Cheng.

References

[1] Christoph Englert et al. 'Pharmapolymers in the 21st century: Synthetic polymers in drug delivery applications'. In: *Progress in Polymer Science* 87 (Dec. 2018). ISSN: 00796700.

[2] Anisha A. D'souza and Ranjita Shegokar. 'Polyethylene glycol (PEG): a versatile polymer for pharmaceutical applications'. In: *Expert Opinion on Drug Delivery* 13.9 (Sept. 2016). ISSN: 1742-5247.

[3] Afsaneh Lavasanifar, John Samuel and Glen S Kwon. 'Poly(ethylene oxide)-block-poly(l-amino acid) micelles for drug delivery'. In: *Advanced Drug Delivery Reviews* 54.2 (Feb. 2002). ISSN: 0169409X.

[4] Chun Li. 'Poly(l-glutamic acid)–anticancer drug conjugates'. In: *Advanced Drug Delivery Reviews* 54.5 (Sept. 2002). ISSN: 0169409X.

[5] Younsoo Bae and Kazunori Kataoka. 'Intelligent polymeric micelles from functional poly(ethylene glycol)-poly(amino acid) block copolymers'. In: *Advanced Drug Delivery Reviews* 61.10 (Aug. 2009). ISSN: 0169409X.

[6] Stijn F. M. van Dongen et al. 'Biohybrid Polymer Capsules'. In: *Chemical Reviews* 109.11 (Nov. 2009). ISSN: 0009-2665.

[7] Sarah Hehir and Neil R Cameron. 'Recent advances in drug delivery systems based on polypeptides prepared from N -carboxyanhydrides'. In: *Polymer International* 63.6 (June 2014). ISSN: 09598103.

[8] Gerhard Bilek et al. 'Liposomal Nanocontainers as Models for Viral Infection: Monitoring Viral Genomic RNA Transfer through Lipid Membranes'. In: *Journal of Virology* 85.16 (2011), pp. 8368–8375. ISSN: 0022-538X.

[9] Zhou J Deng et al. 'Layer-by-Layer Nanoparticles for Systemic Codelivery of an Anticancer Drug and siRNA for Potential Triple-Negative Breast Cancer Treatment'. In: *ACS Nano* 7.11 (2013), pp. 9571–9584.

[10] Siyuan Chen and Rongjun Chen. 'A Virus-Mimicking, Endosomolytic Liposomal System for Efficient, pH-Triggered Intracellular Drug Delivery'. In: *ACS Applied Materials & Interfaces* 8.34 (Aug. 2016). ISSN: 1944-8244.

[11] J. A. Hubbell and A. Chilkoti. 'Nanomaterials for Drug Delivery'. In: *Science* 337.6092 (July 2012). ISSN: 0036-8075.

[12] Simona Mura, Julien Nicolas and Patrick Couvreur. 'Stimuli-responsive nanocarriers for drug delivery'. In: *Nature Materials* 12.11 (Nov. 2013). ISSN: 1476-1122.

[13] M.E. Eccleston, N.K.H. Slater and B.J. Tighe. 'Synthetic routes to responsive polymers; co-polycondensation of tri-functional amino acids with diacylchlorides'. In: *Reactive and Functional Polymers* 42.2 (Nov. 1999). ISSN: 13815148.

[14] M.E Eccleston et al. 'pH-responsive pseudopeptides for cell membrane disruption'. In: *Journal of Controlled Release* 69.2 (Nov. 2000). ISSN: 01683659.

[15] Sivaramakrishnan Ramadurai et al. 'Dynamic studies of the interaction of a pH responsive, amphiphilic polymer with a DOPC lipid membrane'. In: *Soft Matter* 13.20 (2017). ISSN: 1744-683X.

[16] Shuzhe Wang and Fernando Bresme. 'Simulation Studies on the Lipid Interaction and Conform-

ation of Novel Drug-Delivery Pseudopeptidic Polymers'. In: *The Journal of Physical Chemistry B* 121.39 (Oct. 2017). ISSN: 1520-6106.
[17] Giulia Rossi and Luca Monticelli. 'Simulating the interaction of lipid membranes with polymer and ligand-coated nanoparticles'. In: *Advances in Physics: X* 1.2 (Mar. 2016). ISSN: 2374-6149.
[18] Mark James Abraham et al. 'Gromacs: High performance molecular simulations through multi-level parallelism from laptops to supercomputers'. In: *SoftwareX* 1-2 (Sept. 2015), pp. 19–25. ISSN: 23527110.
[19] M.C. Nicklaus and team. *NCI/CADD Group Chemoinformatics Tools and User Services*. URL: https://cactus.nci.nih.gov/#4.
[20] Alpeshkumar K. Malde et al. 'An Automated force field Topology Builder (ATB) and repository: Version 1.0'. In: *Journal of Chemical Theory and Computation* 7.12 (Dec. 2011), pp. 4026–4037. ISSN: 15499626.
[21] Wei Huang, Zhixiong Lin and Wilfred F. van Gunsteren. 'Validation of the GROMOS 54A7 Force Field with Respect to β-Peptide Folding'. In: *Journal of Chemical Theory and Computation* 7.5 (May 2011). ISSN: 1549-9618.
[22] Eberhard Engel and Reiner M. Dreizler. *Density Functional Theory*. Theoretical and Mathematical Physics. Berlin, Heidelberg: Springer Berlin Heidelberg, 2011. ISBN: 978-3-642-14089-1.
[23] Hwankyu Lee and Ronald G. Larson. 'Molecular dynamics simulations of PAMAM dendrimer-induced pore formation in DPPC bilayers with a coarse-grained model'. In: *Journal of Physical Chemistry B* 110.37 (Sept. 2006), pp. 18204–18211. ISSN: 15206106.
[24] Selina Nawaz et al. 'Interactions of PEO-PPO-PEO block copolymers with lipid membranes: A computational and experimental study linking membrane lysis with polymer structure'. In: *Soft Matter* 8.25 (July 2012), pp. 6744–6754. ISSN: 1744683X.
[25] Antonio De Nicola et al. 'Micellar drug nanocarriers and biomembranes: How do they interact?' In: *Physical Chemistry Chemical Physics* 16.11 (Mar. 2014), pp. 5093–5105. ISSN: 14639076.
[26] *Downloads — Biocomputing — University of Calgary*. URL: http://wcm.ucalgary.ca/tieleman/downloads.
[27] Berk Hess et al. 'LINCS: A Linear Constraint Solver for molecular simulations'. In: *Journal of Computational Chemistry* 18.12 (Sept. 1997), pp. 1463–1472. ISSN: 01928651.
[28] Mark J. Abraham and Jill E. Gready. 'Optimization of parameters for molecular dynamics simulation using smooth particle-mesh Ewald in GROMACS 4.5'. In: *Journal of Computational Chemistry* 32.9 (July 2011), pp. 2031–2040. ISSN: 01928651.
[29] Schrödinger LLC. 'The PyMOL Molecular Graphics System, Version
1.8'. Nov. 2015. URL: https://pymol.org/2/.
[30] *High performance computing — Research groups — Imperial College London*. URL: https://www.imperial.ac.uk/computational-methods/hpc/.
[31] Sébastien Buchoux. 'FATSLiM: a fast and robust software to analyze MD simulations of membranes'. In: *Bioinformatics* 33.1 (Jan. 2017). ISSN: 1367-4803.
[32] Sayan Dutta et al. 'Calcein Release Assay to Measure Membrane Permeabilization by Recombinant Alpha-Synuclein'. In: *BIO-PROTOCOL* 10.14 (2020). ISSN: 2331-8325.
[33] Shankar Kumar et al. 'THE weighted histogram analysis method for free-energy calculations on biomolecules. I. The method'. In: *Journal of Computational Chemistry* 13.8 (Oct. 1992), pp. 1011–1021. ISSN: 1096987X.
[34] Z.V. Leonenko et al. 'Investigation of Temperature-Induced Phase Transitions in DOPC and DPPC Phospholipid Bilayers Using Temperature-Controlled Scanning Force Microscopy'. In: *Biophysical Journal* 86.6 (June 2004). ISSN: 00063495.
[35] Vitaly Chaban. 'Computationally efficient prediction of area per lipid'. In: *Chemical Physics Letters* 616-617 (Nov. 2014). ISSN: 00092614.
[36] Emily M. Curtis and Carol K. Hall. 'Molecular dynamics simulations of DPPC bilayers using "IIME", a new coarse-grained model'. In: *Journal of Physical Chemistry B* 117.17 (May 2013), pp. 5019–5030. ISSN: 15205207.
[37] Neha Shafique et al. 'Quantifying the Heterogeneous Dynamics of a Simulated Dipalmitoylphosphatidylcholine (DPPC) Membrane'. In: *The Journal of Physical Chemistry B* 120.23 (June 2016). ISSN: 1520-6106.
[38] G. Firpo et al. 'Permeability thickness dependence of polydimethylsiloxane (PDMS) membranes'. In: *Journal of Membrane Science* 481 (May 2015). ISSN: 03767388.
[39] Ernest Awoonor-Williams and Christopher N. Rowley. 'Molecular simulation of nonfacilitated membrane permeation'. In: *Biochimica et Biophysica Acta (BBA) - Biomembranes* 1858.7 (July 2016). ISSN: 00052736.

Techno-economic analysis of a novel hydrogen powered air-source absorption heat pump for domestic heating

Aniruddh Krishnaswamy
Corinne Stollery
Department of Chemical Engineering, Imperial College London, UK

December 17, 2020

Abstract

This paper presents the design and thermo-economic analysis of a novel single-effect air-source absorption heat pump powered with a hydrogen boiler to provide zero-carbon heat. An analysis of the potential to supply homes with hydrogen and the current aborption heat pump literature is carried out and NH_3-H_2O is chosen as the desired refrigerant. Thermodynamic correlations of the cycle are formulated and data extracted from the NIST Reference Fluid Thermodynamic and Transport Properties Database, REFPROP, supplies properties at each stage. Mass and energy balances and combustion equations were formulated and computed on MATLAB for cycle performance, sizing and cost calculations. The temperature of water heated by hydrogen supplied to the generator, demand temperature, air temperature, total heat output, excess air ratio, cost of hydrogen and the temperature of boiler flue gas are used as input data. The COP at an air and demand temperature of 285 K and 320 K respectively was determined as 1.58 when powered with water heated to 420 K by the hydrogen boiler. This requires about 0.2 kgh^{-1} supply of hydrogen. The total cost of the heat pump was estimated to be just below £5000 and operational fuel costs were assessed against average UK heating demand. Performance sensitivity was executed and environmental credentials, efficiency, competition against electrification and the deployment potential of the hydrogen heat pump were discussed.

Keywords: hydrogen, absorption heat pump, ammonia, absorption, decarbonisation, catalytic boiler

Nomenclature	
Q_k	Heat transfer rate of component k [kW]
T_i	Temperature of stream i [K]
P_i	Pressure of stream i [kPa]
h_i	Enthalpy of stream i [J/kg]
η	Isentropic efficiency
ε	Heat exhanger effectiveness factor
m_i	Mass flowrate of stream i [kg/s]
x_i	Concentration in stream i [mass frac]
f	Solution circulation ratio
W_k	Work output of component k [kW]
COP	Coefficient of performance
Cp	Heat capacity [J/kgK]
Subscripts	
gen	Generator
cond	Condenser
evap	Evaporator
abs	Absorber
SHX	Solution heat exchanger
k	Component
fg	Flue gas
s	Losses from boiler

1 Introduction

The urgent need for climate change mitigation has lead to ambitious decarbonisation targets. The UK has committed to eliminate annual greenhouse gas emissions by 2050 under the Climate Change Act 2008 [1] and due to the prevalence of natural gas, heating is a significant contributor to these emissions. To achieve this target, the heating of all buildings and most industrial processes must undergo decarbonisation [2]. Of the 17% of carbon emissions from heating in buildings, about 13-14% can be attributed to UK households [3]. To cut these emissions, advancements in efficient, sustainable heat generation technologies must occur and low-carbon solutions delivered to households.

There are many challenges facing the decarbonisation of domestic heating, including meeting the increasing demand for heat in a sustainable, cost-effective way. The UK is dominated by the natural gas grid and it is hard and expensive for established buildings on the grid to be retrofitted with new technologies [4]. The UK housing stock has poor energy efficiency, there is a lack of public awareness of low-carbon heating and low carbon heating is expensive for regular households.

Currently, less than 5% of home heating is low carbon and the main technologies that are likely to be rolled out to UK buildings include heat pumps and hydrogen boilers [5]. Transitioning the natural gas grid to supply boilers with hydrogen offers the same current functionality, with no CO_2 emissions at the point of use. Hydrogen provides an attractive opportunity to re-utilise the existing grid infrastructure, saving resources and time [6].

Heat pumps are another attractive option for the de-

livery of low-carbon heat. They are a substantially lower carbon system than gas-based or direct electric solutions and extract otherwise useless low-heat energy from the air, improving the efficiency [7]. The Committee on Climate Change has indicated that gas boiler installations should cease by 2035 in order to achieve the UK's decarbonisation targets and heat pumps are a promising technology to replace them [2].

This study assesses the thermo-economic feasibility of using heat from a hydrogen boiler to power an absorption heat pump, providing zero carbon household-level heating.

2 Background

The Committee on Climate Change's *Hydrogen in a low-carbon economy* report finds that hydrogen can make an important contribution to long-term decarbonisation if combined with greater energy efficiency. It reports that heat pumps offer the potential to provide heat efficiently for most of the time, and hydrogen boilers can be used on the coldest winter days to meet peak demands [8]. Boilers can also be synced to follow the grid loading pattern, so they can operate on any excess energy the grid is carrying - this is more likely to become an issue as the electricity grid becomes more renewable and therefore more intermittent.

Northern Gas Networks commissioned a feasibility study, the H21 project, examining how the North of England could be converted to 100% hydrogen. In this study, cost estimates for the full switch from natural gas were produced in a conversion period lasting three years. The need for further work regarding detailed engineering design of hydrogen appliances was outlined. There is currently low demand for hydrogen appliances due to the absence of piped hydrogen, this feasible conversion would motivate the market to employ technologies such as hydrogen powered heat pumps [9].

D. Hart et al demonstrated a 'full contribution' residential heat provision which involved the complete, long-term uptake of hydrogen across the economy [10]. In this scenario, the natural gas boilers in most houses are replaced by hydrogen boilers and some solid-wall houses have hybrid heat pumps integrated with hydrogen boilers for peak heat demands. Other than this mention, current literature lacks studies of hydrogen powered heat pumps, neglecting the potential they will have in a hydrogen economy.

Heat pumps are efficient, low-carbon providers of domestic heat but are often powered by electricity at a compressor, which must be sourced renewably to provide zero-carbon heat. When supplied with a renewable power source, absorption heat pumps are a fully decarbonised heating technology and can also utilise the capability of existing supply infrastructure. Absorption heat pumps extract additional heat from the air at the evaporator, so a greater amount of heat can be supplied at the condenser and absorber. The technology has been assessed to save primary energy by 20-40% compared with conventional fuel systems and studies have shown that they improve efficiency and capacity of district heating networks [11].

Absorption systems have been widely studied for refrigeration purposes and are now gaining attention for heating capabilities. A key advantage is reliability; the heat provider to the generator can be used as an auxillary heat source when the heat demand cannot be reached by the heat pump on particularly cold days. Wu et al. experimentally investigated the performance characteristics of novel absorption heat pumps and provided a comparative analysis of emissions and performance. It was found that air-source absorption heat pumps have significant advantages regarding CO_2 emissions, especially under lower ambient temperatures, with gas-fired air-source absorption heat pumps having an absolute performance advantage over other heating systems modelled [12].

Although $H_2O-LiBr$ systems are the more commonly studied for absorption heating due to better safety and higher efficiency [13], Chen et al. concluded that, $H_2O-LiBr$ systems are limited in heat supply applications due to solution crystallization and a high refrigerant freezing point, making it impossible to utilise source temperatures lower than 5 °C at the evaporator [14]. This is impractical for the colder months in the UK climate therefore NH_3-H_2O is the chosen refrigerant for this study.

An existing experimental work studied a gas-fired residential NH_3-H_2O absorption heat pump to produce hot water. It measured a COP in the range of 1.44-1.63 when supplying 45 °C hot water under an ambient of 20 °C [15]. Wu and Ran investigated the applicability of NH_3-H_2O water-source absorption heat pumps and proved that a developed prototype can operate under evaporator inlet temperatures as low as -18 °C [13].

Literature investigating the integration of renewable power sources with absorption heat pumps tends to focus on solar energy which provides significant reductions in air pollution, however is extremely reliant on solar radiation [16]. The combination with a hydrogen power source reduces this reliability if it can be sustainably supplied to houses.

Although NH_3-H_2O absorption systems have been experimentally explored, an in-depth techno-economic analysis of this concept, capturing both how performance and cost depend on the operating conditions as well as the chosen cycle configuration and component size, has not been identified in literature. Thus, insights into the potential of this system as a competitive alternative to hydrogen boilers have not been attained. The novelty of this work lies in the development of a comprehensive thermodynamic and component-costing model of a hydrogen-powered, single-effect NH_3-H_2O absorption heat pump. Performance parameters will be analysed in alignment with annual UK domestic heating demand and the capital component and annualised cost of the system will be measured, as well as the sizing of the system with a focus on UK households.

Section 3 describes the system configuration of the absorption heat pump cycle and hydrogen boiler to be combined and outlines the methods required to thermo-economically model the proposed system. Section 4 provides the results and chosen operating and sizing parameters as well as analysis of input sensitivity to system performance. Section 5 analyses environmental and market potential and Section 6 presents concluding remarks.

3 Methodology

3.1 Combined Model

The two models described in Sections 3.2 and 3.3 are linked via the Q_{gen} value. That is, the heat determined to be required by the heat pump cycle in the generator is fed to the hydrogen boiler model which calculates and outputs a mass flowrate of hydrogen required.

3.2 Heat Pump Cycle

3.2.1 System Configuration

A schematic diagram of the ammonia-water absorption heat pump is shown in Figure 1. The proposed system replaces the compressor typically used in electric heat pumps with a single-stage absorption cycle consisting of a generator, solution heat exchanger and absorber, as well as an electrically powered pump and refrigerant expansion valve. For this study, ammonia and water are used as the refrigerant and absorbent respectively. The high pressure units are the condenser, generator and solution heat exchanger, while the low pressure units are the evaporator and absorber.

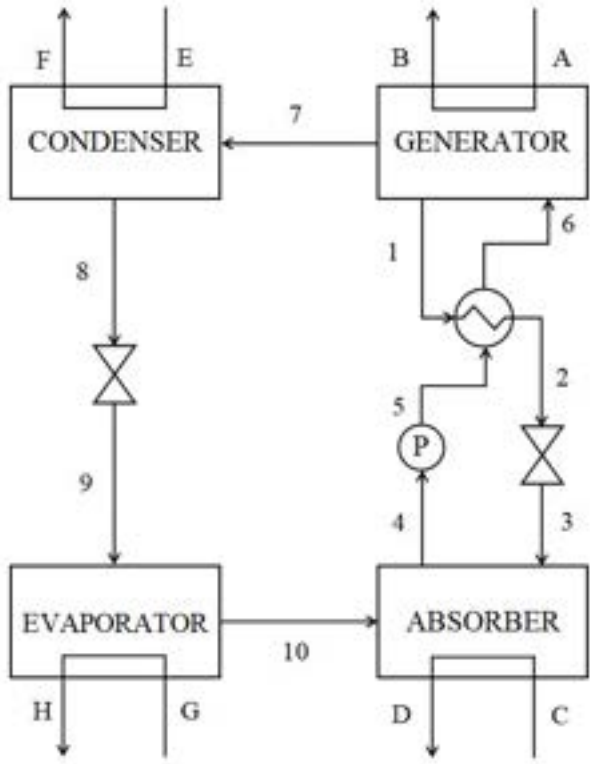

Figure 1: Schematic diagram of the absorption heat pump cycle.

Referring to the stream labelling in Figure 1, stream 1 represents the 'weak' NH_3-H_2O solution present as a subcooled liquid following heat input from the hydrogen boiler, Q_{gen}, and enters the counter-flow solution heat exchanger as the hot stream. Following this, stream 2 enters the expansion valve and exits as a saturated liquid, stream 3. Stream 4 consists of the strong refrigerant solution as a saturated liquid and is compressed to a high pressure in the pump. Stream 5 is preheated in the solution heat exchanger by recovering heat from the weak solution and exits as stream 6 into the generator.

Saturated refrigerant vapour exits the generator in stream 7 and condenses into a liquid in stream 8. This enters another expansion valve and stream 9 enters the evaporator and becomes vapourised in stream 10, and then absorbed by the strong stream in the absorber.

Streams A and B represent heated water from the hydrogen boiler and streams C, D, E and F are water supply streams for household heating, heated by the heat of solution released in the absorber. Stream E is heated due to the condensation of the refrigerant in the condenser and stream C is heated due to heat released in the absorber. Streams G and H contain air from the heat pump surroundings, this heat obtained is considered as a free resource.

3.2.2 Thermodynamic Correlations

The thermodynamic properties of each stream in the system must be known to calculate energy balances, the coefficient of performance and component design specifications. This was executed by using known parameters to extract properties from the NIST Reference Fluid Thermodynamic and Transport Properties Database, REFPROP, and computing equations on MATLAB. The assumptions for the following calculations are [17]:

- The systems operate at steady state conditions
- Heat losses and pressure drops in components and piping are negligible
- Ammonia/water solution is saturated in the generator and absorber outlet
- Refrigerant leaving the condenser is a saturated liquid
- Hot and cold temperature differences in the generator and evaporator are 5 °C
- All valves are isenthalpic
- The isentropic efficiency of the pump is equal to 0.8
- The heat exchanger effectiveness factor is equal to 0.8
- 5 °C of superheating in the evaporator is assumed for performance calculations

The demand temperature and pinch point temperature are set as 320 K and 5 K respectively and the outlet streams of the heat providing components (T_8 and T_4) can be calculated. Assuming saturated liquid leaves the condenser, P_8 and h_8 can be extracted from REFPROP. This gives the high pressure of the cycle. From assuming saturation and knowing P_{high}, all properties of stream 7, the generator outlet, can be extracted from REFPROP.

$$T_8 = T_4 = T_{demand} + T_{pp} \tag{1}$$

$$P_{high} = P_8 = P_7 = P_6 = P_5 = P_2 = P_1 \tag{2}$$

The low pressure of the cycle is calculated from the outlet of the evaporator, assuming it is a saturated vapour. T_{10} is calculated in Equation 3 and following the assumption, the pressure and enthalpy of this stream can be extracted from REFPROP.

$$T_{10} = T_{air} - T_{pp} \tag{3}$$

$$P_{low} = P_{10} = P_9 = P_3 = P_4 \tag{4}$$

By assuming isenthalpic expansion and knowing P_9, T_9 can be found. There is also enough information to calculate h_{10}. This stream enters the absorber where water is introduced to the cycle. The solution concentrations of the strong and weak stream are calculated using the nonlinear system solver, fsolve, with the knowledge of temperature, pressure and assuming saturation. From this, h_4 and s_4 can be calculated and using s_4 and P_5, the $h_{5,ideal}$ is calculated. Using an isentropic efficiency of 0.8, h_5 is calculated as shown in Equation 6. From this, all the thermodynamic properties of stream 5 can be calculated.

$$T_1 = T_{gen} - T_{pp} \tag{5}$$

$$h_5 = h_4 + \frac{(h_{5,ideal} - h_4)}{\eta} \tag{6}$$

The concentration of stream 1 is calculated in the same way as the strong stream and assuming saturated solution, all thermodynamic properties of this stream can be found. Stream 1 enters the solution heat exchanger and its effectiveness is used to calculate the temperature gradient, as shown in Equation 7. A heat exchanger effectiveness of 0.8 is used.

$$T_2 = T_1 - \varepsilon(T_1 - T_5) \tag{7}$$

With knowledge of temperature and pressure, h_6 can be extracted from REFPROP. Assuming isenthalpic expansion across the expansion valve, all the thermodynamic properties for stream 3 can also be found.

$$h_2 = h_3 \tag{8}$$

3.2.3 Mass and Energy Balances

Each cycle component is treated as a control volume with inlet and outlet streams and no accumulation. Mass conservation must be satisfied as demonstrated in Equation 9.

$$\sum_i m_{i,in} x_{i,in} - \sum_i m_{i,out} x_{i,out} = 0 \tag{9}$$

The solution circulation ratio is defined as the ratio between the weak solution mass flow rate entering the generator and the refrigerant vapour mass flow rate leaving the generator [18]. From manipulation of Equation 9, the ratio can be given in terms of the the strong and weak stream concentrations, as demonstrated in Equation 10.

$$f = \frac{m_6}{m_7} = \frac{x_1}{x_1 - x_4} \tag{10}$$

The energy balance for each component in the cycle gives the following:

$$Q_{gen} = m_7 h_7 + m_1 h_1 - m_6 h_6 \tag{11}$$

$$Q_{cond} = m_7(h_7 - h_8) \tag{12}$$

$$Q_{evap} = m_9(h_{10} - h_9) \tag{13}$$

$$Q_{abs} = m_{10} h_{10} + m_3 h_3 - m_4 h_4 \tag{14}$$

$$Q_{SHX} = m_5(h_6 - h_5) \tag{15}$$

$$W_{pump} = m_4(h_5 - h_4) \tag{16}$$

Through use of the above equations, the mass flow rates of each stream in the cycle can be calculated.

$$m_{10} = \frac{Q_{cond} + Q_{gen}}{h_7 - h_8 + h_{10} + (f-1)h_3 - f h_4} \tag{17}$$

$$m_4 = f m_{10} \tag{18}$$

$$m_3 = m_4 - m_{10} \tag{19}$$

Knowledge of the mass flow rates enables the enthalpy of stream 6 to be calculated. From h_6 and P_6, T_6 can be extracted from REFPROP and the thermodynamic properties of all cycle streams is accounted for.

$$h_6 = h_5 + \frac{m_1}{m_4}(h_1 - h_2) \tag{20}$$

3.2.4 Cycle Performance

The cycle performance is evaluated by the coefficient of performance, a ratio between the heat output and heat and power input.

$$COP = \frac{Q_{abs} + Q_{cond}}{W_{pump} + Q_{gen}} \tag{21}$$

The supply water is heated utilising the energy from the absorber and the condenser. It is noted that Q_{evap} is not accounted for in this coefficient due to this heat being essentially free, extracted from the air.

3.2.5 Design Specifications

The heat exchange area of each component in the cycle can be obtained from the heat transfer equation [17].

$$A_k = \frac{Q_k}{U_k LMTD_k} \tag{22}$$

where A is heat transfer area, Q is heat transfer flow rate through the component, U is heat transfer coefficient which is considered as 1.6, 1.1, 0.6, 0.9 and 1 kW/m^{2}K for the generator, solution heat exchanger, absorber, evaporator and condenser respectively [19] and LMTD is the logarithmic mean temperature difference which is calculated by Equation 23.

$$LMTD_k = \frac{(T_{h,i} - T_{c,i}) - (T_{h,o} - T_{c,o})}{\ln \frac{T_{h,i} - T_{c,i}}{T_{h,o} - T_{c,o}}} \tag{23}$$

where subscripts h and c represent hot and cold streams, and subscripts i and o represent inlet and outlet streams.

3.2.6 Component Costings

The cost functions of components and equipment used in the cycle are summarised in Table 1. The correlations come from the work of Olympios et al [20]. TC refers to total cost; the sum of the cost of the listed components.

Table 1: Table of cost functions for different components and the variables upon which these depend.

Component	Dependent variable	Cost function [£]
Generator	Heat exchange area [m^2]	173 + 282A
Solution heat exchanger	Heat exchange area [m^2]	173 + 282A
Condenser	Heat exchange area [m^2]	173 + 282A
Absorber	Heat exchange area [m^2]	173 + 282A
Evaporator	Heat exchange area [m^2]	270A
Pump	Work output [kW]	$512W^{0.46}$
Miscellaneous	Total component costs	0.2TC

3.3 Catalytic Hydrogen Boiler

A catalytic hydrogen boiler is used to provide heating to the generator. Catalytic boilers are not traditional 'boilers' in the sense that they catalytically convert the fuel to its products in the absence of a flame rather than combusting it. This results in negligible production of nitrogen oxide emissions [21]. The hydrogen boiler is modelled by a separate reaction chamber and heat exchanger which heats water to flow to the generator. This model is based upon a modified natural gas boiler as functionally they behave very similarly [22].

The following assumptions were made when modelling this system:

- The reaction of hydrogen in the boiler is complete and with dry air
- The mass and energy balances are at steady state

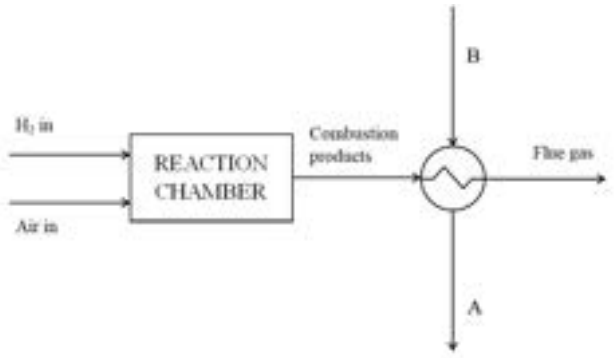

Figure 2: Schematic diagram of the catalytic hydrogen boiler model.

The reaction taking place in the combustion chamber is as follows:

$$H_2 + \lambda(O_2 + 3.76N_2) \xrightarrow{Pt} H_2O + \frac{3.76\lambda}{2}N_2 + \frac{\lambda\text{-}1}{2}O_2 \tag{24}$$

where λ is the excess air ratio and 3.76 represents the ratio of nitrogen to oxygen in air. In our model, we have assigned λ to be equal to 1.13, in line with observed values in boilers [22].

Consequently, the total molar flowrate of the flue gases out of the reaction chamber is simply the sum of the stoichiometric coefficients of the products, multiplied by the molar flowrate of hydrogen in. This is given by:

$$\dot{n}_{fg} = \dot{n}_{H_2}\left(1 + \frac{3.76\lambda}{2} + \frac{\lambda - 1}{2}\right) \tag{25}$$

Simplified, this gives:

$$\dot{n}_{fg} = \dot{n}_{H_2}(0.5 + 2.38\lambda) \tag{26}$$

The mole fraction of each component in the flue gas is calculated using the individual component flowrates divided by the flue gas molar flowrate. These are given in Table 2.

Table 2: Table of component molar flowrates and fractions in the flue gas.

Component	Molar flowrate	Mole fraction
H_2O	$\dot{n}_{H_2}$	$\frac{1}{0.5+2.38\lambda}$
N_2	$\dot{n}_{H_2}\frac{3.76\lambda}{2}$	$\frac{1.88\lambda}{0.5+2.38\lambda}$
O_2	$\dot{n}_{H_2}\frac{\lambda-1}{2}$	$\frac{0.5(\lambda-1)}{0.5+2.38\lambda}$
Total	$\mathbf{\dot{n}_{H_2}(0.5+2.38\lambda)}$	**1**

Hydrogen reacts in the catalytic boiler at approximately 300°C [23]. The heat capacity of the products in the flue gas at this temperature are found via REFPROP. A weighted flue gas molar heat capacity is then calculated by multiplying the mole fractions (shown in Table 2) of each component with their respective molar heat capacity. This stays constant and is independent of the amount of hydrogen fed to the combustion chamber.

The energy from combustion is transferred to the flue gas via two effects; through sensible heat energy, described in Equation 27 and through the latent heat of vaporisation of water, described in Equation 28.

$$\dot{E}_{fg,T} = \dot{n}_{fg}\bar{C}_{p_{fg}}\left(T_{fg} - T_0\right) \tag{27}$$

where T_0 is our environment temperature.

$$\dot{E}_{fg_L} = \dot{n}_{fg}x_{H_2O}Ma_{H_2O}L_{H_2O} \tag{28}$$

where x_{H_2O} is the mole fraction of water in the stream, Ma_{H_2O} is the molar mass of water and L_{H_2O} is the latent heat of vapourisation of water.

Summing these two effects gives our total energy transferred to the flue gas, as described in Equation 29.

$$\dot{E}_{fg} = \dot{E}_{fg_T} + \dot{E}_{fg_L} \tag{29}$$

The Q_{gen} value from the heat pump cycle previously is fed into Equation 30 to provide a required amount of hydrogen gas. $\dot{E}_s$ accounts for heat losses in the boiler system and is considered given the high temperatures involved. It is approximated to be 1% of the sum of Q_{gen} and $\dot{E}_{fg}$.

$$E_{fuel} = Q_{gen} + \dot{E}_{fg} + \dot{E}_s \tag{30}$$

Finally, our E_{fuel} value can be divided by the lower heating value of hydrogen (by mass), H_u, to provide the required mass flowrate of hydrogen into our boiler as described in Equation 31.

$$\dot{m}_{fuel} = \frac{E_{fuel}}{H_u} \tag{31}$$

4 Results

4.1 Base Case Parameters

The following parameters as displayed in Table 3 were decided as the base case for the MATLAB model.

Table 3: Input parameters into MATLAB model.

Parameter	Value	Units
T_A	420	K
T_{demand}	320	K
T_{air}	285	K
T_{sh}	5	K
Q_{op}	7	kW
λ (excess air ratio)	1.13 [22]	-
H_2 unit cost	0.076 [9]	kWh
T_{fg}	300	°C

These base case parameters were selected following analysis of other similar units and research into the required attributes for a domestic heat pump. 7 kW was chosen as Q_{op} as this was the highest heating demand at any point in the year for an average household in the UK [3].

4.2 Outputs

4.2.1 Parameters

Following execution of the base case parameters as inputs, the following results displayed in Table 4 are obtained from the MATLAB model.

Table 4: Output parameters following MATLAB execution of base case.

Parameter	Value	Units
COP	1.58	-
H_2 required	0.20	kg/h
$Q_{generator}$	4.40	kW
$Q_{absorber}$	4.40	kW
$Q_{condenser}$	2.60	kW
$Q_{evaporator}$	2.60	kW
Q_{HX}	3.40	kW
W_p	0.031	kW
P_{high}	2100	kPa
P_{low}	550	kPa

Figure 3 depicts a Sankey Diagram, showing where power is sourced from and where it flows to in the heat pump. This is idealistic with losses being neglected within the heat pump cycle however, it shows a large proportion of energy is lost through flue gases.

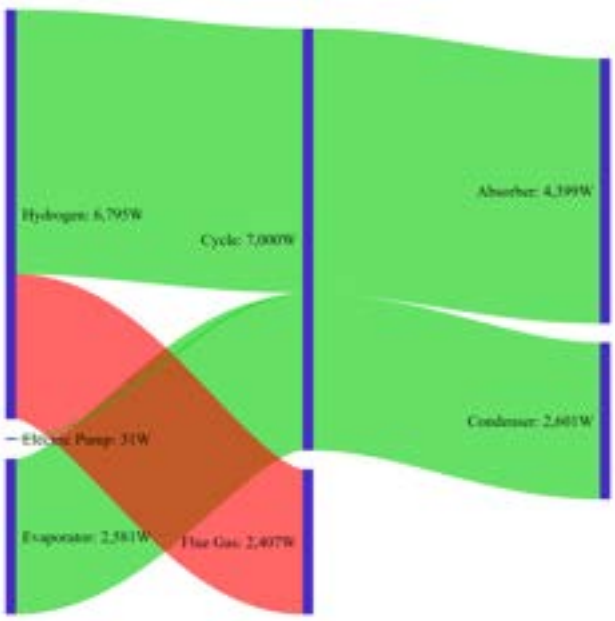

Figure 3: Sankey Diagram depicting power flows in the base case.

4.2.2 Component design and cost

Through use of the correlations in Sections 3.2.5 and 3.2.6 the heat exchange area and cost of each component is calculated and displayed in Table 5. The cost of a new catalytic hydrogen boiler is from Speirs et al [24]. After addition of miscellaneous costs (pipework, labour, etc.) and a factor accounting for taxes and profits, the total cost is estimated to be just below £5000.

Table 5: Cost of each component in the base case.

Component	Exchange Area [m^2]	Cost [£]
Generator	0.19	380
Solution heat exchanger	0.13	370
Absorber	0.65	480
Evaporator	0.67	180
Condenser	0.61	470
Hydrogen boiler	-	2200
Miscellaneous	-	390
Profit/tax factor	-	390
Total cost	-	**4860**

4.2.3 Heat pump performance

Figure 4 illustrates how the performance of the hydrogen heat pump is effected by the temperature demanded of the system. It can be seen that COP decreases when higher temperatures are demanded and at our chosen demand temperature of 320 K, the COP is 1.58, providing a trade-off between the heat pump performance and temperature output.

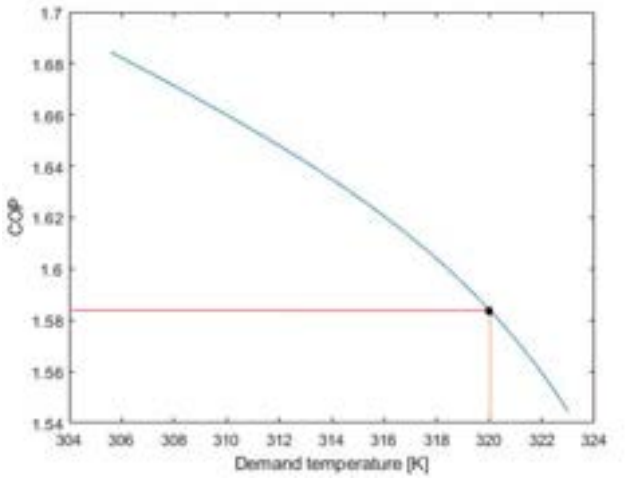

Figure 4: Graph of Coefficient of Performance with varying demand temperature and indication of chosen output.

Figure 5 demonstrates how the COP of the thermodynamic model varies for a range of air and generator temperatures. For the air temperature, UK average monthly temperature markers are given from data in 2019 [25] indicating how the hydrogen heat pump produces less heat for a given heat and power input in winter. The heat pump will perform more effectively in the summer months as expected due to higher heat input at the evaporator. The COP increases with T_{gen} which means that the heat pump performs more effectively when more heat is supplied from the hydrogen boiler.

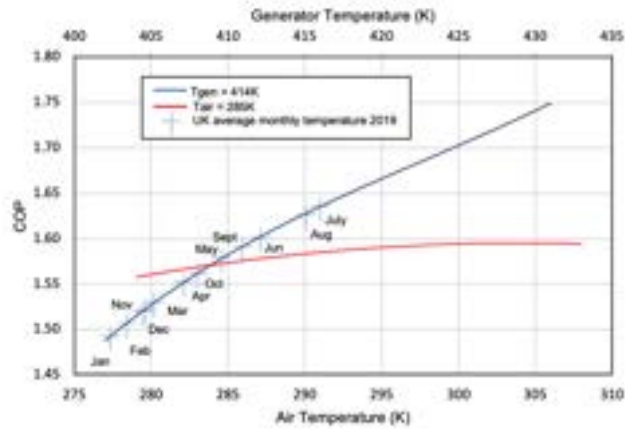

Figure 5: Graph of Coefficient of Performance with varying air and generator temperatures and average monthly UK air temperatures.

4.2.4 Operational cost

Figure 6 depicts how the operational (fuel) cost per hour of running the heat pump at 7kW decreases as the air temperature increases. This seems to be a broadly linear relationship in the range depicted with the cost decreasing by approximately 0.2p per degree of temperature increase.

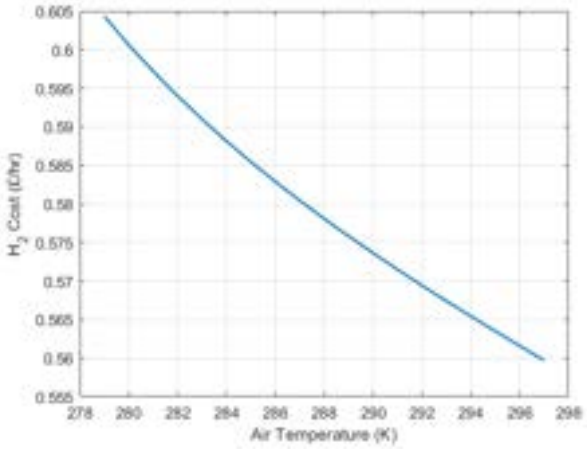

Figure 6: Graph of operational cost per hour at base case scenario with changing air temperature.

5 Discussion

5.1 Environmental Credentials

The inherent goal of this technology is to provide a fully decarbonised heating system for a household level application. This goal is dependent on the ability to provide renewable hydrogen to buildings, most probably via the national gas grid. The Royal Society of Chemistry have studied the regional transition of the heating sector from a natural gas-based infrastructure to hydrogen and it was found that a low-carbon hydrogen supply can be developed cost-effectively through the deployment of reforming technologies with CCS. This is feasible through use of large scale hydrogen storage in salt caverns and CO_2 storage in deep geological reservoirs [26]. This is promising for the hydrogen powered heat pump market and confirms the technology's ability to provide zero-carbon heat.

The power source of the electric solution pump is another external dependency this technology faces in order to be 100% zero carbon. This depends on the energy mix of the grid at the time, as the pump is electrically powered. At the time of writing, the latest UK government data (Q1 2020) shows 47% of energy comes from renewable sources [27] and with recent government commitments, this is likely to rise over time. Regardless, the pump consumes a fairly negligible 31 W in our base case scenario and so does not severely affect the 'green credentials' of this heat pump system.

The heat pump under review here uses an $NH_3 - H_2O$ refrigerant. Ammonia is an established refrigerant commonly used in industry but is not so common domestically due to some of its inherent limitations environmentally and physically. Hence, it may be worth investigating other refrigerant systems such as $H_2O - LiBr$, especially in geographies where the air temperature tends to be higher allowing alternative refrigerant systems such as these to function. Environmentally, ammonia is very toxic however the smell can normally be identified before it reaches critical concentrations in the air [28]. There is arguably more risk when these toxic chemicals are used domestically and as such, any parts of the system in contact with ammonia must be

sufficiently proofed to ensure they can withstand any ruptures. These additional costs have not been considered in this paper. Physically, ammonia is corrosive and more so when there are impurities present. Care must be taken to ensure there are rigid safety procedures in case of any leaks and appropriate training must be undertaken by contractors to mitigate risks during installation and charging.

5.2 Efficiency

Following the reaction chamber, the flue gases are at at a temperature of around 300 °C. As described in section 4.2, an energy analysis on the reaction in the hydrogen catalytic boiler suggests that in the base case, approximately 35% of the heat of reaction exits the boiler in the form of internal energy of the flue gas whilst the remaining 65% is transferred to the generator. This provides immense potential for flue gas heat recovery however this was not investigated in this study. The boiler modelled in this study is a non-condensing boiler resulting in a low efficiency. This boiler efficiency could be increased by considering a multi-stage heat exchange network within the boiler: a condensing boiler.

5.3 Hydrogen vs. Electrification

Heat pumps will undoubtedly play a significant role in the future heating technology space but conventional electrically powered systems are likely to be a popular alternative. The market viability of the hydrogen powered heat pump proposed in this paper will be dependent on these alternative competitors. Electrifying heat ties its carbon footprint to that of the power sector, where there is a clear path to decarbonisation through renewable energy. However, adding the burden of domestic heating onto the electric grid will require infrastructure reinforcement although this will likely be a future requirement due to increasing energy demands regardless. This requirement could be partially relieved by improving heating efficiencies in the UK housing stock.

One advantage of hydrogen powered heating over electricity is that a hydrogen gas supply to households has other uses such as gas hobs for cooking. Electric hobs can be used but provide less control of cooking temperatures and are generally less efficient for cooking applications. In addition, the ability to use current gas grid infrastructure for hydrogen supply is an effective use of existing resources.

5.4 Market Viability

Costs are an important metric in judging how successful the uptake of these heat pumps would be if they were to be rolled out for domestic heating. The total cost of the units described in this paper are estimated to be £4860 and households will also incur significant operational costs due to the cost of hydrogen being priced around £0.076 per kWh [9]. However, this figure is likely to naturally decrease over time as alternative hydrogen production methods come online and generate competition in the market.

The average household is unlikely to be able to afford to pay for these units upfront and so government incentives will be required to encourage purchasing. Alternatively, zero/low interest payment plans will have to be devised in order to stimulate take up. In order to further incentivise households to purchase these units, governments could use one of two key methods. First, they could impose heavy carbon taxes on natural gas and other fossil fuels, increasing the operational costs of traditional boilers and thus forcing people away from these legacy systems. This is unlikely given the UK government is considering banning the sale of new natural gas boilers by 2025 [29] at the latest and so it seems a less aggressive tactic has been adopted. This could be implemented in tandem with the second method of incentivising households to switch, through subsidies. Both the capital and operational costs of these units are very high and so subsidies are likely to be necessary to promote uptake of these units. The UK government has a track record of providing grants for technologies that decarbonise domestic energy consumption: for example, at the time of writing there exists the *Domestic Renewable Heat Incentive Scheme* which provides a grant to encourage homeowners to replace fossil fuel based systems with renewable heating systems. Air source heat pumps form the vast majority of renewable heating systems chosen under this scheme, validating that this financing model would likely work if implemented for hydrogen fuelled air-source heat pumps.

Table 6: Approximate cost of hydrogen prior to and post combustion following efficiency calculations.

Unit	Cost in [£/kWh]	Boiler efficiency	Cycle efficiency	Cost out [£/kWh]
H_2 boiler	0.076 [9]	0.65	-	0.117
Heat pump incl. H_2 boiler	0.076 [9]	0.65	1.56	0.075

Table 6 shows the retail cost of hydrogen (Cost in) and the real cost per kWh of energy (Cost out) by dividing by the efficiency figures. A comparison is also shown between the regular hydrogen boiler and the integrated hydrogen heat pump system showing that in the base case, the integrated system is cheaper. The cycle efficiency used in this instance is the COP. A more detailed and accurate calculation of the final consumer cost using the heat pump is given in Table 7.

Table 7: Step-by-step calculation of per-kWh cost of hydrogen to the consumer.

ID	Parameter	Value	Unit	Source
1	Power	7	kW	Table 3
2	H_2 cost	0.076	£/kWh	[9]
3	H_2 density	33.6	kWh/kg	[30]
4	H_2 cost	2.55	£/kg	ID2 × ID3
5	H_2 required	6.38×10^{-5}	kg/s	Table 4
6	Factor	3600	s/hr	-
7	Cost per hour	0.592	£/hr	ID5 × ID6
8	Cost per kWh	0.085	£/kWh	ID7 ÷ ID1

Disregarding flue gas heat recovery, alternative cost calculations as shown in Table 7, give a final cost to the consumer of £0.085 per kWh. It is noted that the minor discrepancies between this price and the one given in Table 6 are due to W_p not being taken into account in the latter. When the air temperature falls, the hydrogen boiler will take

precedence as the most price-efficient method of generating heat and so a control system is proposed to switch between the individual boiler and the whole system at the correct point.

Although it may be more efficient to heat the generator directly with the flue gas of the catalytic hydrogen boiler, this does not allow for the switch between the boiler and whole system when the air temperature decreases below the point at which operating the whole system heat pump is more efficient. In warmer climates, it may make more sense to power the system without the intermediary water loop however this is unlikely to be the case in seasonal countries. Additionally, the water loop provides a buffer as the flue gas is at an extreme temperature for the generator.

Figure 7 was produced by using the Watson model of UK heating demand [3]. This model provides hourly data on the UK's heating power requirement and subsequently an average per household. This was converted to a daily average power requirement which was input to the MATLAB model to provide an operational hydrogen cost for each day. As expected, the UK's seasonal nature causes far higher demand during the winter months and lower demand during the summer months.

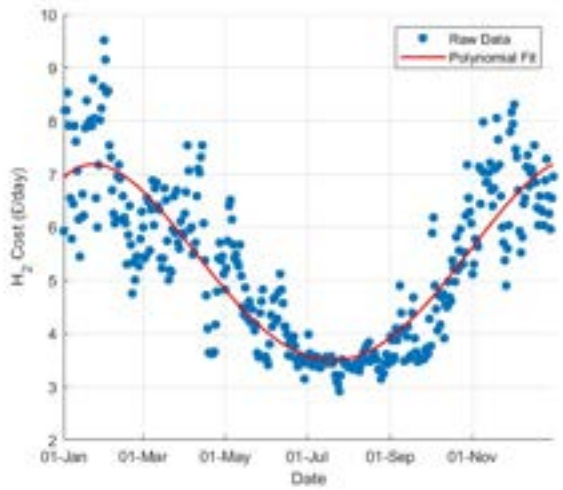

Figure 7: Graph of fuel cost per day based on average heating demand in the UK [3].

Table 8: Capital and operating cost comparison of hydrogen powered air source heat pump systems and natural gas boilers.

System	Capital costs [£]	Operational costs per annum [£]
H_2 powered air source heat pump	4860	1150 [9]
Natural gas combi-boiler	2000 [31]	572 [32]

Table 8 concludes by showing the stark difference in cost between a hydrogen powered air source heat pump and natural gas combi-boiler. These costs have not been annualised as both systems' lifetimes are similar. The incumbent natural gas boiler is significantly cheaper in both aspects and this highlights why there is currently little incentive for households to switch. In order to encourage uptake now, subsidies and carbon taxes must be implemented to make the economic case for purchasing a hydrogen powered air source heat pump viable.

6 Conclusions

The hydrogen powered air-source absorption heat pump designed in this paper provides a viable method of decarbonising domestic heating at the point of use in the UK. There are two externalities, the source of hydrogen and grid electricity mix, that dictate whether this is a truly zero-carbon solution however both are heading in the right direction. The base case model provides a 7 kW unit for hot water and heating in the home and further units could be designed to meet different capacity requirements. Although this is far more expensive than the equivalent traditional natural gas boiler, as shown in Table 8, further research in the sector and optimisation of this model will cause the price to decrease. In particular, new hydrogen production techniques such as electrolysis using renewable electricity will generate competition in the hydrogen supply market driving the operational cost down.

Future research should investigate the potential of using hydrogen fuel cells as substitutes for hydrogen boilers in order to reduce costs. Quantitative analysis comparing the merits of this solution versus electrification of heating should also be examined when proposing a final solution. The viability of this system also needs to be analysed in other geographies as it is highly dependant on air source temperature.

Acknowledgments

The authors would like to express their gratitude towards Mr Andreas Olympios and Dr Antonio Marco Pantaleo for their proactive supervision and assistance whilst undertaking this research.

References

[1] UK Public General Acts. Climate change act 2008 c. 27, 2008.

[2] Committee on Climate Change. Net zero - technical report. Technical report, May 2019.

[3] S. D. Watson, K. J. Lomas, and R. A. Buswell. Decarbonising domestic heating: What is the peak gb demand? *Energy Policy*, 126:533–544, March 1, 2019.

[4] Nick Eyre and Pranab Baruah. Uncertainties in future energy demand in uk residential heating. *Energy Policy v.87*, pages 641–653, Dec 2015.

[5] Thomas Nowak. White paper: Heat pumps - integrating technologies to decarbonise heating and cooling, Nov 07, 2018.

[6] Prepared Element Energy Ltd for the Department for Business, Energy, and 2018 Industrial Strategy November. Hydrogen supply chain evidence base.

[7] Greater London Authority. Low carbon heat: Heat pumps in london. Technical report, Sept 2018.

[8] David Joffe, Sarah Livermore, and Mike Hemsley. Hydrogen in a low-carbon economy. Technical report, Climate Change Committee, 2018.

[9] Dan Sadler, Henrik Solgaard Anderson, Martin Sperrink, and Al Cargill. H21 north of england. Technical report, 2018.

[10] F. Lehner P. Dodds N. Hughes B. Fais N. Sabio D. Hart, J. Howes and M. Crowther. Scenarios for deployment of hydrogen in meeting carbon budgets (e4tech). Technical report, 2015.

[11] Wei Wu, Baolong Wang, Wenxing Shi, and Xianting Li. Absorption heating technologies: A review and perspective. *Applied Energy*, 130:51–71, October 1, 2014.

[12] Wei Wu, Xianting Li, and Tian You. *Low Evaporation Temperature Absorption Heat Pump*, pages 75–108. Absorption Heating Technologies: Efficient Heating, Heat Recovery and Renewable Energy. Springer Singapore, Singapore, 2020. ID: Wu2020.

[13] Wei Wu, Siyuan Ran, Wenxing Shi, Baolong Wang, and Xianting Li. Nh3-h2o water source absorption heat pump (wsahp) for low temperature heating: Experimental investigation on the off-design performance. *Energy*, 115:697–710, November 15, 2016.

[14] Yi Chen, Wei Han, and Hongguang Jin. An absorption–compression refrigeration system driven by a mid-temperature heat source for low-temperature applications. *Energy*, 91:215–225, November 1, 2015.

[15] Michael Garrabrant, Roger Stout, Paul Glanville, Janice Fitzgerald, and Chris Keinath. Development and validation of a gas-fired residential heat pump water heater - final report; sponsor org.: Usdoe office of energy efficiency and renewable energy (eere); usdoe ee office of building technologies (ee-2j). Technical report, 2013.

[16] Wei Wu, Baolong Wang, Tian You, Wenxing Shi, and Xianting Li. Configurations of solar air source absorption heat pump and comparisons with conventional solar heating. *Applied thermal engineering*, 141:630–641, 2018.

[17] Iman Janghorban Esfahani, Yong Tae Kang, and ChangKyoo Yoo. A high efficient combined multi-effect evaporation–absorption heat pump and vapor-compression refrigeration part 1: Energy and economic modeling and analysis. *Energy (Oxford)*, 75:312–326, Oct 1, 2014.

[18] Berhane H. Gebreslassie, Eckhard A. Groll, and Suresh V. Garimella. Multi-objective optimization of sustainable single-effect water/lithium bromide absorption cycle. *Renewable Energy*, 46:100–110, October 1, 2012.

[19] Hadi Ghaebi, Towhid Parikhani, and Hadi Rostamzadeh. A novel trigeneration system using geothermal heat source and liquefied natural gas cold energy recovery: Energy, exergy and exergoeconomic analysis. *Renewable energy*, 119:513–527, Apr 2018.

[20] Andreas V. Olympios, Antonio M. Pantaleo, Paul Sapin, and Christos N. Markides. On the value of combined heat and power (chp) systems and heat pumps in centralised and distributed heating systems: Lessons from multi-fidelity modelling approaches. *Applied energy*, 274:115261, Sep 2020.

[21] Paul E. Dodds, Iain Staffell, Adam D. Hawkes, Francis Li, Philipp Grünewald, Will McDowall, and Paul Ekins. Hydrogen and fuel cell technologies for heating: A review. *International Journal of Hydrogen Energy*, 40(5):2065–2083, February 9, 2015.

[22] Meryem Terhan and Kemal Comakli. Energy and exergy analyses of natural gas-fired boilers in a district heating system. *Applied thermal engineering*, 121:380–387, Jul 2017.

[23] Giacomini. Hydrogem, the hydrogen boiler by giacomini.

[24] Jamie Speirs, Paul Balcombe, Erin Johnson, Jeanne Martin, Nigel Brandon, and Adam Hawkes. A greener gas grid: What are the options. *Energy Policy*, 118:291–297, 2018.

[25] Statista. Uk: average temperature by month 2020.

[26] Nixon Sunny, Niall Mac Dowell, and Nilay Shah. What is needed to deliver carbon-neutral heat using hydrogen and ccs? *Energy Environmental Science*, 13(11):4204–4224, -11-12 2020.

[27] Energy Industrial Strategy Department for Business. Uk energy statistics, q1 2020. Technical report, Department for Business, Energy Industrial Strategy, Jun 25 2020.

[28] B. O. Bolaji and Z. Huan. Ozone depletion and global warming: Case for the use of natural refrigerant – a review. *Renewable and Sustainable Energy Reviews*, 18:49–54, February 1, 2013.

[29] Damian Carrington. Ban new gas boilers in uk from 2025 or risk missing net zero target, says cbi, -07-22T05:01:03.000Z 2020.

[30] Olu Ajayi-Oyakhire. Hydrogen - untapped energy? Technical report, IGEM, 2018.

[31] TheHeatingHub. Guide to new boiler installation costs , Jan 27 2020.

[32] UKPower. Compare energy prices per kwh .

Numerical Modelling with Particles of Taylor-Couette Graphene Exfoliation

Douglas Lau & Gordon Lee

Department of Chemical Engineering, Imperial College London, South Kensington Campus, London SW7 2AZ, United Kingdom

Abstract

Graphene is a versatile two-dimensional material with much industrial potential. However, its adoption has been limited by the lack of mature large-scale production methods. Recently, a Taylor-Couette flow device was developed and demonstrated great potential as a method to exfoliate graphene. In this study, a Computational Fluid Dynamics model is developed using OpenFOAM to explore the particle-fluid interactions within this device. Fluid flow is simulated using the Large-Eddy Simulation with Wall Adapting Local Eddy-viscosity method and particles are simulated using a point-particle approach with two-way coupling. Simulations at Reynolds numbers (Re) of 6200, 8300, and 10350 are used to understand and improve the process. In the model, the number and strength of Taylor vortices is found to decrease when graphite particles are added. Exfoliation is found to occur locally at the walls and there is preferential movement of particles towards the outer wall. Some particle movement towards the inner wall is observed at higher Re, which is desirable due to higher local shear rates. Particles are also found to accumulate in pockets between vortices where there is minimal exfoliation and possible methods to reduce this are discussed. Overall, it is found that operation at higher Re is beneficial for exfoliation.

Keywords: ***graphene, Taylor-Couette, liquid exfoliation, computational fluid dynamics, OpenFOAM, Taylor Vortices***

Introduction

Graphene is rapidly capturing the attention of the nanomaterials sector as a versatile substance with potentially transformative effects across a wide variety of industries. As a two-dimensional (2D) material consisting of sp^2-bonded carbon atoms packed into a dense honeycomb crystal lattice [1], graphene possesses a range of remarkable properties such as high electrical and thermal conductivities, high tensile strength, and high optical transmissivity while retaining out-of-plane flexibility [2, 3]. Bi-layer and few-layer graphene sheets are equally of interest, possessing similar properties to single-layer graphene [4]. With such properties, there is much potential for the industrial application of graphene in functional electronic devices, energy harvesting & storage, optoelectronics, sensors, thermal dissipation films, anti-corrosion primers, and other applications [5, 6].

Whilst the interest in graphene technology has dramatically increased in recent years, with the British government investing over £20 million into graphene-related research [7] and more than 38,000 publications on the topic of graphene in 2019 alone[1], the production rate of graphene in industry unfortunately still lags behind. Consequently, any potential implementation of graphene in industry is currently limited by the lack of mature large-scale production methods. Numerous techniques have been developed that can produce graphene of varying quality. However, all such techniques are complex and energy intensive and only produce small quantities of graphene. Thus far, there exists no simple process that allows for a high production rate of good quality graphene [8].

Graphene production techniques can be broadly categorised into "bottom-up" and "top-down" methods. The bottom-up method involves the chemical reaction of hydrocarbon precursors to produce 2D sheets of graphene. Typically, graphene derived from bottom-up methods are of high quality, characterised by having highly controlled layer numbers ranging between one (single-layer graphene) to ten (few-layer graphene). However, a major drawback of the bottom-up method is that it suffers from very low production rates [9, 10]. Top-down methods, on the other hand, produce graphene at a higher rate but at the cost of quality. Such methods begin with graphite as a feedstock and utilise exfoliation methods whereby van der Waals forces between graphitic layers are overcome to produce graphene sheets [11].

There are many applications in industry where high quality graphene is unnecessary such as in composites, coatings, and flexible electronics. Due to the breadth of applications, low cost, and high scalability potential, it is likely that top-down methods will become the primary source of mass-produced graphene [10, 12]. Accordingly, this study will focus on the top-down method of producing graphene, specifically investigating the liquid exfoliation of graphene in a Taylor-Couette flow device.

Computational Fluid Dynamics (CFD) modelling allows for complex three-dimensional (3D) fluid flows to be solved in timely manner. With the advent of high performance computing these complex flows have been numerically simulated, allowing for the close analysis of the complete flow field which cannot easily be done experimentally. An additional advantage of CFD over experimental methods is its adaptability and resource efficiency. It facilitates the investigation of the effects of different parameters on fluid flow, eliminating the need to devise multiple physical experiments. Unsurprisingly, CFD has become a popular tool in engineering analytics. Its role in engineering prediction has proven to be so strong that it is now viewed as equal in stature and importance to experiment and theory [13].

[1]This figure was sourced from the ISI Web of Science Core Collection database. Search criteria are: Topic = "Graphene", Custom Year Range = "2019 - 2019".

This study takes full advantage of OpenFOAM, an open source CFD toolbox, to simulate the addition of graphite particles in a Taylor-Couette flow device for graphene exfoliation. The behaviour of this multiphase system is analysed at different solvent Reynolds numbers, with particular interest in the dynamics of graphite particles.

Background

The first isolation and characterisation of a graphene flake was performed in 2004 by Novoselov et al. via mechanical exfoliation. This process consisted of the repeated manual application of adhesive tape on the surface of highly oriented pyrolytic graphite (HOPG), thereby allowing a normal force to be exerted in order to separate layers of graphene. With each exfoliation cycle, the graphitic layer decreased in thickness until single-layer or few-layer graphene was produced. While the group was able to reliably produce few-layer graphene up to 10 μm in size, the method employed was extremely time and labour intensive and could not be scaled up. Consequently, many later studies have focused on scaling up graphene production.

As presented in a 2015 review by Yi and Shen, two main mechanical exfoliation routes emerged. The first, based on the original experiment by Novoselov et al., was exfoliation via the normal force. The second was exfoliation via the shear force. Due to the self-lubricating property of graphite in the lateral direction, it is possible to apply a shear force to promote the relative motion between graphite layers, leading to the exfoliation of graphene sheets.

Studies in the late 2000s gave rise to non-chemical, liquid exfoliation methods. Hernandez et al. demonstrated in 2008 that graphene could be dispersed and exfoliated via sonication in organic solvents such as n-methylpyrrolidone (NMP). This was possible as the energy required for exfoliation was balanced by the surface energy of NMP. The group was able to produce high quality single-layer graphene at yields of ~1 wt%, with the potential to increase yields to ~12 wt% with further process refinement. However, using organic solvents such as NMP was not without its drawbacks. Such solvents were expensive and required special care to handle. Post-processing to recover graphene was also difficult due to their tendency to have high boiling points. Following this, Lotya et al. developed a method in 2009 to disperse and exfoliate graphene in a surfactant-water solution. Although water on its own had too high a surface energy to act as an effective exfoliant for graphene, it was shown that the addition of sodium dodecylbenzene sulfonate (SDBS), an ionic surfactant, imparted an effective charge onto graphene flakes and allowed for a graphene dispersion stabilised by electrostatic repulsion.

In 2014 Paton et al. demonstrated high shear mixing of graphite as a scalable alternative to sonication, with the former being a more mature and widely available technology. The group reported that exfoliation of graphene occurs once local shear rate exceeds approximately 10^4 s^{-1}, with quality and size indistinguishable from that produced by sonication. Tran et al. built on these findings and developed a method for producing high quality graphene using a Taylor-Couette flow device in which a graphite-solvent solution was sheared between a rapidly rotating inner cylinder and stationary outer cylinder. The group reported that when rate of rotation of the inner cylinder exceeded a critical value, Taylor vortices began to appear in regular intervals along the cylinder axis as the basic shear flow became unstable and transitioned to a secondary flow. The high local shear rate within these vortex cells along with high wall shear stress enabled the exfoliation of graphene sheets. In addition to experimental work, Tran et al. performed CFD simulations to attempt to predict local distributions of shear stress and pressure. The group's simulations predicted that maximum wall shear stress and pressure increased alongside rate of rotation of the inner cylinder.

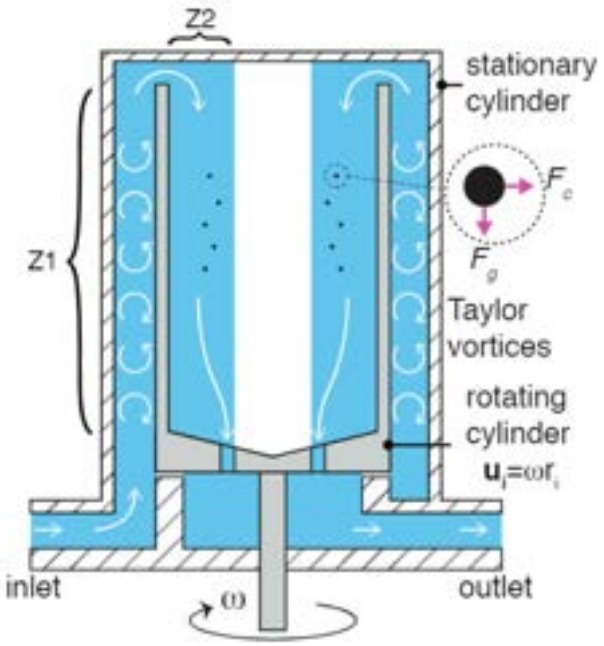

Figure 1: Schematic of the liquid exfoliation Taylor-Couette flow device from Stafford et al. Reproduced with permission from ref. [20]. CC BY-NC-ND 4.0.

Recently, Stafford et al. developed and patented a continuous exfoliation device based on Taylor-Couette flow. The flow device, shown in Figure 1, is made of a stationary outer cylinder and a hollow inner rotating cylinder and contains two zones. The first is the Taylor vortex zone (Z1) where conditions for exfoliation are met. The second is the inner cylinder zone (Z2) where the fluid mixture exits. A secondary purpose of Z2 is to control concentration saturation of graphene. The group found this production method to be effective, producing graphene at concentrations 14 times higher than the shear mixing method of Paton et al., despite equivalent process volumes and precursor conditions. Stafford et al. also developed a CFD model using OpenFOAM to simulate hydrodynamics of the Taylor-Couette process, in particular the Taylor vortex zone (Z1). The group utilised Large-Eddy Simulation (LES) with Wall Adapting Local Eddy-viscosity (WALE) sub-grid scale approach to

model turbulence. Newtonian fluids were modelled to reflect solvents used experimentally, however, the graphite phase was neglected. Consequently, the CFD model produced was effectively a single-phase simplification of the actual process and ignored particle interactions.

This study builds upon and refines the aforementioned CFD model by including the graphite phase and considering particle-fluid interactions. This study specifically investigates the behaviour of particles in the Taylor-Couette system and how particles and flow structures influence each other in the context of graphene exfoliation.

Methodology

Model Setup

Fluid dynamics simulations for this study were performed using OpenFOAM on Imperial College London's High Performance Computing cluster. The CFD model setup shown in Figure 2 considers flow of an incompressible, isothermal Newtonian fluid between a stationary outer cylinder ($r = R_2, u_\theta = 0$) and rotating inner cylinder ($r = R_1, u_\theta = \omega R_1$) with angular velocity ω.

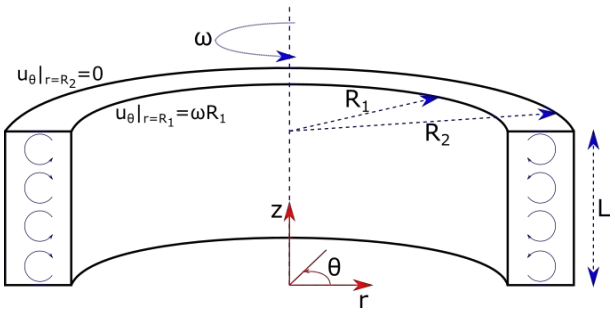

Figure 2: Schematic of the Taylor-Couette simulation setup.

The fluid flow can be described using the following continuity equation and momentum balance equation,

$$\nabla \cdot \mathbf{u} = 0 \tag{1}$$

$$\rho\left(\frac{\partial \mathbf{u}}{\partial t} + \mathbf{u}\cdot\nabla\mathbf{u}\right) = -\nabla p + \mu\nabla^2\mathbf{u} + \rho g\hat{\mathbf{z}} \tag{2}$$

where $\mathbf{u}$ denotes velocity, t denotes time, p denotes pressure, μ denotes dynamic viscosity, ρ denotes density, g denotes gravitational acceleration, and $\hat{\mathbf{z}}$ denotes the unit vector in the z-direction.

Nondimensionalisation of the governing equations was implemented via the following scaling,

$$\tilde{\mathbf{u}} = \frac{\mathbf{u}}{R_1\omega},\ \tilde{\mathbf{x}} = \frac{\mathbf{x}}{d},\ \tilde{t} = \frac{t}{d/R_1\omega},\ \tilde{p} = \frac{p}{\rho(R_1\omega)^2} \tag{3}$$

resulting in the following dimensionless momentum equation,

$$\frac{\partial\tilde{\mathbf{u}}}{\partial\tilde{t}} + \tilde{\mathbf{u}}\cdot\tilde{\nabla}\tilde{\mathbf{u}} = -\tilde{\nabla}\tilde{p} + \frac{1}{Re}\tilde{\nabla}^2\tilde{\mathbf{u}} + \frac{1}{Fr^2}\tilde{\mathbf{z}} \tag{4}$$

where,

$$Re = \frac{\rho R_1\omega d}{\mu},\ Fr = \frac{R_1\omega}{\sqrt{gd}} \tag{5}$$

are the dimensionless Reynolds number and Froude number, respectively. Note that $d = R_2 - R_1$ is the width of the gap between inner and outer cylinders.

No slip boundary conditions were implemented at the surface of each cylinder,

$$\tilde{u}|_{r=R_1} = \tilde{\theta},\ \tilde{u}|_{r=R_2} = 0 \tag{6}$$

and a periodic boundary condition was imposed for the annular flow region. The initial flow condition was set as $\mathbf{u}(r,\theta,z)|_{t=0} = 0$. These conditions result in a model that simulates pure Taylor-Couette flow, allowing for the investigation of Taylor vortices.

Model domain dimensions were set up to replicate the radial geometry of the Taylor-Couette flow device developed by Stafford et al., with $R_1 = 0.0505$ m, $R_2 = 0.0525$ m, and $d = 0.002$ m. The domain length was chosen to be $L = 2\pi d$, which is consistent with simulations performed by Dong. The dimensionless mesh size was chosen to be $r = 8.9 \times 10^{-3}$, $\theta = 0.51$, and $z = 0.079$, which corresponds to a mesh with 40 cells in r, 80 cells in z, and 320 cells in θ. Note that this was lower than the single-phase model developed by Stafford et al., where a mesh was set up with 80 cells in r, 180 cells in z, and 720 cells in θ (dimensionless mesh size was $r = 4.45 \times 10^{-3}$, $\theta = 0.11$, and $z = 0.035$). Lower resolution simulations were performed in this study due to time constraints as well as problems implementing a point-particle approach at small mesh sizes. A time-step of 0.0005 s was selected such that the Courant number did not exceed 0.5 to ensure temporal accuracy and numerical stability of the simulation.

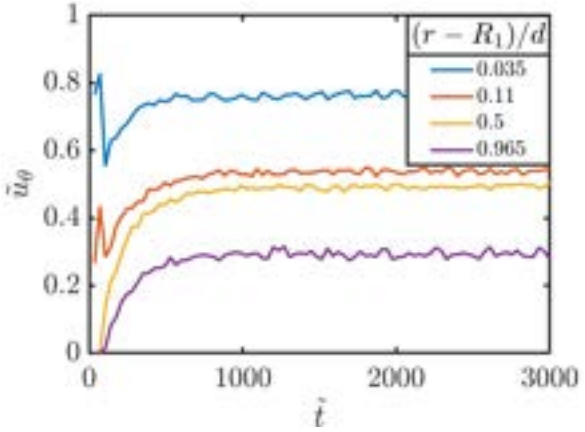

Figure 3: Evolution of dimensionless velocities in the θ-direction over dimensionless time for the single-phase CFD simulation without graphite particles.

To ensure all flow structures and phenomena were fully developed, simulations in this study were carried out to at least $\tilde{t} = 1000$. This number was based off results from the single-phase simulations without graphite particles. As shown in Figure 3, dimensionless velocities in the single-phase simulations reached a plateau by $\tilde{t} = 1000$, suggesting that flows were fully developed.

Simulation of the Liquid Solvent

To replicate experiments performed on the Taylor-Couette flow device NMP was selected as the simulated solvent and three rotational speeds, $\omega = 105, 140,$ and 174 rad s^{-1}, were investigated. Thus, model fluid properties were defined as $\rho = 1000$ kg m^{-3} and $\nu = 1.7 \times 10^{-6}$ m^{2}s^{-1} and dimensionless parameters corresponding to the three rotational speeds were chosen ($Re = 6200, 8300,$ and 10350, respectively).

For turbulent flows at the Reynolds numbers of interest, direct numerical simulation (DNS) of the governing equations was computationally intractable. As such, the computational requirement was reduced by performing Large-Eddy Simulation (LES) to model turbulent motion to a certain scale. At scales smaller than the grid size, the Wall Adapting Local Eddy-viscosity (WALE) sub-grid method was used [22]. The LES-WALE method models turbulence through an additional eddy viscosity term, ν_t. When combined with the molecular viscosity term, ν, effective viscosity can be found, $\nu_e = \nu + \nu_t$. The eddy viscosity term is written as,

$$\nu_t = (C_w \Delta)^2 \frac{(S^d_{ij} S^d_{ij})^{\frac{3}{2}}}{(\bar{S_{ij}} \bar{S_{ij}})^{\frac{5}{2}} + (S^d_{ij} S^d_{ij})^{\frac{5}{4}}} \tag{7}$$

where,

$$\bar{S_{ij}} = \frac{1}{2}\left(\frac{\partial \bar{u_i}}{\partial x_j} + \frac{\partial \bar{u_j}}{\partial x_i}\right) \tag{8}$$

$$S^d_{ij} = \frac{1}{2}\left(\frac{\partial \bar{u_k}}{\partial x_i}\frac{\partial \bar{u_j}}{\partial x_k} + \frac{\partial \bar{u_k}}{\partial x_j}\frac{\partial \bar{u_i}}{\partial x_k}\right) - \frac{1}{3}\delta_{ij}\frac{\partial \bar{u_k}}{\partial x_l}\frac{\partial \bar{u_l}}{\partial x_k} \tag{9}$$

is the deformation tensor of the resolved field and the traceless symmetric part of the square of the velocity gradient tensor, respectively. Note that δ_{ij} is the Kronecker delta and C_w is a constant set at 0.5 as suggested by Stafford et al.. Further details of this method are discussed in the aforementioned paper, which this CFD model is based on, and in Nicoud and Ducros.

Injecting Particles into the Simulation

The method prevously described only models a single-phase liquid and does not consider the graphite phase. To inject graphite particles into the simulation, a point-particle approach using the Maxey-Riley equation was selected. This equation describes the motion of a particle in a viscous fluid [23] and is written as,

$$m_i \frac{d\mathbf{v}_i(t)}{dt} = \mathbf{F_B} + \mathbf{F_{PG}} + \mathbf{F_{AM}} + \mathbf{F_D} + \mathbf{F_{hist}} \tag{10}$$

where particle velocity $\mathbf{v}_i$ is derived from the kinematic equation,

$$\frac{d\mathbf{x}_i(t)}{dt} = \mathbf{v}_i \tag{11}$$

and $\mathbf{x}_i$ is the position of particle i. The terms in the right-hand side of the Maxey-Riley equation represent all forces acting on the particle, namely the buoyancy force, force of the undisturbed velocity field, added mass force, drag force, and the Basset history force, respectively. A full analysis of these forces can be found in Kuerten. It is important to note that the particle drag force used in this study differed from that in the aforementioned paper as the graphite particles were not spherical. Instead, a modified drag force taken from Haider and Levenspiel was used to account for their eccentricity. This drag force is written as,

$$\mathbf{F_D} = \frac{24}{Re}\left(1 + A \times Re^B\right) + \frac{Re \times C}{Re + D} \tag{12}$$

where A, B, C, and D are empirical model coefficients related to particle sphericity, ϕ. Particle sphericity is defined as,

$$\phi = \frac{s}{S} \tag{13}$$

where s is the surface area of a sphere with the same volume as the particle and S is the actual surface area of the particle. To be consistent with experiments, sphericity of the graphite particles was set at $\phi = 0.59$.

Particle diameter was chosen to be 20 microns, which is smaller than that used in experiments. This deviation arose due to problems with the point-particle approach which required particle size to be less than mesh cell size. This was why, as mentioned previously, simulations were performed at lower resolutions (and thus higher mesh sizes) than the single-phase cases.

As recommended by Kuerten, two-way coupling was also performed as particle volume fraction was calculated to be $\Phi = 10^{-6}$. At these volume fractions, the influence of particles on fluid flow and the influence of fluid on the particles themselves must be accounted for. Interactions between particles do not yet need to be considered, only coming into play at even higher volume fractions.

Further details of the point-particle approach and two-way coupling method are discussed in Kuerten. The DPMFoam solver in OpenFOAM was utilised to implement the LES with point-particle approach [25].

Model Validation

The single-phase LES model developed by Stafford et al. was validated against the DNS performed by Dong.

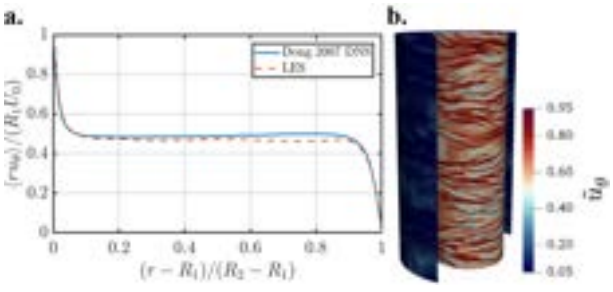

Figure 4: (a) Comparison of dimensionless angular momentum versus dimensionless length data between single-phase simulation (LES) and DNS performed by Dong. **(b)** Velocity contour of the single-phase simulation.

Figure 4**a** shows that the single-phase LES model, which forms the basis of the model developed in this study, is in agreement with the results from DNS of

Taylor-Couette flow performed by Dong within the range of Reynolds number investigated ($3000 < Re < 13000$). A qualitative comparison of instantaneous velocity contours extracted from the LES (Figure 4**b**) and DNS models by Dong also agrees. Thus, the numerical results generated in this study have been validated.

Results & Discussion

Figure 5 shows a comparison of streamline plots between the single-phase simulations and the graphite particles simulations at varying Reynolds numbers. These plots were taken at an instantaneous moment in time and are a slice of the annular flow region. Note that the colour scales are not the same. The scale for single-phase cases (Figure 5**a**) is velocity in the θ-direction while the scale for the cases with particles (Figure 5**b**) is particle concentration. Streamlines are overlaid on top to show the direction of travel of a fluid element.

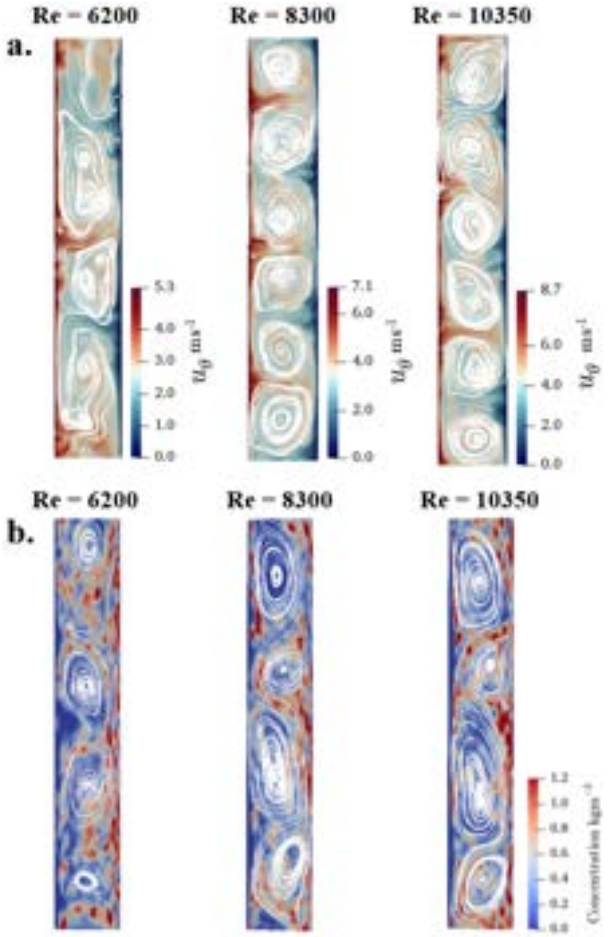

Figure 5: Streamline plots are taken as a slice of the annular flow region at an instantaneous moment in time. The inner and outer cylinder walls are the left and right-hand side of the plots, respectively. (**a**) Single-phase without graphite particles. (**b**) With graphite particles.

The streamlines for the single-phase simulations show four Taylor vortices at a Reynolds number of 6200 and six Taylor vortices for Reynolds numbers of 8300 and 10350, whereas the streamline plots for the graphite particles simulations show four Taylor vortices across all Reynolds numbers investigated. The observed reduction in Taylor vortices may be influenced by pockets of graphite particles that have accumulated at the outer cylinder wall. A previous study suggested that flow in the separation and jet impingement regions (fluid moving away from the wall and fluid moving towards the wall, respectively) play a critical role in the dynamics of Taylor vortices. The appearance of a strong periodic secondary flow in the flow separation region of the outer cylinder wall carries momentum flux from adjacent Taylor vortices and leads to the decrease in strength of these vortices and an imbalance between the two counter-rotating pairs [26]. There is evidence of this imbalance in sizes of vortex pairs (Figure 5**b**), especially for Reynolds numbers of 8300 and 10350. Another study corroborates this conclusion, suggesting that large momentum fluxes cause a decrease in the number of vortex pairs [27]. Evidence suggests that graphite particles at the outer cylinder wall play a role in transporting momentum away from Taylor vortices, leading to the observed decrease in the number of vortices between the single-phase simulations and the simulations with particles. It is important to note that the graphite particles simulations were performed at a lower resolution than the single-phase simulations. Thus, there is opportunity for further investigation into this phenomenon via higher resolution simulations. In the context of the exfoliation of graphene, a decrease in strength and number of Taylor vortices is disadvantageous. This is due to the resultant decrease in local shear rate, which is the primary mechanism for exfoliation. In general, smaller vortices rotate at higher velocities as individual fluid elements travel shorter distances. As such, a higher number of smaller vortices is more desirable for exfoliation due to increased shear rates.

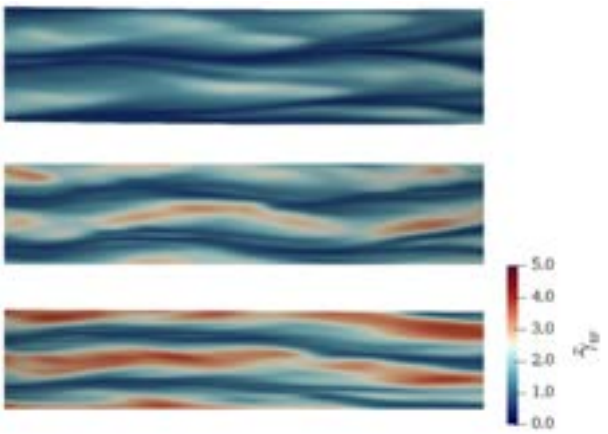

Figure 6: Shear rate map of the inner cylinder wall. The scale has been normalised to show regions where $\tilde{\gamma}_w > 1.0$ have local conditions sufficient for exfoliation. The Reynolds numbers from top to bottom are 6200, 8300, and 10350, respectively.

Figure 6 shows local shear rates at the inner cylinder wall for Reynolds numbers of 6200, 8300, and 10350 from top to bottom, respectively. Note that the scale has been normalised with respect to $\gamma = 10^4$ s^{-1}, the minimum shear rate required for exfoliation. Thus, exfoliation can occur in regions where $\tilde{\gamma}_w > 1.0$. It is observed

that shear rate at the inner cylinder wall increases with Reynolds number, leading to an increased regions of exfoliation. This is expected, as increasing the rate of rotation of the inner cylinder leads to larger velocity gradients, and thus larger shear stresses, due to the no-slip property of the wall. As regions of high shear correspond to the position of the Taylor vortices, vortical flow structures are apparent in the shear rate maps, with these vortices exhibiting wavy behaviour along the θ-direction. This wavy vortex flow is known to arise at high Reynolds numbers. With regards to the exfoliation of graphene, it is clear that increasing the rotational velocity of the inner cylinder, and thus increasing operational Reynolds number, is advantageous.

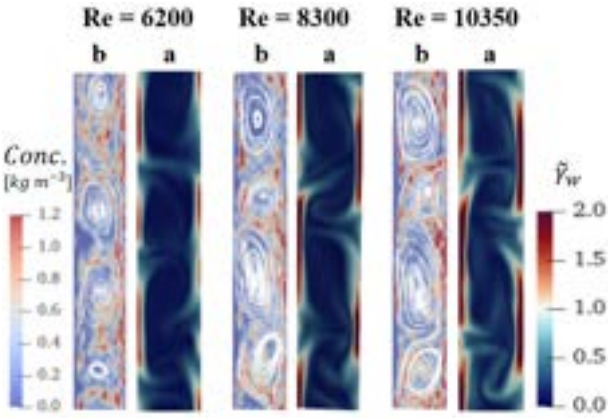

Figure 7: Comparison of shear rate maps of a slice of the annular flow region with concentration plots. (**a**) Shear rate maps. (**b**) Concentration plots with streamlines overlaid on top.

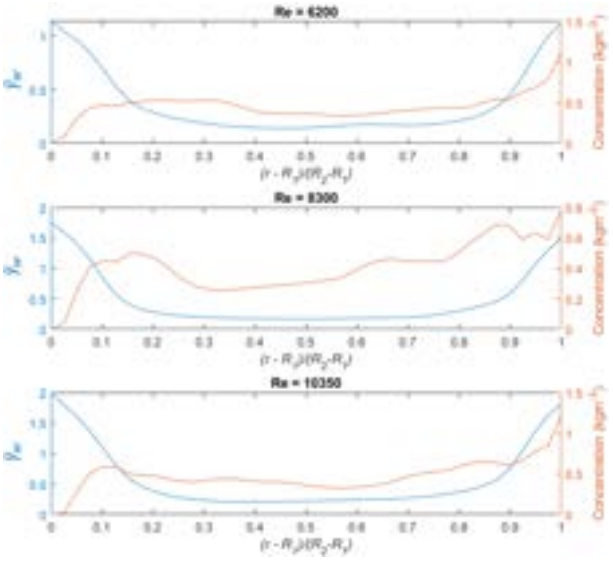

Figure 8: Average normalised shear rate (blue) and average concentration (orange) with respect to normalised radial position (henceforth referred to as $\tilde{r}$) in the annular flow region. Averaging was performed in the θ and z-direction to obtain average values by "fluid layer" in the radial direction.

From the shear rate maps of a slice of the annular flow region (Figure 7**a**), it is clear that the regions of high shear and thus exfoliation are locally concentrated at the wall directly adjacent to the Taylor vortices. Again, this is due to the rotation of these vortices and the no-slip property of the walls. As such, it is generally desired that graphite particles migrate towards the walls to benefit exfoliation. There are already strong indications of this. It is observed that graphite particles avoid stagnation zones at the centre of Taylor vortices and that there is preferential movement towards the stationary outer cylinder wall (Figure 5**b**). Indeed, plots of average particle concentration with respect to normalised radial position, $\tilde{r}$, confirm this (Figure 8, orange). There is a general trend for all Reynolds numbers that average particle concentration increases as $\tilde{r}$ approaches unity (the stationary outer cylinder wall). Note that there are also local maxima between $\tilde{r} = 0.1$ and $\tilde{r} = 0.2$ (close to the rotating inner cylinder wall). At the outer cylinder wall, average particle concentrations reach global maxima of 1.1230 kg m^{-3}, 0.7816 kg m^{-3}, and 1.2279 kg m^{-3} for Reynolds numbers of 6200, 8300, and 10350, respectively. The observed preferential movement of graphite particles to the outer cylinder wall is likely due to turbophoresis. In non-homogeneous turbulent flows, particles tend to migrate towards regions of lower turbulence kinetic energy near a stationary wall [23].

Although preferential movement of particles towards the stationary outer cylinder wall is desirable, it would be even more desirable for particles to migrate towards the rotating inner cylinder wall where there are higher average shear rates. Figure 8 shows that average normalised shear rates (blue) increase to reach local maxima at the walls. Average normalised shear rates are higher at the inner cylinder wall ($\tilde{\gamma}_w$ = 1.1345, 1.7577, and 1.9918 for Re = 6200, 8300, and 10350, respectively) than at the outer cylinder wall ($\tilde{\gamma}_w$ = 1.1229, 1.4813, 1.8072 for Re = 6200, 8300, and 10350, respectively). The difference in shear rates can be attributed to the fact that the inner cylinder wall is rotating and the outer cylinder wall is stationary. Additionally, regions of exfoliation appear to cover a larger proportion of the inner cylinder wall than the outer cylinder wall. This is especially pronounced at the Reynolds number of 10350 (Figure 7**a**, Re = 10350). Both higher average shear rates and larger exfoliation regions are incentives for further investigation into influencing graphite particles to preferentially move towards the inner cylinder wall. Already, there is some indication of this at higher Reynolds numbers (Figure 7**b**, Re = 8300 and Re = 10350). As mentioned previously, there are local maxima for average particle concentration near the inner cylinder wall. For Reynolds numbers of 8300 and 10350, there is a average particle concentration is 0.4969 kg m^{-3} at $\tilde{r} = 0.15$ and 0.5857 kg m^{-3} at $\tilde{r} = 0.10$, respectively (Figure 8). As such, evidence suggests that operating at higher Reynolds numbers benefits exfoliation.

It is important to note, however, that these average values overlook the reality that local shear rates and local particle concentrations are not uniform in the z-direction. While there is preferential movement of graphite particles towards the outer cylinder wall, particles tend to accumulate in pockets between Taylor vortices. When Figure 7**a** and Figure 7**b** are overlaid on top of each other, it is clear that these pockets do not line up with regions of exfo-

liation. From particle concentration plots, there is evidence that graphite particles at the edge of these stagnation pockets escape and migrate towards exfoliation regions, likely a result of being dragged along by the Taylor vortices. However, it is still undesirable to have large stagnation pockets at the walls. As such, there is opportunity for further investigation into methods of reducing these stagnation pockets. The introduction of baffles into the Taylor-Couette system could be of interest as it has been previously shown to increase the number of Taylor vortex pairs [27] and may also act to disrupt the formation of stagnation pockets at the walls. Operation by varying inner cylinder rotational speed, and thus Reynolds number, with time could also be of interest as a means to "pulse" the exfoliation regions. Simulations are currently performed at a constant rotational velocity and Reynolds number with no time-dependency.

Conclusions & Outlook

The Taylor-Couette flow model was successfully refined by introducing graphite particles into the simulation via the point-particle approach. With this, analysis on the interactions between particles and fluid flow structures in the context of the liquid exfoliation of graphene was completed. It was found that the number of Taylor vortices in the graphite particles simulations was lower than in the single-phase simulations. This may be a result of the influence of pockets of accumulated graphite particles at the outer cylinder wall on promoting a periodic secondary flow and transporting momentum away from the vortices. In terms of exfoliation, the observed decrease in number and strength of Taylor vortices is disadvantageous. It was also found that regions of high shear, and thus regions of exfoliation, are locally concentrated at the wall directly adjacent to the vortices due to the combined effect of the rotation of the vortices and the no-slip property of the walls. It was shown that increasing the rotational velocity of the inner cylinder, and thus increasing the Reynolds number, is advantageous for exfoliation due to higher local shear rates at the walls. Simultaneously, it was found that particles tend to migrate towards the outer cylinder wall, with maximum average particle concentrations at the outer wall of 1.1230 kg m^{-3}, 0.7816 kg m^{-3}, and 1.2279 kg m^{-3} for Reynolds numbers of 6200, 8300, and 10350, respectively. This phenomenon was likely due to the effect of turbophoresis. While migration to the stationary outer cylinder wall is desirable, analysis showed that it would be more advantageous if particles could be influenced to migrate to the rotating inner cylinder wall as the local average shear rate at the inner cylinder wall was higher than at the outer cylinder wall. There were signs of this migration at higher Reynolds numbers, with local maximum average particle concentrations near the inner wall of 0.4969 kg m^{-3} and 0.5857 kg m^{-3} for Reynolds numbers of 8300 and 10350, respectively. This was further evidence suggesting that operating at higher Reynolds numbers is beneficial for exfoliation. However, although preferential movement of graphite particles towards the walls was observed, it was also found that they tended to accumulate in pockets between Taylor vortices in zones of minimal exfoliation. These large stagnation pockets are not desirable for exfoliation. Overall, evidence suggests that the operation of the Taylor-Couette flow device at high rotational velocities, and thus high Reynolds numbers, is advantageous for the liquid exfoliation of graphene.

With increased interest in graphene production over the past few years, further research into understanding the Taylor-Couette flow device is warranted, especially as it has demonstrated its potential. There are many avenues of research that could be of particular interest, such as an investigation into the influence of graphite particle size on flow structures and exfoliation due to potential differences in momentum transfer. As a continuation of the present study, higher resolution graphite particle simulations can be performed to further investigate how the pockets of accumulated graphite particles at the outer cylinder wall affect flow structures. Further investigation into influencing particles to migrate towards the rotating inner cylinder wall can also be done. Finally, further investigation into reducing stagnation pockets and increasing the number of Taylor vortices can be performed in an effort to enhance exfoliation, possibly through the introduction of baffles into the Taylor-Couette system or operation by varying inner cylinder rotational speed and Reynolds number with time.

Acknowledgements

The authors would like to thank Usmaan Farooq, Dr Jason Stafford, Dr Camille Petit, and the Matar Fluids Group for the helpful discussions, guidance, and technical support offered throughout this research.

References

[1] Wonbong Choi, Indranil Lahiri, Raghunandan Seelaboyina, and Yong Soo Kang. Synthesis of graphene and its applications: A review. *Critical Reviews in Solid State and Materials Sciences*, 35(1):52–71, 2010. doi: 10.1080/10408430903505036.

[2] Caterina Soldano, Ather Mahmood, and Erik Dujardin. Production, properties and potential of graphene. *Carbon*, 48(8):2127–2150, 2010. doi: 10.1016/j.carbon.2010.01.058.

[3] Jelle Vekeman, José Sánchez-Marín, Alfredo Sánchez de Merás, Inmaculada Garcia Cuesta, and Noelia Faginas-Lago. Flexibility in the graphene sheet: The influence on gas adsorption from molecular dynamics studies. *The Journal of Physical Chemistry C*, 123(46):28035–28047, 2019. doi: 10.1021/acs.jpcc.9b07503.

[4] C. N. R. Rao, Kanishka Biswas, K. S. Subrahman-

yam, and A. Govindaraj. Graphene, the new nanocarbon. *Journal of Materials Chemistry*, 19(17): 2457, 2009. doi: 10.1039/b815239j.

[5] Yanwu Zhu, Hengxing Ji, Hui-Ming Cheng, and Rodney S Ruoff. Mass production and industrial applications of graphene materials. *National Science Review*, 5(1):90–101, 2017. doi: 10.1093/nsr/nwx055.

[6] Xiaoyue Xiao, Yichun Li, and Zhaoping Liu. Graphene commercialization. *Nature Materials*, 15 (7):697–698, 2016. doi: 10.1038/nmat4665.

[7] Edward P. Randviir, Dale A.c. Brownson, and Craig E. Banks. A decade of graphene research: production, applications and outlook. *Materials Today*, 17(9):426–432, 2014. doi: 10.1016/j.mattod.2014.06.001.

[8] Les Johnson and Joseph Meany. Mass-producing graphene. *American Scientist*, 106(3):176, 2018. doi: 10.1511/2018.106.3.176.

[9] Yuan Li and Nitin Chopra. Progress in large-scale production of graphene. part 2: Vapor methods. *JOM*, 67(1):44–52, December 2014. doi: 10.1007/s11837-014-1237-z.

[10] Jason Stafford, Andrius Patapas, Nwachukwu Uzo, Omar K. Matar, and Camille Petit. Towards scale-up of graphene production via nonoxidizing liquid exfoliation methods. *AIChE Journal*, 64(9): 3246–3276, 2018. doi: 10.1002/aic.16174.

[11] Yuan Li and Nitin Chopra. Progress in large-scale production of graphene. part 1: Chemical methods. *JOM*, 67(1):34–43, December 2014. doi: 10.1007/s11837-014-1236-0.

[12] Josphat Phiri, Patrick Gane, and Thad C. Maloney. General overview of graphene: Production, properties and application in polymer composites. *Materials Science and Engineering: B*, 215:9–28, January 2017. doi: 10.1016/j.mseb.2016.10.004.

[13] John F. Wendt and John D. Anderson. *Computational fluid dynamics: an introduction*. Springer, 2010.

[14] K. S. Novoselov, A. K. Geim, S. V. Morozov, D. Jiang, Y. Zhang, S. V. Dubonos, I. V. Grigorieva, and A. A. Firsov. Electric field effect in atomically thin carbon films. *Science*, 306(5696):666–669, 2004. ISSN 00368075, 10959203.

[15] Min Yi and Zhigang Shen. A review on mechanical exfoliation for the scalable production of graphene. *Journal of Materials Chemistry A*, 3(22):11700–11715, 2015. doi: 10.1039/c5ta00252d.

[16] Yenny Hernandez, Valeria Nicolosi, Mustafa Lotya, Fiona M. Blighe, Zhenyu Sun, Sukanta De, I. T. McGovern, Brendan Holland, Michele Byrne, Yurii K. Gun'Ko, John J. Boland, Peter Niraj, Georg Duesberg, Satheesh Krishnamurthy, Robbie Goodhue, John Hutchison, Vittorio Scardaci, Andrea C. Ferrari, and Jonathan N. Coleman. High-yield production of graphene by liquid-phase exfoliation of graphite. *Nature Nanotechnology*, 3(9): 563–568, August 2008. doi: 10.1038/nnano.2008.215.

[17] Mustafa Lotya, Yenny Hernandez, Paul J. King, Ronan J. Smith, Valeria Nicolosi, Lisa S. Karlsson, Fiona M. Blighe, Sukanta De, Zhiming Wang, I. T. Mcgovern, and et al. Liquid phase production of graphene by exfoliation of graphite in surfactant/water solutions. *Journal of the American Chemical Society*, 131(10):3611–3620, 2009. doi: 10.1021/ja807449u.

[18] Keith R. Paton, Eswaraiah Varrla, Claudia Backes, Ronan J. Smith, Umar Khan, Arlene O'Neill, Conor Boland, Mustafa Lotya, Oana M. Istrate, Paul King, and et al. Scalable production of large quantities of defect-free few-layer graphene by shear exfoliation in liquids. *Nature Materials*, 13(6):624–630, 2014. doi: 10.1038/nmat3944.

[19] Tuan Sang Tran, Seung Jun Park, Sung Sic Yoo, Tae-Rin Lee, and TaeYoung Kim. High shear-induced exfoliation of graphite into high quality graphene by taylor–couette flow. *RSC Advances*, 6(15):12003–12008, 2016. doi: 10.1039/c5ra22273g.

[20] Jason Stafford, Nwachukwu Uzo, Usmaan Farooq, Silvia Favero, Si Wang, Hseuh-Hung Chen, Anouk L'Hermitte, Camille Petit, and Omar Matar. Universal scaling and real-time monitoring of the production of liquid exfoliated graphene. [Preprint] 2020. Available from: doi.org/10.26434/chemrxiv.11628267.v1.

[21] S. Dong. Direct numerical simulation of turbulent taylor–couette flow. *Journal of Fluid Mechanics*, 587:373–393, August 2007. doi: 10.1017/s0022112007007367.

[22] F. Nicoud and F. Ducros. *Flow, Turbulence and Combustion*, 62(3):183–200, 1999. doi: 10.1023/a:1009995426001.

[23] J. G. M. Kuerten. Point-particle DNS and LES of particle-laden turbulent flow - a state-of-the-art review. *Flow, Turbulence and Combustion*, 97(3):689–713, September 2016. doi: 10.1007/s10494-016-9765-y.

[24] A. Haider and O. Levenspiel. Drag coefficient and terminal velocity of spherical and nonspherical particles. *Powder Technology*, 58(1):63–70, May 1989. doi: 10.1016/0032-5910(89)80008-7.

[25] Jeroen Hofman. Understanding dpmfoam/mppicfoam. *Eindhoven University of Technology, Eindhoven*, 2015.

[26] M. A. Razzak, B. C. Khoo, and K. B. Lua. Numerical study on wide gap taylor couette flow with flow transition. *Physics of Fluids*, 31(11):113606, November 2019. doi: 10.1063/1.5125640.

[27] V. Sinevic, R. Kuboi, and A.W. Nienow. Power numbers, taylor numbers and taylor vortices in viscous newtonian and non-newtonian fluids. *Chemical Engineering Science*, 41(11):2915–2923, 1986. doi: 10.1016/0009-2509(86)80022-7.

Exploratory Framework towards Developing a Predictive Model for Teamwork in Engineering Teams

Karyshma Gill and Jodie Lee
Department of Chemical Engineering, Imperial College London, U.K.

Abstract

This study provides an initial framework to guide predictive modelling to aid in the formation of high-performing teams. From literature review, a series of diversity impact factors (DIF) and team outcome parameters were identified. DIFs of interest were MBTI personality types, locus of control, goal orientations and procrastination. Team outcome parameters studied were team self-efficacy, team behaviour and team performance. Information on DIFs, team self-efficacy and team behaviour outcomes were collected through retroactive survey data for the Strategy of Design project from final year undergraduates in the Department of Chemical Engineering at Imperial College London. Scores obtained by each team indicated their performance. A combination of statistical methods was used to rank DIFs by relative importance. Rankings were then aggregated to identify important predictors. Homogeneity in DIFs was positively related to team behaviour outcomes, indicating a complementary model, which seemed to point towards possible tensions between diversity and team effectiveness. Team behaviour outcomes better explained variance in team performance than DIFs, which indicated a possible input-process-output model with direct and indirect effects. Future modelling efforts may be complicated by multi-collinearity and suppressor variables. However, average rankings seem to indicate that future models should focus on goal orientation and procrastination tendencies.

Keywords*:* personality, locus of control, goal orientation, team effectiveness, engineering teams, relative importance, multiple regression, relative weights

1. Background

Teams are increasingly becoming integral parts of modern organisations. Cleland (1996) advocates the usage of teams as key organisational elements in the design and execution of strategic management initiatives as they are conducive to cost-reduction, innovation, creativity, productivity, and risk-taking.

Unsurprisingly, employers have taken note and are increasingly requiring students to be effective team players. This had led accreditation institutions such as the Institution of Chemical Engineers (IChemE), the International Accreditation Board for Engineering and Technology (ABET), and the Accounting Education Change Commission (AECC) to compel higher education institutions to introduce and develop team-working elements into their curricula.

In designing suitable curricula, higher education institutions (HEIs) often adopt a three-pronged approach (Ventura-Medina, 2020) – identifying intended learning outcomes (ILOs), providing meaningful learning opportunities and assessing the achievement of these outcomes amongst students. ILOs tend to be guided by both accreditation requirements and employer demands. In the context of teamwork, many universities have developed appropriate pedagogies to incorporate these elements, most commonly through the usage of problem-based learning and coursework.

However, assessing teamwork outcomes is hard. Current assessment modes tend to emphasise product-related skills by assigning scores on completed products. However, the effectiveness of such approaches are uncertain. Adams *et al.* (2002) claim that although assessing product-related outcomes help students see the benefits of working in teams, most students remain sceptical on the purported pedagogical benefits. Instead, they are generally frustrated by their past experiences in teamwork, most notably, the social-loafing effect and thus prefer being assessed on individual work.

Educational researchers have found correlations between team processes and factors such as the method of instruction used (Bobbitt *et al.*, 2000), students' preference for teaching methods (Anderton-Lewis and King, 1995), learning styles (Gardner and Korth, 1998), team composition (Miller and Polito, 1999), team longevity (Urch and Hayes 2000), attitude towards teamwork (Chalupa *et al.*, 1997) and team incentives such as the usage of grades as motivators (Ravenscroft and Buclkess, 1995).

However, most of this research is reported in the management and psychology literature, meaning that the generalizability of this work to engineering student teams is often unclear. Additionally, although controlling the factors discussed above should theoretically improve learning experiences, practically balancing these characteristics during team assignment in large classes is often difficult.

This study is an exploratory framework towards designing a predictive model to produce better engineering design teams. A 'better' team is defined as a productive, high-performing team that allows individual members to thrive.

In developing an exploratory framework, theoretical and practical implications will be considered. Theoretical considerations include shortlisting relevant diversity attributes through extensive literature review, understanding the influence on dimension diversity on team outcomes and identifying the underlying structure of interaction between team attributes and team outcomes. Practical considerations include identifying problematic characteristics that may affect the predicting power of future models designed and identifying important predictor variables for future works to focus on.

2. Introduction

To understand team work, many researchers adopt an input-process-output model (Hackman, 1990; Guzzo and Dickson, 1996) as shown in Figure 1.

Figure 1. Graphical representation of input-process-output (IPO) model

This model describes the influence of a combination of inputs on team processes, and subsequently team outputs. Hackman (1990) groups these inputs into three categories: individual-level factors (e.g. team-member attributes), group-level factors (e.g. structure and size) and environmental-level factors (e.g. task characteristics and reward mechanisms). In this study, we focused only on individual-level inputs, specifically specific attributes of team members (e.g. motivation, personality). The main purpose of this study was to assess how diversity in member attributes in functioning student teams relate to team outcomes and to develop a framework to guide future model building in predicting team effectiveness.

Team Composition

Each team member has a specific set of psychological and emotional predispositions which affect team effectiveness (Guzzo and Dickson, 1996). These attributes include team personality, task type, project length, and organisation culture. This study focuses on team personality attributes and assumes organisation culture, task type, and project length are controlled.

In operationalizing team compositions, researchers have predominantly adopted two methods – calculating trait elevation and calculating trait diversity (Van Vianen and De Dreu, 2010). Trait elevation is defined by the averaged individual scores for a trait, whilst trait diversity (TD) is represented by a team's variance or standard deviation score for a specific construct.

Muchinsky and Monahan (1987) proposed two distinct models of person-environment fit which aim to explain when homogenous (low TD) or heterogenous (high TD) teams result in better job performance. The supplementary model of person-environment fit hypothesises that homogeneity in individual team members' attributes improve team compatibility and cohesion, ensuring better communication and increased team motivation, thus leading to better team performance. The second model, known as the complementary model of person-environment fit suggests that team performance is improved when team members' attributes are diverse, as this allows each member to add unique contributions and perspectives which are necessary for team success.

Research examining the relationship between TD of and group effectiveness remain mixed. Some research suggest a supplementary model of TD results in more effectiveness in predicting team performance (Day and Bedeian, 1995). Others suggest more effective performance results arise from a complementary model of TD (Mello and Ruckes, 2006). Hackman (1990) hypothesised that team performance is a function of both similar and diverse traits. Thus, certain traits may enhance performance when the team is homogenous, whereas others may enhance performance when the team is diverse. This study focuses on diversity of attributes which are henceforth referred to as Diversity Impact Factors (DIFs).

Much of the focus on the role of personality in team performance has been on the OCEAN and MBTI models. Other traits, such as locus of control (LOC) have received less attention. LOC is defined as the extent to which individuals believe they have control over the outcome of events. Individuals are hypothesised to have either internal or external LOC. Those with internal LOC believe that their success or failure in an endeavour is dependent on their efforts while individuals with external LOC believe that their success or failure is dependent on factors outside their control such as fate. Boone and Hendriks (2009) suggest that fundamental attitudinal differences increase likelihood of tensions and conflicts, causing homogenous LOC management teams to achieve higher performance metrics. Barrick *et al.* (1998) hypothesises that this is because LOC diversity is related to diversity in certain traits of the Big Five, causing diversity in LOC to adversely affect team functions by decreasing team cohesion.

There has been little research on the importance of goal orientation at a team level although studies have indicated the role of goal orientation in predicting outcomes for individuals in educational and organisational settings (Pieterse, 2009a). Goal orientation refers to an individuals' disposition towards developing and validating one's ability in achievement settings. This is typically measured across two dimensions – learning orientation and performance orientation. Learning orientation describes the desire to understand concepts in depth and develop mastery in a task, whilst performance orientation reflects the desire to demonstrate competence in comparison to others and to receive favourable judgements of performance. Pieterse (2009) suggests that individual goal orientations may translate to a team, potentially affecting group functioning. Although studies have reported positive relationships between elevations in individual mastery approach and to team efficacy (LePine, 2005; Porter, 2005), the effects of diversity in goal orientations on team outcomes are still uncertain.

Many studies have investigated the effects of individual-level procrastination on performance. Although many researchers suggest procrastination negatively affects behavioural outcomes, cognitive components and performance (Bond and Feather 1988; Harriot and Ferrari 1996), more recent studies have indicated that procrastination can induce short-term benefits as it can aid in temporarily regulating negative emotions (Baumeister *et al.*, 1994). In a team setting, research has shown team procrastination to have a negative relationship with team performance as it increased team members' collective stress levels (Van Hooft and Van Mierlo, 2018).

Team Effectiveness (TE)

It is difficult to conduct a cross-study comparison due to the multi-dimensionality inherent in team effectiveness and poor conceptualisation by researchers. Brannick and Prince (1997) proposed that a comprehensive measure of team effectiveness should consider both the individual and the team, be able to capture the process and the outcome, and be able to describe and diagnose performance to provide developmental feedback to teams.

In practice, however, due to the challenges in formulating this, previous research on team effectiveness have mainly utilised two models – a unidimensional model that aims to characterise team performance by using objective measures such as productivity, quality of work and/or timeliness (Guzzo and Dickson, 1996), and a multi-variate model that attempts to capture the multi-dimensionality of team effectiveness by identifying other dependent factors (Hackman, 1990). Examples of factors previously considered include performance behaviours (Beal *et al.*, 2003), team satisfaction (Gladstein, 1984) and team viability (Sundstrom, De Meuse and Futrell, 1990).

In an attempt to synthesise previous bodies of research, Cohen and Bailey (1997) hypothesised that team effectiveness measures could be classified into three broad dimensions – performance effectiveness, individual attitudinal outcomes and behavioural outcomes. However, they cautioned against developing an overarching formula of team effectiveness, arguing that the multi-dimensionality of the construct required researchers to make value judgements in developing models of effectiveness that were tailored to the characteristics of the teams being studied, especially the types of teams (e.g. project, management, work team), task features (e.g. interdependence, autonomy) and team composition (e.g. size, tenure, diversity).

To articulate the specific manifestation of these dimensions in an academic setting, Adams *et al.* (2002) proposed the following mathematical formulation of team effectiveness,

$$TE = f(P, B, A) \quad (1)$$

where the performance indicator (P) would measure the extent to which student deliverables met the specifications of the task set; the behaviour index (B) would measure the inner workings of the team and team processes; the attitude indicator (A) would determine individual team member's confidence in the team.

However, the lack of systematic evaluation of the construct validity of the team effectiveness (i.e. researchers primarily examine one or two dimensions of team effectiveness in a given study) means to date, there has not been a comprehensive analysis between the dimensions of team effectiveness, or within a category. In addition, the extent to which the dimensions combine to shape students' overall perception of teamwork remain unclear. This is primarily due to difficulties in evaluating certain dimensions of teamwork, especially those with subjective outcomes such as behavioural aspects and attitudinal outcomes. Multiple instruments have been derived to overcome this. Of these, instruments which report both high reliability and validity are the Team Effectiveness Questionnaire from the London Leadership Academy and a self-efficacy questionnaire proposed by Bandura (2005).

Modelling

Researchers often aim to reduce multi-variate data sets to a more manageable, and more illustrative form. This is typically done by considering the relative importance of various predictors. Johnson and Lebreton (2004) define relative importance as the contribution each predictor makes to the total predicted criterion variance, both when a predictor is considered on its own and in combination with other predictors. A variety of indices have been proposed to evaluate the relative importance of predictors; these include simple correlation coefficients, regression weights, and partial correlations.

Mac Nally (2000) suggests this is important for 2 reasons. First, researchers may seek to develop a single predictive model for a given dependent variable as a function of several independent variables. To improve future prediction estimates, Breiman (1995) suggests the inclusion of fewer independent variables. Second, researchers may be interested in identifying the independent variables that are most likely to causally influence the dependent variables. This is especially useful, when further studies and experiments would be required to test the causal nature of relationships.

It can be difficult to develop a predictive model for team outcomes based on a large set of predictor variables. A simplified model is needed whereby as few predictors as possible are kept. This is because including more predictors tend to overfit the data. This effect is particularly amplified when there are as many independent variables as samples, leading to a perfect fit.

3. Methods

3.1. Data Collection

3.1.1. Participants and Procedure

The participants in this research were 4th year students at the Department of Chemical Engineering at Imperial College London. A personalised link to the survey was generated using Qualtrics and e-mailed to all participants. Participants' were informed of the confidentiality and anonymity of their responses. Out of the 117 students invited to participate in this survey, 94 completed the survey (80% response rate). 71% respondents were male and 29% female.

The survey comprised of 2 main parts: the first part collected data on the students' individual inherent attributes and the second part collected data on the students' perceptions of their teamwork during the Strategy of Design (SoD) project in their previous academic year. This meant that this survey was retroactive as it required students to reflect on their past experiences.

The SoD project was chosen as its scope most closely resembled that of engineering design, i.e. students worked in groups with minimal supervision and guidance to develop a conceptual design and relevant documentation for a chemical process given resource

constraints and process specifications. This project ran for 4-weeks from 17/2/2020 – 15/3/2020. Group allocation was done by the module leader and 19 teams of 6-7 were formed.

3.1.2. Measures

10 predictor variables and 7 criterion variables were analysed in this study. To collect necessary data, three sets of measures were collected: inherent student attributes, team effectiveness measures and team performance as summarised below. Validated surveys were used to collect data on the students' attributes (personality types, locus of control, goal orientations) and on the team effectiveness measures, with the exception of procrastination.

Personality. Individual personality types were evaluated using the Montgomery Shorter Sorter questionnaire, which is an abbreviated version of the Keirsey Temperament Sorter. This questionnaire, based on MBTI personality types, consists of a 38-item instrument with only two possible responses for each item. Example items include: "When dealing with others do you try to be (a) firm and objective (b) gentle and sympathetic".

Locus of Control. Locus of control was measured using the 28-item Duttweiler Control Index as proposed by Duttweiler (1984). Each item was rated on a 5-point Likert scale (1 = strongly agree, 5 = strongly disagree), measuring the extent to which the respondents agree. Example items include "If I want something, I work hard to get it".

Goal Orientation. This was evaluated using a shortened version of the 12-item Achievement Goal Questionnaire-Revised (AGQ-R) proposed by Elliot and Murayama (2008). A 5-point Likert scale was used to rate the respondents' levels of agreement with each item. Example items include: "My aim is to completely master the material presented in this class". Goal orientation is comprised of 4 aspects: mastery approach, mastery avoidance, performance approach and performance avoidance, with each aspect measured by 2 items.

Procrastination. This was measured by 2 questions proposed by Psychology Today. Respondents were asked to provide the extent to which they agreed with the items on a 5-point Likert scale. Example item includes "I do most of the work close to the deadline". Though a validated survey was not used to measure this construct, the internal consistency of this measure was computed.

Team Effectiveness. Team effectiveness was assessed by an adapted version of the NHS Team Effectiveness Questionnaire (TEQ), which evaluated several dimensions of team effectiveness such as: purpose and goals, team roles, team relationships, team processes and team problem solving in which each dimension was measured by 7-items. Respondents rate their levels of agreement to each item on a 5-point Likert scale.

Team Self-Efficacy. This was evaluated with a 4-item scale developed by Bandura (2005) which assessed the team member's belief in oneself to work well within a team. This was evaluated with a 4-item scale developed by Bandura (2005) which assessed the team member's belief in oneself to work well within a team. An example item includes "Rate your degree of anxiety in working in this team throughout the project" on a scale between 1 to 5, with 5 indicating high degree of anxiety.

Team Performance. Grades awarded by module supervisors to teams were taken as an indicator of their performance. This score was collected and anonymised by the project supervisors on behalf of the student researchers and are graded on a scale of 0-100.

3.2. Data Operationalisation

For quality control purposes, only teams with at least 4 respondents were considered. In total, 17 teams were examined in this study. Internal reliability estimates were computed for each construct to assess the consistency of results across items for the attributes and outcomes as shown in Table 1.

Table 1: Attributes and team outcomes nomenclature, survey instrument used to measure each construct and Cronbach's alpha reliability estimates

Variables	Instrument Used	α*
Inputs		
Extraversion/Introversion (EI)	Montgomery Shorter Sorter	.724
Sensing/Intuition (SN)	Montgomery Shorter Sorter	.573
Thinking/Feeling (TF)	Montgomery Shorter Sorter	.777
Judging/Perceiving (JP)	Montgomery Shorter Sorter	.659
Locus of Control (LOC)	Duttweiler Scale	.850
Mastery Approach (MAP)	Revised AGQ-R	.552
Mastery Aversion (MAV)	Revised AGQ-R	.767
Performance Approach (PAP)	Revised AGQ-R	.862
Performance Aversion (PAV)	Revised AGQ-R	.848
Procrastination (PRO)	Psychology Today	.794
Outputs		
Team Self-Efficacy (TSE)	Bandura Scale	-
Team Effectiveness	NHS TEQ	
Purpose & Goals (P&G)		.818
Roles (ROL)		.838
Relationships (REL)		.874
Processes (PR)		.804
Problem-Solving (PS)		.827

*α: Cronbach alpha reliability estimate

As the survey data measured attributes and team outcomes on an individual-level, the collected data was then operationalised as follows to obtain a team-level variable. The standard deviations of the team members' scores for a given team for each attribute was computed, and returned a corresponding DIF. The team self-efficacy and team effectiveness scores for each team were computed by taking an aggregate score (mean) across all team members for a given team. For the feasibility of future statistical analysis, discrete MBTI data was transformed to a continuous scale of -1 to 1. Extroversion (E), sensing (S), thinking (T) and perceiving (P) were assigned a positive score whilst their counterparts for each dimension, i.e. introversion (I), intuition (N), feeling (F) and perceiving (P) were assigned negative values.

3.3. Data Analysis

Given the multivariate nature of data collected, it was assumed that variables (and their residuals) were normally distributed, and that predictors and dependent variables had a linear relationship. DIFs and team outcomes were then compared using four main statistical techniques: zero-order correlations, partial correlations, standardised regression coefficients (β-coefficients), and Johnson's relative weights (RW) analysis. Predictor importance was assessed via a rank ordering of the magnitude of relevant coefficients obtained.

Analysis was primarily conducted through the combination of MATLAB (RW analysis) and the General Linear Module (GLM) of IBM SPSS statistical software package, version 23.0.

Zero-order correlation. The zero-order correlation measures the direct effect of the predictor on the dependent variable, while ignoring the effect of other variables. As such, it is unable to partition the shared variance between two or more correlated predictors into the variance attributable to each predictor. Therefore, when predictor variables are correlated, interpreting the variable importance assigned by this index poses a significant challenge since individual correlations do not accurately reflect the contributions of the correlated variables.

Partial correlation. The partial correlation measures the direct impact of a predictor on the dependent variable after the influence of other predictor variables have been removed. This means that unlike zero-order correlations which measures the predictive power of predictors in isolation, partial correlations provide an indication of the predictive power of predictors in the presence of other predictors. Like zero-order correlations, partial correlations are unable to partition the shared variance between multiple correlated predictors and the dependent variable, meaning the interpretation of variable importance is unclear when predictors are correlated to each other.

Standardised regression coefficients. β-coefficients explain the change in the dependent variable from a change on one standard deviation in the predictor variables. A reliance on this analysis assumes that changes in one standard deviation of individual predictors are comparable. Additionally, interpretation of this index is difficult wen predictors are collinear as a higher value is typically assigned to the variable with the larger zero-order correlation.

Relative weights. Relative weights (RW) explain the proportionate contributions of each predictor to the overall linear regression effect R^2 in its direct effect and effect when combined with other variables. This analysis was done using MATLAB using the following procedure. Original predictor variables (X_i) are transformed into a set of uncorrelated, orthogonal principal components (Z_j) that are maximally related to the predictors but uncorrelated with each other. Original predictor variables are then regressed onto the uncorrelated components with regression coefficients represented by λ_{ij}. The relative weights are calculated by the following equation. For example, the relative weight for the original variable x_i is given by:

$$\varepsilon_i = \lambda_{ij}^2 \beta_j^2 \quad (2)$$

To facilitate the selection of a smaller subset of predictors of highest relative importance, an average across rank orderings generated across statistical methods was done as suggested by Kruskal (1987). This is assumed to be a valid strategy as it reduces the limitations of each of the statistical methods discussed and allows us to consider which predictors may be of interpretable interest in future model-building endeavours.

4. Results and Discussion

This section will aim to further develop a conceptual understanding underpinning the possible interactions of the DIFs identified and to offer practical and actionable recommendations to further develop a comprehensive modelling approach towards this problem. Discussion is structured as follows: 1) Theoretical underpinnings where we discuss possible conceptual frameworks that explain our data structure and 2) Modelling recommendations where we offer recommendations to guide future work based on the structure of our data.

4.1. Theoretical Underpinnings

How are our DIFs affecting team outcomes?

Preliminary scatter-plot analysis of predictors against team outcome variables indicated that data obtained was relatively scattered across most DIF-team outcome combinations with the exception of EI-P&G. This indicates that the relationships obtained should not be used to make definitive conclusions about the relationships in the data.

It can be observed from Figure 2 that with the exception of academic score, most of the team outcomes were negatively correlated with the predictors. The predictors that showed positive relationships typically had smaller magnitudes of its zero-order correlation coefficients which could potentially indicate spurious effects. This would seem to indicate the preference for a supplementary DIF model under high-stress and time-restrictive settings, where grades are used as a primary motivator. Homogeneity in DIFs in these settings appear to positively impact team outcomes due to improved team cohesion, increased team motivation and better communication.

However, academic performance was positively impacted by heterogeneity for LOC and goal orientation dimensions, indicating a complementary model of attributes might be necessary to explain these observations. This is possibly because in a group setting, a combination of goal orientations is necessary to ensure the team completes the tasks to a high standard according to specifications in a timely manner with minimal conflict. Given that the combination of all DIFs explain the least amount of variance for this outcome (~30%), some caution should be taken in accepting this hypothesis.

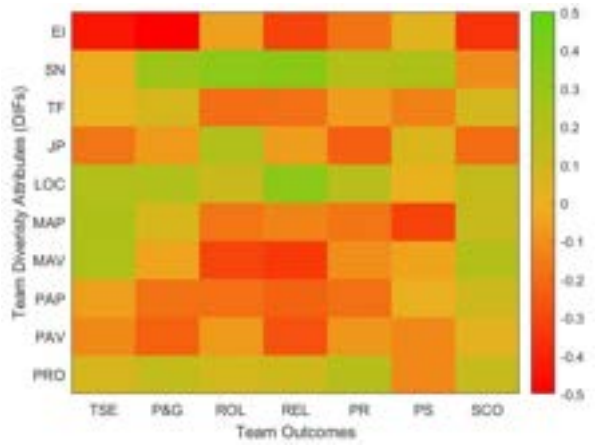

Figure 2. Zero-order correlation heatmap between team diversity attributes (DIFs) and team outcomes.

When looking at individual DIFs, EI, JP, MAP and MAV appear to have negative relationships across all team outcome dimensions, while TF seems to have spurious effects with all team dimensions except for PS and ROL. LOC, SN, and PRO tendencies seem to positively impact team outcomes whilst the effect of PAP and PAV are mixed across all outcomes studied.

These preliminary results indicate possible conflicts between team diversity and team outcomes, specifically with personality and goal orientations. Therefore, in an academic setting, the desire to select students who will perform well together should be balanced with the desire to select diverse teams.

What is the explanatory power of DIFs for individual team outcomes?

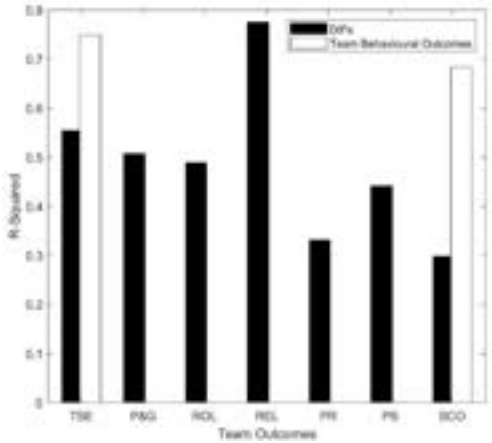

Figure 3. R^2 values of linear regression model for regressing each team outcome on all DIFs (black) and regressing academic score and team self-efficacy on team behaviour outcomes (white).

It is assumed that the R^2 values for each outcome indicated the explanatory power of the combination of DIFs chosen for each team outcome. This means that outcomes with high R^2 values predicted by the combination of DIFs chosen were sufficient in explaining the variance while low R^2 values potentially indicated the unsuitability of DIFs chosen in capturing the variation in that team outcome.

As displayed on Figure 3, the combination of DIFs showed a strong fit ($R^2 > 0.70$) for relationships ($R^2 = .77$), moderate fit for team self-efficacy, purpose and goals, roles, and problem-solving, and a weak fit with team processes and academic scores.

To further understand the underlying structure behind our data, the explanatory power of the combination of DIFs for a specific team outcome was compared to the explanatory power of a combination of team behaviour variables. The following observations were made. The explanatory power of the DIFs for team academic score ($R^2 = .298$) was relatively poor when compared to the explanatory power of team behaviour outcomes to academic scores ($R^2 = .683$). Similar trends albeit not as pronounced were observed in team self-efficacy. When regressed on DIFs, $R^2 = .550$ was reported as compared to $R^2 = .683$ when regressed on team behaviour outcomes.

The combination of these variables seemed to suggest a slightly more-complicated IPO model where the DIFs influence the academic scores, and team self-efficacy through two routes: a direct route and an indirect route. In the direct route, the DIF contributed directly to the difference in team outcomes specifically academic score and team self-efficacy. In the indirect route, the DIFs influenced the process i.e. team behaviour outcomes such as P&G, ROL, REL etc. which subsequently influenced the output. An alternative model that could explain our data is shown in Figure 4. The relative importance of the direct and indirect paths proposed would have to be further confirmed through path analysis.

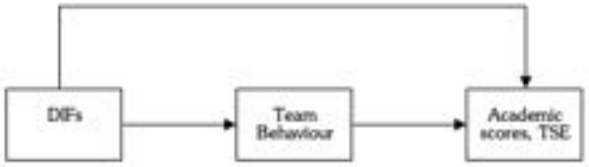

Figure 4. Model of DIFs influence on team self-efficacy and academic score via their direct and indirect paths

4.2. Practical Implications

What are problematic characteristics in dataset that may complicate future modelling attempts?

Good predictor models aim to have as few predictors (DIFs) as possible as this prevents overfitting and allows the model to have better predicting power. It is commonly assumed that variables and the corresponding residuals are distributed normally, variables exhibit similar variances, and variables are independent from each other.

It was noted by Nathans, Oswald and Nimon (2001) that behavioural scientists primarily validate their statistical findings using zero-order correlations and standardised β-coefficients. However, interpretation of these coefficients is only straight-forward when DIFs are uncorrelated. In comparing rankings generated for DIFs by various statistical methods, the following characteristics were noticed.

First, for all team behaviour outcomes, zero-order correlations and Johnson's relative weights analysis consistently ranked SN as one of the top 5 predictors but β-coefficients did not. This was likely due to the non-normal distribution of the residuals of SN, possibly indicating the non-normal distribution of the SN DIF. At a team level, the SN DIF reported a skewness of -1.37, which was the highest skew reported, indicated the existence of a negative skew in this dimension. Conceptually, this meant that teams were predominantly homogenous in the SN dimension, which was likely due to the prevalence of the sensing attribute at an individual level.

Second, in comparing rankings generated by the zero-order correlation and β-coefficients, the difference in importance assigned to DIFs were noted. For example, when comparing the rankings generated by the zero-order correlation and β-coefficient for purpose and goals, PRO, TF and JP were assigned higher weightages by the latter although they displayed near-zero zero-order correlations, possibly indicating that these DIFs may not have a relationship with P&G but are correlated with other DIFs. This could indicate that TF and JP act as suppressor variables. The presence of such suppressors are unexpected and hard to interpret based on existing frameworks, possibly implying a complex statistical relationship as a consequence of multicollinearity.

Third, in noting the differences between rankings obtained by zero-order correlation and partial correlations, it was noted that DIFs behaved differently when control variables were introduced. For some pairs of DIFs-team outcomes such as MAV-TSE, correlations were strengthened when control variables were introduced through the partial correlation. This serves as a confirmation of the direct relationship between these pairs. For other pairs such as LOC-PR, however, introducing control variables significantly weakened the zero-order correlations generated. Breiman (1995) suggests that this could possibly indicate that the initial correlations involving these DIFs were spurious (i.e. return a value/weight of zero).

Fourth, in preliminary attempts to synthesise a feasible structure for the DIFs and team outcomes identified, we tested the significance of differences among zero-order and first-order correlations using the Z transformation. Upon analysis, it was discovered that DIFs differed from zero-order correlations by a maximum of 2 σ. DIFs that exhibited differences larger than 1 sigma were PAV-TSE, PRO-TSE, PAP-ROL, PRO-PS, PAP-PS, SN-PS and all DIF-REL combinations. Goldsmith (1977) suggests that this could possibly indicate the relative importance of considering the control variables in determining a feasible model. From a strategic perspective, results obtained suggest that it might be difficult to create an explanatory model to explain the interactions of DIFs with team relationships and suggest optimising for other team outcomes instead.

Fifth, it was noted that across all team outcome variables, rankings by β-coefficients consistently rank PRO and/or PAV as important predictors of team outcomes, despite the relatively weak zero-order correlations. Additionally, rankings seem to indicate the importance of mastery and performance goal orientations in comparison to personality diversity attributes. When looking at variances in these DIFs across teams, it was noticed that these DIFs had significantly larger variances than their counterparts, i.e. σ^2_{PRO}= .515 and σ^2_{PAV}= .719 in comparison to σ^2_{EI}= .032. The 10 times difference in the variance of the personality DIF versus the goal orientation DIF seem to suggest that in partitioning shared variance, these DIFs were assigned higher weightings, possibly due to their larger variance.

Sixth, our data shows relatively large and unexpected change in the magnitude of zero-order correlations and β-coefficients. For example, the PAV-P&G zero-order correlation was estimated as r = -.229, but β-coefficient was estimated as β = -.996. For uncorrelated DIFs, Johnson and Lebreton (2004) suggest that zero-order correlations and β-weights should be equivalent. Therefore, the inequivalence in values reported could indicate substantial degree of multicollinearity and/or the presence of shared variances between DIF variables. This is further supported by the difference in relative rankings of DIF by β-coefficients and zero-order correlations.

Additionally, analysing zero-order correlations between PAV, PR and other DIFs revealed significant contributions between PAV-TF (r = .493), PAV-PAP (r = .609), and PR-MAP (r = .511). This collinearity may have caused high β weights to be assigned to PRO and PAV.

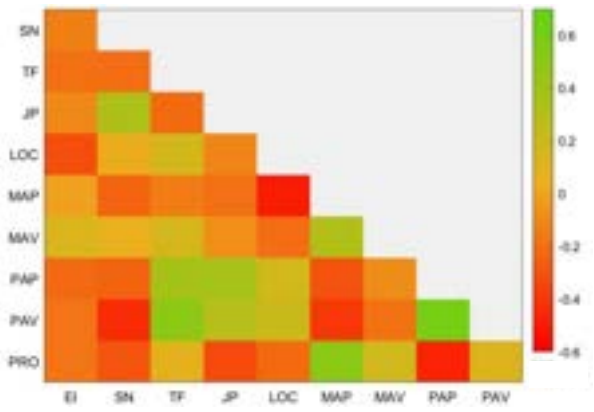

Figure 5. Zero-order correlation heatmap between team diversity attributes (DIFs)

Murray and Conner (2009) suggest that this multicollinearity could be problematic as it may inflate standard errors for predictor coefficients with a concurrent increase in Type II error, cause instability in coefficients estimated and rank variables erroneously. Although there is a large range of suggested cut-off values, Murray (2009) reports that conventionally, remediation is not recommended unless pair-wise correlations exceed ~ .80. However, the moderate correlations as shown in Figure 5 (PAP-PAV, r = .609, MAP-PRO, r = .511) between DIFs seemed to be sufficient to cause inaccurate model parametrisation and

may have resulted in an inaccurate assessment of variable importance.

To address this multi-collinearity, relative weights (RW) was introduced as it reflects the true contributions of the DIF towards the variance in team outcomes. Although RW tackles this multi-collinearity, its usage has limited utility as it is not able to represent the direction of the effect. This means it has limited use in extending theoretical and conceptual frameworks to current understanding of DIFs in an education setting.

However, there is a possibility that the degree of multicollinearity has been overestimated. Given that a combination of 17 variables (10 DIFs and 7 team outcomes) were studied in a sample of 17 teams, Flack and Chang (2012) suggest that it is likely that the model has retained noise.

Note that the variables were not screened using statistical significance. This was primarily because the statistical significance is not an indicator of the variable importance, but rather reflects the strength of confidence in making an inference about an unknown parameter based on a statistic.

In conclusion, an overreliance on traditional measures of variable importance such as the zero-order correlation and β-coefficients are likely to lead to the misidentification of important variables. This is because such measures tend to obscure problematic structures in data structures. Additionally, when predictor variables exhibit multi-collinearity, and possible spuriousness like that exhibited by the DIFs studied, the relative importance ranked by various statistical methods may diverge. Therefore, to identify important variables, insights generated from multiple statistical methods should be utilised. These insights combined with theoretical and conceptual understanding will generate good models.

Which DIFs are most significant in affecting team outcomes?

The ranking of DIFs were generated based on adequacy, i.e. the proportion of the total explainable variance that it contributed to.

However, in considering the most significant variables to include in a model, simple single analysis methods measuring marginal contributions of DIFs (e.g. β-coefficients and partial correlations) and those do not consider marginal contributions (e.g. zero-order correlations) did not agree with each other, painting conflicting pictures of DIF importance, especially in instances where multi-collinearity and/or suppressor variables exist. To overcome this, the rankings generated by various statistical methods were averaged to obtain the most significant DIF for each team outcome as summarised in Figure 4.

From Figure 6, it can be noted that PRO and learning orientations, such as MAP, MAV and PAV consistently rank as one of the top 5 predictors across team outcome. This is possible due to a larger variation in these dimensions at an individual level. This seems to suggest that in settings such as the Department of Chemical Engineering where a combination of the academic requirements and technical relevance of the course result in a student body that is relatively homogenous in terms of personality, goal orientations and procrastination tendencies seem to be able to explain the variations in team performance.

Figure 6. Averaged rankings of top 5 DIF predictors across all team outcomes

We do not claim that the correlations above imply causation. The validation of the rankings of variable importance suggested can only be done experimentally. However, this approach does allow the generation of testable hypothesis regarding alternative team formation strategies that can be subsequently consolidated to a 'predictory' model.

5. Limitations

As with any survey experimental design, our findings and conclusions should be interpreted considering the boundary conditions and constraints. Firstly, findings may not be applicable and generalisable to other contexts outside engineering projects and of this particular study population as this study was a single faculty-institution study, i.e. it focused on teams in Chemical Engineering in Imperial College London. Future replications in different disciplines of engineering or a different undergraduate population may help to corroborate the external validity of this research and improve the generalisability. Additionally, care should be taken in interpreting these results as only a sample size of 17 teams were involved in this study.

Secondly, effects of nonresponse bias may have caused errors in the estimated team DIF and aggregate team outcome. This could reduce the representativeness of team values obtained. Though missing data was handled by taking a mean where possible, this could have distorted the estimation of these parameters due to variation between the true mean values and the actual mean values obtained from the sample. Additionally, the voluntary nature of this study which led to a high response rate (~80%) may have led to the underrepresentation of several student archetypes, i.e. students who were likely to respond to this survey would have been those that had had extremely positive or negative experiences with the project. This means that the data may not represent a subset of students who were neutral about the project.

In addition, recall bias might have arisen due to the retrospective nature of this study. There could possibly have been a lack of accuracy and precision in recalling past teamwork experiences when answering the team outcomes survey. This is particularly significant in our cohort as Covid-19 measures meant groups of students started isolating themselves in the final week of the

project. This could be reduced by repeating this study in a dynamic manner, i.e. in surveying the students throughout the teamwork process.

Furthermore, response bias may have caused students to provide answers that align with the supervisors' views. Although there were attempts to minimise this by anonymising students' responses, student self-censorship in reporting past experiences remain a concern.

Finally, the two survey questions that measured the procrastination construct require further investigation and validation, despite reporting high internal validities. Alternatively, this construct could be re-tested using existing validated instruments should be used to measure this.

6. Conclusion and Outlook

In conclusion, this study reviewed various theoretical frameworks and models of teamwork and explored how inherent diversity attributes influence team outcomes.

In high pressure settings where grades act as a primary motivator, preliminary evidence obtained indicate a complementary model fit for team behavioural outcomes since it was found to be positively related to homogeneity of diversity attributes and a supplementary model fit for team performance outcomes as it was found to be positively related to heterogeneity in certain attributes. This seemed to indicate possible tensions between diversity and team effectiveness.

Secondly, an examination of the data seemed to support an input-process-output (IPO) model with direct and indirect effects. This means that for team outcomes such as team performance and team self-efficacy, variances in the outcomes were better explained by team behaviour (process) which was influenced by the DIFs (inputs).

Thirdly, there were several complicating characteristics in the underlying data that may affect future modelling efforts, most notably multi-collinearity and the presence of suppressor variables which caused a divergence in the rankings of variable importance across the methods. This indicates the importance of using multiple statistical methods to generate rankings for comparisons in subsequent exploratory research aimed at identifying top predictors.

Finally, averaging the rankings obtained indicate the relative importance of the diversity in learning orientations and procrastination tendencies in influencing team outcomes, particularly in a similar study setting with homogenous personality types.

The present study was retrospective and relied on self-reporting from individual group members. Therefore, future studies should adopt a more dynamic approach and conduct its research during an engineering project. Additionally, this study only focused on inherent member attributes, which is only one broad area of inputs in a teamwork model. Future studies could explore how other categories of inputs beyond the individual-level can affect team effectiveness, including the group-level factors, such as group size, and environmental-level factors, such as project types.

In applying this study, it should be remembered that this study only provides an exploratory framework to identify variables that may be significant in affecting team effectiveness. However, educational researchers interested in studying possible interventions necessary to improve this outcome should look at the possibility of interaction effects amongst the diversity attributes and team outcomes e.g. if two diversity attributes will have a significant interaction effect on team relationships.

Acknowledgements

We would like to thank members of their cohort for participating in the present study, particularly those who candidly expressed their views on team formation in Imperial during the post-survey discussions. We would also like to express our gratitude to Dr Vijesh Bhute and Dr Marsha Maraj for their invaluable support, guidance and feedback throughout the project.

References

Adams, S. G. *et al.* (2002) 'A conceptual model for the development and assessment of teamwork', in *ASEE Annual Conference Proceedings*. doi: 10.18260/1-2--10049.

Bandura, A. (2005) *Self-Efficacy Beliefs of Adolescents*.

Barrick, M. R. *et al.* (1998) *Relating Member Ability and Personality to Work-Team Processes and Team Effectiveness*, *Journal of Applied Psychology*.

Beal, D. J. *et al.* (2003) 'Cohesion and Performance in Groups: A Meta-Analytic Clarification of Construct Relations.', *Journal of Applied Psychology*, 88(6). doi: 10.1037/0021-9010.88.6.989.

Bobbitt, L. M. *et al.* (2000) 'Integrating Marketing Courses to Enhance Team-Based Experiential Learning', *Journal of Marketing Education*, 22(1), pp. 15–24. doi: 10.1177/0273475300221003.

Boone, C. and Hendriks, W. (2009) 'Top Management Team Diversity and Firm Performance: Moderators of Functional-Background and Locus-of-Control Diversity', *Management Science*, 55(2), pp. 165–180. doi: 10.1287/mnsc.1080.0899.

Bradley-Geist, J. C. and Landis, R. S. (2012) 'Homogeneity of Personality in Occupations and Organizations: A Comparison of Alternative Statistical Tests', *Source: Journal of Business and Psychology*, 27(2), pp. 149–159. doi: 10.1007/sl0869-01.

Brannick, M. T. and Prince, C. (1997) 'An overview of team performance measurement', *Team performance assessment and measurement. Theory, methods, and applications*.

Breiman, L. (1995) 'Better subset regression using the nonnegative garrote', *Technometrics*, 37(4). doi: 10.1080/00401706.1995.10484371.

Cohen, S. G. and Bailey, D. E. (1997) 'What Makes

Teams Work: Group Effectiveness Research from the Shop Floor to the Executive Suite', *Journal of Management*, 23(3). doi: 10.1177/014920639702300303.
Day, D. V. and Bedeian, A. G. (1995) 'Personality similarity and work-related outcomes among african-american nursing personnel: A test of the supplementary model of person-environment congruence', *Journal of Vocational Behavior*, 46(1), pp. 55–70. doi: 10.1006/jvbe.1995.1004.
Duttweiler, P. C. (1984) 'The Internal Control Index: A Newly Developed Measure of Locus of Control', *Educational and Psychological Measurement*, 44(2), pp. 209–221. doi: 10.1177/0013164484442004.
Elliot, A. J. and Murayama, K. (2008) 'On the Measurement of Achievement Goals: Critique, Illustration, and Application', *Journal of Educational Psychology*, 100(3). doi: 10.1037/0022-0663.100.3.613.
Flack, V. F. and Chang, P. C. (2012) 'Frequency of Selecting Noise Variables in Subset Regression Analysis: A Simulation Study'. doi: 10.1080/00031305.1987.10475450.
Gladstein, D. L. (1984) 'Groups in Context: A Model of Task Group Effectiveness', *Administrative Science Quarterly*, 29(4). doi: 10.2307/2392936.
Goldsmith, John R and Goldsmith, J R (1977) *Paths of Association in Epidemiological Analysis: Application to Health Effects of Environmental Exposures**, *International journal of Epldtmfology C Oxford Unlvarafty Pros*. Available at: https://academic.oup.com/ije/article/6/4/391/718876.
Guzzo, R. A. and Dickson, M. W. (1996) 'TEAMS IN ORGANIZATIONS: Recent Research on Performance and Effectiveness', *Annual Review of Psychology*, 47(1). doi: 10.1146/annurev.psych.47.1.307.
Hackman, R. J. (1990) 'Conclusion: Creating More Effective Work Groups ni Organizations', *Groups that work (and those that doesn't)*.
Hamilton, B. H., Nickerson, J. A. and Owan, H. (2003) *Team Incentives and Worker Heterogeneity: An Empirical Analysis of the Impact of Teams on Productivity and Participation*, *Journal of Political Economy*.
Van Hooft, E. A. J. and Van Mierlo, H. (2018) 'When teams fail to self-regulate: Predictors and outcomes of team procrastination among debating teams', *Frontiers in Psychology*, 9(APR). doi: 10.3389/fpsyg.2018.00464.
Johnson, J. W. and Lebreton, J. M. (2004) 'History and Use of Relative Importance Indices in Organizational Research', *Organizational Research Methods*, 7(3), pp. 238–257. doi: 10.1177/1094428104266510.
Kruskal, W. (1987) 'Relative Importance by Averaging Over Orderings', *The American Statistician*, 41(1). doi: 10.2307/2684310.
Livingstone, D. and Lynch, K. (2002) 'Reflections on 'Group Project Work and Student-centred Learning', *Journal of Geography in Higher Education*, 26(2), pp. 213–215. doi: 10.1080/03098260220144739.
London Leadership Academy, N. (no date) *Leading Teams: Team Effectiveness Diagnostic*. Available at: https://www.londonleadershipacademy.nhs.uk/sites/default/files/Team_effectiveness_diagnostic-LAL1.pdf (Accessed: 11 December 2020).
Mello, A. S. and Ruckes, M. E. (2006) 'Team composition', *Journal of Business*, pp. 1019–1039. doi: 10.1086/500668.
Muchinsky, P. M. and Monahan, C. J. (1987) *What Is Person-Environment Congruence? Supplementary versus Complementary Models of Fit*, *Journal of Vocational Behavior*.
Murray, K. and Conner, M. M. (2009) 'Methods to quantify variable importance: implications for the analysis of noisy ecological data', *Ecology*, 90(2), pp. 348–355. doi: 10.1890/07-1929.1.
Mac Nally, R. (2000) 'Regression and model-building in conservation biology, biogeography and ecology: The distinction between - and reconciliation of - "predictive" and "explanatory" models', *Biodiversity and Conservation*, 9(5). doi: 10.1023/A:1008985925162.
Nathans, L. L., Oswald, F. L. and Nimon, K. (2001) 'Interpreting Multiple Linear Regression: A Guidebook of Variable Importance', 17(9).
Neuman, G. A., Wagner, S. H. and Christiansen, N. D. (1999) *The Relationship Between Work-Team Personality Composition and the Job Performance of Teams*.
Pieterse, A. N. (2009) *Goal Orientation in Teams: The Role of Diversity*.
Sundstrom, E., De Meuse, K. P. and Futrell, D. (1990) 'Work teams: Applications and effectiveness.', *American Psychologist*, 45(2). doi: 10.1037/0003-066X.45.2.120.
Today, P. (no date) *Procrastination Test - Abridged*. Available at: https://www.psychologytoday.com/us/tests/career/procrastination-test-abridged (Accessed: 16 December 2020).
Ventura-Medina, E. (2020) *Chemical Engineering Education in the Age of Disruption - Features - The Chemical Engineer*. Available at: https://www.thechemicalengineer.com/features/chemical-engineering-education-in-the-age-of-disruption/ (Accessed: 16 December 2020).
Van Vianen, A. E. M. and De Dreu, C. K. W. (2010) 'European Journal of Work and Organizational Psychology Personality in teams: Its relationship to social cohesion, task cohesion, and team performance'. doi: 10.1080/13594320143000573.

Optimising the synthesis of MIL-53(Al) on ceramic hollow fibre substrate for the adsorptive removal of diclofenac from water

Jenny Lim[1] and Chen Yang Ng[1]

Department of Chemical Engineering, Imperial College London, U.K.

Abstract: Metal organic frameworks, specifically MIL-53(Al), has been shown to be a promising adsorbent due to its advantageous structural characteristics and high structural stability. Typically, MIL-53(Al) is used in powder form for commercial applications, making it difficult to recover. Therefore, this study aims to fabricate MIL-53(Al) on ceramic hollow fibre substrate supports for use in adsoprtion processes as a solution to this problem. The effects of synthesis time and mass of benzenedicarboxylic acid powder used for synthesis on adsorption performance of the product were also investigated. The synthesised product was then characterised and its adsorption performance determined via testing with samples of diclofenac solution. Characterisation techniques show that MIL-53(Al) was successfully synthesised on the ceramic hollow fibre support. Experimental results also show that in general, adsorption performance of the product decreases with increasing mass of benzenedicarboxylic acid used for synthesis. Additionally, an overall U-shaped trend was observed for the relationship between synthesis time and adsorption performance. The synthesis conditions that gave the highest adsorption of diclofenac, 40.6 $\mathrm{mg\,L^{-1}}$, and exhibited an adsorption capacity of 163 $\mathrm{mg\,g^{-1}}$, was at synthesis time of 12 hours and 0.5 g of benzenedicarboxylic acid used.

Keywords: MIL-53(Al), Diclofenac, Metal-organic frameworks (MOFs), Ceramic Hollow Fibre, Adsorption

1 Introduction

Metal-organic frameworks (MOFs) are made up of an array of metal ions with organic ligands linking them together. As such, MOFs can be considered organic-inorganic hybrid porous materials. There has been significant interest in MOFs and their applications in recent years, given their numerous advantageous characteristics such as their flexibility in tuning of pore size and pore shape, high porosity, large surface area and high thermal stability [1, 2]. Hence, MOFs have been employed in a wide range of applications which include energy storage [3], biological imaging [4] and catalysis [5]. In particular, MOFs have shown great potential as attractive adsorbents for water purification [6].

Aluminium-based MOFs are of particular interest as they have been shown to be highly stable in the presence of water and organic solvents and also when exposed to heating. In addition, they are effective in the sorption of various organic and inorganic compounds [7]. Thus, the aluminium-based MOF from the MIL (Materials Institute Lavoisier) family, MIL-53(Al), was selected to be used in this study. MIL-53(Al), which is constructed from secondary building units (SBUs), has higher stability than pure metal ion network vertices and other aluminium-based MOFs [8, 9]. Furthermore, MIL-53(Al) has been shown to be resistant to hydrolysis under neutral and acidic conditions, successfully maintaining its crystallinity and porosity [10].

MIL-53(Al) is most commonly used in powder form in adsorption processes [11]. However, powdered adsorbents suffer from the fact that they are difficult to recover. In commercial applications, after the adsorbent is loaded into the process and has adsorbed the residual organic matter and micropollutants, they are typically disposed of along with the sludge. This leads to increased water treatment costs as there is a need for fresh adsorbent to be continuously supplied. An interesting solution to this would be to grow MIL-53(Al) MOFs on supports for ease of recovery and regeneration. Interestingly, a novel reactive seeding procedure was used to synthesise MIL-53(Al) membranes, where an alumina support was used as the aluminium precursor to react with 1,4-benzenedicarboxylic acid to form a seed layer [12, 13]. This step was then followed by a secondary growth process to form the membrane layer, ensuring strong bonding between the porous support and MOF crystals [13]. This study proposes applying the same principles to obtain high binding strength between MIL-53(Al) and the support, with ceramic hollow fibre substrates being used as the aluminium precursor. As the synthesised product is intended to be used as an adsorbent rather than as a membrane in this study, the secondary growth process step was not carried out.

Ceramic hollow fibre substrate was selected as the support because of its long finger-like structure on the inner and outer walls and sponge-like structure at the center of the fibre, as shown in Figure 1, that contributes to its high porosity and strong mechanical strength. It has been used in a variety of applications such as production of graphene membranes for use in high temperature membrane reactors [14], microfiltration [15] and development of efficient catalytic converters [16]. Moreover, the presence of α-alumina in the production of ceramic hollow fibres makes it suitable to be used as an aluminium precursor for MIL-53(Al).

Studies thus far have tested the performance of

MIL-53(Al) as an adsorbent using various compounds such as Hg^{2+} [17], hydrogen sulfide [18] and nitrobenzene [19]. However, in this study, the adsorptive performance of MIL-53(Al) synthesised on ceramic hollow fibre substrates was tested using a common non-steroidal anti-inflammatory drug - Diclofenac.

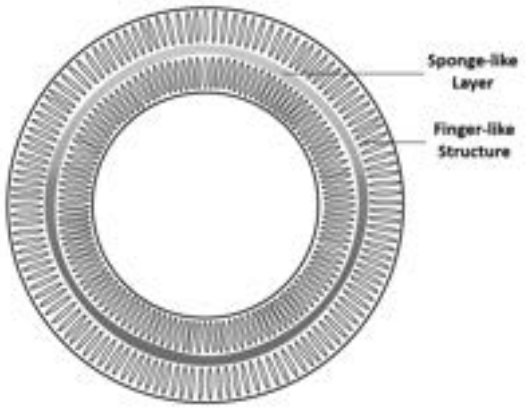

Figure 1: Cross-sectional area of ceramic hollow fibre support with finger-like micro-channels originating from both lumen and shell sides sandwiching a sponge-like layer that is enclosed by thin barrier layers

Non-steroidal anti-inflammatory drugs (NSAID) are a class of medication commonly used for the treatment of fever, inflammation, stiffness, menstrual cramps and other causes of long term pain. Diclofenac (2-[2-(2,6-dichloroanilino)phenyl]acetic acid, DCF) is a common NSAID frequently detected in sewage treatment plants, whose primary routes for entry into the environment are the effluent discharge from wastewater treatment plants after incomplete removal and disposal of sludge on land [20]. NSAIDs such as DCF are reported to have significant ecotoxicological effects. It has been reported that the application of NSAIDs altered the number and activity of soil micro-organisms, reducing their catabolic properties and disturbing the functioning of soil [21]. According to recent environmental reports, trace concentrations of DCF in aquatic environments have also been shown to pose a threat to fish and other non-target aquatic organisms by damaging their hatching at exposure concentrations as low as 0.001 - 10 $mg\,L^{-1}$ and leading to marked alterations in their reproduction being observed at concentrations around 10 - 50 $mg\,L^{-1}$ [22, 23].

Currently, DCF is commonly removed in full-scale wastewater treatment plants using conventional activated sludge, activated sludge with biological nutrient removal, membrane bioreactors and moving bed biofilm reactors [24]. However, DCF has exhibited low solid water-diffusion coefficients, in the range of 1.2 - 2.7 (where a value of above 2.5 is required for efficient sorption), leading to its ineffective sorption to sludge [25, 26]. A biodegradability study has also shown the biodegradation of DCF to be slow, making it insufficient for effective removal from wastewater [27]. Due to these limitations, the current industrial methods to remove DCF are insufficient, with only an average of 20 - 50% elimination being reported [28–30]. Tertiary treatment methods being considered include ozonation, reverse osmosis, UV radiation and chlorination. However, adsorption still shows superiority in wastewater treatment due to its low operation cost, absence of secondary pollution and high removal efficiency [31]. Therefore, it is imperative to investigate new adsorbents for the effective removal of DCF.

To date, various materials have been studied for the adsorption of DCF from aqueous environments. These include activated carbon [32–34], silica and carbonaceous solids [35], activated biochars [36], magnetic nanoparticles [37, 38], carbon nanotubes [39], covalent organic frameworks (COFs) [40] and zeolites [41–43]. However, there exist significant deficiencies with these materials, including and not limited to high costs, complex fabrication methods and inferior adsorption performances, which restrict their widespread practical applications. MOFs, specifically MIL-53(Al), is a promising alternative and potential solution to this problem. Therefore, this study intends to analyse key parameters such as synthesis time and mass of ligand used for synthesis, in order to determine the optimal synthesis conditions of MIL-53(Al) on ceramic hollow fibre substrates for adsorptive removal of DCF from water.

2 Materials and Methods

2.1 Materials

98% pure 1,4-benzenedicarboxylic acid (BDC) powder and α-alumina (Al_2O_3) powder (0.5 - 1 μm, 99.99+% metal basis, surface area 4 - 6 $m^2\,g^{-1}$ were purchased from Sigma-Aldrich and Inframat Advanced Materials respectively for the synthesis of MIL-53(Al) on ceramic hollow fibre substrate. For the washing of the synthesised product, analytical grade dimethyl sulfoxide (DMSO) and methanol were obtained from VWR Chemicals and used as supplied without modifications. Diclofenac, which was purchased from Sigma-Aldrich, was used together with de-ionized (DI) water to prepare DCF aqueous solutions with a concentration of 46 $mg\,L^{-1}$.

2.2 Fabrication of Ceramic Hollow Fibre

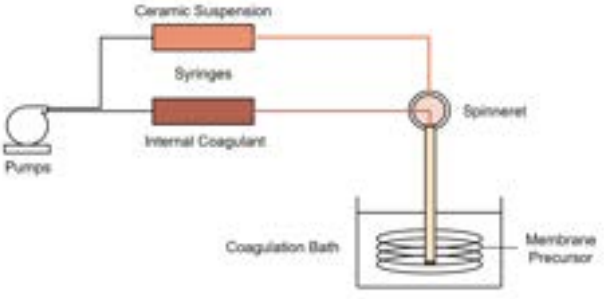

Figure 2: Schematic diagram of phase-inversion assisted extrusion process which was used to fabricate ceramic hollow fibre support

Micro-structured ceramic hollow fibre substrates were produced using a phase-inversion assisted extru-

sion process as described in a previous study [44]. In essence, poly(methyl methacrylate) (PMMA), N-Methyl-2-pyrrolidone (NMP) and Arlacel P135 dispersant, which act as the polymer binder, solvent and additive respectively, were extruded through a spinneret together with α-alumina powder into an external water bath (Figure 2). The final ceramic hollow fibre substrate was obtained after the intermediate product was straightened, dried, cut and sintered at an elevated temperature. The detailed methodology for the production of ceramic hollow fibre substrates can be found in a study by Tan *et al.* [45].

2.3 Synthesis of MIL-53(Al) on Ceramic Hollow Fibre Substrate

Varying amounts of BDC (0.5, 1.0, 1.5 and 2.0 g) were first mixed with 18 g of DI water. The mixture was then placed into a Teflon-lined steel autoclave together with 0.11 g of ceramic hollow fibre substrate. The autoclave was placed in a mechanical convection laboratory oven under 220 °C for different periods of time (12, 24, 36, 48 h). After completion of the reaction, the autoclave was allowed to cool to room temperature naturally. To remove excess BDC, the synthesised product was soaked in DMSO for 48 h. The synthesised product was then taken from the DMSO and soaked in methanol for another 24 h to remove the DMSO solvent. Finally, to ensure any remaining solvent residue is removed, the ceramic hollow fibre support with MIL-53(Al) grown on it was heated to 100 °C for 24 h.

2.4 Characterisation

In this study, powdered X-ray diffraction (XRD) tests were conducted using a X'Pert PRO PANalytical X-ray diffractometer, where the step size used was 0.02°and the 2θ range was 5.0 - 90°. The XRD patterns of MIL-53 (Al) crystals were obtained from a database from the Cambridge Crystallographic Data Centre (CCDC), and was linked to a previous study [46]. Similarly, the XRD patterns of α-alumina (Al_2O_3) powder [47] and 1,4-benzenedicarboxylic acid (BDC) powder [48] were obtained from the American Mineralogist Crystal Structure Database.

The surface morphology of the synthesised product was observed with a scanning electron microscope (SEM) at an electron beam voltage of 5kV. For the Brunauer-Emmett-Teller (BET) surface area analysis, nitrogen physisorption was carried out at 77 K on the synthesised product using an analyser from Quantachrome Instruments. Thermogravimetric analysis (TGA) data was collected from a STA 449 F5 Jupiter®, where a ramp rate of 10°C min^{-1} was used to heat the samples from 30°C to 700°C, before allowing the sample to sit for 5 minutes at 700°C. Finally, to determine the amount of DCF adsorbed, ultraviolet–visible spectrophotometry (UV-Vis) was performed using a Thermo Scientific NanoDrop 2000 spectrophotometer, where DCF solution samples were compared against a blank solution without any DCF present.

2.5 Adsorption Experiments

The adsorption experiments were performed by adding the MIL-53(Al)-Ceramic Hollow Fibre substrate products to 25 mL of DCF solution which had an initial concentration of 46 mg L^{-1}. After sealing the mixtures, they were then thoroughly mixed at 50 RPM and at room temperature for a predetermined amount of time to ensure complete adsorption. The final concentration of DCF in the solution was then measured using the UV-Vis spectrophotometer as mentioned above. The amount of DCF adsorbed was then calculated using Equation 1.

$$q = \frac{(C_0 - C_f) \times V}{m} \tag{1}$$

where q is the amount of DCF adsorbed per unit mass of MIL-53(Al) (mg g^{-1}), C_0 is the inital concentration of DCF (mg L^{-1}), C_f is the final concentration of DCF (mg L^{-1}), V is the volume of DCF solution used (L) and m is the mass of MIL-53(Al) synthesised on the ceramic hollow fibre substrate (g).

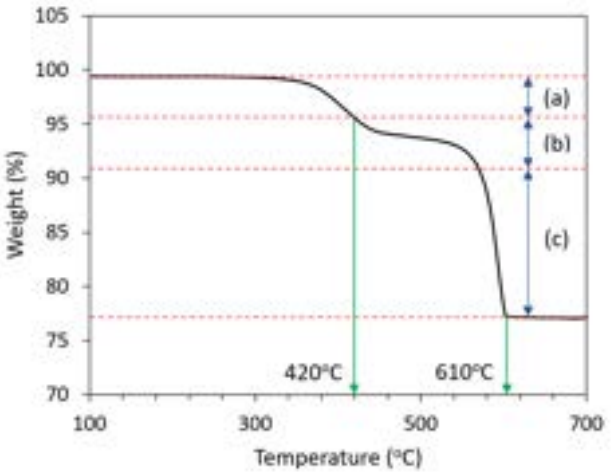

Figure 3: TGA with mass loss from (a) excess BDC (89.39%), (b) excess BDC (remaining 10.61%) and (c) BDC removed from the MIL-53 (Al)-Ceramic Hollow Fibre product

In order to calculate m, the mass of MIL-53(Al) synthesised on the ceramic hollow fibre substrate, TGA was carried out. The thermal stability of MIL-53(Al) from previous studies [49] show a gradual weight loss below 100°C, which has been attributed to be due to the removal of H_2O, followed by a long plateau before the decomposition of the MOF, beginning at approximately 520°C.

Figure 3 shows that a slight initial weight loss due to removal of H_2O is still expected. However, after a shorter plateau than is typically observed, decomposition of excess BDC ligands then begins at a temperature of approximately 320°C. This difference in TGA results with previous studies is expected due to the presence of the ceramic hollow fibre and the fact that the MIL-53(Al) was synthesised on the surface of the ceramic hollow fibre support, making it more difficult to remove any residual free BDC ligands in the pores of the support. In this first stage, 3(a), a majority of

the excess BDC (89.39%) is removed. After a short plateau, the remainder of the excess BDC is then removed in stage 3(b). Directly following this, the MIL-53(Al) begins to decompose as expected at approximately 520°C. From the mass change of the final stage, 3(c), the total mass of BDC present in the MIL-53(Al) can be obtained. Using the stoichiometric ratio of BDC to MIL-53(Al), the total mass of MIL-53(Al) on the synthesised product was then calculated. To determine the exact percentage split between stages 3(a) and 3(b), TGA was performed on a sample of pure BDC ligand.

3 Results and Discussion

3.1 Characterisation

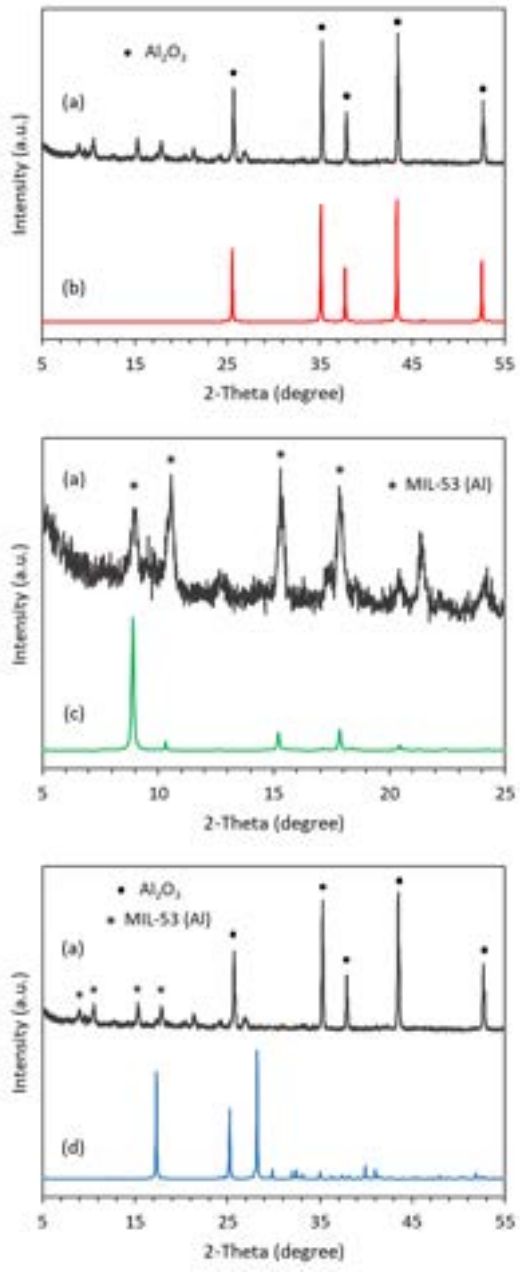

Figure 4: X-Ray diffraction patterns: (a) MIL-53(Al) crystals synthesised on ceramic hollow fibre substrate, (b) α-alumina (Al_2O_3) powder, (c) MIL-53(Al) crystals and (d) 1,4-benzenedicarboxylic acid (BDC) powder

Presented in Figure 4 are the XRD profiles collected for (a) the synthesised MIL-53(Al)-Ceramic Hollow Fibre compound, (b) α-alumina powder, (c) pure MIL-53(Al) crystals and (d) BDC powder. By comparing 4(a) and 4(b), it can be seen that the peaks at 25.7, 35.3, 37.9, 43.5 and 52.6 degrees in 4(a) correspond to that of 4(b). This shows that α-alumina is present in the synthesised compound, which is as expected due to the use of significant amounts of α-alumina powder for synthesis of the ceramic hollow fibre substrate.

Similarly, since both 4(a) and 4(c) have peaks at 9.0, 10.5, 15.3 and 17.8 degrees, it can be conclusively shown that MIL-53(Al) crystals were successfully synthesised on the ceramic hollow fibre as desired. The intensity of the peaks for the MIL-53(Al) crystals in 4(a) are noticeably smaller than that of alumina since the proportion of α-alumina present in the MIL-53(Al)-Ceramic Hollow Fibre product is significantly higher. Finally, from 4(a) and 4(d), it can be observed that they do not share any common peaks. This suggests there is no excess BDC present in the synthesised product after DMSO was used to remove residual free BDC ligands.

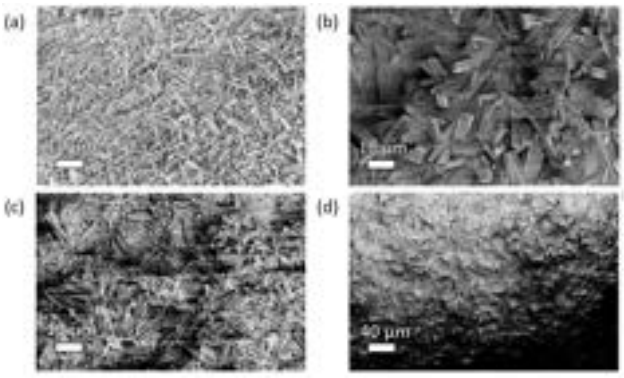

Figure 5: SEM images of MIL-53(Al) synthesised on ceramic hollow fibre substrate with a fixed synthesis time of 12 h and varying amounts of BDC reactant used for synthesis: (a) 0.5 g, (b) 1.0 g, (c) 1.5 g and (d) 2.0 g

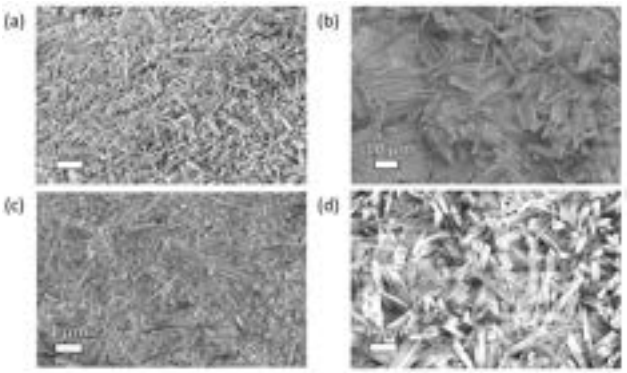

Figure 6: SEM images of MIL-53(Al) synthesised on ceramic hollow fibre substrate with a fixed amount (0.5 g) of BDC reactant used for synthesis and varying synthesis times: (a) 12 h, (b) 24 h, (c) 36 h and (d) 48 h

From Figures 5, 6 and 7, the morphology and size of the MIL-53(Al) crystals can be determined. In all the

SEM images, the MIL-53(Al) are seen to be mostly composed of uniform cuboid spindle-shaped crystals. From Figure 5, 5(a) is observed to have the most uniform and smallest crystals. Additionally, the MIL-53(Al) crystals in 5(a) are the most homogeneous as the ceramic hollow fibre structure that acts as the support appears to be fully covered by the crystals. It is worth noting that the crystals in 5(b) seem to be larger and less homogeneous than both 5(a) and 5(c). From Figure 6, it is seen that the crystals in 6(a) and 6(d) are more uniform and homogeneous than those in 6(b) and 6(c). In particular, 6(c) shows the most irregularly shaped crystals. Lastly, Figure 7 shows a zoomed out version of 6(b). Figure 7 shows that there is a high loading of MIL-53(Al) crystals on the finger-like micro-channels of the ceramic hollow fibre substrate. This proves that MIL-53(Al) crystals are growing not only on the surface, but also on the inner layers of the ceramic hollow fibre substrate, thus increasing the surface area available for adsorption.

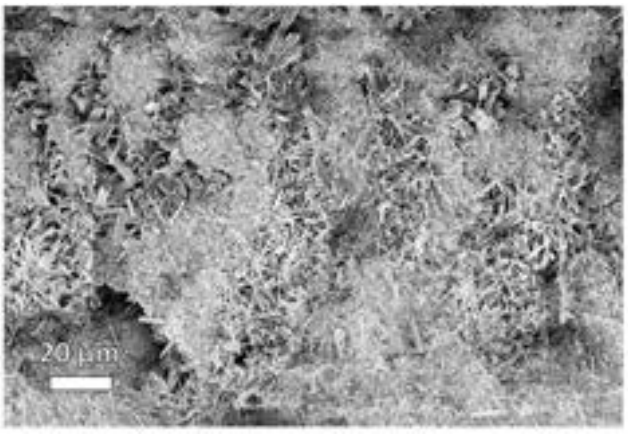

Figure 7: Zoomed out SEM image of MIL-53 (Al) synthesised on ceramic hollow fibre substrate with synthesis time of 24 h and 0.5 g of BDC for synthesis

3.2 Adsorption Experiments

Based on the XRD pattern of BDC, Figure 4(d), it was hypothesised that the absence of the corresponding BDC peaks in the synthesised MIL-53(Al) product X-Ray diffraction pattern, Figure 4(a), indicated that there were no residual BDC ligands remaining on the synthesised product. However, a decrease in weight of the sample starting at approximately 320°C can be seen from the TGA results as shown in Figure 3. This corresponds to the temperature at which pure BDC begins to decompose, which was identified via TGA that was performed on a sample of pure BDC ligand. Thus, this initial weight loss at stage 3(a) of Figure 3 can be inferred to have been caused by the decomposition of residual BDC ligands on the synthesised product that had not reacted with the aluminium precursor or been washed away with DMSO. This indicates there was still residual BDC ligand remaining on the synthesised product, which is in contrast to the results of the XRD previously discussed in Section 3.1. It was suggested that the BDC was not detected in the XRD due to the mass of free BDC ligand remaining being insignificant when compared to the mass of both MIL-53(Al) crystals and the ceramic hollow fibre.

The results of Figure 8 are in agreement with the SEM images shown in Figure 5, showing that the mass of MIL-53(Al) formed when 1.0 g of BDC was used is less than that formed when 0.5 g of BDC was used. However, this contradicts the overall trend (red dashed line) observed in Figure 8 that suggests a higher mass of MIL-53(Al) should be produced when increasing amounts of BDC is used for synthesis. This predicted trend is in line with theory that indicates more products are formed when larger amounts of reactant(s) are used, assuming that the reactant(s) are in excess, which is true in this case due to increasing amounts of MIL-53(Al) being obtained when higher amounts of BDC, i.e. 1.5 g and 2.0 g, were used for synthesis. Therefore, the inconsistent result observed at synthesis time of 12 h and 1.0 g of BDC used is suggested to have been caused by an error made during the synthesis process for this particular sample. The synthesis of a new sample at these conditions to validate the predicted trend could not be carried out due to time and equipment limitations.

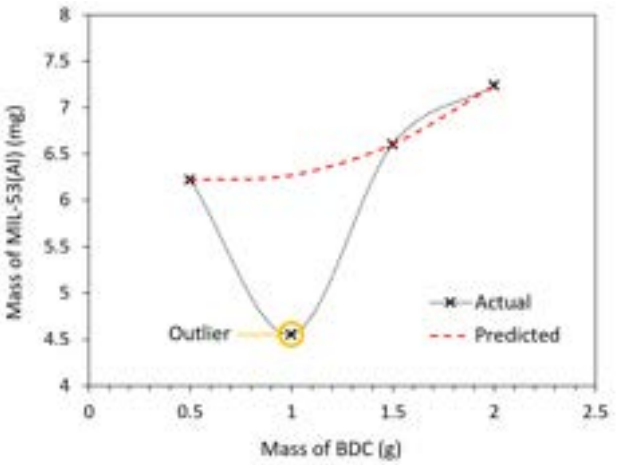

Figure 8: Effect of mass of BDC used for synthesis on mass of MIL-53(Al) formed for a fixed synthesis time of 12 h

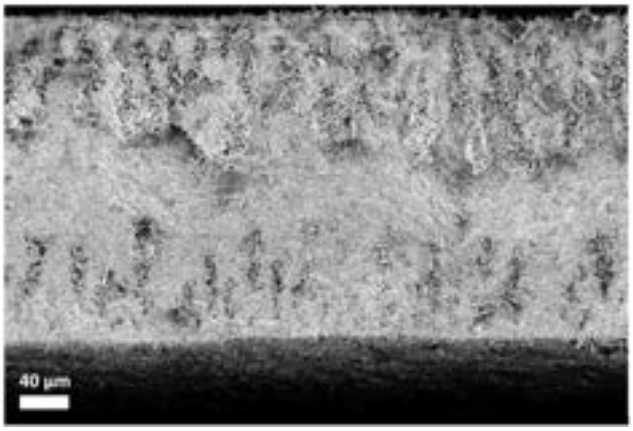

Figure 9: SEM image of cross-sectional area of the synthesised product with MIL-53(Al) crystals growing on the finger-like structures of the ceramic hollow fibre support

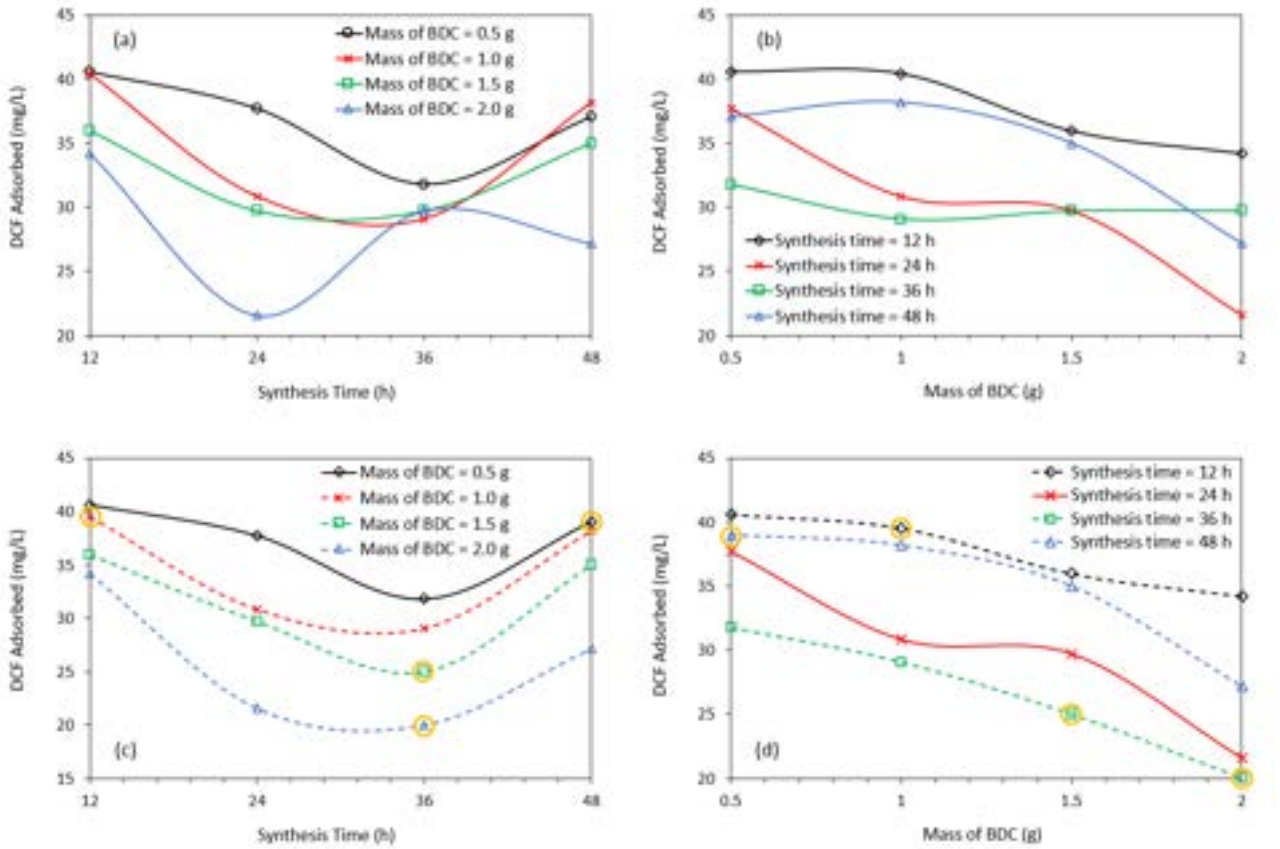

Figure 10: (a) Effect of synthesis time on adsorption performance of MIL-53(Al)-Ceramic Hollow Fibre adsorbent - experimental data, (b) Effect of mass of BDC used for synthesis on adsorption performance of MIL-53(Al)-Ceramic Hollow Fibre adsorbent - experimental data, (c) Effect of synthesis time on adsorption performance of MIL-53(Al)-Ceramic Hollow Fibre adsorbent - with predicted data points highlighted in circles and (d) Effect of mass of BDC used for synthesis on adsorption performance of MIL-53(Al)-Ceramic Hollow Fibre adsorbent - with predicted data points highlighted in circles

Figure 10(b) shows that in general, the adsorption of DCF decreases with increasing amounts of BDC used during synthesis. Building upon the aforementioned hypothesis that higher amounts of BDC used for synthesis leads to more MIL-53(Al) being formed, this decrease in adsorption performance may seem counter-intuitive. However, this decreased adsorption performance could be due to the blockage of pores. There are two main types of pores to consider in this study, pores inside the MIL-53(Al) crystals and the pores of the ceramic hollow fibre substrate, as seen in the SEM image of the cross-sectional area of the synthesised MIL-53(Al)-Cereamic Hollow Fibre product (Figure 9).

It is suspected that higher amounts of BDC used for synthesis would lead to more free BDC ligands blocking both these pores. Blockage of pores inside the MIL-53(Al) crystals would lead to a decrease in free adsorption sites for adosorption of DCF, thus reducing adsorption performance. Additionally, blockage of the pores of the ceramic hollow fibre support would lead to smaller pore sizes in the support, preventing DCF solution from even reaching the MIL-53(Al) crystals inside the ceramic hollow fibre structure, making it impossible for the MOFs to adsorb the DCF. This coupled pore blockage effect could explain the decrease in adsorption performance with increasing mass of BDC used for synthesis. However, there were four data points that did not adhere to this overall trend, specifically at the synthesis conditions of: 36 h and 1.5 g, 36 h and 2.0 g, 12 h and 1.0 g and 48 h and 1.0 g, so reasonable predictions were made for these four data points, as highlighted in circles in Figures 10(c) and 10(d), to show the overall effects of varying synthesis times and mass of BDC used for synthesis. Once again, retests at these four sets of synthesis conditions to validate the predictions made were unable to be carried out due to time limitations.

The graph of varying mass of BDC used for synthesis after adjusting for these four sets of synthesis conditions (Figure 10(d)) shows a clear decrease in amount of DCF adsorbed with increasing amounts of BDC used for synthesis. Based on the range of mass of BDC used for synthesis tested, it can also be inferred that the lowest mass of BDC, 0.5 g, gives the highest adsorption performance.

Based on Figure 10(c), it is evident that a synthesis time of 12 h gives the highest adsorption of DCF. It is also interesting to note that there is an initial decrease in adsorption performance with increasing synthesis time, before a minimum point is reached somewhere between 24 h and 36 h and the trend is reversed. This leads to an interesting hypothesis that at long enough synthesis times, free BDC ligands become the limiting reactant, causing the excess BDC ligands which were

Table 1: Comparison of adsorption capacities of DCF using various adsorbents from this study and literature

Adsorbents	q_{max} (DCF) mg g^{-1}	BET Surface Area m^2 g^{-1}	Total Pore Volume cm^3 g^{-1}	References
PPhA	21	1231	0.62	[35]
CNT/Alumina Hybrid	27	237	0.60	[39]
Activated Carbon (Olive Waste)	56	793	0.59	[32]
CTAB-ZIF-67	61	1103	0.34	[42]
Activated Carbon (Commercial)	76	870	0.44	[33]
ZIF-8 / MAF-4	100	1073	0.51	[43]
NH_2-UiO-66	106	902	0.35	[33]
Zeolite with Cetylpyridinium Chloride	160	68	-	[41]
UiO-66	189	1082	0.44	[33]
OH-MCOF	203	90	-	[40]
18% SO_3H-UiO-66	263	910	0.59	[33]
Activated Biochars	372	1360	0.95	[36]
Fe_3O_4@MOF-100(Fe)	377	198	-	[38]
PCDM-1000	400	1855	-	[43]
MIL-53(Al) Powder	422	1100 - 1500	0.51	[11]
OAC (2.0)	487	704	0.35	[34]
CDM6-K1000	503	3123	1.77	[50]
MIL-53(Al) on Ceramic Hollow Fibre	163	6.836	0.016	Present Study

originally blocking the pores to be reduced via reaction to form more MIL-53(Al) crystals. This leads to a decrease in the pore blockage effect, thus increasing adsorption of DCF. Additionally, the four predicted data points, highlighted in circles, also fit the overall trend observed for synthesis time in Figure 10(c), further reaffirming that the predictions made were reasonable and should be the expected results.

From the BET analysis carried out, a BET surface area of 6.836 $m\,g^{-2}$ for the synthesised MIL-53(Al) on ceramic hollow fibre was obtained. This is extremely low compared to other adsorbents as shown in Table 1. There are two two main factors for this. The first being pore blockage of the MIL-53(Al) by free BDC ligands preventing N_2 gas from reaching the adsorption sites, thus limiting adsorption of the gas molecules. The second is the fact that this calculated value is normalised against the mass of the sample, which in this case includes the mass of the unreacted aluminium precursor, MIL-53(Al) with free adsorption sites, MIL-53(Al) with pores blocked by BDC ligands and free BDC ligands. Although all four components contribute to the overall mass of the sample, only the unreacted aluminium precursor and MIL-53(Al) with free adsorption sites contribute to the surface area, resulting in this reduced value. As such, this significantly lower BET surface area is most likely due to the combined effects of these two factors. This same reasoning can also be used to justify the low total pore volume of 0.016 $cm^3\,g^{-1}$ obtained, which is significantly lower than that of other common adsorbents such as activated carbon, zeolites and UiO-66, as shown in Table 1.

Figure 11 compares the adsorption performance of the synthesised MIL-53(Al)-Ceramic Hollow Fibre product in this study against other adsorbents found in literature. Despite the pore blockage by free BDC ligands, the final product still performed better (in terms of DCF adsorbed per mass of adsorbent) than many other traditional adsorbents. In particular, the adsorption performance of the synthesised product (163 $mg\,g^{-1}$) is much higher than that of conventional adsorbents such as activated carbon (76 $mg\,g^{-1}$), which is most commonly used in commercial applications.

It can also be seen from Table 1 that the maximum adsorption capacity of DCF per unit mass of MIL-53(Al), q_{max}, is less than half that of pure MIL-53(Al) powder. Once again, this reduced value could be due to the pore blockage from residual BDC ligands, possibly due to incomplete washing with DMSO. DMSO was selected as the solvent for washing in this study due to the high solubility of BDC in DMSO at room temperature (0.2 g $g_{solvent}{}^{-1}$) compared to other solvents such as dimethylformamide (0.074 g $g_{solvent}{}^{-1}$), methanol (0.001 g $g_{solvent}{}^{-1}$) and water (0.000017 g $g_{solvent}{}^{-1}$) [51]. However, a study by Karolina *et al.* [51] has shown that ionic liquids could serve as more promising solvents to be used in future studies for better removal of DMSO whilst ensuring the environmental sustainability of this fabrication process. Therefore, it cannot be concluded based on this study alone that the adsorption performance of MIL-53(Al) on ceramic hollow fibre is inferior to that of pure MIL-53(Al) powder and a fairer comparison where the MIL-53(Al)-Ceramic Hollow Fibre product is ensured to be free of residual BDC ligands would need to be carried out to accurately compare its adsorption performance to that of other adsorbents.

4 Conclusion

In conclusion, MIL-53(Al) was successfully synthesised on ceramic hollow fibre substrates, with the final product characterised by XRD, SEM, TGA and nitrogen adsorption. XRD analysis showed that both MIL-53(Al) crystals and alumina were present in the product in significant quantities. Furthermore, SEM showed that the MIL-53(Al) crystals were homogeneously grown on the surface of the ceramic hollow fibre substrate at the optimal synthesis conditions. From the TGA results, the overall trend showed that there was a positive relationship between the mass of BDC used for synthesis and the mass of MIL-53(Al) crystals formed, which was as expected. Lastly, the BET surface area and total pore volume were determined to

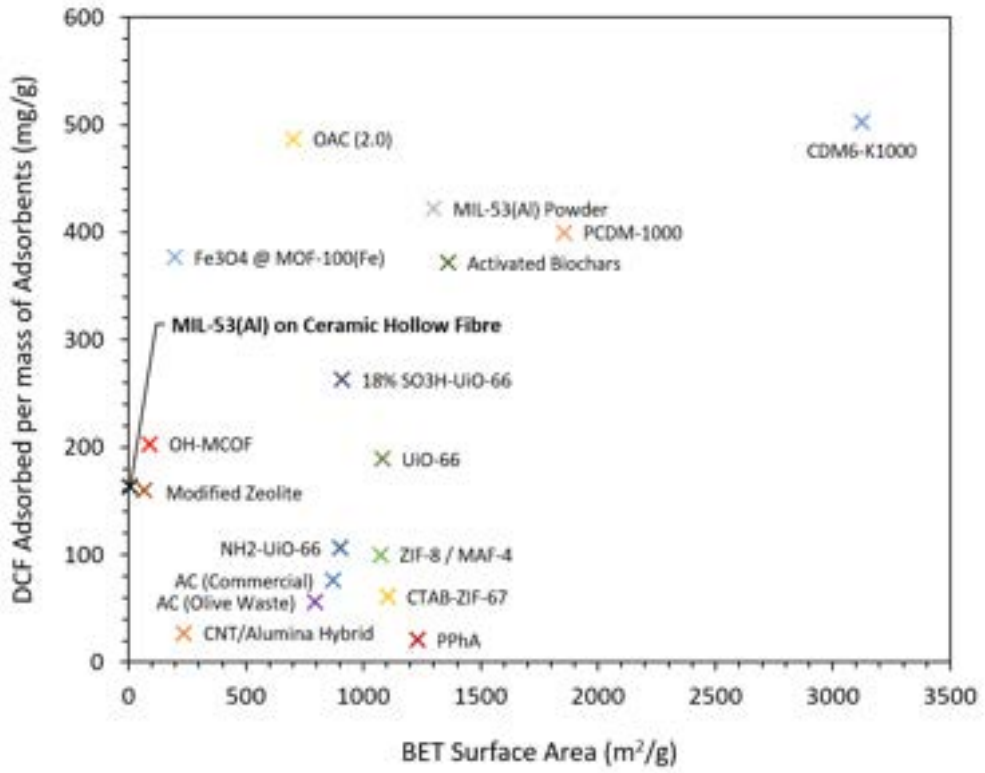

Figure 11: Scatter plot of adsorptive performance of various adsorbents for the removal of DCF from water

be 6.836 $m^2\,g^{-1}$ and 0.016 $cm^3\,g^{-1}$ respectively.

The overall trend for mass of BDC used for synthesis showed that as larger amounts of BDC is used, more MIL-53(Al) crystals is formed but less DCF is adsorbed. This is mainly due to increasing amounts of residual BDC ligands, which based on TGA results have been shown to still be present, blocking the pores of both the MIL-53(Al) crystals and the ceramic hollow fibre substrate. On the other hand, a U-shaped trend is observed for the relationship between synthesis time and adsorption performance. At a minimum point somewhere between 24 h and 36 h, free BDC becomes the limiting reactant and reacts to form more MIL-53(Al), thus reducing pore blockage and increasing adsorption performance. From this study, the product which adsorbed the highest amount of DCF, 40.6 $mg\,L^{-1}$, was synthesised using 0.5 g of BDC and a synthesis time of 12 h. The trends for both synthesis time and mass of BDC used for synthesis holds true for the majority of data points obtained. There were four data points that did not adhere to the overall trends and this was hypothesised to have been caused by both experimental and equipment errors. This hypothesis was unable to be confirmed through re-runs of the experiment at those sets of synthesis conditions due to time constraints. In future studies, it is suggested that re-runs of these four sets of synthesis conditions and duplicate experiments be carried out.

The maximum adsorption capacity of DCF for the MIL-53(Al)-Ceramic Hollow Fibre product was determined to be 163 $mg\,g^{-1}$. While this value is higher than the adsorption capacities of some conventional adsorbents such as activated carbon and other MOFs such as ZIF-8, it is significantly lower when compared to the adsorption performance of pure MIL-53(Al) powder. It was hypothesised that the adsorbent was not performing at its maximum capacity due to the presence of free BDC ligands blocking its pores, resulting in reduced free adsorption sites available for adsorption. Despite this, the final product still performed relatively well, suggesting it has the potential to be a highly efficient adsorbent. Therefore, further analysis and studies should be carried out to determine its suitability for commercial applications.

5 Outlook

Although the adsorption of the MIL-53(Al)-Ceramic Hollow Fibre product (163 $mg\,g^{-1}$) did not perform as well as pure MIL-53(Al) powder (422 $mg\,g^{-1}$), there is still a promising future for this product as its full potential was not achieved due to the presence of BDC blocking its pores. As such, future experimental studies after ensuring there is no residual BDC remaining can be carried out for fair comparison with other adsorbents. Additionally, after determining a method for complete removal of BDC, this study should be repeated to investigate any changes in trends for synthesis time and mass of BDC used for synthesis. Some possible suggestions to ensure complete removal of BDC include the use of different solvents, a longer washing time or the use of ultrasonic vibration during the washing process.

Apart from adsorption performance (total amount of DCF adsorbed), another key factor that should be considered is the adsorption efficiency of the adsorbent. Adsorption efficiency, which is defined as the DCF adsorbed per mass of adsorbent, is useful to compare the

performance of different adsorbents on the same basis. A more efficient adsorbent will be more economical since a smaller amount of adsorbent would be required to adsorb the same amount of DCF. Due to time and equipment limitations, TGA (which is needed to determine the adsorption efficiency) could not be carried out for all samples produced. In a future continuation of this study, it would be interesting to compare both the adsorption performance and adsorption efficiency of samples for each set of synthesis conditions.

In this study, a limited range of synthesis conditions were tested. The results show that the highest amount of DCF was adsorbed using 0.5 g of BDC for synthesis. However, since no peak in the performance was observed, a lower mass of BDC, i.e. between 0 and 0.5 g, may yield even better results. Similarly, no peaks for synthesis time were observed despite the results at 12 h being better than that at 48 h. As such, synthesis times of less than 12 h and more than 48 h should also be considered and compared to determine the ideal trade-off between synthesis time and additional adsorption performance. Moreover, temperature and pH, which are other important synthesis process conditions to be investigated, can also be considered for a more in-depth optimisation study.

The adsorption performance of the synthesised product can also be tested using other common NSAIDs such as naproxen and ibuprofen. An adsorbent that can perform well for several types of NSAIDs is desirable as this would allow it to adsorb multiple compounds effectively at the same time. However, in cases where several adsorbates are of interest, it may also be useful to consider a co-adsorption experiment. This would allow any effects different adsorbates may have in the presence of each other to be studied in greater detail to ensure that the adsorption performance of one compound is not negatively impacting the adsorption of another.

Another important aspect that should be considered is the equilibrium and kinetic studies of the MIL-53(Al)-Ceramic Hollow Fibre product. The equilibrium model, also called an isotherm, is essential for understanding how the adsorbate interacts with the adsorbent and other adsorbate molecules. Some common isotherms of adsorption include Langmuir, Freundlich and Temkin. Furthermore, during scaling-up, mass transfer analysis should be conducted to determine the breakthrough point, the time at which regeneration of the adsorbent will be required. Finally, the performance of the adsorbent should then be tested using real wastewater samples, in order to determine the efficacy of the synthesised product.

Acknowledgements

The authors are thankful to Mr Tongrong Wu for performing the experiment and collecting the data on our behalf due to the COVID-19 restrictions in the laboratory. The authors also gratefully acknowledge the support provided by the Department of Chemical Engineering at Imperial College London.

References

1. Hasan, Z., Jeon, J. & Jhung, S. H. Adsorptive removal of naproxen and clofibric acid from water using metal-organic frameworks. *Journal of Hazardous Materials* **209-210,** 151–157 (2012).
2. Dhaka, S. *et al.* Metal–organic frameworks (MOFs) for the removal of emerging contaminants from aquatic environments. *Coordination Chemistry Reviews* **380,** 330–352 (2019).
3. Guo, F. *et al.* Dual-metal-organic frameworks derived manganese and zinc oxides nanohybrids as high performance anodes for lithium-ion batteries. *Journal of Alloys and Compounds* **852,** 156814 (2020).
4. Younis, S. A., Bhardwaj, N., Bhardwaj, S. K., Kim, K.-H. & Deep, A. Rare earth metal–organic frameworks (RE-MOFs): Synthesis, properties, and biomedical applications. *Coordination Chemistry Reviews,* 213620 (2020).
5. Feng, X., Song, Y. & Lin, W. Transforming Hydroxide-Containing Metal–Organic Framework Nodes for Transition Metal Catalysis. *Trends in Chemistry* **2,** 965–979 (2020).
6. Jun, B.-M. *et al.* Applications of metal-organic framework based membranes in water purification: A review. *Separation and Purification Technology* **247,** 116947 (2020).
7. Samokhvalov, A. Aluminum metal–organic frameworks for sorption in solution: A review. *Coordination Chemistry Reviews* **374,** 236–253 (2018).
8. Wu, T., Prasetya, N. & Li, K. Recent advances in aluminium-based metal-organic frameworks (MOF) and its membrane applications. *Journal of Membrane Science* **615,** 118493 (2020).
9. Colombo, V. *et al.* High thermal and chemical stability in pyrazolate-bridged metal–organic frameworks with exposed metal sites. *The Royal Society of Chemistry* **2,** 1311–1319 (2011).
10. Qian, X. *et al.* Structure stability of metal-organic framework MIL-53 (Al) in aqueous solutions. *International Journal of Hydrogen Energy* **38,** 16710–16715 (2013).
11. Karami, A., Sabouni, R. & Ghommem, M. Experimental investigation of competitive co-adsorption of naproxen and diclofenac from water by an aluminum-based metal-organic framework. *Journal of Molecular Liquids* **305,** 112808 (2020).
12. Hu, Y. *et al.* Metal–organic framework membranes fabricated via reactive seeding. *Chem. Commun.* **47,** 737–739 (2011).
13. Nan, J., Dong, X., Wang, W. & Jin, W. Formation mechanism of metal–organic framework membranes derived from reactive seeding approach. *Microporous and Mesoporous Materials* **155,** 90–98 (2012).
14. Chi, Y., Chong, J. Y., Wang, B. & Li, K. Pristine graphene membranes supported on ceramic hollow fibre prepared via a sacrificial layer assisted CVD approach. *Journal of Membrane Science* **595,** 117479 (2020).
15. Chong, J. Y., Wang, B. & Li, K. High performance stainless steel-ceramic composite hollow fibres for microfiltration. *Journal of Membrane Science* **541,** 425–433 (2017).
16. Mahyon, N. I. *et al.* Integrating Pd-doped perovskite catalysts with ceramic hollow fibre substrate for efficient CO oxidation. *Journal of Environmental Chemical Engineering* **8,** 103897 (2020).
17. Zhang, L. *et al.* NH2-MIL-53(Al) Metal–Organic Framework as the Smart Platform for Simultaneous High-Performance Detection and Removal of Hg2+. *Inorganic Chemistry* **58,** 12573–12581 (2019).

18. Hamon, L. *et al.* Comparative Study of Hydrogen Sulfide Adsorption in the MIL-53(Al, Cr, Fe), MIL-47(V), MIL-100(Cr), and MIL-101(Cr) MetalOrganic Frameworks at Room Temperature. *Journal of the American Chemical Society* **131,** 8775–8777 (2009).
19. Patil, D. V. *et al.* MIL-53(Al): An Efficient Adsorbent for the Removal of Nitrobenzene from Aqueous Solutions. *Industrial & Engineering Chemistry Research* **50,** 10516–10524 (2011).
20. Caliman, F. A. & Gavrilescu, M. Pharmaceuticals, Personal Care Products and Endocrine Disrupting Agents in the Environment – A Review. *CLEAN – Soil, Air, Water* **37,** 277–303 (2009).
21. Cycoń, M., Borymski, S., Żołnierczyk, B. & Piotrowska-Seget, Z. Variable effects of non-steroidal anti-inflammatory drugs (NSAIDs) on selected biochemical processes mediated by soil microorganisms. *Frontiers in Microbiology* **7,** 1969 (2016).
22. Lee, J., Ji, K., Lim Kho, Y., Kim, P. & Choi, K. Chronic exposure to diclofenac on two freshwater cladocerans and Japanese medaka. *Ecotoxicology and Environmental Safety* **74,** 1216–1225 (2011).
23. Folarin, O., Otitoloju, A. & Amaeze, N. Comparative Ecotoxicological Assessment of Acetaminophen and Diclofenac using Freshwater African Catfish Clarias gariepinus (Burchell 1822). *Journal of Applied Sciences and Environmental Management* **22,** 1519–1525 (2018).
24. Vieno, N. & Sillanpää, M. Fate of diclofenac in municipal wastewater treatment plant — A review. *Environment International* **69,** 28–39 (2014).
25. Carballa, M., Fink, G., Omil, F., Lema, J. M. & Ternes, T. Determination of the solid–water distribution coefficient (Kd) for pharmaceuticals, estrogens and musk fragrances in digested sludge. *Water Research* **42,** 287–295 (2008).
26. Ternes, T. A. *et al.* A rapid method to measure the solid–water distribution coefficient (Kd) for pharmaceuticals and musk fragrances in sewage sludge. *Water Research* **38,** 4075–4084 (2004).
27. Suárez, S., Carballa, M., Omil, F. & Lema, J. M. How are pharmaceutical and personal care products (PPCPs) removed from urban wastewaters? *Reviews in Environmental Science and Bio/Technology* **7,** 125–138 (2008).
28. Radjenović, J., Petrović, M. & Barceló, D. Fate and distribution of pharmaceuticals in wastewater and sewage sludge of the conventional activated sludge (CAS) and advanced membrane bioreactor (MBR) treatment. *Water Research* **43,** 831–841 (2009).
29. Quintana, J. B., Weiss, S. & Reemtsma, T. Pathways and metabolites of microbial degradation of selected acidic pharmaceutical and their occurrence in municipal wastewater treated by a membrane bioreactor. *Water Research* **39,** 2654–2664 (2005).
30. Joss, A. *et al.* Biological degradation of pharmaceuticals in municipal wastewater treatment: Proposing a classification scheme. *Water Research* **40,** 1686–1696 (2006).
31. Ren, Z., Shao, L. & Zhang, G. Adsorption of Phosphate from Aqueous Solution Using an Iron–Zirconium Binary Oxide Sorbent. *Water Air Soil Pollution* **223,** 4221–4231 (2012).
32. Baccar, R., Sarrà, M., Bouzid, J., Feki, M. & Blánquez, P. Removal of pharmaceutical compounds by activated carbon prepared from agricultural by-product. *Chemical Engineering Journal* **211-212,** 310–317 (2012).
33. Hasan, Z., Khan, N. A. & Jhung, S. H. Adsorptive removal of diclofenac sodium from water with Zr-based metal–organic frameworks. *Chemical Engineering Journal* **284,** 1406–1413 (2016).
34. Bhadra, B. N., Seo, P. W. & Jhung, S. H. Adsorption of diclofenac sodium from water using oxidized activated carbon. *Chemical Engineering Journal* **301,** 27–34 (2016).
35. Turk Sekulic, M. *et al.* Surface functionalised adsorbent for emerging pharmaceutical removal: Adsorption performance and mechanisms. *Process Safety and Environmental Protection* **125,** 50–63 (2019).
36. Jung, C. *et al.* Competitive adsorption of selected non-steroidal anti-inflammatory drugs on activated biochars: Experimental and molecular modeling study. *Chemical Engineering Journal* **264,** 1–9 (2015).
37. Ghosh, S., Badruddoza, A. Z. M., Hidajat, K. & Uddin, M. S. Adsorptive removal of emerging contaminants from water using superparamagnetic Fe3O4 nanoparticles bearing aminated -cyclodextrin. *Journal of Environmental Chemical Engineering* **1,** 122–130 (2013).
38. Zheng, X. *et al.* Facile synthesis of Fe3O4@MOF-100(Fe) magnetic microspheres for the adsorption of diclofenac sodium in aqueous solution. *Environmental Science and Pollution Research* **25,** 31705–31717 (2018).
39. Wei, H. *et al.* Regenerable granular carbon nanotubes/alumina hybrid adsorbents for diclofenac sodium and carbamazepine removal from aqueous solution. *Water Research* **47,** 4139–4147 (2013).
40. Mi, X. *et al.* Adsorptive removal of diclofenac sodium from aqueous solution by magnetic COF: Role of hydroxyl group on COF. *Colloids and Surfaces A: Physicochemical and Engineering Aspects* **603,** 125238 (2020).
41. Krajišnik, D. *et al.* Properties of diclofenac sodium sorption onto natural zeolite modified with cetylpyridinium chloride. *Colloids and Surfaces B: Biointerfaces* **83,** 165–172 (2011).
42. Lin, K.-Y. A., Yang, H. & Lee, W.-D. Enhanced removal of diclofenac from water using a zeolitic imidazole framework functionalized with cetyltrimethylammonium bromide (CTAB). *Rsc Advances* **5,** 81330–81340 (2015).
43. Bhadra, B. N., Ahmed, I., Kim, S. & Jhung, S. H. Adsorptive removal of ibuprofen and diclofenac from water using metal-organic framework-derived porous carbon. *Chemical Engineering Journal* **314,** 50–58 (2017).
44. Kingsbury, B. F. & Li, K. A morphological study of ceramic hollow fibre membranes. *Journal of Membrane Science* **328,** 134–140 (2009).
45. Tan, X., Liu, S. & Li, K. Preparation and characterization of inorganic hollow fiber membranes. *Journal of Membrane Science* **188,** 87–95 (2001).
46. Loiseau, T. *et al.* A Rationale for the Large Breathing of the Porous Aluminum Terephthalate (MIL-53) Upon Hydration. *Chemistry – A European Journal* **10,** 1373–1382 (2004).
47. Lewis, J., Schwarzenbach, D. & Flack, H. D. Electric field gradients and charge density in corundum, -Al2O3. *Acta Crystallographica Section A* **38,** 733–739 (1982).
48. Bailey, M. & Brown, C. J. The crystal structure of terephthalic acid. *Acta Crystallographica* **22,** 387–391 (1967).
49. Qian, X. *et al.* Structure stability of metal-organic framework MIL-53 (Al) in aqueous solutions. *International Journal of Hydrogen Energy* **38,** 16710–16715 (2013).
50. An, H. J., Bhadra, B. N., Khan, N. A. & Jhung, S. H. Adsorptive removal of wide range of pharmaceutical and personal care products from water by using metal azolate framework-6-derived porous carbon. *Chemical Engineering Journal* **343,** 447–454 (2018).
51. Karolina, M., Ewa, P., Aleksander, G., Piotr, L. & Anna, C. Studies on the Solubility of Terephthalic Acid in Ionic Liquids. *Molecules* **25** (2020).

Modelling of Paracetamol Crystallisation in Ethanol Solution

Aiman Syahirah Ahmad Dzulfakhar and Sim En You
Department of Chemical Engineering, Imperial College London, U.K.
Compiled December 17, 2020

Abstract

This work focuses on the modelling of secondary nucleation as well as explaining the deficiencies in current growth and dissolution equations. The modelling used in this paper is based on paracetamol crystals in ethanol solution for seeded batch cooling crystallisation process. The modelling is conducted in gPROMS FormulatedProducts® 1.6.0. Both Mersmann's and Evans' kinetics were studied and used to describe activated and attrition nucleation respectively. The values of each kinetic parameter of the above mechanisms were determined by carrying out the parameter estimation using experimental data from literature, which are the mass fraction change of the paracetamol in the solution versus time and the particle size distribution of paracetamol crystals. It was found that Mersmann's kinetics alone does not fully describe the whole secondary nucleation mechanism as it did not achieve a satisfactory fit with experimental data. On the other hand, a model with both Mersmann's activated secondary nucleation and Evans' attrition secondary nucleation kinetics provided a closer fit to experimental data. As for the growth rate equation used, it was found that the power-law growth equation is insufficient to fully describe the growth rate behaviour of crystals alone especially in industrial crystallisers because it does not take into account the self-healing mechanism of crystals. An equation which is a function of surface energy and molar strain energy is postulated to account for the presence of self-healing in crystals.

Keywords: Crystallisation, Paracetamol, gPROMS, Secondary nucleation

1 Introduction

The production of high-quality pharmaceutical drugs is paramount in improving human lives. Hence, the pharmaceutical industry plays a vital role in the policy surrounding research, discovery and development of new medicines which would benefit patients who require advanced scientific developments in medicine and health-care systems (Durrant 2001). Aside from that, the pharmaceutical industry is moving away from blockbuster drugs manufactured in tonne batches which leads to a large amount of wastage and is shifting towards targeted medicines manufactured in small batches based on the digital design which shows that the entire pharmaceutical industry is in an urgent need of both innovative technological solutions (Rantanen and Khinast 2015).

One of the crucial steps in the production of pharmaceutical goods is the crystallisation process where the desired product is separated from the liquid phase. The aim of this process is to obtain a higher purity percentage of the active pharmaceutical ingredients (APIs) in stable solid form so it can be used in producing pharmaceutical medicine since most drugs in the industry are small organic molecules. Reportedly, more than 90% of APIs would go through a crystallisation purification step at some stage of their production cycles to remove impurities (Variankaval, Cote, and Doherty 2008). Although paracetamol has many other purification methods such as distillation and chromatography, in terms of purity and cost, crystallisation is the preferred purification method (Chemistry 2009).

However, high purity is not the only concern for the final solid form products. The medicine performance is significantly impacted by numerous crystal characteristics such as the crystal form and polymorphs, particle size and the solubility in the human body (Bučar, Lancaster, and Bernstein 2015). Also, the mechanism of crystal nucleation and growth has not been fully grasped in the scientific world, which is a challenge in obtaining high-quality pharmaceutical products. Therefore, it is essential to understand the mechanisms in more depth to decide the best-operating conditions to obtain the desired crystal product in a crystalliser (Chen et al. 2011).

Currently, lab experiments are carried out to determine the crystallisation process and mechanisms; however, this method takes a long time to obtain a beneficial result. A few works have been done on process modelling of crystallisers on gPROMS® and some studies have also been done on how crystallisation is strongly influenced by fluid flow using tools such as computation fluid dynamics (CFD) (Oh et al. 2020). Hence, this research project focuses on constructing a computational model to control the paracetamol crystallisation process and investigate the mechanisms by using gCRYSTAL® program under gPROMS FormulatedProducts® 1.6.0.

gCRYSTAL® has an advanced crystallisation library where it enables scientists and engineers to screen the formulations with complex phase structures for quality attributes which allows it to be manufactured easily and clearly; thus the whole formulation and manufacturing design space could be explored (Process Systems Enterprise Ltd. n.d.(a)). This software utilises kinetic models which assist in monitoring the crystals' progression in every life cycle (i.e. birth, growth and agglomeration) and the population balance model (i.e. particle size distribution) to reproduce the crystallisation process.

Currently, in literature, several papers have looked at primary nucleation and growth and dissolution in detail. A generic power-law equation has also been used to describe the secondary nucleation process. This research paper aims to develop a deeper understanding of secondary nucleation mechanism (activated and attrition) and develop a model to attain kinetics of secondary nucleation using parameter estimation. This would also enable one to develop a deeper understanding of the underlying mechanisms of secondary nucleation and its impact on particle size distribution as well as mass fraction changes. This would also benefit the pharmaceutical industry as it will be more cost-effective, reducing the wastage of API materials and experimental efforts in developing process models and control strategies. An investigation on self-healing crystal was also carried out to highlight the inefficiencies in the current power-law equation used for growth and dissolution. Lastly, a detailed workflow is presented on how to tackle parameter estimation to save time and obtain more accurate results.

2 Background

This section aims to achieve two things, firstly to provide an overview of the principles being the crystallisation process. Secondly, to explain how the theory of nucleation and growth fits with the models used in gPROMS®.

2.1 Nucleation

There are two main types of nucleation, primary and secondary nucleation. Primary nucleation refers to a nucleation process that occurs in a crystal-free solution. Whereas secondary nucleation describes the formation of nuclei in the supersaturated solution where solute crystals are present in the solution. This paper will mainly focus on secondary nucleation; hence the following sections would explain secondary nucleation mechanisms in greater depth.

2.1.1 Primary Nucleation

Primary nucleation can be further split in two, primary homogeneous nucleation and primary heterogeneous nucleation. In homogeneous nucleation, the nuclei appearing in the homogeneous solution is spontaneously driven by the supersaturation force of the solution, whereas heterogeneous nucleation is the formation of nuclei induced by foreign bodies in the environment (Liu 2000). The foreign bodies can be any insoluble solid materials such as the dust particles (Mullin 2001). Homogeneous nucleation rarely occurs. Most of the time, it is catalysed by a heterogeneity (Ohring 1995). This is because some impurities lower the energy barrier on the nucleation process as there is an increase in solute concentration on the local surface spot (Thakur et al. 2007).

The mechanisms that can be applied in gCRYSTAL® program for the primary nucleation is the empirical power-law equation or the classical kinetics (Mullin 2001), which is represented in the form of the Arrhenius reaction velocity equation.

2.1.2 Secondary Nucleation

Formation of crystals through secondary nucleation can be distinguished into three different ways initial breeding, needle breeding (dendrite breeding), and attrition breeding.

Initial Breeding

Initial breeding mechanism is the process where small crystalline dust on crystal surface detaches itself from the crystal seed forming secondary nuclei (Myerson and Ginde 2002).

Initial breeding is not a dominant mechanism because the crystalline dust on the crystal surface is limited (Agrawal and Paterson 2015). Besides, this form of secondary nucleation could and should be inhibited by pre-treating the seed crystal (Myerson and Ginde 2002) before conducting the experiment.

Needle Breeding

Needle breeding, also known as dendrite breeding, is where dendrites are formed on the crystal surfaces, detaches itself from the crystal surface either due to collision or shear. This process is known in gCRYSTAL® as activated nucleation and the mechanism can be described by Mersmann's activated kinetic model (A. Mersmann, Braun, and Löffelmann 2002). The equation of Mersmann's activated nucleation is shown below in Equation 1:

$$J_{sec} = A_t \left[exp\left(ln\, k_s\right) \frac{D_{AB}}{d_m^4} \cdot exp\left(-\pi \left(K\, ln\left(\frac{C_c}{C^*} \right) \right)^2 \frac{1}{\nu\, ln\, S_a} \right) \right] \quad (1)$$

where A_t is the total surface area of crystal, $ln\, k_s$ is the natural logarithm of pre-exponential rate constant, D_{AB} is the diffusion coefficient of solute in the liquid phase, d_m is the diameter of the solute molecule, K is the solubility factor, ν is the number of entities, $C^*$is the solubility of the solute,C_c is the mass density of crystal and S_a the supersaturation ratio of the solution.

The dominance of a particular mechanism is influenced by several factors, mainly agitation speed and supersaturation level. At relative supersaturation of a solution larger than 0.1, needle breeding is more dominant than attrition breeding (A. Mersmann, Braun, and Löffelmann 2002).

Attrition breeding

Attrition breeding occurs due to the removal of fragments from the parent crystal due to collisions with each other (crystal-crystal interactions) or some other objects (crystal-impeller interactions). At low levels of supersaturation (< 0.1), attrition breeding is the dominant secondary nucleation mechanism where the generated fragments act as nuclei and are likely to be a major source of secondary nucleation in industrial crystallisers (Agrawal and Paterson 2015).

The first mechanistic description of the mechanical interaction of the crystals with crystalliser is developed by Ottens in which the nucleation rate of the crystals is assumed to be proportional to the product of collision energy and frequency of collision (Ottens E. P. K. 1973). Besides, to account for the phenomenon that larger crystals are more prone to attrition, a lower bound of integration was also introduced into the distribution.

The basic approach of Ottens was further modified by Evans T. 1974. However, other than crystal-impeller collisions due to bulk flow and crystal-crystal collisions due to turbulence, additional collision mechanisms like crystal impeller collisions due to turbulence, and crystal-crystal collisions induced by gravity were also added.

The Evans kinetic model is the recommended model in gPROMS® for the secondary nucleation arising from attrition describes the approach above and the equation is seen below:

$$J_{sec_ci} = \exp(ln\, k_{n_ci})\, \sigma^{n_{ci}}\, \frac{N_Q}{N_P} k_v \rho_c\, \varepsilon \int_{L_{min_ci}}^{\infty} nL^3\, dL \quad (2)$$

where J_{sec_ci} is the secondary rate due to crystal-impeller collisions, lnk_{n_ci} is the natural logarithm of the proportional factor for crystal–impeller collisions, σ is the relative supersaturation, n_{ci} is the supersaturation dependency of the secondary nucleation rate for crystal–impeller collisions, N_Q is the impeller flow number, N_P is impeller power number, k_v is volume shape factor, ρ_c is crystal density, ε is the energy dissipating rate, L_{min_ci} is particle size above which crystals are prone to attrition for crystal–impeller collisions and n is number density of particles.

2.2 Growth and Dissolution

The growth rate of a crystal face is dependent on its growth mechanism, which ultimately decides the crystal size (L. Li 1992). Therefore, to predict the final particle size distribution of a crystal, it is crucial to understand the growth mechanism. Volmer 1939 described the crystal growth process as a discontinuation process, taking place by adsorption on the crystal surface. There are three generally accepted mechanisms of the above mentioned kind of crystal growth, each of which reflects a particular range of supersaturation; screw dislocation (BCF) mechanism, Birth & Spread (B & S) mechanism and rough interfacial growth model with increasing supersaturation (Nguyen 2014).

These considerations are taken into account in Mersmann's two steps kinetic which proposes that the crystal growth contains two steps, which are the mass transfer of solute molecule from bulk phase to the liquid-crystal interface and the integration of solute molecule on the crystal surface (Alfons Mersmann et al. 1988). When the supersaturation level of the solution is high, the mass transfer step is considered as the primary rate control step, which can be shown as below:

$$G(L) = k_d(L)\left[\frac{C_{bulk} - C_{int}(L)}{\rho_{crys}}\right] \quad (3)$$

where G is the linear growth rate of crystal, k_d is the mass transfer coefficient, C_{bulk} is the concentration of the solute in the bulk phase, $C_{int}(L)$ is the concentration of the solute at liquid-crystal interface and ρ_{crys} molar density of the crystal.

3 Methods

Flowsheet construction of the APIs seeded crystallisation process was done in gCRYSTAL® program in gPROMSFormulatedProducts® 1.6.0 and is explained in detail in this section. The parameter estimation process of the secondary nucleation is also briefly described in this section.

3.1 Flowsheet Construction

This research paper aim is to study the kinetics of secondary nucleation and crystal growth. Hence, a paracetamol-ethanol cooling crystallisation flowsheet was constructed in gCRYSTAL® program to achieve the aim. The components included in this flowsheet are global specification, a seed pot, Mixed Suspension-Mixed Product Removal (MSMPR) crystallisers, temperature sensor and controller and a liquid composition sensor.

3.1.1 Global Specification

The starting point in developing a model in gCRYSTAL® is to determine the required details in the global specification unit which are the physical and chemical properties of the chemical components for both the liquid and crystal phases and the solubility of the paracetamol in ethanol solution. In paracetamol-ethanol crystallisation, only the paracetamol crystals' properties are considered as ethanol has a freezing point of -114°C (Sigma-Aldrich 2020a) and this value is lower than the set operating temperature. Hence, no ethanol crystal will be formed during the process.

For the liquid phase, the properties required in the global specification sheet are the molecular weights, the mass density, the mass-specific heat capacity and the dynamic viscosity of each component. Both mass density and dynamic viscosity specifications are important as both may influence the secondary nucleation and crystal growth rate estimation. The specification of the mass-specific heat capacity is essential in energy balance calculation.

As for the crystal phase, the properties required and need to be determined are the mass density, the mass-specific heat capacity, enthalpy of crystallisation and volume shape factor of crystals. Both mass density and volume shape factor of crystals specification can influence the crystal volume estimation, which will affect the secondary nucleation rate estimation and the particle size distribution (PSD) of the final product in the crystalliser. As for the liquid phase, the mass-specific heat capacity of crystal is essential in energy balance calculation.

Lastly, the solubility of paracetamol solution needs to be specified as well in the global specification sheet. Equation 4 is used to represent some of the properties in gCRYSTAL® program is shown below:

$$x = a + b\,T + c\,T^2 + d\,T^3 + \frac{e}{T} + \frac{f}{T^2} \quad (4)$$

where x is the liquid or crystal properties such as the mass density, the mass-specific heat capacity, the dynamic viscosity and the solubility of the solute. a, b, c, d, e, and f are properties coefficients which need to be determined. T is the temperature of solution in Kelvin (K).

3.1.2 Seed Pot

A seed pot unit was added to the simulation as the inlet of the MSMPR crystalliser. A few properties of the seed crystal were acquired, which are the bulk density, crystal density and the initial particle size distribution of the seed crystals. As mentioned before, the seed pot acts as the inlet to the crystalliser; hence the mass and feeding time of the seed crystal can be controlled. Other than that, this also allows the seed crystals to be added when the concentration of the solution is inside the metastable zone during the cooling process. Moreover, the seed pot also allows some flexibility on the crystallisation process by allowing the option of adding more seed crystals multiple times.

3.1.3 MSMPR Crystalliser

In the flowsheet, the simulation of the batch crystalliser process was modelled by using the MSMPR crystalliser model. It is connected to a seed pot as the inlet stream and a blank outlet was chosen as no products leave the batch crystalliser during the batch period. Assumptions made on the development of MSMPR in the gCRYSTAL® program are the vessel is well mixed, the liquid and solid phases in bulk are in thermal and mechanical equilibrium where it is operated under the same temperature and pressure, and liquid and solid phases are not in chemical equilibrium where both solid and liquid phases have different chemical compositions during the process (Process Systems Enterprise Ltd. 2015).

The crystallisation process kinetics and the initial conditions of the solution can be specified in the MSMPR crystalliser model. In gCRYSTAL® program, the kinetics of secondary nucleation such as the Mersmann's kinetic of activated nucleation, the Evans' kinetic of attrition nucleation and the empirical power-law equation which were introduced in Section 2.1.2 are accessible and can be specified. The values of the kinetics chosen will be discussed and justified later in Section 5. The mass fraction of paracetamol and ethanol at the liquid phase was established. The initial conditions of the solution, such as the mass of paracetamol crystals and liquid, were specified in the MSMPR model as well.

3.1.4 Controllers and Sensors

To ensure continuous crystal growth, it is paramount for the concentration of the solution to be within the metastable zone throughout the experiment. A temperature controller coupled with a temperature sensor could be used to specify a cooling curve, ensuring that the concentration of the solution is always in the metastable zone. A liquid composition sensor, on the other hand, could track the change of liquid composition over time. Lastly, a PSD sensor is used to report the particle size distribution of the desired product over time.

3.1.5 Seeded Crystallisation Process Flowsheet

A flowsheet was established in gCRYSTAL® program using the methods illustrated above as shown below:

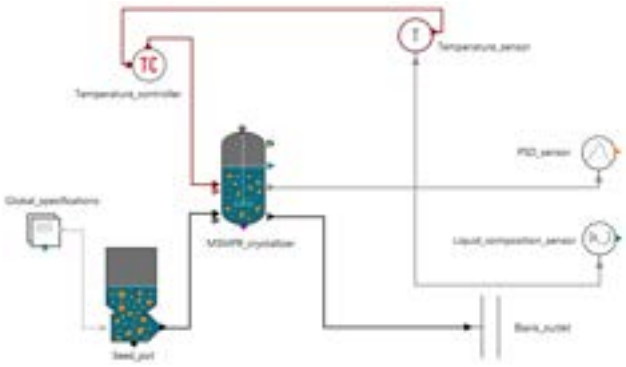

Figure 1: Flowsheet of the seeded paracetamol-ethanol crystallisation process in gCRYSTAL program.

3.2 Literature Experiment Data

For parameter estimation, three sets of experimental data (S03, S03-R and S05) was taken from the literature (Frawley et al. 2012) which comprise of the change of mass fraction of paracetamol in ethanol solution and the particle size distribution (PSD) of paracetamol crystal product. The operating conditions of all three sets of experimental data are summarised in Table 1.

For the change of mass fraction of paracetamol, the data was obtained from data points of supersaturation ratio graph in (Frawley et al. 2012) and converted into mass fraction of paracetamol in the liquid phase. As for the PSD of the final product of all three experiments, the volume frequency which can be read from the graph, is converted into volume fraction by using Equation 5. Then, the cumulative volume density of PSD is calculated by summing up all the volume fraction for each set of data using Equation 6.

$$\text{Volume fraction} = \frac{\text{Volume frequency}}{100} \tag{5}$$

$$\text{Cumulative volume density} = \sum_{1}^{n} \text{Volume frequency} \tag{6}$$

A plot of volume density graph versus parameter diameter bin was done to acquire the values of 5%, 10%, 16%, 25%, 50%, 75%, 84%, 90%, and 95% quantiles. Then, these values are imported into the program. Then all experiments chosen were set up in the gCRYSTAL® program with specified conditions, as shown in Table 1.

3.3 Parameter Estimation

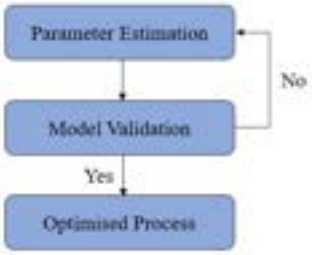

Figure 2: Summary of workflow in when doing parameter estimation.

The parameter estimation in the gCRYSTAL® program is essential to measure the secondary nucleation kinetics. This process consists of three stages, as depicted in Figure 2. The first stage involves estimating the kinetics of the chosen model. To estimate the kinetics of the chosen model, the model has to be trained with experiment data. One is also required to enter an initial estimated value, as well as the upper and lower bounds for each kinetic parameter that is to be estimated.

The gCRYSTAL® program estimates the kinetic parameters by minimising the Maximum Likelihood objective function, which is given as Equation 7 below (Process Systems Enterprise Ltd. n.d.(b)):

$$\phi = \frac{1}{2}\, min \sum_{i=1}^{NE} \sum_{j=1}^{NV_i} \sum_{k=1}^{NM_{ij}} \left[ln(\sigma_{ijk}^2) + \frac{(\widetilde{z_{ijk}} - z_{ijk})^2}{\sigma_{ijk}^2} \right] \tag{7}$$

where ϕ is the maximum likelihood objective function, NE, NV_i, and NM_{ij} are the number of experiments, the number of variables in experiment i and the number of the measurements of variable j in experiment i respectively. $\widetilde{z_{ijk}}$ and z_{ijk} are the k^{th} measured value and the estimated value of the variable j in experiment i respectively, and σ_{ijk}^2 is the variance.

From Equation 7, two things were learnt and gained. Firstly, it is non-linear in nature, which means that the initial values and bounds are very important to ensure that the final solution is neither sub-optimal nor infeasible. Secondly, an increase in the number of variables to be estimated or experiment to be trained with could increase the time complexity by an order which would increase the model run time significantly.

After the model has been trained, it is then validated with another experiment with either similar or slightly different conditions to check whether the predicted model produced results that are within the literature range. If the fit is not within the literature range, Stage 1 is repeated where the initial conditions and bounds are tweaked. On the other hand, if it is within the literature range, then this is now the optimised process which is Stage 3 in Figure 2.

4 Results

4.1 Global Specification

4.1.1 Liquid Phase Properties

The molecular weight of paracetamol and ethanol were found as 0.15316 kg/mol and 0.04607 kg/mol, respectively (Sigma-Aldrich 2020b). Other liquid properties were found and are detailed as below:

Mass Density

Ethanol is taken as the main component in the paracetamol system, so the density of the system is taken to be the density of ethanol. The values in Table 2 was obtained by fitting the mass density coefficients with mass density data at different temperatures using Equation 4 (EngineeringToolBox.com 2020a).

Table 2: Mass density coefficients of paracetamol-ethanol system in the liquid phase.

Coefficients	Paracetamol and Ethanol
a	930
b	-0.113
c	-0.125

Heat Coefficient

By fitting the mass-specific heat data of ethanol (EngineeringToolBox.com 2020c) into Equation 4, the heat coefficients can be calculated and is summarised in Table 3:

Table 3: Mass specific heat coefficients of paracetamol-ethanol system in the liquid phase.

Coefficients	Paracetamol and Ethanol
a	-2286
b	20.47
c	-0.01400

Table 1: Experimental conditions of under-seeded secondary nucleation experiments (Frawley et al. 2012).

Exp. No.	Temperature (°C)	Seed Mass (g)	Initial Mass of Liquid Phase (kg)	Initial Mass of Ethanol in Liquid Phase (kg)	Initial Mass Fraction (kg/kg)
S03 / S03-R	20	1.0335	505.051	395.84	0.216
S05	20	3.0215	494.782	398.84	0.199

Dynamic Viscosity

The dynamic viscosity coefficients can be calculated in the same way as above. The value of each coefficient is shown in Table 4 (EngineeringToolBox.com 2020b):

Table 4: Dynamic viscosity coefficient of the liquid phase.

Coefficients	Ethanol
a	0.02676
b	-1.504E-4
c	2.156E-7

4.1.2 Crystal Properties

The melting point of paracetamol is 169°C (Ellis 2002) which is much higher than the maximum temperature the experiment is conducted. In the solid-state, the mass density of paracetamol can be approximated to have a constant density of 1260 kg/m^3 (Sigma-Aldrich 2020b).

The mass-specific heat capacity of the paracetamol crystal at different temperature can be found from literature (Sacchetti 2000) and is fitted in Equation 4 to find the coefficients which are given in Table 5.

Table 5: Crystal properties of paracetamol crystal.

Coefficients	Paracetamol
a	1388.9
b	-5.727
c	0.0165

The enthalpy of paracetamol crystallisation is -21.7 kJ/mol (-159000 J/kg) (Fujiwara et al. 2002). The volume shape factor, on the other hand, is 0.866 for Form 1 of paracetamol crystal (Frawley et al. 2012).

4.1.3 Solubility

The solubility of paracetamol in ethanol is paramount in determining whether the crystal will grow or dissolve, as well as determining the types of nucleation and crystal growth mechanisms. The solubility of paracetamol in ethanol at different temperatures were obtained from Fernandez 1999 and fitted in Equation 4 to obtain the coefficients given in Table 6. It was also found that a 1% change in solubility would increase the particle size distribution of the lower quantiles by approximately 8.5%; therefore it is essential to enter the coefficients for solubility as accurate as possible in the model.

Table 6: Solubility coefficients of paracetamol in ethanol.

Coefficients	Paracetamol
a	0.9996
b	-8.646E-3
c	1.961E-1

4.2 Primary Nucleation and Growth and Dissolution Rates

The kinetics required to be entered into the model for primary nucleation and growth were obtained from the literature (Frawley et al. 2012) and is detailed in Table 7 below. These values were obtained from previously evaluated experiments from isothermal seeded batch experiments in the literature (Niall A. Mitchel 2011).

Table 7: Primary, growth and dissolution kinetic parameters.

Crystallisation Kinetics	Kinetics Parameter	Values
Power Law Primary Nucleation	$ln\ k_n$ (ln (# / m^3 · s)	19.40
	n (-)	2.276
	$E_{A,n}$ (kJ/mol)	0.000
Power Law Crystal Growth Kinetics	k_g (m/s)	9.979
	$E_{A,g}$ (kJ/mol)	40.56
	g (-)	1.602

Custom kinetics models were used in this case as opposed to the power-law equations provided in gCRYSTAL®, as the driving forces used in the expressions provided by Frawley considered supersaturation on a solvent basis, which is different from the solution basis used for the implemented/standard model options for each crystallisation mechanism in the well-mixed crystalliser model.

5 Discussion

5.1 Mersmann Kinetics Only

To estimate the secondary growth kinetics - activated. The parameter estimation was carried out using the mass fraction data from experiment S03 and the estimated kinetics were validated on experiment S03-R and S05 from Frawley et al. 2012. The initial conditions of the respective experiments are shown in Table 1. As discussed in Section 2.1.2, if the relative solution of the solution is above 0.1 (0.149 kg paracetamol/kg solution), activated secondary nucleation (needle breeding) will be the dominant secondary nucleation mechanism. Therefore, secondary nucleation due to attrition is deemed to be negligible.

The Mersmann kinetics is estimated based on the mass fraction data of paracetamol from the liquid composition sensor. The linear variance model was chosen to be the variance model of the liquid composition sensor to take into account the uncertainty of the measured experimental data. The equation of the linear variance model can be seen in Equation 8 below:

$$\sigma_{ijk} = | \alpha z_{ijk} + \beta | \tag{8}$$

where α is the constant relative term and β is the constant term of the sensor.

The values of α and β were taken as 0.001 and 0.007 respectively. This value was obtained by taking the average of the max-min for each point of time, in experiments S02, S03, S05, S06 of Frawley which are experiments conducted over approximately similar experimental conditions (Frawley et al. 2012).

In gCRYSTAL®, only two models were available to model needle breeding secondary nucleation, which are the power-law and Mersmann's kinetics. Mersmann's kinetics model was chosen because the model was created specifically to model needle breeding and is based on the diffusion of solute molecules onto nuclei

present at the surface of larger solute crystals. From Equation 1, three entities need to be provided to the gCRYSTAL® model which are the number of entities ν, the natural logarithm of the pre-exponential rate constant, $ln\ k_s$ and the solubility factor, K.

For Mersmann's activated kinetic, the number of entities ν can be specified as 1 since the paracetamol molecule will not be ionised during the crystallisation process (Mersmann 1995). The parameter estimation process was then carried out to determine the values of $ln\ k_s$ and K. Due to the lack of literature papers on Mersmann kinetics, the initial value, upper and lower bounds of $ln\ k_s$ were taken as -35.00, 0, 50 which are the default values provided by gCRYSTAL®. Whereas the initial value of K was taken as 0.355 with an upper and lower bound of 0.31 and 0.414 respectively (A. Mersmann, Braun, and Löffelmann 2002).

The estimated result of the kinetic parameters for Mersmann's kinetic is summarised in Table 8 below.

Table 8: Mersmann estimated parameters.

Kinetic Parameter	Initial Guess Value	Upper Bound	Lower Bound	Final Value
$lnk_s(-)$	-35.00	-50.00	0.00	-50.00
K(-)	0.340	0.311	0.420	0.357

The estimated parameters on experiment S03 is then validated on the mass fraction curve of experiment S03-R. The result is shown in Figure 3. From Figure 3, it can be seen that the predicted mass fraction values are slightly below the experimental data. The explanation of this poor fit would be discussed later.

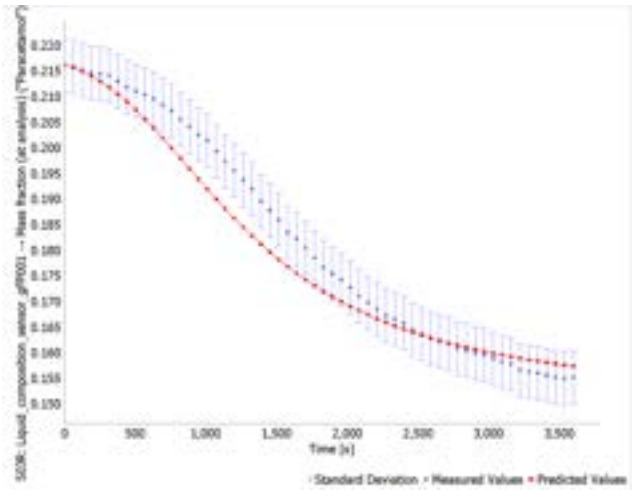

Figure 3: Comparison of the predicted mass fraction curve and the experimental mass fraction curve for experiment S03-R.

Next, the particle size distributions (PSD) of the model was also compared with the PSD of the experiment, as seen in Table 9 and Table 10.

Table 9: PSD quantiles of model with Mersmann kinetics only.

Quantiles	Particle Diameter (μm)
5%	206
10%	235
16%	260
25%	292
50%	373
75%	477
84%	537
90%	598
95%	685

Table 10: PSD quantiles of experiment S03-R from Frawley et al. 2012.

Quantiles	Particle Diameter (μm)
5%	35
10%	70
16%	105
25%	145
50%	250
75%	385
84%	490
90%	550
95%	600

From Table 9 and 10, the predicted particle size distribution is almost twice the size of the actual experimental distribution for lower quantiles. Although increasing the value of $ln\ k_s$ in Mersmann's kinetics might lead to better fit for particle size distribution yet it would lead to a worse fit for the mass fraction of paracetamol, this is observed in the sensitivity analysis conducted on Mersmann's kinetics.

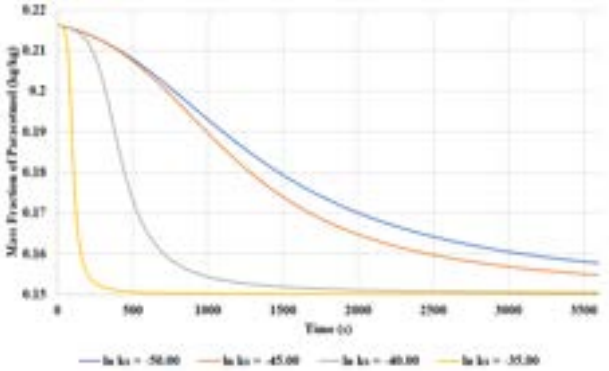

Figure 4: Mass fraction of paracetamol with different $ln\ k_s$.

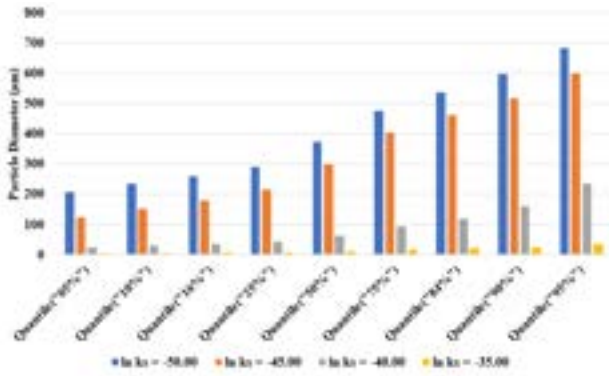

Figure 5: Particle size distribution with different $ln\ k_s$.

Among the two Mersmann kinetics that was required to be entered into the model are $ln\ k_s$ and K. The solubility factor, K, showed very little variability in both the mass fraction of paracetamol and PSD compared to $ln\ k_s$. Figure 4 and 5 shows the changes in liquid mass fraction of paracetamol and the particle size distribution of the crystals as $ln\ k_s$ is varied.

A lower PSD distribution could be achieved by increasing $ln\ k_s$ as seen in Figure 4. However, the increase in $ln\ k_s$ also decreases the mass fraction of paracetamol in the liquid. In Figure 3 and Table 9 mass fraction of paracetamol in liquid needs to increase and particle size needs to decrease. The objective function in parameter, the parameter estimation process is pulled in two different directions, thus by getting a good fit in one aspect would lead to a poor result in the other; thus we can conclude

that Mersmann's kinetics alone would not produce a satisfactory model to model secondary nucleation in this system.

There are two possible reasons why the mass fraction of paracetamol in the liquid is being underestimated, whereas the particle size distribution of paracetamol is being overestimated. First, an overestimated growth rate. The kinetics of the power-law equation used to model growth rate is obtained from Niall A. Mitchel 2011, the overestimation of the growth rate is not impossible due to the stochastic nature of the crystallisation process, this is clearly seen by a similar experiment conducted by Worlitschek and Mazzotti 2004, which resulted in different growth rate kinetics. The second reason is that the model is severely underestimating the number of small crystals present in the system. This is because currently, the model only took into account secondary nucleation due to needle breeding and neglected attrition. A smaller average particle size would also mean less solute consumption leading to a higher mass fraction of paracetamol graph. This is because the change in solute concentration due to growth is proportional to the cube of crystal size(Frawley et al. 2012). Thus, a larger crystal would cause a bigger change in solute concentration compared to a smaller crystal.

5.2 Evans and Mersmann Kinetics

Secondary nucleation due to attrition is also added to the model using Evans' kinetics. Evans' kinetics requires three input parameters which are the rate constant ($ln\ k_{n_ci}$), size above which crystals undergo attrition (L_{min_ci}) and supersaturation order (n_{ci}). The initial guess values of these kinetics parameters were taken as 9.0087, 540.822, 3.14 respectively (Wang 2019) before rerunning the parameter estimation resulting in a final value of 11.0409, 473.063, 0.00 for the rate constant, size of crystals and supersaturation order. Other initial values were also compared, however, the initial values above resulted in the lowest value for the objective function, more of this process will be discussed in Section 5.4. The particle size distribution of the model with both Mersmann and Evans is observed in Table 11, whereas the mass fraction of paracetamol in the liquid is observed in Figure 6.

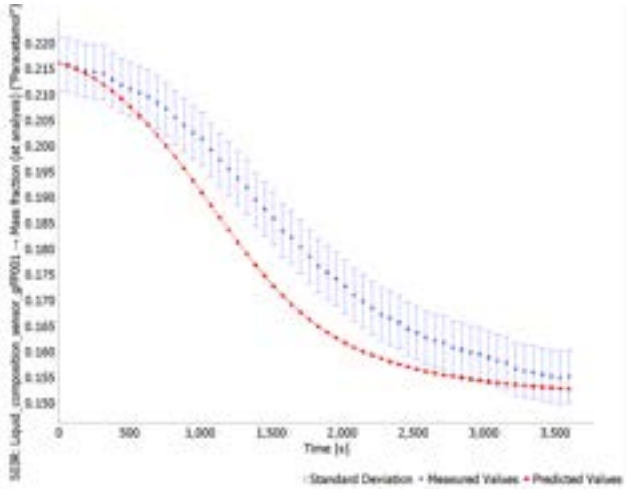

Figure 6: Mass fraction of paracetamol in liquid with Mersmann's and Evans kinetics.

The model is further validated on experiment S05 and showed an equally satisfactory fit similar to the result of S03-R. From the results of Table 11, it is confirmed that secondary nucleation due to attrition cannot be neglected as initially presumed. Surprisingly, even with the decreased average particle size, the mass fraction of paracetamol decreased slightly. The reason for this is because even though the average size of particle decreased using up less solute, yet the total number of crystals has increased due to attrition. This is confirmed by the PSD sensor in the flowsheet model, which showed an overall increase in the cumulative volume density of paracetamol crystals when switched from Mersmann's kinetic only to Mersmann's and Evans kinetics. On the other hand, the particle size distribution in Table 11 showed a good fit and is very similar to that of the actual experiment result in Table 10.

Table 11: PSD quantiles when Evans and Mersmann kinetic applied.

Quantiles	Particle Diameter (μm)
5%	47
10%	69
16%	93
25%	141
50%	273
75%	386
84%	445
90%	503
95%	584

Sensitivity analysis was also carried out on the three Evans kinetic parameters. Among the three kinetic parameters, the rate constant $ln\ k_{n_ci}$ shows the most variability when its value is changed and the results are shown in Figure 7 and Figure 8. This is mainly because it is a constant in an exponential term, which would have a signifiant effect on the rate. The changes produced by L_{min_ci} and n were negligible. The small change in n was because it is the exponential term for relative supersaturation, of which value in this particular experiment is between 0 and 1. However, it is still worth noting that the current model treats the secondary nucleation attrition rate to be independent of the saturation level of the solution.

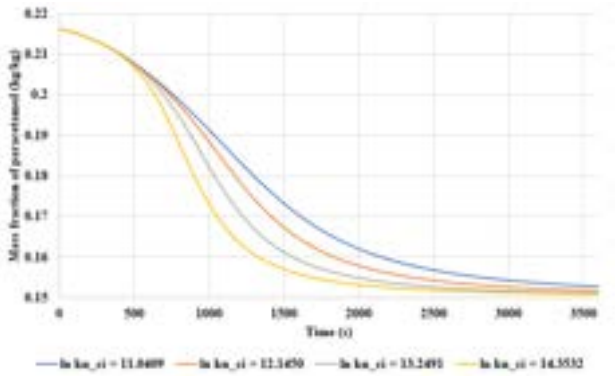

Figure 7: Mass fraction of paracetamol with different $ln\ k_{n_ci}$.

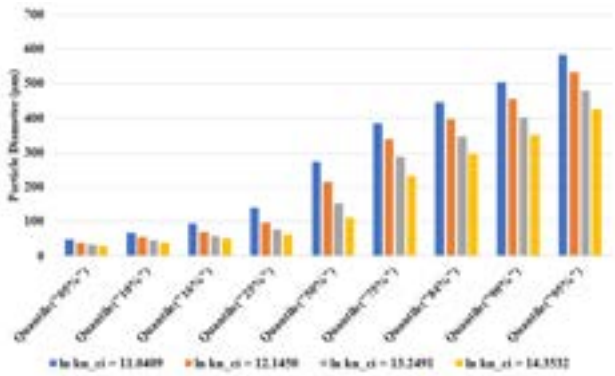

Figure 8: Particle size distribution with different $ln\ k_{n_ci}$.

5.3 Self-Healing of Crystals

The growth rate mechanism in the two-step Mersmann kinetics, as well as the power-law used in the model only, takes into account the mass transfer and surface integration step of the process. However, it has been found that the growth rate of a whole crystal and the growth rate of a broken crystal differs. This is due to a phenomenon knows as self-healing mechanism of crystals.

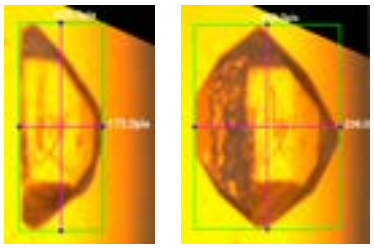

(a) Initial crystal size **(b)** Final crystal size

Figure 9: Left image shows the crystal fragment right image shows crystal after regeneration.

The self-healing hypothesis was investigated using a paracetamol and ethanol system similar to the case of the batch crystallisation. Paracetamol crystals were cut in half along its cleavage plane facet (001), exposing the high energy facets (010). These crystals fragments were then left in saturated solutions of various supersaturation.

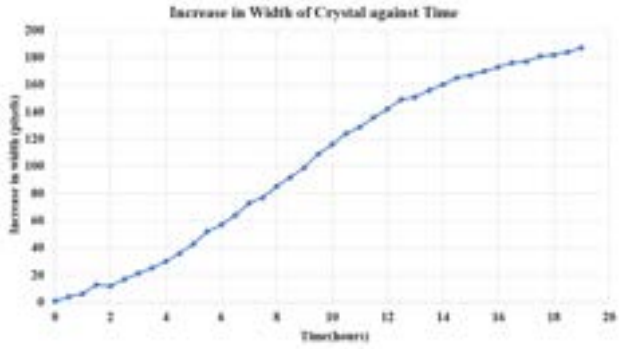

Figure 10: A graph plot on change of width length of the crystal against time.

The growth rate of these broken crystal fragments was measured. The OpenCV library for PythonTM programming language is used to measure the increase in length and width of the crystal as oppose to direct measurements methods as this reduces errors. Figure 9 shows an example of such measurement. The growth rates of the crystals were plotted against time and the results are observed in Figure 10.

The steeper gradient is 5 hours into the experiment when the crystal is repairing compared to 18 hours, and this shows that while the crystal is repairing itself, its growth rate increases. After it approaches complete restoration of its broken facet, the growth rate slows down.

The power-law equation used to model growth does not take into account the growth rate changes caused by the regeneration of crystals; therefore, a new model has to be proposed to get more accurate results.

A quantitative model was proposed by Mersmann and Gahn, which account for the brittle fracture and subsequent growth and dissolution of these fragments due to crystal-impeller interactions. To better understand the full growth mechanism for smaller broken crystal, it is first essential to go into detail the mechanism of larger unbroken crystals. As described briefly in Section 2.2 in the Mersmann 2-step kinetic, the solute must first diffuse from the bulk solution to the interface, followed by the integration of solute into the crystal lattice. By using a semi-empirical assumption, the integration step is assumed to be a second-order reaction with respect to supersaturation, giving the following growth rate equation (Alfons Mersmann et al. 1988).

$$\frac{G(L)}{2k_d(L)} = \frac{\Delta c}{c_s} + \frac{k_d(L)}{2k_r c_s} - \sqrt{\left(\frac{k_d(L)}{2k_r c_s}\right)^2 + \left(\frac{k_d(L)}{k_r c_s}\right)\frac{\Delta c}{c_s}} \quad (9)$$

where k_d is the mass transfer coefficient, k_r is the integration rate constant, c_s the molar concentration of the crystallising substance and Δc is the supersaturation.

The driving force for crystal growth in the equation above is the supersaturation.

$$\Delta c = c - c^* \quad (10)$$

where the saturation concentration c* is generally considered to be a constant. However for attrition fragments, to account for the anamolous growth behavior it has been suggested by Garside and Davey that individual strain energies of the crystals also have to be taken into account by the model. This led to c* being modified to give the equation below.

$$c^*_{real} \sim c^* \exp\left(\frac{w_s}{RT}\right) \quad (11)$$

where c* is now the solubility of a perfect crystal only. Thus, the molar strain energy w_s in the crystal, induced by lattice strain, will increase its solubility. This leads to a decrease of the driving force for growth or even to the dissolution of fragments ($c^* > c$).

However, the experiment conducted on crystal self-healing in Figure 10 showed that instead of growing slower, the growth rate increases. Thus, this equation does not fully describe the phenomenon observed. The reason for this could also be attributed to the increase in surface energy when the crystal is broken. The growth rate of the crystal especially of the high surface energy facet (cleavage plane) is considerably faster. This is in accordance with crystals growing to minimise the free surface energy as postulated by Gibbs (1878). Overall, from the experiments conducted, it can be postulated that the increase in growth rate due to surface energy outweighs the decrease in growth rates due to the increase in supersaturation. This indicates that currently, small broken fragments would have a faster growth rate. Currently, there is no such equation in the literature that takes into account both the change in surface energy as well as the change in solubility due to lattice strain. The modified Mersmann and Gahn's equation above comes the closest yet more experiments need to be conducted to add in the effect of surface energy.

5.4 Parameter Estimation Workflow

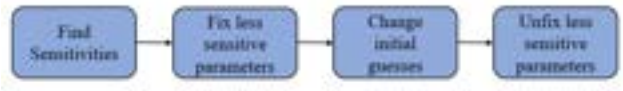

Figure 11: Parameter estimation detailed process.

The parameter estimation process can be broken down into four stages, as seen in Figure 11. Firstly, it is to find the sensitivities of the different kinetics that are being estimated. The sensitivities of the different kinetics would allow one to know which kinetics would produce the biggest change, and would also give a broad

approximation of the range of the upper and lower bounds of the parameter to be estimated. Secondly, after finding the sensitivities of each kinetic parameter, fix the parameters which are less sensitive to change, which means it does not change the output by much. By fixing these parameters, only the most sensitive parameters are estimated. This allows the parameter estimation model to compute fewer variables, thus saving computational time. Next, iteratively change the initial guess. It is advised to use a handful of initial values and choose the final result, which produces the lowest objective function. This step is necessary because of the non-linear nature of the optimisation model. Lastly, using the final kinetic that is estimated, unfix the kinetics that was fixed previously and rerun the parameter estimation process. This is to fine-tune all the parameters.

6 Conclusions

The main purpose of this paper is to develop a working model to understand and measure the kinetics of secondary nucleation process successfully. To achieve this objective, justifiable thermo-physical properties are used in the model. After which parameter estimation was carried out on Mersmann secondary nucleation kinetics only as well as a combination of Evans and Mersmann kinetics. The main findings of the paper are summarised as follows.

Firstly, activated secondary nucleation alone using Mersmann equation did not manage to achieve a good fit with experimental results; this is because the model overestimated the particle size distribution of paracetamol crystals. A combination of activated secondary nucleation modelled with the Mersmann equation and secondary nucleation due to attrition modelled using Evans kinetics produced a much smaller crystal particle distribution which fitted the PSD distribution of the experiment. However, the mass fraction of paracetamol fit was slightly worse, indicating that the growth rate of crystals is too high.

The power-law growth equation used to measure growth assumed that crystal of all sizes has the same growth rate. However, experiments conducted proved that smaller broken crystal fragments have a much higher growth rate compared to larger crystals; this is because of the self-healing mechanism of broken fragments. Lastly, in order to achieve better results in parameter estimation, it is advised to do sensitivity analysis on the different kinetics first, then running the parameter estimation process on more sensitive kinetics while fixing the kinetic parameters that are less sensitive. This is then followed by testing a range of random initial values to find the best optimum, before unfixing the less sensitive kinetics and rerunning the parameter estimation process to fine-tune the model.

7 Outlook

The findings of this paper could be used as a supporting tool within the pharmaceutical industry; however, more work needs to be done in the future to develop a specific model for specific API requirements.

Currently, there are still limitations to the model, mainly the limited number of kinetics available in the gCRYSTAL® program. It is advised to take advantage of the custom equation modelling function in future flowsheets in gCRYSTAL®, as this would allow one to try out different kinetic equations. Due to COVID-19, there is also limited experimental data which the current model can be trained on. Hence, more experiments could be done by testing more seeded crystallisation experiments with different operating conditions to produce a more robust model. This could include different seeding temperature, different crystal seed mass input and different cooling rates of the process.

Besides, there is also the possibility to test the performance of the model on other small organic molecules such as aspirin or benzoic acid, as these small molecules have a similar molecular structure where carboxylic end group is present in the molecule. Moreover, the product's kinetics and properties could also affect the simulation results. The effect of surface energies could also be investigated on using a microreactor; doing this would allow one to develop a more accurate growth and dissolution equation which incorporates the self-healing phenomenon.

Lastly, it is also worthwhile to model a continuous crystallisation process instead of batch crystallisation. This is because there are several advantages to a continuous process which includes high output, more consistent production and easier scale-up.

Nomenclature

α	Constant relative term, [-]
β	Constant term of sensor, [-]
Δc	Absolute supersaturation, [kg/m^3 solution]
ν	Number of entities, [-]
ϕ	Maximum likelihood objective function
ρ_c	Crystal density, [kg/m^3]
ρ_{crys}	Molar density of crystal, [mol/m^3]
σ	Relative supersaturation, [-]
ε	Energy dissipating rate, [m^2/s^3]
A_t	Total surface area of crystal, [m^2/m^3]
C^*	Solubility of the solute, [kg/m^3]
c^*	Equilibrium concentration, [kmol/m3]
C_c	Mass density of crystals, [kg/m^3]
c_s	Molar concentration of crystallising substance, [kmol/m^3]
C_{bulk}	Concentration of solute in bulk phase, [mol/m^3]
$C_{int}(L)$	Concentration of the solute at liquid-crystal interface, [mol/m^3]
d_m	Molecular diameter of the solute molecule, [m]
D_{AB}	Diffusion coefficient of solute in the liquid phase, [m^2/s]
$exp\ (ln\ k_s)$	Efficiency factor, [-]
$G(L)$	Linear growth rate of crystal, [m/s]
J_{sec_ci}	Secondary rate due to crystal-impeller collisions, [#/m^3·s]
J_{sec}	Activated secondary nucleation, [#/m^3·s]
K	Solubility factor, [-]
k_d	Mass transfer coefficient, [m/s]
k_r	Integration rate constant, [m^4/kmol·s]
k_v	Volume shape factor, [-]
L_{min_ci}	Particle size above which crystals are prone to attrition for crystal–impeller collisions, [m]
$ln\ k_{n_ci}$	Natural logarithm of proportional factor for crystal-impeller collisions, [ln (#/m^3·s)]
n	Number density of particles, [#/m^3·m]
N_P	Impeller power number, [-]
N_Q	Impeller flow number, [-]
n_{ci}	Supersaturation dependency of the secondary nucleation rate for crystal–impeller collisions, [-]
R	Molar gas rate constant, [J/mol K]
S_a	Supersaturation ratio of the solution, [-]
T	Temperature, [K]
w_s	Molar strain energy in the crystal, [J/mol]
MSMPR	Mixed Suspension-Mixed Product Removal

References

Agrawal, S.G. and A.H.J. Paterson (2015). "Secondary Nucleation:Mechanisms and models". In: pp. 698–706. DOI: https://doi.org/10.1080/00986445.2014.969369.

Bučar, Dejan-Krešimir, Robert W. Lancaster, and Joel Bernstein (2015). "Disappearing Polymorphs Revisited". In: *Angewandte Chemie International Edition* 54.24, pp. 6972–6993. DOI: 10.1002/anie.201410356.

Chemistry, Royal Society of (2009). *Paracetamol*. URL: https://www.stem.org.uk/resources/elibrary/resource/29688/paracetamol.

Chen, Jie et al. (2011). "Pharmaceutical Crystallization". In: *Crystal Growth & Design* 11.4, pp. 887–895. DOI: 10.1021/cg101556s.

Durrant, C. (2001). "The responsibility of the pharmaceutical industry". In: *Clinical Microbiology and Infection* 7, pp. 2–4. DOI: https://doi.org/10.1046/j.1469-0691.2001.00077.x..

Ellis, Frank (2002). "Paracetamol - a curriculum resource". In: *Royal society of Chemistry*. DOI: https://edu.rsc.org/.

EngineeringToolBox.com (2020a). *Ethanol - Density and Specific Weight*. URL: https://www.engineeringtoolbox.com/ethanol-ethyl-alcohol-density-specific-weight-temperature-pressure-d_2028.html (visited on 10/21/2020).

— (2020b). *Ethanol - Dynamic and Kinematic Viscosity*. URL: https://www.engineeringtoolbox.com/ethanol-dynamic-kinematic-viscosity-temperature-pressure-d_2071.html (visited on 10/21/2020).

— (2020c). *Ethanol - Specific Heat, Cp and Cv*. URL: shorturl.at/dwACG (visited on 10/21/2020).

Evans T. Margolis G., Sarofim A. F. (1974). "Models of secondary nucleation attributable to crystal-crystallizer and crystal-crystal collisions". In: *AIChe Journal*.

Fernandez, C. (1999). "Effect of the nature of the solvent on the crystallization of paracetamol." In: *14th International Symposium on Industrial Crystallization Symposium on Industrial Crystallization*.

Frawley, Patrick et al. (June 2012). "The effects of supersaturation, temperature, agitation and seed surface area on the secondary nucleation of paracetamol in ethanol solutions". In: *Chemical Engineering Science* 75, pp. 183–197. DOI: 10.1016/j.ces.2012.03.041.

Fujiwara, M. et al. (2002). "Paracetamol Crystallization Using Laser Backscattering and ATR-FTIR Spectroscopy: Metastability, Agglomeration, and Control". In: *Crystal Growth and Design* 2, pp. 363–370. DOI: https://doi.org/10.1021/cg0200098.

L. Li, N.Rodríguez-Hornedo (1992). "Growth kinetics and mechanism of glycine crystals". In: *Journal of Crystal Growth* 121, pp. 33–38. DOI: https://doi.org/10.1016/0022-0248(92)90172-F.

Liu, X.Y. (2000). "Heterogeneous nucleation or homogeneous nucleation?" In: *J.Chem.Phys* 112. DOI: https://doi.org/10.1063/1.481644.

Ltd., Process Systems Enterprise (2015). *gCRYSTAL Model Documentation - Crystalliser MSMPR*. 4.2, pp. 1–46.

— (n.d.[a]). *gPROMS FORMULATEDPRODUCTS - Integrated digital design of robust formulated products and their manufacturing processes*. Accessed: 2020-12-06. URL: https://www.psenterprise.com/products/gproms/formulatedproducts.

— (n.d.[b]). *Workflow for Parameter Estimation*.

Mersmann (1995). *Crystallization Technology Handbook*. Vol. 13. DOI: https://doi.org/10.1080/07373939508917003.

Mersmann, A., B. Braun, and M. Löffelmann (2002). "Prediction of crystallization coefficients of the population balance". In: *Chemical Engineering Science* 57 (20), pp. 4267–4275. DOI: https://doi.org/10.1016/S0009-2509(02)00343-3.

Mersmann, Alfons et al. (1988). "Attrition and secondary nucleation in crystallizers". In: *Chemical Engineering & Technology* 11.1, pp. 80–88. DOI: https://doi.org/10.1002/ceat.270110112.

Mullin, J.W. (2001). *Crystallization, 4th edition*, pp. 181–215. DOI: https://doi.org/10.1016/B978-075064833-2/50007-3.

Myerson, Allan S. and Rajiv Ginde (2002). *Crystals, crystal growth, and nucleation*, pp. 33–65. DOI: https://doi.org/10.1016/B978-075067012-8/50004-5.

Nguyen, T. T. H. (2014). "Precision measurement of the growth rate and mechanism of ibuprofen 001 and 011 as a function of crystallization environment†". In: *CrystEngComm* 21. DOI: https://pubs.rsc.org/en/content/articlelanding/2014/ce/c4ce00097h#!divAbstract.

Niall A. Mitchel Clifford T. OCiardha, Patrick J.Frawley (2011). "Estimation of the growth kinetics for the cooling crystallisation ofparacetamol and ethanol solutions". In: *Journal of Crystal Growth* 328.

Oh, Dong-Hoon et al. (2020). "Software Platform for Computation Fluid Dynamics Simulation of Mixing and Crystallization in a Stirred Vessel". In: *Crystal Growth & Design* 20, pp. 1172–1185. DOI: https://doi.org/10.1021/acs.cgd.9b01465.

Ohring, Milton (1995). *Engineering Materials Science*, pp. 249–297. DOI: https://doi.org/10.1016/B978-012524995-9/50030-1.

Ottens E. P. K., de Jong E. J. (1973). "A model for secondary nucleation in a stirred vessel cooling crystallizer". In: *Industrial Engineering chemistry Fundamentals*.

Rantanen, Jukka and Johannes Khinast (2015). "The Future of Pharmaceutical Manufacturing Sciences". In: *Journal of Pharmaceutical Sciences* 104.11, pp. 3612–3638. DOI: 10.1002/jps.24594.

Sacchetti, M. (2000). "Thermodynamic Analysis of DSC Data for Acetaminophen Polymorphs". In: *Journal of Thermal Analysis and Calorimetry* 63. DOI: https://doi.org/10.1023/A:1010180123331.

Sigma-Aldrich (2020a). *Ethanol*. URL: https://www.sigmaaldrich.com/catalog/search?term=ethanol&interface=All&N=0&mode=partialmax&lang=en&region=GB&focus=product (visited on 12/06/2020).

— (2020b). *Paracetamol*. URL: https://www.sigmaaldrich.com/catalog/product/sial/p0300000?lang=en&region=GB&cm_sp=Insite-_-caSrpResults_srpRecs_srpModel_paracetamol-_-srpRecs3-1 (visited on 12/06/2020).

Thakur, Anil S et al. (Oct. 2007). *Improved success of sparse matrix protein crystallization screening with heterogeneous nucleating agents*. DOI: https://doi.org/10.1371/journal.pone.0001091.

Variankaval, Narayan, Aaron S. Cote, and Michael F. Doherty (June 2008). *From form to function: Crystallization of active pharmaceutical ingredients*. URL: https://aiche.onlinelibrary.wiley.com/doi/full/10.1002/aic.11555.

Volmer, M. (1939). *Kinetic der Phasenbildung*.

Wang, Haiting (2019). "Modelling of the seeded crystallization process and the investigation of the secondary nucleation and crystal growth mechanisms". In:

Worlitschek, Jörg and Marco Mazzotti (2004). "Model-Based Optimization of Particle Size Distribution in Batch-Cooling Crystallization of Paracetamol". In: *American Chemical Society*.

Investigation of the Thermodynamic Stability of the Precious Metal-Free Catalysts for the Oxygen Reduction Reaction

Chumphot Ngammekchay and Christos Christoforou
Department of Chemical Engineering, Imperial College London, U.K.

Abstract The ever-increasing demand for clean energy has driven the development of new sustainable energy technologies to battle global warming. Fuel cell technology is a promising and completely green alternative to the combustion of fossil fuels when sourcing the electricity renewably. With strategies in place by major markets such as the EU, US and Japan to integrate renewable hydrogen energy in society, the effective use of fuel cells for power generation is of paramount importance. Currently, platinum-group metals (PGMs) are used as the electrocatalyst for the cathodic reaction in fuel cells, since they demonstrate the best catalytic activity. However, for feasible commercialisation of fuel cells, it is of utmost significance to overcome the cost and scarcity barriers imposed by the reliance on precious metals. Dual-metal atom catalysts (DACs) have the propensity to improve catalytic performance, whilst shifting towards the use of abundant, cheaper metals. This paper investigates the electronic structure and total energy of pristine graphene and N-doped graphene by *ab initio* calculations using density function theory (DFT) in CP2K. Band structure calculations were performed to verify the accuracy of the constructed models. The thermodynamic stabilities of substrates for single-metal atom catalysts (SACs) and DACs were compared, by computing the energy of formation for each system examined. For the DAC substrate, the nitrogen defects closest to one another displayed the most thermodynamically favourable energy of formation, due to the charge delocalisation of the free electrons acting to stabilise the structure. Despite the simplest SAC precursor showing the greatest stability, it is essential to place emphasis on the under-researched DACs given that they offer the potential to shift away from the use of uneconomic precious metals. The future outlook of DACs is outlined for further investigations with the main goal of disseminating the large-scale utilisation of fuel cells.

Introduction

It is unequivocal that anthropogenic activities have been responsible for the constantly increasing concentration of carbon dioxide (CO_2) in the atmosphere since the Industrial Revolution in the 18th and 19th centuries (Bereiter, et al., 2015). This increase is strongly correlated with the rise in the average global temperature in what is referred to today as global warming (NASA, 2020). Cleaner processes of energy production have to be developed to keep the global temperature rise well below 2ºC above the pre-industrial levels according to the Paris Agreement ratified by 189 countries (UNFCCC, 2020).

Hydrogen is a greener alternative energy carrier to fossil fuels as it does not produce CO_2 in power generation processes. However, whether the process is entirely renewable depends on the sources of hydrogen supplied. Currently, most of the hydrogen is produced by natural gas reforming which uses fossil fuels, the major hindrance towards the international climate goal (IEA, 2019). Alternatively, hydrogen can be produced by electrolysis of water via the hydrogen evolution reaction (HER) and the oxygen evolution reaction (OER) (Abbasi, et al., 2019). 'Green hydrogen' can be produced if the electricity used is powered by a renewable resource (Geopura, 2020) such as solar energy.

According to the European Commission (2020), the European Union (EU) Hydrogen Strategy will accelerate the installation of renewable hydrogen electrolysers, targeting a large-scale deployment from 2030 onwards even in sectors that are difficult to achieve decarbonisation. The increasing significance of fuel cells is exemplified by the inclusion of hydrogen energy research and development in national strategies of the major markets including USA, China, Europe and Japan (Deloitte, 2020).

In fuel cells, hydrogen is used as a feedstock as it supplies H^+ ions for the oxygen reduction reaction (ORR) producing electricity and water as the only by-product (U.S Department of Energy, 2020). Currently, noble-metal nanoparticles are the most commonly used electrocatalysts for this reaction due to their high apparent activity (Lu, et al., 2020). Such heterogeneous catalysts are usually wasteful as the metal atoms at the surface predominantly participate in the reaction, leaving the inaccessible atoms unused. Hence, the research area of single-metal atom catalysts (SACs) has been evolving as atomic-scale catalytic sites maximise the atom utilisation of those precious metals. Moreover, the strong metal-substrate coordination helps enhance the stability of the metal atom. This favourable interaction can be engineered to improve the selectivity of the reaction of interest (Lu, et al., 2020). However, SACs are usually kept to a low metal loading around 1.0 wt% to avoid aggregation due to high surface energy of isolate atoms (Hou, et al., 2020). Furthermore, the major shortcoming of SACs is the linear scaling relationship between the energy of adsorption of the reaction intermediates, namely oxygen and hydroxyl group for ORR, resulting in the noble metals once again exhibiting the highest catalytic activity (Nørskov, et al., 2004). For large-scale

commercialisation of fuel cell to be feasible, a more sustainable and inexpensive alternative must be developed using more abundant metals.

Dual-metal atom catalysts (DACs) are a further development from SACs containing two metal centres instead of one. Recently, they have gained a lot of research attention due to their greater metal loading and higher geometrical flexibility of active sites compared to SACs (Kandula, et al., 2018).

Carbon-based materials are a favourable support for the metal atoms owing to their abundance, low cost and stability (Guo, et al., 2020). It has been demonstrated that Zn-Co atomic pairs coordinated on N-doped carbon support (Zn/CoN-C) could elongate the O=O bond length and hence facilitate the binding of oxygen onto the active site (Lu, et al., 2019). This bond cleavage is fundamental for the four-electron reduction pathway of oxygen to water, rather than the two-electron pathway which produces hydrogen peroxide (Song & Zhang, 2008).

An alternative electrocatalyst needs to be developed economically by exploiting inexpensive, abundant metals to rapidly disseminate the technology while also considering the robustness and the catalytic performance. Therefore, further investigations into DACs could potentially yield a suitable and cost-effective catalyst.

This report aims to understand how the doping of DACs in a carbon matrix affects the binding energies of the reaction intermediates of the ORR. The main objectives are to understand the basics of density functional theory (DFT) and apply it to perform calculations on the abovementioned systems. A model was developed by initially performing *ab initio* calculations for pristine graphene systems. DFT parameters were adjusted to meet the convergence criterion and the electronic structures were compared with literature to validate the robustness of the model. The energy of formation of the three and six N-doped graphene, precursors for N-doped SACs and DACs respectively, were calculated to compare their thermodynamical stability.

Background

To study systems at a quantum level, the DFT approach is considered the best compromise between accuracy and computational costs (Crocombette & Willaime, 2020). DFT is a framework employed to acquire an approximate solution to the Schrödinger equation for many-electron systems. The Born-Oppenheimer approximation is vital for DFT calculations, whereby the nuclei are treated as fixed charges, so the dynamics of nuclei and electrons can be decoupled. Using this approximation, the problem is simplified to solving the ground state of electrons for one fixed set of atomic positions (Sholl & Steckel, 2009).

Using fundamental mathematical theorems developed by Kohn and Hohenberg, the electron density corresponding to the solution of Schrödinger's equation can be reduced to the electron density that minimises the energy functional of the system. This simplifies the complexity and the computational cost significantly (Sholl & Steckel, 2009). By solving a set of equations defined by Kohn and Sham iteratively, the electron density can then be used to compute the total energy of the system.

To perform an electronic structure calculation using DFT, several parameters require definition. The ***k***-point grid is a way of sampling the reciprocal space in which finite number of vectors are contained within the first Brillouin zone of the periodic cell. Choosing a sufficiently dense set of ***k***-points is vital in obtaining reliable approximations to the electronic potential from a filled electronic band (Archer, 2004). Another parameter is the pseudopotential which replaces the strong Coulombic potential and the core electrons with a smoothed potential. A multitude of pseudopotentials for different elements is available for application in DFT codes (Goedecker, et al., 1995; Hartwigsen, et al., 1998; Krack, 2005). Moreover, basis sets are sets of known functions used to signify wavefunctions (Feller & Dixon, 2018). To determine the most suitable basis set, a balance must be found between the computational cost required and the ability to minimise the total energy of the system. Additionally, cut-off energy needs to be defined to avoid dealing with infinite sums. It represents the upper bound beyond which the kinetic energies of plane waves are not considered.

Fuel cells convert chemical energy from fuels such as hydrogen to produce electricity efficiently with heat and water being the only by-products (U.S Department of Energy, 2020). The basic physical structure of a single cell comprises of an electrolyte layer contacting a porous anode and cathode on either side (Giorgi & Leccese, 2013). Hydrogen oxidation reaction (HOR) occurs at the anode, where an electron is released into the external circuit. This external circuit is completed at the cathode where oxygen reduction reaction (ORR) occurs, consuming the electron. The full circuit is completed as either H^+ or OH^- ions (in acidic and alkaline environment respectively) are transferred across an electrolyte layer connecting the two electrodes.

Two of the main types of fuel cells, namely alkaline (AFC) and polymer electrolyte membrane (PEMFC) use hydrogen as fuel to produce

electricity. AFCs are the more mature technology, and are well-established in industry, with research on these reported from 1920 (Sotouchi, 2003). Despite AFCs being one of the cheapest and most efficient fuel cell technologies available, CO_2 poisoning of the electrolyte is preventing them from being the most prevalent in the market (Ni, et al., 2006). PEMFCs, on the other hand, possess several advantages such as fast start-up, simple operation and high voltage efficiency (Ni, et al., 2006). The main disadvantage, however, is that PGM catalysts are required, raising the overall cost of the fuel cell production.

The cathodic ORR reaction demonstrates sluggish kinetics and is significantly slower than the HOR at the anode. This necessitates the development of an alternative catalyst to the conventional PGM catalyst to improve the process performance and facilitate the commercialisation of fuel cells. There are two known routes for the ORR reaction to proceed; namely a four-electron reduction route whereby H_2O and OH^- are formed in acidic and alkaline media respectively, or a two-electron reduction route where hydrogen peroxide (H_2O_2) is produced as a by-product (Song & Zhang, 2008). It is thus important for the catalyst developed to favour the four-electron reduction route so as to prevent the production of the undesired H_2O_2 by-product.

The key properties that must be considered when establishing the suitability of a catalyst for any given reaction are activity, selectivity, stability and resistance to chemical poisoning. Activity can be qualitatively assessed using the Sabatier principle (Sabatier, 1911) which states that the optimal catalyst should bind oxygen strongly enough to facilitate the cleavage of the O=O bonds but simultaneously weak enough to allow for the desorption of intermediates and products from the active site. The renowned volcano plots illustrate the correlation between catalytic activity and interaction strength of reaction intermediates with the catalyst. A notable limitation of this technique is that other factors affecting rate of reaction are not considered; for example, some metals such as nickel cannot be observed at given potentials without being covered by an oxide layer (Ghosh, et al., 2016). Nevertheless, the Sabatier principle, although not quantitative in nature, can still be used to make qualitative predictions.

By examining the volcano plot figure by Nørskov, et al. (2004), it can be deduced qualitatively that platinum (Pt) is the best catalyst for the ORR reaction given that it demonstrates the highest catalytic activity. Given that Pt still demonstrated sluggish activity, either more effective use of Pt or new catalysts with a different material must be developed.

SACs are a class of catalysts that have gained research attention in the past decade where catalytically active single, isolated metal atoms are attached to support structures (Cheng, et al., 2019). This technique allows superior metal atom utilisation which inevitably makes the catalyst more cost-effective as less of the valuable Pt remains unused. However, similarly to nanoscale metal catalysts, the linear scaling relationships associated with the volcano plots remain relevant. Therefore, SACs do not provide a prospective pathway to move away from using PGM as catalysts for the ORR reaction.

The limited supply of Pt is a key factor affecting the high price it is associated with. Up to 80% of global Pt resources are found in South Africa and Russia only (Sealy, 2008). Two potential approaches to replace the use of PGM include: considering different precious metals (e.g., Pd and Ru) as indicated by the aforementioned volcano plot (Nørskov, et al., 2004). However, prices and stock availability will still be an issue. Alternatively, the use of more abundant, non-precious metals instead of Pt offers a more appealing prospect.

The development of DACs is a novel alternative to PGM catalysts, with DACs defined as catalytic sites comprising of two active metal atoms in atomic proximity to one another. Inspired by dual-centre biological enzymes, haem-copper oxidases (HCOs), Gong, et al. (2018) demonstrated an improved performance using a Fe,Mn–N/C catalyst in Zn-air battery compared to the conventional Pt/C catalyst. They reported a reduced energy barrier for the protonation of O* to HO*, a vital step in the ORR mechanism. DAC further maximise the atomic utilisation, and allow for the use of non-precious metals such as Fe, Zn or Co. Moreover, with DACs the strong interaction between the double-metal atoms and the supporting substrate material enhances the intrinsic activity of the active sites (Lu, et al., 2020). In addition, the synergy between the metal diatoms has a great auxiliary advantage for the rupture of the O=O bond (Liu, et al., 2020). Thus, the use of DACs provides the opportunity to break the linear scaling relationships associated with SACs.

Reported works on DACs have mostly been applied to ORR and CO_2 reduction (Zhang, et al., 2020). An example includes the experiment by Wu (2018), where a Fe-Co/N/C DAC was tested in an H_2/air fuel cell and achieved approximately 76% of the power density of the commercial Pt/C catalyst. This demonstrates a great potential for further optimisation of the DAC to eventually be used as the

main catalyst in the fuel cell reaction (Wang, et al., 2017). Unfortunately, the lack of successful results of DAC in H_2/air fuel cells in the representative working condition means that further work is required for the potential to be realisable. Improvements in activity and durability of alternative electrocatalysts are required so that they can be successfully deployed in large scale. The main challenge of DACs involves the identification of the two metal centres, so methods such as DFT should continue to be employed to gather information about geometric arrangement and electronic structure of the metal centres in DACs.

The determination of the substrate supporting the dual-metal atoms is required. The discovery of graphene in 2004 (University of Manchester, 2004), together with the development of the DFT in the late 20th century (Jones & Gunnarsson, 1989), has led to an increasing research interest in graphene-supported heterogeneous catalysts due to its exceptional electronic properties, extremely large surface-to-volume ratio (Yam, et al., 2020) and mechanical and thermal stability (Julkapli & Bagheri, 2015). Moreover, interactions between graphene and the supported metal atoms are highly tuneable via physical or chemical methods. The biggest issue in graphene-based catalysis is to find both effective and pragmatic ways of activating the graphene (Yam, et al., 2020).

The direct way of controlling the electrical and magnetic properties of graphene is to dope different elements such as nitrogen, sulphur or by defect engineering (Hou, et al., 2013). Nitrogen-doped (N-doped) graphene has shown wide applications in lithium-ion batteries (Reddy, 2010) as well as catalysis for various reactions. The well-bonded nitrogen atom could drastically alter the electronic performance by offering more active sites and enhancing the interaction between the carbon structure formed and lithium. Thus, it is expected to improve the kinetics of lithium diffusion and transfer, which would be beneficial to its electrochemical performance. Therefore, N-doped graphene was tested considering its potential to be a promising material for hydrogen fuel cells.

Computational Methods

Ab-initio molecular dynamic calculations were carried out using the Quickstep module in CP2K with periodic boundary conditions using Goedecker-Teter-Hutter/Perdew-Burke-Ernzerhof (GTH-PBE) pseudopotentials (Goedecker, et al., 1995; Hartwigsen, et al., 1998; Krack, 2005) and TZVP-MOLOPT-GTH basis sets (VandeVondele & Hutter, 2007) for both carbon and nitrogen atoms. The cut-off energy was tuned to 300 Ry with 12 x 12 x 1 ***k***-point grid using the Monkhorst-Pack method to sample the Brillouin zone (Monkhorst & Pack, 1976) for a 2-atom unit cell to satisfy the total energy convergence criterion of 1 meV/atom. The exchange-correlation potential was described by the PBE functionals (Perdew, et al., 1996), using the generalised gradient approximation.

Based on the laws of thermodynamics, Eq. 1 was used to calculate the energy of formation of the N-doped graphene, E_f, as shown below:

$$E_f = E_d + n_C E_C - \frac{1}{2} n_N E_{N_2} - E_g, \qquad (1)$$

where E_d is the total energy of N-doped graphene, n_C is the number of carbon atom 'removed' from the pristine graphene and E_C is the energy of the pristine graphene per carbon atom, n_N is the number of nitrogen atom in the N-doped graphene, E_{N_2} is the total energy of pure nitrogen and E_g is the total energy of pristine graphene.

Therefore, the total energy of pristine graphene was calculated as the reference system. Similar calculations for three N-doped graphene, six N-doped graphene and isolated nitrogen molecules were then performed for the calculation of E_f as described by Eq. 1.

Reference System

Pristine graphene was modelled using a 2-atom hexagonal unit cell. Subsequently, supercell with 32 atoms (4 × 4 unit cells), 128 atoms (8 × 8 unit cells) and 288 atoms (12 × 12 unit cells) were modelled and the total energy of these systems were compared to the unit cell. The density of the ***k***-point grid was adjusted to remain comparable for calculations using larger supercells to maintain analogous levels of convergence in ***k*** space.

The Fermi energy obtained from the DFT calculations were set to the zero-energy level before plotting the band structure of pristine graphene as shown in Figure 1. The band gap is zero at the symmetry point K which is in quantitative agreement with a similar investigation of graphene band structure (Castro Neto, et al., 2009; Kozlov, et al., 2011). The DFT model was deemed to be robust as the electronic structure of the system was well-reproduced.

To model a single graphene layer, geometry optimisation calculations showed that a vacuum distance c = 18.0 Å was required to decouple the interactions between neighbouring layers in the periodic system. The optimal lattice parameter a was determined by fitting the total energy of the system into the Murnaghan's equation of state (Murnaghan, 1944). This yielded a = 2.46730 Å as shown in Figure 2 in a hexagonal 2-atom unit cell. The C–C bond length was calculated to be 1.424 Å using the

cosine rule. This agrees closely to the experimental value of 1.421 Å (Ergun, 1973).

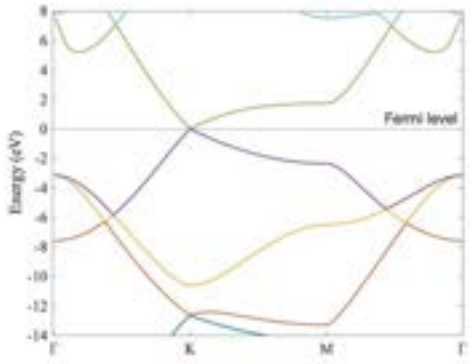

Figure 1. Band structure of pristine graphene

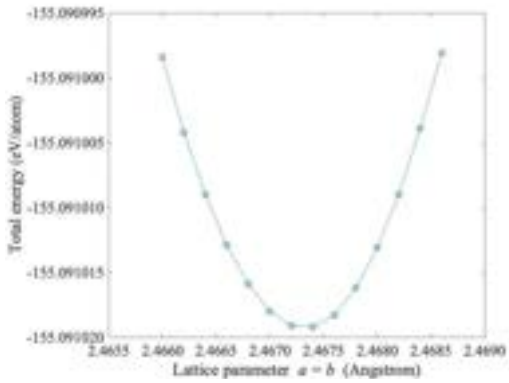

Figure 2. Plot of total energy per atom against lattice parameter $a = b$ for the optimisation of lattice parameter of pristine graphene

Results

N-doped graphene, as a precursor of a DAC, was modelled using the atomic positions adapted from a paper which investigates DACs with various combinations of metal atoms for ORR (Zhu, et al., 2019). The system was studied using the same three supercell sizes as pristine graphene to assess the effects of the distance between neighbouring defects. The visualisation of the supercell is shown in Figure 3. For all the supercell geometry optimisation calculations for six N-doped graphene for DACs, the C–C bond length was 1.423 Å while the C–N bond length was 1.354 Å.

The band structure of the six N-doped graphene is shown in Figure 4. The band gap opened up at the symmetry point K with a value of 0.46 eV, agreeing closely with a reported value of 0.45 eV (Sharma, et al., 2017).

The energy of formation (normalised per nitrogen atom substituted for comparison) was then calculated using Eq. 1. The results are tabulated in Table 1. Moreover, the energy of formation of three N-doped graphene, precursors for an SAC, were also calculated using Eq. 1 to compare with DAC precursors. These structures, adapted from a paper on single-atom copper catalyst (Anon., n.d.), include models of M–N_3, M–N_3–C and M–N_3–* where M is a site for a metal atom and * is a vacant site shown in Figure 5.

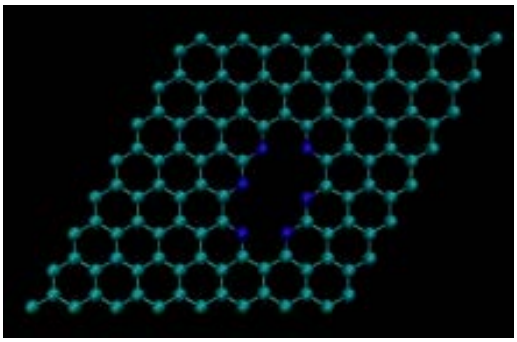

Figure 3. Top view of the optimised structure of six N-doped graphene, a DAC precursor. Adapted from (Zhu, et al., 2019).

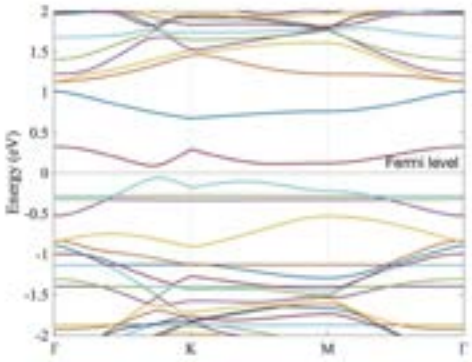

Figure 4. Band structure of six N-doped graphene

Discussion

Mathematically, the objective of electronic density calculations is to find a solution to the Kohn-Sham equations through the use of a specific exchange-correlation functional, for a set of atoms with periodic boundary conditions. Consequently, the calculation of energy of formation using Eq. 1 within the realms of DFT was well-defined and provided a dependable indication of the stabilities of the various substrate precursors that were studied. By contrast, obtaining the energy of formation accurately from experiments is strenuous. For example, establishing the enthalpy of formation in a direct manner is only feasible through calorimetry which requires heat of combustion values (Mole, et al., 1996).

Numerical imprecision associated with DFT calculations exists, as systematic yet unknown errors arise due to the inexact nature of the exchange-correlation functional. Despite the numerical inaccuracy, the concept of physical accuracy does nevertheless yield the prospect of making comparisons between similar states. Furthermore, it has been shown that the systematic error is similar between two states, so in essence the evaluation of relative energies improves the accuracy of DFT as opposed to the comparison of absolute energies (Sholl & Steckel, 2009).

Table 1. Energy of formation of N-doped graphene

Structure	Distance between the centres of adjacent sites (Å)	Energy of formation, E_f (eV)	Energy of formation per N atom, $E_{f,N}$ (eV/atom)
Precursors for DAC (Figure 3)			
32 atoms (4 × 4 unit cells)	9.8692	-7.483	-1.247
128 atoms (8 × 8 unit cells)	19.7384	-5.415	-0.903
288 atoms (12 × 12 unit cells)	29.6076	-5.683	-0.947
Precursors for SAC (Figure 5)			
M–N_3	9.8692	-3.084	-1.542
M–N_3–C	9.8692	-0.697	-0.232
M–N_3–*	9.8692	0.811	0.270

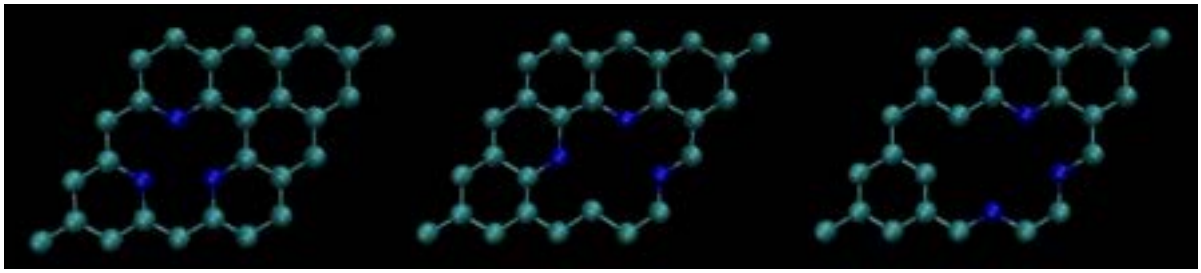

Figure 5. Top view of the optimised structures of SAC precursors: M–N_3 (left), M–N_3–C (centre) and M–N_3–* (right) where M is a site for a metal atom and * is a vacant site. Adapted from (Yang, et al., 2019).

It is also worth noting that when defining the parameters under which DFT is executed, the selection of large enough cut-off energy and ***k***-point grid would result in more well-converged numerical solutions to the exact solution of the Kohn-Sham equations for infinite dimensions. Intuitively, there is a trade-off associated with the solution precision and computational cost associated with it, therefore this has to be accounted for in the determination of the optimal parameters.

As periodic boundary conditions were used, the system was duplicated in all directions. Thus, it was important to determine the vacuum distance to ensure that the results obtained were representative of a single isolated graphene layer, without any interactions from the adjacent layers.

Out of the three supercell sizes studied for the DAC precursors, the energy of formation reveals that the nitrogen defects thermodynamically favour being closer to one another. This is demonstrated by the lowest energy of formation per nitrogen atom in the supercell of 32 atoms where the distance between the centres of adjacent sites is 9.8694 Å. However, this value is only valid when comparing the three supercell sizes studied, so the prospect of the defects being located closer to each other could potentially result in stronger interactions among themselves, affecting the stability of the substrate formed.

Since nitrogen atoms contain one more electron than carbon atoms, the defects possess a higher charge distribution between the nitrogen nuclei and their lone pairs, compared to only one free electron per carbon atom in pristine graphene. The favouring of shorter distances between defects is due to the extra charges of the non-bonding electrons dispersing over a larger area. This enhanced charge delocalisation gives rise to greater stability of the system (Housecroft & Constable, 2010).

The electronic structure of the substrate was studied from an atomic point of view, firstly by plotting the band structure of pure graphene. The linear dispersion of the π band (where the valence band and the conduction band meet at the K point of the hexagonal Brillouin zone) suggests that the charge carriers in graphene can be considered as massless Dirac fermions (Hwang, et al., 2011). From the band structure in Figure 1, it can be inferred that pure graphene possesses a stable hybrid structure and high charge carrier mobility (Olaniyan, et al., 2016).

Furthermore, the band gap opening of 0.46 V at the symmetry point K (Dirac point) in the six N-doped graphene can be explained by symmetry breaking caused by nitrogen doping. This phenomenon has been experimentally illustrated using scanning tunnelling spectroscopy and angle-resolved photoemission in a paper studying the band gap opening in the Ag/Cu(111) interface which is also characterised by hexagonal supercells (Vasseur, et al., 2013). It is worth noting that calculating band gaps within the framework of DFT usually results in an underestimation, hence the actual value for the band gap could be greater than reported (Morales-Garcia, et al., 2017). This is due to the fact that DFT is a ground state theory so the energy bands far away from the Fermi level are not meaningful.

The calculated C–N bond is slightly shorter than the C–C bond as nitrogen is more electronegative than carbon on the Pauling electronegativity scale, with a value of 3.04 and 2.55 respectively (Pauling, 1931). This is shown by the somewhat distorted lattice structure in Figure 3. The increase in electronegativity in the N-doped graphene, together with the electron lone pairs on each nitrogen atoms, interacts more strongly with the metal atoms. This is beneficial for the ORR, when compared to DACs without nitrogen doping, as the metal atoms will be bound more strongly to the vacancies and hence less strongly to oxygen atom participating in the reaction.

According to the Sabatier principle, the optimal catalyst should have an intermediary bond strength with reaction intermediates (Sabatier, 1911). This means that the optimal catalyst should neither bind too weakly, hindering the activation of reactants, nor too strongly, obstructing the desorption of products (Medford, et al., 2015). Using the qualitative principle, it has been concluded that the best catalyst for ORR should have binding energies for oxygen and hydroxyl group similar to that of Pt(111) as illustrated in the volcano-shaped plot (Nørskov, et al., 2004). Therefore, nitrogen doping is a potential solution to lowering the oxygen binding energy on the substrate, which is reported to be -204 kJ/mol on Fe atoms in pristine graphene without nitrogen doping (cf. -124 kJ/mol on Pt (111)) (Kropp & Mavrikakis, 2019).

The formation of M–N_3, precursor for SAC, is more thermodynamically favourable than the formation of the most stable DAC precursor as anticipated due to its higher surface energy resulting from the greater number of vacancies (Chen, et al., 2019). Despite SACs having been investigated for a longer time, it does not show the potential to shift away from the use of expensive noble metals. On the other hand, DACs offer a higher adjustability of the electronic structure due to their ability to host two metal atoms, between which the synergy can be optimised to the reaction of interest. Therefore, further investigations on DACs could provide a pathway towards a more sustainable, inexpensive electrocatalyst for the ORR.

Conclusion

In this paper, a DFT-based study was conducted on the substrates, three and six N-doped graphene, to assess the thermodynamic stability of potential precursors for SAC and DAC. To gain a fundamental understanding of the DAC system, it was paramount to create a reference model of the substrate in its simplest form; one layer of pristine graphene. Various parameters required to run the electronic structure calculations such as cut-off energy, the k-point grid, basis set and vacuum distance were obtained by running geometry optimisation to relax the system by reaching convergence at the minimum total energy. Numerical tolerance tests ensured the error of all calculations converged to 1 meV/atom. A band structure calculation was carried out for pristine graphene with a zero band gap obtained, and the lattice parameter was determined. Both the band structure and lattice parameter were in experimental in agreement with literature values, indicating the model was well-defined and results were reproducible.

The model was further developed through the introduction of nitrogen atoms based on the atomic positions of a DAC investigated by (Zhu, et al., 2019). This N-doped graphene DAC precursor was modelled at three supercell sizes to assess the effects of the distance between neighbouring defects. The evaluation of thermodynamic stability was performed through comparison of the energy of formation. By normalising the formation energy per nitrogen atom substituted, the precursors for SAC and DAC could be effectively compared. It was clearly determined that nitrogen defects being in closer proximity to each other were more stabilised systems due to the effect of enhanced charge delocalisation being felt more strongly. Thus, for DAC the supercell with the least distance between centres of adjacent sites was found to have the lowest normalised energy of formation, at -1.247 eV. Based on the laws of thermodynamics, this indicates that the lowest energy of formation structure would be the most favourable to synthesise out of the structures studied.

In addition, similar analysis was performed on the SAC precursors, and the results displayed that the system modelled with a metal and 3 nitrogen atoms (M–N_3) was the most stable thermodynamically when compared to M–N_3–C and M–N_3–*, with a normalised energy of formation of -1.542 eV. This signifies a higher stability relative to the most stable DAC precursor, due to its higher surface energy as a consequence of its greater number of vacant sites. Moreover, based on the calculations performed, it was determined that the system M–N_3–* was thermodynamically infeasible, and could not occur spontaneously.

In conclusion, DFT is a powerful framework which can provide qualitative indications to which structure configuration results in the most favourable thermodynamic stability. Despite the precursor for SAC being the most stable, it does not allow the shift away from Pt-based metals used for electrocatalysis. Therefore, further investigations on the binding energies of the oxygen and hydroxyl groups should be conducted as a function of the metal atoms. Moreover, the catalytic activity of the

prospective catalysts should be examined in a further study to allow for the optimisation of parameters such as ORR kinetics.

Outlook

To further expand on the findings of this paper, an investigation on the thermodynamics of the reaction intermediates adsorbed on the dual-metal atom site is essential. Most importantly, the binding energies of oxygen and hydroxyl group should be examined as a function of the metal atoms used and compared to those for the Pt(111) catalyst (Nørskov, et al., 2004). In addition, different combinations of metal atoms used in the DACs should then be explored.

The next logical step would be to assess the mechanical stability of the materials by evaluating their finite-temperature elastic constants. This can be done by *ab initio* molecular dynamics simulations as they can circumvent the difficulty of having to take into account the atomic motions (Shulumba, 2015).

Subsequently, the performance of these DACs should be investigated – with parameters of interest including kinetics of ORR and thermal stability. It is desirable to ensure comparable, if not even better, catalytic activity to that of the existing PGM catalysts. Moreover, it is essential for the DAC to be resistant to potentially harsh temperatures in working conditions for its establishment as a viable alternative to PGM catalysts.

The last step that follows would then be to experimentally synthesise the computationally designed DACs. Synthesis methods of N-doped graphene such as a hydrothermal process using graphene oxide as a precursor followed by an annealing treatment has been successfully demonstrated (Zheng, et al., 2013). Other novel synthesis methods include one-step pyrolysis using biomass citric acid and dicyandiamide (Gu, et al., 2018), chemical vapour deposition (CVD) (Maldonado, et al., 2006), arc-discharge method (Panchakarla, et al., 2009) and solvothermal method (Choucair, et al., 2009).

All in all, there are many challenges ahead for both theoretical and experimental researchers to find potential DACs to replace the Pt-based electrocatalyst used in fuel cells. After the prospective catalysts have been discovered, they must work hand-in-hand with engineers to scale up the production so that this novel technology becomes ubiquitous.

Acknowledgement

The authors would like to thank Dr Cucinotta, Y. Zhang and A. Pedersen for their support over the duration of this research project.

References

Abbasi, R. et al., 2019. A Roadmap to Low-Cost Hydrogen with Hydroxide Exchange Membrane Electrolyzers. *Adv. Mat.,* 31(31), p. 1805876.
Anon., n.d.
Archer, T. D., 2004. *Computer Simulations of Calcite,* s.l.: s.n.
Bereiter, B. et al., 2015. Revision of the EPICA Dome C CO2 record from 800 to 600 kyr before present. *Geophys. Res. Lett.,* 42(2), pp. 542-549.
Castro Neto, A. H. et al., 2009. The electronic properties of graphene. *Rev. Mod. Phys.,* 81(1), pp. 109-162.
Cheng, N., Zhang, L., Doyle-Davis, K. & Sun, X., 2019. Single-Atom Catalysts: From Design to Application. *Electrochemical Energy Reviews,* Volume 2, pp. 539-573.
Chen, Y. et al., 2018. Single-Atom Catalysts: Synthetic Strategies and Electrochemical Applications. *Joule,* 2(7), pp. 1242-1264.
Chen, Z. W., Chen, L. X., Yang, C. C. & Jiang, Q., 2019. Atomic (single, double, and triple atoms) catalysis: frontiers, opportunities, and challenges. *J. Mat. Chem. A,* 7(8), pp. 3492-3515.
Choucair, M., Thordarson, P. & Stride, J., 2009. Gram-scale production of graphene based on solvothermal synthesis and sonication. *Nat. Nanotech.,* Volume 4, p. 30.
Crocombette, J.-P. & Willaime, F., 2020. Ab initio electronic structure calculations for Nuclear Materials.
Dai, J. & Yuan, J., 2010. Adsorption of molecular oxygen on doped graphene: Atomic, electronic, and magnetic properties. *Phys. Rev. B.*
Deloitte, 2020. *Fueling the Future of Mobility: Hydrogen and fuel cell solutions for transportation,* s.l.: Deloitte.
EERE, 2020. *Hydrogen Resources.* [Online]
Available at: https://www.energy.gov/eere/fuelcells/hydrogen-resources
[Accessed 30 Nov 2020].
Ergun, S., 1973. Structure of Graphite. *Nat. Phys. Sci.,* Volume 241, p. 65.
European Commission, 2003. *European Commission.* [Online]
Available at: fch.europa.eu/sites/default/files/documents/hlg_vision_report_en.pdf
European Commission, 2020. *European Commission.* [Online]
Available at: ec.europa.eu/commission/presscorner/detail/en/fs_20_1296

FCHEA, 2020. *Fuel Cell Basics.* [Online]
Available at: http://www.fchea.org/fuelcells
Feller, D. & Dixon, D. A., 2018. Density Functional Theory and the Basis Set Truncation Problem with Correlation Consistent Basis Sets: Elephant in the Room or Mouse in the Closet?. *J. Phys. Chem..*
Geopura, 2020. *What is green hydrogen? And why should we start using it?.* [Online]
Available at: https://www.geopura.com/blog/why-we-should-start-using-green-hydrogen-in-2019/
[Accessed 30 Nov 2020].
Ghosh, P., Senthilarasu, S., Nixon, T. & Krishnamurthy, S., 2016. Influence of Nanostructures in Perovskite Solar Cells. *Mat. Sci. and Mat. Eng..*
Giorgi, L. & Leccese, F., 2013. Fuel Cells: Technologies and Applications. *The Open Fuel Cells Journal,* Volume 6, pp. 1-20.
Goedecker, S., Teter, M. & Hutter, J., 1995. Separable Dual Space Gaussian Pseudo-potentials. *Phys. Rev. B,* 54(3), pp. 1703-1710.
Gong, S. et al., 2018. Designing highly efficient dual-metal single-atom electrocatalysts for the oxygen reduction reaction inspired by biological enzyme systems. *J. Mat. Chem. A,* Volume 6, p. 13254.
Gu, D. et al., 2018. Facile Synthesis of N-Doped Graphene-Like Carbon Nanoflakes as Efficient and Stable Electrocatalysts for the Oxygen Reduction Reaction. *Nano-Micro Lett.,* Volume 10.
Guo, J. et al., 2020. Graphitic-N-rich N-doped graphene as a high performance catalyst for oxygen reduction reaction in alkaline solution. *Int. J. of Hydrogen Energy,* 45(56), pp. 32402-32412.
Hartwigsen, C., Goedecker, S. & Hutter, J., 1998. Relativistic separable dual-space Gaussian pseudopotentials from H to Rn. *Phys. Rev. B,* 58(7), pp. 3641-3662.
Hou, C.-C., Wang, H.-F., Li, C. & Xu, Q., 2020. From metal–organic frameworks to single/dual-atom and cluster metal catalysts for energy applications. *Ener. & Env. Sci.,* Volume 13, p. 1658.
Housecroft, C. E. & Constable, E. C., 2010. *Chemistry : An Introduction to Organic, Inorganic, and Physical Chemistry.* s.l.:s.n.
Hou, Z. et al., 2013. Electronic structure of N-doped graphene with native point defects.
Hwang, C., Shin, S., Choi, S.-M. & Kim, N., 2011. The stability of graphene band structures against an external periodic perturbation ; Na on Graphene.
Hydrogenics, 2020. *Fuel cells.* [Online]
Available at: https://www.hydrogenics.com/technology-resources/hydrogen-technology/fuel-cells/
[Accessed 30 Nov 2020].
IEA, 2019. *The Future of Hydrogen.* [Online]
Available at: https://www.iea.org/reports/the-future-of-hydrogen
Jones, R. O. & Gunnarsson, O., 1989. The density functional formalism, its applications and prospects. *Rev. Mod. Phys.,* 61(3), p. 689.
Julkapli, N. M. & Bagheri, S., 2015. Graphene supported heterogeneous catalysts: An overview. *Int. J. of Hydrogen Energy,* 40(2), pp. 948-979.
Kandula, S., Shrestha, K. R., Kim, N. H. & Lee, J. H., 2018. Fabrication of a 3D Hierarchical Sandwich Co9S8/α-MnS@N–C@MoS2 Nanowire Architectures as Advanced Electrode Material for High Performance Hybrid Supercapacitors. *Small,* 14(23), p. 1800291.
Kolev, S., 2017. Ab-Initio Molecular Dynamics Simulation of Graphene Sheet.
Kozlov, S. M., Viñes, F. & Görling, A., 2011. Bandgap Engineering of Graphene by Physisorbed Adsorbates. *Adv. Mat..*
Krack, M., 2005. Pseudopotentials for H to Kr optimized for gradient-corrected exchange-correlation functionals. *Theoretical Chemistry Accounts,* Volume 114, pp. 145-152.
Kropp, T. & Mavrikakis, M., 2019. Transition Metal Atoms Embedded in Graphene: How Nitrogen Doping Increases CO Oxidation Activity. *ACS Cat.,* 9(8), p. 6864–6868.
Lanzara, A., 2015. *Graphene Gets a Good Gap.* [Online]
Available at: https://physics.aps.org/articles/v8/91
[Accessed 2 Dec 2020].
Liu, J., Cao, D., Xu, H. & Cheng, D., 2020. From double-atom catalysts to single-cluster catalysts: A new frontier in heterogeneous catalysis. *Nano Select,* pp. 1-20.
Lu, B., Liu, Q. & Chen, S., 2020. Electrocatalysis of Single-Atom Sites: Impacts of Atomic Coordination. *ACS Cat.,* 10(14), pp. 7584-7618.
Lu, Z. et al., 2019. An Isolated Zinc–Cobalt Atomic Pair for Highly Active and Durable Oxygen Reduction. *Angewandte Chemie International Edition,* 58(9), pp. 2622-2626.
Machado, B. F. & Serp, P., 2011. Graphene-based materials for catalysis. *Catalysis, Science & Technology,* pp. 54-75.
Maldonado, S., Morin, S. & Stevenson, K. J., 2006. Structure, composition, and chemical reactivity of carbon nanotubes by selective nitrogen doping. *Carbon,* 44(8), pp. 1429-1437.
McKerracher, C. et al., 2020. *Electric Vehicle Outlook 2020,* s.l.: BloombergNEF.
Medford, A. J. et al., 2015. From the Sabatier principle to a predictive theory of transition-metal heterogeneous catalysis. *J. Cat.,* Volume 328, pp. 36-42.
Mole, S. J. M., Zhou, X. & Liu, R., 1996. Density Functional Theory (DFT) Study of Enthalpy of Formation. 1. Consistency of DFT Energies and Atom Equivalents for Converting DFT Energies into Enthalpies of Formation. *J. Phys. Chem.,* Volume 100, pp. 14665-14671.

Monkhorst, H. J. & Pack, J. D., 1976. Special points for Brillouin-zone integrations. *Phys. Rev. B,* 13(12), pp. 5188-5192.
Morales-Garcia, A., Rosendo, V. & Illas, F., 2017. An Empirical, yet Practical Way To Predict the Band Gap in Solids by Using Density Functional Band Structure Calculations. *J. Phys. Chem..*
Murnaghan, F. D., 1944. The Compressibility of Media under Extreme Pressures. *PNAS,* 30(9), pp. 244-247.
NASA, 2020. *NASA/JPL Edu.* [Online]
Available at: https://www.jpl.nasa.gov/edu/teach/activity/graphing-global-temperature-trends/
[Accessed 30 Nov 2020].
Ni, M., Leung, M. & Leung, D., 2006. Technological development and prospect of alkaline fuel cells. *Proceedings of 16th World Hydrogen Energy Conference ,* pp. 33-39.
Nørskov, J. K. et al., 2004. Origin of the Overpotential for Oxygen Reduction at a Fuel-Cell Cathode. *J. Phys. Chem.,* 108(46), p. 17886–17892.
Olaniyan, O. et al., 2016. Exploring the stability and electronic structure of beryllium and sulphur co-doped graphene: a first principles study. *RSC Advances.*
Panchakarla, L. et al., 2009. Synthesis, structure and properties of boron and nitrogen doped graphene. *Adv. Mater.,* Volume 21, p. 4726.
Pauling, L., 1931. The Nature of the Chemical Bond. Application of Results Obtained from the Quantum Mechanics and from a Theroy of Paramagnetic Susceptability of the Structure of Molecules. *J. Am. Chem. Soc.,* 53(4), p. 1367–1400.
Perdew, J., Burke, K. & Ernzerhof, M., 1996. Generalized Gradient Approximation Made Simple. *PRL,* 77(18), pp. 3865-3868.
Reddy, A., 2010. Synthesis Of Nitrogen-Doped Graphene.
Sabatier, P., 1911. Hydrogénations et déshydrogénations par catalyse. *Ber. Dtsch. Chem. Ges.,* Volume 44, pp. 1984-2001.
Sahu, S. & Rout, G. C., 2017. Band gap opening in graphene: a short theoretical study. *Int. Nano Lett.,* pp. 81-89.
Sealy, C., 2008. The problem with platinum. *Mater. Today,* 11(12), pp. 65-68.
Sharma, R. et al., 2017. Investigation on effect of boron and nitrogen substitution on electronic structure of graphene. *FlatChem,* Volume 1, pp. 20-33.
Sholl, D. & Steckel, J., 2009. Density Functional Theory- A Practical Introduction.
Shulumba, N., 2015. *Vibrations in solids : From first principles lattice dynamics to high temperature phase stability,* s.l.: s.n.
Song, C. & Zhang, J., 2008. Electrocatalytic Oxygen Reduction Reaction. *PEM Fuel Cell Electrocatalysts and Catalyst Layers,* pp. 89-134.
Sotouchi, H., 2003. Alkaline Fuel Cells. *Energy Carriers And Conversion Systems.*
U.S Department of Energy, 2020. *Energy Efficiency & Renewable Energy Department.* [Online]
Available at: https://www.energy.gov/eere/fuelcells/fuel-cells
UNFCCC, 2020. *The Paris Agreement.* [Online]
Available at: https://unfccc.int/process-and-meetings/the-paris-agreement/the-paris-agreement
[Accessed 30 Nov 2020].
University of Manchester, 2004. *Discovery of graphene.* [Online]
Available at: https://www.graphene.manchester.ac.uk/learn/discovery-of-graphene/
[Accessed 5 Dec 2020].
VandeVondele, J. & Hutter, J., 2007. Gaussian basis sets for accurate calculations on molecular systems in gas and condensed phases. *J. Chem. Phys.,* Volume 127, p. 114105.
Vasseur, G. et al., 2013. Effect of Symmetry Breaking on Electronic Band Structure: Gap Opening at the High Symmetry Points. *Symmetry,* 5(344-354).
Wang, H., 2011. Nitrogen-doped graphene nanosheets with excellent lithium storage properties. *J. Mater. Chem..*
Wang, J., Huang, Z., Liu, W. & Chang, C., 2017. Design of N-Coordinated Dual-Metal Sites: A Stable and Active Pt-Free Catalyst for Acidic Oxygen Reduction Reaction. *J. Am. Chem. Soc..*
Wu, G. et al., 2018. Atomically dispersed manganese catalysts for oxygen reduction in proton-exchange membrane fuel cells. *Nature Catalysis,* Volume 1, p. 935–945.
Yam, K. M. et al., 2020. Graphene-Based Heterogeneous Catalysis: Role.
Yang, X., Wang, A. & Qiao, B., 2013. Single-atom catalysts: a new frontier in heterogeneous catalysis.
Yang, Z. et al., 2019. Directly transforming copper (I) oxide bulk into isolated single-atom copper sites catalyst through gas-transport approach. *Nat. Comm.,* Volume 10, p. 3734.
Zhang, J. et al., 2020. Supported dual-atom catalysts: Preparation, characterization, and potential applications. *Chinese J. Catal.*
Zheng, B., Wang, J., Wang, F.-B. & Xia, X.-H., 2013. Synthesis of nitrogen doped graphene with high electrocatalytic activity toward oxygen reduction reaction. *Electrochem Comm,* Volume 28, pp. 24-26.
Zhu, X. et al., 2019. Activity Origin and Design Principles for Oxygen Reduction on Dual- Metal-Site Catalysts: A Combined Density Functional Theory and Machine Learning Study. *J. Phys. Chem. Lett.,* Volume 10, pp. 7760-7766.

Investigating Entrepreneurial Intention among Chemical Engineering students and Developing tailored Entrepreneurship Education

Sasangee Dissanayake and Pravin Suduwelikanda
Department of Chemical Engineering, Imperial College London, U.K.

Abstract: The chemical engineering industry is shifting to a predominantly technology-based industry which has led to significant growth in certain fields and the need for innovation; promoting entrepreneurial activities. Higher education institutions in the UK have progressed to develop curricula that focus on innovation and the promotion of entrepreneurial education in engineering. A gap was identified between entrepreneurial intention of engineering students and subsequent choosing of entrepreneurship as a career path. To address this, research was conducted in the Department of Chemical Engineering at Imperial College London with the objectives of quantifying intent, identifying the extent of existing support and how best to supplement entrepreneurial education. Data was gathered using a questionnaire and through interviews with students, alumni and academics. Students were found to have high intention but a lack of awareness. A hierarchal regression model was used to identify impact of intention, awareness and education on specific and transferable skills. Students were found to be lacking in entrepreneurial specific skills and awareness the most important variable to address. A course was developed based of key findings to bridge the gap with a focus on collaborating with industry and learning by doing to invoke higher order cognitive skills sufficient for entrepreneurship.

Introduction

The chemical engineering industry is at a crossroads; it is undergoing rapid transitioning from traditional process engineering to a predominantly technology-based industry. [1] There is significant growth in fields such as environmental engineering and biotechnology, which are increasingly adapting new computational engineering approaches. [1] The introduction of Industry 4.0 along with machine learning and big data [2] have caused a paradigm shift in chemical engineering. However, such digitalisation [3] are accompanied by new complications and barriers that need to be overcome. This has led to a prevailing increase in innovation and enterprise opportunities [4] for developing new products and processes within the realms of today's environmental laws and sustainability goals.

The Institution of Chemical Engineers (IChemE) has taken increased interest in enabling digital literacy and efforts to 'harness innovations created through systems thinking, artificial intelligence and automation' as part of their 2024 Strategy. It states that 'the discipline must adopt new concepts and integrate them into curricula, so that finally, innovative and more sustainable processes will break through into industry'. Meeting these innovation and entrepreneurship criteria require concentrated effort and some crucial cultural changes from Higher education institutions (HEI) such as Imperial College London (Imperial).

Entrepreneurship education in the UK has progressed over the last 10 years and more recently been part of interdisciplinary teaching within engineering degrees. Entrepreneurship drivers for engineering students are based around development of new technologies. Such activity has shown a positive trend in recent years. [29]

Initial investigations display that 7 Russel Group Universities offer a course with an entrepreneurship module and two of these courses explicitly mention entrepreneurship in their Degree Title. This signifies that entrepreneurship whilst deemed important has yet to be fully implemented. However, the scope and direction of these are unclear and though there is progress; there is a sufficient lack of research mentioned in literature for the domain of engineering undergraduate programmes in the UK landscape. As such, adequate research must be carried out for the development and implementation of such courses in Engineering Degree Programmes.

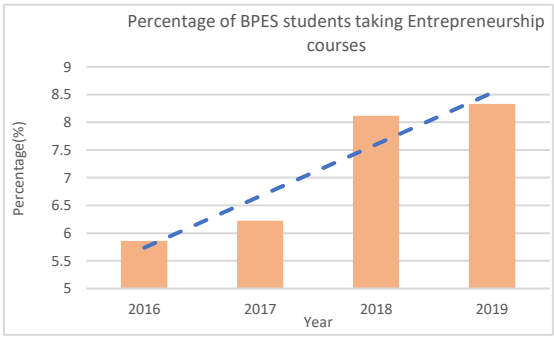

Figure 1 – Graph showing percentage of BPES students taking entrepreneurship

This project investigates the entrepreneurial intention and awareness of Chemical Engineering students at Imperial College London. A key motivation of this research also encompasses a core element of Imperial College London's new teaching strategy which involves using 'students as partners' in co-creating curricula. [report] Given the high importance of this field of education, the purpose of this study was to investigate student attitudes toward entrepreneurship and examine how a medium of entrepreneurial support could be

provided to bridge the gap between intention and execution.

The main research questions are:

1. **How is entrepreneurship supported in undergraduate degree programs?**
2. **What is the extent of entrepreneurial intent undergraduate students in the department?**
3. **What are the major gaps in entrepreneurship education tailored to chemical engineering students?**
4. **What is the best method to deliver this education and what key learning objectives must be satisfied?**

There are major differences in the area of academic entrepreneurship as opposed to technical entrepreneurship [5]. Great significance is given to academic entrepreneurship at research intensive HEI's such as Imperial College London. The extent of entrepreneurship at HEIs is documented in literature based on spinoffs resulting from academic entrepreneurship. However, there is no mention of data pertaining to the formation of start-ups by students and graduates as these are excluded from the academic entrepreneurship category [19]. With students showing promising potential and immediate graduates successfully creating start-ups, it is understood that research must be done in implementing an effective framework to support students in accomplishing technical entrepreneurship. In order to cater to these needs, higher education institutions are developing a growing number of entrepreneurship education programs that consist of integration with university technology transfer offices (TTOs) [6]. This has been researched by Imperial Innovations with a focus on limitations and the direction of transformation of such TTOs [22].

Teaching entrepreneurship is very much different to teaching other business subjects [13] such as accounting, economics or strategic management. This is because in the context of Higher Education, such courses have been prominent over many years and the concepts and theories have been developed and rationalised in such a way that it can be taught and learned in a lecture. This would essentially involve traditional teaching methods where the professor delivers a lecture enforcing theoretical knowledge and solution approaches to students. However, in the domain of entrepreneurship education, teaching methods differ, and the teaching theory must be explored practically [25]. This form of education improves students' skills, perception and entrepreneurial drive as well as intent [14] through teaching 'for' entrepreneurship as opposed to teaching 'about' it. Students who end up pursuing entrepreneurial avenues are expected to have self-motivation and many promising personal attributes owing to risk taking and creativity [24].

The relevance of this research is impactful in the broad scope of engineering and education and encompasses several stakeholders including students, educational institution, the industry and government. Thus, entrepreneurship education is highly interdisciplinary [28]

If provided with sufficient educational methods; the integration of these personal attributes along with taught skills can lead to the creation of an enterprise [7] It is prevalent that such education is best received when the lecturer conducting lessons has personal interest and experience in the practicalities of entrepreneurship and that they can drive a change or reinforcing of this mindset to students with intent[8] Courses are expected to induce high level thinking while handling conceptual and technical knowledge, with a key direction of engaging students in several unconventional teaching methods.[21]

A multi-step approach which involves an understanding of the correlation between many variables such as entrepreneurial intent, awareness and education on an undergraduate students' technical and transferable skillset will be investigated. This study will take a robust approach involving an iterative model to understand the gap in curriculum for chemical engineering students with entrepreneurial intent. Using key findings from the model, insights from interviews and taking a broad view of course development, a course outline will be created. Emphasis will be given to developing technical and transferrable skills between many taxonomies available in literature. Particularly Bloom's Taxonomy will be used to design the module objectives to evoke higher order learning and cognitive thinking skills.

Background

There is a continuous transformation in entrepreneurship pedagogies as the field of entrepreneurship becomes more dominant and promising as a career avenue. This is driven by increasing demand from industries and the market [23].

The general trend shows an increase in entrepreneurship education across many domains. New interdisciplinary programs use faculty teams to develop programs for the non-business students, and there is a growing trend in courses specifically designed for engineering and science students.

Whether or not entrepreneurship can be taught and how to deliver this effectively has been under investigation for years [10] and it is becoming prominently evident that necessary skills can be honed with the right mode of entrepreneurial education [11] and the effectiveness of such modes

have been predominantly driven by intention. [12] Entrepreneurial intent is a result of an individual's personal independence, self-fulfilment and self-discipline [H]. Student's personal motivation and intellectual curiosity are major drivers as is documented in literature [15] Previous research has been done in drawing links between entrepreneurial intention, awareness, self-efficacy and the role of entrepreneurship education [16][26]

Some entrepreneurship research examines the impact of intention and learned behaviours on actions of an individual and their performance capability [17]. The effect of perceived norms and social norms have also investigated and were found to have a moderating effect on the outcomes. [27] In another research, a model variant that includes EE as a strong determinant of EI was developed [26]. This model shows that the family background and personality traits have a direct impact on EI of an individual and it also appreciated that education developed a sense of initiative. Whereas earlier models justify the use of full correlations, recent studies have instead shown the partial effects of these variables, which introduces the significance of cognitive traits.

Whilst such models have been improved and documented in research, only few investigations explore these model in relation to developing or further improving education. Entrepreneurial education in higher education institutions should be fully reviewed and changed. Clear goals should be set regarding the development of graduates who are more entrepreneurially oriented.

In the initial research of the entrepreneurial landscape, the UCAS website [35] was used as a means of identifying current entrepreneurial options available to students in Russel Group universities. These universities are the most comparable to Imperial due to having similar standards of entry and receiving similar funding from the government. Several filters were used to focus the results. The course had to have at least one module of Entrepreneurial Studies. To ensure that cultural and social norms were as consistent as possible, only universities in England were looked at. In addition, only the upper end of the UCAS Tarif at 144+ was observed to better isolate the presence of Russell group universities. Using these filters 7 Russel Group universities were found to offer courses with entrepreneurship of which only 2 had entrepreneurship in the title. These courses were all tailored towards business students. The only exception was Manchester university which offered a biology based entrepreneurial course. Also evident was that universities of all types tended to offer entrepreneurial studies in relation to the creative arts. This is theorised to be due to the lower initial investment of a start-up in these fields compared to engineering

Methodology

Two key methods of data collection were employed during this research; a survey (modified version of the Liñán and Chen questionnaire) [37] and interviews.

Methodology - Questionnaire

The data for this study was collected from 110 undergraduate students in their second, third or fourth year of study from the Department of Chemical Engineering at Imperial College London. First year undergraduates were excluded from the study as they were considered to have not had sufficient time to formulate a career goal [27].

A modified version of the Liñán-Chen questionnaire catered to chemical engineers was handed out using the online survey software Qualtrics. A third of students voluntarily replied expressing their views with two students (one male and female) per year being interviewed as part of a focus group. Alongside these students, three recently graduated alumni and two academics pursuing entrepreneurial activities were also interviewed.

Based on the literature review, the Liñán-Chen questionnaire was deemed to be the most appropriate to use as it is a validated survey and was created with the intention of standardising comparison of entrepreneurial research. It is a questionnaire with each determinant being measured using a multi item scale where respondents are asked to indicate their level of agreement/ knowledge on a 7-point rating scale from 1 (total disagreement to 7 (total agreement). It measures intention, abilities and attitudes but also has the capacity to measure knowledge of the entrepreneurial landscape, family background, work experience and career goals. Furthermore, the robustness of this questionnaire has been tested over many cultures and social settings.

The survey was modified before being sent out to students, in order to gather more concise data, in line with the research objectives. All scales were narrowed down to a 5-point system to reduce ambiguity and the number of statements relevant to

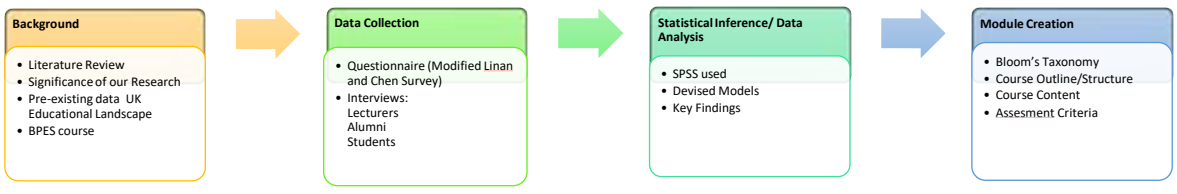

Figure 2 – Flowchart showing the outline and stage composition

each attribute are summarised in (A.3). A new section was added which focused on technical aspects of chemical engineering - this modification was necessary because the original survey was not intended for the explicit creation of a course. During the modification process, questions that explored barriers of entry were added for a more complete idea of challenges faced by students who intend on pursing a role in technical entrepreneurship. Finally, several open-ended questions were also added to gather thorough insight of individuals' thoughts and ideas.

Interviews

Several face-to-face interviews were conducted to further consolidate findings and understand key takeaways based on the personal experience of academics involved in the entrepreneurial landscape, immediate graduates who have successfully created a start-up and a focus group of students.

Questions asked from academics were (A.2.1) regarding their experience with entrepreneurship, the teaching of entrepreneurship, what technical areas need to be addressed in education tailored to chemical engineers, what the major barriers to entry are for undergraduates and what fields seem the most promising in industry. Questions for alumni (A.2.2) were focused more so on the path taken to get there, what support was provided from the college and what was lacking in curricula that needs to be implemented. The data gathered from the interviews are qualitative and were used to reinforce decisions on course content and for complete understanding of Imperial's existing system for supporting entrepreneurship.

Student focus groups were utilised to answer questions regarding their experiences, career goals, the risks and limitations they see in entrepreneurship and what support they would like in the future.

Data Analysis

The survey contained several questions which asked students to state their agreement with statements in a set. The 5-point scale was used which ranged from very negative (1) to very positive (5) answers. The mean of each individual statement set was then taken as the value of the variable; and as such survey analysis was easy to quantify yet vigorous.

It was necessary to isolate the areas lacking in the current entrepreneurial skillset of students. For this reason, the skills were subdivided into two variables. The first was Entrepreneurial Specific Skills (ESS). These are skills that would prove especially useful to students pursuing entrepreneurship over other career paths such as financial awareness, knowledge of laws and marketing. The average response over 11 statements from Q41 were used. The second is Entrepreneurial

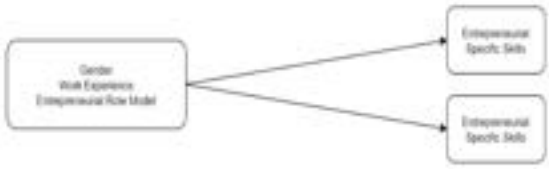

Figure 3 – Initial stage of hierarchal regression

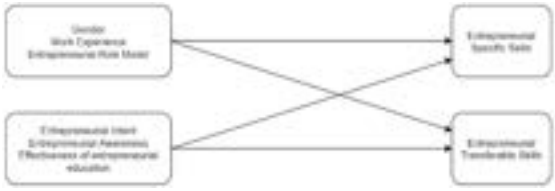

Figure 4 – Second stage and final stage of hierarchal regression

Transferable Skills (ETS) which are skills beneficial to any career such as innovation, communication, and resilience. The average response of 7 statements from Q34 were used.

To understand how to best augment the skillsets of the students, the effect of 3 independent factors were analysed. The first is the Entrepreneurial Intention (EI) of the student evaluated over 10 statements from Q23 and Q26. These range from the attractiveness of the career path to their determination to start a firm. The second looked at their awareness of the entrepreneurial environment (EA) encompassing knowledge about several entrepreneurial support bodies inside (e.g. entrepreneurial society) and outside imperial (e.g. Engineering council). The average response of 10 statements from Q17 and Q18 were used. Lastly the Effectiveness of Entrepreneurial Education (EEE) was explored. This is the perceived benefit that students have received from existing entrepreneurial courses. This was done by averaging the response of 5 statements about how the education improved several "soft aspects" such as general entrepreneurial knowledge and the preference to be an entrepreneur.

Several controls were also used to ensure accurate depictions of data. These are the gender of

Variable	Statements Analysed	Cronbach Alpha
ESS	11 (Agreement 1 – 5)	0.928
ETS	7 (Agreement 1 – 5)	0.806
EI	10 (Agreement 1 – 5)	0.949
EA	10 (Agreement 1 – 5)	0.939
EEE	5 (Agreement 1 – 5)	0.911

Table 1 – Table of variables showing the number of statements analyzed, the answer range and Cronbach's Alpha

the student (G), whether the student had previous work experience (WE) and if the student had a role model who was an entrepreneur (ERM). The latter two consisted of a simple question asking if they

have had work experience/an entrepreneur role model (Yes=1, No=0). The former had a question asking to identify their preferred gender (Male=0, Female=1, Other=2, Not specified=3).

A dual model approach was used. The first used ESS as the dependent variable and the second used ETS as the dependent variable. All calculations mentioned here forth were done using the SPSS data handling software. This software was chosen as it has the capacity to quickly calculate all statistical values required and the data is easily exported to and from Qualtrics. Firstly, Cronbach's Alpha was calculated as shown on Table 1 per statement set, to test the internal consistency. Hierarchal regression was then used to test the effect of the Pearson Correlation (R) on each model. This method was used as it allows the effect of one variable on a dependent to be observed whilst under the moderating effect of other variables. Initially in each case, the impact of the control variables on the dependent were assessed to ensure that they had no statistically significant input into the variance of the dependent. Following this the independent variables were added for regression. The variance inflation factor (VIF) was also calculated to ensure that the independents had no highly linear relation which may skew the results. A single tailed test at the 95% confidence interval was used in all cases to test significance.

Results and Discussion - Initial Observations

Sub- Model	R	R Square	R Square Change	F Change	Sig. F Change
1.1	0.502[a]	0.252	0.252	1.794	0.189
1.2	0.926[b]	0.858	0.607	18.564	0.000*
2.1	0.407[a]	0.166	0.166	1.389	0.274
2.2	0.773[b]	0.597	0.432	6.438	0.004*

Table 2 – Table showing models and sub models of hierarchal regression

	Mean	Std. Dev	Std. B	Sig	VIF	ESS	G	WE	ERM	EA	EI	EEE
ESS	2.735	0.927				1.000	-0.011	0.010	-0.237	0.824	0.475	0.169
G	0.640	0.860	-0.034	0.818	1.314		1.000	0.155	-0.156	0.005	0.220	0.003
WE	0.400	0.500	0.135	0.416	1.649			1.000	0.036	-0.106	-0.378	0.125
ERM	0.280	0.458	0.031	0.822	1.157				1.000	-0.322	-0.299	-0.094
EA	2.059	0.978	0.901	0.000	2.173					1.000	0.676	0.355
EI	3.588	0.855	0.012	0.961	3.511						1.000	0.458
EEE	3.408	1.017	-0.169	0.295	1.554							1.000

Table 3 – Table showing results of model 1.2

	Mean	Std. Dev	Std. B	Sig	VIF	ESS	G	WE	ERM	EA	EI	EEE
ETS	3.503	0.583				1.000	-0.324	-0.065	-0.192	0.651	0.380	0.456
G	0.640	0.860	-0.297	0.100	1.314		1.000	0.155	-0.156	0.005	0.220	0.003
WE	0.400	0.500	-0.045	0.819	1.649			1.000	0.036	-0.106	-0.378	0.125
ERM	0.280	0.458	-0.052	0.751	1.157				1.000	-0.322	-0.299	-0.094
EA	2.059	0.978	0.622	0.011	2.173					1.000	0.676	0.355
EI	3.588	0.855	-0.147	0.607	3.511						1.000	0.458
EEE	3.408	1.0173	0.304	0.120	1.554							1.000

Table 4 – Table showing results of model 2.2

From the data it can be seen that of the 110 students partaking in the survey 54.4% are from outside the UK with 23%, 19% and 48% from second, third, and fourth years respectively [A.3]. It was gathered from the interviews that fourth-year students are more inclined to consider all career prospects due to their imminent graduation hence the larger participant ratio in the survey. Further stats show 39.1% of participants are female, 40% have some form of work experience and 28% have a role model whom is an entrepreneur. This shows that the spread of participants is fairly representative.

Respondents show an overwhelmingly positive favour towards extra entrepreneurial education being provided as a course or module with 48.1% preferring it as their main form of entrepreneurial support as shown on graph X. For this reason, a course will be the only education medium considered moving forwards. A majority (69.7%) also wish for this support to be tailored towards chemical engineers. Despite this, only 39.7% of students would prefer to pursue entrepreneurship in a chemical engineering sector. This can be inferred as a consequence of the low awareness exhibited by students (2.059) shown in tables 3 and 4. Students lacking awareness will be unaware of prominent fields of chemical engineering to pursue entrepreneurship. However, the question itself is fairly restrictive as the non-chemical engineering option covers considerably more sectors. Another reason may be the tendency of chemical engineering students to apply their transferable skills and mindset to other sectors, as brought up during the interviews by alumni. By consideration of both these factors, the value is not wholly unexpected and is still significant enough that the department should consider providing additional support for these students. The proposed course whilst focused on chemical engineering should still support students with intent in other sectors. When asked about which year students would prefer the course to be introduced, most preferred third year. This is a reasonable point at which to introduce such a module as it may be included in the list of electives available. Second and fourth year accumulated similar votes with there being a clear preference against first year.

When directly asked, a majority of students listed “lack of knowledge of start-up ecosystem”, “lack of financial knowledge” and “lack of knowledge of laws/regulations” as their perceived barriers to entry. These all fall under ESS and should therefore be aspects of focus on the specific skills section of the module. When asked which transferable skills to include, many students showcased indifference answering yes to inclusion of all listed skills [A.3]. As student generally ranked themselves much higher for ETS (3.503) than ESS (2.735) a major focal point should be addressing the weaknesses brought forth for specific skills.

Many students, in both interviews and the survey, state that the current workload of chemical engineering requires too much memorisation and that entrepreneurship is learnt better via application. Thus, when considering assessment for the module, the proposal of a standard examination received very negative feedback. A coursework style project-based assessment was proposed instead which garnered more positive feedback. This is in line with previous research [25].

From table 3, students in chemical engineering show an above average EI (3.588) stating it as an “attractive” and “satisfying” career path given the “opportunity and resources”. When asked simply “have you considered becoming an entrepreneur”, 44.1% of students answered yes with another 32.4% considering it. In fact, 73.2% of respondent’s valued entrepreneurship as being equal or greater than another career path. The outlying issues lie in that many consider entrepreneurship to have more disadvantages than advantages. 77.4% of people consider entrepreneurship to be too risky and consider engineering as a safer choice. 53% state they lack the knowledge of the practical details with 59.1% citing they lack the funds to pursue the venture. The module created should to this end help provide this know-how by covering risk mitigation and loan acquisition strategies to circumvent the above issues. It is also noteworthy that EI displays significant negative correlation with WE and ERM i.e. students with work experience and/or entrepreneurial role models are less likely to want to be entrepreneurs. For WE, this can be inferred to be due to the propensity of students to undertake work experience due to it boasting higher employment rate [36]. Therefore, these students are more inclined to find employment than become entrepreneurs. In the case of ERM however, it is likely due to many respondents having a lack of knowledge of their role model’s entrepreneurial activities with most having only some (28.6%) to moderate (28.6%) understanding with very few expressing an in-depth understanding (11.9%). These relations however are not the focus of this project but lay the foundation for future research.

EEE is also above average (3.4080) highlighting the importance of relevant entrepreneurial education. 37.3% of students have taken what they consider to be courses that are entrepreneurship education. These are unanimously business-related courses demonstrating the lack of entrepreneurial content in base chemical engineering [A.3]. A large majority of students have gained decent benefit from taking the courses with 88.8% of students having stated that EE given by Imperial has increased their knowledge of the entrepreneurial environment by a moderate to great extent. All these finding consolidate previous literature [A.3]. A further 88% state that the courses have similarly improved their necessary abilities to

be an entrepreneur. 68% also expressed increased intention and preference to be an entrepreneur showing that the presence of entrepreneurial education is effective at promoting entrepreneurship as a viable career path and students' favour towards it. EEE does however also express the most standard deviation of all variables.

EA is the only variable expressing a lower-than-average response. Students are generally unaware of all the resources available to them via a multitude of organisations both within and outside Imperial. Even the most commonplace ones such as IChemE and the Imperial College Student Union have as much as 68.9% and 44.6% respectively of respondents expressing no understanding of the support given. This is a major issue that needs to be addressed in the module.

Results and Discussion – Statistical Model

The initial internal consistency of the Liñán-Chen survey is very high as it is a validated survey. As modifications were made it was necessary to ensure that this was still the case. The Cronbach's alpha for all sets of statements in the modified survey is well above the recommended value of 0.7 and hence continue to display high internal consistency. In addition, the variance inflation factors are much lower than 10 therefore, the issue of multicollinearity is non-existent.

As seen in table 1 sub-model 1.1 shows that the impact of the G, WE and ERM variables on the variance in both models are not statistically significant. Hence it is possible to progress the hierarchal regression. Sub-model 1.2 shows statistical significance in the R square change as per the F test. From tables 2 and 3 it can be seen that EA is the only independent variable for which the Beta value (0.901) is significant ($0.011<0.05$). In other words, as EA increases an almost equivalent change is observed in ESS. This reemphasises the importance of addressing awareness in the course as it has a substantial impact on ESS. Other independent correlations are also observed to isolate individual impacts. EI and EA independently show strong correlation with ESS at 0.824 and 0.475, respectively. Intention should therefore also be nurtured in the course. This is however less of an issue as shown previously, the mere presence of relevant entrepreneurial education is sufficient to elevate EI. This ties in with existing research [26]

Model 2.1 shows a similar trend to model 1.1 with the control variables being insignificant. Likewise, model 2.2 only has the beta coefficient of EA as significant although it is considerably lower. Hence EA, while still significant in developing ETS, is more effective in developing ESS. In terms of independent correlations, EI and EA are still significant although less so and do not need to be directed as much to improve ETS. The only other difference is that EEE is also significantly correlated to ETS. This implies that current entrepreneurial education is effective at improving ETS but less so at improving ESS. Therefore, the course needs to focus on addressing ESS over ETS.

On their own all independent variables show varying degrees of positive correlation with ETS or ESS however EEE in sub-model 1.2 and EI in sub-model 2.2 show a negative beta value. This phenomenon occurs as the beta coefficient accounts for all variables in the system whereas the correlations isolate the individual impact of a variable on the dependent. EI and EEE are particularly vulnerable to this as they express more significant correlations with other independent variables when isolated.

Results and Discussion – Interviews

The key insights from interviews with lecturers in business and chemical engineering were around the significant growth and scope for enterprise in certain sectors such as biotechnology and environmental engineering. This is supported by literature and the direction of growth in the chemical engineering industry as a whole [5][30]. Lecturers also mentioned that the lack of awareness was because students did not have links with relevant industrial professionals who might be looking for a specific technological solution. However, given Imperial College London's close links with industry, this collaboration would be sufficiently simple to implement and must be provided to students with entrepreneurial intention to provide a solid base for education.

From interviews with lecturers it is also apparent that entrepreneurial support is generally only made at available at PhD or Postgraduate level and is lacking for undergraduates; this is more relevant to academic enterprise rather than technical enterprise but focus must be given to implementing a supportive framework for undergraduates who want to pursue entrepreneurship. This circumvents the issue of a student's efforts towards entrepreneurship being delayed due to insufficient support at an undergraduate level.

Lastly after mentioning the intention to create a course of entrepreneurial support, the lecturers suggested that the course either focus on promoting entrepreneurship or assisting existing students with entrepreneurial intent but not both. Due to the already high intention amongst students, the latter was decided as the focal point especially since the presence of effective education has already been shown to increase EI and hence no extra focus is required. In relation to this, the high failure rate of start-ups was also addressed. As mentioned previously, this is what incurs the high perceived risk of entrepreneurship and will be tackled in the form of risk mitigation strategies [31].

Based on interviews with alumni, the most prevailing consensus is the transitioning to Industry 4.0, the need for innovation and how there is so much potential for undergraduates to explore these innovative technologies to create a start-up. It was mentioned that Opportunity Recognition is a key aspect of any enterprise and that these avenues can be introduced to students as part of a course. Alumni gave feedback on how the existing framework naturally expects undergraduates to take up a job or continue with further studies upon graduation and that the entrepreneurship route is not focused on. However, with the right framework and the provision of necessary support, students with such technical knowledge and high order cognitive skills would be encouraged to take up alternate graduate routes.

Another key goal highlighted was to expose students to already existing external organisations and the support they may provide at an undergraduate level until such a framework is implemented within the College. Also, the idea of allowing creativity to manifest and reducing the restriction imposed through assessment and exams was mentioned and thus, the idea of the main assessment being the development of a 'proof of concept' for a technological solution was suggested. Therefore, the module will be assessed on how innovative the solution is, to what extent it works to address the industrial problem and how well it is received during the pitch by industrial experts and investors.

Creating the Course

Figure 5 – Diagram of Bloom's Taxonomy

The key findings from Model 1 and Model 2 were used, along with input from interviews with lecturers in business and chemical engineering and feedback from students and alumni, to formulate a module. The module focuses on the development of both ETS and ESS with an extensive focus on EA, due to the significance of it being emphasised by both models and the general lack of awareness by students. Imperial College London's framework for new programme proposal was used to create an outline of the module. The final outline is a 12-week module comprising of 12 lecture hours and 10 hours of enterprise based technical project work.

The course content is differentiated from existing entrepreneurship modules with a key focus on educating students and creating awareness of technological aspects in addition to generic entrepreneurial skills; these comprise of but are not limited to the understanding of emerging technologies in the Chemical Engineering Industry, barriers to entry in scientifically advanced domains, the importance of Intellectual Property and relevant regulations and law[32]. This course is intended to fill the gap in skillset particularly ESS that is not covered by the currently available BPES entrepreneurship modules. A.0 in the appendix shows the course details with a week to week outline with suggested sample learning objectives for each week, these were devised using action verbs obtained in relation to Bloom's Taxonomy. As gathered from research, entrepreneurship cannot be learnt just by teaching and some personal traits need to be inherent in a student from the start. Thus, teaching methods must involve many open-ended discussions and debates with lectures creating a space for discussions which elevate creativity, stimulate innovative thinking, and develop higher order cognitive skills.

As suggested by lecturers and alumni entrepreneurs, the assessment of this module was devised in a way to learn by doing and as such, it will consist of two summative assessments; an essay (10%) a summative report (30%), followed by one final enterprise pitch (60%) with the key criteria being the development of a technologically sound working 'proof of concept' model that addresses an industrial issue. The pitch panel must consist of external stakeholders including industrial experts and investors. In order to successfully carry out this project; students will be connected to industrial personnel and this collaboration will direct students and focus their interest in areas of industry that require solutions from technical enterprises thus paving the pathway to building a proof of concept.

Conclusion

After conducting the initial background research, a lack of tailored support was identified in entrepreneurial education provided to engineering students. Overall, students studying chemical engineering at Imperial College London displayed high intent showing that the lack of tailored entrepreneurial education was not due to a lack of interest. In fact, students preferred chemical engineering tailored entrepreneurial education. A general lack of awareness of available support was identified amongst students. Awareness was also found to be the most important aspect to develop both entrepreneurial specific and transferable skills. Furthermore, existing entrepreneurial education

provided at Imperial was found to be subpar in stimulating entrepreneurial specific skills but sufficient for entrepreneurial transferable skills. A medium of entrepreneurial support was therefore to be designed to fill the gap. An elective was the desired form of entrepreneurial support with 3rd year being the preferred time of introduction. This course was then designed to explicitly address the afore mentioned problems. The objectives of the course are to utilise higher orders of Bloom's Taxonomy to inspire creative thinking. Other key factors included are industry 4.0 and growing chemical engineering fields. Lastly due to the inherent mindset needed for entrepreneurship, a coursework assessment method was utilised to encourage learning through actions. As this module was designed heavily based of student input, the students are co-creators and as such are incentivised to follow through with their commitment to the course. This is unique to existing entrepreneurial courses.

Limitations

There are several limitations to this research – the first and most prominent limitation is one that is common in the pedagogical research domain which is the reliance of self-evaluation of individuals when attempting a questionnaire. This judgement is hard to normalise however we believe that this was mitigated by using a validated and robust questionnaire. Another limitation is that participants are human and are subject to acquiescence bias which might have added extra ambiguity and a over predicted positive intention, but the surveys were conducted anonymously and thus it would have prompted participants to respond more genuinely. Lastly this is a forerunner concept for research as this specific area of incorporating entrepreneurship into chemical engineering curriculum has not been addressed before and so requires further research to develop on this foundation.

Recommendations

- While the module recommended by this project should prove useful in addressing the student's skill gap, it is crucial to understand that it is an initial concept. The module itself must be trialled and amended based off feedback from trained educators and students. This should be done in an iterative process.
- Following this it is necessary to run another survey to record the change in the student's self-assessment after the module has been implemented to see if it has succeeded in bridging the skill gap and how it may still be improved.
- As mentioned before, there also exists the potential for future research to further narrow and eventually close the engineering entrepreneurial education gap.
- Highlighted in the model were several significant correlations such as that of EI with ERM and WE. While explanations were proposed for these relations they were not explicitly tested. As entrepreneurial intention is a common area of research, exploration of these relations may prove productive.
- Other areas highlighted for development are the relations interchangeably between EI, EA and EEE. As is often the case in a focused study such as this, the independent variables may not be fully independent, and any such interrelations need to be examined.

Acknowledgements

We would like to thank Dr. Marsha Maraj for all her supervision and support throughout this research project and her guidance for the direction of the research. We would also like to thank Dr. Klaus Hellgardt.

References

1. Vision 2020: Computational Needs of the Chemical Industry)
2. Daugherty et al., (2015)
3. Mckinsey Digital (2016)
4. Education in Chemical Entrepreneurship: Towards Technology Entrepreneurship for and in Chemistry-Related Enterprises Wolfgang Runge and Stefan Bräse. (2009)
5. Managing Innovation: Integrating Technological, Market and Organizational Change Tidd, Bessant and Pavitt 2001:352 (2005)
6. Knowledge Based View of University Tech Transfer—A Systematic Literature Review and Meta-Analysis (2020)
7. What's hot in entrepreneurship research 2013? Andreas Kuckertz (2013)
8. Entrepreneurship and Enterprise Education in Schools and Colleges: Insights from UK Practice, Allan Gibb (2017)
9. Innovative Teaching Methods and Entrepreneurship Education: A Review of Literature B.Adedeji (2018)
10.
11. The emergence of entrepreneurship education Kuratko (2005),
12. ((Kuehn, 2008).
13. (Gartner & Vesper, 1994)
14. (Martin, B.C., mcnally, J.J. and Kay, M.J. (2013). Examining the formation of human capital in entrepreneurship: A meta-analysis of entrepreneurship education out-comes. Journal of Business Venturing, 28: 211–224 https://doi.org/10.1016/j.jbusvent.2012.03.002
15. (Kuratko and Naffzier, 1993–4; Young, 1997).
16. Martin et al., 2013, Souitaris et al., 2007).
17. Krueger et al., 2000,
18. (B9_Bae et al., 2014, B31_Chen et al., 1998.
19. Cross-faculty proximity and academic entrepreneurship: the role of business schools M. Goethner (2019)

20. Startups by recent university graduates and their faculty: Implications for university entrepreneurship policy T. Astebro (2012)
21. Enterprise and Entrepreneurship Education: Guidance for UK Higher Education Providers (2018)
22. UK University Technology Transfer: behind the headlines (2015)
23. Entrepreneurship and Enterprise Education in Schools and Colleges: Insights from UK Practice Allan Gibb 2017
24. The moderating role of higher education on entrepreneurship Zeliha İlhan Ertuna, Eda Gurel (2011)
25. When theory is invisible and hidden in practice - a qualitative study of one entrepreneurship course (2016)
26. Entrepreneurial Intention among Engineering Students and Its Main Determinants Emilia Hermana, 0F* 2019
27. Entrepreneurial Intention of Engineering Students: The Role of Social Norms and Entrepreneurial Self-Efficacy 2019
28. Developing Professional and Entrepreneurship Skills of Engineering Students Through Problem-Based Learning: A Case Study in Brazil 2020
29. The impact of new technologies on the labour market and the social economy 2018
30. Industrie 4.0: What Does It Mean for Chemical Companies? Valentijn de Leeuw (2017)
31. A risk mitigation approach for concurrent engineering projectsb. Kayis (2008)
32. The significance of studying legal protection of rights on innovative creations: the case of entrepreneurship education r. Zakieva et al. (2019)
33. Entrepreneurship, start-up costs and employment R. Fonseca (2001)
34. Innovative Teaching Methods and Entrepreneurship Education: A Review of Literature B. Adedeji et al (2018)
35. https://www.ucas.com/ [Accessed October 2020]
36. https://www.prospects.ac.uk/jobs-and-work-experience/work-experience-and-internships [Accessed November 2020]
37. Liñán, F., & Chen, Y.-W. (2009). Development and Cross-Cultural Application of a Specific Instrument to Measure Entrepreneurial Intentions. Entrepreneurship Theory and Practice, 33(3), 593-617.

Data-Driven State of Charge Estimation in Li-ion Batteries under Dynamic Operating Conditions

Cox Joseph
Department of Chemical Engineering, Imperial College London, U.K.

***Abstract*—Lithium-ion batteries are predicted to dominate the Electric Vehicle (EV) market for the next decade, with further applications in consumer electronics and energy storage. Li-ion batteries have high sensitivity to battery operating conditions; Therefore, the role of a Battery Management System, to ensure the battery operates safely and reliably, is critical in Li-ion batteries. State of charge (SOC) is a key indicator of the current state of a battery. This study takes a data-driven approach to develop accurate SOC estimation models. LIONSIMBA, a Li-ion Simulation Battery Toolbox, is used to simulate dynamic battery data which resembles operating conditions and loads seen in real-world applications. The data generated is used to train and test three different neural network structures: A simple recurrent neural network, a nonlinear autoregressive network with exogenous inputs (NARX) and a long short term memory network (LSTM). Network fitting and generalisation performance is tested against established EV battery discharge regimes, at constant and varying ambient temperature. The results show that the NARX network is accurately able to estimate SOC under dynamic loads, with a Root Mean Square Error (RMSE) of less than 0.2% for the Urban Dynamometer Driving Schedule (UDDS), at constant and varying ambient temperature.**

***Keywords*—Li-ion batteries, State of charge, Recurrent neural network, Battery Management Systems (BMS), Electric vehicles**

I. Introduction

An insight report published by The World Economic Forum predicts global battery demand will grow by a factor of 14 between 2018 and 2030 (The World Economic Forum 2019). Battery applications fueling this growth include electric mobility, energy storage and consumer electronics. A battery technology which has seen considerable advancements in performance, and reduction in price is Lithium-ion (Li-ion) batteries; Li-ion battery prices for electric vehicle applications have fallen by almost 90% since 2010 (IEA 2020*a*). In comparison to alternative battery technologies, Li-ion batteries have a high specific energy, low self-discharge rate and long cycle-life (Yu et al. 2017). A disadvantage of Li-ion batteries is that they are highly sensitive to battery operating conditions; Thermal runaway and battery degradation can be caused by by mechanical, electrical or heat abuses (How et al. 2019). Innovation in the area of battery technology has been 'spearheaded' by lithium-ion batteries, particularly for Electric Vehicle applications (IEA 2020*c*).

A battery consists of the battery, and also the battery-management-system (BMS). The BMS controls the battery during operation to ensure that it operates safely and reliably (Chaturvedi et al. 2010). Additionally, the BMS handles cell balancing and thermal management of the battery (Hannan et al. 2017). In order to do this, the BMS must monitor the current state of the battery. One of the key indicators of a battery's current state is the state of charge:

$$SOC = \frac{C_{curr}}{C_{full}} \tag{1}$$

where C_{curr} is the capacity of the battery in its current state and C_{full} is the capacity of the battery in its fully-charged state (Ng et al. 2020). SOC is a key indicator which is not directly measurable. It remains complex to model due to the non-linear and time-varying dependencies which it admits (Hannan et al. 2017). Accurate SOC estimation can improve battery lifespan, ensure safe and efficient operation, and also improve range predictions.

Li-ion batteries are likely to dominate the EV market for the next decade (IEA 2020*b*). Li-ion batteries used in electric vehicle applications experience a broad range of operating conditions throughout their lifetime. Key variables including power/current load, initial and final SOC, ambient temperature and battery temperature can vary greatly across driving cycles and battery lifetime; These fluctuations are observed in battery data from real EV driving cycles (Trifonov 2020).

The key contributions of this study are as follows:

- LIONSIMBA, a Li-ion Simulation Battery Toolbox by Torchio et al., is used to generate dynamic battery data which resembles operating conditions and loads seen in real-world applications
- Three shallow neural network structures are trained and tested using generated simulation data, under additional uncertainties such as varied initial SOC and ambient temperature
- Model performance is tested under established electric vehicle battery discharge regimes

II. Background

A. SOC Estimation Methods

SOC estimation methods can be categorised by 5 main methodologies (Xiong et al. 2017):

1) **Look-up table methods** rely on physical properties and parameters which can be directly measured such as Open Circuit Voltage (OCV), Terminal Voltage and Impedance. Look-up tables map the relationship between measurable properties and SOC.

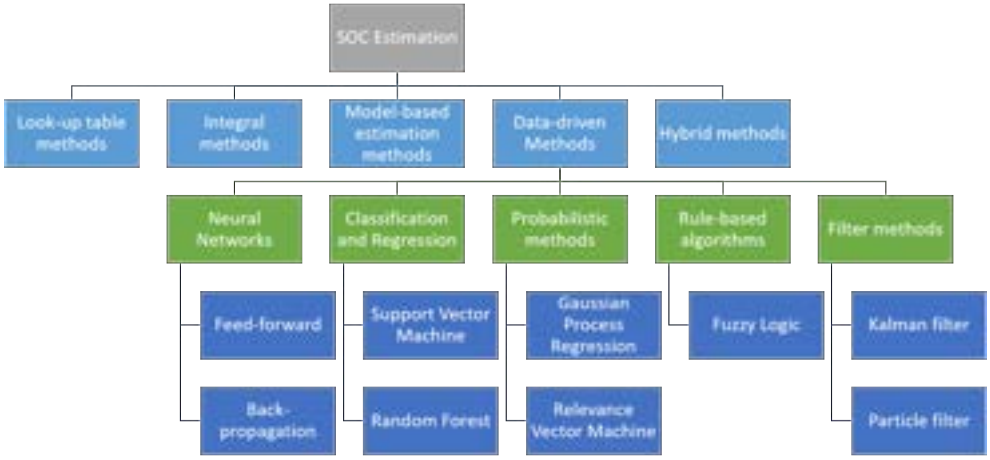

Fig. 1. SOC Estimation Methods

2) **Integral methods** use charge/discharge current as an input, and are often referred to as Coulomb-counting methods. A limitation of these methods is that the initial SOC must be known.
3) **Model-based estimation methods** include electrochemical models, equivalent circuit models and electrochemical impedance models. Electrochemical models, also known as Physics-based models, are computationally demanding to solve (Ng et al. 2020). The development of these models also requires a lengthy amount of time and extensive experimentation (How et al. 2019). Equivalent circuit models are based on small AC-signal perturbations of the battery; This means they have a limited applicability (Chaturvedi et al. 2010). In spite of this, ECMs are the major models that are widely used in BMS, for online SOC estimation (Ng et al. 2020).
4) **Data-driven estimation methods** are able to accurately model the nonlinear relationship between input(s) and output(s), without requiring in-depth knowledge of battery parameters. The performance of these models is heavily reliant on the quality and quantity of training data (Hannan et al. 2020).
5) **Hybrid methods** combine multiple approaches in order to benefit from the advantages of each (Hannan et al. 2017). These can combine data-driven and model-based estimation methods to provide accurate, online SOC-estimation.

B. Comparing model-based estimation and data-driven models

Model-based estimation methods, particularly electrochemical models, are able to achieve good accuracy and robustness if parameters are accurately determined, but they generally offer a slow online execution time (Hossain Lipu et al. 2020). Conversely, data-driven models provide fast execution time, and can also achieve good accuracy if data is sufficient (Ng et al. 2020). Another advantage of data-driven models is that in-depth knowledge of Chemical and Physical processes is not required, so data-driven models can be developed in a shorter time-frame (Hannan et al. 2020);

C. Data-driven models

Figure 1 shows some of the most prominent data-driven techniques used to estimate state of charge in Li-ion batteries. Ng et al. and Hossain Lipu et al. through their reviews of data-driven models, found that the most common inputs for SOC estimation are current, voltage and temperature. Li et al. found that battery temperature and discharge time were the main influence factors on state of charge under dynamic discharge. There are a diverse range of methodologies used to collect experimental battery data. Additionally, a varied combination of established battery datasets are used to train data-driven models. This makes it difficult to directly compare different data-driven techniques for SOC estimation. Although neural networks are expensive to train relative to other techniques, they often yield the best fitting function when a large quantity of data is available (Ng et al. 2020).

D. Data generation for dynamic modelling

The data used to train and test data-driven models is often limited to experimental data, and established battery datasets such as NASA's randomized battery usage datasets (Bole et al. 2014). The range of operating conditions that can be simulated in the lab are bounded; As stated by How et al., 'LIB can be subject to more environment dynamics in a real-world application that can never be simulated in the laboratory.' They went on to suggest that SOC estimation models should be analysed under various uncertainties such as temperature, aging cycle, and noise effects.

III. Methods

A. Data Generation

LIONSIMBA is a Li-ion Simulation Battery Toolbox developed by Torchio et al.. This toolbox consists of a set of fully customizable functions implemented in MATLAB (MathWorks® 2020*d*) and is suitable for simulating the

dynamic behavior of Li-ion batteries (Torchio et al. 2016). This toolbox uses a finite volume method for a pseudo two-dimensional (P2D) Li-ion battery model, where the spatial domain is discretized. The P2D model is comprised of coupled nonlinear partial-differential algebraic equations relating to the conservation of mass, charge and energy in each section of the battery. The toolbox is additionally able to model the thermal profile of the battery. The P2D model equations, boundary conditions and numerical reformulation are fully detailed by Torchio et al.. This toolbox is used extensively to simulate a Li-ion battery under varied operating conditions.

Data-driven dynamic SOC models are frequently trained and tested using dynamometer driving cycles for vehicle testing, which consist of velocity-time profiles (Hossain Lipu et al. 2020). A relationship between the acceleration of the vehicle and battery power/current is assumed. Bizeray (2016) assumed input current was proportional to vehicle acceleration, where a peak acceleration corresponded to a extreme 15C discharge rate. Conversely, Yang et al. found that current varies between approximately -4C and 2C during driving cycles. To ensure that model training and testing data resembled real-world usage, a BWM-i3 EV battery dataset consisting of over 70 driving cycles was analysed; It was found that the C-rate varied between -6.7C and 2.4C, for a $60Ah$ battery (Trifonov 2020).

The method followed by Bole et al. to generate NASA's 'Randomized Battery Usage Data Set 1' involved randomly varying current between -4.5A and -0.75A during a 'random walk' discharge, over periods of 5 minutes. As a goal of this study is to model highly dynamic battery systems such as in EVs, a 1 second period was initially selected. Input currents between the range of -6C and 3C were randomly selected following a similar methodology to NASA's Randomized Battery Usage Data Set. This method failed to accurately capture the distribution of currents when compared to real EV driving cycles, and the profiles produced was overly-dynamic (Trifonov 2020).

Alternatively, for NASA's 'Randomized Battery Usage Data Set 6', a customized probability distribution was used; Current loads were randomly selected from this distribution and applied to the battery (Bole et al. 2014). Analysing the EV battery dataset further, it was found that the the mean and standard deviation of battery currents were -8.4Am^{-2} (-0.3C) and 21.6Am^{-2} (0.7C) respectively (Trifonov 2020). Rather than a customized probability distribution, a truncated normal distribution was used. Figure 2 shows that the distribution of currents for the EV dataset is not strictly normal, but this approximation is sufficient to select current loads which resemble real-world usage.

$$I \sim \mathcal{N}(\mu, \sigma^2) \tag{2}$$

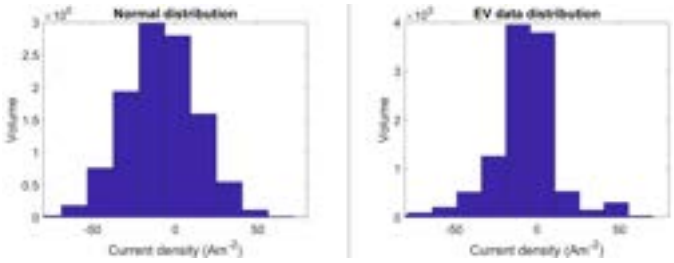

Fig. 2. Truncated normal distribution (left) and BMW-i3 EV driving cycle dataset (Trifonov 2020) distribution (right)

where I is the current density load in Am^{-2}, μ is equal to -8.4Am^{-2}, and σ is equal to 21.6Am^{-2} (The mean and standard deviation from the BWM-i3 EV battery dataset by Trifonov). This distribution was truncated between -6C and 3C. Input currents were randomly selected from this distribution and applied for a period between 0.5 and 5 seconds. This time period range was chosen so that the simulated data consists of highly dynamic, and steady periods of operation.

B. Neural Networks

An individual neuron in a neural network can be thought of as its own linear regression model. It is composed of input data, weights, biases and output data (IBM Cloud Education 2020). Each neuron input, X_i has a weight assigned to it, W_i. Each neuron also has a bias term, $bias$.

$$Z = \sum_{i=1}^{n} W_i X_i + bias \tag{3}$$

$$Y = f(Z) \tag{4}$$

The activation function is applied to the pre-activation value, Z; This yields the predicted probability, Y (Yiu 2019). The activation function is often a non-linear function, such as a sigmoid function. Three neural network structures were selected for dynamic SOC estimation: Simple recurrent neural network; Nonlinear autoregressive network with exogenous inputs, and long-short term memory network. These network structures were chosen as they have shown strong performance in estimating SOC, under dynamic current loads and operating uncertainties in previous studies (Hossain Lipu et al. 2020).

*1) **Recurrent Neural Network**:* Any network which contains a cycle within its network connections, is a recurrent neural network (Jurafsky & Martin 2019). This cycle means that the output of at least one of the neurons is dependent on the output of a previous neuron. For a simple recurrent neural network, the activation value for the hidden layer, h_t, and the output, y_t, are calculated by:

$$h_t = f_h(Uh_{t-1} + WX_t + b_h) \tag{5}$$

$$Y_t = f_y(Vh_t + b_y) \tag{6}$$

where the input and output at time t are denoted by X_t and Y_t. b_h and b_y are biases, and f_h and f_y are activation

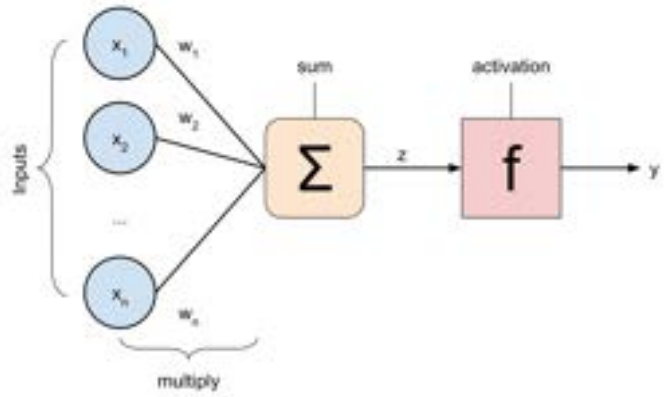

Fig. 3. Representation of a single neuron (Cingillioglu 2019)

functions. The default activation functions for layrecnet in MATLAB were used, f_h is a hyperbolic tangent sigmoid function, and f_y is a linear function. Here, W is the weight for the input and V is the weight for the hidden layer.

Figure 4 shows an example recurrent neural network structure, with 10 nodes in its hidden layer and a single node in its output layer. The input variable at time t has a dimension of 4, and is denoted by $X_i(t)$. The output from a hidden layer node is denoted by $h_k(t)$:

$$h_j(t) = f_h\Big(\sum_{i=1}^{4} W_{ij}X_i(t) + \sum_{k=1}^{10} U_{kj}h_k(t-1)) + b_{hj}\Big) \quad (7)$$

Here U_{kj} denotes the weight at node j, for the hidden layer output 'cycled' from node k. W_{ij} is the weight for input i at node j.

$$Y(t) = f_y\Big(\sum_{j=1}^{10} V_j h_j(t)) + b_y\Big) \quad (8)$$

where $i \in [1\ \ 4]$, $j \in [1\ \ 10]$, $k \in [1\ \ 10]$. As seen before, f_h and f_y are the activation functions. Figure 4 also shows the delays on each of the inputs. The regular inputs have no delay and the hidden layer output has a delay of 1.

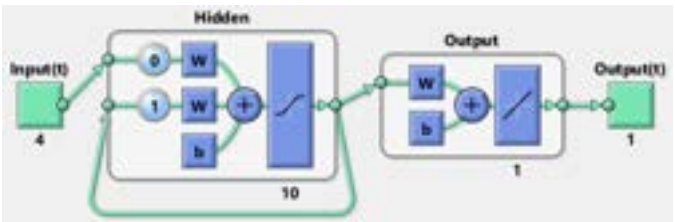

Fig. 4. MATLAB layrecnet (MathWorks® 2020*b*)

*2) **Nonlinear auto-regressive network with exogenous inputs**:* The NARX network is a recurrent dynamic network, with feedback connections that enclose several layers of the network (MathWorks® 2020*e*). It is frequently used in time-series modelling, because future output signals can be regressed against previous outputs, in addition to external inputs. Rather than cycling the hidden layer output as seen by the simple recurrent neural network, the output of the output layer has recurrent connections to the hidden layer. The hidden and output layer outputs for the example NARX structure displayed by figure 5, can be expressed as follows:

$$h_j(t) = f_h\Big(\sum_{i=1}^{4} W_{ij}X_i(t) + U_j y_{t-1} + b_{hj}\Big) \quad (9)$$

Here U_j denotes the weight for the previous output from the output layer, at node j. W_{ij} is the weight for input i at node j. The default activation functions for layrecnet in MATLAB were used, f_h is a hyperbolic tangent sigmoid function, and f_y is a linear function. $i \in [1\ \ 4]$, $j \in [1\ \ 10]$.

$$Y(t) = f_y\Big(\sum_{j=1}^{10} V_j h_j(t)) + b_y\Big) \quad (10)$$

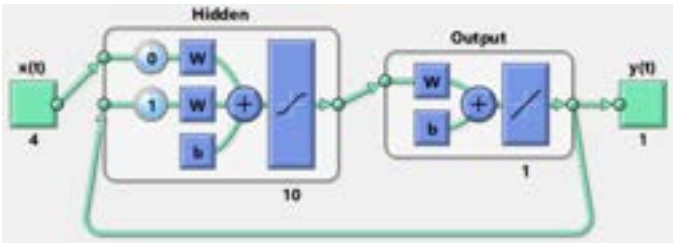

Fig. 5. MATLAB narxnet (MathWorks® 2020*e*)

*3) **Long-short term memory network**:* LSTM networks are a type of RNN that aim to overcome the 'short-term memory' problem of conventional RNN; The gradient vanishes for data that is further back in the sequence. An LSTM network selectively retains relevant information and forgets irrelevant information (MathWorks® 2020*c*). The general form for each of these outputs is (Sanjeevi 2018) (Mittal 2019):

$$f_t = \sigma(W_f X_t + U_f h_{t-1} + b_f) \quad (11)$$

$$g_t = tanh(W_g X_t + U_g h_{t-1} + b_g) \quad (12)$$

$$i_t = \sigma(W_i X_t + U_i h_{t-1} + b_i) \quad (13)$$

$$o_t = \sigma(W_o X_t + U_o h_{t-1} + b_o) \quad (14)$$

$$C_t = f_t C_{t-1} + i_t g_t \quad (15)$$

$$h_t = o_t tanh(C_t) \quad (16)$$

Where σ is a sigmoid function and the remaining variables are as defined in 5. g_t is more commonly denoted by $\tilde{c}_t$.

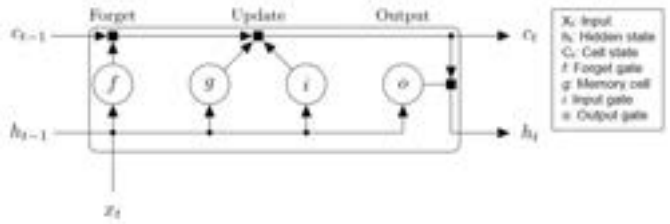

Fig. 6. Long Short-Term Memory block (MathWorks® 2020*c*)

C. Data preprocessing and Training

Each of the 3 networks were trained an tested in MATLAB (MathWorks® 2020*d*). The structure for a RNN (layrecnet) and NARX (narxnet) network, as shown by Figure 4 and Figure 5, consists of a hidden layer and an output layer. For an LSTM network (lstmlayer), the structure consists of an input layer, LSTM layer, fully-connected layer and a regression layer.

- Network inputs were Current, Voltage, Temperature and Time, and output was SOC
- All inputs and targets were normalised before training between the range of $[-1, 1]$, using minimum and maximum values
- For RNN and NARX network, target data was shifted to account for the delay
- All inputs and targets were padded so all sequences were of equivalent length
- Discharge cycles were randomly split into training and testing cycles with a ratio of 70:30, as used by Hannan et al.. The testing data was further split into validation and testing data with a ratio of 1:2.

The host computer was configured with Core i7 2.3GHz processor and 8 GB RAM with MATLAB R2020b - academic use, version 9.9.0.1467703 (MathWorks® 2020*d*).

D. Model performance

Two key performance measures were used to analyse model performance: The root mean square error (RMSE) and mean absolute error (MAE). All figures in the following sections display RMSE and MAE with units of SOC (%).

$$RMSE = \sqrt{\frac{\sum_{t=1}^{N} (Predicted_t - Actual_t)^2}{N}} \tag{17}$$

$$MAE = \frac{\sum_{t=1}^{N} \left| Predicted_t - Actual_t \right|}{N} \tag{18}$$

In addition to testing SOC prediction accuracy on 'testing data', the networks were also tested on unseen dynamic driving profiles: EPA Urban Dynamometer Driving Schedule (UDDS) (EPA 2015*a*); Supplemental FTP driving schedule (US06) (EPA 2015*b*); Dynamic Stress Test (DST) (USABC 1996) and a constant current discharge at the nominal current rate (-1C). These test profiles were generated following an equivalent methodology using the LIONSIMBA toolbox (Torchio et al. 2016). The US Advanced Battery Consortium defines two variable power discharge regimes in the Electric Vehicle Battery Testing procedures manual; The Federal Urban Driving Schedule (FUDS) which is identical to the EPA UDDS, and the DST. Therefore these two profiles, in addition to the US06 and a constant current discharge were chosen to test generalization performance.

IV. Results and Discussion

A. Constant Ambient Temperature - Network training

100 discharge cycles, each consisting of a maximum of 1000 time periods were simulated using LIONSIMBA for network training and testing. For each cycle, the initial SOC and depth of discharge were varied randomly between the bounds displayed by Table 1. The current profile was randomly generated from the truncated normal distribution, previously detailed by Equation 2. The ambient temperature was held constant at 25 $^{\circ}C$ for each cycle. The initial battery temperature at time zero, was set equal to ambient temperature.

TABLE I
Range of Simulated Operating Conditions - Constant Ambient Temperature

Parameter	Lower bound	Upper bound
Initial SOC (%)	10	90
Depth of discharge (%)	0	Initial SOC
Current ($C-rate$)	-3	6

For RNN and NARX network training, the default Levenberg-Marquardt backpropagation training function was used, with the default mean square-error performance function. Conversely, as a sequence network in MATLAB, the LSTM network was trained using the Adam (adaptive moment estimation) optimizer. All 3 networks were trained over 1000 epochs, as used by Hannan et al.. Training was stopped after 1000 epochs, or once validation tests were satisfied.

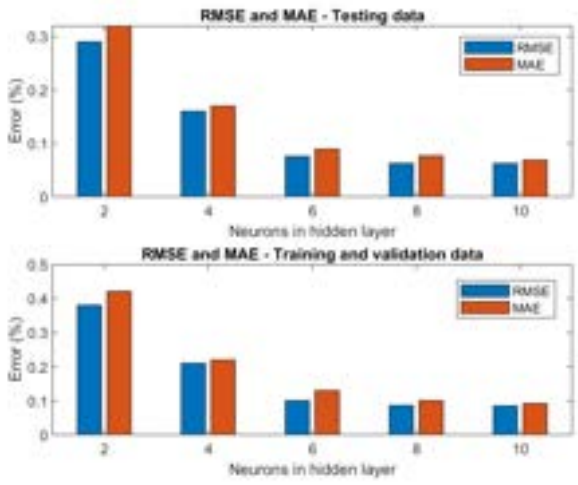

Fig. 7. RNN training and testing - SOC estimation errors

TABLE II
NETWORK TESTING RESULTS - CONSTANT AMBIENT TEMPERATURE

	Testing data (298.15K)		UDDS (298.15K)		US06 (298.15K)		DST (298.15K)		Constant Current (298.15K)	
Network	RMSE	MAE	RMSE	MAE	RMSE	MAE	RMSE	MAE	RMSE	MAE
RNN	0.062	0.077	0.58	0.43	0.27	0.19	2.69	2.21	1.98	1.77
NARX	0.022	0.033	0.17	0.13	0.016	0.0089	13.9	9.64	0.29	0.20
LSTM	0.23	0.19	1.19	0.81	0.53	0.30	1.20	1.06	0.99	0.82

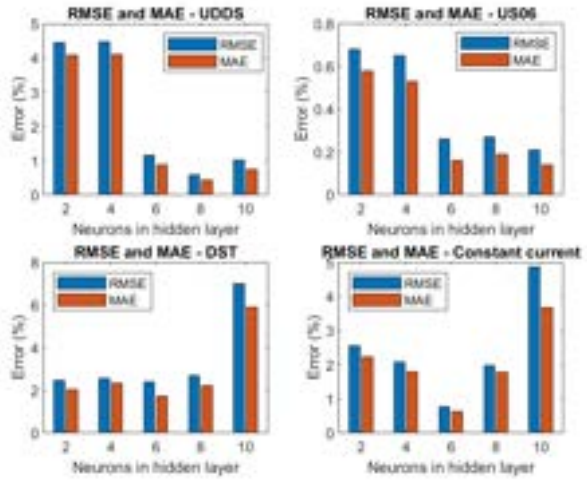

Fig. 8. RNN cycle testing - SOC estimation errors

To prevent over-fitting and ensure that the networks maintain a strong generalisation performance over a wide range of operating conditions, each network was trained with a single hidden layer. As shown by figure 7, the simple RNN fits the training and testing data better, as the number of neurons in the hidden layer is increased. Increasing network capacity (number of neurons/layers) is expected to increase performance on training data (Brownlee 2018).

Conversely, the error does not show a monotonous decrease for the 4 unseen testing cycles, displayed by figure 8. The error for 3 out of the 4 tests was higher for a structure of 10 neurons, than at 8 neurons. As the number of neurons is increased above a given value, although the training/testing error may continue to decrease, the generalization performance may become worse when the network is presented with new data. This is a sign that the network is over-fitting. A method to improve generalization performance is to use a network just large enough to provide an adequate fit (MathWorks® 2020*a*). For the simple RNN structure, an 8 neuron network showed the best combined fitting and generalisation performance.

An equivalent methodology was used to select the number of hidden units for the NARX and LSTM networks. The relevant figures for these are displayed by 'B. Supplementary Network Training Figure(s)'. The NARX network was trained in open loop and tested in closed loop. Analogous to the RNN, the NARX network showed an improvement in training and testing error as the number of neurons was increased. When the number of neurons was increased significantly above 10, the generalization performance was poorer.

The LSTM network continued the trend of improved training and testing performance as the number of hidden layer units wad increased, with the exception of 8 hidden layers. There was not a clear trend in generalization performance for the unseen cycle tests with the number of hidden layer units. This network structure also showed to be more sensitive to the randomness dictating the training/testing data division and network initialisation. A network with 4 hidden layer units was found to give the best balance between fitting and generalization performance.

B. Constant Ambient Temperature - Network testing

As shown by table 2, the NARX network shows the lowest RMSE and MAE for all unseen testing cycles, excluding the DST. The DST consists of a series of current pulses applied to the battery over a 360s (720 time-step) interval. Lin et al. found that although NARX networks do not circumvent the problem of long-term dependencies and vanishing gradients, it is easier to discover long-term dependencies with gradient descent in NARX architectures. Therefore, the NARX was expected to perform better than the simple RNN structure, even in the absence of sufficient training data. NARX's large deviation when extrapolating time is likely because of how the error is able to back-propagate through recurrent connection between output layer output, and hidden layer; Time is not only extrapolated, but is also a key network input used to estimate SOC.

All of the networks initially perform well under the DST until approximately 10000 time steps. The poor performance following this time-step is likely a result of the training data; Each individual cycle in the training data had a maximum time-step of less than 6000. As shown by figure 10, the LSTM network is able to extrapolate well and fits the DST with a RMSE of 1.20%, even though there was no training data beyond 6000 time-steps for each cycle. This is because the LSTM network is able to overcome the 'short-term' memory effect seen by the simple RNN and NARX structure, through its memory cell. Thus, the network is better suited to extrapolate time steps and and map long-term dependencies.

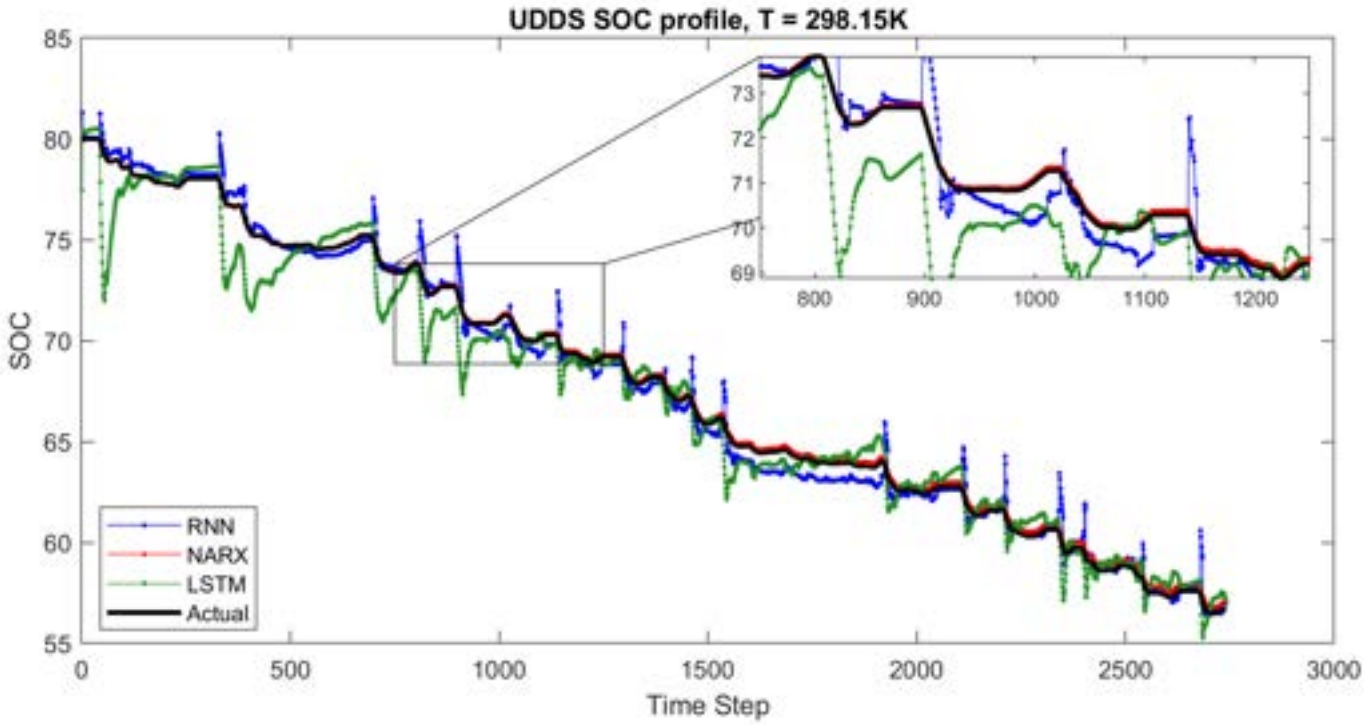

Fig. 9. UDDS cycle testing SOC profile (1 time-step is equivalent to 0.5 seconds)

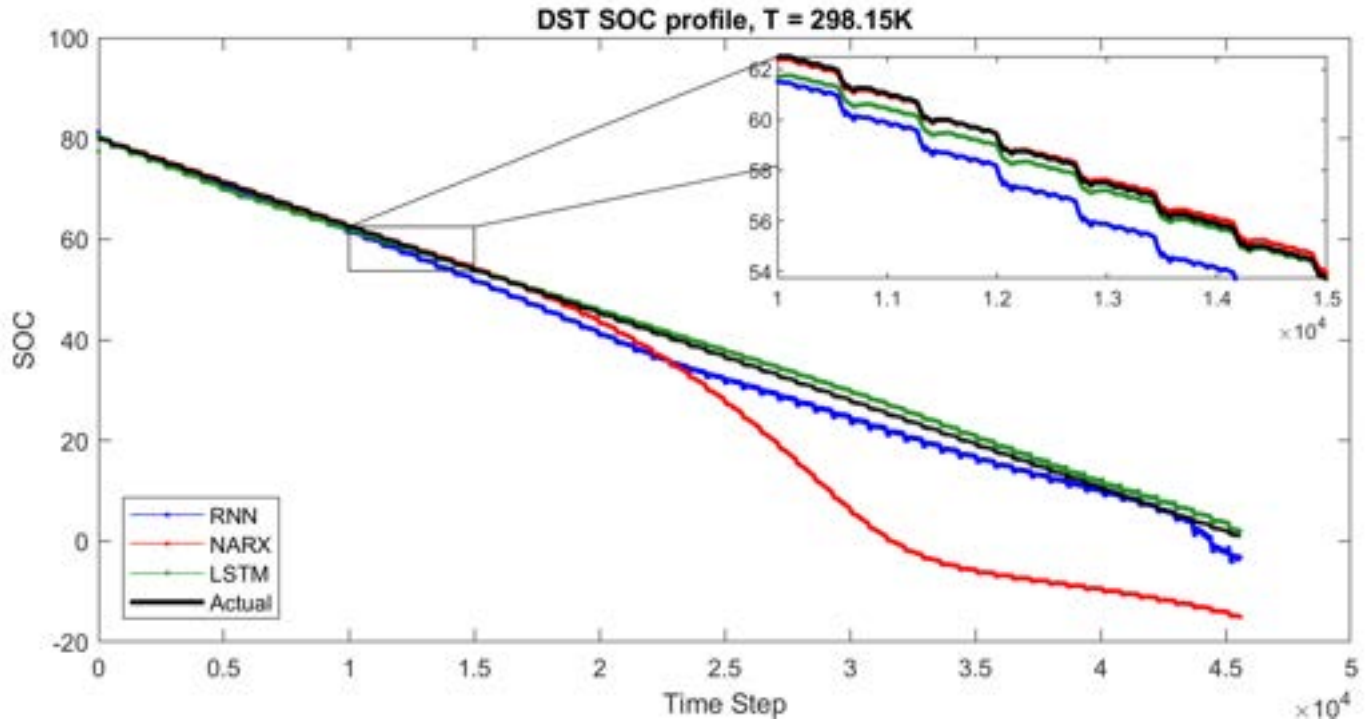

Fig. 10. DST cycle testing SOC profile (1 time-step is equivalent to 0.5 seconds)

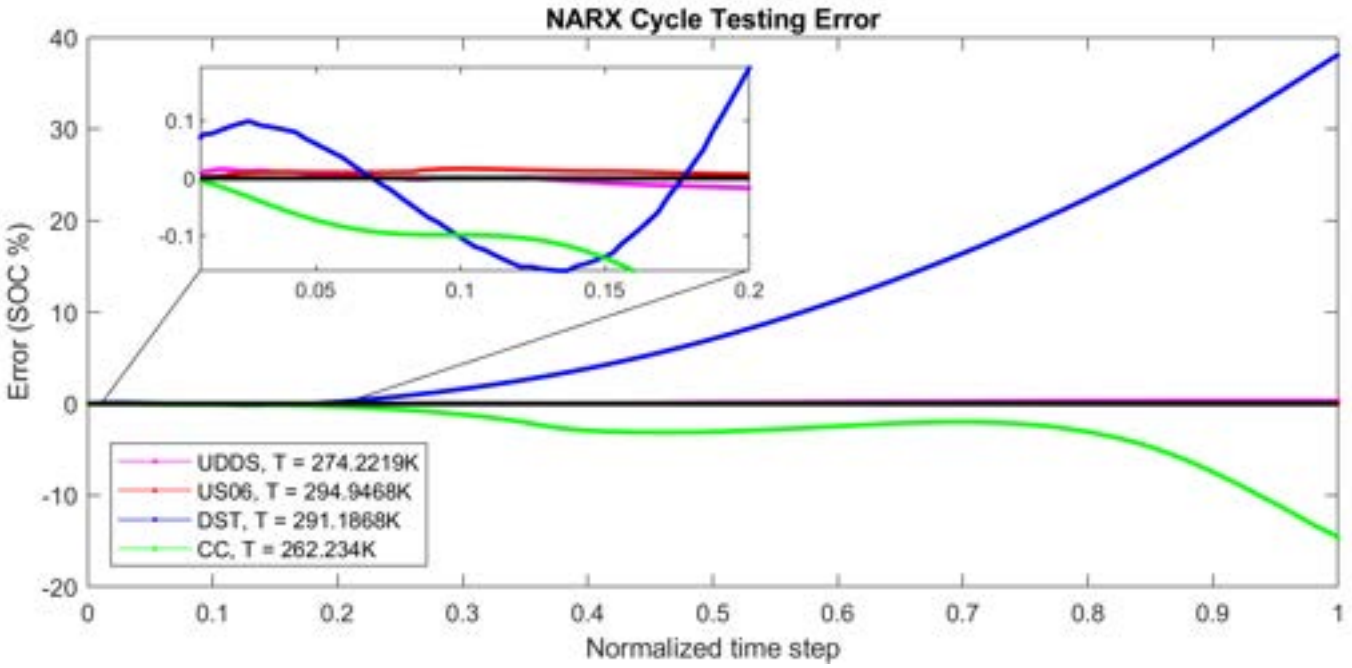

Fig. 11. Cycle testing SOC estimation error for varying ambient temperature

All three Networks generally performed better on dynamic UDDS and US06 driving cycles, than DST and constant current discharge cycles. This shows that the training data was able to capture the relationship between the inputs and SOC for real EV driving cycles well. Conversely, the training data was less sufficient under steady current loads, as the networks performed worse under profiles with long periods of steady operation.

The SOC estimated by the LSTM and simple RNN, showed sharp fluctuations when SOC changed abruptly over a short time period; This can be seen by figure 9. The LSTM and simple RNN structures contain a considerably greater number of parameters than the NARX network. On top of this, NARX networks typically converge much faster than alternative RNN structures (Lin et al. 2001). Therefore, the NARX network was trained to a greater extent, and fitted dynamic training data better over the same number of epochs. This is supported by the higher error under 'Testing data' seen by the other two networks, displayed by Table 2.

C. Varying Ambient Temperature

TABLE III
RANGE OF SIMULATED OPERATING CONDITIONS - VARYING TEMPERATURE

Parameter	Lower bound	Upper bound
Initial SOC (%)	10	90
Depth of discharge (%)	0	Initial SOC
Current ($C - rate$)	-3	6
Ambient Temperature ($^{\circ}C$)	-20	50

Following the same methodology as before, a second dataset was generated of 100 discharge cycles, each consisting of a maximum of 1000 time periods. Hossain Lipu et al. in their 'data-driven SOC performance analysis under different uncertainties' found that ambient temperature for battery operation was generally varied incrementally between -20°C and 50°C. Therefore, ambient temperature was randomly varied between these bounds, as shown by Table 3.

Table 4 displays the testing errors for each of the two NARX networks that were trained. These two networks had the same structure, of 10 neurons in their hidden layers. The first was trained on the constant ambient temperature dataset outlined in the previous section, and the second was trained on the varying ambient temperature dataset. Table 4 shows that the network makes less accurate estimations, when the additional uncertainty of varying temperature is factored in.

Both Hannan et al. and Chemali et al. found that SOC error rates decline as the temperature increases, as a result of the rise in the electrolyte activity inside the Li-ion battery cell. This effect was also seen here; The SOC RMSE increased by over 15 times for the constant current test at 262K. For the US06 test at a higher temperature of 294.9K, the RMSE only increased by a factor of 2 relative to the constant ambient temperature case. To further explore this effect, the testing cycles could be simulated over additional random temperatures.

As seen before, the error is lower for the dynamic driving

TABLE IV
NARX NETWORK RESULTS - CONSTANT AND VARIED AMBIENT TEMPERATURE

Constant Ambient Temperature	Testing data (298.15K)		UDDS (298.15K)		US06 (298.15K)		DST (298.15K)		Constant Current (298.15K)	
Network	RMSE	MAE	RMSE	MAE	RMSE	MAE	RMSE	MAE	RMSE	MAE
NARX	0.022	0.033	0.17	0.13	0.016	0.0089	13.9	9.64	0.29	0.20
Varied Ambient Temperature	Testing data (253.15-323.15K)		UDDS (274.2K)		US06 (294.9K)		DST (291.2K)		Constant Current (262.2K)	
Network	RMSE	MAE	RMSE	MAE	RMSE	MAE	RMSE	MAE	RMSE	MAE
NARX	0.11	0.14	0.17	0.12	0.033	0.026	15.9	11.1	4.3	2.95

profiles, than for the profiles that consist of long periods of steady operation. This is due to the aforementioned insufficiency of the training data to capture steady current loads. The model shows a high accuracy for the UDDS and US06 driving cycles, even under varied ambient temperature conditions; The RMSE is less than 0.2% for these two cycles. Once again, the estimated SOC for the DST profile diverged dramatically after approximately 0.2 normalised time-steps. This was a result of the limited number of time-steps in the training data.

V. CONCLUSION

In a final analysis, this study offers 3 main contributions. Two dynamic datasets were generated using LIONSIMBA Li-ion Simulation Battery Toolbox, at both constant and varying ambient temperature, to simulate the loads and operating conditions of a Li-ion battery in a real EV application. Additional uncertainties such as initial SOC and depth of discharge were randomly varied, between simulated cycles. Using these datasets, three different shallow neural networks structures were trained and tested. Each network was tested under established EV battery discharge regimes, in addition to a portion of the generated data. The NARX network showed the strongest fitting and generalization performance; This model was accurately able to estimate SOC directly from Current, Voltage, Temperature and Time, when tested against dynamic driving cycles; The RMSE and MAE of the SOC estimations made by the NARX network at a constant ambient temperature were 0.17 and 0.13 for UDDS, and 0.016 and 0.0089 for US06, respectively. Additionally, the NARX network performed well under varying ambient temperature conditions; The RMSE and MAE of the estimations made by the NARX network were 0.17 and 0.12 for UDDS, and 0.033 and 0.026 for US06, respectively. The model did not perform as well under sustained-steady periods of operation; This was caused by insufficient training data for steady current loads. This provides an opportunity for further study, to improve the SOC estimation accuracy by strengthening the sufficiency of simulated training data, and improving the network-training methodology.

REFERENCES

Bizeray, A. (2016), State and parameter estimation of physics-based lithium-ion battery models, PhD thesis, University of Oxford.

Bole, B., Kulkarni, C. & M., D. (2014), 'Randomized battery usage data set'.
URL: *http://ti.arc.nasa.gov/project/prognostic-data-repository*

Brownlee, J. (2018), 'How to avoid overfitting in deep learning neural networks'. Date accessed: 12/12/2020.
URL: *https://machinelearningmastery.com/introduction-to-regularization-to-reduce-overfitting-and-improve-generalization-error/*

Chaturvedi, N. A., Klein, R., Christensen, J., Ahmed, J. & Kojic, A. (2010), 'Algorithms for advanced battery-management systems', *IEEE Control Systems Magazine* **30**(3), 49–68.

Chemali, E., Kollmeyer, P. J., Preindl, M., Ahmed, R. & Emadi, A. (2018), 'Long short-term memory networks for accurate state-of-charge estimation of li-ion batteries', *IEEE Transactions on Industrial Electronics* **65**(8), 6730–6739.

Cingillioglu, N. (2019), 'Imperial college machine learning - neural networks'. Date accessed: 02/12/2020.

EPA (2015*a*), 'Urban dynamometer driving schedule'.
URL: *https://www.epa.gov/vehicle-and-fuel-emissions-testing/dynamometer-drive-schedules*

EPA (2015*b*), 'Us06 supplemental ftp driving schedule'.
URL: *https://www.epa.gov/vehicle-and-fuel-emissions-testing/dynamometer-drive-schedules*

Hannan, M. A., Lipu, M. S., Hussain, H. & Mohamed, A. (2017), 'A review of lithium-ion battery state of charge estimation and management system in electric vehicle applications: Challenges and recommendations', *Renewable and Sustainable Energy Reviews* **2013**(ISSN 1364-0321), 834–854. https://doi.org/10.1016/j.rser.2017.05.001.

Hannan, M., Lipu, M., Hussain, A. & et al (2020), 'Toward enhanced state of charge estimation of lithium-ion batteries using optimized machine learning techniques', *Sci Rep* **10**(4687).

Hossain Lipu, M., Hannan, M., Hussain, A., Ayob, A., Saad, M. H., Karim, T. F. & How, D. N. (2020), 'Data-driven state of charge estimation of lithium-ion batteries: Algorithms,

implementation factors, limitations and future trends', *Journal of Cleaner Production* **277**, 124110.
URL: *http://www.sciencedirect.com/science/article/pii/S095965262034155X*

How, D. N. T., Hannan, M. A., Hossain Lipu, M. S. & Ker, P. J. (2019), 'State of charge estimation for lithium-ion batteries using model-based and data-driven methods: A review', *IEEE Access* **7**, 136116–136136.

IBM Cloud Education (2020), 'Neural networks'. Date accessed: 02/12/2020.
URL: *https://www.ibm.com/cloud/learn/neural-networks*

IEA (2020*a*), Clean energy innovation, Technology report, International Energy Agency. https://www.iea.org/reports/clean-energy-innovation.

IEA (2020*b*), Global ev outlook 2020, Energy report, International Energy Agency. www.iea.org/reports/innovation-in-batteries-and-electricity-storage.

IEA (2020*c*), Innovation in batteries and electricity storage, Technology report, International Energy Agency. www.iea.org/reports/innovation-in-batteries-and-electricity-storage.

Jurafsky, D. & Martin, J. (2019), *Speech and Language Processing*, 3rd draft edn, Publisher.

Li, C., Chen, Z., Cui, J., Wang, Y. & Zou, F. (2014), The lithium-ion battery state-of-charge estimation using random forest regression, *in* '2014 Prognostics and System Health Management Conference (PHM-2014 Hunan)', pp. 336–339.

Lin, T., Horne, W., Tino, P. & Giles, C. (2001), 'Learning long–term dependencies is not as difficult with narx recurrent neural networks', *IEEE Trans. Neural Netw.* **7**.

MathWorks® (2020*a*), 'Improve shallow neural network generalization and avoid overfitting'. Date accessed: 11/12/2020.
URL: *https://www.mathworks.com/help/deeplearning/ug/improve-neural-network-generalization-and-avoid-overfitting.html*

MathWorks® (2020*b*), 'layrecnet, documentation'. Date accessed: 02/12/2020.
URL: *https://www.mathworks.com/help/deeplearning/ref/layrecnet.html*

MathWorks® (2020*c*), 'Long short-term memory (lstm)'. Date accessed: 02/12/2020.
URL: *https://www.mathworks.com/discovery/lstm.html*

MathWorks® (2020*d*), *MATLAB version 9.9.0.1467703 (R2020b - academic use)*, The MathWorks Inc., Natick, Massachusetts.

MathWorks® (2020*e*), 'narxnet, documentation'. Date accessed: 02/12/2020.
URL: *https://www.mathworks.com/help/deeplearning/ref/narxnet.html*

Mittal, A. (2019), 'Understanding rnn and lstm'. Date accessed: 03/12/2020.
URL: *https://towardsdatascience.com/understanding-rnn-and-lstm-f7cdf6dfc14e*

Ng, M., Zhao, J., Yan, Q. & et al (2020), 'Predicting the state of charge and health of batteries using data-driven machine learning', *Nat Mach Intell* **2**(3), 161–170.

Sanjeevi, M. (2018), 'Chapter 10.1: Deepnlp — lstm (long short term memory) networks with math'. Date accessed: 03/12/2020.
URL: *https://medium.com/deep-math-machine-learning-ai/chapter-10-1-deepnlp-lstm-long-short-term-memory-networks-with-math-21477f8e4235*

The World Economic Forum (2019), A vision for a sustainable battery value chain in 2030, Insight report, The World Economic Forum; The Global Battery Alliance.
URL: *http://www3.weforum.org/docs/WEF_A_Vision_for_a_Sustainable_Battery_Value_Chain_in_2030_Report.pdf*

Torchio, M., Magni, L., Gopaluni, R. B., Braatz, R. D. & Raimondo, D. M. (2016), 'LIONSIMBA: A matlab framework based on a finite volume model suitable for li-ion battery design, simulation, and control', *Journal of The Electrochemical Society* **163**(7), A1192–A1205.
URL: *https://iopscience.iop.org/article/10.1149/2.0291607jes*

Trifonov, M. S. J. B. D. (2020), 'Battery and heating data in real driving cycles'.
URL: *https://dx.doi.org/10.21227/6jr9-5235*

USABC (1996), *ELECTRIC VEHICLE BATTERY TEST PROCEDURES MANUAL*, 2 edn, USABC.
URL: *https://avt.inl.gov/sites/default/files/pdf/battery/usabc_manual_rev2.pdf*

Xiong, R., Cao, J., Quanqing, Y., Hongwen, H. & Fengchun, S. (2017), 'Critical review on the battery state of charge estimation methods for electric vehicles', *IEEE Access* **6**(Electronic ISSN: 2169-3536), 1832 – 1843. https://ieeexplore.ieee.org/abstract/document/8168251.

Yang, F., Zhang, S., Li, W. & Miao, Q. (2020), 'State-of-charge estimation of lithium-ion batteries using lstm and ukf', *Energy* **201**, 117664.
URL: *http://www.sciencedirect.com/science/article/pii/S0360544220307714*

Yiu, T. (2019), 'Understanding neural networks'. Date accessed: 02/12/2020.
URL: *https://towardsdatascience.com/understanding-neural-networks-19020b758230*

Yu, Q., Xiong, R., Lin, C., Shen, W. & Deng, J. (2017), 'Lithium-ion battery parameters and state-of-charge joint estimation based on h-infinity and unscented kalman filters', *IEEE Transactions on Vehicular Technology* **66**(10), 8693–8701.

Molecular modelling absorption of solutes in amorphous domain of semicrystalline polymers

Sirui Huang, Chris HZ Chua
Department of Chemical Engineering, Imperial College London, U.K.

Abstract The absorption of various organic solutes, namely alkanes, aromatics, cyclics and branched alkanes, into semicrystalline polyethlene is modelled using two theories, SAFT-γ Mie in conjunction with the Michaels-Hausslein theory. Absorption results are compared with experimental results from previous work of various authors, and fitting them by adjusting the weight fraction of tie chains in the polymer, f. Good agreement is obtained for benzene, as each isotherm modelled can be matched to the corresponding experimental isotherm with no significant overpredictions or underpredictions, while some agreement is found for other molecules. The SAFT-γ Mie EoS was verified with good agreement by fitting absorption isotherms of fully amorphous polyethylene above the T_m generated by the EoS with experimental results for methane and cyclohexane.

Introduction

Polymers can be defined as macromolecules comprised of many repeat units of smaller molecules. The discovery of catalysts such as Ziegler-Natta have advanced the mass production and specialisation post-polymerisation of many polymers in use today. The wide utility and versatility polymers, both man-made and biological, can be attributed to their thermophysical and chemical properties, such as high ductility, toughness, chemical resistance and sorption capacity. An in-depth understanding of the phase behaviour of solute-polymer systems is critical in the polymer production process and to discover potential industrial applications. Under typical gas-phase polymerisation reaction conditions, monomers diffuse into the amorphous region and form a vapour-liquid equilibrium (VLE) with liquid polyethylene (PE), which exists in a semicrystalline state. In semicrystalline polymers, two phases are present: amorphous and crystalline domains. The crystalline region consists of crystal lamellae of regular folding chains, which are generally assumed to be impermeable to solutes. In the amorphous region, different types of polymer chains are present: tie chains that are connected at both ends to different crystals, loops that exit and return to the same crystal, free ends that have one unattached end extending from the crystal, and floating chains that are not attached to a crystal. The tie chains are stretched when the solvent penetrates the amorphous polymer network and elastically deform. The chains exert a constraint pressure and decreases the solubility of solvent in the polymer compared to that in a purely amorphous polymer under similar conditions. Previous attempts to model polymer solubility use fluid theories which ignore elasticity effects, and treat the polymer as a subcooled polymer melt, thus significantly overpredicting solubility. To accurately model solubility of semicrystalline polymers, a suitable fluid theory in conjunction with elastic factor modifications are required.

Background

Various fluid theories have been developed to model the VLE of polymer systems: activity coefficient approaches, lattice models, and equations of state (EoS). Activity coefficient approaches accurately model activity coefficients of gases in polymers and are able to describe VLE as well as LLE in binary mixtures, but fail to model pressure effects. Commonly used approaches include UNIFAC-FV (Oishi and Prausnitz, 1978) and polymer-NRTL method (Chen, 1993). Lattice models such as the Sanchez-Lacombe equation of state (Lacombe and Sanchez, 1976), attempted to account for compressibility effects by describing a compressible version of the Flory-Huggins lattice model (Flory, 1942; Huggins, 1941), which incorporates volume effects via vacant lattice sites. A weakness of both approaches is that interaction parameters required to describe the phase equilibria over a large temperature, pressure and composition ranges are state-dependent. Continuum-based EoS approaches, in contrast, are advantageous in the sense that they can be applied over wide temperature and pressure ranges.

Statistical associating fluid theory (SAFT) approaches, which is based on the first-order thermodynamic perturbation theory of Wertheim (1984), describe mixtures of associating fluids and are one of the most widely used continuum-based approaches today. Each molecule is divided into a number of spherical segments known as monomers, which interact with other monomers through pairwise dispersion interactions while also possessing association sites that mediate short-ranged molecular inter-

actions. SAFT-γ Mie EoS, which was formulated by Papaioannou, Lafitte, et al. (2014). is the latest EoS iteration in the SAFT family, and improves upon SAFT-VR Mie EoS using the Barker–Henderson (Barker and Henderson, 1967) high-temperature perturbation expansion up to third order in the free energy of the monomer and a second-order expansion for the radial distribution function of the reference monomer fluid. SAFT-γ Mie also incorporates a group contribution framework for fused heteronuclear molecular models, with Mie potential interactions between segments, and is able to model various complex molecules with similar chemical monomers.

Attempts by previous authors to studying solubility in semicrystalline polymers have used different fluid-theory approaches with modifications to account for the elastic effect. Doong and Ho (1991) used UNIFAC and solubility parameter methods which combined with the Michaels–Hausslein (MH) (Michaels and Hausslein, 1965) and Flory–Rehner (FR) (Flory and Rehner, 1943) theories for the prediction of the solubility for several polyethylene/solvent systems, and found reasonable alignment in UNIFAC-MH theory, with error of 10%. Banaszak et al. (2004) studied the absorption of ethylene and 1-hexene in polyethylene using PC-SAFT simulations in conjunction with MH theory and verified their simulations with experimental results obtained by Novak et al. (2004) for the same system. They concluded that these elastic constraints play an important role in the solvent solubility for temperatures below the melting point of the polymer. In most cases, the polymer-solute cases studied are simple solutes in the same functional family.

This paper aims to extend the predictive capabilities of SAFT-γ Mie in conjunction with Michaels-Hausslein theory by modelling the phase behaviour of polyethylene in VLE with a variety of organic compounds including alkanes, alkenes, aromatics and cyclic compounds. The solution predictions are verified by comparison with experimental results studied in previous work. Further, absorption isotherms above the T_m are generated using SAFT-γ Mie EoS and fitted with experimental data in order to verify the SAFT-γ Mie EoS is able to accurately model VLE properties above the melt.

Theory

Saft-γ Mie

The Mie potential between segments k and l is given by

$$\Phi_{kl}(r_{kl}) = C_{kl}\epsilon_{kl}\left(\left(\frac{\sigma_{kl}}{r_{kl}}\right)^{\lambda^r_{kl}} - \left(\frac{\sigma_{kl}}{r_{kl}}\right)^{\lambda^a_{kl}}\right) \quad (1)$$

where r_kl represents the distance between two segments and C_kl is given by

$$C_{kl} = \frac{\lambda^r_{kl}}{\lambda^r_{kl} - \lambda^a_{kl}}\left(\frac{\lambda^r_{kl}}{\lambda^a_{kl}}\right)^{\frac{\lambda^a_{kl}}{\lambda^r_{kl}-\lambda^a_{kl}}} \quad (2)$$

such that min $\Phi^{Mie}_{kl}(r) = -\epsilon_{kl}$. Each monomer k may possess any number $N_{st,k}$ of different types of association sites, with each site having multiplicity $n_{k,a}$. The interaction potential between site a on monomer k and site b on monomer l is governed by equation (3):

$$\Phi^{HB,ab}_{kl}(r_{kl,ab}) = \begin{cases} \epsilon^{HB}_{kl,ab} & \text{if} r_{kl,ab} \leq r^c_{kl,ab} \\ 0 & \text{otherwise} \end{cases} \quad (3)$$

The interaction between any distinct pair of monomers is defined by the four dispersion parameters σ_{kl}, ϵ_{kl}, λ^r_{kl}, λ^a_{kl} and by the eventual $\epsilon^{HB}_{kl,ab}$, $H^{HB}_{kl,ab}$ for every pair (a_k, b_l) of sites. λ^a_{kl} is set to 6 to reflect the form of dipole interaction. The unlike interaction parameters ($k \neq l$) are calculated with combining rules from corresponding qualities that describe the like interactions ($k = l$). An additional shape factor S_k is introduced to account for the contribution of each group to the total free energy.

Parametrisation

SAFT-γ Mie parameters for the molecules are obtained from table 1, which are regressed to pure-component vapour-liquid equilibrium data, as well as single phase densities at given temperatures and pressures. Polyethylene is modelled as monodisperse, consisting of 100% ethylene repeat units with no branching, with a fixed molecular weight of 10,000 g mol^{-1}. Monodispersity model assumption is justified as there is a weak correlation of polydispersity with vapour-liquid equilibrium properties Paricaud et al. (2004).

Michaels-Hausslein Theory

The Michaels-Hausslein theory (equation (4)) postulates that the the tension in the tie chains is in equilibrium with the driving force of crystallisation.

$$\Delta G^{crys} \approx \Delta H^{crys}\left(1 - \frac{T}{T_m}\right) \quad (4)$$

The chemical potential of the polymer in the amorphous phase equals that of the crystalline phase in thermodynamic equilibrium.

$$\mu_2^a = \mu_2^c \tag{5}$$

μ_2^a consists of the chemical potential of the amorphous chain in the presence of penetrant μ_2^m plus the chemical potential due to the elastic constraints on the chain μ_2^e. μ_2^m can be expressed by and μ_2^c is expressed by equation (4), equation (5) can be rewritten as.

$$\begin{aligned} -RT\left(\frac{V_2}{V_1}\right)(\phi_1 - \chi\phi_1^2) + \mu_2^e = \\ -\Delta H_2\left[1 - \frac{T}{T_m}\right] \end{aligned} \tag{6}$$

with ΔH_2 as the molar heat of fusion and T_m as melting point. Similarly, the solute chemical potential in the amorphous phase μ_1^e equals the chemical potential in the vapour phase. μ_1^v, which

$$\mu_1^m + \mu_1^e = \mu_1^v \tag{7}$$

equation (8) for polymer phase pressure is obtained using general thermodynamic relationships, in accordance with Banaszak et al. (2004).

$$\begin{aligned} &P^{\text{amph P, elastic}} = \\ &-3\left(\frac{RT}{\bar{\nu}_P^{\text{amph P}}}\right) \\ &\frac{\left[\frac{\Delta H_2}{R}\left(\frac{1}{T} - \frac{1}{T_m}\right) + \frac{\mu_{\text{P}}^{\text{pure amph P, res}}}{RT}\right]}{\left(\frac{3}{2f\phi_{\text{P}}^{\text{amph P}}} - 1\right)} \end{aligned} \tag{8}$$

where T_m is the melting temperature, $\bar{\nu}_P^{\text{amph P}}$ is the partial molar volume of species i in the amorphous polymer phase, and $\phi_{\text{P}}^{\text{amph P}}$ is the volume fraction of the polymer in the amorphous polymer phase.

Coarse graining

Coarse-grained models represent groups of atoms in each interaction site and is used to represent large molecules. The molecular EoS-based approach in SAFT-γ Mie relies on macroscopic experimental data and uses a top-down approach, which derive coarse-grained force field parameters which reproduce macroscopic experimental properties. Table 1 summarises the references of the values used in the model.

Methodology

Total solubility is calculating using equation (9), given crystallinity, ω_c

$$S_{ab} = \omega_a S_{am} = (1 - \omega_c)S_{am} \tag{9}$$

Solubility in the amorphous domains in obtained by equating the chemical potential of the solute in the gas phase, which is in equilibrium with the amorphous domains.

$$\begin{aligned} &\delta\mu_s^*(T, P, n_s, n_p) = \\ &\mu_s^{EoS}(T, P + P_c, n_s, n_p) - \mu_s^{EoS}(T, P, n_s, n_p) \end{aligned} \tag{10}$$

The chemical potential of the solute is calculated by equation (10), with constraint pressure obtained by recursively solving for $P^{\text{amph P,elastic}}$ in equation (8).

Experimental

The papers in which the solubility experimental data were obtained used gravimetric sorption methods with polyethylene of varying crystallinity, density and T_m. T_m and H_m were obtained through differential scanning analysis, with crystallinity obtained based on measured H_m. Due to missing T_m and H_m data in some instances, a standard T_m and H_m, were chosen by averaging out data applicable. Where specified, the polyethylene films were washed with toluene between use and the solutes used were of reagent grade purity. Doong and Ho (1991) found absorption results of polyethylene were independent of film history in temperature ranges of 30 °C to 60 °C, which is in line with experimental temperature ranges of other molecules studied.

Results and Discussion

A series of solubility plots are generated with solubility in terms of gram of solute per 100 gram of polymer plotted against pressure in kPa. The model data is plotted as smooth lines, while the experimental data is plotted as data points. The vertical dotted line in the graph indicates the vapour limit of the solute, beyond which LLE between polymer-solute occurs, which is beyond the scope of this paper. f is chosen by prioritising fit between SAFT predictions and that of the lowest isotherm.

Alkanes

N-hexane is examined, using data from Liu and Neogi (1988). The coarse graining groups CH_2 and CH_3 are used for this molecule. The polymer used had a crystallinity, ω_c, of 0.53. A good agreement

Table 1: Summary of coarse graining values reference

group k	group l		
	CH_3		
CH_3	Papaioannou, Lafitte, et al. (2014)	CH_2	
CH_2	Papaioannou, Lafitte, et al. (2014)	Papaioannou, Lafitte, et al. (2014)	CH
CH	Dufal et al. (2014)	Dufal et al. (2014)	Dufal et al. (2014)
aCH	Dufal et al. (2014)	Dufal et al. (2014)	Dufal et al. (2014)
$aCCH_3$	Hutacharoen et al. (2016)	Hutacharoen et al. (2016)	
$aCCH_2$	Dufal et al. (2014)	Dufal et al. (2014)	Dufal et al. (2014)
cCH_2	Dufal et al. (2014)	Dufal et al. (2014)	Dufal et al. (2014)
	aCH		
aCH	Dufal et al. (2014)	$aCCH_3$	
$aCCH_3$	Papaioannou, Calado, et al. (2016)	Papaioannou, Calado, et al. (2016)	$aCCH_2$
$aCCH_2$	Dufal et al. (2014)		Dufal et al. (2014)
cCH_2			
	cCH_2		
cCH_2	Dufal et al. (2014)		

between the data can be found at $f = 0.33$, as seen in figure 1. The solubility increases with decreasing temperature, and this is due to the number of tie chains in the amorphous domain of the polymer increasing with temperature. In this case, the solubility at higher temperatures are underpredicted. A f value of 0.20 is found to fit 60 °C well, at the expense of a poor fit for other isotherms. As chain length of polymer increases, the predictive power of the SAFT equations of state deteriorates, as the parameters obtained from Papaioannou are optimised for short chain alkanes and branched alkanes.

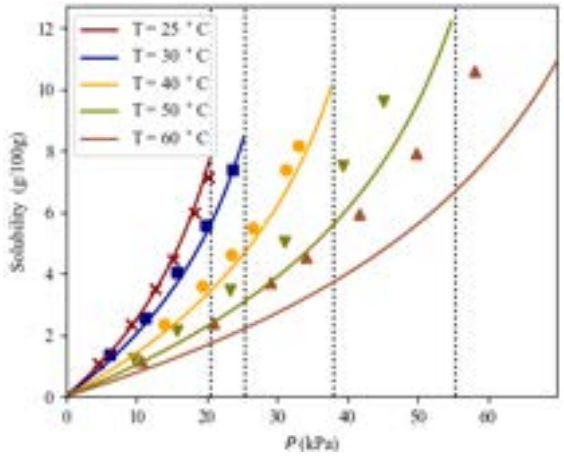

Figure 1: Solubility of n-hexane based on model predictions, with experimental data from Liu and Neogi (1988), $\omega_c = 0.53$, $f = 0.33$

Aromatics

Next, a series of aromatic compounds is modelled and plotted, with experimental data obtained from Doong and Ho (1991). The coarse graining group aCH is used for the aromatic carbons. The polymer used has a crystallinity of 0.45. The results can be found in figure 2, and their corresponding f values in table 2.

The model first calculated the solubility of benzene in PE, and the results can be found in figure figure 2a. A good agreement is obtained between the model data and the experimental data and $f = 0.32$ is obtained. A good agreement can also be found for toluene, mesitylene, and prehnitine, which used an additional coarse graining group $aCCH_3$. The results for toluene and mesitylene can be found in figures 2c and 2d respectively. Their respective f values are 0.47 and 0.52. In the case of mesitylene, there are some overprediction of the solubility in PE at higher temperatures.

Next, the solubility of n-propylbenzene and n-butylbenzene is modelled with the additional coarse graining group $aCCH_2$. The result for the former can be found in figure 2b. A good agreement is found between the model data and the experimental data, however, the f value obtained in these cases are very low, at 0.11 and 0.12 respectively, which is much lower than values previously obtained in literature. Therefore, the models were recomputed at a lower melting temperature of 374 K for the polymer, based on the data from Doong and Ho (1991), instead of the averaged T_m of 410 K, in order to increase these f values and bring them closer towards commonly accepted literature values. The driving force of crystallisation ΔG is proportional to the degree of undercooling, $T_m - T$, as seen from equation (4). Thus, for all temperaetures, reducing T_m decreases the driving

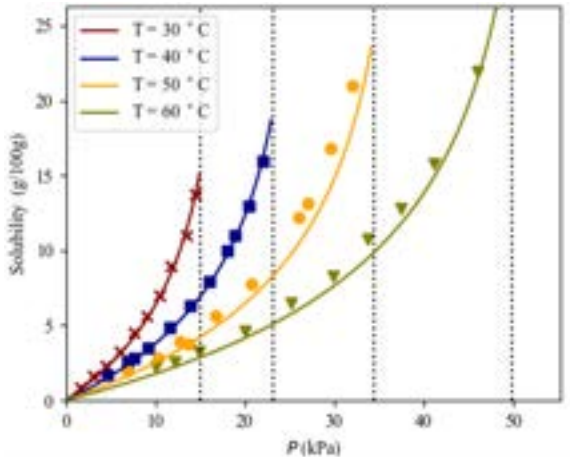

(a) Solubility for benzene, T_m =410 K, $f = 0.32$

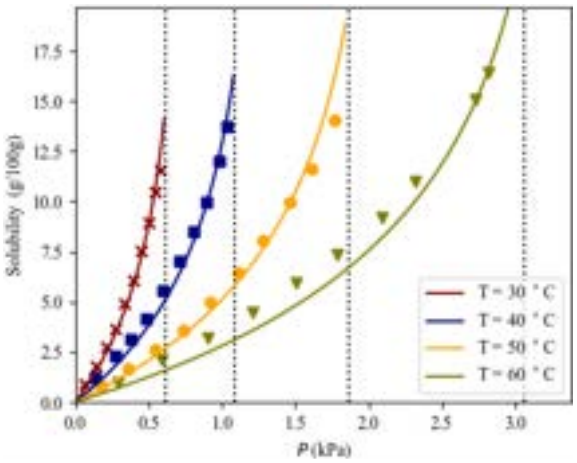

(b) Solubility for n-propylbenzene, T_m =410 K, $f = 0.11$

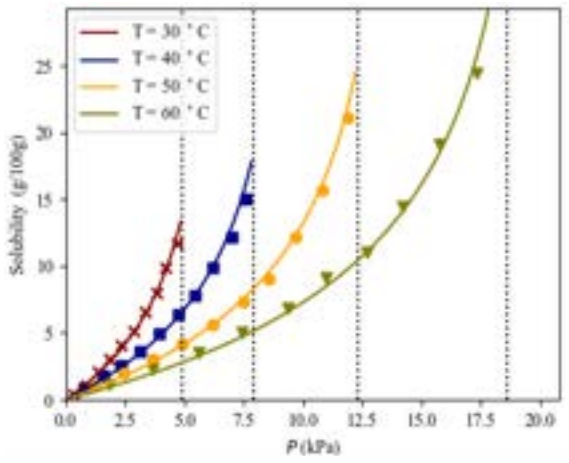

(c) Solubility for toluene, T_m =410 K, $f = 0.47$

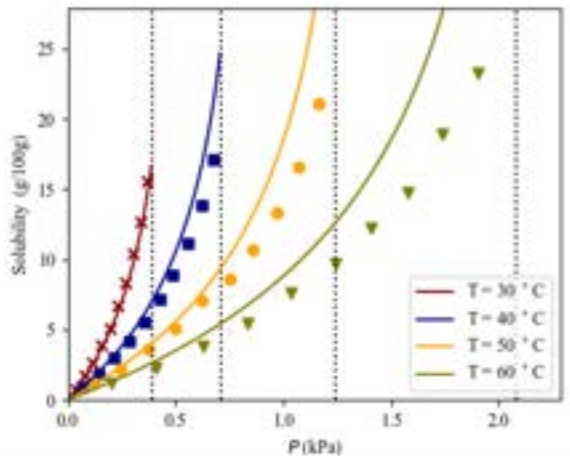

(d) Solubility for mesitylene, T_m =410 K, $f = 0.52$

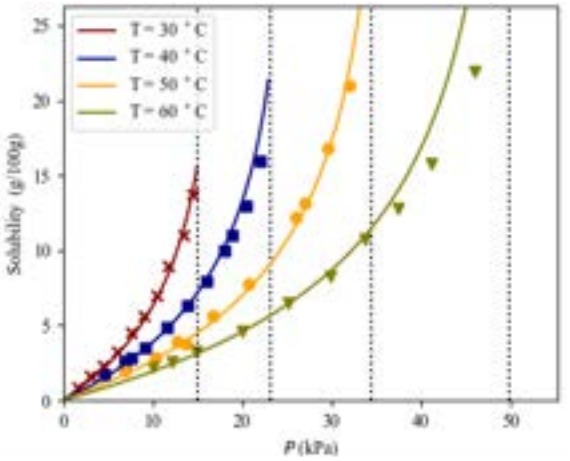

(e) Solubility for benzene, T_m =374 K, $f = 0.42$

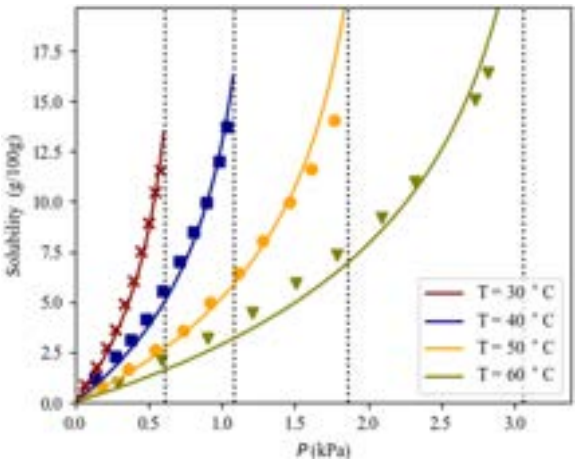

(f) Solubility for n-propylbenzene, T_m =374 K, $f = 0.16$

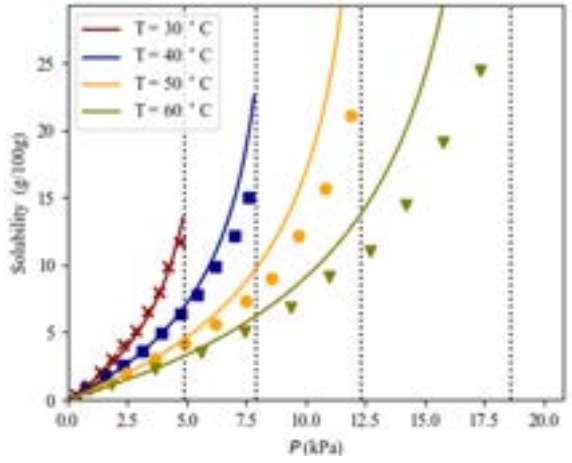

(g) Solubility for toluene, T_m =374 K, $f = 0.60$

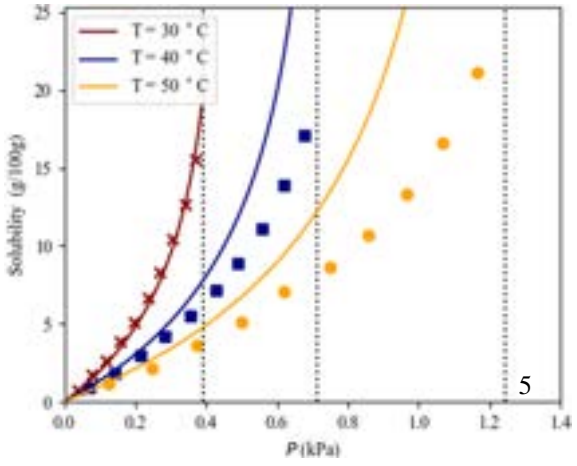

(h) Solubility for mesitylene, T_m =374 K, $f = 0.65$

Figure 2: Solubility of aromatics in PE based on model predictions, with experimental data from Doong and Ho (1991), $\omega_c = 0.45$

force ΔG, meaning that the tie chains will exert less stress on the polymer. Therefore, a higher value of f is required to obtain the same solubility. The results are shown in figures 2e to 2h.

Figure 2e shows the solubility of benzene in PE with a melting temperature of 374 K. A good agreement is maintained between the model data and experimental data, and f increased from 0.32 to 0.42. Therefore, this model is shown to be able to capture the solubility relationship with pressure well even when the melting temperature of the polymer changes.

Figure 2f shows the solubility of n-propylbenzene in PE with the lower melting temperature. A good agreement is also maintained between the data sets, and f increased from 0.11 to 0.16. Although the new f value is still low, it is an improvement as it is now within 0.1 of commonly accepted values in literature.

New values of f are also obtained for toluene and mesitylene, and the results are shown in figures 2g and 2h respectively. The f values increased from 0.47 to 0.60 and from 0.52 to 0.65 respectively. The agreement between the data sets worsened for both cases, with the model overpredicting the solubility of the solutes in PE more at the higher temperatures.

Table 2: Summary of f values obtained for PE

	f	
	T_m =410 K	T_m =374 K
benzene	0.32	0.42
n-propylbenzene	0.11	0.16
n-butylbenzene	0.12	0.17
toluene	0.47	0.60
mesitylene	0.52	0.65
prehnitene	0.53	0.65

Doong and Ho (1991) calculated a f value of 0.373 to fit their readings, and based on the model values in table 2, benzene can be considered to be well-modelled, and further comparisons should be made with respect to benzene, which also showed good agreement with the experimental data.

As seen from table 2, the f values increased by about 0.1 when the melting temperature of the polymer is decreased from 410 K to 374 K. A range of values are also obtained, ranging from 0.11 to 0.53 for T_m =410 K and from 0.16 to 0.65 for T_m =374 K. However, only one value should be obtained as f is a parameter of the polymer, and it is not dependent on the solute. Therefore, it is postulated that the solutes could have changed the crystallinity of the polymer when they dissolve, and thereby changing the f values as well, since the tie chains are strained when solutes dissolve into the polymer. In addition, the methodology used by Doong and Ho (1991) involved reusing the polymer, with it being outgassed between measurements for each solute. This could also have the effect of changing the actual crystallinity of the PE sample, leading to additional deviation from the actual solubility. Additional work is required to verify the readings and test the postulate.

The model consistently only overpredicts the solubility at higher temperatures, and not lower, in the case of toluene and mesitylene, as shown in figures 2d, 2g and 2h. In addition, the f values. Therefore, it can also be theorised that the coarse graining parameters for the groups $\mathrm{aCCH_3}$, which are present in toluene and mesitylene, to be poorly calibrated. f is also a parameter that changes with temperature, as crystallinity changes with temperature, but most literature, particularly the ones cited in this paper, assume it to be constant as crystallinity is a weak dependence on temperature in a range far below T_m. In the temperature ranges of 30C to 60C in this experiment, Charlesby and Callaghan, 1958 found that crystallinity varies by 10%. It could be the case that this model is particularly sensitive to such variation of f with temperature, and hence f needs to be parameterised to change with temperature. It is also possible that there are intertwined loops in the PE sample used by Doong and Ho (1991), as the model only overpredicts the solubility compared to their data. These intertwined loops function like tie chains as they exert additional stress between the lamellae, but are not counted as such and do not contribute to the f value. Therefore, the experiments produced lower than expected solubility results, and hence the model would be seen to have overpredicted based on those experiments. Therefore, additional experiments should be done to verify and recalibrate the interactions between $\mathrm{aCCH_3}$ and other groups, and to parameterise f according to temperature.

Cyclics

Experimental solubility data obtained from Rausch et al. (2011) was plotted on model data using the coarse graining group $\mathrm{cCH_2}$ for the cyclic carbons, and the results are shown in figure 3. The crystallinity of PE was 0.776 and the f value obtained was 0.30. As the experiment was done over a low range of pressures, hence solubility is a linear function of vapour pressure, in accordance with Henry's Law.

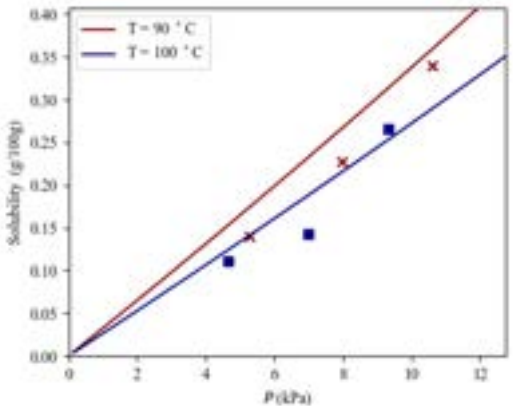

Figure 3: Solubility of cyclohexane based on model predictions, with experimental data from Rausch et al. (2011), $\omega_c = 0.776$, $f = 0.30$

Branched Alkanes

Sorption data of isobutane was modelled with the coarse graining groups cCH and CH_3, and isotherms are plotted with experimental data by Dos Santos et al. (1974). The results are shown in figure 4. The crystallinity of PE was 0.45 and the f value obtained was 0.25. The solubility at higher temperatures were underpredicted, as was the case for hexane, suggesting that additional calibration may be needed for the group CH_3. A further caveat is that an average T_m was used for this instance, which could lead to errors in a similar fashion as Doong.

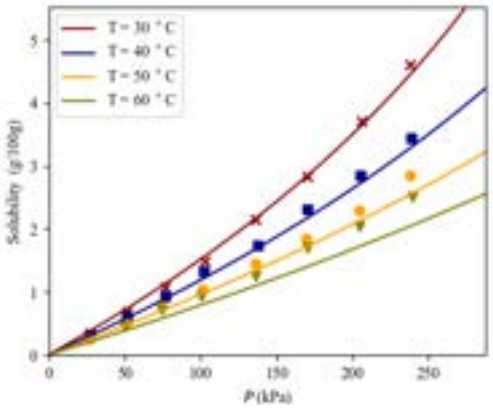

Figure 4: Solubility of isobutane based on model predictions, with experimental data from Dos Santos et al. (1974), $\omega_c = 0.45$, $f = 0.25$

Validation of SAFT-γ Mie in polymer melt

Thus far, the dual theory model with SAFT-γ Mie and the Michaels-Hausslein theory had produced results that deviate from experimental data from various authors. Therefore, experimental data of sorption of different molecules in PE melt are obtained from different authors, and compared with the model data. By conducting the modelling in the polymer melt, Michaels-Hausslein theory is removed from the model as the melt phase has no crystallinity and hence no tie chains. SAFT-γ Mie is also optimsed for 2-phase fluid systems, and modelling the solubility at polymer melt conditions would reproduce such systems, thus giving better insight as to the validity of using SAFT-γ Mie in the model.

First, cyclohexane is revisited with the data provided by Rausch et al. (2011), and the results are shown in figure 5. The model data and experimental data produced some agreement, particularly at 160 °C. There might be some errors with the experimental data, however, as the experimental isotherms appear to intersect and the points do not extrapolate to the origin for the other temperatures, which should be the expected behaviour.

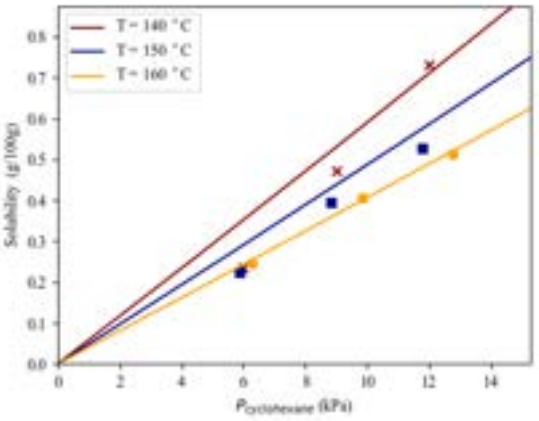

Figure 5: Solubility of cyclohexane in PE melt based on model predictions, with experimental data from Rausch et al. (2011)

Next, a experimental sorption data set of methane from Lundberg (1964) was used to compare with the model, and the results are shown in figure 6. There is good agreement between the different data sets, with only deviations at higher pressures and temperatures. SAFT-γ Mie starts to overpredict solubility at pressures exceeding 300 kPa. The top-down approach of SAFT-γ Mie prioritises transferability by fitting experimental data over a range of state points in the group leads to deviations in outlier molecules. In this case, the parameters for methane might not be optimised as it is the smallest alkane molecule. Nevertheless, there is good agreement between SAFT and experimental data in the pressure scales in which VLE

occurs between semicrystalline polyethylene-solute pairs below the melt temperature.

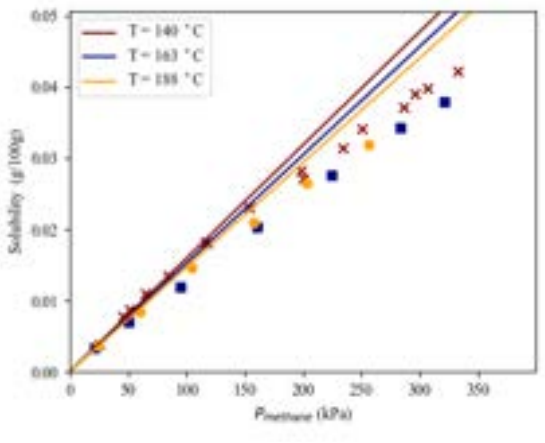

Figure 6: Solubility of methane in PE melt based on model predictions, with experimental data from Lundberg (1964)

Conclusion

SAFT-γ Mie with Michaels-Hausslein theory is able to produce good semi-quantitative predictions of absorption of a wide range of solutes in the amorphous domain of semicrystalline polyethylene, in line with experimental data. It is observed that solubility decreases with increasing temperature at a given pressure for solutes, in agreement with experimental data. SAFT-γ Mie produced good agreement with the experimental data for benzene, as each model isotherm can be fitted to the corresponding experimental isotherm with no consistent overpredictions or underpredictions over a range of temperatures and different polymer melting temperatures. Some agreement are also found for other molecules, where there are consistent overpredictions or underpredictions.

The sorption model is validated to be well-characterised by a single parameter f. As f is a polymer-sample dependent property, it should be independent of the solute pair. Thus, universal transferability of the f parameter to different polymer-solute systems might be hindered. Additional recalibration needs to be done on the coarse graining groups for higher temperatures and pressures, as well as for the groups $\mathrm{aCCH_3}$, $\mathrm{aCCH_2}$, and $\mathrm{CH_3}$, in order to increase the predictive ability of this model.

SAFT-γ Mie has been shown to be a valid EoS to model absorption above T_m for alkanes and branched alkanes, where polyethylene is fully amorphous. Good agreement between model data and experimental data is found for those ranges. However, additional calibrations can be done in order to maximise the predictive ability of this model, as well as other SAFT-γ Mie applications in general.

A factor currently hindering SAFT-γ Mie a fully quantitative VLE solubility prediction is the many sources of error. Examples include optimised SAFT parameters, reproducibility of experimental data, and the assumptions used in modelling the f parameter in Michaels-Hausslein theory. Future work to ensure comparability include calibrating SAFT parameters for VLE below T_m and standardising polymer thermophysical data and thermal history, to minimise uncertainty due to fortuitous cancellation of errors.

For future considerations, this model can be extended to more complex compounds, such as biological polymers with complex intermolecular attractions involving hydrogen bonding, so that the model can be used to predict sorption data for real-life applications, such as the sorption of solutes into polymeric membranes and packaging for industrial purposes, as well as natural and synthetic fibres with commercial purposes.

References

Banaszak, B.J., Lo, D., Widya, T., Ray, W.H., Pablo, J.J. de, Novak, A., and Kosek, J., 2004. Ethylene and 1-hexene sorption in LLDPE under typical gas phase reactor conditions: a priori simulation and modeling for prediction of experimental observations. *Macromolecules* [Online], 37(24) (), pp.9139–9150. Available from: https://doi.org/10.1021/ma0491107.

Barker, J.A. and Henderson, D., 1967. Perturbation theory and equation of state for fluids. II. a successful theory of liquids. *The journal of chemical physics* [Online], 47(11) (), pp.4714–4721. Available from: https://doi.org/10.1063/1.1701689.

Charlesby, A. and Callaghan, L., 1958. Crystallinity changes in irradiated polyethylenes. *Journal of physics and chemistry of solids* [Online], 4(4) (), pp.306–314. Available from: https://doi.org/10.1016/0022-3697(58)90081-7.

Chen, C.-C., 1993. A segment-based local composition model for the gibbs energy of polymer solutions. *Fluid phase equilibria* [Online], 83 (), pp.301–312. Available from: https://doi.org/10.1016/0378-3812(93)87033-w.

Doong, S.J. and Ho, W.S.W., 1991. Sorption of organic vapors in polyethylene. *Industrial & engineering chemistry research* [Online], 30(6) (), pp.1351–1361. Available from: https://doi.org/10.1021/ie00054a042.

Dos Santos, M.L., Corrêa, N.F., and Leitao, D.M., 1974. Interaction of polyethylene with isobutane, isobutylene, 1-butene and normal butane. *Journal of colloid and interface science* [Online], 47(3) (), pp.621–627. Available from: https://doi.org/10.1016/0021-9797(74)90239-2.

Dufal, S., Papaioannou, V., Sadeqzadeh, M., Pogiatzis, T., Chremos, A., Adjiman, C.S., Jackson, G., and Galindo, A., 2014. Prediction of thermodynamic properties and phase behavior of fluids and mixtures with the SAFT-γ Mie group-contribution equation of state. *Journal of chemical & engineering data* [Online], 59(10) (), pp.3272–3288. Available from: https://doi.org/10.1021/je500248h.

Flory, P.J., 1942. Thermodynamics of high polymer solutions. *The journal of chemical physics* [Online], 10(1) (), pp.51–61. Available from: https://doi.org/10.1063/1.1723621.

Flory, P.J. and Rehner, J., 1943. Statistical mechanics of cross-linked polymer networks II. swelling. *The journal of chemical physics* [Online], 11(11) (), pp.521–526. Available from: https://doi.org/10.1063/1.1723792.

Huggins, M.L., 1941. Solutions of long chain compounds. *The journal of chemical physics* [Online], 9(5) (), pp.440–440. Available from: https://doi.org/10.1063/1.1750930.

Hutacharoen, P., Dufal, S., Papaioannou, V., Adjiman, C.S., Jackson, G., and Galindo, A., 2016. Prediction of liquid-liquid partitioning and solubility of apis with the SAFT-γ Mie EoS approach.

Lacombe, R.H. and Sanchez, I.C., 1976. Statistical thermodynamics of fluid mixtures. *The journal of physical chemistry* [Online], 80(23) (), pp.2568–2580. Available from: https://doi.org/10.1021/j100564a009.

Liu, C. and Neogi, P., 1988. Sorption of benzene and n-hexane in polyethylene. *Journal of membrane science* [Online], 35(2) (), pp.207–215. Available from: https://doi.org/10.1016/s0376-7388(00)82444-8.

Lundberg, J.L., 1964. Diffusivities and solubilities of methane in linear polyethylene melts. *Journal of polymer science part a: general papers* [Online], 2(9) (), pp.3925–3931. Available from: https://doi.org/10.1002/pol.1964.100020909.

Michaels, A.B. and Hausslein, R.W., 1965. Elastic factors controlling sorption and transport properties of polyethylene. *Journal of polymer science part c: polymer symposia* [Online], 10(1) (), pp.61–86. Available from: https://doi.org/10.1002/polc.5070100107.

Novak, A., M.Bobak, Kosek, J., Banaszak, B.J., Lo, D., Widya, T., Ray, W.H., and Pablo, J.J. de, 2004. Manuscript in preparation.

Oishi, T. and Prausnitz, J.M., 1978. Estimation of solvent activities in polymer solutions using a group-contribution method. *Industrial & engineering chemistry process design and development* [Online], 17(3) (), pp.333–339. Available from: https://doi.org/10.1021/i260067a021.

Papaioannou, V., Calado, F., Lafitte, T., Dufal, S., Sadeqzadeh, M., Jackson, G., Adjiman, C.S., and Galindo, A., 2016. Application of the SAFT-γ Mie group contribution equation of state to fluids of relevance to the oil and gas industry. *Fluid phase equilibria* [Online], 416 (), pp.104–119. Available from: https://doi.org/10.1016/j.fluid.2015.12.041.

Papaioannou, V., Lafitte, T., Avendaño, C., Adjiman, C.S., Jackson, G., Müller, E.A., and Galindo, A., 2014. Group contribution methodology based on the statistical associating fluid theory for heteronuclear molecules formed from mie segments. *The journal of chemical physics* [Online], 140(5) (), p.054107. Available from: https://doi.org/10.1063/1.4851455.

Paricaud, P., Galindo, A., and Jackson, G., 2004. Modeling the cloud curves and the solubility of gases in amorphous and semicrystalline polyethylene with the SAFT-VR approach and flory theory of crystallization. *Industrial & engineering chemistry research* [Online], 43(21) (), pp.6871–6889. Available from: https://doi.org/10.1021/ie049592a.

Rausch, J.L., Schulz, T.C., and Danner, R.P., 2011. Solubility and diffusivity of cyclohexane in high density polyethylene. *Journal of applied polymer science* [Online], 124(5) (), pp.4315–4321. Available from: https://doi.org/10.1002/app.35433.

Wertheim, M.S., 1984. Fluids with highly directional attractive forces. i. statistical thermodynamics. *Journal of statistical physics* [Online], 35(1-2) (), pp.19–34. Available from: https://doi.org/10.1007/bf01017362.

Catalyst Design Study for the Catalytic Conversion of Ethanol to 1-Butanol and Butadiene via the Guerbet and Lebedev reactions.

Anshoor Yusra and Ayandipo Rafiah

Department of Chemical Engineering, Imperial College London, U.K.

Abstract

The use of bioethanol as a reagent in the production of fuels and a wide range of chemicals has seen growing interest due to its reduced environmental impacts, as a renewable chemical, compared to fossil fuel alternatives. 1-butanol and 1,3-butadiene (BD) are two desirable compounds that can be derived from bioethanol through the Guerbet and Lebedev reaction pathways, respectively. The application of 1-butanol as a fuel in the automotive industry has demonstrated several advantages over ethanol, such as poor solubility and a higher energy density. Moreover, BD shows great industrial importance, being a critical monomer in the production of several polymers such as synthetic rubbers. Due to the high potential of these processes, this review outlines the catalysts employed for the Guerbet and Lebedev reactions to date, focusing briefly on homogeneous catalysts, and more specifically on heterogeneous catalysts. This is followed by a discussion on the catalytic systems, including suggested areas of research for future studies. Techno-economic analysis was also utilised to assess the economic viability of both pathways based on currently available catalytic systems.

Keywords: Catalyst, Ethanol, 1-butanol, 1,3-butadiene, Guerbet, Lebedev

Introduction

In the early 20th century, Professor Hale, a member of the faculty at the University of Michigan advocated the use of agricultural carbohydrates as feedstock for many commercial products produced industrially. However, the application and further development of his idea lost traction in the 1950s as the exploration of inexpensive petroleum products emerged.[1] Now, the gradual transition to cleaner and more sustainable energy sources due to global concerns of climate change has led to the increased interest in producing fuels and chemicals from renewable biomass such as plants and agricultural waste.

Bioethanol is one of the major compounds produced in large quantities from fermentation of renewable biomass and is mainly used as a blending agent with gasoline fuel.[2] However, several hurdles restrict the extensive application of ethanol in the automotive industry. For example, ethanol has a relatively low energy density (24MJ/L vs 34.2MJ/L for gasoline), can result in corrosion of engine components and has a large affinity for water. Consequently, there is much interest for the development of a chemical route for the conversion of ethanol to heavier alcohols. 1-butanol has an energy density (29.2 MJ/L) similar to gasoline and poor solubility in water (74 g/L) thus alleviating many of the problems associated with ethanol.[3]

Methods known for the synthesis of butanol include the ABE fermentation process where mixtures of acetone, butanol and ethanol are produced using strains of the *Clostridium acetobutylicum bacterium*[4] and the hydroformylation/hydrogenation of propylene. These routes are challenging due to the existence of selectivity and separation issues.[5]

Alternatively, 1-butanol can be synthesised through the Guerbet reaction, a direct chemical route reliant on the coupling of ethanol. Ethanol is initially dehydrogenated to form acetaldehyde; aldol coupling, and dehydration then occur to form crotonaldehyde, which further undergoes hydrogenation to form 1-butanol. Other reactions involving intermediates of the reaction network occur simultaneously, resulting in heavier alcohols and other by-products.[6]

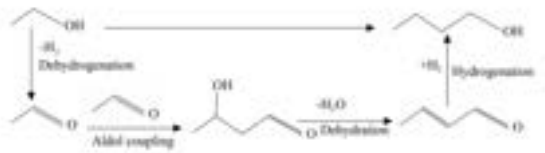

Figure 1. Guerbet Reaction Pathway

Ethanol is also a useful feedstock for the production of 1,3-butadiene (BD). BD is of significant economic importance in the polymers industry, being involved in the production of synthetic rubbers such as styrene – butadiene rubber and polybutadiene rubber. The production of BD is currently heavily reliant on fossil fuels, with the predominant production method utilising the C4 fraction produced in the steam cracking of naphtha.[7] BD is a by-product of this process, the desired product being ethene. The market price of BD has increased as a result of its reduced production due to the rise in oil prices and desire for lighter hydrocarbons. This is challenged further by the increased production of shale gas which reduces the amount of ethene required through the cracking process. Shale gas contains ethane which can be dehydrogenated to produce the ethene desired. This

alternative route provides competition, exacerbating the volatility of BD prices.[8]

Using biobased feedstock, BD can be produced from two routes; The two-step Ostromiselensky process involves the partial dehydrogenation of ethanol to acetaldehyde followed by recombination to form BD.[9] Figure 2 shows the Lebedev pathway, where acetaldehyde is formed from ethanol, after which aldol coupling of acetaldehyde occurs to form acetaldol. Acetaldol is then dehydrated forming crotonaldehyde, which is reduced with ethanol via the Meerwein-Ponndorf-Verley (MPV) reaction to crotyl alcohol and later dehydrated to produce BD.[10] Similar to the Guerbet reaction, side reactions occur producing by-products such as ethylene and butene.

The ability to tailor the product selectivity and yield of these processes is essential. The objective of this review is to assess the performances of the catalytic systems for the Guerbet and Lebedev reactions which have been developed to date. Furthermore, the review aims to discuss the technical and economic aspects of the global reactions and provide suggestions for the direction of future research.

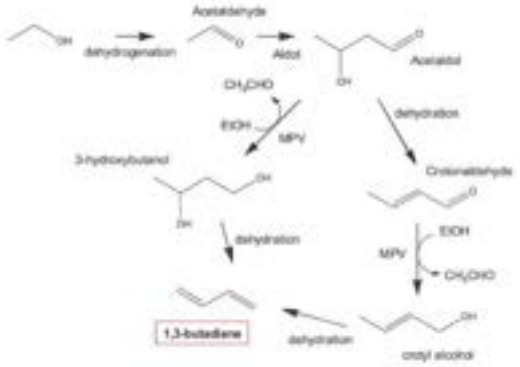

Figure 2. Lebedev Reaction Pathway.[11]

Homogeneous catalysts

The use of homogeneous catalysts for the upgrading of ethanol to 1-butanol has been a continued area of research for several years. Homogeneous catalysts typically proceed at lower temperatures than those required by heterogeneous catalysts and so allow the reaction to take place in the liquid phase. A base was commonly utilised to catalyse the aldol coupling step of the Guerbet mechanism, alongside a precious metal catalyst (such as Ru or Ir) to catalyse the dehydrogenation and hydrogenation steps. Koda *et al.* developed an iridium-based homogeneous catalyst ([Ir(acac)(cod)]) that achieved 51% 1-butanol selectivity at 41% conversion when used alongside an ethanol sodium ethoxide (EtONa) base, 1,7-octadiene as an additive and dppp ligand at 120˚C .[12] However, pre-activation by stirring the reaction mixture for 2 h at room temperature before the reaction was necessary to achieve a high turnover number (TON, moles product formed / mol active metal). An increase in catalyst loading as well as decreasing the reaction temperature, also resulted in a decrease in TON. No reaction was seen to take place in the absence of base, suggesting its critical role in the upgrading of ethanol to 1-butanol.

The investigation of ruthenium-based systems was also investigated by Dowson *et al.*, using $[\{RuCl_2(n^6\text{-p-cymene})\}_2]$ as a catalyst precursor with two molar equivalents (Ru/L 1:1) where L are bidentate phosphine ligands. In the absence of the diphosphine ligand, low base catalytic activity (6.9% conversion) was observed. The small-bite-angle bis(diphenylphosphanyl)methane ligand gave an excellent result with 20.4% conversion, 17.5% 1-butanol yield and 90% selectivity after 4h. Running the reaction for a duration longer than 4h did not result in an increase in any of the parameters. It is important to note that the pre-activation reported by Koda and co-workers was not required to achieve the high TON of 204. The ability for the catalyst to control base-catalysed aldol condensation of acetaldehyde was the main reason for its superior performance.

Ruthenium P−N (phosphine-amine) ligand complexes were developed by Wingad *et al.* in 2015, building upon the ruthenium-based catalysts previously studied by this group.[13] The use of a phosphine-amine ligand and EtONa base alongside the ruthenium-based catalyst resulted in a high selectivity of 93% at a higher conversion of 31% (TON, 301), significantly outperforming the results seen by Koda *et al*. The high selectivity of the system was suggested to be due to a 'metal-templated aldol condensation', however this is an area still under study. At water concentrations of 5% vol, higher conversion and selectivity were recorded when a P-N ligand was used compared to when a ddpm ligand was used, showing the water tolerance as a result of the P-N ligand. Ethanol feed produced from biomass will often contain small amounts of water and so water tolerance proves an advantage of this system.

The aldol coupling step is often catalysed by simple bases such as EtONa, however EtONa has poor selectivity towards the crotonaldehyde product. This results in the formation of side products due to a lack of control of the aldol coupling step and therefore, a decrease in 1-butanol selectivity. This issue was tackled by Chakraborty *et al.* in 2015.[14] An iridium-based catalyst with a nickel or copper hydroxide complex as the base, was utilised in a tandem catalytic approach. 1-butanol selectivity greater than 99% was achieved at an ethanol conversion of 37% (TON, 185) and a temperature of 150˚C when using the nickel complex as the base. The steric hinderance of the bulky ligands present on the complexes were used as a means of controlling the product selectivity. Through selectively coupling aldehyde molecules, crotonaldehyde was

produced as the sole product of this coupling step, resulting in the high selectivity achieved by this approach. However, this optimisation of selectivity resulted in a lower TON of 185.

TON is an important parameter that expresses the stability of a catalyst and so a high TON is often necessary for large-scale industrial application (i.e. the transport sector). In 2016, Tseng *et al* reported an amide-derived N,N,N-Ru (II) catalyst with a focus on improving TON and ethanol conversion.[15] The catalyst achieved a TON of 530 at an ethanol conversion of 53% and a 1-butanol selectivity of 37%. Increased ethanol conversion and TON were reached though the addition of triphenylphosphine (PPh_3) which served to prevent the decarbonylation pathway of the ethanol reactant.

In contrast to the Guerbet condensation of ethanol, the upgrading of ethanol to BD, *via* the Lebedev pathway has not been reported in open literature. This is most likely due to the high temperatures required, meaning the reaction usually takes place in the vapour phase. Therefore, the use of a homogeneous catalyst would most likely be ruled out.

Heterogeneous catalysts for Guerbet reaction

A review of the current literature revealed that frequently used catalysts for the Guerbet reaction included hydroxyapatites (HAP), aluminium oxide support doped with various metals and MgO, with a variety of other catalysts proving effective for the conversion of ethanol to 1-butanol. These catalysts were utilised in both flow and batch conditions.

Maio *et al.* reported a relatively high 1-butanol yield of 23.7% under mild conditions (250°C, 5h) using the inexpensive Ni-MgO catalyst (Table 1, Entry 1).[16] Recycling experiments using this catalyst indicated good catalyst activity over six cycles but there was a reduced yield after first use of Ni-MgO catalyst (23.7% to 19.5%). The small particle size of nickel and good distribution on the MgO carrier resulted in superior productivity of 1.88 $g_{but}g_{cat}^{-1}h^{-1}$.

Sun *et al.*[6] have reported at 320°C the production of 1-butanol over a copper and nickel doped porous metal oxide (PMO) catalyst with a 1-butanol selectivity of 70% using a weighted hourly space velocity (WHSV) of 3.99 h^{-1} (Table 1, Entry 2). Conversion over the Cu10Ni10-PMO catalyst was 56% and the productivity (0.705 $g_{but}g_{cat}^{-1}h^{-1}$) of the doped catalysts were approximately 3 times higher than those with dopants absent. Recycling experiments showed good robustness after 7 cycles, with a drop in 1-butanol yield from 22% to 14% and within range 10-14% afterwards with the relative product distribution staying constant.

Barrett *et al.* were able to demonstrate the change in selectivity over a copper-doped PMO catalyst upon the exposure to ppm quantities of a chloride source.[17] In the presence of the $MgCl_2.6H_2O$ additive to the Cu_{20}PMO catalyst, the substrate conversion rose from 43% to 59% (Table 1, Entry 3). The 1-butanol yield increased to 28% from 10% while that of ethyl acetate was observed to reduce proving there was a suppression in its formation. It was evident that the addition of Cl^- enhances catalyst productivity as the productivity of this system at 320°C, 0.748 $g_{but}g_{cat}^{-1}h^{-1}$, was slightly higher than observed by Sun et al using copper and nickel doped PMOs (Table 1, Entry 2). The catalyst showed high stability, producing high and relatively constant ethanol conversion and 1-butanol selectivity over 17 runs.

Ghaziaskar *et al.* achieved an optimal 1-butanol selectivity of 61.7% and yield of 21.6% at an ethanol conversion of 35% at 250˚C over 8% Ni alumina supported catalyst (Table 1, Entry 4).[18] At these conditions, a productivity of 1.11 $g_{but}g_{cat}^{-1}h^{-1}$ was achieved. Moreover, the catalyst demonstrated a high level of stability with product yields remaining relatively constant for 18h.

Tsuchida *et al.* studied the influence that varying the Ca/P ratio of the HAP catalyst would have on the upgrading of ethanol to 1-butanol through controlling the solution pH during synthesis.[19] Selectivity to 1-butanol was seen to increase with an increase in Ca/P ratio. At 20% conversion, HAP with a Ca/P ratio of 1.67 resulted in a 1-butanol selectivity of 69.8% at 298˚C (Table 1, Entry 5).

Silvester *et al.* investigated the reactivity of ethanol over a series of carbonate-containing hydroxypatites (HAPs) with different Ca/P ratios.[2] The optimal ratio of acid to base sites was found to be approximately 5 and best performance was obtained over the HAP-CO_3 catalyst which had a 60% selectivity to 1-butanol at 400°C (Table 1, Entry 6). Carbonate substitution did not have a negative effect on the catalyst stabilisation as ethanol conversion was reported stable during a 24h reaction run.

For the first time, Wang *et al.* were able to report the superior catalytic activity of calcium carbide (CaC_2) in the condensation of ethanol to 1-butanol (Table 1, Entry 7).[20] A yield of 24.5% 1-butanol and low selectivity of 39.3% was achieved at a temperature of 275°C. The productivity of the system decreased significantly during the reaction suggesting that there was a change in the catalytic components. In order to obtain a productivity of 0.174 $g_{but}g_{cat}^{-1}h^{-1}$, the reaction time was shortened to 6h at the expense of product yield.

Dispersion of MgO on an activated carbon (AC) support has been proposed by Cimino *et al.* as a novel catalyst for the upgrading of ethanol to 1-butanol.[21] The optimal catalytic conditions at 400˚C and a GHSV of 330 h^{-1} were found to correspond to

Table 1: Catalysts for the Guerbet reaction

Entry[a]	Catalyst	Device Mode	T (˚C)	WHSV (h^{-1})	X (%)	$Y_{1\text{-but}}$ (%)	$S_{1\text{-but}}$ (%)	Productivity ($g_{1\text{-but}}g_{cat}^{-1}h^{-1}$)
1[16]	Ni-MgO	B	250	-	44.3	23.7	53.5	1.88
2[6]	Cu10Ni10-PMO	C	320	3.99	56.0	22.0	70.0	0.705
3[17]	140ppm Cl^- with Cu_{20}PMO	B	320	-	59.0	28.0	53.0	0.748
4[18]	8% Ni/ɣ-Al_2O_3	C	250	6.40	35.0	21.6	61.7	1.11
5[19]	Ca-HAP (Ca/P = 1.67)	C	298	0.560	20.0	14.0	69.8	0.063
6[2]	HAP-CO3	C	400	8.30	21.0	12.6	60.0	0.840
7[20]	CaC_2	B	275	-	62.4	24.5	39.3	0.174
8[21]	20%MgO/AC	C	400	0.380	68.0	12.5	18.4	0.0382
9[22]	Cu_{10}MMO	B	350	-	79.6	25.4	32.0	-
10[23]	RuNi@MOF	B	170	-	11.2	8.85	79.0	-

[a]Reference for each catalyst. Abbreviations: C, Continuous; B, Batch; X, EtOH conversion; Y, Yield; S, Selectivity.

20% MgO/AC. This produced a 12.5% 1-butanol yield at an ethanol conversion of 68% (Table 1, Entry 8). This result was due to the high dispersion of the MgO on the AC support, which has a large surface area in comparison to the alternative alumina support used in comparison. However, the formation of MgO aggregates at loadings above 20% caused a decrease in both conversion and yield.

Through the use of a surface response model, Siqueira *et al.* optimised the catalyst load, reaction temperature and reaction time over a copper mixed metal oxide (MMO) catalyst in order to maximise the conversion of ethanol to 1-butanol.[22] The result was a Cu_{10}MMO catalyst achieving an ethanol conversion of 79.6% and a 1-butanol selectivity of 32% at 350˚C and 5h (Table 1, Entry 9). Through this study, reaction time was found to be the most important of the tested parameters.

Neumann *et al.* investigated Ru and Ni nanoparticles dispersed on a metal organic framework (MOF) with a focus on obtaining a catalyst with the ability to differentiate between ethanol and 1-butanol, so that high activity would be seen with respect to the ethanol reactant, whereas negligible activity would be seen for 1-butanol.[23] The result was a selectivity of 79% at an ethanol conversion of 11.2% and low temperature of 170˚C (Table 1, Entry 10), with selectivity reaching greater than 99% at lower conversions. The catalyst was seen to incorporate characteristics of both heterogeneous and homogeneous catalysts, producing the observed results at low temperatures.

Heterogeneous catalysts for Lebedev reaction

The Lebedev reaction of ethanol to BD has been studied over a range of catalysts with extensive research performed using MgO/SiO_2 systems, with or without the use of a metal promoter.
More recent studies have shown an increase in the use of Zr-Zn based catalytic systems.

Among more than 500 materials tested, Corson *et al.* showed 2%Cr_2O_3-59%MgO-39%SiO_2 catalyst performed best for the Lebedev reaction.[24] At 400°C and WHSV of 0.4 h^{-1}, the catalyst produced 38% yield of BD with 56% selectivity corresponding to a productivity of 0.09 $g_{BD}g_{cat}^{-1}h^{-1}$ (Table 2, Entry 1). The addition of a small amount of chromium oxide clearly resulted in higher BD yield and selectivity compared to the unmodified $MgO\text{-}SiO_2$ samples. However, there was a decrease in selectivity of BD, despite higher yield when the reaction was carried out at temperatures higher than 400°C.

Makinsha *et al.* demonstrated the increase in ethanol conversion and BD yield by the modification of the magnesia-silica binary system using a consecutive impregnation step. $MgO\text{-}SiO_2$ containing CuO promoter yielded 58.2% BD with a 60% selectivity at a high ethanol conversion of 97.5% (Table 2, Entry 2).[25] The effect of different preparation methods on performance was explored including mechanical mixing of calcined magnesium oxide and silica, magnesium hydroxide and silica and wet-kneading of magnesium hydroxide and silica, this was found to be negligible in impact.

Lewandowski *et al.* reported the applicability of ZrO_2/ZnO incorporated into $MgO{:}SiO_2$ for the conversion of ethanol to BD.[8] (95:5) $MgO{:}SiO_2$_ZrZn produced a 25% BD yield with a high selectivity of 62.6% (Table 2, Entry 3). The addition of Zr(IV) and Zn(II) increased the system selectivity by catalysing the aldol condensation and dehydration steps of the reaction mechanism.

A trimetallic silica supported catalyst ($Cu_{1.0}Hf_{3.0}Zn_{0.5}$/ SiO_2), developed by Baerdemaeker *et al.* at 360˚C, achieved a BD selectivity of 72% at a high ethanol conversion of 99% (Table 2, Entry 4).[26] Hf was utilised in preference to Zr due to its

Table 2. Catalysts for Lebedev Reaction

Entry[a]	Catalyst	Device Mode[b]	T (˚C)	WHSV (h^{-1})	X (%)	Y_{BD} (%)	S_{BD} (%)	Productivity ($g_{BD}g_{cat}^{-1}h^{-1}$)
1[24]	Cr_2O_3-MgO-SiO_2	C	400	0.400	68.0	38.0	56.0	0.09
2[25]	CuO/MgO–SiO_2	C	350	0.205	97.5	58.2	60.0	0.070
3[8]	MgO:SiO_2_ZrZn	C	325	0.300	40.0	25.0	62.6	0.075
4[26]	$Cu_{1.0}Hf_{3.0}Zn_{0.5}$/ SiO_2	C	360	0.210	99.0	71.6	72.0	0.090
5[27]	MgO-SiO_2	C	450	4.10	95.0	73.2	77.0	1.35
6[28]	Cs_2O-1ZnO-5ZrO_2/SiO_2	C	400	1.00	97.7	54.5	55.8	0.320
7[29]	MgO−SiO_2	C	450	4.10	68.0	41.5	61.0	0.998
8[30]	Ag–ZrO_2/SiO_2	C	325	0.474	86.9	62.4	71.8	0.174
9[31]	CuTaSiBEA	C	325	0.5	87.9	63.8	72.6	0.190
10[32]	talc with zinc	C	400	8.34	45.7	22.1	48.3	1.08

[a]Reference for catalysts. Abbreviations: C, Continuous; B, Batch; X, EtOH conversion; Y, Yield; S, Selectivity.

reduced formation of the unwanted ethylene by-product, resulting in a higher BD selectivity at increased loadings.

A hierarchical flower-like MgO-SiO_2 catalyst with an MgO:SiO_2 ratio of 65:35 at 450˚C was reported by Huang *et al.* to produce 95% ethanol conversion and a 77% BD selectivity with a high productivity of 1.35 $g_{BD}g_{cat}^{-1}h^{-1}$ (Table 2, Entry 5).[27] The catalyst preparation method was demonstrated to have a large influence on catalytic activity, with wet kneading resulting in higher activity.

Patil *et al.* focused their study on the effect of alkali metal supporters and the role of acid-base sites in the conversion of ethanol to BD when using a silica supported ZnO-ZrO_2 catalyst.[28] They found that the use of caesium as the alkali metal supporter produced the required balance of acid-base sites, resulting in optimal catalysis of the aldol condensation step. At 400˚C, the Cs_2O-1ZnO-5ZrO_2/SiO_2 catalyst reached a 97.7% ethanol conversion and a 55.8% BD selectivity with a 0.320 $g_{BD}g_{cat}^{-1}h^{-1}$ (Table 2, Entry 6).

Li *et al*. utilised reverse impregnation to prepare MgO-SiO_2 catalysts with nanosheets, nanodisks and flower-like morphology to determine the influence of morphology on catalytic activity during the conversion of ethanol to BD.[29] The most promising catalyst was observed to be the flower-like MgO-SiO_2, which achieved a BD selectivity of 61% at an ethanol conversion of 68% at 450˚C, corresponding to a productivity of 0.998 $g_{BD}g_{cat}^{-1}h^{-1}$ (Table 2, Entry 7).

Pang *et al.* demonstrated the critical role of surface interfaces in the reaction of ethanol to BD. They found that at 325˚C, a 2%Ag–4%ZrO_2/SiO_2 catalyst achieved 86.9% ethanol conversion and a 71.8% BD selectivity at a WHSV of 0.474 h^{-1} (Table 2, Entry 8).[30] This corresponded to a productivity of 0.174 $g_{BD}g_{cat}^{-1}h^{-1}$. Moreover, the addition of Ag was seen to have a large effect on the ethanol conversion, with a 0.7% decrease in loading resulting in a 32% decrease in conversion due to its role in the dehydrogenation step.

Over a tantalum-containing SiBEA zeolite with isolated framework mononuclear Ta(V) doped with Cu, Kyriienko *et al.* achieved 87.9% conversion of ethanol to yield 63.8% BD with a productivity of 0.19 $g_{BD}g_{cat}^{-1}h^{-1}$ (Table 2, Entry 9).[31] Active sites formed upon the doping of the zeolite seemed more stable as there is a higher stability in ethanol conversion, selectivity and yield of BD observed when compared to other samples prepared in the investigation.

Results by Sekiguchi *et al.* showed that talc containing 1.4wt% ZnO produced 21.1% yield of BD from 45.7% conversion of ethanol after 7 h on stream (Table 2, Entry 10).[32] The rate of butadiene production was significantly increased by the presence of small amounts of Zn in talc. This amount was essential for generating catalytic activity whilst also contributing to prolonging the catalyst life.

Discussion – Guerbet

Due to the variety of reaction steps involved in the Guerbet reaction, it is vital that catalysts for the conversion of ethanol to 1-butanol have multifunctional properties. The acidity and basicity of the catalysts influence the key reaction steps with dehydration usually catalysed by acid sites and basic sites being favourable for dehydrogenation. A balance between these acidic and basic properties is essential to achieve high catalyst productivity and selectivity since the product 1-butanol can undergo several side reactions, mainly dehydration.

Therefore, acid-base ratio is a very important parameter for the success of the Guerbet reaction.

Equimolar amounts of copper and nickel dopants can be introduced to tune catalytic activity of porous metal oxides (PMO). The composition of acid sites is reduced when compared to undoped MgAl-PMO and an improved selectivity to 1-butanol proves the correlation between acidity and basicity levels and reactivity. Cu dopants help to control the balance of these sites in mixed metal oxides (MMO). The increased basicity speeds up the rate of ethanol dehydrogenation, producing superior conversions as a result. Without the nickel dopant beside copper in the PMO, the 1-butanol yield is identical to the undoped catalyst due to the formation of ethyl acetate as the main product. A Cu-Ni alloy phase in the system which could be formed during the reaction is responsible for catalyst stability as there are stronger interactions between dehydrogenation metals enabling robustness after several cycles. It would be ideal to test the effects of nickel dopant alongside copper in MMOs in order to boost selectivity and productivity.

As hydroxyapatites (HAP) have a predominantly acidic nature, it is modified to decrease acid site density and thus increase basicity when applied to the Guerbet process. The basic character of carbonate rich apatites produces a high productivity with a larger than previously reported Ca/P ratio of 5. Within the HAP structure, Ca^{2+} provides Lewis acid sites whilst the O from phosphate ions acts as the base site. At a Ca/P ratio of 1.62, the distance between the two ions facilitates the entrapments of hydrogen on the catalyst surface enabling it to take part in the mechanism instead of escaping as hydrogen gas (as observed in MgO supported catalysts). With HAPs showing excellent characteristics as support catalysts, focus should be on the modification of base sites to achieve higher catalytic activity.

The alkyl moiety of CaC_2 contributes positively to its application in the Guerbet process. Whilst Ca^{2+} similar to HAP, provides acid sites, the compound as a whole is susceptible to nucleophilic attack of the acid terminal hydrogen which promotes hydrogen transfer. However, deactivation occurs as the catalyst converts to C_2H_2 due to the formation of H_2O in ethanol condensation. As a result, productivity decreases significantly during the reaction so reaction time must be shortened to obtain optimal productivity. The effects of catalyst composition change on yield could be countered by increasing the catalyst loading but a method of maintaining productivity at a constant level must by devised because an increased loading reduces the catalyst efficiency.

Specific adsorbates like chlorine can be useful in tuning the selectivity of mixed phase catalysts. Chlorine modification of copper doped PMO reduces the surface basicity of the catalyst and suppresses the formation of ethyl acetate resulting in a slightly improved 1-butanol yield and productivity. It should be noted that an increased chloride concentration increases Cu sintering and reduces catalyst surface area. Continued research into the addition of adsorbates to marginally improve existing systems would be beneficial because this study shows its implementation can increase 1-butanol yield and productivity by 27% and 6% respectively (when compared to Cu10Ni10-PMO catalyst). Methods to reduce effects on catalyst activity (sintering) should also be explored.

Amongst all catalysts, conversion, and productivity increase with temperature. Operation at elevated temperatures is not beneficial though, due to the negative impact on 1-butanol yield as self-coupling and coupling with ethanol reactant led to the formation of unwanted heavier alcohols thus reducing selectivity.

In the PMO systems, reactions between 180°C and 220°C took place in the liquid phase. Higher temperatures provided supercritical conditions which facilitated mass transfer, this is the reason for its excellent operation at 320°C. It was observed that at higher reaction temperatures, ethanol dehydration is the dominant reaction, this is supported by the observation of less than 25% conversion on MMO catalysts at temperatures below 300°C. Calcination temperature of the MMO catalyst is also essential in achieving the correct balance of acidic and basic sites. Higher temperatures were found to decrease basic sites whilst leaving acidic sites unchanged.

Ethanol conversion and 1-butanol yield initially increase with increasing time on stream. The dynamics of catalyst properties during the reaction affect performance as changing compositions may cause deactivation.

The use of subcritical ethanol as the reaction medium favours the formation of acetals whereas supercritical ethanol led to the preferential formation of the 1-butanol product in some nickel doped alumina systems. This is due to a drop in ethanol density along with the fact that sub and super critical conditions favour compounds with higher solubility in sub and supercritical ethanol. It is evident that optimal operational and substrate conditions will depend on the unique characteristics of each system as this result was not observed across all studies.

The ability of metal organic frameworks (MOF) to differentiate between ethanol and 1-butanol with high activity towards ethanol is a

promising feature of the system. Low Ru loading was needed for efficient alloying which was necessary in the maintenance of catalytic activity. High activity was observed at temperatures as low as 170°C which is the lowest among heterogeneous catalysts used in the direct conversion of ethanol to 1-butanol. Therefore, it would be beneficial to explore this novel system further by studying the effects of different alloyed metals in order to optimise production and promote industrial application.

Discussion – Lebedev

The effect of temperature on the Lebedev reaction is well established in past studies and so is an area that is unlikely to benefit much from further investigation. The general trend found in conversion was that an increase in temperature resulted in a subsequent increase in conversion. However, the BD selectivity demonstrated an inverted U-shaped trend, with an increase in temperature initially causing an increase in BD selectivity and reaching a maximum, as seen in systems such as the flowerlike $MgO\text{-}SiO_2$ and $Cs_2O\text{-}1ZnO\text{-}5ZrO_2/SiO_2$ catalyst. This maximum was found by many studies to be in the 300˚C to 450˚C range, depending on the catalyst used. A further increase in temperature resulted in a relatively large decrease in BD selectivity. The observed peak was explained as a result of the competitive reactions of ethanol to acetaldehyde, which shows a downward trend with temperature, and ethanol to ethylene, whose production increased with temperature. Therefore, at higher temperatures, the dehydration reaction to ethylene is dominant.

Similar to the Guerbet reaction, the catalysts for the Lebedev process require bifunctionality. The complex reaction network demands a balance in the amount and strength as well as the ideal proximity of acid/base and redox sites, where the density of these sites was typically measured using techniques such as temperature programmed desorption. However, study into the direct influence of each site and its configuration, on the activity of the catalyst is an area that requires further study. In $MgO\text{-}SiO_2$ and $ZnO/ZrO_2\text{-}SiO_2$ systems, Mg/Si or Zn/Zr ratios, dopant loading, and preparation methods were commonly investigated factors that had an impact on the balance of various sites on the catalyst. This in turn influenced the observed catalytic activity (in terms of ethanol conversion and BD selectivity).

It was found that the dehydrogenation step typically proceeds over basic sites, whereas acidic sites were found to promote the dehydration pathway. An increase in Mg/Si ratio was generally seen to result in an increase in basic sites, due to MgO, and a decrease in acidic sites on the catalyst, where this acidity originates from the SiO_2 support. As a result, ethanol conversion increases and ethylene selectivity decreases with an increase in MgO content. However, BD selectivity is seen to increase with Mg/Si ratio only to a given point before decreasing, as seen for the hierarchical flower-like $MgO\text{-}SiO_2$. This highlights the importance of not only basic sites, but also the presence of acid sites in the Lebedev reaction mechanism. It has been suggested that adjacent acid and base sites are crucial for the aldol condensation and MPV steps. In $ZnO/ZrO_2\text{-}SiO_2$ systems, the addition of ZnO introduced basic sites to the system whereas ZrO_2 added acidic sites. High Zn/Zr ratios were often unfavourable due to the excessive reduction of acidic sites, leading to lower BD yields. The Mg/Si and Zn/Zr ratios showed similar trends in that an intermediate ratio, balancing acid and base sites was crucial for optimising BD yield and selectivity. Varying the Zn/Zr ratio had a more significant impact on activity in comparison to impacts brought about by changes in dopants loading.

Different preparation methods for the binary Mg-Si materials were carried out to obtain samples with variations in strength and location of base and acid sites. Catalysts prepared using a Sol-gel method were found to have a higher amount of strong acid sites and so favoured the dehydration pathway. In contrast, catalysts prepared through the wet kneading process had a significantly higher number of base sites, resulting in the highest BD yield of the methods investigated due to the dehydrogenation pathway being favoured. The importance of surface interfaces has been greatly emphasised in these preparation methods. Mg-O-Si interfaces are formed due to the interaction of MgO with SiO_2. This interaction is strengthened by the wet kneading process resulting in the higher activity observed. Moreover, catalysts prepared though the physical mixture of MgO and SiO_2 had a significantly lower BD yield than the wet kneaded samples which reinforced the critical role of the interaction between MgO and SiO_2 as well as the proximity of these sites.

The better performance of the flower-like morphology, mentioned in the heterogeneous catalyst section above, was due to the higher synergy between MgO and SiO_2. The favoured formation of Mg-O-Si bonds over Si-O-Si bonds resulted in more interfacial Mg-O-Si bonds being formed than seen in the nanosheet and nanodisk structures. This trend in activity also followed the acid-base site pattern, with flower-like giving the highest base/acid site ratio and nanodisk giving the lowest ratio. The formation of Zr-O-Si interfaces in $ZrO_2\text{-}SiO_2$

systems due to high ZrO_2 dispersion resulted in a decrease in strong acid sites and the formation of medium and weak Lewis acid sites. Therefore, the aldol condensation reaction was favoured over the dehydration reaction. Further study into the relationship between these interfaces and catalytic activity could potentially be a beneficial direction to move in for the Lebedev reaction.

Productivities are often an important indicator for industrial application of a catalytic system. The hierarchical flower-like MgO-SiO_2 catalytic system developed by Huang et al recorded a productivity of 1.35 $g_{BD}g_{cat}^{-1}h^{-1}$, which is the highest among the catalytic systems investigated for both MgO-SiO_2 and ZnO/ZrO_2-SiO_2 systems. This was achieved whilst also maintaining a high BD yield of 73.2%. Moreover, the Flower-like MgO−SiO_2 catalyst also had a significantly higher productivity compared to the alternative MgO-SiO_2 catalysts. Both catalysts place an emphasis on the influence of surface interactions and so this may potentially be an important factor when considering the productivity. These catalytic systems have been operated using dry feed conditions, whereas the ethanol feed used in industry will often contain some water. Therefore, investigations into catalytic activities under wet feed conditions would be beneficial for future studies.

Techno-Economic Analysis

Techno-economic analysis of the Guerbet and Lebedev reaction process was carried out by Nezam *et al.* and Camacho *et al.* using $NiLa_2O_3/Al_2O_3$ and Hf-Zn catalyst systems repectively, with anhydrous ethanol as the feed.[33,34]

In the Guerbet process, ethanol is converted to 1-butanol in a jacketed stainless steel up-flow packed bed reactor at temperatures ranging between 210℃ and 250℃. The plant is to fulfil a capacity of 75,000 tonne/yr. Fresh ethanol is combined with recycled ethanol, pressurised, and preheated to the reaction temperature before being passed into the reactor. Generated steam used to remove heat from the reactor partially preheats the reactor feed. After a series of separations, five outlet streams are produced: pure water, azeotropic ethanol/water mixture recycled to the reactor, light by-products used as steam for heat generation, 1-butanol and C6+ alcohols (sold as co-products). Separation costs are reduced by ensuring sufficient ethanol is present in the reactor effluent so all the water can be removed in the distillate as the formation of a 1-butanol-water azeotrope is avoided.

The techno-economic analysis determines the required selling price of 1-butanol as a function of return on investment. Price of ethanol is taken as the average wholesale price over recent periods - \$0.53/kg. Catalyst cost is conservatively estimated as nickel and lanthanum oxide are both inexpensive materials. The maximum per-pass conversion required to avoid the significant costs associated with obtaining dry 1-butanol from the 1-butanol/water azeotrope is 40%. Limiting the conversion is seen to have a positive effect on system productivity as the Ni-MgO catalyst studied by Maio *et al.* results in the best productivity ($1.88g_{but}g_{cat}^{-1}h^{-1)}$ in this study at a conversion of 44.3%.

At 40% ethanol conversion, the corresponding minimum selling price (MSP) is estimated to be between \$1.55/kg to \$1.60/kg. As feedstock costs make up a large proportion of operating costs, the MSP is very sensitive to the market price of ethanol. A significant increase in conversion of ethanol in the plant is not favourable however, as a larger reactor is needed and smaller amounts of ethanol in the reactor effluent lead to 1-butnaol/water azeotrope which will increase utility and thus operating costs.

In the Lebedev process, bioethanol (with wet feed conditions, 93 wt % ethanol) is converted to 200,000 tonne/year of BD under industrial conditions in a furnace reactor (which is modelled as a yield reactor). Fresh and recycled ethanol are combined before a subsequent reaction occurs in the reactor. A series of separations are carried out on the reactor effluents, including adsorption/desorption, extractive distillation, liquid-liquid separation, distillation, molecular sieving and high-pressure distillation. This resulted in seven outlet streams from the system: a purified ethanol stream recycled to the reactor, a residual fuel stream (which is a mixture of polar compounds), a wastewater stream (water with polar compound impurities) and separate high purity acetaldehyde, butene, hydrogen, ethylene, and propylene streams (sold as co-products).

Analysis was carried out using scenarios with differing carbon yield and selectivity. Higher productivity results in less ethanol feed (17%) needed per ton of BD produced due to the higher conversion and selectivity. Less by-products are produced meaning reduced solvent amounts are needed for separations and less utilities are consumed. Therefore, catalysts with higher selectivity led to lower raw ethanol requirements and reduced energy consumption (12%), so catalyst selectivity is an important factor to make the economics favourable.

Techno-economic analysis results in an estimated MSP of \$2.05/kg for BD. The MSP is mainly determined by the operating costs whilst the contribution of the capital costs is marginal. Ethanol accounts for 86.8% of operating costs so similar to

1-butanol, the MSP is sensitive to the price of ethanol which is highly volatile.

It should be noted that 1-butanol as a fuel component is currently not economical as the price fails to compete with current gasoline prices. The probability of profitability for the Lebedev process is low because the MSP is higher than the mean market price. Although the primary cost driver of both process economics is ethanol feed costs, a suitable combination of ethanol, 1-butanol and BD market process is required to make the process economical.

Greenhouse gas (GHG) emissions of the process are largely influenced by ethanol feedstock source.[35] Although there are uncertainties in farming practices, biorefinery operations and transport distance/modes, analysis by Shylesh *et al.* showed that BD derived from sugarcane and corn stover ethanol sources is a net carbon negative product. Emissions were decreased by 150% and 140% for sugarcane and corn stover ethanol sources respectively when compared to the production of petroleum-based BD. The economics of the bioethanol route could be further improved if the decrease in GHG emissions compared to the fossil fuel route is subsidised.

Conclusion

The catalytic upgrade of ethanol to 1-butanol and 1,3-butadiene (BD) has been an area of much research due to the potential to produce these products from a renewable source. Despite the advantages of homogeneous catalysts due to lower reaction temperatures, heterogeneous catalysts are often preferred for industrial application due to lower associated separation costs, as the catalyst can be easily recovered from the reaction mixture. For the Guerbet catalysts, it has been suggested that methods to reduce effects on catalyst activity (sintering) should be explored to develop more stable catalysts. Moreover, further research into novel catalytic systems, such as Ru and Ni on MOF, would be beneficial due to the high selectivity achieved at lower temperatures. For the Lebedev catalytic systems, additional study into the relationship between surface interfaces and catalytic activity was suggested as a beneficial direction for future research. Research on both the Lebedev and Guerbet catalytic systems are primarily carried out utilising dry feed conditions and so investigation into these catalytic systems using wet feed conditions would be of great use. Techno-economic analysis has determined the minimum selling price (MSP) of both products to be highly sensitive to raw ethanol price. The upgrading of ethanol to 1-butanol was found not to be economically viable, whereas the profitability of ethanol to BD was low and greatly influenced by the systems selectivity as well as the market price of BD.

References

(1) Caes *et al.* (2015) Biomass to Furanics: Renewable Routes to Chemicals and Fuels. *ACS Sustainable Chem. Eng.* 3, 2591-2605. Available from: doi: 10.1021/acssuschemeng.5b00473

(2) Silvester *et al.* (2015) Reactivity of Ethanol over Hydroxyapatite-based Ca-enriched Catalysts with Variuos Carbonate Contents. *Catal. Sci. Technol.* 5, 2994-3006. Available from: doi: 10.1039/C5CY00327J

(3) Balat. (2016) Production of Bioethanol from Lignocellulosic Materials via the Biochemical Pathway: A Review. *Energy Conversion and Management*. 52,858-875. Available from: doi: 10.1016/j.enconman.2010.08.013

(4) Meramo-Hurtado *et al.* (2020) Comparison of Biobutanol Production Pathways via Acetone-Butanol-Ethanol Fermentation using a Sustainability Exergy-based Metric. *ACS Omega.* 30, 18710-18730. Available from: doi: 10.1021/acsomega.0c01656

(5) Pruett. Hydroformylation (1979). *Adv. Organomet. Chem.* 17, 1-60. Available from: doi: 10.1016/S0065-3055(08)60320-2

(6) Sun *et al.* (2017) Efficient Catalytic Conversion of Ethanol to 1-Butanol via the Guerbet Reaction over Copper and Nickel Doped Porous Metal Oxides. *ACS Sustainable Chem. Eng.* 5, 1738-1746. Available from: doi:10.1021/acssuschemeng.6b02494

(7) Ullmann (2000) *Ullmann's Encyclopedia of Industrial Chemistry.* 6th ed. New York, Wiley. Available from: doi:10.1002/14356007

(8) Lewandowski *et al.* (2014) Investigations into the Conversion of Ethanol to 1,3-Butadiene Using MgO:SiO2 Supported Catalysts. *Catalysis Communications.* 49, 25-28. Available from: doi:10.1016/j.catcom.2014.02.003

(9) Makshina *et al.* (2014) Review of Old Chemistry and New Catalytic Advances in the On-Purpose Synthesis of Butadiene. *Chem Soc. Rev.* 43, 7917-7953. Available from: doi:10.1039/C4CS00105B

(10) Pomalaza *et al.* (2016) Recent Breakthroughs in the Conversion of Ethanol to Butadiene. *Catalysis.* 6, 203. Available from: doi:10.3390/catal6120203

(11) Jones *et al.* (2011) Investigations into the Conversion of Ethanol to 1,3-Butadiene. *Catal. Sci. Technol.* 1,267-272. Available from: doi:10.1039/C0CY00081G

(12) Koda *et al.* (2009) Guerbet Reaction of Ethanol to n-Butanol Catalyzed by Iridium Complexes. Chemistry Letters. 38, 838-839. Available from: doi:10.1246/cl.2009.838

(13) Wingad *et al.* (2015) Catalytic Conversion of Ethanol to n-Butanol Using Ruthenium P−N Ligand

Complexes. ACS catalysis. 5, 5822-5826. Available from: doi:10.1021/acscatal.5b01327
(14) Chakraborty et al. (2015) Highly Selective Formation of n-Butanol from Ethanol through the Guerbet Process: A Tandem Catalytic Approach. Journal of the American Chemical Society. 137, 14264-14267. Available from: doi:10.1021/jacs.5b10257
(15) Tseng *et al.* (2016) Upgrading Ethanol to 1-Butanol with a Homogeneous Air-Stable Ruthenium Catalyst. Chemical communications (Cambridge, England). 52, 2901-2904. Available from: doi: 10.1039/C5CC09913G
(16) Wang *et al.* (2020) Efficient One-Pot Valorization of Ethanol to 1-Butanol Over an Earth-Abundant Ni-MgO Catalyst Under Mild Conditions. *Sustainable Energy Fuels*. 4, 1612-1615. Available from: doi: 10.1039/C9SE01236B
(17) Barrett *et al.* (2018) A Pinch of Salt Improves n-Butanol Selectivity in the Guerbet Condensation of Ethanol over Cu-doped Mg/Al Oxides. *ACS Sustainable Chem Eng.* 6, 15119-15126. Available from: doi: 10.1021/acssuschemeng.8b03589
(18) Ghaziaskar *et al.* (2013) One-Step Continuous Process for the Production of 1-Butanol and 1-Hexanol by Catalytic Conversion of Bioethanol at its Sub-/Supercritical State. RSC advances. 3, 4271. Available from: doi: 10.1039/c3ra00134b
(19) Tsuchida *et al.* (2008) Reaction of Ethanol over Hydroxyapatite Affected by Ca/P Ratio of Catalyst. Journal of catalysis. 259, 183-189. Available from: doi: 10.1016/j.jcat.2008.08.005
(20) Wang *et al.* (2019) Efficient Conversion of Ethanol to 1-Butanol and C5-C9 Alcohols over Calcium Carbide. *RSC Adv.* 9, 18941-18948. Available from: doi: 10.1039/c9ra02568e
(21) Cimino *et al.* (2019) MgO Dispersed on Activated Carbon as Water Tolerant Catalyst for the Conversion of Ethanol into Butanol. Applied sciences. 9, 1371. Available from: doi: 10.3390/app9071371
(22) Siqueira *et al.* (2019) Highly Selective 1-Butanol Obtained from Ethanol Catalyzed by Mixed Metal Oxides: Reaction Optimization and Catalyst Structure Behaviour. *Molecular catalysis*. 476, 110516. Available from: doi: 10.1016/j.mcat.2019.110516
(23) Neumann *et al.* (2019) Metal−Organic Framework-Derived Guerbet Catalyst Effectively Differentiates between Ethanol and Butanol. Journal of the American Chemical Society. 141, 17477-17481. Available from: doi: 10.1021/jacs.9b08968
(24) Corson *et al*. (1950) Butadiene from ethyl alcohol; Catalysis in the One and Two Step Process. *Ind. Eng. Chem*. 42, 359-373. Available from: doi: 10.1021/ie50482a039
(25) Makshina *et al*. (2012) Catalytic study of the Conversion of Ethanol to 1,3-Butadiene. *Catalysis Today*. 198, 338-344. Available from: doi: 10.1016/j.cattod.2012.05.031
(26) Baerdemaeker *et al.* (2015) Bimetallic Zn and Hf on Silica Catalysts for the Conversion of Ethanol to 1,3-Butadiene. ACS Catal. 6, 3393-3397. Available from: doi: 10.1021/acscatal.5b00376
(27) Huang *et al*. (2017) Highly Active and Selective Binary MgO–SiO2 Catalysts for the Production of 1,3-Butadiene from Ethanol. Catal. Sci. Technol. 7,168-180. Available from: doi: 10.1039/c6cy02091g
(28) Patil *et al*. (2017) Improving 1,3-Butadiene Yield by Cs Promotion in Ethanol Conversion. Applied Catalysis A. 543, 67-74. Available from: doi: 10.1016/j.apcata.2017.05.025
(29) Li *et al.* (2019) Morphological Control of Inverted MgO-SiO2 Composite Catalysts for Efficient Conversion of Ethanol to 1,3-Butadiene. Applied Catalysis A. 577, 1-9. Available from: doi: 10.1016/j.apcata.2019.03.007
(30) Li *et al*. (2020) Conversion of Ethanol to 1,3–Butadiene over Ag–ZrO2/SiO2 Catalysts: The Role of Surface Interfaces. Journal of Energy Chemistry. 54, 7-15. Available from: doi: 10.1016/j.jechem.2020.05.038
(31) Kyriienko *et al.* (2017) Ethanol Conversion into 1,3-Butadiene by the Lebedev Method Over MTaSiBEA Zeolites (M = Ag, Cu, Zn). *ACS Sustainable Chem Eng.* 5, 2075-2083. Available from: doi: 10.1021/acssuschemeng.6b01728
(32) Sekiguchi *et al*. (2015) One-Step Catalytic Conversion of Ethanol to 1,3-Butadiene Using Zinc-Containing Talc. *Catalysis Communications*. 68, 20-24. Available from: doi: 10.1016/j.catcom.2015.04.023
(33) Nezam *et al*. (2019) Continuous Condensed-Phase Ethanol Conversion to Higher Alcohols: Experimental Results and Techno-economic Analysis. *Journal of Cleaner Production.* 209, 1365-1375. Available from: doi: 10.1016/j.jclepro.2018.10.276
(34) Camacho *et al.* (2020) Techno-economic and Life-Cycle Assessment of One-Step Production of 1,3-Butadiene from Bioethanol Using Reaction Data under Industrial Operating Conditions. *ACS Sustainable Chem, Eng.* 8,10201-10211. Available from: doi:10.1021/acssuschemeng.0c026
(35) Shylesh *et al.* (2016) From Sugars to Wheels: The Conversion of Ethanol to 1,3-Butadiene over Metal-Promoted Magnesia-Silicate Catalysts. *ChemSusChem.* 9, 1462-1472. Available from: doi:10.1002/cssc.2016000195

Surrogate Modelling of Spray Dispersion using Computational Fluid Dynamics & Machine Learning

Dominik Klotz and Samuel Dale

Department of Chemical Engineering, Imperial College London, U.K.

Abstract *Spray-mist deposition from vehicles is an important phenomenon in several fields including pesticide application and disinfection of large areas. Here, the feasibility of the use of machine learning (ML) to generate surrogate models of spray behaviour from computational fluid dynamics (CFD) data is investigated. CFD is used to model a single cone spray nozzle using a Lagrangian-Eulerian approach, with pesticide spray modelled as a kinematic particle cloud. A self-generated computational pipeline is used to produce 5550 distinct simulations with variation of multiple physical parameters. A 600 pixel image of spray deposition at each simulation time is produced for each simulation and is used to train various classes of ML algorithms. The strongest surrogate model approaches were found to be based on a self-developed traversing local frame on which a Gaussian process regressor was trained, achieving a maximum root relative mean error of 1.3%, and thresholding of the deposition images with binary images being used for classifier training which showed an overall accuracy of 78%. The potential of surrogate modelling of this type of chaotic flow behaviour was thus shown. This technique is potentially suitable for active control of spray dispersion due to its expected advantages of high accuracy and configurability with low end-user computing times.*

1 Introduction

Spray-mist deposition from either terrestrial vehicles, aircraft or, increasingly, unmanned aerial vehicles (UAVs) is the dominant route of pesticide application. Globally, 3.5 Mt of pesticides are projected to have been applied during 2020 [1]. Depending on the mode of pesticide application, up to 75% of the applied volume does not reach the intended target area – the annual cost of environmental and societal damage by unnecessary pesticide exposure is estimated to amount to up 10 billion US dollars in the US alone [1, 2].

In order to apply pesticides, solutions of varying pesticide and additive compositions are sprayed out via boom arrangements of several nozzles; the atomisation process results in broadly distributed spray droplet diameters on the order of magnitude of μm. Lower droplet diameters achieve better, uniform active component coverage of the plant foliage but are more susceptible to downwind displacement [3]. Horizontal downwind drift of spray droplets outside their intended area of deposition is referred to as spray drift, and is the primary pathway for off-target pesticide deposition [4].

Efforts to mitigate spray drift have lead to positive results, particularly the development of drift-reducing nozzles (DRN) [5], control of atomisation and evaporation properties via additive by-mixtures [6], and introduction of agricultural buffer zones [7]. Accurate monitoring of dispersion effects, and thus the establishment of conclusive cause-effect relationships in legislation, is incredibly difficult due to weather-sensitivity and non-periodic spraying schedules [8]. Regulatory agencies have established various safety requirement schemes, created extensive rating frameworks for various nozzle types and placed heavy weighting on the wide-spread roll out of DRNs [9, 10]. The classification schemes usually rely on comparison to a reference nozzle under specified wind tunnel conditions. Comparative experiments under strictly defined conditions provide adequate results for differentiation of individual nozzle designs and their spray drift potentials, but provide limited information for modelling of actual field spray drift behaviour [3].

With the rise of precision agriculture [11] and smart farming [12], the level of technological capabilities in the agricultural sector is primed to enter a new phase. Application of sophisticated sensor and control techniques via UAVs will enable optimally targeted application of pesticides [13–15] – and the development of easily deployable, highly accurate spray drift models will be required to successfully adapt and control spraying schedules in real time, enabling further reduction of the environmental impact of pesticide usage.

Spray dispersion from UAVs has found wider use in 2020, with efforts to modify agricultural UAVs for disinfectant spraying taking place in response to the COVID-19 pandemic [16] and the rapid roll-out of commercial UAV disinfection services having occurred [17]. Reduction of spray drift is important here to ensure effective disinfection of the desired surface and prevent environmental contamination by dispersed disinfectant.

This report sets out to develop a data-driven surrogate model (SM) of the spray drift phenomenon, ca-

pable of achieving highly accurate results at low computational costs and being useful for real-time control of spray-mist deposition. Development of a validated computational fluid dynamics (CFD) simulation (3.1) and integration into a custom computational pipeline (3.2) allowed for generation of high quality synthetic CFD data used to train multiple classes of ML algorithms to produce surrogate models of spray behaviour (3.3). Analysis showed that the most successful approach was based on image thresholding and classification of individual pixels (4.2.4), with a self-developed traversing local frame regressor also showing promise (4.2.4). The potential of ML-based surrogate modelling of spray behaviour was demonstrated, with potential applications in active control of spray dispersion or in nozzle design studies.

2 Background

Currently available spray drift models can be compartmentalised into four main approaches, summarised in order of increasing complexity from (1) to (4) in table 1 [18–23]. Atmospheric plume dispersion and multiple regression are computationally inexpensive, but provide only limited accuracy: they remain extensively used in the assessment of long term exposition and emission rates, and drift buffer zone assessment [3, 18]. Pure droplet-tracking methods solve the Lagrangian equations of motion of discrete particle clouds with a stochastic component (random walk models), while treating the surrounding atmospheric wind field in a simplified, correlation-based manner [20, 21]. Full CFD studies add a further layer of complexity by solving the Navier-Stokes (NS) equations, usually additionally employing turbulence modelling for the wind field. They then take one of two primary approaches: Eulerian/Lagrangian (E/L) or Eulerian/Eulerian (E/E). The former computes the movement of a Lagrangian particle cloud using two-way interaction between the fluid and the discrete phase [24], whereas the latter computes droplet and wind phase as fluids via the NS, possibly utilizing interface capturing volume of fluid (VoF) methods [23].

Classes of problem with negligible diffusion are well-described by an E/L framework as numerical diffusive effects form an inherent part of E/E solution methods [25]. In particular, drag force-dominated application settings with constant interface topologies are preferentially formulated in the E/L view when compared to the "pure" two-fluid E/E approach. The phase fraction function employed in the classic two-fluid approach neglects any possible geometrical information about the phase boundary and treats each computational cell as a homogeneous mixture of both phases, which is not desirable in the description of a shape-sensitive force such as drag [26].

The individual tracking of large numbers of Lagrangian particles and their interactions as employed in E/L formulations is usually associated with higher computational cost than comparable E/E implementations; however, prior CFD studies show that the number of Lagrangian particles required to accurately model spray drift behaviour is relatively low [27]. Additionally, inclusion of evaporation effects does not significantly increase accuracy [28]. The volume fraction of the droplet phase (Φ_p) encountered within agricultural sprays places the spray cloud in the upper region of dilute suspensions [29], providing justification for the dominance of E/L approaches in available spray drift CFD studies. The dominance of this approach is further explained by the easily accessible implementation of Lagrangian particle clouds in several CFD software packages, shipping with a wide variety of configurable subroutines. Considering the combined ease of use, physically justified range of applicability to the considered phenomenon and particularly the ability to directly specify several key properties of the droplet phase [30, 31], the E/L approach – in conjunction with experimental data for different nozzle types – was chosen to be the preferred framework for the formulation of the CFD setup in this study.

Experimental spray drift measurements have been carried out extensively. Nuyttens et al. carried out detailed measurement of spray drift variation with droplet size and nozzle type by use of spray collectors and phase Doppler particle analysis downwind of a single mounted nozzle in a wind tunnel [32]. Their wind tunnel setup follows ISO 22856:2008 [33] in line with governmental DRN accreditation schemes [10], and similar setups have been utilised in numerous experimental studies [27, 34, 35]. The extremely controlled nature of these wind tunnel experiments makes the data ideal for CFD validation. Further studies approach drift measurement through diverse methods, in-

Table 1: Existing spray deposition modelling techniques.

	droplets	atmosphere	dynamic	time resolution	accuracy	commercial implementations
(1) Plume dispersion	concentration	matrix	no	months	low	ADMS
(2) Multiple regression	concentration	matrix	no	days	intermediate	DriftSIM
(3) Droplet tracking	discrete	correlated	yes	real time	high	AgDRIFT
(4) Euler/Lagrange CFD	discrete	Navier Stokes	yes	real time	very high	-
Euler/Lagrange SM	density	Navier Stokes	yes	real time	high (projected)	-

cluding specialised test benches, other lab-based studies and measurements in the field [36–38]. The experimental setups of these studies vary significantly in terms of nozzle setups, atmospheric conditions and drift collection schemes, making comparsion to other studies complex.

The application of data-driven statistical surrogate modelling has been part of numerical fluid dynamics since the early days of the field. Kolmogorov, one of the founders of statistical learning theory and esteemed turbulence researcher, considered the turbulence phenomenon to be one of the most crucial application domains of statistical learning [39]. Large quantities of high-dimensional data were an everyday reality in the field long before the term Big Data was coined [39]. Applications of general Deep Neural Networks (DNN) [40], or more specific Recurrent Neural Networks such as Long-Short-Term-Memory (LSTM) [41, 42], Convolutional Neural Networks and Encoders (CNN) [42, 43] and Gaussian Process Regressions (GPR) [43] have shown promising results in the development of reduced order models. Most of these approaches however can be interpreted as image-to-image regression or image evolution models – modelling the evolution of some field quantity which can be interpreted as an image (such as the velocity field from synthetic CFD data) using an initial field as input parameter. Prior research results on whole image regression, or the prediction of an output image using only a few key physical parameters of the system as inputs, were found to be very sparse. While incredibly interesting for computational scientists, the development of accurate whole image regression models provides a difficult, yet exciting challenge – as will become clearer in the following pages.

3 Methods

3.1 CFD simulation of spray dispersion

The open source CFD toolbox OpenFOAM v6 was used to develop the computational implementation of the Eulerian/Lagrangian simulation of the spray drift case. Several tutorial cases (`AachenBomb, InjectionChannel, motorBike`) provided partial templates for the setup.

The layout of the wind tunnel used by Nuyttens et al. [32] was taken as a sensible basis for the domain of the CFD simulation, allowing comparability of results and validation of the numerical results. Domain geometry is indicated in figure 1. The standard `BlockMesh` mesh generation utility was used, with uniform grading in all three dimensions of the generated mesh. The final mesh resolution was set at $[70, 20, 20]$ resulting in 28,000 cells and 80,100 internal faces.

The discrete droplet phase was implemented as a Lagrangian particle model using the `kinematicCloud` class, which offers integrated support of a wide range of additional sub-models for particle forces, properties and injection models. In line with properties of standard pesticide formulations, particle properties were taken to be those of water at 25 °C and 1 atm. Drag forces were calculated using the `sphereDrag` sub method. Stochastic dispersion modelling via the `stochasticDispersionRAS` method, a stochastic `isotropyModel` and simple relaxation `dampingModel` completed the physical description of the Lagrangian particle cloud. A local `patchInteractionModel` was specified to allow escape of particles from the computational domain without any patch interaction.

The nozzle was consciously chosen not to be modelled using a specific mesh representation of a real nozzle – this would have also substantially increased the computational complexity of the simulation. A more generalised representation of the nozzle using the `InjectionModel` class provides a better basis to develop a more abstract model capable of simulating various nozzle makes, by specifying a set of characteristic input parameters obtained from experimental studies. The `ConeInjection` sub class implemented a disk-

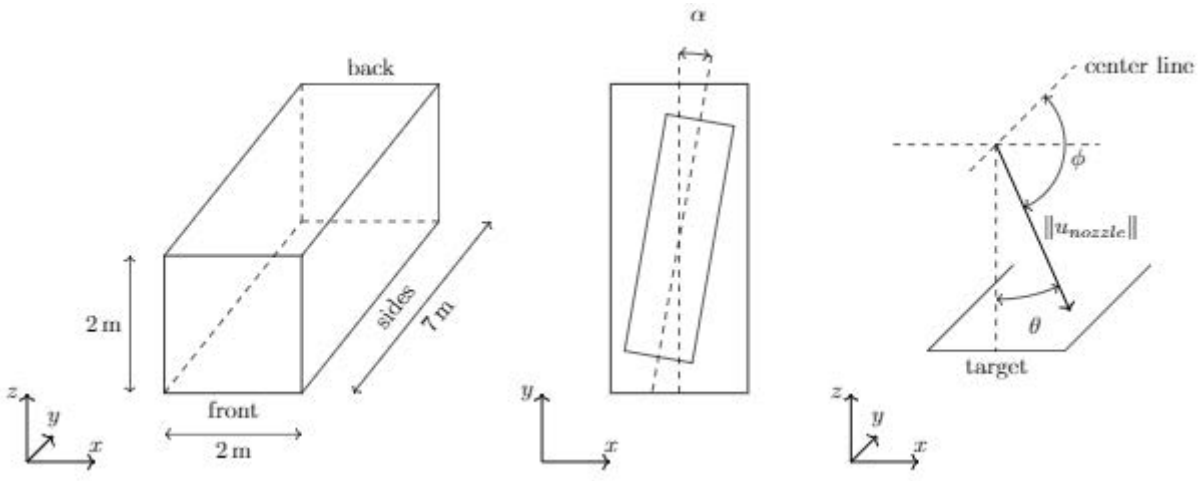

Figure 1: From left to right: computational domain; deposition target and wind angle; nozzle orientation

Table 2: Boundary- and Initial Conditions

	$\boldsymbol{U}$	p	k	ϵ	ν_t
ground	`noSlip`	`zeroGradient`	`kqRWallfunction`	`epsilonWallfunction`	`nutkWallFunction`
top	`fixedValue`	`zeroGradient`	`zeroGradient`	`zeroGradient`	`calculated`
sides	`fixedValue`	`zeroGradient`	`inletOutlet`	`inletOutlet`	`calculated`
front (inlet)	`fixedValue`	`zeroGradient`	`fixedValue`	`fixedValue`	`calculated`
back (outlet)	`inletOutlet`	`fixedValue`	`inletOutlet`	`inletOutlet`	`calculated`
internalField	$(\,u_x,\,0,\,0\,)\,\mathrm{m\,s^{-1}}$	$0\,\mathrm{Pa}$	$1.3\,\mathrm{m^2\,s^{-2}}$	$1\,\mathrm{m^2\,s^{-3}}$	$0\,\mathrm{m^2\,s^{-1}}$

shaped source of 10 mm diameter, emitting 5.7×10^4 particles of the `kinematicCloud` at a parcel size of one over a spray angle of 80°. The nozzle outlet was located 1 m above the floor of the domain and 0.5 m from its front. Parcels were specified on the basis of mass, with the density being fixed as described above and the droplet diameters being distributed according to a Rosin–Rammler distribution. Hence the variable input parameters for the nozzle are given by particle diameter distribution's parameters, the initial particle velocity and the nozzle orientation via the azimuthal and polar angles.

Turbulence was modelled using a k–ϵ model, with initial turbulent kinetic energy and dissipation rate values being based on atmospheric measurements [44]. k–ϵ is known to under-predict effects of turbulence on lateral dispersion [31], which was aimed to be compensated by introduction of a stochastic component with `StochasticDispersionRAS`. Boundary and initial conditions were set as outlined in table 2 under the assumption that the domain is wide enough to employ far-field boundary conditions on the top and side faces of the domain. The initial velocity field and the fixed boundary values are given by a unidirectional velocity field of magnitude u_x, corresponding to the mean wind speed. The case was then solved with the incompressible, two-way interaction solver `MPPICFoam` using the divergence schemes Gauss upwind for k and ϵ, Gauss linear upwind for $\boldsymbol{u}$ and Gauss linear corrected for the Laplacian scheme.

The ground deposition density data was extracted from the Lagrangian particle trajectories using the `ParticleCollector` function object, which allows the user to specify a polygonal surface and "collect" the total mass of particles having passed through it. A self-developed Python utility function was used to generate a rectangular grid of specified resolution of independent `ParticleCollector` instances. A "deposition target" resembling a row of crop of size 6 m by 2 m was defined upon which the `ParticleCollector` grid was placed. To simulate non-frontal winds without altering the CFD setup, the nozzle, the target and correspondingly the `ParticleCollector` grid were rotated around the target's center by an angle α, providing a lateral wind field from the perspective of the target / row of crop.

The data was then extracted from the individual instances using a further Python utility function outputting a single `NumPy` matrix of dimension $[x_{\text{cells}}, y_{\text{cells}}, t_{\text{cells}}]$, with t being the number of time step outputs – equivalent to a collection of t snapshots of the deposition density field at a grid resolution of $[0, x_{\text{cells}}] \times [0, y_{\text{cells}}]$. These snapshots can be interpreted as images of the deposition field, with each cell's spray deposition value corresponding to a pixel's colour scale of the image, and will be referred to as as such throughout.

Mesh independence studies were performed on the simulation to ensure adequate mesh density. The main output variable of interest was the deposition density distribution – therefore, the variable of interest for comparison of mesh densities is this density distribution. The number of mesh elements in a simulation was varied, keeping element aspect ratio identical. These simulations were then run and variation in the variable of interest (drift percentages) was then calculated from `ParticleCollector` and average mean square error between each between this output for each simulation against the next least dense simulation calculated. The final timestep is taken to indicate steady state. Drift percentages ($D\%$) were calculated as the ratio of mass deposited ($m_d(x_i)$) on cell x_i to total mass introduced (m_{total}):

$$D\% = \frac{m_d(x_i)}{m_{total}} \times 100 \tag{1}$$

Validation of CFD results against experimental data was performed using 3 independent data sets. Spray cloud properties for three individual nozzles were taken from a detailed phase doppler particle analysis study by Nuyttens et al. [32] and used to derive the shape and scale parameters of the underlying Rosin–Rammler Distribution. The geometric dimensions of the validation simulations were in accordance with ISO22856 [45] and the setups of the experimental studies. A `ParticleCollector` grid with made 0.1 m sided squares parallel to the frontal wind was placed at a height of 0.1 m, corresponding to usual foliage height.

3.2 Computational pipeline

The validated CFD model was then integrated into a `Nextflow` (a workflow manager for the creation and

execution of data-driven computational pipelines in a fluent domain-specific language) data pipeline. This enabled a controlled workflow for the computation of over 5500 simulations of automatically varied parameters which can be specified in a single file. Additionally, `Nextflow` allowed native batching of runs on the Imperial College High Performance Cluster, while also enabling parallel computing at the process level.

A `Nextflow` channel iteratively executes a process for every set of parameters in an input `.csv` file. The process itself is a `bash` script which is executed in a dynamically created work directory, into which the OpenFOAM template case and the utility scripts are copied. Several self-developed Python scripts, making use of the `pyFoam` module, are called automatically to read the run parameters, create the specific OpenFOAM case and the `ParticleCollector` instances. The case is run using `MPPICFoam` and further Python scripts are called to extract a `.npy` file of particle collector outputs over time. A minimum working example of the final computational pipeline is provided in a GitHub repository [46].

Table 3 lists the constraints imposed on the five input variables specifying wind velocity and direction, nozzle orientation, and exit velocity (with the particle size distribution being fixed for a given nozzle). Samples were then drawn from the resulting space via Latin hypercube sampling, using a space filling sampling criterion, and processed via the computational pipeline.

Table 3: Ranges of simulation input sample space

	lower	upper	unit
wind velocity	0.5	6.5	$\mathrm{m\,s^{-1}}$
wind angle	0	10	°
nozzle θ	-45	45	°
nozzle ϕ	-45	45	°
exit velocity	2.5	3.5	$\mathrm{m\,s^{-1}}$

3.3 Surrogate model construction

3.3.1 Black-box approaches

Initial exploratory surrogate model construction was performed using a variety of regression models from the `scikit-learn` module. Input parameters were scaled using the `StandardScaler` procedure, and the individual $[30, 20]$ matrices were flattened to a drift-percentage normalised one-dimensional output vector of length 600. After randomly splitting the dataset in a train and validation set (80/20), several Multilayer Perceptrons (MLP), Random Forest Regressors (RFR) and a Gaussian Process Regressors (GPR) models were trained using different hyperparameter variations – each attempting to predict the entire image from the five input parameters.

In addition, pixel to pixel (P2P) ensemble regression was performed by training an individual MLP and GPR for each pixel of the particle collector, as opposed to training one model for the whole collector. This was designed to reduce the effect of information density issues and complexity of whole-image output scales (see 5.2.1). The lack of success of these approaches lead to development of more advanced surrogate modelling methods, as outlined in the following paragraphs.

3.3.2 Pesticide drift surrogate model

A custom image regression algorithm was formulated for surrogate modelling of pesticide drift. A pixel frame of size 2x2 traverses the image at a stride of (2,2). In each frame, a local coordinate system $\{0,1\} \times \{0,1\}$ is defined and treated as an additional pixel feature, providing relative spatial positioning information of the pixels to the model. Smoothness is imposed by including the current mean pixel value, and assigning it a relative position at the centre of the frame $(0.5, 0.5)$. The input vector is then formed by concatenating the vector of run parameters with the local pixel coordinates for the five points, while the output vector is constructed by stacking the vectors of pixel values and the computed mean vector. A GPR was then trained for each frame, fundamentally providing the model with built-in prediction uncertainty quantification. At the specified resolution, this results in training 150 individual frame models – each only focusing on a subset of the image, but from which the whole image can be easily reconstructed. Regression scoring on the test set is conducted on a frame by frame basis, resulting in an image of coefficients of determination providing more holistic information of true regression performance.

Conceptual unit testing of the proposed algorithm was conducted on synthetically constructed dispersion fields to provide a benchmark on less chaotic data. The data was generated from Gaussian' curves with a constant mean and standard deviation following geometric Brownian motion with positive drift in wind direction. White noise was added to all data points, and the proposed algorithm, a P2P GPR and whole-image GPR were trained as benchmarks. The proposed algorithm was then applied to a CFD data set with a compressed parameter space (nozzle angles were restricted to $\pm\,10°$ and wind velocity only up to $5\,\mathrm{m\,s^{-1}}$) to produce a less chaotic dataset and evaluated for its performance.

3.3.3 Disinfectant drift surrogate model

The surrogate modelling task was reformulated for disinfection application as a binary decision of sufficient application of disinfectant volume at some point on the spray target. The CFD output images were processed into binary images using a defined threshold of $7.9\,\mathrm{ml\,m^{-2}}$, corresponding to both a deposition rate higher than one obtained by uniform deposition across the entire target, and slightly above the recommended application volume of spray mist surface disinfection with dilute hydrogen peroxide. The pixel by pixel approach was to predict a binary variable for

each pixel from the 5 input parameters – again training 600 individual classifiers on the entire thresholded CFD dataset, pixel to pixel. A neural network with two hidden layers at 25 neurons each, using a hyperbolic tangent as activation function and lowered convergence tolerance of 10^{-6}, was chosen as the final model architecture. Performance was evaluated via the cross-image mean accuracy, the position dependent accuracy as an accuracy image, and the false positive rate – particularly crucial in the disinfection application.

4 Results

4.1 Validation of the CFD simulation

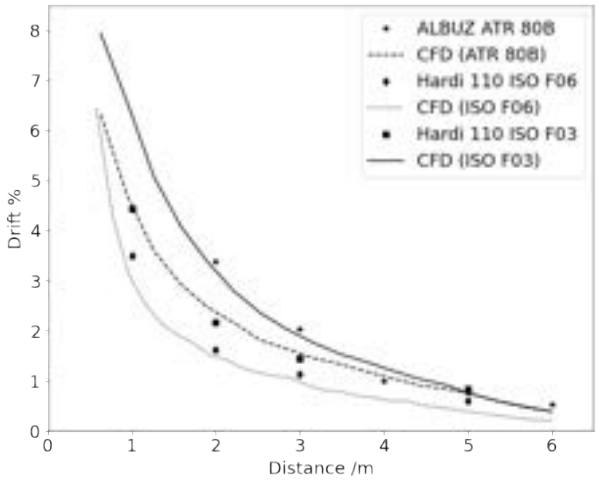

Figure 2: Validation curves for three nozzle designs

The CFD simulation required both validation against experimental results from literature, and verification of mesh independence. Validation results are presented in figure 2. CFD-predicted drift percentages at varying distance downwind from the nozzle (lines) are compared to experimental results for three different nozzle types (points) from three literature sources [27, 34, 35], showing good adherence of the model's predictions to all three nozzle types. Mesh independence analysis showed a mean square error (MSE) of the resulting deposition fields between successive mesh gradings of $[63,18,18]$ and $[70,20,20]$ to be $<1.8\times10^{-5}$; hence the mesh grading of $[70,20,20]$ with 2.8×10^{4} elements was deemed sufficient.

4.2 Surrogate modelling

4.2.1 Exploratory analysis of the generated training data

In total, data from more than 5500 individual CFD simulations was successfully generated – amounting to more than 100.000 snapshots and 6×10^{7} data points. The resulting deposition fields showed an astonishing variety of spatial structures.

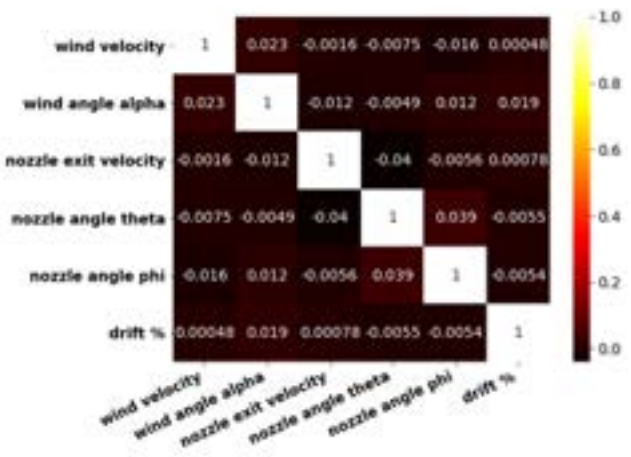

Figure 3: Correlation matrix for entire training dataset – note near-zero correlations for all variables

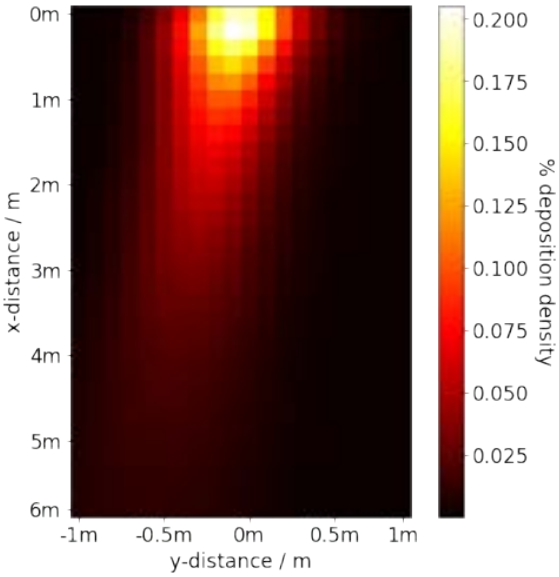

Figure 4: The mean deposition density image of all generated 5500 CFD simulations – note skew of mean to left due to variation of wind angle only in this direction relative to head-on

Correlations between individual cell deposition densities and input parameters (figure 3) were very low, further illustrating and quantifying the complexity of the underlying phenomenon. The large variety of plume shapes seems promising with regards to application of active control to influence downwind spray deposition, with the nozzle orientation in particular having a very intricate interaction with the resulting deposition field and hence ability to counteract wind influences – however, it also provides testimony to the challenging problem of modelling these interactions in a surrogate model. The mean image of all generated snapshots can be found in figure 4. The mean approximately follows simple Gaussian plume dispersion behaviour on the first metre, but deviates significantly further downwind. It is interesting to note that while

the mean at first follows the expected diagonal line along the centre of the wind angle variation, deposition behaviour further downwind becomes increasingly dispersed – from visual inspection of several deposition density images, it seems that the effects of the nozzle orientation and wind direction interplay are particularly pronounced in the more dilute region of the spray.

4.2.2 Black box approaches

Black box whole-image regression techniques showed poor results. Reduction of position dependent accuracy metrics to a single scalar by aggregation functions such as the mean R^2 or root relative mean square error (RRMSE) indicated low performance off all 3 regressors (MLP: $R^2 < 0$, RRMSE 20%; RFR: $R^2 < 0$, RRMSE 11%; GPR: $R^2 < 0$, RRMSE 29%), but pre-aggregation performance data showed significant differences in areas of low vs. high deposition(RRMSE $< 0.1\%$ vs. $> 40\%$).

Classic regression metrics showed higher performance of the P2P approach over the whole-image model: the average prediction error was reduced (MLP RRMSE $< 18\%$). However, visual inspection of the P2P model revealed no recognition of the spatial image structures and characteristic plume shapes. While this clearly showed the need for the more advanced surrogate modelling techniques, it also further illustrated the difficulty of formulating appropriate loss functions for position-dependent output accuracy, providing a challenge both in assessment of the model and appropriate application-specific formulation of the underlying optimisation problem of the machine learning algorithms.

4.2.3 Pesticide drift surrogate model

After promising performance in the proof-of-concept test (R^2 proposed 0.34 vs P2P, whole-image ≈ 0), the proposed algorithm was applied to the described CFD data set of 400 runs with a reduced parameter space. The RRMSE image, shown in figure 5, shows particularly strong performance of the regression in the the key downwind area of the deposition density image. The maximum RRMSE across the image on the test split of the reduced data set was 1.3%, ensuring good accuracy throughout and placing the model in a range appropriate for active control purposes. The R^2 score indicates that more than 80% of the variance found in the data set can be accounted for by the model. Given the very low RRMSE, the lower-than-expected R^2 value might be a result of the imposed smoothness condition introducing additional variance, with the calculated mean being considered a frame feature. This possibly indicates a smoothness/variance trade off – partly caused by the discrete, comparatively coarse grid nature of the `ParticleCollector`. The proposed algorithm compares favourable to the whole-image and the pixel to pixel regression attempts, with whole image GPR regression on the reduced parameter set performing more than four times worse than the proposed algorithm (but significantly better than on the large dataset; RRMSE 8%) and pixel to pixel regression also performing better on the reduced parameter dataset, but also significantly worse than the proposed algorithm with an achieved RRMSE of 11%. Visual inspection of CFD ground-truth output / surrogate output pairs also confirmed the better performance of the proposed algorithm in correctly recognising and reproducing physically sensible plume shapes, of which a particular example is also illustrated in figure 5.

4.2.4 Disinfectant drift surrogate model

The classification model for spray drift disinfection achieves an overall average accuracy of 78% with a false positive rate of 12%, at a standard decision threshold of 0.5. The accuracy image (figure 6) shows an interesting spatial trend with the area of lowest accuracy being present in the dilute border region of the spray, and ac-

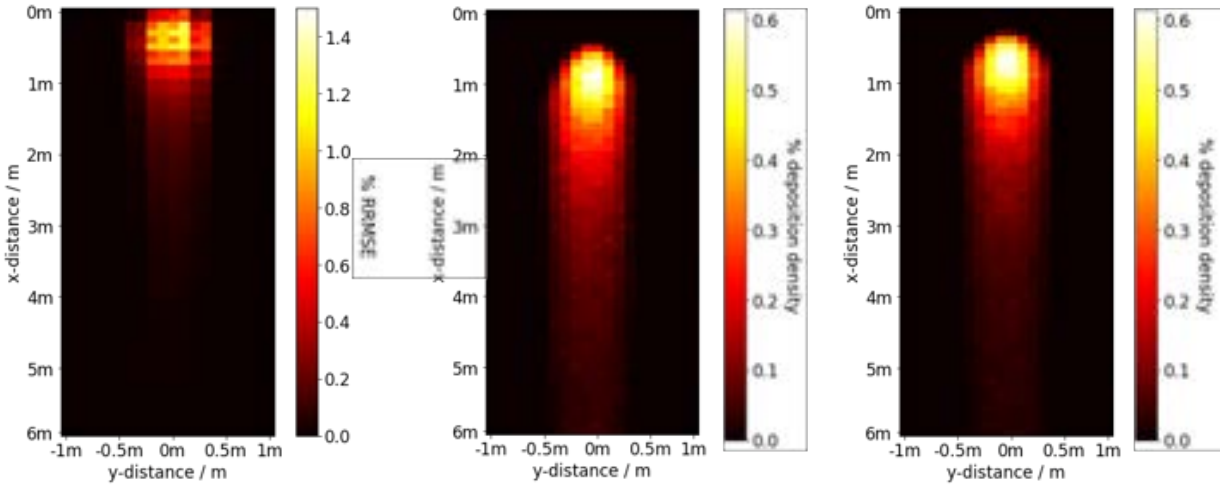

Figure 5: From left to right: relative root mean square error (RRMSE) of the proposed whole image regression algorithm; an exemplary CFD deposition density output image compared to; the deposition density image predicted by the proposed algorithm

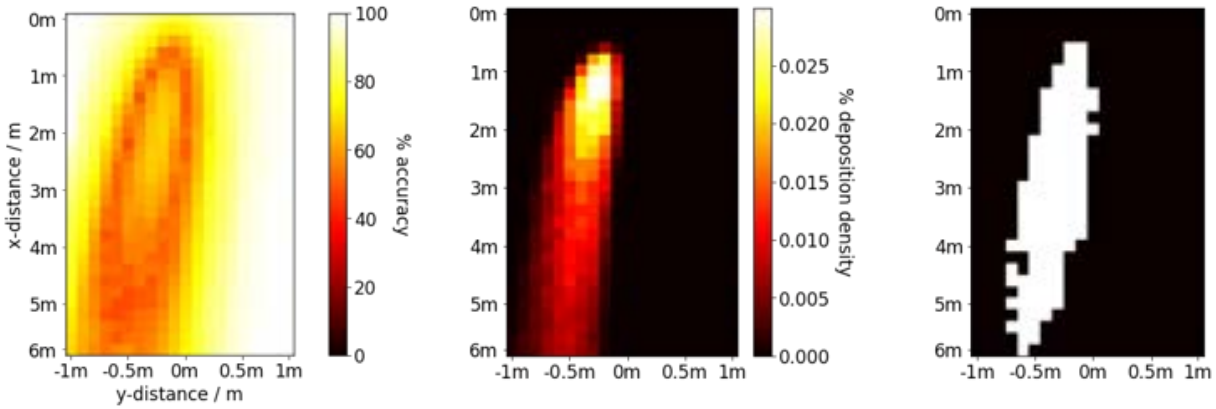

Figure 6: From left to right: classifier accuracy of the proposed disinfection threshold classification algorithm; an exemplary CFD deposition density output image compared to; the binary disinfection image predicted by the proposed algorithm with white indicating areas of sufficient disinfectant application

curacy increasing both inwards towards the plume and the outermost spray regions. The current threshold, set above the recommended application volume limit, mitigates the current false positive rate by providing a safety margin. The classifier can be easily adjusted to incorporate different safety margins and or decision thresholds, and could in it's current state be configured to provide a meaningful active control model for UAV spray mist surface disinfection.

5 Discussion

5.1 Efficacy of CFD models

Comparison to literature data indicated that the CFD model is accurate to those scenarios tested. Easy transferability of the `kinematicCloud` and `coneInjection` modelling approach to different nozzle makes was indicated by the testing for different nozzle designs. However, experimental data for every single permutation of input parameter is not available – it can be predicted that, as physical variations compared to these cases were relatively limited (e.g. Reynolds numbers remain in similar ranges), the validity over the tested sample space is acceptable, but this could not be absolutely verified. Additionally, the model was formulated for comparability to literature studies as opposed to specific industrial scenarios (e.g. 20 nozzles on a tractor-towed pesticide sprayer), although the method could certainly be adapted to this by future researchers.

5.2 Surrogate modelling

5.2.1 Model formulation issues

Initial whole-image MLP and GPR showed a stagnant decrease of training loss, relatively non-smooth predictions and their predicted output images converged to the mean of all training images, usually indicating that the model is not sufficiently complex to capture the underlying relationship. RFRs produced output features with more noticeable spatial distinctions, but also did not capture the true image structure sufficiently to be chosen as the most applicable algorithm.

Additionally, the commonly used regression metrics and loss functions showed limited applicability to whole image regression. R^2 values in image regression would become position-dependent, and hence effectively also give an 'image of determination'. R^2 and RRMSE figures for these approaches indicated poor overall performance, hence development of the other approaches to tackle the problem. Three key issues leading to low regressor performance were identified:

1. Low information density for prediction of 600 values from just five input parameters
2. Extremely low covariances between the feature space and the deposition data
3. Large variations in magnitude of output values, which cannot be uniformly scaled

P2P ensemble regression was used as a simple potential solution to these difficulties. This was effectively a failure as it did not recognise the spacial structure of the images. This is obscured by removing the spatial relationships between pixels and the effects of noisy variation in pixel values are even more apparent. It became clear that this type of application requires a specifically constructed approach to surrogate modelling. The main challenges to whole-image regression in this application setting are thus summarised:

1. Imposition of output smoothness and compactness
2. Imposition of spatial structure information
3. Robustness of the method to scale of parameters
4. A position-dependent goodness-of-fit assessment metric

Revisiting the requirements of the two use cases of a spray drift surrogate model outlined in the introduction revealed some differences. For disinfection and decontamination procedures, the key performance measure can be interpreted as a binary decision: whether a

sufficient amount of active component has been applied to a specific area. For drift-reducing active control of agricultural sprays however, a detailed pesticide deposition field output is required. A individually tailored ML approach to each of these differing requirements was deemed necessary to achieve the required accuracy. A disinfection spray drift surrogate model can hence be formulated as a classification problem, using some deposition threshold of applied active component per unit area; the classification approach would allow working on a simple $\{0,1\}$ output scale with reduced importance of the wider spatial structure, while having clearly defined performance metrics in the accuracy and false-positive rate. The pesticide drift surrogate must be a regression model that can – at least in some localised sub-domain – learn from the spatial structures and provide a smooth output result, while preferably being capable of built in uncertainty quantification.

5.2.2 Pesticide drift surrogate model

The traversing local frame regression showed highly promising results in the current application as well as general whole image regression; the ability to preserve the spatial relationships within the image whilst reducing the effects of a lack of information density and local output scale comparability. Regression scoring showed strong results on both synthetic Gaussian data and CFD data, providing a near instantaneously evaluable surrogate model of adequate accuracy for active control application – albeit on a reduced physical parameter space. Further research is required to extend the proposed algorithm to larger, more complex CFD datasets. The primary next step would be the development of a simple to use, modular code base for the proposed algorithm enabling investigation into different hyperparameter combinations, frame sizes and strides, as well as possible whole image regression scenarios outside the spray drift phenomenon.

5.2.3 Disinfection drift surrogate model

The constant threshold value is a key explanation behind the shape of accuracy plot (figure 6), the value of $7.9\,\mathrm{ml\,m^{-2}}$ having been chosen as a good fit overall for most images. ROC-AUC optimisation of decision thresholds for individual classifiers should enable further decrease of the false positive rate, by reflecting the preference of specificity over sensitivity for a disinfection application. This would increase descriptiveness of plume shape, but complicate the training methodology due to the ensemble nature of the classifier and associated worries of local overfitting. This technique was overall shown to be a strong predictor of both plume shape and the key performance indicator of the desired application setting. The surrogate model hence produces good estimates of surface coverage in only a few miliseconds, compared to the average computing time of two hours of the developed CFD simulation. Further research would likely provide potential for additional accuracy improvements focusing not only on ROC tailoring but also Bayesian hyperparameter optimisation of the underlying neural network.

5.2.4 Numerical assessment of descriptiveness of shape

Although assessment of shape sensitivity of models was made visually, a numerical method for comparison of this was not found. The hence not optimal loss function used in the algorithmic training of ML methods impacts performance as networks better describing the true shape cannot be directly searched for. It is assumed that increased R^2 and reduced RRMSE will in general indicate better shape descriptions: this may not always be true, however. For example, a model could have significant variation in every pixel compared to the true values, resulting in poor RRMSE values, but describe overall plume shape relatively well. If a metric of description of shape could be formulated as a loss function, model training and selection could be significantly enhanced and help find drift models of lower generalisation error in the complex parameter space. This would perhaps be more effective when training on larger images; converting the 600 pixel images used here to edge vectors, the first step in numerical shape description, was found not be effective due to the coarse variation in spatial structure.

6 Conclusion

In the course of this investigation, a validated CFD model for spray drift from a single nozzle was produced, a custom computational pipeline for generating CFD data on remote clusters was produced and various approaches to generating surrogate models of spray dispersion were evaluated. In this case, black box models used for whole-image regression showed no efficacy in predicting spray patterns and pixel-to-pixel regression on an unprocessed image failed to predict spatial structures within the image. The traversing local frame regression approach described spatial structure and was overall an effective predictor of spray behaviour. Similarly, the thresholding and classification-based approach described plume shape well. Bayesian hyperparameter optimisation could be used to improve on these results. Improved implementation of this modelling strategy could show utility in the active control of spray dispersion.

More radically, the problem could be rephrased for image-to-image regression, with an additional particle collector placed under the nozzle, perhaps an image relayed from a camera on a real-life nozzle. This would help solve the information density problem faced by the surrogate modelling approaches and potentially reduce the sensor array needed in a real-life control problem.

The computational tools developed for this project are publicly available for adaptation and use in further research [46].

7 Acknowledgements

Special thanks is given to Dr Lachlan Mason, Gabriel Farah, Dr Indranil Pan and Dr Themistoklis Botsas for their invaluable aid and support with this project.

References

(1) Sharma, A. et al. *SN Applied Sciences* **2019**.
(2) Pimentel, D.; Burgess, M. In *Integrated Pest Management*, 2014.
(3) Felsot, A. S. et al. *Journal of Environmental Science and Health - Part B Pesticides, Food Contaminants, and Agricultural Wastes* **2011**.
(4) Stephenson, G. R. et al. *Pure and Applied Chemistry* **2006**.
(5) Nuyttens, D. et al. *Communications in agricultural and applied biological sciences* **2009**.
(6) Hilz, E.; Vermeer, A. W. *Crop Protection* **2013**, *44*, 75–83.
(7) De Snoo, G. R.; De Wit, P. J. In *Ecotoxicology and Environmental Safety*, 1998.
(8) Matthews, G. *Outlooks on Pest Management* **2008**, *19*, 278–279.
(9) Van de Zande, J. et al. *Spray drift and off-field evaluation of agrochemicals in the Netherlands*; tech. rep.; Plant Research International, 2007.
(10) Rautmann, D. In, 2013.
(11) Stafford, J. V. *Journal of Agricultural and Engineering Research* **2000**.
(12) Walter, A. et al. Smart farming is key to developing sustainable agriculture, 2017.
(13) Mahbub, M. *Internet of Things* **2020**.
(14) Lottes, P. et al. In *2017 IEEE International Conference on Robotics and Automation (ICRA)*, 2017, pp 3024–3031.
(15) Skotadis, E. et al. *Computers and Electronics in Agriculture* **2020**, *178*, 105759.
(16) Eddy, Y. et al. *Revista Argentina de Clínica Psicológica* **2020**, *29*, 221.
(17) EagleHawk Drone-Enabled Disinfectant Spraying `https://www.eaglehawk.io/drone-enabled-disinfectant-spraying` (accessed 12/21/2020).
(18) Bache, D. H.; Sayer, W. J. *Agricultural Meteorology* **1975**.
(19) Zhu, H. et al. *International Conference on Pesticide Application for Drift Management* **2004**.
(20) Teske, M. E. et al. *Environmental Toxicology and Chemistry* **2002**.
(21) Butler Ellis, M.; Miller, P. *Biosystems Engineering* **2010**, *107*, 169–177.
(22) Duga, A. T. et al. *Biosystems Engineering* **2017**, *154*, Engineering Approaches for Reducing Spray Drift, 62–75.
(23) Parra, H. G. et al. In *New Knowledge in Information Systems and Technologies*, ed. by Rocha, Á. et al., Springer International Publishing: Cham, 2019, pp 812–822.
(24) Zhang, B. et al. *Biosystems Engineering* **2018**, *166*, 184–199.
(25) Subramaniam, S. Lagrangian-Eulerian methods for multiphase flows, 2013.
(26) Cristini, V.; Tan, Y. C. Theory and numerical simulation of droplet dynamics in complex flows - A review, 2004.
(27) Baetens, K. et al. *Computers and Electronics in Agriculture* **2007**.
(28) Woods, N. et al. *Journal of environmental quality* **2001**, *30*, 697–701.
(29) Elghobashi, S. *Applied Scientific Research* **1994**, *52*, 309–329.
(30) Arshad, S. Report - Descriptions and comparisons of sprayFoam, reactingParcelFoam, and basicSprayCloud, basicReactingCloud, 2014.
(31) Nygren, A. Modeling of Spray Formation and Development in OpenFOAM with Application to Diesel and Alcohol Fuels, 2018.
(32) Nuyttens, D. et al. *Biosystems Engineering* **2009**.
(33) BS ISO 22856:2008: Equipment for crop protection. Methods for the laboratory measurement of spray drift. Wind tunnels, eng, 2009.
(34) Nuyttens, D. et al. *Communications in agricultural and applied biological sciences* **2008**.
(35) Torrent, X. et al. *Crop Protection* **2017**.
(36) Nuyttens, D. et al. *Biosystems Engineering* **2017**.
(37) Nuyttens, D. et al. *Transactions of the ASABE* **2009**.
(38) Butler Ellis, M. C. et al. *Biosystems Engineering* **2010**.
(39) Brunton, S. L. et al. *Theoretical and Computational Fluid Dynamics* **2020**, *34*, 333–337.
(40) Kutz, J. N. *Journal of Fluid Mechanics* **2017**, *814*, 1–4.
(41) Mohan, A. T.; Gaitonde, D. V. A Deep Learning based Approach to Reduced Order Modeling for Turbulent Flow Control using LSTM Neural Networks, 2018.
(42) Hasegawa, K. et al. In *ASME-JSME-KSME 2019 8th Joint Fluids Engineering Conference, AJKFluids 2019*, 2019.
(43) Maulik, R. et al. Latent-space time evolution of non-intrusive reduced-order models using Gaussian process emulation, 2020.
(44) Han, J. et al. An Estimation of Turbulent Kinetic Energy and Energy Dissipation Rate Based on Atmospheric Boundary Layer Similarity Theory, 2000.
(45) BS ISO 22866:2005: Equipment for crop protection. Methods for field measurement of spray drift, eng, 2006.
(46) Klotz, D.; Dale, S. driftml GitHub repo `https://github.com/klotzd/driftml`.

Technoeconomic Assessment of Hybrid Renewable Energy Systems for a Hotel in Egypt

Hassan Jawwad and Mustafa Nasar
Department of Chemical Engineering, Imperial College London, U.K.

Abstract Egypt has recently launched an energy diversification strategy, the 2035 Integrated Sustainable Energy Strategy, which aims to step up the development of renewable energy and energy efficiency in the country. As Egypt's tourist sector rapidly grows, there is an increasing burden on existing power plants and increased CO_2 emissions. This report compares 5 hybrid renewable energy systems (HRES) against a list of technoeconomic criteria in order to determine the optimal system that satisfies the electricity, heating and hot water demands of a hotel in Fayoum, Egypt. The selected HRES consists of 1 wind turbine, 40 m^2 of PV-T collectors and a 70 kW biomass boiler. The electricity, heating and hot water coverages provided by this system are 8.8%, 15.8% and 30.4% respectively. The system has an $LCOE_{ElecEq}$ of 0.0617 \$/kWh, a payback period of 18.2 years and achieves a 30% reduction in annual CO_2 emissions versus a fossil fuel-backed system. A sensitivity analysis reveals that the financial KPIs were most sensitive to discount rate and hence this must be carefully assessed in light of Egypt's unstable political and economic past.

1. Introduction

Two major issues facing the world today are resource scarcity and environmental degradation. Many countries are taking steps to tackle these challenges and international treaties, like the Paris Agreement, have been enacted to address the issue of climate change. To ensure continuous security and stability of their energy supply, Egypt has launched an energy diversification strategy, known as the 2035 Integrated Sustainable Energy Strategy (ISES), which aims to step up the development of renewable energy and energy efficiency in the country [1]. Global utilisation of renewable energy resources has risen rapidly in recent years, with the share of global power generation from renewables (excluding hydropower) almost doubling from 6.9% in 2011 to 13.4% in 2019 [2]. Egypt has signed up to the United Nations Framework Convention on Climate Change (UNFCCC), meaning it is committed to lowering its dependence on fossil fuels. Currently, 68% of Egypt's power generation is from natural gas [3].

Tourism is recognized as one of the largest contributors to economic growth in Egypt, representing an 11.5% share of GDP and 19.5% share of foreign currency income [4]. Figure 1 demonstrates the expected growth in hotel guest room numbers following predictions from the Egyptian government's plan to attract more tourists to the country [5]. Between 2004 and 2017, the number of guest rooms increased by 71,000 which is equivalent to 220 new hotels and resorts. As new tourism developments take place in Egypt, there is a growing burden on existing power plants and increased CO_2 emissions.

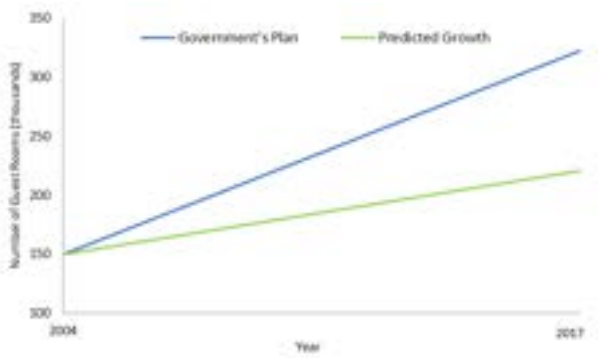

***Figure 1**: Growth in guest room numbers in Egypt*

Energy efficiency can help reduce hotels' operating expenses, with the transition to renewables expected to cut Egypt's energy costs by 7 \$/MWh [6]. However, the real gains in energy efficient transition lie in softer benefits like improvements in health, comfort, better marketing and public relations, and stronger employee morale while promoting environmental restoration, economic prosperity, and social welfare. Moreover, Egypt is split by the River Nile, with many regions in the south still not connected to the national grid. Egypt is keen to invest in tourism along the Red Sea, meaning there is a need for not only infrastructure, but also power supply in these remote regions.

One way to achieve the transformation is through hybrid renewable energy systems (HRES). An HRES is a combination of various renewable energies within a comprehensive system that offers a more reliable and less costly solution compared to reliance on any single resource [7]. An HRES is highly flexible for co-generation of electricity and heating and can reduce the influence of intermittency of different renewables. Solar power is a promising source of renewable energy in Egypt because of the country's geographic position in the sun belt, allowing it to receive a solar radiation of 2000-3000 kWh/m^2 annually. Egypt also enjoys excellent wind due to its proximity to the Gulf of Suez with an average wind speed of 10.5 m/s [8]. As a result, solar and wind are selected as the two main renewable sources in the HRES studied in this report. This falls in line with ISES 2035, which has a goal of electricity generation from wind and solar to equal 14% and 25% respectively by 2035 [1]. In addition, the Egyptian government has enacted regulations to assist wind and solar developers in integrating these resources into Egypt's energy mix, such as the "Build-Own-Operate" policy and zero custom duties on wind equipment [9].

The aim of this study is to determine an optimal hybrid renewable energy system that will supply the electricity, heating and hot water demands of a hotel in Fayoum, Egypt based on technoeconomic criteria in line with the targets of ISES 2035. Various solar technologies (PV panels, evacuated tube collectors (ETCs), and PV-thermal (PV-T) collectors), wind turbines and biomass boilers are considered.

2. Background

The individual technologies implemented in the HRES proposed by this study (see Section 3.1.) have been

researched extensively in previously published works. A particular area of growing interest is PV-T solar collectors due to the combination of solar cells and solar collectors in a single unit to output both electricity and thermal energy leading to greater overall efficiency. Recent work has shown that PV-T hybrid technology is maturing and now has lower payback periods than comparable PV systems [10].Solar water heating systems based on ETC technology have shown great potential for use in not only the residential sector, but also in industry where the outlet water temperature requirements are higher than houses or hotels [11]. In China particularly, continuous research and development on evacuated tube collectors has led to greatly increased usage of the technology which now has low initial investment requirements and short payback periods [12].

Ahmed et al. performed a study on an HRES combining wind turbines, PV panels, and biomass to meet the demands of the local population in Kallar Kahar, Pakistan [13]. They obtained a levelized cost of electricity of 0.05744 $/kWh for the system that can generate more than 50MW. In 2019, a paper published by Kai Wang et al. involved a detailed analysis comparing the performances of PV, ETC, and PV-T solar technologies to supply the electricity and heat demands of a sports centre in Bari, Italy [14]. The study involved a technoeconomic assessment of the solar technologies implemented on a 4000 m^2 installation area and showed that PV panels were the most financially feasible solar technology for the large demands of a sports centre.

This paper intends to build further on these past studies by combining previous knowledge of the different available solar technology types with the benefits of an HRES. It aims to understand the technoeconomic feasibility of an HRES in a region with a higher annual solar radiation than that available in Europe. Past studies have focused mostly on cases in Europe while this study analyses the performance of an HRES in the less explored tourist sector of Egypt.

3. Methodology

3.1. Technology combinations for proposed HRES

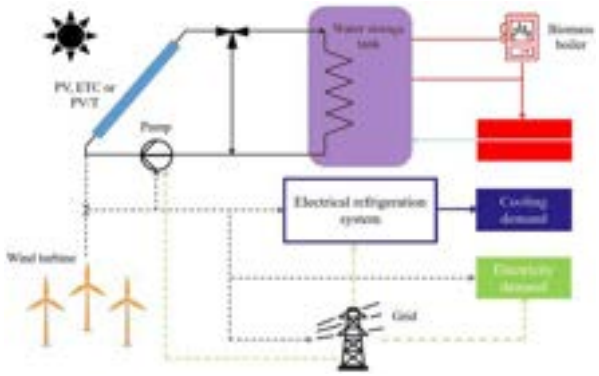

***Figure 2**: Proposed HRES for the hotel in Fayoum, Egypt*

The proposed hybrid renewable energy system (HRES) for the selected hotel in Fayoum, Egypt is shown in Figure 2. PV solar panels and PV-T solar collectors serve the local electricity demand in combination with wind turbines. The wind turbine selected for the HRES is *XZERES Skystream 3.7*. Any shortage in electricity is bought from the grid whilst any surplus electricity generation is exported to the grid via net metering. ETC and PV-T solar thermal collectors generate thermal energy to meet the hotel's heating and hot water demands. Their thermal output is stored in a water storage tank via a heat transfer loop. The capacity of the water storage tank is sized according to the installation area of the collectors by using a ratio of 50 L per unit area of collectors based on the works of Kai *et al* [14]. The stored energy can be upgraded to the required temperature, 50°C for heating and 55°C for hot water, by a back-up biomass boiler if necessary. The hot water outlet temperature is higher as it is needed for showering, dishwashing, etc.

Five systems under this HRES configuration, summarised in Table 1, are investigated in this study. These are:

i. System 1: Wind, PV, Biomass

This system purely generates electricity through PV solar panels and wind turbines. There is no production of thermal energy through the solar or wind technologies. Instead, the back-up biomass boilers are used to satisfy the heating and hot water demands. The electrical parameters and installation area of the PV panels are outlined in Table 2.

ii. System 2: Wind, ETC, Biomass

This system purely generates thermal energy through ETC collectors. The parameters and installation area of the ETC are outlined in Table 2 The capacity of the water storage tank is as described above. Electricity is generated from wind turbines.

iii. System 3: Wind, PV-T, Biomass

This system uses the hybrid PV-T technology to generate both thermal energy and electricity. Thermal energy is stored in a water storage tank that is the same as the one described above. The technical specifications of the PV-T collector are given in Table 2. Wind turbines also supplement electricity generation.

iv. System 4: Wind, PV, ETC, Biomass

An alternative method to generate both electricity and thermal energy from the given area is to install separate PV panels and ETC collectors. Therefore, a combined PV + ETC + WT system is also assessed. The area allocated to each solar technology is 50% of the total available area, which is constant for each system. The technical specifications of these technologies are that described in Table 2.

v. System 5: Wind, PV, PV-T, Biomass

A second alternative for the compound generation of electricity and thermal energy is the combination of PV panels and PV-T collectors, alongside wind turbines. The area allocated to each solar technology is 50% of the total available area. The technical specifications of these technologies are that described in Table 2

Table 1: *Summary of HRES variations*

System	Solar Technology	Wind Turbine	Biomass Boiler
1	PV	✓	✓
2	ETC	✓	✓
3	PV-T	✓	✓
4	0.5 PV + 0.5 ETC	✓	✓
5	0.5 PV + 0.5 PV-T	✓	✓

Table 2: *Technoeconomic specification of HRES technologies*

Technology	Parameter	Value	Reference
PV	Area per panel	1.55 m^2	[15]
	Reference electrical efficiency	14.7 %	
	Temperature coefficient	-0.45 %/K	
	Capital cost	276 $/$m^2$	
ETC	Area per collector	2 m^2	[16]
	Intercept thermal efficiency	76.8 %	
	1st-order heat loss coefficient	1.36	
	2nd-order heat loss coefficient	0.0053	
	Capital cost	364 $/$m^2$	
PV-T	Area per collector	1.55 m^2	[15]
	Reference electrical efficiency	14.7 %	
	Temperature coefficient	-0.45 %/K	
	Intercept thermal efficiency	72.6 %	
	1st-order heat loss coefficient	3.325	
	2nd-order heat loss coefficient	0.0176	
	Capital cost	365 $/$m^2$	
Wind turbine	Capital cost	6140 $/unit	[17]
Storage tank	Capital cost	0.874*Tank Volume + 763500	[18]
Boiler	Capital cost	600 $/kW	[19]

Note: The annual operating & maintenance cost of all units in the HRES is 1% of their capital cost [14]

3.2. Key performance indicators

The feasibility of the 5 systems analysed in this study was understood by comparing a list of key performance indicators: levelised cost of electricity, coverage, payback period and CO_2 emissions reduction.

i. Levelised cost of electricity (*LCOE*)

The levelised cost of electricity is the lowest price at which electricity can be sold to break even. *LCOE* was chosen as a KPI because it enables a fair comparison of systems with unequal capital costs and different sizes of technologies used. This is because *LCOE* reflects a per unit cost of electricity generated with the risk of each system accounted for in a specific discount rate. Moreover, this KPI allows us to compare the cost of electricity generated from the HRES against electricity purchased from the grid.

3 types of *LCOE* were considered in this study. The first *LCOE* accounted for electricity generated (*LCOE*), the second accounted for thermal energy generated ($LCOE_{\text{Thermal}}$), and the third accounted for electricity and thermal energy generated ($LCOE_{\text{ElecEq}}$). $LCOE_{\text{ElecEq}}$ requires the conversion of thermal energy into electricity through a conversion factor based on the following formulae:

$$Electricity\ Equivalent\ Cooling = \frac{Thermal\ Energy\ Removed\ for\ Cooling}{6.3116 \times e^{-0.023 \times T_{ambient}}} \quad (1)$$

$$Electricity\ Equivalent\ Heating = \frac{Thermal\ Energy\ Required\ for\ Heating}{2.2244 \times e^{0.0264 \times T_{ambient}}} \quad (2)$$

$$Electricity\ Equivalent\ Hot\ Water = \frac{Thermal\ Energy\ Required\ for\ Hot\ Water}{0.98} \quad (3)$$

$$Electricity\ Generated\ Equivalent = Electiricity\ Generated + Electricity\ Equivalent\ Heating + Electricity\ Equivalent\ Hot\ Water \quad (4)$$

All 3 types of *LCOE* are then calculated using the same following formula:

$$LCOE = \frac{C_0 + \sum_{i=1}^{n} C_{O\&M}\,(1+i_F)^{i-1}(1+d)^{-i}}{\sum_{i=1}^{n} Q(1+d)^{-i}} \quad (5)$$

where:
C_0 = Capital Cost [$]
$C_{O\&M}$ = Annual Operating and Maintenance Cost [$/year]
i_f = Inflation Rate
d = Discount Rate
Q = Electricity Generated (*LCOE*), Thermal Energy Generated ($LCOE_{\text{Thermal}}$) or Electricity Generated Equivalent ($LCOE_{\text{ElecEq}}$) [kW]

ii. Coverage

Coverage is an important KPI because it indicates how much of the hotel's electricity, heating and hot water demands are met through the cheaper and greener HRES versus the grid. Using the estimated electricity, heating and hot water generation and input demand data for the hotel in Fayoum, the model calculates the following annual coverages:

$$Electricity\ Coverage = \frac{Annual\ Electricity\ Generation}{Annual\ Electricity\ Demand} \quad (6)$$

$$Heating\ Coverage = \frac{Annual\ Heat\ Generation}{Annual\ Heat\ Demand} \quad (7)$$

$$Hot\ Water\ Coverage = \frac{Annual\ Hot\ Water\ Generation}{Annual\ Hot\ Water\ Demand} \quad (8)$$

iii. Payback period (*PBP*)

Payback period is an indicator for evaluating the time taken to return the upfront investment of the HRES. It was chosen as a KPI as it is an effective measure of the investment risk that would be made by the hotel. Hotels need to recover upfront capital quickly so they can use it for their high running costs. The payback period for the HRES is calculated using the following formula:

$$Payback\ Period = \frac{ln\left[\frac{C_0(i_F - d)}{C_S} + 1\right]}{ln\left(\frac{1 + i_F}{1 + d}\right)} \quad (9)$$

where:
C_0 = Capital Cost [$]
C_S = Cost Savings [$/year]
i_F = Inflation Rate
d = Discount Rate

iv. Reduction in CO_2 emissions

The environmental benefit of renewable energy technologies has been the main driving force behind their increasing adoption. As a signee of the United Nations Framework Convention on Climate Change (UNFCCC), Egypt has made it a top priority to reduce its carbon emissions with a specific focus on the energy sector. In this study, the annual reduction in CO_2 emissions is used as an indicator of the environmental benefit of each HRES variation.

The amount of CO_2 reduced through use of renewable energy can be calculated by determining the amount of CO_2 generated when the same amount of thermal energy or electricity is produced on a fossil fuel basis. For this, the CO_2 emission factors for electricity and thermal energy generation from fossil fuels in Egypt are required. The CO_2 emission factor for a biomass boiler is also needed.

$$Annual\ CO_2\ Reduction_{Electricity} = CO_2\ Emission\ Rate_{Electricity,ng} \times Electricity\ Coverage \quad (10)$$

$$Annual\ CO_2\ Reduction_{Thermal} = (CO_2\ Emission\ Rate_{Thermal,ng} - CO_2\ Emission\ Rate_{Biomass}) \times (Heating\ Gen + Hot\ Water\ Gen) \quad (11)$$

$$Annual\ CO_2\ Reduction_{Total} = Annual\ CO_2\ Reduction_{Electricity} + Annual\ CO_2\ Reduction_{Thermal} \quad (12)$$

3.3. Selection of optimal HRES using KPIs

The KPIs defined in Section 3.2. were used to select the optimal HRES that would provide maximum electricity, heating and hot water coverage at the lowest $LCOE_{ElecEq}$ within the useful lifetime of the HRES. Subsequently, the reduction in CO_2 emissions of each system was also contrasted. The selection process consisted of step-by-step process detailed below:

To select the optimal system size within each of the 5 systems

i. The selected system size must be able to payback its investment cost within the system's useful lifetime of 25 years [14].
ii. The selected system size must have an $LCOE_{ElecEq}$ that is lower than the current buying price of electricity from the grid in Fayoum, Egypt – 0.062 $/MWh [20].
iii. Applying i. and ii. creates a satisfactory range of system sizes within each of the 5 systems. Then, the size of system that provides the maximum electricity, heating and hot water coverages within the defined range is selected.

To select the optimal system across all 5 systems

iv. The payback periods of the 5 selected system sizes are then compared to select the system size with the smallest payback period.
v. As an additional comparison point, the reduction in CO_2 emissions of each of the 5 selected systems is also compared. The highest reduction in CO_2 emissions is the most favourable option.

3.4. Algorithm for simulating HRES performance

The model for the proposed configuration was formulated using MATLAB R2018b with the REFPROP 9.0 (2016) fluid property database from NIST used as an add-on. The developed model simulates the performance of the wind turbines and solar technologies being utilised under a set of conditions.

The specific technology being used for the wind turbines and the solar panels can be changed in the model, leading to different electricity outputs, heat outputs, capital costs, and operation and maintenance

costs. This allows for optimisation and selection of the optimal technology for this specific case study.

To estimate the half hourly electricity and heat generation from the system, the model uses half hourly wind speed and solar irradiance as input variables. This weather data was provided by our partners at Fayoum University in Egypt. Details can be found in Appendices B and C.

Annual heating, hot water, and electricity coverages are determined by the algorithm using Equations 6, 7, and 8.

The hotel's annual cost savings from the implementation of the proposed HRES is calculated using the following formula:

$$\begin{aligned} Annual\ Cost\ Saving \\ &= Heating\ Cost\ Saving \\ &+ Hot\ Water\ Saving\ Cost \\ &+ Electricity\ Saving\ Cost \\ &+ Sold\ Electricity\ Cost - \\ &- Biomass\ Cost\ -\ OM\ Cost \end{aligned} \quad (13)$$

where:

Heating Cost Saving = Annual savings due to reduction in heat energy required from fossil fuels for the space heating

Hot Water Saving Cost = Annual savings due to reduction in heat energy required from fossil fuels for hot water

Electricity Saving Cost = Annual savings due to reduction in the electricity required from the grid

Sold Electricity Cost = Annual profit from selling electricity back to grid during times of low demand or high generation

Biomass Cost = Annual cost of biomass for the biomass boiler

OM Cost = Annual operation and maintenance cost of the HRES

After the electricity and thermal energy output from the configuration is estimated, the model works to meet the remaining electricity, heating and hot water demands. This is done by calculating the half hourly amount of electricity that needs to be purchased from the grid and the half hourly mass of biomass required to be combusted by the biomass boiler to meet heating and hot water demands.

The algorithm calculates the payback period for the HRES using Equation 9. The *LCOE*, $LCOE_{Thermal}$, and $LCOE_{ElecEq}$ are calculated using Equation 5.

The model repeats the calculation for a range of wind turbine numbers and solar areas. The number of wind turbines ranges from 1 to 10 (max.) and the solar area ranges from 20 m^2 to 200 m^2 (max.) with 20 m^2 intervals, based on the space constraints of the hotel.

4. Results & Discussion

4.1. Simulation parameters

Table 3 summarises the parameters used in the simulations of the five HRES variations under investigation.

***Table 3**: Input parameters*

Parameter	Value
Discount rate, d	4.00% [21]
Inflation rate, i_F	2.92% [22]
Electricity buy price	0.062 $/MWh [20]
Electricity sell price	0.056 $/MWh [20]
Biomass price	19.5 $/kg
Lifetime	25 [14]
CO_2 Emission $Rate_{electricity,ng}$	0.59 @/MWh [3]
CO_2 Emission $Rate_{thermal,ng}$	0.30 @/MWh [23]

Forecasts of Egypt's future economic atmosphere predict a movement towards lower inflation and discount rates than those in Egypt's politically unstable past [24]. The discount and inflation rates in this study were based on a relatively stable African economy, South Africa, to reflect Egypt's future vision.

4.2. Criteria-based selection of HRES

The hybrid renewable energy systems analysed in this study all consist of wind turbine(s), solar technologies, and a 70 kW biomass boiler. The boiler is sized to be slightly larger than the maximum combined heating and hot water demands of hotel, 66.67 kW, such that it can satisfy them without any contribution from the solar thermal collectors. The systems differ from one another based on the type(s) of solar technology being utilised.

The number of wind turbines and the solar areas in each system were optimised to ensure that the $LCOE_{ElecEq}$ was lower than the grid electricity buying price in Fayoum, Egypt (0.062 $/kWh) and the payback period was lower than the lifespan of the HRES (25 years) whilst maximising electricity, heating and hot water coverages. The red circles on Figures 3-15 indicate the optimal system size and corresponding coverage. It should be noted that coverage only accounts for contributions from wind and solar technologies.

i. System 1: Wind, PV, Biomass

The selected system consisted of 1 wind turbine, 100 m^2 of PV panels and a 70kW biomass boiler. Its $LCOE_{ElecEq}$ was 0.0618 $/kWh and the *PBP* was 18.6 years. The annual electricity coverage provided by the wind turbine and PV panels was 13.3%. The remaining electricity demand was fulfilled by purchasing electricity from the grid while the entire heating and hot water demands were fulfilled using the biomass boiler.

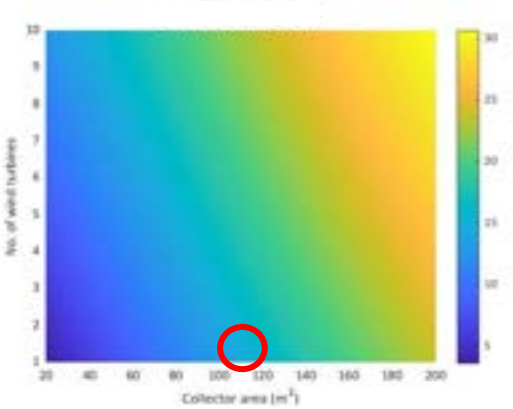

***Figure 3:** System 1 - electricity coverage*

ii. System 2: Wind, ETC, Biomass

The selected system consisted of 1 wind turbine, 20 m^2 of ETC and a 70 kW biomass boiler. Its $LCOE_{ElecEq}$ was 0.0641 $/kWh and the *PBP* was 19.9 years. The annual electricity coverage provided by the wind turbine was 1.1%. The annual heating and hot water coverages provided by the ETC were 7.6% and 8.4% respectively. The remaining electricity demand was fulfilled by purchasing electricity from the grid while the remaining heating and hot water demands were fulfilled using the biomass boiler. This system was discarded from further analysis due to an out-of-bound $LCOE_{ElecEq}$.

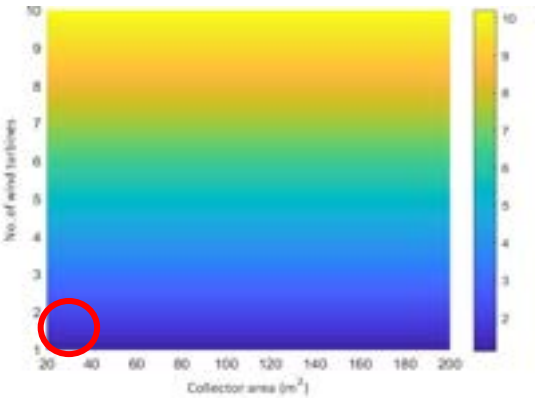

Figure 4: *System 2 - electricity coverage*

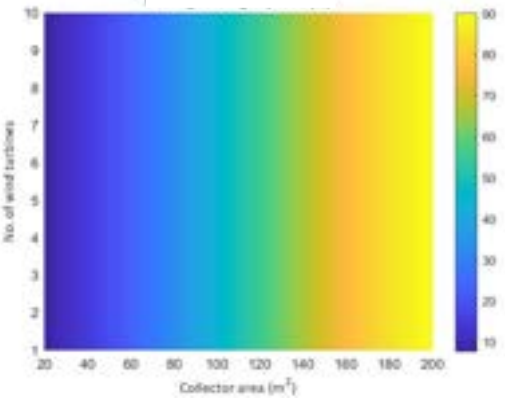

Figure 5: *System 2 - heating coverage*

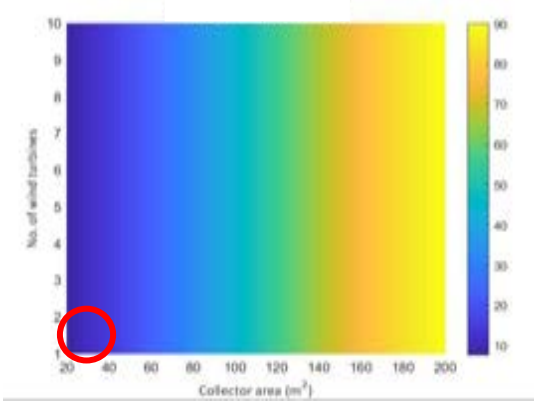

Figure 6: *System 2 - hot water coverage*

iii. System 3: Wind, PV-T, Biomass

The selected system consisted of 1 wind turbine, 40 m^2 of PV-T collectors and a 70 kW biomass boiler. Its $LCOE_{ElecEq}$ was 0.0617 $/kWh and the *PBP* was 18.2 years. The annual electricity coverage provided by the wind turbine and PV-T collectors was 8.8%. The annual heating and hot water coverages provided by the PV-T collectors were 15.8% and 30.4% respectively. The remaining electricity demand was fulfilled by purchasing electricity from the grid while the remaining heating and hot water demands were fulfilled using the biomass boiler.

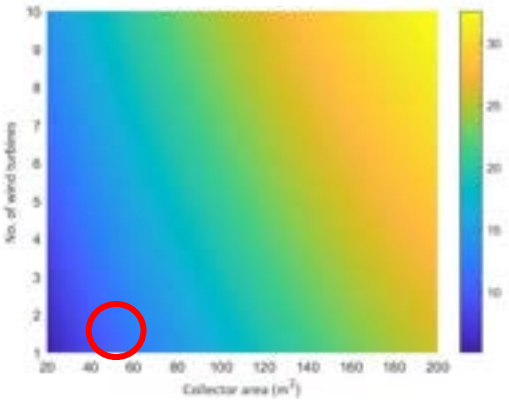

Figure 7: *System 3 - electricity coverage*

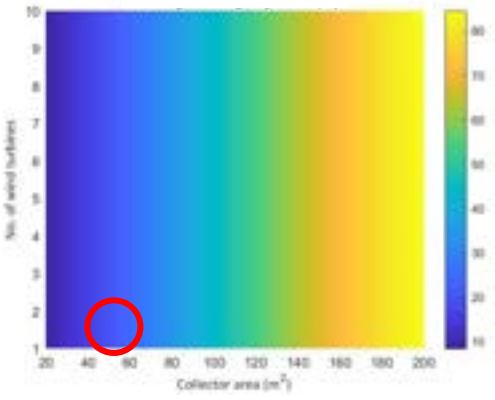

Figure 8: *System 3 - heating coverage*

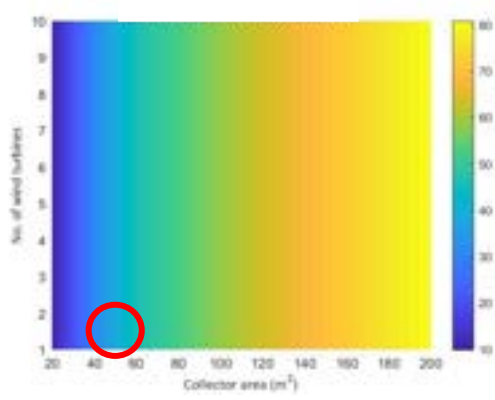

Figure 9: *System 3 - hot water coverage*

iv. System 4: Wind, PV, ETC, Biomass

The selected system consisted of 1 wind turbine, 10 m^2 of PV panels, 10 m^2 of ETC and a 70 kW biomass boiler. Its $LCOE_{ElecEq}$ was 0.0618 $/kWh and the *PBP* was 19.0 years. The annual electricity coverage provided by the wind turbine and PV panels was 3.6%. The annual heating and hot water coverages provided by the ETC were 4.6% and 4.0% respectively. The remaining electricity demand was fulfilled by purchasing electricity from the grid while the remaining heating and hot water demands were fulfilled using the biomass boiler.

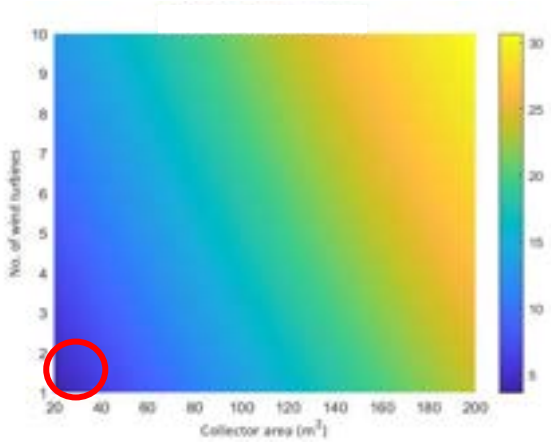

Figure 10: *System 4 - electricity coverage*

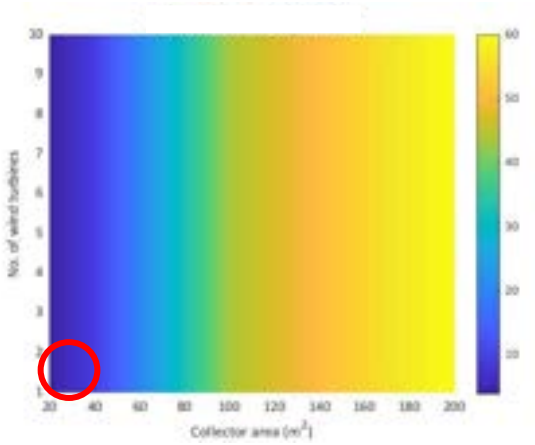

Figure 11: *System 4 - Heating Coverage*

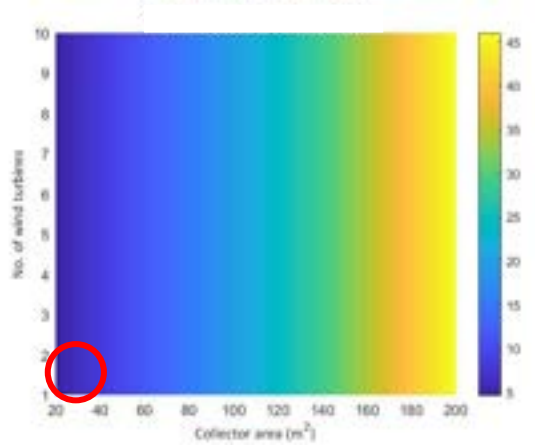

Figure 12*: System 4 - hot water coverage*

v. System 5: Wind, PV, PV-T, Biomass

The selected system consisted of 1 wind turbine, 30 m^2 of PV panels, 30 m^2 of PV-T collectors and a 70 kW biomass boiler. Its $LCOE_{ElecEq}$ was 0.0618 $/kWh and the *PBP* was 18.4 years. The annual electricity coverage by the wind turbine and solar technologies was 14.3%. The annual heating and hot water coverages by the solar technologies were 11.8% and 19.7% respectively. The remaining electricity demand was fulfilled by purchasing electricity from the grid while the remaining heating and hot water demands were fulfilled using the biomass boiler.

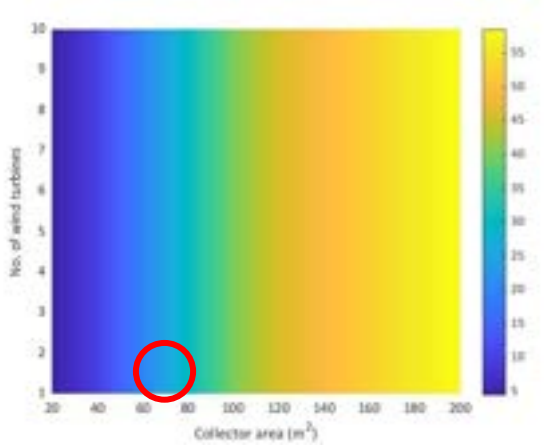

Figure 13: *System 5 - electricity coverage*

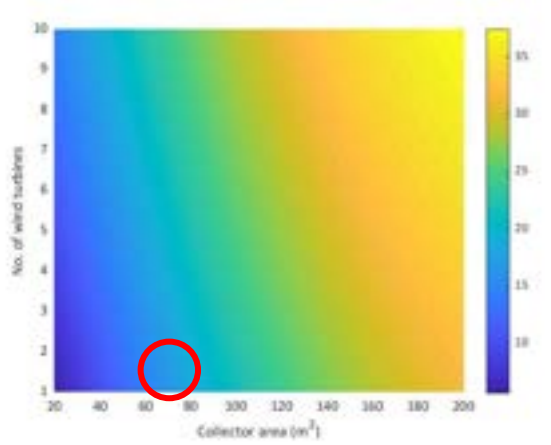

Figure 14: *System 5 - heating coverage*

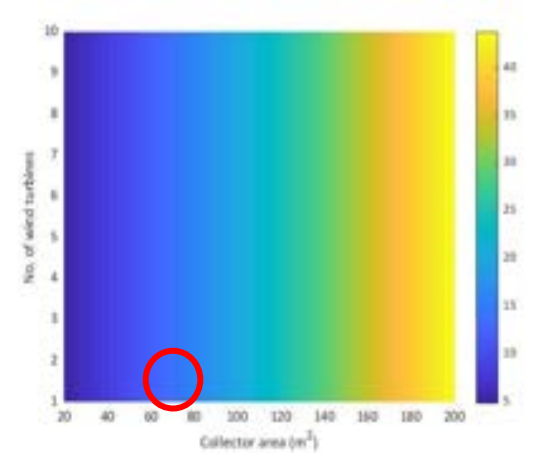

Figure 15: *System 5 - hot water coverage*

4.3. Environmental advantage of HRES utilisation

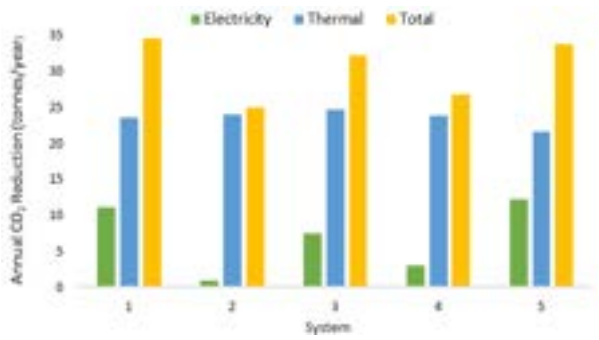

Figure 16: *Annual reduction in CO_2 emissions*

68% of the energy generation in Egypt comes from natural gas. The CO_2 emission reductions due to avoided consumption of this fossil fuel are shown in Figure 16. In line with expectations, the largest reduction in carbon emissions, 34.65 $tonnes_{CO2}$/year, was achieved by System 1 (WT+PV) due to the high electricity generation of this system. The smallest reduction in carbon emissions, 24.90 $tonnes_{CO2}$/year, came from System 2 (WT+ETC) because only one wind turbine contributes to electricity generation in this system. System 3 (WT+PV-T) achieved the highest reduction in carbon emissions amongst the three systems containing co-generation solar technologies, with a reduction value of 32.17 $tonnes_{CO2}$/year. This was due to the large electricity generation coming from the hybrid feature of PV-T technology in this system.

Table 4: *Decrease in CO_2 emissions of HRES vs. natural gas*

System	1	2	3	4	5
% Annual Decrease in CO_2 Emissions	33	23	30	25	31

Table 4 displays the annual reduction in CO_2 emissions if an HRES is implemented in the hotel versus the case where the hotel's electricity, heating and hot water demands are met entirely through natural gas. The largest decrease in CO_2 emissions can be achieved by System 1. Around 77% of an average hotel's CO_2 footprint comes from energy consumption, making these CO_2 reductions particularly important in the movement towards decarbonisation [25]. Given the growth of Egypt's tourist sector, the implementation of HRES in hotels could make meaningful contributions to curbing climate change. Renewable Energy Certificates or other contractual instruments used to monetize the addition of renewable energy to the grid could further incentivise this transition.

4.4. Seasonal behaviour of a selected HRES

Transient analysis was conducted on System 3 to understand how the electricity, heating and hot water coverages vary by hour over a year for the HRES. The results were consistent over the two seasons analysed: a mild winter (November-April) and a hot summer (May-October). To showcase the transient analysis for both seasons, a week in each season is chosen: June 22nd to 28th for summer and December 22nd to 28th for winter.

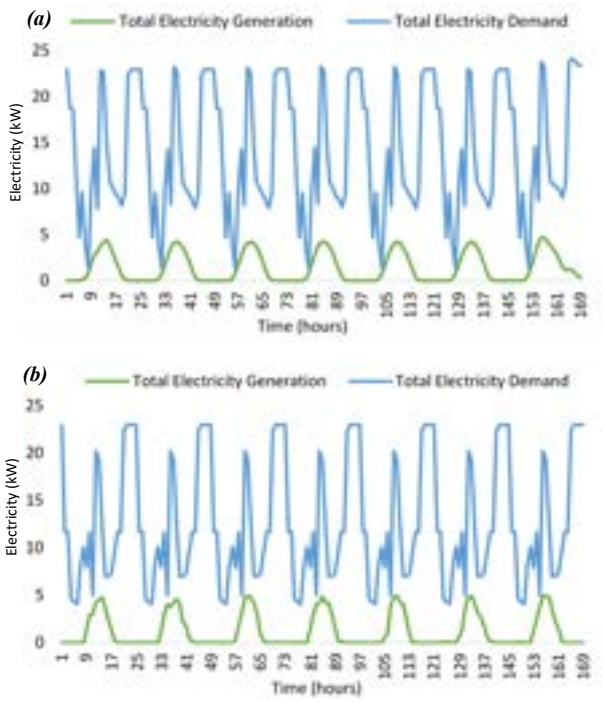

Figure 17: *Hourly electricity demand of hotel in Fayoum, Egypt and electricity generation by proposed HRES during: (a) June 22nd – 28th and (b) December 22nd – 28th*

Figure 17 shows how the hourly electricity demand and generation from the wind turbine and the PV-T collector varied through a typical week in both seasons. As expected, the electricity generation was at its highest during the daytime when solar irradiance was the most. Electricity generation fell considerably as the solar irradiance decreased in the evening and night-time. This trend was consistent through the week for both seasons. It was observed that solar irradiance, and hence the electricity generation, was consistent on most days with only minor fluctuations due to differing weather conditions. The peak electricity generation was similar for both seasons, reaching just under 5 kW during the daytime. In summers, solar irradiance was high with relatively low wind speeds but in winters, wind speed was high and solar irradiance was relatively lower. This complementary nature of the two energy resources ensured that electricity generation from the HRES is fairly consistent throughout the year. Due to the low coverage, at almost no time during the day was electricity sold to the grid. Overall, electricity coverage for both seasons was around the expected 8.8% with the remaining electricity demand being satisfied using electricity from the grid.

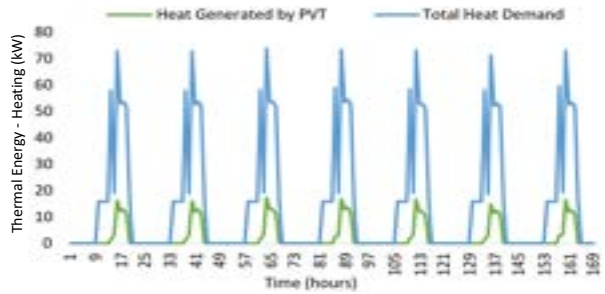

Figure 18: *Hourly heating demand of hotel in Fayoum, Egypt and heating generation by solar technologies in proposed HRES during December 22nd – 28th*

Figure 18 shows the how hourly heating demand and generation from the PV-T collector varied in a typical week in winter. There was no heating demand in summer months and so, that figure was not provided. Heating generation varied with solar irradiance and ambient temperature as expected. As Figures 17 and 18 show, heating generation peaked at a later time during the day than electricity generation as heating generation corresponds to increasing heating demand. Generation and demand were both consistent through the week with generation peaking at 15 kW. Overall, annual heating coverage was 15.8% with the remaining heating demand being satisfied using the biomass boiler.

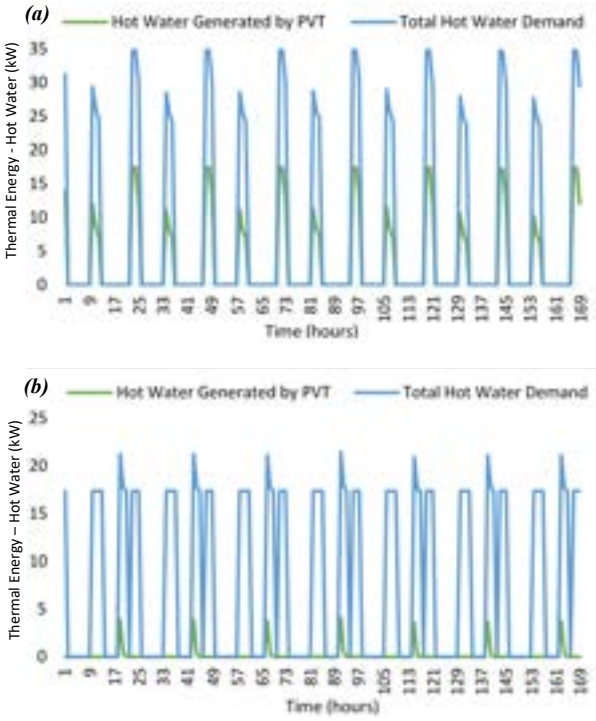

Figure 19: *Hourly hot water demand of hotel in Fayoum, Egypt and hot water generation by solar technologies in proposed HRES during: (a) June 22nd – 28th and (b) December 22nd – 28th*

Figure 19 shows how the hourly hot water demand and generation from the PV-T collector varied through a typical week in both seasons. Here, the times of demand overlap consistently with times of generation as hot water is only generated when the demand requires water to be removed from the storage tank. Demand data from the hotel showed that during each half hour, either there was a demand of 17400 kW or there was no demand at all. This consistent demand data was likely obtained from the usage of a fixed wattage electric heater for the hot water. Such an electric heater would be activated in times of high demand, producing 17,400 kW for the entire half hour. Hot water generation from the PV-T collector was higher in summer months with peak generation ranging from 10-18 kW. In the winter week, the hot water generation was much lower, peaking at 3kW, due to lower solar irradiance and ambient temperatures. There was greater fluctuation in hot water generation from the PV-T collector through the week than for electricity generation. This indicates that the hot water generation was more sensitive to fluctuations in weather conditions due to contribution from only one energy source. Overall, annual hot water coverage from the PV-T collector was 30.4% with the remaining hot water demand being satisfied using the biomass boiler.

4.5. Sensitivity analysis on $LCOE_{ElecEq}$ and PBP

A sensitivity analysis was performed on results from System 3 to understand the effect of changes in discount rate, inflation rate, grid electricity prices, and biomass prices on the financial KPIs: $LCOE_{ElecEq}$ and *PBP*.

Table 5: *Sensitivity of LCOE and PBP to changes in discount rate*

Change	Discount Rate (%)	% Change in $LCOE_{ElecEq}$	% Change in *PBP*
-15%	3.40	-5.0	-5.5
-10%	3.60	-3.4	-3.8
-5%	3.80	-1.7	-1.9
Base	4.00	0.0	0.0
+5%	4.20	1.7	+2.0
+10%	4.40	3.4	+4.2
+15%	4.60	5.2	+6.4

The financial KPIs were sensitive to discount rate with the *PBP* changing by a slightly higher percentage than the $LCOE_{ElecEq}$ for the same percentage change in discount rate. A 15% increase in discount rate increased the *PBP* by 1.2 years while a 15% decrease led to the *PBP* decreasing by 1 year. However, any increase (up to 15%) or decrease (up to 15%) in the discount rate kept the *PBP* lower than the lifetime of the technology, which is 25 years, allowing the HRES to meet the goals of the project. However, even a 5% increase in the discount rate led to an $LCOE_{ElecEq}$ greater than the grid electricity price, which is $0.062/kWh. This would make grid electricity cheaper than the electricity generated by the HRES.

Table 6: *Sensitivity of LCOE and PBP to changes in inflation rate*

Change	Inflation Rate (%)	% Change in $LCOE_{ElecEq}$	% Change in *PBP*
-15%	2.482	-0.8	+4.1
-10%	2.628	-0.6	+2.7
-5%	2.774	-0.3	+1.3
Base	2.920	0.0	0.0
+5%	3.066	0.3	-1.3
+10%	3.212	0.6	-2.5
+15%	3.358	0.9	-3.7

The sensitivity analysis on inflation rate showed that the financial KPIs are much less sensitive to it than discount rate. In fact, $LCOE_{ElecEq}$ only increased by 0.9% when the inflation rate increased by 15%. *PBP* remained under 25 years for any increase or decrease in inflation rate up to 15%. A 15% increase in inflation rate decreased the *PBP* by 0.7 years while a 15% decrease led to the *PBP* increasing by 0.8 years. Similar to discount rate, the inflation rate in Egypt has also seen decreases of around 10% in the recent past. Policymakers have set targets to continue with such decreases till 2022, making discount and inflation rates important decision variables to test [26].

Table 7: *Sensitivity of PBP to changes in price of biomass fuel*

Change	Biomass Price ($/kg)	% Change in *PBP*
-15%	16.575	-1.4
-10%	17.550	-1.0
-5%	18.525	-0.5
Base	19.500	0.0
+5%	20.475	+0.5
+10%	21.450	+1.0
+15%	22.425	+1.5

Table 8: *Sensitivity of PBP to changes in prices of grid electricity*

Change	Electricity Buy Price ($)	Electricity Sell Price ($)	% Change in *PBP*
-15%	0.0527	0.0476	+3.5
-10%	0.0558	0.0504	+2.3
-5%	0.0589	0.0532	+1.1
Base	0.0620	0.0560	0.0
+5%	0.0651	0.0588	-1.1
+10%	0.0682	0.0616	-2.2
+15%	0.0713	0.0644	-3.2

As expected, only the *PBP* was sensitive to changes in grid electricity and biomass prices whilst $LCOE_{ElecEq}$ was unaffected. It should be noted that sensitivity to grid electricity price was determined by assessing coupled variations in electricity buying and selling price because they are mutually dependent factors. *PBP* was more sensitive to grid electricity prices than it was to biomass price, but less than it was to discount and inflation rates. An increase in grid electricity price by 15% caused the *PBP* to decrease by 3.2%, or 0.6 years, while the same percentage increase in biomass price caused the *PBP* to increase by only 1.5%, or about 0.3 years.

Understanding the sensitivity of the *PBP* to electricity grid electricity prices was an essential part of this study as these have seen major fluctuations over recent years. In the 2019-20 fiscal year, Egypt's electricity prices rose by an average 14.9% [27]. These price changes are less drastic for consumers utilising large amounts of electricity so the hotel analysed in this study would see electricity price hikes lower than the country average. In fact, an increase in grid electricity prices decreased the *PBP* of the HRES as shown in Table 8, further increasing the system's practicality.

5. Conclusion

This study analysed 5 combinations of a wind turbine, three solar technologies (PV, PV-T and ETC) and a biomass boiler to understand the optimal HRES that would meet the electricity, heating and hot water demands of a hotel in Fayoum, Egypt. A summary of the results can be found in Appendix D.

All tested systems, except for System 2 (consisting of ETC as the sole solar technology) had both a *PBP* shorter than the lifetime of the individual technologies and an $LCOE_{ElecEq}$ lower than the buying price of grid electricity. System 2 was considered infeasible due to the ETC's high capital cost for the large demands of the hotel, making it difficult for this system to meet the strict *LCOE* and *PBP* requirements set by the study.

The recommended HRES for the hotel in Fayoum, Egypt is System 3, consisting of 1 wind turbine, a 40m^2 PV-T collector and a 70 kW biomass boiler. This system had the lowest $LCOE_{ElecEq}$ ($0.0617/kWh) and the shortest *PBP* (18.2 years). Compared to costs of hybrid renewable energy systems analysed in previous studies such as Sharafi *et al*, this system had a relatively low capital cost of $106,000 [28]. System 3 did not offer the highest electricity coverage (8.8%) but unlike the PV system which delivered a higher value, it also provided heating (15.8%) and hot water (30.4%) coverages due to the hybrid nature of the PV-T collectors. System 3 also achieved a high reduction in CO_2 emissions, 30%, compared to the scenario in which the hotel's energy demands were met entirely by natural gas. To understand the effect of Egypt's past political and economic instability, this study also performed a sensitivity analysis of $LCOE_{ElecEq}$ and *PBP* to discount and inflation rates as well as biomass and grid electricity prices. This revealed that the selected HRES's financial feasibility is most strongly affected by discount rate, with just a 5% increase in discount rate making the system electricity more expensive than the grid.

Even though PV-T collectors are not as readily available in the current market as PV panels or ETCs, they have displayed their feasibility in commercial uses as shown in this study [29]. As the manufacturing scale of PV-T collectors increases, their costs will likely decrease. The growing potential of PV-T collectors will allow for an accelerated global transition to renewables.

6. Outlook

Further actions are needed to fully understand the potential of implementing hybrid renewable energy systems for tourist facilities in Egypt. It is recommended to test PV panels, ETC and PV-T collectors with different technoeconomic parameters (see Table 2) to gauge their effect on the system's $LCOE_{ElecEq}$ and coverages. For example, a cheaper wind turbine, such as *Leading Edge LE-600* (2038 $/unit), is predicted to result in a system with a higher electricity coverage for the same $LCOE_{ElecEq}$ [30]. Furthermore, the size of the water storage tanks can be optimised to meet the heating and hot water demands whilst minimising the capital cost of the HRES and heat losses from the tank. An alternative to the biomass boiler is a geothermal heat pump. The *LCOE* of geothermal energy is 0.021 $/kWh lower than that of biomass power. Moreover, Egypt has a large geothermal potential with substantial geothermal resources locked up radiogenic granite basins in its Eastern region. For example, the El Faliq granite reservoir can generate up to 7x10^9 kWh of electricity [31]. Although Egypt does not have an official CO_2 emissions penalty yet, it is also useful to calculate the cost savings made by the imposition of a carbon tax because it is a likely scenario already enacted in 25 countries [32]. CO_2 penalties in comparable economies, such as South Africa, can be used for preliminary calculations. Finally, different financial KPIs, such as net present value (NPV), may be calculated as an additional indicator of the financial feasibility of the systems.

References

[1] T. Khitous, "How Egypt Banks on Renewables to Meet Expected Surge of Energy Demand," [Online]. Available: https://www.altenergymag.com/article/2020/07/how-egypt-banks-on-renewables-to-meet-expected-surge-of-energy-demand/33511. [Accessed 05 01 20].

[2] S. N., "Renewable Power Generation Share Worldwide 2019," [Online]. Available: https://www.statista.com/statistics/489131/share-of-renewables-in-power-generation-globally/. [Accessed 05 01 20].

[3] A. S. Emara, "Egypt's Energy Planning and Management in View of the Commitments to the Framework Convention on Climate Change".

[4] A. M. G. T. K. Aladassy, "Towards optimum energy performance measures for existing hotels in Egypt," 2016.

[5] H. B. M. Georgei I, "Energy Use In Sharm El-Sheikh Resort in Egypt," *Int. J. Sus. Dev. Plann.,* vol. 7, no. 4, pp. 412-427, 2012.

[6] I. R. E. Agency, Renewable Energy Outlook: Egypt, 2018.

[7] A. Maheri, "Using new methodology to improve renewable energy efficiency," University of Aberdeen, [Online]. Available: https://www.abdn.ac.uk/stories/improving-energy-efficiency/index.html. [Accessed November 2020].

[8] Energypedia, "Egypt Energy Situation," [Online]. Available: https://energypedia.info/wiki/Egypt_Energy_Situation. [Accessed October 2020].

[9] T. W. Bank, "Clean Energy: Scaling up Wind Power in Egypt," 12 08 20. [Online]. [Accessed 05 01 2021].

[10] V. Y. M. K. Y. E. C. Oner, "Photovoltaic Thermal (PVT) Solar Panels," 2016.

[11] C. L. J. G. J. Porras-Prieto, "Energy Saving in an ETC Solar System to Produce High-Temperature Water," *Energies,* 2018.

[12] R. M. G. S. Qiu S., "Evacuated tube collectors: A notable driver behind the solar water heater industry in China".

[13] J. I. M. K. A. I. W. Ahmad, "Technoeconomic analysis of a wind-photovoltaic-biomass hybrid renewable energy system for rural electrification: A case study of Kallar Kahar," *Energy,* 2018.

[14] K. H. M. M. C. Wang, "Technoeconomic assessments of hybrid photovoltaic-thermal vs. conventional solar-energy systems: Case studies in heat and power provision to sports centres," *Applied Energy,* 2019.

[15] A. R. I. Z. C. N. M. Maria Herrando, "A comprehensive assessment of alternative absorber-exchanger designs for hybrid PVT-water collectors," *Applied Energy,* vol. 235, pp. 1583-1602, 2019.

[16] Kingspan, "Kingspan Thermomax DF400 Evacuated Tube Collectors," [Online]. Available: https://www.kingspan.com. [Accessed October 2020].

[17] XZERES, "SKYSTREAM 3.7," [Online]. Available: https://www.xzeres.com/?page_id=351. [Accessed October 2020].

[18] A. J. F. I. Z. C. N. M. Maria Herrando, "Technoeconomic modelling and optimisation of solar combined heat and power systems based on flat-box PVT collectors for domestic applications," *Energy Conversion and Management,* vol. 175, pp. 67-85, 2018.

[19] Treco, "How much does a biomass boiler cost?," [Online]. Available: https://www.treco.co.uk/news/article/how-much-doe-a-biomass-boiler-cost. [Accessed October 2020].

[20] Egyptian Electric Holding Company, "Annual Report EEHC," 2017-18.

[21] C. B. Rates, "Worldwide Central Bank Rates," 2020. [Online]. Available: http://www.cbrates.com/. [Accessed 05 01 2021].

[22] inflation.eu, "Current inflation South Africa - CPI inflation," [Online]. Available: https://www.inflation.eu/en/inflation-rates/south-africa/current-cpi-inflation-south-africa.aspx. [Accessed October 2020].

[23] T. P. O. o. S. a. Technology, "Carbon Footprint of Heat Generation (May 2016)," 2016.

[24] H. E. M. Abdelkader, "Political Instability and Economic Growth in Egypt," *Review of Middle East Economics and Finance,* 2017.

[25] A. Group, "Planet 21: Our Building," [Online]. Available: https://group.accor.com/en/commitment/planet-21/building. [Accessed December 2020].

[26] C. B. o. Egypt, "Egypt Interest Rate," 24 12 2020. [Online]. Available: https://tradingeconomics.com/egypt/interest-rate. [Accessed 05 01 2020].

[27] E. Today, "Egypt applies new electricity prices as of July 1," 01 07 2019. [Online]. Available: https://www.egypttoday.com/Article/3/72314/Egypt-applies-new-electricity-prices-as-of-July-1. [Accessed 05 01 2020].

[28] M. E. T. Y. B. E. L. Sharafi, "Optimal design of hybrid renewable energy systems in buildings with low to high renewable energy ratio," *Renewable Energy,* 2015.

[29] S. 2. Power, "Photovoltaic thermal hybrid solar collector," 02 2020. [Online]. Available: https://solar2power.pt/photovoltaic-thermal-hybrid-solar-collector/. [Accessed 05 01 2021].

[30] L. Edge, "LE-600 Small Wind Turbine," [Online]. [Accessed 05 01 2021].

[31] D. L. A. A. A. N. Chandrasekharam, "Geothermal energy potential of eastern desert region, Egypt," *Environmental Earth Sciences,* 2016.

[32] C. Chow, "Carbon Tax: A Shared Global Responsibility For Carbon Emissions," 24 01 2020. [Online]. Available: https://earth.org/carbon-tax-a-shared-global-responsibility-for-carbon-emissions/. [Accessed 05 01 2021].

Techno-Economic Analysis of Photocatalytic Reduction of CO_2

Hengrui Lu and Sulaiman Qureshi
Department of Chemical Engineering, Imperial College London, U.K.

Abstract Photocatalytic reduction of carbon dioxide to solar fuels has received significant attention as an approach of CO_2 mitigation, that can be used in tandem with existing carbon capture and storage (CCS) technologies. While there has been much development into the photoreduction reaction itself and the corresponding catalysts, few have focused on relevant techno-economic analysis (TEA) on large scale CO_2 reduction. The models that have been built also required further investigation and could be potentially optimized. This work aims to build on a previous TEA developed for a system with an annual feed of 100,000 tonnes of CO_2 that is converted to methane by looking at four alternative products. Namely, carbon monoxide, ethene, methanol and ethanol. The model also includes developing technologies' that are used for product separation. It was found out that under current market conditions, ethanol is the most promising product, as 15% conversion of CO_2 is needed for the process to become profitable, followed by methanol and ethene, at 35% and 46%, respectively. The production of carbon monoxide is not economically feasible with the current model. Various photocatalytic parameters were altered to investigate the limitation and feasibility of the system under the changing conditions.

1. Introduction

Climate change has gradually become one of the most important issues faced globally, especially due to the overreliance on greenhouse gas producing fossil fuels for many years. As the global energy demand continues to increase year on year, the use of these fuels has led to an overabundance of CO_2 into the atmosphere (Shown et al., 2014). Thus, seeking an economically viable solution to reduce the large amounts of CO_2 present is of major importance. There are technologies to reduce the CO_2 in the atmosphere such as carbon capture and storage (CSS), however this tends to be relatively costly, and suffers from many technology related hurdles Therefore, exploring alternative solutions that can work alongside CSS such as carbon capture and utilisation(CCU) is of great interest (Galadima and Muraza, 2019). One such CCU avenue to pursue is the reduction of CO_2 into fuels and other hydrocarbons, as not only does this reduce the amount of CO_2 released into the atmosphere but also helps meet chemical and energy demands. Various research breakthroughs have been made in making such technology more viable, however the current state of such technology is not yet at a level where it can be implemented on an industrial scale (Herron et al., 2015).

There are multiple reduction processes that can be used, which can be broken down into four main groups: Thermochemical, electrochemical, biochemical and photochemical/photocatalytical (Herron et al., 2015; Yaashikaa, Senthil Kumar, Varjani and Saravanan, 2019) Each have their own merits and drawbacks, however the focus on this paper will be on photocatalytic reduction/photoreduction of CO_2. This technology is chosen over the others as it is regarded as more environmentally friendly, given it is a solar driven process. As it is reliant on light irradiance, it has the potential to be less costly than other methods so may have greater economic viability. (Martins et al., 2020 ;Yaashikaa, Senthil Kumar, Varjani and Saravanan, 2019) Despite this it does have its own drawbacks, such as lower conversions and catalytic activity when compared to other methods (Bushuyev et al., 2018; Yaashikaa, Senthil Kumar, Varjani and Saravanan, 2019).

Photocatalytic reduction can be undertaken via two routes depending on the reducing agent, either hydrogenation via H_2 or artificial photosynthesis via H_2O. H_2 is regarded superior reducing agent, in terms of productivity as it is a far more efficient than H_2O, offering productivity values approximately 3 magnitudes higher when compared to those achieved via H_2O (Albero, Peng and García, 2020). However, on an industrial scale the demand of the reducing agent would be far higher, and if chosen, would require additional H_2 from industrial production, such as water splitting, resulting in higher energy as well as material cost. Alsayegh, Johnson, Ohs and Wessling, 2019). From an industrial and environmental perspective, using H_2O is ideal due to its low cost and the high demand that comes with such a scale. The low productivity rates that arise as a result of using H_2O is something that unfortunately cannot be avoided as a result. These reactions under lab conditions typically have very low solar to fuel efficiencies (STF), often far less than 1% (Albero, Peng and García, 2020). It has been suggested that a minimum STF of 10% would be required for economic viability (Wu, Huang, Ye and Li, 2017).

The most common products and better understood reduction reactions between CO_2 and H_2O are those that produce C1 products. These reactions typically have simpler kinetics and as are better understood as a result. Although, there are many other solar products that can be produced through photocatalysis, such as C2+ products. These products tend to have for more complicated reaction kinetics and are regarded as black box reactions. However, they often have greater market values than C1 products, thus may present better economic viability (Albero, Peng and García, 2020). Selectivity towards different products in the photocatalytic reduction of CO_2 is affected by various factors, choice of catalyst and reaction conditions can be modified to obtain a desired product. Often when driving selectivity towards C2+ products, a co-catalyst is needed due to the nature of the products produced. Furthermore, it is common that mixtures are typically produced when driving towards C2+ products, requiring complicated and sometimes not fully developed separation technologies (Fu et al., 2020).

There has been much academic research and development into understanding the use of various photocatalysts in photoreduction of CO_2 to produce solar fuels. Comparatively research into techno economic models for photocatalysis of CO_2 via artificial photosynthesis are sparse. This may be attributed to fact that artificial photosynthesis tends to be less efficient than hydrogenation (Albero, Peng and García, 2020). As there has been some development into a techno-economic assessment (TEA) for the photocatalytic production of methanol via hydrogenation, where the H_2 is sourced through photocatalytic water splitting. The main findings in the model were that, even in the best-case scenario, a methanol market price of 0.96$/kg is required to break even. This is much higher than the current market price of 0.58$/kg, thus more development is needed so that it can be competitive with conventional production of methanol. Furthermore, the model also has safety concerns, as H_2 and O_2 are produced in tandem, posing a risk of ignition (Alsayegh, Johnson, Ohs and Wessling, 2019). Other reduction methods have also received some attention regarding techno-economic development, such as thermochemical and electrochemical. It was found that in a model based on thermochemical reduction to produce methanol, a market price of 1.22$/kg was required, again much higher than the current market price (Kim et al., 2011).Electrocatalysis also shows some promise, with the model being able to remain economically viable producing formic acid and CO (Jouny, Luc and Jiao, 2018).

A techno-economic model for the photocatalysis of CO_2 to produce methane was developed over the past year as part of a master's thesis. This model demonstrates how the photocatalytic conversion of CO_2 to methane could potentially be performed on a large scale. Furthermore, it also shows the economic viability of large scale photoreduction. This report aims to expand on the techno-economic model developed for the photocatalysis of CO_2. Whereas the current model just looks at one product, it will be expanded to the production of other solar products (Xiong, 2020). The purpose of this is to better understand whether there is economic viability of production of other hydrocarbons, such as C2 products, and to understand the limits that the model can be pushed to, while still maintaining the economic viability.

2. Background

2.1 Products

Through reduction, it is possible to acquire products such as CO, CH_3OH, CH_4 etc., The previous model has been focused on reduction to CH_4 for its comparably high selectivity and decent economic potential (Xiong, 2020). However, this section will focus on other products with potential that were considered and provide justifications on the ones which were ultimately chosen to move forward with. Many potential products were looked at, each showing various degrees of promise. As seen in Table 1 the initial products considered can be found, with the corresponding catalyst employed to produce them under lab conditions, and the maximum selectivity achieved. It was decided to focus on the following products when conducting simulations of the model, methanol, ethanol, ethene and carbon monoxide.

Table 1 *solar products considered ref (1,7,11,17,21,25-28,31,37,41)*

Product	Formula	Price /kg ($)	Selectivity (%)	Catalyst
Methane	CH_4	0.18	100	Pt-TiO_2
Methanol	CH_3OH	0.58	67.5	Ni loaded TiO_2
Ethene	C_2H_4	1.3	7	TiO_2/AuPd
Ethanol	C_2H_5OH	1	69.7	TiO_2 with Cu nanotubes
Ethane	C_2H_6	4	40	Au nanoparticles
Propane	C_3H_8	8	17.9	CdS/TiCU nanotubes
Propene	C_3H_6	0.9	1.3	Same catalyst as propene
Acetaldehyde	CH_3CHO	4.5	100	Graphene oxide (GO)/ Cu nanoparticles
Carbon monoxide	CO	0.06	60.8	Ni-doped $ZnCo_2O_4$ WO_3

2.1.1 CO

Carbon monoxide is the simplest C1 product from reduction. Despite being a non-organic chemical, CO can be subsequently transformed into more useful chemicals or fuels through FTS or other synthetic strategies (Cheng, Zhang, Zhu and Wang, 2020). The reaction in the process utilizes water as the reducing agent, which results in the production of H_2 as a by-product, the separation of CO and H_2 most likely would result in additional cost applying membranes and other utilities. However, not separating the two gases would make it a syngas product, which could in turn raise its commercial value. Syngas has a wide usage across the world and is a great replacement of fossil fuel. Current market prices of syngas are reported as 2.54 $/1000$ft^3$(www.eia.gov, n.d.). The market for syngas is expected to grow by greater than 10% in the upcoming 5 years (Xiong et al., 2020).

2.1.2 CH_3OH

Methanol is another C1 product worth considering from the photocatalytic reduction of CO_2. As an important liquid fuel, as well as the precursor of many commodity chemicals, methanol can be found in the manufacture of many consumer and industrial products. One of the most important usage of methanol is its role as a feedstock to produce chemicals (Mao et al,. 2012). In terms of fuel, methanol is known as a key component in biodiesel, a renewable fuel that can be used in place of, or blended with, conventional diesel fuel, which could potentially reduce emissions. In the future, methanol is expected to become a maritime fuel that meets shipping industry's

emission regulation in a cost-effective manner (Wu, 2009).

2.1.3 C_2H_4

Ethene is another valuable product that can be manufactured from the reduction of CO_2. It is a vital raw material and precursor to many other chemicals, the largest use of ethene is polymerization, which takes up half of the annual ethene production. It can be used to produce plastics such as polyethene, which is recyclable and can be reused to make other products. It is also at the forefront of environmental research as various methods being studied to make polyethene more biodegradable (Essentialchemicalindustry.org, 2015). The global ethene market size reached a value at around $222.1 billion in 2019. Having grown at a compound annual growth rate (CAGR) of 5.25% since 2015, by 2023, this number is estimated to grow at a CAGR of 4.77% and reach nearly $267.6 billion, showing a huge demand for ethene production (www.polarismarketresearch.com, n.d.).

2.1.4 C_2H_5OH

Like methanol, ethanol can be mixed with gasoline and to produce biodiesel. Several studies have shown that by using ethanol fuels, the emission of greenhouse gases can be reduced to up to 30% in every mile, significantly reducing the impact on the environment (Green Coast, 2019). In addition, since ethanol is produced from CO_2 via this route, it is possible to achieve carbon neutrality. Despite being a beneficial fuel, there are some drawbacks related to ethanol. The prices of ethanol vary and fluctuate greatly, which is highly location-dependent, for example in the Midwest, the ethanol market price is lower due to the high availability of corn (Grandviewresearch.com, 2019). In 2019, the global market of ethanol was valued at $89.1 billion, the market size is projected to register a CAGR of 4.8% from 2020 to 2027 (www.globalinforesearch.com, n.d.). The demand for the product is mainly driven by growing usage of the product as a biofuel (biofuels-news.com, n.d.).

2.2 Catalysts

As mentioned previously, the choice of catalyst can have a major effect in driving the reaction to certain products. Photocatalysts absorb light, bringing to a higher energy to drive a photoreaction. In the case of CO_2 reduction, the energy is provided to the CO_2 and H_2O molecules so that a reduction reaction can occur (Oshida 2013). The effectiveness of photocatalysts can be compared through apparent quantum yield which is given by the ratio of reacted electrons to the number of incident photons. (Xiong, 2020). Much of the research into producing solar products has only been done on a lab scale, thus they have been able to make use of experimental catalysts that are very costly and tend to not be available on an industrial scale. The following catalysts are some of those which have potential to be used in the large scale photocatalysis of CO_2.

2.2.1 Titania catalysts

Transition metal-doped titanium oxide (M-TiO_2) is a classic photocatalyst. TiO_2 is an inexpensive, highly stable semiconductor that has great potential for large scale synthesis, but it is restricted by the activation of UV light. Metal doping is used extensively to advance efforts at modifying TiO_2 to operate more efficiently under visible light (Moma and Baloyi, 2019).The doping of metal onto TiO_2 results in a shift in the absorption spectrum to longer wavelengths, which favors the use of visible light to photoactivate the TiO_2 (Tasbihi et al., 2018).

Various transition metals can be used to dope titania, the most commonly used metals are Ag, Cu and Pt, the specific metal doped on the catalyst is dependent on the desired product and selectivity. For example, platinum-titania catalyst is ideal for the reduction of CO_2 to methane, it would simultaneously ensure a high yield as well as selectivity; Other catalysts, such as copper-doped titania, opens up the option to convert CO_2 to methanol, the use of copper instead of platinum indicates that the total cost of the catalyst would also go down significantly, while making a compromise on the overall yield (Slamet et al.,2005)

2.2.2 Tungsten oxide

Thanks to its highly tuneable structure and unique physicochemical properties, tungsten oxides receive considerable attention in photocatalysis, electrochemistry as well as phototherapy. Through manipulation of the crystal structure, the properties of the catalyst can be changed, which can prove beneficial depending on the process. Compared to its crystalline counterpart, amorphous tungsten oxide has a higher photocatalytic activity, at the cost of poor structural and chemical stability. With bandgap ranging from 2.6 to 3.2 eV, tungsten oxide is one of the most popular catalysts in the field of photocatalytic reactions, including CO_2 reduction. For WO_3, the low conduction band level (lower than -0.1V vs SNHHE, pH=7) inherently limits its application for CO2 reduction, it also suffers from sluggish kinetics of holds, slow charge transfer at the semiconductor/electrolyte interface (Huang et al., 2015)

2.2.3 Graphene oxide

Because of its unique 2D carbon structure, graphene oxide (GO) sheets have highly tuneable electronic properties. GO is a new type of two-dimensional carbon sheets, that have similar properties to an insulating material with a wide band gap. Its electronic structure is dependent on the stoichiometric carbon to oxygen atomic ratio. In the past years, graphene oxide has raised great attention for photocatalytic performance and demonstrated as an efficient electron acceptor to improve the charge transfer and effectively reduce recombination of the electron-hole pairs in the composite to improve the photoactivity. The bandgap of GO offers the possibility to convert CO_2 to methanol, which favours solar energy harvesting, the reported productivity of methanol using GO as catalyst is also significantly higher than that of using TiO_2 (Hsu et al., 2013)

2.2.4 Carbon nitride

Carbon nitride (C_3N_4) is a nanomaterial that is capable of absorbing visible light and utilize the energy in the photons to catalyse chemical reactions of industrial interest. It is very easy to produce on an industrial scale with widely available, cost-effective precursors. The advantage of using carbon nitride is manifold, including its stability, being a robust material and can be easily recycled, it could be used to replace expensive and potentially harmful metal-based catalysts (Filippini et al.,2020)

3. Model development

The basis for this paper is a TEA model used to develop the large-scale photocatalytic conversion of CO_2 using Pt-TiO_2 as the photocatalyst. The reaction takes place as a gas-solid binary reaction, where the feed remains gaseous. As discussed, earlier metal doped titanium oxide presents numerous advantages as a catalyst. The purpose of the TEA is to analyse the performance process on technical as well as economic scale. This can be done through a combination of first modelling the process, and an economic evaluation. Followed by a sensitivity analysis. Much of this section will be based on the work found in the previous model. (Xiong, 2020)

The process model is developed using the scope of the process as a basis. A continuous CO_2 reduction process contains the following stages, CO_2 capture, conversion, separation, purification, storage and fuel/chemical utilisations. The reactor used and separation technologies are all dependant on the process. However, in regards to photocatalytic reduction of CO_2, there is not yet a standard reactor used in an industrial context. The economic model looks at estimating the operating and capital costs of the system.

Using the process model and economic model in tandem, a sensitivity analysis can be performed. This allows for investigation into the process while it operates under different parameters and conditions. Using the data generated, technical and economic performance indicators can be calculated. Common technical indicators are CO2 conversion, production rate and the solar to fuel efficiency (STF). While being a good indicator, STF does also have a theoretical limit. The highest STF efficiency achieved so far for photoreduction is 19.1%, and similar values are required for the process to be competitive.

$$Conversion = \frac{moles\ of\ CO_2\ reacted\ per\ pass}{moles\ of\ CO_2\ fed\ into\ reactor\ per\ pass} \quad (1)$$

$$\eta_{STF} = \frac{r_{fuel}(mol\ s^{-1}) \times \Delta G\ (J\ mol^{-1})}{P_{solar}(W\ m^{-2}) \times Area\ (m^2)} \quad (2)$$

Where r_{fuel} is the rate of production, ΔG is the Gibbs free energy for the reaction, P_{solar} is the solar irradiance and area is the area irradiated.

Economic performance can be assessed based on the following indicators, economic potential (EP), simple payback time, and return on investment (ROI). EP is an annualised indicator, that if positive suggests economic viability. Simple payback time and ROI are both indicators that suggest profitability. The difference between the two is that ROI includes location dependant taxation, whereas the former does not.

$$EP = annual\ revenue - total\ anualised\ cost \quad (3)$$

Where annual revenue is the total product price per year, and total annualised cost corresponds to the annualised capital costs and the operating costs.

$$Simple\ payback\ \ time = \frac{total\ investment}{annualised\ cash\ flow} \quad (4)$$

Where total investment is the total capital cost, and annualised cash flow is the gross profit per year.

$$ROI = \frac{net\ annual\ profit}{total\ investment} \quad (5)$$

Where net annual profit is the net gross profit per year after taxes.

3.1 Model parameters

Development of the model first requires a CO_2 feedstock, which can be obtained a source directly or ambient air. The cheapest approach in this regard is to use the CO_2 produced by a high emission process. The model is based on the using half of a CO_2 waste stream produced in an ethylene oxide plant, approximately 100,000 tonnes per year (0.2104 kmol/s). Choice of photoreactor is also highly dependent on the demands of the process. An optical fibre reactor is chosen as it is an ideal configuration for scale up and allows for a fast mass transfer rate. The parameters chosen for the base case of model can be found in Table 2, justification for the choice of these parameters can be found in the previous authors work.

Table 2 *Parameters used for the process model*

Base case	Decisions
Reactor type	Optical fibre
Feed temp	70 C
CO_2 feed rate	100,000 tonnes per year
H_2O/CO_2 feed ratio of the system	Stoichiometric ratio
Annual operating hours (sunshine hours)	3000 hours
Plant lifetime	25 years
Location	Pasadena, Texas, the U.S.

3.2 Separation technologies

The process also makes use of technologies that are still currently in development in the removal of oxygen, and unreacted CO_2. Oxygen removal works on the basis of sulphide deoxidation. Two removal columns are required, one is used for oxygen removal and the other for sulphide regeneration. Carbon monoxide is used as the reducing gas for this process. For the removal of CO_2 from the methane stream, a two-stage membrane-based

solution is employed. A compressor and two coolers are also required to pre-treat the feet to the required conditions for separation. Both removal units are simulated as separation units within the Aspen flow sheeting.

3.3 Assumptions

3.3.1 Process model

In the Aspen simulation, Peng-Robinson equation of state is used, as the equation is capable of handling both vapor and liquid properties of the products studied in the simulation. The simulation aims to investigate the feasibility of photocatalytic reduction of CO_2 in an ideal scenario, therefore complete separation is assumed for each of the separation unit.

3.3.2 Economic model

Several assumptions are made on the economic model. Piping and additional instrumentation costs are assumed to be negligible. ISBL investment (Inside battery limits), OSBL investment(Outside battery limit), engineering cost, contingency charges and working capital all make up the total investment. Costing of each of these can be based on the ISBL and OSBL and are summarised in Table 3. Furthermore, a standard commercial loan for the equipment costs with an interest of 5% and no tax breaks are assumed.

Table 3 *Economic model variables used in KPI calculations*

Cost	Calculation
ISBL	/
OSBL	40% of ISBL
Engineering cost	10% of ISBL + OSBL
Contingency charges	10% of ISBL + OSBL
Working capital	15% of ISBL + OSBL

3.3.3 Findings of the previous model

It was found that in the previous model, a minimum conversion of 42% is needed for the economic potential of the process to remain positive. Increasing the conversion does not increase the amount of product, therefore the revenue remains unchanged. However, at higher conversions the operating costs are reduced thus increasing the EP of the process. It was also found that the process has a STF efficiency of approximately 17.5% which suggests that large scale CO_2 photoreduction could become a competitive process in the future.

A sensitivity analysis was also performed where various parameters were changed to understand the effect on the system. Market prices and location were found to have the largest impact on economic viability of the model. Change in location had a noticeable affect especially, as this in turn changes the number of sunshine hours per year and the level of taxation. Furthermore, the market price of the product also varies from location to location.

The model suffers from various limitations, a major one being that conversions found under lab conditions are far lower than what is needed for economic viability. The model also makes use of novel technologies that have only been tested on a lab scale, so may not be suitable for industrial use.

3.4 Differences between models

For keeping consistency, the operating parameters for the base case were kept same: 3000 hours of annual sunshine time, 100,000 tonnes CO_2 feed, and 25 years project lifetime. This ensures consistency between the two models and allows for easy comparison. A Pt-TiO_2 catalyst is also used for cost estimations, however as other products are being assessed the viability of using other catalysts can be assessed using a sensitivity analysis. The assumptions made in the previous model are also taken as the same.

3.4.1 Modifications to the Process

As the products that were being considered were not as well researched as methane, it was decided that the production rate chosen would be in proportion to the production rate of methane, 1361g_{cat}·h Therefore, for a C1 product the rate would remain the same, while for a C2 product it would be halved due to the stochiometric ratio. The production rate chosen for the product and equations can be seen in Table 4.

Table 4 *Production rate and equations of products chosen*

Solar product	Equation	Production rate(μmol/g_{cat}·h)
CH_3OH	$CO_2 + 2H_2O \rightarrow CH_3OH + 1.5O_2$	1361
C_2H_5OH	$2CO_2 + 3H_2O \rightarrow C_2H_5OH + 3O_2$	680.5

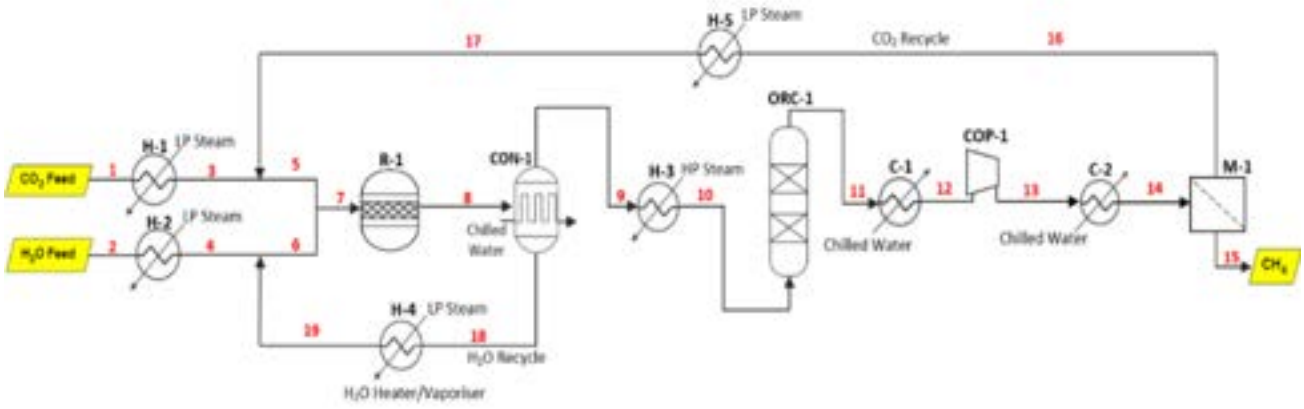

Figure 1. *Unmodified process flow diagram* (Xiong., 2020)

C_2H_4	$2CO_2 + 2H_2O \rightarrow C_2H_4 + O_2$	680.5
CO	$CO_2 + 2H_2O \rightarrow CO + H2 + O_2$	1361

The process will need certain modification to suit the production need, for products that are required in liquid form, namely methanol and ethanol, a DSTWU distillation column capable of achieving >99% product purity is added after the condenser so that the desired product may be separated from the recycled water stream, the utilities subsequent to O_2 removal column were removed, since they are no longer needed; For the gaseous products (CO and ethene), the process was kept the same, however the simulation also assumes that the technology used for CO_2-methane separation can be applied to ethene and CO. The previous process model and modified one can be seen in Figures 1 and 2 respectively.

This project is broken down into two steps: Simulations were conducted on Aspen Plus v9.0. The simulations run for the base model for each process were performed with various conversions of CO_2 (20% - 80%),which aims to investigate the process performance. The data acquired would be used for techno-economic analysis and subsequent sensitivity analysis with Microsoft Excel. The sensitivity analysis is performed on the base case for each product with a CO_2 conversion of 50%.

4. Results and discussion

4.1 Base Case

As discussed before, the simulations for different desired products were conducted based on the 100% selectivity assumption. A demonstration of the calculations for the techno economic model performed on the base case of 50% CO_2 conversion can be found in the appendix.

As shown in Figure 3, at higher CO_2 conversions, regardless of chosen product, better EPs are generated. The number of moles of carbon that goes in the plant equals the number of moles that comes out (0.2104 kmol/s). Therefore, the revenues of products stay the same as the feed rate was kept constant throughout. As conversion increase both the capital and operational costs fall, albeit at different rates depending on the product. Figure 4 shows the decrease of these costs with increasing conversion, which in turn causes the EP for each product to increase. At higher conversions, the system has less unreacted CO_2 and H_2O. Therefore, less duty is required as there a less moles required to be separated and recycled. At lower conversions, more reactants are recycled, thus the corresponding duty of the units is higher. Both ethene and CO processes benefit significantly from increasing conversion, this can be attributed to the fact that in the unmodified process there are more units such as heaters or compressors. Therefore, at higher conversions the duty of the unmodified and ethene process decreases at a faster rate. This is demonstrated by the annualised

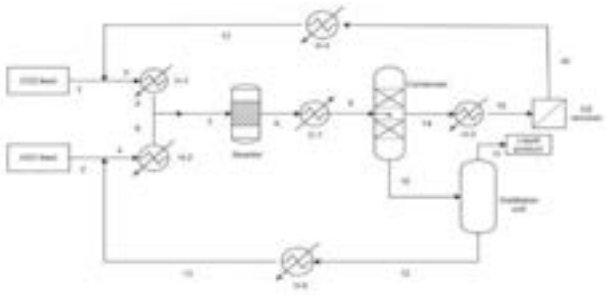

Figure 2. *Modified process flow diagram*

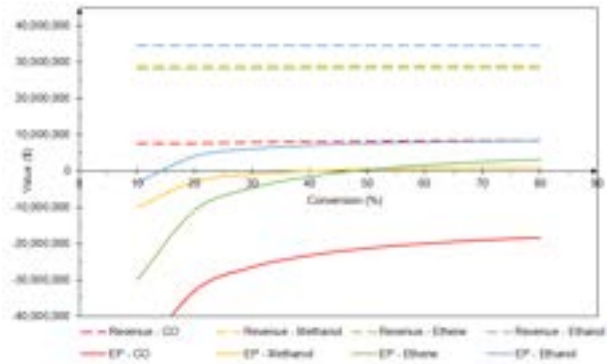

Figure 3. *EP and revenue of the different products*

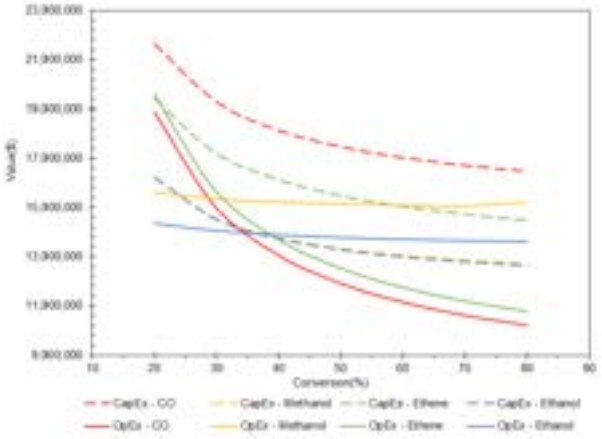

Figure 4. *Annual CapEx and OpEx of the different products*

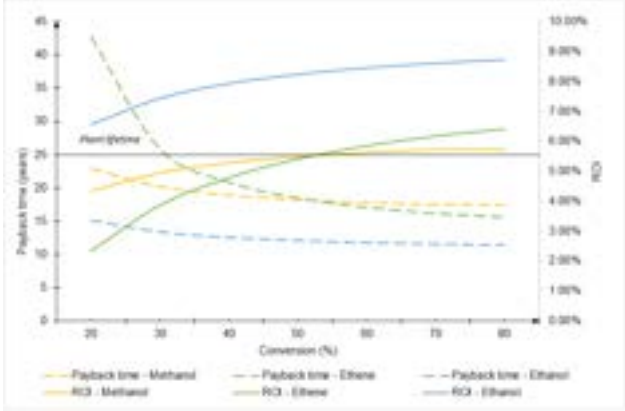

Figure 5. *Economic performance indicators of the different products*

operating cost (OpEx) and annualised capital cost (CapEx) curves for ethene and CO in Figure 4.

The liquid products ethanol and methanol also benefit from increasing conversion but not in directly the same way. Although EP does decrease with increasing conversion as previously mentioned the change and operating and capital cost vary from that of the liquid products. They both decrease; however it is noticeable that the CapEx curves for ethanol and methanol decrease at a faster rate than the OpEx curves as seen in Figure 4. The greater decrease in capital cost rather than operating cost can be explained by the condenser duty. While for all other units, the duty does decrease with conversion thus reducing the operational cost, with regards to the liquid products only, condenser duty increase. The increase demand of the condenser can be explained by the fact that the product is also condensed instead of just H_2O as before.

It can also be seen from Figure 3, ethanol has a critical conversion of 15% the methanol process requires a conversion of 35% to be profitable, whereas that for ethene is 46%. Carbon monoxide, however, is not economically viable under the current model, as it does not generate a positive EP on any trial conversion. It is worth noting that the for the ethene and methanol EP curves, that despite methanol having a lower critical conversion, after 53% conversion, ethene overtakes methanol and has a larger EP. This could be due to the fact that as ethene is a C2 product is has a higher market value than methanol, and in the unmodified process used for ethene the operating costs decrease at a faster rate with conversion.

The economic performance indicators are represented in Figure 5. Given the carbon monoxide process was found to be economically unviable, its corresponding indicators are not featured. As the EP is negative the findings for the other indicators are invalid. For the same reasons discussed with EP, as conversion increases, the process has a shorter payback time and higher ROI, therefore better economic performance. Both methanol and ethanol have payback time less than 25 years (plant lifetime) at all trial conversions, whereas ethene needs at least 30% conversion. At 80% conversion, all the processes have more than 10 years payback time, amongst them, only ethanol has shorter time than the industry average payback period of 15 (Leanmanufacture, 2020). The ROI values of all three processes are reasonable and even outperform the methane process, the highest being 9.00%, achieved by ethanol at 80% conversion, even then it is still lower than 10.29%, the average value of industry (CSIMarket, 2020).

The STF efficiencies of different processes were also calculated, using equation 2. At base case, methanol has an STF efficiency of 17.5%, while that for ethene and ethanol is 8.75%. Methanol has a similar value as methane in the previous work, the similarity could be explained by the fact that both are C1 product, therefore sharing the same stoichiometric ratio. For C2 products, the fuel produced is only half of number of moles CO_2 that is fed in. The change in STF efficiency is attributed to the change in production rates shown in Table 4. Despite this as discussed previously a STF efficiency of 10% is required for economic viability (Wu, Huang, Ye and Li, 2017). For C1 products the process achieves this with an STF efficiency of 17.5%, while for the C2 products it does get close at 8.75% which shows promise.

4.2 Sensitivity analysis

Parameters in the models are usually uncertain and fluctuating. Therefore, a sensitivity analysis is done to investigate how changes in certain parameters impact the general viability of the process, as well as to understand the limitation of the system.

4.2.1 H_2O/CO_2 feed ratio

In previous iterations, an analysis on changes of H_2O/CO_2 feed ratio was conducted on the 50% conversion base case. Similar procedure was carried out for the current study, as it features different products.

Increasing H_2O/CO_2 feed ratio will lead to loss in EP of the process, which is largely due to the rise in operating costs, as more water needs to be heated and recycled: For the ethene process, as shown in Figure 6, when the feed ratio is increased in the minimum, the EP becomes negative, therefore, the ROI and payback time of these feed ratios are invalid, again this is due to the production of ethene uses the unmodified process, which has more utilities. Methanol processes, however, due to reduced utilities, can tolerate some increases before becoming unprofitable, its operating cost increases at a slower rate. Ethanol, however, due to its market value and using modified process, does not generate negative EPs as water feed is increased. Despite of this, increasing feed ratio may not be beneficial for liquid products, as the purity will

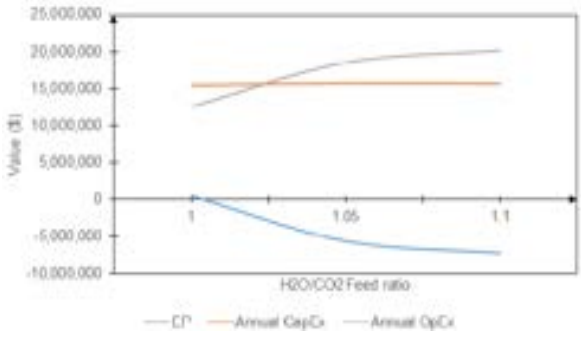

Figure 6. *Ethene process performance for 1.0, 1.05, 1.1 feed ratio*

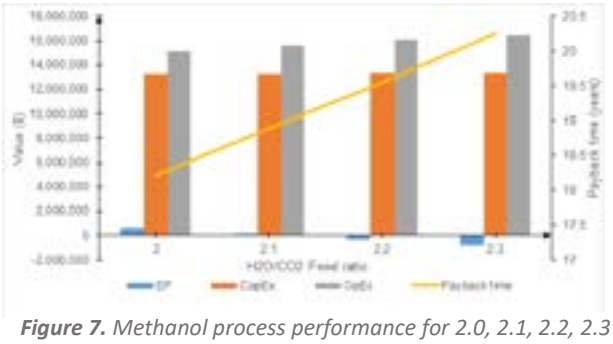

Figure 7. *Methanol process performance for 2.0, 2.1, 2.2, 2.3 feed ratios*

decrease. The economic performance of methanol and ethanol are shown in Figure 7 and 8, respectively.

4.2.2 Catalyst cost

Various photocatalyst are able to convert CO2 to various products. The cost of the respective catalyst can also have an impact on the economic viability of the plant. Variation in the catalyst cost allows to test how the system would be able to work with other, potentially more costly catalysts. As discussed previously the choice of photocatalyst will have a major impact on the product, therefore it is of great importance, that the process can handle changes in the catalyst cost.

As shown in Figure 9, utilisation of a more expensive catalyst will lead to a fall in EP as the capital cost is higher: Ethene and methanol start to generate negative EPs as the catalyst cost increases to around 5%, the payback time of these two products also increases, however, methanol at a faster rate. The rise in catalyst cost does not affect ethanol as great as the previous two products, as its simple payback time hardly changes. The maximum changes the ethanol process can tolerate at 50% conversion is a 71% increase in catalyst cost. For the trial changes of catalyst price, all the processes have shorter period than the plant lifetime; However, even when using a cheaper catalyst, methanol and ethene still have relatively long payback time.

4.2.3 Product price

The prices of chemical product tend to fluctuate; therefore, it is very important to assess the economic viability of the process under certain changes of the target product price.

Decreasing the product price will lead to loss in revenue, therefore loss in EP, it will also result in longer payback time, as seen in Figure 10. Both ethene and methanol are sensitive to changes in their prices, as negative EPs can be seen when their respective market price drop to below 98% of the original, their payback time still stay within 25 years plant lifetime; When both at higher percentage of market prices, ethene tends to have shorter payback time than methanol. Ethanol does not become unprofitable until its price drops to below 80%, when increased to even higher market values, a payback time less than 10 years can be achieved.

5. Conclusion and Future Work

In this project, the techno-economic model and the simulation for different CO_2 conversion processes were successfully built and evaluated. The viability of each process, under certain changes in various factors were also successfully evaluated.

The results from the base case analysis show that under the current model, ethanol is the most promising product, with a critical conversion of 15% for the process to become economically viable; Methanol and ethene are also competitive products (35% and 46% respectively). However, beyond a certain conversion, ethene's EP overtakes that of methanol. The production of carbon monoxide is not profitable, as its market price

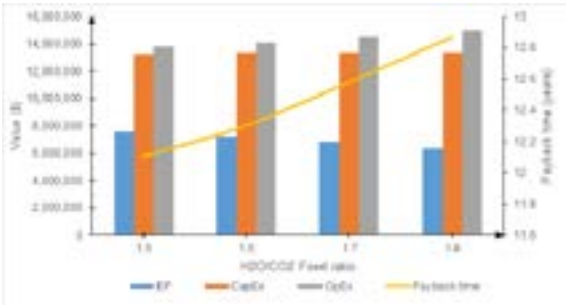

Figure 8. *Ethanol process performance for 1.5, 1.6, 1.7, 1.8 feed ratios*

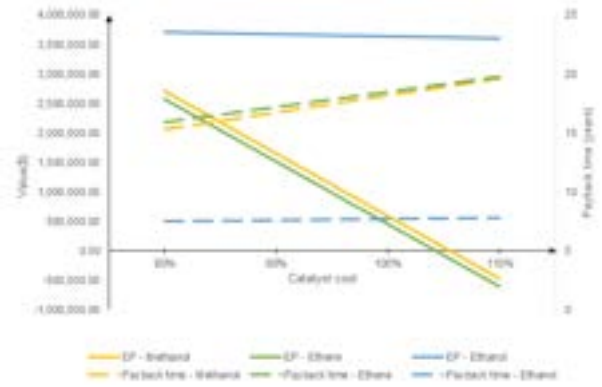

Figure 9. *Process performances with catalyst price change*

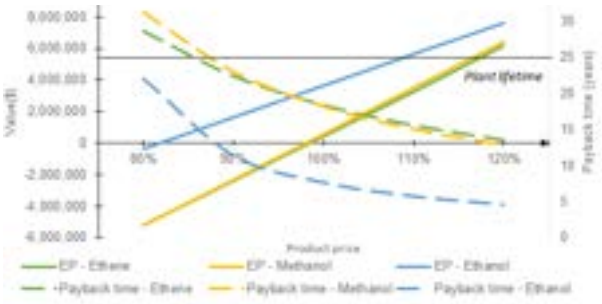

Figure 10. *Process performances with product price change*

is simply too low to generate a positive EP. Furthermore, even when it was looked at selling it as a syngas product, it was still unable to produce a positive EP. Generally speaking, liquid products are more favourable because of the reduced utilities in the process.

Sensitivity analysis shows that the H_2O/CO_2 feed ratio has large impact on the process. A lower feed ratio results in less water to be recycled in the process, therefore less duty is required, and a better EP can be achieved. The same can be said for at higher conversions. From the analysis, ethanol shows the most tolerance to changes in the parameters. Although the process does show promise and has the potential economic viability for large scale production far more development into CO_2 photoreduction is needed.

Therefore, it is suggested that experiments regarding the photocatalytic conversion of CO_2 to ethanol should be carried out, so the process may be better understood, and conversion rates can be brought

to a level where the process can be competitive, so that selectivity can be increased from the reported 69.7%.

References

[1]Albero, J., Peng, Y. and García, H., 2020. Photocatalytic CO2 Reduction to C2+ Products. ACS Catalysis, 10(10), pp.5734-5749.

[2] Alsayegh, S., Johnson, J., Ohs, B. and Wessling, M., 2019. Methanol production via direct carbon dioxide hydrogenation using hydrogen from photocatalytic water splitting: Process development and techno-economic analysis. Journal of Cleaner Production, 208, pp.1446-1458.

[3]biofuels-news.com. (n.d.). CropEnergies predicts higher EU ethanol demand as restrictions ease | Biofuels International Magazine. [online] Available at: https://biofuels-news.com/news/cropenergies-predicts-higher-eu-ethanol-demand-as-restrictions-ease/ [Accessed Dec. 2020].

[4]Bushuyev, O., De Luna, P., Dinh, C., Tao, L., Saur, G., van de Lagemaat, J., Kelley, S. and Sargent, E., 2018. What Should We Make with CO2 and How Can We Make It?. Joule, 2(5), pp.825-832.

[5]Caravaca, A., Garcia-Lorefice, W., Gil, S., de Lucas-Consuegra, A. and Vernoux, P., 2019. Towards a sustainable technology for H2 production: Direct lignin electrolysis in a continuous-flow Polymer Electrolyte Membrane reactor. Electrochemistry Communications, 100, pp.43-47.

[6]Cheng, M., Zhang, X., Zhu, Y. and Wang, M., 2020. Selective photocatalytic reduction of CO2 to CO mediated by a [FeFe]-hydrogenase model with a 1,2-phenylene S-to-S bridge. Chinese Journal of Catalysis, 42(2), pp.310-319.

[7]Chen, Q., Chen, X., Fang, M., Chen, J., Li, Y., Xie, Z., Kuang, Q. and Zheng, L. (2019). Photo-induced Au–Pd alloying at TiO2 {101} facets enables robust CO2 photocatalytic reduction into hydrocarbon fuels. *Journal of Materials Chemistry A*, 7(3), pp.1334–1340.

[8]CSIMarket. (2020) Chemical Manufacturing Industry. Available from: https://csimarket.com/Industry/industry_ManagementEffectiveness.php? ind=101 [Accessed Dec 2020]

[9]Essentialchemicalindustry.org. (2015). Ethene (Ethylene). [online] Available at: https://www.essentialchemicalindustry.org/chemicals/ethene.html.

[10]Filippini, G., Longobardo, F., Forster, L., Criado, A., Di Carmine, G., Nasi, L., D'Agostino, C., Melchionna, M., Fornasiero, P. and Prato, M. (2020). Light-driven, heterogeneous organocatalysts for C–C bond formation toward valuable perfluoroalkylated intermediates. Science Advances, 6(46), p.eabc9923.

[11]Fu, J., Jiang, K., Qiu, X., Yu, J. and Liu, M., 2020. Product selectivity of photocatalytic CO2 reduction reactions. Materials Today, 32, pp.222-243.
Galadima, A. and Muraza, O., 2019. Catalytic thermal conversion of CO2 into fuels: Perspective and challenges. Renewable and Sustainable Energy Reviews, 115, p.109333.

[12]Grandviewresearch.com. (2019). Ethanol Market Size, Share, Trends | Global Industry Report, 2025. [online] Available at: https://www.grandviewresearch.com/industry-analysis/ethanol-market.

[13]Green Coast (2019). 11 Important Ethanol Pros and Cons You Need to Know. [online] Green Coast. Available at: https://greencoast.org/ethanol-pros-and-cons/.

[14]Herron, J., Kim, J., Upadhye, A., Huber, G. and Maravelias, C., 2015. A general framework for the assessment of solar fuel technologies. Energy & Environmental Science, 8(1), pp.126-157.

[15]Hsu, H.-C., Shown, I., Wei H.Y., Chang, Y.-C., Du, H.-Y., Lin, Y.-C. and Chen, K.-H. (2013). Graphene oxide as a promising photocatalyst for CO2 to methanol conversion. Nanoscale, 5(1), pp2.62-268

[16]Huang, Z.-F., Song, J., Pan, L., Zhang, X., Wang, L. and Zou, J.-J. (2015). Tungsten Oxides for Photocatalysis, Electrochemistry, and Phototherapy. Advanced Materials, 27(36), pp.5309–5327.

[17]Iqbal, F., Mumtaz, A., Shahabuddin, S., Abd Mutalib, M.I., Shaharun, M.S., Nguyen, T.D., Khan, M.R. and Abdullah, B. (2020). Photocatalytic reduction of CO2 to methanol over ZnFe2O4/TiO2(p–n) heterojunctions under visible light irradiation. *Journal of Chemical Technology & Biotechnology*, 95(8), pp.2208–2221.

[18]Jouny, M., Luc, W. and Jiao, F., 2018. General Techno-Economic Analysis of CO2 Electrolysis Systems. Industrial & Engineering Chemistry Research, 57(6), pp.2165-2177.

[19]Kim, J., Henao, C., Johnson, T., Dedrick, D., Miller, J., Stechel, E. and Maravelias, C., 2011. Methanol production from CO2 using solar-thermal energy: process development and techno-economic analysis. Energy & Environmental Science, 4(9), p.3122.

[20]Leanmanufacture. (2020) Payback Period. Available from:

http://www.leanmanufacture.net/kpi/paybackperiod.aspx [Accessed Dec 2020].

[21]Liu, K., Li, X., Liang, L., Wu, J., Jiao, X., Xu, J., Sun, Y. and Xie, Y. (2018). Ni-doped ZnCo2O4 atomic layers to boost the selectivity in solar-driven reduction of CO2. *Nano Research*, 11(6), pp.2897–2908.

[22]Mao, J., Peng, T., Zhang, X., Li, K. and Zan, L. (2012). Selective methanol production from photocatalytic reduction of CO2 on BiVO4 under visible light irradiation. Catalysis Communications, 28, pp.38–41.

[23]Martins, P., Kappert, S., Nga Le, H., Sebastian, V., Kühn, K., Alves, M., Pereira, L., Cuniberti, G., Melle-Franco, M. and Lanceros-Méndez, S., 2020. Enhanced Photocatalytic Activity of Au/TiO2 Nanoparticles against Ciprofloxacin. Catalysts, 10(2), p.234.

[24]Moma, J. and Baloyi, J. (2019). Modified Titanium Dioxide for Photocatalytic Applications. Photocatalysts - Applications and Attributes. [online] Available at: https://www.intechopen.com/books/photocatalysts-applications-and-attributes/modified-titanium-dioxide-for-photocatalytic-applications.

[25]Park, H., Ou, H.-H., Colussi, A.J. and Hoffmann, M.R. (2015). Artificial Photosynthesis of C1–C3 Hydrocarbons from Water and CO2 on Titanate Nanotubes Decorated with Nanoparticle Elemental Copper and CdS Quantum Dots. *The Journal of Physical Chemistry A*, 119(19), pp.4658–4666.

[26]Sharma, A. and Lee, B.-K. (2017). Photocatalytic reduction of carbon dioxide to methanol using nickel-loaded TiO2 supported on activated carbon fiber. *Catalysis Today*, 298, pp.158–167.

[27]Shi, W., Guo, X., Wang, J.-C., Li, Y., Liu, L., Hou, Y., Li, Y. and Lou, H. (2020). Enhanced photocatalytic 3D/2D architecture for CO2 reduction over cuprous oxide octahedrons supported on hexagonal phase tungsten oxide nanoflakes. *Journal of Alloys and Compounds*, 830, p.154683.

[28]Shown, I., Hsu, H., Chang, Y., Lin, C., Roy, P., Ganguly, A., Wang, C., Chang, J., Wu, C., Chen, L. and Chen, K., 2014. Highly Efficient Visible Light Photocatalytic Reduction of CO2 to Hydrocarbon Fuels by Cu-Nanoparticle Decorated Graphene Oxide. Nano Letters, 14(11), pp.6097-6103.

[29]Slamet, Nasution, H.W., Purnama, E., Kosela, S. and Gunlazuardi, J. (2005). Photocatalytic reduction of CO2 on copper-doped Titania catalysts prepared by improved-impregnation method. Catalysis Communications, 6(5), pp.313–319.

[30]Tasbihi, M., Kočí, K., Edelmannová, M., Troppová, I., Reli, M. and Schomäcker, R. (2018). Pt/TiO2 photocatalysts deposited on commercial support for photocatalytic reduction of CO2. Journal of Photochemistry and Photobiology A: Chemistry, [online] 366, pp.72–80. Available at: https://www.sciencedirect.com/science/article/pii/S1010603017316404.

[31]Wang, W.-N., An, W.-J., Ramalingam, B., Mukherjee, S., Niedzwiedzki, D.M., Gangopadhyay, S. and Biswas, P. (2012). Size and Structure Matter: Enhanced CO2 Photoreduction Efficiency by Size-Resolved Ultrafine Pt Nanoparticles on TiO2 Single Crystals. *Journal of the American Chemical Society*, 134(27), pp.11276–11281.

[32]Wu, J.C.S. (2009). Photocatalytic Reduction of Greenhouse Gas CO2 to Fuel. Catalysis Surveys from Asia, 13(1), pp.30–40.

[33]Wu, J., Huang, Y., Ye, W. and Li, Y., 2017. CO2Reduction: From the Electrochemical to Photochemical Approach. Advanced Science, 4(11), p.1700194.

[34]www.eia.gov. (n.d.). *Texas Natural Gas Industrial Price (Dollars per Thousand Cubic Feet)*. [online] Available at: https://www.eia.gov/dnav/ng/hist/n3035tx3m.htm.

[35]www.polarismarketresearch.com. (n.d.). Ethylene Market Size, Share, Trends, Value | Industry Report 2020-2026. [online] Available at: https://www.polarismarketresearch.com/industry-analysis/ethylene-market [Accessed Dec. 2020].

[36]www.globalinforesearch.com. (n.d.). globalinforesearch.com Industry Analysis, Market Research Analysis,GIR reports. [online] Available at: https://www.globalinforesearch.com/Global-Pharmaceutical-Ethanol_p510708.html [Accessed Dec. 2020].

[37]Xia, X.-H., Jia, Z.-J., Yu, Y., Liang, Y., Wang, Z. and Ma, L.-L. (2007). Preparation of multi-walled carbon nanotube supported TiO2 and its photocatalytic activity in the reduction of CO2 with H2O. *Carbon*, 45(4), pp.717–721.

[38]Xiong, X 2020. 'A Techno-Economic Analysis of Photocatalytic Systems for CO2 Photoreduction', Masters thesis, Imperial College London, London.

[39]Xiong, X., Mao, C., Yang, Z., Zhang, Q., Waterhouse, G.I.N., Gu, L. and Zhang, T. (2020). Photocatalytic CO 2 Reduction to CO over Ni Single Atoms Supported on Defect-Rich Zirconia. Advanced Energy Materials, 10(46), p.2002928.

[40]Yaashikaa, P., Senthil Kumar, P., Varjani, S. and Saravanan, A., 2019. A review on photochemical, biochemical and electrochemical transformation of CO2

into value-added products. Journal of CO2 Utilization, 33, pp.131-147.

[41]Yu, S., Wilson, A.J., Heo, J. and Jain, P.K. (2018). Plasmonic Control of Multi-Electron Transfer and C–C

Technoeconomic and Life Cycle Analysis of Single Cell Proteins

Mustafa Baig and Muhammad Yahya Anjum
Department of Chemical Engineering, Imperial College London, U.K

Abstract

With the human population increasing at an alarming rate, moving to alternate food sources has become a necessity to prevent a food crisis in the future. This is what makes research into the production of Single Cell Proteins essential. Two methods of including SCP in the diet of humans were considered in the report. The Quorn ™ production process provides protein that can directly be consumed by humans. The Bath production process provides a feed for animals which can then be the source of proteins for humans. ASPEN Plus was used to simulate the two processes. Both processes were compared in terms of final cost in terms of protein consumption for humans and a life cycle analysis was carried out to compare the environmental impacts. The life cycle analysis was done using openLCA. Having carried out the investigation, it was clear that Quorn ™ is a more sustainable option compared to Bath and definitive steps should be taken to increase its market share in the world.

Key words: Single cell protein, *Fusarium Venenatum*, *Methylococcus Capsulatus*, ASPEN Plus, open LCA

1 Introduction

The rate at which the human population is growing has led to a significant increase in the demand for food supply. The human population is projected to grow to 8.3 billion by 2030 and up to 9.1 billion by 2050. Traditional food sources are likely to be severely overburdened due to this (United Nations, 2019). Increasing the production of meat and dairy is not a suitable option as 1,250 million tonnes would need to be produced yearly which is simply unsustainable. This is because the efficiency of converting feed to meat and dairy products is quite low and almost 6 kg of plant protein is required to produce 1 kg of meat protein (Ritala, et al., 2017). The obvious solution to counter the stark difference in demand and supply is the introduction of single cell protein (SCP).

SCP is protein that is produced in microbial or algal cells. It can be used directly as human feed or fed to animals which are later consumed by humans. The process involved in producing SCP is essentially fermentation where the microbes or algae are cultivated by providing them with a specific substrate and a nutrient and oxygen supply. SCP provide sufficient protein to humans and animal which is vital for muscle growth, providing structure and essential body activities like digestion and blood clotting (Millward, 2013). In extreme cases, protein may even be used as a source of energy for the body. SCP can be produced from bacterial, algae, fungi and even genetically modified organisms. However, this report only investigates SCP produced from fungi (mycoprotein) and bacteria.

The mycoprotein chosen for this investigation was Quorn ™ which is suitable for human use. It is produced from the cultivation of the fungus *Fusarium. Venenatum* and uses glucose as its substrate. It was the first cultured protein that was exclusively produced for human use and development for its production started in the 1960s. After a rigorous screening process, *F. Venenatum A3/5* was selected as the protein source and production started in 1984 by

Marlow Foods Limited. Quorn ™ was first sold in 1985 and the brand has since seen substantial growth and success. By 1997, they were able to commission two new fermenters which resulted in Quorn ™ sales rocketing up to £74 million per year. In 2002, it was approved by the FDA and this finally, opened the American markets (Moore, et al., 2011).

On the other hand, the bacterial SCP that was investigated was *Methylococcus Capsulatus* (Bath) which feeds on methane gas and can be used as animal feed. Unlike the mycoprotein, this process has not been scaled up industrially and research is still being carried out on it. The groundwork was started by Imperial Chemical Industries Ltd in 1968 in the U.K. but has seen many roadblocks on the way. The reason *M. Capsulatus* was chosen for this investigation was because its substrate, methane, is widely available and is a by-product of many agricultural processes (Mosier, et al., 1998).

The main aim of this investigation was to make a comparison between SCP as human feed and animal feed. This comparison was made in terms of production, costing and a life cycle analysis (LCA). The findings from this techno-economic analysis can be used to plan ahead in terms of how much funding would be required to increase the share of SCP in human and animal feed. It also goes one step further and looks into the advantages and disadvantages of human and animal feed and the results can be used to prioritise one over the other.

2 Background

Due to the value of SCP in the world today, significant research has already taken place in this field. This research mainly involves the various SCP production systems with their specific substrates and processes. Anupama & Ravindra, 2000 gives a holistic view of the world of SCP and the nutritional value associated with each type. Weibe, 2004 laid out the foundation of the production of Quorn™ and the intricacies of its process. Øverland, et al., 2010 also holds great significance as the report provides great insight on methane-utilising bacteria as a feed source. However, the scope of both these papers is limited to only the production and not the economic and environmental impact of the products. This is a clear literature gap in this field and has been worked on extensively in this report. Another literature gap is in the comparison of human-grade and animal-grade SCP which is the foundation of this report. Lastly, an integral part of this report was the ASPEN Plus simulation of the processes. Humbird, et al., 2011 have done similar work and have provided extensive details on their process simulation.

3 Materials & Methods

In order to compare the two protein sources, in terms of production costs and environmental impact, it was important to first develop the process sheets for the two reactions. This was done on Aspen Plus and can be seen in Appendix Section A.1 and A.2. The physical properties for *F.Venenatum* and *M. Capsulatus* are not available in the standard Aspen Plus property databases. In fact, many of the properties necessary to simulate the process could not be found online and were required to be estimated.

3.1 Quorn Production

3.1.1 Design Basis

The plant size was set to produce 30kmol/hr based on the Quorn 2155m^3 air-lift fermenter commissioned in 1993 (Moore, et al., 2011). The plant is expected to be operational for 8,410 hours a year with an expected uptime of 96%. The annual feedstock requirement for the production process designed is 39,000 tonnes. The flowrates for each reactant were set according to the stoichiometric equation for the reaction with ammonia and phosphoric acid in excess. The stream data can be found in Appendix Section A.2.

3.1.2 Properties of *F. Venenatum*

F. Venenatum was designed as a conventional solid on Aspen. The dry weight composition of the elements present was used to determine the Molecular Formula (Calculation can be found

in Appendix Section B). The Molecular weight was then determined. The enthalpy of formation is estimated by first using the Mahler Correlation (Guy Marlair, 1999) to find the Heat of Combustion for Fusarium and then using Hess' Law. This is shown in Appendix Section B.2.

Kopp's Law states that the heat capacity of compounds depends on the sum of heat capacities of individual components present in the compound (Encyclopedia, n.d.). Since *F.Venenatum* has a composition similar to that of the bacterium Zymo in the NREL study, the same polynomial for solid heat capacity was used (Putsche, 1996). The coefficients for the solid heat capacity polynomial in ASPEN are given in Table 1.

The solid density of the biomass was simply assumed to be similar to that of starch, just like the NREL study (Humbird, et al., 2011).

Table 1: Physical properties of *F.Venenatum,* used in Aspen, along with methods used to calculate them.

Properties	Value	Method
Molecular Weight	27.249	Calculated directly
Solid Heat of Formation at 298.15 K	-4.9 x 10^8 J/Kmol	Calculate ΔH_c using Mahler's Correlation and then ΔH_f
Solid Heat Capacity	Term 1: 38409 Term 7: 298.15 Term 8: 1000	Kopp's Law
Solid Density	1.5 g/cc	Similar to starch

3.1.3 Process Flow Sheet Description

B100: The fermenter was designed as a R_{stoic} reactor operating at 30°C. The reactor is fed with a feed containing glucose as a substrate along with ammonia, oxygen and phosphoric acid. Ammonia serves as a source of nitrogen for the growth of the protein. Phosphoric acid serves as the source of phosphate ions and helps maintain the culture at a pH of 6.0. The reaction taking place is shown by the equation:

$$0.485\ C_6H_{12}O_6 + 1.8493\ O_2 + 0.173\ NH_3 + 0.0151\ H_3PO_4 \rightarrow\ CH_{1.98}N_{0.173}O_{0.647}P_{0.0151} + 2.202\ H_2O + 1.91\ CO_2 \quad (1)$$

B101: A flash vessel is installed to separate the gases in the output stream. The gas stream coming out of the flash contains 96% CO_2 which must be captured to avoid having adverse effects on the environment.

B102: The vessel was installed in order to reduce the RNA content of the Myco-protein in order to make it suitable for human consumption. High nucleic acid content in human food causes the blood uric acid value to rise, leading to a disease called gout. In order to reduce the RNA content, to limit ingestion from SCP to 2g per day as recommended by WHO (Moore, et al., 2011), the biomass temperature is raised to 74°C for 30 minutes (Weibe, 2004). This step stops biomass growth as it activates enzymes that break down RNA to nucleotides that diffuse into the culture broth.

B103: The Myco-protein is harvested by separating it from the water in a centrifuge. The product is obtained in the form of a paste.

3.2 Bath Production

3.2.1 Design Basis

The plant size was set in order for the product to contain the same amou°3nt of protein as that in the Quorn production process mentioned above. The feedstock flowrate is set according to the stoichiometric equation for the reaction with ammonia in excess.

3.2.2 Properties of *M. Capsulatus*

M. Capsulatus was designed as a conventional solid on Aspen. Since limited data is available on *M. Capsulatus,* the dry weight composition of the elements present in a similar bacteria known as *E. Coli* were used to obtain the molecular formula of the biomass as they are similar kinds of bacteria (Moore, et al., 2011). The molecular weight was then determined. The enthalpy of formation was then calculated by using the method used for *F. Venenatum*. Like in the case of *F. Venenatum*, the polynomial and solid density were obtained from the NREL study.

Table 2: Physical properties of *M.Capsulatus* and the methods used to calculate them.

Properties	Value	Method
Molecular Weight	22.844	Calculated directly
Solid Heat of Formation at 298.15 K	-1.46 x 10^8 J/Kmol	Calculate ΔH_c using Mahler's Correlation and then ΔH_f
Solid Heat Capacity	Term 1: 38409 Term 7: 298.15 Term 8: 1000 1	Kopp's Law
Solid Density	1.5 g/cc	Similar to starch

3.2.3 Process Flow Sheet Description

B2: The fermenter was designed as a R_{stoic} reactor operating at 30°C. The reactor is fed with a feed containing methane as a substrate along with ammonia, oxygen and phosphoric Acid. The role of ammonia and phosphoric acid has been described previously in Section 3.1.3. The reaction taking place is shown by the equation:

$$1.874\ CH_4 + 2.568\ O_2 + 0.24\ NH_3 + 0.024\ H_3PO_4 \rightarrow CH_{1.92}N_{0.24}O_{0.3}P_{0.024} + 3.184\ H_2O + 0.874\ CO_2 \quad (2)$$

B3: A flash vessel is installed to separate the gases in the output stream. The gas stream coming out of the flash contains CO_2 and ethane. These can be separated in order to be used further.

B4: The SCP is harvested by separating it from the water in a centrifuge. The product is obtained in the form of a paste.

It is important to note that there is no need for an RNA reduction step in the production of Bath. This is because it is not consumed by humans directly and is fed to animals. In animals, the uric acid produced from the breakdown of nucleic acid is converted to soluble acid allantoin which is then excreted. (Moore, et al., 2011)

3.3 Costing

The cost of each process was divided into two parts: capital cost and operating cost. The capital cost included the cost for setting up the process equipment, infrastructure and storage tanks. Energy and raw material costs form the bulk of the operating costs. Raw material costs were found in literature and adjusted according to the current index (Warren D. Seider, 1999) and details of these calculations can be found in Appendix Section C.1. Salaries and other overheads were assumed to be negligible compared to these costs.

The two single cell proteins studied are different because one is fed directly to humans while the other needs to be fed to animals first. In order to have a fair comparison of the costs, it is important to include the costs related to farming in order to raise animals for human consumption. The costs of setting up a farm and raising calves on a SCP feed were added to the Bath production cost.

To compare the final cost of feeding protein to humans using the two products, the capital

cost for the two processes was amortised over a period of 25 years. This was done due to the assumption of the plant life being 25 years. The capital cost for each 2 year period was then obtained and added to the operating cost for this period. A 2 year period was chosen as this is the time it takes for a calf to grow into a cattle for meat production. The capital cost values were obtained from a UC Davis Study (Rebecca K. Ozeran, 2019) and can be seen in Table 3.

3.3.1 **Capital Cost**

The equipment cost was calculated using the Guntherie's method in Product and Process Design Principles by Sieder (Warren D. Seider, 1999). The equipment costs included the cost of storage tanks, reaction vessels and the centrifuge. In the case of Bath, the cost of farming machinery, buildings and calves was also included to the overall capital cost.

Storage Tanks: The raw materials for each plant are stored in storage tanks to have enough supply for a few weeks. All liquid raw materials are stored in spherical storage tanks at atmospheric pressure due to the pressure range being between 0-30 psig. The correlation used for the f.o.b cost at CE index of 500 is given by the equation

$$C_P = 60V^{0.72} \quad (3)$$

where V is the tank volume in gallons.

For gaseous raw materials, the tank volume is given in cubic feet and the correlation:

$$C_P = 3170V^{0.43} \quad (4)$$

For each raw material, the volumetric flow rate required per day was obtained from ASPEN and was multiplied by the number of days the tanks were expected to store supply for. The data for these calculations can be found in Appendix Section C.1.

Pressure Vessels: In order to find the purchase cost of the pressure vessels, the method of Mulet, Corripio, and Evans (1981a, b) was employed. The f.o.b purchase cost at a CE index of 500 is given by the equation

$$C_P = F_M C_V + C_{PL} \quad (5)$$

The term C_V takes into account the cost of the empty vessel including nozzles, manholes and supports depending on the weight of the vessel W. The term C_{PL} takes into account the added cost of ladders and platforms for each vessel. C_{PL} depends on the inner diameter of the vessel. Correlations were used to determine the weight and a diameter to height ratio of 1:4 was assumed for the stirred tank. The calculations can be seen in Appendix Section C.4 and C.5.

The size of the flash vessel is determined using the liquid and vapour flow rates and the respective densities. The calculations can be seen in Appendix Section C.6.

Centrifuge: The centrifuge cost is estimated using the correlation for a continuous reciprocating pusher for a stainless-steel centrifuge:

$$C_P = 150000S^{0.3} \quad (6)$$

where S is the Tons of solid/hr

The total f.o.b costs are added and then corrected according to the current CE index of 662 to give the bare-module cost. This is obtained by using the latest available index of 618.7 from 2019 (Jenkins, 2020) and adjusting it with an inflation rate of 7%.

The main fermenter in the Quorn production process is a unique state-of-the-art fermenter. The cost was, therefore, obtained from literature instead of being estimated using the method above. The capital cost obtained from literature was \$37.5m (Moore, et al., 2011). A similar fermenter is used in the Bath production process. Equation 7 was used to scale down the literature value for Quorn in order to obtain the cost of the fermenter used in Bath production. The average value of m = 0.6 was taken. The cost obtained was \$13.8m.

$$\frac{\text{Cost}_2}{\text{cost}_1} = \left(\frac{\text{Capacity}_2}{\text{Capacity}_1}\right)^m \quad (7)$$

Following Guntherie's method, 10% of the total equipment cost was added as costs for site and buildings. The cost of off-site facilities was obtained using Equation 8.

$$C_{\text{of fsite facilities}} = 1,500,000 + 0.05C_{\text{TBM}} \quad (8)$$

3.3.2 Operating Cost

The amount of heat needed to be removed and supplied to the process equipment along with the cost of raw material was used to determine the annual operating cost for each process. Steam at 150 psig MP steam was used to heat the effluent. Cooling water is used to cool down the streams.

Fermenter: The heat of formation for the two products is used to calculate the Heat of Reaction of the reaction taking place in the fermenter using Equation 9 (calculation shown in Appendix Section C.9). This is then used to determine the flow rate (F_1) of cooling water required using the heat capacity of water of 4.187 kJ/kgK and a ΔT of 5 using Equation 10.

$$\Delta H_R = \Delta H_f(Products) - \Delta H_f(Reactants) \quad (9)$$

$$F_1 \times 4.187 \times 10^3 \times 5 = Molar\ extent\ of\ reaction \times \Delta H_R \quad (10)$$

The annual flow of water required and hence the cost of cooling can then be calculated.

Other Equipment: In addition to the fermenter, the Quorn Production process requires heating in the CSTR for RNA reduction, and in Heater 1. Steam at 150 psig is used for this. A similar method to the one used for the fermenters is used where flow of steam is calculated to provide latent heat to bring the temperature change. The heat required this time is calculated using the average heat capacity of streams obtained from ASPEN. This is then used to determine the annual cost. The calculations can be found in Appendix Section C.9.

The cost for other equipment is calculated using the equation below

$$Heat\ (Provided, Removed) = Temp\ Change \times Average\ heat\ capcity\ of\ stream \times Flow\ rate \quad (11)$$

The amount of steam required can then be calculated from the equation

$$Steam\ Required = \frac{Heat\ Provided}{Latent\ heat\ of\ steam} \quad (12)$$

Note that these costs are according to the index in 2006 i.e. 500 and must be corrected to a value of the current index i.e. 662 as in Appendix C.10.662 as shown in Table 20 in Appendix Section C.10.

Cattle Farming Cost

As mentioned earlier, to have a fair comparison, a cattle farm was assumed to be run with the cattle being fed with Bath. This farm then produced protein for human consumption and allowed comparison with Quorn. The amount of protein required by an adult cow on a daily basis was used to determine the number of cattle that could be grown on the feed from the Bath Plant over a 2 year period. On average a cow was assumed to require 2.5 kg of protein a day which is an average of the daily protein requirement for a calf (2 kg) and an adult cow (3 kg) (Ondarza, n.d.). This allowed the output from our Bath process to feed 260 cows over a 2 year period. Calculations can be seen in Appendix Section C.11. The number of cows is similar to that in the UC Davis Study (Rebecca K. Ozeran, 2019). The capital and operating costs of beef production were, therefore, directly obtained from the study and included in our analysis. The exact values can be found in Table 3. It is important to note that a conversion factor of 2.45 kg protein in Bath feed for 1 kg of Beef protein was applied. This calculation was done

based on the ratios provided in literature (Ritala, et al., 2017).

Table 3: The table shows the costs associated with cattle farming

		Cost
Machinery		$84,500.00
Building, and Equipment		$323,800.00
Livestock Cost		$37,700.00
	Total	$446,000.00
Annual Op. Cost		**$71,521.00**

The costs from Table 3 are added to that of Bath production. The cost of protein available to humans is then calculated and compared in Figure 5.

3.4 Life Cycle Analysis

A life cycle analysis assessment was carried out to evaluate the environmental impact of both processes. The software openLCA was used to carry out this analysis. The functional unit used to compare the two processes was taken to be per 100g of protein consumed by humans. Thus, the process of feeding *M. Capsulatus* to animals which would later be consumed by humans was taken into account. This allowed a like-for-like comparison between the two processes. The mode of assessment adopted for this LCA was cradle-to-gate. This method involves the environmental impact of the processes from the extraction of raw materials until it is transported to the consumer. An inventory analysis was carried out for both processes (details shown in Appendix Section D.1) and the impact evaluation approach that was used was the mid-point method.

4 Results & Discussion

4.1 Costing

To produce 612 tonnes of protein, the capital cost of Quorn ™ production ended up being $50.1m compared to $20.1m for Bath production. On the other hand, the operating cost for Quorn ™ production was $10.94m/year compared to $0.8m/year for Bath production. The breakdown of these costs can be seen in Table 4, Table 5 and Table 6. A thorough breakup of the costs and the calculations involved can be found in Appendix Section C.

Table 4: Capital cost breakdown of Quorn

Type	Subtype	$m
Vessels	Reactor	37.5
	Stirred Tank	0.05
	Flash	0.63
Centrifuge	-	0.39
Misc.	Storage Tank	3.7
	Site and Buildings	7.8

Table 5: Capital cost breakdown of Bath production

Type	Subtype	$m
Vessels	Reactor	13.8
	Flash	0.07
Centrifuge	-	0.2
Misc.	Storage Tank	2.1
	Site and Buildings	3.9

Table 6: Operating cost breakup of both processes

	Quorn ($m/year)	Bath ($m/year)
Energy	0.44	0.38
Raw Materials	10.5	0.42

However, as mentioned in Section 3.3, a more accurate comparison was needed to take into account the costs associated with feeding Bath to animals before being fed to humans. The normalised results can be seen in **Error! Reference source not found.** and the cost of Sainsbury's beef was used as a reference to

compare the economic viability. The calculation involved in finding out the cost of Sainsbury's beef can be seen in Appendix Section C.2. It was evident that the cost of producing Bath exceeds Quorn and it would be fair to say that it is currently economically infeasible to produce it. A major factor for this is that Quorn ™ production has achieved economies of scale due to the years of research and development that has taken place. Bath production, on the other hand, is still only possible at a laboratory level which explains the high costs associated with it. In addition, the losses in protein due to low conversion decreases the overall efficiency of the process resulting in higher costs. Quorn ™ is also cheaper compared to the average Sainsbury's beef which explains why they have been able to stay competitive for so long and continue to grow.

Furthermore, the oxygen storage tanks form a major part of the capital cost in both processes. These costs can be reduced by investing in an air separation unit which would further bring down the capital cost and make both forms of SCP more economically competitive.

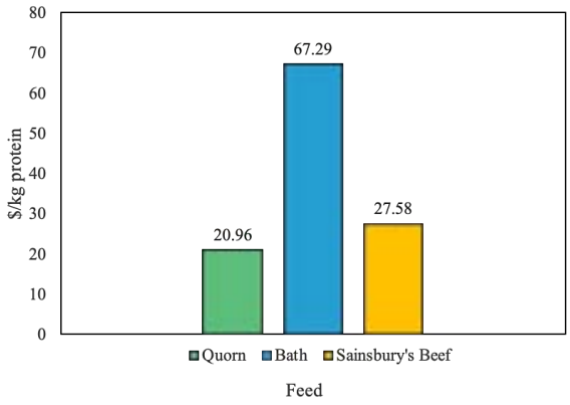

Figure 1: Cost comparison of different feeds

4.2 Life Cycle Analysis

The results were normalised to take into account the protein conversion factor in the same way as described in Section 3.3

4.2.1 Terrestrial Acidification

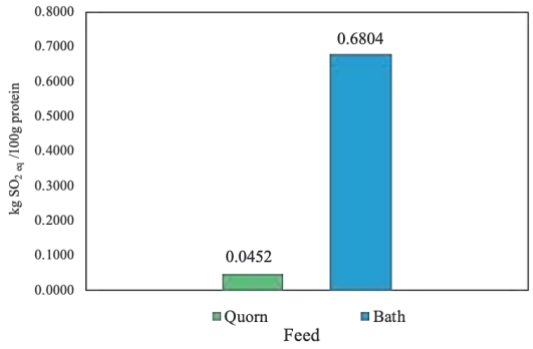

Figure 2: Effect of both processes on terrestrial acidification

As shown in Figure 2, the production of Bath contributes drastically more than the production of Quorn ™ in terms of terrestrial acidification. This is due to a greater amount of ammonia being released in Bath production to produce the same amount of human consumable protein. Although ammonia is a reactant in both processes, some of it remains unused and is part of the effluent. The ammonia that is released seeps into the soil causing a chemical imbalance resulting in a lower pH. This further leads to the concentration of aluminium ions increasing in the soil and causes discolouration of plant tissue and seed germination failure. The end result of terrestrial acidification is a significant decrease in biodiversity (Zvereva, et al., 2007)

4.2.2 Marine Eutrophication

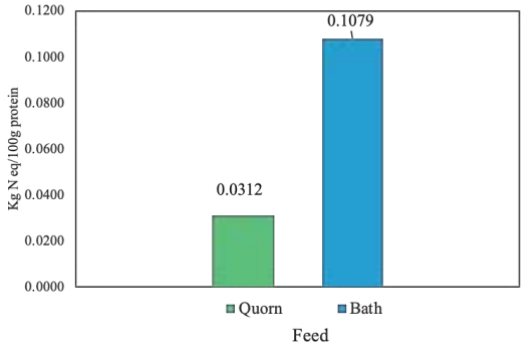

Figure 3: Effect of both processes on marine eutrophication

Similar to terrestrial acidification, the results for marine eutrophication showed that Bath

has a greater contribution per kg of consumable protein. This can clearly be seen in Figure 3. This was a direct result of more nitrogen and phosphorous containing emissions in Bath production. These emissions have adverse consequences on the marine ecosystem. This increased supply of nutrients leads to an algal bloom on the surface. It reduces water quality, clarity and can be quite toxic. Due to this algal bloom, the amount of sunlight entering the water decreases. This can be quite disastrous as the marine animals need light to catch prey and marine plants need it for photosynthesis. Lastly, when the algae die, microbes decompose them and this leads to oxygen depletion in the marine ecosystem (Jessen & Bednarz, 2015)

4.2.3 Particulate Matter (PM) Formation

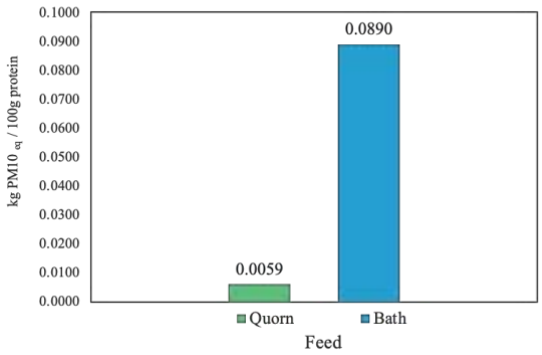

Figure 4: Effect of both processes on PM formation

The results showed that the process of manufacturing Bath was causing almost 15 times more PM formation compared to Quorn™. This can once again be traced back to greater ammonia emission while producing Bath. However, PM formation is a direct result of ammonia being released into the atmosphere as a gas from the flash vessel. The ammonia is transformed into secondary aerosols and the formation of ammonium sulfate and ammonium nitrate takes place. This has very detrimental consequences as it leads to respiratory diseases and cardiovascular illnesses (Gong, et al., 2013)

4.2.4 Greenhouse Gas (GHG) Emission

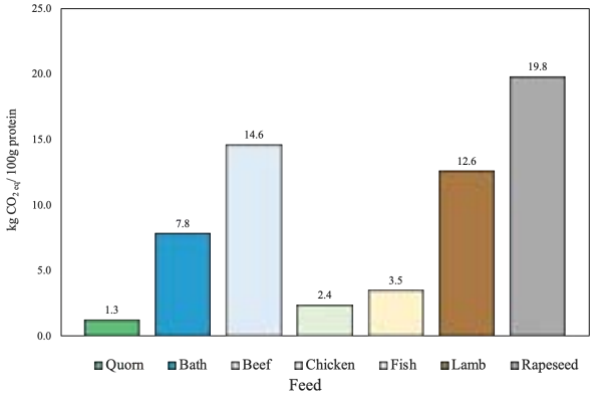

Figure 5: GHG emission comparison of different feeds

The results from the GHG emissions were pivotal to analyse the environmental sustainability of the two processes. GHG emissions are a very important indicator as these emissions absorb and emit infrared radiation directly resulting in global warming and all the negative impacts associated with it (Easterbrook, 2016). The unit of comparison was taken to be equivalent CO_2 /100g protein as this takes into account other greenhouse gases like methane as well.

As Figure 5 shows, the process of producing Bath released 6 times more equivalent CO_2. A major reason for this is due to the fact that the substrate for *M. Capsulatus* is methane. However, methane is fed to the reactor in the form of natural gas which contains 75% methane and 25% ethane by volume. Ethane, a greenhouse gas, is unused in this reaction and is eventually released into the atmosphere.

However, if you compare the SCP to their traditional counterparts, they are still producing less equivalent CO_2. The results showed that beef was the biggest contributor towards climate change amongst human-grade feed. The values for the traditional food sources were calculated using their protein content and carbon footprint per kg live weight which were all available through literature (Ritchie, 2020). For rapeseed, a common source of animal fodder, the equivalent CO_2 is on the higher side as a significant amount of

N_2O is released in its production. Nitrous oxide is a type of greenhouse gas where 1kg of N_2O is equivalent to 298kg of CO_2 (Climate Change Connection, 2007).

5 Conclusion

After completing the investigation, it is obvious that SCP is the answer to the food shortage that is being predicted. However, it is clear that increasing the share of Quorn ™ in our diet is a more favourable option compared to feeding Bath to livestock. Despite Bath's high protein content, its low protein conversion efficiency makes it effectively redundant to pursue. Quorn™ is more economically feasible and environmentally friendly as discussed in Section 4.1 and 0 respectively. It has very high capital and operating costs associated with it but that is expected given the scale it has achieved. Furthermore, their annual sales show that these costs are definitely recoverable. Quorn's carbon footprint is also significantly less compared to traditional food sources. Taking all these factors into account, there is every reason for Quorn ™ to increase its market share as long as it can be marketed successfully and enough awareness can be raised about the benefits of SCP.

6 Future Outlook

There are a few improvements that can be suggested to improve the validity of the results and broaden the scope of this investigation. Firstly, more accurate modelling would significantly increase the accuracy of the ASPEN Plus simulations. As mentioned in Section 3.2.2, the properties of *M. Capsulatus* were assumed to be similar to *E.Coli*. As there is a literature gap in the chemical composition of *M. Capsulatus*, molecular spectroscopy would be required to find this information. Although this would be an expensive exercise, it would definitely make the results more reliable. Furthermore, it was evident that Bath is not economically viable, and a different strain of bacterial SCP should be looked into. The same approach should be adopted where the SCP is compared to Quorn ™ in terms of production, costing and environmental impact. Some potential strains are *Bacillus Subtillis* and *Haloarcula* sp. IRU1 which feed on ram horn and petrochemical wastewater respectively (Ritala, et al., 2017). Both these strains have a protein content of more than 70% which makes them suitable options.

One area of research that should be looked into is the introduction of a heat exchanger network. This would be possible for Quorn™ production as there are two streams being heated and one stream being cooled. This was not possible in this investigation as the values of heat capacity provided by ASPEN Plus were in the order of 10^{19} W/K (Pinch point analysis can be seen in Appendix Section E). Due to this, it was not possible to create a heat exchange network that could be replicated in the real world. This problem would also be solved if more accurate modelling was possible as mentioned earlier.

Having discussed the technical aspect of this investigation, it is equally important to carry out an extensive market survey. This would enable us to find any potential limitations in increasing Quorn's market share in the world and the volumes that can potentially be supplied. As taste is very subjective, it is imperative that region dependant demands are also looked into to make it a product that is accepted worldwide. Once research is carried out on these subjects, it will be possible to find the optimal blend of SCP for humans, SCP for animals and traditional sources in our diet as it is not possible to rely on just one source.

7 Bibliography

Anon., n.d. *NIST Chemistry WebBook.* [Online]
Available at: https://webbook.nist.gov/chemistry/
[Accessed 20 December 2020].

Anupama, R. & Ravindra, 2000. Value-added food:: Single cell protein. *Biotechnology Advances,* 18(6), pp. 459-479.

Climate Change Connection, 2007. *CO2 Equivalents.* [Online]
Available at: https://climatechangeconnection.org/emissions/co2-equivalents/
[Accessed 2020].

Easterbrook, D., 2016. Greenhouse Gases. In: *Evidence-Based Climate Science (Second Edition).* s.l.:Elsevier, pp. 163-173.

Encyclopedia, B. C., n.d. *Big Chemical Encyclopedia.* [Online]
Available at: https://chempedia.info/info/kopp_s_law/
[Accessed 20 12 2020].

Gong, L., Lewicki, R., Griffin, R. J. & Tittel, F. K., 2013. Role of atmospheric ammonia in particulate matter formation in Houston during summertime. *Atmospheric Environment,* Volume 77, pp. 893-900.

Guy Marlair, C. C. A. T., 1999. *An analysis of some practical methods for estimating heats of combustion in fire safety studies,* Edimbourg, United Kingdom: s.n.

Humbird, D. et al., 2011. *rocess Design and Economics for Biochemical Conversion of Lignocellulosic Biomass to Ethanol,* s.l.: National Renewable Energy Laboratory.

Jenkins, S., 2020. *2019 CHEMICAL ENGINEERING PLANT COST INDEX ANNUAL AVERAGE.* [Online]
Available at: https://www.chemengonline.com/2019-chemical-engineering-plant-cost-index-annual-average/
[Accessed 20 12 2020].

Jessen, C. & Bednarz, V. N., 2015. Marine Eutrophication. *Environmental Indicators,* pp. 177-203.

Millward, D., 2013. Protein: Requirements and Role in Diet. *Encyclopedia of Human Nutrition (Third Edition),* pp. 131-138.

Moore, D., Robson, G. D. & Trinci, A. P., 2011. 21st Century Guidebook to Fungi. *The Quorn fermentation and evolution in fermenters,* Volume II.

Mosier, A. R., Duxbury, J. & Freney, J., 1998. Mitigating Agricultural Emissions of Methane. *Climatic Change,* Issue 40, pp. 39-80.

Ondarza, M. B. d., n.d. *Protein Milkproduction.com.* [Online]
Available at: http://www.milkproduction.com/Library/Scientific-articles/Nutrition/Protein/
[Accessed 20 12 2020].

Putsche, R. J. W. a. V., 1996. *Development of an ASPEN PLUS Physical Property Database for Biofuels Components,* s.l.: s.n.

Rebecca K. Ozeran, D. S. D. A. S., 2019. *SAMPLE COSTS FOR BEEF CATTLE.* [Online]
Available at: https://coststudyfiles.ucdavis.edu/uploads/cs_public/55/4a/554ac9bf-286e-448b-8930-de1cfc02dcd1/2019beefcowcalfcentralsanjoaquinvalley.pdf
[Accessed 20 12 2020].

Ritala, A., Häkkinen, S. T., Toivari, M. & Wiebe, M. G., 2017. Single Cell Protein—State-of-the-Art, Industrial Landscape and Patents 2001–2016. *Frontiers in Microbiology ,* Volume 8.

Ritchie, H., 2020. *Less meat is nearly always better than sustainable meat, to reduce your carbon footprint.* [Online]
Available at: https://ourworldindata.org/less-meat-or-sustainable-meat
[Accessed 2020].

United Nations, 2019. *Department of Economic and Social Affairs.* [Online] Available at: https://population.un.org/wpp/Download/Standard/Population/

Warren D. Seider, J. S. D. R. L. a. S. W., 1999. *PRODUCT AND PROCESS DESIGN PRINCIPLES.* Third Edition ed. s.l.:Donald Fowley.

Weibe, M. G., 2004. Quorn™ Myco-protein — Overview of a successful fungal product. *Mycologist,* 18(1), pp. 17-20.

Wooley, R. &. P. V., 1996. *Development of an ASPEN PLUS physical property database for biofuels components,* s.l.: s.n.

Wooley, R. &. P. V., 1996. *Development of an ASPEN PLUS physical property database for biofuels components,* s.l.: s.n.

Øverland, M., Tauson, A.-H., Shearer, K. & Skrede, A., 2010. Evaluation of methane-utilising bacteria products as feed ingredients for monogastric animals. *Archives of animal nutrition,* Issue 64, pp. 171-189.

Zvereva, E., Toivonen, E. & Kozlov, M., 2007. Changes in species richness of vascular plants under the impact of air pollution: A global perspective. *Global Ecology and Biogeography,* Issue 17, pp. 305-319.

Author Index

Linked to paper number

Abraham, Deborah 39
Anwary, Soleiman N. 13
Anshoor, Yusra 59
Anjum, Muhammad Yahya 65
Ayandipo, Rafiah 59
Baig, Mustafa 65
Banks, Mason 5
Barreyre, Robin 30
Bin Rizal, Rizqin Naim 16
Boghii, Maxim 44
Borys, Alessia 40
Brooker, Christopher 25
Charaschanya, Theeranai 31
Charos, Athanasios 8
Chaudhry, Raaghav 25
Chen, Lian 58
Christoforou, Christos 54
Chua, Chris H.Z. 57
Clancy, Rebecca L. 10
Cox, Joseph 56
Dale, Samuel 61
Davidson, Joseph 1
Dholakia, Darshil 41
Diane, Onalethata 39
Dischamps, Laetitia 1
Dissanayake, Sasangee 55
Duru, Naomi 20
Dzulfakhar, Aiman Syahirah Ahmad 53
Ejikeme, Sochi 63
Feng, Mingzhe 42
Furlonge, Isaac 32
Ganesan, Rajaram 14
Gill, Karyshma 51
Gulliford, Miles 6
Hua, Weicheng 2
Huang, Licheng 43
Huang, Sirui 57
Hussain, Hamza Riaz 7
Husin, Marissa Adila Binti 27
Jawwad, Hassan 62
Jones, Marie 38
Joshi, Sharada 24
Kang, Beom Seok 46
Khaitan, Varnaraj 14
Kandiah, Mathusan 41
Kim, Jiwon 15
Klotz, Dominik 61
Koh, Yu Shan 26
Krishnaswamy, Aniruddh 48
Lai, Matthew 32
Lau, Douglas 49
Lee, Jodie 51
Lee, Gordon 49
Lee, Seyoung 15
Lee, Wei Yang 33
Lee, Zong Hao 26
Lema Botelho, Miguel 28
Leong, Jun Hong 34
Lim, Jenny 52
Liu, Yuyi 43
Liu, Yuxin 47
Loh, Christine Pei Ying 60
Lu, Hengrui 64
Matabudul, Manjeeta 5
Mistry, Dhylan 23
Mehmet, Layla 37
Morakotkarn, Chayut 58
Mornto, Aris 21
Nasar, Mustafa 62
Ng, Chen Yang 52
Ngammekchay, Chumphot 54
Ngu, Ming Jiun 35
Ogbobi, Helen 22
Ooi, Wei Loon 16
Orlebar, Richard 6
Otakoro, Aghogho 24
Pandya, Hiren H. 17
Perez Tabarnero, Ines 7
Piliounis, Michael 8
Pratt, Michael 36
Qureshi, Sulaiman 64
Reading, Jonathan 36
Richardson, Andreas T. D. 10
Rigby, Charles W. 13
Rodríguez, Lucía 37
Sim, Megan 2
Sathasivam, Vikneswaran 27
Sivanesakanthan, Janusshan 44
Stollery, Corinne 48
Suduwelikanda, Pravin 55
Tan, Benjamin Isaac 18
Tan, Chen Horng 3

Tan, Kuan Yang 34
Tan, Lay Ping 35
Tan, Rou Jing 28
Tan, Stephen 19
Tang, Vanessa 45
Thurairatnam, Sathurthini 60
Tonus, Alessandro 45
Tosti di Valminuta, Gianluigi 4
Trotta, Federico 29
van Surell, Noah 38
Vimalendiran, Shav 23
Wade-Smith, Florence 11
Walker, Pierre J. 50
Wang, George Jing 29
West, James A. 21
Wijekoon, Malinya 22
Whittington, Luke 9
Woolley, Richard L. 17
Wongwaisayawan, Thanat 3
Wu, Hiu Lam Athena 19
Wu, Yuting 46
Ye, Jiahao 12
Yiakoumi, Nicolas 47
You, Sim En 53
Yuwono, Henrico 42
Zagorulko, Maria 4
Zeeuw, Philip 9
Zhao, Tianpu 50
Zheng, Mingchuan 20
Zhu, Yichuan 12
Zhang, Yihan 33

Supervisor Index

Linked to paper number

Adjiman, Claire S.	34, 44
Bhute, Vijesh	51
Cabral, Joao	8, 20, 40
Ceroni, Francesca	22
Chachuat, Benoit	2, 16, 56
Chen, Rongjun	36, 41, 47
del Rio Chanona, Antonio	13, 42
Eslava, Salvador	21
Fennell, Paul	17, 25
Galindo, Amparo	46
Guo, Miao	65
Hammond, Ceri	30, 59
Hawkes, Adam	26, 28, 39
Heng, Jerry	23, 32, 53
Hellgardt, Klaus	5, 38, 63
Jackson, George	18, 50, 57
Kazarian, Sergei	58
Kontoravdi, Cleo	1, 33, 45
Li, Kang	52, 60
Luckham, Paul	35
Markides, Christos	4, 48, 62
Marsha Maraj	55
Matar, Omar K.	43, 49, 61
Petit, Camille	64
Pini, Ronny	11
Papathanasiou, Maria	3, 12, 15
Polizzi, Karen	19
Shah, Nilay	6, 9, 37
Tighe, Chris	14, 24, 31
Titirici, Magda	7, 29, 54
Trusler, J.P. Martin	27
Yetisen, Ali	10
Xu, X. Yun	36